Transactions of the ASME

Technical Editor, L. B. FREUND

Division of Engineering
Brown University
Providence, R.I. 02912

APPLIED MECHANICS DIVISION

Chairman, M. M. CARROLL
Secretary, J. R. RICE
Associate Editors,
T. BELYTSCHKO
D. B. BOGY
R. M. CHRISTENSEN
R. J. CLIFTON
T. L. GEERS
MAURICE HOLT
THOMAS J. R. HUGHES
W. D. IWAN
W. G. KNAUSS
F. A. LECKIE
FRANCIS C. MOON
J. W. NUNZIATO
R. H. PLAUT
R. T. SHIELD
J. G. SIMMONDS
K. R. SREENIVASAN
J. S. WALKER
Z. WARHAFT
G. A. WEMPNER
L. T. WHEELER
S. E. WIDNALL

BOARD ON COMMUNICATIONS
Chairman and Vice-President
K. N. REID, JR.

Members-at-Large
W. BEGELL
J. T. COKONIS
W. G. GOTTENBERG
F. LANDIS
J. R. LLOYD
R. E. NICKELL
J. ORTLOFF
C. PHILLIPS
R. E. REDER
F. W. SCHMIDT

President, L. S. FLETCHER
Exec. Dir.
PAUL ALLMENDINGER
Treasurer, ROBERT A. BENNETT

PUBLISHING STAFF
Mng. Dir., Pub., J. J. FREY
Dep. Mng. Dir., Pub.
JOS. SANSONE
Managing Editor,
CORNELIA MONAHAN
Production Editor, REMO SALTA
Prod. Asst., MARISOL ANDINO

The Journal of Applied Mechanics (ISSN 0021-8936) is published quarterly for $100 per year by The American Society of Mechanical Engineers, 345 East 47th Street, New York, NY 10017. Second class postage paid at New York, NY and additional mailing offices. POSTMASTER: Send address changes to The Journal of Applied Mechanics, c/o THE AMERICAN SOCIETY OF MECHANICAL ENGINEERS, 22 Law Drive, Box 2300, Fairfield, NJ 07007-2300.
CHANGES OF ADDRESS must be received at Society headquarters seven weeks before they are to be effective. Please send old label and new address.

PRICES: To members, $24.00, annually; to nonmembers, $100.00. Add $6.00 for postage to countries outside the United States and Canada.

STATEMENT from By-Laws. The Society shall not be responsible for statements or opinions advanced in papers or . . . printed in its publications (B7.1, Par. 3).

COPYRIGHT © 1985 by the American Society of Mechanical Engineers. Reprints from this publication may be made on condition that full credit be given the TRANSACTIONS OF THE ASME, JOURNAL OF APPLIED MECHANICS, and the author, and date of publication be stated.

INDEXED by the Engineering Index, Inc.

Journal of Applied Mechanics

Published Quarterly by The American Society of Mechanical Engineers

VOLUME 52 • NUMBER 4 • DECEMBER 1985

TECHNICAL PAPERS

743 VLFEM Analysis of a Two-Dimensional Cochlear Model (85-WA/APM-17)
C. E. Miller

752 A Change in Wave Type Modeled by the Variable Coefficient Korteweg-deVries Equation
M. S. Cramer, S. H. Nguyen, M. E. Bowman, and B. E. McCown

759 The Effect of Inertia in Lubrication Flow Including Entrance and Initial Conditions (85-WA/APM-1)
J. A. Tichy and P. Bourgin

766 Flow Driven by a Finite, Shrouded Spinning Disk With Suction
J. M. Hyun

771 Cavitation Boundary Shapes for Submerged Short Journal Bearings Using Newtonian Lubricants (85-WA/APM-7)
R. H. Buckholz

777 Asynchronous Instability of a Rotating Centrifuge Partially Filled With Fluid
C. A. Cheng, A. S. Berman, and T. S. Lundgren

783 Falkner-Skan Solution for Gravity-Driven Film Flow
H. I. Andersson and T. Ytrehus

787 Free Edge Strain Concentrations in Real Composite Laminates: Experimental-Theoretical Correlation (85-WA/APM-10)
C. T. Herakovich, D. Post, M. B. Buczek, and R. Czarnek

794 On the Comparison Between Microscopic and Macroscopic Instability Mechanisms in a Class of Fiber-Reinforced Composites
N. Triantafyllidis

801 Reduction of Free-Edge Stress Concentration
P. R. Heyliger and J. N. Reddy

806 Thermal Expansion Coefficients and Thermal Stresses in an Aligned Short Fiber Composite With Application to a Short Carbon Fiber/Aluminum (85-WA/APM-11)
Y. Takao and M. Taya

811 Short Subsurface Cracks Under Conditions of Slip and Stick Caused by a Moving Compressive Load (85-WA/APM-15)
S. Sheppard, J. R. Barber, and M. Comninou

818 Characteristics of the Elastic Field of a Rigid Line Inhomogeneity
Z. Y. Wang, H. T. Zhang, and Y. T. Chou

823 The Crack Problem for Bonded Nonhomogeneous Materials Under Antiplane Shear Loading (85-WA/APM-8)
F. Erdogan

829 Continuous Damage Mechanics Revisited: Basic Concepts and Definitions (85-WA/APM-5)
D. Krajcinovic

835 Elastic Field of a Partially Debonded Elliptic Inhomogeneity in an Elastic Matrix (Plane-Strain)
B. L. Karihaloo and K. Viswanathan

841 Eddy Current Flow Near Cracks in Thin Plates
C. Y. Hui and A. Ruina

847 *Saint-Venant End Effects for Incremental Plane Deformations of Incompressible Nonlinearly Elastic Materials*
R. Abeyaratne, C. O. Horgan, and D.-T. Chung

853 The Dynamic, Steady-State Propagation of an Antiplane Shear Crack in a General Linearly Viscoelastic Layer
J. R. Walton

857 A New Endochronic Approach to Computational Elastoplasticity: Example of a Cyclically Loaded Cracked Plate (85-WA/APM-4)
O. Watanabe and S. N. Atluri

865 The Plastic Spin
Y. F. Dafalias

872 A New Approach to Large Deflection Analyses of Spherical and Cylindrical Shells
G. C. Sinharay and B. Banerjee

877 *An Extended Shakedown Theory for Structures That Suffer Cyclic Thermal Loading Part 1:* Theory
A. R. S. Ponter and S. Karadeniz

883 An Extended Shakedown Theory for Structures That Suffer Cyclic Thermal Loading Part 2: Applications
A. R. S. Ponter and S. Karadeniz

890 Free Vibration of a Point-Supported Spherical Shell
T. Irie, G. Yamada, and Y. Muramoto

897 Dynamics of Viscoelastic Structures – A Time-Domain, Finite Element Formulation
D. F. Golla and P. C. Hughes

(Contents continued on Inside Back Cover)

Downloaded 04 May 2010 to 171.66.16.49. Redistribution subject to ASME license or copyright; see http://www.asme.org/terms/Terms_Use.cfm

CONTENTS (CONTINUED)

907 **Nonlinear Asymptotic Solution of the Reissner Plate Equations**
L. A. Taber

913 **Load-Supporting Fluid-Filled Cylindrical Membranes** (85-WA/APM-14)
V. Namias

919 **Three-Dimensional Dynamic Response of Buried Pipelines to Incident Longitudinal and Shear Waves** (85-WA/APM-13)
S. K. Datta, P. M. O'Leary, and A. H. Shah

927 **Vibration of a Cracked Cylindrical Shell of Rectangular Planform** (85-WA/APM-2)
R. Solecki and F. Forouhar

933 **Beams in Receding/Advancing Contact: Dundurs Problems** (85-WA/APM-3)
T. P. Pawlak, N. J. Salamon, and F. F. Mahmoud

937 **Point-Force Excitation of an Elastic Plate With an Embedded Cavity** (85-WA/APM-9)
A. Boström and A. Karlsson

943 **Singular Value Decomposition for Constrained Dynamical Systems**
R. P. Singh and P. W. Likins

949 **Asymptotic Modal Analysis and Statistical Energy Analysis of Dynamical Systems** (85-WA/APM12)
E. H. Dowell and Y. Kubota

958 **Multi-Harmonic Analysis of Dry Friction Damped Systems Using an Incremental Harmonic Balance Method** (85-WA/APM-16)
C. Pierre, A. A. Ferri, and E. H. Dowell

965 **Stochastic Response of Nonlinear Dynamic Systems Based on a Non-Gaussian Closure** (85-WA/APM-6)
R. A. Ibrahim, A. Soundararajan, and H. Heo

BRIEF NOTES

Stability of Annular Sector Plates With Clamped Radial Edges **971**
I. E. Harik

Electric-to-Pneumatic Transducer and its Use for Reading Braille **973**
R. Caen and C. Fonade

Long Wavelength Elastic Scattering From a Planar Distribution of Inclusions **974**
J. Baik and R. B. Thompson

976 Moving Load on Initially Stressed Orthotropic Cylindrical Shells Filled With Liquid
S. Chonan

977 Axial Stress-Time History Measurements in Impulsively Loaded Aluminum Rods Using the Double Gauge Technique
Z. Rosenberg, M. Mayseless, and Y. Partom

979 Solutions of Multiple Crack Problems of Elastic Half-Plane
Y. Z. Chen

DISCUSSION

982-983 Discussion on previously published paper by **S. Cheng and F. B. He**

983 Discussion on previously published paper by **N. Katsube**

BOOK REVIEWS

984 ***Computational Methods for Transient Analysis*** edited by **Ted Belytschko and Thomas J. R. Hughes** . . . Reviewed by **P. Burgers**

984 ***Random Vibrations of Elastic Systems*** by V. V. Bolotin . . . Reviewed by **S. H. Crandall**

985 ***Books Received by the Office of the Technical Editor***

ERRATA

896 ***Erratum on "Large Deflection Behavior of Simply Supported Laminated Panels Under In-Plane Loading," by*** **Y. Zhang and F. L. Matthews** and published in the September 1985 Issue

912, 926, 932	Worldwide Mechanics Meeting List
751, 758, 782, 793, 822, 828	Applied Mechanics Symposium Proceedings
846, 882, 889, 918, 981	Applied Mechanics Symposium Proceedings
786	Change of Address Form
988	Postdoctoral Research Awards

Downloaded 04 May 2010 to 171.66.16.49. Redistribution subject to ASME license or copyright; see http://www.asme.org/terms/Terms_Use.cfm

VLFEM Analysis of a Two-Dimensional Cochlear Model

C. E. Miller
Department of Biomedical Engineering,
Duke University,
Durham, N.C. 27706

A hybrid technique named here the Very Large Finite Element Method (VLFEM) is developed to analyze a two-dimensional model of the cochlea of the inner ear. In this method, the domain is divided into elements of constant material properties and the exact solution to the model equations obtained in each element. This involves two forms of eigenexpansion, allowing a one-dimensional instead of two-dimensional discretization. The discretization is related to the rate of change of the wavenumber of traveling waves on the elastic partition, producing an optimal mesh spacing. A full characterization of the multiple complex wavenumbers is obtained. The results of this analysis for partition (basilar membrane) amplitude and phase exactly correspond to those from previous finite difference and finite element analyses, but less computing effort is required for the same accuracy of results. Reflected waves, abrupt changes in material properties, and arbitrary boundary conditions pose no difficulties for VLFEM analysis, an advantage over the WKB (or LG) technique used previously on this problem.

Introduction

This article demonstrates a new means of analysis of the "classical" two-dimensional cochlear model. This model is suitable for studying gross movements within the cochlea, containing the basic physics of the problem without the computational complications of three-dimensional models. Steele and Taber (1979b), comparing mathematical calculations to experimental results, show the one-dimensional longwave model to be grossly in error compared to their fully three-dimensional model. In contrast, they find a two-dimensional approximation to be surprisingly close to the three-dimensional analysis, agreeing in phase and location of peak, but differing slightly in sharpness of peak.

The two-dimensional model is that used by Lesser and Berkley (1972). Many different techniques have been used for efficient solution of the equations of the model. Viergever (1980) divides the classes of solution in two: direct numerical techniques and approximate techniques involving asymptotics.

First in the class of exact techniques is the method of Lesser and Berkley (1972). They express the fluid velocity potential in the form of a truncated Fourier series and use a fast Fourier transform (FFT) algorithm to find the coefficients of the series by matching the boundary conditions at the basilar membrane. Allen and Sondhi (1979) also use FFT techniques, but on integral equations developed by Allen (1977) for a two-dimensional model. Their time-domain solution incorporates signal-dependent properties and requires 40 ms/time step on an array processor for 512 equally spaced points. Neely (1977) uses the finite difference method with a 245 × 8 grid, requiring 70 s on a PDP-10 to calculate the response for one set of parameters. Viergever (1980) uses a finite element approach with a 238 × 11 grid, requiring 100 s on an IBM 370/158. His solution is virtually identical to the finite difference solution.

The asymptotic techniques consist of short-wavelength (shortwave), long-wavelength (longwave), and WKB (or LG) analyses. The shortwave approach, where the wavelength of motion on the basilar membrane is small compared with channel height, was proposed by Ranke (1931) and reintroduced by Siebert (1974). Investigators using the longwave approach, where waves on the basilar membrane are long compared to channel height, include Viergever and Kalker (1975) and Sondhi (1978).

The WKB (or LG) approach does not have the limitations of the longwave or shortwave methods. Steele and Taber (1979a) demonstrate excellent agreement between their WKB solution and the finite difference results of Neely (1977). The method is computationally fast while retaining the physics of the problem, but limited in the problems it can handle. Membrane impedance must vary slowly in comparison with wavelength or, equivalently, reflection of the traveling wave must be negligible, to insure its accuracy.

Both categories of techniques, exact and approximate, have drawbacks. The exact numerical methods can be very accurate but generally require large amounts of computing time and do not give physical insight into the problem. The asymptotic methods do give insight into the physics, but cannot match all boundary conditions or handle rapid changes in basilar membrane properties.

Contributed by the Applied Mechanics Division and presented at the Winter Annual Meeting, Miami, Fla., November 17-21, 1985, of THE AMERICAN SOCIETY OF MECHANICAL ENGINEERS.

Discussion on the paper should be addressed to the Editorial Department, ASME, United Engineering Center, 345 East 47th Street, New York, N.Y. 10017, and will be accepted until two months after final publication of the paper itself in the JOURNAL OF APPLIED MECHANICS. Manuscript received by ASME Applied Mechanics Division, October, 1984; final revision, March, 1985. Paper No. 85-WA/APM-17.

Copyright © 1985 by ASME
Downloaded 02 May 2010 to 171.66.16.54. Redistribution subject to ASME license or copyright; see http://www.asme.org/terms/Terms_Use.cfm

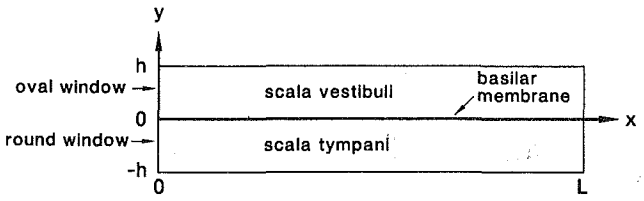


Fig. 1 Two-dimensional, two-channel cochlear model. Scalae vestibuli and tympani are fluid-filled. The basilar membrane is linearly viscoelastic with no coupling in the x direction. Sound pressure at the eardrum causes piston-like motion of the stapes, which fills the oval window and causes motion of the enclosed fluid and basilar membrane.

The method described here, called the VLFEM, is part exact and part approximate. The problem domain is divided into subregions, or elements, each having constant material properties. An exact solution to the governing equations is obtained in each element. Matching of pressure and velocity between elements yields a set of global equations, as in the finite element approach, which are solved for the nodal velocities. Low cost and accuracy are shown here by comparing results obtained with the VLFEM to those obtained with some of the other methods mentioned above. As will be seen, this technique can also be used to judge the validity of assumptions made in other types of analyses, since it maintains the "exact" form of the solution. The range of possibilities is extensive, some of the most promising being investigation of the dynamics of the hair cell structure, resonance phenomena in the cochlea, and reflection from sharply tuned or active cochlear structures.

I Model

The standard assumptions are made to ignore coiling, Reissner's membrane, and all structures of scala media except the basilar membrane. Scalae vestibuli and tympani have equal, constant cross sections and rigid walls. The fluid filling the two channels is linear, incompressible, and inviscid. No quantity varies in the z direction. See Viergever (1980) for a discussion of the validity of many of these assumptions. Finally, the basilar membrane is represented by a point impedance function; there is no coupling between points in the x direction. Figure 1 shows the corresponding model.

The equations for the model are formulated in terms of the velocity potential $\phi(x, y, t)$ for the fluid. For an incompressible, inviscid fluid, the velocity potential obeys Laplace's equation:

$$\nabla^2\phi(x, y, t) = 0 \tag{1}$$

The velocity component of the fluid in the x direction is u, where

$$u(x, y, t) = \frac{\partial\phi}{\partial x} \tag{2}$$

and the component in the y direction is v, where

$$v(x, y, t) = \frac{\partial\phi}{\partial y} \tag{3}$$

The pressure at any point in the fluid is

$$p(x, y, t) = -\rho\frac{\partial\phi}{\partial t} \tag{4}$$

Since the fluid is incompressible, an inward motion of the stapes results in a simultaneous equal outward motion of the round window. Pressure in the two chambers is antisymmetric; thus only one chamber of the model (the upper) is discussed here.

The normal fluid velocity at the rigid walls is zero. The corresponding boundary conditions are

$$\frac{\partial\phi}{\partial y} = 0 \quad \text{at} \quad y = h \tag{5}$$

and

$$\frac{\partial\phi}{\partial x} = 0 \quad \text{at} \quad x = L \tag{6}$$

The stapes fills the oval window and vibrates with unit displacement at radian frequency ω. The boundary condition at the stapes is thus

$$\frac{\partial\phi}{\partial x} = i\omega e^{i\omega t} \quad \text{at} \quad x = 0 \tag{7}$$

This displacement boundary condition is chosen to match the assumption of Neely (1980). Since the model is linear, the solution for the unit-velocity condition ($\partial\phi/\partial x = e^{i\omega t}$ at $x = 0$) can be obtained from that of the unit-displacement condition by dividing by $i\omega$. Only the steady-state response is desired; thus all quantities will have time dependence $e^{i\omega t}$. In the following equations, explicit time dependence is not shown.

At $y = 0$, the impedance of the fluid must match that of the membrane. The basilar membrane is described by a point impedance function $Z(x; i\omega)$, where

$$Z(x; i\omega) = \frac{K(x)}{i\omega} + R(x) + i\omega M(x) \tag{8}$$

Here K, R, and M are stiffness, damping, and mass factors per unit area of the basilar membrane. This membrane impedance is the ratio of pressure across the membrane to velocity of the membrane. Thus

$$-\frac{2p(x, 0, t)}{v(x, 0, t)} = \frac{K(x)}{i\omega} + R(x) + i\omega M(x) \tag{9}$$

where the factor of 2 comes from the antisymmetry of pressure in the two chambers.

Expressing the relationship in terms of ϕ,

$$\frac{\partial\phi}{\partial y} = -\phi\frac{2\rho\omega^2}{K + i\omega R - M\omega^2} \quad \text{at} \quad y = 0 \tag{10}$$

Figure 2 illustrates the complete boundary value problem as posed in (1), (5), (6), (7), and (10).

II Element Approach

(a) Single Element. An exact solution to the problem illustrated in Fig. 2 is possible only for certain variations $K(x)$, $R(x)$, and $M(x)$. The simplest case allowing an analytical solution is the case of constant membrane impedance. Consider one section of the cochlear model extending from $x = x_1$ to $x = x_2$ and let the membrane impedance be constant in this domain. The fluid velocity potential satisfying Laplace's equation in the domain and the rigid-wall boundary condition at $y = h$ can be found by separation of variables as

$$\phi = [Ae^{-i\kappa x} + \tilde{A}e^{i\kappa x}] \quad \cosh \quad (\kappa\tilde{y}) \tag{11}$$

where $\tilde{y} = (y - h)$ and A, $\tilde{A}$ are complex constants.

The boundary condition at $y = 0$ determines κ. From (10), κ must satisfy the equation

$$\kappa h \quad \tanh \quad (\kappa h) = \frac{2\rho\omega^2 h}{K + i\omega R - M\omega^2} \tag{12}$$

Here κ is the (complex) wavenumber for traveling waves on the basilar membrane, equal to $2\pi/\lambda$. Equation (12) is the eikonal equation for dispersive waves, expressing the relationship between wavenumber and frequency. Because of the cyclic nature of the tanh function for complex arguments (period $i\pi$), there are an infinite number of values κ_n satisfying this equation. The complete solution is a linear combination of these values,

Downloaded 02 May 2010 to 171.66.16.54. Redistribution subject to ASME license or copyright; see http://www.asme.org/terms/Terms_Use.cfm

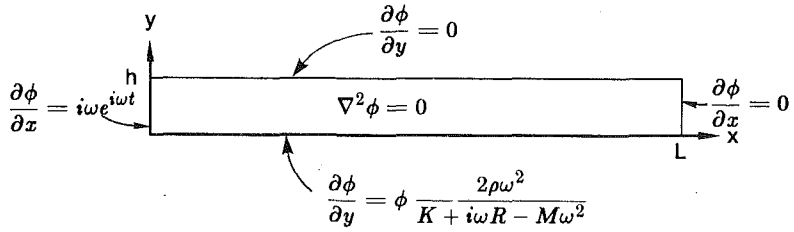


Fig. 2 Boundary-value problem for the two-dimensional model

$$\phi = \sum_{n=0}^{\infty} [A_n e^{-i\kappa_n x} + \tilde{A}_n e^{i\kappa_n x}] \quad \cosh \quad (\kappa_n \tilde{y}) \tag{13}$$

This is a generalized Fourier series for the traveling wave. The κ_n arise from the solution of the ordinary differential equation

$$Y''(y) - \kappa^2 Y(y) = 0 \tag{14}$$

and are thus the eigenvalues of the problem. The functions $\cosh(\kappa_n \tilde{y})$ are the corresponding eigenfunctions Y_n. They are orthogonal to the complex conjugates of the eigenfunctions of the adjoint problem,

$$\int_{-h}^{0} (\cosh \quad \kappa_n \tilde{y}) \, \overline{(\cosh \quad \kappa_r^+ \tilde{y})} \, d\tilde{y} = 0, \quad n \neq r \tag{15}$$

Here κ_r^+ are the eigenvalues of the adjoint problem with an appropriate numbering, found by substituting $\tilde{Z}$ for Z in the boundary condition at $y = 0$. This property allows choice of the coefficients A and $\tilde{A}$ to fit boundary conditions at x_1 and x_2.

For positive, real values of K, R, and M, the eigenvalues or wavenumbers lie in the second and fourth quadrants of the complex plane. Only the fourth-quadrant values will be included in κ_n, as the $\tilde{A}$ terms in equation (13) include the second-quadrant values. For no damping, or $R = 0$, one eigenvalue, κ_0, lies on the positive real axis while the others, κ_I, lie on the negative imaginary axis. With small damping, the "imaginary" wavenumbers, κ_I for $I > 0$, have a small real part and the "real" wavenumber, κ_0, has an imaginary part whose magnitude depends on the value of $(K - M\omega^2)$.

***(b)* Multiple Elements.** The solution thus obtained for one region of constant properties can be extended to the entire model. The x direction of the cochlear model is divided into ne elements, in which all material properties are constant with respect to x. Within each element, the solution is as obtained in the last section. The ends of these elements are x_A, where

$$0 = x_1 < x_2 < \ldots < x_{ne} < x_{ne+1} = L \tag{16}$$

The elements are numbered consecutively, element e having nodes x_e and x_{e+1}. The continuous variation of membrane impedance $Z(x)$ is thus approximated by a discrete variation, with the impedance Z^e for element e being

$$Z^e = Z\left(x = \frac{x_e + x_{e+1}}{2}\right) \tag{17}$$

Let ξ be the x coordinate local to each element,

$$\xi^e = x - x_e \tag{18}$$

The ends or nodes of each element are

$$\begin{aligned} \xi_1^e &= 0 \\ \xi_2^e &= x_{e+1} - x_e \end{aligned} \tag{19}$$

The velocity potential within each element is then

$$\phi^e(\xi^e, \quad \tilde{y}) = \sum_{n=0}^{\infty} [A_n^e e^{-i\kappa_n^e \xi^e} + \tilde{A}_n^e e^{i\kappa_n^e \xi^e}] \quad \cosh \quad (\kappa_n^e \tilde{y}) \tag{20}$$

where the superscript e refers to quantities local to the element.

The coefficients A_n^e and $\tilde{A}_n^e$ are determined by the boundary conditions at ξ_1^e and ξ_2^e. Pressure and velocity must be continuous between elements; thus

$$\left.\begin{aligned} p^e(\xi_2^e, \tilde{y}) &= p^{e+1}(\xi_1^{e+1}, \tilde{y}) \\ u^e(\xi_2^e, \tilde{y}) &= u^{e+1}(\xi_1^{e+1}, \tilde{y}) \end{aligned}\right\} e = 1, 2, \ldots, (ne-1) \tag{21}$$

The conditions at $x = 0$ and $x = L$ give two additional equations. For example, if $u(0, \tilde{y}) = u_0(\tilde{y})$ and $u(L, \tilde{y}) = u_L(\tilde{y})$, then

$$u_0(\tilde{y}) = u^1(\xi_1^1, \tilde{y}) \tag{22}$$

and

$$u_L(\tilde{y}) = u^{ne}(\xi_2^{ne}, \tilde{y}) \tag{23}$$

The $(2 \times ne)$ equations (21)–(23) must be solved simultaneously for A_n^e and $\tilde{A}_n^e$, $e = 1, \ldots, ne$. This is facilitated by expressing the solution in each element in terms of a common set of orthogonal functions. Coefficients can then be equated directly between elements and discretization in the y direction is eliminated.

A good choice for the basis is the cosine function. It is odd like the cosh function and, with $(m\pi\tilde{y}/h)$ as argument, its derivative is zero at $\tilde{y} = 0$. Let each eigenfunction in every element be represented as

$$\cosh \quad (\kappa_n^e \tilde{y}) = \sum_{m=0}^{\infty} a_{nm}^e \quad \cos \quad \left(\frac{m\pi\tilde{y}}{h}\right) = \sum_{m=0}^{\infty} c_m \tag{24}$$

where the a_{nm}^e are complex constants. Using the orthogonality property of the cosine series, the coefficients are obtained as

$$a_{nm}^e = \begin{cases} \dfrac{(-1)^m \kappa_n^e h \quad \sinh \quad (\kappa_n^e h)}{(\kappa_n^e h)^2 + (m\pi)^2} & m = 0 \\ \dfrac{2(-1)^m \kappa_n^e h \quad \sinh \quad (\kappa_n^e h)}{(\kappa_n^e h)^2 + (m\pi)^2} & m = 1, 2, \ldots \end{cases} \tag{25}$$

The element fluid pressure is then

$$p^e(\xi^e, \tilde{y}) = -i\omega\rho \sum_{m=0}^{\infty} \sum_{n=0}^{\infty} [A_n^e e^{-i\kappa_n^e \xi^e} + \tilde{A}_n^e e^{i\kappa_n^e \xi^e}] a_{nm}^e \quad \cos \quad \left(\frac{m\pi\tilde{y}}{h}\right) \tag{26}$$

and the element fluid velocity in the x direction is

$$u^e(\xi^e, \tilde{y}) = i \sum_{m=0}^{\infty} \sum_{n=0}^{\infty} k_n^e h [-A_n^e e^{-i\kappa_n^e \xi^e} + \tilde{A}_n^e e^{i\kappa_n^e \xi^e}] a_{nm}^e \quad \cos \quad \left(\frac{m\pi\tilde{y}}{h}\right) \tag{27}$$

Downloaded 02 May 2010 to 171.66.16.54. Redistribution subject to ASME license or copyright; see http://www.asme.org/terms/Terms_Use.cfm

Table 1 Values of α_1, α_2, n, and m for (39) and (40)

	Index q	$1 \le q \le nm$	$nm < q \le 2nm$
α_1	r	-1	$+1$
α_2	s	ξ_1	ξ_2
n	r	$q-1$	$q-(nm+1)$
m	s	$q-1$	$q-(nm+1)$

Letting the subscript m denote the coefficient of the cos $(m\pi\tilde{y}/h)$ term,

$$p_m^e(\xi^e) = -i\omega\rho \sum_{n=0}^{\infty} [A_n^e e^{-i\kappa_n^e \xi^e} + \tilde{A}_n^e e^{i\kappa_n^e \xi^e}] a_{nm}^e \tag{28}$$

and

$$u_m^e(\xi^e) = i \sum_{n=0}^{\infty} [-A_n^e e^{i\kappa_n^e \xi^e} + \tilde{A}_n^e e^{i\kappa_n^e \xi^e}] a_{nm}^e \tag{29}$$

then the continuity conditions (21) become

$$\begin{aligned} p_m^e(\xi_2^e) &= p_m^{e+1}(\xi_1^{e+1}) \\ u_m^e(\xi_2^e) &= u_m^{e+1}(\xi_1^{e+1}) \end{aligned} \quad \begin{cases} m = 0, 1, 2, \ldots \\ e = 1, 2, \ldots, (ne-1) \end{cases} \tag{30}$$

Note that the independent variable $\tilde{y}$ has been eliminated in going from (21) to (30), allowing discretization in the x direction only.

(c) **Truncation.** The question to be answered now is where to truncate the infinite series of (26) and (27). For small $|\kappa_n h|$, the series (24) converges vary rapidly. For example,

$$\begin{aligned} |\kappa_n h| = 0.1 &\rightarrow \left| \frac{c_1}{c_0} \right| \le 10^{-3} \\ |\kappa_n h| = 1 &\rightarrow \left| \frac{c_5}{c_0} \right| \le 4 \times 10^{-3} \end{aligned} \tag{31}$$

Let nm be the number of modes or the number of terms of the series used. For three-place accuracy, we can take $nm = 2$ in the first case and $nm = 6$ in the second. As $|\kappa_n h|$ increases, nm must increase to obtain the same relative accuracy.

Next, consider the eigenfunction series. Looking only at the case of the right-traveling wave (the case of the left-traveling wave is analogous), let

$$\sum_{n=0}^{\infty} A_n e^{-i\kappa_n x} \cosh(\kappa_n \tilde{y}) = \sum_{n=0}^{\infty} d_n \tag{32}$$

If the damping factor R is small, a good approximation for the eigenvalues is

$$\kappa_n \approx (a_n - in\pi),\ n > 0,\ a_n \ll 1 \tag{33}$$

and the terms of the series are bounded by

$$|d_n| \le A_n \exp(-n\pi x),\ n > 0 \tag{34}$$

If all A_n are of the same order of magnitude, then at $x = 1$,

$$\left| \frac{d_2}{d_1} \right| \approx 4 \times 10^{-2}, \left| \frac{d_3}{d_1} \right| \approx 2 \times 10^{-3}, \left| \frac{d_4}{d_1} \right| \approx 8 \times 10^{-5} \tag{35}$$

If κ_0 has a negligible imaginary part, d_0 is substantially larger than d_1. Thus for three-place accuracy, $nm = 4$ is certainly sufficient and we may even use $nm = 2$ or 3.

(d) Matrix Representation. Trunation of the series in n and m now allows the derivation of matrix representations for (30). Define the *element eigenfunction coefficient vector* $\mathbf{A}$ as

$$\mathbf{A}^e = \{A_0^e, A_1^e, \ldots, A_{nm-1}^e, \tilde{A}_0^e, \tilde{A}_1^e, \ldots, \tilde{A}_{nm-1}^e\} \tag{36}$$

The *nodal pressure vector* $\mathbf{p}^e$ is

$$\mathbf{p}^e = \{p_0^e(\xi_1^e), p_1^e(\xi_1^e), \ldots, p_{nm-1}^e(\xi_1^e), p_0^e(\xi_2^e), p_1^e(\xi_2^e), \ldots, p_{nm-1}^e(\xi_2^e)\} \tag{37}$$

and the *nodal velocity vector* $\mathbf{u}^e$ is

$$\mathbf{u}^e = \{u_0^e(\xi_1^e), u_1^e(\xi_1^e), \ldots, u_{nm-1}^e(\xi_1^e), u_0^e(\xi_2^e), u_1^e(\xi_2^e), \ldots, u_{nm-1}^e(\xi_2^e)\} \tag{38}$$

The $\mathbf{A}^e$, $\mathbf{p}^e$, and $\mathbf{u}^e$ have length $2 \times nm$. The terms of the *element nodal pressure coefficient matrix* $\mathbf{P}^e$ are

$$\mathbf{P}_{rs}^e = -i\omega\rho \exp(\alpha_1 i\kappa_n^e \alpha_2) a_{nm}^e \tag{39}$$

and of the *element nodal velocity coefficient matrix* $\mathbf{U}^e$ are

$$\mathbf{U}_{rs}^e = i\alpha_1 \exp(\alpha_1 i\kappa_n^e \alpha_2) \kappa_n^e \alpha_{nm}^e \tag{40}$$

where α_1, α_2, n, and m are given in Table 1. The following relationships then hold:

$$\mathbf{p}_r^e = \mathbf{P}_{rs}^e \mathbf{A}_s^e \quad r, s = 1, 2, \ldots, 2nm \tag{41}$$

$$\mathbf{u}_r^e = \mathbf{U}_{rs}^e \mathbf{A}_s^e \quad r, s = 1, 2, \ldots, 2nm \tag{42}$$

If the *element stiffness matrix* $\mathbf{K}$ is defined as

$$\mathbf{K}_{rs}^e = \mathbf{P}_{rs}^e [\mathbf{U}_{rs}^e]^{-1} \tag{43}$$

then the relationship between nodal pressures and velocities for element e is

$$\mathbf{p}^e = \mathbf{K}^e \mathbf{u}^e \tag{44}$$

III Implementation

The computational effort in the analysis of the model is divided into two parts: (1) calculation of the wavenumber κ_n for each element of the model, and (2) formation of element arrays, assembly into the global matrix, and solution of the global equations.

(a) **Calculation of Wavenumber.** The parameters necessary for determination of the wavenumbers κ_n^e are ρ, h, $K(x)$, $R(x)$, $M(x)$, and ω. Calculation of wavenumbers begins at $x_1 = 0$. Subsequent element nodes x_{A+1} are chosen such that $[\kappa_n(x_{A+1}) - \kappa_n(x_A)]/\kappa_n(x_A) \le \Delta_\kappa$ for $n = 0, 1, \ldots, nm$. This produces an optimal element discretization.

At each x_A, the wavenumbers κ_n are found as the roots of the equation

$$f = \kappa_n h \tanh(\kappa_n h) - \frac{2\rho\omega^2 h}{K + i\omega R - M\omega^2} = 0 \tag{45}$$

where all parameters are evaluated at x_A. The problem is first cast in the form of a nonlinear least-squares minimization problem. Let $f_1 = \Re\{f\}$ and $f_2 = \Im\{f\}$. If $\mathbf{z}$ is the vector defined by $\mathbf{z} = (\Re\{\kappa h\}, \Im\{\kappa h\})$, then the problem is to minimize $F = f_1(\mathbf{z})^2 + f_2(\mathbf{z})^2$. A finite difference, Levenberg-Marquardt algorithm with strict descent is used.[2] Iterations are halted and a value of $\mathbf{z}$ accepted when $F \le 10^{-11}$. Since the algorithm finds local minima, good starting guesses are required for all vaues of κ_n desired. Asymptotic approximations are possible in some regions. Letting

$$\alpha = \frac{2\rho\omega^2 h}{K + i\omega R - M\omega^2} \tag{46}$$

then starting approximations for the real root are

$$\kappa_0 h(x_A) = \begin{cases} \alpha & \text{if } \Re\{\alpha\} \ge 2.5 \\ \sqrt{\alpha} & \text{if } 0.0 < \Re\{\alpha\},\ \Im\{\alpha\} \le 0.01 \end{cases} \tag{47}$$

and for the imaginary root are

$$\kappa_n h(x_A) = \left(\frac{\Im\{\alpha\}}{n\pi}, \frac{\Re\{\alpha\}}{n\pi} - n\pi \right) \text{ if } \frac{|\Re\{\alpha\}|}{(n\pi)^2}, \frac{|\Im\{\alpha\}|}{(n\pi)^2} \le 0.01 \tag{48}$$

[2] ZXSSQ, International Mathematical and Statistical Libraries, Houston, TX.

Downloaded 02 May 2010 to 171.66.16.54. Redistribution subject to ASME license or copyright; see http://www.asme.org/terms/Terms_Use.cfm

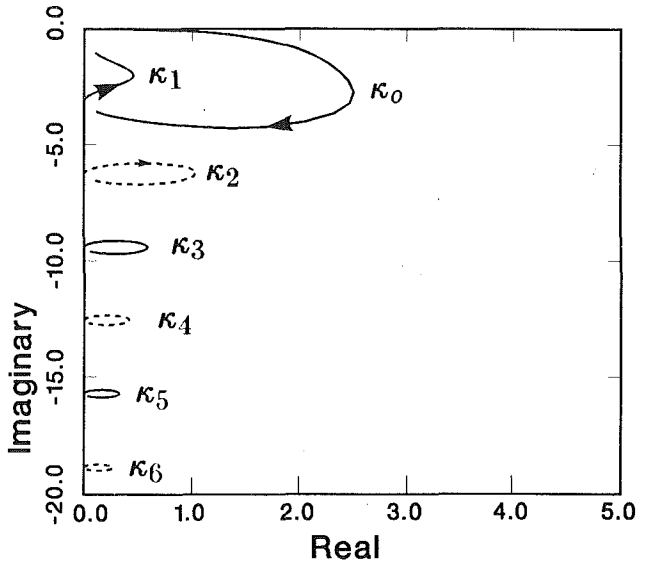


Fig. 3(*a*)

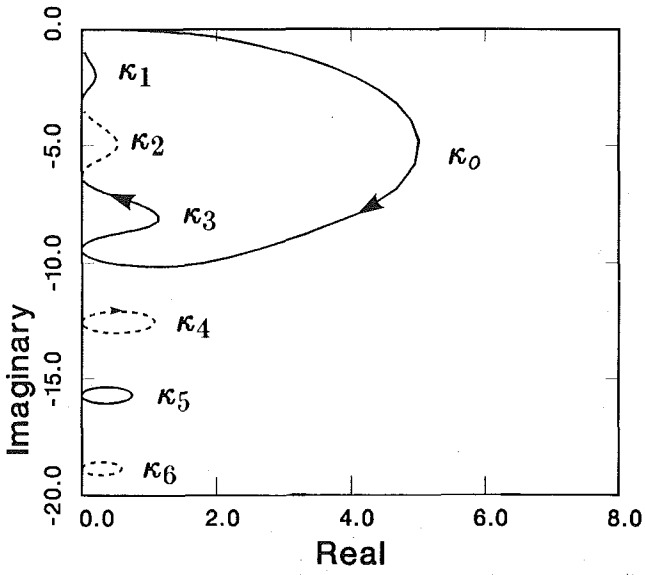


Fig. 3(*b*)

Fig. 3 Locus of wavenumbers $\kappa_{\hat{n}}$, the roots of equation (45), for the parameters of Table 2 and frequencies: (*a*) 0.8 kHz; (*b*) 1.6 kHz. Distance from stapes *x* increases from 0.0 to 35.0 on the curves in the directions indicated by arrows.

Otherwise, Taylor series approximations are made:

$$\kappa_n h(x_A) = \kappa_n h(x_{A-1}) + [x_{A-1} - x_A] \frac{d\kappa_n h}{dx}(x_{A-1}) \tag{49}$$

If the initial approximations are not good enough, calculations can be started at some x sufficiently negative to insure validity and then stepped forward to the region of interest.

(*b*) Element Arrays and Assembly. Formation of the global problem begins after files of nodal coordinates x_A and wavenumbers $\kappa_n(x_A)$ are created. First, the files are read and the element wavenumbers κ_n^e formed as $\kappa_n^e = [\kappa_n(x_e) + \kappa_n(x_{e+1})]/2$ for $e = 1, 2, \ldots, ne$. One file need not apply to the entire domain $x = 0$ to L; a file representing one set of model parameters may be used for one region and another file representing a different set of model parameters used for another region.

Next, a matrix is formed which, given the element node and mode number, locates the element equation in the set of global equations. For each element, $\mathbf{P}^e$ and $\mathbf{U}^e$ are calculated as defined in (39) and (40) as a preliminary to calculating $\mathbf{K}^e$ from (43). The blocked form of these matrices simplifies the calculations. Each $\mathbf{K}^e$ adds to the global stiffness matrix, which is stored in band form. Boundary conditions dictate the formation of the global pressure vector. The global stiffness matrix is then factored and solved to obtain the global velocity vector.

From the global velocity vector, the element nodal velocities $\mathbf{u}^e$ are extracted and used to calculate the element eigenfunction coefficients $\mathbf{A}^e$ as in (42). The terms of (20) are evaluated at the element midpoints and summed from $n = 0$ to $(nm - 1)$ to obtain ϕ^e. From this, basilar membrane deflection at the element midpoints is obtained as

$$\int \frac{\partial \phi}{\partial y}\bigg|_{y=0} dt$$

and normalized to stapes displacement.

There are $2 \times nm$ element equations and $nm \times (ne - 1)$ global equations (NEQS). The bandwidth of the global "stiffness" matrix (BW) is $(4 \times nm) - 1$. The number of operations required for formation of the element stiffness matrix is proportional to $nm^2 \times ne$, for factorization of the global matrix to $\text{BW}^2 \times \text{NEQS}$, and for solution of the global equations to $2 \times \text{BW} \times \text{NEQS}$. Thus formation grows as nm^2, factorization as nm^3, and solution as nm^2. An "average" size problem solved here is $ne = 48$ and $nm = 3$. For this, NEQS = 141 and BW = 11.

Table 2 Parameters for the two-dimensional cochlear model

$L = 35$ mm
$h = 1$ mm
$\rho = 0.001$ g/mm^3
$K(x) = 10e^{-0.2x}$ μN/mm^3
$R(x) = 2.0$ μNs/mm^3
$M(x) = 1.5 \times 10^{-3}$ g/mm^2

IV Results

One important result of this study is a characterization of the wavenumber κ as it depends on basilar membrane impedance. This behavior gives insight into the validity of the solution method. The accuracy of the solution depends on two parameters: nm, the number of modes of pressure or velocity at each node, and Δ_κ, the relative change in wavenumber κ between nodes. The effect of each of these factors on the accuracy of the VLFEM is examined by comparing results with varying refinement in both parameters to those of the finite difference, finite element, and WKB methods. The model parameters used for all of the results shown here except those in section (e) are given in Table 2. All calculations were done a Digital VAX 11/782.

(*a*) Behavior of Wavenumber. As noted earlier, the wavenumbers κ_n can be typified as real wavenumber κ_0 or the imaginary wavenumbers κ_I for $I > 0$. This nomenclature is in accordance with their values for $R = 0$. Figure 3 shows the locus of κ_n for two different frequencies, 0.8 and 1.6 kHz, and the model parameters of Table 2. The coordinate x is a parameter of the curves, increasing from 0.0 to 35.0 in the directions shown. The following discussion refers to Fig. 3(*a*) to illustrate the ideas presented.

Looking first at the behavior of κ_0 with increasing x, two regions in the locus plot can be distinguished. The first is the region before the *in vacuo* resonance point x_{res} [$\Re\{\kappa_0\} \leq 1.0$, $x \leq 23.6$ in Fig. 3(*a*)]. Here $[K(x) - M\omega^2] > 0$ and $[\kappa h \tanh(\kappa h)] > 0$. In this stiffness-dominated region, κ_0 has a very small imaginary part. As $K(x)$ decreases with increasing x, $\Im\{\kappa_0\}$ becomes more negative until $K(x) = M\omega^2$, when it is

Downloaded 02 May 2010 to 171.66.16.54. Redistribution subject to ASME license or copyright; see http://www.asme.org/terms/Terms_Use.cfm

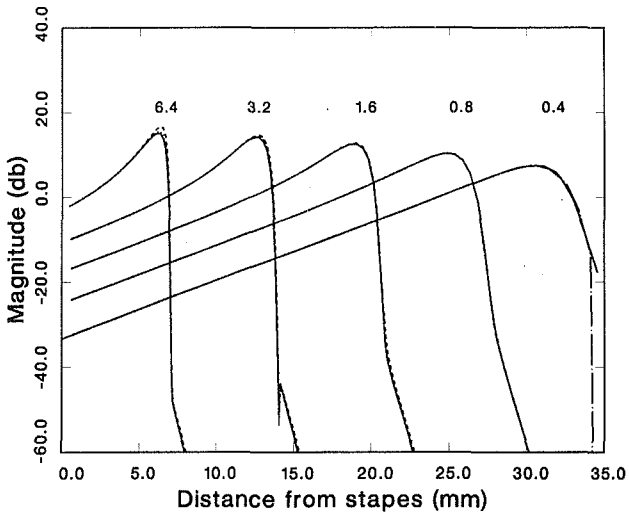


Fig. 4(*a*)

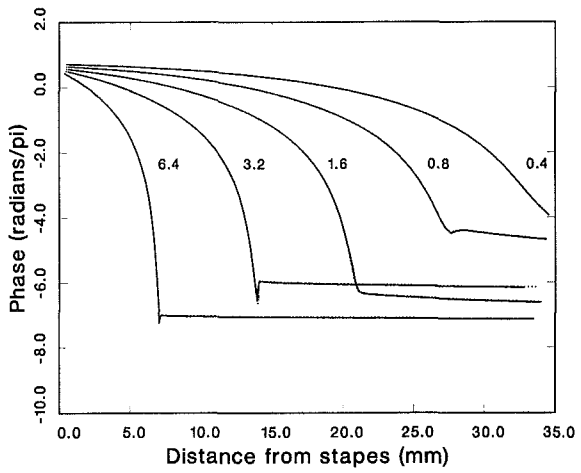


Fig. 4(*b*)

Fig. 4 Ratio of basilar membrane/stapes displacement: (*a*) amplitude, and (*b*) phase. Model parameters are those of Table 2 and curve labels are stapes frequency in kHz. Element discretizations for each frequency were chosen with $\Delta_\kappa = 0.4$, representing 48, 44, 44, 42, and 38 elements for 6.4, 3.2, 1.6, 0.8, and 0.4 kHz, respectively. Solid lines: five modes ($nm = 5$); dotted lines: three modes; dashed lines: two modes; chain-dotted line for 0.4 kHz: five modes with boundary condition $p = 0$ at $x = 35.0$. The five-mode solution in each case exactly overlays the eight-mode solution.

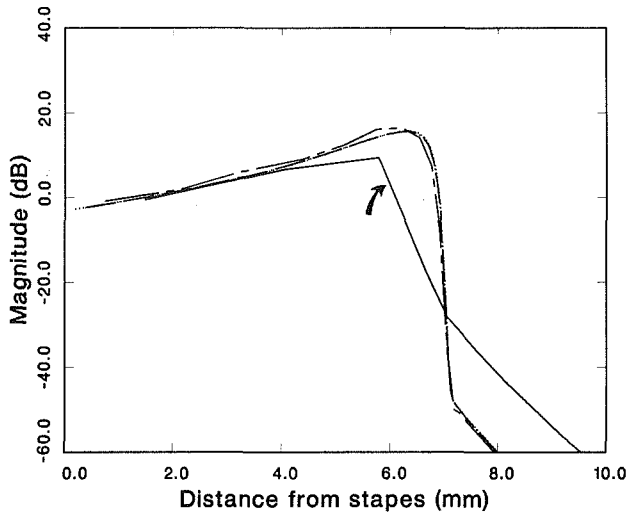


Fig. 5(*a*)

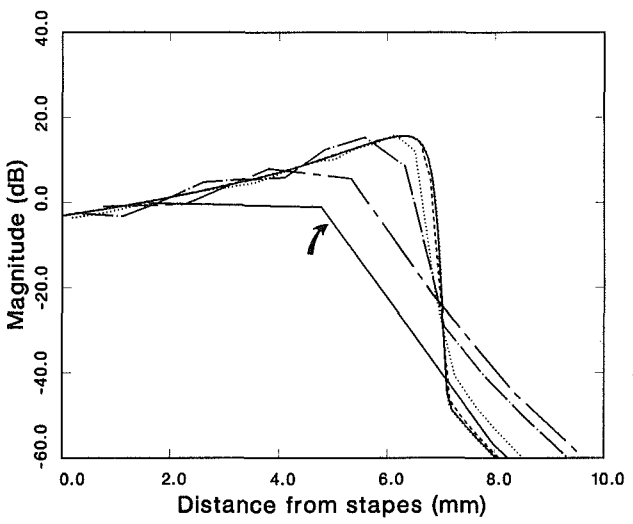


Fig. 5(*b*)

Fig. 5 Convergence with element discretization for 6.4 kHz, three modes: (*a*) optimal mesh, and (*b*) uniform mesh. Arrow shows direction of increasing number of elements (ne). First solid line: $ne = 12$; chain-dashed line: $ne = 24$; chain-dotted line: $ne = 48$; first dotted line: $ne = 96$; dashed line: $ne = 192$; second solid line: $ne = 384$; second dotted line: $ne = 768$. The curves $ne = 192, 384$, and 768 do not appear in (*a*).

maximal [$x = 27.9$, $\kappa_0 = (1.4, -4.3)$]. $\Re\{\kappa_0\}$ increases with increasing x but peaks [$x = 26.5$, $\kappa_0 = (2.44, -2.15)$] before x_{res} and is already decreasing when $\Im\{\kappa_0\}$ is maximal. Beyond x_{res}, in the mass-dominated region, $\Re\{\kappa_0\}$ decreases and $\Im\{\kappa_0\}$ becomes less negative as the wavenumber nears the imaginary axis.

Now look at the locus of the κ_I. They remain close to the imaginary axis with $\Im\{\kappa_I\} \approx -I\pi$ in the stiffness-dominated region. As $K(x)$ decreases, $\Re\{\kappa_I\}$ increase. The real parts of the κ_I enclosed by the locus of κ_0 (only κ_1 in Fig. 3(*a*)) peak when the real part of κ_0 peaks [$x = 26.5$, $\kappa_1 = (0.46, -2.0)$]. The real parts of the κ_I not enclosed by κ_0 ($\kappa_2, \kappa_3, \ldots$) peak at x_{res} [$x = 27.9$, $\kappa_2 = (1.1, -6.4)$]. Beyond these points, $\Re\{\kappa_I\}$ decrease. The behavior of $\Im\{\kappa_I\}$ also depends on whether or not they are enclosed by κ_0. For κ_I that are (κ_1), $\Im\{\kappa_I\}$ becomes less negative with increasing x. For κ_I that are not enclosed by κ_0 ($\kappa_2, \kappa_3, \ldots$), the opposite is true: $\Im\{\kappa_I\}$ become more negative as x increases.

The calculation of κ_n for $n = 1$ to 5 at $\Delta_\kappa = 0.4$ for one frequency requires about 7 s. This represents approximately 250 calls to the root-finding routine.

(*b*) Number of Modes. Section II part (c) has already shown how the accuracy of the approximations depends on the number of modes nm in the series for pressure and velocity (see (37) and (38)). The ratio of basilar membrane to stapes displacement amplitude and phase was calculated for $nm = 2$, 3, 5, and 8 for each of five input frequencies and is shown in Fig. 4. For all 20 cases, $\Delta_\kappa = 0.4$. Referring first to Fig. 4(*a*) for amplitude, for every frequency, the curves of the five-mode solution exactly overlay those of the eight-mode solution. The curves of the three-mode solution coincide with the five-mode solution everywhere but at the amplitude peak for 6.4 kHz. At this location, $|\kappa_0| \approx 30$ and the cosine series does not converge as rapidly as for smaller $|\kappa_n|$. Even the two-mode solution is almost indistinguishable from the five-mode solution except at the peak amplitudes for 6.4, 3.2, and 1.6 kHz, where again the reason is that $|\kappa_0|$ is large. As seen in Fig. 4(*b*), the two-mode solution for phase is virtually identical to the five-mode solution.

Downloaded 02 May 2010 to 171.66.16.54. Redistribution subject to ASME license or copyright; see http://www.asme.org/terms/Terms_Use.cfm

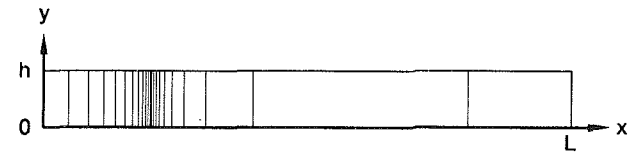


Fig. 6(*a*)

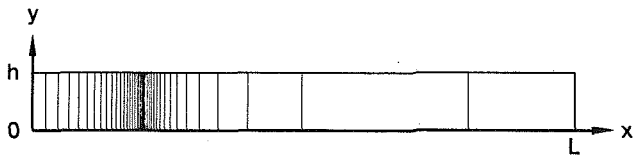


Fig. 6(*b*)

Fig. 6 Optimal element discretizations of the model domain for 6.4 kHz. Here L = 35.0 mm and *in vacuo* resonance, $K(x) = M\omega^2$, occurs at 7.1 mm, where the elements are smallest. (*a*) $\Delta_\kappa = 0.8$, $ne = 24$; (*b*) $\Delta_\kappa = 0.4$, $ne = 48$.

The 6.4, 3.2, 1.6, and 0.8 kHz, five-mode solutions of Fig. 4(*a*) and 4(*b*) agree completely with the finite difference solutions published by Neely (1977, 1981). Neely's boundary condition at $x = L$ is $p = 0$ instead of $u = 0$ as used here, but this does not affect the results for these frequencies since disturbances caused by stapes vibration do not reach the apex. For frequencies of 0.4 kHz and lower, however, disturbances will reach the apex. The chain-dotted line in Fig. 4(*a*) for 0.4 kHz shows model response with $p = 0$ at $x = L$. Neely's result for the same frequency differs from this, probably due to the manner in which the finite difference boundary condition must be implemented, for his basilar membrane/stapes displacement amplitude does not go to zero ($-\infty$ dB) at the apex as would be expected for zero pressure. Steele and Taber's (1979a) results for a WKB analysis of the model agree with the finite difference results and thus the present results in location and magnitude of peak for frequencies above 1.6 kHz. They differ by about 4 dB in amplitude for the lower frequencies and predict a more rapid post-peak drop-off for all frequencies. Viergever (1980) shows results from a finite element scheme to be equivalent to results from the finite difference scheme, so these are also equivalent to the present results.

(*c*) Element Discretizations. Here we look at the effect of element discretization on the accuracy of the solution. The element size for the VLFEM used here is chosen by specifying the change of κ from one node to the next. Since the solution is expressed in terms of κ, this produces an *optimal* mesh spacing: The elements are smallest where the solution is changing most rapidly. Figures 5(*a*) and 5(*b*) illustrate the advantages of this optimal spacing in accuracy and calculation time. Figure 5(*a*) shows the amplitude solution for 6.4 kHz and three modes. The 48-element solution for $\Delta_\kappa = 0.4$ is barely distinguishable from the 96-element solution for $\Delta_\kappa = 0.2$. Figure 8(*b*) also shows 6.4 kHz, three-mode amplitude solutions but for uniform discretizations with 12, 24, 48, 96, 192, 384, and 768 elements. Here the 384-element solution is very close to the 768-element solution. The advantages of the optimal discretization are evident from these figures, requiring 1/8 as many elements as the uniform discretization for the same level of accuracy. Since factorization and solution fo the global stiffness matrix depend linearly on ne, the optimal discretization also requires 1/8 the computing time.

Figure 6 shows the optimal discretizations used to obtain the results of Fig. 5(*a*). For these, $x_{res} = 7.1$ mm. Here κ changes most rapidly and the elements are smallest.

(*d*) Element Eigenfunction Coefficients. The vector $\mathbf{A}^e$ of

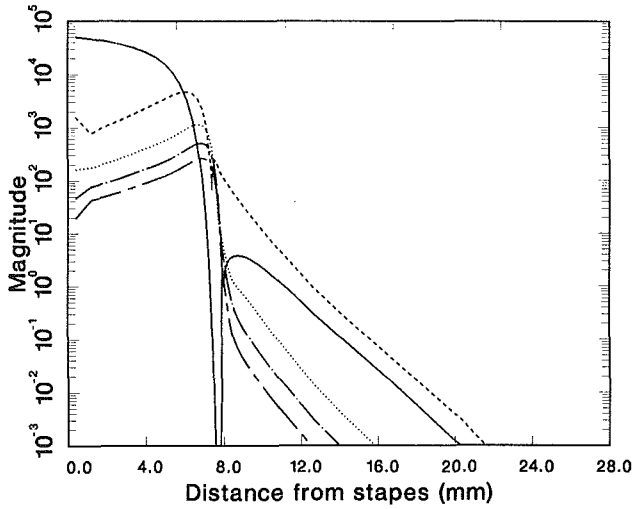


Fig. 7(*a*)

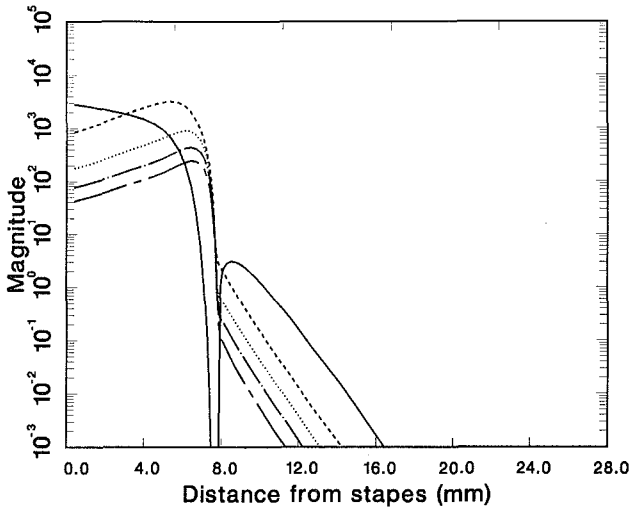


Fig. 7(*b*)

Fig. 7 Magnitude of the element eigenfunction coefficients for 6.4 kHz plotted for element midpoint: (*a*) coefficients of right-traveling wave A_n; (*b*) coefficients of left-traveling wave $\tilde{A}_n$

eigenfunction coefficients is calculated for each element to obtain the complete solution within that element. Examination of these coefficients shows the contribution of each of the eigenfunction modes ($\cosh \kappa_n \tilde{y}$) to the total solution. Figure 7(*a*) shows the coefficients A_n on the right-traveling wave and Fig. 7(*b*) the coefficients $\tilde{A}_n$ of the left-traveling wave. For both, input frequency is 6.4 kHz, $nm = 3$, and $\Delta_\kappa = 0.4$.

In Fig. 7(*a*), we see that A_0 is dominant until $x = 5.8$ mm, a point basal to the amplitude peak of 6.2 mm and the resonance point $x_{res} = 7.1$ mm. A_0 decreases beyond 5.8 mm until it is minimal at 7.7 mm, wherafter it again increases. However, beyond this minimum it is never greater than A_1. At $x = 0$, the magnitude of $\tilde{A}_0$ is 6×10^{-3} times the magnitude of A_0. $\tilde{A}_1$ is greater than $\tilde{A}_0$ from $x = 3.0$ to 8.2.

(*e*) Effects of Lower Mass. Figure 8 shows model behavior with parameter $M = 5 \times 10^{-5}$ g/mm^2, 1/30 the value for mass given in Table 2. All other parameters remain the same. This value is much more physically reasonable, but the other was selected by previous investigators to give optimal agreement with experimental measurements. The amplitude peaks of Fig. 8 are less sharp and post-peak drop-off less

Downloaded 02 May 2010 to 171.66.16.54. Redistribution subject to ASME license or copyright; see http://www.asme.org/terms/Terms_Use.cfm

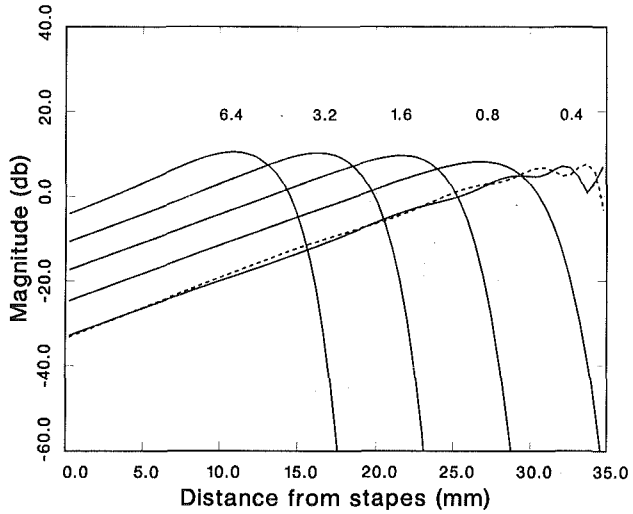


Fig. 8 Basilar membrane/stapes displacement amplitude for low mass model, $M = 5 \times 10^{-5}$. All solutions are for three modes and $\Delta_\kappa = 0.2$. Labels give input frequency in kHz. Dashed line for 0.4 kHz is the solution for boundary condition $p = 0$ at $x = L$. The response for all other frequencies is unchanged by this boundary condition.

rapid than those of Fig. 4(*a*). The 0.4 kHz response shows the effects of reflection at the apex.

V Discussion

I have chosen to compare the present VLFEM results to those of the finite difference and finite element methods because, of all published results from "exact" solution methods, these are the most complete and appear the most accurate. With proper choices of Δ_κ, the element discretization control, and *nm*, the number of modes of pressure and velocity, the present method produces the same results as these other methods. It has two significant advantages over finite differences and finite elements, however. First, it maintains a physically meaningful form of solution. As seen in Fig. 7, this allows determination of the individual coefficients of the Fourier decomposition of the traveling wave. Calculation of the wavenumber is a bonus of this method.

The second advantage is a reduction in computing effort due to reduction of number of elements needed in both x and y directions. The number of modes *nm* in VLFEM corresponds to the number of elements in the y direction *ny* in the finite element method (FEM) in the order of global equations and the bandwidth. An important consideration in choosing *nm* or *ny* is what mode shape or spatial frequency can be resolved in the y direction. In VLFEM, an additional half-sine wave is resolved for each increment of *nm*. A good engineering approximation of the half-sine wave requires four linear elements. Thus *nm* can typically be 1/4 of *ny* to resolve the same variation in y. Indeed, the VLFEM solution with $nm = 3$ gives the same results as an FEM solution (Viergever, 1980) with $ny = 11$.

In VLFEM, adaptive mesh spacing and the use of exact functions as basis functions reduces the number of elements needed in the x direction, *ne*, from that in FEM. The present results show good convergence with $ne = 48$, while FEM may require four times this number.

Viergever (1980) reports a FEM solution with 238×11 grid to require 100 s on an IBM 370/158; the VLFEM solution with $ne = 48$ and $nm = 3$ producing identical results requires 13.2 s on a VAX 11/780, a machine with 0.7 times the floating-point throughput (Dongarra, 1984). If a wavenumber file already exists, VLFEM requires 6.2 s. Comparison of times on different machines and with different programming times may be misleading, however.

Now the VLFEM must be compared to the approximate analysis methods of cochlear mechanics. I use the WKB (or LG) method as the benchmark approximate method, in agreement with Steele and Taber (1979a), Viergever (1980), and deBoer and Viergever (1982) that it is the approximate method most appropriate in the study of cochlear mechanics. Based on times reported by Steele and Taber (1979a) and Steele and Miller (1980), and machine estimates of Dongarra (1984), the two-mode solution requires five times the work of the standard WKB and 11 times the work of the improved WKB (or two and four times the work if wavenumber files are already generated). However, this two-mode solution is more accurate than these corresponding asymptotic solutions. The advantage in accuracy is due to three factors: ability to match boundary conditions, ability to handle reflected waves, and inclusion of additional solution modes.

The WKB solution has the form

$$\phi = \Phi(x) \quad \exp \quad \left[i\left(\omega t - \int_0^x \kappa(x)\,dx\right) \right] \quad \cosh \quad (\kappa \tilde{y}) \qquad (50)$$

where Φ is an amplitude function that depends on x. There are no free constants to match boundary conditions at $x = 0$ and $x = L$. This problem was not significant in the model used here, since the boundary condition at the apex is not important for any but the low frequencies and the WKB solution is almost constant at the base. The method would not function as well with other models requiring more effort to match boundary conditions.

Results from the VLFEM demonstrate why the WKB method works in certain regions and why it fails in others. For the example of Fig. 7, all coefficients of the left-traveling or reflected waves are at least two orders of magnitude below those of the right-traveling waves before the amplitude peak. For this particular set of parameters, then, the WKB assumption of no reflection is a good one. Before x_{res}, A_0 is much larger than A_1, so use of only κ_0 is also a good approximation. Beyond x_{res}, the A_1 terms in the series solution are largest. A WKB solution using only κ_0 thus predicts too rapid a post-peak drop-off, as seen in the results of Steele and Taber (1979a). Viergever's (1980) LG solution uses the κ_0 term before x_{res} and the κ_1 term beyond x_{res}. Figure 7(*a*) shows why this combination produces more accurate results.

The WKB approach necessitates a priori discard of part of the solution by using only one mode. In the VLFEM, we can decide how many modes to include and then, by studying results such as Figs. 4 and 7, discard certain parts and know exactly what we are discarding. Note a reflected component of the solution must always be present in combination with its corresponding right-traveling mode.

Although results are presented here for only one very specific set of parameters, this method is by no means limited to models of this form and its greatest benefit is to more complicated models. Nonconstant $M(x)$ and $R(x)$ are handled as easily as the variable $K(x)$. None need to be continuous functions of x; for example, a heavy mass may be added in one region, $x = x_a$ to x_b, as in the cochlea of the greater horseshoe bat. Mass and stiffness may also be removed in such a region: The result is a hole in the basilar membrane, such as occurs in the cochlea of the goose. A discrete set of resonators may also be added. In addition, other parameters normally constant such as scala height h may vary with x; this allows analysis of a model with a hole in the wall of one scala.

Until now, the WKB method was the only one available fast enough to use for parameter studies in two-dimensional cochlear mechanics. The VLFEM now provides an alternative. The calculation time is low enough for rapid analysis

Downloaded 02 May 2010 to 171.66.16.54. Redistribution subject to ASME license or copyright; see http://www.asme.org/terms/Terms_Use.cfm

of many different cases. It is structured so that convergence of the solution is easily verified and accuracy is assured. Finally, it can handle complicated two-dimensional models and may be extended to three-dimensional models, thus giving solutions to some very interesting problems of cochlear mechanics.

Acknowledgments

This work was supported by grants to Stanford University from the National Science Foundation and the National Institute of Neurological and Communicative Disorder and Stroke. The author would like to acknowledge helpful suggestions from Professor C. R. Steele, which motivated the element-level approach to the problem. Thanks go to Dr. J. M. Winget for review of the manuscript.

References

Allen, J. B., 1977, "Two-Dimensional Cochlear Fluid Model: New Results," *J. Acoust. Soc. Am.*, Vol. 61, pp. 110–119.

Allen, J. B., and Sondhi, M. M., 1979, "Cochlear Macromechanics: Time Domain Solutions," *J. Acoust. Soc. Am.*, Vol. 66, pp. 123–132.

deBoer, E., and Viergever, M. A., 1982, "Validity of the Liouville-Green (or WKB) Method for Cochlear Mechanics," *Hearing Research*, Vol. 8, pp. 131–155.

Dongarra, J. J., 1984, "Performance of Various Computers Using Standard Linear Equations Software in a FORTRAN Environment," preprint, Mathematics and Computer Science Division, Argonne National Laboratory.

Gill, P. E., Murray, W., and Wright, M. H., 1981, *Practical Optimization*, Academic Press, New York.

Lesser, M. B., and Berkley, D. A., 1972, "Fluid Mechanics of the Cochlea. Part 1," *J. Fluid Mechanics*, Vol. 51, pp. 497–512.

Neely, S. T., 1977, "Mathematical Models of the Mechanics of the Cochlea," E.D. Thesis, California Institute of Technology, Pasadena, CA.

Neely, S. T., 1981, "Finite Difference Solution of a Two-Dimensional Model of the Cochlea," *J. Acoust. Soc. Am.*, Vol. 69, pp. 1386–1393.

Peterson, L. C., and Bogert, B. P., 1950, "A Dynamical Theory of the Cochlea," *J. Acoust. Soc. Am.*, Vol. 22, pp. 369–381.

Seibert, W. M., 1974, "Ranke revisited—A Simple Short-Wave Cochlear Model," *J. Acoust. Soc. Am.*, Vol. 56, pp. 594–599.

Steele, C. R., 1974, "Behavior of the Basilar Membrane with Pure-Tone Excitation," *J. Acoust. Soc. Am.*, Vol. 55, pp. 148–162.

Steele, C. R., and Miller, C. E., 1980, "An Improved WKB Calculation for a Two-Dimensional Cochlear Model," *J. Acoust. Soc. Am.*, Vol. 68, pp. 147–148.

Steele, C. R., and Taber, L. A., 1979a, "Comparison of WKB and Finite Difference Calculations for a Two-Dimensional Cochlear Model," *J. Acoust. Soc. Am.*, Vol. 65, pp. 1001–1006.

Steele, C. R., and Taber, L. A., 1979a, "Comparison of WKB Calculations and Experimental Results for Three-Dimensional Cochlear Models," *J. Acoust. Soc. Am.*, Vol. 64, pp. 1007–1018.

Viergever, M., 1980, *Mechanics of the Inner Ear*, Academic thesis, Delft University Press, Delft.

Viergever, M. A., and Kalker, J. J., 1975, "A Two-Dimensional Model for the Cochlea," *J. Engineering Math.*, Vol. 9, pp. 353–365.

Downloaded 02 May 2010 to 171.66.16.54. Redistribution subject to ASME license or copyright; see http://www.asme.org/terms/Terms_Use.cfm

M. S. Cramer
Associate Professor,
Department of Engineering Science
and Mechanics,
Virginia Polytechnic Institute and
State University,
Blacksburg, Va. 24061

S. H. Nguyen
System Product Division,
D2G6/050-1,
IBM Corporation,
Rochester, Minn. 55901

M. E. Bowman
Equipment Engineering Department,
Bldg. 322-M,
E. I. DuPont-Savannah River Plant,
Aiken, S.C. 29801

B. E. McCown
Dynamics Technology Branch,
Boeing Vertol,
Philadelphia, Pa.

A Change in Wave Type Modeled by the Variable Coefficient Korteweg-deVries Equation

Strongly shoaling solutions to the variable coefficient Korteweg-deVries equation have been obtained for arbitrary initial or off-shore waveforms and depth variations. Although the solutions were capable of exhibiting dispersive behavior off-shore, the near-shore behavior was always found to be governed by a variable coefficient Burger equation. Conditions under which the wave slope became infinite were given in terms of the initial shape of the wave and the depth variation. These solutions are valid when $\alpha << \delta << 1$, *where* α *is the ratio of the initial wave amplitude to the depth and* δ *is the ratio of the initial length of the wave to the length scale associated with the depth variation. Numerical solutions of this equation were also found; these were in excellent agreement with the asymptotic results.*

1 Introduction

One of the most important problems in physical oceanography is the description of surface gravity waves as they propagate in water of variable depth. An extremely useful tool in the study of this phenomenon is the variable coefficient Korteweg-deVries equation. This equation contains the most important effects of modulation due to depth variation, nonlinearity, and dispersion. It has been shown that this equation can describe the gradual modulation of solitary waves and cnoidal wavetrains, see [1–3], as well as the shoal-induced fissioning of solitary waves, see, e.g., [4–6]. These studies have all been concerned with the behavior of a single type of wave as it is modulated by the depth variation. Generally, we would expect a change in the type of wave as it approaches a beach. The description of such changes and the relation between near and off-shore conditions are of central interest and have been discussed by a number of authors; see, e.g., [7–10]. Because of the combined difficulties associated with depth variations, nonlinear free-surface conditions, and dispersion the previous studies have obtained the near to off-shore relation through various patching schemes. These schemes suffer from the fact they rely on arbitrary, although in many cases reasonable, matching conditions for the near and off-shore solutions. Furthermore, these cannot take into account in a systematic way the wide variety of phenomena, i.e., wave fissioning, plunging, etc., which previous investigations have shown to be possible.

Because of the importance of the Korteweg-deVries equation in the theory of free-surface waves and a number of other fields, see, e.g., Lamb [11], and, in order to make a first step toward developing a rigorous theory of the off to near-shore transition, the main objective of the present study is to show how the variable coefficient Korteweg-deVries equation may be used to model changes in wave type triggered by depth variations. Furthermore, one of the advantages of this work is that the relative simplicity of the Korteweg-deVries equation permits a clearer understanding of the physical processes at work and the fact that the results are in complete accord with the qualitative behavior of shoaling waves, see, e.g., the experiments of [9]. Under the conditions described in the following, we have used the method of matched asymptotic expansions to show that over most of their propagation, waves may be described by the linearized dispersive version of this equation. Near the shore, it is shown that dispersive effects are negligible and nonlinear effects predominate. The wave therefore steepens until its slope becomes infinite. At this stage the theory of the Korteweg-deVries equation breaks down and a more accurate analytical model will need to be applied. For the sake of convenience, we will refer to the point at which the slope first becomes infinite as the break point.

Contributed by the Applied Mechanics Division for publication in the JOURNAL OF APPLIED MECHANICS.

Discussion on this paper should be addressed to the Editorial Department, ASME, United Engineering Center, 345 East 47th Street, New York, N.Y. 10017, and will be accepted until two months after final publication of the paper itself in the JOURNAL OF APPLIED MECHANICS. Manuscript received by ASME Applied Mechanics Division, August, 1983; final revision, January, 1985.

Copyright © 1985 by ASME
Downloaded 02 May 2010 to 171.66.16.54. Redistribution subject to ASME license or copyright; see http://www.asme.org/terms/Terms_Use.cfm

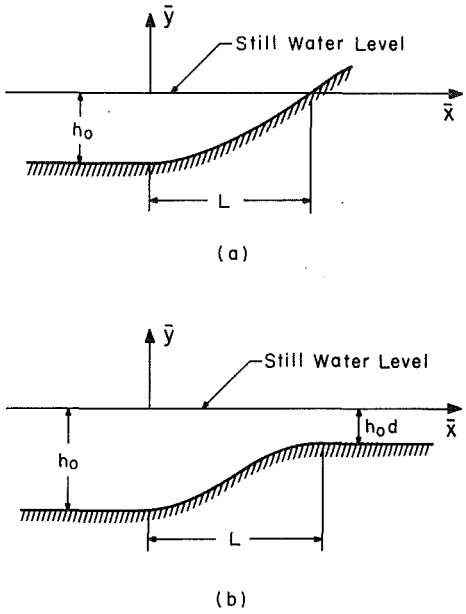


Fig. 1 Typical bathymetries. The undisturbed water level is taken to be $\bar{y} = 0$ and L may be considered to be the length scale characteristic of the depth variation. (a) Closed beach and (b) shelf; d is the ratio of shelf depth to the deep water depth.

However, it is essential to note that the physical significance of this point is to signal the need for a more accurate theory which, in turn, may be used to calculate the actual point of physical breaking.

In the next section, we introduce the variable coefficient Korteweg-deVries equation and indicate the conditions under which our results will be valid. Section 3 contains the main analysis of the paper and in Section 4 we compare these results to numerical solutions of the exact Korteweg-deVries equation. Because of the wide variety of behavior found in theories of free-surface waves and, in particular, described by the Korteweg-deVries equation, we have compared our results to a selection of the most closely related and relevant previous investigations in Section 5.

2 Problem Formulation

We will consider one-dimensional surface waves of length λ and amplitude a. These propagate into water whose depth, $H(\tilde{x})$, is given by

$$H = h_0 h\left(\frac{\tilde{x}}{L}\right),$$

where $\tilde{x}$ is the distance measured parallel to the free surface in the direction of propagation and L is a length scale measuring the rate of depth change. As suggested by Fig. 1, we will take $H \equiv h_0$, i.e., $h = 1$, for $\tilde{x} \le 0$ and, for a closed beach, we will also take $h(1) \equiv 0$. When the parameters

$$\alpha \equiv \frac{a}{h_0}, \quad \mu \equiv \frac{h_0}{\lambda}, \quad \text{and} \quad \delta \equiv \frac{\lambda}{L}$$

are all small, Johnson [4] and Ostrovskiy and Pelinovskiy [2] have shown that the wave motion is governed by the following equation

$$\eta_x + \frac{3}{2}\alpha h^{-\frac{3}{2}}\eta\eta_\tau + \mu^2\frac{h^{1/2}}{6}\eta_{\tau\tau\tau} + \frac{\delta}{4}\frac{h'}{h}\eta = 0, \tag{1}$$

where the actual displacement of the fluid surface from its unperturbed position is given by $\alpha h_0 \eta$ and

$$x = \frac{\tilde{x}}{\lambda}, \quad h = h(x\delta) \quad \text{and} \quad h'(x\delta) \equiv \frac{dh}{dx\delta}.$$

This equation has been written in a coordinate system which moves at the speed of a linearized shallow water wave; thus,

$$\tau \equiv \frac{1}{\delta}\int_0^{x\delta}\frac{dp}{\sqrt{h(p)}} - t,$$

where t is the nondimensional time obtained by scaling the actual time by $\lambda/\sqrt{gh_0}$ and g is the acceleration of gravity. In the following analysis it will be convenient to write this basic equation by replacing x and $\eta(x, \tau)$ by $\tilde{x} \equiv x\delta$ and $u(\tilde{x}, \tau) \equiv h^{1/4}(\tilde{x})\eta(\tilde{x}, \tau)$. We will therefore seek solutions to the following initial value problem

$$u_{\tilde{x}} + \frac{\nu}{6}h^{1/2}u_{\tau\tau\tau} + \frac{3}{2}\epsilon h^{-\frac{7}{4}}uu_\tau = 0 \tag{2}$$

$$u(0,\tau) = F(\tau),$$

where $\nu \equiv \mu^2/\delta$, $\epsilon \equiv \alpha/\delta$, F is some prescribed, sufficiently smooth function of τ and $h = h(x\delta) = h(\tilde{x})$. The solutions obtained here are expected to be valid when $\epsilon = o(1)$. The parameter ν is required to be bounded at most; i.e., $\nu = 0(1)$. The results obtained will also be valid for the case $\mu^2 = 0(\alpha)$, i.e., $\nu = 0(\epsilon) = o(1)$; thus, this theory may also describe the shoaling of a solitary wave. In the case of a constant slope beach having a 1:100 rate of depth change and an initial depth of 30m, a solitary wave of amplitude 0.3m will satisfy these conditions.

3 Asymptotic Solutions

We first seek solutions to (2) that are valid for $h \neq 0$, i.e., $\tilde{x} \neq 1$. We therefore consider an outer or off-shore expansion

$$u = U_0(\tilde{x}, \tau; \nu) + 0(\epsilon).$$

Substitution of this in (2) shows that U_0 satisfies

$$U_{0\tilde{x}} + \frac{\nu h^{1/2}}{6}U_{0\tau\tau\tau} = 0$$

$$U_0(0,\tau) = F(\tau).$$

If we define

$$z \equiv \int_0^{\tilde{x}} h^{1/2}(p)\,dp,$$

where $0 \le z \le \int_0^1 h^{1/2}(p)\,dp$ when $0 \le \tilde{x} \le 1$, we can convert this to an equivalent flat-bottom problem,

$$U_{0z} + \frac{\nu}{6}U_{0\tau\tau\tau} = 0$$

$$U_0(0,\tau) = F(\tau).$$

When $F(\tau) \equiv \cos\tau$, it can be shown that a solution is

$$U_0(\tilde{x}, \tau) = \cos T, \tag{3}$$

where $T \equiv \tau + (\nu/6)z = \tau + (\nu/6)\int_0^{\tilde{x}} h^{1/2}(p)\,dp$. If we assume that U_0 and therefore F approach zero sufficiently fast as $\tau \to \pm\infty$, Fourier transforms may be used to obtain fairly general solutions for U_0; these are

$$U_0(z,\tau) = \frac{1}{\sqrt{2\Pi}}\int_{-\infty}^{\infty} f(p)e^{-ip(\tau + (\nu/6)zp^2)}\,dp \tag{4}$$

where $f(p)$ is the Fourier transform of $F(\tau)$. The convolution theorem may be used to show that

$$U_0(z,\tau) = \left(\frac{2}{\nu z}\right)^{1/3}\int_{-\infty}^{\infty} F(\eta)Ai\left[\left(\frac{2}{\nu z}\right)^{1/3}(\tau - \eta)\right]d\eta \tag{5}$$

where Ai is the Airy integral defined by

$$Ai(w) \equiv \frac{1}{2\Pi}\int_{-\infty}^{\infty} e^{i(sw + \frac{1}{3}s^3)}\,ds.$$

The off-shore solution is particularly simple when ν is also

Downloaded 02 May 2010 to 171.66.16.54. Redistribution subject to ASME license or copyright; see http://www.asme.org/terms/Terms_Use.cfm

small. These results are easily obtained by a formal expansion of (4) for small ν:

$$U_0(z,\tau) = F(\tau) - \frac{z\nu}{6} F'''(\tau) + 0(\nu^2) \approx F(\tau),$$

where the inversions

$$F(\tau) = \frac{1}{\sqrt{2\Pi}} \int_{-\infty}^{\infty} f(p) e^{-ip\tau} dp$$

$$F'''(\tau) = \frac{1}{\sqrt{2\Pi}} \int_{-\infty}^{\infty} [ip^3 f(p)] e^{-ip\tau} dp,$$

have been used. The cosine wave yields similar results, viz, $U_0 \approx \cos\tau$. Thus, when $\nu = 0(\epsilon) = o(1)$ dispersive effects can be neglected over this part of the propagation and the wave evolution is correctly described by the linear long wave theory of Green, see, e.g., Lamb [12, Section 185]; note that this includes the important special case of a solitary wave. When $\nu = 0(1)$, the dispersion is noticeable when $\tilde{x} = 0(1)$ and the initial waveform is modified according to (5).

If higher order terms in this small ϵ expansion are examined, we find that this perturbation scheme breaks down as $\tilde{x} \to 1$. We shall therefore seek a second approximation to (2) which is valid near the shore. To do this we define a near-shore or inner variable

$$\hat{x} \equiv \frac{\tilde{x} - 1}{\Delta} \tag{6}$$

as well as an inner expansion

$$u = u_0(\hat{x}, \tau) - o(1).$$

Here $\hat{x}$ is of order one in the inner region and the scaling factor $\Delta = \Delta(\epsilon) = o(1)$ will be determined in the course of the analysis.

In the following it will also be useful to have an explicit expansion of $h = h(\tilde{x})$ near $\tilde{x} = 1$. We will assume that this is of the form

$$h(\tilde{x}) = h(1 + \Delta\tilde{x}) \sim \Delta^m \hat{h}(\hat{x}) + o(\Delta^m) \tag{7}$$

for $\Delta = o(1)$ and $\hat{x} = 0(1)$. The exponent $m > 0$ and function $\hat{h}(\hat{x})$ will depend on the particular bathymetry considered. For example, the closed beach having

$$h(\tilde{x}) \sim (1 - \tilde{x})^n \quad \text{as} \quad \tilde{x} \to 1$$

will correspond to an $m = n$ and $\hat{h}(\tilde{x}) \equiv (-\tilde{x})^n$. For a shelf given by

$$h(\tilde{x}) \equiv \begin{cases} 1 & \text{for} \quad \tilde{x} \le 0 \\ \dfrac{1+d}{2} + \dfrac{1-d}{2} \cos\Pi\tilde{x} & \text{for} \quad 0 \le \tilde{x} \le 1 \\ d & \text{for} \quad \tilde{x} \ge 1, \end{cases}$$

where we assume that $d = 0(\Delta^2) = o(1)$, we find that $m = 2$ and

$$h(\hat{x}) = \begin{cases} \hat{d} + \dfrac{\Pi^2 \hat{x}^2}{4} & \text{for} \quad \hat{x} \le 0 \\ \hat{d} & \text{for} \quad \hat{x} \ge 0, \end{cases}$$

where $\hat{d} \equiv \Delta^{-2} d = 0(1)$.

When the inner expansion and relations (6) and (7) are substituted in (2) and when we seek a reasonable balance of terms, we find that

$$\Delta = \epsilon^{\frac{4}{7m-4}} \quad \text{and} \quad m > \frac{4}{7}$$

and that u_0 must satisfy

$$u_{0\hat{x}} + \frac{3}{2} \hat{h}^{-\frac{7}{4}} u_0 u_{0\tau} = 0.$$

For the sake of convenience, we have replaced the order symbol with an equality in the expression for Δ. The equation for u_0 is immediately recognized as a variable coefficient version of the inviscid Burger's equation. Its solution is easily obtained by the method of characteristics; this may be written

$$u_0(\hat{x}, \tau) = G(\tau_\infty) \tag{8}$$

on lines

$$\tau = \tau_\infty + \frac{3}{2} G(\tau_\infty) I(\hat{x}),$$

where

$$I(\hat{x}) \equiv \int_{-\infty}^{\hat{x}} \hat{h}^{-\frac{7}{4}}(p)\, dp \tag{9}$$

and G is, at this stage, arbitrary. An alternative, implicit form of this solution may be obtained by combining equations (8) to yield

$$u_0(\hat{x}, \tau) = G\left(\tau - \frac{3}{2} G I(\hat{x})\right).$$

Our description of the near-shore region is complete once the function G is determined. This will be done by requiring that u_0 match the off-shore solution (5). The formalism of the method of matched asymptotic expansions will be used, see, e.g., Van Dyke [13]. When the near-shore solution

$$u = G\left(\tau - \frac{3}{2} G I(\hat{x})\right) + o(1)$$

is recast in the off-shore variables and expanded for $\epsilon \to 0$ and $\hat{x}$ fixed we have

$$u \sim G(\tau),$$

since $I(\hat{x}) = I\left(\dfrac{\hat{x}-1}{\Delta}\right) \to 0$ as $\Delta = \epsilon^{\frac{4}{7m-4}} \to 0$. When the off-shore solution

$$u = \left(\frac{2}{\nu z}\right)^{1/3} \int_{-\infty}^{\infty} F(\eta) Ai\left[\left(\frac{2}{\nu z}\right)^{1/3} (\tau - \eta)\right] d\eta + o(1)$$

is recast in the near-shore variables and expanded for $\hat{x}$ fixed and $\epsilon \to 0$, we have

$$u \sim \left(\frac{2}{\nu z_1}\right)^{1/3} \int_{-\infty}^{\infty} F(\eta) Ai\left[\left(\frac{2}{\nu z_1}\right)^{1/3} (\tau - \eta)\right] d\eta,$$

where $z_1 \equiv z(1) = \int_0^1 h^{1/2}(p)\, dp$, which is always bounded. The usual matching principle requires that these match; thus

$$G(\tau) \equiv \left(\frac{2}{\nu z_1}\right)^{1/3} \int_{-\infty}^{\infty} F(\eta) Ai\left[\left(\frac{2}{\nu z_1}\right)^{1/3} (\tau - \eta)\right] d\eta \tag{10}$$

for all τ. Thus, near the shore, $u \approx u_0$, where u_0 can be calculated from equations (8), (9), and (10); analogous results may be obtained for the wavetrain solution having $F(\tau) = \cos\tau$. In the case $\nu = o(1)$, it is easily seen that $G(\tau) = F(\tau)$ and therefore

$$u = F(\tau_\infty)$$

$$\text{on} \quad \tau = \tau_\infty + \frac{3}{2} F(\tau_\infty) I(\hat{x}), \tag{11}$$

to lowest order in ν and ϵ. As a check, we have carried out

Downloaded 02 May 2010 to 171.66.16.54. Redistribution subject to ASME license or copyright; see http://www.asme.org/terms/Terms_Use.cfm

higher order expansions and matchings; the results presented here are seen to be completely consistent with these.

It is well known that the waveform described by (8)–(10) will steepen at the front face or faces and ultimately becomes triple-valued; this is due to the convergence and crossing of the characteristic lines in (8). As pointed out in the introduction, we refer to the point at which the slope, i.e., $u_{0\tau}$, first becomes infinite as the breaking point. The characteristic lines in (8) may be used to show that this occurs at a point or points $\hat{x}_b$ given by the implicit formula

$$I(\hat{x}_b) \equiv \frac{2}{3} \frac{1}{(-G')|_{\max}}. \tag{12}$$

Here $G' \equiv dG(\tau)/d\tau$ and $(-G')|_{\max}$ is the maximum value of $-G'$; typically, although not necessarily, this is an inflection point. For most bathymetries I is a monotonic positive function of $\hat{x}$. Thus, only positive values of $(-G')|_{\max}$ will yield solutions for $\hat{x}_b$; that is, breaking only occurs at portions of the wave having $u_\tau < 0$.

A concise statement of the breaking condition is that the incoming wave develops an infinite slope when

$$\tilde{x} - 1 = x\delta - 1 = 0\left(\epsilon^{\frac{4}{7m-4}}\right)$$

and depth $h_b = 0(\epsilon^{4m/7m-4})$, where (7) has been used. The actual wave height is given by $\alpha\ h_0 h^{-1/4}\ u(\hat{x},\tau)$ and is therefore of order $h_0\ \alpha^{6m-4/7m-4}\ \delta^{m/7m-4}$ at breaking; here the fact that $u = 0(1)$ has been used. For a beach of constant slope, i.e., $h = 1 - x\delta$, $m \equiv 1$ and the previous wave height estimate becomes $h_0\ \alpha^{2/3}\ \delta^{1/3} = o(h_0)$.

It is also of interest to point out that when $\nu = 0(1)$, these results will depend on ν through the incoming waveform, see, for example, (12). When $\nu = o(1)$, e.g., a solitary wave, $G(\tau) \equiv F(\tau)$ and the near-shore solution is independent of ν and therefore $\mu \equiv h_0/\lambda$. Thus, when $\nu = o(1)$, dispersive effects are negligible over the whole flow field and, for this particular case, solutions to the initial value problem (2) can be approximated to lowest order by those of Burger's equation.

4 Numerical Results

In this section, we compare numerical solutions of (2) to our asymptotic results. Cramer, McCown, and Bowman [14] applied the finite difference scheme developed by Zabusky and Kruskal [15], Vliegenthart [16], and Johnson [5] to cases similar to those considered here. However, as the wave steepened in the near-shore region, oscillations and spikes were generated which were seen to be purely numerical in nature. In the present study these difficulties are eliminated through use of the implicit scheme described in the following.

The basic approach was to first recast equation (2) in a finite difference form. The $\tilde{x}$ derivative was forward differenced while the derivatives with respect to τ were central differenced; the nonlinear term uu_τ was written

$$u_{i,j+1} \frac{u_{i+1,j+1} - u_{i-1,j+1}}{2\Delta\tau},$$

where the i and j refers to the τ and $\tilde{x}$ directions and $\Delta\tau$ denotes the step size in τ. Equation (2) can now be written

$$-C_j u_{i-2,j+1} + D_{i,j} u_{i-1,j+1} + u_{i,j+1} - D_{i,j} u_{i+1,j+1} + C_j u_{i+2,j+1} = u_{i,j}, \tag{13}$$

where

$$C_j \equiv \frac{\nu}{12} h_j^{1/2} \frac{\Delta\tilde{x}}{(\Delta\tau)^3},$$

$$D_{i,j} \equiv 2C_j - \frac{3}{4}\epsilon h_j^{-7/4} \frac{\Delta\tilde{x}}{\Delta\tau} u_{i,j+1},$$

$$h_j \equiv h(j\Delta\tilde{x})$$

and $\Delta\tilde{x}$ is the step size in the $\tilde{x}$ direction. At each $\tilde{x}$ step, equation (13) was solved for $u_{i,j+1}$; because of the nonlinearity associated with the coefficients $D_{i,j}$, this was carried out iteratively. In all the results presented next, step sizes of $\Delta\tilde{x} = 0.001$ and $\Delta\tau = 0.1$ were found to yield sufficient accuracy.

One of the simplest and most interesting cases involves waves of the solitary wave type. We will therefore take our initial condition to be

$$F(\tau) = \operatorname{sech}^2\tau$$

and to illustrate the effect of shoaling, we have taken $\nu = 4/3$ $\epsilon = 0(1)$. When the depth is uniform, i.e., $h(\tilde{x}) \equiv 1$, the resultant wave will ultimately fission; however, as predicted in the preceding section, the wave slope becomes infinite long before this can occur. For the sake of simplicity, the beach slope was taken to be constant. That is,

$$h = \begin{cases} 1 & \tilde{x} \le 0 \\ 1 - \tilde{x} & 0 \le \tilde{x} \le 1; \end{cases}$$

thus, the shore is located at $\tilde{x} = 1$ or $x = \delta^{-1}$.

In each case, the asymptotic solution has been calculated from equations (11). For the beach and wave profile described in the foregoing, these may be written

$$u(\tilde{x},\tau) = \operatorname{sech}^2\tau_\infty$$

$$\tau = \tau_\infty + 2(-\hat{x})^{-\frac{3}{4}} \operatorname{sech}^2\tau_\infty, \tag{14}$$

where τ_∞ may be regarded as a parameter and $\hat{x} = (\tilde{x} - 1)$ $\epsilon^{-4/3}$.

Our theory is not valid after the wave slope becomes infinite. We have therefore terminated the computation when such infinite slopes are predicted by (12). For the case considered here, the value of h for which this occurs was found to be

$$h_b \equiv 1 - \tilde{x}_b = (2\epsilon|F'|_{\max})^{\frac{4}{3}}$$

$$h_b = \left(\frac{8}{3\sqrt{3}}\epsilon\right)^{\frac{4}{3}}, \tag{15}$$

since $|F'|_{\max} = \frac{4}{3\sqrt{3}}$ for this case.

In Figs. 2–4, the evolution of a wave having ϵ equal to 0.100, 0.050, and 0.025 has been depicted. The solid lines are the numerical solutions to (2) and the dotted lines the asymptotic theory. For each value of ϵ, the last figure corresponds to the break point given by (15); i.e., the point where the asymptotic theory predicts infinite slopes. Even in these extreme cases, the numerical oscillations found by [14] were eliminated through use of our implicit scheme. To check the ability of our scheme to compute solutions with relatively steep slopes, we applied this to appropriately chosen Burger equations and then compared the results with exact solutions obtained by the method of characteristics. Up to, but, obviously not beyond the break point, these agree very well and we conclude that the main discrepancy seen in Figs. 2–4 is due to the errors inherent in the asymptotic approximation.

For the case $\epsilon = 0.100$, inspection of Fig. 2 shows that the approximation provided by the asymptotic theory is not particularly good. However, as the small parameter ϵ is decreased, the agreement with the numerical solutions becomes better and better until at $\epsilon = 0.025$, the agreement is very good over virtually all the waveform. We therefore conclude that in the limit $\epsilon \to 0$, the asymptotic theory gives a valid approximation to equation (2) up to the predicted break point.

Downloaded 02 May 2010 to 171.66.16.54. Redistribution subject to ASME license or copyright; see http://www.asme.org/terms/Terms_Use.cfm

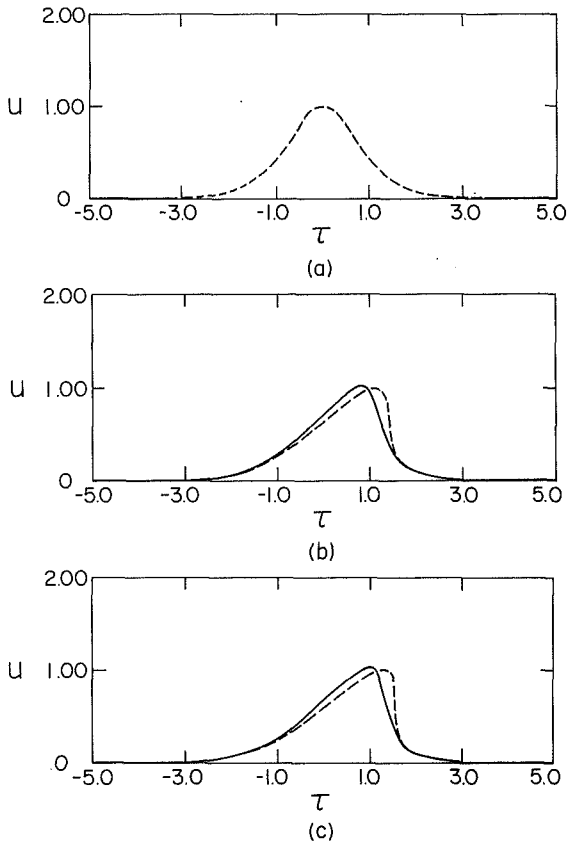


Fig. 2 Wave evolution for solitary wave profile $u(0, \tau) = \text{sech}^2 \tau$ and $\epsilon = 0.100$, $\nu = 0.133$. Asymptotic theory ----, numerical solution ——. (a) $\bar{x} = 0$, (b) $\bar{x} = 0.90$, (c) $\bar{x} = 0.918$.

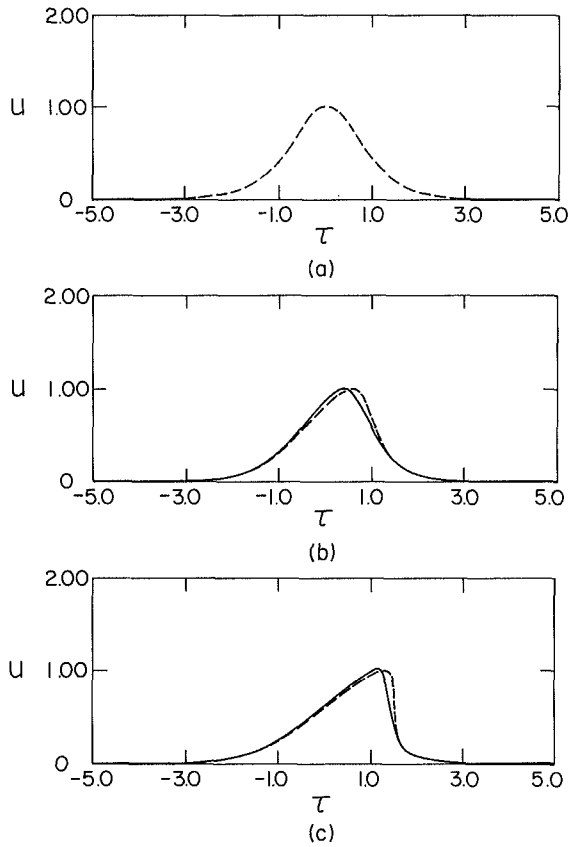


Fig. 3 Wave evolution for $\epsilon = 0.050$, $\nu = 0.067$. Asymptotic theory ----, numerical solution ——. (a) $\bar{x} = 0$, (b) $\bar{x} = 0.900$, (c) $\bar{x} = 0.967$.

5 Discussion of Related Studies

The present study is primarily concerned with solutions to the variable coefficient Korteweg-deVries equation. In this section we compare these results with previous investigations of the Korteweg-deVries equation as well as more general theories.

The analytical studies of Johnson [1, 4–5] and Tappert and Zabusky [6] resemble ours in the sense that each used the variable coefficient Korteweg-deVries equation as a starting point. The fact that the wave behavior observed differs is because different choices of the small parameters α and δ were taken. In each of the previous investigations, solitary waves were considered so that α was always chosen to be of order μ^2. When

$$\delta << \alpha << 1, \quad \text{i.e.,} \quad \epsilon >> 1,$$

the solitary wave could adjust to the relatively slow depth changes. This case was described by Johnson [1] who showed that the wave amplitude varied inversely with the undisturbed depth. The basic wave profile was essentially unchanged although a long flat tail was generated. Svendsen and Hansen [3] and Ostrovskiy and Pelinovskiy [2] have considered the analogous case of slowly varying cnoidal waves. When

$$\delta = 0(\alpha), \quad \text{i.e.,} \quad \epsilon = 0(1),$$

the solitary wave is not able to adjust and will fission as the depth decreases. This has been computed by Johnson [5] using the Korteweg-deVries equation and Madsen and Mei [17] using Boussinesq equations.

Finally, if

$$\alpha << \delta << 1, \quad \text{i.e.,} \quad \epsilon = o(1),$$

the depth change is so rapid relative to the response time of

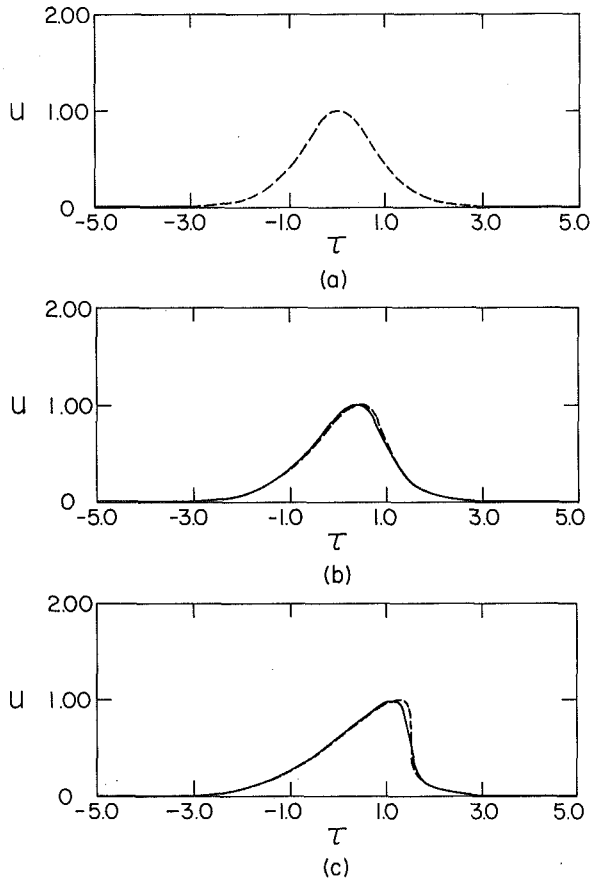


Fig. 4 Wave evolution for $\epsilon = 0.025$, $\nu = 0.033$. Asymptotic theory ----, numerical solution ——. (a) $\bar{x} = 0$, (b) $\bar{x} = 0.950$, (c) $\bar{x} = 0.987$.

Downloaded 02 May 2010 to 171.66.16.54. Redistribution subject to ASME license or copyright; see http://www.asme.org/terms/Terms_Use.cfm

the solitary wave, the variation of the wave will simply be that of the linear long wave theory. If the depth variation corresponds to a shelf, the wave will arrive on the shelf with the Green's law, i.e., $h^{-1/4}$, amplification and corresponding length change. Because the relation between the amplitude to length no longer corresponds to a solitary wave, further propagation will result in fissioning at times of order α^{-1}. This process has been described in detail by Johnson [4] and Tappert and Zabusky [6]. However, if the depth goes to zero, i.e., a closed beach, or the shelf depth is sufficiently small, the processes described in the present paper will take place. Because of the singularity associated with the nonlinear term in (2), the wave can no longer be described by the $\nu \equiv 0$, $\epsilon \equiv 0$ version of (2), at least when h is small. The dominance of the nonlinear term then results in the strong steepening described in the previous sections. Thus, the work presented here uses the same parameter range examined by [4, 6]. However, it differs because a near-shore region where the depth is small is analyzed. Furthermore, solutions corresponding to $\nu = 0(1)$ were given in addition to the $\nu = o(1)$ solutions corresponding to solitary waves.

An analogous description of changing wave type has been given by Flick [10] who extended the work of Svendsen and Brink-Kjaer [18] to relate deep water Stokes waves to a shallow water cnoidal wavetrain; in contrast to the work presented here, the bottom was taken to vary so slowly that each wavetrain could be described by the flat-bottom theory. A second frequently quoted study is due to Carrier [19] which gives an extensive description of the off-shore wave evolution through an analysis of the linearized equations. The near-shore behavior was assumed to be governed by the nonlinear nondispersive theory. The initial condition for this was obtained by equating the linear and nonlinear solutions, although no specification of the point is given. The work presented here is narrower in scope but simultaneously goes further in that we illustrate the dependence of the observed behavior not only on the small parameters α, μ, and δ but more importantly, on their relative values. This fact can be seen by comparing the parameter ranges employed by [1, 4–6]. Further evidence of the importance of the relative values of the parameters can be seen by examining the large ν solutions to (2). It is expected that it can be shown that this limit corresponds to transitions between shoaling Stokes' wavetrains and shoaling cnoidal wavetrains.

Although this paper is primarily concerned with solutions to (2), it is of interest to determine the relation of these solutions to those of the exact water wave equations. One of the most important assumptions made in the derivation of (1) is that the ratios associated with the initial parameters α, μ, and δ are always small. That is, we assume that the wave amplitude is always small compared to the depth and that the length of the wave is large compared to the depth and small compared to a local measure of the bathymetry scale length, i.e., $|(1/H)\ dH(\tilde{x})/d\tilde{x}|^{-1}$. A second important assumption is that we can ignore the reflected waves generated by the shoaling. In most theories involving equation (1), these can be ignored once the small δ is satisfied. In the case of wavetrains, Kajiura [20] has shown that destructive interference plays a significant role in further reducing the amplitude of these. Although it is expected that most of these assumptions will fail sufficiently close to shore, our only interest here is in the description of the wave evolution up to the break point; thus, the key question in the present study is whether these ratios and waves remain small up to the point at which breaking occurs.

To shed some light on this question, Cramer et al. [14] have combined the solutions obtained here with the appropriate form of the linearized long wave equations to derive a set of conditions under which (2) is a reasonable approximation to the exact water wave equations. When $m < 2$, it was shown that in addition to requiring that $\alpha << \delta$, we need to require that

$$\delta << \alpha^{\frac{2}{5}\frac{2-m}{m}}.$$

and when $m > 2$, no additional constraints are necessary. However, these are local conditions analogous to those given by [3, 21] and say nothing about cumulative effects, the most important of these being related to the reflected waves. Although we can find no other studies that address this particular question, recent numerical investigations do suggest that our results can provide a good approximation to shoaling waves. Peregrine [22] has solved a set of Boussinesq equations to describe a solitary wave as it propagates over a gently sloping beach. His results are seen to be in qualitative agreement with those presented here. In addition, the reflected wave was seen to be at least an order of magnitude smaller than the main wave and amplification rate was also essentially that predicted here. Chwang and Wu [23] have also used Boussinesq equations to study the shoaling of cylindrical solitary waves. Again, we see an amplification of the wave followed by a sharp steepening near shore. The wave was followed by a very low amplitude tail, again suggesting that reflections are negligible; however, this conclusion is obscured somewhat by the fact that part of this tail is due to the axisymmetric geometry. The experimental studies of Kishi and Saeki [9] also confirm this tendency.

To put our results in perspective, we therefore need to make two points. First, we feel the asymptotic analysis presented in Section 3 and verified in Section 4 provides valid approximate solutions to the variable coefficient Korteweg-deVries equation. These complement the previous studies of this equation by taking into account the singularity associated with vanishing h and shown how this can trigger a change in wave type. Secondly, although previous numerical and experimental investigations clearly indicate that our results give the correct qualitative picture of shoaling waves, we feel the question of the precise relation of the present work to solutions of the exact water wave equations remains open; this is primarily due to the commonly employed assumption which neglects reflected waves. To answer this, further numerical and experimental work needs to be carried out. A reasonable numerical approach would be to apply the schemes employed by [17, 22, 23, or 24] to the Boussinesq equations.

6 Conclusions

The method of matched asymptotic expansions has been used to obtain approximate solutions of the variable coefficient Korteweg-deVries equation. Under the conditions stated, the depth variation was rapid enough to change the basic wave type. Over much of the propagation nonlinear effects were negligible and the wave evolution was given by the outer or off-shore solution (5). Because of the amplification and effective lengthening of the wave, we find that, near the shore, dispersive effects are negligible and nonlinear effects predominate. This near-shore solution can be calculated from equations (8)–(10) and the break point is given by (12). The numerical computations presented in Section 4 verify that our analytical results are a valid asymptotic approximation to exact solutions of (2), in the sense that the latter will approach our solutions in the limit of vanishing $\epsilon \equiv \alpha/\delta$, at least up to the predicted break point.

The importance of the present study is that it shows how the variable coefficient Korteweg-deVries equation can be used to model the change in wave type from a linear, possibly dispersive, wave to a nondispersive nonlinear wave near the shore and has delineated the conditions under which this may occur.

Finally, we note that once our theory predicts infinite wave

Downloaded 02 May 2010 to 171.66.16.54. Redistribution subject to ASME license or copyright; see http://www.asme.org/terms/Terms_Use.cfm

slopes, the approximations leading to the original Korteweg-deVries equation break down and a more general theory is needed to compute the details of breaking. In this respect, we have followed previous investigators, see, e.g., [8, 22, 21, and 23] in applying long wave theory to describe the approach to wave breaking and should be regarded in the same light as these studies. Furthermore, the continuation of the computation would be carried out in essentially the same manner as for these theories.

Acknowledgment

This work was initiated and carried out while the first author, M. S. Cramer, participated in the ASEE/NAVY Summer Faculty Research Program at the NRL. The fourth author, B. E. McCown, was supported by NRL under contract number N00173-80-M-7172.

References

1 Johnson, R. S., "On an Asymptotic Solution of the Korteweg-deVries Equation With Slowly Varying Coefficients," *J. Fluid Mech.*, Vol. 60, 1973, pp. 813–824.

2 Ostrovskiy, L. A., and Pelinovskiy, E. N., "Wave Transformation on the Surface of a Fluid of Variable Depth," *Atmospheric and Ocean Physics*, Vol. 6, 1970, pp. 934–939.

3 Svendsen, I. A., and Hansen, J. B., "On the Deformation of Periodic Long Waves Over a Gently Sloping Bottom," *J. Fluid Mech.*, Vol. 87, 1978, pp. 433–448.

4 Johnson, R. S., "On the Development of a Solitary Wave Moving Over an Uneven Bottom," *Proc. Camb. Phil. Soc.*, Vol. 73, 1973, pp. 183–203.

5 Johnson, R. S., "Some Numerical Solutions of a Variable-Coefficient Korteweg-deVries Equation (With Applications to Solitary Wave Development on a Shelf)," *J. Fluid Mech.*, Vol. 54, 1972, pp. 81–91.

6 Tappert, F. D., and Zabusky, N. J., "Gradient-Induced Fission of Solitons," *Phys. Rev. Lett.*, Vol. 27, 1971, pp. 1774–1776.

7 Ursell, F., "The Long-Wave Paradox in the Theory of Gravity Waves," *Proc. Camb. Phil. Soc.*, Vol. 49, 1953, pp. 685–694.

8 Amein, M., "A Method for Determining the Behavior of Long Waves Climbing a Sloping Beach," *J. Geophysical Res.*, Vol. 71, 1966, pp. 401–410.

9 Kishi, T., and Saeki, H., "The Shoaling, Breaking and Run-up of the Solitary Wave on Impermeable Rough Slopes," *Proc. 10th Conf. on Coastal Eng.*, 1966, pp. 322–348.

10 Flick, R. E., *Study of Shoaling Waves in the Laboratory*, Ph.D. Dissertation, 1978, UCSD, San Diego.

11 Lamb, G. L., Jr., *Elements of Soliton Theory*, Wiley-Interscience, New York, 1980.

12 Lamb, H., *Hydrodynamics*, Dover, 1932.

13 Van Dyke, M., *Perturbation Methods in Fluid Mechanics*, Parabolic Press, 1975.

14 Cramer, M. S., Bowman, M. E., and McCown, B. E., *NRL Memorandum Report 4444*, 1981.

15 Zabusky, N. J., and Kruskal, M. D., "Interaction of Solitons in a Collisionless Plasma and the Recurrence of Initial States," *Phys. Rev. Lett.*, Vol. 15, 1965, pp. 240–243.

16 Vliegenthart, A. C., "On Finite-Difference Methods for the Korteweg-deVries Equation," *J. Eng. Math.*, Vol. 5, 1971, pp. 137–155.

17 Madsen, O. S., and Mei, C. C., "The Transformation of a Solitary Wave Over an Uneven Bottom," *J. Fluid Mech.*, Vol. 39, 1969, pp. 781–791.

18 Svendsen, I. A., and Brink-Kjaer, O., "Shoaling of Cnoidal Waves," *Proc. 13th Conf. on Coastal Engr.*, 1972, pp. 365–383.

19 Carrier, G. F., "Gravity Waves in Water of Variable Depth," *J. Fluid Mech.*, Vol. 24, 1966, pp. 641–659.

20 Kajiura, K., "On the Partial Reflection of Water Waves Passing Over a Bottom of Variable Depth," *International Union of Geodesy and Geophysics, Monograph 24, Tsunami Symposia*, 1961, pp. 206–230.

21 Varley, E., Venkataraman, R., and Cumberbatch, E., "The Propagation of Large Amplitude Tsunamis Across a Basin of Changing Depth, Part I. Off-Shore Behavior," *J. Fluid Mech.*, Vol. 49, 1971, pp. 775–801.

22 Peregrine, D. H., "Long Waves on a Beach," *J. Fluid Mech.*, Vol. 27, 1967, pp. 815–827.

23 Chwang, A. T., and Wu, T. Y., "Cylindrical Solitary Waves," *Waves in Water of Variable Depth*, Springer-Verlag.

24 Witting, J. M., *NRL Memorandum Report 5001*, 1982.

Downloaded 02 May 2010 to 171.66.16.54. Redistribution subject to ASME license or copyright; see http://www.asme.org/terms/Terms_Use.cfm

The Effect of Inertia in Lubrication Flow Including Entrance and Initial Conditions

J. A. Tichy
Associate Professor of
Mechanical Engineering,
Rensselaer Polytechnic Institute,
Troy, N.Y. 12181
Mem. ASME

P. Bourgin
Laboratoire de Mécanique des Fluides,
Ecole Centrale de Lyon,
Ecully, France 69130
Assoc. Mem. ASME

This study is concerned with the influence of fluid inertia in thin film steady or transient laminar flows, emphasizing the role of initial conditions and inlet boundary conditions. Most existing studies implicitly omit these effects due to the method of formulation or the type of problem studied. In the present study, linearization for the convective inertia terms is used to transform the problem to a coordinate system which results in a simple diffusion equation. Closed-form solutions are obtained, considering initial or entrance conditions in the classical manner. Predictions are tested against cases for which solutions exist in the literature and against a numerical solution and excellent agreement is found. For simple squeeze films, large discrepancies from lubrication theory are found at short times following the start-up, or at moderate Reynolds numbers. In the steady flow case, fluid is assumed to enter the bearing with a slug flow profile. The inlet pressure is determined by coupling the bearing flow with the upstream inviscid flow. Large discrepancies from lubrication theory are found at Reynolds numbers where the lubrication theory was previously thought to be satisfactory. The load may increase or decrease, depending on the upstream conditions.

Introduction

This paper is concerned with the effect of fluid inertia in thin, lubricating films. The flow is incompressible, two-dimensional, and both the transient and steady-state cases are considered. The general idea of the present paper is to seek linearized approximations for the inertia terms of the Navier-Stokes equations, and to solve the resulting equations by conventional means. Such a solution was very recently obtained by Tuck and Bentwich [1] (October 1983) for the steady plane slider bearing and their results compare favorably with a numerical solution. In the present paper, the Tuck and Bentwich method is modified slightly for steady flow and generalized for the unsteady case. An alternative physical explanation for the linearization is also put forth. An important consideration is that entrance and initial conditions must be carefully applied.

In steady lubrication applications, fluid inertia effects are thought to be present only in fairly extreme conditions. However, such extreme conditions are becoming more common due to the higher speeds of modern machinery and the use of low-viscosity lubricants in many specialized applications. For the transient case, the importance of fluid inertia in *typical* squeeze film bearing operation is becoming widely recognized [2, 3].

Contributed by the Applied Mechanics Division and presented at the Winter Annual Meeting, Miami, Fla., November 17–21, 1985 of THE AMERICAN SOCIETY OF MECHANICAL ENGINEERS.

Discussion on this paper should be addressed to the Editorial Department, ASME, United Engineering Center, 345 East 47th Street, New York, N.Y. 10017, and will be accepted until two months after final publication of the paper itself in the JOURNAL OF APPLIED MECHANICS. Manuscript received by ASME Applied Mechanics Division, July, 1984. Paper No. 85-WA/APM-1.

Since the governing Navier-Stokes equations are highly nonlinear, analytical solutions can only be obtained in limiting cases or by approximation. One may categorize most of the existing pertinent literature based on solution technique, as follows: (*a*) small Reynolds number perturbation, and (*b*) averaging the momentum across the film to eliminate the nonlinearities and the cross-film dependence. In this paper we use the term Reynolds number to mean the usual "modified" or "reduced" Reynolds number of lubrication analysis.

Some literature in both categories is now briefly discussed. The Reynolds number perturbation technique for steady flow in slider bearings is presented in Pinkus and Sternlicht [4]. Perturbation solutions for various types of squeezing flow are presented by Ishizawa [5] (parallel disks), Tichy [6] (parallel one-dimensional bearing), and many others.

Results from various cross-film averaging are due to Milne [7] (one-dimensional steady bearings), Fritz [8] (one-dimensional transient bearings), Smalley et al. [9] (two-dimensional steady bearings), and Elrod et al. [10] (two-dimensional transient bearings). There are many others. In many cases the details of evaluating the inertia integrals may vary but the basic technique is the same.

The approximate methods listed in the foregoing cannot properly consider the problem of entrance conditions or initial conditions. In the case of small Reynolds number perturbation studies, only a small correction to lubrication theory can, in priciple, be made. One is not free to choose the inlet or initial conditions. This situation is not a problem if the Reynolds number is in fact small—indeed the perturbation solution may be regarded as "exact" in this case. However,

Copyright © 1985 by ASME
Downloaded 02 May 2010 to 171.66.16.54. Redistribution subject to ASME license or copyright; see http://www.asme.org/terms/Terms_Use.cfm

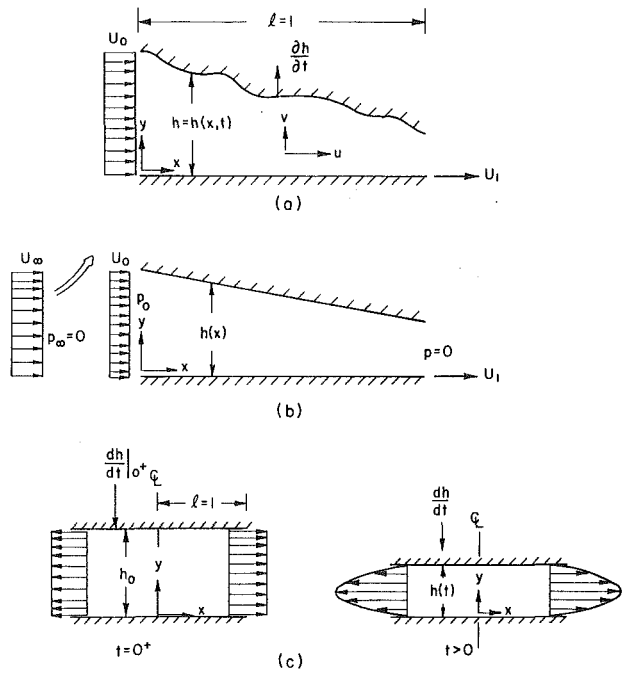


Fig. 1 Thin film flow geometry. (*a*) General case; (*b*) steady case, plane slider; (*c*) pure squeeze case, sudden start.

investigators are wont to extend the perturbation results to modified Reynolds numbers of, say, 10 (hardly a small number) to infer conclusions regarding load. Due to the implicit omission of entrance and flow development effects, such conclusions may be suspect.

The second method of approximation, cross-film averaging, will not properly account for entrance or initial condition effects, even though the filmwise spatial derivative or time derivative may be retained. It is the development from potential flow to viscous flow that produces the discrepancy from lubrication theory. Cross-film averaging tends to wipe out the differences from one profile to another, other than the total momentum flux.

Inlet pressure conditions have been considered by Pan [11], Constantinescu et al. [12], and Tipei [13] but they have not coupled their analyses with a solution for the complete bearing, including flow development. In Elrod's paper [10], entrance effects are discussed and surely appreciated, but not taken into account per se. Among the few papers considering *initial* conditions in unsteady flow are those due to Jones and Wilson [14] and Hamza [15], who develop short-time asymptotic solutions. We believe that due to flow entrance or initial conditions, the inertia effect may become important at more moderate conditions than was previously thought.

In fluid mechanics, since Schlichting's classical study of entry flow in a channel [16], there is a long tradition of assuming that the entrance velocity condition to a narrow channel is the uniform or "slug" flow profile. The fluid outside the gap may be treated as a potential flow, obeying Bernoulli's equation, which seems to be a reasonable assumption for lubrication in the absence of specific information concerning conditions outside the bearing. More recent work by Van Dyke [17] and Wilson [18] shows that there are theoretical difficulties with the uniform entrance assumption; specifically Schlichting's analysis must be properly considered as a downstream expansion, which is fortunately still accurate near the entrance. In the present approximate study of lubrication flows, however, we retain the slug profile entrance condition which is consistent with the linear diffusion-type equations obtained.

Analysis

Consider the combined sliding and squeezing two-dimensional laminar flow of a thin lubricating film; see Fig. 1. The usual governing continuity and momentum equations for the laminar incompressible flow of a Newtonian fluid are used here in dimensionless form:

$$\frac{\partial u}{\partial x}+\frac{\partial v}{\partial y}=0 \tag{1}$$

$$\mathrm{Re}\left(\frac{\partial u}{\partial t}+u\frac{\partial u}{\partial x}+v\frac{\partial u}{\partial y}\right)=-\frac{\partial p}{\partial x}+\frac{\partial^2 u}{\partial y^2} \tag{2}$$

$$0=\frac{\partial p}{\partial y}. \tag{3}$$

where x and y are coordinate directions along and across the film, u and v are the corresponding flow velocities, t is time, and p is fluid pressure. The symbol Re denotes the "modified" or reduced Reynolds number.

Tuck and Bentwich considered the steady problem, $\partial u/\partial t = 0$, and linearized the inertia terms with

$$\begin{aligned} u&=\tilde{u}+u_1 \qquad p=\tilde{p}+p_1 \\ v&=\tilde{v}+v_1 \end{aligned} \tag{4}$$

where $(\tilde{u}, \tilde{v}, \tilde{p})$ represents the inviscid solution. An inviscid solution must satisfy equations (1)–(3), omitting the $\partial^2 u/\partial y^2$ term, and on both surfaces must obey:

$$(\mathbf{V}_{\text{surface}}-\tilde{\mathbf{V}})\cdot\mathbf{n}=0 \tag{5}$$

where $\mathbf{n}$ is the unit normal vector to the surface. Quadratic terms such as $u_1\partial u_1/\partial x$ were neglected. If the following transformation is made

$$X=\int_0^x \frac{dx'}{h}, \tag{6a}$$

$$Y=\frac{y}{h(x)}, \tag{6b}$$

where h is the film thickness, the governing equations are approximated by a diffusion equation for the shear term $\partial u_1/\partial y$,

$$\left(\frac{\partial u_1}{\partial y}\right)_{YY}=\mathrm{Re}\left(\frac{\partial u_1}{\partial y}\right)_X \tag{7}$$

Tuck and Bentwich solved equation (7) by Laplace transform techniques and presented figures for the pressure profiles at several Reynolds numbers, compared to an "exact" numerical solution. An important feature of their analysis is that the inlet pressure and velocity conditions are coupled through the Bernoulli equation:

$$p(0)=\frac{\mathrm{Re}}{2}[1-U_0^2], \tag{8}$$

rather than specifying one or the other, assuming for the far upstream conditions $U_\infty = 1, p_\infty = 0$.

Let us generalize Tuck and Bentwich's method for an unsteady film $h = h(x, t)$ by approximating the inertia terms in the following way:

$$\frac{\partial u}{\partial t}+u\frac{\partial u}{\partial x}+v\frac{\partial u}{\partial y}\simeq\frac{\partial u}{\partial t}+\tilde{u}\frac{\partial u}{\partial x}+\tilde{v}\frac{\partial u}{\partial y}, \tag{9}$$

with $(\tilde{u}, \tilde{v}, \tilde{p})$ being the inviscid solution:

$$\tilde{u}=\frac{1}{h}\left[C(t)-\int_0^x\frac{\partial h}{\partial t}\,dx\right] \tag{10a}$$

$$\tilde{v}=\frac{y}{h}\left(\frac{\partial h}{\partial t}+\frac{\partial h}{\partial x}\tilde{u}\right) \tag{10b}$$

It is interesting to note that equation (10*a*) also represents the

Downloaded 02 May 2010 to 171.66.16.54. Redistribution subject to ASME license or copyright; see http://www.asme.org/terms/Terms_Use.cfm

average (across the film) of the inertialess velocity. In the inviscid case, the "constant" C is arbitrary, depending on the imposed velocity at the inlet ($x = 0$). However, if we consider equation (10a) to represent the inertialess velocity, then C equals $h_m/2$, where h_m is the film thickness at the zero pressure-gradient location. In either case, the $\bar{v}$ component, equation (10b), is determined from continuity.

We now seek a transformation

$$\xi = g(x,t) \quad \eta = y/h(x,t), \quad \tau = t \tag{11}$$

such that

$$\frac{Du}{Dt} \equiv \frac{\partial u}{\partial t} + \bar{u}\frac{\partial u}{\partial x} + \bar{v}\frac{\partial u}{\partial y} = \frac{\partial u}{\partial \tau}. \tag{12}$$

If the function g is defined by

$$\xi = g(x,t) = \int_0^x h\, dx' - \int_0^t C\, dt' \tag{13}$$

and the approximation (9) and (10) is used, the governing equations (1)–(3) transform to the linear system

$$h\frac{\partial u}{\partial \xi} - \eta\frac{\partial h}{\partial \xi}\frac{\partial u}{\partial \eta} + \frac{1}{h}\frac{\partial v}{\partial \eta} = 0 \tag{14a}$$

$$\mathrm{Re}\, h^2\frac{\partial u}{\partial \tau} = -h^3\frac{\partial p}{\partial \xi} + \frac{\partial^2 u}{\partial \eta^2} \tag{14b}$$

$$0 = \frac{\partial p}{\partial \eta}. \tag{14c}$$

Note that equation (14b) is a diffusion equation for u, with a time-dependent coefficient h^2, and source term $h^3\partial p/\partial\xi$; and ξ treated as a parameter.

A physical interpretation of the mathematics presented in the foregoing is now offered. In the Lagrangian representation (i.e., following the fluid particle) the material time derivative of a quantity can be denoted as

$$\frac{Du(x,y,t)}{Dt} = \frac{\partial u}{\partial t}\bigg|_{x_p,y_p}, \tag{15}$$

the subscripts x_p, y_p meaning that the position of the particle is held constant in the differentiation. Obviously this can only occur if the coordinate system (x_p, y_p) follows the particle. Equation (15) is useful in principle, but not in practice, since a transformation from the spatial coordinates (x, y) to the particle coordinates (x_p, y_p) cannot be obtained except in some trivial cases. In equation (12), the symbol $\partial u/\partial\tau$ automatically means that ξ and η are held constant. Comparing equations (12) and (15), one sees that the coordinates (ξ, η) "approximately" follow the particle since partial differentiation with respect to τ (holding ξ and η constant) nearly equals D/Dt.

For steady flow, the transformation is simply

$$\xi = \int_0^x h\, dx' \tag{16a}$$

$$\eta = y/h(x) \tag{16b}$$

which leads to

$$h\frac{\partial u}{\partial \xi} - \eta\frac{1}{h}\frac{dh}{dx}\frac{\partial u}{\partial \eta} + \frac{1}{h}\frac{\partial v}{\partial \eta} = 0 \tag{17a}$$

$$\mathrm{Re}\, Ch^2\frac{\partial u}{\partial \xi} = -h^3\frac{dp}{d\xi} + \frac{\partial^2 u}{\partial \eta^2}. \tag{17b}$$

Equation (17b) is again a diffusion equation. The coordinate ξ in equation (17b) plays nearly the same role as the transformed time τ in equation (14b). If we then apply the following transformation:

$$\xi^* = \int_0^\xi \frac{d\xi'}{Ch^2} = \int_0^x \frac{dx'}{Ch}, \quad \eta^* = \eta, \tag{18}$$

the coordinates (ξ^*, η^*) are the same as Tuck and Bentwich's (X, Y).

The Plane Slider Bearing. Before solving several transient flow problems, the plane slider bearing is considered and the results compared with Tuck and Bentwich's linearized solution, and their numerical solution. The boundary conditions on equations (17) are

$$\xi^* = 0: \quad u = U_0$$

$$\eta^* = 0: \quad u = 1, \quad v = 0$$

$$\eta^* = 1: \quad u = 0. \tag{19}$$

The system of equations (15)–(19) is a "well-posed problem" if $dp/d\xi^*$ is known. In fact, this is not the case, but we have the additional condition

$$Q = h\int_0^1 u\, d\eta^* = U_0, \tag{20}$$

which serves to determine the pressure gradient, as in the Reynolds equation development. Finally, the fact that $p = 0$ at the film end $\xi^* = \xi_f^*$ is sufficient to define p itself.

For the plane slider bearing U_0 is unspecified at the onset, but treated as known. The constant C is equal to the inviscid solution arbitrary inlet velocity, cf., equation (10a), but let us set it equal to the lubrication theory flow rate:

$$C = \frac{h_m}{2},$$

$$h = 1 + mx = e^{mh_m\xi^*/2},$$

$$\xi^* = \frac{2}{mh_m}\ln(1+mx), \tag{21}$$

where h_m is the film thickness at the zero pressure gradient location for the inertialess (lubrication theory) solution.

By tedious but conventional application of classical solutions and techniques in Carslaw and Jaegar [19]:

$$u(\xi^*,\eta^*) = u_A(\xi^*,\eta^*) + u_B(\xi^*,\eta)$$

$$u_A(\xi^*,\eta^*) = -\frac{2}{\mathrm{Re}}\Bigg\{\sum_{1,3,\ldots}^{M\to\infty}[\cos n\pi\eta^* - 1]e^{-n^2\pi^2\xi^*/\mathrm{Re}}$$

$$\cdot\int_0^{\xi^*} e^{n^2\pi^2\xi'/\mathrm{Re}} f_{1A}(\xi')\,d\xi' + \sum_{2,4,\ldots}^{M\to\infty}[\cos n\pi\eta^* - 1]e^{-n^2\pi^2\xi^*/\mathrm{Re}}$$

$$\cdot\int_0^{\xi^*} e^{n^2\pi^2\xi'/\mathrm{Re}} f_{2A}(\xi')\,d\xi'\Bigg\}$$

$$u_B(\xi^*,\eta^*) = 1 + [U_0 - 1]\mathrm{erf}\sqrt{\frac{\mathrm{Re}}{4\xi^*}}\,\eta^*$$

$$+ U_0\left[\mathrm{erf}\sqrt{\frac{\mathrm{Re}}{4\xi^*}}\,(1-\eta^*) - \mathrm{erf}\sqrt{\frac{\mathrm{Re}}{4\xi^*}}\right], \tag{22}$$

with the function f_{1A} determined, in principle, from $u(\xi^*, 1) = 0$:

$$\frac{4}{\mathrm{Re}}\sum_{1,3,\ldots}^{M\to\infty} e^{-n^2\pi^2\xi^*/\mathrm{Re}}\int_0^{\xi^*} e^{n^2\pi^2\xi'/\mathrm{Re}} f_{1A}(\xi')\,d\xi'$$

$$= -u_B(\xi^*,1) = -U_1\left(1 - \mathrm{erf}\sqrt{\frac{\mathrm{Re}}{4\xi^*}}\right), \tag{23}$$

and f_{2A} from equation (20):

$$\frac{2}{\mathrm{Re}}\sum_{2,4,\ldots}^{M\to\infty} e^{-n^2\pi^2\xi^*/\mathrm{Re}}\int_0^{\xi^*} e^{n^2\pi^2\xi'/\mathrm{Re}} f_{2A}(\xi')\,d\xi'$$

Downloaded 02 May 2010 to 171.66.16.54. Redistribution subject to ASME license or copyright; see http://www.asme.org/terms/Terms_Use.cfm

$$= \frac{Q}{h} - \int_0^1 u_A(\xi^*,\eta^*)d\eta^*$$

$$= \frac{Q}{h} - \frac{U_1}{2} - \left(U_0 - \frac{1}{2}U_1\right)\operatorname{erf}\sqrt{\frac{\mathrm{Re}}{4\xi^*}} - (2U_0 - U_1)$$

$$\cdot\sqrt{\frac{4\xi^*}{\pi\mathrm{Re}}}\,(e^{-\mathrm{Re}/4\xi^* - 1}) \tag{24}$$

If we define $\omega = \partial u/\partial\eta^*$ as a vorticity-like variable, differentiating equation (17*b*) with respect to η^* gives the homogeneous diffusion equation:

$$\mathrm{Re}\frac{\partial\omega}{\partial\xi^*} = \frac{\partial^2\omega}{\partial\eta^{*2}}. \tag{25}$$

At the inlet, $\omega = 0$ (since $u \equiv U_0$) except at the two bearing surfaces where vorticity sources must be applied to satisfy the nonslip boundary conditions $\eta = 0$: $u = U_1$, $\eta = 1$: $u = 0$. The "*B*" solution of equation (22) is the sum of these vorticity sources:

$$\omega_B = \frac{2(U_0 - U_1)}{\sqrt{\pi}}\sqrt{\frac{\mathrm{Re}}{4\xi^*}}e^{-\frac{\mathrm{Re}}{4\xi^*}\eta^{*2}}$$

$$- \frac{2U_0}{\sqrt{\pi}}\sqrt{\frac{\mathrm{Re}}{4\xi^*}}e^{-\frac{\mathrm{Re}}{4\xi^*}(1-\eta^*)^2} \tag{26}$$

which satisfies (25) as well as the inlet boundary conditions. It turns out that the functions f_1 and f_2 of equations (22)–(24) are defined by

$$f_1(\xi^*) = \omega(\xi^*,0) + \omega(\xi^*,1)$$
$$f_2(\xi^*) = \omega(\xi^*,0) - \omega(\xi^*,1) \tag{27}$$

with the corresponding A and B components. Since the B solution fully accounts for the vorticity requirements at $\xi^* = 0$, $f_{1A}(0) = f_{2A}(0) = 0$.

From routine manipulations of equations (17), (18), (25), and (27) we obtain the pressure gradient:

$$\frac{h}{C}\frac{dp}{d\xi^*} = \left.\frac{\partial\omega}{\partial\eta^*}\right|_{\eta^*=0} = -(f_{2A} + f_{2B}) - \mathrm{Re}\,Q\frac{\partial}{\partial\xi^*}\left(\frac{1}{h}\right), \tag{28}$$

where f_{2A} is later determined in the following from a numerical inversion procedure on equation (24), and f_{2B} is determined directly from equations (26) and (27).

A small FORTRAN computer program was written to evaluate expressions for the solution, equations (22); and to determine by inversion of equations (23) and (24) the functions $f_{1A}(\xi^*)$ and $f_{2A}(\xi^*)$. The ξ^* domain is broken into N segments of length $\Delta\xi^*$. The value of f at each new position ξ^*_{I+1}, is found in terms of all previous $f(\xi^*_I)$, using $f(0) = 0$. Thus, the program marches through ξ^* space, calculating the new values of f at each location and evaluating the velocity profile from equation (22), and the source term from equation (28) as it goes along. When the program reaches the end of the ξ^* domain, it integrates the pressure gradient backwards (toward $\xi^* = 0$) to obtain the pressure, beginning at $p(\xi^*_f) = 0$.

We now consider the entrance effect in a plane slider bearing. Recall from the boundary conditions (19) that the inlet velocity U_0 is unknown. In fact U_0 can be determined by applying Bernoulli's equation to the region outside the film, see Fig. 1(*b*). In dimensionless form,

$$p(0) = \frac{\mathrm{Re}}{2}[U_\infty^2 - U_0^2 - \text{upstream loss}] \tag{29}$$

which assumes that the far-upstream pressure is ambient. The far-upstream velocity may be essentially that of the runner ($U_\infty = 1$), in which case the fluid outside the bearing is decelerated to U_0 (<1) and the inlet pressure $p(0)$ will be

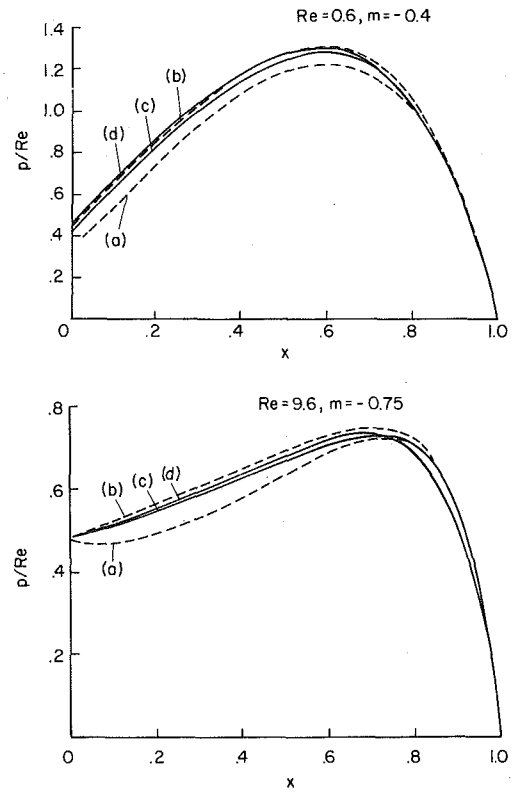


Fig. 2 Comparison with Tuck and Bentwich's solution – plane slider-bearing pressure profiles. (*a*) Exact numerical solution, reference [1]; (*b*) linearized solution, reference [1]; (c) small Re perturbation solution; (*d*) present solution.

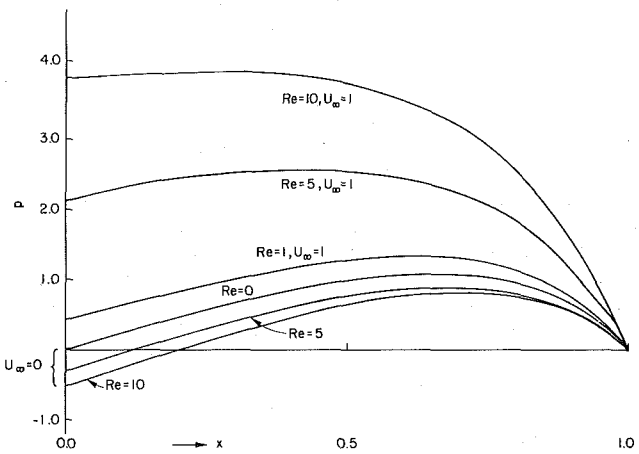


Fig. 3 Plane slider bearing pressure profiles. Upstream loss coefficient $k = 0$, slope $m = -0.5$.

greater than ambient; depending, of course, on the loss. On the other hand, the far-upstream velocity may be essentially zero, in which case $p(0)$ will be *less* than ambient.

For the plane slider bearing, the computer program assumes a U_0, calculates the pressure gradient at each ξ^* and then integrates from ξ^*_f back to $\xi^* = 0$. The Bernoulli condition (29) is then tested, an improved estimate for U_0 is made, and the process continued until equation (29) is satisfied.

To compare with Tuck and Bentwich, we neglect the upstream losses, however references [11, 12] suggest loss coefficients $k \approx 0.3$, where loss $= k\,\mathrm{Re}U_\infty^2/2$. Two different conditions for U_∞ are assumed: $U_\infty = 0$ and $U_\infty = 1$. Figure 2 shows a comparison between our results and Tuck and Bentwich's, and excellent agreement is found. Our solution can even be considered as a slight improvement of their

Downloaded 02 May 2010 to 171.66.16.54. Redistribution subject to ASME license or copyright; see http://www.asme.org/terms/Terms_Use.cfm

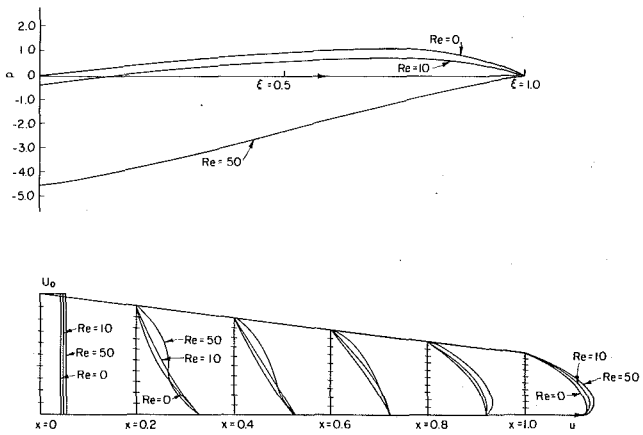


Fig. 4 Velocity profile development of the plane slider bearing

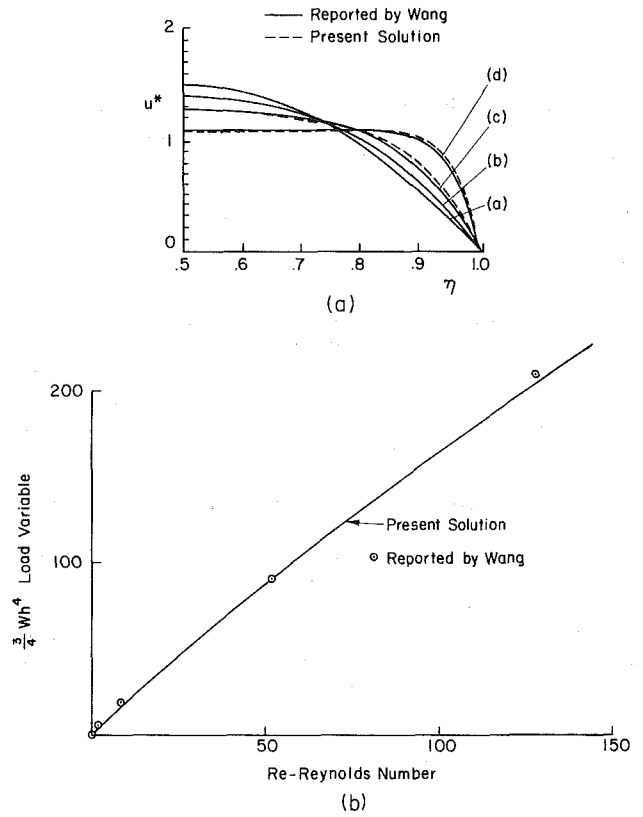


Fig. 5 Comparison with Wang's solution – parallel squeeze film, $h = \sqrt{1-t}$. Velocity profile and load variable. (*a*) Re = 0.; (*b*) Re = 4.16; (*c*) Re = 13.7; (*d*) Re = 121.

linearized solution. Figure 3 portrays some additional pressure profiles. Since U_0 is typically $\sim 1/3$, it turns out that the inlet pressure jump is highly sensitive to the upstream velocity U_∞. Load may either be increased or decreased, depending on U_∞.

For Re < 10 the influence of inertia is small except for the effect of the inlet pressure jump. If the inlet pressure is forced to be zero (not shown), the effect of inertia on load is less than 1 percent for Re = 10. However, when the inlet pressure jump is taken into account, fluid inertia has a large influence on the load. These results are consistent with recent experiments [20].

Velocity profile development is shown in Fig. 4 for $U_\infty = 0$. As Reynolds number increases, the flow rate $Q = U_0$ also increases. The negative inlet pressure jump primarily accounts for the reduced load. The opposite situation (increased load)

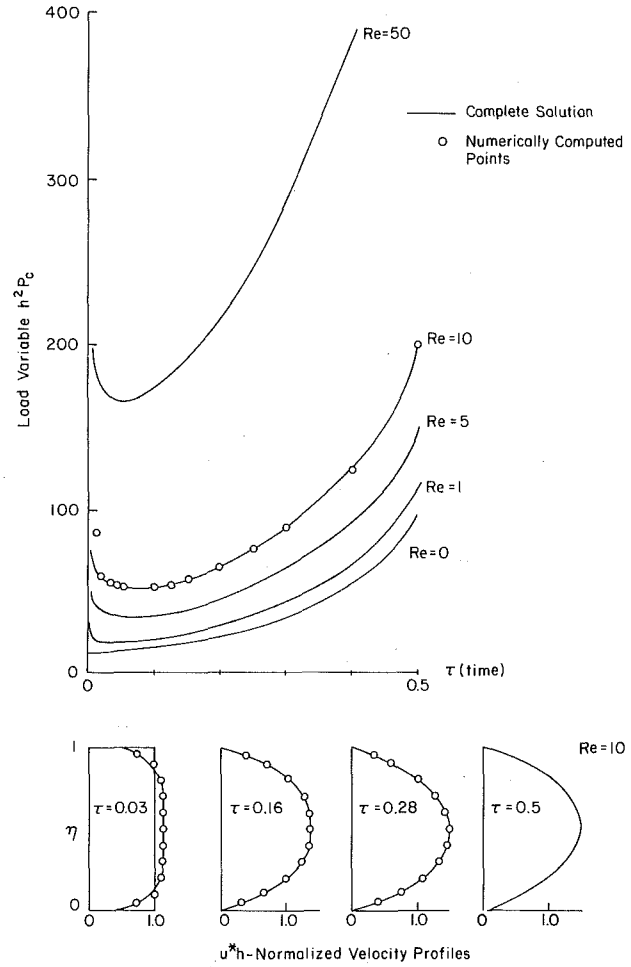


Fig. 6 Parallel squeeze film with a sudden start

exists for $U_\infty = 1$. For Re = 10, most velocity profile development occurs in the first 10 percent of the bearing length, but for Re = 50 flow development occurs over most of the length.

Transient Flow Examples—Pure Squeezing of Parallel Plates. For this case $h = h(t)$; see Fig. 1(*c*). If $x = 0$ is located at the midpoint of the plates, $\tilde{u}(0, t) = 0$; hence

$$\tilde{u} = -\frac{x}{h}\frac{\partial h}{\partial t}, \quad \tilde{v} = \frac{y}{h}\frac{\partial h}{\partial t}, \quad g = xh(t) = \xi. \tag{30}$$

The ξ-dependence can be eliminated from equations (14) by the change of dependent variables:

$$u = \xi\, u^*(\eta, \tau), \quad v = v^*(\tau, \eta) \quad p = \frac{1}{2}(h^2 - \xi^2)p_c(\tau) \tag{31}$$

to obtain

$$h^2 u^* + \frac{\partial v^*}{\partial \eta} = 0$$

$$\mathrm{Re}\frac{\partial u^*}{\partial \tau} = h^3 p_c^* \frac{\partial^2 u^*}{\partial \eta^2}. \tag{32}$$

One can show that the load W is directly proportional to $h^2 p_c^*$.

(*a*) *Wang's Squeeze Film Problem,* $h = \sqrt{1-t}$. It has recently been shown that exact similarity solutions exist for certain squeeze film problems, namely when $h = \sqrt{1-t}$, reference [21]. Using equation (32), we get

$$\tau = -ln(1-t) \tag{33}$$

The boundary conditions are

Downloaded 02 May 2010 to 171.66.16.54. Redistribution subject to ASME license or copyright; see http://www.asme.org/terms/Terms_Use.cfm

$$\eta=0: \quad u^*=U_1=0, \quad v^*=0$$
$$\eta=1: \quad u^*=0 \tag{34}$$

Global continuity must be obeyed, i.e.,

$$-\frac{\partial h}{\partial t}x=\int_0^h u\,dy, \tag{35}$$

$$Q=\frac{1}{h^3}e^{3/2\tau}=\int_0^1 u\,dy \tag{36}$$

Because the solution is of the similarity type, no initial conditions are imposed, i.e., the initial velocity profile is "similar" to the profile at any other time.

The system of equations (32)-(36) is the same as (17)-(20) with τ replacing ξ^*, and slightly different expressions for the source (pressure) term and the flow rate Q. The solution is thus given by equations (22)-(28), making the appropriate substitutions. The "B" solution represents vorticity sources on the plates due to a sudden start at $\tau = 0$, however the "B" solution is not required in this case.

Assuming that f_2 is proportional to $e^{3/2\tau}$ and neglecting in the solution terms $\exp(-n^2\pi^2\tau/\mathrm{Re})$ in comparison to 1, f_2 is found to be:

$$f_2=\frac{e^{3/2\tau}}{4\alpha(\mathrm{Re})}, \tag{37}$$

where

$$\alpha(\mathrm{Re})=\sum_{n=1}^{M\to\infty}\frac{1}{n^2\pi^2+\frac{3}{2}\mathrm{Re}}=\frac{\sqrt{\frac{3\mathrm{Re}}{2}}-\tanh\sqrt{\frac{3\mathrm{Re}}{2}}}{3\mathrm{Re}\tanh\frac{\sqrt{3\mathrm{Re}}}{2}} \tag{38}$$

The velocity field is found after straightforward but lengthy calculation,

$$u^*=e^{3/2\tau}\sqrt{\frac{3\mathrm{Re}}{2}}\,\frac{\cosh\sqrt{\frac{3\mathrm{Re}}{2}}-\cosh\left(\sqrt{\frac{3\mathrm{Re}}{2}}\eta\right)}{\sqrt{\frac{3\mathrm{Re}}{2}}\cosh\sqrt{\frac{3\mathrm{Re}}{2}}-\sinh\sqrt{\frac{3\mathrm{Re}}{2}}} \tag{39}$$

The pressure gradient is obtained from the balance of momentum equation:

$$\frac{\partial p}{\partial\xi}=\frac{1}{h^3}\frac{\partial^2 u}{\partial\eta^2}-\frac{\mathrm{Re}}{h^2}\frac{\partial u}{\partial\tau}\cong -\frac{1}{2}\xi e^{3\tau^*}\left(\frac{3\mathrm{Re}}{2}\right)^{3/2}\frac{1}{\sqrt{\frac{3\mathrm{Re}}{2}}-\tanh\sqrt{\frac{3\mathrm{Re}}{2}}} \tag{40}$$

The pressure boundary conditions being $p(x=\pm\,1/2,\ t)=0$ one gets, as the normal force (load) per unit length

$$W(t)=2\int_0^1 p\,dx=\frac{1}{3}\frac{1}{h^4}\left(\frac{3\mathrm{Re}}{2}\right)^{3/2}\frac{\cosh\sqrt{\frac{3\mathrm{Re}}{2}}}{\sqrt{\frac{3\mathrm{Re}}{2}}-\tanh\sqrt{\frac{3\mathrm{Re}}{2}}} \tag{41}$$

The present approximate solution is compared to Wang's exact solution. Several velocity profiles and the loads are compared in Fig. 5. The agreement is very good over a wide range of Reynolds numbers.

(*b*) *Constant Squeezing Rate.* Let us now consider the case of a sudden beginning of squeezing from rest, i.e.,

$$t\le 0 \quad h=1$$
$$0\le t<1 \quad h=1-t \tag{42}$$

hence

$$\tau=\frac{t}{1-t} \tag{43}$$

The initial condition is

$$\tau=0^+: \quad u^*=U_0=1, \tag{44}$$

which is the same as that used by Jones and Wilson [14] and Hamza [15]. Immediately after the squeezing starts ($\tau = 0^+$) an outward slug flow occurs as viscous effects propagate into the film. As before, global continuity must be obeyed, i.e.,

$$t\ge 0 \quad -\frac{\partial h}{\partial t}x=\int_0^h u\,dy \tag{45}$$

$$\tau\ge 0^+ \quad Q=-\frac{1}{h^4}\frac{\partial h}{\partial\tau}=\frac{1}{h^2}=\int_0^1 u\,d\eta. \tag{46}$$

Again, the solution is essentially given by equations (22)-(28) with appropriate substitutions. The behavior is depicted in Fig. 6. The time interval considered is between start-up, and when the plates reach one-half the initial gap. Normalized velocity profiles are shown for several instants of time, for the case Re = 10. This Reynolds number is based on the initial film thickness, while the instantaneous value is Re • h. The load (h^2p_c) versus time is also shown for four Reynolds numbers. Clearly there is a large error relative to lubrication theory. A discrepancy from lubrication theory occurs due to the initial conditions (near $\tau = 0$), but a large error also exists for quasisteady conditions (τ large). This latter condition is different than the plane slider bearing where for Re = 10, the lubrication theory pressure gradient is quite accurate for large ξ^*.

We seek to verify the approximate method presented by an "exact" numerical solution for the squeeze film case. Fortunately this case is easier than in the plane slider case because the initial condition can be applied in a straightforward manner, without the "coupling" of inlet pressure and velocity. The x-coordinate can be eliminated as an independent variable by a similar change of variables to equations (31). The governing equations are

$$hu^*+\frac{\partial v}{\partial\eta}=0, \tag{47a}$$

$$\mathrm{Re}h^2\left(\frac{\partial u^*}{\partial t}+u^{*2}+\frac{v}{h}\frac{\partial u^*}{\partial\eta}\right)=h^2p^*+\frac{\partial^2 u^*}{\partial\eta^{*2}} \tag{47b}$$

$$v=v(\eta) \quad u=xu^*(t,\eta) \quad p=\frac{1}{2}(1-x^2p_c^*(t) \tag{47c}$$

with the same boundary and initial conditions as in the foregoing.

These equations are solved by a fully implicit matrix inversion scheme which marches through time. The x-momentum discretized balance equation is obtained from a control volume formulation as suggested in Patankar's text [22]. The problem is treated as a transient linearized one-dimensional heat conduction-convection problem. The u^{*2} and $h^2p_c^*$ terms of equation (47b) are treated as heat sources and the nonlinear coefficient v/h is updated each successive iteration. For most runs there were 20 grid steps across the film ($\Delta\eta = 0.05$) and 50 time steps ($\Delta t = 0.01$). The calculations were checked under several conditions at $\Delta\eta = 0.01$, and agreement was found to be within 2 percent. The numerically computed points are also shown in Fig. 6

Downloaded 02 May 2010 to 171.66.16.54. Redistribution subject to ASME license or copyright; see http://www.asme.org/terms/Terms_Use.cfm

Conclusions

We conclude that the method proposed here is suitable for study of fluid inertia effects in lubrication including the effects of entrance and initial conditions. The method is based on linearizing the inertia terms of the Navier-Stokes equations by transformation to a coordinate system that approximately follows the fluid particle. Both the transient and steady cases are considered. The basic developing character of the flow is retained (in a temporal or spatial sense), as opposed to other types of approximations. Results are achieved in closed form, although a small computer program is required to perform numerical integration and series summation.

Predictions of the model agree favorably with the existing results in the literature. Three cases are discussed: (*a*) the plane slider bearing, (*b*) a pure squeeze film with $h = \sqrt{1-t}$, for which an exact solution exists, and (*c*) the pure squeeze film at constant approach velocity. In all cases agreement with published results or numerical solutions is excellent.

We believe the proposed method will be useful because accurate results can be obtained for many practical problems in fairly simple closed form. The accuracy may deteriorate, or results may be difficult to obtain, either for very large Reynolds number or very near the entrance (or initial time). However, complications also arise in these cases when purely numerical solutions are used. In addition, such numerical solutions are expensive and cumbersome, a fact also noted by Tuck and Bentwich [1]. Carrier [23] and Sparrow et al. [24] have shown that similar linearizations are accurate for large Reynolds number in related flows.

In the parallel-surface squeeze film where constant velocity squeezing is begun suddenly, large inertia effects exist immediately following the start. The inertia correction is greater than 100 percent for $\mathrm{Re} > 5$ or $t/\mathrm{Re} < 0.004$. Such initial phenomena always exist for small times, regardless of the instantaneous Reynolds number. This result may be of interest in the case of reported work on squeeze films for viscometry, polymer testing, etc.

The entrance flow problem, while mathematically analogous in the present model, is more complex. The reason is that the inlet condition is strongly coupled to conditions upstream of the bearing, as discussed by several authors. The Bernoulli effect may cause a large pressure jump at the inlet which is of order Re relative to the viscous pressure generated in the bearing. The jump may be positive or negative depending on the upstream velocity and losses. Upstream flow losses will (algebraically) decrease the pressure jump. The effect of the jump may dominate the entire pressure profile. Without detailed information on the upstream conditions it is impossible to predict the effect of inertia on load, especially due to the likelihood of large upstream losses as lubricant enters the bearing. The traditional a priori assumption of ambient inlet pressure cannot, in general, be justified. At modified Reynolds number of 5, where many authors suggest that the inertia effect is small (< 10 percent), inlet conditions may cause a substantial error in lubrication theory.

Finally, a few remarks regarding limitations and accuracy of the method are appropriate. Clearly, the method is valid only when the thin film equations are in force. For $x \ll \mathrm{Re}^{-1}$, an upstream expansion must be used, comprising all terms of the Navier-Stokes equations, as shown by Van Dyke [17]. Fortunately, Schlichting's boundary layer analysis [16] is, in fact, very accurate even for very small $x\mathrm{Re}^{-1}$ (negligible error at $x\mathrm{Re}^{-1} \sim 0.002$, cf. Van Dyke's Fig. 3). We may imagine analogous results just after the start of squeezing flows.

Borrowing the terminology of Van Dyke's text [25], the present analysis is an example of the "method of composite equations," i.e., an ad hoc correction for nonuniformity near the entrance or initial conditions. As such, we put forth an "irrational but useful approximation," i.e., it does not become exact in any known limit. Many other examples are cited in [25]. Therefore it is not possible to make a formal estimate of errors in each succeeding approximation. Note, however, that correct predictions are made for stresses in the upstream boundary layer flow (constant $\cdot \sqrt{\mathrm{Re}x^{-1}}$), and far downstream flow (1 + constant $\cdot$ Reh). Small errors exist only in the values of the constants.

Acknowledgment

The research described herein was funded, in part, by the United States National Science Foundation, Grant No. MEA-80-18028. This support is gratefully acknowledged.

References

1 Tuck, E. O., and Bentwich, M., "Sliding Sheets: Lubrication with Comparable Viscous and Inertia Forces," *Journal of Fluid Mechanics*, Vol. 135, 1983, pp. 51-69.

2 Tichy, J. A., "The Effect of Fluid Inertia in Squeeze Film Damper Bearings: A Heuristic and Physical Description," ASME Paper No. 83-GT-177.

3 Tecza, J. A., Giordano, J. C., Zorzi, E. S., and Drake, S. K., "Squeeze Film Damper Technology: Part II—Experimental Verifications Using a Controlled Orbit Test Rig," ASME Paper No. 83-GT-248.

4 Pinkus, O., and Sternlicht, B., *Theory of Hydrodynamic Lubrication*, McGraw-Hill, New York, 1961, pp. 351-367.

5 Ishizawa, S., "The Unsteady Laminar Flow Between Two Parallel Disks with Arbitrary Varying Gap Width," *Bull. of Japan Soc. Mech. Eng.*, Vol. 9, No. 35, 1966, pp. 533-550.

6 Tichy, J. A., and Modest, M. F., "A Simple Low Deborah Number Model for Unsteady Hydrodynamic Lubrication, Including Fluid Inertia," *Journal of Rheology*, Vol. 24, No. 6, 1980, pp. 829-845.

7 Milne, A. A., "On the Effect of Lubricant Inertia in the Theory of Hydrodynamic Lubrication," ASME *Journal of Basic Engineering*, Vol. 81, 1959, p. 239.

8 Fritz, R. J., "The Effect of an Annular Fluid on the Vibration of a Long Rotor: Part I—Theory," ASME *Journal of Basic Engineering*, 1970, pp. 923-929.

9 Smalley, A. J., Vohr, J. H., Castelli, V., and Wachmann, C., "An Analytical and Experimental Investigation of Turbulent Flow in Bearing Films Involving Convective Fluid Inertia Forces," ASME *Journal of Lubrication Technology*, Vol. 96, 1974, pp. 151-157.

10 Elrod, H. G., Anwar, I., and Colsher, R., "Transient Lubricating Films With Inertia," ASME Paper No. 82-Lub-12.

11 Pan, C. H. T., "Calculation of Pressure, Shear, and Flow in Lubrication Films for High Speed Bearings," ASME *Journal of Lubrication Technology*, Vol. 96, 1974, pp. 80-94.

12 Constantinescu, V. N., and Galetuse, S., "On the Possibilities of Improving the Accuracy of the Evaluation of Inertia Forces in Laminar and Turbulent Films," ASME *Journal of Lubrication Technology*, Vol. 96, 1974, pp. 69-79.

13 Tipei, N., "Flow Characteristics and Pressure Head Build-up at the Inlet of Narrow Passages," ASME *Journal of Lubrication Technology*, Vol. 100, 1978, pp. 47-55.

14 Jones, A. F., and Wilson, S. D. R., "On the Failure of Lubrication Theory in Squeezing Flows," ASME *Journal of Lubrication Technology*, Vol. 97, 1975, pp. 101-104.

15 Hamza, E. A., and MacDonald, D. A., "A Fluid Film Squeezed Between Two Parallel Plane Surfaces," *Journal of Fluid Mechanics*, Vol. 109, 1981, pp. 147-160.

16 Schlichting, H., "Laminare Kanaleinaufströmung," *Z. angew. Math. Mech.*, Vol. 14, 1934, pp. 368-373.

17 Van Dyke, M., "Entry Flow in a Channel," *Journal of Fluid Mechanics*, Vol. 44, Pt. 4, 1970, pp. 813-823.

18 Wilson, S. R., "Entry Flow in a Channel, Part 2," *Journal of Fluid Mechanics*, Vol. 46, Pt. 4, 1971, pp. 787-799.

19 Carslaw, H. S., and Jaeger, J. C., *Conduction of Heat in Solids*, 2nd Ed., Oxford University Press, Oxford, 1959, pp. 92-133.

20 Tichy, J. A., and Chen, S.-H., "Plane Slider Bearing Load Due to Fluid Inertia—Experiment and Theory," ASME *Journal of Tribology*, Vol. 107, 1985, pp. 32-38.

21 Wang, C. Y., "The Squeezing of a Fluid Between Two Plates," ASME JOURNAL OF APPLIED MECHANICS, Vol. 43, 1976, pp. 579-583.

22 Patankar, S. V., *Numerical Heat Transfer and Fluid Flow*, McGraw-Hill, 1981.

23 Lewis, J. A., and Carrier, G. F., "Some Remarks on the Flat Plate Boundary Layer," *Quart. Appl. Math.*, Vol. 7, No. 2, 1949, pp. 228-234.

24 Sparrow, E. M., Lin, S. H., and Lundgren, T. S., "Flow Development in the Hydrodynamic Entrance Region of Tubes and Ducts," Physics of Fluids, Vol. 7, No. 3, 1964, pp. 338-347.

25 Van Dyke, M., *Perturbation Methods in Fluid Mechanics*, Parabolic Press, Stanford, Calif., 1975.

Downloaded 02 May 2010 to 171.66.16.54. Redistribution subject to ASME license or copyright; see http://www.asme.org/terms/Terms_Use.cfm

Flow Driven by a Finite, Shrouded Spinning Disk With Suction

J. M. Hyun
Department of Mechanical Engineering,
Clarkson University,
Potsdam, NY 13676
Mem. ASME

Numerical solutions are presented for the flow driven by a spinning disk which forms an endwall of a finite, closed cylinder. The effects of imposing a uniform suction (or blowing) through the spinning disk in finite configuration are investigated. The Reynolds number is large and the cylinder aspect ratio is $0(1)$. Finite-difference techniques are employed to integrate the time-dependent Navier-Stokes equations. The initial state is taken to be a uniform axial motion. Integration is performed until an approximate steady state is attained. When there is no suction, the infinite disk model is shown to provide a qualitatively representative approximation to the flow in the central core region. As a suction (blowing) is imposed, the core rotation rate in the case of finite configuration becomes smaller (larger) than that for the case of no suction, which is in disagreement with the predictions of the infinite disk model. These significant discrepancies point to a fundamental difficulty of the infinite disk model to adequately describe the real flow in finite geometry when there is a mass flux across the system boundary. Plots showing the meridional stream function at various times are constructed. Details of the flow structure in the approximate steady state are analyzed. When there is a suction, a strong Ekman layer is present on the spinning disk but the Ekman layer on the stationary disk fades. When there is a blowing, a strong Ekman layer forms on the stationary disk. It is shown that the dynamic effects influencing the character of the flow are confined to these Ekman layers.

1 Introduction

The flow of an incompressible, viscous fluid in a finite, closed cylinder when one of its endwall disks is spinning has received considerable attention in recent years (e.g., see [1-5]). For definiteness, we envision the axis of the cylinder to be vertical and the spinning disk to be the bottom endwall of the cylinder. From a theoretical standpoint, this internal flow displays an intricate interplay between the transverse pressure gradients, the Coriolis acceleration, and the viscous effect. The shrouded spinning disk is also a useful experimental apparatus to study convective transport processes that occur in engineering applications. As is the case for the majority of these applications, we shall consider the situations for which the Reynolds number $\mathrm{Re}=\Omega h^2/\nu$ is large, and the cylinder aspect ratio $h/a \sim 0(1)$, where ν is the kinematic viscosity of the fluid, Ω the rotation rate of the disk, h the height, and a the radius of the cylinder.

When the Reynolds number is large, the flow characteristics can be divided into the essentially inviscid core and the boundary layers enclosing the core. The key ingredient in the dynamic process is the fluid pumping mechanism in the Ekman layers which form on the horizontal endwall disks. When there is a difference in rotation rates between the core and the disk, a small axial velocity is induced by the Ekman layer. By this mechanism, the Ekman layer strongly influences the behavior of the inviscid core flow. Over much of the disk radius, the interior fluid is sucked into the bottom Ekman layer, pushed radially outward in the layer, and ejected back into the interior along the sidewall. This establishes the secondary flows, which form a counterclockwise circulation in the meridional plane.

The theoretical investigations of flows near a rotating disk have been built largely on the infinite disk model (e.g., see [6]). The assumption of an infinite disk configuration admits the similarity transformations, which result in a set of coupled ordinary differential equations. The infinite disk model captures the qualitative essentials of the flow for certain limiting cases, at least in the central region near the axis. The basic results of this model have been well summarized [7].

The modification in the flow brought about by the imposition of an axial velocity within a rotating fluid has been investigated by several authors (e.g., see the papers cited in [8]). These previous papers adopted the infinite disk model to determine the effects of suction (or blowing) through the spinning disk. In particular, [8] obtained numerical solutions for the large Reynolds number flow between two parallel infinite disks (one stationary and the other rotating at Ω) when there is a uniform suction through the rotating disk. It is important to recognize that, within the infinite disk model, as the fluid is drawn out through the rotating disk, the fluid at large radii moves radially inward to maintain mass continuity. There is no corresponding suction of fluid through the

Contributed by the Applied Mechanics Division for publication in the JOURNAL OF APPLIED MECHANICS.
Discussion on this paper should be addressed to the Editorial Department, ASME, United Engineering Center, 345 East 47th Street, New York, N.Y. 10017, and will be accepted until two months after final publication of the paper itself in the JOURNAL OF APPLIED MECHANICS. Manuscript received by ASME Applied Mechanics Division, April, 1984; final revision, March, 1985.

Copyright © 1985 by ASME
Downloaded 02 May 2010 to 171.66.16.54. Redistribution subject to ASME license or copyright; see http://www.asme.org/terms/Terms_Use.cfm

stationary infinite disk. The strength of suction is measured by the suction parameter S, which is the imposed suction velocity at the spinning disk referred to the axial velocity scale $\mathrm{Re}^{-1/2}\Omega h$, where h is the axial separation between the two disks. Reference [8] presented the results for $0.0 \le S \le 2.0$. When there is no suction ($S=0$), the core rotation rate is 0.313Ω and the Ekman layer exists on both disks. As the suction increases, the inviscid core rotates more rapidly and the downward axial velocity increases. When $S=1.3494$, the angular velocity in the core reaches Ω and the Ekman layer on the spinning disk vanishes. A further increase in suction causes the fluid in the core to rotate faster than Ω and the Ekman layer reappears on both disks, but the direction of the radial flow in the bottom Ekman layer is reversed.

It is surprising that, according to the infinite disk model solutions of [8], the core rotation rate exceeds that of the spinning disk under sufficiently strong suction. An important question is whether these idealized, infinite disk model predictions can adequately depict the real flows in finite geometry. The present paper addresses this question; we shall determine the effects of the imposition of the axial velocity on the flow in a finite cylinder driven by a spinning endwall disk. As was pointed out in [9], the angular velocity of the sidewall does not affect the essential dynamics of the interior flow. In line with the approach taken in [10], therefore, the sidewall of the cylinder is fixed to the spinning disk.

Physically, this situation can be modeled by sucking fluid with uniform vertical velocity, $w_s = -S\mathrm{Re}^{-1/2}\Omega h$, through the porous, spinning bottom disk. It is important to realize that, since the configuration is finite, we have to allow an exactly equal uniform suction through the porous, stationary top disk to achieve mass continuity. In this paper, we shall also encompass the cases when a blowing is applied through the disks, i.e., $S<0$.

We have acquired comprehensive flow data by employing a finite-difference numerical model to integrate the time-dependent Navier-Stokes equations. The initial flow was taken to be an axial motion with uniform velocity $w_s = -S\mathrm{Re}^{-1/2}\Omega h$. At the initial instant, the bottom disk starts impulsively to rotate at Ω and this rotation rate is maintained thereafter. By using the time-stepping method, the integration is performed until an approximate steady state is reached, when the temporal variations of the flow variables are very small.

Details of the time evolution of the flow are obtained. In this paper we present new results on the radial and axial structures of the approximate steady flow in finite geometry over a range of suction parameter $-2.0 \le S \le 2.0$. The character of the flow is distinctly different depending on whether the type of the imposed axial velocity at the spinning disk is of suction ($S>0$), or of blowing ($S<0$), or of no suction ($S=0$). The present results exhibit significant discrepancies from the predictions of the infinite disk model. Most prominent is that, contrary to the similarity solutions, the core rotation rate in finite configuration is shown to be smaller than that of the spinning disk even under strong suction. The present study sheds light on the more fundamental question regarding the applicability of the infinite disk model. It is concluded that the infinite disk model does not provide an adequate representation to the real flow in finite geometry if there is a net mass flux across the boundary of the container.

2 The Model

The governing equations are the time-dependent, axisymmetric, incompressible Navier-Stokes equations written for cylindrical coordinate (r,θ,z) with respective velocity components (u,v,w). These are

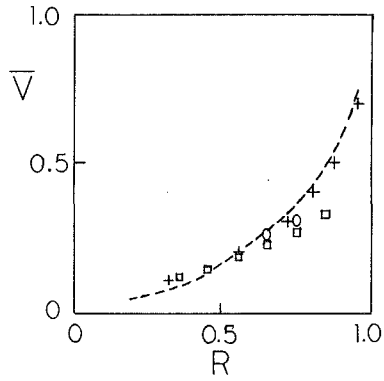


Fig. 1 Comparison between results for azimuthal velocity $\bar{V}=v/a\Omega$ at the middepth $z/h=0.5$ for $S=0$. ---- the present numerical results; + numerical data from reference [10] for $\mathrm{Re}=10^3$, $h/a=0.07$; ○ experimental values from reference [10] for $\mathrm{Re}=10^3$, $h/a=0.07$; □ experimental values from reference [10] for $\mathrm{Re}=10^3$, $h/a=0.07$, but with a stationary sidewall.

$$\frac{\partial u}{\partial t} = -\frac{1}{r}\frac{\partial}{\partial r}(ru^2) - \frac{\partial}{\partial z}(uw) - \frac{1}{\rho}\frac{\partial p}{\partial r} + \frac{v^2}{r} + \nu\left(\nabla^2 u - \frac{u}{r^2}\right), \tag{1}$$

$$\frac{\partial v}{\partial t} = -\frac{1}{r}\frac{\partial}{\partial r}(ruv) - \frac{\partial}{\partial z}(vw) - \frac{vu}{r} + \nu\left(\nabla^2 v - \frac{v}{r^2}\right), \tag{2}$$

$$\frac{\partial w}{\partial t} = -\frac{1}{r}\frac{\partial}{\partial r}(ruw) - \frac{\partial}{\partial z}(w^2) - \frac{1}{\rho}\frac{\partial p}{\partial z} + \nu\nabla^2 w, \tag{3}$$

$$\frac{1}{r}\frac{\partial}{\partial r}(ru) + \frac{\partial w}{\partial z} = 0, \tag{4}$$

where $\nabla^2 = (1/r)\,\partial/\partial r\,(r\partial/\partial r) + \partial^2/\partial z^2$, p is the reduced pressure, and ρ is the density.

The initial conditions for the fluid are

$$u = v = 0, w = w_s \quad \text{for} \quad t = 0, \tag{5}$$

and the boundary conditions are

$$u = 0,\ v = r\Omega,\ w = w_s \quad \text{at} \quad z = 0 \text{ (the bottom disk)}, \tag{6}$$

$$u = v = 0,\ w = w_s \quad \text{at} \quad z = h \text{ (the top disk)}, \tag{7}$$

$$u = w = 0,\ v = a\Omega \quad \text{at} \quad r = a \text{ (the sidewall)}. \tag{8}$$

To satisfy numerical stability requirements, the boundary conditions at the central axis are applied at a small, but finite radius $r = r_i$. Thus, we have [11]

$$u = v = 0,\ \partial w/\partial r = 0 \quad \text{at} \quad r = r_i.$$

We employed the finite-difference techniques to solve this system of equations. The details of the numerical methods used, including the finite-differencing schemes, were given in [11].

3 Results and Discussion

Numerical computations were performed using the following geometrical and fluid parameters: $a=10.15$ cm, $h=10.05$ cm, $\Omega=0.211$ rad/s, and $\nu=9.3\times10^{-3}$ cm^2/s, which give $\mathrm{Re}[\equiv\Omega h^2/\nu]=2.29\times10^3$. These values were chosen from the laboratory experiments of reference [12] for the nonlinear spin-up in a rigidly rotating cylinder.

Calculations were made using a 30×32 grid in the $(r\text{-}z)$ plane. The sensitivity of this numerical model to grid size was tested by reference [11]. The stretching of the grid enabled us to place about eight grid points in the Ekman layer. The time step used was $\Delta t = 0.05$–0.20 s, which assured accuracy and satisfied the computational stability criteria [11]. For a given set of parameters, the computer time to integrate the

Downloaded 02 May 2010 to 171.66.16.54. Redistribution subject to ASME license or copyright; see http://www.asme.org/terms/Terms_Use.cfm

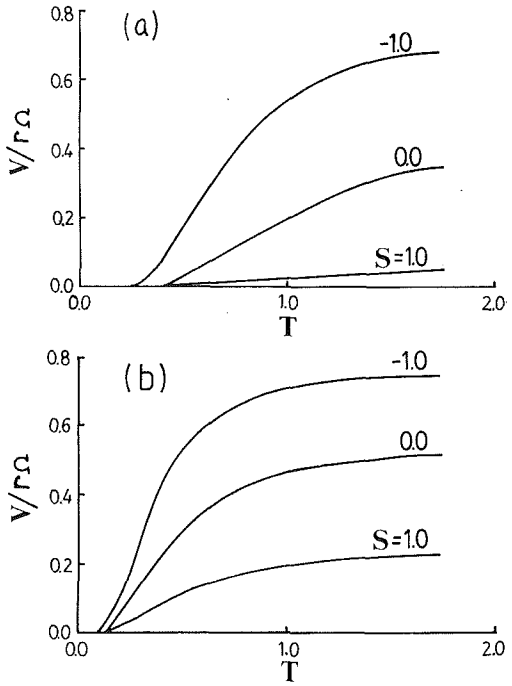


Fig. 2 Plots of the scaled angular velocity versus time. (*a*) at $R = 0.5$, $Z = 0.5$, and (*b*) at $R = 0.75$, $Z = 0.5$.

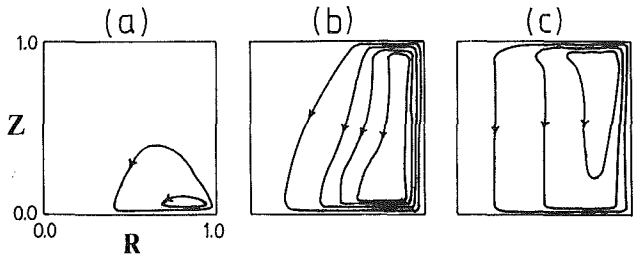


Fig. 3 Plots of the meridional stream function ψ for the case of no suction ($S = 0$). Values of ψ are expressed in units of $\mathrm{Re}^{-1/2}\Omega h^2 a$, and $\Delta\psi$ *denotes the contour increment.* (*a*) at $T = 0.014$. $\psi_{max} = 0.22$, $\psi_{min} = 0$, $\Delta\psi = 0.07$; (*b*) at $T = 0.58$. $\psi_{max} = 0.36$, $\psi_{min} = 0$, $\Delta\psi = 0.09$; (*c*) at $T = 2.18$. $\psi_{max} = 0.40$, $\psi_{min} = 0$, $\Delta\psi = 0.13$.

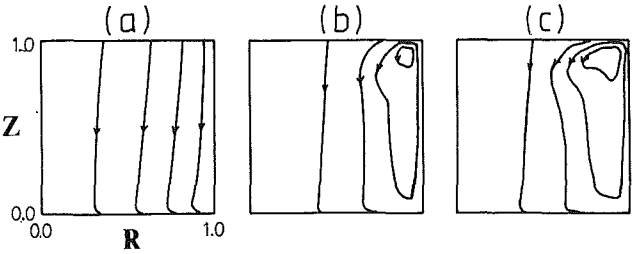


Fig. 4 Same as in Fig. 3, except for a suction ($S = 1.0$). (*a*) at $T = 0.019$. $\psi_{max} = 0.57$, $\psi_{min} = 0$, $\Delta\psi = 0.13$; (*b*) at $T = 0.70$. $\psi_{max} = 0.81$, $\psi_{min} = 0$, $\Delta\psi = 0.22$; (c) at $T = 2.22$. $\psi_{max} = 0.83$, $\psi_{min} = 0$, $\Delta\psi = 0.22$.

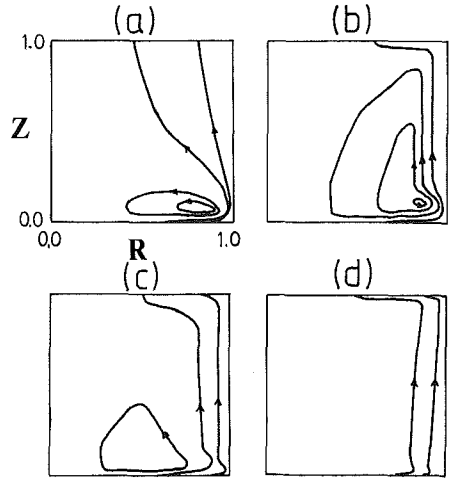


Fig. 5 Same as in Fig. 3 except for a blowing ($S = -1.0$). (*a*) at $T = 0.04$. $\psi_{max} = 0.49$, $\psi_{min} = -0.51$, $\Delta\psi = 0.22$; (*b*) at $T = 0.16$. $\psi_{max} = 0.73$, $\psi_{min} = -0.51$, $\Delta\psi = 0.33$; (c) at $T = 0.62$. $\psi_{max} = 0.22$, $\psi_{min} = -0.51$, $\Delta\psi = 0.22$; (*d*) at $T = 1.41$. $\psi_{max} = 0.21$, $\psi_{min} = -0.51$, $\Delta\psi = 0.22$.

equations up to one spin-up time scale, $\tau \equiv \mathrm{Re}^{1/2}\Omega^{-1} \cong 227$ s, was approximately 1 hour on an IBM 4341 Computer. The time-marching integration was terminated when an approximate steady state is attained. For convenience, the approximate steady state was arbitrarily taken to be the state when the flow variables at $r/a = 0.5$, $z/h = 0.5$ changed less than 0.1 percent over the time interval $t/\tau = 0.1$.

The reliability and accuracy of the present numerical model have been validated previously for spin-up flows in a rigidly rotating cylinder by checking the model predictions against the laser-Doppler velocimeter measurements in the laboratory [11, 12]. Regarding the present flow problem in hand, the numerical results for the case of no suction ($S = 0$) were compared with the available data for moderate and large Re in finite geometry reported in the literature [1, 3–5, 10]. No experimental or numerical data exist for the same geometrical and fluid parameters as used in the present study. However, when these data are rendered in scaled nondimensional form, the present numerical results are shown to be consistent with the available data. Figure 1 is an example of such comparisons. No experimental or numerical data have appeared in the literature for the flow in finite configuration when there is a suction (or blowing).

The salient features of the computed results are presented in Figs. 2–9. Only the representative and physically illuminating cases of $S = 1.0$, $S = 0.0$, and $S = -1.0$ will be discussed. These three cases exemplify the class of flow with suction ($S > 0$), no suction ($S = 0$), and blowing ($S < 0$), respectively. A change in the value of S within a given class causes only quantitative changes. In the figures, the nondimensional quantities are $T \equiv \mathrm{Re}^{-1/2}\Omega t$, $Z \equiv z/h$, $R \equiv r/a$.

Figure 2 illustrates the time evolution of the angular velocity in the core. Firstly, it is clear that the transient flow is characterized by the spin-up time scale τ. At $T = 1.5$, for example, the fluid at $R = 0.75$ has almost attained the steady state, whereas at $R = 0.50$ the flow still evolves slowly. It is well known that, when there is no suction, the similarity solution gives the steady-state core rotation rate as $0.313\,\Omega$ in the limit $\mathrm{Re} \to \infty$. As shown in curve for $S = 0.0$ in Fig. 2(*a*), the steady state core rotation rate at $R = 0.5$ is slightly larger than 0.313Ω. This is attributable to the finite value of Re and to the presence of the rotating sidewall. Obviously, the applicability of the infinite disk model cannot persist at larger radii because of the influence of the sidewall.

As the fluid suction is imposed, Fig. 2 demonstrates that the core rotation rate in finite configuration is smaller than that for the case of no suction. This is in basic disagreement with the results of reference [8] based on the infinite disk model. To obtain an understanding for the physical process at work, we shall examine the qualitative features of the entire flow field when a suction (or blowing) is applied.

We first consider the infinite disk model. As the fluid at a given radial location is sucked out through the spinning disk, mass continuity calls for the fluid at infinity to move radially inward. The fluid coming from infinity carries higher angular momentum; thus, the effect of suction is to increase the angular momentum in the core region of interest. In the core away from the Ekman layers, angular momentum is con-

Downloaded 02 May 2010 to 171.66.16.54. Redistribution subject to ASME license or copyright; see http://www.asme.org/terms/Terms_Use.cfm

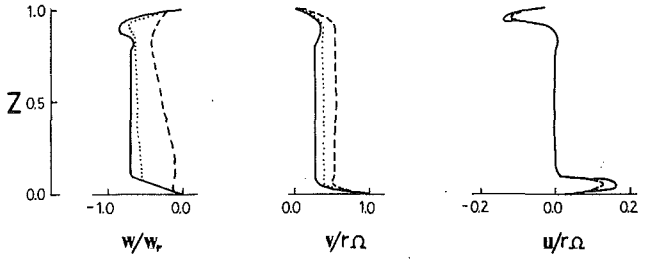


Fig. 6 Profiles of the velocity components in the steady state for $S = 0$. The radial locations are ____ $R = 0.25$, ... $R = 0.50$, ---- $R = 0.75$. The vertical velocity is scaled by $W_r = \mathrm{Re}^{-1/2}\Omega h$.

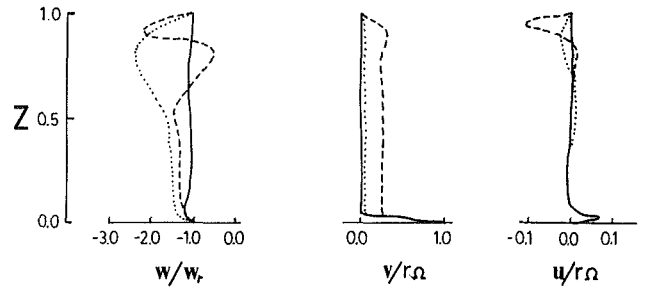


Fig. 7 Same as in Fig. 6, except for $S = 1.0$.

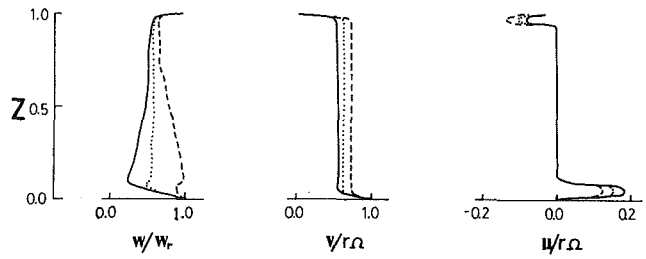


Fig. 8 Same as in Fig. 6, except for $S = -1.0$.

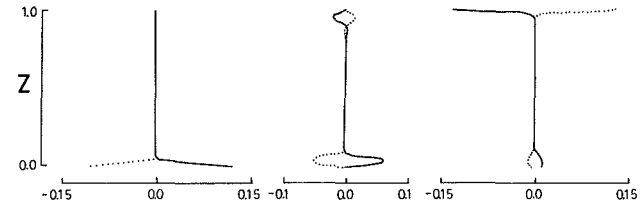


Fig. 9 Plots of the sum of the advection terms (shown by dots) and of the viscous term (shown by solid line) in equation (2) in the steady state at $R = 0.5$. The abscissa denotes the magnitude of these terms in units of cm/s^2. (*a*) $S = 1.0$, (*b*) $S = 0.0$, (*c*) $S = -1.0$.

served in the absence of viscosity. As the fluid moves radially inward, its radius decreases and, consequently, the angular velocity increases to conserve angular momentum. This is the mechanism by which the core rotation rate under suction becomes larger than that for the case of no suction. Further increase in suction causes a larger amount of fluid of higher angular momentum to move inward; therefore, the core rotation rate under sufficiently strong suction exceeds the rotation rate of the spinning disk. The numerical results of reference [8] are consistent with this physical reasoning.

For the flow in a finite, closed cylinder, a suction through the spinning bottom disk requires an equal suction through the stationary top disk. The fluid that is being sucked through the top disk carries no angular momentum initially. The effect of suction is to pull the fluid of zero angular momentum downward into the core. Consequently, the angular momentum in the core is lowered, and the core rotation rate under suction is smaller than that for the case of no suction. An increase in suction enhances this process and, therefore, the core rotation rate decreases further. A similar argument applies to the case of blowing; a blowing causes the fluid of high angular momentum, which originates from the spinning disk, to more upward into the core. Accordingly, the core rotation rate under blowing becomes larger than that for the case of no blowing.

The striking qualitative discrepancy between the infinite disk solutions of reference [8] for the case of suction and the present results underscores a fundamental difficulty of the infinite disk model to represent the real flow in finite configuration when there is a mass flux across the system boundary.

Figures 3–5 depict the secondary flow patterns in the meridional plane. The meridional stream function ψ is defined such that $u = (1/r)(\partial\psi/\partial z)$, $w = -(1/r)(\partial\psi/\partial r)$. Figure 3 is for the case of no suction. Plots describing the meridional flows when there is no suction were presented previously by [1–5]. At very early times [see Fig. 3(*a*)], the fluid very near the spinning disk is pushed radially outward. This causes the fluid in the interior to be drawn into the bottom layer, and a counterclockwise meridional circulation forms. At early times, however, the bottom Ekman layer has not fully developed and, therefore, the Ekman pumping is weak. The weak meridional flow is confined to the region near the spinnind disk. At intermediate times [see Fig. 3(*b*)], the Ekman pumping has intensified and the circulation penetrates up to the top disk. An Ekman layer appears on the top disk and grows in strength. At large times when the approximate steady state is attained [see Fig. 3(*c*)], the meridional flow in the core consists of purely axial downward motion sustained by the Ekman suction (blowing) at the spinning (stationary) disk. Clearly, the return circuit is in the sidwall vertical boundary layer.

The modifications in the meridional flow brought about by the imposition of a suction are displayed in Fig. 4. At very early times (see Fig. 4(*a*)), the bottom Ekman layer is weak; the meridional flow does not deviate much from the uniform downward axial motion of the initial state. At intermediate times (see Fig. 4(*b*)), the meridional circulation is substantial due to the well-developed Ekman layer on the spinning disk. In the central region, say $R < 0.9$, the downward axial motion is enhanced by the Ekman pumping. Near the sidewall, a vertical boundary layer is established to accommodate the return circuit of the counterclockwise meridional circulation. These patterns of the meridional flow persist to large times. In the approximate steady state (see Fig. 4(*c*)), the counterclockwise circulation is present at large radii, say $R > 0.6$, and a predominantly downward axial motion occurs in the central region.

Figure 5 illustrates the meridional flow when a blowing is applied. At early times (see Fig. 5(*a*)), the influence of the bottom Ekman layer is restricted to a small corner area. The upward axial motion, which was given in the initial state, still prevails over a large portion at large radii. At intermediate times (see Fig. 5(*b*)), the bottom Ekman layer has grown to build a considerable counterclockwise circulation. The return circuit of the meridional circulation near the sidewall is enhanced by the blowing. As time progresses further, the core rotation rate increases under blowing (see Fig. 2). This implies that the difference in rotation rate between the core and the spinning disk is reduced. As a consequence, the Ekman pumping weakens at large times. This results in diminishing counterclockwise circulation, as shown in Fig. 5(*c*). At very large times [see Fig. 5(*d*)], the downward axial motion generated by the Ekman pumping almost balances the upward motion imposed by the blowing in the bulk of the interior, say

Downloaded 02 May 2010 to 171.66.16.54. Redistribution subject to ASME license or copyright; see http://www.asme.org/terms/Terms_Use.cfm

$R<0.8$. Thus, only the upward axial flow in the return circuit near the sidewall remains to be noticeable in the meridional flow field.

To examine the details of the steady flow structure, the vertical profiles of the three velocity components at different radii are constructed. Figure 6 shows such plots for the case of no suction. As can be seen in Fig. 3(*c*), the axial motion in the bulk of the interior is downward, driven by the Ekman pumping at the spinning disk. The downward axial velocity is large at small radii, and the axial motion weakens at large radii. At very large radii, where the vertical boundary layer is present near the sidewall, the axial motion is upward to accommodate the return circuit of the meridional circulation. In the inviscid core, the azimuthal velocity is substantially uniform in the vertical direction. The Ekman layers form on both disks. Owing to the presence of the rotating sidewall, the scaled angular velocity increases at large radii. The radial velocity is very small in the core. The fluid is pushed radially outward (inward) in the Ekman layer on the spinning (stationary) disk. Apart from the region at large radii where the influence of the rotating sidewall is significant, the flow structure shown in Fig. 6 is consistent with the infinite disk solutions for no suction [see Fig. 1 of reference [8]). This demonstrates that, when there is no suction imposed at the disk, the infinite disk model provides an adequate approximation to the real flow in finite geometry in the central core region away from the sidewall.

Figure 7 shows the steady flow structure when a suction is imposed. The downward axial velocity has intensified [compare the abscissa of Fig. 7(*a*) with that of Fig. 6(*a*)]. As was discussed earlier, the core rotation rate under suction is smaller than that for no suction. The Ekman layer is present on the spinning disk, but on the stationary disk the Ekman layer fades except at relatively large radii. The radial velocity in the core is very small. The meridional flow at small radii is predominantly downward. It is notable that the meridional flow at large radii exhibits appreciable vertical variations, especially in the upper half region [see curves for $R=0.75$ in Fig. 7(*a*) and (*c*)]. This is due to the concentration of the counterclockwise meridional circulation at large radii [see Fig. 4(*c*) for cross-referencing].

Figure 8 shows the steady flow structure when a blowing is applied. The axial motion is predominantly upward. At small radii, the imposed upward axial motion is retarded by the downward flow induced by the Ekman pumping. At large radii, this retardation is reduced and the upward motion increases in magnitude. As can be observed in Fig. 2, the core rotation rate is larger than that for no blowing ($S=0$). The Ekman layer is present on both disks. The radial velocity is very small in the core, but the radial flow is appreciable in the Ekman layers.

It is informative to gauge the weight of various dynamic effects affecting the steady flow by inspecting the relative sizes of the representative terms in the equations of motion. Figure 9 shows the vertical profiles at $R=0.5$ of the advection effect, represented by the first three terms on the right-hand side of equation (2), and of the viscous term in equation (2). When there is a suction [see Fig. 9(*a*)], all the dynamic effects are restricted principally to the Ekman layer on the spinning disk. The strong viscous effect is balanced by the advection effect in the Ekman layer. A further breakdown reveals that the inviscid dynamic effect is dominated by the vertical advection, $-\partial(vw)/\partial z$. This term becomes substantial in the Ekman layer where the velocity shear $\partial v/\partial z$ becomes large. It is apparent in Fig. 9(*a*) that in the bottom Ekman layer the viscous effect accelerates the flow, whereas the advection decelerates the flow by entraining the fluid of low angular momentum from above.

Where there is no suction [see Fig. 9(*b*)], a strong Ekman layer appears on the spinning disk, whereas the Ekman layer on the stationary disk is weak. Near the spinning disk, in a similar manner to Fig. 9(*a*), the viscous effect accelerates the flow and the advection decelerates the motion. In the weak Ekman layer on the stationary disk, the influence of these two effects is opposite to that in the layer on the spinning disk.

Figure 9(*c*) shows that, when there is a blowing, much of the action is confined to the Ekman layer on the stationary disk. The viscous effect is to retard the flow, whereas the advection accelerates the flow by bringing in the fluid of high angular momentum from below.

4 Conclusion

Numerical solutions were obtained for the flow in a finite, closed cylinder driven by its spinning bottom endwall disk. When there is no suction ($S=0$), the predictions of the infinite disk model are shown to be representative of the flow in the central core. As a suction (blowing) is imposed through the disks, the core rotation rate becomes smaller (larger) than that for $S=0$. The present finding is in basic disagreement with the infinite disk solution for suction. This discrepancy can be explained by examining how the angular momentum in the core is affected by the action of suction (or blowing) in the two models.

Detailed analyses of the flow structure in the approximate steady state point to the following observations. For $S=0$, the Ekman layer forms on both disks. Both the advection effect and the viscous effect are confined to these Ekman layers. In the bulk of the meridional plane, the secondary flow consists of purely downward axial motion. For the case of a suction ($S>0$), a strong Ekman layer is present on the spinning disk but the Ekman layer fades on the stationary disk. The downward axial motion is enhanced by the imposition of suction. For the case of a blowing ($S<0$), the Ekman layer on the spinning disk is weak, and a strong Ekman layer appears on the stationary disk. The secondary flow diminishes in the bulk of the meridional plane.

References

1 Pao, H.-P., "A Numerical Computation of a Confined Rotating Flow," ASME JOURNAL OF APPLIED MECHANICS, Vol. 37, 1970, pp. 480–487.

2 Tomlan, P. F., and Hudson, J. L., "Flow Near an Enclosed Rotating Disk: Analysis," *Chemical Engineering Science*, Vol. 26, 1971, pp. 1591–1600.

3 Lugt, N. J., and Haussling, H. J., "Development of Flow Circulation in a Rotating Tank," *Acta Mechanica*, Vol. 18, 1973, pp. 255–272.

4 Alonso, C. V., "Steady Laminar Flow in a Stationary Tank With a Spinning Bottom," ASME JOURNAL OF APPLIED MECHANICS, Vol. 42, 1975, pp. 771–776.

5 Bertela, M., and Gori, F., "Laminar Flow in a Cylindrical Container with a Rotating Cover," ASME *Journal of Fluids Engineering*, Vol. 104, 1982, pp. 31–39.

6 Batchelor, G. K., "Note on a Class of Solutions of the Navier-Stokes Equations Representing Steady Rotationally-Symmetric Flow," *Quarterly Journal of Mechanics and Applied Mathematics*, Vol. 4, 1951, pp. 29–41.

7 Greenspan, H. P., *The Theory of Rotating Fluids*, Cambridge University Press, Cambridge, 1968.

8 Wilson, L. O., and Schryer, N. L., "Flow Between a Stationary and a Rotating Disk With Suction," *Journal of Fluid Mechanics*, Vol. 85, 1978, pp. 479–496.

9 Venezian, G., "Nonlinear Spin-Up," *Topics in Ocean Engineering*, Vol. 2, 1970, pp. 87–96.

10 Dijkstra, D., and Van Heijst, G. J. F., "The Flow Between Two Finite Rotating Disks Enclosed by a Cylinder," *Journal of Fluid Mechanics*, Vol. 128, 1983, pp. 123–154.

11 Warn-Varnas, A., Fowlis, W. W., Piacsek, S., and Lee, S. M., "Numerical Solutions and Laser Doppler Measurements of Spin-Up," *Journal of Fluid Mechanics*, Vol. 85, 1978, pp. 609–639.

12 Hyun, J. M., Leslie, F., Fowlis, W. W., and Warn-Varnas, A., "Numerical Solutions for Spin-Up from Rest in a Cylinder," *Journal of Fluid Mechanics*, Vol. 127, 1983, pp. 263–281.

Downloaded 02 May 2010 to 171.66.16.54. Redistribution subject to ASME license or copyright; see http://www.asme.org/terms/Terms_Use.cfm

Cavitation Boundary Shapes for Submerged Short Journal Bearings Using Newtonian Lubricants

R. H. Buckholz
Department of Mechanical Engineering,
Columbia University,
New York, N.Y. 10027

Cavitation boundary shapes for submerged short journal bearings are investigated in this study. In this analysis, the Reynolds lubrication equation is approximated by using the bearing slenderness ratio as a small parameter. The slenderness ratio appears explicitly in the Reynolds lubrication equation. The lubrication equation is solved subjected to the boundary condition of a subambient value for the cavitation pressure and the additional Reynolds' free-surface boundary condition along the unknown cavitation boundary. The Ocvirk short bearing solution is shown to fail near the leading edge of the cavitation region, and a matched asymptotic theory is used to determine the shape and location of this cavitated region. Cavitation bubble location and size are shown to depend on bearing aspect ratio, journal eccentricity, and cavitation pressure. Finally the present journal bearing analysis is limited to those cases where the cavitation region has a large axial extent.

1 Introduction

Fluid film journal bearings are used to stabilize and restrict the motion of a rotating shaft. During this process gas bubbles often form when the lubricating fluid film is swept into the diverging portion of the journal bearing gap. Subambient pressures inside these gas bubbles have been measured, and the cavitation pressure is relatively constant throughout the bubble. There has been much interest in predicting the shape and location of these cavitated regions. Both bearing load and attitude angle are dependent on the cavitation bubble size and location. It was realized long ago that cavitation regions must be accounted for in journal bearing performance models. This cavitation phenomenon is initiated in the journal bearing when sufficiently high journal eccentricities cause the fluid pressure in the diverging gap to fall below some cavitation pressure.

Gumbel [5] first treated journal bearing cavitation by omitting the subambient portion of the pressure; he considered the fluid film pressure in the converging portion of the fluid film gap. In addition, a subsequent refinement to Gumbel's approximation is that the pressure gradient is required to vanish at the cavitation boundary location. Swift [10], Stieber [9], and Floberg [5] argued that the pressure gradient must vanish at the start of cavitation. This specification of a subsidiary boundary condition results in a mathematically nonlinear free boundary value problem. This subsidiary condition has been applied by several investigators who used numerical analysis to treat fluid film cavitation. The details of the boundary shape – on the downstream side of the maximum cavitation bubble width – require a mass continuity boundary condition to locate the trailing edge of the cavitation bubble. Thus, this part of the free-surface problem is also nonlinear. Floberg presents a numerical solution to Reynolds equation – including cavitation – for a bearing having unity aspect ratio, eccentricity 0.6, and a cavitation pressure of -0.1. Calculation of bearing loads using Floberg's theory compared well with experimental data. Numerical methods are used to handle the cavitated regions in journal bearing; however, programming complexities do occur. Elrod [3] proposed a numerical method to reduce the programming difficulties associated with fluid film cavitation. His numerical scheme conforms to the Reynolds boundary condition and to the requirement for mass conservation. It should be noted that the details of the cavitation shape are not always obtained since the method employed requires interpolation between grid points.

Numerical methods for journal bearing applications are well developed; however – as pointed out by Pan [8] – the short bearing theory remains a useful and practical approach for rotor-bearing dynamics, dampers, and shaft steel applications. We are concerned here with applying the Reynolds free-surface boundary condition to the short bearing geometry. An asymptotic approximation method is used to predict the cavitation boundary shape. We seek a uniformly valid approximation to small journal bearing aspect ratio

Contributed by the Applied Mechanics Division and presented at the Winter Annual Meeting, Miami, Fla., November 17-21, 1985 of THE AMERICAN SOCIETY OF MECHANICAL ENGINEERS.

Discussion on this paper should be addressed to the Editorial Department, ASME, United Engineering Center, 345 East 47th Street, New York, N.Y. 10017, and will be accepted until two months after final publication of the paper itself in the JOURNAL OF APPLIED MECHANICS. Manuscript received by ASME Applied Mechanics Division, August, 1984; final revision, January, 1985. Paper No. 85-WA/APM-7.

Copyright © 1985 by ASME
Downloaded 02 May 2010 to 171.66.16.54. Redistribution subject to ASME license or copyright; see http://www.asme.org/terms/Terms_Use.cfm

configurations for the case of cavitation regions that have a large axial extent.

Pan [7] applied the Reynolds free-surface cavitation condition to the journal bearing pressure field; he calculated the pressure by using Ocvirk's short bearing analysis. Thus, he obtained an analytical result for the cavitation boundary location applicable to journal bearings operating at fixed conditions. These results he obtained by expanding the pressure in a regular asymptotic series for small bearing aspect ratio. However, the azimuthal pressure derivative effect is important near the leading edge of the cavitation region (Buckholz [1, 2]). The shape of the cavitation region – as predicted by Pan – is not consistent with the shape Floberg obtained. Furthermore, the cavitation boundary location – given by Pan – is independent of the bearing aspect ratio. In a short bearing analysis, without cavitation bubbles, Buckholz [1] included the azimuthal derivatives in Reynolds equation near the axial fluid film edges. He used a matched asymptotic theory. Buckholz also calculated the cavitation boundary location – for short bearings – by using Reynolds free-surface condition and zero cavitation pressure boundary conditions to solve the Reynolds equation.

2 An Improved Cavitation Boundary Calculation Using Matched Asymptotic Theory

The lubrication theory developed here is for an incompressible and isoviscous lubricant. The cavitation pattern treated is the *O* type [Pan, 8]. The small slenderness ratio theory presented in the following analysis describes the region in a thin layer before the fluid film cavitation as a boundary layer. The cavitation boundary is assumed to extend over most of the axial bearing length. Therefore, the Reynolds cavitation condition can not be applied directly to Ocvirk's [6] short bearing solution since azimuthal derivatives are not included in the approximated differential equation – the Ocvirk equation – for the pressure. A matched asymptotic theory is used to solve the Reynolds lubrication equation. As will be shown in the following analysis, the three independent parameters are: the aspect ratio λ, the journal eccentricity ϵ, and the cavitation pressure.

2a Boundary Layer Solution to Reynolds Lubrication Equation. The Reynolds equation was nondimensionalized using the bearing radius R, the bearing length L, the journal bearing clearance C, the journal angular rotation ω, and the fluid viscosity μ. The nondimensional parameters and variables are defined as:

$$\lambda = L/2R \tag{2.1a}$$

$$\bar{h} = h/C = (1 - \epsilon\cos\eta) \tag{2.1b}$$

$$\bar{P} = 2PC/3\mu\omega L^2 \tag{2.1c}$$

$$\zeta = 2Z/L \tag{2.1d}$$

$$\eta = X/R \tag{2.1e}$$

The nondimensional bearing sliding direction is η and the axial direction is ζ. The nondimensional Reynolds equation is:

$$\lambda^2 \frac{\partial}{\partial\eta}\left(\bar{h}^3 \frac{\partial\bar{P}}{\partial\eta}\right) + \frac{\partial}{\partial\zeta}\left(\bar{h}^3 \frac{\partial\bar{P}}{\partial\zeta}\right) = \epsilon\sin\eta \tag{2.2}$$

A regular perturbation expansion for the pressure – using λ as a small parameter – is assumed:

$$\bar{P} = \sum_{n=1}^{\infty} \nu_n(\lambda)\bar{P}_{on}(\zeta,\eta) \tag{2.3}$$

This expansion is substituted into the nondimensional Reynolds equation and the limit $\lambda \to 0$ is applied. The resulting equation is:

$$\frac{\partial^2\bar{P}_{01}}{\partial\zeta^2} = \epsilon\sin\eta/\bar{h}^3 = Q(\eta), \quad \nu_1(\lambda) = 1 \tag{2.4}$$

The associated boundary conditions for the preceding equation are zero pressure along the axial bearing end. The solution is given in the following:

$$\bar{P}_{01} = -\frac{1}{2}(1-\zeta^2)\epsilon\sin\eta/(1-\epsilon\cos\eta)^3 \tag{2.5}$$

The leading order scaling for the outer solution is $\bar{P}_1$ and the first correction scales on λ^2. To study the region near the fluid film cavitation boundary, it is useful to rescale the azimuthal coordinate, using the slenderness ratio (Buckholz [1, 2]). For the region near η_1 the variable η^* is defined as:

$$\eta^* = (\eta_1 - \eta)/\lambda \tag{2.6}$$

In this new coordinate system the Reynolds equation has the following form:

$$\frac{\partial}{\partial\eta^*}\left(\bar{h}^3 \frac{\partial\bar{P}^*}{\partial\eta^*}\right) + \frac{\partial}{\partial\zeta}\left(h^3 \frac{\partial\bar{P}^*}{\partial\zeta}\right) = \epsilon\sin\eta \tag{2.7}$$

The asymptotic expansion for the pressure in the boundary layer region is given as:

$$\bar{P}^* = \sum_{n=1}^{\infty} \nu_n^*(\lambda)\bar{P}_{on}^*(\zeta,\eta^*) \tag{2.8}$$

where ν_n^* is an asymptotic sequence. The leading order differential equation for the boundary layer pressure, $\bar{P}_{01}^*$, is:

$$\frac{\partial}{\partial\eta^*}\left\{\bar{h}^3(\eta_1)\frac{\partial\bar{P}_{01}^*}{\partial\eta^*}\right\} + \frac{\partial}{\partial\zeta}\left\{\bar{h}^3(\eta_1)\frac{\partial\bar{P}_{01}^*}{\partial\zeta}\right\} = \epsilon\sin\eta_1 \tag{2.9}$$

The associated boundary conditions and matching conditions for the preceding elliptic equation are given in the following where π_c is the cavitation pressure, ζ_0 is the cavitation boundary width, and the pressure at the bearing axial ends is zero.

$$\bar{P}_{01}^*(\zeta = \pm 1, \eta^*) = 0 \tag{2.10a}$$

$$\bar{P}_{01}^*(\zeta, \eta^* = 0) = \pi_c, \qquad \zeta\epsilon[0,\zeta_0] \tag{2.10b}$$

$$\bar{P}_{01}^*(\zeta, \eta^* = 0) = P^{II}(\zeta), \qquad \zeta\epsilon[\zeta_0, 1] \tag{2.10c}$$

$$\lim_{\eta\to\eta_1}\left(\sum_{n=1}^{\infty}\nu_n(\lambda)\bar{P}_{on}(\zeta,\eta)\right) = \lim_{\eta^*\to\infty}\left(\sum_{n=1}^{\infty}\nu_n^*(\lambda)\bar{P}_{on}^*(\zeta,\eta^*)\right) \tag{2.10d}$$

The boundary layer solution is given as

$$\bar{P}_{01}^* = \epsilon\sin\eta_1\left\{-(1-\zeta^2) + \sum_{n=0}^{\infty} A_n\cos\gamma_n\zeta e^{-\gamma_n\eta^*}\right\} \Big/ 2(1-\epsilon\cos\eta_1)^3 \tag{2.11}$$

where

$$\gamma_n = \left(n + \frac{1}{2}\right)\pi$$

A composite solution that is uniformly valid for the boundary layer region and Ocvirk region is found (Buckholz [2]).

$$P_{cs} = -\frac{1}{2}(1-\zeta^2)\epsilon\sin\eta/(1-\epsilon\cos\eta)^3 + \frac{1}{2}\epsilon\sin\eta_1\sum_{n=0}^{\infty} A_n\cos\gamma_n\zeta e^{-\gamma_n\eta^*}/(1-\epsilon\cos\eta_1)^3 \tag{2.12}$$

However, the location of the boundary layer at η_1 must be determined from the Reynolds free-surface condition.

2b The Cavitation Boundary Calculation. The constants A_n in the composite solution for the pressure are determined by matching the pressure to the cavitation pressure π_c for $\zeta\epsilon[0,\zeta_0]$, and to the pressure in region two for $\zeta\epsilon[\zeta_0,1]$. In general, a boundary layer region is needed for the pressure in

Downloaded 02 May 2010 to 171.66.16.54. Redistribution subject to ASME license or copyright; see http://www.asme.org/terms/Terms_Use.cfm

region 2. The transition in pressure between region 1 and region 2 should be smooth. This requires matching the two boundary layer solutions. As an alternative to the consideration of cavitation bubbles of all sizes, the class of wide cavitation bubbles is instead considered. This results in some mathematical simplification. The scope of the present work is limited to cavitation bubbles that have a large axial extent.

The azimuthal extent of the boundary layer in region 1 is λ (i.e., the bearing slenderness ratio). The finite width of the fluid film located between the cavitation bubble edge and the bearing edge may be regarded as a short bearing, and the slenderness ratio for this region is λ'; thus the boundary layer extent in region 2 is λ', where $\lambda' = (1-\zeta_0)\lambda$. This is a multiple parameter problem for λ and λ'. To obtain the pressure field and the cavitation boundary location, it is necessary to include the boundary layer shown as region 1. The region 2 boundary layer is used to connect region 1 to the short bearing theory along the bearing edge. The extent of the boundary layer in region 2 is λ'; this corresponds to a few degrees in the azimuthal direction. To obtain a completely uniformly valid leading order approximation, it is necessary to include the two boundary layer regions. However, since λ' is small, it is possible to omit the boundary layer in region two, provided one is willing to accept a slight discontinuity in azimuthal derivative of the pressure at the boundary $\zeta = \zeta_0$. We turn now to solving for the constants A_n in the composite solution to Reynolds equation. This requires the specification of the pressure along the curve $\eta^* = 0$. The cavitation bubble is assumed to extend from $\zeta = 0$ to $\zeta = \zeta_0$, and the short bearing solution is assumed to hold from $\zeta = \zeta_0$ to $\zeta = 1$. The resulting equation for the pressure along the curve $\zeta^* = 0$ is:

$$Q(\eta_1)\left(-\frac{1}{2}(1-\zeta^2)+\sum_{n=0}^{\infty}\frac{1}{2}A_n\cos\gamma_n\zeta\right) = \begin{cases}\pi_c & 0\le\zeta\le\zeta_0\\ p^{II} & \zeta_0\le\zeta\le 1\end{cases} \tag{2.13}$$

where p^{II} is the pressure in the narrow fluid film near the bearing edge. The orthogonaility condition is applied to determining the A_n's in the preceding equation. The details for determining the A_n's are given in Appendix *I*; the result for the A_n's is:

$$A_n = (4\sin\gamma_n\zeta_0/\gamma_n^3)Q(\eta_1) \tag{2.14}$$

The composite solution for the upstream pressure, region 1, is given in the following:

$$P_{cs} = -\frac{1}{2}(1-\zeta^2)\epsilon\sin\eta/(1-\epsilon\cos\eta)^3 + \frac{1}{2}\epsilon\sin\eta_1\sum_{n=0}^{\infty}\frac{4\sin\gamma_n\zeta_0}{\gamma_n^3}\cos\gamma_n\zeta e^{-\gamma_n\eta}\Big/(1-\epsilon\cos\eta_1)^3 \tag{2.15}$$

The Reynolds cavitation boundary condition is applied to the foregoing composite solution; thus:

$$\frac{\partial P_{cs}}{\partial\eta}\Big)_{\eta=\eta_1} = 0, \quad \zeta\epsilon[0,\zeta_0] \tag{2.16}$$

and

$$-\frac{1}{2}(1-\zeta^2)\frac{\partial}{\partial\eta}\left(\frac{\epsilon\sin\eta}{(1-\epsilon\cos\eta)^3}\right)_{\eta=\eta_1} + \frac{\epsilon\sin\eta_1}{2(1-\epsilon\cos\eta_1)}\sum_{n=0}^{\infty}A_n\cos\gamma_n\zeta\left(\frac{\gamma_n}{\lambda}\right) = 0 \tag{2.17}$$

The expression for A_n is substituted into equation (2.17); the following implicit expression for $\eta_1 = \eta_1(\zeta,\lambda)$ is obtained:

$$\frac{\lambda(1-\zeta^2)\tfrac{1}{2}}{\Sigma\gamma_n A_n\cos\gamma_n\zeta} = \frac{\epsilon\sin\eta_1(1-\epsilon\cos\eta_1)}{(\cos\eta_1 - 3\epsilon + 2\epsilon\cos^2\eta_1)} \tag{2.18}$$

This expression for $\eta_1(\zeta,\lambda)$ is identical to that obtained by Buckholz for the nonsubmerged bearing, if the limit of ζ_0 going to 1 is taken. The location of the cavitation boundary in region 2 and 3 is given here by:

$$\zeta_0 = 1 - \sqrt{-2\pi_c/Q(\eta_1)} \tag{2.19}$$

where

$$Q(\eta_1) = \epsilon\sin\eta_1/(1-\epsilon\cos\eta_1)^3$$

The preceding result is identical to that obtained by Pan – he used Ocvirk's short bearing theory and Reynolds cavitation condition – for the shape of the cavitation boundary away from the nose. The cavitation boundary location given by equation (2.19) was obtained by applying the Reynolds free-surface condition to the Ocvirk solution. However, it is interesting to note that equation (2.19) can also be obtained directly from a matched asymptotic theory for the case of ζ_0 near 1(i.e., wide cavitation bubbles). This analysis is given in Appendix *II*. The entire cavitation boundary shape is determined from equations (2.18) and (2.19); equation (2.18) is used to determine $\eta_1(\zeta)$ for $\zeta\epsilon[0,\zeta_0]$.

Some simplification occurs for cavitation boundaries that begin near the minimum fluid film gap. For this case the equation (2.19) is rewritten as:

$$\eta_1 = \lambda(1-\zeta^2)\frac{1}{2}\Big/\sum_{n=0}^{\infty}\gamma_n A_n\cos\gamma_n\zeta \tag{2.20}$$

The relationship between cavitation pressure, journal eccentricity, and cavitation boundary width is as follows:

$$\frac{\pi_c}{\lambda}4\sum_{n=0}^{\infty}\frac{\sin 2\gamma_n\zeta_0}{\gamma_n^2}\Big/(1-\zeta_0^2)(1-\zeta_0)^2 = -\frac{\epsilon}{(1-\epsilon)^3} \tag{2.21}$$

This approximation obviously deteriorates as the leading edge of the cavitation boundary moves away from the minimum gap.

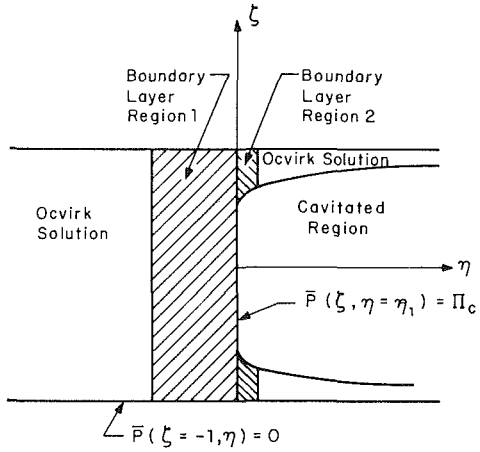


Fig. 1 Sketch showing the different flow regions. Far upstream of the cavitation boundary, the Ocvirk solution (the outer region) is valid; upstream of the leading edge of cavitation, a region 1 boundary layer solution is valid, just downstream of cavitation incipience, a region 2 boundary layer is shown, and between the cavitation boundary and the bearing edge (region 3), the Ocvirk solution is valid

3 Results

We turn now to finding the cavitation boundary shape for a few specific cases. As an example, the cavitation boundary shape is determined for $\lambda = 0.4$, $\zeta_0 = 0.8$ and for eccentricities 0.1 and 0.6 The cavitation incipience region, $\zeta\epsilon[0, 0.8]$, is determined from equation (2.18), while the remaining part of the cavitation curve is determined from equation (2.19). The cavitation pressure for Fig. 2 is $\pi_c = -0.0068$, and for Fig. 3, $\pi_c = 0.035$. The cavitation boundary shape predicted by Pan is also shown. Since Pan used Ocvirk's solution, in the diverging

Downloaded 02 May 2010 to 171.66.16.54. Redistribution subject to ASME license or copyright; see http://www.asme.org/terms/Terms_Use.cfm

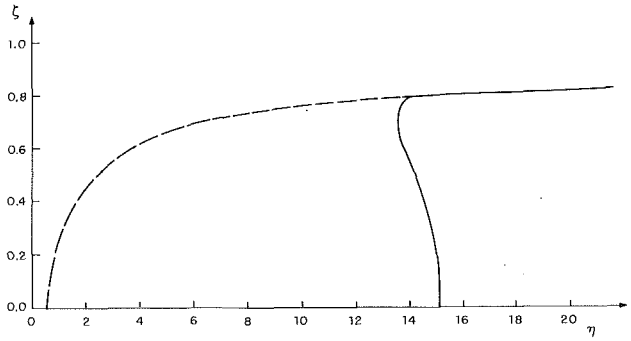


Fig. 2 Plot of cavitation boundary location for $\lambda = 0.4$ and $\epsilon = 0.1$: the curve (———)indicates the new cavitation boundary location; the curve (·····) indicates Pan's cavitation boundary prediction ($\pi_c = 0.00068$)

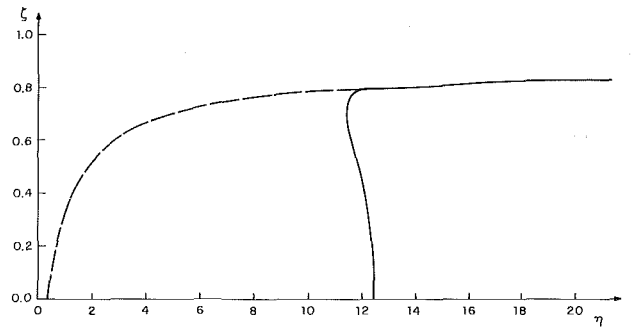


Fig. 3 Plot of cavitation boundary location for $\lambda = 0.4$ and $\epsilon = 0.6$ the curve (———)indicates the new cavitation boundary location, the curve (·····) indicates Pan's cavitation boundary prediction ($\pi_c = -0.035$)

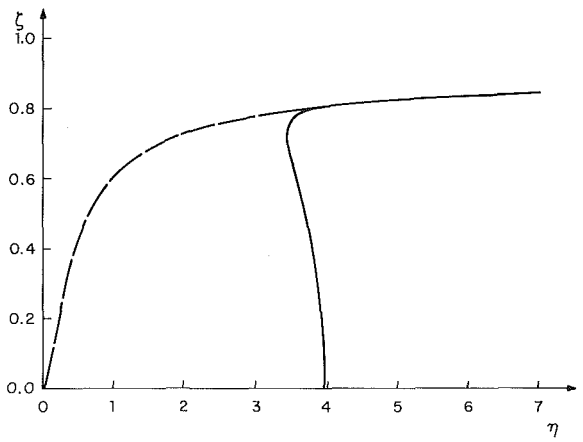


Fig. 4 Plot of cavitation boundary location and shape for $\lambda = 0.1$

portion of the fluid film gap, his solution will always underpredict the angle for centerline cavitation incipience. Here, the newly predicted cavitance boundary shape is qualatively similiar to that obtained by Floberg; both Floberg's result and this result show a region where the function $\eta_1(\zeta)$ becomes multiple valved.

A second set of results is given for $\lambda = 0.1$ and $\zeta_0 = 0.8$. For this smaller aspect ratio the cavitation incipience is seen to occur nearer to the minimum gap. Therefore, equation (2.20) can be used to determine the cavitation boundary shape for $\zeta \epsilon [0, 0.8]$. The cavitation boundary shape does not have an explicit dependence on the journal eccentricity. This result is consistent with the result obtained by Buckholz [1, 2] for Newtonian and power-law non-Newtonian fluids. But, the cavitation boundary shape does depend on ζ_0, which is related to the eccentricity; hence the dependence on eccentricity is implicit through ζ_0. The dependence of the cavitation pressure on eccentricity is shown directly by equation (2.21). The

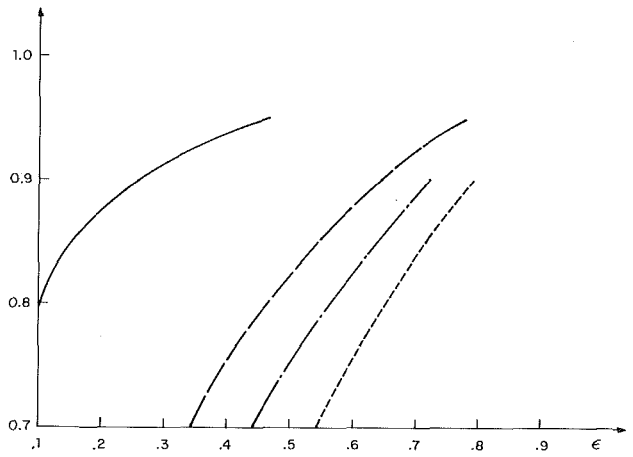


Fig. 5 Cavitation boundary width as a function of eccentricity for fixed values of the parameter π_c/λ, $\pi_c/\lambda = -0.0017$ (———), $\pi_c/\lambda = -0.04$ (– –), $\pi_c/\lambda = -0.08$ (– · –), $\pi_c/\lambda = 0.2$ (----)

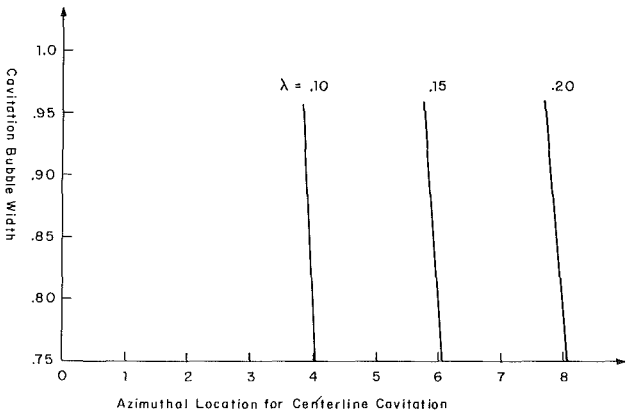


Fig. 6 Axial cavitation bubble width as a function of centerline cavitation bubble location for fixed values of the aspect ratio

cavitation boundary shape for $\lambda = 0.1$ and $\zeta_0 = 0.8$ is given in Fig. 4.

It is of interest to observe the location of the cavitation boundary for both a changing eccentricity and a fixed cavitation pressure; as the eccentricity increases, the isobars move toward the bearings axial ends. Thus, the cavitation boundary will move as the eccentricity changes. Figure 5 shows that the axial extent of the cavitation boundary, for fixed π_c/λ, is a function of the eccentricity.

The effect of increasing journal eccentricity for fixed π_c/λ is shown to increase the width of the cavitation bubble. Likewise, the effect of decreasing π_c/λ while holding the eccentricity fixed is shown to decrease the width of the cavitation bubble, Fig. 5.

The effect of λ and ζ_0 on the axial centerline cavitation bubble location is shown in Fig. 6. A small change in azimuthal location, for fixed λ, is shown to occur for changing ζ. The more important parameter for locating the centerline cavitation is λ. As λ increases, the fluid film penetrates farther into the diverging portion of the gap.

4 Discussion

The effect of fluid film cavitation in short bearings is shown to depend on retaining the azimuthal derivative term in the Reynolds lubrication equation. The azimuthal mass flux near the onset of cavitation is shown to depend on both the Couette velocity component and the Poiseuille velocity component. The Poiseuille azimuthal mass flux term is absent from the

Downloaded 02 May 2010 to 171.66.16.54. Redistribution subject to ASME license or copyright; see http://www.asme.org/terms/Terms_Use.cfm

Ocvirk approximation. A discussion of this boundary layer flow was given by Buckholz [2]. As pointed out earlier, the azimuthal scale of the boundary layer in the region upstream of cavitation is 0 (λ). The location of the centerline cavitation incipience is determined directly by assigning a value to the subambient cavitation pressure and satisfying the Reynolds free-surface condition; the leading edge shape is determined directly from the upstream pressure expansion. Downstream of the cavitation incipience region the fluid film pressure distribution is determined from the Ocvirk solution. The shape of the cavitation boundary agrees qualitatively with results obtained by Floberg [4] and with the shape given by Buckholz [2] for zero cavitation pressure. It should be noted that hydrodynamic bearing loads calculated based on this theory will increase slightly from that previously predicted by Pan. The cavitation boundary shape and location – for nonzero λ – differ significantly from that given by Pan. The fluid film can extend further into the diverging portion of the gap. This is likely to affect the squeeze film bearing loads where the extended fluid film can sustain more load. Analytical results were obtained for the cavitation boundary location as a function of the three parameters: bearing aspect ratio, journal eccentricity, and the cavitation pressure. It would be useful to extend the present analysis to include nonaxisymmetric cavitation shapes due to an imposed axial pressure gradient. All the required approximations follow from the series approximations given here. Pan [6] presented such an analysis, but azimuthal derivatives in Reynolds equation were not included.

References

1 Buckholz, R. H., Lin, J., and Pan, C. H. T., "The Role of Axial Edge Effects and Cavitation in Lubrication for Short Journal Bearings," JOURNAL OF APPLIED MECHANICS, Vol. 52, 1985.

2 Buckholz, R. H., "On The Role of a Non-Newtonian Fluid in Short Bearing Theory," ASME *Journal of Tribology*, Vol. 107, 1985, pp. 68-74.

3 Dubois, G. B., and Ocvirk, F. W., "Analytical Derivation of Short Bearing Approximation to Full Journal Bearings," NACA Report 1157, 1953.

4 Elrod, H. G., "A Cavitation Algorithm," ASME *Journal of Lubrication Technology*," Vol. 103, 1981, pp. 350-354.

5 Floberg, L., "Cavitation Boundary Condition With Regard to the Number of Streamers and Tensile Strength of the Liquid," *Acta Poly. Scan.*, 1965, ME19.

6 Gumbel, Everling, Reibung, and Schmierung in *Maschinenhav*, Krayn, Berlin, 1925, pp. 49-52.

7 Pan, C. H. T., "An Improved Short Bearing Analysis for the Submerged Operation of Plain Journal Bearings and Squeeze-Film Dampers," ASME *Journal of Lubrication Technology*, Vol. 102, 1980, pp. 320-332.

8 Pan, C. H. T., and Ibrahim, R. A., "Cavitation in a Short Bearing with Pressurized Lubricant Supply," ASME *Journal of Lubrication Technology*, Vol. 103, 1981, pp. 337-349.

9 Stieber, W., Das Schwimmlager, Berlin, Ver. Dtsch. Ing., 1933.

10 Swift, H. W., "The Stability of Lubricating Films in Journal Bearings," *J. Inst. Civ. Eng*, 1931, pp. 267-288.

APPENDIX *I*

We seek to evaluate the A_n's using the eigenfunction orthogonality condition. The expression for the A_n's is given in the following:

$$A_n = \frac{\int_0^{\zeta_0} (\pi_c + \frac{1}{2}(1-\zeta^2)Q(\eta_1))\cos\gamma_n\zeta d\zeta + \int_{\zeta_0}^1 (P^{II} + \frac{1}{2}(1-\zeta^2)Q(\eta_1)\cos\gamma_n\zeta d\zeta}{\int_0^1 \cos^2\gamma_n\zeta d\zeta} \qquad (I-1)$$

The following two integrals are easily obtained:

$$\int_0^1 \cos^2\gamma_n\zeta d\zeta = \frac{1}{2}$$

$$\int_0^1 \left(\pi_c + \frac{1}{2}(1-\zeta^2)Q(\eta_1)\right)\cos\gamma_n\zeta d\zeta = \frac{\pi_c(-1)^n}{\gamma_n} + \frac{(-1)^n}{\gamma_n^3}Q(\eta_1) \qquad (I\text{-}3)$$

The third integral is evaluated using integration by parts. Thus:

$$\int_{\zeta_0}^1 (P^{II} - \pi_c)\cos\gamma_n\zeta d\zeta = \frac{-\pi_c(-1)^n}{\gamma_n} - \int_{\zeta_0}^1 \frac{\partial P^{II}}{\partial\zeta}\frac{\sin\gamma_n\zeta}{\gamma_n}d\zeta \qquad (I-4)$$

where

$$P^{II}(\eta=\eta_1,\zeta_0)=\pi_c, P^{II}(\eta=\eta_1,\zeta=1)=0$$

Using integration by parts again, and the Reynolds free-surface condition,

$$\partial P^{II}(\eta=\eta_1,\zeta_0)/\partial\zeta = 0$$

we obtain:

$$\int_{\zeta_0}^1 (P^{II} - \pi_c)\cos\gamma_n\zeta d\zeta = -\frac{\pi_c}{\gamma_n}(-1)^n - \int_{\zeta_0}^1 \frac{\partial^2 B^{II}}{\partial\zeta^2}\frac{\cos\gamma_n\zeta}{\gamma_n^2}d\zeta \qquad (I\text{-}5)$$

Since the short bearing solution is used to determine the pressure in region two, we have

$$\frac{\partial^2 P}{\partial\zeta^2} = \epsilon\sin\eta_1/(1-\epsilon\cos\eta_1)^3 \qquad (I-6)$$

thus

$$\int_{\zeta_0}^1 (P^{II} - \pi_c)\cos\gamma_n\zeta d\zeta = -\frac{\pi_c}{\gamma_n}(-1)^n - \left(\frac{(-1)^n - \sin\gamma_n\zeta_0}{\gamma_n^3}\right)Q(\eta_1) \qquad (I\text{-}7)$$

The final result for the A_n is

$$A_n = (4\sin(\gamma_n\zeta_0)/\gamma_n^3)Q(\eta_1) \qquad (I\text{-}8)$$

APPENDIX *II*

We seek a uniformly valid approximation to the Reynolds equation for small aspect ratio that connects the short bearing solution upstream of the cavitated region to the short bearing solution downstream of the cavitated region. Here it will be shown that a boundary layer in region two is not necessary for wide cavitation bubbles. The boundary valve problem for the boundary layer region is given in the following

$$\nabla^2 P = Q(\eta_1) \qquad (II\text{-}1A)$$

$$P(\eta^*,\zeta=\pm 1)=0 \qquad (II\text{-}1B)$$

$$\lim_{\eta^*\to\infty} P = -\frac{1}{2}(1-\zeta^2)Q(\eta_1) \qquad (II-1C)$$

$$\lim_{\eta^*\to\infty} P = -\frac{1}{2}(1-\zeta^2)Q(\eta_1) + (1-\zeta)\zeta_0 Q(\eta_1) \qquad (II-1D)$$

$$P(\eta^*,\zeta_0(\eta^*)) = \pi_c \qquad (II\text{-}1E)$$

$$\nabla P(\eta^*,\zeta_0(\eta^*)) = 0 \qquad (II\text{-}1F)$$

Equation (*II*-1*A*) is the field equation (i.e., Reynolds equation); equation (*II*-1*B*) is the axial edge boundary condition; equations (*II*-1*C*) and (*II*-1*D*) are the matching conditions; equation (*II*-1*E*) is the cavitation condition; and

Downloaded 02 May 2010 to 171.66.16.54. Redistribution subject to ASME license or copyright; see http://www.asme.org/terms/Terms_Use.cfm

equation (*II*-1*F*) is the Reynolds free-surface condition. Note that equation (*II*-1*C*) is the upstream Ocvirk solution and (*II*-1*D*) is the downstream Pan solution. A solution having the following form is sought:

$$P = -\frac{1}{2}(1-\zeta^2)Q(\eta_1) + P_H \qquad (II\text{-}2)$$

where P_H is the homogeneous solution. Clearly the solution P_H must satisfy the following equations:

$$\nabla^2 P_H = 0 \qquad (II\text{-}3A)$$

$$P_H(\eta^*, \zeta = \pm 1) = 0 \qquad (II\text{-}3B)$$

$$\lim_{\eta^* \to \infty} P_H = 0 \qquad (II\text{-}3C)$$

$$\lim_{\eta^* \to \infty} P_H = (1-\zeta)\zeta_o Q(\eta_1) \qquad (II\text{-}3D)$$

In addition to the preceding conditions, the cavitation and Reynolds boundary conditions must also be satisfied by the entire solution. The homogeneous solution P_H can be found by the superposition of fundamental solutions to Laplace's equation, which automatically satisfy equation (*II*-3*B*). This fundamental solution is given below:

$$\bar{P}_H = \frac{1}{2} ln\left(\frac{\cosh\eta^*\pi/2 - \cos\zeta\pi/2}{\cosh\eta^*\pi/2 + \cos\zeta\pi/2}\right) \qquad (II\text{-}4)$$

Equation (*II*-4) is the fluid mechanical analog of a point vortex, between two parallel plates that are located at $\zeta = \pm 1$. We recognize that a distribution of point vortices along the journal bearing centerline starting at $\eta^* = 0$ and extending to $\eta^* \to \infty$ is also a solution to Laplaces equation. Therefore:

$$\bar{P}_H = Q(\eta_1)\int_0^\infty \frac{1}{2}\kappa(\bar{\eta}) ln\left(\frac{\cosh\eta'\pi/2 - \cos\zeta\pi/2}{\cosh\eta'\pi/2 + \cos\zeta\pi/2}\right) d\bar{\eta} \qquad (II\text{-}5)$$

where $\eta' = \eta^* + \bar{\eta}$, and $\kappa(\bar{\eta})$ is the unknown singularity strength along the centerline. The total pressure is given in the following:

$$P = -\frac{1}{2}(1-\zeta^2)Q(\eta_1)$$

$$+\int_0^\infty \frac{1}{2}\kappa(\bar{\eta}_1) ln\left(\frac{\cosh\eta'\pi/2 - \cos\zeta\pi/2}{\cosh\eta'\pi/2 + \cos\zeta\pi/2}\right) Q(\eta_1) d\bar{\eta} \qquad (II\text{-}6)$$

The cavitation pressure condition, $P = \pi_c$, and the Reynolds condition in region *II*, $\partial P/\partial\zeta = 0$, are:

$$\pi_c = -\frac{1}{2}(1-\zeta^2)Q(\eta_1)$$

$$+ Q(\eta_1)\int_0^\infty \frac{1}{2}\kappa(\bar{\eta}) ln\left(\frac{\cosh\eta'\pi/2 - \cos\zeta\pi/2}{\cosh\eta'\pi/2 + \cos\zeta\pi/2}\right) d\bar{\eta} \qquad (II\text{-}7A)$$

$$0 = \zeta_0 + \pi/4 \sin\zeta\pi/2 \int_0^\infty \frac{\kappa(\bar{\eta})}{\cosh\eta'\pi/2} \times$$

$$\times\left(\frac{1}{1 - \dfrac{\cos\zeta_0\pi/2}{\cosh\eta'\pi/2}} - \frac{1}{1 + \dfrac{\cos\zeta_0\pi/2}{\cosh\eta\pi/2}}\right) d\bar{\eta} \qquad (II\text{-}7B)$$

The shape of the cavitation boundary in region 2 is $\zeta_0(\eta)$. Equations (*II*-7*A*) and (*II*-7*B*) are nonlinear integral equations for $\kappa(\bar{\eta})$ and $\zeta_0(\eta)$. In general a numerical solution is required. Here we take advantage of the wide bubble approximation by defining the parameter τ as follows:

$$\tau = \cos(\pi\zeta/2)/\cosh\eta'\pi/2 \qquad (II\text{-}8)$$

Equations (*II*-7*A*) and (*II*-7*B*) are expressed in terms of τ, using a geometric series approximation to the integrand; these expansions are given in the following:

$$\pi_c = -(1-\zeta_0^2)\frac{1}{2}Q(\eta_1) - \frac{1}{2}\int_0^\infty \kappa(\bar{\eta})2\{\tau + \tau^3/3 + \tau^5/5 + \ldots\} d\bar{\eta} \qquad (II\text{-}9)$$

$$0 = \zeta_0 + (\pi/4)\sin\zeta_0\pi/2 \int_0^\infty \frac{\kappa(\bar{\eta})}{\cosh\eta'\pi/2}\{2 + 2\tau^2 + 2\tau^4 + \ldots\} d\bar{\eta} \qquad (II\text{-}10)$$

In the case of wide cavitation bubbles we have $\tau << 1$; thus, the preceding two equations are expressed as:

$$\frac{\pi_c}{Q(\eta_1)} = -\frac{1}{2}(1-\zeta_0^2) - \frac{1}{2}\cos\zeta_0\pi/2 \int_0^\infty \frac{\kappa(\bar{\eta})2}{\cosh\eta'\pi/2} d\bar{\eta} \qquad (II\text{-}11)$$

$$0 = \zeta_0 + (\pi/4)\sin\zeta_0\pi/2 \int_0^\infty \frac{\kappa(\bar{\eta})2}{\cosh\eta'\pi/2} d\bar{\eta} \qquad (II\text{-}12)$$

The foregoing equations can be solved for ζ_0 and the result is:

$$\zeta_0 = 1 - \sqrt{-2\pi_c/Q(\eta_1)} \qquad (II\text{-}13)$$

We recognize the preceding result as the Ocvirk short bearing solution for regions 2 and 3. Thus, it is shown that Ocvirk's short bearing theory is a valid approximation for the pressure in region two.

Downloaded 02 May 2010 to 171.66.16.54. Redistribution subject to ASME license or copyright; see http://www.asme.org/terms/Terms_Use.cfm

Asynchronous Instability of a Rotating Centrifuge Partially Filled With Fluid

C. A. Cheng

A. S. Berman

T. S. Lundgren

Department of Aerospace Engineering and Mechanics, University of Minnesota, Minneapolis, Minn. 55455

An experimental investigation of the asynchronous whirl motion of a partially filled rotating centrifuge on an elastic support system has been performed. Whirl runout amplitudes are measured and the data are used to deduce the stability boundaries of the asynchronous whirl. The effects of various parameters on the stability boundaries are studied systematically. These parameters are the fill ratio, mass ratio, Reynolds number, and the damping of the elastic support system. The experimental results are compared with theoretical predictions based on a linear analysis. Free surface shapes are compared with results of nonlinear analysis.

Introduction

For a centrifuge operating at high rotating speeds, it is known that, when there is liquid trapped in the centrifuge, the centrifuge will undergo unstable whirling motion over a range of operating speeds. This whirling motion is asynchronous, the whirl frequency being different from the operating frequency of the centrifuge.

In his experiments examining the effects of reduced critical speed due to liquid trapped in a rotating centrifuge, Kollmann [1] found a range of operating speeds at which unstable whirl occurred. No definite explanation of the phenomenon was attempted but it was presumed to be caused by some sort of waves in the liquid.

Epishev [2] analyzed the case of a very thin liquid layer in the rotating centrifuge and the mass of liquid was assumed negligible. He considered that the self-excited oscillations were maintained by energy absorbed from the motor that drove the centrifuge and transmitted by friction to the liquid layer in the centrifuge. Ehrich [3] incorporated the viscosity of the liquid in his analysis and assumed that the circumferential velocity of the spun-up liquid (in a coordinate system attached to the rotating centrifuge) varied linearly with the radial distance from the center of centrifuge. Both analyses predicted self-excited asynchronous whirl onset at an operating speed above the critical speed of the centrifuge system.

Wolf [4] considered an inviscid, incompressible fluid in a rotating centrifuge which was assumed to undergo a uniform, circular whirling motion. He coupled the liquid momentum to the motion of the centrifuge which was subjected to a linear restoring force provided by the elastic shaft on which the centrifuge was mounted. A linear analysis predicted the overall bounds of the range of operating speeds at which unstable, asynchronous whirl occurred. Wolf examined the dependency of the extent of this unstable region on the volume and density of the fluid load, and good agreement between the experimental results and the theory was observed, except for very small fluid load.

Hendricks and Morton [5] extended Wolf's work by including the viscosity of liquid in the centrifuge and the damping effect of the support system. A linear analysis was used to predict the range of operating speeds at which the system was unstable when the fill ratio, mass ratio, Reynolds number, and external damping were specified. They reported a numerical study of the effects of these parameters on the stability boundaries, but no extensive experiments were performed to verify the accuracy of the predictions.

It is the goal of this paper to present the results of a systematic experimental investigation of the effects of those parameters that Hendricks and Morton judged to be important on the stability boundaries for the asynchronous whirling motion of a partially filled rotating centrifuge.

Apparatus and Instrumentation

Equipment has been designed to monitor closely the asynchronous whirling motion and to control carefully the variables that affect the whirl phenomenon. Figure 1 is a schematic diagram of the equipment, which is basically a centrifuge mounted on a platform and coupled to an elastic support system. The centrifuge is a lucite cylinder of inner diameter 0.12 m and height 0.06 m. A short centrifuge is used so that the thickness variation of the spun-up liquid film from top to bottom of centrifuge is kept below about 5 to 10 percent for the range of operating speeds investigated. The top of the cylinder is covered by a lucite lid with a hole in the center for adding or removing liquid. The lower end of the cylinder has a lucite flange which is mounted to an aluminum circular base by six uniformly spaced screws. The aluminum base is mounted on the shaft of the servomotor that drives the

Contributed by the Applied Mechanics Division for publication in the JOURNAL OF APPLIED MECHANICS.

Discussion on this paper should be addressed to the Editorial Department, ASME, United Engineering Center, 345 East 47th Street, New York, N.Y. 10017, and will be accepted until two months after final publication of the paper itself in the JOURNAL OF APPLIED MECHANICS. Manuscript received by ASME Applied Mechanics Division, June, 1984; final revision, November, 1984.

Copyright © 1985 by ASME

Downloaded 02 May 2010 to 171.66.16.54. Redistribution subject to ASME license or copyright; see http://www.asme.org/terms/Terms_Use.cfm

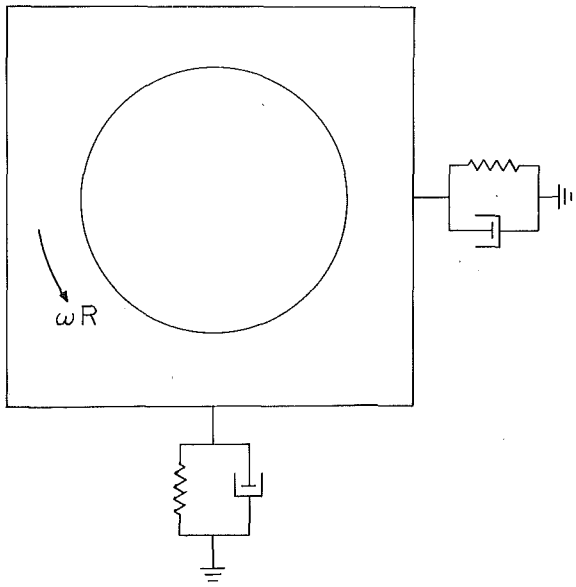


Fig. 1 Schematic diagram of rotor system

centrifuge and the motor is fixed to the platform. When the centrifuge undergoes pure rotational motion, the platform is stationary, but when the centrifuge undergoes whirling motion and moves away from its equilibrium position, the platform moves with it. The platform is a rectangular aluminum plate with a circular hole in the center and a cylindrical sleeve welded to the bottom surface which houses the servomotor.

The platform is coupled to the elastic support system through two sets of linear bearings and is free to move in two mutually perpendicular directions. The motion in a plane perpendicular to the axis of rotation of the centrifuge is resisted by linear restoring forces and viscous damping forces provided by the support system. The elastic support system has a double cantilever spring and a piston-type damper in each direction of motion. The spring constants and damping factors associated with each degree of freedom can be matched closely. The effective length of a double cantilever spring is determined by the positions of clamps at the two ends. These effective lengths can be adjusted so as to match the resonant frequencies and thus the spring constants associated with either degree of freedom. The viscous damper is a hypodermic syringe filled with silicone oil supplied by an oil reservoir through tubing. The damping factor varies with the length and diameter of the tubing and the viscosity of silicone oil in it. A clamp on the tubing provides fine tuning for matching the damping forces in the two directions. The masses associated with either direction of motion are balanced by means of two metal frames in the support system. Each frame moves with the whirling platform in only one direction and they are built in such a way that the masses moving in the two directions are equal. The total mass (includes the centrifuge, platform and metal frame) moving in each direction is approximately 20 kg. The support system has a steel plate foundation firmly fixed to a large concrete pier which is part of the foundation of the building. This eliminates any interaction between the whirling centrifuge and the surroundings.

The experiments are designed to measure the whirl amplitude and frequency as functions of operating speed. Speed measurements are accomplished with the aid of a Bentley magnetic probe which is fixed on the platform and mounted at an appropriate distance above the screws on the lower flange of the centrifuge. During rotational motion of the centrifuge, when a screw passes under the magnetic probe, the probe generates a signal which is amplified and fed to a counter. For each revolution of the centrifuge, six pulses are recorded by the counter, so when the counter is opened for a 10-second period, the counter displays the rotational speed in RPM. The rotational speed can be thus determined to the precision of 5 RPM, which amounts to about 0.5 percent of the average operating speed.

Whirl amplitude is defined as the displacement of the center of the centrifuge from its equilibrium position when it whirls. And whirl frequency is the angular velocity of the displaced center of centrifuge around its equilibrium position. Whirl amplitudes and frequencies are determined by signals obtained from a noncontact linear proximity measuring system. A Kamen variable impedance transducer displacement measuring system is used and it outputs an analog voltage signal directly proportional to the distance between its sensor and a metallic target. The proximity probe has a frequency response from 0 to 50 kilohertz, is calibrated in place, and has a sensitivity of about 80 millivolts per millimeter. In each direction of motion of the platform, there is a metallic target mounted on the platform with its surface perpendicular to the direction of motion and its center aligned with the center of the centrifuge. A sensor of the proximity probe system is fixed to the steel plate foundation and in a position parallel to and at a distance from each target surface. The analog voltage outputs from the proximity probe electronics are fed to the two channels of a Hewlett-Packard Model 3582A spectrum analyzer. The spectrum analyzer has a A/D converter which converts an analog signal to a digital signal. A built-in microcomputer then performs a discrete Fourier transform to convert a finite segment of discrete time data into a discrete frequency spectrum. The amplitudes of the synchronous as well as asynchronous whirl are displayed as functions of frequency. For most operating conditions, the spectrum analyzer is set at a frequency span of 25 Hz, for which the resolution is 0.2 Hz and the amplitude sensitivity is set so that an amplitude resolution of 0.01 mV, or 0.0125 mm is achieved.

Procedure

A goal of this investigation is the experimental determination of the effects of variables such as volume, density, and viscosity of fluid in the centrifuge, and the damping forces and spring forces of the elastic support system, on the stability boundaries of asynchronous whirl. Hence these variables, as well as the whirl amplitude and frequency, must be measured. The density and viscosity of the fluid are determined by conventional methods using specific gravity bottles and Fenske viscometers, respectively. The method used to determine the damping coefficient and resonant frequency is summarized here. The elastic support system is assumed to be a two degree of freedom, viscous damped, linear oscillator. A 5-gram weight is mounted on one of the six screws on the lower flange of the centrifuge to provide a driving force which produces a synchronous runout. By examining the phase of the driving force (determined from the magnetic probe signal) and the synchronous runout (determined from the proximity probe signal) on a dual-trace oscilloscope, the resonant frequency can be determined from the operating frequency at which the two signals are 90 deg out of phase. The synchronous runout amplitude at resonance is obtained from the proximity probe signal fed to the spectrum analyzer. Then, measurements of runout amplitude are made at three operating frequencies about 1.5 to 2.0 times the resonant frequency. These data are used in an iteration scheme which is basically a four-point curve fitting to determine the damping coefficient of the elastic support system. In most experiments, the resonant frequency of the system is set at 1100 to 1200 RPM, while the damping

Downloaded 02 May 2010 to 171.66.16.54. Redistribution subject to ASME license or copyright; see http://www.asme.org/terms/Terms_Use.cfm

coefficient is in the range of 0.08 to 0.10 of the critical damping. From measurements made before and after each whirl run, it may be concluded that the resonant frequency and damping coefficient can be measured with a precision of about 5 percent.

After the resonant frequencies and damping coefficients associated with the two degrees of freedom have been determined, the 5-gram weight is removed and the centrifuge is loaded with a known amount of fluid, whose density and viscosity are known. Fluid temperature is measured before and after each whirl experiment and the mean temperature is used for determination of the fluid viscosity. In general, the temperature of fluid rises by three to five degrees Celsius during the experiment. The centrifuge is spun up and the operating speed is gradually increased until asynchronous whirl appears. The analog signals from the two proximity probes are fed to the two channels of the spectrum analyzer which is interfaced with a digital computer that controls the analyzer operation. It has been observed that, depending on the operating speed, the whirl amplitude may be steady or modulated. The phenomenon of modulated whirl amplitude was studied and reported elsewhere [6]. When the whirl amplitude is modulated, "peak averaging" on the spectra sampled by the spectrum analyzer is taken, otherwise, "RMS averaging" is used. In either case, the averaged spectral data are transferred to the digital computer and stored on magnetic tape for further analysis. The operating speed at which each whirl amplitude measurement is made is obtained from the digital counter and input to the computer. For each whirl experiment, the operating speed is manually adjusted to cover the region in which asynchronous whirl exists and whirl measurements are made with both increasing and decreasing operating speed. After each whirl experiment, measurements of resonant frequency and damping coefficient are repeated.

Results

It has been observed that during a whirl experiment, at operating speeds below a certain critical value, the centrifuge is in pure rotational motion about its geometric center. When operating speed exceeds this lower critical speed, the centrifuge moves away from its equilibrium position and whirls at a frequency lower than the operating frequency. Further increase in operating speed first leads to a rapid increase in whirl amplitude until the whirl amplitude reaches its maximum at a certain speed. Beyond that speed, an increase in operating speed results in a gradual decrease in whirl amplitude until the whirl vanishes and the centrifuge resumes pure rotational motion about its geometric axis. The operating speeds at which whirl first appears and ultimately disappears are called the lower and upper stability boundaries and define a range of operating frequencies at which the centrifuge is unstable and asynchronous whirl exists.

It has been found that for the apparatus used, the damping coefficient can only be determined with reasonable accuracy for runout amplitudes greater than about 0.025 mm. For runout amplitudes smaller than that, friction in the system bearings elsewhere in the system becomes comparable to the viscous damping and the system no longer behaves as a linear viscous damped oscillator. For this reason, it is not appropriate to consider the operating speed at which the observed whirl amplitude vanishes to be the stability boundary of asynchronous whirl at the given operating conditions. Instead of attempting a parametric study of the unstable, asynchronous whirl boundaries, the parametric dependence of contours of finite whirl amplitudes greater than 0.025 mm is investigated.

Data for this parametric study are deduced from whirl amplitude versus operating speed curves obtained from a series of whirl experiments. Figure 2 is a typical whirl amplitude curve in which the runout amplitudes in both directions of motion are shown. It presents data obtained in a whirl experiment with 250 cu. cm of silicone oil in the centrifuge. The whirl amplitude rises so sharply with operating speed near the lower stability boundary that no significant data can be obtained in that range of operating speeds. Consequently for most of the parametric studies, only the effects on the upper stability boundaries are presented.

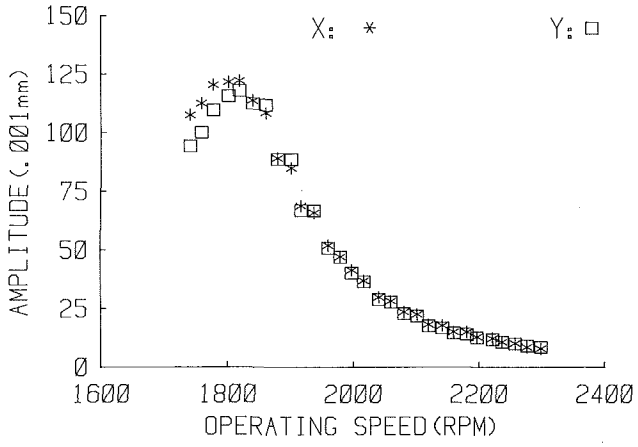


Fig. 2 Typical whirl amplitude curve (fill ratio = 0.21, mass ratio = 0.032, Re = 4×10^4, damping coefficient = 0.08)

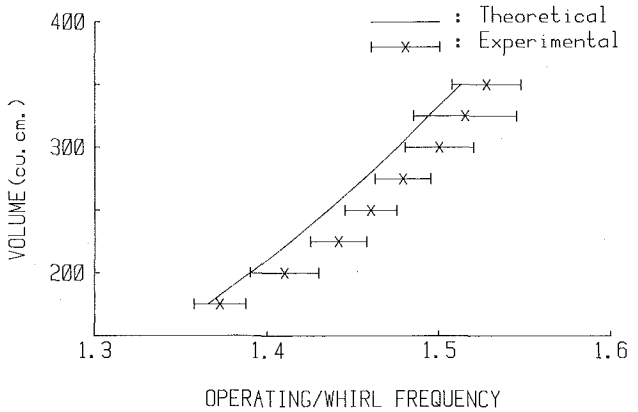


Fig. 3 Comparison of experimental and predicted whirl frequency (mass ratio = 0.034, Re = 5.7×10^5, damping coefficient = 0.09)

Experiments show that the ratio of operating to whirl frequency is essentially constant over the range of operating frequencies above that of maximum whirl amplitude. The value of this ratio is averaged over the range of operating speeds near the upper stability boundary and the means and standard deviations for different fluid loads are presented in Fig. 3. Also shown in Fig. 3 is the value of this ratio at the upper stability boundary predicted by Hendricks and Morton's linear stability theory plotted as a function of fluid load. The agreement between the experimental results and the predictions is satisfactory.

In the parametric studies, the data corresponding to whirl amplitudes of 0.025 mm, 0.075 mm, and 0.125 mm obtained from interpolation of whirl amplitude curves will be presented. They will be shown on figures along with the "zero whirl amplitude" operating speeds at the upper stability boundaries predicted from Hendricks and Morton's linear theory at corresponding operating conditions. In Hendricks and Morton's linear analysis, the Ekman boundary layers at the top and bottom of the centrifuge have been ignored by assuming the centrifuge is long. In this report, the height of

Downloaded 02 May 2010 to 171.66.16.54. Redistribution subject to ASME license or copyright; see http://www.asme.org/terms/Terms_Use.cfm

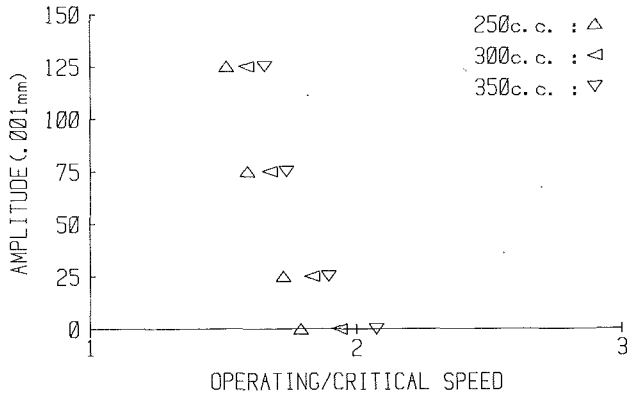


Fig. 4 Effect of fill ratio (mass ratio = 0.032, Re = 3.4×10^4, damping coefficient = 0.09)

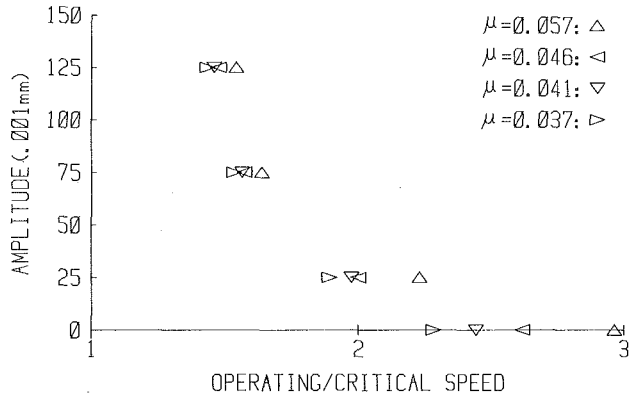


Fig. 5 Effect of mass ratio (fill ratio = 0.14, Re = 7.4×10^5, damping coefficient = 0.09)

centrifuge is finite but the Ekman numbers corresponding to the experimental conditions are of order 4.4×10^{-5}. The Ekman suction velocity is less than 1 percent of the perturbation velocity and should not introduce substantial discrepancy in the comparisons of experimental results with Hendricks and Morton's analysis.

Effect of Fill Ratio

The fill ratio is the ratio of unperturbed uniform film thickness of spun-up fluid layer to the inner radius of the centrifuge. For a given centrifuge, the fill ratio depends on the volume of fluid in the centrifuge. Figure 4 presents the summary of three whirl experiments with fluid loads ranging from 250 to 350 cu. cm of silicone oil. It indicates that when other parameters are kept unchanged, an increase in volume of fluid (and thus fill ratio) moves the constant whirl amplitude contours to higher operating speeds and it agrees with the predicted effect on the stability boundary based on Hendricks and Morton's analysis. A visual extrapolation of the measured finite whirl amplitudes suggests the whirl amplitudes will vanish at operating speeds consistent with those predicted by the linear stability theory.

Effect of Mass Ratio

Mass ratio is the ratio of fluid that fills the centrifuge to the mass of centrifuge (including parts that move with the centrifuge during whirl) and it has been found to be an important parameter in the study of asynchronous whirl. In this study, cesium chloride solutions of different concentrations have been used to provide a mass ratio ranging from 0.04 to 0.06. Cesium chloride solution has the advantage that its kinematic viscosity varies little with changes in concentration and density. Hence, experiments can be carried out with fluids of different densities but similar Reynolds numbers. Figure 5 shows the effect of mass ratio on the whirl amplitude contours deduced from a series of whirl experiments with 175 cu. cm of cesium chloride solutions. The predicted stability boundaries computed from Hendricks and Morton's theory are plotted on the zero whirl amplitude axis. It can be concluded that the experimental data indicate results consistent with the theory, namely, an increase in mass ratio results in a wider range of operating speeds at which unstable, asynchronous whirl exists.

Effect of Reynolds Number

The Reynolds number in the study of asynchronous whirl is defined by

$$\mathrm{Re} = \frac{\omega_0 R^2}{\nu}$$

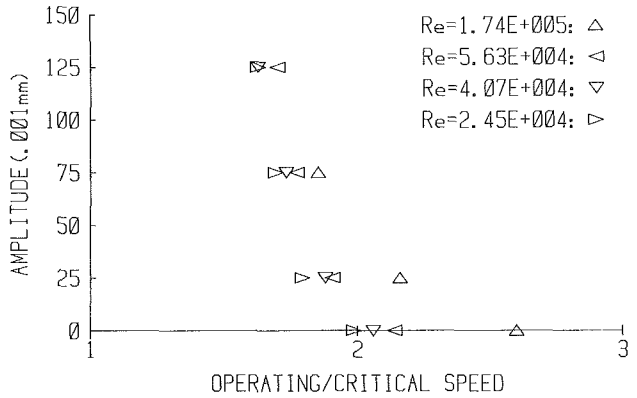


Fig. 6 Effect of Reynolds number (fill ratio = 0.30, mass ratio = 0.032, damping coefficient = 0.09)

where

ω_0 is the resonant frequency of the support system
R is the inner radius of centrifuge
ν is the kinematic viscosity of fluid in the centrifuge.

For the study of the effect of Reynolds number, silicone oils of kinematic viscosity (nominal value at 20°C) ranging from 3 to 20 centistokes have been used. With these fluids, whirl experiments were performed with Reynolds numbers ranging from 24480 to 17400 and the results are summarized in Fig. 6. The upper stability boundaries predicted by Hendricks and Morton's linear analysis corresponding to each whirl experiment are shown on the zero whirl amplitude axis. The experimental data agree with the theory in indicating that higher Reynolds number (lower kinematic viscosity) moves the upper stability boundaries to higher operating speeds.

Effect of Damping Coefficient

The dimensionless damping coefficient is defined as the ratio of the damping constant of the elastic support system to the critical damping constant. Different damping coefficients were obtained by filling the piston-type dampers with silicone oils of kinematic viscosities of 13.3, 20.0, and 30.0 centistokes and this provided damping coefficients ranging from 0.065 to 0.120 of the critical damping. With the same fluid load of 250 cu. cm of silicone oil, whirl experiments were carried out with different damping forces and the results are presented in Fig. 7. The data ponts for zero whirl amplitude are the upper stability boundaries predicted by linear stability analysis. Although the constant finite whirl-amplitude contours for different dampings do not appear in the same sequence as that

Downloaded 02 May 2010 to 171.66.16.54. Redistribution subject to ASME license or copyright; see http://www.asme.org/terms/Terms_Use.cfm

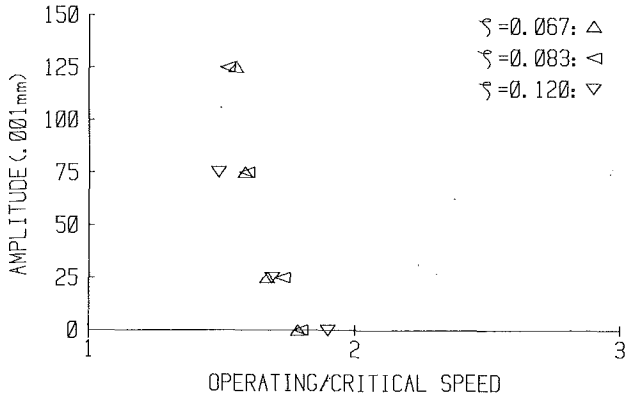


Fig. 7 Effect of damping coefficient (fill ratio = 0.21, mass ratio = 0.032, Re = 4×10^4)

of the predicted stability boundaries, an extrapolation of the experimental data for each damping reveals that the stability boundaries obtained by such extrapolation are consistent with the theoretical predictions. The difference in external damping significantly changes not only the position, but also the slope of the whirl amplitude curves so that the curves cross each other.

From the results shown so far, it can be concluded that effects of these parameters on the stability boundaries obtained experimentally are consistent with the predictions of the linear analysis of Hendricks and Morton.

During the acquisition of the whirl-amplitude data, visual observation of the free surface of the spun-up fluid film revealed some interesting phenomena. It was observed that the waves on the free fluid surface were remarkably uniform from top to bottom of the centrifuge. Since the film thickness variation from top to bottom, which is the only factor that will contribute to axial dependence of the whirl motion, is kept below about 10 percent, it may be assumed that the whirl motion is two-dimensional. With stroboscopic illumination synchronized to whirl frequency, photographs of the fluid film were taken by a precision view camera. The fluid film thickness distribution is measured from each of these 3 in. × 5 in. photographs to the precision of 0.0125 mm and the normalized film thickness is plotted as a function of angular position along the circumference. The film thickness is normalized to $(h\text{-}ho)/\mu ho$, where h is the actual film thickness, ho is the average unperturbed film thickness for the fluid load, and μ is the mass ratio. The measured film thickness distribution is compared to the theoretical film thickness distribution predicted by a nonlinear analysis and reported elsewhere [6].

Results from a whirl experiment with a fluid load of 175 cu. cm of water where Reynolds number is 57,6500, mass ratio is 0.0339 and damping coefficient is 0.095 are presented in Figs. 8 to 11. Figure 8 is the film thickness distribution when a hydraulic jump with several waves and turbulence behind it occur on the film surface. When operating speed is raised, the waves behind the hydraulic jump flatten and the film surface changes to that shown in Fig. 9. Further increase in operating speed results in modulation of whirl amplitude mentioned earlier. Visual observation reveals that this modulation is associated with periodic or aperiodic breaking and reformation of the hydraulic jump. Figure 10 shows the film thickness distribution when whirl amplitude is modulating. It suggests that the hydraulic jump is breaking and the waves behind it are decaying to form a solitary wave on the film surface. At higher operating speeds, the whirl amplitude stabilizes and a solitary wave exists on the otherwise smooth surface as indicated in Fig. 11. In each of the preceding figures, the theoretical result is computed by a numerical

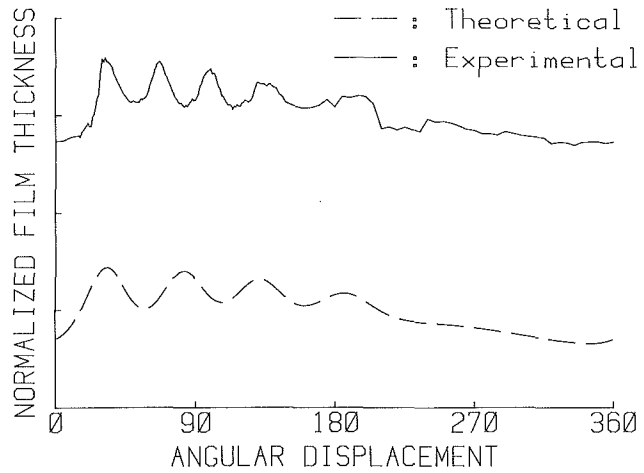


Fig. 8 Film thickness distribution (ω/ω_0 = 1.324, fill ratio = 0.14, mass ratio = 0.034, Re = 5.7×10^5, damping coefficient = 0.09)

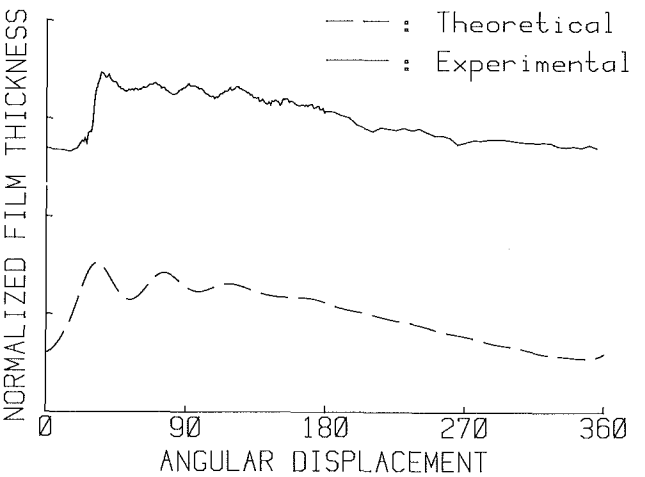


Fig. 9 Film thickness distribution (ω/ω_0 = 1.375, fill ratio = 0.14, mass ratio = 0.034, Re = 5.7×10^5, damping coefficient = 0.09)

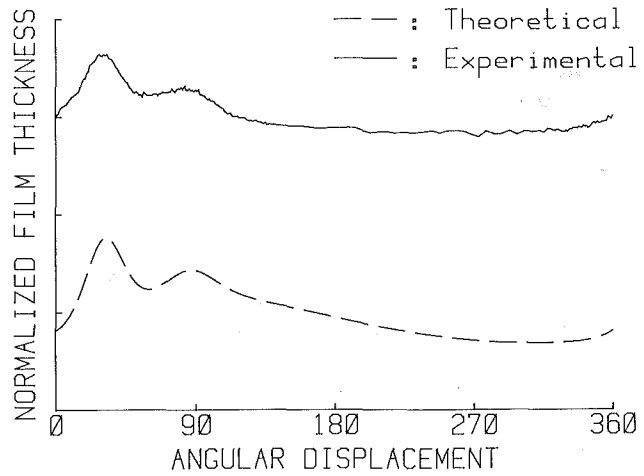


Fig. 10 Film thickness distribution (ω/ω_0 = 1.619, fill ratio = 0.14, mass ratio = 0.034, Re = 5.7×10^5, damping coefficient = 0.09)

method described in [7] at the corresponding operating conditions except that the operating speed is about 10 percent lower than that of the experiment.

Downloaded 02 May 2010 to 171.66.16.54. Redistribution subject to ASME license or copyright; see http://www.asme.org/terms/Terms_Use.cfm

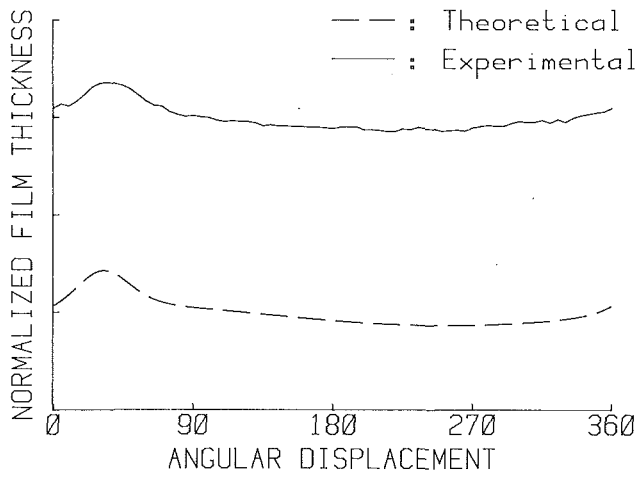


Fig. 11 Film thickness distribution (ω/ω_0 = 1.744, fill ratio = 0.14, mass ratio = 0.034, Re = 5.7×10^5, damping coefficient = 0.09)

Conclusion

An experimental investigation of the asynchronous instability of a partially filled rotating centrifuge has been completed. It indicates that the asynchronous whirling motion is associated with a hydraulic jump and/or waves propagating on the spun up fluid film surface. A study of the effects of various parameters on the stability boundaries leads to the following conclusions. (1) The region of instability widens with increase in fluid load. (2) Higher mass ratio widens the region of instability. (3) Higher Reynolds number widens the region of instability. (4) Higher external damping widens the region of instability. These results are in satisfactory agreement with the predictions of Hendricks and Morton's linear analysis.

Acknowledgments

The authors are grateful to Professor S. L. Hendricks of the Virginia Polytechnic Institute and State University, Blacksburg, Virginia, for providing the FORTRAN program that allows the computation of the stability boundaries based on the linear analysis. Financial assistance from the Union Carbide Corporation, Nuclear Division, Separation Systems Department, Oak Ridge, Tenn. made the completion of this study possible.

References

1 Kollmann, F. G., "Experimentelle und theoretische Untersuchungen uber die Kritischen Drehzahlen flussigkeitsgefullter Hohlkorper," *Forschung auf dem Gebiete des Ingenieurwesens*, Ausgabe B, Vol. 28 1962, pp. 115–123 and 147–153.

2 Epishev, L. V., "On the Dynamic Instability of a Revolving Rotor Partly Filled With a Liquid," *Nauchnye doklady vysshei shkoly, series Mashinostroenie i priborostroenie*, 1959, No. 2, pp. 66–74.

3 Ehrich, F. F., "The Influence of Trapped Fluid on High Speed Rotor Vibration," ASME *Journal of Engineering for Industry*, Vol. 89, 1967, pp. 806–812.

4 Wolf, J. A., Jr., "Whirl Dynamics of a Rotor Partially Filled With Liquid," ASME JOURNAL OF APPLIED MECHANICS, Vol. 35, 1968, pp. 676–682.

5 Hendricks, S. L., and Morton, J. B., "Stability of a Rotor Partially Filled With a Viscous Incompressible Fluid," ASME JOURNAL OF APPLIED MECHANICS, Vol. 46, 1979, pp. 913–918.

6 Berman, A. S., Lundgren, T. S., and Cheng, C. A., "Asynchronous Whirl in a Rotating Cylinder Partially Filled With Liquid," *Journal of Fluid Mechanics*, Vol. 50, 1985, pp. 311–327.

7 Cheng, C. A., "Self-Induced Asynchronous Instability in a Partially Filled Rotating Centrifuge on an Elastic Support System," Ph.D. Thesis, University of Minnesota, Minneapolis, Minn., Nov. 1983.

Downloaded 02 May 2010 to 171.66.16.54. Redistribution subject to ASME license or copyright; see http://www.asme.org/terms/Terms_Use.cfm

Falkner-Skan Solution for Gravity-Driven Film Flow

H. I. Andersson

T. Ytrehus

The Norwegian Institute of Technology,
N-7034 Trondheim–NTH, Norway

It is demonstrated that the development of a viscous film flow down along a vertical wall can be described by the classical Falkner-Skan equation from aerodynamic boundary layer theory for the particular parameter-value m = ½. This leads to a well-known exact solution for the velocity field, as long as the viscous boundary layer can be considered not to interact with the free surface of the film. An exact reference solution for developing film flow is thus made available, against which approxiate solutions may be tested for accuracy.

Introduction

An important class of exact solutions to the boundary layer version of the viscous fluid flow equations was discovered by Falkner and Skan (1931), and was later explored numerically by Hartree (1937). It was established that, for problems without finite geometrical length-scales and for certain external inviscid flow-behavior, the governing partial differential equations for the boundary layer motion could be transformed into the following third-order ordinary differential equation,

$$f''' + ff'' + \beta(1 - f'^2) = 0 \quad \text{where} \quad \beta = \frac{2m}{m+1}, \tag{1}$$

which can be solved by standard numerical techniques to an arbitrary high degree of accuracy. This is an example of a so-called similarity solution in fluid mechanics.

More specifically, the Falkner-Skan similarity solutions arise in aerodynamic boundary layer flows along semi-infinite wedge-shaped bodies and around sharp corners, in which cases the external velocity $U(x)$ becomes proportional to x^m:

$$U(x) = Cx^m \tag{2}$$

where x measures the local distance along the wall, and where m relates to the wedge-angle θ_w, or, to the angle of the corner by $\theta_w = \beta\pi$; see e.g. Evans (1968). In the absence of external forces, the boundary layer flow is then completely controlled by the pressure gradient

$$\frac{1}{\rho}\frac{dp}{dx} = -U\frac{dU}{dx} \sim mx^{2m-1} \tag{3}$$

as implied by the Bernoulli theorem at the outer edge of the viscous domain. The driving pressure gradient is therefore in general proportional to a power in x, except in the singular case $m = ½$ for which it becomes a constant.

It is the contention of the present paper to demonstrate that this special case of $m = ½$ also corresponds to the boundary layer development in a gravity-driven hydraulic film flow down a vertical wall, the constant gravity acceleration then corresponding to the constant pressure gradient in equation (3). From this observation it follows that the exact Falkner-Skan solution for an aerodynamic boundary layer on a wedge with the particular opening angle $\theta_w = 2\pi/3$ also solves the hydrodynamic boundary layer problem in film flow down a vertical wall. It is a remarkable fact that this exact solution

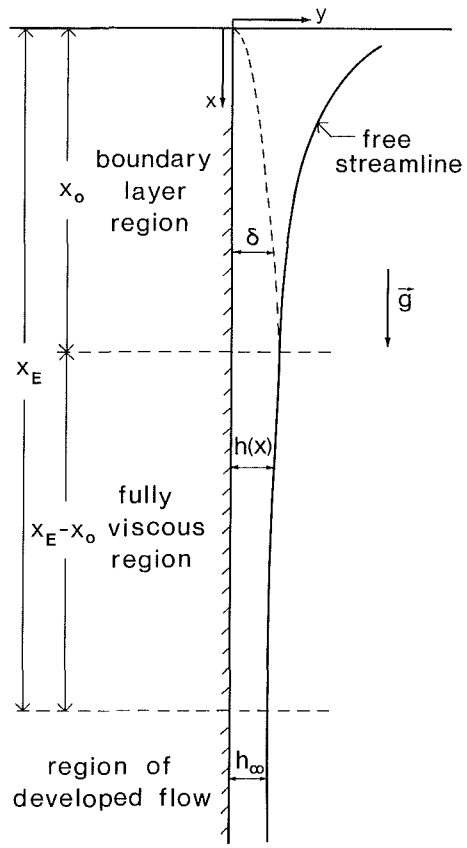


Fig. 1 Coordinate system and notations

Contributed by the Applied Mechanics Division for publication in the *Journal of Applied Mechanics*.

Discussion on this paper should be addressed to the Editoral Department, ASME, United Engineering Center, 345 East 47th Street, New York, N.Y. 10017, and will be accepted until two months after final publication of the paper itself in the *Journal of Applied Mechanics*. Manuscript received at ASME Applied Mechanics Division, December, 1984; final revision, January, 1985.

Copyright © 1985 by ASME

Downloaded 02 May 2010 to 171.66.16.54. Redistribution subject to ASME license or copyright; see http://www.asme.org/terms/Terms_Use.cfm

has escaped the attention of the numerous investigators of laminar film flow and related hydraulic phenomena over the years.

Analysis

With reference to Fig. 1 we consider the inlet region, or, equivalently, the boundary layer region in the film flow down along a vertical wall.

This region is distinguished from the rest of the flow field by the existence of a viscous boundary layer whose thickness $\delta(x)$ is smaller than the corresponding local film thickness $h(x)$.

Between the boundary layer and the free streamline bordering the atmosphere, there is inviscid, quasi-one-dimensional flow with downward velocity $U(x)$ and with constant pressure p_0. For this flow the Bernoulli equation yields,

$$\tfrac{1}{2}U^2 - gx = 0 \tag{4}$$

assuming zero velocity (and infinite film thickness) at the entrance of the wall, $x = 0$. From this equation two simple results are derived:

$$U(x) = \sqrt{2gx} \tag{5a}$$

and

$$U\frac{dU}{dx} = g, \tag{5b}$$

the latter of which presenting the formal equivalence with equation (3) for the case $m = \frac{1}{2}$.

In the viscous boundary layer the Navier-Stokes equation for incompressible flow reduces to

$$u\frac{\partial u}{\partial x} + v\frac{\partial u}{\partial y} = g + \nu\frac{\partial^2 u}{\partial y^2} \tag{6}$$

with boundary conditions

$$u(x,0) = 0 \tag{7a}$$

$$v(x,0) = 0 \tag{7b}$$

$$u(x,y) \to U(x) \quad \text{as} \quad y \to \delta \tag{7c}$$

Introducing the similarity variables as suggested by Hartree (1937)

$$\psi = \sqrt{\frac{4}{3}U\nu x}\, f(\eta), \quad \eta = y\sqrt{\frac{3}{4}U/\nu x} \tag{8}$$

where ψ is the physical stream function in the flow problem, such that,

$$u = \frac{\partial \psi}{\partial y}, \quad v = -\frac{\partial \psi}{\partial x}, \tag{9}$$

the boundary layer problem transforms into

$$f''' + ff'' + \frac{2}{3}(1 - f'^2) = 0 \tag{10a}$$

$$f(0) = f'(0) = 0 \tag{10b}$$

$$f'(\eta) \to 1 \quad \text{as} \quad \eta \to \infty \tag{10c}$$

Here, f is a normalized stream function, and $f' \equiv df/d\eta$ has the particular physical significance of the normalized velocity

$$f'(\eta) = \frac{u}{U}, \tag{11}$$

as readily inferred from equations (8) and (9). Furthermore, the second derivative of the function f is related to the shear stress τ by

$$\frac{\tau}{\frac{1}{2}\rho U^2} = f''(\eta)\sqrt{3\frac{\nu}{Ux}} \tag{12}$$

The mathematical problem defined in equations (10) is identical to the Falkner-Skan problem for boundary layer flow along a semi-infinite wedge of angle $\theta_w = 2\pi/3$, $m = \frac{1}{2}$ (Evans (1968)), and may be solved numerically by a shooting method using a standard Runge-Kutta integration procedure. Here, we applied an efficient shooting method developed by Keller (1968) and described for instance by Cebeci and Bradshaw (1977). In this scheme a Newton iteration procedure is employed to provide a quadratic convergence of the iterations. The numerical solution is summarized in Table 1.

Table 1 Falkner-Skan similarity solution for $m = 1/2$

η	$f(\eta)$	$f'(\eta)$	$f''(\eta)$
0.0	0.0	0.0	1.03890
0.1	0.00508	0.10056	0.97230
0.2	0.01989	0.19447	0.90605
0.3	0.04376	0.28179	0.84052
0.4	0.07603	0.36261	0.77607
0.5	0.11607	0.43705	0.71303
0.6	0.16324	0.50528	0.65176
0.7	0.21692	0.56747	0.59257
0.8	0.27654	0.62387	0.53575
0.9	0.34151	0.67471	0.48158
1.0	0.41130	0.72028	0.43029
1.1	0.48540	0.76087	0.38208
1.2	0.56332	0.79681	0.33710
1.3	0.64462	0.82840	0.29545
1.4	0.72887	0.85601	0.25719
1.5	0.81570	0.87996	0.22232
1.6	0.90475	0.90058	0.19081
1.7	0.99572	0.91823	0.16257
1.8	1.08831	0.93320	0.13747
1.9	1.18228	0.94582	0.11537
2.0	1.27740	0.95637	0.09607
2.2	1.47038	0.97232	0.06505
2.4	1.66598	0.98296	0.04264
2.6	1.86331	0.98983	0.02704
2.8	2.06174	0.99412	0.01658
3.0	2.26085	0.99671	0.00982
3.2	2.46035	0.99822	0.00561
3.4	2.66009	0.99907	0.00310
3.6	2.85995	0.99953	0.00165
3.8	3.05989	0.99977	0.00085
4.0	3.25985	0.99989	0.00042

The Falkner-Skan solution is exact in the sense that the partial differential equation (6) is exactly represented by the ordinary differential equation (10*a*) in the variables f and η, whose nominal solution may be carried out to an arbitrary degree of accuracy. This is an example within the general class of similarity solutions in fluid mechanics. An obvious advantage in this type of solution is that it represents a two-dimensional field by one-dimensional mathematics, through the function f versus the single independent variable

$$\eta = y\sqrt{\frac{3}{4}U/\nu x}.$$

Results and Discussion

There are two conditions for the validity of the Falkner-Skan solution given in Table 1: first, the entrance velocity at the top of the wall must be equal to zero in order for equation (5*a*) to apply, and secondly, the solution domain must be sufficiently restricted in downstream direction for the boundary condition (10*c*) to be satisfied in some asymptotic sence within the total thickness of the flowing film.

This latter condition means that a maximum value, x_0, of the streamwise coordinate x may be defined such that

$$Q = \psi(\eta_\delta) = \sqrt{\frac{4}{3}U\nu x_0}\, f(\eta_\delta) \tag{13}$$

Downloaded 02 May 2010 to 171.66.16.54. Redistribution subject to ASME license or copyright; see http://www.asme.org/terms/Terms_Use.cfm

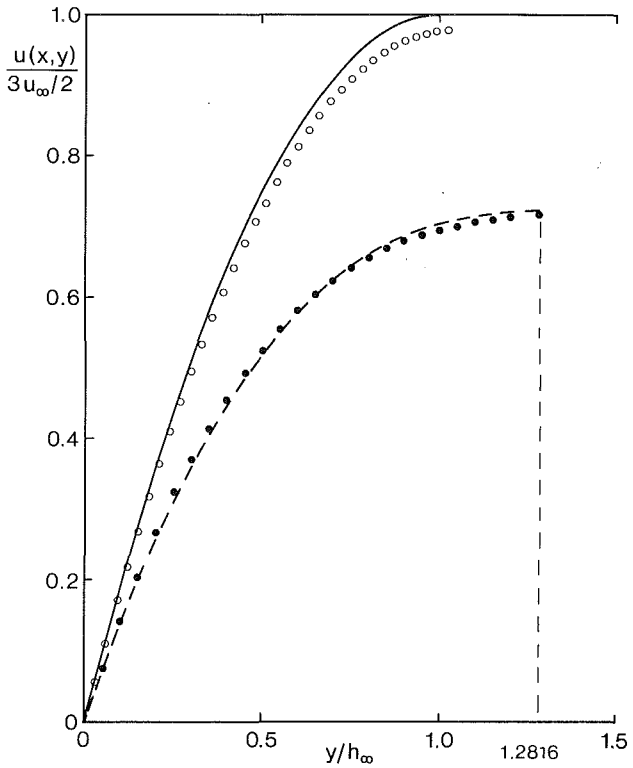


Fig. 2 Dimensionless velocity profiles. • • • similarity solution at $x = x_0$; — — — third-order polynomial; ○ ○ ○ finite difference solution at $x = x_E$; and —— Navier-Stokes solution, equation (17).

Table 2 Results for the boundary layer region

	Falkner-Skan		
	$f'(\eta_\delta) = 0.99$	$f'(\eta_\delta) = 0.999$	Roy (1984)
$\frac{h(0)}{h_\infty}$	∞	∞	1.7100
$\frac{h(x_0)}{h_\infty}$	1.2816	1.4817	1.2686
$\frac{x_0}{h_\infty Q/\nu}$	0.1972	0.1244	0.1449

where Q is the total volumetric flow rate in the film. A slight rearrangement of this expression using equation (5*a*), yields

$$x_0 = \left(\frac{3Q^4}{\nu^2 g}\right)^{1/3} \left(\frac{1}{f(\eta_\delta)}\right)^{4/3} \left(\frac{3}{32}\right)^{1/3} \tag{14}$$

Here, $f(\eta_\delta)$ is the value of the normalized stream function at the edge of the boundary layer, and will, to some extent depend on the definition adopted for δ. For instance, defining δ as the value of y for which $f' \equiv u/U = 0.99$, we have from Table 1:

$$\eta_\delta = 2.6069, \quad f(\eta_\delta) = 1.8702 \tag{15}$$

The numerical factor in equation (14) takes the value of 0.1972 in this case, whereas a δ defined at $f' = 0.999$ would give a value 0.1244 and therefore would decrease x_0 by a factor close to 2/3.

The streamwise extension of the Falkner-Skan solution domain $[0, x_0]$ in the film thus depends on the actual accuracy that is required in the asymptotic approach to the external flow, equation (10*c*). In this domain the boundary layer thickness is given by

$$\delta(x) = \eta_\delta \sqrt{\frac{4}{3}\frac{\nu x}{U}} \sim x^{1/4} \tag{16}$$

as implied by equation (8). Inside the boundary layer the flow is fully described by the solution in Table 1.

To compare the present exact solution with previous approximate results, the profiles are scaled against quantities relating to the asymptotic downstream Navier-Stokes solution for fully developed flow; $\partial u/\partial x = 0$, $v = 0$

$$u = 3u_\infty \left[\frac{y}{h_\infty} - \frac{1}{2}\left(\frac{y}{h_\infty}\right)^2\right] \tag{17}$$

where u_∞ is the asymptotic mean velocity and h_∞ is the asymptotic thickness of the film;

$$h_\infty = (3\nu Q/g)^{1/3}, \quad u_\infty = g h_\infty^2/3\nu \tag{18}$$

In terms of these quantities, the streamwise extension of the boundary layer region, equation (14), can be expressed in dimensionless form as

$$\frac{x_0}{h_\infty Q/\nu} = \left(\frac{1}{f(\eta_\delta)}\right)^{4/3} \cdot \left(\frac{3}{32}\right)^{1/3} \tag{19}$$

which shows that the dimensionless length $x_0/(h_\infty Q/\nu)$ is independent of the physical parameters of the flow.

The film thickness h, which at the particular streamwise position $x = x_0$ becomes equal to the boundary layer thickness given by equation (16), can be scaled against the asymptotic thickness h_∞:

$$\frac{h(x_0)}{h_\infty} = \eta_\delta \cdot \left[\frac{9}{2} f(\eta_\delta)\right]^{-1/3} \tag{20}$$

The comparison between the present results and the recent momentum integral method investigation by Roy (1984) in Table 2, indicates that reasonable results can be obtained by an approximate intergral approach, at least for accelerating films.

A comparison between the Falkner-Skan profile at $x = x_0$ and the Navier-Stokes profile (17) in Fig. 2 indicates the amount of adaptation in the velocity that must take place in the fully viscous region (Fig. 1), downstream of the Falkner-Skan domain, before the film flow is fully developed at $x = x_E$ in Fig. 1. In this adaptation regime there is no external inviscid flow region and the viscous boundary layer interacts directly with the free surface of the film.

The detailed flow behavior in this regime has been calculated by a finite-difference solution technique for thin shear layer equations by Andersson (1984a). Results have been obtained by marching the solution in the streamwise direction, starting with the Falkner-Skan solution at $x = x_0$. A velocity profile at $x = x_E$, defined at $h_E/h_\infty = 1.02$, is included in Fig. 2 for comparison with the Navier-Stokes result.

It is seen that the velocity profile in the finite-difference solution is not yet fully developed, particulary not in the outer part of the flow. This is evidently a result of the cut-off condition $h_E/h_\infty = 1.02$, which is strictly not compatible with the condition $\partial u/\partial x = 0$ ($h = h_\infty$) for the asymptotic solution (17).

It is anticipated that reasonable results for the fully viscous region can be obtained by a simple momentum integral approach. The close correspondence in Fig. 2 between the third-order polynomial assumed by Hassan (1967) and Roy (1984), and the Falkner-Skan profile at $x = x_0$, supports this assumption. The dimensionless cubic profile, which depends only on the local film thickness $h(x)/h_\infty$, reduces to the exact solution (17) as $h(x)$ tends to h_∞.

Assuming this profile to be approximately valid throughout the fully viscous region, the streamwise extension of this region, from $h(x_0)/h_\infty = 1.2816$ to $h(x_E)/h_\infty = 1.02$, has been computed from the analytic solution of the momentum integral equation derived by Andersson (1984b). The length of the fully viscous region is given in Table 3, as obtained by the finite-difference and momentum integral

Downloaded 02 May 2010 to 171.66.16.54. Redistribution subject to ASME license or copyright; see http://www.asme.org/terms/Terms_Use.cfm

Table 3 Results for the fully viscous region

	Falkner-Skan		Yilmaz and Brauer (1973)
	Finite-difference	Integral method	
$\frac{x_E - x_0}{h_\infty Q/\nu}$	0.4792	0.4468	-
$\frac{x_E}{h_\infty Q/\nu}$	0.6764	0.6440	0.67

approaches. In both cases, the length of the fully viscous region exceeds the extension of the boundary layer region, as obtained from the Falkner-Skan solution, by a factor greater than two.

There is a close correspondence between the results, although they are originating from two rather different approaches. This may be explained by the fact that the flow is steadily accelerating, which makes the velocity rather insensitive to the particular assumptions made in the moment approach.

By adding the length x_0 of the boundary layer region, Table 2, to the extension of the fully viscous region, Table 3, the total film flow entrance length x_E is obtained, and is included in Table 3.

Yilmaz and Brauer (1973) solved the momentum equation (6) for the film flow by a finite-difference method, starting with a flat profile at $x = 0$ and for initial film thickness ratios $h(0)/h_\infty > 4$. The good agreement between their and our results in Table 3 may be attributed to the fact that the entrance length is approximately constant for $h(0)/h_\infty > 3$ as pointed out by Andersson (1984a).

Conclusions

It has been demonstrated that the solution of a developing film flow on a vertical wall can be obtained from the Falkner-Skan equation in aerodynamic boundary layer theory for the special choice of the parameter $m = 1/2$. The constant gravity term g in the film flow equation then plays the role of the constant pressure gradient in the aerodynamic boundary layer equations.

Since the Falkner-Skan equation has been extensively studied in the past, and its solution has been obtained by accurate methods, a reference solution for developing film flow is thereby made available, against which any approximate solution may be checked.

References

Andersson, H. I., 1984a, "Numerical Solutions of a TSL-Model for Free-Surface Flows," *Notes on Numerical Fluid Mechanics*, Vol. 7, Proceedings of the 5th GAMM-Conference on Numerical Methods in Fluid Mechanics, Pandolfi, M., and Piva, R., eds., Vieweg, Braunschweig, pp. 9–16.

Andersson, H. I., 1984b, "On Integral Method Predictions of Laminar Film Flow," *Chemical Engineering Science*, Vol. 39, pp. 1005–1010.

Cebeci, T., and Bradshaw, P., 1977, *Momentum Transfer in Boundary Layers*, McGraw-Hill, Hemisphere, Washington, pp. 62–69.

Evans, H. L., 1968, *Laminar Boundary Layer Theory*, Addison-Wesley, Reading, Mass., pp. 52–60.

Falkner, V. M., and Skan, S. W., 1931, "Some Approximate Solutions of the Boundary-Layer Equations," *Philosophical Magazine*, VII, Vol. 12, pp. 865–896.

Hartree, D. R., 1937, "On an Equation Occurring in Falkner and Skan's Approximate Treatment of the Equations of the Boundary Layer," *Proceedings Cambridge Philosophical Society*, Vol. 33, pp. 223–239.

Hassan, N. A., 1967, "Laminar Flow Along a Vertical Wall," ASME JOURNAL OF APPLIED MECHANICS, Vol. 34, pp. 535–537.

Keller, H. B., 1968, *Numerical Methods for Two-Point Boundary Value Problems*, Ginn-Blaisdell, Waltham, Mass., pp. 54–61.

Roy, T. R., 1984, "On Laminar Thin-Film Flow Along a Vertical Wall," ASME JOURNAL OF APPLIED MECHANICS, Vol. 51, pp. 691–692.

Yilmaz, T., and Brauer, H., 1973, "Beschleunigte Strömung von Flussigkeitsfilmen an Ebenen Wanden und in Fullkorperschichten," *Chemie-Ingenieur Technik*, Vol. 45, pp. 928–934.

Downloaded 02 May 2010 to 171.66.16.54. Redistribution subject to ASME license or copyright; see http://www.asme.org/terms/Terms_Use.cfm

C. T. Herakovich
Mem. ASME

D. Post
Mem. ASME

M. B. Buczek[1]
Mem. ASME

R. Czarnek

Department of Engineering Science and Mechanics,
Virginia Polytechnic Institute & State University,
Blacksburg, Va. 24061

Free Edge Strain Concentrations in Real Composite Laminates: Experimental-Theoretical Correlation

The magnitude of the maximum shear strain at the free edge of axially loaded $[\theta_2/-\theta_2]_s$ *and* $[(\pm\theta)_2]_s$ *composite laminates was investigated experimentally and numerically to ascertain the actual value of strain concentration in resin matrix laminates and to determine the accuracy of finite element results. Experimental results using moiré interferometry show large, but finite, shear strain concentrations at the free edge of graphite-epoxy and graphite-polyimide laminates. Comparison of the experimental results with those obtained using several different finite element representations showed that a four-node isoparametric finite element provided the best and most trouble-free numerical results. The results indicate that the ratio of maximum shear strain at the free edge to applied axial strain varies with fiber orientation and does not exceed nine for the most critical angle which is 15 deg.*

Introduction

The problem of singular interlaminar stresses at the free edge of a finite width laminated composite structure has been under investigation continuously ever since the original paper of Pipes and Pagano [1]. Numerous papers have been published on the subject over the years. They have included the finite difference solution of Pipes and Pagano, approximate analytical solutions [2–4], finite element solutions [5–8], and several experimental investigations [9–11]. All theoretical investigations have modeled the laminate as combinations of distinct material layers with distinct interfaces. One paper modeled the interface as a separate layer, but still maintained distinct layer interfaces [12]. These papers have predicted large stress gradients in a boundary layer region along the free edges of laminated composites. The idealized model with distinct layers predicts singular interlaminar stresses at the free edge. Of prime importance to the designer are the magnitude and sign of the interlaminar stresses. High tensile interlaminar normal stresses and/or high interlaminar shear stresses can cause delamination failures at relatively low applied loads. This mode of failure is often the dominant mode and thus the great interest in this problem.

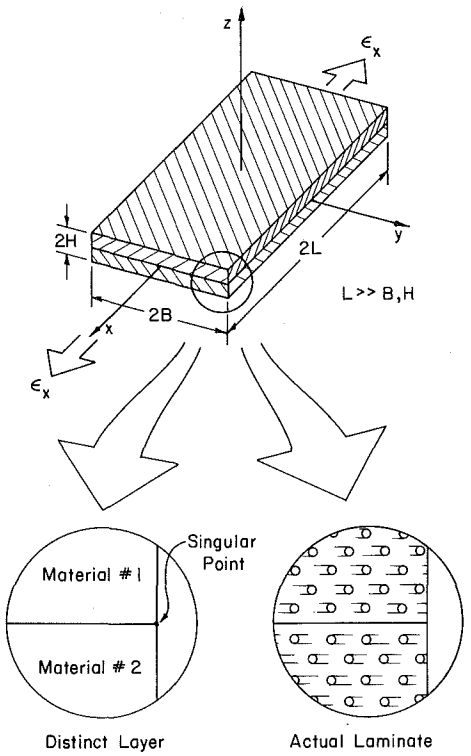


Fig. 1 Distinct layer interface and actual laminate interface

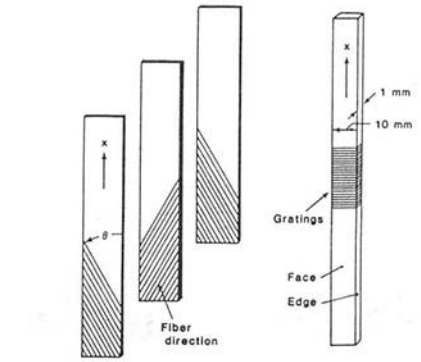
As depicted in Fig. 1, the real world is quite different from the idealized model that has been studied so extensively in the literature. Real laminates do not exhibit distinct interfaces

[1]Now with General Electric, Cincinnati, Ohio.

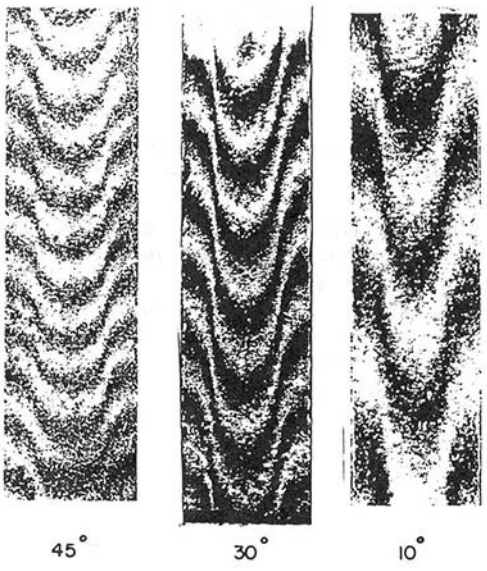
Contributed by the Applied Mechanics Division and presented at the Winter Annual Meeting, Miami, Fla., November 13–17, 1985 of THE AMERICAN SOCIETY OF MECHANICAL ENGINEERS.

Discussion on this paper should be addressed to the Editorial Department, ASME, United Engineering Center, 345 East 47th Street, New York, N.Y. 10017, and will be accepted until two months after final publication of the paper itself in the JOURNAL OF APPLIED MECHANICS. Manuscript received by ASME Applied Mechanics Division, June, 1984; final revision, January, 1985. Paper No. 85-WA/APM-10.

Copyright © 1985 by ASME
Downloaded 02 May 2010 to 171.66.16.54. Redistribution subject to ASME license or copyright; see http://www.asme.org/terms/Terms_Use.cfm



a) Specimens and Gratings



b) Fringe Patterns for $[\theta_2/-\theta_2]_s$ Laminates

Fig. 2 Moire fringe patterns

between layers and hence the mathematical singularity is only an artifact of the idealized model. It is not present in the real world. This is, of course, borne out experimentally by the finite load required to initiate edge failure.

The studies that have been conducted on the idealized model have resulted in a clear understanding of the mechanics of the problem. They have shown the influence of material properties, fiber orientation, and stacking sequence on the distribution of stresses in the boundary layer. Some analytical solutions have also provided results for the order of the singularity [4]. The insight that has been gained as a result of these studies is invaluable. However, failure analysis using these results is limited to the extent that the actual stresses in real composites are different from those predicted using an idealized, distinct interface model.

The intent of this paper is to present accurate experimental results for the maximum shear strain at the free edge for a family of angle-ply laminates and to compare the experimental results with finite element results obtained using a variety of element types and grids. Strains rather than stresses are emphasized in this paper because the moiré technique, which is used for the experimental measurements, provides displacements directly. The gradients of these displacements are the shear strains that can be compared with the strains obtained from the finite element solution. Stresses can be obtained with the appropriate constitutive equation, but this additional computation does introduce another degree of approximation due to the uncertainty associated with the elastic properties of composite materials (i.e., shear modulus and out-of-plane properties in particular).

A second goal of this investigation was to determine a suitable finite element representation for use in failure analysis of real world laminated composites. While the finite element method does not provide an exact solution to the idealized singular problem, it is possible to obtain very accurate predictions of the "real world" strains using the finite element method. The difficulty lies in verification of a satisfactory element and grid. This can be determined only through comparison of theoretical and experimental results.

The experimental results in this paper were obtained using a high resolution moiré interferometry technique developed previously by one of the authors [13]. The finite element results were obtained using an existing code [5] and a program written specifically for this investigation by one of the authors (MBB). Experimental and numerical results were obtained for T300/5208 graphite-epoxy and Celion 6000/PMR-15 graphite-polyimide.

Problem Formulation

The problem under consideration is depicted in Fig. 1. A long, finite width composite laminate is subjected to an imposed axial strain, ϵ_x. The laminate stacking sequence is symmetric about the midplane and balanced with plus and minus theta plies occurring in pairs (not necessarily adjacent). Under these conditions, stresses and strains away from the ends are independent of the axial coordinate x. In general, all six components of stress are nonzero. For thin laminates, the analysis may be restricted to one-quarter of the laminate cross section [14].

This paper will consider only angle-ply laminates. Two stacking sequences are considered, $[\theta_2/-\theta_2]_s$ and $[(\pm\theta)_2]_s$. Fiber orientations of 10, 30, and 45 deg were investigated experimentally. Finite element results were obtained at 10, 15, 20, 25, 30, and 45 deg. These fiber orientations were chosen to survey the range from high to low interlaminar shear strains [15].

In displacement formulations of the finite element method, the fundamental unknowns of the problem are the element nodal point displacements. For the problem under consideration, a generalized plane strain assumption is made from which the most general form of the displacement field is:

$$\begin{aligned} u(x,y,z) &= U(y,z)+x\epsilon_x \\ v(x,y,z) &= V(y,z) \\ w(x,y,z) &= W(y,z) \end{aligned} \tag{1}$$

Given ϵ_x, it is necessary to determine the unknown functions $U(y,z)$, $V(y,z)$, and $W(y,z)$. Four different isoparametric elements were used during the course of this investigation, the three-node constant strain triangle, and four, eight, and nine-node quadrilateral elements. In all cases, minimization of the total potential energy for each element yields a set of simultaneous equations of the form

$$[K^{(e)}]\{U\} = \{F^{(e)}\} \tag{2}$$

where $[K^{(e)}]$ is the element stiffness matrix, $\{U\}$ is the nodal displacement vector, and $\{f^{(e)}\}$ is the element force vector. (The element stiffness matrix and force vector vary with the type of element [16].) The finite element equations (2) are assembled for all elements in the grid and the resulting set of simultaneous equations solved for the unknown nodal displacements.

Displacements at any location within an element can be determined using the element interpolation (shape) functions. Strains are then determined using the well-known strain-displacement relationships. The interlaminar shear strain γ_{xz} will be of prime consideration in this paper. The strain-displacement relationship for this component of strain is

Downloaded 02 May 2010 to 171.66.16.54. Redistribution subject to ASME license or copyright; see http://www.asme.org/terms/Terms_Use.cfm

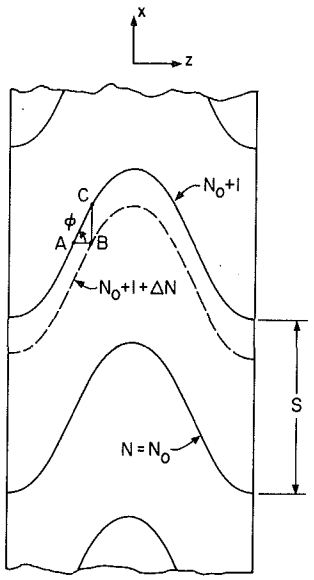


Fig. 3 Typical fringe pattern for $[\theta_2/-\theta_2]_S$ laminate

$$\gamma_{xz} = \frac{\partial U}{\partial z} + \frac{\partial W}{\partial x} \tag{3}$$

However, W is independent of x for this problem and hence

$$\gamma_{xz} = \frac{\partial U}{\partial z} \tag{4}$$

Thus, the strain of interest at any location z on the free edge is equal to the through-the-thickness gradient of the U-displacement curve at that location.

Experimental Program

Moiré interferometry is a whole-field optical technique that produces contour maps (or fringe patterns) of inplane displacement fields [13]. Its sensitivity is in the subwavelength range, viz. 0.417 μm (16.4μ in.) per fringe order for the current work, using a reference grating of 2400 lines/mm (60,960 l/in.). The experimental techniques employed in this investigation are reported in reference [11]. Briefly, high frequency reflection gratings were applied to the face and edge of the laminate (Fig. 2(*a*)) by a relatively easy replication process. Those were viewed by an optical system that uses coherent laser light and produces patterns of inplane displacements. Carrier patterns and optical filtering were employed to cancel effects of initial fringes and yield patterns of the load-induced fringes exclusively.

The specimens were approximately 250-mm (10-in.) long, 12.5-mm (1.5-/in.) wide and 1.0 to 1.3-mm (0.04 to 0.05-in.) thick. They were angle-ply laminates of graphite-epoxy and graphite-polyimide as specified previously. The tensile loads were low, generating axial strains typically ranging about 0.05 percent for the ± 10 deg clustered laminate to a maximum of 0.2 percent for the ± 45 deg alternating laminate.

Moiré interferometry patterns are shown in Fig. 2(*b*) for edge views of $[\theta_2/-\theta_2]_s$ graphite/polyimide specimens. Face and edge views for graphite/epoxy specimens were shown in reference [11]. In all cases, the slopes of the fringes are fairly well defined at the locations where the fringes cross the $+\theta/-\theta$ interface. The relationship between this slope and the interlaminar shear strain γ_{xz} can be derived as follows.

At any point in the interference patter, the fringe order, N_x, is related to the x-component of displacement, u, by

$$u = \frac{1}{f} N_x \tag{4a}$$

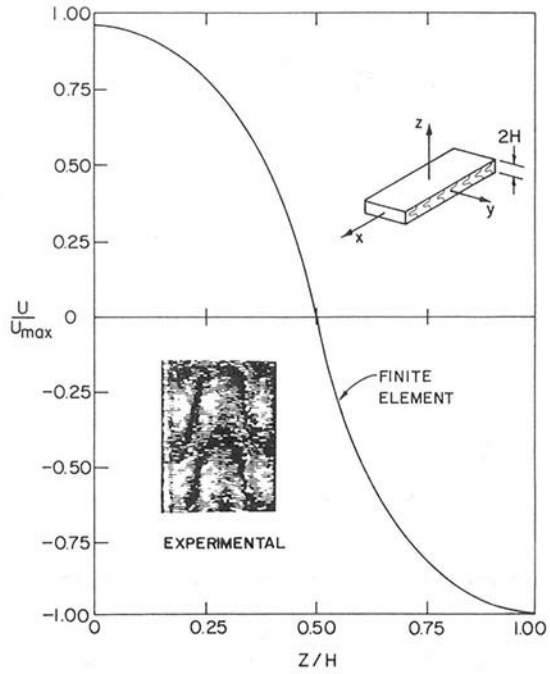


Fig. 4 Experimental and finite element free edge U displacements for a $[30_2/-30_2]_S$ laminate

where f is the frequency of the reference grating, here 2400 lines/mm. The displacement increment, Δu, between two points is proportional to the difference of fringe orders at the points, ΔN, viz.,

$$\Delta u = \frac{1}{f} \Delta N_x \tag{4b}$$

Figure 3 is a schematic illustration of the fringes, with fringe orders enumerated as N_0 and N_0+1. A self-similar curve of fringe order $N_0+1-\Delta N$ can be drawn, where fractional fringe order ΔN can be as small as desired. At point A at the interface between cross-plies, the triangle ABC has leg $AB=\Delta z$ and leg $BC=S\Delta N$. The latter is true because fringe orders change linearly with x in this problem, and therefore fractional distances are proportional to fractional fringe orders, or $BC/S=\Delta N/1$. Accordingly

$$\tan\phi = \frac{BC}{AB} = \frac{S\Delta N}{\Delta z} = \mathrm{Sf}\,\frac{\Delta u}{\Delta z}$$

In the limit as ΔN approaches zero, and using equation (4)

$$\tan\phi = Sf\frac{\partial u}{\partial z} = Sf\gamma_{xz} \tag{5}$$

The normal strain ϵ_x is

$$\epsilon_x = \frac{\partial u}{\partial x} = \frac{1}{f}\frac{\partial N_x}{\partial x}$$

The gradient $\partial N_x/\partial x$ is a constant, namely one fringe per distance S, so

$$\epsilon_x = \frac{1}{f}\left(\frac{1}{S}\right) \tag{6}$$

Thus, equation (6) can be written

$$\frac{\gamma_{xz}}{\epsilon_x} = \tan\,\phi \tag{7}$$

where ϕ is the angle of the tangent to the fringe, measured counter-clockwise from the z-axis. This ratio is a measure of the strain concentration at the free edge and is of prime consideration in the investigation.

Downloaded 02 May 2010 to 171.66.16.54. Redistribution subject to ASME license or copyright; see http://www.asme.org/terms/Terms_Use.cfm

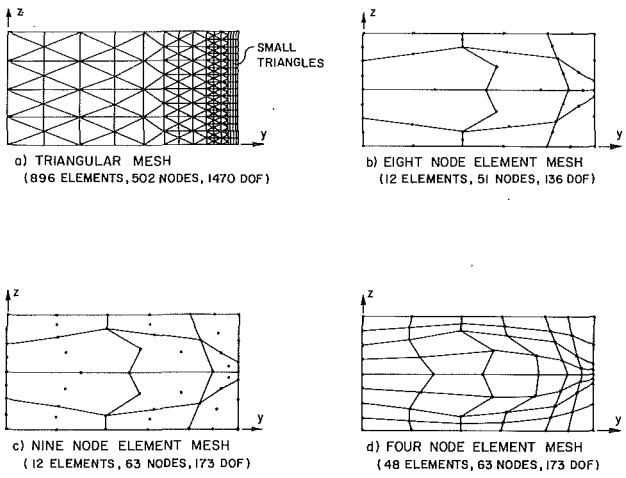


Fig. 5 Finite element representations for $[\theta_2/-\theta_2]_S$ laminates

It is curious and helpful that fringe shape and ϕ are independent of ϵ_x [11]. As a consequence, small inadvertent bending that may have occurred in the experiment would cause ϵ_x to vary across the thickness of the specimen, but the angle ϕ would remain fixed.

Results

Validity of the Finite Element Model. Qualitative comparisons of finite element predictions and moiré results for the through-the-thickness U-displacements at the free edge, Fig. 4, show that the finite element results give a good representation for the form of the actual displacement distributions. The mesh used for these results was an 896 element by 502 node grid of constant strain triangles. After imposing boundary conditions there were 1470 degrees of freedom (DOF). As indicated in Fig. 5(*a*), this grid had a high density of small elements near the edge. There were 32 elements through the thickness of each layer at the free edge. The fringe lines of the moiré pattern correspond to lines of constant U-displacement. These results demonstrate that the finite element model exhibited the same trends as did the "real world" problem as recorded by the moiré fringe patterns, and that the initial assumption of x-independence of (equation (1)) is valid.

Element Dependence. A study was initiated to compare results from the constant strain triangle and several other isoparametric elements. The additional isoparametric elements chosen for study were four, eight, and nine-node elements. The grids for the eight and nine-node element versions were identical 12-element meshes with the nine-node version having an additional node in the interior of each element (Figs. 5(*b*), 5(*c*)). There were 51 nodes in the eight-node version and 63 nodes in the nine-node version. One of two four-node element meshes used in the investigation (Fig. 5*d*) is identical to the nine-node version, but with additional element sides connecting all interior node points. Thus, there are 63 nodes and 48 elements in this grid. The degrees of freedom are identical in this four and the nine-node mesh (173), with the eight-node mesh having fewer DOF (137). The quadrilateral isoparametric meshes (Figs. 5(*b–d*)) are small modifications of the "optimal" mesh as given by Wang and Stango [17]. As with the constant strain triangular mesh, a higher density of smaller elements is used in the vicinity of the expected mathematical singularity.

$[\theta_2/-\theta_2]_S$ Laminates. A primary concern of this investgation was to determine a satisfactory element and grid for accurate prediction of "real world" strains at the free edge of a laminate. A comparison of experimental and theoretical results for the distribution of shear strain through-the-thickness of the free edge of a $[30_2/-30_2]_S$ graphite-epoxy laminate is shown in Fig. 6. The theoretical results were obtained using four different isoparametric finite element

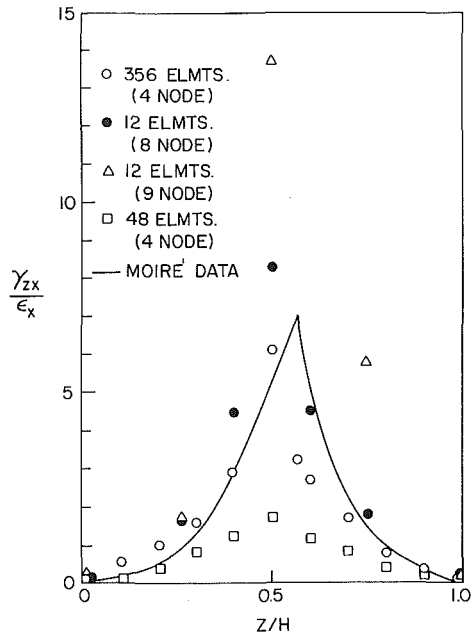


Fig. 6 Strain concentration on free edge of $[30_2/-30_2]_S$ laminate

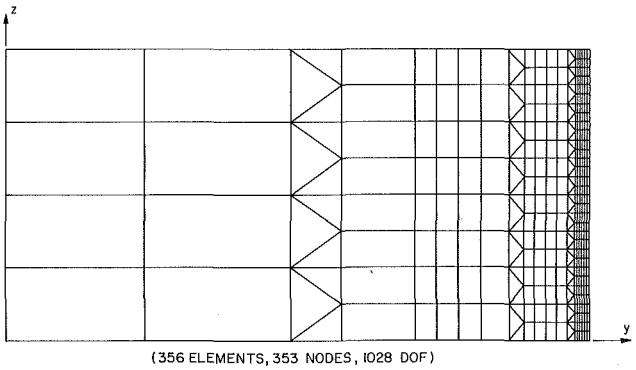


Fig. 7 Dense four-node rectangular element mesh

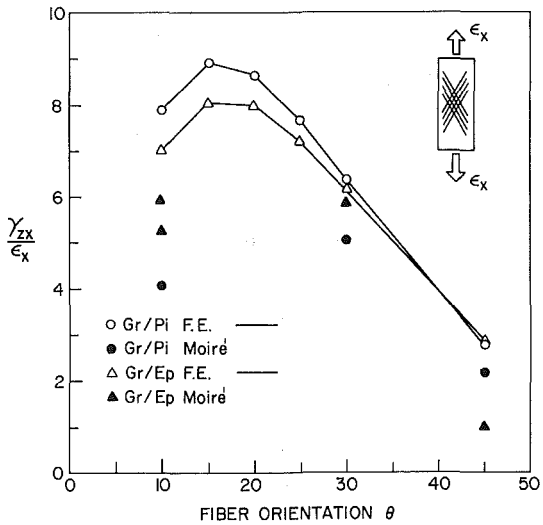


Fig. 8 Theoretical/experimental correlation for maximum strain concentrations on free edge of $[\theta_2/-\theta_2]_S$ laminates

Downloaded 02 May 2010 to 171.66.16.54. Redistribution subject to ASME license or copyright; see http://www.asme.org/terms/Terms_Use.cfm

Table 1 Elastic properties for graphite-epoxy and graphite-polyimide

Property	T300/5208 Gr/Ep	Celion 6000/PMR-15 Gr/Pi
E_1(GPa)	132.0	136.0
E_2(GPa)	10.8	9.79
E_3(GPa)	10.8	9.79
ν_{23}	0.490	0.49
ν_{13}	0.238	0.35
ν_{12}	0.238	0.35
G_{23}(GPa)	3.36	3.36
G_{13}(GPa)	5.65	5.00
G_{12}(GPa)	5.65	5.00

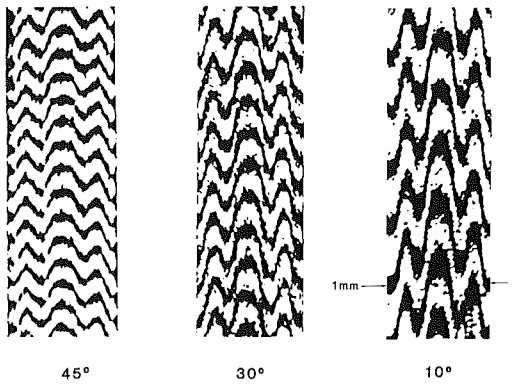


Fig. 9 Moire fringe patterns for $[(\pm\theta)_2]_S$ laminates

representations. In addition to the three representations shown in Fig. 5(*b–5d*), a dense mesh of four-node rectangular elements (356 elements, 353 nodes, and 1028 DOF) was used (Fig. 7). All theoretical and experimental results indicate that the maximum strain occurs at the interface between layers. As indicated in Fig. 6, the maximum strains from the numerical results varied considerably with the element and mesh used. The grid with 12 nine-node elements predicted maximum strains double the actual strains whereas the grid with 48 four-node elements predicted maximum strains 70 percent below the experimental values. The results from the grid of 12 eight-node elements and the 356 element grid of four-node elements were much closer to the actual strains. The maximum strain from the eight-node element mesh was 20 percent higher than the actual value and the maximum strain using the four-node mesh was 13 percent lower than the actual value. Thus, the best results were obtained with the 356 four-node rectangular element grid.

It is noted that the strains found in eight and nine-node elements were first computed at the four Gauss stations used for a four-node linear element and then linearly interpolated to any arbitrary point within the element. This interpolation was necessary to keep the strains bounded when computing near the element corners of the eight and nine-node elements. No such procedures were required with the four-node elements; this is considered to be a significant advantage of the four node element.

Figure 6 also shows that the maximum strain of the actual laminates did not occur at the exact quarter-point line of the specimen thickness. This is because all layers of the actual laminate are not of equal thickness and thus the ± interface is not located exactly at the quarter point as in the idealized model. The maximum strain did occur at the ± interface.

A summary of experimental and numerical results for the maximum free-edge shear strains at the $+\theta/-\theta$ interface of $[\theta_2/-\theta_2]_s$ laminates is presented in Fig. 8. The finite element results were obtained using the 356 element grid of rectangular elements. They indicate that the largest strain concentration occurs at approximately 15 deg for both graphite-epoxy and graphite-polyimide; the maximum strain

Table 2 Experimental results for clustered laminates including variations and error

Specimen	ϕ	γ_{xz}/ϵ_x	Max. variation in ϕ [(a)]	Max. exp. error [(b)]	$\Delta\phi$ [(c)] Min.	$\Delta\phi$ [(c)] Max.
Gr/Ep $[10_2/-10_2]_s$	80.5 deg	6.0	2.7 deg	1 deg	1.7 deg	3.7 deg
Gr/Pi $[10_2/-10_2]_s$	76.3	4.1	1.0	1	0	2
Gr/Pi $[30_2/-30]_s$	78.8	5.1	1.4	1	0.4	2.4
Gr/Pi $[45_2/-45_2]_s$	65.4	2.2	6	3	3	9

(a) Averaged for interfaces on left and right side.
(b) Estimated.
(c) Minimum and maximum variation in ϕ attributable to variations in local specimen properties and dimensions.

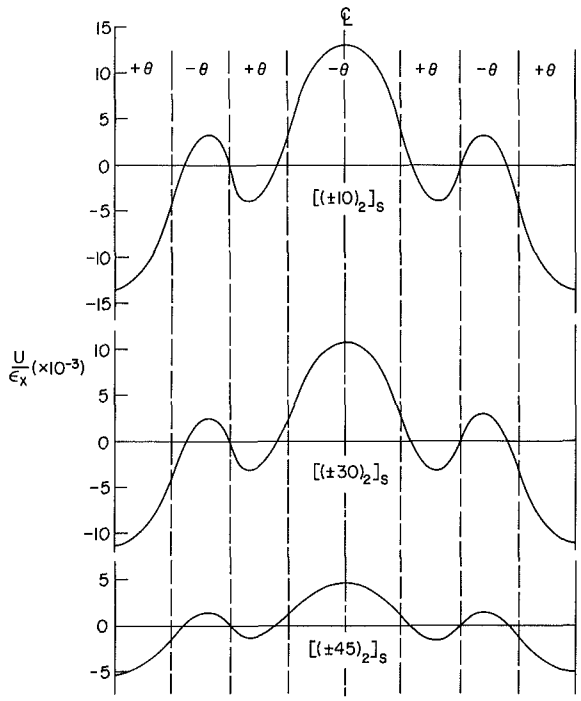


Fig. 10 Theoretical *U* displacements on free edge of $[(\pm\theta)_2]_S$ laminates

concentration factors are 7.9 and 8.9, respectively. The numerical results for the two materials show very similar trends. The strains in the graphite-polyimide are significantly higher than those in the graphite-epoxy in the 10–30 deg fiber orientation range. This difference is because the two materials have different material properties (Table 1).

The experimental results indicate trends similar to the finite element results. Unfortunately, experimental results were not obtained for the most critical fiber orientation. The maximum measured strain concentration γ_{xz}/ϵ_x was 5.9 for the 30 deg graphite-epoxy specimen. However, this value is not significantly greater than the 5.3 value for the 10 deg laminate. The measured strain concentrations were lower than the predicted values in all cases with the difference being largest at the lower fiber angles. It is interesting to note that theory predicts higher strains in the polyimide, but experiment indicates higher strains in the epoxy. This is a clear indication that the input data to the analysis are not an exact representation of the experiment. Materials properties as well as individual layer thicknesses may be in error.

The slopes of fringes at the $+\theta/-\theta$ interface were found to vary for different fringes in the same specimen. Seven pat-

Downloaded 02 May 2010 to 171.66.16.54. Redistribution subject to ASME license or copyright; see http://www.asme.org/terms/Terms_Use.cfm

Table 3 Theoretical-experimental correlation of strain concentrations for alternating laminates

Laminate	Interface 1	2	3	4	5	6
	Magnitude of Experimental γ_{xz}/ϵ_x					
$[(\pm 10)_2]_s$	5.2	4.4	6.8	6.0	4.3	7.2
Avg.			6.4			
Avg.			4.35			
Avg.			6.2			
$[(\pm 30)_2]_s$	3.6	2.4	4.5	5.0	2.9	4.6
Avg.			4.75			
Avg.			2.65			
Avg.			4.1			
$[(\pm 45)_2]_s$	1.7	1.0	2.2	2.0	1.0	2.0
Avg.			2.1			
Avg.			1.0			
Avg.			1.85			
	Magnitude of Theoretical γ_{xz}/ϵ_x					
$[(\pm 10)_2]_s$	5.6	4.1	5.6	5.6	4.1	5.6
$[(\pm 30)_2]_s$	4.7	3.6	4.8	4.8	3.6	4.7
$[(\pm 45)_2]_s$	2.1	1.7	2.2	2.2	1.7	2.1

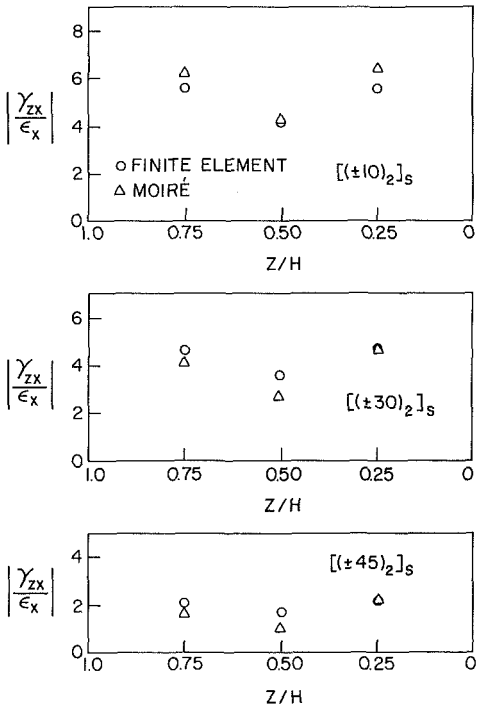


Fig. 11 Theoretical/experimental correlation for free edge strain concentrations in $[(\pm\theta)_2]_s$ laminates

terns were analyzed – four in addition to the three shown in Fig. 2(*b*). The variation is attributed partly to experimental error in determining the slope and partly to point-to-point variations in the specimen material. Table 2 shows the variations attributed to experimental error and the variations attributed to material variations. The material variations appear to be significantly large. Another factor is the difference of fringe slope on the left and right interfaces of the laminate, which verifies the specimen nonuniformity and adds to the variations reported in Table 2.

$[(\pm\theta)_2]_s$ Laminates. The results of the preceding section have shown that the dense four-node rectangular element mesh of Fig. 7 provides reasonably good correlation between theory and experiment for the free edge shear strains in $[\theta_2/-\theta_2]_s$ laminates. Additional evidence from other laminates is necessary before this mesh can be accepted with confidence.

Figure 9 shows moiré fringe patterns for $[(\pm\theta)_2]_s$ graphite-epoxy laminates. The corresponding displacements from the four-node, 356 element mesh are presented in Fig. 10. Comparison of the figures indicates good correlation between theory and experiment.

Results for strain concentrations γ_{xz}/ϵ_x at the free edge of the $[(\pm\theta)_2]_s$ laminates are presented in Table 3 and Fig. 11. These results show that this mesh also provides very good correlation with experiment for the alternating layer stacking sequence. The experimental values in Table 3 are the average from several fringes (4–10) along the length of the specimens. Strain concentrations were determined at each interface (numbered 1–6). It is apparent from the table that the experimental results did not always exhibit symmetric response about the specimen midplane. (The results along a given interface were quite consistent.) The largest differences occurred between the two outermost layers. It is believed that these differences are due to the lack of exact symmetry in the actual specimens. (Experimental error in measuring the strains was discussed previously.)

The average values from both sides of the midplane indicate very good correlation between theory and experiment. In all but two cases the percent difference was less than 14 percent. The maximum difference between average measured value and finite element value was 41 percent.

Comparison of finite element results for the clustered $[\theta_2/-\theta_2]_s$ and the alternating $[(\pm\theta)_2]_s$ laminates indicates that the clustered laminates should exhibit higher strain concentrations for the corresponding fiber orientations. This was generally (but not always) the case for the experimental results.

Conclusions

Experimental results have been presented showing that the maximum shear strains on the free edge of angle-ply laminates are finite. Measured values for the ratio of maximum edge shear strain to applied axial strain did not exceed 7.5 for $[\theta_2/-\theta_2]_s$ and $[(\pm\theta)_2]_s$ laminates. Numerical analysis indicates that the maximum strain concentration for angle-ply laminates would not exceed 9.0 for resin matrix laminates.

Comparison of finite element and experimental results indicates that the most satisfactory and trouble-free numerical results were obtained with a four-node, isoparametric, rectangular element mesh. Good comparison between theory and experiment was obtained or both $[\theta_2/-\theta_2]_s$ and $[(\pm\theta)_2]_s$ laminates using the identical mesh. Experimental results show that there is considerable variation in strains along the length and through the thickness of real

Downloaded 02 May 2010 to 171.66.16.54. Redistribution subject to ASME license or copyright; see http://www.asme.org/terms/Terms_Use.cfm

laminates. These variations are an indication of nonuniformity in the fabricated laminates.

Acknowledgment

This work was supported by the NASA Cooperative Agreement NCC1-15 and NSF Grant MEA 8109230. The authors are also grateful for the assistance of Mr. Duksong Joh with data reduction.

References

1 Pipes, R. B., and Pagano, N. J., "Interlaminar Stresses in Composite Laminates Under Uniform Axial Extension," *J. Composite Materials*, Vol. 4, Oct., 1970, pp. 538–548.

2 Hsu, P. W., and Herakovich, C. T., "Edge Effects in Angle-Ply Composite Laminates," *Journal of Composite Materials*, Vol. 11, Oct. 1977, pp. 422–428.

3 Pagano, N. J., "Free-Edge Stress Fields in Composite Laminates," *Int. J. Solids & Structures*, Vol. 14, 1978, pp. 401–406.

4 Wang, S. S., and Choi, I., "Boundary-Layer Effects in Composite Laminate: Part 2—Free-Edge Stress Solutions and Basic Characteristics," ASME JOURNAL OF APPLIED MECHANICS, Sept. 1982, Vol. 49, pp. 549–560.

5 Herakovich, C. T., Renieri, G. D., and Brinson, H. F., "Finite Element Analysis of Mechanical and Thermal Edge Effects in Composite Laminates," Army Symposium on Solid Mechanics, 1976, *Composite Materials: The Influence of Mechanics of Failure on Design*, Cape Cod, Mass., Sept. 1976, pp. 237–248.

6 Renieri, G. D., and Herakovich, C. T., "Nonlinear Analysis of Laminated Fibrous Composites," VPI-E-76-10, June 1976, 177 pages.

7 Wang, A. S. D., and Crossman, F. W., "Some New Results on Edge Effects in Symmetric Composite Laminates," *J. Composite Materials*, Vol. 11, Jan. 1979.

8 Rybicki, E. F., "Approximate Three-Dimensional Solutions for Symmetric Laminates Under In-Plane Loading," *J. Composite Materials*, Vol. 5, July 1971, pp. 354–360.

9 Pipes, R. B., and Daniel, I. M., "Moiré Analysis of the Interlaminar Shear Edge Effect in Laminated Composites," *J. Composite Materials*, Vol. 5, Apr. 1971, p. 255.

10 Oplinger, D. W., Parker, B. S., and Chiang, F. P., "Edge-Effect Studies in Fiber-Reinforced Laminates," *Experimental Mechanics*, Vol. 14, No. 9, Sept. 1974, pp. 347–354.

11 Czarnek, R., Post, D. and Herakovich, C. T., "Edge Effects in Composites by Moiré Interferometry," *Experimental Techniques*, Vol. 7, No. 1, Jan. 1983, pp. 18–21.

12 Puppo, A. H., and Evensen, H. A., "Interlaminar Shear in Laminated Composite Under Generalized Plane Stress," *J. Composite Materials*, Vol. 4, 1970, pp. 204–220.

13 Post, D., "Moire Interferometry at VPI & SU," *Experimental Mechanics*, Vol. 23, No. 2, June 1983, pp. 203–210.

14 Griffen, O. H., Kamat, M. P., and Herakovich, C. T., "Three Dimensional Inelastic Finite Element Analysis of Laminated Composites," VPI-E-80-28, Virginia Tech, Nov. 1980, 169 pages.

15 Herakovich, C. T., "On the Relationship Between Engineering Properties and Delamination of Composite Materials," *J. Composite Materials*, Vol. 15, July 1981, pp. 336–348.

16 Reddy, J. N., *An Introduction to the Finite Element Method*, McGraw-Hill, New York, 1984.

17 Wang, S. S., and Stango, R. J., "Optimally Discretized Finite Elements for Boundary-Layer Stresses in Composite Laminates," AIAA 82-0748-CP, 23rd Structures, Structural Dynamics and Materials Conference, May 11–12, 1982, New Orleans, La.

Downloaded 02 May 2010 to 171.66.16.54. Redistribution subject to ASME license or copyright; see http://www.asme.org/terms/Terms_Use.cfm

On the Comparison Between Microscopic and Macroscopic Instability Mechanisms in a Class of Fiber-Reinforced Composites

N. Triantafyllidis
Assoc. Mem. ASME

B. N. Maker

Department of Aerospace Engineering,
The University of Michigan,
Ann Arbor, Mich. 48109-2140

To investigate the relation between the macroscopic and microscopic instability predictions for certain microstructured media, we study the stability of an axially stretched fiber-reinforced composite under plane strain conditions. The microstructural instability is attributed to a bifurcation buckling of the fibers while the corresponding macroscopic one occurs at the loss of ellipticity in the homogenized incremental equilibrium equations of the material. The effects of geometry and material properties on those phenomena are analyzed. The macroscopic approach consistently and sometimes considerably overestimates the stable region of the composite. The attractive feature in this work is that all the investigations can be done by using analytical solutions instead of the numerical ones employed in similar investigations so far.

1 Introduction and Motivation

One of the most interesting problems in the study of composite media is the prediction of their failure mechanisms due to adequately large loads. Customarily a composite medium is idealized by a homogeneous continuum whose properties have been obtained by using an appropriate averaging technique (e.g., self-consistent method, homogenization method) which takes into account the solid's microstructure. The question of the composite's stability is usually addressed by investigating the (homogeneous) macroscopic properties of the solid and not by an analysis at the microstructural level. Of the numerous examples of this approach we can state here the Hill-Tsai-Wu (see [1]) failure criterion for fiber-reinforced composites and the work of Rudnicki and Rice [2] for the effects of porosity on the localization strain for microporous metallic aggregates. For a more extensive account on the flow of metals and geomaterials under large strains using the aforementioned approach, the interested reader is referred to S. Nemat-Nasser [3] and references quoted therein. So far relatively few attempts have been made to correlate the stability predictions of the continuum model with the corresponding exact microstructural failure mechanism for a given composite.

One of the first studies in this direction for the case of finitely strained solids was presented by V. Tvergaard [4]. In investigating the effects of voids on the shear band formation of a finitely strained periodic porous material he found the microscopical critical loads and buckling modes and compared them with the predictions of shear band instabilities based on an approximate continuum model of the void-matrix aggregate. More recently Abeyaratne and Triantafyllidis [5] using a consistent homogenization theory approach (needed for proper modeling of the strong interactions between voids) predicted the loss of ellipticity in a finitely strained highly porous periodic elastic material. The overall loss of ellipticity (i.e., the emergence of shear bands) in the homogenized composite is again due to the buckling of the solid at the microstructural level. In view of the composite's geometry though, an exact solution to the corresponding microbuckling problem is very complicated (the method of solution presented in [4] gives only an upper bound for the microbuckling loads) and thus no quantitative comparison between and micro and macrofailure mechanisms was attempted.

The purpose of the present work (which is, so to speak, a continuation of [5]) is a consistent study of the relation between micro and corresponding macroinstability phenomena in finitely strained two-phase composite solids. For more clarity attention will be focused on a model where both the micro and macroinstability problems have an exact analytical solution. As such a case we have decided to investigate a fiber-reinforced composite (made of alternating layers of two different materials) under plane strain conditions and stretched (stretch ratio λ) along x_1, the direction of the reinforcement. The microstructural instability is attributed to a bifurcation (i.e., the loss of uniqueness) of the uniform (i.e., independent of x_1) solution in the form of a wavy pattern. Assuming no layer separation, the bifurcation results for the problem can be obtained in an attractive

Contributed by the Applied Mechanics Division for publication in the JOURNAL OF APPLIED MECHANICS.

Discussion on this paper should be addressed to the Editorial Department, ASME, United Engineering Center, 345 East 47th Street, New York, N.Y. 10017, and will be accepted until two months after final publication of the paper itself in the JOURNAL OF APPLIED MECHANICS. Manuscript received by ASME Mechanics Division, July, 1984.

Copyright © 1985 by ASME
Downloaded 02 May 2010 to 171.66.16.54. Redistribution subject to ASME license or copyright; see http://www.asme.org/terms/Terms_Use.cfm

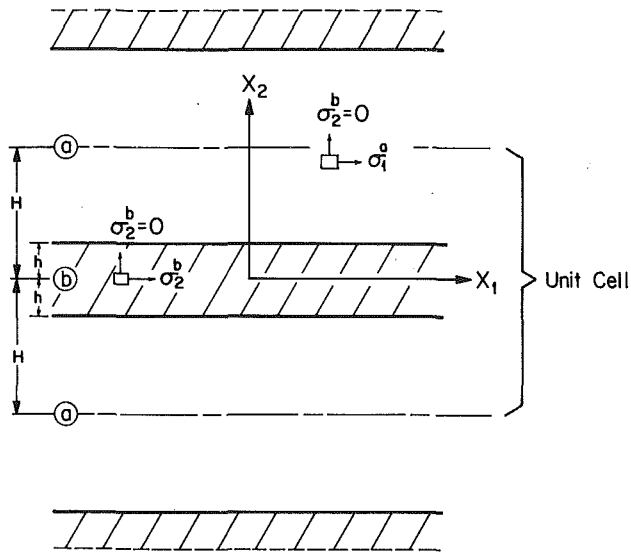


Fig. 1 Schematic representation of the composite

analytical solution (a special case of this problem for layers of equal thickness has been investigated by Biot [6] using a different approach). After calculating the homogenized incremental moduli of the composite we find the macroscopical instability mode which corresponds to the loss of ellipticity in the aforementioned homogenized solid. For given geometry and material properties of the layers we compare the macro and microcritical values for the stretch ratio λ as well as the corresponding instability patterns.

The investigation is carried out for two particular composites. The first application involves a constitutive equation developed by Stören and Rice [7] for modeling the behavior of metals at finite strain while the second one deals with a Mooney-Rivlin solid. The motivation for this choice lies in the different stability properties of the two materials in the finite strain regime. The biggest discrepancies between the micro and macrocritical stretches were found in the case of tension ($\lambda > 1$). For compression the two different mechanisms give the same results for certain range of geometry and material properties. Some very interesting asymptotic (with respect to the wavelength of the bifurcation eigenmode) cases are also discussed. The results prove the dramatic effect of softer inclusions on the stability properties of a two-phase composite and provide a method for quantitative comparison between a macroscopic instability mode and the corresponding microstructural failure mechanism.

2 Microscopic Instability Analysis

2.1 General Problem Formulation. Consider the composite medium, shown in Fig. 1, made of alternating identical layers of two different materials: material (*b*) with thickness $2h$ and material (*a*) with thickness $2(H-h)$. The composite deforms under plane strain conditions and both materials are taken to be incompressible, initially orthotropic (with axes of orthotropy x_1 and x_2) and perfectly bonded between them. At the current state of deformation materials (*a*) and (*b*) are under principal stresses $\overset{a}{\sigma}_1$, $\overset{a}{\sigma}_2$ and $\overset{b}{\sigma}_1$, $\overset{b}{\sigma}_2$ along the x_1, x_2 directions respectively. The corresponding principal stretch ratios $\overset{a}{\lambda}_1$, $\overset{a}{\lambda}_2$ and $\overset{b}{\lambda}_1$, $\overset{b}{\lambda}_2$ satisfy the following kinematical relations in view of the incompressibility and the perfect bonding between layers.

$$\overset{a}{\lambda}_1 = \overset{b}{\lambda}_1 \equiv \lambda, \qquad \overset{a}{\lambda}_2 = \overset{b}{\lambda}_2 \equiv 1/\lambda \tag{2.1}$$

Equilibrium across the (*a*)–(*b*) interface requires

$$\overset{a}{\sigma}_2 = \overset{b}{\sigma}_2 \equiv \sigma_2 \tag{2.2}$$

The question to be addressed in this section is the following: assuming a displacement (or traction) increase at the composite's infinitely remote boundary corresponding to a uniform strain increment $\mathbf{D}$ = constant ($D_{11} = \dot{\lambda}/\lambda$, $D_{22} = -\dot{\lambda}/\lambda$, $D_{12} = 0$) when does the associated incremental solution for the solid cease to be unique, i.e., when a bifurcated solution for the composite occurs?

The prebifurcation state of the solid can be completely specified as a function of the applied stretch ratio λ. The fundamental solution is obviously the one corresponding to a (piecewise) constant stress state. At some stage of deformation suppose that bifurcation is possible so that for a given increment λ there exist two different solutions $\dot{\mathbf{u}}^\alpha$ and $\dot{\mathbf{u}}^\beta$ of the incremental equilibrium equations. Introduce the following notation for the difference between two possible solutions in any field quantity

$$\Delta(\bullet) \equiv (\bullet)^\beta - (\bullet)^\alpha \tag{2.3}$$

Taking for simplicity the reference configuration to coincide with the current one at the onset of bifurcation (so that $\mathbf{u} = 0$ but $\dot{\mathbf{u}} \neq 0$) the incremental equilibrium equations, in terms of the first Piola-Kirchhoff (or nominal) stress $T_{\alpha\beta}$, are

$$[\Delta \dot{T}_{\alpha\beta}],_\alpha = 0 \tag{2.4}$$

while the interface traction continuity condition requires

$$[[\Delta \dot{T}_{2\beta}]] = 0 \tag{2.5}$$

with $[[\bullet]]$ denoting the jump of a field quantity across a layer interface.

Here and subsequently the summation convention for repeated indices is tacitly assumed for all Greek subscripts which always range from 1 to 2. Moreover a comma followed by a subscript denotes differentiation with respect to the corresponding coordinate.

For the case of an incompressible, pressure insensitive and initially orthotropic rate-independent material, the most general structure of its constitutive law is, as first noted by Biot [6]

$$\begin{aligned} \overset{\nabla}{\sigma}_{11} &= 2\mu^* \dot{u}_{1,1} - \dot{p}, \\ \overset{\nabla}{\sigma}_{22} &= 2\mu^* \dot{u}_{2,2} - \dot{p}, \\ \overset{\nabla}{\sigma}_{12} &= \overset{\nabla}{\sigma}_{21} = \mu(\dot{u}_{1,2} + \dot{u}_{2,1}) \end{aligned} \tag{2.6}$$

Where $\overset{\nabla}{\sigma}$ denotes the Jaumann (or corrotational) rate of the Cauchy stress and $\dot{p}$ denotes the hydrostatic pressure increment. The quantities μ and μ^* are called the instantaneous shear moduli and depend in general on the deformation history. A more convenient, for the subsequent analysis, form of (2.6) in terms of the nominal stress rate $\dot{\mathbf{T}}$ is given by (see for example Hill and Hutchinson [8])

$$\dot{T}_{11} = (2\mu^* - \sigma_1)\dot{u}_{1,1} - \dot{p}, \quad \dot{T}_{22} = (2\mu^* - \sigma_2)\dot{u}_{2,2} - \dot{p}$$

$$\begin{aligned} \dot{T}_{12} &= \left(\mu + \frac{\sigma_1 - \sigma_2}{2}\right)\dot{u}_{2,1} + \left(\mu - \frac{\sigma_1 + \sigma_2}{2}\right)\dot{u}_{1,2}, \\ \dot{T}_{21} &= \left(\mu + \frac{\sigma_2 - \sigma_1}{2}\right)\dot{u}_{1,2} + \left(\mu - \frac{\sigma_1 + \sigma_2}{2}\right)\dot{u}_{2,1} \end{aligned} \tag{2.7}$$

In view of the assumed incompressibility $\Delta \dot{u}_{\alpha,\alpha} = 0$, the following potential function ψ can be introduced for convenience

$$\Delta \dot{u}_1 = \frac{\partial \psi}{\partial x_2}, \quad \Delta \dot{u}_2 = -\frac{\partial \psi}{\partial x_1} \tag{2.8}$$

Downloaded 02 May 2010 to 171.66.16.54. Redistribution subject to ASME license or copyright; see http://www.asme.org/terms/Terms_Use.cfm

which upon substitution in the constitutive equations (2.7) gives for the equilibrium equation (2.4)

$$\left(\mu+\frac{\sigma_1-\sigma_2}{2}\right)\psi_{,1111}+2(2\mu^*-\mu)\psi_{,1122}+\left(\mu+\frac{\sigma_2-\sigma_1}{2}\right)\psi_{,2222}=0 \tag{2.9}$$

while the corresponding interface traction continuity conditions (2.5) yield

$$\left[\left[\left(\mu-\frac{\sigma_1-\sigma_2}{2}\right)\psi_{,22}-\left(\mu-\frac{\sigma_1+\sigma_2}{2}\right)\psi_{,11}\right]\right]=0$$

$$\left[\left[\left(\mu-4\mu^*+\frac{\sigma_1+\sigma_2}{2}\right)\psi_{,112}-\left(\mu-\frac{\sigma_1-\sigma_2}{2}\right)\psi_{,222}\right]\right]=0 \tag{2.10}$$

Note that in (2.9) and (2.10) the constants μ, μ^*, σ_1, σ_2 are all functions of the stretch ratio λ. The pertaining explicit functional relations are to be specified subsequently according to the particular constitutive equation choices. The bifurcation problem considered here consists of finding the closest to unity values of λ (one higher for tension, one lower for compression) for which a nontrivial, bounded in $\mathbb{R}^2$, solution to (2.9), (2.10) becomes possible. At this point one can also assume without loss of generality (in view of the material's incompressibility and pressure insensitivity) that the lateral stress $\sigma_2 = 0$. For additional convenience we denote $\sigma_1 \equiv \sigma$.

Observe that in (2.9) the functions μ, μ^*, σ depend solely on x_2 (piecewise constants). Consequently by taking the Fourier transform of (2.9) and (2.10) with respect to x_1 ($x_1 \to \omega$) the initial two-dimensional problem in ψ is reduced to the following one-dimensional problem in terms of its Fourier transform $\tilde{\psi}$: find conditions for the existence of a nontrivial, bounded in x_2, solution $\tilde{\psi}(\omega, x_2)$ to the fourth-order ordinary differential equation

$$\left(\mu+\frac{\sigma}{2}\right)(i\omega)^4+2(2\mu^*-\mu)(i\omega)^2\tilde{\psi}_{,22}+\left(\mu-\frac{\sigma}{2}\right)\tilde{\psi}_{,2222}=0 \tag{2.11}$$

with (piecewise constant) periodic coefficients of period $2H$. In addition at the points of discontinuity of these coefficients i.e., at $x_2 = \pm h + 2nH$; $n \epsilon Z$, the following jump conditions are satisfied

$$[[\tilde{\psi}]]=0, \quad [[\tilde{\psi}_{,2}]]=0$$

$$\left[\left[\left(\mu-\frac{\sigma}{2}\right)(\tilde{\psi}_{,22}-(i\omega)^2\tilde{\psi})\right]\right]=0$$

$$\left[\left[\left(\mu-4\mu^*+\frac{\sigma}{2}\right)(i\omega)^2\tilde{\psi}_{,2}-\left(\mu-\frac{\sigma}{2}\right)\tilde{\psi}_{,222}\right]\right]=0 \tag{2.12}$$

The first two interface conditions are the transformed displacement rate continuity requirements while the last two are the transformed traction rate continuity conditions (2.10). It should be noted at this point that the Fourier transform $\tilde{\psi}(\omega, x_2)$ of ψ (x_1 x_2) is not an ordinary function of ω but a generalized one and thus all subsequent equations in this subsection are taken in the sense of distributions.

From (2.11), in the interval $[-H, H]$, $\tilde{\psi}$ must be of the form

$$\begin{aligned}
\tilde{\psi}(\omega,x_2) &= \sum_{j=1}^{4} A_j^+(\omega)\exp(i\omega\overset{a}{z}_j x_2) \qquad h\le x_2\le H\\
\tilde{\psi}(\omega,x_2) &= \sum_{j=1}^{4} B_j(\omega)\exp(i\omega\overset{b}{z}_j x_2) \qquad -h\le x_2\le h\\
\tilde{\psi}(\omega,x_2) &= \sum_{j=1}^{4} A_j^-(\omega)\exp(i\omega\overset{a}{z}_j x_2) \qquad -H\le x_2\le -h
\end{aligned} \tag{2.13}$$

where z_j ($z_3 = -z_1$, $z_4 = -z_2$) are the four distinct roots of the biquadratic

$$\left(\mu+\frac{\sigma}{2}\right)+2(2\mu^*-\mu)z^2+\left(\mu-\frac{\sigma}{2}\right)z^4=0 \tag{2.14}$$

The a or b superscripts in (2.13) indicate which layer's stresses and moduli have to be used in (2.14). All the roots z_j are assumed to be complex with nonzero imaginary part, thus excluding a loss of ellipticity (shear band) type of instability in either constituent of the composite prior to bifurcation. For a more detailed description of the different regimes in a finitely strained solid and the corresponding physical interpretations, the interested reader is referred to Hill and Hutchinson [8].

The determination of the unknown constants A_j^+, B_j, A_j^- proceeds as follows. From Floquet's theory for ordinary differential equations (see, for example, Ince [9]) the solution of (2.11) and (2.12) has to satisfy the quasiperiodicity conditions

$$\tilde{\psi}(H)=\Lambda\tilde{\psi}(-H),\ \tilde{\psi}_{,2}(H)=\Lambda\tilde{\psi}_{,2}(-H),\ \tilde{\psi}_{,22}(H)=\Lambda\tilde{\psi}_{,22}(H),\ \tilde{\psi}_{,222}(H)=\Lambda\tilde{\psi}_{,222}(-H);\ \Lambda\equiv\exp(iq2H) \tag{2.15}$$

where q is a real number to be subsequently specified. Substituting (2.13) into (2.12) and (2.15) it is found that a nonzero solution to our problem exists (i.e., nonzero coefficients A_j^+, B_j, A_j^-) when

$$\mathrm{Det}[\mathbf{F}-\exp(2iqH)\mathbf{I}]=0;$$

$$\mathbf{F}\equiv\overset{a}{\mathbf{V}}\exp[2i\omega(H-h)\overset{a}{\mathbf{Z}}]\overset{a}{\mathbf{V}}{}^{-1}\overset{b}{\mathbf{V}}\exp[2i\omega h\overset{b}{\mathbf{Z}}]\overset{b}{\mathbf{V}}{}^{-1} \tag{2.16}$$

with the four by four matrices $\mathbf{V}$, $\mathbf{Z}$, and $\mathbf{I}$ given by

$$V_{1i}=1, V_{2i}=z_i, V_{3i}=\left(\mu-\frac{\sigma}{2}\right)(z_i^2-1),$$

$$V_{4i}=\left(\mu-\frac{\sigma}{2}\right)z_i^3+\left(4\mu^*-\mu-\frac{\sigma}{2}\right)z_i \tag{2.17}$$

$$Z_{ij}=z_i\delta_{ij}\ (\text{no sum}), \quad \mathbf{I}=\delta_{ij} \quad 1\le i,j\le 4$$

Observing that Det $\mathbf{F}$ = 1 and that tr ($\mathbf{F}$) = tr ($\mathbf{F}^{-1}$) the characteristic polynomial of $\mathbf{F}$ is

$$\Lambda^4-(\mathrm{tr}\mathbf{F})\Lambda^3+\frac{1}{2}[(\mathrm{tr}\mathbf{F})^2-\mathrm{tr}\mathbf{F}^2]\Lambda^2-(\mathrm{tr}\mathbf{F})\Lambda+1=0 \tag{2.18}$$

with all real coefficients, as it can be easily shown, and with Λ given by (2.15). It is a matter of straightforward algebra to show that $\mathbf{F}$ admits a unimodular (since $q \epsilon \mathbb{R}$, $|\Lambda| = 1$) eigenvalue when the following conditions are met

$$\begin{aligned}
(|\mathrm{tr}\mathbf{F}|+2)^2 &\ge \mathrm{tr}\mathbf{F}^2\ge(|\mathrm{tr}\mathbf{F}|-2)^2 \qquad \text{if } |\mathrm{tr}\mathbf{F}|\ge 4\\
(|\mathrm{tr}\mathbf{F}|+2)^2 &\ge \mathrm{tr}\mathbf{F}^2\ge\frac{1}{2}(\mathrm{tr}\mathbf{F})^2-4 \qquad \text{if } \mathrm{tr}\mathbf{F}\ge 4
\end{aligned} \tag{2.19}$$

Observing that $\mathbf{F} = \mathbf{F}(\lambda)$, the determination of the composite's critical stretch ratio is then achieved as follows: for fixed ω – and for given geometry and material properties – and for $\lambda > 1$ in tension ($\lambda < 1$ in compression) one seeks the lowest (highest) value of λ say $\hat{\lambda}$ for which (2.19) is satisfied. Obviously at $\hat{\lambda}$ one of these three inequalities will be satisfied as an equality. The wanted critical value of the stretch ratio is given by $\lambda_{cr} = \min \hat{\lambda}(\omega)$ ($\lambda_{cr} = \max\hat{\lambda}(\omega)$) over all $\omega \ge 0$. As one can see from (2.16) and (2.18) only positive values of ω need be considered. Results from calculations using specific constitutive models (i.e., using particular functions $\mu^*(\lambda)$, $\mu(\lambda)$ and $\sigma(\lambda)$) will be presented in a subsequent section.

2.2 Critical Stretch Ratios for the Long and Short Wavelength Limits. In determining $\hat{\lambda}(\omega)$ two cases are of particular interest: the long wavelength limit $\omega \to 0$ and the short wavelength limit $\omega \to \infty$. The employed nomenclature stems from the fact that ω is the frequency of the corresponding bifurcation eigenmode $\exp(i\omega x_1) f(\omega, x_2)$.

Downloaded 02 May 2010 to 171.66.16.54. Redistribution subject to ASME license or copyright; see http://www.asme.org/terms/Terms_Use.cfm

2.2.1 Long Wavelength Limit ($\omega \to 0$). A (matrix) series expansion of the exponential terms in $\mathbf{F}$ (see (2.16)) in powers of ω and groupment of the same order terms, yields after some lengthy but straightforward calculations

$$\begin{aligned} \mathrm{tr}\mathbf{F} &= 4+(\omega H)^2\chi+(\omega H)^4\zeta+\ldots; \\ \mathrm{tr}\mathbf{F}^2 &= 4+(\omega H)^2 4\chi+(\omega H)^4(16\zeta+\eta)+\ldots \end{aligned} \tag{2.20}$$

where χ, ζ, and η are given by

$$\chi = \frac{\xi_a^2}{2}\mathrm{tr}(\overset{a}{\mathbf{Z}}{}^2)+\xi_a\xi_b\mathrm{tr}(\overset{a\,a\,a}{\mathbf{V}}\overset{b\,b\,b}{\mathbf{Z}}\mathbf{V}^{-1}\overset{b\,b\,b}{\mathbf{Z}}\mathbf{V}^{-1})+\frac{\xi_b^2}{2}\mathrm{tr}(\overset{b}{\mathbf{Z}}{}^2)$$

$$\begin{aligned} \zeta &= \frac{\xi_a^4}{24}\mathrm{tr}(\overset{a}{\mathbf{Z}}{}^4)+\frac{\xi_a^3\xi_b}{6}\mathrm{tr}(\overset{a\,a\,a}{\mathbf{V}}\overset{a}{\mathbf{Z}}{}^3\mathbf{V}^{-1}\overset{b\,b\,b}{\mathbf{Z}}\mathbf{V}^{-1}) \\ &\quad+\frac{\xi_a^2\xi_b^2}{4}\mathrm{tr}(\overset{a\,a\,a}{\mathbf{V}}\overset{a}{\mathbf{Z}}{}^2\mathbf{V}^{-1}\overset{b\,b\,b}{\mathbf{V}}\overset{b}{\mathbf{Z}}{}^2\mathbf{V}^{-1}) \\ &\quad+\frac{\xi_a\xi_b^3}{6}\mathrm{tr}(\overset{a\,a\,a}{\mathbf{V}}\overset{b\,b\,b}{\mathbf{Z}}\mathbf{V}^{-1}\overset{b\,b\,b}{\mathbf{V}}\overset{b}{\mathbf{Z}}{}^3\mathbf{V}^{-1})+\frac{\xi_b^4}{24}\mathrm{tr}(\overset{b}{\mathbf{Z}}{}^4) \end{aligned}$$

$$\eta = \xi_a^2\xi_b^2[\mathrm{tr}(\overset{a\,a\,a}{\mathbf{V}}\overset{b\,b\,b}{\mathbf{Z}}\mathbf{V}^{-1}\overset{b\,b\,b}{\mathbf{V}}\overset{b\,b\,b}{\mathbf{Z}}\mathbf{V}^{-1})^2-\mathrm{tr}(\overset{a\,a\,a}{\mathbf{V}}\overset{a}{\mathbf{Z}}{}^2\mathbf{V}^{-1}\overset{b\,b\,b}{\mathbf{V}}\overset{b}{\mathbf{Z}}{}^2\mathbf{V}^{-1})]$$

with

$$\xi_a \equiv 2i(1-\epsilon), \quad \xi_b \equiv 2i\epsilon, \quad \epsilon \equiv h/H \tag{2.21}$$

From (2.21) one can deduce the following useful identities

$$\begin{aligned} 2\chi &= \mathrm{trg}^2, \quad 24\zeta+2\eta=\mathrm{trg}^4 \\ \mathbf{g} &= \xi_a\overset{a\,a\,a}{\mathbf{V}}\overset{a}{\mathbf{Z}}\mathbf{V}^{-1}+\xi_b\overset{b\,b\,b}{\mathbf{V}}\overset{b}{\mathbf{Z}}\mathbf{V}^{-1} \end{aligned} \tag{2.22}$$

A further simplification of the foregoing result is possible; upon substitution of (2.17) into (2.22) and using also (2.12) the matrix $\mathbf{g}$ is found to be

$$\begin{aligned} g_{12} &= g_{21}=g_{34}=g_{43}=2i, \quad g_{41}=-2i[(1-\epsilon)\overset{a}{\sigma}+\epsilon\overset{b}{\sigma}]\equiv 2i\upsilon \\ g_{23} &= 2i[(1-\epsilon)/(\overset{a}{\mu}-\overset{a}{\sigma}/2)+\epsilon/(\overset{b}{\mu}-\overset{b}{\sigma}/2)]\equiv 2i\pi \\ g_{32} &= 2i[(1-\epsilon)(4\overset{a}{\mu}{}^*-\overset{a}{\sigma})+\epsilon(4\overset{b}{\mu}{}^*-\overset{b}{\sigma})]\equiv -2i\rho \end{aligned} \tag{2.23}$$

while all the other entries of $\mathbf{g}$ are zero.

Introducing the asymptotic expansions for tr $\mathbf{F}$ and tr $\mathbf{F}^2$ (2.20) into the characteristic equation (2.18) and recalling that $\Lambda = \exp(2iqH)$ one obtains, after grouping the terms of the like order in ωH, that in the limit $\omega H \to 0$

$$\hat{q}^4+\hat{q}^2\chi/4+(\chi^2-\eta-12\zeta)/32=0; \qquad \hat{q}\equiv q/\omega \tag{2.24}$$

which with the help of (2.21)–(2.23) can be rewritten as

$$\hat{q}^4+\hat{q}^2(\pi\rho-2)+(1-\pi\upsilon)=0 \tag{2.25}$$

The existence of a real in ($\hat{q}$) solution of (2.25) signals the presence of a long wavelength bifurcation mode. The parameter $\hat{q}$ admits an interesting physical interpretation: it is the ratio of frequencies of the buckling pattern with respect to the x_2 and x_1 directions, respectively. Consequently $\hat{q} = \tan\phi$ where ϕ is the inclination of the normal (with respect to x_1) to the diagonal of the fundamental rectangle of the quasi periodic buckling eigenmode.

2.2.2 Short Wavelength Limit ($\omega \to \infty$). Unlike the previous case, the determination of the critical stretch $\hat{\lambda}$ (∞) for the short wavelength case is easier achieved by analyzing the initial equations (2.11), and (2.12), (2.15).

From (2.13) $\tilde{\psi}$ (ω, x_2) can be recasted in the more convenient for this case form:

$$\begin{aligned} \tilde{\psi}(\omega,x_2) &= \hat{A}_1^+(\omega)\exp[i\omega\overset{a}{z}_1(x_2-h)] \\ &\quad+\hat{A}_2^+(\omega)\exp[i\omega\overset{a}{z}_2(x_2-h)] \\ &\quad+\hat{A}_3^+(\omega)\exp[-i\omega\overset{a}{z}_1(x_2-H)] \\ &\quad+\hat{A}_4^+(\omega)\exp[-i\omega\overset{a}{z}_2(x_2-H)] \quad \text{for} \quad h\le x_2\le H \\ \tilde{\psi}(\omega,x_2) &= \hat{B}_1(\omega)\exp[-i\omega\overset{b}{z}_1(x_2-h)] \\ &\quad+\hat{B}_2(\omega)\exp[-i\omega\overset{b}{z}_2(x_2-h)] \\ &\quad+\hat{B}_3(\omega)\exp[i\omega\overset{b}{z}_1(x_2+h)] \\ &\quad+\hat{B}_4(\omega)\exp[i\omega\overset{b}{z}_2(x_2+h)] \quad \text{for} \quad -h\le x_2\le h \\ \tilde{\psi}(\omega,x_2) &= \hat{A}_1^-(\omega)\exp[i\omega\overset{a}{z}_1(x_2+H)] \\ &\quad+\hat{A}_2^-(\omega)\exp[i\omega\overset{a}{z}_2(x_2+H)] \\ &\quad+\hat{A}_3^-(\omega)\exp[-i\omega\overset{a}{z}_1(x_2+h)] \\ &\quad+\hat{A}_4^-(\omega)\exp[-i\omega\overset{a}{z}_2(x_2+h)] \quad \text{for} \quad -H\le x_2\le -h \end{aligned} \tag{2.26}$$

where z_1, z_2 are the two roots of (2.14) with positive imaginary parts.

For $\omega \to \infty$ the boundary conditions at the interfaces $x_2 = \pm h$[1] are satisfied (for nontrivial $\tilde{\psi}$ in (2.26)) when

$$\mathrm{Det}\mathbf{W}=0;$$

$$[W_{ij}=\overset{a}{V}_{ij}\ 1\le j\le 2,\ W_{ij}=(-1)^i\overset{b}{V}_{ij-2}\ 3\le j\le 4],\ 1\le i\le 4 \tag{2.27}$$

The preceding condition after considerable manipulations using (2.14) and (2.17) can be equivalently written as

$$\begin{aligned} &(\overset{a}{\mu}-\overset{a}{\sigma}/2)^2[-1+(\overset{a}{z}_1\overset{a}{z}_2)^2-(\overset{a}{z}_1\overset{a}{z}_2)(2-(\overset{a}{z}_1)^2-(\overset{a}{z}_2)^2)] \\ &+(\overset{b}{\mu}-\overset{b}{\sigma}/2)^2[-1+(\overset{b}{z}_1\overset{b}{z}_2)^2-(\overset{b}{z}_1\overset{b}{z}_2)(2-(\overset{b}{z}_1)^2-(\overset{b}{z}_2)^2)] \\ &+(\overset{a}{\mu}-\overset{b}{\sigma}/2)(\overset{b}{\mu}-\overset{b}{\sigma}/2)[2(1+\overset{a}{z}_1\overset{a}{z}_2)(1+\overset{b}{z}_1\overset{b}{z}_2) \\ &+(\overset{a}{z}_1+\overset{a}{z}_2)(\overset{b}{z}_1+\overset{b}{z}_2)(\overset{a}{z}_1\overset{a}{z}_2+\overset{b}{z}_1\overset{b}{z}_2)]=0 \end{aligned} \tag{2.28}$$

which is exactly the condition for the onset of on surface instability at the interface of two finitely strained and perfectly bonded incompressible solids (see, for example, Biot [6]) as one can easily observe from the exponentially decaying eigenmode in (2.26) away from the interfaces $x_2 = \pm h$ (as $\omega \to \infty$).

3 Macroscopic Instability Analysis

The equilibrium (2.4) compatibility (2.8) and constitutive (2.7) equations for the composite can alternatively be put in the form

$$\frac{\partial^2}{\partial x_\alpha \partial x_\beta}\left[L_{\alpha\beta\gamma\delta}\frac{\partial^2\psi}{\partial x_\gamma \partial x_\delta}\right]=0 \tag{3.1}$$

with the periodic in x_2 of period $2H$ functions $L_{\alpha\beta\gamma\delta}(x_2)$ given by

$$\begin{aligned} &L_{1111}=\mu+\sigma/2,\ L_{1122}=L_{2211}=-\mu+\sigma/2,\ L_{2222}=\mu-\sigma/2 \\ &L_{1212}=\mu+\mu^*,\ L_{1221}=L_{2112}=\mu^*-\mu,\ L_{2121}=\mu+\mu^*-\sigma \end{aligned} \tag{3.2}$$

Of interest here is the behavior of the incremental displacement potential ψ^H (where the superscript (H) denotes the dependence of ψ on the period $2H$) as the periodic structure of the composite becomes finer, i.e., as $H \to 0$. The

[1] Note: The Floquet conditions (2.15) in the limit $\omega \to \infty$ turn out to be superfluous.

Downloaded 02 May 2010 to 171.66.16.54. Redistribution subject to ASME license or copyright; see http://www.asme.org/terms/Terms_Use.cfm

basic result from homogenization theory[2] (see, for example, Bensoussan, Lions, and Papanicolaou [10]) establishes that in the limit $H \to 0$, $\psi^H \to \psi^0$ which satisfies

$$\mathcal{L}_{\alpha\beta\gamma\delta} \frac{\partial^2 \psi^0}{\partial x_\alpha \partial x_\beta \partial x_\gamma \partial x_\delta} = 0 \tag{3.3}$$

where the constant (i.e., independent on **x**) homogenized incremental moduli $\mathcal{L}$ are given by

$$\mathcal{L}_{\alpha\beta\gamma\delta} = \frac{1}{2} \int_{-1}^{1} \left[L_{\alpha\beta\gamma\delta}(y_2) + L_{\alpha\beta\epsilon\zeta}(y_2) \frac{d^2 \phi^{\gamma\delta}(y_2)}{dy_\epsilon dy_\zeta} \right] dy_2, \quad y_2 \equiv x_2/H \tag{3.4}$$

in which the functions $\phi^{\gamma\delta}(y_2)$ are periodic in $[-1, 1]$ i.e., $\phi^{\epsilon\zeta}(-1) = \phi^{\epsilon\zeta}(1)$ and satisfy

$$\frac{d^2}{dy_2^2} \left[L_{2222}(y_2) \frac{d^2 \phi^{\epsilon\zeta}}{dy_2^2} \right] = -\frac{d^2}{dy_2^2} L_{22\epsilon\zeta}(y_2), \quad \epsilon = \zeta = 1 \text{ or } \epsilon = \zeta = 2 \tag{3.5}$$

The foregoing result can be straightforwardly obtained using S. Palencia's [11] method of multiple scale expansions i.e., putting $\psi^H(x_1, x_2) = \psi^0(x_1, x_2; y_2) + H\psi^1(x_1, x_2; y_2) + \ldots + H^n \psi^n(x_1, x_2; y_2)$ substituting into (3.1) and subsequently collecting terms of the like order in H. Employing (3.4) and (3.5) the homogenized incremental moduli are found to be

$$\mathcal{L}_{1111} = \langle L_{1111} - L_{1122} L_{2211}/L_{2222} \rangle + \langle L_{2211}/L_{2222} \rangle^2 / \langle L_{2222}^{-1} \rangle$$

$$\mathcal{L}_{1122} = \mathcal{L}_{2211} = \langle L_{1122}/L_{2222} \rangle / \langle L_{2222}^{-1} \rangle, \mathcal{L}_{2222} = 1/\langle L_{2222}^{-1} \rangle$$

all others $\mathcal{L}_{\alpha\beta\gamma\delta} = \langle L_{\alpha\beta\gamma\delta} \rangle$ with $\langle f \rangle \equiv 0.5 \int_{-1}^{1} f(y_2) dy_2$ (3.6)

Thus the investigation of the macroscopic stability properties of the composite is reduced to the examination of the loss of ellipticity in the incremental equilibrium equations of the homogenized material (3.3). The corresponding condition is the existence of real roots n_2/n_1 in the equation

$$\mathcal{L}_{1111} n_1^4 + (2\mathcal{L}_{1122} + 2\mathcal{L}_{1221} + \mathcal{L}_{1212} + \mathcal{L}_{2121}) n_1^2 n_2^2 + \mathcal{L}_{2222} n_2^4 = 0 \tag{3.7}$$

where n_1, n_2 are the direction cosines of the normal **n** to the characteristic direction. Denoting by ϕ the angle formed between **n** and x_1 (i.e., $\tan\phi = n_2/n_1$) and employing (3.6) and (3.2), (3.7) can be rewritten in the form

$$(\tan\phi)^4 + (\pi\rho - 2)(\tan\phi)^2 + (1 - \pi\upsilon) = 0 \tag{3.8}$$

where π, ρ, υ, are the material constants (functions of λ) defined in (2.3).

Observe that the loss of ellipticity condition for the homogenized material (3.8) is identical to equation (2.25) corresponding to the onset of the long wavelength bifurcation instability. This coincidence has to be expected since in both cases (i.e., in (2.25) as well in (3.8)) attention is focused on an instability mode with characteristic wavelength much higher than the unit cell size, i.e., $\omega H \to 0$. It is very interesting however to see how one achieves the same answer for the aforementioned long wavelength instability mode following two completely different analytical procedures.

4 Results From the Study of Two Particular Composites

In the present section the micro and macroinstability behavior of two particular composites is investigated. The first application involves a constitutive equation developed by Stören and Rice [7] for modeling the behavior of metals at finite strain. The second application deals with a Mooney-Rivlin solid. The motivation for this choice lies in the different stability properties of the two materials in the large strain regime, as it will be explained in the sequel.

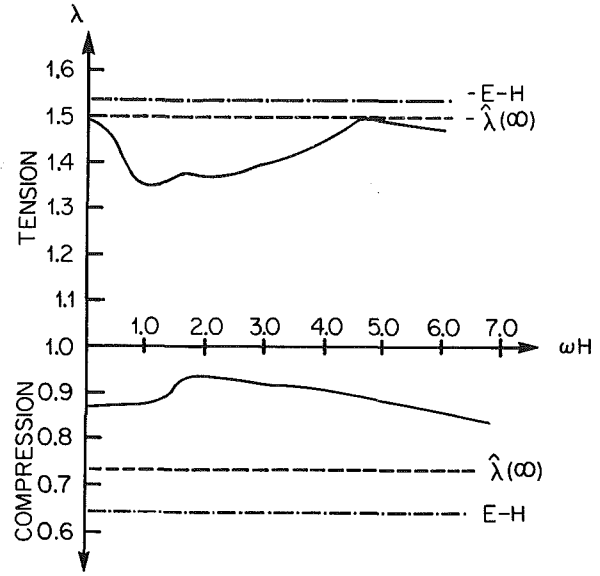


Fig. 2 Dependence of the critical stretch ratio λ on the nondimensionalized eigenmode frequency ωH for the hypoelastic composite with $E_a/E_b = 0.1, m_a = m_b = 4.0, \epsilon = 0.2$

4.1 Stören-Rice Material. The first composite to be considered consists of two alternating series of layers obeying the Stören-Rice [7] deformation theory of plasticity. This hypoelastic constitutive model has been successfully employed to predict the failure strains of finitely deformed metallic sheets. The reason for this model's use in the present work is that it loses ellipticity under plane strain conditions for rather realistic strain levels $0.5 < \lambda < 2$. The incremental moduli μ, μ^* as well as the stress σ under plane strain uniaxial stretching conditions are found to be (see for example Abeyaratne and Triantafyllidis [12] for the corresponding derivations)

$$\mu = \frac{E}{3} \left| \frac{2}{\sqrt{3}} \frac{ln\lambda}{\epsilon_y} \right|^{\frac{1}{m}-1}, \quad \mu^* = \mu/m,$$

$$\sigma = E\epsilon_y \frac{2}{\sqrt{3}} \left| \frac{2ln\lambda}{\sqrt{3}\epsilon_y} \right|^{\frac{1}{m}} \operatorname{sgn}(ln\lambda) \tag{4.1}$$

when the uniaxial stress-strain curve is a power law with hardening exponent m, initial yield strain ϵ_y, and a Young's modulus E (i.e. $(\sigma/\sigma_y)^m = E(\epsilon/\epsilon_y)$; $\sigma_y = E\epsilon_y$). For additional information on this model and its physical relevance in the case of finitely strained metals the interested reader is referred to the original work by Stören and Rice [7].

The dependence of the critical stress $\hat{\lambda}$ on ωH the nondimensional frequency of the buckling eigenmode for a composite with $E_a/E_b = 0.1$, $m_a = m_b = 4.0$ and $\epsilon = h/H = 0.2$ is depicted in Fig. 2. Observe that the lowest (highest) stretch ratio corresponding to the onset of the first microstructural instability in the composite $\lambda_{cr} = \max\hat{\lambda}(\omega H)$ ($\lambda_{cr} = \min\hat{\lambda}(\omega H)$) is $\lambda_{cr} \cong 1.35$ ($\lambda_{cr} \cong 0.95$) while the macroscopic – loss of ellipticity – instability of the homogenized composite occurs at $\lambda = \hat{\lambda}(0) \cong 1.49$ ($\lambda = \hat{\lambda}(0) \cong 0.87$). The dashed lines in both figures indicate the onset of the surface buckling modes at the interface of the composite while the dash-dot lines correspond to the loss of ellipticity of the material which is the same for both layers since $m_a = m_b$

[2] Note: A rigorous mathematical proof of this result requires some restrictive assumptions on **L**.

Downloaded 02 May 2010 to 171.66.16.54. Redistribution subject to ASME license or copyright; see http://www.asme.org/terms/Terms_Use.cfm

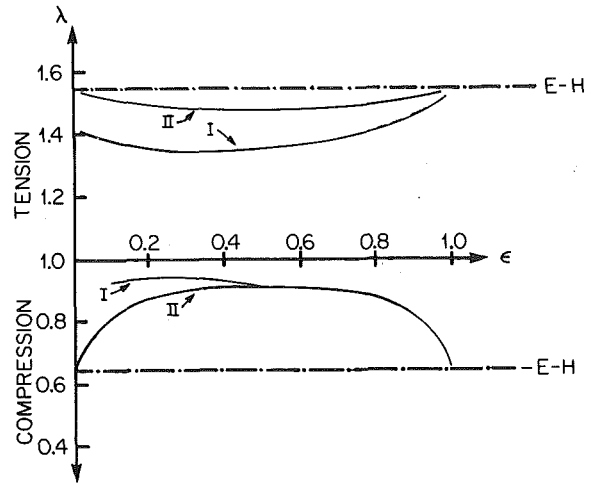


Fig. 3 Dependence of the microscopic (*I*) and macroscopic (*II*) critical stretch ratio λ on the layer thickness parameter ϵ for the hypoelastic composite with $E_a/E_b = 0.1, m_a = m_b = 4.0$

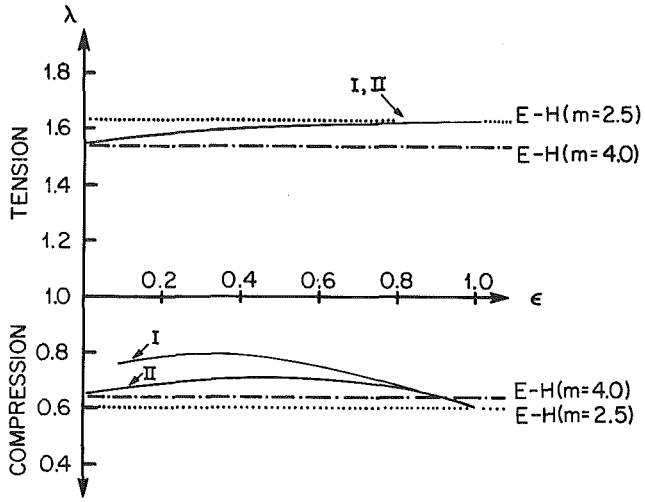


Fig. 4 Dependence of the microscopic (*I*) and macroscopic (*II*) critical stretch ratio λ on the layer thickness parameter ϵ for the hypoelastic composite with $E_a/E_b = 1, m_a = 4, m_b = 2.5$

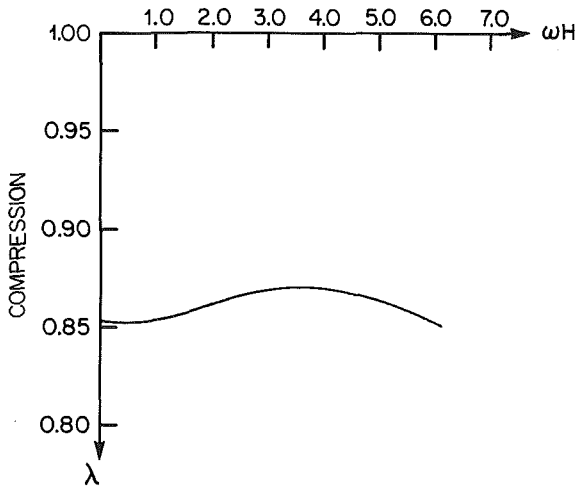


Fig. 5 Dependence of the critical stretch ratio λ on the nondimensionalized eigenmode frequency ωH for the hyperelastic composite with $E_a/E_b = 0.07, \epsilon = 0.1$

(see [12]). The results presented in Fig. 2 are very typical of all such $\hat{\lambda}(\omega H)$ curves obtained for the composites examined in this work.

The comparison between the critical stretch ratios for the onset of the microbuckling (curves *I* correspond to λ_{cr}) and those for the onset of the macroinstability (curves *II* correspond to $\hat{\lambda}(0)$) in a composite with $E_a/E_b = 0.1$, $m_a = m_b = 4$ for both tensile and compressive loading is depicted in Fig. 3 as a function of the composite's geometry, characterized by the thickness ratio $\epsilon = h/H$. Note that in tension the microbuckling instability always precedes the loss of ellipticity in the homogenized material with the biggest difference occurring around $\epsilon = 0.3$ (differences of the order of 30 percent). In compression the differences between the critical stretches corresponding to the onset of macro and microinstability are even greater. First observe that although each layer of the composite loses ellipticity at $\lambda_{cr} \approx 0.65$ the homogenized material loses ellipticity at much lower strains (e.g., $\hat{\lambda}(0) \cong 0.9$ for $\epsilon = 0.5$) Also note that for $\epsilon < 0.5$ (approximately) the microstructural instability occurs at lower strains than the macroscopic one with the difference between the corresponding stretch ratios increasing monotonically as the size of the stiffer inner fiber decreases i.e., as $\epsilon \to 0$. No microscopic instability occurs for $\epsilon > 0.5$.

The stability problem of a composite with two layers of identical initial stiffness, i.e., $E_a/E_b = 1$ but of different hardening exponents $m_a = 4$, $m_b = 2.5$ is examined in Fig. 4. Observe that in tension the lowest critical stretch ratio corresponds to the onset of the long wavelength mode i.e., $\lambda_{cr} = \hat{\lambda}(0)$ and thus the only instability occurring in the composite under tensional loading is the macroscopic one. It is also worth mentioning that the critical stretch in this case, which corresponds to the loss of ellipticity of the homogenized composite lies between the critical stretch ratios for the loss of ellipticity in each layer. Quite a different situation is encountered in the case of compression. There is considerable difference between the onset of the micro and the macroinstabilities which, in a way quite analogous to the compressive behavior of the previous composite (see Fig. 3) increases with decreasing layer thickness ratio ϵ. Note that the two critical stretches coincide for $\epsilon \geq 0.8$ approximately. In addition the behavior of the homogenized material in compression is also of interest in this case since its loss of ellipticity, for a wide range of ϵ, occurs at a strain level significantly inferior to those corresponding to the loss of ellipticity of each layer.

In conclusion one can deduce that the greater the difference in the layer stiffnesses, the more important the discrepancies between the macro and microinstability predictions are. Moreover, in the case of compressive loading, the thinner the stiffest layer is, the lower the critical strain for the onset of microbuckling is, and the bigger the difference between the micro and macroinstability critical stretches becomes.

4.2 Mooney-Rivlin Material. The second composite to be investigated is made up of alternating layers of rubber that obey the Mooney-Rivlin constitutive law. The choice in this case was made on the basis that this model remains always elliptic at any level of strain (see for example Knowles and Sternberg [13]).

For an incompressible, plane strain, uniaxial stress are given by

$$\mu = E(\lambda^2 + \lambda)^{-2}/6, \quad \mu = \mu^*, \quad \sigma = E(\lambda^2 - \lambda^{-2})/3 \tag{4.2}$$

where E is the material's Young's modulus.

The long and short wavelength instabilities present a special interest in this case and will be studied further. For the macroinstability ($\omega H \to 0$) from (4.2) and (2.23) the characteristic equation for the loss of ellipticity in the homogenized composite (3.8) (or (2.25)) assumes the form

$$\hat{q}^4 + \hat{q}^2[(\lambda^4 + 3)s - 2] + 1 + (\lambda^4 - 1)s = 0; \tag{4.3}$$

$$s \equiv [(1-\epsilon)/E_a + \epsilon/E_b][(1-\epsilon)E_a + \epsilon E_b]$$

where s satisfies $s \geq 1$. One can easily verify that for tension ($\lambda > 1$) the homogenized composite remains always elliptic

Downloaded 02 May 2010 to 171.66.16.54. Redistribution subject to ASME license or copyright; see http://www.asme.org/terms/Terms_Use.cfm

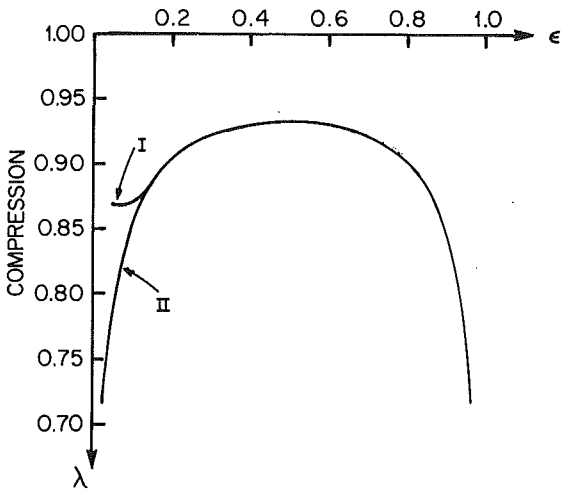


Fig. 6 Dependence of the microscopic (*I*) amd macroscopic (*II*) critical stretch ratio λ on the layer thickness parameter ϵ for the hyperelastic composite with $E_a/E_b = 0.07$

while in compression ($\lambda < 1$) the homogenized composite loses ellipticity at

$$\hat{\lambda}(0) = [(s-1)/s]^{1/4} \tag{4.4}$$

Similarly for the short wavelength limit ($\omega H \to \infty$) from (2.28) surface buckling at the layers' interface is found with the help of (4.2) and (2.14) to occur at (observing that in this case $z_1 = i\lambda^2$, $z_2 = i$)

$$x^6 + x^4(1+3t)/(1+t) + x^2(3-t)/(1+t) - (1-t)/(1+t) = 0$$
$$x \equiv \hat{\lambda}(\infty), \quad t \equiv 2E_aE_b/(E_a^2+E_b^2) \tag{4.5}$$

where $0 \le t \le 1$. One can easily show that in this case (4.5) admits no interlayer surface instability for tensile loading while for compressive loading such an instability always occurs in the interval $0 \le \hat{\lambda}(\infty) \le 0.54$.

For the case of tensile loading the Mooney-Rivlin composite does not seem to admit a microbuckling instability either. Indeed no solution $\hat{\lambda}(\omega H)$ for (2.19) was found in the interval $1 \le \lambda \le 20$, $0 \le \omega H \le 16$ for a wide range of material properties $0.01 \le E_a/E_b \le 1$ and for all possible geometries $0 \le \epsilon \le 1$. Hence only the stability properties of the composite under compressive loading will be investigated.

The typical critical stretch ratio $\hat{\lambda}$ versus nondimensionalized frequency ωH of the buckling eigenmode is shown in Fig. 5 for a composite with $E_a/E_b = 0.07$ and $\epsilon = 0.1$. For this particular case the stretch corresponding to the onset of the first microstructural instability is $\lambda_{cr} = 0.87$.

Finally, Fig. 6 shows the comparison between the critical stretch ratios for the onset of the microbuckling (curve *I* corresponds to $\hat{\lambda}_{cr}$) and those for the onset of the macroinstability (curve *II* corresponds to $\hat{\lambda}(0)$ for a composite with $E_a/E_b = 0.07$ as a function of the layer thickness ratio ϵ. Note that $\lambda_{cr} < \hat{\lambda}(0)$ only for values of $\epsilon < 0.2$ approximately. Also note that the significant reduction for the macroscopic loss of ellipticity strain near $\epsilon = 0.5$ (as it can easily be shown from (4.4) curve *II* passes from $\hat{\lambda} = 0$ at $\epsilon = 0$, $\epsilon = 1$).

5 Conclusions

The purpose of this work has been the consistent quantitative comparison between the macroscopic and the corresponding microscopic instability mechanisms for composite media under finite strain by using a specific example and not the investigation of the stability properties of a particular composite.

Assuming a microbuckling mechanism responsible for the loss of ellipticity in the macroscopical level we have carried out an analytical investigation of the micro and macrostability problem for a fiber-reinforced composite using two different types of constitutive equations. Of the results obtained here the most dramatic evidence of the effect of the microstructure on the overall stability of a medium is the shear band type of instability appearing in the Mooney-Rivlin composite under compression in spite of the fact that the aforementioned material remains pointwise elliptic at any level of strain. This work can also be considered as a first step toward an improved quantitative understanding of the effects of geometry constraint in the stability properties of certain media with microstructure.

Acknowledgments

Support for this work by N.S.F. under Grant MEA - 8116449 is gratefully appreciated. One of us (N.T.) would also like to acknowledge helpful discussions with R. Abeyaratne from Michigan State University during the first stages of this work.

References

1 Tsai, S., and Wu, E., "A General Theory of Strength for Anisotropic Materials," *J. Composite Materials*, Vol. 5, 1971, pp. 58–81.

2 Rudnicki, J., and Rice, J., "Conditions for the Localization of Deformation in Pressure Sensitive Dilatant Materials," *J. Mech. Physics Solids*, Vol. 23, 1975, pp. 371–394.

3 Nemat-Nasser, S., "On Finite Plastic Flow of Crystalline Solids and Geomaterials," ASME JOURNAL OF APPLIED MECHANICS, Vol. 50, 1983, pp. 1114–1126.

4 Tvergaard, V., "Influence of Voids on Shear Band Instabilities Under Plane Strain Conditions," *Int. J. of Fracture*, Vol. 17, 1981, pp. 389–407.

5 Abeyaratne, R., and Triantafyllidis, N., "An Investigation of Localization in a Porous Plastic Material Using Homogenization Theory," ASME JOURNAL OF APPLIED MECHANICS, Vol. 51, 1984, pp. 481–486.

6 Biot, M., *Mechanics of Incremental Deformation*, Wiley, New York, 1965.

7 Stören, S., and Rice, J., "Localized Necking in Thin Sheets," *J. Mech. Physics Solids*, Vol. 23, 1975, pp. 421–441.

8 Hill, R., and Hutchinson, J., "Bifurcation Phenomena in the Plane Strain Tension Test," *J. Mech. Physics Solids*, Vol. 23, 1975, pp. 239–264.

9 Ince, E., *Ordinary Differential Equations*, Dover, 1956.

10 Bensoussan, A., Lions, J., and Papanicolaou, G., *Asymptotic Analysis for Periodic Structures*, North Holland, 1978.

11 Sanchez-Palencia, E., "Comportement Local et Macroscopique d'un type de Milieux Physiques Heterogenes," *Int. J. Eng. Sci.*, Vol. 12, 1974, pp. 331–351.

12 Abeyaratne, R., and Triantafyllidis, N., "On the Emergence of Shear Bands in Plane Strains," *Int. J. Solids Structures*, Vol. 17, 1981, pp. 1113–1134.

13 Knowles, J., and Sternberg, E., "On the Failure of Ellipticity and the Emergence of Discontinuous Deformation Gradients in Plane Finite Elastostatics," *J. of Elasticity*, Vol. 8, 1978, pp. 329–379.

Downloaded 02 May 2010 to 171.66.16.54. Redistribution subject to ASME license or copyright; see http://www.asme.org/terms/Terms_Use.cfm

P. R. Heyliger
Graduate Research Assistant.

J. N. Reddy
Professor.
Mem. ASME

Department of Engineering Science and Mechanics,
Virginia Polytechnic Institute and State University,
Blacksburg, VA 24061

Reduction of Free-Edge Stress Concentration

A quasi-three dimensional elasticity formulation and associated finite element model for the stress analysis of symmetric laminates with free-edge cap reinforcement are described. Numerical results are presented to show the effect of the reinforcement on the reduction of free-edge stresses. It is observed that the interlaminar normal stresses are reduced considerably more than the interlaminar shear stresses due to the free-edge reinforcement.

Introduction

Free edge effects in laminated composites have been studied by numerous investigators [1-17]. These studies indicate the existence of large interlaminar stresses near the free edge of composite laminates under inplane loads.

A proposed method of reducing the intensity of these large stresses is to reinforce the stiffness at the free edge by wrapping a lamina or collection of laminae around the free edge, forming a cap. The cap is intended to reduce the large displacement gradients near the free edge, thereby decreasing the interlaminar stresses and reducing the probability of delamination. Experimental studies indicate that a reinforcing cap is a viable method of maintaining laminate strength [18].

The purpose of this study is to determine the effect of a reinforcing cap on the stress distribution in a symmetric composite laminate under uniform axial extension. Parametric studies are performed by varying the thickness and overlap length of the cap. Numerical results are presented for several representative test cases.

Formulation

The initial work of Pipes and Pagano [1] used the three-dimensional elasticity equations to develop an assumed displacement field for a symmetric laminate (without a cap) under uniform axial extension (see Fig. 1). Using the stress-strain relations for a monoclinic material and the strain-displacement relations for a linearly elastic material, symmetry and antisymmetry conditions can be imposed to give the following displacement field:

$$\begin{aligned} u &= kx + U(y,z) \\ v &= V(y,z) \\ w &= W(y,z) \end{aligned} \tag{1}$$

Since all stresses are independent of the axial coordinate x, the equilibrium equations reduce to:

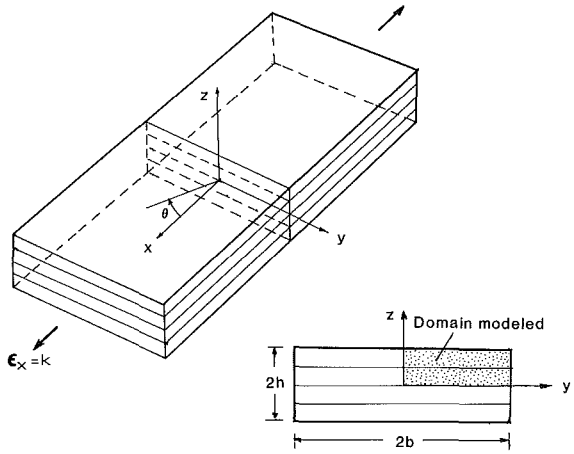


Fig. 1 Laminate geometry and loading (the cap is not shown)

$$\begin{aligned} \tau_{xy,y} + \tau_{xz,z} &= 0 \\ \sigma_{y,y} + \tau_{yz,z} &= 0 \\ \tau_{yz,y} + \sigma_{z,z} &= 0 \end{aligned} \tag{2}$$

Substitution of the displacement field (1) and stress-strain relations into the equilibrium equations (2) yields the following governing equations:

$$\begin{aligned} &C_{66}U_{,yy} + C_{55}U_{,zz} + C_{26}V_{,yy} + C_{45}V_{,zz} + (C_{36} + C_{45})W_{,yz} = 0 \\ &C_{26}U_{,yy} + C_{45}U_{,zz} + C_{22}V_{,yy} + C_{44}V_{,zz} + (C_{23} + C_{44})W_{,yz} = 0 \\ &(C_{45} + C_{36})U_{,yz} + (C_{44} + C_{23})V_{,yz} + C_{44}W_{,yy} + C_{33}W_{,zz} = 0 \end{aligned} \tag{3}$$

These coupled, second order partial differential equations represent a three variable problem in a two-dimensional domain.

The differential equations in (3) are to be solved subject to the appropriate boundary conditions of the problem. The antisymmetry and symmetry about the x-z and x-y planes, respectively, allows us to model only one quadrant of the laminate. The symmetry boundary conditions are given by,

$$\begin{aligned} U_{,z}(y,0) &= 0 \quad & U(0,z) &= 0 \\ V_{,z}(y,0) &= 0 \quad & V(0,z) &= 0 \\ W(y,0) &= 0 \quad & W_{,y}(0,z) &= 0 \end{aligned} \tag{4}$$

Contributed by the Applied Mechanics Division for publication in the JOURNAL OF APPLIED MECHANICS. Discussion on this paper should be addressed to the Editorial Department, ASME, United Engineering Center, 345 East 47th Street, New York, N.Y. 10017 and will be accepted until two months after final publication of the paper itself in the JOURNAL OF APPLIED MECHANICS. Manuscript received by ASME Applied Mechanics Division, August, 1984; final revision, March, 1985.

Copyright © 1985 by ASME
Downloaded 02 May 2010 to 171.66.16.54. Redistribution subject to ASME license or copyright; see http://www.asme.org/terms/Terms_Use.cfm

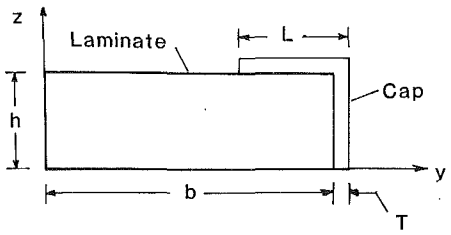


Fig. 2 Domain (a quadrant of the y-z plane shown in Fig. 1) of the capped laminate modeled using FEM

In addition to the displacement boundary conditions (4), the tractions on the boundary planes parallel to the symmetry lines are known. Along the top plane, where the normal vector is parallel to the z axis (i.e., at $z=h$), the traction free conditions give

$$\sigma_z = \tau_{yz} = \tau_{xz} = 0 \tag{5}$$

Similarly, along the outer edge, where the normal vector is parallel to the y axis (i.e., at $y=b$) the traction-free boundary conditions imply,

$$\sigma_y = \tau_{yz} = \tau_{xy} = 0 \tag{6}$$

A comment is in order on the boundary-value problem described above. A cursory look at the differential equations (3) and boundary conditions (4)–(6) shows that we have homogeneous differential equations with homogeneous boundary conditions (hence we must obtain the trivial solution to the problem). However, this is not the case. The problem description is not complete without the specification of the stress boundary conditions on the face of the cross section. These conditions can be expressed in terms of the displacement gradients as (assuming the stress-strain relations of a monoclinic material)

$$\tau_{xz} \equiv C_{45}(V_{,z} + W_{,y}) + C_{55}U_{,z} \tag{7}$$

$$\tau_{xy} \equiv C_{16}k + C_{26}V_{,y} + C_{36}W_{,z} + C_{66}U_{,y} \tag{8}$$

The stress τ_{xy} in (8) includes the initial strain k, and is a nonhomogeneous boundary condition, which gives a nontrivial solution to the problem. This completes the description of the boundary-value problem for the uncapped laminate.

The formulation presented above for an uncapped symmetric laminate can be extended to include the effects of a cap. Indeed, the governing equations and boundary conditions given above will not change for a capped laminate, with the exception of the change in material properties in the cap. The natural boundary conditions given in (6) still apply to the small surface area introduced by the cap whose normal is in the negative y direction and (4) applies to the cap boundary whose normal is in the negative z direction. The inclusion of the cap material must not violate any of the assumptions used to develop the governing equations and boundary conditions (see [1]). For this reason, only unidirectional or symmetric cross-ply (i.e., odd number of layers with material coordinate directions alternatingly oriented at 0 and 90 deg to the laminate coordinates) lamination schemes can be used for the cap since the stress-strain relations for a monoclinic material require symmetry about the midplane of the laminate. The domain of the new problem is shown in Fig. 2 with the necessary geometric variables labeled.

Method of Solution

Variational Formulation. The finite element method is used to obtain an approximate solution to the boundary-value problem described above. Here we use the Ritz finite element model of the equations. The weak (or variational) formulation (see [19]) required for the Ritz finite element models is obtained as follows. The three differential equations in (3) are weighted with the variations δU, δV, and δW of the displacements U, V, and W, respectively, and are integrated over the domain of a typical finite element R^e. The component form of the Green-Gauss theorem is then used to transfer half of the differentiation to the weight functions. For example, consider the first equation in (3). We have

$$0 = \int_{R^e} \delta U[C_{66}U_{,yy} + C_{55}U_{,zz} + C_{26}V_{,yy} + C_{45}V_{,zz}$$

$$+ (C_{36} + C_{45})W_{,yz}]dR = -\int_{R^e} (C_{66}U_{,y}\delta U_{,y} + C_{55}U_{,z}\delta U_{,z}$$

$$+ C_{26}V_{,y}\delta U_{,y} + C_{45}V_{,z}\delta U_{,z}$$

$$+ C_{45}W_{,y}\delta U_{,z} + C_{36}W_{,z}\delta U_{,y})dR$$

$$+ \oint_{S^e} (C_{66}U_{,y}n_y + C_{55}U_{,z}n_z + C_{26}V_{,y}n_y + C_{45}V_{,z}n_z$$

$$+ C_{45}W_{,y}n_z + C_{36}W_{,z}n_y)\,\delta U dS. \tag{9}$$

The final variational form is obtained by including the physical natural boundary conditions of the problem into the variational statement (9). Using (7) and (8), we can write the boundary integral in (9) as

$$\oint_{S^e} [(\tau_{xy} - C_{16}k)n_y + \tau_{xz}n_z]\delta U dS. \tag{10}$$

The final variational form associated with the first equation of (3) for the Ritz finite element model, for a typical element, becomes,

$$\int_{R^e} [(C_{66}U_{,y} + C_{26}V_{,y} + C_{36}W_{,z})\delta U_{,y} + (C_{55}U_{,z} + C_{45}V_{,z}$$

$$+ C_{45}W_{,y})\,\delta U_{,z}\}dR = \oint_{S^e} \delta U(\tau_{xy}n_y + \tau_{xz}n_z)\,dS$$

$$- \oint_{S^e} C_{16}kn_y \delta U dS \tag{11}$$

It is to be understood here that C_{ij} are the material constants of a typical element. The variational form of the remaining two equations can be obtained in a similar manner.

Finite Element Model. The Ritz finite element model of (3) over a typical element can be developed using the variational statements of the type in (11). In the finite element method we seek an approximate solution (U, V, W) in the form (see Reddy [19, 20])

$$U = \sum_{j=1}^{n} \psi_j U_j \qquad \delta U = \psi_i$$

$$V = \sum_{j=1}^{n} \psi_j V_j \qquad \delta V = \psi_i \tag{12}$$

$$W = \sum_{j=1}^{n} \psi_j W_j \qquad \delta W = \psi_i$$

where ψ_j are the interpolation functions (see [19]) and n is the number of nodes in the element. Substituting these approximations into the variational form of the governing equations, we obtain the finite element equations of a typical element:

$$\begin{bmatrix} [K^{11}] & [K^{12}] & [K^{13}] \\ [K^{21}] & [K^{22}] & [K^{23}] \\ [K^{31}] & [K^{32}] & [K^{33}] \end{bmatrix} \begin{Bmatrix} \{U\} \\ \{V\} \\ \{W\} \end{Bmatrix} = \begin{Bmatrix} \{F^1\} \\ \{F^2\} \\ \{F^3\} \end{Bmatrix} \tag{13}$$

Downloaded 02 May 2010 to 171.66.16.54. Redistribution subject to ASME license or copyright; see http://www.asme.org/terms/Terms_Use.cfm

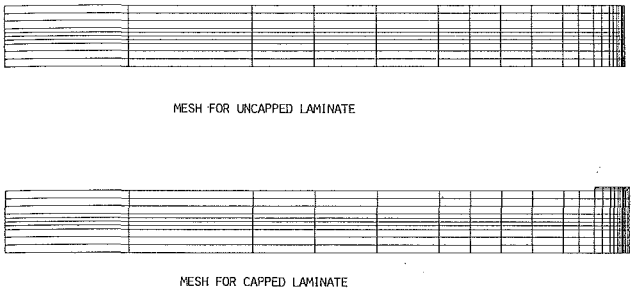


Fig. 3 Finite element meshes used to analyze capped and uncapped laminates

The form of the element stiffness matrices $[K^{\alpha\beta}]$ and force vectors $\{F^{\alpha}\}$ are given in the appendix.

The assembly of the element equations for the entire domain results in the global finite element model

$$[K]\{\Delta\} = \{F\}. \tag{14}$$

These simultaneous algebraic equations are solved after imposing the essential boundary conditions of the problem. In the present study linear rectangular elements are used to represent both geometry and displacements (i.e., isoparametric formulation is used). The finite element meshes used are such that the individual layers are represented by at least one or more elements.

Once the element assembly has been completed, the contributions from the stresses τ_{xy} and τ_{xz} to the element boundary integrals in (9) will cancel at the element interfaces in the domain except on the boundary of the domain, where they are specified to be zero (τ_{xy} along the outer edge and τ_{xz} along the upper surface). Since the material properties can be different for each element, the term in the surface integral involving the initial strain k will be, in general, nonzero between layers and at the outer surfaces of the laminate.

Numerical Examples

Preliminary Remarks. To demonstrate the effects of free edge reinforcement on the interlaminar stresses in symmetric composite laminates under uniform axial extension, several laminates were analyzed with and without a cap. The $[0,90]_s$ and $[\pm 45]_s$ laminates have been studied extensively (see, for example, [14] and [17]) in the analysis of the free edge problem and were studied in this paper for purposes of comparison. The dimensions of the laminate quadrant were taken to be $b=25.4$ cm by $h=2.54$ cm; hence the width to thickness ratio of the laminate is 10. The laminate was subjected to an initial strain of 0.001 cm/cm in all analyses. The following material properties were used for both the laminate and the cap:

$$E_1 = 137.89 \text{ Gpa}$$

$$E_2 = E_3 = 14.48 \text{ Gpa}$$

$$G_{12} = G_{13} = G_{23} = 5.86 \text{ Gpa}$$

$$\nu_{12} = \nu_{13} = \nu_{23} = 0.21$$

These material properties have been frequently used in previous studies.

The upper right hand quadrant of the laminate cross section was modeled using linear finite elements for both the uncapped and capped laminates. A typical finite element mesh for each of these two cases is shown in Fig. 3. The mesh of the uncapped laminate contained 210 elements and the mesh for the capped laminates contained between 246 and 254 elements, depending on the overlap length L of the cap.

The lamination scheme of the cap, as mentioned previously, is limited to at most a cross-ply due to the symmetry requirements about the midplane ($z=0$) of the laminate. However, a cap with its fibers running parallel to the x axis would not provide the needed stiffness or strength through the thickness of the laminate near the free edge, since the transverse or weak axis of the material would then correspond to the z direction of the laminate. For this reason, only a cap with the fibers perpendicular to the x axis were considered in the analyses that follow. More explicitly, the elements in the cap along the top edge of the laminate contain fibers that are parallel to the y axis, and the elements of the cap along the right edge of the laminate contain fibers that are parallel to the z axis. The fibers in the cap are assumed to bend at right angles at the corner of the cap.

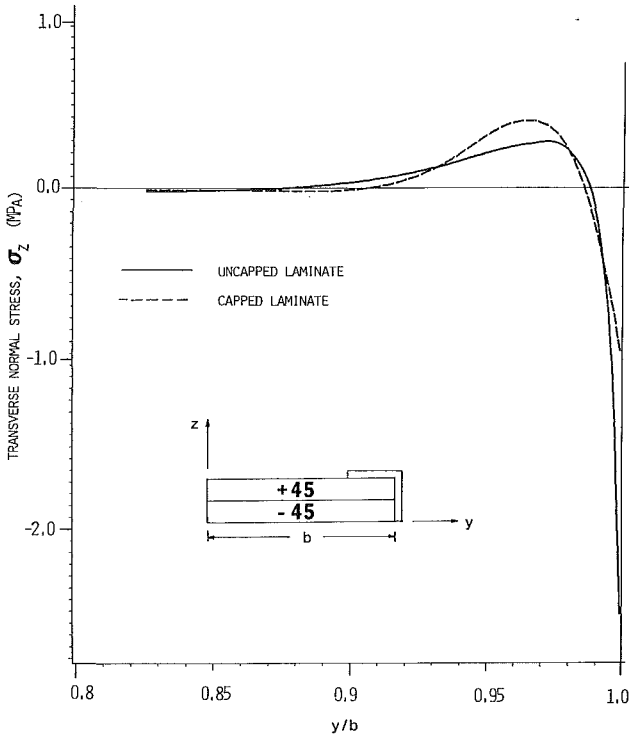


Fig. 4 The distribution of the transverse normal stress (σ_z) along the width (y/b) of the laminate $[45/-45 \text{ deg}]_S$

All stresses in the following examples were computed at the centers of the elements closest to the interface of the two plies. The stresses for the $[\pm 45]_s$ laminate are computed from the uppermost layer of elements in the -45 ply, and the stresses for the $[0, 90]_s$ laminate are computed from the uppermost layer of elements in the 90 ply. All stress distribution plots were smoothed using a spline routine, and are typically plotted only in the region near the free edge, since all interlaminar stresses dissipate at the interior regions of the laminate.

Stress Distributions. Before investigating the effects of a cap on the interlaminar stress distributions in a symmetric composite laminate, analyses were performed on several uncapped laminates to ascertain the accuracy of the formulation developed earlier in this paper by comparing the σ_z and τ_{xz} stress distributions with those reported by earlier investigators for similar laminates. The uncapped laminates are represented by solid lines in all of the examples mentioned below.

The σ_z stress distribution for the $[\pm 45 \text{ deg}]_s$ laminate is shown in Fig. 4. The stress appears to be unbounded near the free edge. The shearing stress τ_{xz} for the same laminate is shown in Fig. 5. Again the stress appears to be singular at the free edge. Finally, the σ_z stress distribution for the $[0, 90]_s$ laminate is shown in Fig. 6 and is also unbounded near the free edge. These results compare favorably with the stress

Downloaded 02 May 2010 to 171.66.16.54. Redistribution subject to ASME license or copyright; see http://www.asme.org/terms/Terms_Use.cfm

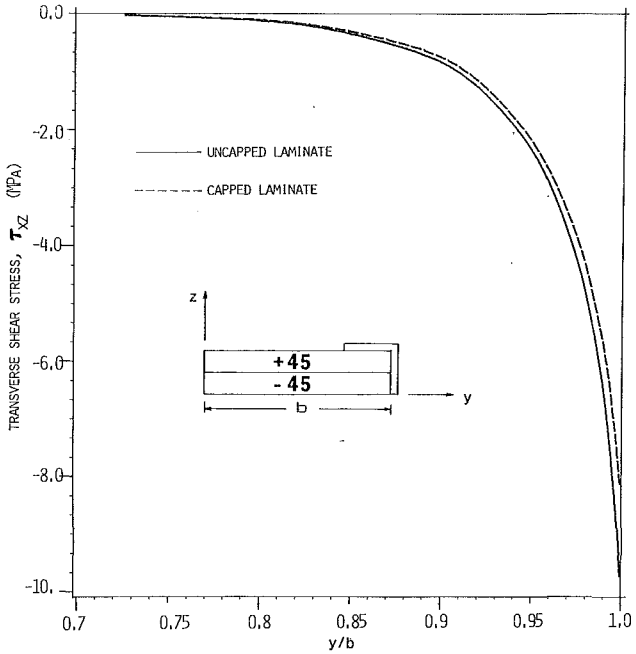


Fig. 5 The distribution of the transverse shear stress along the width of the laminate [45/ – 45 deg]$_s$

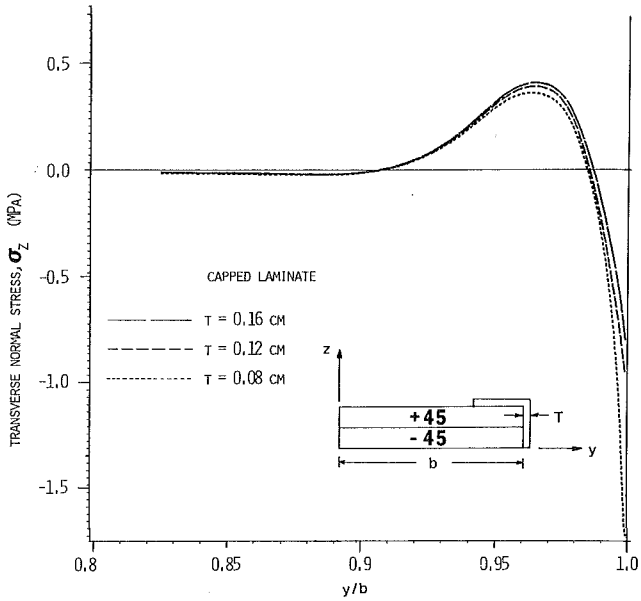


Fig. 7 The distribution of the transverse normal stress along the width of an angle-ply laminate [45/ – 45 deg]$_s$

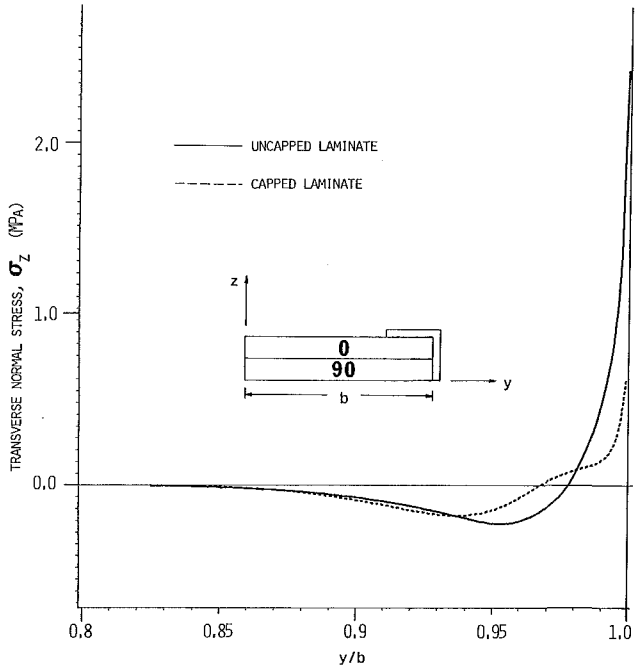


Fig. 6 The distribution of the transverse normal stress along the width of a cross-ply laminate [0/90 deg]$_s$

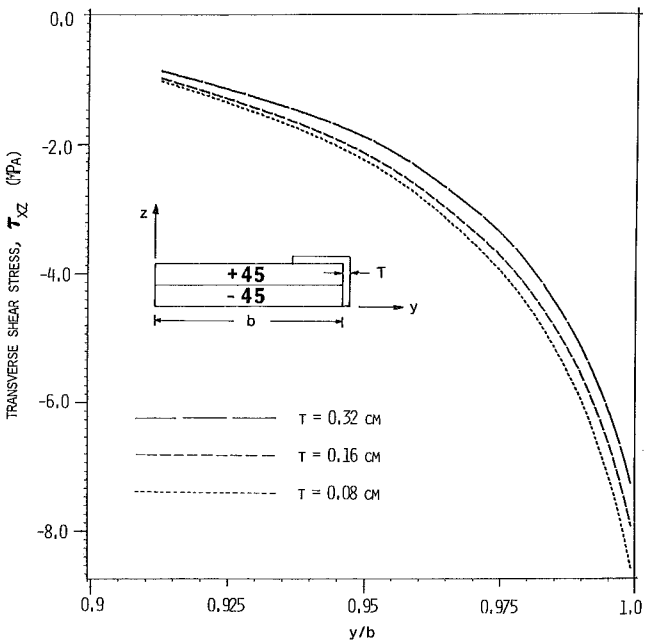


Fig. 8 The distribution of the transverse shear stress along the width for capped angle-ply laminates [45/ – 45 deg]$_s$

distributions reported graphically in earlier works (e.g., references [14] and [17]). Numerical values for the stresses in both laminates are in excellent agreement with the results developed in [9] using similar elements and an identical mesh.

A cap with thickness $T = 0.08$ cm and an overlap length $L = 1.27$ cm was added to the $[\pm 45]_s$ and $[0,90]_s$ laminates to determine the effect of a cap on the interlaminar stress distributions. The stress distributions for the capped laminates are represented by dashed lines in the Figs. 4–6. The added stiffness of the cap appears to create significant reductions for the σ_z and τ_{xz} distributions for both laminates. Considering the σ_z distributions in Figs. 4 and 6, both laminates experience reduced stresses near the free edge. The gradient of the stress near the free edge also appears to have been reduced for both laminates. The maximum value of the stress τ_{xz} in the $[\pm 45]_s$ laminate is also decreased by a noticeable amount as shown in Fig. 5, but the stress distribution for the capped laminate appears to be almost parallel to the stress distribution for the uncapped laminate. Hence it appears that the τ_{xz} stress gradient near the free edge for this laminate is not affected to a significant degree by the addition of a cap.

Additional insight into the effect of a cap may be gained by varying the geometric parameters of the cap, namely the overlap length L and the thickness T. Three different caps with varying overlap lengths were analyzed with the $[\pm 45]_s$ and $[0, 90]_s$ laminates using a constant cap thickness of 0.08 cm. Decreasing the overlap length from 1.27 cm to 0.635 cm results in an increase of the maximum measured normal stress σ_z in the $[0, 90]_s$ laminate of 18 percent. However, increasing the overlap length from 1.27 cm to 2.54 cm results in a

Downloaded 02 May 2010 to 171.66.16.54. Redistribution subject to ASME license or copyright; see http://www.asme.org/terms/Terms_Use.cfm

decrease of only five percent in the maximum normal stress. The changes in the maximum shearing stress τ_{xz} in the $[\pm 45]_s$ laminate are less than one percent for the different overlap length changes. Hence it appears that, once past a certain point, the overlap length has a small effect on the interlaminar stresses.

The cap thickness T was slightly changed to determine its effect on the interlaminar stress distributions for the $[\pm 45]_s$ laminate. The overlap length was kept constant in these comparisons with $L=1.27$ cm. Figure 7 shows the σ_z distributions for the values of $T=0.16$ cm, $T=0.12$ cm, and $T=0.08$ cm. Figure 8 shows the τ_{xz} distributions for the values $T=0.32$ cm, $T=0.16$ cm, and $T=0.08$ cm. The thicker caps appear to create larger reductions for both stresses. The maximum σ_z stress is reduced by a relatively large amount with the first increase in cap thickness, but the reduction is not as large with the next increase in thickness. The reduction in the stress σ_{xz} is, in general, more uniform. Changing the cap thickness causes no radical changes in the pattern of the stress distributions near the free edge.

Summary and Conclusions

Using the governing equations developed by Pipes and Pagano for a symmetric composite laminate under uniform axial extension, the domain of this original problem has been extended to include the addition of a reinforcing cap at the free edge of the laminate. The finite element method was used to obtain approximate interlaminar stress distributions near the free edge for the uncapped and capped laminates. The presence of a cap results in significant reductions in the maximum σ_z and τ_{xz} stresses near the free edge of the laminate. The effects of cap thickness and overlap length variation were also investigated. The change in the cap thickness had a much larger effect on the stress distributions than did the change in the overlap length. The interlaminar normal stresses σ_z were reduced considerably more than the interlaminar shear stresses τ_{xz} due to the free edge reinforcement for all cases studied.

Acknowledgments

The research reported herein was conducted during investigations supported by Office of Naval Research (Mechanics Division) (through Grant N00014-84-K-0552). The authors are grateful for the support.

References

1 Pipes, R. B., and Pagano, N. J., "Interlaminar Stresses in Composite Laminates Under Uniform Axial Extension," *J. Comp. Materials*, Vol. 4, 1970, pp. 538–548.

2 Pagano, N. J., "On the Calculation of Interlaminar Stresses in Composite Laminates," *J. Comp. Materials*, Vol. 8, 1974, pp. 65–82.

3 Pipes, R. B., and Pagano, N. J., "Interlaminar Stresses in Composite Laminates—An Approximate Elasticity Solution," ASME JOURNAL OF APPLIED MECHANICS, Vol. 41, 1974, pp. 668–672.

4 Isakson, G., and Levy, A., "Finite Element Analysis of Interlaminar Shear in Fibrous Composites," *J. Comp. Materials*, Vol. 5, 1971, pp. 273–276.

5 Wang, A. S. D., and Crossman, F. W., "Some New Results on Edge Effects in Symmetric Composite Laminates," *J. Comp. Materials*, Vol. 11, 1977, pp. 92–106.

6 Hsu, P. W., and Herakovich, C. T., "Edge Effects in Angle Ply Composite Laminates," *J. Comp. Materials*, Vol. 11, 1977, pp. 422–428.

7 Renieri, G. D., and Herakovich, C. T., "Nonlinear Analysis of Laminated Fibrous Composites," VPI-76-10, Virginia Polytechnic Institute, 1976.

8 Herakovich, C. T., Renieri, G. D., and Brinson, H. F., "Finite Element Analysis of Mech. and Thermal Edge Effects in Composite Laminates," Army Symposium on Solid Mechanics, 1976, *Composite Materials: The Influence of Mechanics on Failure and Design*, Cape Cod, MA, Sept. 1976, pp. 237–248.

9 Buczek, M. B., Gregory, M. A., and Herakovich, C. T., "CLFE2D-A Generalized Plane Strain Finite Element Program for Laminated Composites Subjected to Mechanical and Hygrothermal Loading," VPI-E-83-40, Virginia Polytechnic Institute, 1983.

10 Wang, J. T. S., and Dickson, J. N., "Interlaminar Stresses in Symmetric Composite Laminates," *J. Comp. Materials*, Vol. 12, 1978, pp. 390–402.

11 Rybicki, E. F., "Approximate Three-Dimensional Solutions for Symmetric Laminates Under Inplane Loading," *J. Comp. Materials*, Vol. 5, 1971, pp. 354–360.

12 Spilker, R. L., and Chou, S. C., "Edge Effects in Symmetric Composite Laminates: The Importance of Satisfying the Traction-Free-Edge Condition," *J. Comp. Materials*, Vol. 14, 1980, pp. 2–20.

13 Altus, E., Rotem, A., and Shmueli, M., "Free Edge Effect in Angle-Ply Laminates—A New Three-Dimensional Finite Difference Solution," *J. Comp. Materials*, Vol. 14, 1980, pp. 21–30.

14 Whitcomb, J. D., Raju, I. S., and Goree, J. G., "Reliability of the Finite-Element Method for Calculating Free-Edge Stresses in Composite Laminates," *Computers and Structures*, Vol. 15, No. 1, 1982, pp. 23–37.

15 Wang, S. S., and Choi, I., "Boundary-Layer Effects in Composite Laminates: Part 2—Free-Edge Stress Solutions and Basic Characteristics," ASME JOURNAL OF APPLIED MECHANICS, Vol. 49, 1982, pp. 549–560.

16 Wang, S. S., and Yuan, F. G., "A Singular Hybrid Finite Element Analysis of Boundary-Layer Stresses in Composite Laminates," *International Journal of Solids and Stresses*, Vol. 19, 1983, pp. 825–837.

17 Pagano, N. J., "Stress Fields in Composite Laminates," *International Journal of Solids and Structures*, Vol. 14, 1978, pp. 385–400.

18 Kim, R. Y., "A Technique for Prevention of Delamination," *Mechanics and Composites Review*, Oct. 28–30, 1981, Dayton, Ohio.

19 Reddy, J. N., *An Introduction to the Finite Element Method*, McGraw-Hill, New York, 1984.

20 Reddy, J. N., *Energy and Variational Methods in Applied Mechanics*, Wiley, New York, 1984.

APPENDIX

Coefficients of the stiffness matrix and force vector in (13)

$$K_{ij}^{11}=\int_R (C_{66}\psi_{i,y}\psi_{j,y}+C_{55}\psi_{i,z}\psi_{j,z})dR$$

$$K_{ij}^{12}=\int_R (C_{26}\psi_{i,y}\psi_{j,y}+C_{45}\psi_{i,z}\psi_{j,z})dR$$

$$K_{ij}^{13}=\int_R (C_{36}\psi_{i,y}\psi_{j,z}+C_{45}\psi_{i,z}\psi_{j,y})dR$$

$$K_{ij}^{22}=\int_R (C_{22}\psi_{i,y}\psi_{j,y}+C_{44}\psi_{i,z}\psi_{j,z})\,dR$$

$$K_{ij}^{23}=\int_R (C_{23}\psi_{i,y}\psi_{j,z}+C_{44}\psi_{i,z}\psi_{j,y})dR$$

$$K_{ij}^{33}=\int_R (C_{33}\psi_{i,z}\psi_{j,z}+C_{44}\psi_{i,y}\psi_{j,y})dR$$

$$\{F_i^1\}=-\oint_{S^e} C_{16}kn_y\psi_i dS+\oint_{S^e} (\tau_{xy}n_y+\tau_{xz}n_z)\psi_i dS$$

$$\{F_i^2\}=-\int_{S^e} C_{12}kn_y\psi_i dS+\int_{S^e} (\sigma_y n_y+\tau_{yz}n_z)\psi_i dS$$

$$\{F_i^3\}=-\oint_{S^e} C_{13}kn_z\psi_i dS+\int_{S^e} (\sigma_z n_z+\tau_{yz}n_y)\,\psi_i dS$$

Downloaded 02 May 2010 to 171.66.16.54. Redistribution subject to ASME license or copyright; see http://www.asme.org/terms/Terms_Use.cfm

Thermal Expansion Coefficients and Thermal Stresses in an Aligned Short Fiber Composite With Application to a Short Carbon Fiber/Aluminum[1]

Y. Takao
Associate Professor,
Research Institute for Applied Mechanics,
Kyushu University,
6-10-1 Hakozaki, Higashi-ku,
Fukuoka 812, Japan

M. Taya
Associate Professor,
Department of Mechanical and
Aerospace Engineering,
University of Delaware
Newark, Del. 19716
Mem. ASME

A formulation to compute the effective thermal expansion coefficients (α_c) of an anisotropic short fiber-reinforced composite and the thermal stress (σ) induced in and around the fiber is developed. The formulation is based on the Eshelby's equivalent inclusion method. Main emphasis is placed on short Carbon fiber/Aluminum. The thermal stress due to a uniform temperature rise ΔT is computed at points just outside the fiber. The effects of various parameters on α_c and σ are also investigated.

1 Introduction

Short fiber-reinforced metal (SFRM) is in high demand due to its ease of fabrication into complicated shapes and the availability of its use under high temperature. When SFRM is to be used at high temperature, one must assess its thermal properties and the extent of the thermal stresses induced in the composite. There have been a large number of models proposed to predict the effective thermal expansion coefficients of the composites, most of which are focused on particulate or continuous fiber composites, for example, [1-8]. The thermal expansion coefficients of a short fiber composite were discussed in [12] where both the matrix and fiber are isotropic. The analysis of the associated thermal stresses has been centered on simpler cases of composites as mentioned in the foregoing [8-10], and on macroscopic curing ply stresses in laminated composites [11].

Among these works, the work of Wakashima et al. [6, 10] is based on a simple model which is called the Eshelby's equivalent inclusion method [13] and it can be extended to the case of SFRM where the fiber is transversely isotropic in its stiffness and thermal expansion coefficients. The thermal stresses just outside the fiber can be easily computed by use of the Hill-Walpole-Mura jump condition [14, 21, 22]. Taya and Mura [15] used the jump condition and Eshelby's method [13] to solve the problem of a fiber-end crack. The extensive examples solved by the Eshelby's method have recently been summarized in a text by Mura [16].

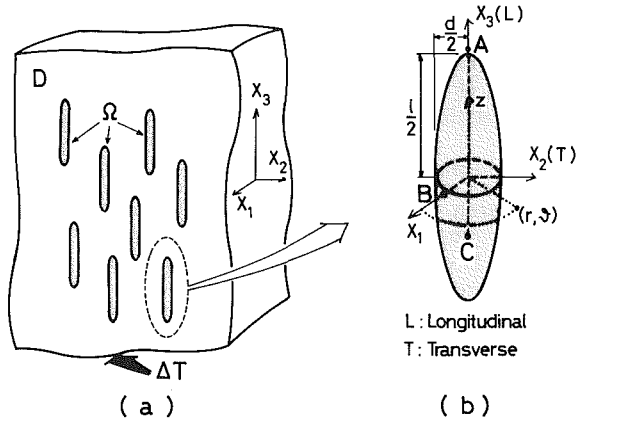


Fig. 1 *(a)* **A calculation model for an aligned short fiber composite and** *(b)* **the calculation points for the stress analysis, *A*, *B*, and *C* with coordinate systems**

Among various SFRM, short Carbon fiber/Aluminum is focused on and the prediction of its thermal expansion coefficients and the thermal stress analysis will be carried out in this paper. The formulation will be described in Section 2 and the numerical results and discussions are presented and compared with the other existing ones in Section 3. Finally the conclusion is given in Section 4.

2 Formulation

Our analytical model consists of aligned short fibers which are transverse isotropic and embedded in an infinite isotropic matrix as shown in Fig. 1. All short fibers are assumed to be prolate spheroid of the same size and aligned along the x_3-

[1]This study was supported by a grant from Honda R&D Company to the University of Delaware.

Contributed by the Applied Mechanics Division and presented at the Winter Annual Meeting, Miami, Fla., November 17-21, 1985 of THE AMERICAN SOCIETY OF MECHANICAL ENGINEERS.

Discussion on this paper should be addressed to the Editorial Department, ASME, United Engineering Center, 345 East 47th Street, New York, NY 10017, and will be accepted until two months after final publication of the paper itself on the JOURNAL OF APPLIED MECHANICS. Manuscript received by ASME Applied Mechanics Division, May 1983, final revision, December, 1984. Paper No. 85-WA/APM-11.

Copyright © 1985 by ASME
Downloaded 02 May 2010 to 171.66.16.54. Redistribution subject to ASME license or copyright; see http://www.asme.org/terms/Terms_Use.cfm

axis, but otherwise distributed randomly in a three-dimensional space. Let the domain of the composite body and fibers, be denoted by D and Ω, respectively. Hence the domain of the matrix becomes $D-\Omega$. The elastic constants of the matrix and fiber are denoted by $\mathbf{C}_m$ and $\mathbf{C}_f$, respectively, and the thermal expansion coefficients of the matrix and fiber are denoted by $\boldsymbol{\alpha}_m$ and $\boldsymbol{\alpha}_f$, respectively. Boldface symbols denote either vectors or tensors. The internal stress $\boldsymbol{\sigma}$ will be induced in the composite due to the mismatch of the thermal expansion coefficients between the fiber and matrix under the temperature change. The internal stress so induced is a function of a position, $\mathbf{x}$. The volume average of $\boldsymbol{\sigma}$ in the matrix domain, $D-\Omega$ is defined as

$$<\boldsymbol{\sigma}>_{D-\Omega}=\mathbf{C}_m\bar{\mathbf{e}} \tag{1}$$

where $<\ >$ denotes the volume average and $\bar{\mathbf{e}}$ is the volume averaged disturbance of strain in $D-\Omega$. Now we introduce a single fiber into the composite, then the stress in Ω is given by

$$\boldsymbol{\sigma}=\mathbf{C}_f(\bar{\mathbf{e}}+\mathbf{e}-\boldsymbol{\alpha}^*) \tag{2}$$

where $\boldsymbol{\alpha}^*$ is the thermal strain due to the mismatch between $\boldsymbol{\alpha}_m$ and $\boldsymbol{\alpha}_f$ under the temperature change ΔT and given by

$$\boldsymbol{\alpha}^*=(\boldsymbol{\alpha}_f-\boldsymbol{\alpha}_m)\Delta T. \tag{3}$$

Based on Eshelby's equivalent inclusion method [6, 13, 16] we can convert the fiber with $\boldsymbol{\alpha}^*$ to the inclusion with $\mathbf{C}_m$, $\mathbf{e}^*$, and $\boldsymbol{\alpha}^*$, in D

$$\boldsymbol{\sigma}=\mathbf{C}_m(\bar{\mathbf{e}}+\mathbf{e}-\boldsymbol{\alpha}^*-\mathbf{e}^*). \tag{4}$$

According to Eshelby [13], the strain induced by $\boldsymbol{\alpha}^*+\mathbf{e}^*$ is represented by

$$\mathbf{e}=\mathbf{S}(\boldsymbol{\alpha}^*+e^*). \tag{5}$$

Here $\mathbf{S}$ is constant in Ω [16]. From equations (2), (4), and (5), we have in Ω

$$\begin{aligned}\boldsymbol{\sigma} &= \mathbf{C}_m\{\bar{\mathbf{e}}+(\mathbf{S}-\mathbf{I})\boldsymbol{\alpha}^*+(\mathbf{S}-\mathbf{I})\mathbf{e}^*\}\\ &= \mathbf{C}_f\{\bar{\mathbf{e}}+(\mathbf{S}-\mathbf{I})\boldsymbol{\alpha}^*+\mathbf{S}\mathbf{e}^*\}\end{aligned} \tag{6}$$

where $\mathbf{I}$ denotes the identity matrix.

In the preceding equations, $\mathbf{e}^*$ is the fictitious strain called "eigenstrain" or "transformation strain" and has some value in Ω, but vanishes in $D-\Omega$. The fact that the volume average of $\boldsymbol{\sigma}$ in D vanishes [17] leads to

$$\bar{\mathbf{e}}+f(\mathbf{S}-\mathbf{I})(\boldsymbol{\alpha}^*+\mathbf{e}^*)=0 \tag{7}$$

where f is the volume fraction of fiber.

A substitution of equation (6) into equation (7) yields

$$\begin{aligned}&[\mathbf{I}-f(\mathbf{S}-\mathbf{I})\{(\mathbf{C}_f-\mathbf{C}_m)(\mathbf{S}-\mathbf{I})+\mathbf{C}_f\}^{-1}(\mathbf{C}_f-\mathbf{C}_m)]\bar{\mathbf{e}}\\ &\quad=-f(\mathbf{S}-\mathbf{I})\{(\mathbf{C}_f-\mathbf{C}_m)(\mathbf{S}-\mathbf{I})+\mathbf{C}_f\}^{-1}\mathbf{C}_f\boldsymbol{\alpha}^*.\end{aligned} \tag{8}$$

This equation provides a solution to $\bar{\mathbf{e}}$.

The volume average of the induced strain in D, $\boldsymbol{\gamma}_D$ is defined by [16]

$$\boldsymbol{\gamma}_D=\frac{1}{V_D}\int_D\{\bar{\mathbf{e}}+\mathbf{S}(\mathbf{e}^*+\boldsymbol{\alpha}^*)\}dV \tag{9}$$

where V_D is the volume of D.

Noting that

$$\int_{D-\Omega}\{\bar{e}+S(e^*+\alpha^*)dV=V_{D-\Omega}\bar{e} \tag{10}$$

$$\int_{\Omega}\{\bar{\mathbf{e}}+\mathbf{S}(\mathbf{e}^*+\boldsymbol{\alpha}^*)\}dV=V_{\Omega}\{\bar{\mathbf{e}}+\mathbf{S}(\mathbf{e}^*+\boldsymbol{\alpha}^*)\} \tag{11}$$

where $V_{D-\Omega}$ is the volume of the matrix, and substituting equations (10) and (11) into (9), we obtain

$$\boldsymbol{\gamma}_D=(1-f)\bar{\mathbf{e}}+f\{\bar{\mathbf{e}}+\mathbf{S}(\mathbf{e}^*+\boldsymbol{\alpha}^*)\}. \tag{12}$$

The thermal expansion coefficients of the composite, $\boldsymbol{\alpha}_c$ is the sum of $\boldsymbol{\alpha}_m$ and $\boldsymbol{\gamma}_D/\Delta T$ and obtained as

$$\boldsymbol{\alpha}_c=\boldsymbol{\alpha}_m+f(\mathbf{e}^*+\boldsymbol{\alpha}^*)/\Delta T \tag{13}$$

where equation (7) was used. This formulation is valid for a wide range of f, i.e., $0\le f\le 1$ (see Appendix A). We note in passing that the number of nonvanishing components of $\mathbf{e}^*$ and $\bar{\mathbf{e}}$ is two due to the transverse isotropy of the fiber, i.e., $e_{11}^*=e_{22}^*$ and e_{33}^*, $\bar{e}_{11}=\bar{e}_{22}$ and $\bar{e}_{33}$. A brief proof of this is given in Appendix B.

The stresses inside the fiber (Ω) can be computed from equation (6) once $\bar{\mathbf{e}}$ and $\mathbf{e}^*$ are solved by use of equations (7) and (8). The stresses just outside Ω can also be obtained as [14]:

$$\sigma_{pq}^{(out)}=\sigma_{pq}^{(in)}+C_{pqmn}\Big\{-C_{klij}(e_{ij}^*+\alpha_{ij}^*)n_1n_n\cdot \cdot\frac{(\lambda+2\mu)\delta_{km}-(\lambda+\mu)n_kn_m}{\mu(\lambda+2\mu)}+e_{mn}^*+\alpha_{mn}^*\Big\} \tag{14}$$

where $\sigma_{pq}^{(out)}$ and $\sigma_{pq}^{(in)}$ are the stresses just outside and inside Ω, respectively, λ and μ are Lame's constants of the matrix, C_{ijkl}

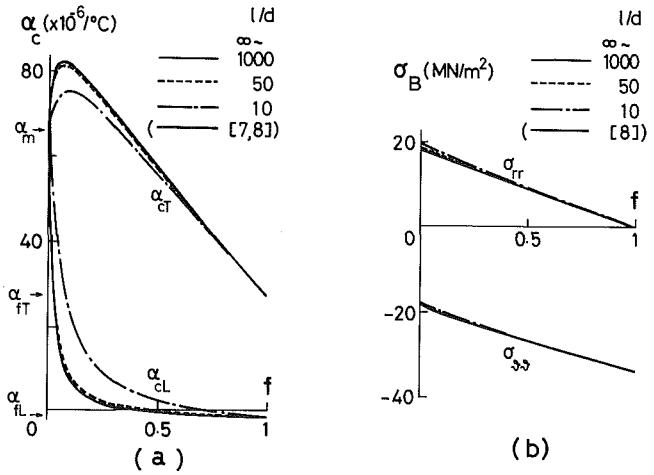


Fig. 2 (a) The thermal expansion coefficients α_c, α_{cL} (longitudinal) and α_{cT} (trasverse), and (b) thermal stresses σ_B at B of Carbon fiber/Epoxy composites (Table 1 and 2) with volume fraction of fiber f for aspect ratio l/d = 10, 50, and 1000 or larger. The results by Ishikawa et al. [7] and Uemura et al. [8] coincide with the solid curve.

Table 1 Material constants for carbon/epoxy composites used in Fig. 3[7]

	Mechanical properties			Thermal expansion coefficients ($\times 10^{-6}$/°C)	
Matrix	Poisson's ratio	0.38			66.0
	Young's modulus	3.43	GN/m^2		
Fiber	C_{11}	28.25	GN/m^2	Longitudinal	−1.5
	C_{33}[a]	234.79		Transverse	27.0
	C_{44}	10.0			
	$C_{66}(2\mu)$[b]	16.02			
	C_{13}	12.14			

[a] Along the fiber direction.
[b] $\sigma_{12}=C_{66}\cdot\epsilon_{12}$ where $\sigma(\epsilon)_{12}$ is the shear stress (strain) in the plane perpendicular to the fiber axis. $C_{66}=C_{11}-C_{12}$.

Downloaded 02 May 2010 to 171.66.16.54. Redistribution subject to ASME license or copyright; see http://www.asme.org/terms/Terms_Use.cfm

is the elastic constants of the matrix and n_i is the x_ith component of the unit vector normal to the surface of Ω. Basically we are concerned with three points at which the stresses are computed, and which are shown in Fig. 1(*b*). A point A is located just outside the end of fiber, at $x_1 = x_2 = 0$ and $x_3 = l/2$, where l is the fiber length, a point B is located just outside the side face of the fiber, at $x_2 = x_3 = 0$ and $x_1 = d/2$, where d is the fiber diameter, and a point C is located inside Ω (note that the stresses inside Ω are uniform). The components of a vector $\mathbf{n}$ at A and B are given by (0, 0, 1) and (1, 0, 0), respectively. Denoting the stress tensor at points A, B, and C by σ_A, σ_B and σ_C, respectively, we can obtain the expression for σ_A and σ_B from equation (14) as

$$\sigma_A = \sigma_C + \begin{Bmatrix} 1 \\ 1 \\ 0 \end{Bmatrix} \frac{2\mu(3\lambda+2\mu)}{(\lambda+2\mu)}(e^*_{11}+\alpha^*_{11}) \tag{15}$$

$$\sigma_B = \sigma_C + \begin{Bmatrix} 0 \\ 2(\lambda+\mu)(e^*_{11}+\alpha^*_{11})+\lambda(e^*_{33}+\alpha^*_{33}) \\ 2(\lambda+\mu)(e^*_{33}+\alpha^*_{33})+\lambda(e^*_{11}+\alpha^*_{11}) \end{Bmatrix} \frac{2\mu}{(\lambda+2\mu)} \tag{16}$$

where only the normal components of stresses, σ_{11}, σ_{22}, and σ_{33} are listed, and σ_c can be directly computed from equation (6).

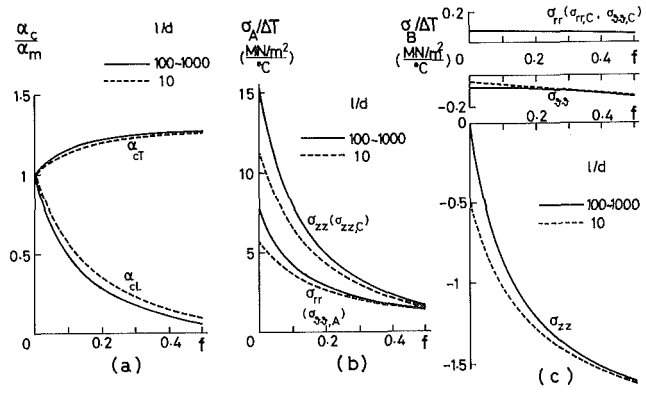


Fig. 3 (*a*) α_c, (*b*) σ_A, and (c) σ_B of short Carbon fiber/Aluminum composites with Table 3 (*SC/A*) versus *f* for *l/d* = 10 and 100 ~ 1000

3 Numerical Results and Discussions

The main target composite in this study is short Carbon fiber Aluminum. However, the theoretical and experimental data on α_c and thermal stresses are not available in the literature. Hence we will compare our results with the previous ones on Carbon/Epoxy [7, 8]. The present results of α_c, the longitudinal (α_{cL}) and the transverse component (α_{cT}) are shown as a function of the fiber volume fraction f for various fiber aspect ratios (l/d) in Fig. 2(*a*). The thermomechanical properties of the constituents of this composite are given in Table 1. The dash-dot, dash, and solid curves correspond to the cases of $l/d = 10$, 50, and $1000 \sim \infty$, respectively. The results by Ishikawa et al. [7] Uemura et al. [8] who studied the case of continuous fiber system are also shown in this figure and coincide with the solid curve ($l/d \geq 1000$). Next the radial (σ_{rr}) and circumferential component ($\sigma_{\theta\theta}$) of σ_B (see Fig. 1(*b*)) are plotted in Fig. 2(*b*) as a function of f for $l/d = 10$, 50, and $1000 \sim \infty$ where the previous results by Uemura et al. [8] are also shown and coincide with the solid curve ($l/d \geq 1000$) of the present result. The data used in this calculation are tabulated in Table 2. Thus, a good agreement between the present results and the previous ones for the continuous anisotropic fiber system is obtained.

Next the numerical results of α_{cL} and α_{cT} of aligned short Carbon fiber/Aluminum are computed based on the present

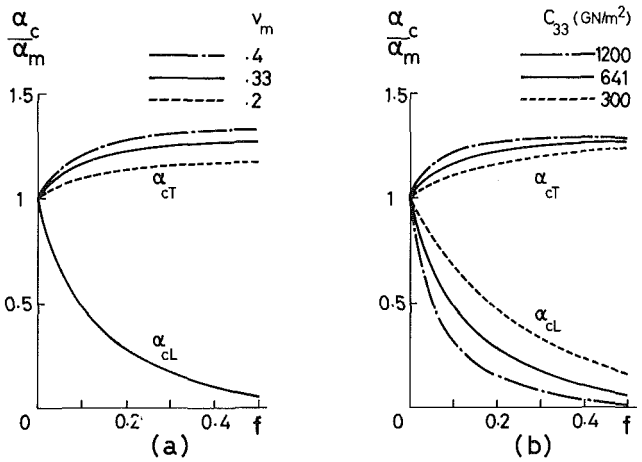


Fig. 4 α_c for (a) the matrix Poisson's ratio $\nu_m = 0.2$, 0.33, and 0.4 and (*b*) the longitudinal stiffness component of the fiber $C_{33} = 300$, 641, and 1200 GN/m^2 of *SC/A* with *l/d* = 100 versus f: Three curves for α_{cL} in (*a*) coincide.

Table 2 Material constants for carbon/epoxy composites used in Fig. 4 [8]

	Mechanical properties			Thermal expansion coefficients ($\times 10^{-6}$/°C)	
Matrix	Poisson's ratio	0.36			70.0
	Young's modulus	3.4	GN/m^2		
Fiber	C_{11}	15.91	GN/m^2	Longitudinal	−0.7
	C_{33}	228.94		Transverse	8.0
	C_{44}	10.0			
	C_{66}	15.48			
	C_{13}	4.90			

Table 3 Material constants for short carbon/aluminum composites (SC/A) [18, 19]

	Mechanical properties			Thermal expansion coefficients ($\times 10^{-6}$/°C)	
Matrix	Poisson's ratio	0.33			23.0
	Young's modulus	73.0	GN/m^2		
Fiber	C_{11}	9.7	GN/m^2	Longitudinal	−1.2
	C_{33}	641.0		Transverse	25.9
	C_{44}	20.6			
	C_{66}	2.1			
	C_{13}	5.9			

Downloaded 02 May 2010 to 171.66.16.54. Redistribution subject to ASME license or copyright; see http://www.asme.org/terms/Terms_Use.cfm

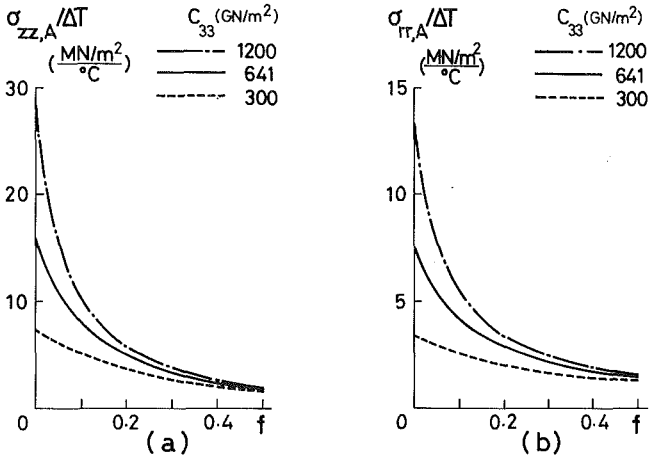


Fig. 5 (*a*) σ_{zz} and (*b*) σ_{rr} at *A* of *SC/A* with $l/d = 100$ versus f for $C_{33} = 300$, 641, and 1200 GN/m^2

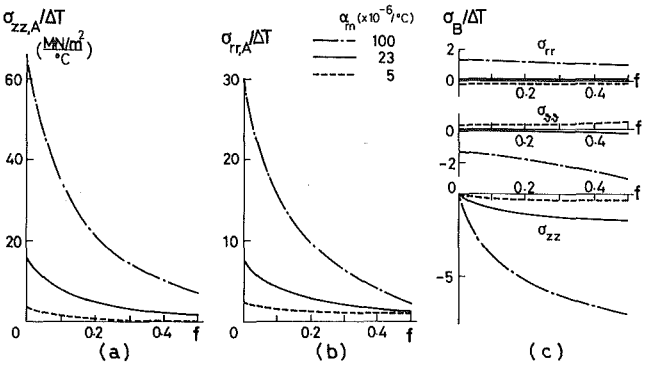


Fig. 6 (*a*) σ_{zz}, (*b*) σ_{rr} at *A*, and (*c*) σ_B of *SC/A* with $l/d = 100$ versus f for the matrix thermal expansion coefficient $\alpha_m = 5$, 23, and 100 × 10^{-6}/°C

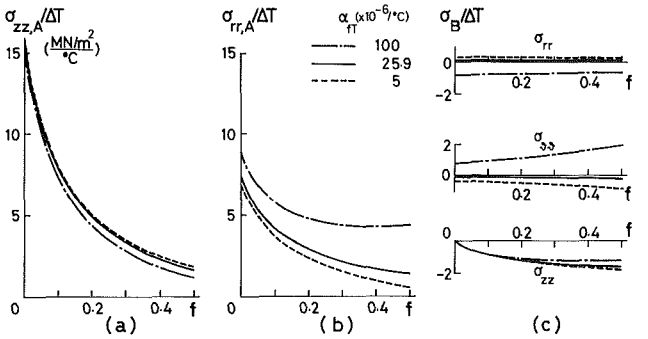


Fig. 7 (*a*) σ_{zz} (*b*) σ_{rr} at *A*, (*c*) σ_B of *SC/A* with $l/d = 100$ versus f for the transverse thermal expansion coefficient of the fiber $\alpha_{fT} = 5$, 25.9, and 100 × 10^{-6}/°C

model and plotted as a function of f for the fiber aspect ratio $l/d = 10$ (dash curve) and $100 \sim 1000$ (solid curve) in Fig. 3(*a*). The data on $\mathbf{C}_m$, $\mathbf{C}_f$, α_m, and α_f of Carbon/Aluminum used in this computation are listed in Table 3 [18, 19]. It should be noted in Fig. 3(*a*) that all the results for $l/d \geq 100$ coincide (given by the solid curve) and the effect of l/d on α_c is negligible in the case of Carbon/Aluminum. Comparing the results of α_{cT} in Fig. 2(*a*) and those in Fig. 3(*a*), α_{cT} for Carbon/Aluminum increases monotonically as f increases, whereas that for Carbon/Epoxy has a peak at $f \cong 0.1$. Next the stresses at points *A*, *B*, and *C* are computed based on the data given by Table 3 and with $l/d = 100$ and are plotted as a function of f for $l/d = 10$ and $100 \sim 1000$ in Figs. 3(*b*) and 3(*c*). Note that $\sigma_{zz,A} = \sigma_{zz,C}$, $\sigma_{rr,A} = \sigma_{\theta\theta,A}$ and $\sigma_{rr,B} = \sigma_{rr,C} = \sigma_{\theta\theta,C}$ (see Fig. 1(*b*)), and ΔT is the temperature change in °C. It follows from Figs. 3(*b*) and (*c*) that the stresses at a point *A* are tensile and their magnitudes are much larger than those at a point *B*. It follows from Fig. 3(*b*) that the stresses just outside the fiber-end (at a point *A*) are quite high and this is more enhanced at a lower volume fraction of fiber f. For example, for $\Delta T = 100$°C, $l/d = 100$ and $f = 0.1$ $\sigma_{zz,A}$ and $\sigma_{rr,A}$ are approximately 750 MN/m^2 and 400 MN/m^2, respectively. The equivalent stress $\bar{\sigma}$ based on the Von-Mises yield criterion is given by

$$2\bar{\sigma}^2 = (\sigma_{zz} - \sigma_{rr})^2 + (\sigma_{rr} - \sigma_{\theta\theta})^2 + (\sigma_{\theta\theta} - \sigma_{zz})^2. \tag{17}$$

At a point *A*, $\sigma_{rr} = \sigma_{\theta\theta}$ and if we use the foregoing numerical values (at $\Delta T = 100$°C, $l/d = 1000$, and $f = 0.1$), we obtain $\bar{\sigma} = 350$ MN/m^2. When Al 6061 is taken as a matrix, the maximum value of the yield stress of Al 6061 (T6) is around 260 MN/m^2 [20]. Thus, even for 100°C temperature rise, the matrix at the fiber end will become yielded. On the other hand, the stresses at a point *B* are not that high except $\sigma_{zz,B}$ at higher volume fraction of fiber as shown in Fig. 3(*c*). When the composite is cooled down, then $\sigma_{zz,B}$ becomes tensile, leading to the possibility of circumferential crackings around the matrix-fiber interface, which may further lead to the debonding of the interface if it is weakly bonded.

We have computed α_c, σ_A and σ_B by changing the material parameters of the matrix and fiber to assess the degree of the effect of each parameter on α's and σ's. The parameters that have strong effect are shown in Figs. 4(*a*) and 4(*b*) for α_{cL} and α_{cT} and Figs. 5, 6, and 7 for σ_A and σ_B as a function of f. In the foregoing calculations, the data given by Table 3 and $l/d = 100$ are used. In these figures the solid curves represent the case of the actual material (Table 3). Figures 4(*a*) and (*b*) show the results of α_{cL} and α_{cT} as a function of f with the parameters being the matrix Poisson's ratio (ν_m) and the fiber axial stiffness (C_{33}), respectively. The effects of C_{33} on $\sigma_{zz,A}$ and $\sigma_{rr,A}$ are given in Figs. 5(*a*) and 5(*b*), respectively. The effects of α_m on $\sigma_{zz,A}$, $\sigma_{rr,A}$ and σ_B are shown in Figs. 6(*a*)–(*c*), respectively. The effects of the transverse thermal expansion coefficient of the fiber (α_{fT}) on $\sigma_{zz,A}$, $\sigma_{rr,A}$ and σ_B are shown in Figs. 7(*a*)–(*c*), respectively. It should be noted that the fiber aspect ratio l/d has some effect on $\sigma_{zz,A}$, $\sigma_{rr,A}$ and $\sigma_{zz,B}$, but has little effect on $\sigma_{rr,B}$ and $\sigma_{\theta\theta,B}$ as evidenced from Figs. 3(*a*) and (*b*).

4 Conclusion

(*i*) The prediction of the thermal expansion coefficients of a short fiber composite and the analysis of the stress in and around the fiber are made for the case of anisotropic fiber with the target composite being a short Carbon fiber/Aluminum.

(*ii*) A number of parametric studies are made as to which parameter has a strong effect on α_c and σ.

References

1 Kerner, E. H., "The Elastic and Thermo-Elastic Properties of Composite Media," *Proceedings of the Physical Society*, Section *B*, Vol. 69, 1956, pp. 808–813.

2 Schapery, R. A., "Thermal Expansion Coefficients of Composite Materials Based on Energy Principles," *Journal of Composite Materials*, Vol. 2, 1968, pp. 380–404.

3 Budiansky, B., "Thermal and Thermoelastic Properties of Isotropic Composites," *Journal of Composite Materials*, Vol. 4, 1970, pp. 286–295.

4 Rosen, B. W., and Hashin, Z., "Effective Thermal Expansion Coefficients and Specific Heats of Composite Materials," *International Journal of Engineering Sciences*, Vol. 8, 1970, pp. 157–173.

5 Law, N., "On the Thermostatics of Composite Materials," *Journal of Mechanics and Physics of Solids*, Vol. 21, 1973, pp. 9–17.

6 Wakashima, K., Otsuka, M., and Umekawa, S., "Thermal Expansions of Heterogeneous Solids Containing Aligned Ellipsoidal Inclusions," *Journal of Composite Materials*, Vol. 8, 1974, pp. 391–404.

7 Ishikawa, T., Koyama, K., and Kobayashi, S., "Thermal Expansion Coefficients of Unidirectional Composites," *Journal of Composite Materials*, Vol. 12, 1978, pp. 153–168.

Downloaded 02 May 2010 to 171.66.16.54. Redistribution subject to ASME license or copyright; see http://www.asme.org/terms/Terms_Use.cfm

8 Uemura, M., Iyama, H., and Yamaguchi, Y., "Thermal Residual Stresses in Filament-Wound Carbon-Fiber-Reinforced Composites," *Journal of Thermal Stresses*, Vol. 2, 1979, pp. 393–412.

9 Weitsman, Y., "Residual Thermal Stresses Due to Cool-Down of Epoxy-Resin Composites," ASME JOURNAL OF APPLIED MECHANICS, Vol. 46, 1979, pp. 563–567.

10 Wakashima, K., Suzuki, Y., and Umekawa, S., "A Micro-Mechanical Prediction of Initial Yield Surface of Unidirectional Composites," *Journal of Composite Materials*, Vol. 13, 1979, pp. 288–302.

11 Hahn, H. T., "Residual Stresses in Polymer Matrix Composite Laminates," *Journal of Composite Materials*, Vol. 10, 1976, pp. 266–278.

12 Nomura, S., and Chou, T. W., "Effective Thermoelastic Contents of Short-Fiber Composites," *International Journal of Engineering Sciences*, Vol. 19, 1981, pp. 1–9.

13 Eshelby, J. D., "The Determination of the Elastic Field of an Ellipsoidal Inclusion, and Related Problems," *Proceedings of the Royal Society of London*, Series *A*, Vol. 241, 1957, pp. 376–396.

14 Walpole, L. J., "The Elastic Field of an Inclusion in an Anisotropic Medium," *Proceedings of the Royal Society of London*, Series *A*, Vol. 300, 1967, pp. 270–289.

15 Taya, M., and Mura, T., "On Stiffness and Strength of an Aligned Short Fiber Reinforced Composite Containing Fiber-End Cracks Under Uniaxial Applied Stress," ASME JOURNAL OF APPLIED MECHANICS, Vol. 48, 1981, pp. 361–367.

16 Mura, T., *Micromechanics of Defects in Solids*, Martinus Nijhoff Publishes, 1982.

17 Mori, T., and Tanaka, K., "Average Stress in Matrix and Average Elastic Energy of Materials With Misfitting Inclusions," *Acta Metallurgica*, Vol. 21, 1973, pp. 571–574.

18 Smith, R. E., "Ultrasonic Elastic Constants of Carbon Fibers and Their Composites," *Journal of Applied Physics*, Vol. 43, 1972, pp. 2555–2561.

19 Harris, S. J., and Marsden, A. L., "Failure Mechanisms in Metal Matrix Composites Reinforced With Small Diameter Brittle Fibers," *The Institute of Metallurgists, Practical Metallic Composites*, Spring Meeting, Series 3, 1974, pp. *B*35–*B*42.

20 *Metals Handbook 9th Edition*, Vol. 2, American Society of Metals.

21 Hill, R., "Discontinuity Relations in Mechanics on Solids," in *Progress in Solid Mechanics 2*, eds. Sneddon, I. N., and Hill, R., North-Holland, Amsterdam, 1961, pp. 245–276.

22 Mura, T., and Cheng, P. C., "The Elastic Field Outside an Ellipsoidal Inclusion," ASME JOURNAL OF APPLIED MECHANICS, Vol. 44, Dec. 1977, pp. 591–594.

APPENDIX *A*

The Modified Eshelby's Method at High Volume Fraction

The basic equations of the present inhomogeneity problem are equations (6), (or (2)), and (7). Equation (6) is correct when the volume fraction $f=0$, which corresponds to the solution by Eshelby [13]. In case of usual composite materials $f \simeq 0.2 \sim 0.6$. The induced strains by fibers that have already been imbedded in the matrix have the significant effects on another fiber that will be imbedded into the matrix. These induced strains are not uniform in the matrix, but are functions of the position. To apply the equivalent inclusion method to this fiber, one needs the eigenstrains as functions of the position. To avoid these difficulties one can consider the volume averaged induced strain $\bar{\mathbf{e}}$, which appears in equation (6). The applicability of equation (6) at wide range of f is shown as follows.

A substitution of $f=0$ into equation (7) yields $\bar{\mathbf{e}}=0$ and equation (6) is reduced to the formulation originally proposed by Eshelby [13]. On the other hand, if we set $f=1$ in equation (7), we obtain

$$\bar{\mathbf{e}} + (\mathbf{S}-\mathbf{I})(\boldsymbol{\alpha}^* + \mathbf{e}^*) = 0 \qquad (A\text{-}1)$$

and by substituting equation (A-1) into equation (6), we have

$$\mathbf{e}^* = 0. \qquad (A\text{-}2)$$

By setting $f=1$ in equation (13) and using equations (A-2) and (3), we obtain

$$\boldsymbol{\alpha}_c = \boldsymbol{\alpha}_m + (\boldsymbol{\alpha}_f - \boldsymbol{\alpha}_m) = \boldsymbol{\alpha}_f. \qquad (A\text{-}2)$$

Thus, the concept of the volume averaged induced strain in the matrix is valid for the entire range of f, $0 \le f \le 1$ (see Fig. 2).

APPENDIX *B*

The tensors, $\mathbf{S}$, $\mathbf{C}_m$, and $\mathbf{C}_f$ has the following structure in matrix form:

$$\mathbf{G} = \begin{pmatrix} G_{11} & G_{12} & G_{13} & & & \\ G_{12} & G_{11} & G_{13} & & \mathbf{0} & \\ G_{31} & G_{31} & G_{33} & & & \\ & & & G_{44} & & \\ & \mathbf{0} & & & G_{55} & \\ & & & & & G_{66} \end{pmatrix} \qquad (B\text{-}1)$$

where $\mathbf{G}$ represents $\mathbf{S}$, $\mathbf{C}_m$, and $\mathbf{C}_f$ and the isotropic plane for the transversely isotropic fiber is taken in the $x_1 - x_2$ plane. The thermal strain $\boldsymbol{\alpha}^*$ has the following form:

$$\boldsymbol{\alpha}^*(\alpha_{11}{}^*, \alpha_{11}{}^*, \alpha_{33}{}^*, 0, 0, 0) \qquad (B\text{-}2)$$

A substitution of equations (B-1) and (B-2) into equation (8) will render that the shear components of $\bar{\mathbf{e}}$ are zero and $\bar{e}_{11} = \bar{e}_{22}$.

Downloaded 02 May 2010 to 171.66.16.54. Redistribution subject to ASME license or copyright; see http://www.asme.org/terms/Terms_Use.cfm

Short Subsurface Cracks Under Conditions of Slip and Stick Caused by a Moving Compressive Load

S. Sheppard
Student Mem. ASME

J. R. Barber

M. Comninou
Mem. ASME

Department of Mechanical Engineering
and Applied Mechanics,
University of Michigan,
Ann Arbor, Mich. 48109

The mechanism of spalling failure in rolling contact is modeled by an elastic half-plane with a subsurface crack parallel to the surface, loaded by a compressive normal force which moves over the surface. Coulomb friction at the crack faces reduces the Mode II Stress Intensity Factors and results in a number of history-dependent slip-stick configurations. The formulation used to study these involves a singular integral equation in two variables which must be solved numerically, and because of the history dependence, requires in an incremental solution. Only crack lengths and coefficients of friction that result in a maximum of two slip or stick zones for any load location are considered in this paper. It is found that the maximum range of stress intensity factors occurs at the trailing crack tip.

Introduction

Steel wheel rims, rails, gear teeth, ball and roller bearings, cams, as well as other members involving a frictional interface and periodic contact loading are all subject to surface degradation. This may manifest itself in the form of pitting (crack originating at the surface), fretting, or spalling (crack originating below to surface). Spalling results from a crack growing parallel to the surface for some distance after which a transverse crack forms, ultimately leading to the detachment of a thin layer of material. These subsurface cracks may be initiated by preexisting defects such as inclusions, gas pores, or local soft spots, or may be generated during the cyclic straining process itself.

A subsurface crack under a static compressive load and a uniform normal pressure in various slip-stick configurations was studied by Chang, Comninou, Sheppard, and Barber [1]. An investigation of the stick-slip zones of a layer pressed on an elastic foundation subjected to a periodic tangential load was carried out by Comninou and Barber [2], but although history dependent, required no incremental formulation. Related static solutions are also given by Comninou et al. [3, 4].

Another contact problem, that of two semi-infinite elastic solids first pressed together, sheared and then at time $t=0$, subjected to a moving force pair at the interface, was studied by Dundurs and Gautesen [5]. A steady-state slip-stick configuration does not occur immediately upon application of the load and therefore a time-dependent solution had to be considered. However, the equations involved were invertible permitting a nonlinear integral equation in one variable to be developed for the unknown stick-slip boundary as a function of load position.

A preliminary study of a subsurface crack subjected to a moving load was carried out by Hearle and Johnson [6]. This problem is also history dependent, but the relevant equations cannot be inverted, hence a solution that involved small load steps, or increments was used. This particular study did not enforce the traction-free boundary condition on the surface of the half-plane and made other approximations which render the accuracy of the reported values of the Mode *II* Stress Intensity Factor (K_{II}) uncertain.

The present paper gives a more exact treatment of the subsurface crack lying parallel to the surface, subjected to a moving compressive normal surface force, as shown in Fig. 1. In particular, we explore the variation of maximum value of K_{II} and its range (ΔK_{II}) with the coefficient of friction (f) and the crack length/depth ratio (L/a). Because of the history dependence, the load sequence is not symmetric and one would not necessarily expect equal variation of K_{II} at the two crack tips.

The Problem Described

Consider the crack geometry depicted in Fig. 1 which represents a subsurface crack subjected to a moving compressive normal force. Distance t measures load position which varies monotonically, and is therefore a timelike variable. With the load P initially located far to the left of the origin, the crack will experience forward slip (top crack face

Contributed by the Applied Mechanics Division and presented at the Winter Annual Meeting, Miami, Fla., November 17–21, 1985 of THE AMERICAN SOCIETY OF MECHANICAL ENGINEERS.

Discussion on this paper should be addressed to the Editorial Department, ASME, United Engineering Center, 345 East 47th Street, New York, N.Y. 10017, and will be accepted until two months after final publication of the paper itself in the JOURNAL OF APPLIED MECHANICS. Manuscript received by ASME Applied Mechanics Division, July, 1984; final revision, April, 1985. Paper No. 85-WA/APM-15.

Copyright © 1985 by ASME
Downloaded 02 May 2010 to 171.66.16.54. Redistribution subject to ASME license or copyright; see http://www.asme.org/terms/Terms_Use.cfm

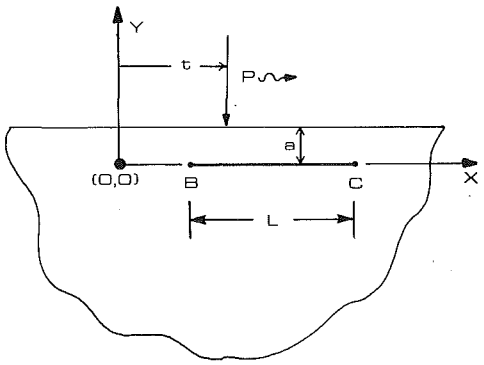


Fig. 1 Geometry of the problem

moving to the right relative to the unloaded crack) throughout its entire length, as shown in Fig. 2(*a*). As the load moves to the right (slowly enough for inertia effects to be ignored) the stress intensity factor K_{II} at both B (leading crack tip) and C (trailing crack tip) and the amount of forward shift continue to increase until the load is at position t_1. If the assumption of full forward slip were retained, further rightward load movement beyond t_1 would cause K_{II} at B to decrease, indicating backslip in a zone adjacent to B. This is inconsistent with the assumption and implies that a locked zone develops at crack tip B, as shown in Fig. 2(*b*).

As the load moves to the right of t_1 this locked zone will continue to grow until the entire crack length is locked (Fig. 2(*c*)), at which point the load is at location t_2. This locked configuration will be retained until load position t_3, where the shear traction at B exceeds the limiting value for backslip.

A backslip zone will grow to the right with additional load movement (Fig. 2(*d*)) until the entire crack is experiencing backslip (load position t_4 and Fig. 2(*e*)). During the initial growth of this backslip zone, there is a positive but decreasing forward shift. With further growth, shift will become increasingly negative until stick once again starts at B (load position t_5).

As the load is moved beyond position t_5, a scenario similar to that described in the foregoing ensues except that the direction of slip is reversed (compare Fig. 2(*a–d*) with Fig. 2(*e–h*)).

At load positions to the right of t_8 the entire crack is experiencing forward slip, as shown in Fig. 2(*i*). This condition results after the crack has been in a fully locked back-shifted configuration (Fig. 2(*g*)). As the load recedes to infinity, this backshift is relieved everywhere by forward slip, leaving the body free of residual stress.

If the crack is of sufficient length, forward slip can begin at B before the stick zone has reached C, giving rise to three or more zones. In this paper we restrict our investigation to cracks for which this does not occur. The two-zone cracks to be considered will be referred to as "short cracks." "Long cracks," which experience three or more zones at some load position(s), will be the subject of a subsequent paper.

Formulation

The problem is formulated by using the solution for a compressive load on an unflawed half-plane, corrected by an additional solution that ensures that appropriate boundary conditions are met along the crack [3, 4]. The unflawed half-plane shear and normal tractions are given by the Flamant solution.

The corrective term is represented by a distribution of edge dislocations of the glide type with density $B_x(x)$. This distribution depends on the position of the load, t, but the dependence is only indicated explicitly when needed for clarity.

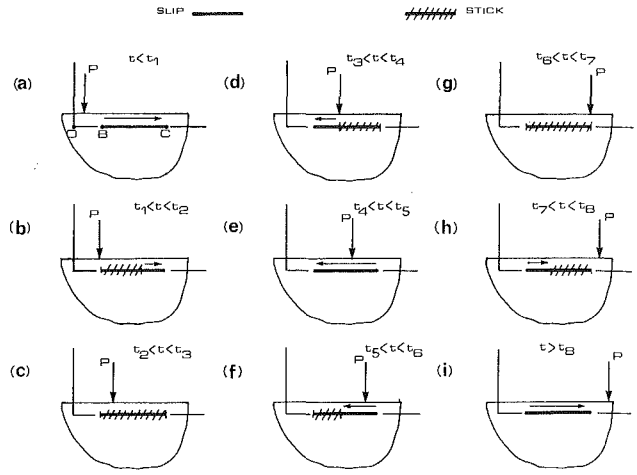


Fig. 2 Sequence of crack configurations as the load position changes

Combining the Flamant terms and the dislocation terms for both shear and normal tractions, we obtain:

$$S(x) = \frac{2Pa^2x_t}{\pi(a^2+x_t^2)^2} + \frac{2\mu}{\pi(\kappa+1)}\int_B^C B_x(\zeta)K_s(x,\zeta)d\zeta \tag{1}$$

$$N(x) = \frac{-2Pa^3}{\pi(a^2+x_t^2)^2} + \frac{2\mu}{\pi(\kappa+1)}\int_B^C B_x(\zeta)K_n(x,\zeta)d\zeta \tag{2}$$

where

$$K_s(x,\zeta) = \frac{1}{x-\zeta} + \frac{x-\zeta}{R}\left(-1+\frac{12a^2}{R}-\frac{64a^4}{R^2}\right) \tag{3}$$

$$K_n(x,\zeta) = \frac{8a^3}{R^2}\left(-3+\frac{16a^2}{R}\right) \tag{4}$$

$$R = 4a^2+(x-\zeta)^2$$

and $x_t = x-t$, μ is the shear modulus, and $\kappa = (3-4\nu)$ plane strain, with ν being Poisson's ratio.

The Mode *II* Stress Intensity Factors at B and C are

$$K_{II}(B) = -\lim_{x\to B}\left(\frac{2\mu}{\kappa+1}B_x(x)\sqrt{2\pi(x-B)}\right) \tag{5}$$

$$K_{II}(C) = \lim_{x\to C}\left(\frac{2\mu}{\kappa+1}B_x(x)\sqrt{2\pi(C-x)}\right) \tag{6}$$

The horizontal shift of the upper crack face relative to the lower face

$$h(x) = u(x,+0)-u(x,-0) \tag{7}$$

is related to $B_x(x)$ by

$$h(x) = -\int_B^x B_x(\zeta)d\zeta \tag{8}$$

We require continuity of displacements throughout the body except at the crack and hence

$$\int_B^C B_x(\zeta)d\zeta = 0 \tag{9}$$

The boundary conditions to be enforced along the crack depend on which of the configurations in Fig. 2 is being described and will be discussed in detail in the following sections, which have been labeled (2*a*)–(2*i*) to correspond with the figure. We assume that Coulomb friction occurs between the crack faces, governed by the equations and inequalities

$$S(x) = -fN(x);\quad \dot{h}>0;\quad \text{forward slip} \tag{10}$$

$$S(x) = fN(x);\quad \dot{h}<0;\quad \text{back slip} \tag{11}$$

$$\dot{h}=0;\quad |S(x)| \le -fN(x);\quad \text{stick}, \tag{12}$$

Downloaded 02 May 2010 to 171.66.16.54. Redistribution subject to ASME license or copyright; see http://www.asme.org/terms/Terms_Use.cfm

where $\dot{h}(x) = dh(x)/dt$ and $N(x) < 0$.

If the expressions for N and S from (1) and (2) are substituted into (10) and rearranged, we obtain

$$\frac{2\mu}{\pi(\kappa+1)}\int_B^C B_x(\zeta)[K_s(x,\zeta)+fK_n(x,\zeta)]d\zeta = \frac{2Pa^2(fa-x_t)}{\pi(a^2+x_t^2)^2} \tag{13}$$

(2*a*) Full Forward Slip ($t<t_1$). The full forward slip configuration is shown in Fig. 2(*a*) and is described by (10) enforced over the range $B<x<C$. Asymptotic analysis by Dundurs and Comninou [7] shows that $B_x(x)$ is square root singular at both tips under full forward slip. Putting equations (9) and (13) into dimensionless form by the change of variables:

$$\delta = (C-B)/(2a); \qquad \sigma = (B+C)/(2a) \tag{14}$$

where

$$\zeta/a = \delta r + \sigma; \qquad x/a = \delta s + \sigma \tag{15}$$

and letting

$$B_x(r) = \frac{P(\kappa+1)}{2\mu a}(1-r^2)^{-1/2}\phi(r) \tag{16}$$

and by discretizing the resulting singular integral equations according to the numerical method of Erdogan, Gupta, and Cook [8], the following series of equations is obtained:

$$\sum_{i=1}^{n}\frac{\phi(r_i)}{n}\left[\frac{1}{(s_k-r_i)}+K(s_k,r_i)\right] = \frac{2[f-(\delta s_k+\sigma)]}{\pi[1+(\delta s_k+\sigma)^2]^2} \tag{17}$$

$$k=1, \ldots, n-1$$

$$\sum_{i=1}^{n}\frac{\phi(r_i)}{n} = 0 \tag{18}$$

where

$$r_i = \cos\left(\frac{2i-1}{2n}\pi\right); \quad i=1, \ldots, n$$

$$s_k = \cos\left(\frac{k}{n}\pi\right); \quad k=1, \ldots, n-1 \tag{19}$$

The n equations represented by (17) and (18) are sufficient for finding the n unknowns $\phi(r_i)$.

The stress intensity factors are obtained by substituting (16) into (5) and (6) as

$$\left(\frac{\pi a^{1/2}}{2P}\right)K_{II}(B) = -\sqrt{2}(\pi/2)^{3/2}\delta^{1/2}\phi(-1) \tag{20}$$

$$\left(\frac{\pi a^{1/2}}{2P}\right)K_{II}(C) = \sqrt{2}(\pi/2)^{3/2}\delta^{1/2}\phi(+1) \tag{21}$$

Values of $\phi(\pm 1)$ are found using the interpolation technique proposed by Krenk [9]. The stress intensity factor at B, given by (20) increases with t until a maximum is reached at $t=t_1$, after which a stick zone starts to develop at B.

(2*b*) Growing Stick Zone ($t_1<t<t_2$). After $K_{II}(B)$ has peaked, a stick zone grows from B toward C upon further load movement. As the transition from stick to slip moves, for example from m_1 to m_2, the dislocation distribution in $m_1<x<m_2$ will be locked in. These locked in dislocations, along with those in the range $B<x<m_1$, will continue to affect shear and normal tractions developed in $m_2<x<C$ even though they have become inactive. It is this continued influence of locked in dislocations that makes the problem history dependent. The approach taken in the following is similar to that developed by Dundurs and Gautesen [5].

For a growing stick zone and a forward slip zone with transition at point m, condition (10) is observed in the range $m<x<C$, while condition (12) prevails in $B<x<m$. Equation (13) is to be integrated over *all* dislocations $B<x<C$, not just those in the slip zone. However, as previously stated, the dislocations in the zone $B<x<m$ are locked in place, and therefore are unaffected by load movement to the right, i.e., $\dot{B}_x = dB_x(\zeta,t)/dt = 0$; $B<\zeta<m$. Differentiating (9) and (13) with respect to t therefore allows the lower bound of integration to be changed from B to m. The resulting equations are

$$\frac{2\mu}{\pi(\kappa+1)}\int_m^C \dot{B}_x(\zeta,t)[K_s(x,\zeta)+fK_n(x,\zeta)]d\zeta = \frac{2Pa^2[4fax_t-3x_t^2+a^2]}{\pi(a^2+x_t^2)^3} \qquad m<x<C \tag{22}$$

$$\int_m^C \dot{B}_x(\zeta,t)d\zeta = 0 \tag{23}$$

Asymptotic analysis [7, 10] shows that the shear tractions must have continuous derivatives with respect to t at m, the transition point between a growing stick zone and a slip zone. Therefore, $\dot{B}_x$ in (22) and (23) is singular at C, and bounded at m and can be represented using a dimensionless formulation for the range $m<x<C$ as:

$$\dot{B}_x(r,t) = \frac{P(\kappa+1)\gamma(r,t)(1+r)^{1/2}}{2\mu a^2(1-r)^{1/2}} \tag{24}$$

where r is given by (15) with δ and σ redefined as

$$\delta = (C-m)/(2a); \qquad \sigma = (C+m)/(2a) \tag{25}$$

Substituting (24) into (22) and (23), and discretizing we find

$$\sum_{i=1}^{n}\frac{2(1+r_i)}{2n+1}\gamma(r_i)[K_s(r_i,s_k)+fK_n(r_i,s_k)] = \frac{2\{4f(\delta s_k+\sigma-t)-3(\delta s_k+\sigma-t)^2+1\}}{\pi(1+(\delta s_k+\sigma-t)^2)^2}; \quad k=1, \ldots, n \tag{26}$$

$$\sum_{i=1}^{n}\frac{2(1+r_i)}{2n+1}\gamma(r_i) = 0 \tag{27}$$

where

$$r_i = \cos\left(\frac{2i-1}{2n+1}\pi\right); \quad i=1, \ldots, n$$

$$s_k = \cos\left(\frac{2k}{2n+1}\pi\right); \quad k=1, \ldots, n \tag{28}$$

Relationships (26) and (27) represent $(n+1)$ equations for the n values of $\gamma(r_i)$ and the transition point m, if the load position t is assumed known. The relation between m and t has to be found by iteration using equation (27) and it is numerically more efficient to fix m and iterate on t rather than vice versa. In this way, the points r_i and s_k, and the kernel matrix have to be calculated only once per step, since only the right-hand side of (26) is affected by the value of t.

The second reason for preferring this approach concerns the history dependence of the problem. Because (26) and (27) have no closed-form solution, the problem must be solved numerically as a series of small load and transition point increments. During this incremental process the effect of the currently active dislocations on shear and normal tractions is continually added to a running total of the effect of *all* dislocations (both locked and active) on shear and normal tractions at a series of fixed "tracer" points. By choosing these "tracer" points as the known m values, the numerical

Downloaded 02 May 2010 to 171.66.16.54. Redistribution subject to ASME license or copyright; see http://www.asme.org/terms/Terms_Use.cfm

evaluation of the traction increments is simplified (see the following).

A check is made at each step to ensure that shift in the currently active zone is in the forward direction. Equation (8) can be written in terms of $\dot{B}_x$, using (9) as:

$$\dot{h}(x) = \int_x^C \dot{B}_x(\zeta)\, d\zeta \tag{29}$$

the right-hand side of which can be evaluated using the trapezoidal rule.

Now that the load position t is known corresponding to the transition point m and the current distribution, the increment in shear and normal tractions at any x caused by the most recent movement in load and transition point can be found. In developing this incremental solution, it is helpful to refer to the current transition and load position as m_{j+1} and t_{j+1}, respectively, and to the previous points as m_j and t_j. The increment ΔS_d in shear traction caused by the load movement from t_j to t_{j+1} can be written as

$$\Delta S_d(x,t) = \frac{2\mu}{\pi(\kappa+1)} \int_{t_j}^{t_{j+1}} \int_{m(z)}^{C} \dot{B}_x(\zeta,z) K_s(x,\zeta)\, d\zeta\, dz \tag{30}$$

where $\dot{B}_x(\zeta, z)$ refers to the derivative of the dislocations that are active when the transition point is at $m(z)$. Remembering that

$$\dot{B}_x(\zeta,z) = \frac{P(\kappa+1)\gamma(\zeta,z)(\zeta - m(z))^{1/2}}{2\mu a^2 (C-\zeta)^{1/2}} \tag{31}$$

the order of integration can be interchanged in (30). The integration with respect to z, the load position dummy variable, can be performed if $\gamma(\zeta,z)$ is assumed to remain constant for a small change in z, and the relationship between m and z is approximated by the piecewise linear form

$$m(z) = m_j + (z - t_j)\frac{(m_{j+1} - m_j)}{(t_{j+1} - t_j)}; \quad m_j < m(z) < m_{j+1} \tag{32}$$

This procedure is used because the term $(\zeta - m(z))^{1/2}$ in $\dot{B}_x$ would give discontinuities in slope at the points m_j if the simpler, piecewise constant integration were used.

We also note that the dislocations in the range $m_j < \zeta < m_{j+1}$ only remain active while $t_j < s < t^*$, where t^* $(< t_{j+1})$ refers to the load position when $m(s) = m_{j+1}$ and can be found from equation (32). Using these results and performing the integration with respect to z gives

$$\Delta S_d(x,t) = \frac{-2(t_{j+1} - t_j)}{3\pi(m_{j+1} - m_j)} \int_{m_j}^{C} \frac{\gamma(\zeta) K_s(\zeta,x)}{(C-\zeta)^{1/2}} [(\zeta - m^*)^{3/2} - (\zeta - m_j)^{3/2}]\, d\zeta \tag{33}$$

where

$$m^* = \zeta; \quad m_j < \zeta < m_{j+1}$$
$$= m_{j+1}; \quad m_{j+1} < \zeta < C. \tag{34}$$

In dimensionless, discretized form, (33) becomes

$$\Delta S_d(x,t)\left(\frac{a}{P}\right) = \frac{-2(t_{j+1} - t_j)}{3(m_{j+1} - m_j)} \sum_{i=1}^{n} \frac{2(1+r_i)}{2n+1} \gamma(r_i) K_s(r_i, s_k)\delta\left[\frac{(r_i - r^*)^{3/2}}{(r_i+1)^{1/2}} - (r_i+1)\right] \tag{35}$$

where

$$r^* = r_i; \quad m_j < a(\delta r_i + \sigma) < m_{j+1}$$
$$= (m_{j+1}/a - \sigma)/\delta; \quad m_{j+1} < a(\delta r_i + \sigma) < C. \tag{36}$$

An expression for the increment in normal tractions N_d can be developed in an analogous manner.

The increment in the shear tractions can be evaluated directly at any point outside of the interval $m_j < x < C$, but *within* this interval, equation (33) is a Cauchy singular integral and the numerical integration procedure is accurate only at the specified collocation points. However, the kernel of the corresponding integral for the increment in normal tractions is bounded for all x and hence condition (10) can be used to evaluate the shear increment at points in the interval $m_{j+1} < x < C$. The technique proposed by Sheppard and Comninou [11] was used to find the shear tractions at a tracer point near B during the first increment only. It was not needed for subsequent increments because the tracer points were chosen to coincide with the transition points.

The change in K_{II} at C caused by an incremental change in the transition point is:

$$\left(\frac{\pi a^{1/2}}{2P}\right)\Delta K_{II}(C) = \pi^{3/2}\delta^{1/2}\gamma(+1)(t_{j+1} - t_j) \tag{37}$$

As the transition point, m, between stick and forward slip is incremented from $B < x < C$ the relationship between S and N in the interval $B < x < m$ is continually monitored to ensure that condition (12) is satisfied. If a violation is found just to the right of B before m has reached C, we are no longer dealing with a "Short Crack" and there will be three zones along the crack: namely backslip in $B < x < q$ such that $B < q < m$, stick in $q < x < m$, and forward slip in $m < x < C$.

The load location t at which the crack has just reached the configuration of full stick is denoted by t_2. Convergence of the incremental procedure was checked by finding $K_{II}(C)$ at $t = t_2$ as a function of the number of incremental steps (e.g., 25 increments were required for convergence for $L/a = 1.00$).

(2C) Full Stick ($t_2 < t < t_3$). Once the load has passed the point t_2, full stick occurs and the solution is obtained by simply updating the contribution from the Flamant solution, while keeping the contribution from the locked in dislocations unchanged. This condition persists until inequality (12) is violated. The nature of this violation is always such as to indicate the development of a backslip zone at B. The load position at which this occurs is denoted by t_3.

(2d) Growing Backslip Zone ($t_3 < t < t_4$). An incremental solution is not required for the growing backslip zone depicted in Fig. 2(*d*). The shear and normal tractions can be written in the form

$$S(x) = \frac{2\mu}{\pi(\kappa+1)} \int_B^q \Delta B_x(\zeta) K_s(x,\zeta)\, d\zeta + \frac{2Pa^2 x_t}{\pi(a^2 + x_t^2)^2} + S_d(x) \tag{38}$$

$$N(x) = \frac{2\mu}{\pi(\kappa+1)} \int_B^q \Delta B_x(\zeta) K_n(x,\zeta)\, d\zeta - \frac{2Pa^3}{\pi(a^2 + x_t^2)^2} + N_d(x) \tag{39}$$

where $S_d(x)$, $N_d(x)$ are the contributions from the dislocations locked in during the preceding full-stick phase, and ΔB_x are the additional dislocations describing the backslip and hence located in the backslip zone defined as $B < x < q$.

Equation (11) is valid in $B < x < q$, and hence, substituting from (38) and (39)

$$\frac{2\mu}{\pi(\kappa+1)} \int_B^q \Delta B_x(\zeta)[K_s(x,\zeta) - fK_n(x,\zeta)]\, d\zeta = fN_d(x) - S_d(x) - \frac{2Pa^2(fa + x_t)}{\pi(a^2 + x_t^2)^2}; \quad B < x < q \tag{40}$$

Also, to comply with equation (9), we require

Downloaded 02 May 2010 to 171.66.16.54. Redistribution subject to ASME license or copyright; see http://www.asme.org/terms/Terms_Use.cfm

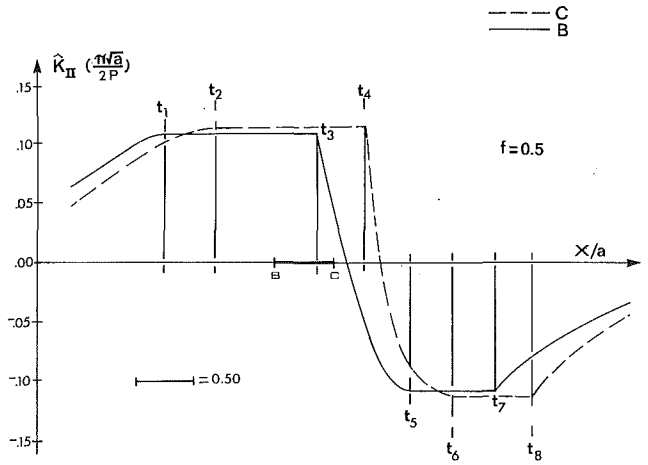


Fig. 3 Stress intensity factors as a function of load position for $L/a = 0.5$; $f = 0.5$. The solid line BC represents the extent of the crack.

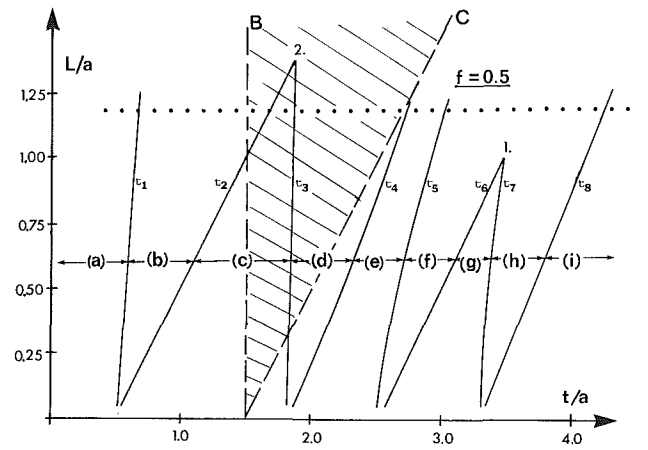


Fig. 4 The transitional load positions t_1, t_2, etc. as functions of crack length L/a for $f = 0.5$. The crack extends between the dashed lines B and C.

$$\int_B^q \Delta B_x(\zeta)\, d\zeta = 0 \tag{41}$$

This currently active distribution of dislocations is singular at the crack tip B and bounded at the stick-slip transition q. We therefore use the representation

$$\Delta B_x(r) = \frac{P(\kappa+1)(1-r)^{1/2}}{2\mu a(1+r)^{1/2}}\,\phi(r) \tag{42}$$

Equations (40) and (41) can then be normalized and discretized, giving $(n+1)$ equations for finding the n values of $\phi(r_i)$ and the load position t for a specified value of q, $B<q<C$. Note that the tractions S_d, N_d are known only at the tracer points m_j. However, they are smooth functions of x and a cubic spline fit is sufficient to give the values at the points s_k.

The change in K_{II} at B from its locked value can also be found:

$$\left(\frac{\pi a^{1/2}}{2P}\right)\Delta K_{II}(B) = -(\pi)^{3/2}\delta^{1/2}\phi(-1) \tag{43}$$

The backslip zone will continue to grow until $q = C$, for which the corresponding load position is denoted by t_4.

(2*e*) Full Backslip ($t_4 < t < t_5$). When the transition point between growing backslip and stick has reached C, the crack experiences full backslip (Fig. 2(*e*)). Once this condition occurs, the problem ceases to be history dependent, since there are no remaining locked-in dislocations. The for-

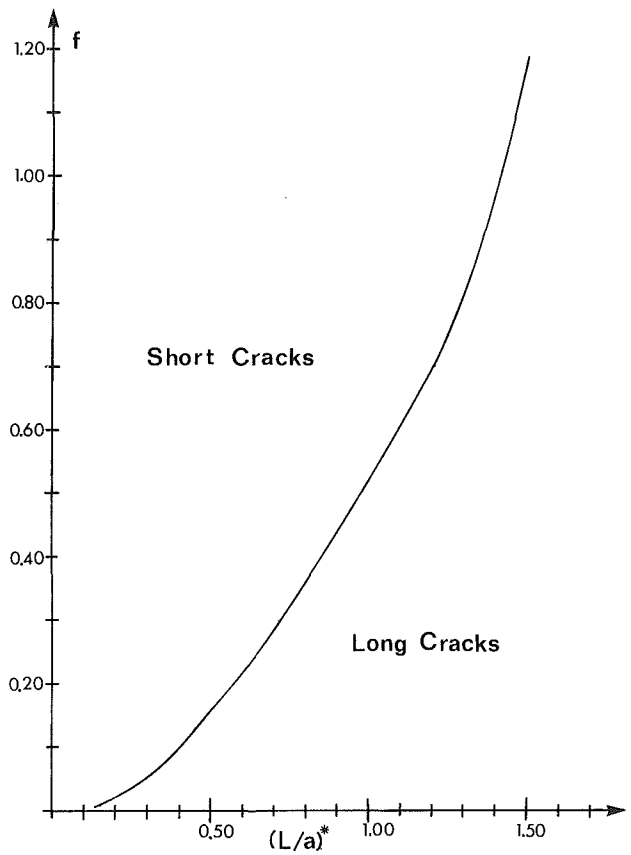


Fig. 5 The critical crack length as a function of crack face coefficient of friction f. Short cracks are those that never experience more than two zones.

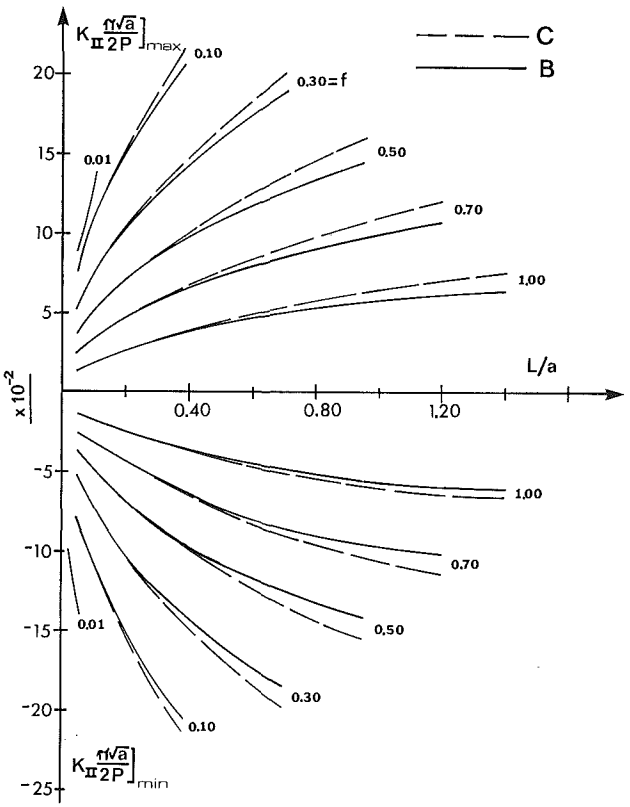


Fig. 6 Maximum and minimum values of stress intensity factors at B and C as functions of crack length L/a for various coefficients of friction

Downloaded 02 May 2010 to 171.66.16.54. Redistribution subject to ASME license or copyright; see http://www.asme.org/terms/Terms_Use.cfm

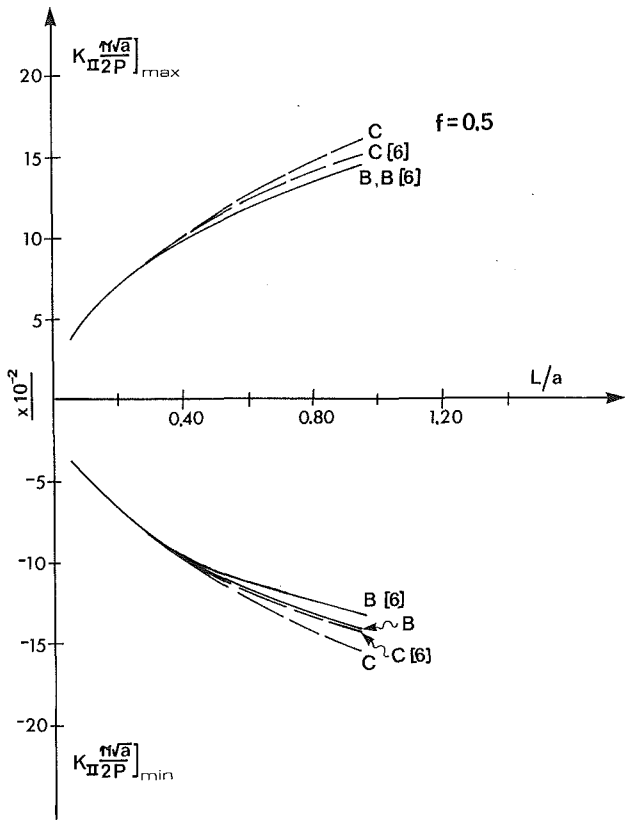


Fig. 7 Comparison of maximum stress intensity factors with the approximate solution of Hearle and Johnson [4]; $f = 0.5$

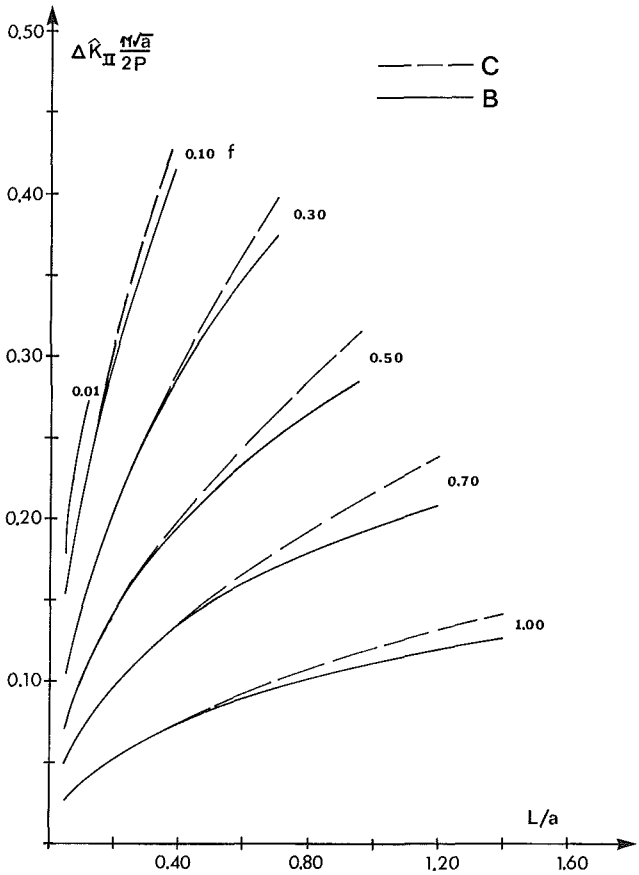


Fig. 8 Effect of crack length L/a on the range of stress intensity factors K_{II} for various coefficients of friction

mulation is identical to that for full forward slip (Section (2*a*)) except that condition (10) is replaced by (11), which is formally equivalent to changing the sign of f in the appropriate equations.

Full backslip persists as long as the solution satisfies

$$\dot{h}(x) < 0; \qquad B < x < C. \tag{44}$$

As in Section (2*a*), this is first violated at B and corresponds to $K_{II}(B)$ reaching a maximum negative value at load position $t = t_5$.

It is interesting to note that (44) is a necessary but not sufficient condition for full backslip to occur, if the previous history is not considered. The load position t_4 at which full backslip starts is determined by the previous history of the process, but the memory of the system is then erased.

(2*f*–*i*) Subsequent Phases ($t > t_5$). After the load passes the point t_5, the crack passes through a sequence of conditions shown in Figs. 2(*f*)-(*i*), which are essentially identical to 2(*b*–*e*), except that the direction of slip is reversed. The formulations used are identical except for a change of sign of f in appropriate equations.

The final phase ($t > t_8$) is one of full forward slip (Fig. 2(*i*)) as the load recedes to infinity, leaving the body in a stress-free state.

Results

The formulation described in the foregoing can be used to explore the variation of stress intensity factors, K_{II}, at B and C with load position t. Figure 3 shows the results obtained for $L/a = 0.5$ and $f = 0.5$. The horizontal portions of the curves correspond to periods when there is a stick zone adjacent to the appropriate crack tip. Each tip experiences a positive and a negative locked period, which represent the maximum and minimum value respectively of K_{II}. The transition points t_1, t_2, etc., mark the beginnings and ends of these periods. Notice that the curves have continuous slope at transitions from slip to stick, but discontinuous slope at transitions from stick to slip.

Similar results were obtained for a range of crack lengths (L/a) and the effect of this parameter on the load locations for the various transitions is illustrated in Fig. 4 for $f = 0.5$. The dashed lines represent the locations of the crack tips B and C.

The lines defining the transitions t_6, t_7 intersect at the point labeled 1 in Fig. 4, corresponding to $L/a = 0.96$. This is the maximum length of crack that can be considered short for $f = 0.5$. Cracks longer then this critical value will start to slip forward at B in configuration 2*f* before the backslip zone at C has shrunk to zero.

A similar intersection between t_2, t_3 occurs at point 2, where $L/a > 1.4$. Cracks in the range $0.96 < L/a < 1.4$, such as that described by the dotted line in Fig. 4 will follow the sequence described in the paper for the first half of the cycle until a three region configuration is developed some time after t_5.

The critical value of crack length $(L/a)^*$, corresponding to point 1 in Fig. 4, was found for coefficients of friction in the range $0.01 < f < 1.1$ and the results are presented in Fig. 5.

The maximum and minimum values of K_{II} at B and C are shown in Fig. 6 as a function of crack length for various coefficients of friction. In each case, the curves are terminated at the critical crack length $(L/a)^*$ defined in Fig. 5. In all cases, increasing crack face friction has a very marked effect in decreasing stress intensity factors, as we would expect. For very short cracks the curves for tips B and C coincide and are symmetrical about zero, indicating that all four extreme values have approximately equal magnitude. These magnitudes increase with crack length, but the values at C become significantly greater than those at B and some asymmetry is developed.

Downloaded 02 May 2010 to 171.66.16.54. Redistribution subject to ASME license or copyright; see http://www.asme.org/terms/Terms_Use.cfm

The results for $f=0.5$ are compared with the approximate solution of Hearle and Johnson [6] in Fig. 7. Their approximation consists of:

(*i*) Using the dislocation solution for the full plane and hence neglecting the influence of the free surface;
(*ii*) Using an inexact model of the locked regions of the crack.

Figure 7 shows that their results are accurate for very short cracks but become less accurate as crack length increases, as we should expect. For longer cracks, their estimates of $K_{II}(B)$ are still very good (within 3 percent) but those of $K_{II}(C)$ are less good (up to 8 percent underestimated). This can be explained by referring to those stages of the solution procedure at which extreme values of K_{II} are obtained. In each case, the maximum of $K_{II}(B)$ follows a period of full slip; the maximum occurs at t_1 following full forward slip and the minimum at t_5 following full backslip. It follows that the estimates of these quantities in [6] are affected only by their approximation (*i*), since no stick zones are involved. By contrast, when $K_{II}(C)$ reaches a maximum (t_2, t_6) there is stick throughout the crack and we conclude that approximation (*ii*) is responsible for the less good estimates of this quantity.

Of particular importance for crack growth is the range of K_{II} (i.e., $\Delta K_{II}=(K_{II\max}-K_{II\min})$), which is shown in Fig. 8. Except for very short cracks, this range is significantly greater at C than at B, indicating a tendency for cracks to grow from the trailing edge under repeated loading; a conclusion that is supported by the experimental evidence of Yoshimura, Rubin, and Hahn [12].

Conclusions

The method described enables the stress field to be found near a subsurface crack subjected to a load moving over the surface. Coulomb friction between the crack faces has a substantial effect in reducing the stress intensity factors at the crack tips and introduces history dependence into the problem.

The stress intensity factors are found to reach higher maximum values at the trailing tip than at the leading tip; a result that is supported by experimental evidence showing that such cracks tend to propagate preferentially from the trailing tip.

The predictions of a previous approximate solution by Hearle and Johnson [6] are shown to be very good for the leading tip, but to underestimate the stress intensity factor at the trailing tip, except for very short cracks.

Acknowledgment

Support by the Office of Naval Research through the contract N00014-K-0287 during the course of this research is gratefully acknowledged.

References

1 Chang, F.-K., Comninou, M., Sheppard, S., and Barber, J. R., "The Subsurface Crack under Conditions of Slip and Stick Caused by a Surface Normal Force," ASME JOURNAL OF APPLIED MECHANICS, Vol. 51, 1984, pp. 311-316.

2 Comninou, M., and Barber, J. R., "Frictional Slip Between a Layer and a Substrate Due to a Periodic Tangential Surface Force," *Int. J. of Solids Structures*, Vol. 19, 1983, pp. 533-539.

3 Comninou, M., Schmueser, D., and Dundurs, J., "Frictional Slip Between a Layer and a Substrate Caused by a Normal Load," *Int. J. Eng. Sci.*, Vol. 18, 1980, pp. 131-137.

4 Comninou, M., Schmueser, D., and Dundurs, J., "Separation and Slip Between a Substrate Caused by a Tensile Load," *Int. J. Eng. Sci.*, Vol. 18, 1980, pp. 1149-1155.

5 Dundurs, J., and Gautesen, A. K., "On the Approach to Steady State for Frictional Contact Under Moving Loads," ASME JOURNAL OF APPLIED MECHANICS, Vol. 50, 1983, pp. 783-788.

6 Hearle, A. D., and Johnson, K. L., "Mode *II* Stress Intensity Factors for a Crack Parallel to the Surface of an Elastic Half-Space Subjected to a Moving Point-Load," submitted to *Journal Mech. Phys. Solids*.

7 Dundurs, J., and Comninou, M., "Some Consequences of the Inequality Conditions in Contact and Crack Problems," *J. Elasticity*, Vol. 9, 1979, pp. 71-82.

8 Erdogan, F., Gupta, G. D., and Cook, T. S., in: *Methods of Analysis and Solution of Crack Problems*, Noordhoff, Leyden, 1973.

9 Krenk, S., "On the Use of the Interpolation Polynomial for Solutions of Singular Integral Equations," *Q. Appl. Math.*, Vol. 32, 1975, pp. 479-484.

10 Comninou, M., Barber, J. R., and Dundurs, J., "Interface Slip Caused by a Surface Load Moving at a Constant Speed," *Int. J. Mech. Sci.*, Vol. 25, 1983, pp. 41-46.

11 Sheppard, S. D., and Comninou, M., "On the Interpolation of Cauchy Integrals," in *Numerical Solution of Singular Integral Equations*, Gerasoulis, A., and Vichnevetsky, R., eds., IMACS, 1984.

12 Yoshimura, H., Rubin, C. A., and Hahn, G. T., "Cyclic Crack Growth Under Repeated Rolling Contact," prepared for Eleventh Canadian Fracture Conference, University of Ottawa, Ontario, Canada, 1984.

Downloaded 02 May 2010 to 171.66.16.54. Redistribution subject to ASME license or copyright; see http://www.asme.org/terms/Terms_Use.cfm

Z. Y. Wang[1]

H. T. Zhang[2]

Y. T. Chou

Department of Metallurgy and Materials Engineering, Lehigh University, Bethlehem, Pa. 18015

Characteristics of the Elastic Field of a Rigid Line Inhomogeneity

Explicit expressions are obtained for the stress and displacement fields near the tip of a rigid line inhomogeneity subjected to an inclined loading. It is shown that the tip stress field, with a square-root singularity, differs in characteristics from that of a slit crack. New designations for the mode of deformation based on the fracture concept are presented and the inhomogeneity extension forces are calculated and discussed.

1 Introduction

The characteristics of the stress field near the tip of a rigid line inhomogeneity have been reported previously [1]. The present paper is a more detailed account of this work.

From the viewpoint of inhomogeneities in solids, a rigid line (the term "inhomogeneity" is omitted for simplicity) and a slit crack are the two extreme cases of a flat inhomogeneity, namely, for a crack $E_1, G_1 \to 0$ and for a rigid line, $E_1, G_1 \to \infty$, where E_1 and G_1 are, respectively, the Young's and shear moduli of the inhomogeneity phase. Although the crack problem has been studied extensively in the past 30 years, investigations on rigid line inhomogeneities have been rather limited. Chou and Wang [1] recently showed that the stress field near the tip of a rigid line subjected to unidirectional tension exhibits a square-root singularity similar to the case of a slit crack. On the other hand, a negative extension force was found which is opposite to that on a crack.

In the present paper we examine a more general case in which the inhomogeneous elastic body is subjected to an inclined loading at infinity. The stress and displacement fields of the elastic system are analyzed using both Eshelby's equivalent-inclusion method and Muskhelishvili's complex-variable method (Section 2). Since the characteristics of the stress field differ from that of a crack, the modes of deformation are redefined for the rigid line case. Subsequently, a new term, "the stress singularity coefficient," is introduced and the inhomogeneity extension force is calculated and discussed (Section 3).

2 Analysis

We consider an elliptic inhomogeneity embedded in an infinite isotropic elastic body with its cylindrical axis parallel to the z-axis of the Cartesian coordinate system xyz (Fig. 1). The boundary of the cross section of the inhomogeneity in the xy plane is described by the ellipse $x^2/a^2 + y^2/b^2 = 1$, where a and b are the semiaxes. (A rigid line inhomogeneity is then the limiting case when $e = b/a \to 0$ and E_1 and $G_1 \to \infty$.) Let the elastic body be subjected to a unidirectional tension $\sigma > 0$ (or a compression if $\sigma < 0$), which makes an angle α with the positive x axis. The boundary value problem can be solved by two methods.

2.1 The Eshelby's Equivalent Inclusion Method. Following the work by Yang and Chou [2, 3], the equivalent eigenstrains for a rigid line are determined by

$$\epsilon_{xx}^C = -\epsilon_{xx}^A, \quad \epsilon_{yy}^C = -\epsilon_{yy}^A, \quad \epsilon_{xy}^C = -\epsilon_{xy}^A \tag{1}$$

where $\epsilon_{xx}^C, \epsilon_{yy}^C, \epsilon_{xy}^C$ are the constrained strains of the equivalent inclusion and $\epsilon_{xx}^A, \epsilon_{yy}^A, \epsilon_{xy}^A$ are the applied strains. For the case $e \ll 1$, the constrained strains may be expressed in terms of the eigenstrains $\epsilon_{xx}^*, \epsilon_{yy}^*$, and ϵ_{xy}^* of the equivalent inclusion by the following relations [4, 5]

$$\epsilon_{xx}^C = \frac{e}{2(1-\nu)}[(3-2\nu)\epsilon_{xx}^* - (1-2\nu)\epsilon_{yy}^*] \tag{2a}$$

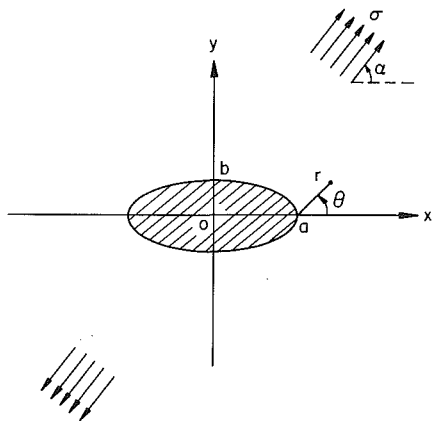


Fig. 1 A rigid line inhomogeneity under the action of an inclined unidirectional loading

[1]On leave from the Central-South Institute of Mining and Metallurgy, Changsha, China.

[2]On leave from Department of Physics, Lanzhou University, Lanzhou, China.

Contributed by the Applied Mechanics Division for publication in the JOURNAL OF APPLIED MECHANICS.

Discussion on this paper should be addressed to the Editorial Department, ASME, United Engineering Center, 345 East 47th Street, New York, N.Y. 10017, and will be accepted until two months after final publication of the paper itself in the JOURNAL OF APPLIED MECHANICS. Manuscript received by ASME Applied Mechanics Division, October, 1984.

Copyright © 1985 by ASME

Downloaded 02 May 2010 to 171.66.16.54. Redistribution subject to ASME license or copyright; see http://www.asme.org/terms/Terms_Use.cfm

$$\epsilon^C_{yy} = \frac{1}{(1-\nu)}[\nu\epsilon^*_{xx} + (1-\nu)\epsilon^*_{yy}] \tag{2b}$$

$$\epsilon^C_{xy} = \epsilon^*_{xy} \tag{2c}$$

where ν is the Poisson's ratio of the matrix and $\epsilon^*_{zz} = 0$ under the plane strain condition. Substituting (2) in (1), we obtain for a rigid line ($e \ll 1$)

$$\epsilon^*_{xx} = -\frac{2(1-\nu)^2}{(3-4\nu)e}\epsilon^A_{xx},\quad \epsilon^*_{yy} = \frac{2\nu(1-\nu)}{(3-4\nu)e}\epsilon^A_{xx},\quad \epsilon^*_{xy} = -\epsilon^A_{xy} \tag{3}$$

In equation (3) both ϵ^*_{xx} and ϵ^*_{yy} are inversely proportional to the semiaxis ratio e of the ellipse, whereas ϵ^*_{xy} is independent of e. As will be seen later, only the two normal components of eigenstrains contribute to the stress singularity of a rigid line, while the shear component ϵ^A_{xy} does not induce any stress singularity. Under the applied stress σ, we have by Hooke's law

$$\epsilon^A_{xx} = \frac{\sigma}{4G}[(1-2\nu)+\cos 2\alpha] \tag{4}$$

$$\epsilon^A_{xy} = \frac{\sigma}{4G}\sin 2\alpha \tag{5}$$

where G is the shear modulus of the matrix. Equations (3)–(5) give the eigenstrains of the flat equivalent inclusion under the action of an inclined loading.

The constrained stress field of a flat inclusion in the matrix was reported previously [5] and the result can be written as follows:

$$\sigma_{xx} = \frac{Ge}{1-\nu}\left\{(3\,\epsilon^*_{xx} - \epsilon^*_{yy})\left[1 + \frac{1}{R}(x\sin\eta - y\cos\eta)\right] + (\epsilon^*_{yy} - \epsilon^*_{xx})\frac{a^2 y}{R^3}\cos 3\,\eta\right\} \tag{6a}$$

$$\sigma_{yy} = -\frac{Ge}{1-\nu}\left\{(\epsilon^*_{xx} + \epsilon^*_{yy})\left[1 + \frac{1}{R}(x\sin\eta - y\cos\eta)\right] + (\epsilon^*_{yy} - \epsilon^*_{xx})\frac{a^2 y}{R^3}\cos 3\,\eta\right\} \tag{6b}$$

$$\sigma_{xy} = \frac{Ge}{1-\nu}\left[-2\,\epsilon^*_{xx}\frac{1}{R}(x\cos\eta + y\sin\eta) + (\epsilon^*_{yy} - \epsilon^*_{xx})\frac{a^2 y}{R^3}\sin 3\,\eta\right] \tag{6c}$$

where

$$R\,e^{i\eta} = \sqrt{a^2 - z^2},\quad z = x + iy \tag{7}$$

Near the tip of the flat inclusion ($r \ll a$), (see Fig. 1), equations (6) approach the following limiting forms,

$$\sigma_{xx} = \frac{G}{1-\nu}\left(\frac{a}{2r}\right)^{1/2} e(\epsilon^*_{yy} - \epsilon^*_{xx})\cos\frac{\theta}{2}\left[1 - \sin\frac{\theta}{2}\sin\frac{3\theta}{2} - \frac{2\,\epsilon^*_{xx}}{\epsilon^*_{yy} - \epsilon^*_{xx}}\right] \tag{8a}$$

$$\sigma_{yy} = \frac{G}{1-\nu}\left(\frac{a}{2r}\right)^{1/2} e(\epsilon^*_{yy} - \epsilon^*_{xx})\cos\frac{\theta}{2}\left[1 + \sin\frac{\theta}{2}\sin\frac{3\theta}{2} + \frac{2\,\epsilon^*_{xx}}{\epsilon^*_{yy} - \epsilon^*_{xx}}\right] \tag{8b}$$

$$\sigma_{xy} = \frac{G}{1-\nu}\left(\frac{a}{2r}\right)^{1/2} e(\epsilon^*_{yy} - \epsilon^*_{xx})\sin\frac{\theta}{2}\left[\cos\frac{\theta}{2}\cos\frac{3\theta}{2} - \frac{2\,\epsilon^*_{xx}}{\epsilon^*_{yy} - \epsilon^*_{xx}}\right] \tag{8c}$$

where (r, θ) are local polar coordinates with the origin at $x = +a$ and $y = 0$.

Substituting (3) and (4) in (8), we obtain the stress field near the tip of a rigid line ($e \to 0$), given by

$$\sigma_{xx} = \frac{\sigma}{4}\left(1 - \frac{1-2\cos 2\alpha}{K}\right)\left(\frac{a}{2r}\right)^{1/2} \cos\frac{\theta}{2}\left[1 + \frac{1}{2}(1+K) - \sin\frac{\theta}{2}\sin\frac{3\theta}{2}\right] \tag{9a}$$

$$\sigma_{yy} = \frac{\sigma}{4}\left(1 - \frac{1-2\cos 2\alpha}{K}\right)\left(\frac{a}{2r}\right)^{1/2} \cos\frac{\theta}{2}\left[1 - \frac{1}{2}(1+K) + \sin\frac{\theta}{2}\sin\frac{3\theta}{2}\right] \tag{9b}$$

$$\sigma_{xy} = \frac{\sigma}{4}\left(1 - \frac{1-2\cos 2\alpha}{K}\right)\left(\frac{a}{2r}\right)^{1/2} \sin\frac{\theta}{2}\left[\frac{1}{2}(1+K) + \cos\frac{\theta}{2}\cos\frac{3\theta}{2}\right] \tag{9c}$$

where we have adopted the notation,

$$K = 3 - 4\nu,\quad 1 < K < 3 \tag{10}$$

for the plane strain deformation. For a plane stress problem, equations (9) are still valid, but with $K = (3-\nu)/(1+\nu)$.

It is worth pointing out that for the eigenstrain component ϵ^*_{xy}, the corresponding constrained stress also contains the factor $e = b/a$, similar to equations (8). (See reference [5].) However, from equations (3) the relation $\epsilon^*_{xy} = -\epsilon^A_{xy}$ is independent of e. Thus, for the limiting case of a rigid line ($e \to 0$) the constrained stresses vanish. The inplane shear ϵ^A_{xy} is compatible with a rigid line and, therefore, does not induce any stress singularity.

From equations (9), two important features are noted. First, the local field has a square-root singularity, and, second, the signs of the stresses change with the value of α. In particular, when

$$\alpha = \alpha_0 = \frac{1}{2}\cos^{-1}\left(\frac{1-K}{2}\right) \tag{11}$$

the local field near the tip vanishes, i.e., the rigid inhomogeneity has no elastic response to the applied stress near its tip (see Fig. 3). Equations (9), which differ from those in reference [6], are confirmed by the results obtained using the Muskhelishvili's complex variable method shown in the next subsection.

2.2 The Muskhelishvili's Complex Variable Method. According to Muskhelishvili [7], the state of stress and displacement of a plane problem (including plane strain deformation $K = 3-4\nu$ and plane stress deformation $K = (3-\nu)/(1+\nu)$) can be determined by two complex potentials, $\varphi(z)$ and $\psi(z)$, and their derivatives, where $z = x + iy$ is a complex variable. For a elliptic inhomogeneity, it is convenient to map the exterior of the ellipse (in the z-plane) onto the exterior of a unit circle (in the ζ-plane) by the equation

$$z = \omega(\zeta) = M\left(\zeta + \frac{m}{\zeta}\right),\quad M > 0,\quad 0 \le m < 1 \tag{12}$$

where M and m are related to the semiaxes of the ellipse, a and b, by

$$a = M(1+m),\quad b = M(1-m) \tag{13}$$

In terms of the variable ζ, the stresses and displacements are given by

$$\sigma_{xx} + \sigma_{yy} = 4\,Re\left[\frac{\varphi'(\zeta)}{\omega'(\zeta)}\right] \tag{14a}$$

Downloaded 02 May 2010 to 171.66.16.54. Redistribution subject to ASME license or copyright; see http://www.asme.org/terms/Terms_Use.cfm

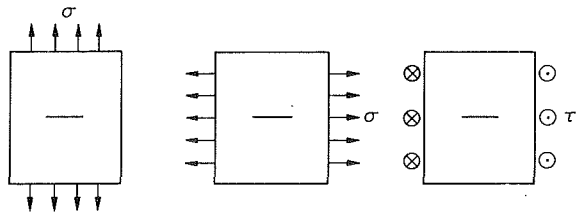


Fig. 2 Three modes of deformation of a rigid line inhomogeneity

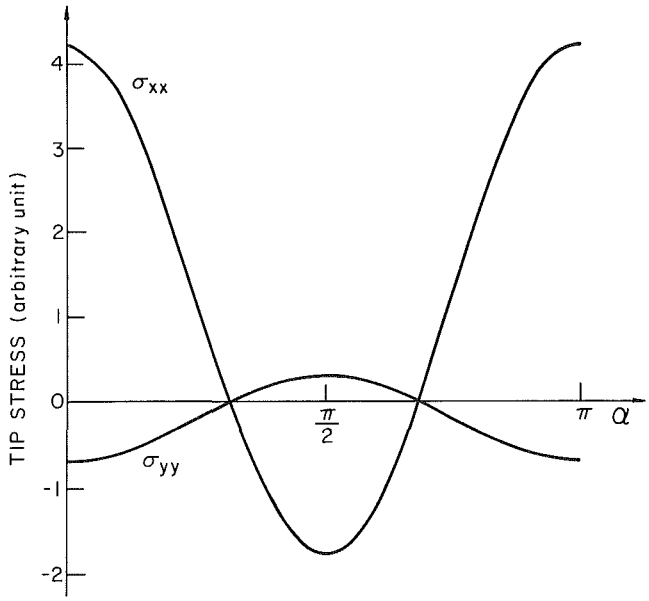


Fig. 3 Variations of σ_{xx} at σ_{yy} with α at $\theta = 0$ near the tip of a rigid line inhomogeneity ($\sigma > 0$ and $\nu = 1/3$). Note that the shear component $\sigma_{xy} = 0$ at $\theta = 0$.

$$\sigma_{yy} - \sigma_{xx} + 2i\sigma_{xy} = 2\left[\frac{\overline{\omega(\zeta)}}{\omega'(\zeta)}\frac{\varphi''(\zeta)\omega'(\zeta) - \varphi'(\zeta)\omega''(\zeta)}{[\omega'(\zeta)]^2} + \frac{\psi'(\zeta)}{\omega'(\zeta)}\right] \quad (14b)$$

$$u_x + i\,u_y = \frac{1}{2G}\left[K\varphi(\zeta) - \frac{\omega(\zeta)}{\omega'(\zeta)}\overline{\varphi'(\zeta)} - \overline{\psi(\zeta)}\right] \quad (14c)$$

where (u_x, u_y) is the displacement vector, *Re* indicates the real part of a complex function, primes denote differentiation, and an overbar denotes the complex conjugate.

For the case of a rigid line under an inclined loading, i.e., $m \to 1$, $e = b/a \to 0$, $a \to 2M$, the two complex potentials are given by

$$\varphi(\zeta) = \frac{\sigma a}{8}\left(\zeta + \frac{1 - 2\cos 2\alpha}{K}\frac{1}{\zeta}\right) \quad (15)$$

$$\psi(\zeta) = \frac{\sigma a}{8}\left[-2e^{-i2\alpha}\zeta + \frac{e^{i2\alpha} - e^{-i2\alpha} + K}{\zeta} - \frac{2\zeta}{\zeta^2 - 1} + \frac{1 - 2\cos 2\alpha}{K}\frac{1 + \zeta^2}{(\zeta^2 - 1)\zeta}\right] \quad (16)$$

With $\varphi(\zeta)$ and $\psi(\zeta)$ known, the stress and displacement fields can be calculated using equations (14). As before, we employ a local coordinate (r, θ) relative to the tip of the rigid line, and define

$$z = a + re^{i\theta} \quad (17)$$

Using equations (12)–(17) and assuming $r \ll a$, the expressions for the stresses near the tip of a rigid line are obtained and are identical to equations (9). In addition, the expressions for the displacements are

$$u_x = \frac{\sigma}{4G}\left(1 - \frac{1 - 2\cos 2\alpha}{K}\right)\left(\frac{ar}{2}\right)^{1/2} \cos\frac{\theta}{2}\left(K + \sin^2\frac{\theta}{2}\right) \quad (18a)$$

$$u_y = -\frac{\sigma}{4G}\left(1 - \frac{1 - 2\cos 2\alpha}{K}\right)\left(\frac{ar}{2}\right)^{1/2} \sin\frac{\theta}{2}\cos^2\frac{\theta}{2} \quad (18b)$$

This treatment was also applied to the case of an inplane shear loading. The results indicate that there is no shear stress singularity as concluded in Section 2.1.

3 Discussion

The preceding analyses appear to be a simple application of the general methods of Eshelby and Muskhelishvili. However, the results obtained are far-reaching. It is recognized that a square-root singularity exists at the tip of a rigid line, similar to the case of a crack.

On the other hand, the detailed characteristics are different in the two extreme cases. For a more appropriate description of the stress singularity, we introduce a new term, "the stress singularity coefficient," for the case of rigid line inhomogeneities.

3.1 The Stress Singularity Coefficient. Upon close examination, we find that there are three distinct modes of deformation which would induce maximum tensile stress or shear stress singularities. In analogy to the case of a crack, they are referred to as Mode *I*, *II*, and *III* deformation for a rigid line inhomogeneity (Fig. 2). To characterize these stress singularities, three corresponding "stress singularity coefficients" are defined.

(*i*) *Mode I Deformation (Tensile Loading).* This mode of deformation is referred to the case where a tensile load is applied perpendicular to the line inhomogeneity, i.e., $\alpha = \pi/2$ and $\sigma > 0$. In this case, the stress singularity coefficient is defined as

$$S_I = \lim_{r\to 0}\,(2\,\pi\,r)^{1/2}\sigma_{yy}(\theta = 0) = \sigma\sqrt{\pi\,a}\,\frac{(K-1)(3-K)}{8K} \quad (19)$$

(*ii*) *Mode II Deformation (Tensile Loading).* In this mode of deformation, a tensile loading is applied parallel to the line inhomogeneity ($\alpha = 0$, $\sigma > 0$). The corresponding stress singularity coefficient is defined by

$$S_{II} = \lim_{r\to 0}\,(2\,\pi\,r)^{1/2}\sigma_{xx}(\theta = 0) = \sigma\sqrt{\pi\,a}\,\frac{(K+1)(3+K)}{8K} \quad (20)$$

Note that unlike the stress intensity factors K_I and K_{II} of a crack, the stress singularity coefficients S_I and S_{II} depend not only on the applied stress σ and the inhomogeneity length a, but also on the material constant K.

(*iii*) *Mode III Deformation (Antiplane Shear Loading).* The analysis of this mode of deformation will be reported in a subsequent paper [8]. Here, for completeness, we list the expression of the stress singularity coefficient for Mode *III* deformation under an antiplane shear stress τ, as

$$S_{III} = \lim_{r\to 0}\,(2\,\pi\,r)^{1/2}\sigma_{xz}(\theta = 0) = \tau\sqrt{\pi\,a} \quad (21)$$

Downloaded 02 May 2010 to 171.66.16.54. Redistribution subject to ASME license or copyright; see http://www.asme.org/terms/Terms_Use.cfm

Table 1 Comparison between stress singularities of a crack and a rigid line inhomogeneity

Slit crack		Rigid line inhomogeneity	
Mode of deformation[a]	Stress intensity factor K	Mode of deformation[b]	Stress singularity coefficient S
I	$K_I = \sigma\sqrt{\pi a}$	I	$S_I = \sigma\sqrt{\pi a}\,\dfrac{(K-1)(3-K)}{8K}$
II	$K_{II} = \tau\sqrt{\pi a}$	II	$S_{II} = \sigma\sqrt{\pi a}\,\dfrac{(K+1)(3+K)}{8K}$
III	$K_{III} = \tau\sqrt{\pi a}$	III	$S_{III} = \tau\sqrt{\pi a}$

[a] See reference [12].
[b] See Fig. 2.

which is independent of the material constant K. Note that in the case of a rigid line, the shear stress is applied in the plane perpendicular to the rigid line, whereas in the case of a crack, the shear stress is applied parallel to the crack.

The definitions of stress singularity coefficients given in the foregoing are based on the viewpoint of fracture.[3] In the case of a rigid line inhomogeneity, both crack nucleation and growth are essential in the process of fracture. In Mode I deformation, a microcrack, if nucleated near the rigid segment by the action of the stress singularity, would grow along the x axis in the applied stress field σ_{yy}. On the other hand, in Mode II deformation, a crack nucleus would propagate in the y direction in the field σ_{xx}.

Now returning to equations (19) and (20), it is seen that

$$S_{II} = \frac{(K+1)(3+K)}{(K-1)(3-K)} S_I \tag{22}$$

For $\nu = 1/3$, $S_{II} = 14\,S_I$ for plane strain and $S_{II} = 15\,S_I$ for plane stress. Thus, for the case of a rigid line inhomogeneity, the most critical state for fracture is the mode II deformation, i.e., when a tensile stress is applied parallel to the rigid line. A comparison between the stress singularities of a crack and a rigid line inhomogeneity is given in Table 1.

Another interesting feature of the local field is the dilatation Δ. From equations (9) it is easy to obtain

$$\Delta = \frac{1-2\nu}{2G}(\sigma_{xx}+\sigma_{yy}) = \frac{1-2\nu}{G}\,\frac{\sigma}{4}\left(1-\frac{1-2\cos 2\alpha}{K}\right)\left(\frac{a}{2r}\right)^{1/2}\cos\frac{\theta}{2} \tag{23}$$

which depends on the angle of inclination α. Unlike the case of a crack where Δ is always positive, the dilatation around the tip of a rigid line may be positive or negative, depending on the angle α. When $\alpha = \alpha_0 = (1/2)\cos^{-1} 1/2\,(1-K)$, $\Delta = 0$. For a material with $\nu = 1/3$, the zero dilatation occurs at $\alpha_0 \cong 55$ deg for plane strain and $\alpha_0 = 60$ deg for plane stress.

3.2 *J* Integral and Inhomogeneity Extension Force. The concept of the energy-momentum tensor [9–11] and the J integral [12, 13] can also be used in the case of a rigid line. We have

$$J = \int_\Gamma \left(U\,dy - \mathbf{T}\cdot\frac{\partial \mathbf{u}}{\partial x}\,ds\right) \tag{24}$$

where Γ is a curve surrounding the tip (starting counterclockwise from the lower surface and ending on the upper surface of the rigid line), U is the strain energy density, $\mathbf{T}$ is the surface traction vector on Γ, $\mathbf{u}$ is the displacement vector, and s is the arc length. As in the case of a crack, the J integral is also path-independent for a rigid line. Thus, we may take Γ as a circle with its center at the rigid line tip. After some calculation, we obtain

$$J = -\sigma^2 \pi a \frac{K(1+K)}{128\,G}\left(1-\frac{1-2\cos 2\alpha}{K}\right)^2 \tag{25}$$

which is always negative, meaning that the applied stress promotes contraction of the rigid line rather than extension. The J integral vanishes at the same α_0 as given by equation (11). From (19)–(21), J is related to the stress singularity coefficients by

$$J_I = -\frac{S_I^2}{2G}\,\frac{k(1+k)}{(1-k)^2} \quad \text{for Mode } I \tag{26}$$

$$J_{II} = -\frac{S_{II}^2}{2G}\,\frac{K(1+K)}{(3+K)^2} \quad \text{for Mode } II \tag{27}$$

$$J_{III} = -\frac{S_{III}^2}{2G} \quad \text{for Mode } III \tag{28}$$[4]

It is worth noting that equation (25) can also be obtained by the equivalent inclusion method. Following references [2, 4], the increase of elastic energy in the body due to the presence of a rigid line is

$$\Delta W = \frac{\pi a^2 e}{2}(\sigma_{xx}^A \epsilon_{xx}^* + \sigma_{yy}^A \epsilon_{yy}^*) \tag{29}$$

Substituting (3) in (29) and using Hooke's law under the plane strain condition, we have

$$\Delta W = -\pi a^2 \frac{2(1-\nu)}{(3-4\nu)} G(\epsilon_{xx}^A)^2 = -\pi a^2 \frac{1+K}{2K} G(\epsilon_{xx}^A)^2 \tag{30}$$

which is in agreement with the result of Yang and Chou [3]. From (4) and (10), equation (30) can be written as

$$\Delta W = -\sigma^2 \pi a^2 \frac{K(1+K)}{128\,G}\left(1-\frac{1-2\cos 2\alpha}{K}\right)^2 \tag{31}$$

A negative ΔW means that the presence of a rigid line would reduce the elastic energy in the deformed body. However, the total free energy (elastic energy in the body, plus the potential

[3] For other purposes, it may be convenient to use a different definition, as proposed in reference [1].

[4] See reference [8].

Downloaded 02 May 2010 to 171.66.16.54. Redistribution subject to ASME license or copyright; see http://www.asme.org/terms/Terms_Use.cfm

energy of the loading mechanism) will increase, and according to Eshelby [14] the interaction energy is equal but in opposite sign to the increase of elastic energy, i.e.,

$$E_{int} = -\Delta W \tag{32}$$

Thus, based on the theory of forces on the elastic singularities [9], the driving force for the growth of the rigid line is

$$F = -\frac{\partial E_{int}}{\partial (2a)} = \frac{\partial (\Delta W)}{\partial (2a)}$$

$$= -\sigma^2 \pi a \frac{K(1+K)}{128\, G}\left(1 - \frac{1-2\cos 2\alpha}{K}\right)^2 \tag{33}$$

which is the same as the J integral given by equation (25). Note that the calculation of ΔW based on the equivalent inclusion concept is simpler than the calculation of the J integral.

These results indicate that contrary to the case of a crack, the applied stress always promotes a contraction of the rigid line inhomogeneity. A possible way to reduce the free energy of the system is the initiation of cracking near the tip of the rigid line. Other physical processes such as interactions with point defects or dislocations may also reduce the total energy of the system.

4 Conclusions

1. Explicit expressions for the stress and displacement fields are obtained near the tip of a rigid line inhomogeneity subjected to an inclined loading. The tip stress field has a square-root singularity.

2. The elastic behavior of the tip stress field of a rigid line is different from that of a crack. In the case of a rigid line inhomogeneity, there is no inplane shear stress singularity.

3. Three modes of deformation based on the fracture concept are proposed and three corresponding stress singularity coefficients are defined.

4. For a rigid line inhomogeneity, the J integral or the energy variation rate is always negative, except for a certain loading direction at which $J = 0$.

References

1 Chou, Y. T., and Wang, Z. Y., "Stress Singularity at the Tip of a Rigid Flat Inclusion," in *Recent Developments in Applied Mathematics*, Ling, F. F., and Tadjbaklish, I. G., eds., Rensselaer Press, 1983, pp. 21–30.

2 Yang, H. C., and Chou, Y. T., "Generalized Plane Problems of Elastic Inclusions in Anistropic Solids," ASME JOURNAL OF APPLIED MECHANICS, Vol. 43, 1976, pp. 424–430.

3 Yang, H. C., and Chou, Y. T., "On Rigid Elliptic Inclusion in Orthotropic Solids," ASME JOURNAL OF APPLIED MECHANICS, Vol. 45, 1978, pp. 683–685.

4 Mura, T., *Micromechanics of Defects in Solids*, Martinus Nijhoff Publishers, Hague, Netherlands, 1982, pp. 150–203.

5 Zhang, H. T., and Zhe, X. L., "Theory of Inclusion and Applications in the Study of Fracture," *Acta Physica Sinica*, Vol. 30, 1981, pp. 761–774.

6 Erdogan, F., and Gupta, D. G., "Stresses Near a Flat Inclusion in Bonded Dissimilar Materials," *Int. J. Solids and Structure*, Vol. 8, 1972, pp. 533–547.

7 Muskhelishvili, N. I., *Some Basic Problems of Mathematical Theory of Elasticity*, Noordhoff Ltd., Groningen, 1953, pp. 104–161; pp. 326–380.

8 Wang, Z. Y., Zhang, H. T., and Chou, Y. T., "Stress Singularity of a Rigid Line Inhomogeneity Under Anti-plane Loading," to be published.

9 Eshelby, J. D., "The Force on an Elastic Singularity," *Phil. Trans. Roy. Soc. London*, Vol. *A*244, 1951, pp. 87–112.

10 Eshelby, J. D., "Energy Relations and the Energy-Momentum Tensor in Continuum Mechanics," in *Inelastic Behavior of Solids*, Kanninen, M. F., et al., eds., McGraw-Hill, New York, 1970, pp. 77–115.

11 Eshelby, J. D., "The Calculation of Energy Release Rates," in *Prospects of Fracture Mechanics*, Sih, G. C., et al., eds., Noordhoff International Publishing, Leyden, 1974, pp. 69–84.

12 Rice, J. R., "Mathematical Analysis in the Mechanics of Fracture," in *Fracture—An Advanced Treatise, II*, Liebowitz, H., ed., Academic Press, New York, 1969, pp. 191–311.

13 Rice, J. R., "A Path Independent Integral and the Approximate Analysis of Strain Concentration by Notches and Cracks," ASME JOURNAL OF APPLIED MECHANICS, Vol. 35, 1968, pp. 379–386.

14 Eshelby, J. D., "The Determination of the Elastic Field of an Ellipsoid Inclusion, and Related Problems," *Proceedings of the Royal Society*, Series *A*, Vol. 241, 1957, pp. 376–396.

Downloaded 02 May 2010 to 171.66.16.54. Redistribution subject to ASME license or copyright; see http://www.asme.org/terms/Terms_Use.cfm

The Crack Problem for Bonded Nonhomogeneous Materials Under Antiplane Shear Loading

F. Erdogan
Department of Mechanical Engineering and Mechanics, Lehigh University, Bethlehem, Pa. 18015
Mem. ASME

The main objective of this paper is the investigation of the singular nature of the crack-tip stress field in a nonhomogeneous medium having a shear modulus with a discontinuous derivative. The problem is considered for the simplest possible loading and geometry, namely the antiplane shear loading of two bonded half spaces in which the crack is perpendicular to the interface. It is shown that the square-root singularity of the crack-tip stress field is unaffected by the discontinuity in the derivative of the shear modulus. The problem is solved for a finite crack and extensive results are given for the stress intensity factors.

1 Introduction

In a nonhomogeneous medium if the elastic moduli are piecewise constant, it is known that the stress field around a crack tip terminating at the interface has a behavior of the form r^{α} where r is the distance from the crack tip and $-1<\alpha<0$ (see, for example, [1, 2]). It is also known that if the nonhomogeneous medium has elastic moduli that are continuous with continuous derivatives, the stress state around the crack tips has the standard square-root singularity [3, 4]. What has not been studied so far is the effect of the discontinuity of the derivatives of elastic moduli on the crack-tip stress singularity for a crack terminating at the plane of discontinuity. In this paper the problem is studied for the simple case of antiplane shear loading of an infinite medium in which the shear modulus μ is a function of x only, $d\mu/dx$ is discontinuous along the $x=0$ plane, and the crack lies in the xz plane (Fig. 1). The main objective of the paper is to investigate the effect of $d\mu/dx$ on the stress singularity. Hence, it is further assumed that μ is an exponential function in x, which appears to lead to a relatively simple formulation of the problem.

2 Formulation of the Problem

The antiplane shear problem for the nonhomogeneous medium shown in Fig. 1 having the elastic properties

$$\mu(x)=\mu_0 e^{\beta x}, x>0;\ \mu(x)=\mu_0 e^{\gamma x},\ x<0, \tag{1}$$

may be formulated as follows:

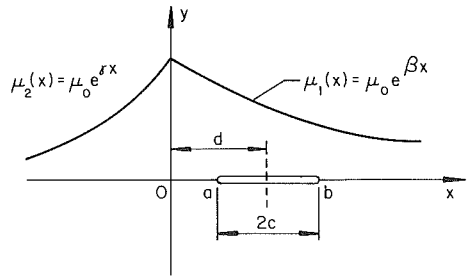


Fig. 1 Geometry for bonded nonhomogeneous half planes

$$\nabla^2 w_1+\beta\frac{\partial w_1}{\partial x}=0,\ 0<x<\infty,\ 0\le y<\infty, \tag{2}$$

$$\nabla^2 w_2+\gamma\frac{\partial w_2}{\partial x}=0,\ -\infty<x<0,\ 0\le y<\infty \tag{3}$$

$$w_1(0,y)=w_2(0,y), \tag{4}$$

$$\sigma_{1xz}(0,y)=\sigma_{2xz}(0,y), \tag{5}$$

$$w_1(x,0)=0,\ 0\le x<a,\ b<x<\infty \tag{6}$$

$$\sigma_{1yz}(x,+0)=p(x),\ a<x<b, \tag{7}$$

where it is assumed that the crack surface traction $p(x)$ is the only nonzero external load and that because of symmetry it is sufficient to consider the problem for $y>0$ only. Expressing the solution of (2) and (3) as

$$w_1(x,y)=\frac{1}{2\pi}\int_{-\infty}^{\infty} f_1(y,\alpha)e^{-i\alpha x}d\alpha + \frac{2}{\pi}\int_0^{\infty} g_1(x,\alpha)\sin y\alpha\, d\alpha, \tag{8}$$

$$w_2(x,y)=\frac{2}{\pi}\int_0^{\infty} g_2(x,\alpha)\sin y\alpha\, d\alpha, \tag{9}$$

we obtain

Contributed by the Applied Mechanics Division and presented at the Winter Annual Meeting, Miami, Fla., November 17–21, 1985 of The American Society of Mechanical Engineers.

Discussion on this paper should be addressed to the Editorial Department, ASME, United Engineering Center, 345 East 47th Street, New York, N.Y. 10017, and will be accepted until two months after final publication of the paper itself in the Journal of Applied Mechanics. Manuscript received by ASME Applied Mechanics Division, September, 1984; final revision, January, 1985. Paper No. 85-WA/APM-8.

Copyright © 1985 by ASME
Downloaded 02 May 2010 to 171.66.16.54. Redistribution subject to ASME license or copyright; see http://www.asme.org/terms/Terms_Use.cfm

$$f_1 = A(\alpha)e^{my},\ g_1 = B(\alpha)e^{nx},\ g_2 = C(\alpha)e^{\lambda x},$$

$$m = -\sqrt{\alpha^2 + i\beta\alpha},\ n = -\alpha_1 - \frac{\beta}{2},\ \lambda = \alpha_2 - \frac{\gamma}{2},$$

$$\alpha_1 = \sqrt{\alpha^2 + \beta^2/4},\ \alpha_2 = \sqrt{\alpha^2 + \gamma^2/4}. \tag{10}$$

The stress components are given by

$$\sigma_{1xz} = \mu_o e^{\beta x}\frac{\partial w_1}{\partial x},\ \sigma_{1yz} = \mu_o e^{\beta x}\frac{\partial w_1}{\partial y},\ (0<x<\infty, 0<y<\infty), \tag{11}$$

$$\sigma_{2xz} = \mu_o e^{\gamma x}\frac{\partial w_2}{\partial x},\ \sigma_{2yz} = \mu_o e^{\gamma x}\frac{\partial w_2}{\partial y},\ (-\infty<x<0, 0<y<\infty). \tag{12}$$

Substituting from (8)–(12) into the continuity conditions (4) and (5) it may easily be shown that

$$C(\alpha) - B(\alpha) = \frac{1}{2\pi}\int_{-\infty}^{\infty}\frac{\alpha A(\rho)d\rho}{\alpha^2 + \rho^2 + i\beta\rho}, \tag{13}$$

$$nB(\alpha) - \lambda C(\alpha) = \frac{1}{2\pi}\int_{-\infty}^{\infty}\frac{i\alpha\rho A(\rho)d\rho}{\alpha^2 + \rho^2 + i\beta\rho}. \tag{14}$$

Defining now

$$g(x) = \frac{\partial}{\partial x}w_1(x,0), \tag{15}$$

from (8), (10), and (6) we find

$$i\alpha A(\alpha) = -\int_a^b g(t)e^{i\alpha t}dt, \tag{16}$$

$$\int_a^b g(t)\,dt = 0. \tag{17}$$

By substituting from (16) into (13) and (14) and by using the residue theorem to evaluate the improper integrals and the condition (17), the unknown functions B and C may be obtained as follows:

$$B(\alpha) = \frac{\alpha\left(\alpha_1 - \alpha_2 + \frac{\gamma-\beta}{2}\right)}{2\alpha_1(\lambda - n)(\alpha_1 - \beta/2)}\int_a^b g(t)e^{-i(\alpha_1 - \beta/2)}dt, \tag{18}$$

$$C(\alpha) = \frac{\alpha}{(\lambda - n)(\alpha_1 - \beta/2)}\int_a^b g(t)e^{-i(\alpha_1 - \beta/2)}dt. \tag{19}$$

Thus $g(t)$ is the only unknown in the problem which may be determined from the remaining boundary condition (7). From (7), (8), (10), (11), (16), and (18) it then follows that

$$\sigma_{1yz}(x,0) = p(x) = \mu_o e^{\beta x}\frac{1}{\pi}\int_a^b [k_1(x,t) + k_2(x,t)]g(t)dt, a<x<b, \tag{20}$$

$$k_1(x,t) = \lim_{y\to+0}\frac{i}{2}\int_{-\infty}^{\infty}\frac{m(\alpha)}{\alpha}e^{my}e^{i\alpha(t-x)}d\alpha, \tag{21}$$

$$k_2(x,t) = \lim_{y\to+0} e^{(t-x)\beta/2} \times\int_0^{\infty}\frac{\alpha^2\left(\alpha_1 - \alpha_2 + \frac{\gamma-\beta}{2}\right)}{\alpha_1(\lambda - n)\left(\alpha_1 - \frac{\beta}{2}\right)}e^{-(t+x)\alpha_1}\cos\alpha y\,dx. \tag{22}$$

Referring to (10) and the regularity conditions at infinity it may be noted that $Re(m)<0$, $Re(n)<0$ and $Re(\lambda)>0$. The singular behavior of the kernels k_1 and k_2 may be obtained from the asymptotic analysis of the integrals in (21) and (22).

By observing that for large values of $\alpha, m(\alpha)\to -|\alpha|$, from (21) we find

$$k_1(x,t) = \lim_{y\to+0}\frac{i}{2}\int_{\infty}\frac{-|\alpha|}{\alpha}e^{-|\alpha|y}e^{i\alpha(t-x)}d\alpha + \frac{i}{2}\int_{-\infty}^{\infty}\left(\frac{m}{\alpha} + \frac{|\alpha|}{\alpha}\right)e^{i\alpha(t-x)}d\alpha \tag{23}$$

where because of uniform convergence, in the second integral the limit has been put under the integral. By evaluating the first integral k_1 is obtained as follows:

$$k_1(x,t) = \frac{1}{t-x} + h_1(x,t), \tag{24}$$

$$h_1(x,t) = Im\left\{\int_o^{\infty}\left(\sqrt{1 + \frac{i\beta}{\alpha}} - 1\right)e^{i\alpha(t-x)}da\right\}. \tag{25}$$

Further examination would show that h_1 has a logarithmic singularity at $t=x$ which can be separated as follows:

$$\begin{aligned} h_1(x,t) &= \int_0^{\infty}\left[\left(1 + \frac{\beta^2}{\alpha^2}\right)^{1/4}\cos\frac{\theta}{2} - 1\right]\sin\alpha(t-x)d\alpha \\ &+ \int_0^{A}\left(1 + \frac{\beta^2}{\alpha^2}\right)^{1/4}\sin\frac{\theta}{2}\cos\alpha(t-x)\,d\alpha \\ &+ \int_A^{\infty}\left[\left(1 + \frac{\beta^2}{\alpha^2}\right)^{1/4}\sin\frac{\theta}{2} - \frac{\beta}{2\alpha}\right]\cos\alpha(t-x)d\alpha \\ &+ \frac{\beta}{2}\int_A^{\infty}\frac{\cos\alpha(t-x)}{\alpha}d\alpha \end{aligned} \tag{26}$$

where

$$\tan\theta = \beta/\alpha \tag{27}$$

and A is any positive constant. In (26) the first three integrals on the right-hand side are bounded for all values of x and t in the closed interval $[a,b]$, $a>0$ and the fourth is a cosine integral which may be expressed as

$$\frac{\beta}{2}\int_A^{\infty}\frac{\cos\alpha(t-x)}{\alpha}d\alpha = -\frac{\beta}{2}\left[\gamma_0 + \log A + \log|t-x| + \int_0^{A(t-x)}\frac{\cos y - 1}{y}dy\right]. \tag{28}$$

where $\gamma_0 = 0.577216$ is the Euler's constant. The kernel $h_1(x,t)$ defined by (25) may now be written as

$$h_1(x,t) = -\frac{\beta}{2}\log|t-x| + h_2(x,t), \tag{29}$$

where h_2 is bounded in $a\le(x,t)\le b, a\ge 0$.

Similar asymptotic analysis would show that the kernel k_2 is bounded for $a>0$ (for which $t+x>0$), and has only a logarithmic end point singularity for $a=0$ (i.e., for $x+t\to 0$). We first write

$$k_2(x,t) = e^{(t-x)\beta/2}\int_0^{\infty}K_2(x,t,\alpha)\cos\alpha y\,d\alpha, \tag{30}$$

$$K_2(x,t,\alpha) = \frac{\alpha^2\left(\alpha_1 - \alpha_2 + \frac{\gamma-\beta}{2}\right)}{\alpha_1(\lambda - n)(\alpha_1 - \beta/2)}e^{-(t+x)\alpha_1}. \tag{31}$$

The limiting behavior of the integrand K_2 for $\alpha\to 0$ and for $\alpha\to\infty$ is

$$K_2 \to K_{2o}(x,t,\alpha) = \frac{2(\gamma-\beta)}{\gamma\beta^2}\alpha^2 e^{-(t+x)\beta/2},\ \text{for } \alpha\to 0, \tag{32}$$

$$K_2 \to K_{2\infty}(x,t,\alpha) = \frac{\gamma-\beta}{4}\frac{1}{\alpha}e^{-\alpha(t+x)},\ \text{for } \alpha\to\infty. \tag{33}$$

Downloaded 02 May 2010 to 171.66.16.54. Redistribution subject to ASME license or copyright; see http://www.asme.org/terms/Terms_Use.cfm

We now express k_2 as

$$k_2(x,t)=\lim_{y\to+0} e^{(t-x)\beta/2}\left[\int_0^{\epsilon} K_{2o}(x,t,\alpha)\cos\alpha y d\alpha + \int_{\epsilon}^{N} K_2(x,t,\alpha)\cos\alpha y d\alpha + \int_N^{\infty} K_{2\infty}(x,t,\alpha)\cos\alpha y d\alpha + \delta\right] \tag{34}$$

where ϵ is a very small and N is a very large constant and the constant δ may be made as small as we please by selecting ϵ sufficiently small and N sufficiently large. Note that in $\epsilon\le\alpha\le N$ K_2 is bounded and hence, the second integral in (34) is finite for all $x\ge 0$, $t\ge 0$. Equation (32) shows that the same is true also for the first integral in (34). The third integral is the exponential integral which may be expanded as

$$\lim_{y\to+0}\int_N^{\infty}\frac{e^{-\alpha(t+x)}}{\alpha}\cos\alpha y d\alpha=\lim_{y\to 0+} Re\{Ei[(t+x-iy)N]\}$$

$$=-\log(t+x)-\log N-\gamma_o-\frac{N^2}{2\cdot 2!}(t+x)^2+\frac{N^3}{3\cdot 3!}(t+x)^3-\ldots \tag{35}$$

where γ_o is the Euler's constant. One may note that if N is nonzero and finite then the exponential integral in (35) and consequently the kernel k_2 is bounded for all x and t in $0<(x,t)<b$ and has only a logarithmic singularity at $x=0=t$. It may now be observed that the kernels $\log(t+x)$ in (35) and $\log|t-x|$ in (29) are square integrable and would have no influence on the singular behavior of the solution of the integral equation (20). The dominant part of the integral equation has only a simple Cauchy kernel for $a=0$ as well as $a>0$ and its solution would be of the form [5]

$$g(t)=\frac{G(t)}{\sqrt{(t-a)(b-t)}},\ (0\le a<t<b). \tag{36}$$

3 Stress Intensity Factors

For $a>0$ we observe that (20) gives $\sigma_{1yz}(x,0)$ for $0<x<\infty$ and the function F defined by

$$F(x)=\int_a^b [h_1(x,t)+k_2(x,t)]g(t)dt \tag{37}$$

is bounded in the closed interval $a\le x\le b$. Thus (20) may be expressed as

$$\frac{1}{\mu_o}e^{-\beta x}\sigma_{1yz}(x,0)=\frac{i}{\pi}\int_a^b\frac{G(t)dt}{(t-x)X^+(t)}+F(x),(0<x<\infty) \tag{38}$$

where

$$X(z)=\sqrt{(z-a)(z-b)},X^+(t)=-X^-(t)$$
$$=\sqrt{(t-a)(t-b)},(z=x+iy). \tag{39}$$

Consider now the function

$$\phi(z)=\frac{1}{2\pi i}\oint_C\frac{G(s)ds}{(s-z)X(s)} \tag{40}$$

where the contour C encircles the crack and z is outside C. By shrinking the contour to the cut, from (38)–(40) it may be shown that

$$\frac{1}{\mu_o}e^{-\beta x}\sigma_{1yz}(x,0)=-\phi(x)+F(x),(0<x<a,b<x<\infty). \tag{41}$$

On the other hand, from (40) it follows that [5]

$$\phi(z)=\frac{G(z)}{X(z)}-P(z) \tag{42}$$

where $P(z)$ is the principal part of G/X at $|z|=\infty$. From (41) and (42) we find

$$\frac{1}{\mu_o}e^{-\beta x}\sigma_{1yz}(x,0)=-\frac{G(x)}{X(x)}+P(x)$$
$$+F(x),(0<x<a,b<x<\infty). \tag{43}$$

By observing that

$$X(x)=\sqrt{(x-b)(x-a)},(x>b);X(x)=-\sqrt{(a-x)(b-x)},(x<a), \tag{44}$$

the Mode *III* stress intensity factors at the crack tips may now be defined and expressed as follows:

$$k_3(b) = \lim_{x\to b}\sqrt{2(x-b)}\sigma_{1yz}(x,0)=-\mu_o e^{\beta b}\frac{G(b)}{\sqrt{(b-a)/2}}$$
$$= -\lim_{x\to b}\mu(x)\sqrt{2(b-x)}g(x), \tag{45}$$

$$k_3(a) = \lim_{x\to a}\sqrt{2(a-x)}\sigma_{1yz}(x,0)=\mu_o e^{\beta a}\frac{G(a)}{\sqrt{(b-a)/2}}$$
$$= \lim_{x\to a}\mu(x)\sqrt{2(x-a)}g(x). \tag{46}$$

For $a=0$ we define the stress intensity factor at the crack tip $x=0$ as follows:

$$k_3(0)=\lim_{x\to -0}\sqrt{-2x}\sigma_{2yz}(x,0). \tag{47}$$

To calculate $k_3(0)$ the asymptotic analysis of σ_{2yz} around the crack tip $x=0$ is needed. From (9), (12), and (19) σ_{2yz} may be expressed as

$$\sigma_{2yz}(x,y) = \mu_o e^{\gamma x}\frac{2}{\pi}\int_0^{\infty}C(\alpha)e^{\lambda x}\alpha\cos\alpha y d\alpha$$
$$= \mu_o e^{\gamma x}\frac{1}{\pi}\int_0^b h_3(x,t)g(t)e^{(\beta t-\gamma x)/2}dt \tag{48}$$

where

$$h_3(x,t)=\lim_{y\to+0}2\int_o^{\infty}\frac{\alpha^2 e^{\alpha_2 x-\alpha_1 t}\cos\alpha y}{(\lambda-n)(\alpha_1-\beta/2)}d\alpha. \tag{49}$$

By observing that $\alpha_1\to\alpha$, $\alpha_2\to\alpha$, $\lambda\to\alpha$, and $n\to-\alpha$ for $\alpha\to\infty$, from (49) we obtain

$$h_3(x,t) = \lim_{y\to+0}\int_o^{\infty}e^{-\alpha(t-x)}\cos\alpha y d\alpha$$
$$+\int_o^{\infty}\left[\frac{2\alpha^2 e^{\alpha_2 x-\alpha_1 t}}{(\lambda-n)(\alpha_1-\beta/2)}-e^{-\alpha(t-x)}\right]d\alpha \tag{50}$$

where the second integral is uniformly convergent. Note that in (50) $t>0$, $x<0$, and $t-x>0$. Thus, from

$$\lim_{y\to+0}\int_o^{\infty}e^{-\alpha(t-x)}\cos\alpha y d\alpha=\lim_{y\to+0}\frac{t-x}{(t-x)^2+y^2}=\frac{1}{t-x}, \tag{51}$$

and (50), σ_{2yz} may be obtained as follows:

$$\sigma_{2yz}(x,0)=\mu_o e^{\gamma x/2}\frac{1}{\pi}\int_o^b\left[\frac{1}{t-x}+H_3(x,t)\right]g(t)e^{\beta t/2}dt, \tag{52}$$

where the bounded kernel H_3 is given by the second integral in (50).

If we now substitute from (36) into (52) and follow an analysis similar to (37)–(44), the asymptotic expression for σ_{2yz} may be written as

$$\sigma_{2yz}(x,0)=\mu_o e^{\gamma x/2}\frac{G(x)e^{\beta x/2}}{\sqrt{(-x)(b-x)}}+K(x) \tag{53}$$

where K is a bounded function. Thus, from (53) and the definition of the stress intensity factor at $x=0$ as given by (47) it follows that

$$k_3(0)=\mu_o\frac{G(0)}{\sqrt{b/2}}=\lim_{x\to 0}\mu(x)\sqrt{2x}g(x). \tag{54}$$

The results obtained in this section clearly show that the

Downloaded 02 May 2010 to 171.66.16.54. Redistribution subject to ASME license or copyright; see http://www.asme.org/terms/Terms_Use.cfm

square-root character of the crack-tip singularity is unaffected by the discontinuity in the derivative of the shear modulus.

From (10) and (22) it may be seen that for $\gamma=\beta$ (i.e., for the case of single nonhomogeneous plane) the kernel k_2 is identically zero and the expressions (24) and (25) defining k_1 remain unchanged. Thus, with $k_2=0$, (20), (24), and (25) give the density function $g(x)$ as defined by (36) and the stress intensity factors are then obtained from (45) and (46).

4 The Rigid Half Space

In the special case of an elastic half space bonded to a rigid half space, $w_2=0$, (8) is still valid and A and B are given by (16) and (13) (with $C=0$), respectively. Following an analysis similar to that of Section 2 (equations (20)–(35)), it may easily be shown that in this case the integral equation (20) becomes

$$p(x) = \mu_0 e^{\beta x}\frac{1}{\pi}\int_a^b\left[\frac{1}{t-x}+h_1(x)-\frac{1}{t+x}e^{\beta(t-x)/2}\right.$$
$$\left.-h_2(x,t)e^{\beta(t-x)/2}\right]g(t)dt,(a<x<b) \tag{55}$$

where h_1 is given by (29) and

$$h_2(x,t)=\int_0^\infty\left[\frac{\alpha^2}{\alpha_1\left(\alpha_1-\frac{\beta}{2}\right)}e^{-\alpha_1(t+x)}-e^{-\alpha(t+x)}\right]d\alpha. \tag{56}$$

We note that for $\beta=0$ h_1 and h_2 vanish and (55) would reduce to the following known integral equation for the homogeneous half plane $x>0$ for which $w(0,y)=0$:

$$\frac{1}{\mu_0}p(x)=\frac{1}{\pi}\int_a^b\left(\frac{1}{t-x}-\frac{1}{t+x}\right)g(t)dt,\ (a<x<b). \tag{57}$$

For $a>0$, clearly the solution of (55) is of the form (36) and the solution may easily be obtained by following the technique described in, for example, [6]. In the limiting case of $a=0$, by expressing the solution of (55) as

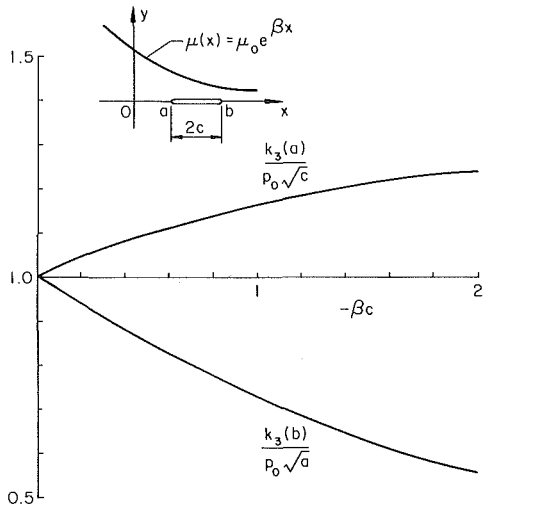


Fig. 2 Stress intensity factors for an infinite nonhomogeneous plane subjected to uniform crack surface traction $\sigma_{yz}(x,0)=-p_0$

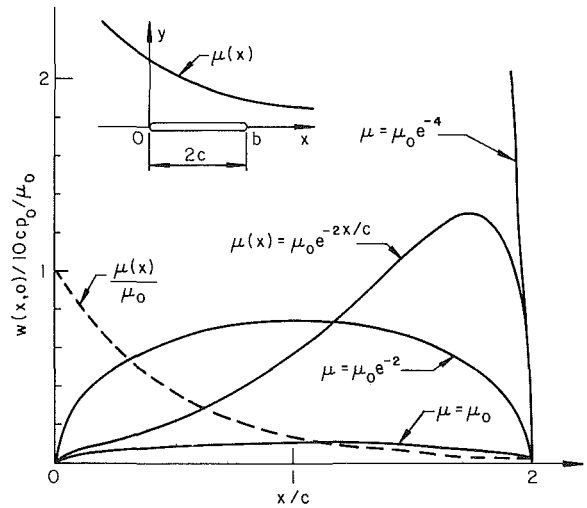


Fig. 3 Crack surface displacement in an infinite nonhomogeneous plane under uniform crack surface shear loading $\sigma_{yz}(x,0)=-p_0$; shear modulus $\mu(x)=\mu_0 e\beta x, \beta c=-2$

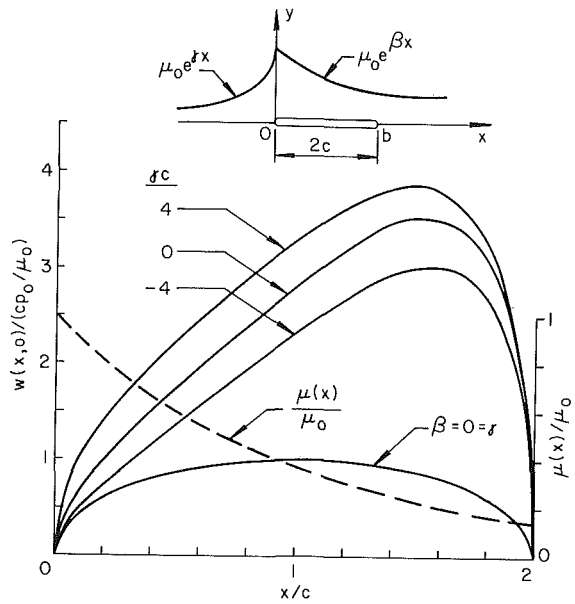


Fig. 4 Crack surface displacement in bonded nonhomogeneous half planes under uniform antiplane shear loading $\sigma_{1yz}(x,0)=-p_0$; $\mu(x)=\mu_0\exp(\beta x), x>0$; $\mu(x)=\mu_0\exp(\gamma x), x<0, \beta=-1$

Table 1 Stress intensity factor ratio $k_3/p_0\sqrt{c}$ in bonded nonhomogeneous half planes, $\gamma=-\beta$

d/c	1.0		1.1		1.25		1.5		2.0		5.0	
βc	$k(a)$	$k(b)$	$k(a)$	$k(b)$	$k(a)$	$k(b)$	$k(a)$	$k(b)$	$k(a)$	$k(b)$	$k(a)$	$k(b)$
−2.0	2.197	0.576	1.813	0.571	1.576	0.566	1.401	0.561	1.284	0.558	1.238	0.556
−1.5	1.943	0.666	1.684	0.657	1.514	0.649	1.377	0.641	1.270	0.633	1.211	0.629
−1.0	1.635	0.783	1.494	0.772	1.395	0.762	1.309	0.750	1.231	0.738	1.165	0.727
−0.5	1.303	0.909	1.252	0.902	1.216	0.894	1.183	0.885	1.149	0.874	1.104	0.857
−0.25	1.143	0.961	1.122	0.958	1.108	0.954	1.096	0.949	1.082	0.943	1.062	0.932
−0.1	1.054	0.986	1.047	0.984	1.042	0.983	1.038	0.981	1.034	0.979	1.028	0.975
0.0	1.0	1.0	1.0	1.0	1.0	1.0	1.0	1.0	1.0	1.0	1.0	1.0
0.1	0.952	1.015	0.958	1.016	0.962	1.018	0.965	1.019	0.968	1.020	0.971	1.023
0.25	0.889	1.038	0.901	1.041	0.909	1.043	0.915	1.046	0.921	1.049	0.927	1.054
0.5	0.799	1.074	0.820	1.078	0.831	1.083	0.841	1.087	0.848	1.092	0.854	1.098
1.0	0.664	1.136	0.693	1.142	0.707	1.149	0.717	1.155	0.723	1.160	0.726	1.163
1.5	0.570	1.185	0.601	1.192	0.615	1.199	0.623	1.204	0.627	1.208	0.629	1.210
2.0	0.503	1.218	0.535	1.224	0.546	1.230	0.553	1.234	0.556	1.237	0.556	1.238

Downloaded 02 May 2010 to 171.66.16.54. Redistribution subject to ASME license or copyright; see http://www.asme.org/terms/Terms_Use.cfm

Table 2 Stress intensity factor ratio $k_3/p_0\sqrt{c}$ in bonded nonhomogeneous half planes

d/c		1.0		1.1		1.25		1.5		2		5	
γc	βc	$k(a)$	$k(b)$	$k(a)$	$k(b)$	$k(a)$	$k(b)$	$k(a)$	$k(b)$	$k(a)$	$k(b)$	$k(a)$	$k(b)$
$\beta c/4$	−0.1	1.034	0.977	1.032	0.976	1.030	0.976	1.029	0.975	1.027	0.974	1.025	0.973
	−0.25	1.082	0.937	1.075	0.936	1.071	0.935	1.066	0.933	1.062	0.932	1.056	0.929
	−0.5	1.155	0.867	1.139	0.865	1.128	0.863	1.118	0.861	1.109	0.858	1.099	0.855
	−1.0	1.273	0.737	1.237	0.735	1.213	0.733	1.192	0.730	1.175	0.728	1.163	0.726
	−1.5	1.363	0.635	1.305	0.633	1.268	0.632	1.240	0.631	1.220	0.629	1.210	0.629
	−2.0	1.423	0.559	1.345	0.558	1.298	0.558	1.265	0.557	1.245	0.556	1.238	0.556
$4\beta c$	−0.25	0.975	0.906	0.999	0.909	1.015	0.912	1.028	0.916	1.040	0.920	1.053	0.927
	−1.0	0.950	0.713	1.036	0.716	1.087	0.719	1.124	0.722	1.150	0.724	1.163	0.726
	−2.0	0.947	0.553	1.094	0.554	1.167	0.555	1.211	0.556	1.233	0.556	1.238	0.556
0	−0.25	1.093	0.941	1.084	0.940	1.077	0.938	1.072	0.936	1.066	0.934	1.057	0.929
	−1.0	1.329	0.743	1.276	0.740	1.241	0.737	1.210	0.733	1.184	0.730	1.164	0.726
	−2.0	1.530	0.561	1.411	0.560	1.338	0.559	1.284	0.557	1.250	0.557	1.238	0.556
$-4\beta c$	−0.25	1.261	0.999	1.207	0.990	1.171	0.981	1.140	0.971	1.109	0.958	1.067	0.535
	−1.0	2.317	0.848	1.881	0.820	1.630	0.794	1.437	0.770	1.283	0.747	1.166	0.727
	−2.0	3.665	0.600	2.440	0.584	1.879	0.573	1.527	0.565	1.316	0.559	1.238	0.556
1	0	1.106	1.038	1.072	1.033	1.052	1.027	1.035	1.021	1.020	1.014	1.004	1.003
−1	0	0.907	0.966	0.935	0.970	0.952	0.975	0.967	0.980	0.980	0.987	0.996	0.997
5	0	1.383	1.097	1.213	1.076	1.132	1.057	1.077	1.040	1.038	1.023	1.005	1.004
−5	0	0.737	0.929	0.834	0.940	0.888	0.952	0.931	0.964	0.965	0.978	0.995	0.996
$\beta c/4$	0.25	0.913	1.049	0.918	1.050	0.921	1.051	0.923	1.052	0.925	1.053	0.927	1.055
	1.0	0.704	1.154	0.715	1.157	0.720	1.159	0.723	1.161	0.725	1.162	0.726	1.163
	2.0	0.537	1.232	0.549	1.234	0.553	1.236	0.555	1.237	0.556	1.238	0.556	1.238
$-4\beta c$	0.25	0.839	1.019	0.868	1.024	0.886	1.030	0.901	1.036	0.913	1.044	0.926	1.053
	1.0	0.595	1.111	0.657	1.123	0.687	1.135	0.707	1.147	0.720	1.157	0.726	1.163
	2.0	0.446	1.201	0.513	1.213	0.537	1.223	0.550	1.231	0.555	1.237	0.556	1.238
$4\beta c$	0.25	0.981	1.074	0.961	1.070	0.950	1.067	0.941	1.063	0.934	1.059	0.928	1.055
	1.0	0.802	1.184	0.758	1.177	0.742	1.172	0.733	1.168	0.728	1.165	0.726	1.163
	2.0	0.618	1.250	0.573	1.245	0.562	1.241	0.558	1.239	0.556	1.238	0.556	1.238
0	0.25	0.908	1.047	0.915	1.048	0.919	1.049	0.922	1.051	0.925	1.052	0.927	1.054
	1.0	0.696	1.151	0.710	1.154	0.717	1.157	0.722	1.159	0.725	1.162	0.726	1.163
	2.0	0.530	1.229	0.546	1.232	0.552	1.235	0.555	1.237	0.556	1.238	0.556	1.238

$$e^{\beta t}g(t) = G(t)(b-t)^{\omega_1}t^{\omega_2}, (-1 < Re(\omega_1, \omega_2) \le 0) \tag{58}$$

and by following the function theoretic method, it may easily be shown that (see, for example, [5] or [6])

$$G(b)\cot\pi\omega_1 = 0, \tag{59}$$

$$G(0)\left(\cot\pi\omega_2 - \frac{1}{\sin\pi\omega_2}\right) = 0. \tag{60}$$

Equations (59) and (60) are identical to the characteristic equations that would result from (57) and give $\omega_1 = -1/2$ and $\omega_2 = 0$ as the acceptable roots. It is, therefore, seen that at $t = 0$ $g(t)$ is bounded. Physically, this result is indeed expected, as the half plane problem with $w_1(0,y) = 0$ corresponds to the antisymmetric problem for the infinite plane for which $\mu(x) = \mu_0 e^{\beta|x|}$, which has a crack on the x axis along $-b < x < b$ subjected to antisymmetric shear tractions $\sigma_{yz}(x,0) = p(x) = -p(-x)$, $(-b < x < b)$.

5 Results and Discussion

The calculated results are shown in Figs. 2–4 and Tables 1 and 2. Figure 2 shows the stress intensity factors for an infinite plane with a shear modulus $\mu(x) = \mu_0 e^{\beta x}$ subjected to uniform shear tractions $\sigma_{1yz}(x,0) = -p_0$. These results are analogous to those given in [4] for the pressurized crack. As in [4], the normalized stress intensity factors are independent of the crack location d (see Fig. 1) and are functions of the dimensionless parameter βc only. At first sight the result given in Fig. 2 to the effect that the stress intensity factor $k_3(a)$ on the stiffer side of the medium is greater than $k_3(b)$ may appear to be somewhat paradoxical. However, this result may easily be explained by considering the corresponding crack surface displacements given in Fig. 3 and obtained from

$$w_1(x,+0) = \int_0^x g(t)dt, \ (0 < x < b). \tag{61}$$

The figure shows the normalized crack surface displacement $w_1(x,+0)$ for the nonhomogeneous infinite medium with $\mu(x) = \mu_0\exp(\beta x)$, $\beta c = -2$, and for the homogeneous planes with shear moduli $\mu = \mu(0) = \mu_0$, $\mu = \mu(c) = \mu_0 \exp(-2)$ and $\mu = \mu(b) = \mu_0\exp(-4)$. In the homogeneous planes the stress intensity factors are independent of μ and are given by

$$k_3(0) = k_3(b) = p_0\sqrt{c}, \tag{62}$$

whereas the crack surface displacement is inversely proportional to μ, i.e.

$$w(x,+0) = \frac{p_0}{\mu}\sqrt{x(b-x)}, \ (0 < x < b). \tag{63}$$

From Fig. 3 it is seen that near the crack tip $x = 0$ the crack surface displacement $w(x,0)$ for the nonhomogeneous medium is greater than that for the homogeneous medium having the modulus $\mu(0) = \mu_0$. Since the stress intensity factor k_3 is related to the magnitude of the crack surface displacement derivative (see (45), (46), and (54)), it would, therefore, be expected that (for $\beta < 0$) at $x = 0$ k_3 for the nonhomogeneous medium would be greater than $p_0\sqrt{c}$, the value for the corresponding homogeneous medium. Even though near $x = b$ $w(x,0)$ is considerably greater than that near $x = 0$, it is still smaller than the displacement for the homogeneous medium having $\mu = \mu(b)$ which also has $k_3(b) = p_0\sqrt{c}$. With (45), this would then explain the trend for the stress intensity factor at $x = b$ shown in Fig. 2, namely that $k_3(b) < p_0\sqrt{c}$.

Some sample results for the crack surface displacement in bonded nonhomogeneous half planes with a crack along $0 < x < b$ are shown in Fig. 4.

For uniform crack surface traction $\sigma_{1yz}(x,0) = -p_0$ Tables 1 and 2 show the calculated stress intensity factors normalized as

$$\frac{k_3(a)}{p_0\sqrt{c}} = k(a), \ \frac{k_3(b)}{p_0\sqrt{c}} = k(b). \tag{64}$$

Downloaded 02 May 2010 to 171.66.16.54. Redistribution subject to ASME license or copyright; see http://www.asme.org/terms/Terms_Use.cfm

Aside from the validity of the general trends given in Fig. 2 for the infinite medium, these results also conform to the broad principle that in bonded nonhomogeneous solids as the crack tip approaches the interface the corresponding stress intensity factor tends to decrease if the crack lies in the medium with the smaller shear modulus and increase if the crack lies in the stiffer medium.

It should perhaps be pointed out that even though the main result of this study, namely, that the square-root nature of the stress singularity is unaffected by the "kink" in $\mu(x)$, is based on a specific choice of the shear modulus ($\mu_0 e^{\beta x}$ for $x>0$, $\mu_0 e^{\gamma x}$ for $x<0$, $\beta \neq \gamma$), clearly the conclusion should be valid for any continuous function $\mu(x)$. One may, therefore, also conclude that the expression

$$k_3(0) = \lim_{x \to 0} \mu(x)\sqrt{2x}\frac{\partial}{\partial x} w(x,0)$$

for the stress intensity factor at a crack tip $x=0$ is valid for any $\mu(x)$ that is continuous at $x=0$.

Acknowledgments

This study was performed at the Fraunhofer-Institut für Feskörpermechanik in Freiburg, Germany while the author was an Alexander von Humboldt Senior U.S. Scientist Awardee. The author would also like to thank Dr. A.C. Kaya for carrying out the numerical calculations.

References

1 Cook, T. S., and Erdogan, F., "Stresses in Bonded Materials With a Crack Perpendicular to the Interface," *Int. J. Eng. Sci.*, Vol. 10, 1972, pp. 667–697.

2 Erdogan, F., and Cook, T. S., "Antiplane Shear Cracks Terminating at and Going Through a Bimaterial Interface," *Int. J. of Fracture*, Vol. 10, 1974, pp. 227–240.

3 Dhalival, R. S., and Singh, B. M., "On the Theory of Elasticity of a Nonhomogeneous Medium," *Journal of Elasticity*, Vol. 8, 1978, pp. 211–219.

4 Delale, F., and Erdogan, F., "The Crack Problem for a Nonhomogeneous Plane," ASME JOURNAL OF APPLIED MECHANICS, Vol. 50, 1983, pp. 609–614.

5 Muskhelishvili, N. I., *Singular Integral Equations*, P. Noordhoff, Groningen, Holland, 1953.

6 Erdogan, F., "Mixed Boundary Value Problems in Mechanics," *Mechanics Today*, Nemat-Nasser, S., ed., Vol. 4, 1978, pp. 1–81.

Downloaded 02 May 2010 to 171.66.16.54. Redistribution subject to ASME license or copyright; see http://www.asme.org/terms/Terms_Use.cfm

D. Krajcinovic
Professor,
Department of Civil Engineering,
Mechanics and Metallurgy,
University of Illinois at Chicago,
Chicago, Ill. 60680
Mem. ASME

Continuous Damage Mechanics Revisited: Basic Concepts and Definitions

The paper proposes a geometrically consistent representation for the set of internal variables defining an arbitrary distribution of flat, planar microcracks. A special averaging procedure in conjunction with a characteristic length leads to an experimentally identifiable measure or damage. The model makes an essential distinction between the active and passive microcrack systems. The progressive deterioration of the material is modeled by a combination of nucleation (activation of new systems) and continued growth or cracks in already active systems.

1 Introduction

The nonlinear behavior of engineering materials arises in general as a consequence of a specific pattern in irreversible changes of the microstructure. In case of ductile metals, the inelastic response (on the macroscale) often reflects twinning and slip on the multitude of crystallographic planes. In case of brittle solids the deviation from the elastic response is a result of the nucleation of new microcracks and the growth of existing microcracks.

The change in the dominant mode of the microstructural change has a profound effect on the macrostructural response in quantitative and qualitative sense. It is, therefore, not surprising that the theory of plasticity, eminently successful in dealing with ductile processes, proved to be of dubious utility in description of phenomena reflecting the change in the density and distribution of microcracks.

The recent development of the continuum damage mechanics (CDM), based on the premise that the present state of the solid may be measured locally by the density, distribution, and shape of microcracks, seems to offer a rational framework for the establishment of methods aimed for the prediction of the nonlinear response of brittle solids. The lack of a physically and geometrically acceptable definition of damage caused some confusion and spawned a host of substantially different methods [1] dealing with the same phenomenon. Consequently, it appears reasonable to focus at the outset on the establishment of a geometrically acceptable definition of basic variables.

While the theory of slip in a single crystal is reasonably well developed (see Hutchinson [2] or Asaro [3]), the extension of such a theory to a polycrystalline solid involving averaging in conjunction with substantial simplifications is too complicated for practical usage. A promising strategy is to establish amacromodel which will broadly mirror the salient trends of the microstructural kinetics "with more or less distortion and blurring of detail" (Hill [4]). Such a continuum macroscopic theory of slip was proposed by Rice [5, 6]. A similar strategy will be pursued in this paper to establish a theory for the nonlinear behavior of solids reflecting changes in the material integrity (i.e. accumulation of damage).

To focus on the most important aspects of the phenomenon, the considerations will be restricted to perfectly brittle solids under isothermal conditions. Furthermore, it will be assumed that the thermodynamics with internal variables applies [7–9] such that the observed nonequilibrium state can be sufficiently well approximated by a constrained state of thermodynamic equilibrium corresponding to the current values of a finite set of internal variables.

2 Basic Concepts

Consider a solid in which the nucleation and growth of microcavities is the only mode for irreversible changes in the microstructure. In a purely geometrical sense all microcavities can be classified with respect to their aspect ratio as microcavities and microcracks.

The influence of a dilute concentration of spheroidal microcavities on the state of the solid locally can be readily defined by a scalar function of coordinates (porosity), i.e., the volume average of voids (Davison et al. [10]). In case of larger concentration (over 10 percent, see [11]) the influence of the cavity shape may render the scalar representation inadequate. In view of the rather definitive treatment of solids containing microcavities proposed in [10] and other theories of porous materials, it appears reasonable to focus on the more contentious problem of solids weakened by an arbitrary distribution of flat, planar microcracks.

2.1 Single Microcrack. Assuming that in first approximation (or the zeroth-order moment theory in sense of Kroner [12]), the shape of the crack is a small effect of higher

Contributed by the Applied Mechanics Division and presented at the Winter Annual Meeting, Miami, Fla., November 17–21, 1985 of THE AMERICAN SOCIETY OF MECHANICAL ENGINEERS.

Discussion on this paper should be addressed to the Editorial Department, ASME, United Engineering Center, 345 East 47th Street, New York, N.Y. 10017, and will be accepted until two months after final publication of the paper itself in the JOURNAL OF APPLIED MECHANICS. Manuscript received by ASME Applied Mechanics Division, February, 1985. Paper No. 85-WA/APM-5.

Copyright © 1985 by ASME
Downloaded 02 May 2010 to 171.66.16.54. Redistribution subject to ASME license or copyright; see http://www.asme.org/terms/Terms_Use.cfm

order[1]. A single (penny-shaped) microcrack of area $\xi^{(i)}$ is defined by an axial vector

$$\xi^{(i)} = \xi^{(i)}\mathbf{N} \qquad (i=1,2,\ldots,n) \tag{1}$$

for which only the direction (normal $\mathbf{N}$) but not the sense is uniquely determined. The majuscules refer to the material coordinates. The change in $\xi^{(i)}$ is the fundamental measure of the local loss of bonds in the material [14].

Thus the internal state of the material weakened by n penny-shaped microcracks is fully defined by n internal variables $\xi^{(i)}$. In a general case the number n is very large and dependent on the size of the specimen. Moreover, the details of the "exact" distribution of microcrack are relatively unimportant since they change from one "identical" specimen to the other. As a consequence it is advisable to introduce the "averaging variables" $\omega^{(j)}$ $(j = 1, 2, \ldots k << n)$ (as in Rice [6]) being an appropriate measure of the microcrack distribution in a sample in a smoothed sense. These averaging variables which to a "suitable approximation" [6] may be considered as internal variables must obviously be related to the original internal variables

$$\omega^{(i)} = \omega(\xi^{(1)}, \xi^{(2)}, \ldots \xi^{(n)}; V^0) \qquad (i=1,2,\ldots k) \tag{2}$$

where V^0 indicates averaging over the volume.

2.2 System of Parallel Microcracks. Consider next a solid weakened by a large (but finite) number n of flat and parallel microcracks. The solution of the problem will obviously be facilitated if n original variables $\xi^{(i)}$ are suitably averaged into $k << n$ variables $\omega^{(j)}$. To retain the insight into the problem these variables ω should be "endowed with a clear physical meaning" [7]. Among several possible averaging processes it appears reasonable to select one providing a direct relation between the representation of the observed microcrack system and the concept of damage. The ratio of the void area to the total virgin area of a cross section is an almost universally accepted measure of damage. While intuitively appealing and physically sound, this proposition must be carefully examined within the context of the general formulation. Since the number of microcracks while large is still finite and the number of cross sections S parallel to the microcrack system infinite, the probability of a cross section S containing a microcrack is zero. The situation is even more obscure in the case or planes at an angle to the microcrack system since they do not suffer any loss of area at all.

The fact that the influence of the microcrack on the amount of the load bearing area in a cross section is related to their proximity implies existence of a characteristic length l. Instead of simple averaging (which would incidentally, in view of an infinite number of cross sections without crack, fail to work) it is more reasonable to revert again to the physics of the problem. Assuming that only those microcracks within the band $(-l < \zeta < l)$ will impair the load bearing capacity of S the area $\bar{\xi}$ of S (Fig. 1) not available for the transmission of stresses is

$$\bar{\xi}(\zeta,\eta) = \sum_i w^{(i)}(\eta_i - \eta)\xi^{(i)}(\zeta,\eta_i) \tag{3}$$

where the weighting function $w(\eta_i - \eta) = w(-\eta_i - \eta)$ reflecting the distance separating the microcrack from the plane S montonically decreases with the increasing distance from S satisfying conditions

$$w^{(i)} = 1 \quad \text{at} \quad \eta_i - \eta = 0$$
$$w^{(i)} = 0 \quad \text{for} \quad |\eta_i - \eta| \geq l$$

The characteristic length l in general depends on the material

[1] The results published by Budiansky and O'Connell [13] indicate that the elastic moduli of the material are quite insensitive to the planform of the microcrack.

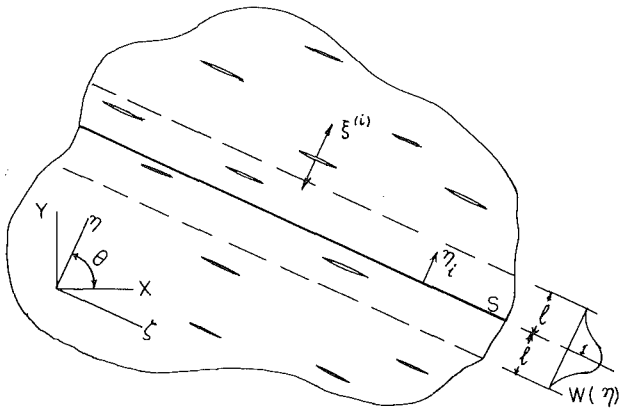


Fig. 1 A system of parallel microcracks $\omega^{(i)}$

and possibly the size of the microcracks as well. In general, the weighting function can conceivably be selected so that it reflects microcrack interaction etc.

Taking a large enough area A of S to contain a representative sample of discontinuity surfaces ξ (such that $\bar{\xi}$ does not vary significantly with ζ), a field of parallel microcracks can be represented by an axial vector

$$\omega_I(\zeta,\eta) = \frac{\bar{\xi}(\zeta,\eta)}{A} N_I = \omega N_I \tag{4}$$

where N_I is the normal to the microcrack field. Expression (4) averages a large number of independent vectorial delta functions (1) into a single vectorial function of coordinates.

2.3 General Microcrack Field. In general, the microdefects in polycrystalline solid with irregular microstructure do not develop in regular patterns. For simplicity consider the case when the normals N_I of all cracks are bedded in parallel planes z = const subtending angles $0 \leq \theta \leq \pi$ with the x-axis (Fig. 1). Furthermore, assign orientation $\theta^{(j)} = (j+1)\Delta\theta$ (where $j = 1, 2, \ldots m$ and $m = \pi/\Delta\theta$) to all cracks with orientations within a given range $(\theta^{(j)} - \Delta\theta \leq \theta^{(j)} \leq \theta^{(i)} + \Delta\theta)$. To each system of parallel microcracks with orientation $\theta^{(i)}$ corresponds an axial vector ω in sense of (4).

Thus, a general microcrack field (with an almost continuously changing θ) discretized into m parallel microcrack systems is represented by m vectorial functions of coordinates ω. These variables fully describe the microstructure within the proposed scheme and will be selected as "average" internal variables in the sense of Rice [6]. The degree of approximation depends on the magnitude of $\Delta\theta$. In the limit as $\Delta\theta \to 0$ or $m \to \infty$ the representation is obviously exact. It is perhaps interesting that a similar approach was suggested by Seaman, et al. [15] within a context of computational model for spalling. The generalization to nonplanar fields is trivial.

Several important implications reside with the representation (4). Firstly, through the characteristic length it entails the choice of scale (see Berg [16]). To capture the physics of the problem the elementary volume (or unit cube, Bishop and Hill [17]) must be large enough to contain sufficient number of microcracks (macrouniformity) and yet small enough to be mapped onto a material point. Additionally, implicit to the representation (4) is the assumption that the concentration of microcracks is dilute enough creating no significant overlap of projections.

2.4 Damage. Central to the proposed model is the distinction between the microcrack field and the concept of damage. To define the damage it is necessary to distinguish between active and passive microcrack systems. A microcrack field will be called active if the local stress or strain field allows discontinuities in the displacement field across the face of the crack. The criteria separating the active from passive

Downloaded 02 May 2010 to 171.66.16.54. Redistribution subject to ASME license or copyright; see http://www.asme.org/terms/Terms_Use.cfm

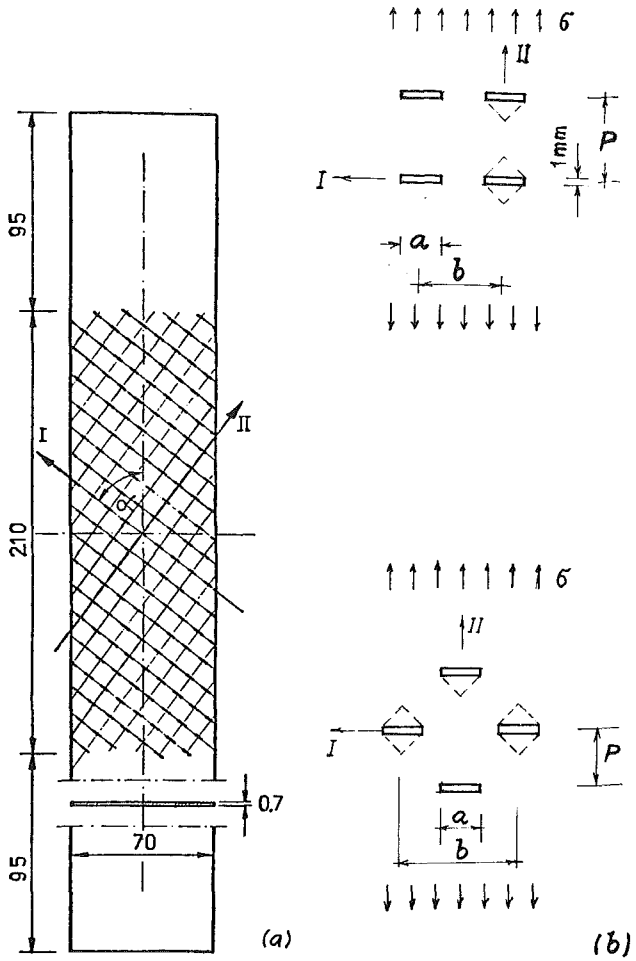


Fig. 2(a) Test specimen from references [20, 21] subjected to uniaxial tension along its axis. (b) Two different perforation patterns: rectangular and diamond, shown for case $\alpha = \pi/2$.

fields are discussed at some length by Horii and Nemat-Nasser [18] and Margolin [19].

In concert with the physical intuition, the scalar measure of the damage D in a plane with normal $\hat{\mathbf{N}}$ will be defined as a sum of projections of all active axial vectors $\omega^{(j)}$ ($j = 1,2, \ldots m_1$) on $\hat{\mathbf{N}}$

$$D^{(\hat{N})} = \sum_{j=1}^{m_1} \omega^{(j)} \mathbf{N}^{(j)} \hat{\mathbf{N}} = \sum_{j=1}^{m_1} \omega^{(j)} \cos\beta_j \tag{5}$$

where the scalar product $\mathbf{N}^{(j)} \cdot \hat{\mathbf{N}} = \cos\beta_j$ is, on purely physical grounds, taken as positive. This defines the orientation of the axial vector ω such that $-\pi/2 \le \beta_j \le \pi/2$. In the limit, as the number of microcrack fields m_1 tends to infinity the equation (5) can be rewritten as

$$D^{(N)} = \int_{\beta_a}^{\beta_b} \omega(\beta)\cos\beta \, d\beta \tag{6}$$

where $\beta_a \le \beta \le \beta_b$ defines the range of active fields.

As an illustration consider uniaxial tension of a brittle cylinder in the direction of the x-axis. The majority of the microcracks will develop in planes perpendicular to the maximum tensile strain. If the specimen is then unloaded and subsequently to a small compressive stress in the direction of the x-axis it will behave as undamaged since all of the existing microcrack fields will be passive, i.e., the damage will change even though the microstructure did not. Consequently, in contrast to the microcrack distribution the damage cannot be chosen as an internal variable since it depends on the state of stress.

The formulated representation allows for an interesting interpretation of the experimental results published by Litewka and Sawczuk [20, 21]. Two sets of metal specimens (aluminum alloy) weakened by two different patterns of machined perforations (5 mm by 1 mm) at different angles α (Fig. 2) were subjected to uniaxial tension. According to the measurements published in [21, 22] the response of the specimen, and in particular its rupture strength, proved to be pattern insensitive.

In view of the rather large dimension of perforation only a qualitative interpretation of these experiments based on the considered theory makes sense. For simplicity, consider only the case when the perforations are perpendicular to the tensile axis (Fig. 2(b)). Select the simplest, bilinear weighting function $w = (l - |\eta|)/l$ (dotted lines in Fig. 2(b)) where l is the radius of the largest "microcrack" (here, $l = a/2$). Adopting the criterion of Paterson [22] (p. 149)], according to which any narrow discontinuity up to several grain diameters in size can be classified as a microcrack, l can also be interpreted in general as a size of the source of inhomogeneity (grain or crystal). This assertion is in agreement with the observation of Hoagland et al. [23] and Pak and Trapeznikov [24] according to which the fracture mechanics leads to unreliable results in case of fissures less than two or three grain diameters in size. Finally, the proposed bilinear weighting (influence) function can be interpreted in sense of the stress diffusion through solids as the boundary (dotted lines in Fig. 2(b)) of the portion of the solid that does not participate in transmitting the stresses.

According to this model, the "damage" peaks in the cross section through the perforations where $D_{\max} = a/b$, for both patterns, and then linearly reduces to zero at $\eta = a/2 < P/2$. Naturally, the damage is identical for the two considered patterns as long as $P > a$. When the pitch reduces to $P < a$ the damage fields associated with the two lines of perforations will obviously interact. Finally, in the limit as $P \to 0$ the damage will obviously double in the case of the diagonal pattern and remain constant for the rectangular pattern. This is clear indication of the existence of a characteristic length.

Another important advantage of the suggested definition of damage is that it establishes a link between CDM and literature dealing with estimates of the elastic compliances of solids permeated by a large number of microcracks. For example, in [13, 18] the elastic compliance of an elastic solid weakened by a random distribution of flat, penny-shaped cracks is found to depend on a crack density parameter na^3 (where n is the number of cracks per unit of volume and a the crack radius). Assuming that all cracks are of the same size and that the stress diffuses through the solid at an angle of 45 deg, the loss of area $\bar{\xi}$ attributable to a single system of parallel microcracks is according to (3) $\bar{\xi} = Ma^3$, where $2Ma$ is the number of cracks of given orientation in volume ($2a \times 1 \times 1$). If the number of microsystems is m_1, then $n = 2m_1M$. For isotropic damage A_v is constant for every system. Letting $m_1 \to \infty$ at $n = \text{const.}$, from (5) it follows that

$$\omega = \frac{na^3}{\pi} \int_0^{2\pi} d\theta \int_0^{\pi/2} \sin \, d\phi = 2na^3 \tag{7}$$

where ϕ and θ are the spherical angles.

3 Microcrack Kinematics

The rate of change of the axial vector (4) consists of two terms

$$\dot{\omega}^{(\alpha)}_I = \dot{\omega}^{(\alpha)} N_I + \omega^{(\alpha)} \dot{N}_I = \dot{\omega}^{(\alpha)} N_I + \omega^{(\alpha)} \dot{\theta}_{IK} N_K \tag{8}$$

where $\dot{\theta}_{IK}$ is the rotation tensor. For small rotations

$$\dot{\omega}^{(\alpha)}_I = \dot{\omega}^{(\alpha)} N_I + \omega^{(\alpha)} e_{IJK} \dot{\theta}_J N_K \tag{9}$$

where e_{IJK} is the alternating tensor and $\dot{\theta}_J$ the change of the

Downloaded 02 May 2010 to 171.66.16.54. Redistribution subject to ASME license or copyright; see http://www.asme.org/terms/Terms_Use.cfm

angle subtended by the normal **N** and the axes of the coordinate system X. The first term in (9) represents the cleavage mode of the microcrack growth while the second term defines the "rotation" of the microcracks associated with the shear force [27]. The relations (8) and (9) tacitly assume that a flat but nonplanar microcrack is equipollent to its largest projection.

To simplify the model, at least loss of accuracy, it appears reasonable to neglect in first approximation the "rotation" of each microcrack system as a second-order effect. The gradual change of the orientation of the entire microcrack field will be reflected solely through the sequential activation of microcrack fields $\omega^{(j)}$. If desired the rotation can be introduced as indicated in references [26, 27].

4 Structure of Constitutive Relations

The essential structure of constitutive relations for the considered class of solids can be effectively established along the lines suggested by Rice [6]. The change in the internal energy u of a sample of initial volume V_0 in transition from one constrained equilibrium state to the neighboring one is

$$V^0\mathbf{S}:\delta\mathbf{E} - f^{(i)}\delta\xi^{(i)} + \theta\delta(V^0\eta) = \delta(V^0 u) \tag{10}$$

where $\mathbf{S}$ is the Kirchoff stress tensor, E the Lagrange (material) strain tensor, $f^{(i)}$ the thermodynamic forces conjugate to internal variables $\xi^{(i)}$, η the entropy, and θ the temperature.

Introducing the Helmholtz free energy density $\psi(\mathbf{E}, \theta, \xi)$ it follows that

$$\mathbf{S} = \frac{\partial\psi}{\partial\mathbf{E}} \tag{11}$$

and

$$f^{(i)} = -V^0\frac{\partial\psi}{\partial\xi^{(i)}} \tag{12}$$

As further shown in [6] if

$$\dot{\xi}^{(i)} = \dot{\xi}^{(i)}(f^{(i)}, \theta, \xi) \tag{13}$$

the flow potential exists and the normality structure of the constitutive equations follows. Note that (13) implies that the rate at which an internal variable changes depends on the stresses only through its conjugate thermodynamic force.

Introducing "average variables" $\omega^{(j)}$ in equations above $R^{(j)}\delta\omega^{(j)}$ replaces $(1/V^0)f^{(i)}\delta\xi^{(i)}$. Consequently, without duplicating details of the derivation presented in [6]

$$R^{(j)} = -\frac{\partial\psi(\mathbf{E},\theta,\omega)}{\partial\omega^{(j)}} \tag{14}$$

Moreover,

$$\dot{\omega}^{(j)} = \frac{\partial\omega^{(j)}(\xi, V^0)}{\partial\xi^{(i)}}\dot{\xi}^{(i)} = \frac{1}{V^0}\frac{\partial f^{(k)}(R,\xi)}{\partial R^{(j)}}\dot{\xi}^{(k)} \tag{15}$$

Consequently, since $\xi^{(i)}df^{(i)}$ (at fixed θ and ξ) is an exact differential, $\dot{\omega}$ is derivable from a potential $\Omega(R, \theta, \xi)$

$$\dot{\omega}^{(i)} = \frac{\partial\Omega(R,\theta,\xi)}{\partial R^{(i)}} \tag{16}$$

where

$$\Omega(R,\theta,\xi) = \frac{1}{V^0}\int_0^{f(R,\xi)}\dot{\xi}^{(i)}(f,\theta,\xi)df^{(i)} \tag{17}$$

If the condition (13) proves to be too restrictive, a potential can also be derived by an appropriate modification of the Drucker's stability postulate. Assuming that the complementary work on the irreversible changes of the crystalline microstructure is nonpositive for a closed loading cycle during which only incremental changes in the damage occur, it directly follows that

$$-\oint\omega^{(i)}dR^{(i)} = (\bar{R}^{(i)} - R^{(i)})d\omega^{(i)} \geq 0 \tag{18}$$

where $\bar{R}(i)$ is the current position of the "damage surface." The inequality (18) ensures the convexity of the flow potential, normality rule for the fluxes, and uniqueness (Hill [28]).

4.1 Helmholtz Free Energy (HFE). A significant step in the formulation of the theory consists of writing the HFE as a scalar invariant of the elastic strain tensor ϵ and a finite number of axial vectors $\omega^{(j)}$ ($j = 1, 2, \ldots m$). The problem of the determination of the basic absolute invariants and the irreducible integrity basis for a symmetric second-order tensor ϵ and a finite set of axial vectors $\omega^{(j)}$ under a full orthogonal group of transformations was addressed by at least two authors (Spencer [29] and Wang [30]) and their results need not be reproduced here. Restricting present considerations to infinitesimal strains and the generalization of the original Kachanov's model [31] the HFE must be quadratic in elastic strain and a homogeneous function of degree one in ω. As an illustration of the procedure take the form of HFE used in [26].

$$\rho\psi = \frac{1}{2}(\lambda+2\mu)\epsilon_{KK}\epsilon_{LL} - \mu(\epsilon_{KK}\epsilon_{LL} - \epsilon_{KL}\epsilon_{LK})$$

$$+\sum_\alpha\sum_\beta(\omega_p^\alpha\omega_p^\beta)^{-1/2}$$

$$(C_1\epsilon_{KL}\epsilon_{MM}\omega_K^\alpha\omega_L^\beta + C_2\epsilon_{KL}\epsilon_{LM}\omega_K^\alpha\omega_M^\beta) \tag{19}$$

where ρ is the mass density assumed to be constant, while λ and μ are Lame constants, which in general can depend on temperature, strain rate, and the density of spheroidal cavities [10]. The two additional parameters C_i define the influence of the microcracks on the free energy.

The stress tensor is from (11)

$$\sigma_{IJ} = \rho\frac{\partial\psi}{\partial\epsilon_{IJ}} = K_{IJKL}\epsilon_{KL} \tag{20}$$

where the stiffness tensor reads

$$K_{IJKL} = \lambda\delta_{IJ}\delta_{KL} + \mu(\delta_{IK}\delta_{JL} + \delta_{IL}\delta_{KJ})$$

$$+\sum_\alpha\sum_\beta(\omega_p^\alpha\omega_p^\beta)^{-1/2}[C_1(\delta_{IJ}\omega_K^\alpha\omega_L^\beta + \delta_{KL}\omega_I^\alpha\omega_J^\beta)$$

$$+C_2(\delta_{JK}\omega_I^\alpha\omega_L^\beta + \delta_{IL}\omega_J^\alpha\omega_K^\beta)] \tag{21}$$

If the direct coupling between various microcrack systems is neglected (i.e., if $\alpha = \beta$) expressions (19) and (21) can be further reduced to a simpler form. In the limit as $m \to \infty$

$$D_{KL} = \lim_{m\to\infty}\sum_{j=1}^{m}\omega^{(j)}N_K^{(j)}N_L^{(j)} =$$

$$= \int_{\theta_b}^{\theta_a}\int_{\phi_b}^{\phi_a}\omega(\theta,\phi)N_{KL}(\theta,\phi)d\phi d\theta \tag{22}$$

with $N_{KL}^{(j)}$ being the dyadic product of axial vectors $N_K^{(j)}$ $N_L^{(j)}$ with products of cosines of spherical coordinates θ and ϕ as its elements. As before, $\theta_a \leq \theta \leq \theta_b$ and $\phi_a \leq \phi \leq \phi_b$ define the set of all active microcrack fields (not necessarily contigious).

Therefore, the expressions for the HFE and the stiffness tensor can finally be written in the form

$$\rho\psi = \rho\psi^e + (C_1\epsilon_{MM}D_{KL} + C_2\epsilon_{LM}D_{KM})\epsilon_{KL} \tag{23}$$

$$K_{IJKL} = K_{IJKL}^e + 2C_1\delta_{IJ}D_{KL} + 2C_2\delta_{IK}D_{JL} \tag{24}$$

where the terms with superscript e refer to the part not af-

Downloaded 02 May 2010 to 171.66.16.54. Redistribution subject to ASME license or copyright; see http://www.asme.org/terms/Terms_Use.cfm

fected by ω (first two terms in (19) and (21)) while the remaining terms reflect the presence of the microcracks.

The second law of thermodynamics, i.e., the Clausius-Duhem inequality [6, 14]

$$\rho\dot{\mathfrak{D}} = \sum_{j=1}^{m_1} R_I^{(j)} \dot{\omega}_I^{(j)} = \sum_{j=1}^{m_1} R^{(j)} \dot{\omega}^{(j)} \geq 0 \tag{25}$$

where $R_I^{(j)} = R^{(j)} N_I^{(j)}$, places further restrictions on the model. From (14) and (19)

$$\begin{aligned} -R_I^{(j)} &= (\omega_p^{(j)} \omega_p^{(j)})^{-1/2} 2\epsilon_{IL} (C_1 \epsilon_{MM} \omega_L^{(j)} + C_2 \epsilon_{LM} \omega_M^{(j)}) \\ &+ (\omega_p^{(j)} \omega_p^{(j)})^{-3/2} \epsilon_{KL} \omega_K^{(j)} \omega_I^{(j)} (C_1 \epsilon_{MM} \omega_L^{(j)} + C_2 \epsilon_{LM} \omega_M^{(j)}) \end{aligned} \tag{26}$$

Passing again to the limit, as the number of microcrack systems tends to infinity, in conjunction with (22) it follows

$$\rho\dot{\mathfrak{D}} = -3\epsilon_{IL}(C_1 \epsilon_{MM} \dot{D}_{IL} + C_2 \epsilon_{LM} \dot{D}_{IM}) \geq 0 \tag{27}$$

It is also interesting to note that **R** has the form of the fracture mechanics "crack resistance force."

4.2 Damage Law. The kinetic equations relating the flux rates $\dot{\omega}^{(i)}$ and their affinities are derived from a potential using either (16) or (18). In principle, to be acceptable a specific form of the flow potential (damage surface) should reflect the salient aspects of the physical phenomenon. The gradual deterioration of the material results from the continuing growth of cracks in the already active systems and the progressive activation (nucleation) of the new systems. Thus the damage surface in many ways resembles the yield surface (Hill [4]) in the slip theories. The elastic region $\Omega < 0$ (the locus of points which can be reached without change in the recorded history) is in the space of thermodynamic forces **R** enclosed by a polyhedral cylinder. Every face of the cylinder corresponds to an active microcrack system.

Denoting by $\bar{R}^{(i)}$ the current position of the face (i) of the damage surface, an active microcrack system $\omega^{(i)}$ is potentially operative if

$$R^{(i)} = \bar{R}^{(i)} \tag{28}$$

Consequently, the system (i) is considered operative if the microcrack density increases, i.e.

$$\dot{\omega}^{(i)} > 0 \quad \text{if} \quad R^{(i)} = \bar{R}^{(i)} \quad \text{and} \quad \dot{R}^{(i)} \frac{\partial \Omega}{\partial R^{(i)}} > 0 \tag{29}$$

The damage rate is from the normality condition (16)

$$\dot{\omega}^{(i)} = \lambda \frac{\partial \Omega}{\partial R^{(i)}} \tag{30}$$

where the scalar λ is determined from the consistency equation. A stress point will during loading in general be attracted to a pointed vertex corresponding to the envelope associated with all operative and potentially operative microcrack systems.

In a general case of loading a point in the **R** space reaches some initial threshold value $\bar{R}_0$ along a preferred direction determined by the prevailing field of elastic strains and the already accumulated (operative) damage. As soon as the condition (28) is reached the cracks in that system are nucleated (if they did not exist previously) or commence their growth (if they were already there). As the external load further increases and as the face $\bar{R}^{(k)}$ translates as the history is being recorded, the stress point will reach the vertex of the damage surface where the faces $\bar{R}^{(k)}$ and $\bar{R}^{(k+1)}$ intersect. The kinetics of the damage growth consist, therefore, of the progressive growth of cracks in the already active systems and the sequential activation (nucleation of cracks) of the new systems. The situation is in principle similar to one discussed in detail by Hill [4] in connection with the slip theory.

To define the microcrack kinetics it is necessary to determine the initial shape of the damage surface (i.e., threshold value $\bar{R}_0^{(i)}$) as well as the manner in which it moves and distorts (i.e., dependence of the crack resistance $\bar{R}_0^{(i)}$ on $\omega^{(j)}$). While some preliminary speculations may be borrowed from the slip theories a comprehensive experimental program using various methods of nondestructive testing (see, for example [32]) will be needed before any more definitive answers can be reached.

5 Summary and Conclusions

The present paper focuses on the basic aspects of the mechanics of solids weakened by an arbitrary distribution of flat, planar microdefects. The solid is assumed to be perfectly brittle, leaving microcracks as the exclusive source of the material nonlinearity.

The proposed model is geometrically consistent and preserves the essential features of the physical process. The gradual deterioration of the material is modeled through nucleation of new microcracks and growth of the already existing microcracks. The distinction between the microcrack distribution and the damage is perhaps the most important feature of the proposed model. Since the damage depends on the state of stress (tension or compression) only the variables defining the microcrack distribution can be chosen as internal variables. Instead of considering every microcrack independently the paper suggests an averaging procedure approximating a multitude of vertorial delta functions ξ by a system of "averaging" internal variables ω in form of vectorial functions of coordinates. The number of variables ω depends on the desired degree of approximation.

In addition to its obvious intuitive appeal the proposed averaging procedure leads to a rational definition of damage based on the Kachanov's damage measure and establishes a direct link to the volume average of defects on which the passive models estimating the elastic compliances of solids with defects are based.

The proposed model, motivated by the micromechanical kinematics, has the mathematical structure not unlike that of some of the slip theories. This should facilitate use of the existing algorithms and numerical schemes after appropriate modifications. The proposed model in the limit becomes equivalent to some of the phenomenological models based on the tensorial damage variable if the status of the microcracks does not change from active to passive and vice versa. Consequently, the equivalence ceases to exist whenever the orientations of the principal axis of the stress or strain tensor change.

Acknowledgment

This research was supported by the U.S. Department of Energy, Office of Basic Energy Sciences, Engineering Research Program to the University of Illinois at Chicago. Numerous discussions and many useful suggestions made by Dr. M. G. Srinivasan (Argonne National Laboratory) and R. Ilankamban (University of Illinois at Chicago) are gratefully acknowledged.

References

1 Krajcinovic, D., "Continuous Damage Mechanics," *Appl. Mech. Rev.*, Vol. 37, 1984, pp. 1-6.

2 Hutchinson, J. W., "Elastic-Plastic Behavior of Polycrystalline Metals and Composites," *Proc. Royal Soc. Lond.*, Series *A*, Vol. 319, 1970, pp. 247-272.

3 Asaro, R. J., "Crystal Plasticity," JOURNAL OF APPLIED MECHANICS, Vol. 50, 1983, pp. 921-934.

4 Hill, R., "The Essential Structure of Constitutive Laws for Metal Composites and Polycrystals," *J. Mech. Phys. Solids*, Vol. 15, 1967, pp. 79-95.

5 Rice, J. R., "On the Structure of Stress-Strain Relations for Time-Dependent Plastic Deformations in Metals," ASME JOURNAL OF APPLIED MECHANICS, Vol. 37, 1970, pp. 728-737.

6 Rice, J. R., "Inelastic Constitutive Relations for Solids: An Integral Variable Theory and its Application to Metal Plasticity," *J. Mech. Phys. Solids*, Vol. 19, 1971, pp. 433-455.

Downloaded 02 May 2010 to 171.66.16.54. Redistribution subject to ASME license or copyright; see http://www.asme.org/terms/Terms_Use.cfm

7 Kestin, J., and Bataille, J., "Irreversible Thermodynamics of Continua and Internal Variables," in *Continuum Models of Discrete Systems*, Provan, J. W. ed., Univ. of Waterloo Press, 1978.

8 Kestin, J., and Rice, J. R., "Paradoxes in Application of Thermodynamics to Strained Solids," in *A Critical Review of Thermodynamics*, Stuart, E. B., et al., eds., Mono Book Corp., Baltimore, 1970.

9 Rice, J. R., "Continuum Mechanics and Thermodynamics of Plasticity in Relation to Microscale Deformation Mechanisms," in *Constitutive Equations in Plasticity*, Argon, A. S., ed., The MIT Press, 1975.

10 Davison, L., Stevens, A. L., and Kipp, M. E., "Theory of Spall Damage Accumulation in Ductile Metals," *J. Mech. Phys. Solids*, Vol. 25, 1977, pp. 11-28.

11 Iwakuma, T., and Nemat-Nasser, S., "Composites With Periodic Microstructure," *Computers and Structures*, Vol. 16, 1983, pp. 13-19.

12 Kroner, E., "Dislocation: A New Concept in the Continuum Theory of Plasticity," *J. Math and Physics*, Vol. 42, 1962, pp. 27-37.

13 Budiansky, B., and O'Connell, R. J., "Elastic Moduli of a Cracked Solid," *Int. J. Solids Structures*, Vol. 12, 1976, pp. 81-97.

14 Davison, L., and Stevens, A. L., "Thermomechanical Constitution of Spalling Elastic Bodies," *J. Appl. Phys.*, Vol. 44, 1973, pp. 668-674.

15 Seaman, L., Curran, D. R., and Shockey, D. A., "Computational Models for Ductile and Brittle Fracture," *J. Appl. Phys.*, Vol. 47, 1976, pp. 4814-4826.

16 Berg, C. A., "Plastic Dilation and Void Interaction," in *Inelastic Behavior of Solids*, Kanninen, M. F., et al., eds., McGraw-Hill, 1970, pp. 171-210.

17 Bishop, J. F. W., and Hill, R., "A Theory of Plastic Distortion of A Polycrystalline Aggregate Under Combined Stress," *Phil. Mag.*, Vol. 42, 1951, pp. 414-427.

18 Horii, H., and Nemat-Nasser, S., "Overall Moduli of Solids With Microcracks:, Load-Induced Anisotropy," *J. Mech. Phys. Solids*, Vol. 31, 1983, pp. 155-171.

19 Margolin, L. G., "Elastic Moduli of a Cracked Body," *Int. J. of Fracture*, Vol. 22, 1983, pp. 65-79.

20 Litewka, A., and Sawczuk, A., "A Yield Criterion for Perforated Sheets," *Ing.-Archiv*, Vol. 50, 1981, pp. 393-400.

21 Litewka, A., and Sawczuk, A., "Experimental Evaluation of the Overall Anisotropic Response at Continuous Damage," tp appear.

22 Paterson, M. S., *Experimental Rock Deformation — The Brittle Field*, Springer-Verlag, 1978.

23 Hoagland, R. G., Hahn, G. T., and Rosenfeld, A. R., "Influence of Microstructure on Fracture Propagation in Rock," *Rock Mechanics*, Vol. 5, 1973, pp. 77-106.

24 Pak A. P., and Trapeznikov, L. P., "Experimental Investigations Based on the Griffith-Irwin Theory Processes on the Crack Development in Concrete," in *Advances in Fracture Research — Fracture 81*, Vol. 4, Francois, D., ed., 1981, pp. 1531-1539.

25 Krajcinovic, D., and Fonseka, G. U., "The Continuous Damage Theory of Brittle Material—Parts I, II," ASME JOURNAL OF APPLIED MECHANICS, Vol. 48, pp. 809-815 and pp. 816-824.

26 Krajcinovic, D., "Constitutive Equations for Damaging Materials," ASME JOURNAL OF APPLIED MECHANICS, Vol. 50, 1983, pp. 355-360.

27 Krajcinovic, D., and Selvaraj, S., "Constitutive Equations for Concrete," in *Proc. Int. Conf. on Constitutive Laws for Engineering Materials*, Desai, C. S., and Gallagher, R. H., eds., Tucson, 1983, pp. 399-406.

28 Hill, R., "Generalized Constitutive Relations for Incremental Deformation of Metal Crystals by Multislip," *J. Mech. Phys. Solids*, Vol. 14, 1966, pp. 95-101.

29 Spencer, A. J. M., "Theory of Invariants," in *Continuum Physics*, Vol. 1, Eringen, A. C., ed., Academic Press, 1971.

30 Wang, C.-C., "A New Representation Theorem for Isotropic Functions," *Arch. Rational Mech. Anal.*, Vol. 36, 1970, pp. 166-197.

31 Kachanov, L. M., "On the Creep Rupture Time," *Izv. AN SSSR, Otd. Tekhn. Nauk*, No. 8, 1958, pp. 26-31 (in Russian).

32 McGonnagle, W. J., "Nondestructive Testing," Chapter 6 in *Fracture, an Advanced Treatise* Vol. 3, Liebowitz, H., ed., Academic Press, 1971.

33 Vakulenko, A. A., and Kachanov, M. L., "Continuum Theory of Cracked Media," *Mekh. Tverdogo Tela*, Vol. 6, 1971, pp. 159-166 (in Russian).

34 Murakami, S., and Ohno, N., "A Continuum Theory of Creep and Creep Damage," in *Creep in Structures*, Ponter, A. R. S., ed., Springer-Verlag, 1981.

35 Leckie, F. A., and Onat, E. T., "Tensorial Nature of Damage Measuring Internal Variables," in IUTAM *Physical Non-Linearities in Structural Analysis*, Hult, J., and Lemaitre, J., eds., Springer-Verlag, 1981.

36 Betten, J., "Damage Tensors in Continuum Mechanics," *J. de. Mec. Theor. et Appl.*, Vol. 2, 1983, pp. 13-32.

APPENDIX

Having in mind the regularity at which the second-order tensors appear in continuum mechanics, it is by no means surprising that various tensor representations of the damage variable found many proponents. The present representation motivated solely by the geometry of the microstructural kinetics is by no means related to those suggested by Vakulenko and Kachanov [33], Murakami and Ohno [34], Leckie and Onat [35], Betten [36], and others. The essential differences between these and present model consists of the introduction of the characteristic length, distinction between the active, operative, and inactive microcrack fields, and distinction between the damage and the microcrack distribution (alluded to in [20, 21]) as presented in this paper.

The mathematical representations introduced in this paper are consistent with the actual geometry in an appropriately smoothed sense with as little arbitrariness as possible. It is, nevertheless, useful to clarify some relatively important though perhaps formal aspects of the model. On the purely physical grounds the scalar measure of the damage $D(\hat{\mathbf{N}})$ in the plane with normal $\hat{\mathbf{N}}$ must be non-negative. Therefore, in (5) $-\pi/2 \leq \beta_j \leq \pi/2$ for all $j = 1$ to m. This amounts to selecting as the normal $\hat{\mathbf{N}}$ to the microcrack field one that subtends the acute angle with $\mathbf{N}$. Once that is done no further ambiguities occur.

An axial (relative, oriented, or pseudo) vector $\mathbf{U}$ transforms according to the rule [29]

$$U_I = |M_{IJ}| M_{IK} \bar{U}_K \tag{A.1}$$

where the determinant $|M_{IJ}|$ of the orthogonal transformations can be either positive (for proper orthogonal transformation) or negative. As a result it readily follows that the scalar product of two relative vectors (5) is an absolute invariant. Moreover, the product of two axial vectors

$$U_I V_K = |M_{IJ}|^2 M_{IJ} M_{KL} \bar{U}_J \bar{V}_K \tag{A.2}$$

transforms (for a full group of orthogonal transformations) as an absolute second-order tensor. Consequently, D_{KL} as defined by (22) for $\alpha = \beta$ is a second-order tensor. However, if $\alpha \neq \beta$ (i.e., in case of a direct interaction of damage fields) this is not necessarily true.

It must also be noted that the tensor D_{KL} can always be uniquely determined knowing $\omega^{(i)}$. The opposite is obviously not true.

Downloaded 02 May 2010 to 171.66.16.54. Redistribution subject to ASME license or copyright; see http://www.asme.org/terms/Terms_Use.cfm

B. L. Karihaloo
Professor,
Department of Civil Engineering
and Surveying,
University of Newcastle,
New South Wales, Australia 2308
Mem. ASME

K. Viswanathan
Principal Scientific Officer,
Defence Science Centre,
Metcalfe House,
Delhi, India 110054

Elastic Field of a Partially Debonded Elliptic Inhomogeneity in an Elastic Matrix (Plane-Strain)

The problem of the stress-field of an elliptic inhomogeneity that has debonded over an arc of its common boundary with a different elastic material is studied under plane-strain conditions. Eshelby's method of equivalent inclusion is employed. The "equivalence relation" is solved by a method that is applicable to any general plane-strain situation. Further, the relative displacements of the debonded faces are derived from the discontinuous behavior of ***individual terms*** *associated with the derivatives of Green's function. Numerical results are presented for the stress-intensity factors at the tips of the debonded arc and the relative displacements across the debond.*

1 Introduction

While the problem of the elastic field due to an inhomogeneity embedded in a matrix has been well studied in recent years [1–3], there does not seem to be much progress in the context of the field due to a partially debonded inhomogeneity. This is in a way due to the fact that the analytical solution by the "boundary-value problem" method is usually very complicated. In a recent investigation [4] (this paper also contains other useful references), the authors demonstrated how Eshelby's method [1] of equivalent inclusions can be adapted to the case of a debonded inhomogeneity in antiplane-strain conditions. In the present work, we extend the previous method to the study of a debonded inhomogeneity under plane-strain conditions. The extension is by no means straightforward, especially when Poisson's ratios of the matrix and inhomogeneity are unequal. In the present work we derive the general solution (for arbitrary Poisson's ratios; $\nu \neq \nu_1$) by a new approach. Additionally, we investigate certain properties of the discontinuous behavior of some of the functions that constitute the various derivative terms of Green's function describing the problem. These are discussed in detail during the derivation of the expressions for relative displacements of the debonded faces. Several numerical examples are given to illustrate the variation of the stress-intensity factors at the tips of the debonded arc in terms of the various material and geometrical parameters of the problem. The shapes of the deformed debond arc are also shown.

2 Statement of the Problem

The geometry of the elliptic inhomogeneity (Ω) and the coordinate axes, together with the debonded arc (Γ) are shown in Fig. 1. (λ, μ) and (λ_1, μ_1) denote the Lamé constants of the matrix and inhomogeneity, respectively.

The elastic equilibrium in the matrix is governed by the equations

$$\sigma_{ij,j}(\mathbf{u}) + X_i = 0 \tag{2.1}$$

where σ_{ij} is the usual stress-operator, $\mathbf{u} = (u_1, u_2)$ is the displacement vector, and X_i $(i = 1, 2)$ are the body force components $\{X_i \equiv X_i(\mathbf{x})\}$.

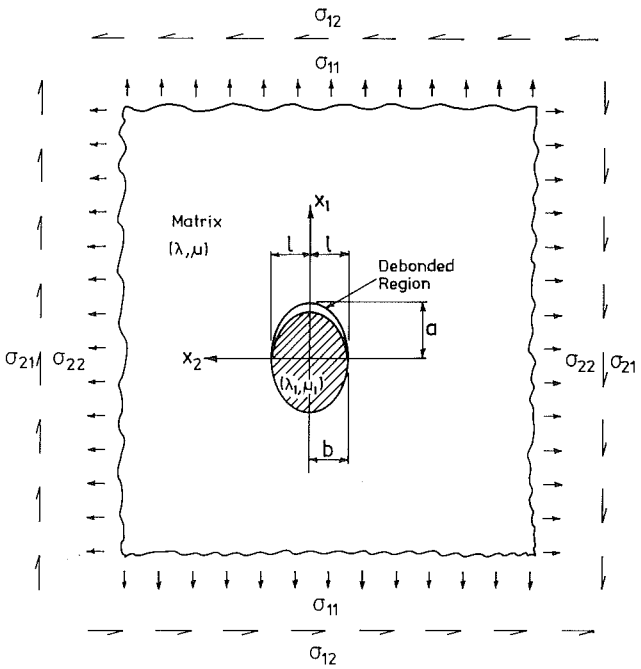


Fig. 1 The elliptic inhomogeneity (Ω) with debonding over an arc (Γ)

Contributed by the Applied Mechanics Division for publication in the JOURNAL OF APPLIED MECHANICS.

Discussion on this paper should be addressed to the Editorial Department, ASME, United Engineering Center, 345 East 47th Street, New York, N.Y. 10017, and will be accepted until two months after final publication of the paper itself in the JOURNAL OF APPLIED MECHANICS. Manuscript received by ASME Applied Mechanics Division, August, 1984; final revision, October, 1984.

Copyright © 1985 by ASME
Downloaded 02 May 2010 to 171.66.16.54. Redistribution subject to ASME license or copyright; see http://www.asme.org/terms/Terms_Use.cfm

The Green's function $G_{km}(x, x')$ is governed by the equation [3]

$$\sigma_{ij,j}(\mathbf{G}^m) = -\delta_{im}\delta(\mathbf{x}-\mathbf{x}') \tag{2.2}$$

where $\mathbf{G}^m$ denotes the vector $G_{km}(\mathbf{x},\mathbf{x}')$ for a fixed m. $\delta_{im} = 0(i \neq m)$, $\delta_{mm} = 1$, denotes the Kronecker delta function, and $\delta(\mathbf{x}-\mathbf{x}')$ the Dirac delta function.

From (2.1) and (2.2) we obtain

$$\int_V [G_{im}(\mathbf{x},\mathbf{x}')\sigma_{ij,j}\{u(\mathbf{x}')\} - u_i(\mathbf{x}')\sigma_{ij,j}\{\mathbf{G}^m(\mathbf{x},\mathbf{x}')\}]dV(\mathbf{x}')$$

$$= \int_V [\delta(\mathbf{x}-\mathbf{x}')\delta_{im}u_i(\mathbf{x}') - X_i(\mathbf{x}')G_{im}(\mathbf{x},\mathbf{x}')]dV(x')$$

$$= u_m(\mathbf{x}) - \int_V X_i(\mathbf{x}')G_{im}(\mathbf{x},\mathbf{x}')dV(\mathbf{x}'); \quad (\mathbf{x}\subset V) \tag{2.3}$$

where V denotes any region in the x_1, x_2 plane. After rearranging the terms in (2.3), we obtain

$$u_m(\mathbf{x}) = \int_V X_i(\mathbf{x}')G_{im}(\mathbf{x},\mathbf{x}')dV(\mathbf{x}') + \int_S [G_{im}(\mathbf{x},\mathbf{x}')\sigma_{ij}\{u(\mathbf{x}')\} - u_i(\mathbf{x}')\sigma_{ij}\{G^m(\mathbf{x},\mathbf{x}')\}]n_j(\mathbf{x}')dS(\mathbf{x}') \tag{2.4}$$

where we have used Green's Theorem to replace the integration over the region V by the equivalent integral over its boundary S. In (2.4), $n_j(\mathbf{x})$ denotes the unit (outward) normal at any point $\mathbf{x}$ on S. We now apply (2.4) to the whole domain and allow S to denote the two faces of the debonded arc Γ. Assuming that $X_i(x)$ vanish outside of Ω, (2.4) finally gives

$$u_m(\mathbf{x}) = \int_\Omega X_i(\mathbf{x}')G_{im}(\mathbf{x},\mathbf{x}')d\Omega(\mathbf{x}') - \fint_\Gamma \gamma_i(\mathbf{x}')\sigma_{ij}\{\mathbf{G}^m(\mathbf{x},\mathbf{x}')\}n_j(\mathbf{x}')d\Gamma(\mathbf{x}') \tag{2.5}$$

The first term under the integral over S in (2.4) vanishes due to the continuity of stresses across Γ, but the second term leads to the integral over Γ in (2.5) with $\gamma_i(\mathbf{x})$ denoting the relative displacement of the two faces of Γ. [The symbol $\fint$ denotes the principal value of the integral].

Following Eshelby [1], we replace the inhomogeneity by the same material as that of the matrix but with a suitable eigenstrain e^*_{ij} so that

$$X_i = -\sigma^*_{ij,j} = -\{\lambda\,\delta_{ij}(e^*_{11}+e^*_{22}) + 2\mu\, e^*_{ij}\}_{,j} \tag{2.6}$$

Thus (2.5) may be rewritten as

$$u_m(\mathbf{x}) = -\int_\Omega \sigma^*_{ij,j}(\mathbf{x}')G_{im}(\mathbf{x},\mathbf{x}')d\Omega(\mathbf{x}') - \fint_\Gamma \gamma_i(\mathbf{x}')\sigma_{ij}\{\mathbf{G}^m(\mathbf{x},\mathbf{x}')\}n_j(\mathbf{x}')d\Gamma(\mathbf{x}') \tag{2.7}$$

Assume the applied field to be $\sigma^0_{ij}(\mathbf{x})$ with the corresponding strains

$$e^0_{ij}(\mathbf{x}) = \sum_{\alpha,\beta} a^{ij}_{\alpha\beta}\, x_1^\alpha\, x_2^\beta \tag{2.8}$$

The Green's function is given by

$$G_{ij}(\mathbf{x},\mathbf{x}') = \frac{1}{8\pi\mu(1-\nu)}\left\{\frac{\bar{x}_i\bar{x}_j}{\bar{R}^2} - (3-4\nu)\delta_{ij}\log\bar{R}\right\} \tag{2.9}$$

where

$$\bar{x}_i = (x_i - x_i'), \qquad \bar{R} = |\mathbf{x}-\mathbf{x}'| \tag{2.10}$$

and $\nu = \lambda/2(\lambda+\mu)$ is Poisson's ratio of the matrix.

3 Equivalence Relation and Boundary Conditions

The equivalence relation for the elliptic inhomogeneity that corresponds to an inclusion with eigenstrains e^*_{ij} according to Eshelby [1] is

$$\sigma_{ij}(\mathbf{u}) + \sigma^0_{ij} - \sigma^*_{ij} = \sigma^{(1)}_{ij}(\mathbf{u}) + \sigma^{(1)0}_{ij}, \quad (\mathbf{x}\subset\Omega) \tag{3.1}$$

where $\sigma^{(1)}_{ij}$ is the stress-operator in the inhomogeneity with (λ,μ) replaced by (λ_1,μ_1). $\sigma^{(1)0}_{ij}$ thus denotes the stress $\sigma^{(1)}_{ij}$ due to the applied strain e^0_{ij}.

Equation (3.1) can be written more compactly as

$$\sigma^*_{ij}(\mathbf{x}) = \bar{\sigma}_{ij}(u(\mathbf{x})) + \bar{\sigma}^0_{ij}(\mathbf{x}), \quad (\mathbf{x}\subset\Omega) \tag{3.2}$$

where $\bar{\sigma}_{ij}$ denotes the stress-operator with (λ,μ) replaced by $(\bar{\lambda},\bar{\mu})$ defined by

$$\bar{\lambda} = \lambda - \lambda_1, \qquad \bar{\mu} = \mu - \mu_1 \tag{3.3}$$

Substitution from (2.7) in (3.2) gives

$$\sigma^*_{ij}(\mathbf{x}) = \bar{\sigma}^0_{ij}(\mathbf{x}) - \int_\Omega \sigma^*_{kl,l}(\mathbf{x}')\;\bar{\sigma}_{ij}\{\mathbf{G}^k(\mathbf{x},\mathbf{x}')\}d\Omega(\mathbf{x}') - \fint_\Gamma \gamma_k(\mathbf{x}')n_l(\mathbf{x}')\sigma_{kl}\{\bar{\sigma}_{ij}(\underline{\mathbf{G}}(\mathbf{x},\mathbf{x}'))\}d\Gamma(\mathbf{x}'), \quad (\mathbf{x}\subset\Omega) \tag{3.4}$$

where $\underline{\mathbf{G}}$ denotes the tensor G_{ij} for short. In (3.4), the derivatives under the stress operator $\bar{\sigma}_{ij}$ are with respect to $\mathbf{x}$ while those under σ_{kl} are with respect to $\mathbf{x}'$.

Next, the boundary conditions are that the stresses across Γ must vanish. This is ensured by taking

$$\{\sigma_{ij}(\mathbf{u}) + \sigma^0_{ij}\}n_j(\mathbf{x}) = 0, \quad (\mathbf{x}\subset\Gamma) \tag{3.5}$$

Using (2.7) here, we get

$$n_j(\mathbf{x})\fint_\Gamma \gamma_k(\mathbf{x}')n_l(x')\sigma_{kl}\{\sigma_{ij}(\underline{\mathbf{G}}(\mathbf{x},\mathbf{x}')\}d\Gamma(\mathbf{x}') + n_j(\mathbf{x})\int_\Omega \sigma^*_{kl,l}(\mathbf{x}')\sigma_{ij}\{\mathbf{G}^k(\mathbf{x},\mathbf{x}')\}d\Omega(\mathbf{x}') = \sigma^0_{ij}(\mathbf{x})n_j(\mathbf{x}), \quad (\mathbf{x}\subset\Gamma) \tag{3.6}$$

4 Solution to (3.4) and (3.6)

Due to the debonding, the eigenstrains e^*_{ij} will consist of both singular and nonsingular parts, the former being absent for perfect bonding. Let us assume that

$$e^*_{ij} = e^{*I}_{ij} + e^{*II}_{ij} \tag{4.1}$$

and correspondingly

$$\sigma^*_{ij} = \sigma^{*I}_{ij} + \sigma^{*II}_{ij} \tag{4.2}$$

Here, e^{*I}_{ij} and σ^{*I}_{ij} denote the nonsingular parts which will be in the form of power-series like the applied fields in (2.8). Thus we assume that

$$e^{*I}_{ij} = \sum_{\alpha=0}^{\infty}\sum_{\beta=0}^{\infty} b^{ij}_{\alpha\beta}x_1^\alpha x_2^\beta \tag{4.3}$$

The expansion coefficients $b^{ij}_{\alpha\beta}$ are to be found in terms of $a^{ij}_{\alpha\beta}$ by equating the nonsingular parts of (3.4). The corresponding equation is

$$\sigma^{*I}_{ij}(\mathbf{x}) = \bar{\sigma}^{(0)}_{ij}(\mathbf{x}) + \int_\Omega \sigma^{*I}_{kl}(\mathbf{x}')\bar{\sigma}_{ij}\{\mathbf{G}^k(\mathbf{x},\mathbf{x}')\}_{,l}d\Omega(\mathbf{x}'); \quad (\mathbf{x}\subset\Omega) \tag{4.4}$$

where we have incorporated an integration by parts in the integral over Ω to cast the foregoing relation in the well-known form in literature; (see [3]).

We substitute from (2.8) and (4.3) in (4.4) and compare the like terms on both sides. The integral over Ω in (4.4) can be evaluated as in our earlier work [4] and we can write it as

$$\int_\Omega \sigma^{*I}_{kl}(\mathbf{x}')\bar{\sigma}_{ij}\{\mathbf{G}^k(\mathbf{x},\mathbf{x}')\}_{,l}\;d\Omega(\mathbf{x}') = \sum_{\alpha,\beta}\bar{C}^{ij}_{\alpha\beta}v_1^\alpha x_2^\beta \tag{4.5}$$

Downloaded 02 May 2010 to 171.66.16.54. Redistribution subject to ASME license or copyright; see http://www.asme.org/terms/Terms_Use.cfm

where $\bar{C}^{ij}_{\alpha\beta}$ are linear expressions in terms of $b^{ij}_{\alpha\beta}$. Thus $b^{ij}_{\alpha\beta}$ can be solved from (4.4) in terms of $a^{ij}_{\alpha\beta}$.

Singular Part of the Eigenstrain. Now we turn to the more difficult part of the solution, viz., the singular part e^{*II}_{ij} of the eigenstrains e^{*}_{ij}. The corresponding eigenstresses σ^{*II}_{ij} satisfy the following relation derived from the equivalence relation (3.4) using the displacement field u_m from (2.7)

$$\sigma^{*II}_{ij}(\mathbf{x}) = -\int_{\Omega} \sigma^{*II}_{\alpha\beta,\beta}(\mathbf{x}')\bar{\sigma}_{ij}\{\mathbf{G}^{\alpha}(\mathbf{x},\mathbf{x}')\}d\Omega(\mathbf{x}')$$

$$-\oint_{\Gamma} \gamma_k(\mathbf{x}')n_l(\mathbf{x}')\sigma_{kl}\{\bar{\sigma}_{ij}(\underline{\mathbf{G}}(\mathbf{x},\mathbf{x}'))\}d\Gamma(\mathbf{x}'), \quad (\mathbf{x}\subset\Omega) \tag{4.6}$$

For the general case of unequal Poisson's ratios ($\nu \neq \nu_1$), the stress operators σ_{ij} and $\bar{\sigma}_{ij}$ are *not* linear multiples of each other. Thus to solve (4.6) for σ^{*II}_{ij}, a more general approach than that used in [4] is required. Towards this end, assume that σ^{*II}_{ij} is given by

$$\sigma^{*II}_{ij}(\mathbf{x}) = \oint_{\Gamma} \gamma_k(\mathbf{x}')n_l(\mathbf{x}')f^{kl}_{ij}(\mathbf{x},\mathbf{x}')d\Gamma(\mathbf{x}') \tag{4.7}$$

Substituting (4.7) into (4.6) and comparing the integrands we obtain the following equation for f^{kl}_{ij}.

$$f^{kl}_{ij}(\mathbf{x},\mathbf{x}') = -\bar{\sigma}_{ij}\{\sigma_{kl}(\underline{\mathbf{G}}(\mathbf{x},\mathbf{x}')\}$$

$$-\int_{\Omega} f^{kl}_{\alpha\beta,\beta}(\mathbf{x}'',\mathbf{x}')\bar{\sigma}_{ij}\{\mathbf{G}^{\alpha}(\mathbf{x},\mathbf{x}'')\}d\Omega(\mathbf{x}'') \tag{4.8}$$

For further simplification, assume that

$$f^{kl}_{ij}(\mathbf{x},\mathbf{x}') = \bar{\sigma}_{ij}(\mathbf{U}^{kl}) \tag{4.9}$$

so that (4.8) gives the equation for $\mathbf{U}^{kl}$ as

$$U^{kl}_{i}(\mathbf{x},\mathbf{x}') = \phi^{kl}_{i}(\mathbf{G}) + I^{kl}_{i}(\mathbf{U}) \tag{4.10}$$

where

$$\phi^{kl}_{i}(\mathbf{G}) = -\sigma_{kl}\{\mathbf{G}^{i}(\mathbf{x},\mathbf{x}')\}$$

$$= \left[\alpha_0 \frac{\bar{x}_i}{\bar{R}^2}\delta_{kl} + \alpha_1 \frac{\bar{x}_k}{\bar{R}^2}\delta_{il} + \alpha_2 \frac{\bar{x}_l}{\bar{R}^2}\delta_{ik} + \alpha_3 \frac{\bar{x}_i\bar{x}_k\bar{x}_l}{\bar{R}^4}\right] \tag{4.11}$$

$$\bar{x}_i = (x'_i - x_i),$$

$$\alpha_0 = -\{\lambda(4\nu-2)+2\mu\}/8\pi\mu(1-\nu),$$

$$\alpha_1 = \alpha_2 = -(4\nu-2)/8\pi(1-\nu) = -\alpha_0,$$

$$\alpha_3 = 1/2\pi(1-\nu); \quad \left\{\nu = \frac{\lambda}{2(\lambda+\mu)}\right\}, \tag{4.12}$$

and

$$I^{kl}_{i}(\mathbf{U}) =$$

$$-\int_{\Omega} \bar{\sigma}_{\alpha\beta,\beta}\{\mathbf{U}^{kl}(x'',x')\}G_{\alpha i}(\mathbf{x},\mathbf{x}'')d\Omega(\mathbf{x}'') \tag{4.13}$$

Since Green's function satisfies the equation

$$\sigma_{ij,j}\{\mathbf{G}^{m}(\mathbf{x},\mathbf{x}')\} = -\delta_{im}\delta(\mathbf{x}-\mathbf{x}'), \tag{4.14}$$

it can easily be shown from (4.13) that

$$\sigma_{ij,j}(\mathbf{I}^{kl}) \equiv \bar{\sigma}_{ij,j}(\mathbf{U}^{kl}) \tag{4.15}$$

The form of equation (4.11) which is the "free" term of the equation (4.10) suggests that the solution of the latter may be assumed in the form

$$U^{kl}_{i} = A\frac{\bar{x}_i\delta_{kl}}{\bar{R}^2} + B\frac{\bar{x}_k}{\bar{R}^2}\delta_{il} + C\frac{\bar{x}_l}{\bar{R}^2}\delta_{ik} + D\frac{\bar{x}_i\bar{x}_k\bar{x}_l}{\bar{R}^4} \tag{4.16}$$

From (4.15) it then follows by direct substitution and comparison of like terms on both sides, that

$$I^{kl}_{i} = A'\frac{\bar{x}_i}{\bar{R}^2}\delta_{kl} + B'\frac{\bar{x}_k}{\bar{R}^2}\delta_{il} + C'\frac{\bar{x}_l}{\bar{R}^2}\delta_{ik} + D'\frac{\bar{x}_i\bar{x}_k\bar{x}_l}{\bar{R}^4} \tag{4.17}$$

where

$$A' = (\bar{\lambda}/\lambda)A, \qquad B' = \left(\frac{\bar{\lambda}+\bar{\mu}}{\lambda+\mu}\right)B$$

$$C' = \left(\frac{\bar{\lambda}+\bar{\mu}}{\lambda+\mu}\right)C, \qquad D' = (\bar{\mu}/\mu)D \tag{4.18}$$

Finally, the coefficients A, B, C, D are found by substituting from (4.11), (4.16), and (4.17) into the identity (4.10), and so giving

$$A = (\lambda/\lambda_1)\alpha_0, \qquad B = \left(\frac{\lambda+\mu}{\lambda_1+\mu_1}\right)\alpha_1$$

$$C = \left(\frac{\lambda+\mu}{\lambda_1+\mu_1}\right)\alpha_2, \qquad D = (\mu/\mu_1)\alpha_3 \tag{4.19}$$

The relations (4.18) and (4.19) lead to the following values for A', B', C', D':

$$A' = (\bar{\lambda}/\lambda_1)\alpha_0, \qquad B' = \left(\frac{\bar{\lambda}+\bar{\mu}}{\lambda_1+\mu_1}\right)\alpha_1$$

$$C' = \left(\frac{\bar{\lambda}+\bar{\mu}}{\lambda_1+\mu_1}\right)\alpha_2, \quad D' = (\bar{\mu}/\mu_1)\alpha_3 \tag{4.20}$$

This completes the determination of f^{kl}_{ij} defined in (4.9). Finally, (4.7) gives the solution to the equivalence relation (4.6) for the general case of unequal Poisson's ratios. The functions $\gamma_k(\mathbf{x})$ in (4.7) are determined from the boundary conditions (3.6). It is easily seen that (3.6) gives by virtue the equations (4.7)–(4.13),

$$n_j(\mathbf{x})\oint_{\Gamma} \gamma_k(\mathbf{x}')n_l(\mathbf{x}')\sigma_{kl}\{\sigma_{ij}(\underline{\mathbf{G}}(\mathbf{x},\mathbf{x}'))\}d\Gamma(\mathbf{x}')$$

$$-n_j(\mathbf{x})\oint_{\Gamma} \gamma_k(\mathbf{x}')n_l(\mathbf{x}')\sigma_{ij}\{\mathbf{I}^{kl}(\mathbf{x},\mathbf{x}')\}d\Gamma(\mathbf{x}')$$

$$= n_j(\mathbf{x})\sigma^{0}_{ij}(\mathbf{x}) + n_j(\mathbf{x})\sum_{\alpha,\beta} C^{ij}_{\alpha\beta}x_1^{\alpha}x_2^{\beta}; \quad [x\subset\Gamma] \tag{4.21}$$

The second term on the right-hand side of (4.21) arises from the surface integral in (3.6) due to the nonsingular part σ^{*I}_{ij} of the eigenstress. To solve (4.21) for $\gamma_k(\mathbf{x})$ we assume that (for $|x_2| \leq l$ on Γ)

$$\gamma_k(\mathbf{x}) = \frac{1}{2\pi}(l^2 - x_2^2)^{-1/2}(\gamma_0{}^k + \gamma_1{}^k x_2 + \gamma_2{}^k x_2^2 + \ldots\ldots) \tag{4.22}$$

We also note that

$$(n_1,n_2) = \left(\frac{x_1}{a^2},\frac{x_2}{b^2}\right)/T(\mathbf{x}) \tag{4.23}$$

$$T(\mathbf{x}) = (x_1^2/a^4 + x_2^2/b^4)^{1/2} \tag{4.24}$$

and, since

$$x_1 = a(1 - x_2^2/b^2)^{1/2}, \quad (\mathbf{x}\subset\Gamma) \tag{4.25}$$

it follows that

$$d\Gamma(\mathbf{x}') = T(\mathbf{x}')(a^2/x'_1)dx'_2 \tag{4.26}$$

Thus (4.21) finally reduces to

$$\frac{1}{2\pi}\int_{-l}^{l} \frac{(l^2 - x_2'^2)^{1/2}F_i(x_2,x'_2)}{(x'_2 - x_2)^2}dx'_2 = p_i(x_2); \quad (|x_2| \leq l) \tag{4.27}$$

where (subscript l not to be confused with debond half length l)

$$F_i(x_2,x'_2) = (\gamma_0 + \gamma_1{}^k x'_2 + \gamma_2{}^k x_2'^2 + \ldots\ldots)\phi_{ik}, \tag{4.28}$$

Downloaded 02 May 2010 to 171.66.16.54. Redistribution subject to ASME license or copyright; see http://www.asme.org/terms/Terms_Use.cfm

$$\phi_{ik} = T(\mathbf{x}) n_j(\mathbf{x}) \left\{ n_l(\mathbf{x}') \frac{d\Gamma(\mathbf{x}')}{dx_2'} \right\} (x'_2 - x_2)^2 \times [\sigma_{kl}\{\sigma_{ij}(\underline{\mathbf{G}}(\mathbf{x},\mathbf{x}'))\} - \sigma_{ij}\{\mathbf{I}^{kl}(\mathbf{x},\mathbf{x}')\}] \quad (4.29)$$

and

$$p_i(x_2) = T(\mathbf{x})[n_j(\mathbf{x})\sigma^0_{ij}(\mathbf{x}) + n_j(\mathbf{x}) \sum_{\alpha,\beta} C^{ij}_{\alpha\beta} x_1^\alpha x_2^\beta]; \quad (\mathbf{x} \subset \Gamma) \quad (4.30)$$

Following the procedure adopted in [4], we expand the functions $\phi_{ik}, p_i(x_2)$ in the following form

$$P_i(x_2) = \sum_m p_{im} {x_2}^m \quad (4.31)$$

$$\phi_{ik} = \sum_{m,n} r^{ik}_{mn} x_2^m {x_2'}^n. \quad (4.32)$$

Then (4.28) gives

$$F_i(x_2, x_2') = \sum_{m,n} \alpha^i_{mn} x_2^m {x_2'}^n \quad (4.33)$$

where

$$\alpha^i_{pq} = \sum_{m \le q} \gamma^k_m r^{ik}_{pm'} \quad (m' = q - m). \quad (4.34)$$

We recall that summation over repeated indices is assumed.

The Cauchy-type integrals in (4.27) can be evaluated term by term to result in a power series in x_2. Then a comparison of like terms in (4.27) determines the expansion coefficients (α^i_{mn}). When the latter are substituted in (4.34) it is possible to solve for (γ^i_m), and thus the functions $\gamma_k(\mathbf{x})$ in (4.22) are fully determined.

5 Stress Intensity Factors

The singular part of u_m in (2.7) is

$$u^s_m(\mathbf{x}) = -\oint_\Gamma \gamma_i(\mathbf{x}')\sigma_{ij}\{\mathbf{G}^m(\mathbf{x},\mathbf{x}')\} n_j(\mathbf{x}') d\Gamma(\mathbf{x}') + \oint_\Gamma \gamma_i(\mathbf{x}') n_j(\mathbf{x}') I^{ij}_m(\mathbf{x},\mathbf{x}') \quad d\Gamma(\mathbf{x}'), \quad (5.1)$$

where we have made use of relations (4.7)–(4.13).

Thus the stresses across Γ are given by their components

$$\tau_i \equiv \sigma_{ij} n_j = -n_j(\mathbf{x}) \oint_\Gamma \gamma_k(\mathbf{x}') n_l(\mathbf{x}') [\sigma_{kl}\{\sigma_{ij}(\underline{\mathbf{G}}(\mathbf{x},\mathbf{x}'))\} - \sigma_{ij}\{\mathbf{I}^{kl}(\mathbf{x},\mathbf{x}')\}] d\Gamma(\mathbf{x}') \quad (5.2)$$

$$= -\frac{1}{2\pi T(\mathbf{x})} \oint_\Gamma \frac{(l^2 - x_2'^2)^{1/2} \left(\sum_{m,n} \alpha^i_{mn} x_2^m {x_2'}^n \right)}{(x_2' - x_2)^2} dx_2' \quad (5.3)$$

[vide (4.21)–(4.33)].

Evaluating the integral term by term, we obtain

$$\tau_i = -\frac{1}{2\pi T(\mathbf{x})} [\alpha^i_{00} x_2 + \alpha^i_{01} x_2^2 + \alpha^i_{02} x_2^3 + \ldots\ldots + \alpha^i_{10} x_2^2 + \alpha^i_{11} x_2^3 + \alpha^i_{12} x_2^4 + \ldots\ldots + \alpha^i_{20} x_2^3 + \alpha^i_{21} x_2^4 + \alpha^i_{22} x_2^5 + \ldots\ldots + \ldots\ldots] \frac{1}{(x_2^2 - l^2)^{1/2}}; \quad (|x_2| \to l + 0) \quad (5.4)$$

Resolving τ_i in the normal and tangential directions and letting $x_2 \to \pm l$, we obtain the stress intensity factors at the tips of Γ as follows. The normal and tangential stresses are

$$\sigma_{nn} = \tau_i n_i = K_I^\pm / (2\pi d_0)^{1/2} \quad (5.5)$$

$$\sigma_{nt} = \tau_i t_i = K_{II}^\pm / (2\pi d_0)^{1/2} \quad (5.6)$$

where

$$K_I^\pm = K_1^\pm n_1^\pm + K_2^\pm n_2^\pm \quad (5.7)$$

$$K_{II}^\pm = K_1^\pm t_1^\pm + K_2^\pm t_2^\pm \quad (5.8)$$

$$K_i^\pm = \pm \frac{(\pi l)^{1/2} a (1 + a^2 l^2 / b^4)^{1/4}}{2\left(1 - \frac{l^2}{b^2} + \frac{a^2 l^2}{b^4}\right)^{1/2}} \times [\alpha^i_{00} \pm (\alpha^i_{01} + \alpha^i_{10}) l + (\alpha^i_{02} + \alpha^i_{11} + \alpha^i_{20}) l^2 + \ldots\ldots], \quad (i = 1,2) \quad (5.9)$$

$$\mathbf{n}^\pm \equiv (n_1^\pm, n_2^\pm) = \{(1 - l^2/b^2)^{1/2}, \quad \pm a\, l/b^2\}/T_0$$

$$\mathbf{t}^\pm = (\mp n_2^\pm, \pm n_1^\pm)$$

$$T_0 = \left(1 - \frac{l^2}{b^2} + \frac{a^2 l^2}{b^4}\right)^{1/2} \quad (5.10)$$

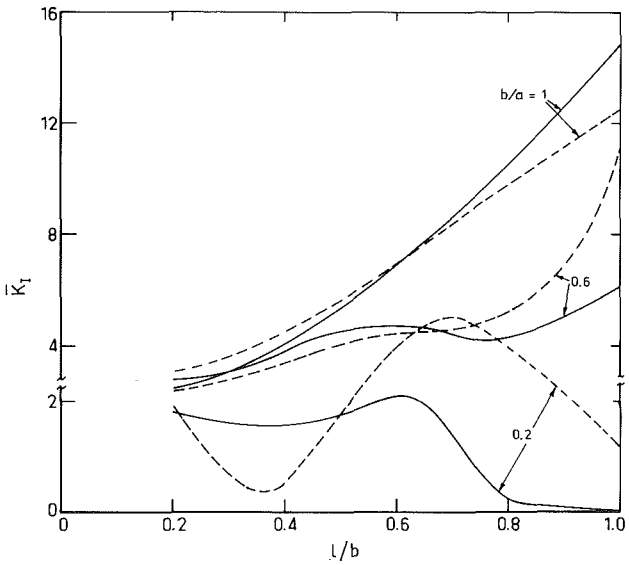


Fig. 2 Stress-intensity factor $\bar{K}_I$ as a function of the debond size (l/b) for $\lambda_1/\lambda = 20$ due to the uniform applied field (7.1). $\nu = 0.3$, $\nu_1 = 0.35$ (solid lines), and $\nu = 0.35$, $\nu_1 = 0.3$ (broken lines).

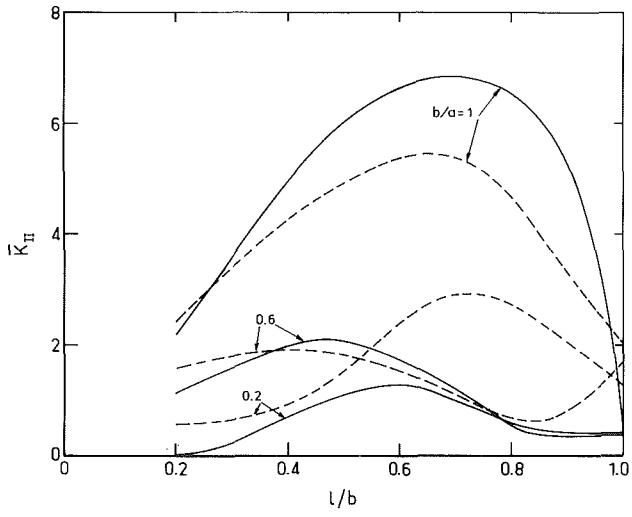


Fig. 3 Stress-intensity factor $\bar{K}_{II}$ as a function of the debond size (l/b) for $\lambda_1/\lambda = 20$ due to the uniform applied field (7.1). $\nu = 0.3$, $\nu_1 = 0.35$ (solid lines), and $\nu = 0.35$, $\nu_1 = 0.3$ (broken lines).

Downloaded 02 May 2010 to 171.66.16.54. Redistribution subject to ASME license or copyright; see http://www.asme.org/terms/Terms_Use.cfm

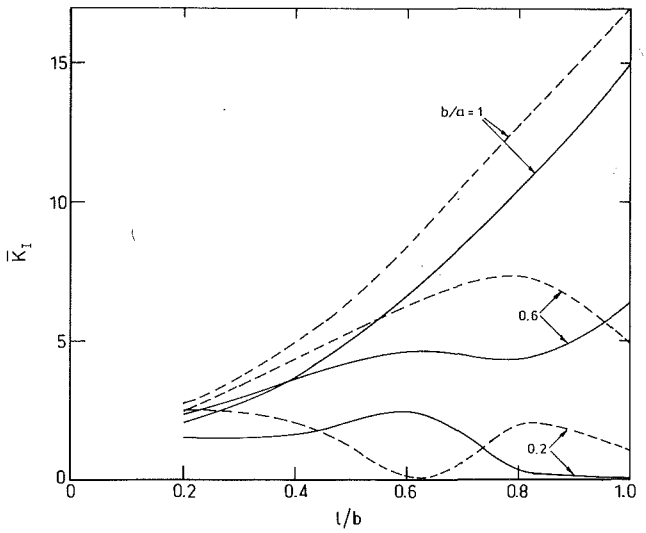


Fig. 4 Stress-intensity factor $\bar{K}_I$ as a function of the debond size (l/b) due to the inhomogeneous applied field (7.3) for $\lambda_1/\lambda = 20$, $\nu = 0.3$, $\nu_1 = 0.35$. (Solid lines represent $x_2 > 0$ side of debond, and broken lines represent $x_2 < 0$ side of debond.)

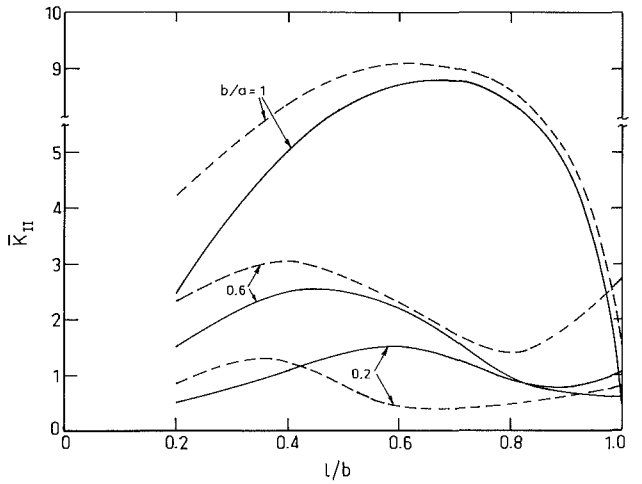


Fig. 5 Stress-intensity factor $\bar{K}_{II}$ as a function of debond size (l/b) due to the nonhomogeneous applied field (7.3) for $\lambda_1/\lambda = 20$, $\nu = 0.3$, $\nu_1 = 0.35$. (Solid lines represent $x_2 > 0$ side of debond, and broken lines, $x_2 < 0$ side of debond.)

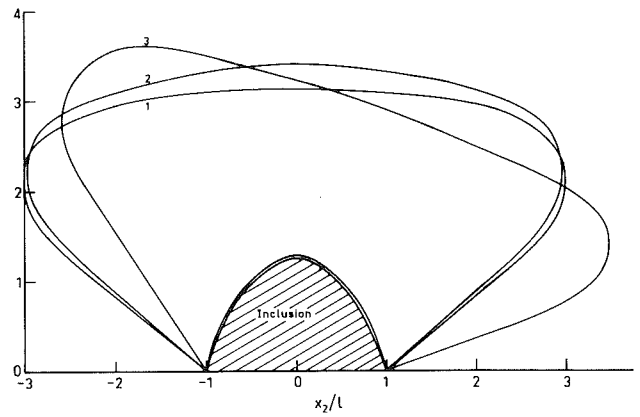


Fig. 6 The deformed shapes of the debonded elliptic arc Γ for $b/a = 0.2$, $l/b = 0.6$, and $\nu = 0.3, \nu_1 = 0.35$. (1) $\lambda_1/\lambda = 20$, for uniform applied field (7.1). (2) $\lambda_1/\lambda = 50$, for uniform applied field (7.1). (3) $\lambda_1/\lambda = 20$, for nonhomogeneous applied field (7.3).

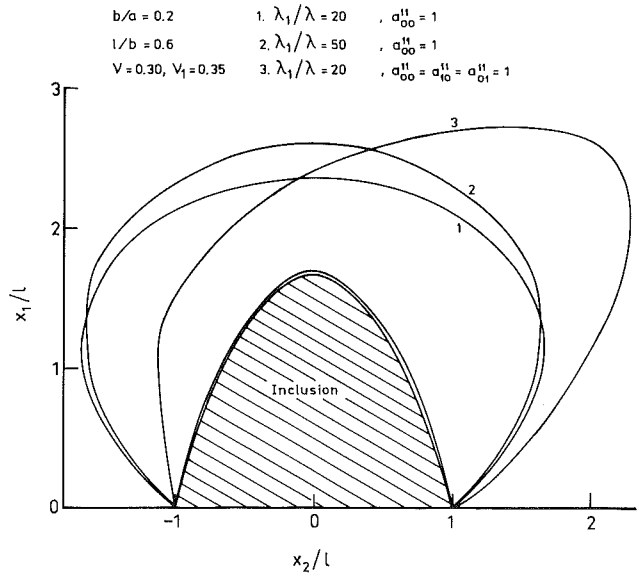


Fig. 7 The deformed shapes of the debonded elliptic arc Γ for $b/a = 0.4$, $l/b = 0.8$, and $\nu = 0.3$, $\nu_1 = 0.35$. (1) $\lambda_1/\lambda = 20$, for uniform applied field (7.1). (2) $\lambda_1/\lambda = 50$, for uniform applied field (7.1). (3) $\lambda_1/\lambda = 20$, for nonhomogeneous applied field (7.3).

The $(\pm)$ signs in these equations refer to the tips $x_2 = \pm l$, and d_0 is the distance along the tangent from these points. We also define the nondimensional stress-intensity factors by

$$\bar{K}^{\pm}_{I,II} = K^{\pm}_{I,II}/(\mu l^{1/2}) \tag{5.11}$$

6 Relative Displacements Across the Debond Faces

Let Δu_m denote the relative displacements across the faces of the debonded arc Γ. From the expression (5.1) for the singular part of the displacements, we obtain

$$\Delta u_m = \Delta u^{(1)}_m + \Delta u^{(2)}_m. \tag{6.1}$$

The two terms on the right-hand side of (6.1) correspond to the two integrals in (5.1). From the equation (4.14), defining Green's function, we know the standard result

$$\Delta[\sigma_{ij}\{\mathbf{G}^m(\mathbf{x},\mathbf{x}')\}n_j] = -\delta_{im}\delta(\xi - \xi') \tag{6.2}$$

where ξ denotes the tangential coordinate vector at any point on Γ. Thus, from the first integral in (5.1) we readily obtain the result

$$\Delta u^{(1)}_m = \gamma_m(\mathbf{x}) \tag{6.3}$$

To obtain $\Delta u^{(2)}_m$ from the remaining integral in (5.1), we need to know the behavior of $I^{ij}_m(\mathbf{x},\mathbf{x}')\, n_j(\mathbf{x}')$ across Γ. The following results concerning the behavior of the various terms of $I^{ij}_m n_j$ arising from (4.17) are easily worked out:

$$\Delta\left[\frac{\bar{x}_j}{\bar{R}^2}\,\delta_{im}n_j\right] = 2\pi\delta_{im}\delta(\xi - \xi') \tag{6.4}_1$$

$$\Delta\left[\frac{\bar{x}_i\bar{x}_j\bar{x}_m}{\bar{R}^4}\,n_j\right] = \pi\delta_{im}\delta(\xi - \xi') \tag{6.4}_2$$

$$\Delta\left[\frac{\bar{x}_m}{\bar{R}^2}\,\delta_{ij}n_j\right] = \Delta\left[\frac{\bar{x}_i}{\bar{R}^2}\,\delta_{mj}n_j\right] = 2\pi\delta(\xi - \xi')n_i n_m \tag{6.4}_3$$

Thus the second integral in (5.1) gives, using (4.17) and (6.4),

$$\Delta u^{(2)}_m = 2\pi\gamma_k(\mathbf{x})[(A' + B')n_k n_m + \delta_{mk}(C' + \tfrac{1}{2}D')] \tag{6.5}$$

Combining (6.3) with (6.5), we find the total relative displacements across Γ to be

$$\Delta u_m = \Delta u^{(1)}_m + \Delta u^{(2)}_m$$
$$= \gamma_m(\mathbf{x}) + 2\pi\gamma_k(\mathbf{x})[(A' + B')n_k n_m + \delta_{mk}(C' + \tfrac{1}{2}D')] \tag{6.6}$$

Downloaded 02 May 2010 to 171.66.16.54. Redistribution subject to ASME license or copyright; see http://www.asme.org/terms/Terms_Use.cfm

7 Numerical Results

To illustrate the procedure, we consider the following two examples:

Example (*i*).

$$e^0_{11} = 1, \quad e^0_{22} = 0, \quad e^0_{12} = 0 \tag{7.1}$$

In this case, (2.8) gives

$$\begin{aligned} &a^{11}_{00} = 1, \\ &a^{11}_{00} = a^{11}_{11} = \ldots\ldots\ldots = 0 \\ &a^{12}_{mn} = a^{22}_{mm} = 0, \quad \text{for all } m \text{ and } n \end{aligned} \tag{7.2}$$

The solution will be symmetric about the line $x_2 = 0$, in view of the homogeneous far-field deformation.

Example (ii). Here the applied far-field deformation is nonhomogeneous:

$$\begin{aligned} e^0_{11} &= 1 + x_1 + x_2 \\ e^0_{12} &= e^0_{22} = 0 \end{aligned} \tag{7.3}$$

Again, from (2.8), it follows that

$$\begin{aligned} &a^{11}_{00} = a^{11}_{10} = a^{11}_{01} = 1, \quad \text{and } a^{11}_{mn} = 0; \\ &\qquad \text{for all other values of } m \text{ and } n, \\ &a^{12}_{mn} = a^{22}_{mn} = 0; \text{ for all values of } m \text{ and } n. \end{aligned} \tag{7.4}$$

Clearly, the results will no longer be symmetric about $x_2 = 0$.

Figures 2–5 give the stress intensity factors $\bar{K}_I$ and $\bar{K}_{II}$ for various values of the elastic constants λ_1/λ, ν, ν_1, and the aspect ratios b/a and l/b. Both the homogeneous and nonhomogeneous deformations are considered. In all the cases, the vaues of $\bar{K}_I$ and $\bar{K}_{II}$ change significantly with the type of loading, as well as the aspect ratios.

Figures 6 and 7 show the shapes of the deformed arc of debonding Γ for two combinations of aspect ratios $b/a = 0.2$, $l/b = 0.6$ (Fig. 6) and $b/a = 0.4$, $l/b = 0.8$ (Fig. 7). As in the preceding numerical examples the elastic constants were chosen to be $\lambda_1/\lambda = 20$ and 50, and $\nu = 0.3$, $\nu_1 = 0.35$ and both the types of loading (7.1) and (7.3) were considered. It is evident that the type of far-field deformation plays a dominant role in the debonding of the inclusion from the matrix and in its eventual separation from the latter.

8 Conclusions

We have solved the general case of the inhomogeneity problem with partial debonding over an arc Γ when Poisson's ratio of the matrix is different from that of the inhomogeneity. A new approach has been developed for solving Eshelby's equivalence relation. Further, several new results were obtained regarding the discontinuous behavior of the constituent terms of the derivatives of Green's function which eventually helped in developing simple expressions for the relative displacements across the debonded faces.

9 Acknowledgments

The visit of K. Viswanathan to the University of Newcastle was funded by a grant (F8215322) to B. L. Karihaloo under the Australian Research Grants Scheme.

References

1 Eshelby, J. D., "The Determination of the Elastic Field of an Ellipsoidal Inclusion and Related Problems," *Proceedings of the Royal Society*, Series *A*, Vol. 241, 1957, pp. 376–396.

2 Eshelby, J. D., "Elastic Inclusions and Inhomogeneities," Progress in Solid Mechanics, Sneddon and Hill, eds., Vol. 2, North-Holland, Amsterdam, 1961, pp. 89–140.

3 Mura, T., "The Continuum Theory of Dislocations," *Advances in Materials Research*, Vol. 3, Herman, H., ed., Wiley-Interscience, New York, 1968.

4 Karihaloo, B. L., and Viswanathan, K., "Elastic Field of an Elliptic Inhomogeneity With Debonding Over an Arc (Antiplane Strain)," ASME, JOURNAL OF APPLIED MECHANICS, Vol. 52, 1985, pp. 91–97.

Downloaded 02 May 2010 to 171.66.16.54. Redistribution subject to ASME license or copyright; see http://www.asme.org/terms/Terms_Use.cfm

C. Y. Hui

A. Ruina
Department of Theoretical and Applied Mechanics, Cornell University, Ithaca, N.Y. 14853

Eddy Current Flow Near Cracks in Thin Plates

The problem of magnetically induced eddy current flow in a thin cracked plate is posed and solved for a few special cases. The current density is singular at the tip of a nonconducting crack. The strength of this singularity, denoted M, *is found by reducing the eddy current problem to a conduction problem and then using the mathematical methods of fracture mechanics.* M *is found for a small crack in a current field, a small crack in a round plate with spatially uniform magnetic field, and a half-cracked round plate with spacially uniform magnetic field.*

Introduction

Mukherjee, Morjaria, and Moon [1, 2] have solved some problems of eddy current flow in thin plates containing nonconductive cracks numerically. They observed in their solutions a singularity in the induced current density at the tips of the cracks. A similar singularity has been observed at a crack tip in a thick slab (Kahn, Spal, and Feldman [3]) in simple conduction problems (Horie et al. [4]) where an analogy with the singularity in stress at the tip of a crack in an elastic solid was noted [4].

Mukherjee et al. [1, 2] motivate their work by the following consideration. The stress singularity at crack tips leads to crack growth and structural failure. Thus, the detection of cracks is important for evaluation of structural integrity. By using magnetically induced currents, cracks might be located by the local heating near the crack tip (as seen on an infrared camera, say). The variations in sample's resistance is already used as a measure of crack growth by various investigators [5–7]. Michael, Waechter, and Collins [8] discuss a magnetically induced current method applicable to surface cracks in thick plates. The method proposed by Mukherjee et al. differs from this in that it could be used to locate cracks in thin plates. To test the applicability of this idea one must be able to determine the induced current in a plate with a crack.

Following the formulation of Mukherjee et al. [1, 2] we have found some solutions for induced current analytically. We have verified their computer results in some cases.

This paper begins with an introduction to the equations governing eddy current flow. Then, by reducing the problem to a simple conduction problem, and by using the fracture mechanics analogy of Horie et al. [4], we find the intensity of the singularity of current for a few idealized problems.

1 Equation Summary

In this section we review the equations governing eddy current flow in a cracked thin plate made of a conducting material. The eddy current is induced by a time varying magnetic field $\mathbf{B}^0$ applied outside the plate. The applied field $\mathbf{B}^0$ can have arbitrary spatial distribution but must vary sufficiently slowly so that skin effects can be neglected.

Following Mukherjee, Morjaria, and Moon [1], let (x, y) denote a cartesian coordinate system in the plane of the plate, then the in plane current density $\mathbf{J}(x, y)$ is divergence free ($\nabla \cdot \mathbf{J} = 0$) and is given in terms of a stream function $\psi(x, y)$:

$$\mathbf{J} = \mathbf{k} \times \nabla\psi, \text{ i.e., } \begin{cases} J_x = -\psi_{,y} \\ J_y = \psi_{,x} \end{cases} \tag{1.1}$$

where $\mathbf{k}$ is a unit vector normal to the plate and ∇ is the gradient operator in the variable (x, y). The in plane current density $\mathbf{J}$ is related to the inplane electric field $\mathbf{E}$ by Ohm's law, i.e.,

$$\mathbf{J} = \sigma\mathbf{E} \tag{1.2}$$

where σ is the conductivity of the homogeneous isotropic plate. For the inplane field $\mathbf{E}$, Faraday's law of induction becomes:

$$\nabla \times \mathbf{E} = \frac{\partial B_3}{\partial t} \tag{1.3}$$

where $B_3 \equiv \mathbf{k} \cdot \mathbf{B}$ and t denotes time. Combining equations (1.1)–(1.3) gives

$$\nabla^2\psi = -\sigma\frac{\partial B_3}{\partial t} = -\sigma\frac{\partial}{\partial t}(B_3^0 + B_3^I) \tag{1.4}$$

Equation (1.4) governs the stream function ψ in the plate. B_3 has been decomposed into B_3^0, the applied field, and B_3^I, the magnetic field induced by $\mathbf{J}$. In the subsequent analysis, we will neglect the self-field term B_3^I in equation (1.4). As observed by Yuan [1], the self-field term can be ignored if the resulting skin depth δ due to the applied field $\mathbf{B}^0$ is much greater than the geometric mean of the plate thickness h and the crack length l. Under this assumption, the governing equation (1.4) reduces to

$$\nabla^2\psi = -\sigma\frac{\partial B_3^0}{\partial t} \tag{1.5}$$

Contributed by the Applied Mechanics Division for publication in the JOURNAL OF APPLIED MECHANICS.

Discussion on this paper should be addressed to the Editorial Department, ASME, United Engineering Center 345 East 47th Street, New York, N.Y. 10017, and will be accpeted until two months after final publication of the paper itself in the JOURNAL OF APPLIED MECHANICS. Manuscript received by ASME Applied Mechanics Division, February, 1984.

Copyright © 1985 by ASME
Downloaded 02 May 2010 to 171.66.16.54. Redistribution subject to ASME license or copyright; see http://www.asme.org/terms/Terms_Use.cfm

The appropriate boundary conditions for equation (1.5) in a cracked plate are

$$\mathbf{J}\cdot\mathbf{n}=0 \tag{1.6}$$

on all the crack faces and the plate boundary. Also, still following Mukherjee et al. [1] we note that the net magnetic flux through the crack is zero because the crack is assumed to be flat and have negligible area on the x, y plane. By the integral form of Faraday's law this implies that the $\mathbf{J}$ field has no net circulation around the crack faces. That is,

$$\underset{\text{around crack face}}{\oint \mathbf{J}\cdot ds} \quad = \quad \underset{\text{around crack face}}{\sigma\oint \mathbf{E}\cdot ds} \quad = \underset{\text{crack opening area}}{\sigma\int \frac{\partial B}{\partial t}dA}=0 \tag{1.7}$$

2 Reduction of Governing Equations to a Conduction Problem

Using the principle of superposition, the eddy current flow problem (equations (1.3)-(1.7)) can be readily reduced to a conduction current problem with suitable modification of the variables and boundary conditions involved. Let $\mathbf{E}$ be the actual inplane electric field satisfying the governing equations (equations (1.3)-(1.5)) and the boundary conditions (equations (1.6) and (1.7)). Let $\mathbf{E}_p$ be the solution of the *crack-free* eddy current problem. That is, $\mathbf{E}_p$ is the particular solution of the same governing differential equations as $\mathbf{E}$ but the boundary condition imposed on $\mathbf{E}_p$ is

$$\mathbf{J}_p\cdot\mathbf{n}\equiv\sigma\mathbf{E}_p\cdot\mathbf{n}=0 \tag{2.1}$$

on the plate boundary only. We thus anticipate that $\mathbf{E}_P$ is a smooth function in the interior of the plate. Define the field due to a new conduction problem $\mathbf{E}_c$ by

$$\mathbf{E}_c\equiv\mathbf{E}-\mathbf{E}_p \tag{2.2}$$

Since $\mathbf{E}$ and $\mathbf{E}_p$ both satisfy equations (1.1)-(1.3) it is clear that $\mathbf{E}_c$ satisfies:

$$\begin{aligned}\nabla\times\mathbf{E}_c&=0\\ \nabla\cdot\mathbf{E}_c&=0\end{aligned} \tag{2.3}$$

inside the cracked plate. These equations will be satisfied identically by a harmonic function f_c related to $\mathbf{E}_c$ by

$$\mathbf{E}_c=\nabla f_c \tag{2.4}$$

where f_c satisfies

$$\nabla^2 f_c=0. \tag{2.5}$$

The altered boundary conditions are

$$\mathbf{J}_c\cdot n=0 \tag{2.6}$$

on the plate boundary and

$$\mathbf{J}_c\cdot\mathbf{n}=\sigma(\mathbf{E}-\mathbf{E}_p)\cdot\mathbf{n}=-\mathbf{J}_p\cdot\mathbf{n} \tag{2.7}$$

on the crack faces, where

$$\mathbf{J}_c\equiv\sigma\mathbf{E}_c=\sigma\nabla f_c \tag{2.8}$$

Notice that $\nabla\cdot\mathbf{J}_c = 0$ by equation (2.3) or (1.1). The function f_c can be interpreted as the electric potential in a conduction current problem in a cracked plate with no applied time-varying magnetic field.

To summarize, the solution of the eddy current problem in a cracked plate is the superposition of two solutions ($\mathbf{E} = \mathbf{E}_c + \mathbf{E}_p$): $\mathbf{E}_p$, the electric field in an uncracked plate and $\mathbf{E}_c$, a new conduction solution in the cracked plate that satisfies equations (2.4)-(2.7).

3 Fracture Analogy

An analogy can be drawn between the eddy current flow in a thin plate when reduced to a conduction problem (equations (2.3)-(2.8)), and antiplane elastic deformation (T. Horie et al., [4]). The analogy allows us to apply well known elasticity results without rederivation. In particular, elastic fracture mechanics results for cracked bodies can be used to calculate the intensity of the singularity of the current flow in a conductor with a crack. The antiplane elasticity problem will now be described and simultaneously correlated term by term with the eddy current problem.

In antiplane shear the only nonzero elastic displacement $w(x, y)$ is perpendicular to the x, y plane and is analogous to the electric potential f in the reduced conduction problem. The elastic strain is the gradient of the displacement $\gamma = \nabla w$ in analogy to the relation $\mathbf{E}_c = \nabla f_c$. The shear stress $\tau = (\tau_{xz}, \tau_{yz})$ is related to shear strain by the shear modulus G, $\tau = G\gamma$, analogous to $\mathbf{J}_c = \sigma\mathbf{E}_c$.

Force balance for a continuum element requires the equilibrium equation $\nabla\cdot\tau = 0$ analogous to conservation of charge $\nabla\cdot\mathbf{J}_c = 0$.

Boundary conditions in an elasticity problem can be the specification of displacement w or traction $\tau\cdot\mathbf{n}$ on boundary curves. This is analogous to specification of the potential f_c or specification of the current flux $\mathbf{J}_c\cdot\mathbf{n} = \sigma\mathbf{E}_c\cdot\mathbf{n}$.

The combination of the definition of strain, the stress-strain relation, and the equilibrium equation yields the Laplace equation for displacement $\nabla^2 w = 0$ analogous to $\nabla^2 f_c = 0$.

Our primary interest is with the intensity of the singularity of solutions at a crack tip. The asymptotic displacement and stress field near the tip of a crack is well known in elastic fracture mechanics. With reference to the coordinates shown in Fig. 1 the asymptotic field ($\rho \to 0$) is given by:

$$w=(2K/G)[\rho/2\pi]^{1/2}\sin(\theta/2)+\text{Constant} \tag{3.1}$$

$$\tau_x=-\frac{K}{\sqrt{2\pi\rho}}\sin\frac{\theta}{2} \qquad \tau_y=\frac{K}{\sqrt{2\pi\rho}}\cos\frac{\theta}{2} \tag{3.2}$$

where K, the "stress intensity factor," is the only free parameter in the asymptotic stress field and is determined by the external loading and geometry. Many solutions and solution techniques have been developed in fracture mechanics to find K for various loadings and crack geometries.

In analogy with the fracture mechanics result, the near crack tip electrical potential f_c and current density $\mathbf{J}_c$ are given by

$$f_c=(2M/\sigma)[\rho/2\pi]^{1/2}\sin(\theta/2)+\text{Constant} \tag{3.3}$$

$$J_{cx}=-M/(2\pi\rho)^{1/2}\sin(\theta/2), \qquad J_{cy}=M/(2\pi\rho)^{1/2}\cos(\theta/2) \tag{3.4}$$

Since the current density in the conduction problem $\mathbf{J}_c$ has a $\rho^{-1/2}$ singularity as $\rho \to 0$ and $\mathbf{J}_p$ is smooth, the current density in the eddy current problem $\mathbf{J} = \mathbf{J}_p + \mathbf{J}_c$ will also have an $\rho^{-1/2}$ singularity of the same strength, i.e.,

$$\mathbf{J}\sim\mathbf{J}_c \quad \text{as} \quad \rho\to 0 \tag{3.5}$$

At this point we would like to refer to the following observation: Calculation of the self-field B_3^I due to $\mathbf{J}_c$, using the BIOT-SAVART Law [9], shows that B_3^I is nonsingular. Thus inclusion of the self-field B_3^I (as in equation (1.4)) does not alter the existance of the $\rho^{-1/2}$ current density singularity.

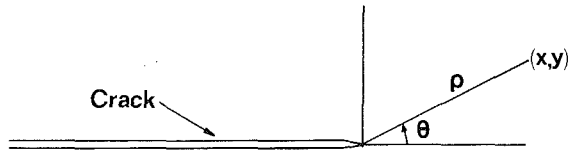


Fig. 1 Points near the tip of a crack are identified by the coordinates ρ, θ

Downloaded 02 May 2010 to 171.66.16.54. Redistribution subject to ASME license or copyright; see http://www.asme.org/terms/Terms_Use.cfm

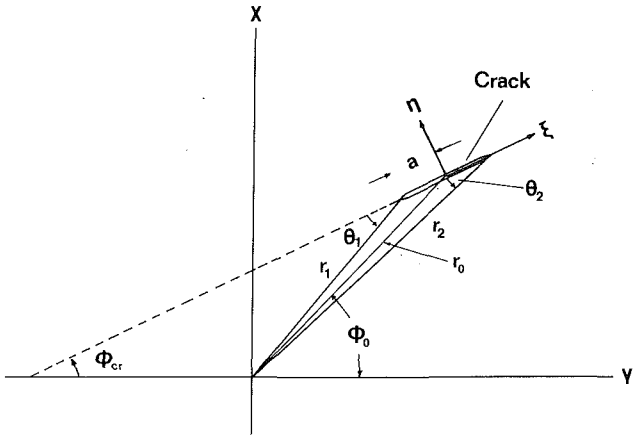


Fig. 2 Axisymmetric magnetic field is applied at the origin of the coordinate system shown. The crack of length $2a$ is centered at (r_0, ϕ) and oriented at the angle ϕ_{cr}. The local coordinates η, ξ as well as the variables $r_1, r_2, \theta_1, \theta_2$ are used in the analysis.

(For very high frequencies the self-field may alter the strength M of the singularity, however.)

For future use we note that single-valued displacement w is insured by the compatability relation $\partial\gamma_x/\partial y = \partial\gamma_y/\partial x$, and the integral condition around the crack $\oint \boldsymbol{\gamma} \cdot d\mathbf{s} = 0$. These are analogous to $\partial E_{cx}/\partial y = \partial E_{cy}/\partial x$ and the integral condition around the crack $\oint \mathbf{E}_c \cdot d\mathbf{s} = 0$, a consequence of Faraday's law, equation (1.7).

4 Current Intensity Factor for Small Cracks

Results of the preceding section will be used to compute the current intensity factor M for a small crack of length $2a$ inside a thin plate. The small crack approximation applies whenever

$$a \ll L$$

where L is any relevant in plane dimension (e.g., the uncracked ligament of the plate). The characteristic distances of the spatial variations of B_3 need not be large compared to a, however.

A local cartesian coordinate system (ξ, η) centered midway between the crack tip will now be introduced to expedite the analysis. This coordinate system is illustrated in Fig. 2, with ξ being the coordinate along the crack face.

The current intensity factor M is the amplitude of the near tip asymptotic solution (3.3) for $(\rho \to 0)$ of $\nabla^2 f_c = 0$ subjected to the boundary conditions:

$$\begin{aligned} &\nabla f_c \cdot \mathbf{n} = 0 \quad \text{on the plate boundary} \\ &\nabla f_c \cdot \mathbf{n} = -\mathbf{J}_p \cdot \mathbf{n} \quad \text{on the crack faces.} \end{aligned} \tag{4.1}$$

Assume for the moment that $j(\xi) \equiv \mathbf{J}_p \cdot \mathbf{n}$ is known on the crack face (recall that $\mathbf{J}_p$ is the solution of the eddy current problem in the same plate with no crack). The small crack assumption allows us to approximate the solution of the governing equations using a crack in an infinite plane, i.e.,

$$\left.\begin{aligned} &\nabla^2 f_c = 0 \\ &\nabla f_c \to 0 \quad \text{as} \quad \sqrt{x^2+y^2} \to \infty \\ &\nabla f_c \cdot \mathbf{n} = -j(\xi) \quad \text{on the crack face} \end{aligned}\right\} \tag{4.2}$$

This approximation will be tested by a sample comparison with numerical results of Mukherjee et al. [1].

The antiplane shear solution of a crack of length $2a$ in an infinite elastic plate with shear modulus G is well known and is given in Rice [10]. Quoting this fracture mechanics result in terms of the analogy of the last section, M at $\xi = \pm a$ is given by

$$M(\text{at } \xi = \pm a) = \frac{\pm 1}{(\pi a)^{1/2}} \int_{-a}^{a} j(\xi) \left(\frac{a \pm \xi}{a \mp \xi} \right)^{1/2} d\xi \tag{4.3}$$

where M is positive for counterclockwise current flow around the crack tip. If $j(\xi)$ is a sufficiently smooth function, so that it can be expanded about the origin $\xi = 0$ in a convergent power series for $|\xi| \le a$

$$j(\xi) = j_0 + j_1 \xi + \ldots = \sum_{n=0}^{\infty} j_n \xi^n \tag{4.4}$$

with

$$j_n = \frac{1}{n!} \frac{d^n j(\xi)}{d\xi^n} \bigg|_{\xi=0}$$

Equation (4.3) gives:

$$\begin{aligned} M(\xi = \pm a) &= \frac{\pm 1}{(\pi a)^{1/2}} \sum_{n=0}^{\infty} j_n \int_{-a}^{a} \xi^n \left(\frac{a \pm \xi}{a \mp \xi} \right)^{1/2} d\xi \\ &= \frac{1}{(\pi a)^{1/2}} \sum_{n=0}^{\infty} j_n I_n^{\pm} \end{aligned} \tag{4.5}$$

Integrals of the type $I_n^{\pm}$ can be evaluated using contour integration as

$$\left.\begin{aligned} &I_n^{\pm} = (\pm 1)^n \pi \left(\sum_{k=0}^{n+1} \alpha_{n+1-k} \beta_k \right) a^{n+1} \\ &\text{with} \\ &\alpha_k = \frac{1/2(1/2-1)\ldots(1/2-k+1)}{k!} \quad k \ge 1 \\ &\beta_k = \frac{1/2(1/2+1)\ldots(1/2+k-1)}{k!} \quad k \ge 1 \end{aligned}\right\} \quad \alpha_0 = \beta_0 = 1 \tag{4.6}$$

Hence

$$M(\xi = \pm a) = \pm (\pi a)^{1/2} \sum_{n=0}^{\infty} (\pm 1)^n j_n a^n \left(\sum_{k=0}^{n+1} \alpha_{n+1-k} \beta_k \right)$$

If the applied magnetic field does not vary significantly in distances on the order of a, then, consistent with the small crack assumption, $j(\xi)$ can be approximated by the first term of equation (4.5), i.e.,

$$M(\xi = \pm a) = M = \pm (\pi a)^{1/2} j_0 \tag{4.7}$$

If the current does vary significantly over the length of the crack, higher-order terms from equation (4.6) are needed. Here we will only include the second-order terms, i.e.,

$$M(\xi = \pm a) \cong \pm (\pi a)^{1/2} [j_0 \pm a j_1/2] \tag{4.8}$$

In problems with special symmetry j_0 may equal zero (e.g., a center crack in a uniform field). In the cases we consider later the inclusion of the second-order term is sufficient to find M with reasonable accuracy.

5 Evaluation of M and Comparison With Numerical Results

The results of the previous sections allow us to obtain several simple analytic solutions for eddy current problems in a cracked plate. The current intensity factor M will be evaluated for three problems: (1) a crack in an infinite plate with the applied magnetic field $B_0 = g(r)h(t)$; (2) a small crack in a circular plate with spatially constant B_0; (3) a half-cracked circular plate with spatially constant B_0.

1. Infinite Cracked Plate With Axisymmetric $B_0 = g(r)h(t)$. A localized magnetic field of the form $B_0(r, \phi, t) =$

Downloaded 02 May 2010 to 171.66.16.54. Redistribution subject to ASME license or copyright; see http://www.asme.org/terms/Terms_Use.cfm

$g(r)h(t)$, with $g(r) \to 0$ for large r, is applied to an infinite plate with a crack; where (r, ϕ) is a polar coordinate system at a fixed point defined as the origin of the plate. The position and orientation of the crack, with respect to the origin, can be arbitrary. They are completely specified by the coordinate of the center of the crack at (r_0, ϕ_0) and the angle of inclination ϕ_{cr} of the crack with respect to the line $\phi = 0$. The crack has a total length of $2a$. The geometry is illustrated in Fig. 2.

For an axisymmetric B_0, the particular solution $\mathbf{J}_p$ is given by:

$$\mathbf{J}_p = \sigma_0 h'(t) J_\phi \hat{\phi} \tag{5.1}$$

with

$$J_\phi = -r^{-1}\int_0^r \eta g(\eta)\, d\eta, \quad h'(t) = dh(t)/dt \tag{5.2}$$

where $\hat{\phi}$ is the circumferential unit vector associated with the polar coordinate system (r, ϕ). Using equation (5.1), and the geometry in Fig. 2, $j(\xi)$ is:

$$j(\xi) = \sigma_0 h'(t) J_\phi(R)[\xi + r_0 \cos(\phi_0 - \phi_{cr})]/R \tag{5.3}$$

with

$$R \equiv \sqrt{r_0^2 + 2\xi r_0 \cos(\phi_0 - \phi_{cr}) + \xi^2} \tag{5.4}$$

The current intensity factor at $x = \pm a$ is given by equation (4.5), i.e.,

$$M(\pm a) = \pm (\pi a)^{-1/2}\int_{-a}^{a} j(\xi)\left[\frac{a \pm \xi}{a \mp \xi}\right]^{1/2} d\xi \tag{5.5}$$

In general, equations (5.3)–(5.5) cannot be evaluated exactly. But usually one can express $j(\xi)$ in terms of a convergent power series about $\xi = 0$ in the interval $|\xi| \le a$. M can then be approximated to any degree of accuracy using equations (4.5) and (4.6). As a concrete example, the following two cases are considered:

Case 1*a*: $g(r) = \dfrac{2}{\pi}\delta(r^2)$, i.e., $B_0 = \delta(x)\delta(y)h(t)$

where δ is the dirac delta function.

For Case 1*a*:

$$J_\phi = -\sigma_0 h'(t) r^{-1}/2\pi \tag{5.6}$$

Hence

$$j(\xi) = -\sigma_0 h'(t)[\xi + r_0 \cos(\phi_0 - \phi_{cr})]/2\pi R^2 \tag{5.7}$$

By equation (4.3),

$$M(\pm a) = \frac{\mp \sigma_0 h'(t)}{2\pi}(\pi a)^{-1/2} \int_{-a}^{a}\left[\frac{\xi + r_0\cos(\phi_0 - \phi_{cr})}{R^2}\right]\left(\frac{a \pm \xi}{a \mp \xi}\right)^{1/2} d\xi \tag{5.8}$$

The preceding integral can be evaluated exactly as:

$$M(\pm a) = -\frac{\sigma_0 h'(t)}{2(\pi a)^{1/2}}\left|1 - \left(\frac{r_1}{r_2}\right)^{\pm 1/2} \cos[(\theta_1 - \theta_2)/2]\right| \tag{5.9}$$

where

$$0 < \theta_1 < \pi$$
$$0 < \theta_2 < \pi$$

where r_1, r_2, θ_1, and θ_2 are as defined by Fig. 2.

Equation (5.9) admits further simplification when the crack plane is orientated radially to the origin (i.e., $\phi_0 = 0$ or π). The crack face, then, either contains the origin and $\cos[(\theta_1 - \theta_2)/2] = 0$ or, the crack face does not contain the origin and $\cos[(\theta_1 - \theta_2)/2] = 1$. In the first case, the current intensity factor M is given by:

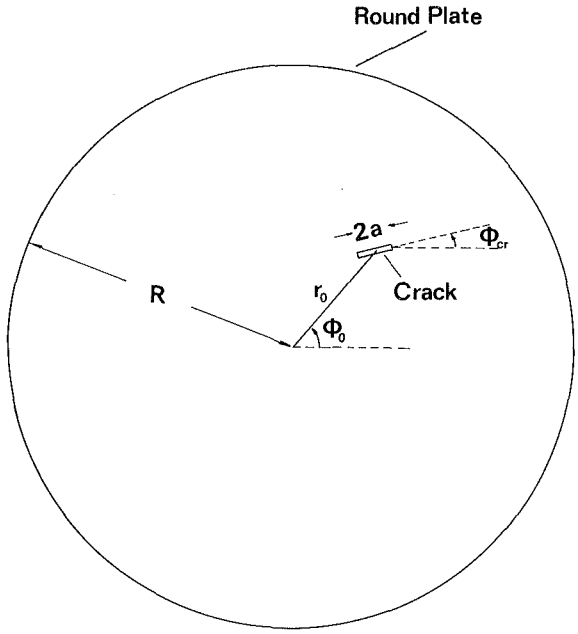


Fig. 3 A crack is located in a round plate of radius R with a uniform magnetic field. The crack position is given by r_0, ϕ_0 and the crack orientation by ϕ_{cr}.

$$M = -\frac{\sigma_0 h'(t)}{2(\pi a)^{1/2}} \tag{5.10}$$

and, surprisingly, is independent of the position of the magnetic source on the crack face. For the second case;

$$M\pm = -\frac{\sigma_0 h'(t)}{2(\pi a)^{1/2}}\left|1 - \left(\frac{r-a}{r+a}\right)^{\pm 1/2}\right| \tag{5.11}$$

where + refers to the crack tip furthest away from the source.

If the crack is sufficiently far away from the magnetic source so that the variation of the induced current is small along its length, equation (5.8) reduces to (by setting $\xi = 0$ and $r_0 = R$)

$$M = \mp \frac{\sigma_0 h'(t)}{2\pi r_0}(\pi a)^{-1/2}\cos(\theta_0 - \phi_{cr}) \tag{5.12}$$

The delta function solution in the foregoing could be used as a Green's function for superposition in more complex applied magnetic fields. We make no further use of this solution here, however.

In general, we may be interested in a local but nonsingular applied magnetic field B. As an example, we choose:

Case 1*b*: $g(r) = \dfrac{1}{\pi\lambda^2} e^{-\left(\frac{r}{\lambda}\right)^2}$

where λ is a representative length scale. The constants are chosen so that as $\lambda \to 0$, the two-dimensional delta function is obtained.

As before,

$$J_\phi = -\sigma_0 h'(t)\frac{1}{2\pi r}\left|1 - e^{-\left(\frac{r}{\lambda}\right)^2}\right| \tag{5.13}$$

Hence

$$M(\pm a) = \pm (\pi a)^{-1/2}\int_{-a}^{a}\left[\frac{\xi + r_0\cos(\phi_0 - \phi_{cr})}{R}\right] J_\phi\left[\frac{a \pm \xi}{a \mp \xi}\right]^{1/2} d\xi \tag{5.14}$$

where R is given by (5.4).

Downloaded 02 May 2010 to 171.66.16.54. Redistribution subject to ASME license or copyright; see http://www.asme.org/terms/Terms_Use.cfm

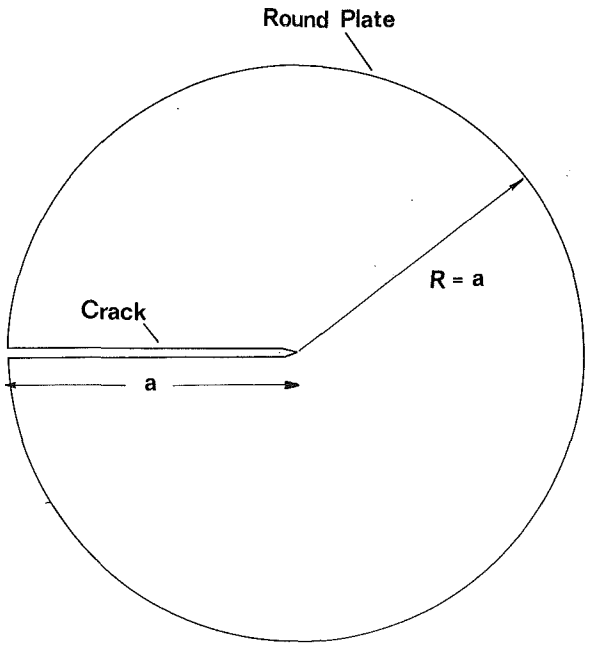


Fig. 4 A uniform magnetic field is applied to a half-cracked round plate of radius $R = a$

In general, $M(\xi = \pm a)$ can be evaluated using equations (4.4) and (4.5). However, if the crack is small enough so that the magnetic field $B(r, t)$ does not vary appreciably along its length, i.e.,

$$a \ll \lambda \tag{5.15}$$

then one can use the first term approximation of J_ϕ in equation (5.14), i.e., $R \sim r_0$ and $\xi \sim 0$. $M(\xi = \pm a)$ is then given by equations (5.13) and (5.14) as:

$$M(\pm a) = \mp \sigma_0 h'(t)(\pi a)^{1/2}\cos(\theta_0 - \phi_0)\frac{1}{2\pi r_{cr}}\left(1 - e^{-\left(\frac{r_0}{\lambda}\right)^2}\right) \tag{5.16}$$

The result here approaches the previous delta function results (i.e., equation (5.12)) for $\lambda \to 0$.

2. Round Plate, Small Crack. A small crack of length $2a$ in a circular plate of radius R is pictured in Fig. 3. The length and position of the crack is such that the small crack assumption of section 4 is satisfied. The applied magnetic field will be of the form $B(r, t) = B_0 h(t)$, where B_0 is a constant. The polar coordinate system (r, ϕ) is positioned at the center of the plate. The position and orientation of the crack can be assumed as arbitrary as long as the small crack assumption is not violated. Their specification is exactly the same as for problem one.

In this case $\mathbf{J}_p$ is given by

$$\left.\begin{aligned} \mathbf{J}_p &= J_\phi \hat{\phi} \\ J_\phi &= -1/2\sigma_0 B_0 r h'(t) \end{aligned}\right\} \tag{5.17}$$

The small crack assumption allows us to approximate the current intensity using equation (5.5). The current intensity factor $M(\pm a)$ is given by

$$M(\pm a) = \mp \frac{\sigma_0 h'(t) B_0}{2[\pi a]^{1/2}} \int_{-a}^{a} [\xi + r_0\cos(\phi_0 - \phi_{cr})]\left[\frac{a \pm \xi}{a \mp \xi}\right]^{1/2} d\xi \tag{5.18}$$

and is calculated to be

$$M(\pm a) = \mp \frac{\sigma_0 h'(t) B_0}{2}\left[r_0\cos(\phi_0 - \phi_{cr}) \pm \frac{a}{2}\right](\pi a)^{1/2} \tag{5.19}$$

Equation (5.19) points out that, for small cracks, the magnitude of the current intensity factor is smallest for the centrally located crack ($r_0 = 0$). Also, if we move the crack along the line $\phi = 0$ [which implies $\phi = \phi_{cr} = 0$], the magnitude of the current intensity in the right-hand crack tip is always larger. Indeed, the centrally located crack is a special case in which the second-order term of the expansion in equation (4.8) becomes important. This is reflected in the numerical calculation of Morjaria, et al. [1] which indicates that the current intensity is much stronger for the off-center crack. A comparison (using equation (5.16)) with their numerical results indicates an excellent agreement for the current intensity factor of a centrally located crack if $a/L = 0.05$; where L is the length of the side of the square plate. For the case if $a/L = 0.1$, the deviation of the numerical and theoretical result for M is less than 2 percent. Recalling that a is half the crack length, these results substantiate our claim for the small crack approximation formulated in the earlier sections.

The current intensity factor for the off-centered crack is compared with the same numerical computations, although the numerical data does not really satisfy our small crack assumption. For the case of $a/L = 0.1$, the center of the crack being displaced to the right by a distance of one crack length, the difference between the numerical result and results given by equation (5.19) is 11 percent for the current intensity factor of the right crack tip and 8 percent for the left crack tip.

3. Half-Cracked Round Plate. A crack of length a inside a circular plate of radius $2a$ is shown in Fig. 4. The center of the plate coincides with the crack tip. The applied magnetic field is of the same for as problem 2.

The complete solution of this boundary value problem can be obtained by conformal mapping or by using infinite series. The infinite series solution is given by Timoshenko for a mathematical equivalent torsional problem and will be presented below. Both approaches were used to evaluate the current intensity factor, leading to exactly the same results. The complete current field $\mathbf{J}$ is found to be [1]:

$$J_\theta = \frac{\sigma_0 B_0 h'(t)}{4}\left[-2r(1 - \cos 2\theta) + \frac{32a^2}{\pi}\sum_{n=1,3,5\ldots}^{\infty}(-1)^{(n+1)/2}\left(\frac{r}{a}\right)^{\frac{n}{2}-1}\frac{\cos(n\theta/2)}{(n^2-16)}\right] \tag{5.20}$$

$$J_r = \frac{\sigma_0 B_0 h'(t)}{4}\left[-2r\sin 2\theta - \frac{-32a^2}{\pi}\sum_{n=1,3,5\ldots}^{\infty}(-1)^{(n+1)/2}\left(\frac{r}{a}\right)^{\frac{n}{2}-1}\frac{\sin(u\theta/2)}{(n^2-16)}\right] \tag{5.21}$$

The dominant term as $r \to 0$ is given by

$$\left.\begin{aligned} J_\theta &= \left(\frac{\sigma_0 B_0 h'(t)}{2\pi}\right)\left[\frac{16}{15}\right] r^{-1/2} a^{3/2}\cos\theta/2 \\ J_r &= \frac{\sigma_0 B_0 h'(t)}{2\pi}\left[\frac{16}{15}\right] r^{-1/2} a^{3/2}\sin\theta/2 \end{aligned}\right\} \tag{5.22}$$

Thus the current intensity factor at the crack tip is

Downloaded 02 May 2010 to 171.66.16.54. Redistribution subject to ASME license or copyright; see http://www.asme.org/terms/Terms_Use.cfm

$$M(a) = M = \frac{\sigma_0 B_0 h'(t)}{\sqrt{2\pi}} \left(\frac{16}{15} \right) a^{3/2} \tag{5.23}$$

Acknowledgment

C. Y. Hui was supported in this work by the National Science Foundation Grant No. NSF82-04675. The authors would like to thank Frank Moon for valuable discussions.

References

1 Mukherjee, S., Morjaria, M., and Moon, F. C., "Eddy Current Flows Around Cracks in Thin Plates for Nondestructive Testing," ASME JOURNAL OF APPLIED MECHANICS, Vol. 49, June 1982, pp. 389-395.

2 Morjaria, M. A., Mukherjee, S., and Moon, F. C., "A Boundary Integral Method for Eddy Current Flow Around Cracks in Thin Plates," IEEE *Transaction on Magnetics*, Vol. Mag-18, March 1982, pp. 467-472.

3 Kahn, A. H., Spal, R., and Feldman, A., "Eddy Current Losses due to a Surface Crack in Conducting Material," *Journal of Applied Physics*, Vol. 48, No. 11, Nov. 1977, p. 4454.

4 Horie, T., Yagawa, G., Ando, Y., Masuda, M., "Fracture Mechanics Analysis Related to Electromagnetic Force," NEVT Research Report 81-03.

5 Johnson, H. H., "Calibrating the Electric Potential Method for Studying Slow Crack Growth," *Material Research and Standards*, Sept., 1965, pp. 442-445.

6 Clark, G., and Knott, J. F., "Measurement of Fatigue Cracks in Notched Specimens by Means of Theoretical Electrical Potential Calibrations," *J. Mech. Phys. Solids*, 1975, Vol. 23, pp. 215-276.

7 Ritchie, R. O., and Bathe, K. J., "On the Calibration of the Electrical Potential Technique for Monitoring Crack Growth Using Finite Element Methods," *International Journal of Fracture*, Vol. 15, No. 1, Feb. 1979, pp. 47-55.

8 Michael, D. H., Walchter, R. T., and Collins, R., "The Measurement of Surface Cracks in Metals by Using a.c. Electric Fields," *Proc. Royal Soc.*, Series *A*, Volume 381, 1982, pp.139-157.

9 Yuan, K. Y., "Finite Element Analysis of Magnetoelastic Plate Problems," Dept. of Structural Engineering Report No. 81-4, Cornell University.

10 Rice, J. R., "Mathematical Analysis in the Mechanics of Fracture," in *Fracture*, Liebowitz, ed., Vol. 2, Academic Press, New York, 1968, pp. 191-311.

11 Timoshenko, *Theory of Elasticity*, McGraw Hill, 1934, pp. 313-314.

Downloaded 02 May 2010 to 171.66.16.54. Redistribution subject to ASME license or copyright; see http://www.asme.org/terms/Terms_Use.cfm

Saint-Venant End Effects for Incremental Plane Deformations of Incompressible Nonlinearly Elastic Materials

R. Abeyaratne
Assoc. Mem. ASME

C. O. Horgan
Mem. ASME

D.-T. Chung
Graduate Student.

College of Engineering,
Michigan State University,
East Lansing, Mich. 48824

This paper is concerned with assessing the extent of Saint-Venant end effects within the theory of small deformations superposed on a large deformation for plane strain of homogeneous, isotropic, incompressible materials. The problem considered is that of plane deformation of a body which in its undeformed configuration, occupies a semi-infinite strip. The long sides of the strip are free of traction while the short side is subjected to prescribed normal and shear tractions. A purely normal tensile traction is applied uniformly at the remote end. For the case of slightly nonuniform end tractions at the near end, it is shown that the resulting stress distribution differs from that of homogeneous uniaxial tension by an exponentially decaying function of the distance from the end of the strip. The decay rate is characterized explicitly in terms of the strip width, the remotely applied tensile load, and constitutive parameters. Numerical results are provided for the Mooney-Rivlin material and power-law materials which either harden or soften in tension.

1 Introduction

The fundamental issues giving rise to the consideration of Saint-Venant's principle in elasticity are well known in the *linear* theory and the implications for practical stress analysis are widely understood. A recent review is given in [1]. In contrast, investigations of Saint-Venant's principle in the context of *finite* elasticity are comparatively few and of relatively recent origin (see, for example, the discussion in [1]). Some recent studies on the effect of nonlinearity on Saint-Venant's principle are [2, 3] which treat finite antiplane shear deformations of homogeneous isotropic incompressible materials, [4] which is concerned with a theory of plane strain with sufficiently small strains and strain gradients, and [5] in which three-dimensional deformations are considered. In all of these papers, qualitative methods for nonlinear partial differential equations are used to derive lower *bounds* for the rate of exponential decay of end effects arising from either self-equilibrated end loads [3, 5] or end loads statically equivalent to uniform shear [2] and to uniform tension or compression [4].

The present paper is concerned with assessing the extent of Saint-Venant end effects within the theory of small deformations superposed on a large deformation ([6]) for plane deformations of homogeneous, isotropic, incompressible materials. The problem considered is that of plane deformation of a body which in its undeformed configuration, occupies a semi-infinite strip. The long sides of the strip are free of traction while the short side is subjected to prescribed normal and shear tractions. A purely normal tensile traction is applied uniformly at the remote end. The case of compression is not considered in order to avoid possible instabilities of the semi-infinite strip. If the tractions at the accessible end of the strip *were* uniformly distributed, a possible corresponding deformation state is that of homogeneous uniaxial tension. The principle of Saint-Venant type established here compares this state of uniaxial tension with that arising from *slightly* nonuniform end tractions. Specifically, we show that the stress components in these two states differ by an exponentially decaying function of the distance from the end of the strip and provide an explicit characterization for the decay rate in terms of the strip width, the remotely applied tensile load and constitutive parameters.

The basic boundary-value problem arising here can be formulated as a boundary-value problem for a single fourth-order (elliptic) linear partial differential equation with constant coefficients (Section 3). The *exact* rate of exponential decay of end effects can be analyzed on employing an eigenfunction approach (Section 4), similar to the well-known method using the Papkovich-Fadle eigenfunctions in linear isotropic elasticity [7], and their analogs for the anisotropic case [8]. The decay rate is characterized in terms of a complex eigenvalue with smallest real part.

In Section 5, the specific examples of the Mooney-Rivlin material and power-law materials, which either harden or

Contributed by the Applied Mechanics Division for publication in the JOURNAL OF APPLIED MECHANICS.

Discussion on this paper should be addressed to the Editorial Department, ASME, United Engineering Center, 345 East 47th Street, New York, N.Y. 10017, and will be accepted until two months after final publication of the paper itself in the JOURNAL OF APPLIED MECHANICS. Manuscript received by ASME Applied Mechanics Division, April, 1984; final revision, January, 1985.

Copyright © 1985 by ASME
Downloaded 02 May 2010 to 171.66.16.54. Redistribution subject to ASME license or copyright; see http://www.asme.org/terms/Terms_Use.cfm

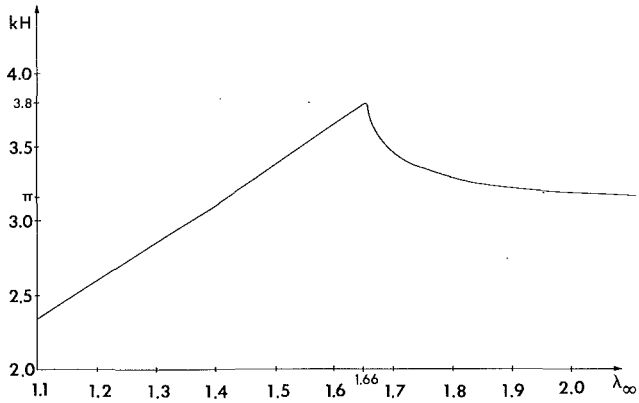


Fig. 1 The decay rate versus the applied stretch for the Mooney-Rivlin material

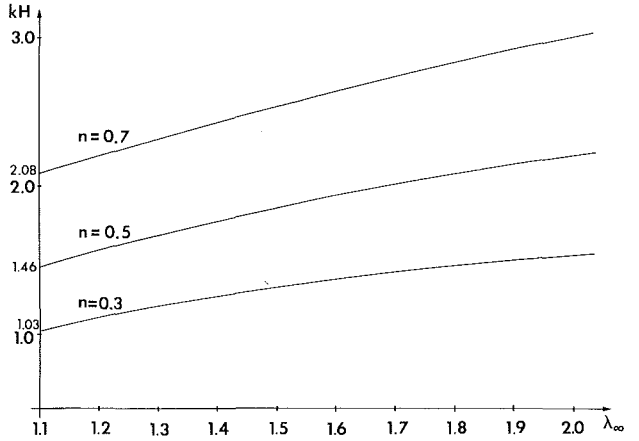


Fig. 2 The decay rate versus the applied stretch for power-law materials (hardening, $n<1$)

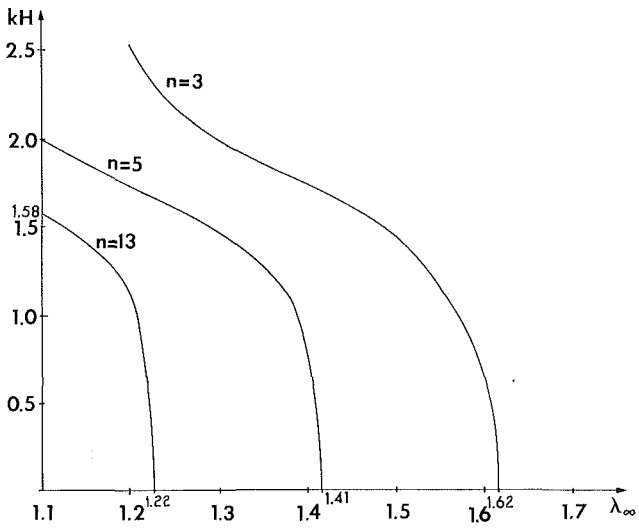


Fig. 3 The decay rate versus the applied stretch for power-law materials (softening, $n>1$)

soften in tension, are discussed. Figures 1–3 display the variation of the decay rate with the applied stretch. For the Mooney-Rivlin material (Fig. 1), the decay rate first increases with the applied stretch and decreases thereafter. An asymptotic formula for the decay rate for large load is obtained. For hardening power-law materials (Fig. 2) the decay rate increases with both the applied stretch and material hardening parameter. On the other hand, for softening power-law materials (Fig. 3), the decay rate decreases with these quantities.

2 Preliminaries

Let D_0 denote the undeformed cross section of a right cylinder in the (X_1, X_2)-plane. A plane deformation of the body, parallel to the (X_1, X_2) - plane, is described by $\mathbf{y} = \mathbf{y}(\mathbf{X}) = \mathbf{X} + \mathbf{u}(\mathbf{X})$ which maps D_0 onto a domain D^*. Here $\mathbf{X}$ and $\mathbf{y}$ denote the position vectors of a particle before and after deformation, respectively, and $\mathbf{u}$ is the displacement vector. The deformation gradient tensor field is defined by $\mathbf{F}(\mathbf{X}) = \nabla \mathbf{y}(\mathbf{X})$ and incompressibility implies that

$$\det \mathbf{F}(\mathbf{X}) = 1 \quad \text{on} \quad D_0. \tag{2.1}$$

In view of (2.1), the principal stretches of the deformation can be written as $\lambda_1 = \lambda^{-1}(>0)$, $\lambda_2 = \lambda\ (>0)$ and the invariant $I = \text{tr}\,\mathbf{F}\mathbf{F}^T$ takes the form

$$I = \text{tr}\mathbf{F}\mathbf{F}^T = \lambda^2 + \lambda^{-2}. \tag{2.2}$$

Next, let $\mathbf{S}(\mathbf{X})$ and $\boldsymbol{\sigma}(\mathbf{y})$ be the first Piola-Kirchhoff and the (symmetric) Cauchy stress tensor fields, respectively, $\mathbf{S} = \boldsymbol{\sigma}\mathbf{F}^{-T}$. Equilibrium, in the absence of body forces, requires that div $\boldsymbol{\sigma}(\mathbf{y}) = \mathbf{0}$ on D^*.

Finally, we turn to the constitutive relation for the incompressible, isotropic, homogeneous, nonlinearly elastic material at hand. Let $W(I)$ with $W' > 0$ denote the strain energy density function[1], characterizing the in-plane behavior of the material. The stresses $\boldsymbol{\sigma}$ and $\mathbf{S}$ are now given by

$$\boldsymbol{\sigma} = 2W'(I)\mathbf{F}\mathbf{F}^T - p\mathbf{1}, \quad \mathbf{S} = 2W'(I)\mathbf{F} - p\mathbf{F}^{-T}, \tag{2.3}$$

where p denotes the pressure.

In the particular case of *plane strain uniaxial tension*, $\sigma_{11} = \sigma_{12} = 0$, $\sigma_{22} = \sigma$, one finds from (2.2), (2.3) that $\sigma = \hat{\sigma}(\epsilon)$, where the response function $\hat{\sigma}$ and the strain ϵ are defined by

$$\hat{\sigma}(\epsilon) = 2(\lambda^2 - \lambda^{-2})W'(\lambda^2 + \lambda^{-2}),\ \epsilon = (\lambda - \lambda^{-1})/2. \tag{2.4}$$

We say that the material is *hardening* or *softening* at a certain strain level ϵ (in tension) if

$$\frac{d}{d\epsilon}\left(\frac{\hat{\sigma}(\epsilon)}{\epsilon}\right) > 0 \quad \text{or} < 0, \tag{2.5}$$

respectively. For example, for an Ogden-type [9] material, with $W = (\mu/2)(\lambda^\alpha + \lambda^{-\alpha} - 2)$, $\mu, \alpha > 0$, it follows from (2.4) that $\hat{\sigma} = (\mu\alpha/2)(\lambda^\alpha - \lambda^{-\alpha})$ which can be shown to be hardening or softening at all (tensile) deformations according as $\alpha > 1$ or $\alpha < 1$, respectively. Note that $\alpha = 2$ corresponds to the Mooney-Rivlin material. Similarly a power-law material $\hat{\sigma}(\epsilon) = \beta\epsilon^{1/n}$, $\beta, n > 0$, hardens or softens when $n < 1$ or $n > 1$, respectively.

The system of governing partial differential equations, written in terms of u_1, u_2, and p, can be shown to be elliptic at some point in D_0 and at a certain deformation level, if and only if, (see [10]),

$$W'(\lambda^2 + \lambda^{-2}) + 2(\lambda - \lambda^{-1})^2 W''(\lambda^2 + \lambda^{-2}) > 0. \tag{2.6}$$

It will be assumed throughout this paper that (2.6) holds so that *ellipticity* prevails. It can be readily shown from (2.4)–(2.6) that a state of uniaxial tension that is hardening is necessarily elliptic. Thus an Ogden material with $\alpha > 1$ and a power-law material with $n < 1$ are always elliptic. On the other hand, for softening materials in general, ellipticity holds only for sufficiently small values of λ. For example, a power-law material with $n > 1$ is elliptic in the range $1 < \lambda < \lambda_e$ and loses ellipticity at $\lambda = \lambda_e$ where

$$\lambda_e = (n^{1/2} + 1)/(n - 1)^{1/2}. \tag{2.7}$$

3 Formulation of Boundary-Value Problem

Suppose now that the undeformed cross section of the body is a semi-infinite strip of width $2H$, $D_0 = \{(X_1, X_2) |$

[1] The invariant I_3 is equal to unity for ischoric deformations, and plane strain, $I_1 = I_2 (\equiv I + 1)$.

Downloaded 02 May 2010 to 171.66.16.54. Redistribution subject to ASME license or copyright; see http://www.asme.org/terms/Terms_Use.cfm

$-H<X_1<H,\ X_2>0\}$. The long faces of the strip are assumed to be free of traction, so that

$$S_{21}=S_{11}=0 \quad \text{on} \quad X_1=\pm H,\quad X_2>0. \tag{3.1}$$

A purely normal tensile traction S_{22} is applied uniformly at the remote end, so that

$$S_{22}=S_\infty>0,\quad S_{12}=0 \quad \text{as} \quad X_2\to\infty,\quad -H<X_1<H. \tag{3.2}$$

Both normal and shear tractions are applied on the end $X_2=0$,

$$S_{22}=S_\infty+f(X_1),\quad S_{12}=g(X_1)$$
$$\text{on} \quad X_2=0,\quad -H<X_1<H. \tag{3.3}$$[2]

Here $f(X_1)$ and $g(X_1)$ are given, and overall force and moment equilibrium require that

$$\int_{-H}^{H} f(X_1)dX_1=\int_{-H}^{H} g(X_1)dX_1=0,$$
$$\int_{-H}^{H}[y_2(X_1,0)g(X_1)-y_1(X_1,0)f(X_1)]dX_1 \tag{3.4}$$
$$=S_\infty\int_{-H}^{H} y_1(X_1,0)dX_1,$$

respectively, where $(y_1,\ y_2)$ are the deformed coordinates. Note that $(3.4)_1$ are restrictions on the data while $(3.4)_2$ is a compatibility relation between the data and the deformation (cf. Gurtin [11]).

If the distribution of normal and shear stress on the end $X_2=0$ was uniform (and so $f=g\equiv 0$) a possible deformation, pressure, and stress state corresponds to a homogeneous state of plane-strain uniaxial tension ($S_\infty>0$, $\lambda_\infty>1$):

$$S_\infty=2\lambda_\infty^{-1}(\lambda_\infty^2-\lambda_\infty^{-2})W'(\lambda_\infty^2+\lambda_\infty^{-2}),\ \sigma_\infty=S_\infty\lambda_\infty, \tag{3.5}$$

$$y_1=\lambda_\infty^{-1}X_1,\ y_2=\lambda_\infty X_2,\ p=\sigma_\infty/(\lambda_\infty^4-1), \tag{3.6}$$

$$\sigma_{11}=\sigma_{12}=0,\ \sigma_{22}=\sigma_\infty. \tag{3.7}$$

The half-width of the deformed strip is

$$h=H\lambda_\infty^{-1}. \tag{3.8}$$

In the present study we restrict attention to the case in which f and g are both small. Then, one would expect the various elastostatic fields to differ only slightly from those given by (3.5)–(3.7), allowing one to carry out an analysis based on the theory of small deformations superposed on a large deformation. Thus, we assume that

$$y_1=\lambda_\infty^{-1}X_1+\tilde{u}_1(x_1,x_2),\quad y_2=\lambda_\infty X_2+\tilde{u}_2(x_1,x_2),$$
$$p=\sigma_\infty/(\lambda_\infty^4-1)+\tilde{p}(x_1,x_2), \tag{3.9}$$

where we have set $x_1=\lambda_\infty^{-1}X_1$, $x_2=\lambda_\infty X_2$, and $|\tilde{u}_{\alpha,\beta}|$, $|\tilde{p}_{,\alpha}|$ are assumed to be small compared to unity. Here a comma followed by a subscript denotes partial differentiation with respect to the corresponding x-coordinate. Linearization of the incompressibility condition (2.1) based on the small displacement gradient $\tilde{u}_{\alpha,\beta}$ gives

$$\tilde{u}_{\alpha,\alpha}=0 \quad \text{on } D, \tag{3.10}$$

where D denotes the strip $\{(x_1,\ x_2)\,|-h<x_1<h,\ x_2>0\}$. Similarly, linearization of the constitutive relation $(2.3)_1$ leads to

$$\tilde{\sigma}_{11}\equiv\sigma_{11}=L_{11}\tilde{u}_{1,1}-\tilde{p},\quad \tilde{\sigma}_{22}\equiv\sigma_{22}-\sigma_\infty=L_{22}\tilde{u}_{2,2}-\tilde{p}$$
$$\tilde{\sigma}_{12}=\tilde{\sigma}_{21}\equiv\sigma_{12}=L_{12}\tilde{u}_{1,2}+L_{21}\tilde{u}_{2,1} \tag{3.11}$$

where the (constant) incremental moduli $L_{\alpha\beta}(\neq L_{\beta\alpha})$ are

$$L_{11}=4\lambda_\infty^{-2}[W'+(\lambda_\infty^{-2}-\lambda_\infty^2)W''],$$
$$L_{22}=4\lambda_\infty^2[W'+(\lambda_\infty^2-\lambda_\infty^{-2})W'']L_{12}=2\lambda_\infty^2W',\ L_{21}=2\lambda_\infty^{-2}W'. \tag{3.12}$$

Here, and henceforth, W' and W'' are evaluated at $I=\lambda_\infty^2+\lambda_\infty^{-2}$. Linearization of $\mathbf{S}=\sigma\mathbf{F}^{-T}$ yields the following expressions for the Piola-Kirchhoff stress $\mathbf{S}$,

$$\tilde{S}_{11}\equiv S_{11}=\lambda_\infty\tilde{\sigma}_{11},\quad \tilde{S}_{22}\equiv S_{22}-S_\infty=\lambda_\infty^{-1}(\tilde{\sigma}_{22}+\sigma_\infty\tilde{u}_{1,1}),$$
$$\tilde{S}_{12}\equiv S_{12}=\lambda_\infty^{-1}\tilde{\sigma}_{12},\quad \tilde{S}_{21}\equiv S_{21}=\lambda_\infty(\tilde{\sigma}_{21}-\sigma_\infty\tilde{u}_{1,2}). \tag{3.13}$$

The linearized equilibrium equations $\tilde{\sigma}_{\alpha\beta,\beta}=0$ on D hold if and only if the stress components are expressed in terms of an Airy stress function $\Phi(x_1,x_2)$ by

$$\tilde{\sigma}_{11}=\Phi_{,22},\quad \tilde{\sigma}_{22}=\Phi_{,11},\quad \tilde{\sigma}_{12}=\tilde{\sigma}_{21}=-\Phi_{,12}. \tag{3.14}$$

Equations (3.10), (3.11), and (3.14) are readily shown to lead to the following compatibility equation for Φ:

$$L_{21}\Phi_{,1111}+(L_{11}+L_{22}-L_{12}-L_{21})\Phi_{,1122}$$
$$+L_{12}\Phi_{,2222}=0 \quad \text{on } D. \tag{3.15}$$

Turning finally to the boundary conditions on the strip, we find from (3.1)–(3.3), (3.8), (3.10), (3.13), (3.14) that

$$\Phi_{,22}=0,\ (L_{11}+L_{22}+\sigma_\infty)\Phi_{,221}-\sigma_\infty\Phi_{,111}=0$$
$$\text{on} \quad x_1=\pm h, x_2>0, \tag{3.16}$$

$$\Phi_{,12}=0,\ (L_{11}+L_{22}-\sigma_\infty)\Phi_{,11}+\sigma_\infty\Phi_{,22}=0$$
$$\text{as} \quad x_2\to\infty,\ |x_1|<h, \tag{3.17}$$

$$\Phi_{,12}=-\lambda_\infty g,\ (L_{11}+L_{22}-\sigma_\infty)\Phi_{,11}$$
$$+\sigma_\infty\Phi_{,22}=\lambda_\infty f(L_{11}+L_{22}) \quad \text{on} \quad x_2=0,\ |x_1|<h. \tag{3.18}$$

It can be shown that the ellipticity condition (2.6) implies that the fourth-order partial differential equation (3.15) is elliptic everywhere on D. We are concerned in what follows with investigating the spatial decay behavior of solutions of the boundary-value problem (3.15)–(3.18), where f and g satisfy $(3.4)_1$. We note that, upon linearization, the moment condition $(3.4)_2$ becomes

$$\int_{-h}^{h} x_1 f(\lambda_\infty x_1)dx_1=-S_\infty\int_{-h}^{h}\tilde{u}_1(x_1,0)dx_1. \tag{3.19}$$

As observed previously, this is a compatibility relation between the data and the displacement. It is of interest to note that if the ground state was undeformed, ($S_\infty=0$, $\lambda_\infty=1$), (3.19) then becomes the classical moment restriction on data of the infinitesimal problem.

4 Eigenfunctions and Eigenvalues

We seek solutions of equation (3.15) in the form

$$\Phi(x_1,x_2)=e^{-\gamma x_2}F(x_1), \tag{4.1}$$

where γ is a constant. Substituting (4.1) into equation (3.15) yields the fourth-order ordinary differential equation

$$L_{21}F^{iv}+(L_{11}+L_{22}-L_{12}-L_{21})\gamma^2F''+L_{12}\gamma^4F=0, \tag{4.2}$$

on $-h<x_1<h$, where the prime denotes differentiation with respect to x_1. The boundary conditions (3.16), on using (4.1), read

$$F(\pm h)=0,(L_{11}+L_{22}+\sigma_\infty)\gamma^2F'(\pm h)-\sigma_\infty F'''(\pm h)=0. \tag{4.3}$$

Equations (4.2) and (4.3) constitute an eigenvalue problem for the ordinary differential equation (4.2) with eigenvalue parameter γ. Eigenvalue problems of this type occur in a variety of situations arising in linear elasticity and for Stokes

[2] Since in the sequel we restrict attention to the case where f and g are small, results for the equivalent Cauchy traction problem follow directly from those obtained here with $\sigma_\infty=S_\infty\lambda_\infty$.

Downloaded 02 May 2010 to 171.66.16.54. Redistribution subject to ASME license or copyright; see http://www.asme.org/terms/Terms_Use.cfm

flows and have attracted considerable recent attention (see e.g., [12]). For linear isotropic plane elasticity, the resulting eigenfunctions are the well-known Papkovich-Fadle eigenfunctions, the completeness of which have been recently established by Gregory [13]. Corresponding results for the eigenfunctions of (4.2), (4.3) are as yet unknown.

A solution of (4.2) is sought in the form

$$F(x_1) = e^{\mu\gamma x_1}, \ \mu = \text{constant}, \tag{4.4}$$

which leads to the characteristic equation

$$L_{21}\mu^4 + (L_{11} + L_{22} - L_{12} - L_{21})\mu^2 + L_{12} = 0, \tag{4.5}$$

a quadratic equation for the quantity μ^2. It is convenient in what follows to consider three separate cases, according to whether the discriminant Δ of (4.5), given by

$$\Delta \equiv (L_{11} + L_{22} - L_{12} - L_{21})^2 - 4L_{21}L_{12}, \tag{4.6}$$

is positive, negative, or zero, respectively. Using (3.12), we find

$$\begin{aligned}\Delta &= 4(\lambda_\infty^2 - \lambda_\infty^{-2})^2[W' + 2(\lambda_\infty + \lambda_\infty^{-1})^2 W''][W' \\ &\qquad + 2(\lambda_\infty - \lambda_\infty^{-1})^2 W''], \\ &= \frac{1}{2}(\lambda_\infty + \lambda_\infty^{-1})^3(\lambda_\infty - \lambda_\infty^{-1})\frac{d}{d\epsilon}\left(\frac{\hat{\sigma}}{\epsilon}\right)\Big|_{\epsilon_\infty}[W' \\ &\qquad + 2(\lambda_\infty - \lambda_\infty^{-1})^2 W''],\end{aligned} \tag{4.7}$$

where $\epsilon_\infty = (\lambda_\infty - \lambda_\infty^{-1})/2 > 0$. Equation (2.4) has been used to obtain the second version of (4.7). By virtue of the ellipticity assumption (2.6) the last term in (4.7) is positive and so our classification depends on whether $d/d\epsilon(\hat{\sigma}/\epsilon)|_{\epsilon_\infty}$ is positive, negative, or zero, respectively.

Case *A* $d/d\epsilon(\hat{\sigma}/\epsilon)|_{\epsilon_\infty} > 0$ **(Hardening).** In this case, it can be shown from (4.7), (3.12), and (2.6) that $L_{11} + L_{22} - L_{12} - L_{21}$ is positive and so the roots μ of (4.5) are purely imaginary. Since these roots occur in conjugate pairs, they may be written as $\mu_{1,2} = \pm iq_1$, $\mu_{3,4} = \pm iq_2$ where $q_\alpha (\alpha = 1,2)$ are real and are given by

$$q_{1,2} = \{[(L_{11} + L_{22} - L_{12} - L_{21}) \mp \sqrt{\Delta}]/2L_{21}\}^{1/2}. \tag{4.8}$$

Thus, from (4.4) and (4.8), the general solution of (4.2) in this case may be written as a linear combination of sines and cosines of the arguments $\gamma q_1 x_1$, $\gamma q_2 x_2$. On substitution into the boundary conditions (4.3), this leads to a transcendental equation for the (generally complex) eigenvalues γ. The resulting eigenfunctions may be separated into even and odd functions corresponding to symmetric and antisymmetric deformations, respectively. It can be shown that the even eigenfunctions[3] are

$$F(x_1) = \frac{\cos\gamma q_1 x_1}{\cos\gamma q_1 h} - \frac{\cos\gamma q_2 x_1}{\cos\gamma q_2 h}, \tag{4.9}$$

where γ is given as the root of the transcendental equation

$$\begin{aligned}&(L_{11} + L_{22} + \sigma_\infty + \sigma_\infty q_1^2) q_1 \tan(\gamma q_1 h) \\ &\qquad = (L_{11} + L_{22} + \sigma_\infty + \sigma_\infty q_2^2) q_2 \tan(\gamma q_2 h).\end{aligned} \tag{4.10}$$

Case *B* $d/d\epsilon(\hat{\sigma}/\epsilon)|_{\epsilon_\infty} < 0$ **(Softening).** In this case, the roots μ of (4.5) may be written as $\mu_{1,2} = (p \pm iq)$, $\mu_{3,4} = -(p \pm iq)$ where p,q are real and are given by

$$p = \left\{\frac{1}{2}\left(\frac{L_{12}}{L_{21}}\right)^{1/2} - \frac{(L_{11} + L_{22} - L_{12} - L_{21})}{4L_{21}}\right\}^{1/2}, \tag{4.11}$$

$$q = \left\{\frac{1}{2}\left(\frac{L_{12}}{L_{21}}\right)^{1/2} + \frac{(L_{11} + L_{22} - L_{12} - L_{21})}{4L_{21}}\right\}^{1/2}. \tag{4.12}$$

[3] In the sequel, we confine attention to consideration of *even* eigenfunctions since one expects that the corresponding Airy stress function (4.1), and hence the corresponding stresses, decay more slowly than those corresponding to the odd eigenfunctions.

The even eigenfunctions are

$$F(x_1) = \frac{\cosh\gamma p x_1 \cos\gamma q x_1}{\cosh\gamma p h \cos\gamma q h} - \frac{\sinh\gamma p x_1 \sin\gamma q x_1}{\sinh\gamma p h \sin\gamma q h}, \tag{4.13}$$

where

$$a\sin(2\gamma q h) = b\sinh(2\gamma p h). \tag{4.14}$$

Here a and b are given by

$$\begin{aligned}a &= \{L_{11} + L_{22} + \sigma_\infty(1 - p^2 + 3q^2)\}p, \\ b &= -\{L_{11} + L_{22} + \sigma_\infty(1 - 3p^2 + q^2)\}q.\end{aligned} \tag{4.15}$$

Case *C* $d/d\epsilon(\hat{\sigma}/\epsilon)|_{\epsilon_\infty} = 0$. In this case, we see from (4.7) that the discriminant $\Delta = 0$. The roots μ of (4.5) may be written as $\mu_{1,2} = ir$, $\mu_{3,4} = -ir$, where r is real and is given by

$$r = \left(\frac{L_{11} + L_{22} - L_{12} - L_{21}}{2L_{21}}\right)^{1/2} = \left(\frac{L_{12}}{L_{21}}\right)^{1/4}. \tag{4.16}$$

The even eigenfunctions are

$$F(x_1) = \frac{\cos\gamma r x_1}{\cos\gamma r h} - \frac{x_1 \sin\gamma r x_1}{h\sin\gamma r h}, \tag{4.17}$$

where

$$\frac{\sin(2\gamma r h)}{2\gamma r h} = -\frac{\{L_{11} + L_{22} + \sigma_\infty + \sigma_\infty r^2\}}{\{L_{11} + L_{22} + \sigma_\infty + 3\sigma_\infty r^2\}}. \tag{4.18}$$

By virtue of (3.12) and $(4.16)_2$, we have $r = \lambda_\infty$. Since $\hat{\sigma}'(\epsilon_\infty) = \sigma_\infty/\epsilon_\infty$ in Case *C*, (2.4), (3.5), and (3.12) may be used to show that equation (4.18) simplifies to read

$$\frac{\sin(2\gamma H)}{2\gamma H} = \frac{-(1 + \lambda_\infty^2)}{3\lambda_\infty^2 - 1}. \tag{4.19}$$

5 Stress Decay: Examples

The preceding considerations suggest that the solution to the boundary-value problem (3.15)–(3.18) and (3.4) may be sought as an infinite series of the form (4.1), summed over the eigenfunctions and eigenvalues of (4.2), (4.3). Assuming the completeness of these eigenfunctions, it follows that the dominant exponential decay rate for Φ is given by the real part γ_1 of the eigenvalue γ with *smallest real part*. Thus, in view of (3.13) and (3.14), the Piola-Kirchhoff stresses $S_{11}(X_1, X_2)$, S_{12}, S_{21}, and $S_{22} - S_\infty$ all have an exponentially decaying factor e^{-kX_2}, where the *characteristic decay rate* k is given by

$$kH = \gamma_1 \lambda_\infty H = \gamma_1 h \lambda_\infty^2, \tag{5.1}$$

with corresponding *characteristic decay length* $ln(100)/k$. Thus, to determine the decay rate, we need to find $\gamma_1 h$ from the transcendental equations (4.10), (4.14), and (4.19). In what follows, we discuss this in several different contexts.

***(i)* Mooney-Rivlin Material.** Here we have $W = \mu/2(\lambda^2 + \lambda^{-2} - 2)$ where μ is the ground-state shear modulus. It follows from (3.12) that

$$L_{12} = \mu\lambda_\infty^2, \quad L_{21} = \mu\lambda_\infty^{-2}, \quad L_{11} + L_{22} = 2\mu(\lambda_\infty^2 + \lambda_\infty^{-2}). \tag{5.2}$$

Since this material is hardening at all deformations, Case *A* applies. It follows from (5.2) and (4.8) that $q_1 = 1$, $q_2 = \lambda_\infty^2$ and so the transcendental equation (4.10) now reads

$$4\tan(\gamma h) = \lambda_\infty^2(\lambda_\infty^2 + \lambda_\infty^{-2})^2 \tan(\gamma h \lambda_\infty^2). \tag{5.3}$$

The roots γh of (5.3) are complex in general. In Table 1, we have tabulated the roots of smallest real part for different values of the stretch λ_∞, and the corresponding values of the decay rate k as given by (5.1). The latter results are displayed graphically in Fig. 1. Observe that as λ_∞ increases, kH increases until $\lambda_\infty \simeq 1.659$ and decreases thereafter. It was found that the root γh of smallest real part is complex on the former range and real on the latter.

It is of interest to derive an asymptotic estimate for the decay rate k for large values of the load S_∞ (i.e., $\lambda_\infty >> 1$). Under this condition, the transcendental equation (5.3) has a

Downloaded 02 May 2010 to 171.66.16.54. Redistribution subject to ASME license or copyright; see http://www.asme.org/terms/Terms_Use.cfm

smallest real root. Using appropriate Taylor expansions in (5.3), it can be shown that (cf. [8], p. 428) $\gamma h \simeq \pi/\lambda_\infty^2$ as $\lambda_\infty \to \infty$ and so from (5.1) we obtain

$$kH \sim \pi \quad \text{for large } S_\infty, \tag{5.4}$$

for the Mooney-Rivlin material. From Table 1 it is seen that this asymptotic formula is accurate for values of λ_∞ exceeding approximately 2.

***(ii)* Self-Equilibrated Load ($S_\infty = 0$).** Here we are concerned with the limiting behavior of the decay rate k of (5.1) as $S_\infty \to 0$ (i.e., $\lambda_\infty \to 1$). In this limit the transcendental equations all reduce to

$$\sin(2\gamma H) = -2\gamma H. \tag{5.5}$$

Of course, as expected, this is the well-known transcendental equation governing the even Papkovich-Fadle eigenfunctions of linear isotropic elasticity [7]. It is known that $\gamma_1 H = 2.106$ which from (5.1) yields

$$kH \to 2.106 \quad \text{as} \quad \lambda_\infty \to 1, \tag{5.6}$$

and so the characteristic decay length is approximately one strip width.

***(iii)* Power-Law Material (Hardening, $n<1$).** The commonly used pure power-law form

$$\hat{\sigma}(\epsilon) = \beta \epsilon^{1/n}, \; 0<n<1, \; \beta>0, \tag{5.7}$$

is adopted here and suitably describes more general power-law materials provided the ground-state strain is large. This material is hardening at all deformations and so Case *A* applies. Thus from (2.4), (3.12), and (4.8) we obtain

$$q_{1,2}^2 = \frac{\lambda_\infty^2}{2}(\lambda_\infty + \lambda_\infty^{-1})^2 \left[\frac{1}{n} - \frac{(\lambda_\infty^2 + \lambda_\infty^{-2})}{(\lambda_\infty + \lambda_\infty^{-1})^2} \mp \left(\frac{1-n}{n}\right)^{1/2} \left\{ \frac{1}{n} - \frac{(\lambda_\infty + \lambda_\infty^{-1})^2}{(\lambda_\infty + \lambda_\infty^{-1})^2} \right\}^{1/2} \right]. \tag{5.8}$$

Table 1 Roots of (5.3) with smallest real part and corresponding decay rates. Mooney-Rivlin material

λ_∞	γh	kH
1.1	$1.937 + i0.926$	2.344
1.2	$1.799 + i0.760$	2.591
1.3	$1.683 + i0.616$	2.844
1.4	$1.584 + i0.486$	3.104
1.5	$1.499 + i0.358$	3.372
1.6	$1.426 + i0.208$	3.651
1.659	$1.389 + i0.016$	3.824
1.66	1.368	3.768
1.7	1.201	3.470
1.8	1.018	3.299
1.9	0.896	3.233
2.0	0.800	3.198
5.0	0.126	3.142
7.0	0.064	3.142

Using (2.4), (3.12), and (5.7) the transcendental equation (4.10) may be written

$$\left\{ \frac{(\lambda_\infty + \lambda_\infty^{-1})}{n} + (\lambda_\infty - \lambda_\infty^{-1})(1+q_1^2) \right\} q_1 \tan(\gamma q_1 h) = \left\{ \frac{(\lambda_\infty + \lambda_\infty^{-1})}{n} + (\lambda_\infty - \lambda_\infty^{-1})(1+q_2^2) \right\} q_2 \tan(\gamma q_2 h). \tag{5.9}$$

The roots γh of (5.9) are complex in general. In Table 2, we have tabulated the roots of smallest real part and the corresponding values of kH for different values of λ_∞ and n. The latter results are displayed graphically in Fig. 2. Observe that, for each n, as the stretch λ_∞ increases, the decay rate k increases. Furthermore, for fixed values of λ_∞, the decay rate increases with the hardening exponent n. (It was found that the root γh of smallest real part is in fact real.)

It is of interest to obtain an asymptotic estimate for the decay rate k for large S_∞. As $S_\infty \to \infty$ (i.e., $\lambda_\infty \to \infty$) (5.9) reduces to

$$\frac{n}{(1-n)^3} \tan\left(\gamma h \sqrt{\frac{n}{1-n}}\right) = \lambda_\infty^6 \tan\left(\gamma h \lambda_\infty^2 \sqrt{\frac{1-n}{n}}\right), \tag{5.10}$$

which has a smallest real root. This together with (5.1) yields the asymptotic estimate

$$kH \sim \pi\sqrt{n/(1-n)} \quad \text{for large } S_\infty. \tag{5.11}$$

(It was found that this formula is accurate for values of λ_∞ exceeding approximately 10). As $n \to 1$, the decay rate according to (5.11) tends to infinity. It can be shown that the material approaches a loss of ellipticity in this limit $n \to 1$, $\lambda_\infty \to \infty$ (cf. (2.7)) and that the associated characteristics in the reference configuration are aligned with the short sides of the strip.

***(iv)* Power-Law Material (Softening, $n>1$).** The constitutive law in tension is now given by (5.7) with $n>1$, which is softening at all deformations. Furthermore, recall from (2.7) that the ellipticity condition (2.6) is satisfied only if $\lambda_\infty < \lambda_e$. Thus, in this range Case *B* applies. Therefore from (2.4), (3.12), (4.11), (4.12), and (5.7) we have

$$p^2 = \frac{\lambda_\infty^2}{4}(\lambda_\infty + \lambda_\infty^{-1})^2 \left(\frac{n-1}{n}\right), \quad q^2 = \frac{\lambda_\infty^2}{4}\left\{ \frac{(\lambda_\infty + \lambda_\infty^{-1})^2}{n} - (\lambda_\infty - \lambda_\infty^{-1})^2 \right\}, \tag{5.12}$$

and so, in view of (4.15), the transcendental equation (4.15) may thus be written as

$$\left\{ \frac{1}{n}\left(\frac{\lambda_\infty + \lambda_\infty^{-1}}{\lambda_\infty - \lambda_\infty^{-1}}\right) + 1 - p^2 + 3q^2 \right\} p \sin(2\gamma q h) = -\left\{ \frac{1}{n}\left(\frac{\lambda_\infty + \lambda_\infty^{-1}}{\lambda_\infty - \lambda_\infty^{-1}}\right) + 1 - 3p^2 + q^2 \right\} q \sinh(2\gamma p h). \tag{5.13}$$

Table 2 Roots of (5.9) with smallest real part and corresponding decay rates. Power-law material (hardening, $n<1$)

λ_∞	$n=0.3$		$n=0.5$		$n=0.7$	
	γh	kH	γh	kH	γh	kH
1.1	0.853	1.033	1.209	1.463	1.720	2.081
1.2	0.773	1.113	1.092	1.572	1.527	2.199
1.3	0.702	1.187	0.991	1.674	1.369	2.314
1.4	0.640	1.254	0.903	1.769	1.238	2.426
1.5	0.585	1.315	0.825	1.857	1.126	2.534
1.6	0.535	1.371	0.757	1.939	1.031	2.639
1.7	0.492	1.421	0.697	2.014	0.948	2.739
1.8	0.453	1.467	0.643	2.084	0.875	2.835
1.9	0.418	1.508	0.595	2.149	0.811	2.927
2.0	0.387	1.546	0.552	2.209	0.754	3.014

Downloaded 02 May 2010 to 171.66.16.54. Redistribution subject to ASME license or copyright; see http://www.asme.org/terms/Terms_Use.cfm

Table 3 Roots of (5.13) with smallest real part and corresponding decay rates. Power-law material (softening, $n>1$)

$n=3$		
λ_∞	γh	kH
1.1	$2.003+i0.836$	2.424
1.2	1.755	2.528
1.3	1.182	1.998
1.4	0.886	1.736
1.5	0.637	1.433
1.6	0.268	0.687
1.61	0.182	0.472

$n=5$		
λ_∞	γh	kH
1.1	1.676	2.028
1.2	1.199	1.726
1.3	0.871	1.471
1.4	0.366	0.718
1.411	0.182	0.362
1.412	0.152	0.302
1.413	0.113	0.225
1.414	0.048	0.095

$n=13$		
λ_∞	γh	kH
1.1	1.307	1.582
1.2	0.791	1.139
1.221	0.378	0.563
1.222	0.328	0.489
1.223	0.265	0.397
1.224	0.176	0.263

In Table 3, the roots γh of (5.13) of smallest real part and the corresponding values of kH are tabulated for different values of λ_∞ and n. The latter results are displayed graphically in Fig. 3. Observe from the figure that, for each n, as λ_∞ increases, kH decreases. Notice that in each case the decay rate tends to zero[4] as λ_∞ tends to a critical value and so end effects are propagated without attenuation in this limit. It is readily verified that these values are *less* than the corresponding values of λ_e given by (2.7). They correspond to the stretches at which bifurcation of the strip into a diffuse mode can occur [14].

[4] In the case of hardening materials (Case *A*), this cannot occur since it is readily shown, on using $q_1 < q_2$, that the transcendental equation (4.10) does not have a purely imaginary root.

Acknowledgment

The work of one of the authors (C.O.H.) was supported by the National Science Foundation under Grant MEA-78-26071.

References

1 Horgan, C. O., and Knowles, J. K., "Recent Developments Concerning Saint-Venant's Principle," in *Advances in Applied Mechanics*, Vol. 23, Hutchinson, J. W., and Wu, T. Y., eds., Academic Press, New York, 1983, pp. 179–269.

2 Horgan, C. O., and Knowles, J. K., "The Effect of Nonlinearity on a Principle of Saint-Venant Type," *Journal of Elasticity*, Vol. 11, 1981, pp. 271–291.

3 Horgan, C. O., and Abeyaratne, R., "Finite Anti-Plane Shear of a Semi-Infinite Strip Subject to a Self-Equilibrated End Traction," *Quarterly of Applied Mathematics*, Vol. 40, 1983, pp. 407–417.

4 Breuer, S., and Roseman, J. J., "Saint-Venant's Principle in Nonlinear Plane Elasticity with Sufficiently Small Strains," *Archive for Rational Mechanics and Analysis*, Vol. 80, 1982, pp. 19–37.

5 Knops, R. J., and Payne, L. E., "A Saint-Venant Principle for Nonlinear Elasticity," *Archive for Rational Mechanics and Analysis*, Vol. 81, 1983, pp. 1–12.

6 Green, A. E., Rivlin, R. S., and Shield, R. T., "General Theory of Small Elastic Deformations Superposed on Large Elastic Deformations," *Proceedings of the Royal Society of London*, Series *A*, Vol. 211, 1952, pp. 128–154.

7 Timoshenko, S. P., and Goodier, J. N., *Theory of Elasticity*, 3rd ed., McGraw-Hill, New York, 1970.

8 Choi, I., and Horgan, C. O., "Saint-Venant's Principle and End Effects in Anisotropic Elasticity," ASME JOURNAL OF APPLIED MECHANICS, Vol. 44, 1977, pp. 424–430.

9 Ogden, R. W., "Large Deformation Isotropic Elasticity—On the Correlation of Theory and Experiment for Incompressible Rubberlike Solids," *Proceedings of the Royal Society of London*, Series *A*, Vol. 326, 1972, pp. 565–584.

10 Abeyaratne, R., "Discontinuous Deformation Gradients in Plane Finite Elastostatics of Incompressible Materials," *Journal of Elasticity*, Vol. 10, 1980, pp. 255–293.

11 Gurtin, M. E., *An Introduction to Continuum Mechanics*, Academic Press, New York, 1981.

12 Joseph, D. D., Sturges, L. D., and Warner, W. H., "Convergence of Biorthogonal Series of Biharmonic Eigenfunctions by the Method of Titchmarsh," *Archive for Rational Mechanics and Analysis*, Vol. 78, 1982, pp. 223–274.

13 Gregory, R. D., "The Traction Boundary-Value Problem for the Elastostatic Semi-Infinite Strip; Existence of Solution and Completeness of the Papkovich-Fadle Eigenfunctions," *Journal of Elasticity*, Vol. 10, 1980, pp. 295–327.

14 Hill, R., and Hutchinson, J. W., "Bifurcation Phenomena in the Plane Tension Test," *Journal of the Mechanics and Physics of Solids*, Vol. 23, 1975, pp. 239–264.

Downloaded 02 May 2010 to 171.66.16.54. Redistribution subject to ASME license or copyright; see http://www.asme.org/terms/Terms_Use.cfm

The Dynamic, Steady-State Propagation of an Antiplane Shear Crack in a General Linearly Viscoelastic Layer[1]

J. R. Walton
Department of Mathematics,
Texas A & M University,
College Station, Texas 77843

In a previous paper, the dynamic, steady-state propagation of a semi-infinite antiplane shear crack was considered for an infinite, general linearly viscoelastic body. Under the assumptions that the shear modulus is a positive, nonincreasing continuous and convex function of time, convenient, closed-form expressions were derived for the stress intensity factor and for the entire stress distribution ahead of and in the plane of the advancing crack. The solution was shown to have a simple, universal dependence on the shear modulus and crack speed from which qualitative and quantitative information can readily be gleaned. Here, the corresponding problem for a general, linearly viscoelastic layer is solved. An infinite series representation for the stress intensity factor is derived, each term of which can be calculated recursively in closed form. As before, a simple universal dependence on crack speed and material properties is exhibited.

Problem Formulation

The analysis of dynamic fracture models, that is, models based on the equations of motion of continuum mechanics rather than the equations of equilibrium, has received considerable attention recently in the applied mechanics literature. Principally for the sake of mathematical convenience, most of these studies have been in the context of linear elasticity. Consequently, for elastic material, many canonical boundary value problems have been solved, either in closed form or numerically, for both steady-state and transient modes of crack propagation. For viscoelastic material, however, much less progress has been made in constructing convenient analytical solutions to even the simplest dynamic crack problems.

In [2], an analysis was presented of the dynamic, steady-state propagation of a semi-infinite, antiplane shear crack in a general, infinite, homogeneous, and isotropic linearly viscoelastic body. (See [2] for a discussion of other relevant studies of dynamic viscoelastic crack propagation.) With only very weak assumptions on the shear modulus (specifically, that it be a continuously differentiable, convex and nonincreasing function of time), simple closed-form expressions were constructed for the stress intensity factor and the entire stress field in front of and in the plane of the advancing crack. Moreover, it was shown that if v, c, and c^* denote the crack speed and elastic shear wave speeds corresponding to the zero and infinite time values of the shear modulus, respectively, then for $0 < v < c^*$ the stress field is the same as for elastic material (that is, it is independent of crack speed and material properties), whereas for $c^* < v < c$ the stress field depends on both v and material properties. An important result from this study was that the dependence on v and material properties has a simple universal form from which qualitative and quantitative information can be easily obtained.

In this paper, the corresponding problem for a viscoelastic layer of finite thickness is considered. The finite layer problem is of interest because the model has more relevance to engineering applications and significantly more mathematical complexity than does the infinite layer problem. Of additional importance is the fact that the Riemann-Hilbert method employed in [2] goes through for this more complicated problem. Specifically, the principal obstacle encountered in applying the Riemann-Hilbert method is the evaluation of a certain rather complex appearing combination of functions and integral transforms. It is demonstrated here that a simplification similar to that effected in [2] occurs also for the finite layer problem and that the stress intensity factor has a simple universal dependence on v, material properties, and layer thickness, even for general shear modulus.

It should also be remarked that the approach adopted here has proved to be convenient for the calculation of the angular dependence of the near crack-tip stress field for both the finite and infinite layer problems. These calculations are the subject of a forthcoming paper as is analysis of the substantially more complicated opening mode plane strain problem. This section concludes with the formulation of the appropriate boundary

[1]Supported in part by the Office Naval Research under Contract No. N00014-83-0211.

Contributed by the Applied Mechanics Division for publication in the JOURNAL OF APPLIED MECHANICS.

Discussion on this paper should be addressed to the Editorial Department, ASME, United Engineering Center, 345 East 47th Street, New York, N.Y. 10017, and will be accepted until two months after final publication of the paper itself in the JOURNAL OF APPLIED MECHANICS. Manuscript received by ASME Applied Mechanics Division, July, 1984.

Copyright © 1985 by ASME
Downloaded 02 May 2010 to 171.66.16.54. Redistribution subject to ASME license or copyright; see http://www.asme.org/terms/Terms_Use.cfm

value problem and the derivation of the corresponding Riemann-Hilbert problem.

The governing field equations for the motion of the linearly viscoelastic layer are

$$\begin{aligned} \sigma_{ij,j} &= \rho\, u_{i,tt}, \quad -\infty < x_1 < \infty, \quad -h \le x_2 \le h, \\ \epsilon_{ij} &= (u_{i,j} + u_{j,i})/2, \\ \sigma_{ij} &= 2\mu^* d\epsilon_{ij} + \delta_{ij}\lambda^* d\epsilon_{kk} \end{aligned}$$

where σ_{ij}, ϵ_{ij}, and u_i denote the stress, strain, and displacement fields, respectively. The summation convention is in effect, $f_{,i}$ denotes partial differentiation of the function f, and $\mu^* d\epsilon$ denotes the Riemann-Stieltjes convolution

$$\mu^* d\epsilon = \int_{-\infty}^{t} \mu(t-\tau)\, d\epsilon(\tau).$$

Since the body is assumed to be in a state of antiplane strain deformation, the only equation of motion not identically satisfied is

$$\mu^* d\Delta u_3 = \rho\, u_{3,tt}$$

where Δu_3 denotes the two-dimensional Laplacian, $\Delta = \partial^2/\partial x_1^2 + \partial^2/\partial x_2^2$. A semi-infinite crack is assumed to be propagating to the right with constant speed v along the x_1-axis. The crack is subjected to a traveling distribution of applied tractions, $\sigma_{23}(x_1, 0, t) = f(x_1 - vt)$ for $x_1 \le vt$, while on the upper and lower surfaces of the layer two possible boundary conditions are considered, fixed grip and traction free, i.e.

$$\begin{aligned} &I. \quad u_3(x_1, \pm h, t) = 0, \quad -\infty < x_1 < \infty \\ &II. \quad \sigma_{23}(x_1, \pm h, t) = 0, \quad -\infty < x_1 < \infty. \end{aligned}$$

Therefore, adoption of the Galilean variables $x = x_1 - vt$, $y = x_2$ yields the boundary value problem

$$\mu^* d\Delta u_3 = \rho\, v^2 u_{3,xx} \quad |y| < h, |x| < \infty \tag{1.1}$$

$$\sigma_{23}(x,0) = \frac{\partial}{\partial y}(\mu^* d u_3) = f(x), \quad x < 0$$

$$u_3(x,0) = 0, \quad x > 0 \tag{1.2}$$

$$I. \quad u_3(x, \pm h) = 0, \quad |x| < \infty$$

or

$$II. \quad \sigma_{23}(x, \pm h) = 0, \quad |x| < \infty. \tag{1.3}$$

The next series of steps are similar to those in [2] and only will be summarized here.

Use will be made of the Fourier transform defined by

$$\hat{f}(p,y) = \int_{-\infty}^{\infty} e^{ipx} f(x,y)\, dx = F_+(p,y) + F_-(p,y)$$

$$F_+ = \int_0^{\infty} e^{ipx} f(x,y)\, dx,$$

$$F_- = \int_{-\infty} e^{ipx} f(x,y)\, dx.$$

Transforming (1.1), solving the resulting ordinary differential equation, and applying the boundary conditions (1.3) yields

$$\hat{u}_3(p,y) = A_1(p) \begin{cases} \sinh(\gamma(p)(h-y)) & I \\ \cosh(\gamma(p)(h-y)) & II \end{cases}$$

with $\gamma^2 = p^2 + ipv/\hat{\mu}(-vp)$. As will be discussed later, it is convenient to choose a square root of γ^2 with positive real part. Applying the boundary conditions (1.2) produces the relation on $y = 0$

$$\hat{\sigma}_{23}^+ + \hat{\sigma}_{23}^- = v\hat{\mu}(-vp)\gamma_1(p)\hat{u}_{3,1} \quad \begin{cases} \coth(h\gamma(p)), & I \\ \tanh(h\gamma(p)), & II \end{cases} \tag{1.4}$$

where $\sigma_{23}^+ + \sigma_{23}^-$ denote the restrictions of σ_{23} to the positive and negative x-axis, respectively.

Equation (1.4) may be viewed as the Riemann-Hilbert problem

$$F^+(p) = G(p)F^-(p) + g(p) \tag{1.5}$$

where

$$\begin{aligned} F^+(p) &= \hat{\sigma}_{23}^+ \\ F^-(p) &= \hat{u}_{3,1}^- \\ g(p) &= -\hat{\sigma}_{23}^- = -\hat{f} \end{aligned}$$

$$G(p) = v\hat{\mu}(-vp)\gamma(p) \begin{cases} \coth(h\gamma(p)), & I \\ \tanh(h\gamma(p)), & II \end{cases}$$

It is easily demonstrated a posteriori that $\sigma_{23}^+(x, 0)$ and $u_{3,1}^-(x, 0)$ are such that $F^+(z) = \hat{\sigma}_{23}^+$ and $F^-(z) = \hat{u}_{3,1}^-$ define functions analytic for $I_m(z) \gtrless 0$, respectively, and are such that the limits

$$F^{\pm}(p) = \lim_{q \to 0^{\pm}} F^{\pm}(p + iq)$$

exist and satisfy (1.5). In the next section the Riemann-Hilbert problem (1.5) is solved and the stress intensity factor calculated.

Problem Solution

To solve (1.5) it is necessary to determine the mapping properties of the coefficient $G(p)$. (See [1], for example, for a detailed discussion of the theory of Riemann-Hilbert boundary problems.) As in [2], it is convenient to rewrite $G(p)$ as

$$G(p) = \operatorname{sgn}(p) G_1(p) G_2(p)$$

where

$$G_1(p) = i\bar{\mu}(-vp)\gamma_1(p) \tag{2.1}$$

$$G_2(p) = \begin{cases} \coth(h|p|\gamma_1(p)), & I \\ \tanh(h|p|\gamma_1(p)), & II \end{cases} \tag{2.2}$$

$$\gamma_1(p) = [1 - \rho v^2/\bar{\mu}(-pv)]^{1/2} \tag{2.3}$$

$$\bar{\mu}(-vp) = ipv\hat{\mu}(-vp) = \mu(0) + \int_0^{\infty} e^{-ivpt}\, d\mu(t). \tag{2.4}$$

For what follows it is sufficient (but clearly not necessary) to assume, as in [2], that the shear modulus, $\mu(t)$, is positive, continuously differentiable, nonincreasing, convex, and such that $\mu(\infty) = \lim_{t \to \infty} \mu(t) > 0$. These assumptions are still sufficiently general to include all physically reasonable examples. Moreover, an easy adaptation of the analysis presented here permits use of the pure power-law model, $\mu(t) = \mu_c(t/tc)^{-\alpha}$, which provides an effective characterization of many real materials.

For convenience the following observations from [2] are recorded here:

(*i*) $\bar{\mu}(0) = \mu(\infty) \le Re(\bar{\mu}(-vp)) \le \mu(0) = \bar{\mu}(\infty)$

(*ii*) $Im(\bar{\mu}(-vp)) = -Im(\bar{\mu}(vp))$

(*iii*) $\arg(\bar{\mu}(-vp)) \begin{cases} \ge 0, & p > 0 \\ \le 0, & p < 0 \end{cases}$

Downloaded 02 May 2010 to 171.66.16.54. Redistribution subject to ASME license or copyright; see http://www.asme.org/terms/Terms_Use.cfm

(*iv*) $Im(\gamma_1^2(-p)) = -Im(\gamma_1^2(p))$

$Re(\gamma_1^2(-p)) = Re(\gamma_1^2(p))$

(*v*) $Im(\gamma_1^2(p)) > 0,\ 0 < p < \infty$

(*vi*) $1-(v/c^*)^2 = \gamma_1^2(0) \le Re(\gamma_1^2(p)) \le \gamma_1^2(\infty) = 1-(v/c)^2$

where $c^* = (\mu(\infty)/\rho)^{1/2}$ and $c = (\mu(0)/\rho)^{1/2}$ are the elastic shear wave speeds corresponding to the value of $\mu(t)$ for infinite and zero time.

To take the square root of $\gamma_1^2(p)$ it is necessary to distinguish two cases

1. $0 < v < c^*$
2. $c^* < v < c$.

Taking the branch cut for $\gamma_1(p)$ to be the negative real axis assures that $\gamma_1(p)$ has positive real part. Hence for Case 1, $\gamma_1(p)$ is Hölder continuous for all real p and

(*vii*) $Im(\gamma_1(p)) = -Im(\gamma_1(-p))$

$Re(\gamma_1(p)) = Re(\gamma_1(-p))$

(*viii*) $Im(\gamma_1(p)) > 0,\ 0 < p < \infty$

(*ix*) $(1-(v/c^*)^2)^{1/2} = \gamma_1(0) \le \gamma_1(\infty) = (1-(v/c)^2)^{1/2}$,

whereas for Case 2, (*vii*) and (*viii*) still hold but $\gamma_1(p)$ is discontinuous for $p = 0$. In particular,

(*x*) $\gamma_1(\pm\infty) = (1-(v/c)^2)^{1/2}$

$\gamma_1(0\pm) = \pm i((v/c^*)^2 - 1)^{1/2}$.

The image in the complex plane of the real p-axis under the transformation $\gamma_1(p)$ is illustrated in Fig. 1 of [2] for both Cases 1 and 2.

Following the solution method employed in [2], we first consider the problem of finding functions $\underline{X}^{\pm}(z)$ analytic for $Im(z) \gtrless 0$, respectively, and that satisfy the homogeneous boundary relation

$$\underline{X}^{+}(p) = G(p)\underline{X}^{-}(p). \tag{2.5}$$

Auxiliary functions $\underline{X}_i^{\pm}(z)$, $i = 1, 2$ are defined by

$$\underline{X}_i^{+}(p) = G_i(p)\underline{X}_i^{-}(-p).$$

Then clearly,

$$\underline{X}^{\pm}(z) = \omega^{\pm}(z)\underline{X}_1^{\pm}(z)\underline{X}_2^{\pm}(z) \tag{2.6}$$

where $\omega^{\pm}(z)$ denote branches of $z^{1/2}$ whose branch cuts are the negative and positive imaginary axes, respectively (see [2]).

The functions $\underline{X}_1^{\pm}(z)$ were constructed in [2], but here only the boundary limit $\underline{X}_1^{\pm}(p)$ is needed. It was shown in [2] that

$$\omega^{+}(p)\underline{X}_1^{+}(p) = \begin{cases} (-ip)^{1/2}\,|G_1(\infty)|^{1/2}, & \text{Case 1} \\ (q_0-ip)^{1/2}\,|G_1(\infty)|^{1/2}, & \text{Case 2} \end{cases}$$

where q_0 is the unique positive solution to

$$vq_0\int_0^{\infty}\mu^*(t)e^{-q_0vt}dt = (v/c)^2. \tag{2.7}$$

In (2.7) $\mu^*(t)$ denotes a normalized modulus given by

$$\mu^*(t) = \mu(t)/\mu(0).$$

The central focus of this paper is the construction of the asymptotic form of $\sigma_{23}^{+}(x,0)$ for x near zero. To that end, much of the derivation presented in [2] is valid here also. In particular, it can be concluded that

$$F^{\pm}(z) = \underline{X}^{\pm}(z)\frac{1}{2\pi i}\int_{-\infty}^{\infty} g(\tau)/\underline{X}^{+}(\tau)\frac{d\tau}{\tau-z},$$

$$\sigma_{23}^{+}(x) = \frac{1}{2\pi}\int_{-\infty}^{\infty} e^{-ixp}\underline{X}^{+}(p)dp\frac{1}{2\pi i}\int_{-\infty}^{\infty} g(\tau)/\underline{X}^{+}(\tau)\frac{d\tau}{\tau-p}$$

and for x near zero, the dominant term in the asymptotic expansion of $\sigma_{23}^{+}(x)$ is given by

$$\sigma_{23}^{+}(x) \sim x^{-1/2}\frac{|G_1(\infty)|^{1/2}}{\sqrt{\pi}}\frac{1}{2\pi}\int_{-\infty}^{\infty} g(\tau)/\underline{X}^{+}(\tau)d\tau = Kx^{-1/2}. \tag{2.8}$$

The coefficient K is the stress intensity factor. It should be remarked that (2.8) is valid for the finite layer problem because $G_2(\infty) = 1$.

In [2] a simple closed-form expression for K was constructed through the device of introducing the function $h(x)$ for which

$$1/\underline{X}^{+}(\tau) = \int_{-\infty}^{\infty} e^{-i\tau x}h(x)dx \tag{2.9}$$

and from which it follows that

$$K = -|G_1(\infty)|^{1/2}\frac{1}{\sqrt{\pi}}\int_{-\infty}^{0}\sigma_{23}^{-}(x)h(x)dx. \tag{2.10}$$

The principal result of [2] was the proof that

$$h(x) = |G_1(\infty)|^{-1/2}H(-x)|x|^{-1/2}\begin{cases} 1, & \text{Case 1} \\ e^{xq_0}, & \text{Case 2} \end{cases} \tag{2.11}$$

where $H(x)$ is the Heaviside step function,

$$H(x) = \begin{cases} 1, & x > 0 \\ 0, & x < 0. \end{cases}$$

For a layer of finite thickness, lines (2.8)-(2.10) are still valid, but with $\underline{X}^{+}(\tau)$ given by (2.6). Consequently, the simple form (2.11) for $h(x)$ does not hold; the contribution from $\underline{X}_2^{+}(p)$ must be incorporated into the solution. It is convenient to remark here that since $G_2(p)$ for problems *I* and *II* are just reciprocals, the same is true for $\underline{X}_2^{\pm}(z)$. Therefore, it is necessary to consider only one of the cases, say *I*.

Evaluating $\underline{X}_2^{+}(p)$ is the central problem. Clearly, from the general theory of Riemann-Hilbert boundary value problems ([1]), it follows that

$$\underline{X}_2^{\pm}(z) = \mathbf{e}^{\Gamma_2^{\pm}(z)}$$

with

$$\Gamma_2^{\pm}(z) = \frac{1}{2\pi i}\int_{-\infty}^{\infty}\log(G_2(\tau))\frac{d\tau}{\tau-z}. \tag{2.12}$$

The integral in (2.12) can be evaluated by a technique similar to that employed in the analysis in [2] of the case $c^* < v < c$. Moreover, only the boundary limit $\underline{X}_2^{+}(p)$ is needed in the computation of the stress field. As in [2], it is necessary to consider the two Cases 1 and 2, separately.

Case 1. $0 < v < c^*$. The function $\log(G_2(\tau))$, $\tau > 0$ has a natural extension, $\log(G_2(z))$, to a function analytic in the fourth quadrant, i.e., for $z = \tau - iq$ with $\tau, q > 0$. Computing the boundary limit $\lim_{\tau\to 0+}\log(G_2(\tau - iq))$ yields

$$\begin{aligned}\lim_{\tau\to 0+}\log(G_2(\tau-iq)) &= \log(\coth(-iqh\gamma_1(-iq))) \\ &= \log(i\cot(hq\gamma_1(-iq))).\end{aligned} \tag{2.13}$$

Since $q\gamma_1(-iq)$ is an increasing function of q, there exists a sequence of numbers, $\{a_n\}_{n=0}^{\infty}$, such that

$$\begin{aligned} ha_{2n}\gamma_1(-ia_{2n}) &= n\pi, \quad n = 0,1,\ldots \\ ha_{2n+1}\gamma_1(-ia_{2n+1}) &= (n+1/2)\pi, \quad n = 0,1\ldots \end{aligned} \tag{2.14}$$

In light of (2.3), (2.14) can be rewritten

$$\begin{aligned} va_{2n}\int_0^{\infty}\mu^*(t)\exp[-vta_{2n}]dt &= (v/c)^2/[1-(n\pi/ha_{2n})^2] \\ va_{2n+1}\int_0^{\infty}\mu^*(t)\exp[-vta_{2n+1}]dt &= (v/c)^2/ \\ &\quad [1-(n+1/2)\pi/ha_{2n+1})^2]. \end{aligned} \tag{2.15}$$

Downloaded 02 May 2010 to 171.66.16.54. Redistribution subject to ASME license or copyright; see http://www.asme.org/terms/Terms_Use.cfm

Consequently,

$$\arg(i\cot(hq\gamma_1(-iq))) = \pi/2 \quad \text{for} \quad a_{2n} < q < a_{2n+1},$$

while

$$\arg(i\cot(hq\gamma_1(-iq))) = -\pi/2 \quad \text{for} \quad a_{2n+1} < q < a_{2(n+1)}.$$

If $\tau < 0$, the function $\log(G_2(\tau))$ has the natural analytic extension $\log(G_2(z))$, $z = \tau - iq$, $q > 0$ given by $\log(G_2(z)) = \log(\coth(-hz\gamma_1(z)))$. Letting z approach the negative imaginary axis results in

$$\lim_{\tau \to 0-} \log(G_2(\tau - iq)) = \log(\coth(ihq\gamma_1(-iq))) = \log(-i\cot(hq\gamma_1(-iq))). \tag{2.16}$$

The function $\Gamma_2^+(z)$ may be computed by replacing the integral in (2.12) over the real axis with the appropriate integrals along the lines $\tau - ia_{2n+1}$, $-\infty < \tau < \infty$ and $-iq$, $0 < q < a_{2n+1}$. Specifically, for $Im(z) > 0$,

$$\Gamma_2^+(z) = \frac{1}{2\pi i}\int_{-\infty}^{\infty} \log(G_2(\tau))\frac{d\tau}{\tau - z}$$

$$= \frac{1}{2\pi i}\left[\int_{\infty - ia_{2n+1}}^{(0+)-ia_{2n+1}} + \int_{(0+)-ia_{2n+1}}^{(0+)-io} + \int_0^{\infty} \log(G_2(\tau))\frac{d\tau}{\tau - z}\right] \tag{2.17}$$

$$+ \frac{1}{2\pi i}\left[\int_{-\infty}^{0} + \int_{(0-)-ia_{2n+1}}^{(0-)-io} + \int_{(0-)-ia_{2n+1}}^{-\infty - ia_{2n+1}} \log(G_2(\tau))\frac{d\tau}{\tau - z}\right] \tag{2.18}$$

$$+ \frac{1}{2\pi i}\left[\int_{(0+)-ia_{2n+1}}^{(0+)-io} + \int_{(0-)-ia_{2n+1}}^{(0-)-io} \log(G_2(\tau))\frac{d\tau}{\tau - z}\right] \tag{2.19}$$

$$+ \frac{1}{2\pi i}\int_{-\infty - ia_{2n+1}}^{\infty - ia_{2n+1}} \log(G_2(\tau))\frac{d\tau}{\tau - z}. \tag{2.20}$$

Lines (2.17) and (2.18) vanish by Cauchy's theorem. The integral in line (2.20) tends to zero as $n \to 0$ uniformly in z for $Im(z) > 0$ and therefore will be denoted by $\epsilon(n)$.

From the foregoing observations and after an obvious change of variables in (2.19) it is now clear that

$$\Gamma_2^+(z) = \epsilon(n) + \frac{1}{2\pi i}\int_0^{a_{2n+1}} [\log(i\cot(th\gamma_1(-it))) - \log(-i\cot(th\gamma_1(-it)))]\frac{dt}{t - iz}$$

$$= \epsilon(n) + \frac{1}{2}\int_0^{a_1} \frac{dt}{t - iz} + \frac{1}{\pi}\sum_{j=1}^{n} \int_{a_{2j-1}}^{a_{2j+1}} \arg(i\cot(th\gamma_1(-it)))\frac{dt}{t - iz}$$

$$= \epsilon(n) + \frac{1}{2}\log\left(\frac{a_1 - iz}{-iz}\right) - \frac{1}{2}\sum_{j=1}^{n}\int_{a_{2j-1}}^{a_{2j}} - \int_{a_{2j}}^{a_{2j+1}} \frac{dt}{t - iz}$$

$$= \epsilon(n) + \frac{1}{2}\log\left(\frac{a_1 - iz}{-iz}\right) - \frac{1}{2}\sum_{j=1}^{n} [2\log(a_{2j} - iz) - \log(a_{2j-1} - iz) - \log(a_{2j+1} - iz)]. \tag{2.21}$$

In (2.21), the limit $Im(z) \to 0+$ is easily taken from which it then follows that

$$\bar{X}_2^+ = (ip)^{-1/2}\bar{Y}_n(p)e^{\epsilon(n)} \tag{2.22}$$

with

$$\bar{Y}_n(p) = \prod_{j=1}^{n}\left[\frac{a_{2j-1} - ip}{a_{2j} - ip}\right](a_{2n+1} - ip)^{1/2}. \tag{2.23}$$

Case 2. $c^* < v < c$. In contrast to Case 1, for Case 2 $\gamma_1(\tau)$ has a natural extension, $\gamma_1(z)$, which is analytic for $Im(z) < 0$ except for a branch cut, $-iq$, $0 < q < q_0$ with q_0 given by (2.7). The same is then true for $\log(G_2(\tau))$ and in particular, $\log(G_2(z))$ is analytic for $Im(z) < -q_0$. After this minor modification is taken into account, the argument utilized in Case 1 applies also for Case 2 and yields the result

$$\bar{X}_2^+(p) = (q_0 - ip)^{-1/2}\bar{Y}_n(p)e^{\epsilon(n)} \tag{2.24}$$

where $\bar{Y}_n(p)$ is still given by (2.23) and the a_n by (2.14). It should be observed that for Case 2, the a_n are such that $q_0 < a_1 < \ldots$ whereas for Case 1, $0 < a_1 < \ldots$. Moreover, the a_n for Case 2 are larger than the corresponding a_n for Case 1.

Calculating $\sigma_{23}^+(x, 0)$ requires the function $\bar{Y}^+(p)$. From (2.6), (2.8)–(2.10), and (2.22)–(2.24) it is easily seen that for both Case 1 and Case 2

$$\bar{X}(p) = \lim_{n\to\infty} |G_1(\infty)|^{1/2}\prod_{j=1}^{n}\left(\frac{a_{2j-1} - ip}{a_{2j} - ip}\right)(a_{2n+1} - ip)^{1/2}, \tag{2.25}$$

$$= \lim_{n\to\infty} \bar{X}_n^+(p)$$

and that

$$K = \lim_{n\to\infty} K_n, \quad K_n = -|G_1(\infty)|^{1/2}\frac{1}{\sqrt{\pi}}\int_{-\infty}^{0} \sigma_{23}^-(x,0)h_n(x)dx$$

with

$$h_n(x) = \frac{1}{2\pi}\int_{-\infty}^{\infty} e^{ixp}/\bar{X}_n^+(p)dp. \tag{2.26}$$

A convenient scheme for inductively approximating the stress intensity factor K can be based on the observation that

$$\prod_{j=1}^{n}\left(\frac{a_{2j} - ip}{a_{2j-1} - ip}\right) = 1 + \frac{b_{n1}}{(a_1 - ip)} + \ldots + \frac{b_{nn}}{(a_{2n-1} - ip)}, \tag{2.27}$$

where

$$b_{nk} = \left[\prod_{j=1}^{n}(a_{2j} - a_{2k-1})\right]\Big/\left[\prod_{j\neq k}^{n}(a_{2j-1} - a_{2k-1})\right]$$

$$= b_{(n-1)k}\left(\frac{a_{2n} - a_{2k-1}}{a_{2n-1} - a_{2k-1}}\right).$$

In light of (2.25)–(2.27) and after some routine integrations it can be shown that for $x < 0$,

$$h_n(x) = |x|^{-1/2}k_n(x)$$

$$k_n(x) = e^{a_{2n-1}x} - 2x\sum_{j=1}^{n} b_{nj}\int_0^1 \exp[x(a_{2n+1}t^2 + a_{2j-1}(1 - t^2))]dt.$$

References

1 Gakov, F. D., *Boundary Value Problems*, Pergamon, London, 1966.

2 Walton, J. R., "On the Steady-State Propagation of an Anti-Plane Shear Crack in an Infinite General Linearly Viscoelastic Body," *Quart. Appl. Math.*, Apr. 1982, pp. 37–52.

Downloaded 02 May 2010 to 171.66.16.54. Redistribution subject to ASME license or copyright; see http://www.asme.org/terms/Terms_Use.cfm

A New Endochronic Approach to Computational Elastoplasticity: Example of a Cyclically Loaded Cracked Plate

O. Watanabe

S. N. Atluri
Mem. ASME

Center for Advancement of Computational Mechanics, School of Civil Engineering, Georgia Institute of Technology, Atlanta, Ga. 30332

In this paper, a methodology for finite-element elastoplastic analyses of structures subjected to cyclic loading, based on a new form of endochronic (internal time) plasticity theory, is presented. In the present version of the endochronic theory, the rate forms of the stress/strain relations (stated here explicitly for plane stress, plane strain, and three-dimensional cases) are entirely analogous to those of the classical (isotropic or kinematic hardening) plasticity theory and, thus, are no more difficult or expensive to implement in computational algorithms. The problem of a double-edge-cracked panel, subjected to monotonic loading as well as to zero-to-tension or tension-compression cyclic external loading, is analyzed. The elastoplastic stress/strain fields at the root of the notch, for each of these loading conditions, are studied in detail. These results are compared and contrasted with those presented recently by Valanis and Fan, and the noted discrepancies are discussed. This paper is limited to considerations of small strains and small displacements only.

1 Introduction

Starting from the pioneering works of Marcal and King (1967), Yamada et al. (1968), and Zienkiewicz et al. (1969) computational elastoplastic analyses have now become commonplace. These earlier approaches employed the simple isotropic hardening plasticity theory and used either the "initial strain/stress" or "tangent stiffness" approaches in the finite-element solution algorithms. To account for anisotropic hardening, the so-called linear kinematic hardening theory of Melan and Prager was widely used in the early days of the era of computational plasticity. Almost simultaneously, the search for constitutive laws that predict cyclic plastic behavior in a more realistic fashion has begun. Among such constitutive models may be mentioned: (*i*) the multiple-yield-surface theories of Mroz (1969), Krieg (1975), Dafalias and Popov (1976); (*ii*) the internal variable theories of Chaboche and Rousselier (1982), of Onat (1981), and others; and (*iii*) the internal time (endochronic) theories of Valanis (1980), Valanis and Fan (1983), and Watanabe and Atluri (1984a,b). A unification of concepts underlying these various theories has recently been attempted by the authors (Watanabe and Atluri, 1984b).

The endochronic theory, as developed by Valanis (1980), results in an integral relation for the stress-deviator in terms of the history of plastic strain and attempts to circumvent the introduction of a "yield-surface." Valanis and Fan (1983) recently developed a *rate* form of the stress/strain relation based on the theory of Valanis (1980). In this *rate form* (which is dimensionally homogeneous in a timelike parameter), the rate of the stress deviator is related *nonlinearly* to the rate of plastic-strain as well as to the history of plastic strain. Thus, Valanis and Fan (1983) used an "initial-strain" type iterative finite-element approach to study the problem of a cyclically loaded double-edge-cracked panel. Apart from the need for iterations based on a linear-elastic stiffness matrix in each increment of loading, the determination of the stress-increment at a material point corresponding to a given strain increment also involves a number of iterations.

On the other hand, using the concepts of an internal time (endochronic) theory, the authors (Watanabe and Atluri 1984a,b) have developed an alternate form of the relation between differential stress and differential strain for use in cyclic plasticity analyses. The approach of Watanabe and Atluri[1] (1984a,b) has the following features: (*i*) The concept of a "yield-surface" is retained; (*ii*) the differential stress is related *linearly* to differential strain, and this relation is essentially similar in its mathematical structure to those of the classical theories of isotropic hardening or of Melan-Prager linear kinematic hardening. Thus, the present endochronic

Contributed by the Applied Mechanics Division and presented at the Winter Annual Meeting, Miami, Fla., November 17-21, 1985 of THE AMERICAN SOCIETY OF MECHANICAL ENGINEERS.

Discussion on this paper should be addressed to the Editorial Department, ASME, United Engineering Center, 345 East 47th Street, New York, N.Y. 10017, and will be accepted until two months after final publication of the paper itself in the JOURNAL OF APPLIED MECHANICS. Manuscript received by ASME Applied Mechanics Division, October, 1984; final revision, February, 1985. Paper No. 85-WA/APM-4.

[1] The fact that Valanis' version of endochronic theory implies a loading surface has also been alluded to by Bazant (1980); and that the constitutive relation can be cast in an incrementally linear form may also be expected on the basis of the observations of Bazant, et al. (1983).

Copyright © 1985 by ASME
Downloaded 02 May 2010 to 171.66.16.54. Redistribution subject to ASME license or copyright; see http://www.asme.org/terms/Terms_Use.cfm

constitutive theory is no more difficult to implement in computational algorithms than the classical theories; and (*iii*) the functions describing the yield-surface translation and expansion are such that the present theory (Watanabe and Atluri 1984a,b) includes, as special cases, the multiple-yield-surface theories (Mroz, 1969; Krieg, 1975; and Dafalias and Popov, 1976) and the other internal variables theories (Choboche and Rousselier, 1982; and Onat, 1981).

In this paper, we give a brief outline of the present rate form of the three-dimensional elastoplastic constitutive law based on an internal time (endochronic) theory. We then give explicit expressions for plane stress and plane strain. We present a "tangent-stiffness" finite-element approach based on these constitutive relations. The stress increment corresponding to a given strain increment, in this approach, may be determined using a simple "radial-return" algorithm as in classical plasticity. We study the problem of a double-edge-cracked plate subject to (*i*) monotonic tensile loading at the upper edge parallel to the crack axis and (*ii*) zero-to-tension as well as tension-compression cyclic loading at the upper edge. In each case, we study the elastoplastic stress/strain fields at the root of the notch, for both plane-stress and plane-strain conditions. These numerical results are compared to those of Valanis and Fan (1983) for certain identical problems. These results indicate, as those of Valanis and Fan (1983), that while the external loading is zero-to-tension or tension-to-compression (symmetric) and periodic in nature, the stress response (especially in the direction of loading) at the root of the notch *does not* exhibit the same symmetry and periodicity as that of the external load. However, the *details* of the stress response at the root of the notch are much different, in magnitude as well as periodic variation, from those of Valanis and Fan (1983). Specifically, the presently computed stress response at the notch-root, in zero-to-tension cyclic loading for both plane stress and plane strain is progressively accumulated, (*ii*) the hysteresis loops gradually saturate, and (*iii*) the peak stress at the instant of stress reversal decreases and converges to a constant value. These detailed comparisons are included in Section 5. The paper ends with a set of concluding comments in Section 6.

2 Nomenclature

Considerations in this paper are limited to small strains and infinitesimal deformations. For simplicity we employ a system of Cartesian coordinates x_i, with unit basis e_i. If $\mathbf{A}(A_{ij}e_ie_j)$ and $\mathbf{B}(B_{mn}e_me_n)$ are two second-order tensors, the notation $\mathbf{A}\cdot\mathbf{B} = A_{ij}B_{mn}e_ie_n$ and $\mathbf{A}:\mathbf{B} = A_{ij}B_{ij}$ is employed.

3A Internal Time (Endochronic) Theory

Let $\mathbf{S}$ be the deviator of Cauchy stress (in the present infinitesimal deformation case, there is no distinction between various stress measures) and $\mathbf{r}$ the deviatoric Cauchy-back-stress, $\boldsymbol{\alpha}$. The differential-strain tensor $d\boldsymbol{\epsilon}$ is written as $d\boldsymbol{\epsilon} = (d\boldsymbol{\epsilon}^e + d\boldsymbol{\epsilon}^p) \equiv (d\mathbf{e}^e + d\mathbf{t}^p) + \mathbf{I}\, d\epsilon^e_m$; thus, the plastic strains considered here are purely distortional. Further, $d\boldsymbol{\epsilon}^p = d\mathbf{e} - (d\mathbf{S}/2\mu_0)$ where μ_0 is the elastic shear modulus. The intrinsic time measure ζ is defined through:

$$d\zeta = (d\mathbf{e}^p : d\mathbf{e}^p)^{1/2} = (de^p_{ij}de^p_{ij})^{1/2} \tag{3.1}$$

The differential intrinsic time dz is defined as:

$$dz = \frac{d\zeta}{f(\zeta)} \tag{3.2}$$

where $f(\zeta)$ is non-negative and $f(0) = 1$. In the intrinsic-time (endochronic) theory, $\mathbf{S}$ is represented (Valanis, 1980; Watanabe and Atluri, 1984a) as:

$$\mathbf{S} = 2\mu_0 \int_0^z \rho(z-z') \frac{\partial \mathbf{e}^p}{dz'}\, dz' \tag{3.3}$$

By differentiating (3.3) with respect to z, one may obtain:

$$d\mathbf{S} = 2\mu_0[\rho(0)d\mathbf{e}^p + \mathbf{h}(z)\,dz] \tag{3.4a}$$

$$= 2\mu_0\left[\rho(0)d\mathbf{e}^p + \mathbf{h}(z)\frac{(d\mathbf{e}^p:d\mathbf{e}^p)^{1/2}}{f(\zeta)}\right] \tag{3.4b}$$

$$= 2\mu_p\left\{d\mathbf{e} + \frac{\mathbf{h}}{\rho(0)}\frac{(d\mathbf{e}^p:d\mathbf{e}^p)^{1/2}}{f(\zeta)}\right\} \tag{3.4c}$$

where

$$\rho(0) = \rho(z=0); \quad \mathbf{h}(z) = \int_0^z \frac{\partial \rho}{\partial z}(z-z')\frac{\partial \mathbf{e}^p}{\partial z'}\, dz' \tag{3.5a,b}$$

$$2\mu_p = 2\mu_0\left\{1+\rho(0)\right\}^{-1}; \quad d\mathbf{e}^p = d\mathbf{e} - \frac{d\mathbf{S}}{2\mu_0} \tag{3.5c,d}$$

Equations (3.3) and (3.4*a*) appear to negate the need for the introduction of a "yield-surface" as in classical plasticity theory. However, the differential relation for deviatoric stress, $d\mathbf{S}$, in equation (3.4), depends *nonlinearly* on the differential plastic strain $d\mathbf{e}^p$ in contrast to a linear relation of the classical plasticity theory. Valanis and Fan (1983) employ (3.4*b*), in conjunction with an "initial-strain" type iterative finite-element algorithm, to solve certain boundary value problems of cyclic plasticity. While specific details of the convergence of iterations in each increment of solution are not indicated by Valanis and Fan (1983), it may be seen that the presence of the nonlinear term involving $(d\mathbf{e}^p)$ on the right-hand side of (3.4), in general, results in a slow process of convergence in each increment. It should be noted that in their development, Valanis and Fan (1983) point out that the chosen kernel $\rho(z)$ should be weakly singular at $z = 0$ in order: (*i*) to obtain closed hysteresis loops in the uniaxial or shear stress/strain space and (*ii*) to ensure initially elastic unloading.

In the following, we present a sketch of an alternate development (Watanabe and Atluri, 1984a) of the differential stress/strain relation of the internal time (endochronic) theory of plasticity where: (*i*) the notion of a "yield-surface" is retained by assuming the kernel $\rho(z)$ to have a singularity at $z = 0$ and (*ii*) the differential stress $d\mathbf{S}$ depends linearly on $d\mathbf{e}^p$ so that expedient finite-element algorithms depending on the concepts of "tangent stiffness" or "initial stress," as elaborately developed for classical plasticity, may be employed. In that sense, the present differential stress/strain relations for endochronic theory are not different in *mathematical structure* from those of classical plasticity (and hence their computational implementation is no different from those of the classical theory). However, through deliberate and specific choices of the functions $\rho(z)$ and $f(\zeta)$, the present theory can account for several phenomenological features of cyclic plasticity that the classical plasticity theory is incapable of.

Toward the objective stated in the foregoing, assume the kernel $\rho(z)$ to be of the form:

$$\rho(z) = \rho_0\delta(z) + \rho_1(z) \tag{3.6}$$

where $\delta(z)$ is a Dirac delta function, and $\rho_1(z)$ is a non-singular function. Use of (3.6) in (3.3) results in:

$$\mathbf{S} = S^0_y\frac{d\mathbf{e}^p}{dz} + \mathbf{r}(z) \tag{3.7a}$$

where

$$\mathbf{r}(z) = 2\mu_0\int_0^z \rho_1(z-z')\frac{d\mathbf{e}^p}{dz'}\, dz' \tag{3.7b}$$

and

$$S^0_y = 2\mu_0\rho_0 \tag{3.7c}$$

As noted by Valanis (1980) and Watanabe and Atluri (1984a), the regions of material behavior may be characterized as:

Downloaded 02 May 2010 to 171.66.16.54. Redistribution subject to ASME license or copyright; see http://www.asme.org/terms/Terms_Use.cfm

(*i*) if $\|\mathbf{S}=\mathbf{r}\|<S_y^0 f(\zeta)$ the material is elastic, (3.8*a*)

(*ii*) if $\|\mathbf{S}-\mathbf{r}\|=S_y^0 f(\zeta)$ and

$(\mathbf{S}-\mathbf{r}):d\mathbf{e}\le 0$ the material is again elastic (3.8*b*)

(*iii*) if $\|\mathbf{S}-\mathbf{r}\|=S_y^0 f(\zeta)$ and $(\mathbf{S}-\mathbf{r}):d\mathbf{e}>0$

then plastic deformation is permissible (3.8*c*)

Thus, in the present theory, $f(\zeta)$ signifies isotropic hardening (yield surface expansion), while $\mathbf{r}$ *denotes kinematic hardening (yield surface translation).*

The present authors (Watanabe and Atluri, 1984a) have shown that the *rate form* of the stress-strain relation arising out of the preceding sketched endochronic theory is entirely analogous in structure to that of the classical theory of plasticity and has the form:

$$d\sigma = 2\mu_0 d\epsilon + \lambda_0(\mathbf{I}:d\epsilon)\mathbf{I} - \frac{2\mu_0(\mathbf{S}-\mathbf{r})<(\mathbf{S}-\mathbf{r}):d\epsilon>}{C(S_y^0)^2 f^2(\zeta)}\Gamma$$

$$\equiv 2\mu_0(d\epsilon - d\epsilon^p) + \lambda_0(\mathbf{I}:d\epsilon)\mathbf{I} \tag{3.9a}$$

or

$$d\epsilon^p = \frac{(\mathbf{S}-\mathbf{r})<(\mathbf{S}-\mathbf{r}):d\mathbf{e}>}{C(S_y^0)^2 f^2(\zeta)} \equiv d\mathbf{e}^p \tag{3.9b}$$

where

$$C = 1 + \rho_1(0) + \frac{(\mathbf{S}-\mathbf{r}):\mathbf{h}^*}{S_y^0 f^2(\zeta)} + \frac{S_y^0 f'}{2\mu_0}; \tag{3.10}$$

and

$$\mathbf{h}^* = \int_0^z \frac{d\rho_1}{dz}(z-z')\frac{d\mathbf{e}^p}{dz'}dz' \tag{3.11}$$

and $\Gamma = 1$ if condition (3.8*c*) holds, i.e., when there is plastic loading;

$\Gamma = 0$ if the material is elastic or undergoes elastic unloading.

Likewise, from (3.7*b*), one finds that:

$$d\mathbf{r} = 2\mu_0\rho_1(0)d\mathbf{e}^p + \frac{2\mu_0\mathbf{h}^*}{f(\zeta)}(d\mathbf{e}^p:d\mathbf{e}^p)^{1/2} \tag{3.12}$$

Thus, in endochronic theory, the evolution equation for the deviatoric Cauchy-back stress is *nonlinear* in the plastic strain rate (this may be labeled as nonlinear kinematic hardening). We now discuss a specific form for the nonsingular kernel $\rho_1(z)$ and the ramifications thereof. It is convenient to assume $\rho_1(z)$ as:

$$\rho_1(z) = \sum_i \rho_{1i} e^{-\alpha_i z} \tag{3.13}$$

Using (3.13) in (3.7*b*) and (3.11), we may write

$$\mathbf{r} = \sum_i \mathbf{r}^{(i)} = \sum_i 2\mu_0 \int_0^z \rho_{1i} e^{-\alpha_i(z-z')}\frac{d\mathbf{e}^p}{dz'}dz' \tag{3.14}$$

$$\mathbf{h}^* \equiv \sum_i \mathbf{h}^{*(i)} \equiv \sum_i \left(-\frac{\alpha_i}{2\mu_0}\right)\mathbf{r}^{(i)} \tag{3.15}$$

Now, one may treat each of the $\mathbf{r}^{(i)}$ as a *secondary* internal variable. Using (3.13) and (3.15) in (3.12), it is easily seen that:

$$\rho_1(0) = \sum_i \rho_{1i} \tag{3.16a}$$

$$d\mathbf{r} = \sum_i d\mathbf{r}^{(i)} \tag{3.16b}$$

$$d\mathbf{r}^{(i)} = 2\mu_0\rho_{1i}d\mathbf{e}^p - \mathbf{r}^{(i)}\alpha_i\frac{d\zeta}{f} \quad \text{(no sum on } i\text{)} \tag{3.16c}$$

$$\equiv 2\mu_0\rho_{1i}d\mathbf{e}^p - \frac{\alpha_i(d\mathbf{e}^p:d\mathbf{e}^p)^{1/2}}{f}r^{(i)} \quad \text{(no sum on } i;\ i=1,2\ldots) \tag{3.16d}$$

where

$$d\mathbf{e}^p = \frac{(\mathbf{S}-\mathbf{r})}{C(S_y^0)^2 f^2(\zeta)} <(\mathbf{S}-\mathbf{r}):d\mathbf{e}> \equiv d\mathbf{e} - \frac{1}{2\mu_0}d\mathbf{S} \tag{3.16e}$$

As noted earlier, the isotropic hardening is represented in the endochronic theory through the relation for self-similar expansion of the yield surface:

$$S_y = S_y^0 f(\zeta) \tag{3.17}$$

where the non-negative $f(\zeta)$, such that $f(0) = 1$, may be assumed as:

$$f(\zeta) = (1+\beta\zeta) \quad \text{(linear form)} \tag{3.18a}$$

or

$$= a + (1-a)\exp(-\gamma\zeta) \quad \text{(saturated form)} \tag{3.18b}$$

Thus,

$$dS_y = S_y^0\beta\, d\zeta \quad \text{(linear)} \tag{3.19a}$$

$$= \gamma(S_y^\infty - S_y)d\zeta \quad \text{(saturated)} \tag{3.19b}$$

In (3.19*b*) S_y^∞ is the saturated radius of the yield surface and is given by:

$$S_y^\infty = S_y^0 a \tag{3.20}$$

It is perhaps worthwhile to summarize the presently derived *rate form* of the relations in endochronic theory [with exponential kernel $\rho_1(z)$] and then contrast them with other relations presented in literature, which, at first glance, may appear to be unrelated to each other.

Table 1 Summary of the present internal-time theory of plasticity

Endochronic theory: [$(\dot{\ })$ denotes a derivative of ( ) with respect to Newtonian-time or a Newtonian-time-like external parameter such as external load]

$\mathrm{tr}(\dot{\sigma}) = (2\mu_0 + 3\lambda_0)\mathrm{tr}(\dot{\epsilon})$; where μ_0, λ_0 are Lamé constants

$$\dot{\mathbf{S}} = 2\mu_0\dot{\mathbf{e}} - \frac{2\mu_0<(\mathbf{S}-\mathbf{r}):\dot{\mathbf{e}}>}{C(S_y^0)'^2 f^2(\zeta)}(\mathbf{S}-\mathbf{r})\Gamma$$

$f(\zeta) = (1+\beta\zeta)$(linear) or $f(\zeta) = [a+(1-a)\exp(-\gamma\zeta)]$(expon)

$$C = 1 + \rho_1(0) + \frac{(\mathbf{S}-\mathbf{r}):\mathbf{h}^*}{S_y^0 f^2(\zeta)} + \frac{S_y^0(df/d\zeta)}{2\mu_0}; \quad S_y^0 = 2\mu_0\rho_0$$

$$\rho(z) \equiv \rho_0\delta(z) + \rho_1(z) = \rho_0\delta(z) + \sum_i \rho_{1i}\exp(-\alpha_i z)$$

$$\mathbf{r} = \sum_i \mathbf{r}^{(i)}; \quad \mathbf{h}^* = \sum_i \mathbf{h}^{*(i)} = \sum_i \left(-\frac{\alpha_i}{2\mu_0}\right)\mathbf{r}^{(i)}$$

Kinematic hardening:

$$\dot{\mathbf{r}}^{(i)} = 2\mu_0\rho_{1i}\dot{\mathbf{e}}^p - \frac{\alpha_i\mathbf{r}^{(i)}}{f}(\dot{\mathbf{e}}^p:\dot{\mathbf{e}}^p)^{1/2} \quad \text{(no sum on } i\text{) for } i=1,2\ldots$$

$$\dot{\mathbf{r}} = \sum_i \dot{\mathbf{r}}^{(i)} = 2\mu_0\rho_1(0)\dot{\mathbf{e}}^p - \sum_i \frac{\alpha_i\mathbf{r}^{(i)}}{f}(\dot{\mathbf{e}}^p:\dot{\mathbf{e}}^p)^{1/2}$$

Isotropic hardening:

$$\dot{S}_y = S_y^0\beta(\dot{\mathbf{e}}^p:\dot{\mathbf{e}}^p)^{1/2} \quad \text{(linear } f\text{)}$$

$$= \gamma\{S_y^\infty - S_y^0[a+(1-a)\exp(-\gamma\zeta)]\}(\dot{\mathbf{e}}^p:\dot{\mathbf{e}}^p)^{1/2} \quad \text{(saturated } f\text{)}$$

(3.21)

3B Other Theories of Plasticity

In comparison to the presently developed internal time (endochronic) theory, other "isotropic hardening" and "kinematic hardening" plasticity theories in literature are summarized in the following:

Downloaded 02 May 2010 to 171.66.16.54. Redistribution subject to ASME license or copyright; see http://www.asme.org/terms/Terms_Use.cfm

Table 2 Summary of other theories of plasticity

Classical theories of plasticity: [($\dot{}$) denotes a derivative of ( ) with respect to a Newtonian-time-like parameter].

(*i*) Prandtl-Reuss isotropic hardening

$$\mathrm{tr}(\dot{\sigma}) = (2\mu_0 + 3\lambda_0)\mathrm{tr}(\dot{\epsilon}) \tag{3.22a}$$

$$\dot{\mathbf{S}} = 2\mu_0\dot{\boldsymbol{\epsilon}} - \frac{3\mu_0\mathbf{S}(\mathbf{S}:\dot{\mathbf{e}})\Gamma}{\bar{\sigma}^2(\bar{\epsilon}^p)\,[1+(1/3\mu_0)H']}; \qquad \begin{array}{l} H' = d\sigma/d\epsilon^p \\ \bar{\sigma} = \text{equivalent stress} \\ \bar{\epsilon}^p = \text{equivalent plastic strain} \end{array} \tag{3.22b}$$

The foregoing can be obtained from the present theory (Table 1) by setting $\rho_1(z) = \mathbf{h}^*(z) = \mathbf{r} = 0$; $d\zeta = (3/2)^{1/2}d\bar{\epsilon}^p$; $S_y^0(\partial f/\partial\zeta) = (2/3)H'$

(*ii*) Linear kinematic hardening (Prager, 1956)

$$\mathrm{tr}(\dot{\sigma}) = (2\mu_0 + 3\lambda_0)\mathrm{tr}(\dot{\epsilon}) \tag{3.22c}$$

$$\dot{\mathbf{S}} = 2\mu_0\dot{\mathbf{e}} - \frac{6\mu_0^2}{(\hat{C}+2\mu_0)(\sigma_y^0)^2} < (\mathbf{S}-\mathbf{r}):\dot{\mathbf{e}} > (\mathbf{S}-\mathbf{r})\Gamma \tag{3.22d}$$

$$\dot{\mathbf{r}} = \hat{C}\,\dot{\mathbf{e}}^p \tag{3.22e}$$

(3.22*c–e*) can be obtained from the present relations (Table 1) by setting $f(\zeta) = 1$; $\rho(z) = \rho_{10} = \text{const}$ (i.e., $h^* = 0$) and $\rho_{10} = (\hat{C}/2\mu_0)$; $S_y^0 = (2/3)^{1/2}\sigma_y^0$.

(*iii*) Mroz-Shrivastava-Dubey (1976), based on an earlier study by Eisenberg and Phillips (1968):

$$\dot{\mathbf{r}} = C(\zeta)\dot{\mathbf{e}}^p - d(\zeta)\mathbf{e}^p\,\dot{\zeta} \tag{3.22d}$$

where $\dot{\zeta} = (\dot{\mathbf{e}}^p:\dot{\mathbf{e}}^p)^{1/2}$

(*iv*) Chaboche and Rousselier (1982) (combined isotropic-kinematic hardening):

Kinematic hardening:

$$\dot{\mathbf{r}} = \sum_i \dot{\mathbf{r}}^{(i)} \tag{3.22e}$$

$$\dot{\mathbf{r}}^{(i)} = C_i\dot{\mathbf{e}}^p - d_i\mathbf{r}^{(i)}\,(\dot{\mathbf{e}}^p:\dot{\mathbf{e}}^p)^{1/2} \quad (\text{no sum on } i) \tag{3.22f}$$

C_i, d_i are constants

Isotropic hardening:

$$\dot{S}_y = b(Q - S_y)\,(\dot{\mathbf{e}}^p:\dot{\mathbf{e}}^p)^{1/2}; \quad S_y = Q\{1-\exp(-b\zeta)\} \tag{3.22g,h}$$

b, Q are constants

It may be easily seen that the present endochronic theory (Table 1) encompasses, as special cases, all the earlier classical theories of plasticity (Table 2). Detailed discussions of this comparison, as well as the interesting aspect of how the multiyield-surface theories of Mroz (1969), Krieg (1975), and Dafalias and Popov (1976) may also be considered as special cases of the present theory, are presented by the authors (Watanabe and Atluri, 1984b).

4 Plane Problems of Plasticity

4.1 Plane Strain. Here $d\epsilon_{33} = d\epsilon_{31} = d\epsilon_{32} = 0$. Defining $\gamma_{12} = 2\epsilon_{12}$, it is easy to derive the relevant plane-strain relations from Table 1 as:

$$\begin{Bmatrix} d\sigma_{11} \\ d\sigma_{22} \\ d\sigma_{12} \end{Bmatrix} = \begin{bmatrix} (\lambda_0+2\mu_0) & & \text{Sym.} \\ \lambda_0 & (\lambda_0+2\mu_0) & \\ 0 & 0 & \mu_0 \end{bmatrix} \begin{Bmatrix} d\epsilon_{11} \\ d\epsilon_{22} \\ d\gamma_{12} \end{Bmatrix}$$

$$- \frac{2\mu_0\Gamma}{C(S_y^0)^2 f^2(\zeta)} \begin{bmatrix} \hat{S}_{11}^2 & & \text{Sym.} \\ \hat{S}_{11}\hat{S}_{22} & \hat{S}_{22}^2 & \\ \hat{S}_{11}\hat{S}_{12} & \hat{S}_{12}\hat{S}_{22} & \hat{S}_{12}^2 \end{bmatrix} \begin{Bmatrix} d\epsilon_{11} \\ d\epsilon_{22} \\ d\gamma_{12} \end{Bmatrix} \tag{4.1}$$

$$d\sigma_{33} = \lambda_0 d\epsilon_{\alpha\alpha} - \frac{2\mu_0(S_{33}-r_{33})}{C(S_y^0)^2 f^2(\zeta)}\,(S_{\alpha\beta}-r_{\alpha\beta})\,d\epsilon_{\alpha\beta}\Gamma \tag{4.2}$$

where

$$\hat{S}_{\alpha\beta} = S_{\alpha\beta} - r_{\alpha\beta};\; S_{33} = -S_{\alpha\alpha};\; r_{33} = -r_{\alpha\alpha};\; \hat{S}_{33} = -\hat{S}_{\alpha\alpha} \tag{4.3}$$

$$\|\mathbf{S}-\mathbf{r}\|^2 = 2(\hat{S}_{11}^2 + \hat{S}_{11}\hat{S}_{22} + \hat{S}_{22}^2 + \hat{S}_{12}^2) \tag{4.4}$$

Yield condition: $\|\mathbf{S}-\mathbf{r}\|^2 - [S_y^0 f(\zeta)]^2 = 0$

$$\rho_1(z) = \sum_i \rho_{1i}\exp(-\alpha_i z);\; \rho_1^{(0)} = \sum_i \rho_{1i} \tag{4.5}$$

$$C = 1 + \sum_i \rho_{1i} + \frac{S_y^0 f'}{2\mu_0} + \frac{1}{S_y^0 f^2}\Big\{\hat{S}_{11}h_{11}^* + \hat{S}_{22}h_{22}^* + (\hat{S}_{11}+\hat{S}_{22})(h_{11}^*+h_{22}^*) + 2\hat{S}_{12}h_{12}^*\Big\} \tag{4.6}$$

$$d\zeta^2 = 2[(de_{11}^p)^2 + (de_{22}^p)^2 + de_{11}^p de_{22}^p] + 1/2(d\gamma_{12}^p)^2 \tag{4.7}$$

$$dr_{\alpha\beta} = \sum_i dr_{\alpha\beta}^{(i)} \tag{4.8a}$$

where

$$dr_{\alpha\alpha}^{(i)} = 2\mu_0\rho_{1i}de_{\alpha\alpha}^p - \frac{\alpha_i}{f(\zeta)}r_{\alpha\alpha}^{(i)}d\zeta \quad (\text{no sum on } \alpha;\; \alpha = 1,2) \tag{4.8b}$$

$$dr_{12}^{(i)} = \mu_0\rho_{1i}d\gamma_{12} - \frac{\alpha_i}{f}r_{12}^{(i)}\,d\zeta \tag{4.8c}$$

$$h_{\alpha\beta}^* = \sum_i \left(-\frac{\alpha_i}{2\mu_0}\right)r_{\alpha\beta}^{(i)} \tag{4.8d}$$

4.2 Plane Stress. As usual, the derivation of the differential stress-strain relation in this case is somewhat tedious. First, note that $d\sigma_{33} = d\sigma_{31} = d\sigma_{32} = 0$. To obtain the stress/strain relations, note from Table 1 that

$$d\epsilon_{\alpha\beta} = d\epsilon_{\alpha\beta}^e + d\epsilon_{\alpha\beta}^p = d\epsilon_{\alpha\beta}^e + de_{\alpha\beta}^p = \frac{1}{2\mu_0}\left[d\sigma_{\alpha\beta} - \frac{\nu_0}{1+\nu_0}d\sigma_{\theta\theta}\delta_{\alpha\beta}\right] + de_{\alpha\beta}^p \tag{4.9}$$

but

$$d\mathbf{e}^p = \frac{<(\mathbf{S}-\mathbf{r}):d\mathbf{e}>}{C(S_y^0)^2 f^2(\zeta)}\,(\mathbf{S}-\mathbf{r}) \tag{4.10}$$

Noting that $d\mathbf{e} = (d\mathbf{S}/2\mu_0) + d\mathbf{e}^p$, we obtain, taking the trace of both sides of (4.10) with $(\mathbf{S}-\mathbf{r})$ and using the resulting expression back in (4.10),

$$d\mathbf{e}^p \equiv C_0(\mathbf{S}-\mathbf{r}) < (\mathbf{S}-\mathbf{r}):d\mathbf{S} > \equiv C_0(\mathbf{S}-\mathbf{r}) < (\mathbf{S}-\mathbf{r}):d\sigma > \tag{4.11}$$

where

$$C_0 = 1/\left[2\mu_0(C-1)S_y^{02}f^2\right] \tag{4.12}$$

Thus

$$de_{\alpha\beta}^p = C_0(S_{\alpha\beta}-r_{\alpha\beta}) < (S_{\mu\nu}-r_{\mu\nu})\,d\sigma_{\mu\nu} > \quad (\alpha,\beta,\mu,\nu = 1,2) \tag{4.13}$$

Using (4.13) in (4.9) and taking the trace of both sides of the resulting equation with $(S_{\alpha\beta}-r_{\alpha\beta})$ yields:

$$(S_{\alpha\beta}-r_{\alpha\beta})\,d\sigma_{\alpha\beta} = \frac{1}{M}\left\{(S_{\alpha\beta}-r_{\alpha\beta})\,d\epsilon_{\alpha\beta} + \frac{\nu_0}{E_0}(S_{\mu\mu}-r_{\mu\mu})\,d\sigma_{\nu\nu}\right\} \tag{4.14}$$

where

$$M = \frac{1}{2\mu_0} + C_0(S_{\alpha\beta}-r_{\alpha\beta})\,(S_{\alpha\beta}-r_{\alpha\beta}) \tag{4.15}$$

Using (4.13) and (4.14) in (4.9), one obtains,

Downloaded 02 May 2010 to 171.66.16.54. Redistribution subject to ASME license or copyright; see http://www.asme.org/terms/Terms_Use.cfm

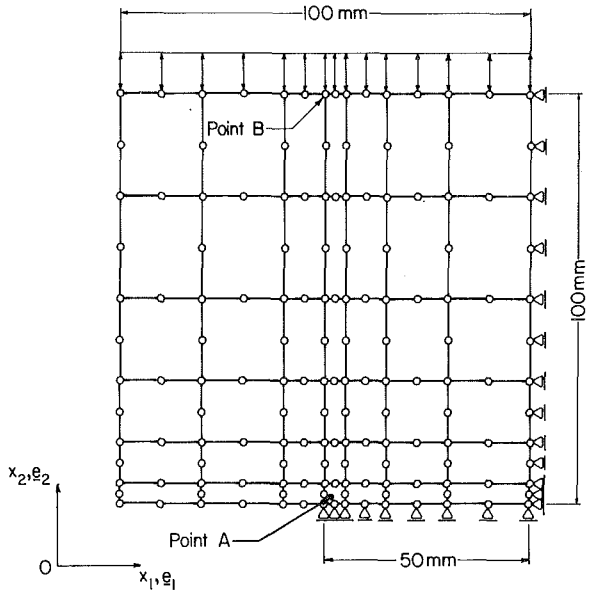


Fig. 1 Finite element model of a double-edge-cracked (DEC) tension specimen

$$\frac{1}{2\mu_0} d\sigma_{11} - \left\{ \frac{\nu_0}{E_0} - A(S_{11} - r_{11}) \right\} (d\sigma_{11} + d\sigma_{22}) = d\epsilon_{11} - B(S_{11} - r_{11})$$

$$\frac{1}{2\mu_0} d\sigma_{22} - \left\{ \frac{\nu_0}{E_0} - A(S_{22} - r_{22}) \right\} (d\sigma_{11} + d\sigma_{22}) = d\epsilon_{22} - B(S_{22} - r_{22})$$

$$\frac{1}{2\mu_0} d\sigma_{12} + A(S_{12} - r_{12})(d\sigma_{11} + d\sigma_{22}) = d\epsilon_{12} - B(S_{12} - r_{12}) \tag{4.16}$$

where

$$A = \frac{\nu_0 C_0}{E_0 M} (S_{\alpha\alpha} - r_{\alpha\alpha}) \tag{4.17a}$$

$$B = \frac{C_0}{M} (S_{\alpha\beta} - r_{\alpha\beta}) d\epsilon_{\alpha\beta} \tag{4.17b}$$

By using the definition of engineering strain, i.e., $\gamma_{12} = 2\epsilon_{12}$, the relations (4.16) may be inverted to find:

$$\begin{Bmatrix} d\sigma_{11} \\ d\sigma_{22} \\ d\sigma_{12} \end{Bmatrix} = \frac{E_0}{Q} \begin{bmatrix} \left(\hat{S}_{22}^2 + 2P\right) & & \text{Sym.} \\ \left(-\hat{S}_{11}\hat{S}_{22} + 2\nu_0 P\right); & \left(\hat{S}_{11}^2 + 2P\right) & \\ -\left(\frac{\hat{S}_{11} + \nu_0 \hat{S}_{22}}{1+\nu_0}\right)\hat{S}_{12}; & -\left(\frac{\hat{S}_{22} + \nu_0 \hat{S}_{11}}{1+\nu_0}\right)\hat{S}_{12}; & \frac{R}{2(1+\nu_0)} + \frac{1-\nu_0}{2E_0 C_0} \end{bmatrix} \begin{Bmatrix} d\epsilon_{11} \\ d\epsilon_{22} \\ d\gamma_{12} \end{Bmatrix} \tag{4.18}$$

where $\hat{S}_{\alpha\beta} = S_{\alpha\beta} - r_{\alpha\beta}$

$$P = \frac{\hat{S}_{12}^2}{1+\nu_0} + \frac{1}{2E_0 C_0}; \quad R = \hat{S}_{11}^2 + 2\nu_0 \hat{S}_{11}\hat{S}_{22} + \hat{S}_{22}^2$$
$$Q = R + 2(1-\nu_0^2)P \tag{4.19}$$

and the plastic strain increments are given by:

$$\begin{Bmatrix} d\epsilon_{11}^p \\ d\epsilon_{22}^p \\ d\gamma_{12}^p \end{Bmatrix} = C_0 \begin{bmatrix} \hat{S}_{11}^2 & & \text{Sym.} \\ \hat{S}_{11}\hat{S}_{22} & \hat{S}_{22}^2 & \\ 2\hat{S}_{11}\hat{S}_{12} & 2\hat{S}_{22}\hat{S}_{12} & 4\hat{S}_{12}^2 \end{bmatrix} \begin{Bmatrix} d\sigma_{11} \\ d\sigma_{22} \\ d\sigma_{12} \end{Bmatrix} \tag{4.20}$$

Note that the expressions for $\|\mathbf{S} - \mathbf{r}\|^2$; $\rho_1(z)$; C; $d\zeta^2$, $dr_{\alpha\beta}$, and $h^*_{\alpha\beta}$, in the plane-stress case, are identical to those in equations (4.4), (4.5), (4.6), (4.7), (4.8*a*), and (4.8*d*), respectively.

When classical isotropic hardening rule is used, as noted in Table 1, $\rho_1(z) = 0$; $\mathbf{r} = \mathbf{h}^* = 0$; $C = 1 + (H'/3\mu_0)$. Thus, C_0 of (4.12) becomes

$$C_0 = \frac{1}{2\mu_0 (H'/3\mu_0)(2/3)\bar{\sigma}^2} = \frac{9}{4\bar{\sigma}^2 H'} \tag{4.21}$$

It can be easily verified that for isotropic hardening, when C_0 is given by (4.21), the present results reduce to those of Yamada et al. (1968), even through the present derivation is different from that of Yamada et al. (1968).

5 Finite Element Analysis and Numerical Results

5.1 Finite Element Analysis. In so far as the presently developed theory results in a linear relation between the differential stress $d\sigma_{ij}$ and the differential strain $d\epsilon_{ij}$, and since the differential plastic strain $d\mathbf{e}^p$ is related to $d\boldsymbol{\epsilon}$ as in (3.9*b*), the implementation of the present endochronic theory in a finite-element algorithm is *no different* from that of the classical theory of isotropic hardening or Prager-hardening plasticity theory (Marcal and King, 1967; Yamada et al., 1968; Zienkiewicz et al., 1969; and Krieg and Key, 1976). For this reason, all details of finite-element algorithms are omitted here. However, we note briefly that one may use the elastic-plastic "tangent stress/strain" relations derived in equation (3.9*a*) (for the three-dimensional case) or in Section 4 for plane stress/strain to obtain "tangent stiffness" matrices for each finite element. Alternatively, one may use an initial strain/stress apporach. Irrespective of the type of finite-element approach (tangent-stiffness/initial strain/stress) that is used, the integration of the constitutive relation, i.e., to determine $d\sigma_{ij}$ for a given $d\epsilon_{ij}$, may proceed in any number of ways—for instance, the popular "radial return" method (Krieg and Key, 1976). In contrast, the type of differential stress/strain relations derived by Valanis and Fan (1983) mandates the use of an *initial-strain* method, requiring a number of iterations to account for plastic pseudoforces arising out of the nonlinear part in the $d\mathbf{S}$ versus $d\mathbf{e}^p$ relation [see (3.4*c*)]. Furthermore, in the approach of Valanis and Fan (1983), the stress integration for a given history of strain [see equations (3.4*c*) and (3.5*d*)], by itself, requires a number of iterations.

In the present series of computations, a tangent-stiffness approach is used, in conjunction with eight-node isoparametric finite elements. A 2 × 2 Gauss quadrature is employed.

5.2 Numerical Results. All the results presented here pertain to the behavior of a double-edge-cracked square plate

Downloaded 02 May 2010 to 171.66.16.54. Redistribution subject to ASME license or copyright; see http://www.asme.org/terms/Terms_Use.cfm

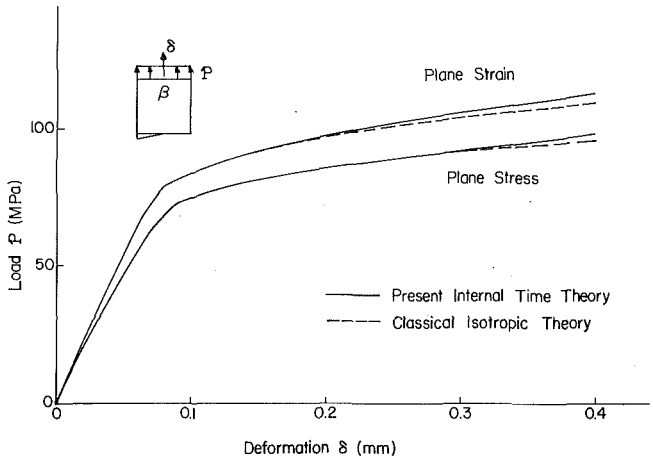


Fig. 2 Load-deflection curve under *monotonic loading* and comparison with isotropic hardening theory

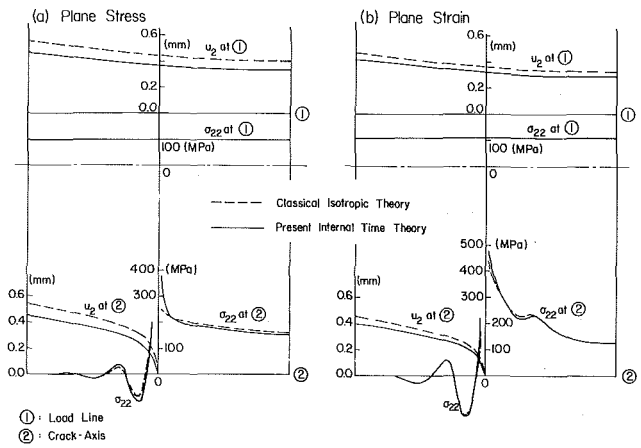


Fig. 3 Elastoplastic solutions for displacement and stress at the loaded edge, and near the crack-axis, for monotonic loading

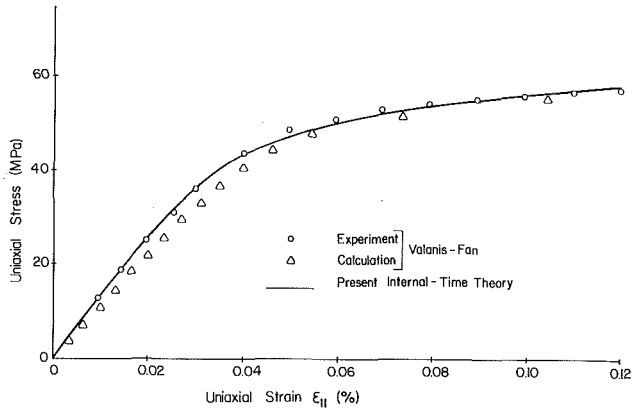


Fig. 4 Uniaxial stress/strain curve for OFHC copper

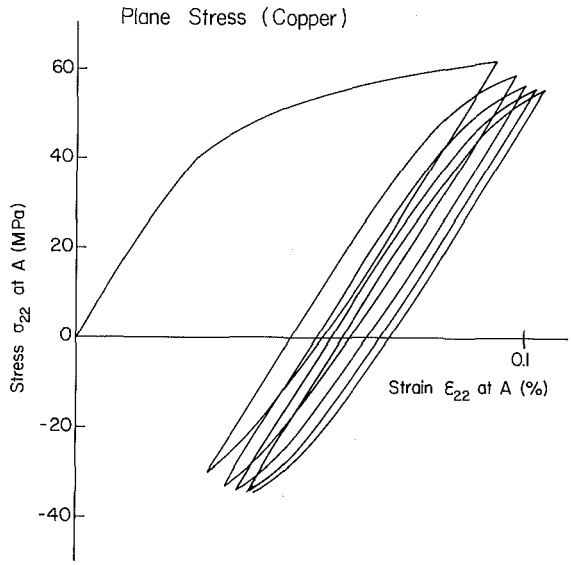


Fig. 5 Stress/strain (σ_{22} versus ϵ_{22}) response at notch-root (point *A* in Fig. 1) in a DEC copper (OFHC) sheet subject to zero-to-tension external cyclic loading (plane stress)

subjected to monotonic or cyclic (zero-to-tension as well as tension-compression) loading. The external load is assumed to be uniformly distributed at the upper and lower edges of the plate. Because of the symmetry of loading and geometry, a quarter of the plate is modeled by finite elements, as shown in Fig. 1, with 42 elements and 284 degrees of freedom. For future reference, we designate the Gauss integration point closest to the crack-tip as point "*A*" and the point at the center of the upper edge of the modeled region as point "*B*".

5.2.1 Monotonic Loading. The material constants used correspond to SUS 304 stainless steel (see Watanabe and Atluri, 1984a): $E_0 = 153.8$ GPa; $\nu_0 = 0.3$; $\sigma_y^0 = 112.8$ MPa. The kernel $\rho_1(z)$ is approximated as: $\rho_1(z) = [\rho_{11}\exp(-\alpha_{12}z)] + \rho_{12}$, with $\rho_{11} = 9.298 \times 10^{-2}$; $\alpha_1 = 314$; $\rho_{12} = 3.511 \times 10^{-4}$. The isotropic hardening function, i.e., $f(\zeta)$, is assumed to be $f = 1 + 5.0\zeta$. Figure 2 shows the load (P) versus deflection (δ) curve, where δ refers to the deflection at B in the direction of the loading. It is seen that the internal time theory results in a slightly stiffer behavior of the specimen as compared to the classical isotropic hardening theory. For both the cases of plane stress and plane strain, Fig. 3 shows the solutions for displacement u_2 and stress σ_{22} at Gauss points closest to the upper edge of the specimen and at points closest to the crack-axis, respectively, at applied stress levels of 98.1 MPa (i.e., 10 kgf/mm^2, for plane stress) and 107.9 MPa (i.e., 11 kgf/mm^2, for plane strain).

From Figs. 2 and 3, it is seen that for monotonic loading the present endochronic theory agrees fairly well with the classical isotropic hardening theory.

5.2.2 Zero-to-Tension Cyclic Loading. First, for comparison purposes, we solve the same problem as reported in Valanis and Fan's (1983) work. The material is OFHC copper, with $E_0 = 133$ GPa; $\nu_0 = 0.3$; $\sigma_y^0 = 20.0$ MPa. [Recall $S_y^0 = 2\mu_0\rho_0 = \sqrt{2/3}\ \sigma_y^0$]. The kernel $\rho_1(z)$ is approximated, presently, as:

$$\rho_1(z) = \rho_{11}e^{-\alpha_1 z} + \rho_{12}e^{-\alpha_2 z} + \rho_{13}$$

$$[\rho(z) = \rho_0\delta(z) + \rho_1(z)]$$

with $\rho_{11} = 5.979$; $\rho_{12} = 4.886 \times 10^{-1}$; $\rho_{13} = 4.746 \times 10^{-2}$; $\alpha_1 = 41389$; $\alpha_2 = 4497$. The function $f(\zeta)$ is assumed as $f = a + (1 - a)\exp(-\gamma\zeta)$ with $a = 1.01$, and $\gamma = 500$, to be valid in the range $0 < \zeta < 0.3$ percent. These assumptions for $\rho(z)$ and $f(\zeta)$ are different from those in Valanis and Fan (1983), which are: $f(\zeta) = 1 + 0.53(\zeta)^{0.72}$ and $\rho(z) \equiv \rho_1(z) = \Sigma_r \rho_{1r}\exp(-\alpha_r z)$ (see Valanis and Fan, 1983, for specific values for ρ_{1r} and α_r).

Figure 4 shows the uniaxial stress/strain curve as modeled in the foregoing, along with the comparison curve of Valanis and Fan (1983) and the experimentally determined curve. Figure 5 shows the hysteresis loops of (σ_{22} versus ϵ_{22}) behavior, at point A, under *plane-stress* conditions, for a zero-to-tension cyclic loading with the maximum amplitude of applied tension being (18 MPa). Note that for a value of σ_{22} at point A being of the same order as in Fig. 5, the maximum amplitude of zero-to-tension cyclic loading indicated by Valanis and Fan (1983) is 37 MPa—roughly twice that in the

Downloaded 02 May 2010 to 171.66.16.54. Redistribution subject to ASME license or copyright; see http://www.asme.org/terms/Terms_Use.cfm

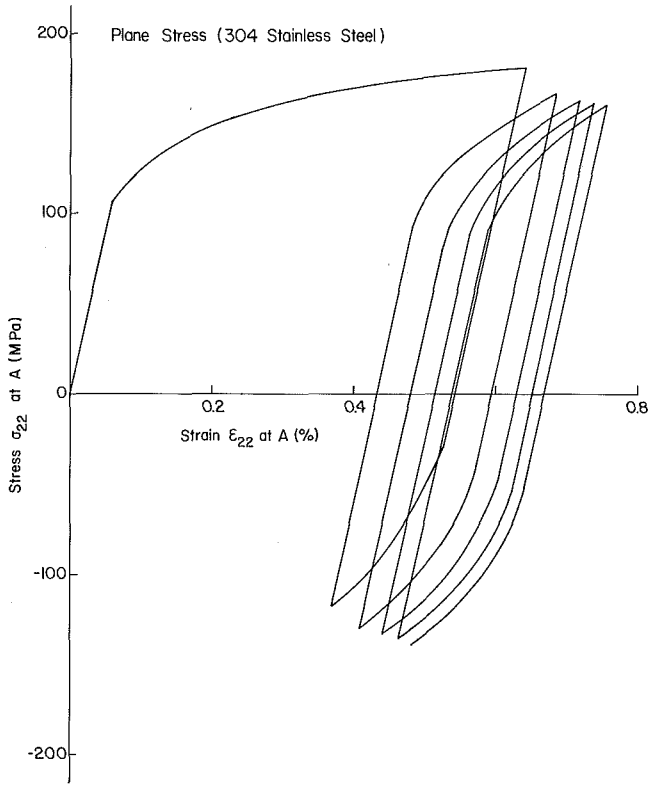


Fig. 6(*a*) Stress response at notch-root (point *A*) in a DEC 304 stainless steel panel subject to zero-to-tension cyclic loading (plane stress)

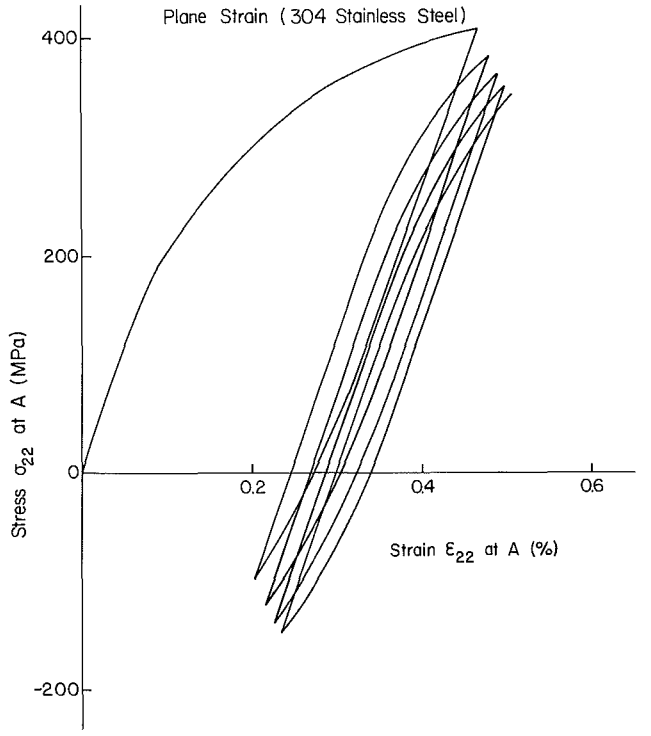


Fig. 6(*b*) Results similar to those in Fig. 6(*a*), except these are for plane strain

Fig. 6

present calculations. Note that, in general, there may be stress singularities near the crack tip, which are not modeled either in the present study or in that of Valanis and Fan (1983). Apart from this, the reasons for a better estimation of stress at point A in the present series of computations, as contrasted

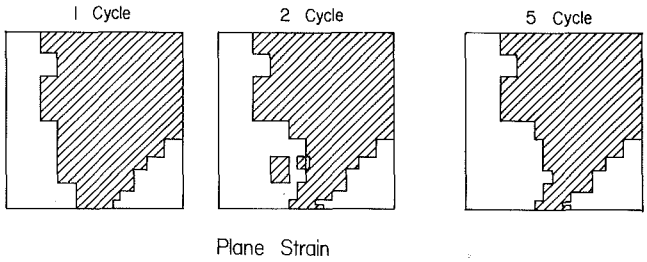


Fig. 7 Plastic zones at points of load reversal in a DEC 304 steel panel, subject to zero-to-tension cyclic loading (plane strain)

to those of Valanis and Fan (1983) are believed to be: (*i*) the user of eight-node parametric elements in the present, as opposed to constant strain triangles by Valanas and Fan (1983); (*ii*) the use of a better finite-element algorithm in the present; and (*iii*) the use of a better algorithm, in the present, for the determination of stresses from the computed strains at each material point. From Fig. 5, it is seen that ratcheting takes place and plastic strain accumulates progressively at point A.

However, the present results shown in Fig. 5 for zero-to-tension cyclic loading have the following features that are *different* from the comparison results presented in Fig. 4 of Valanis and Fan (1983): (*i*) the present hysteresis loops for (σ_{22} versus ϵ_{22}) at the root of the notch, point A, *saturate* gradually, due to the use of a *saturating* function $f(\zeta)$ as in the present, and (*ii*) the amplitude of peak stress at point A, at the instant of stress reversal in the zero-to-tension cyclic loading, decreases gradually and converges to a steady-state value.

As a second example, we consider the zero-to-tension cyclic loading of a double-edge-cracked SUS 304 stainless steel panel with: $E_0 = 153.8$ GPa, $\nu_0 = 0.3$; $\sigma_y^0 = 103.8$ MPa; $\rho_{11} = 1.502 \times 10^{-1}$; $\rho_{12} = 9.298 \times 10^{-2}$; $\rho_{13} = 3.511 \times 10^{-4}$; $\alpha_1 = 2212$; $\alpha_2 = 314$; $a = 1.2$; $\gamma = 25$ [note that $\rho_1(z)$ and $f(\zeta)$, for SUS 304 steel, are assumed to be of the same form as for OFHC copper described earlier].

Figures 6(*a*) and 6(*b*) show the σ_{22} versus ϵ_{22} loops at the root of the notch (point A) of the 304 steel plate subjected to (zero-to-tension) cyclic loading under plane stress (with applied $\sigma_{max} = 73.5$ MPa or 7.5 kgf/mm^2) and plane strain ($\sigma_{max} = 98$ MPa or 10 kgf/mm^2) conditions, respectively. Qualitatively, the stress response is the same as in OFHC copper. Figure 7 illustrates the plastic zones at the instants of reversal of loading at various cycles of zero-tension loading under plane strain. It may be seen that the *elastic* region increases in size progressively, after cyclic tensile loading.

5.2.3 Tension-Compression Cyclic Loading. Here again the considered material is SUS 304 strainless steel, and the problem is that of a double-edge-cracked panel with dimensions as shown in Fig. 1.

The applied loading is uniform at the upper edge of the panel, and varies cyclically from tension to compression, with amplitude of $\pm$ 73.5 MPa ($\pm$ 7.5 kgf/mm^2). Figure 8 shows the overall load versus deflection (at point B) curve for this tension-compression cyclic loading, under plane-stress conditions. The corresponding behavior of σ_{22} versus ϵ_{22} at point A is shown in Fig. 9. From Figs. 8 and 9, it is seen that the hysteresis loops saturate gradually in the present tension-compression cyclic loading, instead of the progressive ratching response observed under zero-to-tension cyclic loading (see Fig. 6(*a*)).

6 Concluding Comments

In all the examples, dealing with either monotonic or cyclic loading, discussed in the foregoing, the increments of external loading are taken to be about 1 MPa. The computational time

Downloaded 02 May 2010 to 171.66.16.54. Redistribution subject to ASME license or copyright; see http://www.asme.org/terms/Terms_Use.cfm

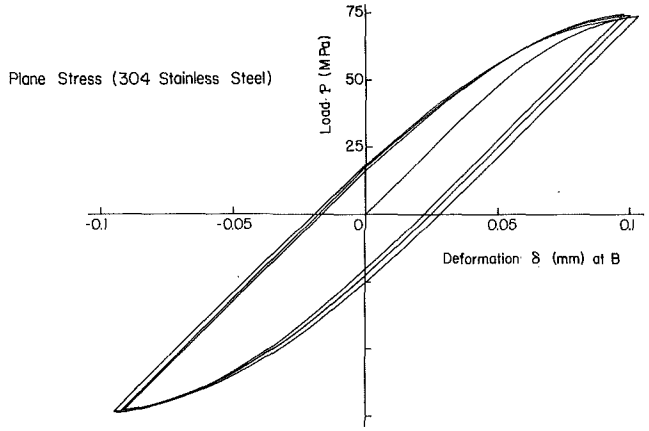


Fig. 8 Hysteresis loops of external load vesus deflection (at point *B*, Fig. 1) for a DEC 304 steel panel, subject to tension-compression cyclic loading (plane stress)

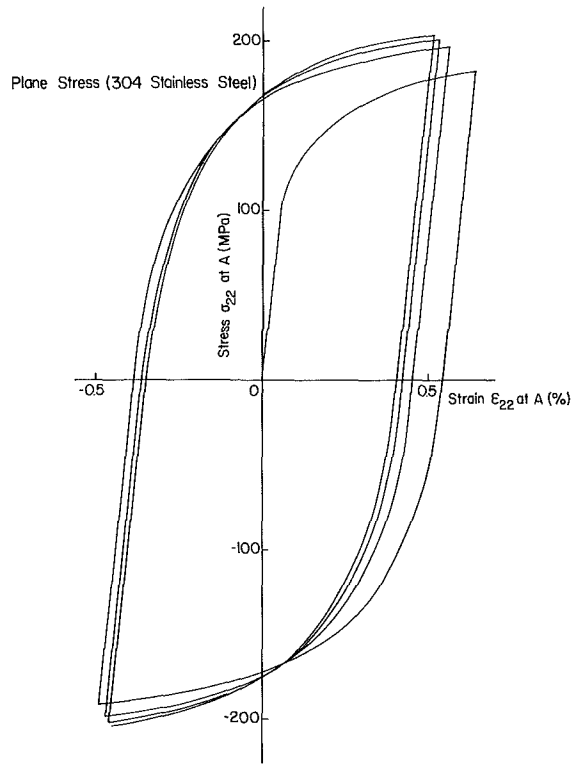


Fig. 9 Stress response at notch-root (point *A*) in DEC 304 steel panel, under tension-compression cyclic external loading (plane stress)

for the present endochronic theory, per increment, was about 3 sec on a CYBER855 and is about the same as for classical isotropic hardening plasticity theory. Considering the facts that: (*i*) the constitutive relations (in differential form) of the present endochronic theory are exactly similar in mathematical structure to those of classical plasticity theory, (*ii*) the computational implementation of the present endochronic theory is no more difficult and no more expensive than a classical isotropic hardening theory, and that (*iii*) the present theory can predict the phenomenological behavior of materials under cyclic loading in a much better fashion, as demonstrated in several examples in this paper, the present constitutive theory may be a viable option for implementation in general purpose computational codes for analyzing structures, especially those susceptible to crack-growth, under cyclic loading.

Acknowledgments

The financial support for this research was provided by the U.S. Office of Naval Research, under contract N00014-78-C-0636 to Georgia Tech. This support, and the encouragement of Drs. Y. Rajapakse and A. Kushner, is greatfully acknowledged. It is a pleasure to thank Ms. J. Webb for her assistance in the preparation of this manuscript.

References

Bazant, Z. P., 1980, "Endochronic Inelasticity and Incremental Plasticity," *International Journal of Solids and Structures*, Vol. 16, pp. 873-901.

Bazant, Z. P., Krizek, R. J., and Shieh, C. L., 1983, "Hysteretic Endochronic Theory for Sand," *Journal of Engineering Mechanics*, ASCE, Vol. 109, pp. 1073-1095.

Chaboche, J. L., and Rousselier, G., 1982, "On the Plastic and Viscoplastic Constitutive Equations, Part I: Rules Developed With Internal Variable Concept; Part II: Application of Internal Variable Concepts to the 316 Stainless Steel," *Inelastic Analysis and Life Prediction in Elevated Temperature Design, ASME PVP—Vol. 59*, Baylac, G., ed., pp. 33-55.

Dafalias, Y. F., and Popov, E. P., 1976, "Plastic Internal Variables Formalism of Cyclic Plasticity," ASME JOURNAL OF APPLIED MECHANICS, Vol. 43, pp. 645-651.

Eisenberg, M. A., and Phillips, A., 1968, "On Nonlinear Kinematic Hardening," *Acta Mechanica*, Vol. 5, pp. 1-13.

Krieg, R. D., 1975, "A Practical Two Surface Plasticity Theory," ASME JOURNAL OF APPLIED MECHANICS, Vol. 42, pp. 641-646.

Krieg, R. D., and Key, S. W., 1976, "Implementation of a Time-Independent Plasticity Theory into Structural Computer Programs," in *Constitutive Equations in Viscoplasticity: Computational and Engineering Aspects*, Stricklin, J. A. et al., eds., AMD-Vol. 20, ASME, pp. 125-137.

Marcal, P. V., and King, I. P., 1967, "Elastic-Plastic Analysis of Two-Dimensional Stress Systems by the Finite Element Method," *International Journal of Mechanical Science*, Vol. 9, pp. 143-155.

Mroz, Z., 1969, "An Attempt to Describe the Behavior of Metals Under Cyclic Loads Using a More General Workhardening Model," *Acta Mechanica*, Vol. 7, pp. 199-212.

Mroz, Z., Shirivastava, H. P., and Dubey, R. N., 1976, "A Nonlinear Hardening Model and Its Application to Cyclic Loading," *Acta Mechanica*, Vol. 25, pp. 51-61.

Onat, E. T., 1981, "Representation of Inelastic Behavior in the Presence of Anisotropy and Finite Deformations," *Proceedings of Research Workshop on Plasticity of Metals at Finite Strain: Theory, Experiment and Computation*, Stanford University, Lee, E. H., and Mallott, R. L., eds., pp. 519-544.

Prager, W., 1956, "A New Method of Analyzing Stresses and Strains in Work-Hardening Plastic Solids," ASME JOURNAL OF APPLIED MECHANICS, Vol. 23, pp. 493-496.

Valanis, K. C., 1980, "Fundamental Consequence of a New Intrinsic Time Measure-Plasticity as a Limit of the Endochronic Theory," *Archives of Mechanics*, Vol. 32, No. 2, pp. 171-191.

Valanis, K. C., and Fan, J., 1983, "Endochronic Analysis of Cyclic Elastoplastic Strain Fields in a Notched Plate," ASME JOURNAL OF APPLIED MECHANICS, Vol. 50, No. 4*a*, pp. 789-794.

Watanabe, O., and Atluri, S. N., 1984a, "Constitutive Modeling of Cyclic Plasticity and Creep, Using an Internal Time Concept," *The International Journal of Plasticity*, in press.

Watanabe, O., and Atluri, S. N., 1984b, "Internal Time, General Internal Variable, and Multi-Yield-Surface Theories of Plasticity and Creep: A Unification of Concepts," *The International Journal of Plasticity*, in press.

Yamada, Y., Yoshimura, N., and Sakurai, T., 1968, "Plastic Stress-Strain Matrix and Its Application for the Solution of Elastic-Plastic Problems by the Finite Element Method," *International Journal of Mechanical Science*, Vol. 10, pp. 343-354.

Zienkiewicz, O. C., Valliapan, S., and King, I. P., 1969, "Elasto-Plastic Solutions of Engineering Problems: 'Initial Stress', Finite Element Approach," *International Journal for Numerical Methods in Engineering*, Vol. 1, pp. 75-100.

Downloaded 02 May 2010 to 171.66.16.54. Redistribution subject to ASME license or copyright; see http://www.asme.org/terms/Terms_Use.cfm

The Plastic Spin

Y. F. Dafalias
Professor of Engineering Science,
Department of Civil Engineering,
University of California at Davis,
Davis, Calif. 95616
Mem. ASME

A macroscopic formulation of large deformations elastoplasticity with tensorial structure variables is presented. The novel features are the effect of constitutive relations for the plastic spin and, to a lesser degree of importance, of elastically embedding the structure variables. The plastic spin constitutive relations are obtained for different kinds of initial and induced anisotropies on the basis of the representation theorems for isotropic second-order antisymmetric tensor-valued functions, and their role is illustrated by the analysis of several examples at large homogeneous deformations. In particular the analysis of simple shear with nonlinear kinematic hardening of the evanescent memory type provides, on the basis of the second Liapunov method for stability, conditions on the material constants for the occurrence or not of stress oscillations with monotonically increasing shear strain.

1 Introduction

The title of this work emphasizes the basic proposition, made by Mandel [1] and Kratochvil [2], that constitutive relations must be provided not only for the plastic rate of deformation but also for the plastic spin within a macroscopic formulation of elastoplasticity. This was motivated by the kinematics of single crystal plasticity where the plastic spin is routinely specified by microscopic analysis. Such constitutive relations, however, have not been systematically considered, derived, and applied within the framework of a macroscopic approach for large elastic and plastic deformations, where the concept of tensorial structure (or internal) variables is utilized to describe the structure of an anisotropic continuum. This is the principal objective of the present work. The proposed general formulation will clearly demonstrate not only the role of the constitutive relations for the plastic spin, but also the consequence of elastically embedding (or convecting) the structure variables. Based on invariance requirements and the representation theorems for isotropic functions [3], specific constitutive relations for the plastic spin will be formulated for different kinds of initial and induced anisotropies, and their effect illustrated by the analysis of several examples at large homogeneous deformations.

Tensors will be denoted usually by boldface characters in direct notation. With the summation convention over repeated indices implied, the following symbolic operations apply: $\mathbf{a}\boldsymbol{\sigma} = a_{ij}\sigma_{jk}$, $\mathbf{a}:\boldsymbol{\sigma} = a_{ij}\sigma_{ji}$, $\mathbf{a}\cdot\boldsymbol{\sigma} = a_{ij}\sigma_{ij}$, $\mathbf{a}\otimes\boldsymbol{\sigma} = a_{ij}\sigma_{kl}$, with proper extension to different order tensors. The prefix *tr* indicates the trace, a superscript T the transpose, subscripts s and a the symmetric and antisymmetric parts, and a superposed dot, the material time derivative or rate. Under an orthogonal transformation $\mathbf{Q}$, the notation $\mathbf{Q}[\mathbf{a}]$ implies the corresponding transformation of the tensor $\mathbf{a}$, e.g., $\mathbf{Q}[\mathbf{a}] = \mathbf{Q}\mathbf{a}\mathbf{Q}^T$ if $\mathbf{a}$ is of second order.

Contributed by the Applied Mechanics Division for publication in the JOURNAL OF APPLIED MECHANICS.

Discussion on this paper should be addressed to the Editorial Department, ASME, United Engineering Center, 345 East 47th Street, New York, N.Y. 10017, and will be accepted until two months after final publication of the paper itself in the JOURNAL OF APPLIED MECHANICS. Manuscript received by ASME Applied Mechanics Division, June 1984.

2 Kinematics of Structured Media

In a macroscopic approach the collection of microscopic entities that define what can be called the substructure of a continuum, can be described by means of tensorial structure variables defined macroscopically at the current configuration κ. With a relative loss of generality for the sake of simplicity, the structure variables will be restricted to second-order tensors $\mathbf{a}$, vectors $\mathbf{m}$, and scalars k, collectively denoted by $\mathbf{s}$, although higher-order tensors can, and must sometimes, be considered [4]. The state variables, therefore, can be defined as the Cauchy stress $\boldsymbol{\sigma}$ (temperature is omitted for simplicity) and the $\mathbf{s}$.

The multiplicative decomposition of the deformation gradient $\mathbf{F}$ into elastic and plastic parts $\mathbf{V}$ and $\mathbf{P}$ [5] such that $\mathbf{V} = \mathbf{V}^T$ [4], yields

$$\mathbf{F} = \mathbf{V}\mathbf{P} \tag{1}$$

The $\mathbf{V}$ defines a macroscopically unstressed configuration κ_0, which can be visualized as being obtained from κ by actual or virtual (if the stress origin is outside the current yield surface) unloading without rotation. Motivated by corresponding concepts of crystal plasticity [6–9], it can be assumed that the $\mathbf{s}$ are elastically embedded so that during the unloading they are transported at κ_0 as second-order tensors $\mathbf{A}$, vectors $\mathbf{M}$, and scalars K, collectively denoted by $\mathbf{S}$. Depending on the particular physical meaning attributed to each $\mathbf{s}$, the transport operation can be expressed by different weighted convected transformations of relative tensors, such as contravariant $\mathbf{A} = |\mathbf{V}|^w\mathbf{V}^{-1}\mathbf{a}\mathbf{V}^{-1}$, $\mathbf{M} = |\mathbf{V}|^w\mathbf{V}^{-1}\mathbf{m}$, covariant $\mathbf{A} = |\mathbf{V}|^w\mathbf{V}\mathbf{a}\mathbf{V}$, $\mathbf{M} = |\mathbf{V}|^w\mathbf{m}\mathbf{V}$, and scalar $K = |\mathbf{V}|^w k$, where $|\mathbf{V}|$ denotes the determinant of $\mathbf{V}$ and w is the weight. Mixed transformations can also be considered, if appropriate. The foregoing transport operations will be symbolized collectively by $\mathbf{S} = \mathbf{V}[\mathbf{s}]$. The transport of $\boldsymbol{\sigma}$ is defined here as the first Piola-Kirchhoff stress in reference to κ_0, $\boldsymbol{\Pi} = |\mathbf{V}|\mathbf{V}^{-1}\boldsymbol{\sigma}\mathbf{V}^{-1}$. Thus, the state variables are defined equivalently either as $\boldsymbol{\sigma}$ and $\mathbf{s}$ at κ, or $\boldsymbol{\Pi}$ and $\mathbf{S}$ at κ_0 since $\mathbf{V}$ will be shown to be a function of them.

The elastic and plastic rate of transformation (deformation and rotation) and the rate of $\mathbf{S}$ can be thought as taking place relatively to the substructure defined at κ_0 by the current

Copyright © 1985 by ASME
Downloaded 02 May 2010 to 171.66.16.54. Redistribution subject to ASME license or copyright; see http://www.asme.org/terms/Terms_Use.cfm

values of $\mathbf{S}$, including orientation [4], followed by a simultaneously occurring rigid body spin ω in order to accommodate the total material spin $\mathbf{W}$. The set of directions created by the tensorial nature of $\mathbf{S}$ (e.g., the eigenvectors of second-order tensors), can be considered as the macroscopic conceptual counterpart of the lattice in single crystals, with the difference that these directions evolve in general with $\mathbf{S}$. For easier interpretation, but without being necessary for the development, the spin ω can be associated with the spin of Mandel's director vectors [1], which at any given instance can be thought as being attached to the substructure. The concept of the spin ω is of cardinal importance because in reference to any fixed cartesian coordinate system the aforementioned rates must be corotational with ω. Defining in general for later use the corotational rates of a tensor $\mathbf{a}$ and a vector $\mathbf{m}$ with respect to an antisymmetric tensor Ω by

$$D\mathbf{a}/Dt = \dot{\mathbf{a}} - \Omega\mathbf{a} + \mathbf{a}\Omega, \quad D\mathbf{m}/Dt = \dot{\mathbf{m}} - \Omega\mathbf{m} \tag{2}$$

and denoting by a superposed $\circ$ the corotational rates with $\Omega = \omega$, the following basic kinematical relations and definitions can be written

$$\dot{\mathbf{F}}\mathbf{F}^{-1} = \dot{\mathbf{V}}\mathbf{V}^{-1} + \mathbf{V}\dot{\mathbf{P}}\mathbf{P}^{-1}\mathbf{V}^{-1} = \omega + \overset{\circ}{\mathbf{V}}\mathbf{V}^{-1} + \mathbf{V}\overset{\circ}{\mathbf{P}}\mathbf{P}^{-1}\mathbf{V}^{-1} \tag{3}$$

$$\mathbf{D}^e = (\overset{\circ}{\mathbf{V}}\mathbf{V}^{-1})_s, \quad \mathbf{D}^p_0 = (\overset{\circ}{\mathbf{P}}\mathbf{P}^{-1})_s, \quad \mathbf{D}^p = (\mathbf{V}\overset{\circ}{\mathbf{P}}\mathbf{P}^{-1}\mathbf{V}^{-1})_s \tag{4}$$

$$\mathbf{W}^e = (\overset{\circ}{\mathbf{V}}\mathbf{V}^{-1})_a, \quad \mathbf{W}^p_0 = (\overset{\circ}{\mathbf{P}}\mathbf{P}^{-1})_a, \quad \mathbf{W}^p = (\mathbf{V}\overset{\circ}{\mathbf{P}}\mathbf{P}^{-1}\mathbf{V}^{-1})_a \tag{5}$$

$$\mathbf{D} = \mathbf{D}^e + \mathbf{D}^p, \quad \mathbf{W} = \mathbf{W}^* + \mathbf{W}^p, \quad \mathbf{W}^* = \omega + \mathbf{W}^e \tag{6}$$

where $\overset{\circ}{\mathbf{V}}$ and $\overset{\circ}{\mathbf{P}}$ are defined according to equations $(2)_1$ and $(2)_2$ with $\Omega = \omega$, respectively; equation $(2)_2$ is used for $\mathbf{P}$ as if it were a vector because $\mathbf{P}$ is attached to κ_0 by its first index only [1]. The superscripts e and p refer to elastic and plastic. The name plastic rate of deformation and plastic spin can be associated with either $\mathbf{D}^p_0$ and $\mathbf{W}^p_0$ at κ_0, or $\mathbf{D}^p$ and $\mathbf{W}^p$ at κ, [10]. It is clear from the foregoing development that the plastic spin expresses the rate of rotation of the continuum with respect to its substructure. Hence, it becomes meaningful for anisotropy where the substructure is characterized by preferred directions.

Anticipating the formulation of the rate constitutive equations and denoting by superposed * and $\triangledown$ the corotational rates with respect to $\mathbf{W}^*$ and $\mathbf{W}$ (Jaumann rates), the following kinematical relations can be written for a representative tensor on the basis of the foregoing kinematics

$$\mathbf{A} = |\mathbf{V}|^w\mathbf{V}^{-1}\mathbf{a}\mathbf{V}^{-1}, \quad \overset{\circ}{\mathbf{A}} = |\mathbf{V}|^w\mathbf{V}^{-1}\overset{\square}{\mathbf{a}}\mathbf{V}^{-1} \tag{7}$$

$$\overset{\square}{\mathbf{a}} = \mathring{\mathbf{a}} - \mathbf{a}\mathbf{V}^{-1}\overset{\circ}{\mathbf{V}} - \overset{\circ}{\mathbf{V}}\mathbf{V}^{-1}\mathbf{a} + w\mathbf{a}tr\mathbf{D}^e = \overset{*}{\mathbf{a}} - \mathbf{a}\mathbf{D}^e - \mathbf{D}^e\mathbf{a} + w\mathbf{a}tr\mathbf{D}^e \tag{8}$$

$$\overset{\vee}{\mathbf{a}} = \dot{\mathbf{a}} - \mathbf{a}\mathbf{F}^{-T}\dot{\mathbf{F}}^T - \dot{\mathbf{F}}\mathbf{F}^{-1}\mathbf{a} + w\mathbf{a}tr\mathbf{D} = \overset{\triangledown}{\mathbf{a}} - \mathbf{a}\mathbf{D} - \mathbf{D}\mathbf{a} + w\mathbf{a}tr\mathbf{D} \tag{9}$$

$$\overset{\vee}{\mathbf{a}} - \overset{\square}{\mathbf{a}} = -\mathbf{a}\mathbf{V}^{-1}\mathbf{P}^{-T}\overset{\circ}{\mathbf{P}}{}^T\mathbf{V} - \mathbf{V}\overset{\circ}{\mathbf{P}}\mathbf{P}^{-1}\mathbf{V}^{-1}\mathbf{a} + w\mathbf{a}tr\mathbf{D}^p \tag{10}$$

and similar relations can be stated for other kinds of transports of tensors, vectors and scalars. In particular equations (7) can be stated in a general symbolic notation as $\mathbf{S} = \mathbf{V}[\mathbf{s}]$, $\overset{\circ}{\mathbf{S}} = \mathbf{V}[\overset{\square}{\mathbf{s}}]$. The superposed $\vee$ denotes the convected derivatives of relative tensors (for $w = 1$, equation (9) yields the Truesdell derivative). The superposed $\square$ denotes the so-called corodeformational rate due to the elastic embedding of $\mathbf{a}$ and the simultaneous corotation of both $\mathbf{a}$ and $\mathbf{V}$ with ω, as can be seen from the use of $\mathring{\mathbf{a}}$ and $\overset{\circ}{\mathbf{V}}$ in equation (8). A final important point is that under a superposed rigid body rotation/reflection at κ defined by an orthogonal tensor $\mathbf{Q}$, the $\mathbf{P}$, $\mathbf{V}$, and ω become $\mathbf{QP}$, $\mathbf{QVQ}^T$, and $\mathbf{Q}\omega\mathbf{Q}^T + \dot{\mathbf{Q}}\mathbf{Q}^T$, correspondingly, because κ_0 must also rotate/reflect by $\mathbf{Q}$ based on the definition of $\mathbf{V}$. Hence, one can show that the σ, $\mathbf{s}$, $\mathbf{\Pi}$, $\mathbf{S}$, and all rates defined in equations (4), (5), (7)–(9), transform only by rotation/reflection under $\mathbf{Q}$.

3 Constitutive Formulation

3.1 Rate Equations. With a scalar loading index λ for a state satisfying a yield criterion, both to be defined in the sequel, the following rate equations can be stated

$$\mathbf{D}^p_0 = <\lambda>\mathbf{N}^p_0(\mathbf{\Pi},\mathbf{S}), \quad \mathbf{W}^p_0 = <\lambda>\Omega^p_0(\mathbf{\Pi},\mathbf{S}) \tag{11}$$

$$\overset{\circ}{\mathbf{S}} = <\lambda>\bar{\mathbf{S}}(\mathbf{\Pi},\mathbf{S}) \tag{12}$$

with $<\lambda> = \lambda$ if $\lambda > 0$ and $<\lambda> = 0$ if $\lambda \leq 0$. The use of $\overset{\circ}{\mathbf{S}}$ in equation (12) follows directly from the discussion preceding equation (2). Based on the transformation law under superposed rigid body rotation/reflection, the corresponding invariance requirements render $\mathbf{N}^p_0$, Ω^p_0 and $\bar{\mathbf{S}}$ isotropic functions of their arguments $\mathbf{\Pi}$ and $\mathbf{S}$ (definition in Appendix). Clearly this does not imply in general that the material is isotropic due to the tensorial nature of $\mathbf{S}$ [4]. Introducing the definitions

$$\mathbf{N}^p = (\mathbf{V}(\mathbf{N}^p_0 + \Omega^p_0)\mathbf{V}^{-1})_s, \quad \Omega^p = (\mathbf{V}(\mathbf{N}^p_0 + \Omega^p_0)\mathbf{V}^{-1})_a \tag{13}$$

equations (4), (5), and (11) yield

$$\mathbf{D}^p = <\lambda>\mathbf{N}^p(\mathbf{\Pi},\mathbf{S}), \quad \mathbf{W}^p = <\lambda>\Omega^p(\mathbf{\Pi},\mathbf{S}) \tag{14}$$

where again $\mathbf{N}^p$ and Ω^p are isotropic functions of $\mathbf{\Pi}$ and $\mathbf{S}$. Similarly one can use relations such as (7)–(9) in conjunction with equations (11) and (14) in order to express equation (12) in terms of rates associated with the values $\mathbf{s}$ at κ. For example, the following set of equivalent forms for the rate equations of $\mathbf{a}$ applies

$$\overset{\circ}{\mathbf{A}} = <\lambda>\bar{\mathbf{A}}(\mathbf{\Pi},\mathbf{S}) \quad \text{or} \tag{15a}$$

$$\overset{\square}{\mathbf{a}} = <\lambda>\bar{\mathbf{a}} \quad \text{with} \quad \bar{\mathbf{A}} = |\mathbf{V}|^w\mathbf{V}^{-1}\bar{\mathbf{a}}\mathbf{V}^{-1}, \quad \text{or} \tag{15b}$$

$$\overset{\vee}{\mathbf{a}} = <\lambda>(\bar{\mathbf{a}} - (\mathbf{a}\mathbf{N}^p + \mathbf{N}^p\mathbf{a}) + (\mathbf{a}\Omega^p - \Omega^p\mathbf{a}) + w\mathbf{a}tr\mathbf{N}^p) \tag{15c}$$

Equation (15b) can be written in general for any $\mathbf{s}$ as $\overset{\square}{\mathbf{s}} = <\lambda>\bar{\mathbf{s}}$ with $\bar{\mathbf{S}} = \mathbf{V}[\bar{\mathbf{s}}]$ when $\mathbf{S} = \mathbf{V}[\mathbf{s}]$. For small elastic deformations one has $\mathbf{V} \simeq \mathbf{I}$ (identity tensor), hence $\mathbf{\Pi} \simeq \sigma$, $\mathbf{S} \simeq \mathbf{s}$ and equation (12) can be written as

$$\overset{\circ}{\mathbf{s}} = <\lambda>\bar{\mathbf{s}}(\sigma,\mathbf{s}), \quad \text{or equivalently} \tag{16a}$$

$$\overset{\triangledown}{\mathbf{a}} = <\lambda>(\bar{\mathbf{a}} + \mathbf{a}\Omega^p - \Omega^p\mathbf{a}), \quad \overset{\triangledown}{\mathbf{m}} = <\lambda>(\bar{\mathbf{m}} - \Omega^p\mathbf{m}), \quad \dot{k} = <\lambda>\bar{k} \tag{16b}$$

with $\bar{\mathbf{s}} = \{\bar{\mathbf{a}}, \bar{\mathbf{m}}, \bar{k}\}$ isotropic functions of σ and $\mathbf{s}$, and where the transition from equation (16a) to (16b) is based on $\omega = \mathbf{W} - \mathbf{W}^p$, valid for $\mathbf{V} \simeq \mathbf{I}$. In equations (15$c$) and (16$b$) observe the clear distinction between the purely constitutive parts $\bar{\mathbf{a}}$, $\bar{\mathbf{m}}$, and the remaining terms due to the kinematics, where the role of the plastic spin via Ω^p is clearly demonstrated. If a tensorial structure variable is purely orientational (such as a preferred direction of the substructure), one must set $\bar{\mathbf{S}} \equiv \mathbf{0}$ or equivalently $\bar{\mathbf{a}} \equiv \mathbf{0}$, $\bar{\mathbf{m}} \equiv \mathbf{0}$. The Almansi plastic strain $\mathbf{A}^p = (1/2)(\mathbf{I} - \mathbf{P}^{-T}\mathbf{P}^{-1})$ can be used, if appropriate, as one of the $\mathbf{S}$, and can be shown that $\mathbf{A}^p = <\lambda>[\mathbf{N}^p_0 - (\mathbf{A}^p\mathbf{N}^p_0 + \mathbf{N}^p_0\mathbf{A}^p) - (\mathbf{A}^p\Omega^p_0 - \Omega^p_0\mathbf{A}^p)]$, consistent with equation (15a). A different plastic deformation measure Δ^p, which is not a true strain measure, could be defined by integration of $\overset{\circ}{\Delta}{}^p = \mathbf{D}^p$ and used as one of the $\mathbf{S}$.

3.2 Elastic Relations With Elastoplastic Coupling and/or Damage. Denoting by $\mathbf{E}^e = (1/2)(\mathbf{V}^2 - \mathbf{I})$ the Green elastic strain, ρ_0 the mass density at κ_0 and $\psi = \bar{\psi}(\mathbf{\Pi},\mathbf{S})$ the complementary free energy per unit mass, isotropic function of $\mathbf{\Pi}$ and $\mathbf{S}$ (invariance), the elastic relations can be obtained from $\mathbf{E}^e = \rho_0(\partial\bar{\psi}/\partial\mathbf{\Pi})$. Since $\mathbf{E}^e$ (and $\mathbf{V}$) is also isotropic function of $\mathbf{\Pi}$ and $\mathbf{S}$, the relation ($A1$) of the Appendix can be applied for $\overset{\circ}{\mathbf{E}}{}^e = \mathbf{V}\mathbf{D}^e\mathbf{V}$ which in conjunction with equation (12) and the foregoing kinematics yields

Downloaded 02 May 2010 to 171.66.16.54. Redistribution subject to ASME license or copyright; see http://www.asme.org/terms/Terms_Use.cfm

$$\mathring{\mathbf{E}}^e = \mathring{\mathbf{E}}^r + \mathring{\mathbf{E}}^c = \underset{\sim}{\mathfrak{L}}^{0-1} : \mathring{\mathbf{\Pi}} + <\lambda>\mathbf{N}_0^c \tag{17a}$$

$$\mathbf{D}^e = \mathbf{D}^r + \mathbf{D}^c = \underset{\sim}{\mathfrak{L}}^{-1} : \overset{\square}{\boldsymbol{\sigma}} + <\lambda>\mathbf{N}^c \tag{17b}$$

$$\underset{\sim}{\mathfrak{L}}^0 = (\rho_0 \partial^2 \bar{\psi} / \partial \mathbf{\Pi} \otimes \partial \mathbf{\Pi})^{-1},$$

$$\mathfrak{L}_{ijkl} = |\mathbf{V}|^{-1} V_{i\alpha} V_{j\beta} V_{k\gamma} V_{l\delta} \mathfrak{L}^0_{\alpha\beta\gamma\delta} \tag{17c}$$

$$\mathbf{N}^c = \mathbf{V}^{-1}\mathbf{N}_0^c\mathbf{V}^{-1} = \rho_0 \mathbf{V}^{-1}[(\partial^2 \bar{\psi}/\partial \mathbf{\Pi} \otimes \partial \mathbf{S}) \cdot \bar{\mathbf{S}}]\mathbf{V}^{-1} - \mathbf{A}^e tr\mathbf{N}^p \tag{17d}$$

where $\mathbf{A}^e = \mathbf{V}^{-1}\mathbf{E}^e\mathbf{V}^{-1}$, $\overset{\square}{\boldsymbol{\sigma}}$ is defined by equation (8) with $w = 1$ and $\boldsymbol{\sigma}$ instead of $\mathbf{a}$, and $\underset{\sim}{\mathfrak{L}}$ are the incremental elastic moduli. The $\mathbf{D}^r$ and $\mathbf{D}^c$ represent the incrementally reversible and elastoplastic coupling or damage induced components of $\mathbf{D}^e$ at κ, counterparts of $\mathring{\mathbf{E}}^r$ and $\mathring{\mathbf{E}}^c$ at κ_0. The $tr\mathbf{N}^p$ in equation (17*d*) appears due to the mass conservation relation $\dot{\rho}_0 + \rho_0 tr\mathbf{D}^p = 0$ at κ_0. The evolution of tensorial $\mathbf{S}$ can alter initial elastic symmetries, unless $\bar{\mathbf{S}} \equiv \mathbf{O}$ (purely orientational) in which case one can still have $\mathbf{N}^c \neq \mathbf{O}$ if $\mathrm{tr}\mathbf{N}^p \neq 0$, equation (17*d*).

3.3 Yield Criterion, Loading Index, and Final Form. A macroscopically smooth yield criterion together with its symmetric stress gradient can be defined by

$$f(\boldsymbol{\sigma}, \mathbf{s}) = 0, \quad \mathbf{N}^n = (\partial f/\partial \boldsymbol{\sigma})_s \tag{18}$$

with f an isotropic function of $\boldsymbol{\sigma}$, $\mathbf{s}$ due to invariance requirements. The dependence of f on the current values $\boldsymbol{\sigma}$, $\mathbf{s}$ at κ is motivated by corresponding formulations in crystal plasticity [6-9] where a resolved shear stress yield threshold τ is defined by $f = \mathbf{m}\boldsymbol{\sigma}\mathbf{n} - \tau = 0$, with $\mathbf{m}$ and $\mathbf{n}$ vectors along the slip and normal to slip plane directions at κ, and which could be considered as being unit vectors at κ_0 [9]. In the same spirit one can express $\mathbf{N}^p$ and $\mathbf{\Omega}^p$ directly as isotropic functions of $\boldsymbol{\sigma}$ and $\mathbf{s}$. Equivalent expressions for f in terms of quantities defined at κ_0 are possible, but a slight advantage of equation $(18)_1$ is that f can be determined in principle without requiring an elastic unloading to κ_0 (possibly only virtual). Since the $\mathbf{s}$ depend on $\boldsymbol{\sigma}$ due to their elastic embedding, one expects that the loading direction will divert from $\mathbf{N}^n$ in a way that will be precisely defined in the sequel.

Due to the isotropy of f, the consistency condition $\dot{f} = 0$ be expressed according to equation (*A*2) of the Appendix in terms of the corotational rates $\overset{*}{\boldsymbol{\sigma}}$, $\overset{*}{\mathbf{s}}$, which in turn can be expressed in terms of $\overset{\square}{\boldsymbol{\sigma}}$ and $\overset{\square}{\mathbf{s}}$ by means of equations similar to (8) with $\mathbf{D}^e$ obtained from equation (17*b*), yielding

$$\dot{f} = \mathbf{N}^n : \overset{*}{\boldsymbol{\sigma}} + (\partial f/\partial \mathbf{s}) \cdot \overset{*}{\mathbf{s}} = (\mathbf{N}^n - \mathbf{Z}^n : \underset{\sim}{\mathfrak{L}}^{-1}) : \overset{\square}{\boldsymbol{\sigma}} + \lambda((\partial f/\partial \mathbf{s}) \cdot \bar{\mathbf{s}} - \mathbf{Z}^n : \mathbf{N}^c) = 0 \tag{19}$$

Use of similar equations to (15*b*) was made for $\overset{\square}{\mathbf{s}}$, and $\mathbf{Z}^n$ is defined in the following equation (25). Equation (19) determines the loading index λ in terms of $\overset{\square}{\boldsymbol{\sigma}}$. On the basis of equations $(6)_1$, (14), (17*b*), (19), and utilizing equation (10) with $w = 1$ and $\boldsymbol{\sigma}$ instead of $\mathbf{a}$ in order to express $\overset{\square}{\boldsymbol{\sigma}}$ in terms of $\overset{\vee}{\boldsymbol{\sigma}}$ (similarly defined from equation (9) with $w = 1$ and $\mathbf{a} = \boldsymbol{\sigma}$), the final form for a state on $f = 0$ is given by

$$\mathbf{D} = \underset{\sim}{\mathfrak{L}}^{-1} : \overset{\square}{\boldsymbol{\sigma}} + <\lambda>(\mathbf{N}^p + \mathbf{N}^c) = \underset{\sim}{\mathfrak{L}}^{-1} : \overset{\vee}{\boldsymbol{\sigma}} + <\lambda>\mathbf{N}' = \mathbf{\Lambda}^{-1} : \overset{\vee}{\boldsymbol{\sigma}} \tag{20}$$

$$\lambda = \frac{\mathbf{N} : \overset{\square}{\boldsymbol{\sigma}}}{H + \mathbf{Z}^n : \mathbf{N}^c} = \frac{\mathbf{N} : \overset{\vee}{\boldsymbol{\sigma}}}{H + \mathbf{Z}^n : \mathbf{N}^c + \mathbf{N} : \mathbf{Z}^p} = \frac{\mathbf{N} : \underset{\sim}{\mathfrak{L}} : \mathbf{D}}{H + \mathbf{N} : \underset{\sim}{\mathfrak{L}} : \mathbf{N}^p + \mathbf{N}^n : \underset{\sim}{\mathfrak{L}} : \mathbf{N}^c} \tag{21}$$

$$\mathbf{\Lambda} = \underset{\sim}{\mathfrak{L}} - \bar{h}(\lambda) \frac{(\underset{\sim}{\mathfrak{L}} : \mathbf{N}') \otimes (\mathbf{N} : \underset{\sim}{\mathfrak{L}})}{H + \mathbf{N} : \underset{\sim}{\mathfrak{L}} : \mathbf{N}^p + \mathbf{N}^n : \underset{\sim}{\mathfrak{L}} : \mathbf{N}^c} \tag{22}$$

$$\mathbf{N}' = \mathbf{N}^p + \mathbf{N}^c - \underset{\sim}{\mathfrak{L}}^{-1} : \mathbf{Z}^p, \quad \mathbf{N} = \mathbf{N}^n - \mathbf{Z}^n : \underset{\sim}{\mathfrak{L}}^{-1}, \quad H = -(\partial f/\partial \mathbf{s}) \cdot \bar{\mathbf{s}} \tag{23}$$

$$\mathbf{Z}^p = -(\boldsymbol{\sigma}\mathbf{N}^p + \mathbf{N}^p\boldsymbol{\sigma}) + (\boldsymbol{\sigma}\mathbf{\Omega}^p - \mathbf{\Omega}^p\boldsymbol{\sigma}) + \boldsymbol{\sigma} tr\mathbf{N}^p \tag{24}$$

$$\mathbf{Z}^n = -(\boldsymbol{\sigma}\mathbf{N}^n + \mathbf{N}^n\boldsymbol{\sigma}) + (\mathbf{N}^n : \boldsymbol{\sigma})\mathbf{I} + \mathbf{\Gamma} \tag{25}$$

$$\mathbf{\Gamma} = \pm\left(\mathbf{a}^T \frac{\partial f}{\partial \mathbf{a}} + \frac{\partial f}{\partial \mathbf{a}} \mathbf{a}^T\right)_s \pm \left(\frac{\partial f}{\partial \mathbf{m}} \otimes \mathbf{m}\right)_s + w\left(\frac{\partial f}{\partial \mathbf{s}} \cdot \mathbf{s}\right)\mathbf{I} \tag{26}$$

with $\bar{h}(\lambda)$ the heavyside step function defined as zero at $\lambda = 0$, and + or − in equation (26) when $\mathbf{a}$, $\mathbf{m}$ are transported from κ to κ_0 by a covariant or contravariant transformation, respectively, of weight w. The $\mathbf{\Gamma}$ encompasses the effect of elastically embedding the $\mathbf{s}$. Many of the features observed in equations (20)-(26) are the macroscopic counterparts of well-established results in microscopic crystal plasticity theories, but appear to be novel in a macroscopic formulation with tensorial structure variables. For example, the $\mathbf{Z}^p$ and $\mathbf{Z}^n$ divert the irreversible rate of deformation and loading directions from $\mathbf{N}^p + \mathbf{N}^c$ and $\mathbf{N}^n$, to $\mathbf{N}'$ and $\mathbf{N}$, respectively, the diversions being of the order stress/elastic moduli. In fact one could broadly associate the $\mathbf{N}'$, $\mathbf{N}$, and $\mathbf{N}^p + \mathbf{N}^c$ with the quantities $\mathbf{P}'$, $\mathbf{Q}$, and $\mathbf{P}$ defined in [7]. With H the plastic modulus, the denominator of the third member of equation (21) corresponds to what is called the effective hardening modulus [11] due to geometrical and elastoplastic coupling (and/or damage) effects expressed by $\mathbf{N} : \mathbf{Z}^p$ and $\mathbf{Z}^n : \mathbf{N}^c$, respectively. The elastoplastic coupling effect has not been considered in [7, 11]. It is possible to have $\mathbf{N}^c \neq \mathbf{0}$ with $\mathbf{N}^p = \mathbf{\Omega}^p = \mathbf{0}$ in which case $f = 0$ acts only as a damage criterion. Certain differences in relation to the aforementioned references are due to the use of different stress rates. In fact one can change the stress rate by properly modifying the elastic moduli and the values of $\mathbf{Z}^p$ and $\mathbf{Z}^n$. For example, assuming for simplicity that $\mathbf{N}^c = \mathbf{0}$, the Jaumann rate $\overset{\triangledown}{\boldsymbol{\tau}} = \overset{\triangledown}{\boldsymbol{\sigma}} + \boldsymbol{\sigma} tr\mathbf{D}$ of the Kirchhoff stress $\boldsymbol{\tau} = \boldsymbol{\sigma}$, but $\dot{\boldsymbol{\tau}} = \dot{\boldsymbol{\sigma}} + \boldsymbol{\sigma} tr\mathbf{D}$, can be used instead of $\overset{\vee}{\boldsymbol{\sigma}}$ by setting $\mathbf{Z}^p = \boldsymbol{\sigma}\mathbf{\Omega}^p - \mathbf{\Omega}^p\boldsymbol{\sigma} + \boldsymbol{\sigma} tr\mathbf{N}^p$, $\mathbf{Z}^n = (\mathbf{N}^n : \boldsymbol{\sigma})\,\mathbf{I} + \mathbf{\Gamma}$ and employing elastic moduli obtained by adding the quantity $(1/2)(\delta_{ik}\sigma_{lj} + \delta_{il}\sigma_{kj} + \delta_{jl}\sigma_{ik} + \delta_{jk}\sigma_{il})$ to $\mathfrak{L}_{ijkl}$, δ_{ij} being the Kronecker delta. For small elastic deformations $\mathbf{V} \simeq \mathbf{I}$ and the effect of elastic embedding is negligible. The corresponding equations can be obtained from equations (20)-(23) by substituting $\mathring{\boldsymbol{\sigma}}$ and $\overset{\triangledown}{\boldsymbol{\sigma}}$ for $\overset{\square}{\boldsymbol{\sigma}}$ and $\overset{\vee}{\boldsymbol{\sigma}}$, respectively, and setting $\mathbf{Z}^n = \mathbf{0}$, $\mathbf{Z}^p = \boldsymbol{\sigma}\mathbf{\Omega}^p - \mathbf{\Omega}^p\boldsymbol{\sigma}$, as obtained directly in [12]. If only the volumetric elastic deformation is finite, one has $\mathbf{V} \simeq |\mathbf{V}|\mathbf{I}$ and all the foregoing relations must be modified accordingly.

4 The Plastic Spin

In a sequence of recent papers [12-14] the author was the first to use the representation theorems for isotropic functions [3] in conjunction with the concept of tensorial structure variables to provide explicit forms of constitutive relations for the plastic spin. Independently Loret [15] obtained similar results. Subsequently the main results presented in [12-14] will be briefly summarized and supplemented by a number of new observations. For simplicity small elastic deformations will be considered, i.e., $\mathbf{\Pi} \simeq \boldsymbol{\sigma}$ and $\mathbf{S} \simeq \mathbf{s}$.

With λ defined from equation (21), the constitutive relation for $\mathbf{W}^p$ depends on $\mathbf{\Omega}^p$, equation (14). In the case of one symmetric tensor structure variable $\mathbf{a}$, the $\mathbf{\Omega}^p$, being an isotropic function of $\boldsymbol{\sigma}$ and $\mathbf{a}$, can be represented by [3]

Downloaded 02 May 2010 to 171.66.16.54. Redistribution subject to ASME license or copyright; see http://www.asme.org/terms/Terms_Use.cfm

$$\Omega^p = \eta_1(\mathbf{a}\sigma - \sigma\mathbf{a}) + \eta_2(\mathbf{a}^2\sigma - \sigma\mathbf{a}^2) + \eta_3(\mathbf{a}\sigma^2 - \sigma^2\mathbf{a}) + \eta_4(\mathbf{a}\sigma\mathbf{a}^2 - \mathbf{a}^2\sigma\mathbf{a}) + \eta_5(\sigma\mathbf{a}\sigma^2 - \sigma^2\mathbf{a}\sigma) \quad (27)$$

where the η_i's are scalar functions (not necessarily polynomial) of the well-known isotropic invariants of σ, $\mathbf{a}$ and any other scalar structure variable k (e.g., equivalent plastic strain). Clearly, the deviatoric parts σ' and $\mathbf{a}'$ can substitute σ and $\mathbf{a}$ in equation (27), by redefining the η_i. If $\mathbf{a}\sigma = \sigma\mathbf{a}$ (i.e., σ and $\mathbf{a}$ are coaxial), which includes as a special case the isotropic one with $\mathbf{a}' = \mathbf{0}$, it follows that $\Omega^p = \mathbf{0}$ even for an anisotropic material. This conclusion can be extended to finite elastic deformations; with $\mathbf{A\Pi} = \mathbf{\Pi A}$ it follows that $\Omega^g_0 = \mathbf{0}$ and that $\mathbf{V}$ and $\mathbf{N}^g_0$ commute (same principal directions as $\mathbf{A}$ and $\mathbf{\Pi}$). Hence, from equations (13) one has $\mathbf{N}^p = \mathbf{N}^g_0$ and $\Omega^p = \mathbf{0}$. The requirement of continuous transition from anisotropy to isotropy and vice-versa is satisfied if the sufficient conditions $lim \eta_i(\mathbf{a}')^{y_i} = \mathbf{0}$ as $\mathbf{a}' \to \mathbf{0}$ are imposed, with y_i the corresponding exponents in equation (27). For a single generator this is also a necessary condition. A discontinuous Ω^p at $\mathbf{a}' = \mathbf{0}$ will cause a corresponding discontinuity in $\mathring{\sigma}$ since it appears in the definition of $\mathbf{\Lambda}$, equation (22), and of λ in terms of $\mathring{\sigma}$, equation (21), via the terms involving $\mathbf{Z}^p$. It was suggested in [12–14] to use the first only generator of equation (27) as a first approximation. The "intensity" of the plastic spin for a given σ on $f = 0$ depends on the η_i, the norm of $\mathbf{a}$ and the degree of noncoaxiality between σ and $\mathbf{a}$, as it can easily be seen by employing the spectral representation for σ and $\mathbf{a}$ in equation (27).

For orthotropic symmetries along three orthonormal vectors $\mathbf{n}_1, \mathbf{n}_2, \mathbf{n}_3$ the structure variables (purely orientational) can be defined by $\mathbf{a}_1 = \mathbf{n}_1 \otimes \mathbf{n}_1$ and $\mathbf{a}_2 = \mathbf{n}_2 \otimes \mathbf{n}_2$, [16, 17]. On the basis of [3] the Ω^p can be represented by

$$\Omega^p = \eta_1(\mathbf{a}_1\sigma - \sigma\mathbf{a}_1) + \eta_2(\mathbf{a}_2\sigma - \sigma\mathbf{a}_2) + \eta_3(\mathbf{a}_1\sigma\mathbf{a}_2 - \mathbf{a}_2\sigma\mathbf{a}_1) + \eta_4(\mathbf{a}_1\sigma^2 - \sigma^2\mathbf{a}_1) + \eta_5(\mathbf{a}_2\sigma^2 - \sigma^2\mathbf{a}_2) + \eta_6(\sigma\mathbf{a}_1\sigma^2 - \sigma^2\mathbf{a}_1\sigma) + \eta_7(\sigma\mathbf{a}_2\sigma^2 - \sigma^2\mathbf{a}_2\sigma) \quad (28)$$

with η_i functions of $tr\sigma$, $tr\sigma^2$, $tr\sigma^3$, $tr\mathbf{a}_1\sigma$, $tr\mathbf{a}_2\sigma$, $tr\mathbf{a}_1\sigma^2$, $tr\mathbf{a}_2\sigma^2$, [16], and any other scalar structure variable. Denoting by a superposed $\hat{}$ the tensor components in reference to a cartesian coordinate system $\hat{\mathbf{x}} = \{\hat{x}_1, \hat{x}_2, \hat{x}_3\}$ along the axes of orthotropy, and assuming that Ω^p is represented by the first three generators only in equation (28) which are linear in σ, one obtains $\hat{\Omega}^p_{12} = \eta_3'\hat{\sigma}_{12}$, $\hat{\Omega}^p_{13} = \eta_2'\hat{\sigma}_{13}$, $\hat{\Omega}^p_{23} = \eta_1'\hat{\sigma}_{23}$ with $\eta_1' = \eta_2$, $\eta_2' = \eta_1$ and $\eta_3' = \eta_1 - \eta_2 + \eta_3$. Defining $\mathbf{N}^p$ from the associated flow rule $\mathbf{N}^p = (\partial f/\partial\sigma)$ with f given by Hill's orthotropic yield criterion [18]

$$f = A(\hat{\sigma}_{11} - \hat{\sigma}_{22})^2 + B(\hat{\sigma}_{22} - \hat{\sigma}_{33})^2 + C(\hat{\sigma}_{33} - \hat{\sigma}_{11})^2 + D\hat{\sigma}^2_{23} + E\hat{\sigma}^2_{13} + F\hat{\sigma}^2_{12} - k^2 = 0 \quad (29)$$

it follows based on the foregoing that

$$\hat{W}^p_{12} = \frac{\eta_3'}{2F}\hat{D}^p_{12}, \quad \hat{W}^p_{13} = \frac{\eta_2'}{2E}\hat{D}^p_{13}, \quad \hat{W}^p_{23} = \frac{\eta_1'}{2D}\hat{D}^p_{23} \quad (30)$$

When the σ' changes sign, and still is on $f = 0$, one expects on physical grounds (sign change of microscopic resolved shear stresses and corresponding shear strain rates) that so does $\mathbf{W}^p$, hence the η_i's must be even functions of σ'. If the orthotropy has the same "intensity" along $\hat{x}_1$ and $\hat{x}_2$ one expects that $\hat{W}^p_{12} = 0$, thus $\eta_3' = 0$. Similarly for η_2' and η_1'. For the fifth class of transverse isotropy characterized by $\mathbf{n}_1$ along $\hat{x}_1$, the structure variable is $\mathbf{a}_1 = \mathbf{n}_1 \otimes \mathbf{n}_1$ [16, 17]. The Ω^p is obtained from equation (28) by setting $\eta_2 = \eta_3 = \eta_5 = \eta_7 = 0$, and the yield criterion from equation (29) with $A = C$, $E = F$ and $D = 2(A + 2B)$. Using only generators linear in σ, equation (30) applies with $E = F$, $\eta_1' = 0$ and $\eta_2' = \eta_3' = \eta_1$. For this case observe that the value $\eta_1/2F = 1$ can be associated with a unidirectionally fiber-reinforced material with $\hat{x}_1$ along the fibers' direction, under the kinematical restriction that plastic shear cannot occur by slip on planes perpendicular to $\hat{x}_1$. Similarly the value $\eta_1/2F = -1$ can be visualized as the case of a deck of cards with $\hat{x}_1$ normal to their planes and where slip is not permitted on planes parallel to $\hat{x}_1$.

5 Kinematic Hardening and Simple Shear

Within the framework of the general development, the following kinematic hardening constitutive model can be proposed

$$f = (3/2)(\sigma' - \alpha):(\sigma' - \alpha) - k^2 = 0 \quad (31)$$

$$\mathbf{D}^p = <\lambda>\mathbf{n}, \ \mathbf{n} = (3/2)^{1/2}(\sigma' - \alpha)/k, \ \mathbf{n}:\mathbf{n} = 1 \quad (32)$$

$$\mathbf{W}^p = <\lambda>\eta_1(\alpha\sigma' - \sigma'\alpha) = (1/2)\rho(\alpha\mathbf{D}^p - \mathbf{D}^p\alpha) \quad (33)$$

$$\mathring{\alpha} = <\lambda>((2/3)h_\alpha\mathbf{n} - (2/3)^{1/2}c_r\alpha) = (2/3)h_\alpha\mathbf{D}^p - ((2/3)\mathbf{D}^p:\mathbf{D}^p)^{1/2}c_r\alpha \quad (34)$$

where clearly f, $\mathbf{D}^p$, $\mathbf{W}^p$, and $\mathring{\alpha}$ are isotropic functions of the state variables σ', α and k, the α represents the usual deviatoric back-stress tensor and k is constant or variable (isotropic hardening). Equation (34) is the finite deformation version of the kinematic hardening rule with evanescent memory originally proposed in [19]. It introduces the positive material constants h_α and c_r which can be calibrated from $\sigma_{11} = \pm[k + (h_\alpha/c_r)\ [1 - \exp(-c_r\,|\epsilon^p|)]]$ obtained from equation (31) and integration of equation (34) for uniaxial loading with ϵ^p the corresponding logarithmic plastic strain. The key equation (33) is obtained from equations (27) and (32) using the first generator only, as originally suggested in [14]. It introduces the material parameter ρ, by setting $\eta_1 = (3/2)^{1/2}(\rho/2k)$, which has the dimensions of (stress)$^{-1}$ and is isotropic function of σ' (or $\sigma' - \alpha$), α, k and any other scalar structure variable such as the equivalent plastic strain, so that $\lim(\rho\alpha) = \mathbf{0}$ as $\alpha \to \mathbf{0}$. Expecting that $\mathbf{W}^p$ changes sign when $\sigma' - \alpha$ does, ρ must be an even function of $\sigma' - \alpha$.

The proposed constitutive model will be used for the analysis of simple shear γ defined by the velocity gradient components

$$D_{12} = D_{21} = W_{12} = -W_{21} = \dot{\gamma}/2, \quad D_{ij} = W_{ij} = 0 \text{ for other } i, j \quad (35)$$

The simple shear analysis has been presented qualitatively, numerically, and analytically for a variety of kinematic hardening models and corotational rates for α [12, 14, 15, 20–24]. In particular the phenomenon of stress oscillations with increasing γ, first reported in [20], prompted investigations on the role of model constants that remained largely numerical or qualitative. In the spirit of [12, 14], where the analytical solution for $c_r = 0$ was provided, sufficient and necessary conditions on h_α, c_r, and ρ for the occurrence or not of such oscillations will be rigorously obtained by analytical means, as well as closed-form expressions on the stress limits as $|\gamma| \to \infty$.

Assuming for simplicity a rigid-plastic response, constant k, $\alpha_{11} + \alpha_{22} = 0$, $\alpha_{13} = \alpha_{23} = 0$ and $\sigma_{33} = 0$, equations (31)–(34) and (35) yield [12, 14]

$$\sigma_{11} = \alpha_{11} = -\sigma_{22} = -\alpha_{22}, \quad \sigma_{12} = \alpha_{12} + \text{sgn}\dot{\gamma}(k/\sqrt{3}) \quad (36)$$

and $\sigma_{13} = \sigma_{23} = 0$, with $\text{sgn}\dot{\gamma}$ = sign of $\dot{\gamma}$ and the evolution of α_{11}, α_{12} governed by the system of nonlinear differential equations

$$d\alpha_{11}/d\gamma = -\text{sgn}\dot{\gamma}(c_r/\sqrt{3})\alpha_{11} + (1 - \rho\alpha_{11})\alpha_{12} \quad (37a)$$

$$d\alpha_{12}/d\gamma = -\text{sgn}\dot{\gamma}(c_r/\sqrt{3})\alpha_{12} - (1 - \rho\alpha_{11})\alpha_{11} + (1/3)h_\alpha \quad (37b)$$

If the assumptions $\alpha_{11} + \alpha_{22} = 0$ and $\sigma_{33} = 0$ were not made,

Downloaded 02 May 2010 to 171.66.16.54. Redistribution subject to ASME license or copyright; see http://www.asme.org/terms/Terms_Use.cfm

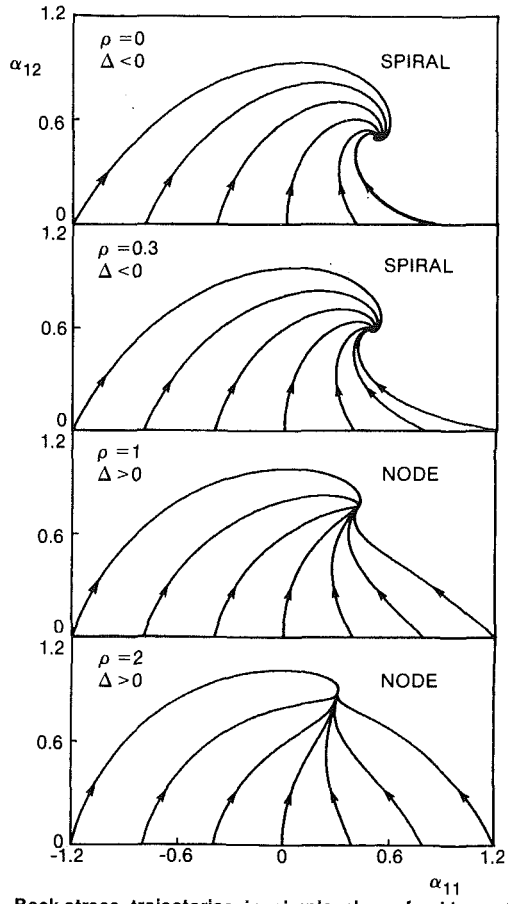


Fig. 1 Back-stress trajectories in simple shear for kinematic hardening with evanescent memory and different values of ρ. Stress quantities are normalized by k.

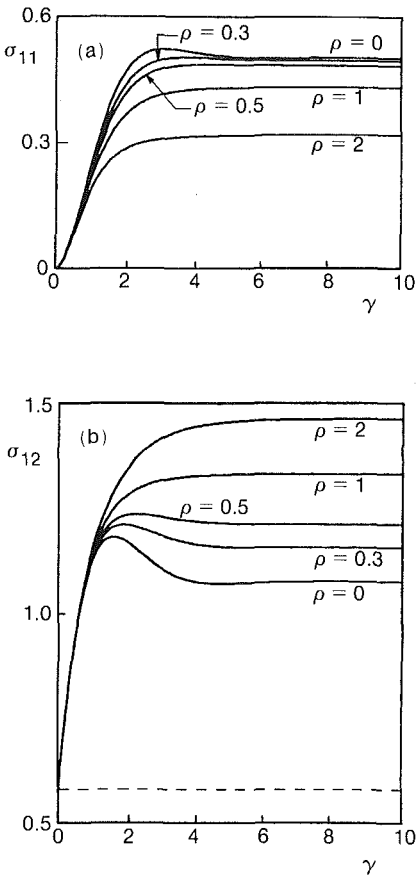


Fig. 2 (*a,b*) Stress-strain in simple shear for kinematic hardening with evanescent memory and different values of ρ. Stress quantities are normalized by k.

one would have obtained $\sigma'_{11} = \alpha_{11}$, $\sigma'_{22} = \alpha_{22}$, $\sigma'_{33} = \alpha_{33} = -2\alpha_{(+)}$, $\sigma_{11} = 3\alpha_{(+)} + \alpha_{(-)} + \sigma_{33}$, $\sigma_{22} = 3\alpha_{(+)} - \alpha_{(-)} + \sigma_{33}$, with $\alpha_{(+)} = (\alpha_{11} + \alpha_{22})/2 = \alpha^0_{(+)}\exp(-c_r|\gamma|/\sqrt{3})$ and $\alpha_{(-)} = (\alpha_{11} - \alpha_{22})/2$ substituting α_{11} in equations (37). Observe that the quantity $(\dot\gamma/2)(1-\rho\alpha_{11})$ represents the ω_{12} component of the spin $\omega = \mathbf{W} - \mathbf{W}^p$, [12], which suggests on physical grounds that $\rho \geq 0$ because otherwise the ω would be "greater" than $\mathbf{W}$ at the first stage of simple shear. Observe also that by setting $c_r = 0$ and $\rho = (2/tr\alpha^2)^{1/2} = (\alpha^2_{11} + \alpha^2_{12})^{-1/2}$ the formulation proposed in [22] is obtained, but the continuity requirement $\lim(\rho\alpha) = \mathbf{0}$ as $\alpha \to \mathbf{0}$ is violated. Henceforth, ρ will be considered constant. For monotonic change of γ, such that $\mathrm{sgn}\dot\gamma = \mathrm{sgn}\gamma$, and $\rho = 0$ which implies the use of Jaumann rates in equation (34), the solution of equations (37) can be obtained in closed form as

$$\alpha_{11} = [h_\alpha/(3+c_r^2)][1 - \exp(-c_r|\gamma|/\sqrt{3})(\cos\gamma + (c_r/\sqrt{3})\sin|\gamma|)] + \exp(-c_r|\gamma|/\sqrt{3})(\alpha^0_{11}\cos\gamma + \alpha^0_{12}\sin\gamma) \quad (38a)$$

$$\alpha_{12} = [(\mathrm{sgn}\gamma)h_\alpha/(3+c_r^2)][(c_r/\sqrt{3}) + \exp(-c_r|\gamma|/\sqrt{3})(\sin|\gamma| - (c_r/\sqrt{3})\cos\gamma)] - \exp(-c_r|\gamma|/\sqrt{3})(\alpha^0_{11}\sin\gamma - \alpha^0_{12}\cos\gamma) \quad (38b)$$

with α^0_{11}, α^0_{12} the values at $\gamma = 0$. For $\rho > 0$ the stability of the system (37) will be first investigated. By standard methods it can be shown that a unique equilibrium point α^e_{11}, α^e_{12} (in fact two such points exist depending on the $\mathrm{sgn}\gamma$) is given by

$$\alpha^e_{11} = (1/3\rho)[2 + (3\sqrt{q} - p)^{1/3} - (3\sqrt{q} + p)^{1/3}] \quad (39a)$$

$$\alpha^e_{12} = \mathrm{sgn}\gamma(c_r/\sqrt{3})\alpha^e_{11}/(1-\rho\alpha^e_{11}) \quad (39b)$$

$$p = 3[c_r^2 - (1/2)\rho h_\alpha + (1/3)],\ q = (1/9)[p^2 + (c_r^2 + \rho h_\alpha - 1)^3] \quad (39c)$$

under the condition $q > 0$ which is sufficient and necessary for α^e_{11} to be the unique real root of the cubic equation $(c_r^2/3)\alpha^e_{11}/(1-\rho\alpha^e_{11}) = \rho(\alpha^e_{11})^2 - \alpha^e_{11} + (1/3)h_\alpha$. A standard investigation of the signs of the left and right-hand sides of this equation, and the fact that the other two roots are complex, yield $0 < \alpha^e_{11} < 1/\rho$. Multiplying now equations (37) by $\mathrm{sgn}\gamma = \mathrm{sgn}\dot\gamma$ (monotonic change of γ), observing that $d|\gamma| = \mathrm{sgn}\dot\gamma d\gamma$ and transferring the origin at α^e_{11}, α^e_{12} without changing notation for the α_{11}, α_{12} for simplicity, equations (37) become

$$d\alpha_{11}/d|\gamma| = -[(c_r/\sqrt{3})\alpha_{11}/(1-\rho\alpha^e_{11})] + \mathrm{sgn}\gamma[(1-\rho\alpha^e_{11})\alpha_{12} - \rho\alpha_{11}\alpha_{12}] \quad (40a)$$

$$d\alpha_{12}/d|\gamma| = -(c_r/\sqrt{3})\alpha_{12} + \mathrm{sgn}\gamma[(2\rho\alpha^e_{11} - 1)\alpha_{11} + \rho\alpha^2_{11}] \quad (40b)$$

Considering the Liapunov function $U = (1/2)(\alpha^2_{11} + \alpha^2_{12})$, use of equations (40) yields $dU/d|\gamma| = -(c_r/\sqrt{3}(1-\rho\alpha^e_{11}))\alpha^2_{11} - (c_r/\sqrt{3})\alpha^2_{12} + (\mathrm{sgn}\gamma)\rho\alpha^e_{11}\alpha_{11}\alpha_{12}$, quadratic in α_{11}, α_{12}. For asymptotic convergence of the system (40) in the whole it suffices to have $q > 0$ (for uniqueness of α^e_{11}) and $dU/d|\gamma| < 0$. On the basis of the sufficient and necessary Sylvester's criterion for negative definiteness [25], the $dU/d|\gamma| < 0$ requires that $1 - \rho\alpha^e_{11} > 0$, already satisfied as shown earlier, and $c_r^2 > (3/4)\rho^2(\alpha^e_{11})^2(1-\rho\alpha^e_{11})$. Observing that the maximum value of the right-hand side of the last inequality is 1/9 for $\alpha^e_{11} = 2/3\rho$, and based on the value of q,

Downloaded 02 May 2010 to 171.66.16.54. Redistribution subject to ASME license or copyright; see http://www.asme.org/terms/Terms_Use.cfm

equation $(39c)_2$, a stronger but simpler and not unduly restrictive sufficient condition for convergence in the whole is

$$c_r > 1/3 \quad \text{and} \quad c_r^2 + \rho h_\alpha > 1 \tag{41}$$

With ν_1, ν_2 the roots and Δ the discriminant of the characteristic equation of the linear approximation of the system (40), it can be shown that $\nu_1 + \nu_2 < 0$, $\nu_1 \nu_2 > 0$, under the previous conditions, and

$$\Delta = (1/3)c_r^2 \rho^2 (\alpha_{11}^e)^2 + 4(1 - \rho\alpha_{11}^e)^3 (2\rho\alpha_{11}^e - 1) \tag{42}$$

Because the origin is not a center for the system (40) and its linear approximation, their phase portraits are qualitatively equivalent. Hence, provided that $q > 0$ and the aforementioned Sylvester's criterion condition, or the stronger conditions (41), are satisfied, and with α_{11}^e given by equation $(39a)$, the sufficient and necessary condition on h_α, c_r, and ρ for which no stress oscillations occur is $\Delta \geq 0$, in which case the equilibrium point is a stable node (inflected if $\Delta = 0$), while for $\Delta < 0$ the equilibrium point is a stable spiral and stress oscillations occur.

Illustration of the foregoing is shown in Figs. 1 and $2(a,b)$ obtained by numerical integration of equations (37) together with equations (36) for $\text{sgn}\dot{\gamma} > 0$. The numerical values of all stress quantities are normalized by k. The values $h_\alpha = 3$ and $c_r = \sqrt{3}$ used in the computation, were found to describe sufficiently well the uniaxial response of commercially pure aluminum. For such values the relations (41) are clearly satisfied for any ρ. Figure 1 shows the back-stress trajectories beginning at $\alpha_{12}^0 = 0$ and different α_{11}^0, while Fig. $2(a,b)$ shows the stress-strain response for $\alpha_{11}^0 = \alpha_{12}^0 = 0$. The α_{12} can be measured from the broken line of Fig. $2(b)$ corresponding to $\sigma_{12} = (1/\sqrt{3})$. The effect of the different values of ρ (normalized by k^{-1}) is clearly demonstrated, and becomes pronounced for $\gamma \geq 1$, approximately. Using equations (39), (42) and the assumed values of h_α, c_r, it can be computed that $\Delta \geq 0$ for $\rho \geq 0.92$, hence, no oscillations occur for $\rho = 1,2$ in the graphs of Fig. 2.

6 Plane Stress for Orthotropic Symmetries

Assume that the orthotropic axes $\hat{x}_1$, $\hat{x}_2$ form an angle θ with the fixed axes x_1, x_2, measured positive counterclockwise from x_1 to $\hat{x}_1$, and that $\hat{x}_3 = x_3$. Assuming rigid-plastic response, the yield criterion (29), $\sigma_{33} = 0$, the associated flow rule and the simple shear velocity gradient (35), the stress components in reference to $\hat{\mathbf{x}}$ are given by

$$\hat{\sigma}_{11}/B = -\hat{\sigma}_{22}/C = \hat{\sigma}_{12}/(X/F\tan 2\theta) = (k/R)\text{sgn}\dot{\gamma}\,\text{sgn}\sin 2\theta \tag{43}$$

and $\hat{\sigma}_{13} = \hat{\sigma}_{23} = 0$, with $X = AB + BC + CA$ and $R = [X(B + C + (X/F\tan^2 2\theta))]^{1/2}$. The interesting problem is to find the law of evolution of θ. Based on equation $(30)_1$, one has $\hat{\dot{W}}_{12}^p = \dot{W}_{12}^p = (\eta_3'/2F)\hat{D}_{12} = (\eta_3'/4F)\dot{\gamma}\cos 2\theta$, where $\hat{\dot{W}}_{12}^p = \dot{W}_{12}^p$ due to the plane transformation. The unit vector $\mathbf{n}_1$ along $\hat{x}_1$ is a purely orientational structure variable and according to equation $(16b)_2$ one has $\overset{\nabla}{\mathbf{n}}_1 = -\mathbf{W}^p\mathbf{n}_1$ (equivalently one may consider the $\mathbf{a}_1$ according to equation $(16b)_1$). Hence, based on the values of W_{12}, W_{12}^p and the $\cos\theta$, $\sin\theta$ components of $\mathbf{n}_1$ in reference to x_1, x_2, the expression for $\overset{\nabla}{\mathbf{n}}_1$ yields

$$d\theta/d\gamma = (1/2)[(\eta_3'/2F)\cos 2\theta - 1] \tag{44}$$

As $|\gamma|$ increases either an equilibrium orientation $\theta_e = (1/2)\cos^{-1}(2F/\eta_3')$ is asympotically reached if $|2F/\eta_3'| \leq 1$, or the axes $\hat{x}_1$, $\hat{x}_2$ rotate indefinitely.

As a second example consider a velocity gradient defined by

$$D_{22} = rD_{11}, D_{33} = -(D_{11} + D_{22}), D_{ij} = 0 \quad \text{for } i \neq j, W_{ij} = 0 \tag{45}$$

with r a real number. The same assumptions of the preceding example yield

$$\hat{\sigma}_1/Q_1 = \hat{\sigma}_{22}/Q_2 = \hat{\sigma}_{12}/Q_3 = (k/Q)\text{sgn}D_{11} \tag{46}$$

where $Q_1 = 2(1+r)A + (1 + r + (1-r)\cos 2\theta)B$, $Q_2 = 2(1+r)A + (1 + r - (1-r)\cos 2\theta)C$, $Q_3 = (X/F)(r-1)\sin 2\theta$ and $Q = [A(Q_1 - Q_2)^2 + BQ_2^2 + CQ_1^2 + FQ_3^2]^{1/2}$. Similarly to the previous case one has $\hat{\dot{W}}_{12}^p = \dot{W}_{12}^p = (\eta_3'/2F)\hat{D}_{12} = (\eta_3'/4F)(r-1)D_{11}\sin 2\theta$, and since $\overset{\nabla}{\mathbf{n}}_1 = \dot{\mathbf{n}}_1$ because $\mathbf{W} = \mathbf{0}$, the evolution of $\mathbf{n}_1$ according to equation $(16b)_2$ is given by $\dot{\mathbf{n}}_1 = -\mathbf{W}^p\mathbf{n}_1$ which yields

$$d\theta/d\epsilon = (c/2)\sin 2\theta, \quad \tan\theta = \tan\theta_0 e^{c\epsilon}, \quad c = (r-1)\eta_3'/2F \tag{47}$$

where e is the basis of the natural logarithm, ϵ the logarithmic strain along x_1, θ_0 the value of θ at $\epsilon = 0$, and equation $(47)_2$ is obtained from equation $(47)_1$ if c is constant. Depending on the signs of $\tan\theta_0$, c and ϵ, the axis $\hat{x}_1$ tends to align with the axis x_1 or x_2 as $|\epsilon|$ increases (for $c = 0 \Rightarrow \theta = \theta_0$). The results expressed by equations (44) and (47) can be given a plausible physical interpretation when $\eta_3'/2F = \pm 1$ for the case of transverse isotropy and the corresponding visualization in terms of a unidirectionally fiber-reinforced material and a deck of cards, discussed at the end of Section 4. A detailed presentation of this case is given in [26].

A remarkable difference exists between the anisotropy induced by kinematic hardening and the initial orthotropic one. In the former case the effect of the plastic spin is pronounced after large strains occurred in order to induce sufficiently "intense" anisotropy, while in the latter case the plastic spin affects the response at the early stage of small to moderate strains due to the pre-existing orthotropy.

7 Discussion and Conclusion

The generality of the development is partially limited because of two restrictions. The first is the omission of tensorial structural variables of higher order than two for reasons of simplicity. Even under this restriction, a sufficiently realistic set of constitutive models can be obtained. Including higher-order tensors can certainly be done along the lines presented in [4, 21]; one should expect then greater difficulties in their experimental determination and more complex expressions for the plastic spin and elastic embedding. The second restriction is the assumption of a smooth yield criterion. While for single crystals there is experimental and theoretical evidence that corners are induced by the superposed action of smooth yield criteria, in materials such as polycrystals for which a macroscopic approach can be applied, no conclusive experimental evidence of macroscopically detectable corners exists at present. Should such evidence become available the present formulation must be extended appropriately.

Within the aforementioned limitations the present work achieved its stated objectives, namely to demonstrate the effect of elastically embedding the structure variables and, mainly, of the constitutive relations for the plastic spin on a macroscopic formulation of anisotropic continua. We would like to emphasize here three points. First, the importance of the forms of equations (15) and (16) for the evolution laws of the structure variables, where the purely constitutive part associated with $\bar{\mathbf{a}}$, $\bar{\mathbf{m}}$, $\bar{\mathbf{s}}$ is clearly distinguished from the kinematical terms associated with $\mathbf{N}^p$ and $\mathbf{\Omega}^p$. Second, the form of the constitutive relations for the plastic spin via $\mathbf{\Omega}^p$, as in equation (27), together with the subsequently discussed continuity requirement as $\mathbf{a}' \to \mathbf{0}$. And third, the fact that Mandel's director vectors are not necessary in general for the definition of the spin ω which simply can be obtained from the kinematics, equation (6), given the constitutive relation for $\mathbf{W}^p$. This has not been recognized in the earlier works of the author [12–14], but has been pointed out in [26]. A number of additional topics including extension to rate dependent viscoplastic response and examples on the effect of elastic embedding, such as in the single slip theory [7, 9], can be

Downloaded 02 May 2010 to 171.66.16.54. Redistribution subject to ASME license or copyright; see http://www.asme.org/terms/Terms_Use.cfm

found in [27] and [28]; reference [28] provides also more details on the calculations performed in the present work.

Much can be gained by parallel microscopic studies but also, vice-versa, the present formulation can serve as a guideline for such studies when the bridging of the gap from micro to macrolevel is attempted by means of proper averaging procedures, through which macroscopic tensorial structure variables emerge. At present one can attempt to calibrate macroscopically constitutive parameters such as ρ and η_3' related to the plastic spin, and whose effect was clearly demonstrated by the theoretical analysis of the cases presented in Sections 5 and 6. For example, the h_α and c_r for the kinematic hardening can be first calibrated from the experimental data of radial deviatoric stress paths (particular case being the uniaxial) where the plastic spin is zero because $\boldsymbol{\alpha}\,\boldsymbol{\sigma}' = \boldsymbol{\sigma}'\boldsymbol{\alpha}$, equations (32)–(34); then the value of ρ can be determined by fitting experimental data where the plastic spin is active and affects the stress-strain response, as shown eloquently in Fig. 2(*a*,*b*) for simple shear. The fact that the aforementioned cases refer to partially idealized situations cannot be overlooked, but at the same time they should not be discarded from a practical point of view before actual experimental data become available for comparison. Even if such data show the weakness of the idealization, the analysis of these examples is of value because it illustrates the way of approach for more complex considerations (e.g., more than one evolving structure variables) within the general formulation.

Finally, observe that the general formulation was presented in terms of the values of the state variables at the current and relaxed configurations as defined by equation (1). Equivalent descriptions in reference to other configurations, such as the isoclinic [1], are also possible; but the important fact is that a change of the mode of description cannot eliminate a physical necessity such as the requirement of constitutive relations for the plastic spin.

8 References

1 Mandel, J., "Plasticité Classique et Viscoplasticité," *Courses and Lectures, No. 97*, International Center for Mechanical Sciences, Udine, Springer, New York, 1971.

2 Kratochvil, J., "Finite-Strain Theory of Crystalline Elastic-Inelastic Materials," *J. Appl. Phys.*, Vol. 42, 1971, pp. 1104–1108.

3 Wang, C. C., "A New Representation Theorem for Isotropic Functions: An Answer to Professor G. F. Smith's Criticism of My Paper on Representations for Isotropic Functions," *Arch. Rat. Mech. Anal.*, Vol. 36, 1970, pp. 198–223.

4 Fardshisheh, F., and Onat, E. T., "Representation of Elastoplastic Behavior by Means of State Variables," *Problems of Plasticity*, Sawczuk, A., ed., Noordhoff, Leyden, 1974, pp. 89–115.

5 Lee, E. H., "Elastic-Plastic Deformations at Finite Strains," ASME JOURNAL OF APPLIED MECHANICS, Vol. 36, 1969, pp. 1–6.

6 Rice, J. R., "Inelastic Constitutive Relations for Solids: An Internal-Variable Theory and its Application to Metal Plasticity," *J. Mech. Phys. Solids*, Vol. 19, 1971, pp. 433–455.

7 Asaro, R. J., and Rice, J. R., "Strain Localization in Ductile Single Crystals," *J. Mech. Phys. Solids*, Vol. 25, 1977, pp. 309–338.

8 Weng, G. J., "The Yield Surface of Single Crystals at Arbitrary Strain," *Acta Mechanica*, Vol. 37, 1980, pp. 231–245.

9 Peirce, D., Asaro, R. J., and Needleman, A., "An Analysis of Nonuniform and Localized Deformation in Ductile Single Crystals," *Acta Metal.*, Vol. 30, 1982, pp. 1087–1119.

10 Nemat-Nasser, S., "On Finite Deformation Elasto-Plasticity," *Int. J. Solids Structures*, Vol. 18, 1982, pp. 857–872.

11 Havner, K. S. and Shalaby, A. H., "Further Investigation of a New Hardening Law in Crystal Plasticity," ASME JOURNAL OF APPLIED MECHANICS, Vol. 45, 1978, pp. 500–506.

12 Dafalias, Y. F., "A Missing Link in the Macroscopic Constitutive Formulation of Large Plastic Deformations," Chapter 8 in *Plasticity Today*, Sawczuk, A., and Bianchi, G., eds., Elsevier Applied Science, U.K., 1985, pp. 135–151. From the International Symposium on Current Trends and Results in Plasticity, CISM, Udine, Italy, June 1983.

13 Dafalias, Y. F., "On the Evolution of Structure Variables in Anisotropic Yield Criteria at Large Plastic Transformations," Volume from the Colloque International du C.N.R.S. No. 351 sur "Critères de Rupture des Matériaux à Structure Interne Orientée", Villard-de-Lans, France, June 1983, Boehler, J. P., ed., Éditions du C.N.R.S., Paris, in press.

14 Dafalias, Y. F., "Corotational Rates for Kinematic Hardening at Large Plastic Deformations," ASME JOURNAL OF APPLIED MECHANICS, Vol. 50, 1983, pp. 561–565.

15 Loret, B., "On the Effects of Plastic Rotation in the Finite Deformation of Anisotropic Elastoplastic Materials," *Mechanics of Materials*, Vol. 2, 1983, pp. 287–304.

16 Boehler, J. P., "A Simple Derivation of Representations for Non-Polynomial Constitutive Equations in Some Cases of Anisotropy," *ZAMM*, Vol. 59, 1979, pp. 157–167.

17 Liu, I. S., "On Representations of Anisotropic Invariants," *Int. J. Eng. Sci.*, Vol. 20, 1982, pp. 1099–1109.

18 Hill, R., *The Mathematical Theory of Plasticity*, Oxford University Press, London, 1950.

19 Armstrong, P. J., and Frederick, C. O., "A Mathematical Representation of the Multiaxial Bauschinger Effect," C.E.G.B. Report RD/B/N 731, 1966.

20 Nagtegaal, J. C., and de Jong, J. E., "Some Aspects of Nonisotropic Work Hardening in Finite Strain Plasticity," in: *Plasticity of Metals at Finite Strain: Theory, Experiment and Computation*, Lee, E. H., and Mallett, R. L., eds., Div. Appl. Mech., Stanford University and Dept. Mech. Eng., R.P.I., 1982, pp. 65–102.

21 Onat, E. T., "Representation of Inelastic Behavior in the Presence of Anisotropy and of Finite Deformations," in: *Recent Advances in Creep and Fracture of Engineering Materials and Structures*, Wilshire, B., and Owen, D. R. J., eds., Pineridge Press, Swansea, U.K., 1982, pp. 231–264.

22 Lee, E. H., Mallet, R. L., and Wertheimer, T. B., "Stress Analysis for Anisotropic Hardening in Finite-Deformation Plasticity," ASME JOURNAL OF APPLIED MECHANICS, Vol. 50, 1983, pp. 554–560.

23 Fressengeas, C., and Molinari, A., "Modèles d'Ecrouissage Cinématique en Grande Déformation," *C.R.A.S.*, Vol. 297, Série II, 1983, pp. 93–96.

24 Johnson, G. C., and Bammann, D. J., "A Discussion of Stress Rates in Finite Deformation Problems," Sandia Report SAND82-8821, Aug. 1982.

25 Ogata, K., *State Space Analysis of Control Systems*, Prentice-Hall, Englewood Cliffs, N.J., 1967.

26 Dafalias, Y. F., "The Plastic Spin Concept and a Simple Illustration of its Role in Finite Plastic Transformations," *Mechanics of Materials*, Vol. 3, 1984, pp. 223–233.

27 Dafalias, Y. F., "A Missing Link in the Formulation and Numerical Implementation of Finite Transformation Elastoplasticity," in: *Constitutive Equations: Macro and Computational Aspects*, William, K. J., ed., ASME, 1984, pp. 25–40.

28 Dafalias, Y. F., "The Plastic Spin," A three-part Report No. 83-1-2-3, Department of Civil Engineering, University of California at Davis, Oct. 1983.

APPENDIX

A scalar, vector, or tensor-valued isotropic function $\mathbf{f}$ of the scalar, vector, and tensor-valued variables $\mathbf{s}$, is defined by $\mathbf{f}(\mathbf{s}) = \mathbf{Q}[\mathbf{f}(\mathbf{Q}^T[\mathbf{s}])]$ for any orthogonal transformation $\mathbf{Q}$. For such a function it can be shown that

$$D\mathbf{f}/Dt = (\partial \mathbf{f}/\partial \mathbf{s}) \cdot (D\mathbf{s}/Dt) \tag{A1}$$

for corotational rates according to equation (2) with respect to any $\boldsymbol{\Omega}$ including $\boldsymbol{\Omega} = \mathbf{0}$, and with the understanding that D/Dt implies the material time derivative for scalar valued quantities. The proof is based on the fact that one can always write $\boldsymbol{\Omega} = \dot{\mathbf{Q}}\mathbf{Q}^T$ since $\mathbf{Q}(t)$ is arbitrary. As an example, for a scalar-valued isotropic function $f(\mathbf{s}) = f(\mathbf{Q}^T[\mathbf{s}])$, one has

$$\dot{f} = \frac{\partial f}{\partial \mathbf{Q}^T[\mathbf{s}]} \cdot \dot{\mathbf{Q}^T[\mathbf{s}]} = \mathbf{Q}^T\left[\frac{\partial f}{\partial \mathbf{s}}\right] \cdot \mathbf{Q}^T\left[\frac{\partial \mathbf{s}}{Dt}\right] = \frac{\partial f}{\partial \mathbf{s}} \cdot \frac{D\mathbf{s}}{Dt}$$

$$= \frac{\partial f}{\partial \mathbf{s}} \cdot \dot{\mathbf{s}} \tag{A2}$$

The proof for tensor-valued $\mathbf{f}$ is longer but similar.

Downloaded 02 May 2010 to 171.66.16.54. Redistribution subject to ASME license or copyright; see http://www.asme.org/terms/Terms_Use.cfm

G. C. Sinharay

B. Banerjee
Department of Mathematics,
Hooghly Mohsin College,
Chinsurah, West Bengal, India

A New Approach to Large Deflection Analyses of Spherical and Cylindrical Shells

In this paper large deflections of thin elastic shallow spherical shell and cylindrical shells are investigated by a new approach. Numerical results for moveable as well as immoveable edge conditions are presented graphically and compared with other known results.

Introduction

It is well known that Berger [1] presented a simplified approach to analyze the large deflections of plates. Berger's method is based onthe neglect of e_2, the second invariant of the middle surface strain. This method has been utilized successfully by many authors in different plate problems. Nash and Modeer [2] extended Berger's method to analyze the nonlinear behavior of thin elastic shallow spherical shells and achieved satisfactory results for immoveable edge conditions only. Nowinski and Ismail [3] followed Berger's line of thought and analyzed quite elegantly the large deflection of cylindrical shell panels.

The present study offers a modified energy expression for deriving the differential equations for a thin elastic shallow spherical shell and for a cylindrical shell panel. Keeping in mind Banerjee's [4] line of thought for large deflections of thin elastic plates, the term $(1-\nu^2)\,u^2/r^2$ in the expression for the total potential energy of a spherical shell is replaced by $\lambda\{1/2(dW/dr)^2 + dW/dr \cdot dZ/dr\}^2$, where λ is a factor depending on the Poisson's ratio of the shell material and $Z=Z(r)$ is the elevation of the middle surface of the shell above the base plane [2] and u, the radial displacement. W is the vertical component of displacement of the middle surface of the shell. As a consequence the partial coupled differential equations have been decoupled and thus simplified. The values of λ have been obtained from the condition of minimum potential energy. The equivalent hypothesis of the present study is similar to that of Banerjee [4] in his corresponding plate problem. In the case of a shell, the radial stretching is proportional to $1/2(dW/dr)^2 + dW/dr \cdot dZ/dr$. This is certainly reasonable, because the contribution of the term $1/2(dW/dr)^2 + dW/dr \cdot dZ/dr$ in the expression for $\epsilon_r = du/dr + 1/2(dW/dr)^2 + dW/dr \cdot dZ/dr$ is greater than that of du/dr in bending. The constant of proportionality is a function of Poisson's ratio ν because ϵ_r and ϵ_θ are mutually perpendicular.

Contributed by the Applied Mechanics Division for publication in the JOURNAL OF APPLIED MECHANICS.

Discussion on this paper should be addressed to the Editorial Department, ASME, United Engineering Center, 345 East 47th Street, New York, N.Y. 10017, and will be accepted until two months after final publication of the paper itself in the JOURNAL OF APPLIED MECHANICS. Manuscript received by ASME Applied Mechanics Division, February, 1984; final revision, November 1984.

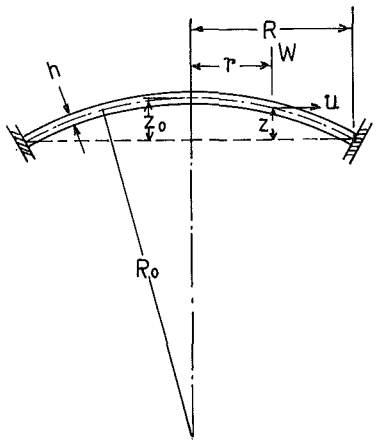


Fig. 1 Geometry of spherical cap

The corresponding differential equation for cylindrical shells in rectangular cartesian coordinates have been deduced following the same method.

Although Berger's method is advantageous for simplicity, it fails miserably for moveable edge conditions. Nowinski and Ohnabe [5] pointed out that Berger's method is meaningful only for the immoveable edge condition.

Formation of Differential Equation for a Thin Spherical Shell.

Let us consider the finite axisymmetric deflection of a thin elastic shallow spherical shell with clamped edges subjected to uniform normal pressure q on its concave surface. The coordinate system to be employed is shown in Fig. 1. The vertical component of the displacement of the middle surface of the shell is denoted by W, considered to be positive in the direction shown. The radial displacement of a point in the middle surface is denoted by u, measured horizontally as shown in the Fig. 1. The elevation of the middle surface of the shell above the base line is denoted by $Z=Z(r)$.

As referred to geometry shown in the Fig. 1, we have $Z=R^2/2R_0(1-r^2/R^2)$, from which dZ/dr is calculated. The total potential energy may be written as

Copyright © 1985 by ASME
Downloaded 02 May 2010 to 171.66.16.54. Redistribution subject to ASME license or copyright; see http://www.asme.org/terms/Terms_Use.cfm

$$U=\frac{D}{2}\int\int\left[(\nabla^2 W)^2-\frac{2(1-\nu)}{r}\frac{dW}{dr}\frac{d^2_W}{dr^2}+\frac{12}{h^2}\{e^2-2(1-\nu)e_2\}\right]rdrd\theta-\int\int qwrdrd\theta$$

where

$$e=\frac{du}{dr}+\frac{u}{r}+\frac{1}{2}\left(\frac{dW}{dr}\right)^2+\frac{dW}{dr}\cdot\frac{dZ}{dr}$$

and

$$e_2=\frac{u}{r}\frac{du}{dr}+\frac{u}{2r}\left(\frac{dW}{dr}\right)^2+\frac{u}{r}\frac{dW}{dr}\cdot\frac{dZ}{dr}$$

$$D=\frac{Eh^3}{12(1-\nu^2)},$$

where e and e_2 are first and second strain invariants, ν is Poisson's ratio, E is Young's modulus, and h is the shell thickness.

Let us now rewrite the potential energy in the following form:

$$U=\frac{D}{2}\int\int\left[(\nabla^2 W)^2-\frac{2(1-\nu)}{r}\frac{dW}{dr}\cdot\frac{d^2W}{dr^2}\right]rdrd\theta+\frac{D}{2}\int\int\frac{12}{h^2}\left[\bar{e}_1{}^2+\lambda\left\{\frac{1}{2}\left(\frac{dW}{dr}\right)^2+\frac{dW}{dr}\cdot\frac{dZ}{dr}\right\}^2\right]rdrd\theta-\int\int qWrdrd\theta \tag{1}$$

Here, the term $(1-\nu^2)u^2/r^2$ has been replaced by $\lambda\{1/2(dW/dr)^2+dW/dr\cdot dZ/dr\}^2$ and

$$\bar{e}_1=\frac{du}{dr}+\frac{\nu u}{r}+\frac{1}{2}\left(\frac{dW}{dr}\right)^2+\frac{dW}{dr}\cdot\frac{dZ}{dr}. \tag{2}$$

Under the preceding assumptions, decoupling of the differential equation is possible and we may apply Euler's variational method to this modified energy expression. Euler's variational equations are

$$\frac{\partial F}{\partial u}-\frac{\partial}{\partial r}\cdot\frac{\partial E}{\partial u_r}=0 \tag{3}$$

and

$$\frac{\partial F}{\partial W}-\frac{\partial}{\partial r}\cdot\frac{\partial F}{\partial W_r}+\frac{\partial^2}{\partial r^2}\cdot\frac{\partial F}{\partial W_{rr}}=0 \tag{4}$$

where F is the integrand in (1).

Let us assume W in the following form

$$W=W_0\left(1-\frac{r^2}{R^2}\right)^2 \tag{5}$$

which clearly satisfies the clamped edge boundary condition. From (3) and (1), we get the following equation determining α:

$$r^{1-\nu}\bar{e}_1=\frac{\alpha^2h^2}{12}(>0) \tag{6}$$

From (4) and (1), and using (6), and $Z=R^2/2R_0(1-r^2/R^2)$, we get the following differential equation governing the deflection W:

$$\nabla^4 W-\alpha^2 r^{\nu-1}\nabla^2 W-\alpha^2(\nu-1)r^{\nu-2}\left(\frac{dW}{dr}-\frac{r}{R_0}\right)-\frac{12\lambda}{h^2}\left[\frac{1}{2r}\left(\frac{dW}{dr}\right)^3+\frac{3}{2}\left(\frac{dW}{dr}\right)^2\frac{d^2W}{dr^2}\right]-\frac{12\lambda}{R_0^2h^2}\left[3r\frac{dW}{dr}+r^2\frac{d^2W}{dr^2}\right]+\frac{12\lambda}{h^2}\left[\frac{3}{R_0}\left\{\left(\frac{dW}{dr}\right)^2+r\frac{d^2W}{dr^2}\cdot\frac{dW}{dr}\right\}\right]=\frac{q}{D}-\frac{2\alpha^2}{R_0}r^{\nu-1} \tag{7}$$

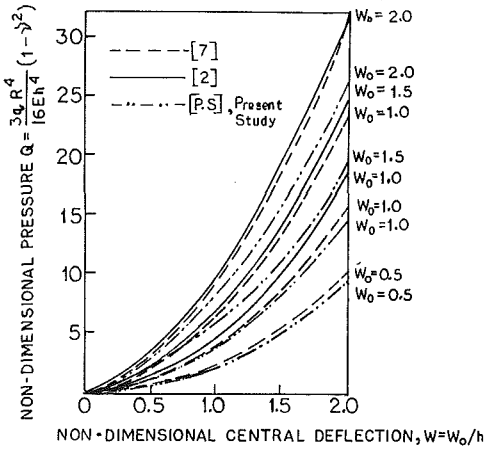


Fig. 2 Center deflection versus pressure for spherical cap (immoveable edge)

For a moveable edge $\alpha=0$, as the inplane radial stress vanishes at the moveable boundary and the expression for the inplane radial stress involves (2), (6), and consequently α.

To solve (6), we put (5) in (6) and integrate over the area of the shell. Thus the equation determining α^2 reduces to

$$\frac{\alpha^2h^2}{12}=\frac{16W_0}{R_0}\cdot\frac{\nu}{(\nu+3)(\nu+5)}R^{1-\nu}+\frac{128W_0^2\nu}{(\nu+3)(\nu+5)(\nu+7)}R^{-\nu-1} \tag{8}$$

To solve (7), we use Galerkin's error-minimizing technique. Putting (5) in (7), and using (8) and applying Galerkin's technique, we get the following equation governing the central deflection W_0/h:

$$\frac{32W_0}{3R^2}+\frac{12}{h^2}\left[\frac{128W_0}{(\nu+3)(\nu+5)(\nu+7)}+\frac{8R^2}{R_0(\nu+3)(\nu+5)}\right]\left[\frac{16W_0\nu}{R_0(\nu+3)(\nu+5)}+\frac{128W_0^2\nu}{R^2(\nu+3)(\nu+5)(\nu+7)}\right]+\frac{12\lambda}{h^2}\left[\frac{64W_0^3}{105R^2}+\frac{4W_0R^2}{15R_0^2}+\frac{4W_0^2}{5R_0}\right]=\frac{q}{D}\cdot\frac{R^2}{6} \tag{9}$$

Evaluation of λ

For a simply supported edge, since the radial strain is small, du/dr can be neglected. For a clamped edge, however, du/dr is minimum at the center and maximum at the edge; therefore, it is quite reasonable to assume $du/dr\approx 1/2$ $[1/2(dW/dr)^2+dW/dr\cdot dZ/dr]$ = the average of the radial strain.

Under this assumption, putting $\partial U/\partial\lambda=0$ for minimum potential energy, λ is obtained as $\lambda\approx 2\nu^2$.

Similarly, for simply supported edge $\lambda\approx\nu^2$.

Numerical Results

Equation (9) can be written as

$$\left[\frac{18432\nu}{(\nu+3)^2(\nu+5)^2(\nu+7)^2}+\frac{24\lambda}{35}\right]\left(\frac{W_0}{h}\right)^3$$

Downloaded 02 May 2010 to 171.66.16.54. Redistribution subject to ASME license or copyright; see http://www.asme.org/terms/Terms_Use.cfm

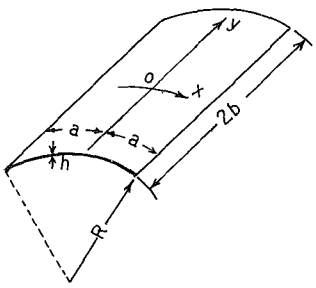


Fig. 3 Geometry of cylindrical panel

$$+\left[\frac{3456\nu}{(\nu+3)^2(\nu+5)^2(\nu+7)}+\frac{9\lambda}{10}\right]\left(\frac{R^2}{R_0h}\right)\left(\frac{W_0}{h}\right)^2$$

$$+\left[1+\left\{\frac{144\nu}{(\nu+3)^2(\nu+5)^2}+\frac{3\lambda}{10}\right\}\left(\frac{R^2}{R_0h}\right)^2\right]\left(\frac{W_0}{h}\right)$$

$$=\frac{3}{16}\cdot\frac{qR^4(1-\nu^2)}{Eh^4}=Q,\quad\text{say}\tag{10}$$

Figure 2 presents a comparative study of the results obtained for central deflection, W_0/h, versus load function, Q, under immoveable edge condition, by Nash and Modeer [2] and Smith [7], and by this present study (using $\nu=0.32$, $\lambda=2\nu^2$) for shallow spherical caps of various geometries. Figure 6 presents a comparative study of the results obtained for central deflection, W_0/h, versus load function, Q, under moveable edge condition, by Ramachandran [9], and by this present study (using $\nu=0.32$, $\lambda=2\nu^2$) for shallow spherical caps of various geometries.

Formation of Differential Equation for Cylindrical Shells

We now approach a problem concerning a circular cylindrical panel uniformly loaded by a normal pressure q. The geometry, the coordinate system, length of the sides, and thickness of the cylindrical shell are shown in Fig. 3.

For definiteness we assume that all edges of the panel are simply supported.

Let K_x and K_y denote the principal curvatures at a point of the middle surface, and u,v,w the components of the displacement.

Rewritting the modified potential energy (as in the case of spherical shell) in cartesian coordinate system for a cylindrical shell, in which $e^2-2(1-\nu)e_2$ is replaced by $\bar{e}^2+\lambda\{1/2(W_x^2+W_y^2)-2KW\}^2$ and using Euler's variational equations, we arrive at the following set of differential equation governing the deflection W:

$$\nabla^4W-\alpha^2(W_{xx}+W_{yy}+2K)-\frac{6\lambda}{h^2}[(W_x^2+W_y^2)(\nabla^2W-2K)$$

$$-4KW(\nabla^2W+2K)+2\{W_x^2W_{xx}+2W_xW_yW_{xy}+W_y^2W_{yy}\}]=\frac{q}{D}\tag{11}$$

where α is determined by

$$\bar{e}=\frac{\alpha^2h^2}{12}=\text{constant}\tag{12}$$

Here,

$$\left.\begin{aligned}\bar{e}&=u_x+\frac{1}{2}W_x^2-K_xW+\nu v_y+\frac{\nu}{2}W_y^2-K_yW\\ \text{and}\quad 2K&=K_x+K_y\end{aligned}\right\}\tag{13}$$

for a movable edge $\alpha=0$.

To solve (12), we integrate over the area

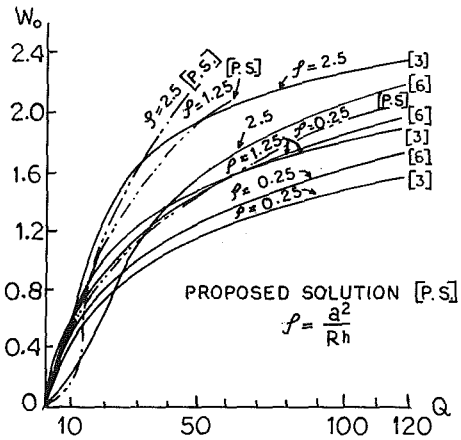


Fig. 4 Center deflection versus reduced load for simply supported square cylindrical panels (immoveable edge)

$$\begin{pmatrix}\text{from } x=-a \text{ to } x=+a\\ \text{from } y=-b \text{ to } y=+b\end{pmatrix}$$

Thus we get

$$\frac{\alpha^2h^2}{12}=\frac{W_0^2\pi^2}{32}\left(\frac{1}{a^2}+\frac{\nu}{b^2}\right)-\frac{8KW_0}{\pi^2}\tag{14}$$

where we assume

$$W=W_0\text{Cos}\frac{\pi x}{2a}\text{Cos}\frac{\pi y}{2b},\tag{15}$$

as a first term approximation. The relation (15) clearly satisfies the boundary condition of simple support.

It is to be noted that the inplane displacements u and v have been eliminated by choice of suitable expressions for these displacements and integrations over the required limits.

To solve (11) we again use Galerkin's error-minizing technique. Putting (15) in (11) and using (14), and applying Galerkin's technique, we get the following equation governing the central deflection W_0/h:

$$W_0\left(\frac{\pi}{2}\right)^4\left(\frac{1}{a^2}+\frac{1}{b^2}\right)^2+\frac{12}{h^2}\left[\frac{W_0^2\pi^2}{32}\left(\frac{1}{a^2}+\frac{\nu}{b^2}\right)\right.$$

$$\left.-\frac{4W_0}{R\pi^2}\right]\left[W_0\left(\frac{\pi}{2}\right)^2\left(\frac{1}{a^2}+\frac{\nu}{b^2}\right)-\frac{16}{R\pi^2}\right]-\frac{16q}{D\pi^2}$$

$$+\frac{6\lambda}{h^2}\left[W_0^3\left(\frac{\pi}{2}\right)^4\left\{\frac{9}{16}\left(\frac{1}{a^4}+\frac{1}{6^4}\right)+\frac{1}{8a^2b^2}\right\}\right.$$

$$\left.-\frac{8}{3R}\left(\frac{1}{a^2}+\frac{1}{b^2}\right)W_0^2+\frac{2W_0}{R^2}\right]=0\tag{16}$$

as, in the case of circular cylindrical shell, $1/2K$ reduces to R, the radius of the shell.

Square Panel

In case of square panel (16) reduces to

$$\frac{3\pi^6}{512}[(1+\nu)^2+5\lambda]\left(\frac{W_0}{h}\right)^3-\left[2\lambda\right.$$

$$\left.+\frac{9(1+\nu)}{8}\right]\pi^2\left(\frac{a^2}{Rh}\right)\left(\frac{W_0}{h}\right)^2+\left[\frac{\pi^6}{64}\right.$$

$$\left.+\frac{3}{4}\left(\lambda\pi^2+\frac{64}{\pi^2}\right)\left(\frac{a^2}{Rh}\right)^2\right]\left(\frac{W_0}{h}\right)=\frac{qa^4}{Dh}=Q,\quad\text{say}\tag{17}$$

Figure 4 presents a comparative study of the results ob-

Downloaded 02 May 2010 to 171.66.16.54. Redistribution subject to ASME license or copyright; see http://www.asme.org/terms/Terms_Use.cfm

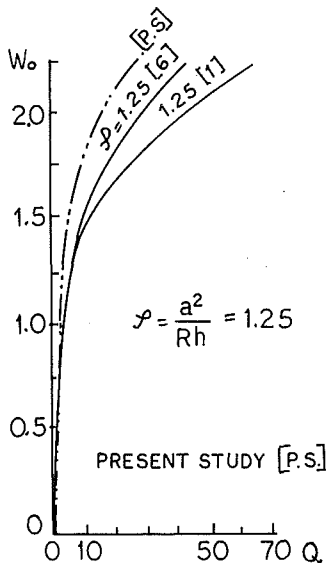


Fig. 5 Center deflection versus reduced load for simply supported infinitely long cylindrical panels (immoveable edge)

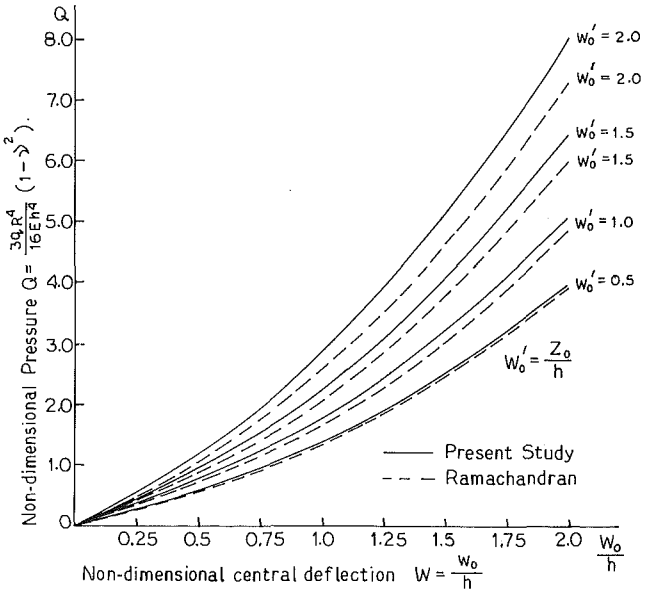


Fig. 6 Center deflection versus pressure for spherical caps (moveable edge)

Table 1 Infinitely long panel with moveable edge, $a^2/Rh = 1.25$

Load Function $Q = \frac{qa^4}{Dh}$	Present Study $\frac{W_0}{h}$
3.292	0.718
4.138	0.88
7.596	1.391
18.694	2.281
28.683	2.751

tained for central deflection, W_0/h, versus load function, Q, by Nowinski and Ismail [3], and by Volmir [6] and by this present study (using $\nu = 0.3$, $\lambda = \nu^2$) for simply supported square panels of various geometries under immoveable edge conditions. The numerical results obtained for central deflection, W_0/h, versus load function, Q, for simply supported square panels of various geometries under moveable edge conditions is presented in Fig. 7 and compared with the results obtained by numerical solutions. It is needless to mention that [3] fails to give any meaningful result under moveable edge condition. The detail calculation of the numerical solutions of the problem is given in the Appendix at the end of the paper.

Infinitely Long Panel ($b \to \infty$)

In this case, (16) reduces to

$$\frac{3\pi^6}{1024}\left[2+\frac{9}{2}\lambda\right]\left(\frac{W_0}{h}\right)^3 - \frac{\pi^2}{8}(9+8\lambda)\left(\frac{a^2}{Rh}\right)\left(\frac{W_0}{h}\right)^2 + \left[\frac{\pi^6}{256} + \frac{3}{4}\left(\lambda\pi^2 + \frac{64}{\pi^2}\right)\left(\frac{a^2}{Rh}\right)^2\right]\left(\frac{W_0}{h}\right) = \frac{qa^4}{Dh} = Q, \quad \text{say} \tag{18}$$

Here, Fig. 5 presents a comparative study of the results obtained for central deflection, W_0/h, versus particular load function, Q by Volmir [6] and Berger [1], and by this present study (using $\nu = 0.3$, $\lambda = \nu^2$, $a^2/Rh = 1.25$), for simply supported infinitely long panel with immoveable edge conditions.

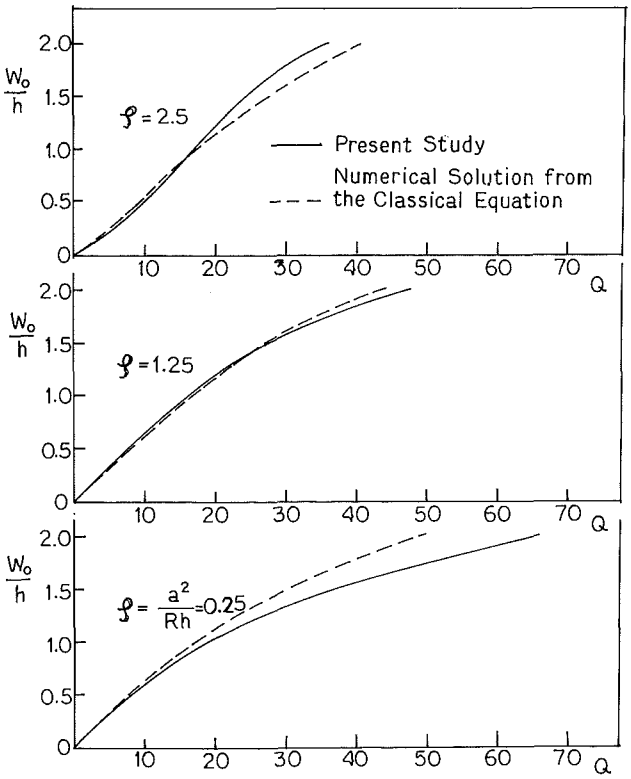


Fig. 7 Center deflection versus reduced load for simply supported square cylindrical panels (moveable edge)

The numerical results obtained for central deflection, W_0/h, versus particular load function, Q, under moveable edge condition is given in tabular form.

Conclusions

It is to be noted that the deflections obtained for plates and shells by experimental study are always higher than those obtained by theoretical approaches. Therefore, the results of the present study are excellent for practical purposes.

From the numerical results the following observations may be made:

(*a*) Berger's method extended by Nash and Modeer [2] for

Downloaded 02 May 2010 to 171.66.16.54. Redistribution subject to ASME license or copyright; see http://www.asme.org/terms/Terms_Use.cfm

a thin shalow spherical shell and by Nowinski and Ismail [3] for cylindrical shell offers reasonably good results only for immoveable edge conditions. In the present study the differential equations have been decoupled and thus simplified in contrast to the set of equations in [8]. Sufficiently accurate results have been obtained both for moveable as well as immoveable edge conditions.

(*b*) From the same cubic equation governing the central deflection, the results both for immoveable as well as moveable edge conditions can be obtained. This is certainly an additional advantage.

(*c*) The modified energy expression suggested in the present study thus conveniently can be employed to study the nonlinear behavior of thin shallow spherical shell and cylindrical shell with ease and accuracy.

References

1 Berger, H. M., "A New Approach to the Analysis of Large Deflection of Plates," ASME JOURNAL OF APPLIED MECHANICS, Vol. 22, 1955, pp. 465-472.

2 Nash, W. A., and Modeer, J. R., "Certain Approximate Analysis of the Non-Linear Behaviours of Plates and Shallow Shells, *Proceedings of the Symposium on the Theory of Thin Elastic Shells* (I.U.T.A.M), (Delft. Int. Sci., N.Y., 1960) 1959, pp. 331-354.

3 Nowinski, J. L., and Ismail, I. A., "Certain Approximate Analysis of Large Deflections of Cylindrical Shells, *ZAMP*, Vol. 15, 1964, pp. 449-456.

4 Banerjee, B., and Datta, S., "A New Approach to an Analysis of Large Deflections of Elastic Plates," *Int. J. of Non-Linear Mechanics*, Vol. 16, No. 1, 1981, pp. 47-52.

5 Nowinski, J. L., and Ohnabe, H., "On Certain Inconsistencies in Berger's Equations for Large Deflections of Elastic Plates," *Int. J. of Mech. Sci*, Vol. 14, 1972, pp. 165-170.

6 Volmir, A. S., *Flexible Plates and Shells* (in Russian), Gos. Iz. Tech. Th. Lit, Moscow, 1956.

7 Smith, E. A., "Large Elastic Deflection of a Nearly Flat Circular Clamped Plate Under Uniform Lateral Loading," Report No. 299, Naval Construction Research Establishment, Dunfermline, Scotland, 1954.

8 Von Karman, Th., and Tsien, Hsue-Shen, "The Buckling of Thin Cylindrical Shells Under Axial Compression," *J. Aero. Sci.*, Vol. 8, 1941, pp. 303-312.

9 Ramachandran, J., "Large Amplitude Vibrations of Shallow Spherical Shell With Concentrated Mass," ASME JOURNAL OF APPLIED MECHANICS, Vol. 43, 1976, pp. 363-365.

APPENDIX

Large Deflection of Cylindrical Square Panel With Moveable Edge by Classical Equation

The integrand F in the total potential energy of the cylindrical square panel is

$$F=\frac{D}{2}[(W_{xx}+W_{yy})^2-2(1-\nu)(W_{xx}W_{yy}-W_{xy}^2)]-qw$$
$$+\frac{6D}{h^2}\left[\left(U_x+\frac{1}{2}W_x^2-K_xW+v_y+\frac{1}{2}W_y^2-K_yW\right)^2\right.$$
$$-2(1-\nu)\left\{\left(U_x-K_xW+\frac{1}{2}W_x^2\right)\left(v_y-K_yW+\frac{1}{2}W_y^2\right)\right.$$
$$\left.\left.-\frac{1}{4}(U_y+v_x+W_xW_y)^2\right\}\right] \tag{19}$$

Applying Euler's variational equations to (19), we get the following three differential equations governing u, v, and w:

$$U_{xx}+\frac{(1-\nu)}{2}U_{yy}+\frac{(1+\nu)}{2}v_{xy}=W_x(K_x+\nu K_y)-W_xW_{xx}$$
$$-\frac{(1-\nu)}{2}W_xW_{yy}-\frac{(1+\nu)}{2}W_yW_{xy} \tag{20}$$

$$v_{yy}+\frac{(1-\nu)}{2}v_{xx}+\frac{(1+\nu)}{2}U_{xy}=W_y(K_y+\nu K_x)-W_yW_{yy}$$
$$-\frac{(1-\nu)}{2}W_yW_{xx}-\frac{(1+\nu)}{2}W_xW_{xy} \tag{21}$$

$$\nabla^4W-\frac{12}{h^2}\left[W_{xx}\left\{U_x+\nu v_y+\frac{1}{2}W_x^2+\frac{\nu}{2}W_y^2-(K_x+\nu K_y)W\right\}\right.$$
$$+W_{yy}\left\{\nu U_x+v_y+\frac{\nu}{2}W_x^2+\frac{1}{2}W_y^2-(\nu K_x+K_y)W\right\}$$
$$+(1-\nu)W_{xy}\{W_xW_y+U_y+v_x\}$$
$$+K_x\left\{U_x+\nu v_y+\frac{1}{2}W_x^2+\frac{\nu}{2}W_y^2-(K_x+\nu K_y)W\right\}$$
$$\left.+K_y\left\{\nu U_x+v_y+\frac{\nu}{2}W_x^2+\frac{1}{2}W_y^2-(\nu K_x+K_y)W\right\}\right]=\frac{v}{D} \tag{22}$$

The solutions of (20) and (21) can be written in the folowing convenient forms:

$$\left.\begin{aligned}U &= Ax+A_1\sin\frac{\pi x}{2a}\cos\frac{\pi y}{2a}+A_2\sin\frac{\pi x}{a}\cos^2\frac{\pi y}{2a}\\ &\quad +A_3\sin\frac{\pi x}{a}\sin^2\frac{\pi y}{2a}\\ v &= By+B_1\sin\frac{\pi y}{2a}\cos\frac{\pi x}{2a}+B_2\sin\frac{\pi y}{a}\cos^2\frac{\pi x}{2a}\\ &\quad +B_3\sin\frac{\pi y}{a}\sin^2\frac{\pi x}{2a}\end{aligned}\right\} \tag{23}$$

and we write

$$W=W_0\cos\frac{\pi x}{2a}\cos\frac{\pi y}{2a}$$

The constants A, B are evidently to be determined from the conditions of moveable edges.

Thus,

$$A=B=-\frac{W_0^2\pi^2}{32a^2} \tag{24}$$

The constants A_i, B_i, $i=1,2,3$ are determined from (20) and (21) with the help of (23) as

$$\left.\begin{aligned}A_1 &= \frac{W_0}{2}\left(\frac{a}{\pi}\right)[K_x(\nu+3)-K_y(1-\nu)]\\ B_1 &= \frac{W_0}{2}\left(\frac{a}{\pi}\right)[K_y(\nu+3)-K_x(1-\nu)]\\ A_2 &= B_2=\frac{W_0^2}{32}\cdot\left(\frac{\pi}{a}\right)(2-\nu)\\ A_3 &= B_3=-\frac{W_0^2}{32},\left(\frac{\pi}{a}\right)\cdot\nu\end{aligned}\right\} \tag{25}$$

Substituting u, v thus determined, and w in (22), and applying Galerkin's procedure, we get the following cubic equation governing the nondimensional central deflection W_0/h:

$$\frac{3\pi^6}{512}(1-\nu^2)\left(\frac{W_0}{h}\right)^3-\frac{5\pi^2}{8}(1-\nu^2)\left(\frac{a^2}{Rh}\right)\left(\frac{W_0}{h}\right)^2$$
$$+\left[\frac{\pi^6}{64}+\frac{3}{16}\pi^2(1-\nu^2)\left(\frac{a^2}{Rh}\right)^2\right]\left(\frac{W_0}{h}\right)=\frac{qa^4}{Dh}=Q \tag{26}$$

Downloaded 02 May 2010 to 171.66.16.54. Redistribution subject to ASME license or copyright; see http://www.asme.org/terms/Terms_Use.cfm

An Extended Shakedown Theory for Structures That Suffer Cyclic Thermal Loading

Part 1: Theory

A. R. S. Ponter
Professor of Engineering,
University of Leicester,
Leicester, LE1 FRH, England

S. Karadeniz
Assistant Professor,
University of Erciyes,
Kayseri, Turkey

The paper describes an extension of classical shakedown theory for structural problems involving constant mechanical loads and cyclic variations in temperature. The objective of the theory is to provide a simple means of distinguishing between circumstances where thermal cycling can cause structural ratchetting for small or zero mechanical loads from those where very substantial thermal stresses can occur with no danger of ratchetting. This distinction is of particular importance in the design of Liquid Metal Fast Breeder Reactors and current design codes do not address this problem directly. An extended definition of material shakedown is described that provides a conservative theory, taking into account cyclic strain hardening. Some simple experiments on a two-bar structure demonstrates the relevance of the theory to observed structural behavior.

1 Introduction

The design of the Liquid Metal Fast Breeder Nuclear Reactor (LMFBR) has posed new and difficult problems of structural stability and integrity. Although the loads generated by structural weight and fluid pressure are low, the rapid response of the core to shutdown conditions results in large and rapid variations in temperature in many of the structural components of the core, its supports, and the heat exchangers. As a result of these situations, which in design code terms involve low primary stresses but high secondary stresses, there has been a desire to acquire a deeper understanding of the effects of thermal loading on the deformation of structures.

For certain structural configurations and thermal gradients it is known that very large fluctuating thermal loads may be tolerated without causing progressive strain growth. In other situations thermal stresses in excess of the initial elastic limit of the material cause incremental growth during each cycle of thermal loading. There is clearly a need to develop a means of classification of the degree of susceptibility of a structure to thermal loads, thereby giving designers some insight into the regions of the design which requires special attention.

This paper discusses a theory that attempts to provide such a classification by extending classical shakedown theory to allow for large thermal loads in excess of yield. The material model adopted and the assumptions made are necessarily simplifications of real material behavior but attempt to include, in a conservative manner, the more important features observed in material tests.

The first section describes the material properties relevant to shakedown, and the results of a two-bar test on 316 SS at 400°C. The importance of cyclic hardening is emphasized and its effects are included in a conservative theory. The following sections contain a description of the theory, which yields limits to the combinations of mechanical loads, and magnitude of thermal loads, which ensure either purely elastic behavior, shakedown (in the classical sense), or plastic shakedown. For low mechanical loads and high thermal loads, the circumstance of particular interest in Fast Reactor Design—the magnitude of the thermal loads that will initiate ratchetting of the structure strongly depends on whether plastic shakedown is possible. The theory yields a simple and easily tested criterion. For sufficiently high thermal loading the thermoelastic stresses will exceed in magnitude twice the yield stress over some volume of material V_F. If we now imagine the structure with this volume of material removed and we find that this weakened structure is still capable of carrying the mechanical load then plastic shakedown will occur for some range of mechanical load. On the other hand, if the weakened structure is not able to carry any mechanical loads because, for example, the removal divides the structure into two separate parts, then no plastic shakedown regime exists and ratchetting can be induced by thermal loads even when the mechanical loads are very small in magnitude or even zero. This distinction is not reflected in design codes, as only the magnitude of the thermal stress is considered. The classic Bree solution [1] is a case where high thermal loads may be tolerated and is the only particular case incorporated into the ASME III code. It is now quite clear that the Bree Diagram is a solution for a very particular problem and that

Contributed by the Applied Mechanics Division for publication in the JOURNAL OF APPLIED MECHANICS.
Discussion on this paper should be addressed to the Editorial Department, ASME, United Engineering Center, 345 East 47th Street, New York, N.Y. 10017, and will be accepted until two months after final publication of the paper itself in the JOURNAL OF APPLIED MECHANICS. Manuscript received by ASME Applied Mechanics Division, September, 1983; Final revision, October, 1984.

Copyright © 1985 by ASME
Downloaded 02 May 2010 to 171.66.16.54. Redistribution subject to ASME license or copyright; see http://www.asme.org/terms/Terms_Use.cfm

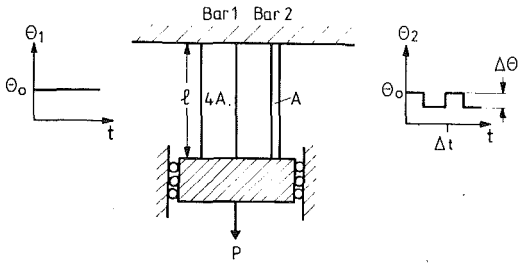


Fig. 1 Two-bar structure

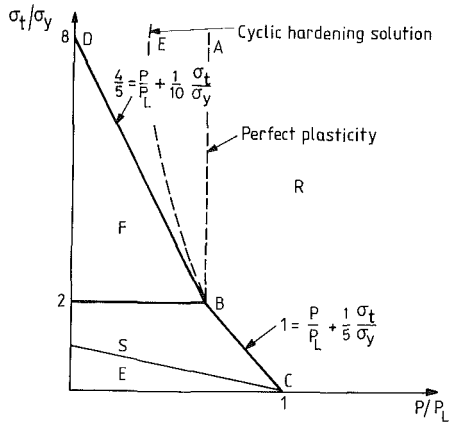


Fig. 2 Modes of behavior of two-bar structure

circumstances exist where thermal loads have a more severe effect.

In an accompanying paper [2] the theory is applied to a set of problems typical of those that occur in Fast Reactor design, by using the upper bound theorem to construct interaction diagrams.

2 Relationship Between Material and Structural Behavior Below the Creep Range

One of the principal problems of predicting the strain growth of structures subjected to thermal loading is assessing the way in which cyclic hardening of the material affects the level of loading at which substantial strain growth occurs. If we refer to the two-bar structure shown in Fig. 1 the various modes of behavior can be understood in the simplest of contexts.

Bar 1 and Bar 2 of area $4A$, and A, respectively, are restrained to remain of equal length and are subject to a constant applied load P while Bar 2 is subjected to periodic drops in temperature $\Delta\theta$ below θ_0. We suppose that the range θ_0 to $\theta_0 - \Delta\theta$ remains outside the creep range so that θ_0 for steels would be at a maximum of 450°C.

The behavior of such a structural model depends on the material behavior. If we adopted the simplest of assumptions, an elastic/perfectly plastic model, the general behavior may be described in terms of the "Bree" diagram shown in Fig. 2, where the normalized constant load P/P_L forms one axis and σ_t/σ_y the other. $P_L = 5A\sigma_y$ is the limit load and $\sigma_t = 4/5\ E\alpha\Delta\theta$ is the maximum thermoelastic stress. In this diagram, four regions E, S, F, and R correspond to differing modes of behavior. In region E purely elastic behavior occurs; in region S shakedown is established after some initial plastic strain which occurs during the first cycle. In F, plastic shakedown is said to occur. Bar 2 suffers a cycle of plastic strains which sum to zero over a cycle and Bar 1 remains elastic. For perfect plasticity the limit to region F is the line $P/P_L = 0.6$ and, provided P does not exceed this value, thermal loads of arbitrary magnitude may occur without any substantial plastic strain growth since Bar 1 remains elastic. The other lines shown in Fig. 2 in this region will be discussed in the following. In the final region, marked R, cyclic growth of strain occurs as structural ratchetting and even small excursions into this region produces unacceptably high accumulated strain over say 100 cycles.

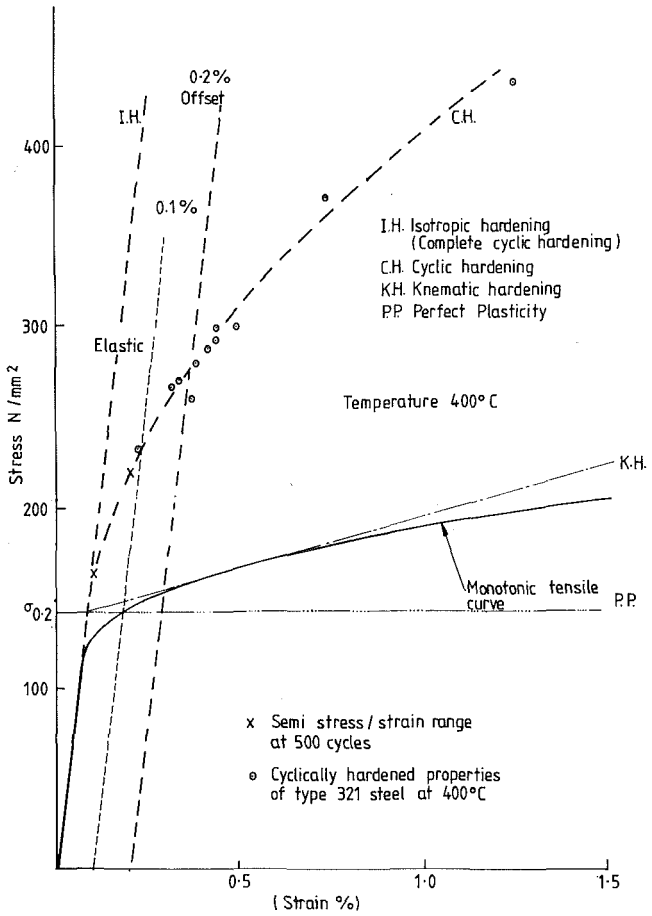


Fig. 3 Cyclic and monotonic stress-strain curve for type 316SS

This traditional model of behavior requires revision as the known behavior of many structural alloys deviates substantially from perfect plasticity. The conventional assumption, that perfectly plastic behavior is always conservative as it does not include strain hardening, is demonstratably not true for the boundary between the F and R regions.

Figure 3 shows the monotonic tensile curve and the cyclic curve for 316 SS at 400°C. The cyclic curve shows the relationship between the semi-stress range and semi-strain range for a reversed strain test carried to 500 cycles. Two features are clear; the monotonic curve shows strain hardening, but the cyclic curve shows very substantial cyclic hardening. The latter feature is, of course, of importance in region F.

The monotonic curve may be modeled using either isotropic or kinematic hardening. However, if we then compute the response of these models under reverse straining their cyclic curves are substantially different. For kinematic hardening the monotonic and cyclic curves are identical, i.e., cycle hardening is underestimated, whereas for isotropic hardening the cyclic behavior eventually becomes elastic and the cyclic hardening is overestimated, as shown in Fig. 3.

The response of two-bar structures to thermal loading has been studied by Megahed [3] and, as a result we can describe in general terms the behavior of our model. For kinematic hardening, within the regions E, S, and F defined by perfect plasticity, no substantial strain growth occurs. In region R an asymptotic state of shakedown, either elastic or plastic, will always occur after a substantial number of cycles, but the total accumulated strain will increase rapidly as the load point

Downloaded 02 May 2010 to 171.66.16.54. Redistribution subject to ASME license or copyright; see http://www.asme.org/terms/Terms_Use.cfm

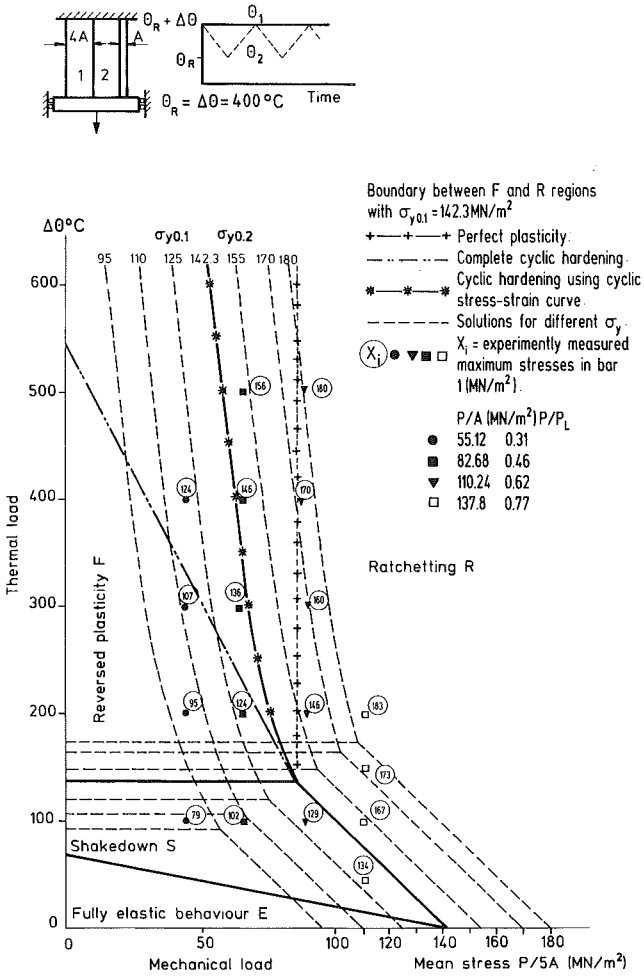


Fig. 4 Experimental results for two-bar tests at 400°C, $E = 145 - 10^3$ MN/m^2, $\alpha = 18, 10^{-6}/°C$, $\sigma_{0.1} = 142\ MN/m^2$, and $\sigma_{0.2} = 155\ MN/m^2$

moves into the R region. The complete solution to the Bree problem [1] by Mulcahy [4] shows this feature very clearly. In fact, using the perfectly plastic solution, with, say, $\sigma_y = \sigma_{0.1}$, gives a boundary to the R region loading states that give plastic strain of the order of 0.1 percent for the kinematic hardening model. Therefore the perfectly plastic solution defines the boundary at which substantial strain growth begins for the kinematically hardening model.

For the isotropic hardening model the behavior for $\sigma_t \leq 2\ \sigma_y$ is identical to that of the kinematic hardening model. However, for higher thermal loading, $\sigma_t > 2\sigma_y$, cyclic hardening occurs and the loading states at which substantial plastic strains begin to occur is given by the line BD of Fig. 2, which lies within the F region of perfect plasticity. The reason for this can be understood when we note that substantial plastic strain occurs as an asymptotic state when the maximum stress in Bar 1 exceeds, say the $\sigma_{0.1}$ proof stress. The greater amplitude of stress in Bar 2 due to cyclic hardening increases this maximum stress in Bar 1 over the value given eiter by perfect plasticity or kinematic hardening. In other words, cyclic hardening reduces the capacity of the structure to withstand thermal loading without strain growth.

This slightly anomolous result has been verified experimentally by simulating the behavior of a two-bar structure by coupling together a Lousenhausen servohydraulic testing machine (Bar 2) and a conventional dead weight tensile testing machine loaded by a jockey-weight which moves along the loading beam (Bar 1). The tests were carried out at a uniform temperature of 400°C and the effect of thermal expansion was simulated by cyclically imposing a voltage bias across the transducer which measured the extension of Bar 1. The details of the tests will be published elsewhere, and here we summarize the results for a sequence of three tests where P/P_L had values 0.31, 0.46, and 0.62 were $\sigma_y = \sigma_{0.1}$. The thermal loading was increased in a number of steps at intervals of $\Delta\theta = 100°C$ from 0°C. At each level of thermal loading 100 cycles occurred. At the end of each sequence the magnitude of stress in Bar 2 showed some small increase per cycle but cyclic behavior was very close to that for 500 cycle shown in Fig. 3. Corresponding to each loading sequence the total accumulated strain at the end of the 100 cycles was governed by the maximum stress in Bar 2. No cyclic hardening had occurred in Bar 1 and the maximum stress and strain corresponded to points on the monotonic stress-strain curve. The numerical values shown in Fig. 4 are the experimentally observed maximum values of stress in Bar 1. Substantial strain growth began to occur once this stress exceeded $\sigma_{0.1}$. Hence a suitable definition of the occurrence of ratchetting in these experiments is when these values exceed 142.3 MN/m^2. We may predict the location of the ratchet boundary corresponding to this definition for differing material assumptions by the following simple calculation.

We observe experimentally that the cyclic state of stress in Bar 2, where cyclic hardening occurs, is such that $\sigma_2^{max} = -\sigma_2^{min}$ except for the lowest values of σ_t, where strain growth is being restrained by the elastic loading and unloading of the Bar 1 in the asymptotic state. If we denote by $\Delta\sigma_2$ and $\Delta\epsilon_2$ the stress and strain (elastic and plastic) amplitudes in Bar 2 in the cyclic state, it is easy to show from compatibility and equilibrium that

$$\Delta\epsilon_2 = -\frac{\Delta\sigma_2}{4E} + \alpha\Delta\theta \tag{1}$$

where α is the linear coefficient of expansion. As the stress in Bar 2 fluctuates between $\pm\ \Delta\sigma_2/2$ irrespective of the value of P, then equilibrium requires that the maximum stress in Bar 1 is given by

$$\sigma_1^{max} = \frac{\Delta\sigma_2}{8} + \frac{P}{4A}, \tag{2}$$

the first term coming from the requirement of equilibrium with Bar 2 and the second from equilibrium with applied load P.

From equations (1) and (2) we may construct the boundary between the F and R regions with differing assumptions. For example, with no cyclic hardening $\Delta\sigma_2 = 2\sigma_y$, and hence from equation (2)

$$P/P_L = 0.6 \tag{3}$$

the boundary for perfect plasticity and kinematic hardening. At the other extreme, for isotropic hardening $\Delta\sigma_2 = E\Delta\epsilon_2$ and hence from equations (1) and (2) the contour of constant σ_1^{max} is given by

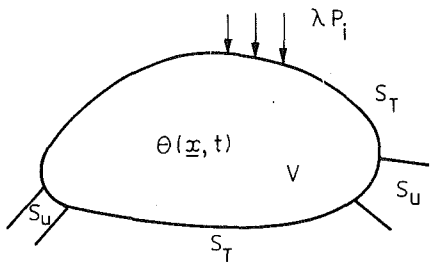
$$\frac{4}{5} = \frac{P}{P_L} + \frac{1}{10}\frac{\sigma_t}{\sigma_y} \tag{4}$$

where $\sigma_y = \sigma_{0.1}$ and $\sigma_t = 4/5\ E\alpha\Delta\theta$. This equation is shown in Figs. 2 and 4.

We may compute an appropriate curve for the material data of Fig. 3 by using, directly, the cyclic curve for the relationship between $\Delta\sigma_2$ and $\Delta\epsilon_2$. This curve is shown in Fig. 4 and is seen to lie between the extremes given by equations (3) and (4).

From equation (2), it can be seen that contours of σ_1^{max} for higher and lower values than $\sigma_{0.1}$ may be easily found as $\Delta\sigma_2$ depends only on $\Delta\theta$. In Fig. 4 a set of such curves are shown which are combined with the shakedown limit for $\sigma_t < 2\sigma_y$ using σ_1^{max} as the yield stress. It can be seen that these contours correlate well with the experimental values of σ_1^{max}.

Downloaded 02 May 2010 to 171.66.16.54. Redistribution subject to ASME license or copyright; see http://www.asme.org/terms/Terms_Use.cfm



σ_t = maximum thermo-elastic effective stress

λ_L = plastic limit load parameter

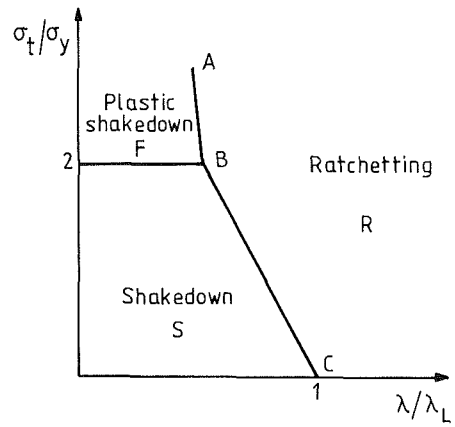


Fig. 5 Schematic representation of general problem

The effects of cyclic hardening are somewhat exaggerated in this structure and we find that the variations of the boundary between the F and R regions is much less marked for problems of design interest. For example, in the classic Bree problem [1] there is no difference and for Bree problems involving transient thermal loading the effect is much less substantial [5, 6]. In all cases where comparisons are possible the assumption of complete cyclic hardening, i.e., the isotropic hardening calculation, produces the more conservative result. In addition we will show in the next section that the entire boundary of the R region may be calculated using an extension of classical shakedown theory. Further the upper bound theorem reduces the problem to a simple quadrature for kinematically determinate structures, which allows a rapid and convenient method of assessing the effects of cyclic thermal loading by simple calculations.

The general problem is shown schematically in Fig. 5. A body with volume V and surface S is subjected to constant surface tractions λP_i on S_T, part of S, where λ is a proportional loading parameter. Over the remainder of S, S_u, displacements are prescribed and within V, at a generic point $\mathbf{x}$, a cyclic history of temperature occurs with cyclic time Δt, given by

$$\theta(\mathbf{x}, t) = \theta_0 + \bar{\theta}(\mathbf{x}, t) \tag{5}$$

where θ_0 denotes some reference temperature. For quasistatic stationary cycling $\bar{\theta}$ has the form

$$\bar{\theta}(\mathbf{x},t) = \Delta\theta\Omega(\mathbf{x})\mu(t) \tag{6}$$
$$0<\mu<1, \quad 0<\Omega<1$$

where $\Delta\theta$ denotes the maximum temperature difference and $\Omega(\mathbf{x})$ a nondimensional shape function. In this case the thermoelastic solution and the maximum effective thermoelastic stress σ_t for the problem will be proportional to $\Delta\theta$, if variations of the elastic moduli with temperature are ignored.

In terms of a (λ, σ_t) diagram, shakedown theory, in the context of a cyclically hardening material, distinguishes between region S, where elastic behavior is established after some growth of strain terminating in a state where the stress everywhere is less than some prescribed value, region F where the same state occurs in part of the structure, and is accompanied by cyclic plasticity of some other part, and region R where continued cyclic growth of the structure to an asymptotic state may occur. In accordance with our observation in the last section, we define a shakedown condition that combines the conventional view of shakedown in terms of a yield stress together with the inclusion of the effects of cyclic hardening. A similar argument has been presented elsewhere [7] based on the notion of material ratchetting and material shakedown where the shakedown theory may be developed in a rigorous manner. The results of that theory are identical to those presented here, although the interpretation of the shakedown state differ.

3 A Theory of Material and Structural Shakedown for Cyclically Hardening Materials

We define histories of stress that will not cause continued strain growth and hence define states of material shakedown. These conditions are expressed in terms of a perfectly plastic model with a yield condition

$$\phi(\sigma'_{ij}) = \sigma_y(\theta); \quad \sigma'_{ij} = \sigma_{ij} - \frac{1}{3}\delta_{ij}\sigma_{kk} \tag{7}$$

where ϕ is homogeneous of degree one in the stress components. The plastic strain increments are given by an associated flow rule,

$$d\epsilon^p_{ij} = d\mu \frac{\partial\phi(\sigma_{ij})}{\partial\sigma_{ij}} \tag{8}$$

wher $d\mu$ is a scaling parameter. In terms of this model we define the following condition of material shakedown for cylic histories of stress that follow straight line paths in stress space.

Assumption 1: Material Shakedown

Material shakedown will occur for a cyclic history of stress $\sigma_{ij}(t)$ and temperature $\theta(t)$ if either of the following conditions are satisfied:

(a) the stress history lies within a yield surface: $\phi[\sigma'_{ij}(t)] \le \sigma_y[\theta(t)]$

(b) the extremes of the stess history are related by $\sigma_{ij}^{\max} = -\sigma_{ij}^{\min}$

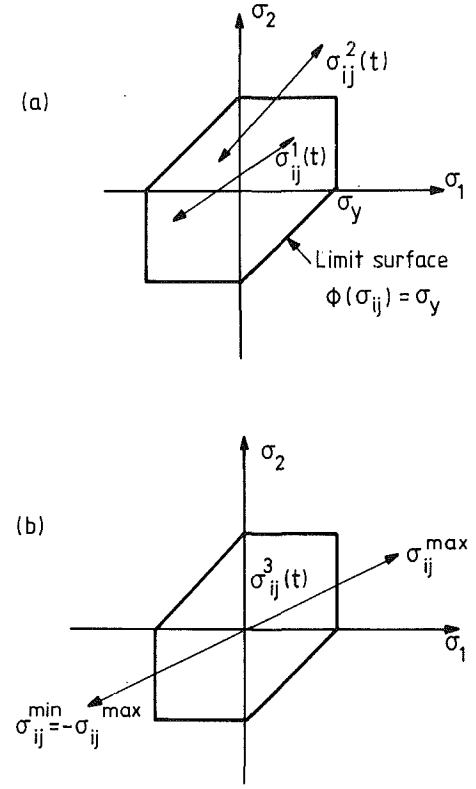
The conditions are shown schematically in Fig. 6. The effect of the variation of temperature during the cycle has not been included in condition (*b*) as there is insufficient experimental evidence to assess its effect.

The material shakedown conditions must be combined with a definition of the form of the stress history. The experiments of Pellissier-Tanon et al. [8] indicate, for uniaxial loading, that the relationship between stress amplitude and strain amplitude is insensitive to the mean stress in the cycle state. This implies that the stress histories belong to the class of histories of the form;

$$\sigma^*_{ij}(t) = \sigma^\theta_{ij}(t) + \lambda\hat{\sigma}^p_{ij} + \bar{\rho}_{ij} \tag{9}$$

where $\sigma^\theta_{ij}(t)$ denotes a thermoelastic/plastic cyclic solution for zero applied load, $\hat{\sigma}^p_{ij}$ is the elastic solution corresponding to applied loads P_i, and $\bar{\rho}_{ij}$ is an arbitrary constant residual stress field. The time constant stresses $\lambda\hat{\sigma}^p_{ij} + \bar{\rho}_{ij}$ are an arbitrary equilibrium stress distribution in equilibrium with applied loads λP_i. The construction of $\sigma^\theta{}_{ij}$ would require a complete description of the cyclic material behavior, which, of course, is not generally available. For stress histories that lie within the yield surface ϕ, the behavior of the cyclic

Downloaded 02 May 2010 to 171.66.16.54. Redistribution subject to ASME license or copyright; see http://www.asme.org/terms/Terms_Use.cfm



σ^1_{ij} – no incremental growth,

σ^2_{ij} – possible incremental growth,

σ^3_{ij} – reversed plasticity condition: no incremental growth.

Fig. 6 Schematic respresentation of material shakedown conditions

component σ^θ_{ij} will be close to the linear elastic solution, but for large fluctuations where condition (*b*) operates, a cyclic stress history will result that lies somewhere between the prediction of perfect plasticity and linear elasticity. It was argued in Section 2 that the assumption of linear elasticity, the completely hardened state, would provide the smallest F region and hence we adopt the following simplifying assumption:

Assumption 2: The Cyclic Stress History

The steady state cyclic stress history has the form

$$\sigma^\theta_{ij} = \hat{\sigma}^\theta_{ij},$$

$\hat{\sigma}^\theta_{ij}(t)$ *is the linear elastic stress history. In all these arguments we ignore, for simplicity, the effect of temperature on the elastic moduli.*

By this means we are not required to know the cyclic material behavior.

The shakedown theorems are now concerned with defining those states of loading for which, in the asymptotic state, no incremental growth of the structure will occur. When the maximum effective thermoelastic stress $\sigma_t \leq 2\sigma_y$ then the theory is identical to classical shakedown theory and shakedown occurs provided there exists a constant residual stress field $\bar{\rho}_{ij}$ so that $\phi(\sigma^*_{ij}(t)) \leq \sigma_y$. However, when $\sigma_t > 2\sigma_y$ we need to use the extended material shakedown Assumption 1(*b*).

The total volume V may be subdivided into two subvolumes; V_S where the history $\sigma_t \leq 2\sigma_y$, so that $\hat{\sigma}^\theta_{ij}$ may, by a rigid body translation in stress space, be contained within the yield surface, and V_F where $\sigma_t > 2\sigma_y$ and where reverse plasticity occurs.

A particular form of the residual stress field $\bar{\rho}_{ij}$ may now be chosen, so that in V_F

$$\bar{\rho}_{ij} = -\frac{1}{2}(\hat{\sigma}^\theta_{ij})^{\max} + \rho^0_{ij} \tag{10}$$

where $(\hat{\sigma}^\theta_{ij})^{\max}$ denotes the value of stress that maximizes $\phi(\hat{\sigma}^\theta_{ij})$, and ρ^0_{ij} an arbitrary stress field in V that ensures that $\bar{\rho}_{ij}$ satisfies the equations of equilibrium.

The total stress history (9) now has the form

$$\sigma^*_{ij} = \bar{\sigma}^\theta_{ij}(t) + \lambda\hat{\sigma}^p_{ij} + \rho^0_{ij} \tag{11}$$

where

$$\bar{\sigma}^\theta_{ij} = \left\{\hat{\sigma}^\theta_{ij}(t) - \frac{1}{2}(\hat{\sigma}^\theta_{ij})^{\max}\right\} \quad \text{in} \quad V_F$$

The condition (*b*) of Assumption (1) is satisfied in volume V_F provided the stress distribution $\sigma^p_{ij} = \lambda\hat{\sigma}^p_{ij} + \rho^0_{ij}$ is either a purely hydrostatic state of stress or zero. For plane stress states, our main concern here, this generally requires that $\sigma^p_{ij} = 0$ within V_F. The problem now reduces to a shakedown problem with V_s. Hence:

Shakedown of the structure will occur if an arbitrary stress field $\sigma^p_{ij} = \lambda\hat{\sigma}^p_{ij} + \rho^0_{ij}$ *exists which satisfies*

(1) $\sigma^p_{ij} = 0$ within V_F

(2) $\phi(\sigma^*_{ij}) \leq \sigma_y$ within V_s, where σ^*_{ij} is given by equation (11).

We will see that the restriction (1) provides the essential step in distinguishing between differing types of thermal loading problems.

For stationary quasistatic loading ρ^0_{ij} is a residual stress field, and condition (2) reduces to the requirement that shakedown should occur in the body with V_F removed and $\hat{\sigma}^\theta_{ij}$ replaced by $\bar{\sigma}^\theta_{ij}$ in the remaining volume V_s.

An important corollary to this result is that the shakedown condition can only be satisfied if there exists regions of V_s capable of transmitting the loads λP_i through the structure. If V_F contains a mechanism of deformation (by, for example, including an entire cross section of the structure which may be activated by the load λP_i), then shakedown will *not* occur once the reverse plasticity condition has been exceeded and this property distinguishes between the existence and nonexistence of an F region. Hence:

No F region exists if, from general equilibrium consideration, components of the applied load λP_i *are transmitted through the volume* V_F.

If a value of λ can be found so that these conditions are satisfied we have constructed a possible asymptotic shakedown state consistent with our material shakedown conditions. In classical shakedown theory the construction of a residual stress field $\bar{\rho}_{ij}$ so that $\hat{\sigma}_{ij} + \bar{\rho}_{ij}$ satisfies yield, guarantees that shakedown will occur. In the present context no such firm result is possible. In constructing this extended form we may only show that: provided complete cyclic hardening occurs in V_F and, as a result, the stress history is determinate by the Assumpiton 1(*b*), then shakedown would occur in the volume V_s if the material in this region were perfectly plastic. An alternative interpretation has been given in [7] where a condition of nonmaterial ratchetting is guaranteed for a certain class of simple equations that describe the long term strain growth of hardening materials due to a cyclic stress history. In the absence of a proper constitutive equation that adequately describes the cyclic behavior of strain hardening metals, it would appear that no firmer result is possible.

Downloaded 02 May 2010 to 171.66.16.54. Redistribution subject to ASME license or copyright; see http://www.asme.org/terms/Terms_Use.cfm

4 Conclusions

The paper is concerned with an attempt to derive simple procedures for distinguishing between structural problems involving substantial thermal loading where structural ratchetting can occur at moderate levels of thermal loading from those where very high levels of thermal loading may be tolerated. This is achieved by deriving an extension of the classical shakedown theory to allow a state of plastic shakedown for a fully cyclically hardening material. Through the discussion of a simple two-bar structure and comparison with experimental results it is shown that a conservative estimate of the boundary between plastic shakedown (where the primary loads are carried through an elastic shakedown region) and ratchetting region can be found by overestimating the cyclic hardening of the material.

The resulting theory does not contain the internal consistency of classical shakedown theory; it does yield a very simple procedure for identifying circumstances where thermal stresses are a potential source of structural ratchetting (in constrast to reverse plasticity which may only be a source of fatigue failure). If the regions of the structure that suffers high levels of thermoelastic stress are such that the primary load cannot be carried by other parts of the structure, then ratchetting can be expected at low levels of primary load. It is interesting to note that the theory places emphasis on the distribution of the volume of material that suffers high levels of thermoelastic stress. The design codes do not, explicitly, make any such distinction although it might be argued that the definition of stress categories includes some elements of such a distinction.

In an accompanying paper [2] a sequence of examples are given, representative of Fast Reactor problems.

References

1 Bree, J., "Elastic-Plastic Behavior of Thin Tubes Subjected to Internal Pressure and Intermittent High Heat Fluxes With Application to Fast Nuclear-Reactor Fuel Elements," *J. Strain Analysis*, Vol. 2, No. 3, 1967, pp. 226–238.

2 Ponter, A. R. S., and Karadeniz, S., "An Extended Theory for Structures that Suffer Cyclic Thermal Loading," Part 2: Applications," ASME JOURNAL OF APPLIED MECHANICS, Vol. 52, 1985, pp. 00–00.

3 Megahed, M. M., "Influence of Hardening Rules on the Elasto-Plastic Behavior of a Simple Structure Under Cyclic Loading," *Int. J. Mech. Sci.*, Vol. 23, 1981, pp. 169–182.

4 Mulcahy, T. M., "Thermal Ratchetting of a Beam Element Having an Idealized Bauschinger Effect," ASME *Journal of Engineering Materials and Technology*, Vol. 96, 1976, pp. 264–271.

5 Karadeniz, S., and Ponter, A. R. S., "The Influnce of Transient Thermal Loading on the Bree Plate; A Simplified Method of Analysis," *Journal of Nuclear Engineering and Design*, Vol. 80, 1984, pp. 359–374.

6 Goodman, A. M., "The Influence of Rapid Thermal Transients on Elastic-Plastic Ratchetting," CEGB, Berkeley Nuclear Laboratories Report No. RD/B/N/4492, 1979.

7 Ponter, A. R. S., "Shakedown and Ratchetting Below the Creep Range," Commission of the European Communities, Nuclear Science and Technology, Directorate-General for Science, Research and Development, Report EUR 8702EN, Office for Official Publications of the European Communities, Luxembourg, 1983.

8 Pellissier-Tenon, A., Rabbi, P., and Arnzallog, C., "Defining a Proper Material Characteristic for the Shakedown Analysis," ASME *3rd Int. Conference on Pressure Vessel Technology*, Tokyo, 1977.

Downloaded 02 May 2010 to 171.66.16.54. Redistribution subject to ASME license or copyright; see http://www.asme.org/terms/Terms_Use.cfm

An Extended Shakedown Theory for Structures That Suffer Cyclic Thermal Loading

Part 2: Applications

A. R. S. Ponter
Professor of Engineering,
Leicester University,
Leicester LE1 7RH, England

S. Karadeniz
Assistant Professor,
Faculty of Engineering,
University of Erciyes,
Kayseri, Turkey

In an accompanying paper an extended shakedown theory was described for structures subjected to constant mechanical loads and cyclically varying thermal loads, a circumstance of interest in Fast Reactor design. In this paper the upper bound theorem is used to construct interactive diagrams for a sequence of sample problems. These examples imply that for many shell problems, where the temperature variations occur along the surface, ratchetting occurs in two distinct ways. For low thermal loading the structure deforms in the same mechanism that occurs at plastic collapse when only the mechanical loads are applied. For high levels of thermal loading the mechanism changes to a local concentration of strain. This behavior differs significantly from that of the Bree problem. In one example this mechanism involves through-thickness shear deformation of a plate; as a consequence the use of thin shell theory which ignores shear deformation in numerical solutions of problems of this type is likely to result in nonconservative estimates of inelastic deformations.

1 Introduction

In an accompanying paper [1] an extended shakedown theory is presented which allows an estimate of the ratchet limit, i.e., both the elastic and plastic shakedown limits, for a structure subject to constant mechanical load and thermal cycling. The plastic shakedown limit is defined by a material ratchetting criteria which allows the possibility that within a part of the volume V_F of the structure the stresses may exceed yield at the extremes of the load cycle, but this volume is attached to material where the stress history lies within yield. By this means elastic shakedown and plastic shakedown may be considered together. The theory has not been developed to the same level of generality as classical shakedown theory, and a simplifying assumption has been introduced, that complete cyclic hardening of the material occurs in V_F, which appears from the study of particular cases to yield a conservative estimate of the ratchet limit.

The purpose of the development of the theory is to provide a means of understanding the important features of the behavior of structures that are subjected to constant mechanical load and cycles of temperature gradient. This problem is of particular importance for Fast Reactor design where the thermal stresses can be very large but the dead load stresses are quite moderate. It is clear that the response of individual structural components can vary considerably depending on the form of the spacial variation of the temperature field. The classic Bree problem [2] of a plate subject to in-plane constant stresses and a fluctuating through-thickness temperature distribution is an example where, for small in-plane stresses, very large thermal stresses may be tolerated without causing cyclic strain growth. This particular solution in the form of the Bree diagram provides the basis of a section of the ASME III design code for nuclear structures. The breadth of applicability of the Bree diagram has never been clear and there has been a tendancy to use it in circumstances that differ markedly from the particular loading situation for which it was developed.

2 The Extended Shakedown Theory

The extension described in [1] is concerned with loading sequences for a structure subject to loads λP_i and a temperature history $\theta(\mathbf{x}, t)$ where for $\lambda = 0$, the shakedown limit has been exceeded. At shakedown the thermoelastic stress history $\hat{\sigma}^{\theta}_{ij}(\mathbf{x}, t)$ is such that there exists a constant residual stress field $\bar{\rho}_{ij}$, such that the stress history

$$\sigma^{*}_{ij} = \hat{\sigma}^{\theta}_{ij} + \bar{\rho}_{ij} \tag{1}$$

lies within yield, given by

$$\phi(\sigma^{*}_{ij}) \leq \sigma_y \tag{2}$$

where σ_y is a uniaxial yield stress and ϕ the yield function, homogeneous of degree unity. Therefore, there will generally exist some volume V_F within which $\hat{\sigma}^{\theta}_{ij}$ cannot be contained

Contributed by the Applied Mechanics Division for publication in the JOURNAL OF APPLIED MECHANICS.
Discussion on this paper should be addressed to the Editorial Department, ASME, United Engineering Center, 345 East 47th Stret, New York, N.Y. 10017, and will be accepted until two months after final publication of the paper itself in the JOURNAL OF APPLIED MECHANICS. Manuscript received by ASME Applied Mechanics Division, September, 1983; final revision, October, 1984.

Copyright © 1985 by ASME
Downloaded 02 May 2010 to 171.66.16.54. Redistribution subject to ASME license or copyright; see http://www.asme.org/terms/Terms_Use.cfm

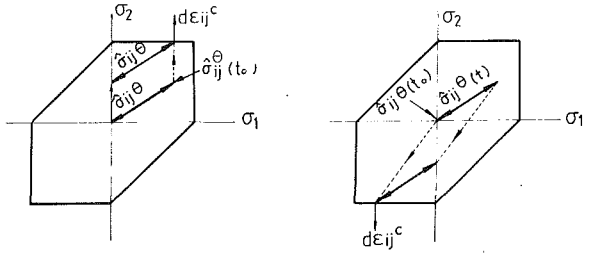


Fig. 1 The definition of t_0: for a prescribed $d\epsilon_{ij}^c$, $\hat{\sigma}_{ij}^{\theta}(t_0)$ contacts the limit surface at the stress point associated with $d\epsilon_{ij}^c$ when the stress trajectory $\hat{\sigma}_{ij}^{\theta}(t)$ is given a rigid body translation in stress space

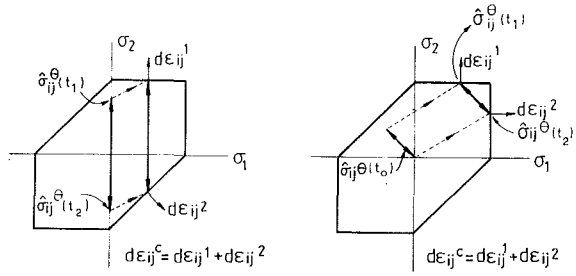


Fig. 2 The definition of t_1 and t_2 on the limit surface touched by the extremes of the translated thermoelastic stress history

within the yield surface by a rigid body translation in stress space. We assume that $\hat{\sigma}_{ij}^{\theta}$ traces a near linear path in stress space. The assessment of the loads λP_i which may now be applied to the structure without inducing ratchetting involves two steps; a residual stress field $\bar{\rho}_{ij}$ is first identified so that

$$\bar{\sigma}_{ij}^{\theta} = \hat{\sigma}_{ij}^{\theta} + \bar{\rho}_{ij} \tag{3}$$

satisfies the nonratchetting condition

$$\bar{\sigma}_{ij}^{\max} = -\bar{\sigma}_{ij}^{\min}. \tag{4}$$

Then plastic shakedown will take place for loads λP_i if elastic shakedown occurs in the remaining volume of the structure V_S, once V_F has been removed and the thermoelastic stresses are augmented by the residual stress field $\bar{\rho}_{ij}$. Hence we look for the maximum value of λ for which there exists within V_S a residual stress field (which is identically zero in V_F) so that the yield condition

$$\phi(\lambda\hat{\sigma}_{ij}^{P} + \bar{\sigma}_{ij}^{\theta} + \bar{\rho}_{ij}) \le \sigma_y \tag{5}$$

is satisfied in V_S.

For all the examples discussed in this paper the thermoelastic stress history varies between extremes $\hat{\sigma}_{ij}^{\theta}(t_1)$ and $\hat{\sigma}_{ij}^{\theta}(t_2)$ along a straight line path in stress space. The residual stress $\bar{\rho}_{ij}$ may then be identified as

$$\bar{\rho}_{ij} = -1/2(\hat{\sigma}_{ij}^{\theta}(t_1) + \hat{\sigma}_{ij}^{\theta}(t_2)) \tag{6}$$

so that

$$\bar{\sigma}_{ij}^{\max} = 1/2(\hat{\sigma}_{ij}^{\theta}(t_1) - \hat{\sigma}_{ij}^{\theta}(t_2)) = -\bar{\sigma}_{ij}^{\min} \tag{7}$$

3 The Upper Bound Shakedown Theorem

A result, which will be particularly helpful in computing shakedown limits for V_s, comes from a simplified form of the upper bound shakedown theorem [3]. Although lower bound results are more satisfactory as an aid to design, the construction of equilibrium stress fields presents difficulties in all but the simplest cases. The modes of deformation that occur in a structure may, however, be easily guessed in many problems and simple upper bounds may be constructed with greater ease. Further, it is well known that satisfactory estimates of limit loads can be found using upper bound theorems even when the assumed collapse mode differs from the exact solutions. As the extended lower bound theorem is identical to the classical result in the reduced volume V_s, this upper bound must also be an upper bound to the shakedown region for the extended theory, and may be used to bound the regions S and F in the Bree diagram. The upper bound is derived in the Appendix and the final result takes the form:

Upper Bound Shakedown Theorem.

An upper bound to the shakedown region is given by the inequality

$$\int_V D(d\epsilon_{ij}^c)\,dV \ge \lambda\int_{S_p}\{P_i du_i^c\}\,dS + \int_V \hat{\sigma}_{ij}^{\theta}(\mathbf{x},t_0)d\epsilon_{ij}^c dV \tag{8}$$

where $d\epsilon_{ij}^c$ denotes a volume conserving compatible strain field which gives rise to displacements du_i^c which satisfy the boundary conditions on S_u. The energy dissipation term is given by

$$D(d\epsilon_{ij}^c) = \sigma_{ij}^c d\epsilon_{ij}^c \tag{9}$$

where σ_{ij}^c is a state of stress on the yield surface associated with $d\epsilon_{ij}^c$.

The final term involves an instant t_0 during the temperature cycle which may be chosen arbitrarily. The optimal bound, however, requires a $t = t_0$, which, for a prescribed $d\epsilon_{ij}^c$, yields a maximum value to this term at each point of the volume.

$$\hat{\sigma}_{ij}^{\theta}(\mathbf{x},t_0)d\epsilon_{ij}^c \ge \hat{\sigma}_{ij}^{\theta}(\mathbf{x},t)d\epsilon_{ij}^c, \quad 0<t<\Delta t \tag{10}$$

In geometric terms, the condition is illustrated in Figs. 1 and 2. The instant t_0 corresponds to the point on the thermoelastic stress history that touches the limit surface at σ_{ij}^c when the entire cyclic stress history $\hat{\sigma}_{ij}^{\theta}$ is translated in stress space by a rigid body translation, when such a translation is possible. In Fig. 2 a case is shown where no such contact point exists, as a rigid body translation does not allow any part of the stress history to contact the stress σ_{ij}^c on the limit surface. In this case $d\epsilon_{ij}^c$ may be subdivided into two components

$$d\epsilon_{ij}^c = d\epsilon_{ij}^1 + d\epsilon_{ij}^2 \tag{11}$$

which correspond to the points on the limit surface touched by the extremes of the translated thermoelastic stress history, as shown in Fig. 2. The corresponding terms on the two sides of the inequality (8) are now replaced by the sum of the terms corresponding to $d\epsilon_{ij}^1$ and $d\epsilon_{ij}^2$,

$$\hat{\sigma}_{ij}^{\theta}(t_0)d\epsilon_{ij}^c = \hat{\sigma}_{ij}^{\theta}(t_1)d\epsilon_{ij}^1 + \hat{\sigma}_{ij}^{\theta}(t_2)d\epsilon_{ij}^2, \tag{12}$$

$$D = \sigma_{ij}^1 d\epsilon_{ij}^1 + \sigma_{ij}^2 d\epsilon_{ij}^2. \tag{13}$$

Alternatively, the mean value $\tilde{\sigma}_{ij}^{\theta}(t)$ may be used (the derivative is given in the Appendix) and the corresponding terms become,

$$\hat{\sigma}_{ij}^{\theta}(t_0)d\epsilon_{ij}^c = \tilde{\sigma}_{ij}^{\theta}d\epsilon_{ij}^c, \quad D = \tilde{\sigma}_{ij}^c d\epsilon_{ij}^c, \tag{14}$$

$$\tilde{\sigma}_{ij}^{\theta} = (\hat{\sigma}_{ij}^{\theta}(t_1) + \hat{\sigma}_{ij}^{\theta}(t_2))/2, \tag{15}$$

and

$$\tilde{\sigma}_{ij}^c = (\sigma_{ij}^1 + \sigma_{ij}^2)/2 \tag{16}$$

4 Application of Shakedown Theorems to Particular Problems

The theory described in the preceding section may be used to estimate the boundaries of the F and S regions, provided the mechanisms of collapse of the structure are known. In this section we discuss four problems of increasing complexity. The first two are kinematically determinate and the solutions are exact. The last two are well-known problems where the mechanisms of plastic collapse without thermal cycling are known, and these are used to estimate an upper bound on the boundary of the elastic shakedown region. In addition, local failure modes are identified which operate when the applied load is small. These calculations tend to indicate that for many plate and shell like structures the F region does not exist and the modes of collapse are of two types, a general mode

Downloaded 02 May 2010 to 171.66.16.54. Redistribution subject to ASME license or copyright; see http://www.asme.org/terms/Terms_Use.cfm

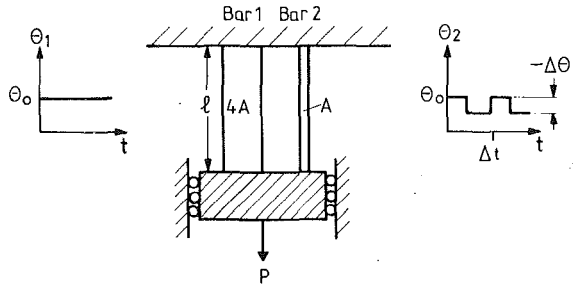


Fig. 3(a) The structure and loading

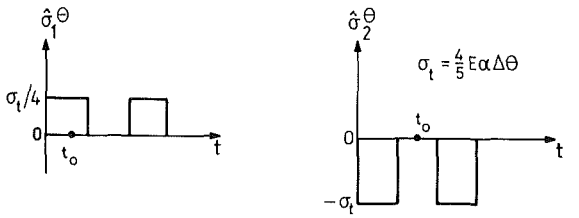


Fig. 3(b) The thermoelastic stress history and t_0 for each bar

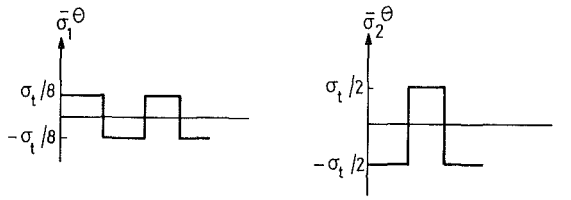


Fig. 3(c) $\bar{\sigma}^\theta = \hat{\sigma}^\theta - 1/2\,(\hat{\sigma}^\vartheta)^{\text{manc}}$ for calculation of *F* region boundary

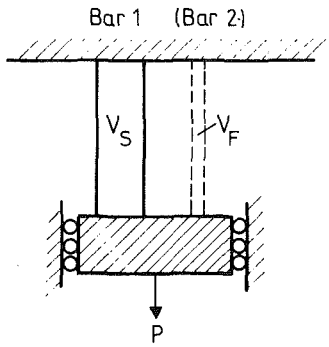


Fig. 3(d) Reduced structure for evaluation of boundary between regions *F* and *R*

Fig. 3 Two-bar structure

identical to the plastic collapse mode and a local mode that is activated when the applied load is small. These local modes, which are contained within the volume V_F and are easily identified, are of principal interest in Fast Reactor design.

(a) A Two-Bar Structure. As an introductory example, the two-bar structure discussed in the accompanying paper [1] will be analyzed. The geometry and thermal loading history are shown in Fig. 3(*a*) and the thermoelastic stress histories are shown in Fig. 3(*b*). The general form of the bound (8) for a two-bar structure is

$$V_1\sigma_y d\epsilon_1^c + V_2\sigma_y d\epsilon_2^c \geq P du^c + \hat{\sigma}_1^\theta(t_0)d\epsilon_1^c V_1 + \hat{\sigma}_2^\theta(t_0)d\epsilon_2^c V_2 \quad (17)$$

where V_1 and V_2 are the material volumes of the two bars. The compatible strains are unique for the problem (implying equality in (17)) and are related by,

$$d\epsilon_1^c = d\epsilon_2^c = \frac{du^c}{l} \quad (18)$$

The thermoelastic stress histories are shown in Fig. 3(*b*) and the values required in (17) are the maximum values:

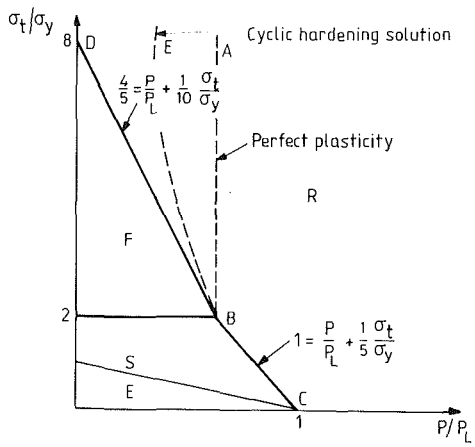


Fig. 4 Ratchet boundaries for two-bar structure. Note that the perfectly plastic solution for the *F-R* boundary is nonconservative.

$$\hat{\sigma}_1^\theta(t_0) = \frac{1}{4}\sigma_t, \quad \hat{\sigma}_2^\theta(t_0) = 0, \quad \sigma_t = \frac{4}{5}E\alpha\Delta\theta.$$

Substituting into (17) and noting that $P_L = 5A\sigma_y$, gives the shakedown limit for $\sigma_t < 2\sigma_y$:

$$1 = \frac{P}{P_L} + \frac{1}{5}\frac{\sigma_t}{\sigma_y} \quad (19)$$

For $\sigma_t > 2\sigma_y$, the thermoelastic stress history is replaced by the history $\bar{\sigma}_1^\theta$ of (3) and (6) as shown in Fig. 3(*c*). The volume V_F where $\Delta\hat{\sigma}_2^\theta > 2\sigma_y$ consists of the volume of Bar 2. Hence the shakedown limit becomes that of the single-bar structure of Fig. 3(*d*) and the bound (17) becomes

$$4Al\sigma_y d\epsilon_1^c > P du^c + 4Al(\sigma_t/8)d\epsilon_1^c, \quad (20)$$

or

$$\frac{4}{5} = \frac{P}{P_L} + \frac{1}{10}\frac{\sigma_t}{\sigma_y}. \quad (21)$$

The shakedown boundaries are shown in Fig. 4 together with the perfectly plastic solution and a solution based on the cyclic hardening curve for the tests on 316 reported in [1]. The result (21) gives a lower bound to these solutions due to the assumption of complete cyclic hardening. Note that the perfectly plastic solution is definitely unsafe.

(b) The Bree Plate [2]. A plate of thickness h is subjected to a linear temperature difference through the thickness which varies between $\Delta\theta$ for $0 < t < \Delta t/2$ and zero for $\Delta t/2 < t < \Delta t$. In the inplane direction x an average stress of σ_p is applied and deformation is restrained in the orthogonal inplane direction y. The distribution of strain is given by

$$d\epsilon_x = d\epsilon = \text{constant}, \quad d\epsilon_y = 0, \quad d\epsilon_z = -d\epsilon$$

The thermoelastic stress history is given by

$$\hat{\sigma}_x^\theta = \sigma_t(1 - 2z/h), \quad 0 < t < \frac{\Delta t}{2}$$

$$= 0 \quad , \quad \frac{\Delta t}{2} < t < \Delta t$$

Hence the thermoelastic stress at time t_0, $\hat{\sigma}_x(t_0)$ in the bound (8), is illustrated in Fig. 5 and given by,

$$\hat{\sigma}_x^\theta(t_0) = \sigma_t(1 - 2z/h), \quad 0 < z < h/2$$

$$= 0 \quad , \quad h/2 < z < h \quad (22)$$

where

$$\sigma_t = \frac{E\alpha\Delta\theta}{2(1-\nu)}$$

Substituting these values into the bound (8) yields, per unit area of plate,

Downloaded 02 May 2010 to 171.66.16.54. Redistribution subject to ASME license or copyright; see http://www.asme.org/terms/Terms_Use.cfm

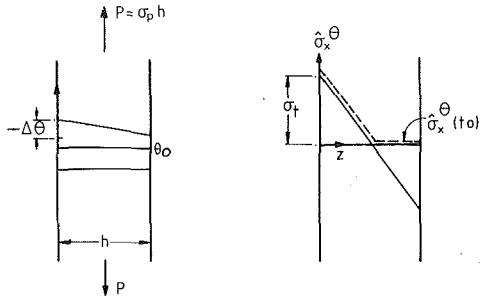


Fig. 5 The Bree problem for $\sigma_t < 2\sigma_y$

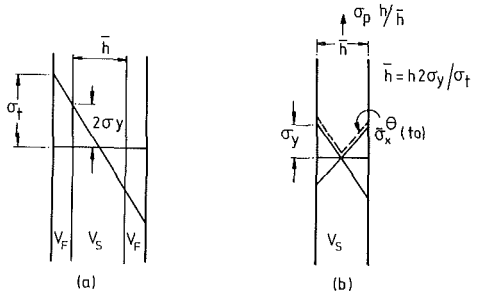


Fig. 6 The Bree problem for $\sigma_t > 2\sigma_y$. (*a*) the definition of V_F and V_S and (*b*) the reduced structure for evaluation of *F*-*R* boundary.

$$h\ \sigma_y d\epsilon = h\ \sigma_p d\epsilon + \left\{ \int_0^h \hat{\sigma}_x^\theta(t_0) dz \right\} d\epsilon \tag{23}$$

i.e.,

$$\sigma_y = \sigma_p + \sigma_t/4.$$

Equality holds in (23) as the problem is kinematically determinate. When the maximum thermoelastic stress exceeds $2\sigma_y$, the volume V_s consists of a plate of thickness $\bar{h} = h\,(2\sigma_y)/\sigma_t$ as shown in Fig. 6. For this reduced problem, the shakedown limit is given by (23) with an increased value of σ_p which must be carried in V_s and $\bar{\sigma}_x^\theta$ replacing $\hat{\sigma}_x^\theta$:

$$\begin{aligned} \bar{\sigma}_x^\theta &= \frac{1}{2}\sigma_t(1-2z/h), && \frac{h-\bar{h}}{2} < z < \frac{h}{2} \\ &= -\frac{1}{2}\sigma_t(1-2z/h), && \frac{h}{2} < z < \frac{h+\bar{h}}{2} \end{aligned} \tag{24}$$

Hence equation (8) becomes, when applied to V_s (see Fig. 6)

$$\sigma_y d\epsilon \bar{h} = \sigma_p \left(\frac{\sigma_t}{2\sigma_y}\right) \bar{h} + \left\{ \int_{\frac{h-\bar{h}}{2}}^{\frac{h+\bar{h}}{2}} \bar{\sigma}_x^\theta dz \right\}$$

i.e.,

$$\sigma_y = \sigma_p \left(\frac{\sigma_t}{2\sigma_y}\right) + \frac{2\sigma_y}{4}$$

or

$$\sigma_y = \sqrt{\sigma_p \sigma_t} \tag{25}$$

Equation (25) is identical to the classical perfectly plastic solution.

For the more general Bree problem when arbitrary average stress σ_1^p and σ_2^p are applied, the analysis requires a strain field involving $d\epsilon_1^c$ and $d\epsilon_2^c$, independent of z and $d\epsilon_z^c = -1/2\,(d\epsilon_1^c + d\epsilon_2^c)$. The bound (8) may then be optimized with respect to the ratio $d\epsilon_1^c/d\epsilon_2^c$ to give the exact solution. The derivation is not given here, but the solution has the following simple form for a Tresca yield condition when σ_1^p and σ_2^p have the same sign:

$$\phi(\sigma_1, \sigma_2) = \sigma_y$$

where

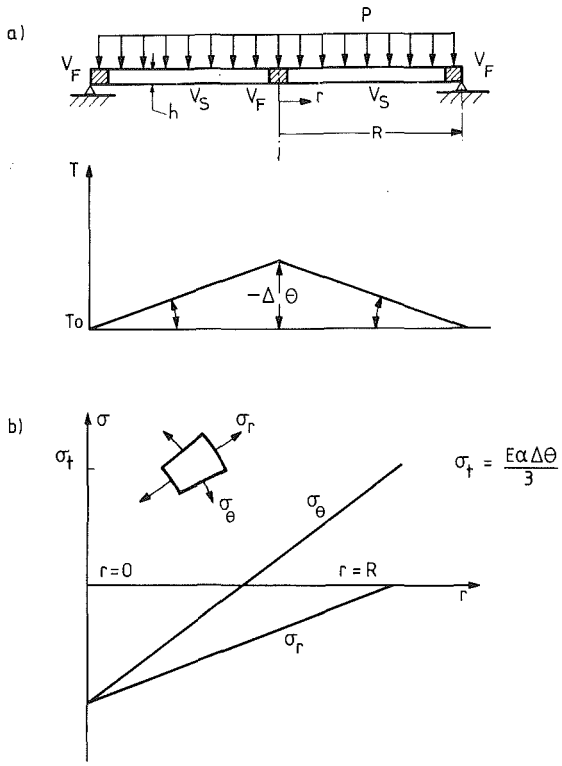


Fig. 7 Circular plate with lateral pressure *P* and linear radial temperature gradient: (*a*) The geometry and (*b*) The thermoelastic solution

$$\left.\begin{aligned} \sigma_1 &= \sigma_1^p + \sigma_t/4 \\ \sigma_2 &= \sigma_2^p + \sigma_t/4 \end{aligned}\right\} \quad \text{for} \quad \sigma_t < 2\sigma_y$$

$$\left.\begin{aligned} \sigma_1 &= (\sigma_1^p \sigma_t + \sigma_y^2)/2\sigma_y \\ \sigma_2 &= (\sigma_2^p \sigma_t + \sigma_y^2)/2\sigma_y \end{aligned}\right\} \quad \text{for} \quad \sigma_t > 2\sigma_y, \tag{26}$$

where

$$\phi(\sigma_1, \sigma_2) = \sigma_I - \sigma_{III}, \quad \sigma_I > \sigma_{II} > \sigma_{III}$$

where σ_I, σ_{II}, and σ_{III} are the principal stresses and

$$\sigma_t = \frac{E\alpha\Delta\theta}{2(1-\nu)}.$$

Hence the solution reduces to the problem of the limit load of a plate, subjected to monotonically increasing orthogonal stress components σ_1 and σ_2.

(*c*) Simply Supported Circular Plate. A circular plate of radius R and thickness h is simply supported around its edge and subjected to a uniform lateral pressure P. A linear radial temperature distribution is imposed cyclically, as shown in Fig. 7(*a*).

The inplane thermoelastic solution is shown in Fig. 7(*b*). For a Tresca yield condition the collapse mechanism for P applied alone [4] consists of a conical deformation pattern (Mechanism *A*) where the increments of curvature are given by

$$d\kappa_\theta = \text{constant}, \quad d\kappa_r = 0, \tag{27}$$

and the limit pressure is given by

$$P_L = \frac{3}{2}\frac{h^2}{R^2}\sigma_y. \tag{28}$$

This mechanism produces, for $\sigma_t < 2\sigma_y$, the upper bound

$$1 = \frac{P}{P_L} + \frac{\sigma_t}{4\sigma_y}. \tag{29}$$

For $\sigma_t > 2\sigma_y$, the volume V_F consists of two regions of the

Downloaded 02 May 2010 to 171.66.16.54. Redistribution subject to ASME license or copyright; see http://www.asme.org/terms/Terms_Use.cfm

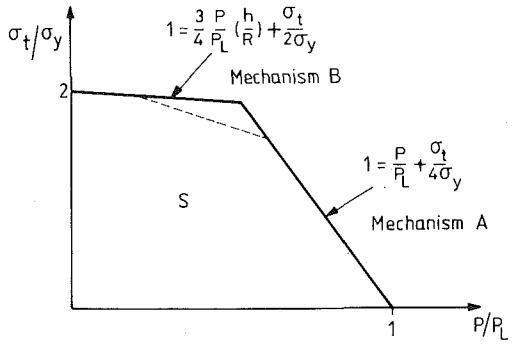


Fig. 8 The Bree diagram for the plate problem of Fig. 7. Note that no *F* region exists as volume V_F shown in (*a*) contains a mechanism that may be activated by *P*.

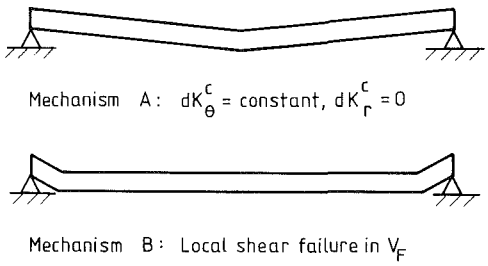


Fig. 9 Collapse mechanism associated with the boundaries of Fig. 2

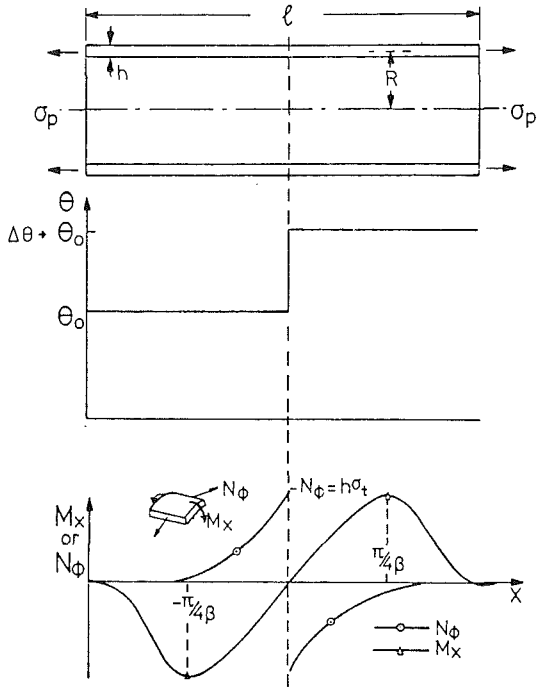


Fig. 10 Thermoelastic stress distribution in the vicinity of a temperature front that moves along the tube

plate, a circular annulus at the periphery and a central area. Both of these volumes contain a mechanism and hence there exists no *F* region. A collapse mechanism *B*, consisting of a local shear mechanism at the support, yields the upper bound

$$1=\frac{3}{4}\frac{P}{P_L}\left(\frac{h}{R}\right)+\frac{\sigma_y}{2\sigma_y} \tag{30}$$

It is important to note that mechanism *B* would not be found from a numerical solution of shell equations, which considered only the curvature and inplane stretching of a plate element. The resulting Bree diagram and the associated mechanisms are shown in Figs. 8 and 9.

The shakedown boundary formed by equations (29) and (30) is an upper bound. Cocks [5] has shown that it is exact, except possibly near the point of intersection of the two lines. A lower bound is given by the dotted line shown in Fig. 8.

(*d*) *Tube Subjected to Axial Stress σ^p and a Temperature Discontinuity $\Delta\theta$ That Moves a Short Distance ΔX.* If a temperature difference $\Delta\theta$ travels, repeatedly in alternating directions, along a length of tube that is very short compared with a characteristic decay length of the thermoelastic solution then the problem is referred to as the short travel problem. The thermoelastic distribution in the vicinity of the temperature front is shown in Fig. 10, [6]. For small $\Delta\theta$ the optimal mechanism (*A*) consists of the collapse mechanism for σ^p acting alone, i.e., a uniform strain field throughout the tube. For sufficiently small travel distance ΔX the bound is given, to first order, by

$$\sigma^p=\sigma_y \quad \text{for} \quad 0<\sigma_t<\frac{\sigma_y}{2},\sigma_t=\frac{E\alpha\Delta\theta}{2}. \tag{31}$$

For this range of $\Delta\theta$ the identification of t_0 within the traversed region is shown in Fig. 11(*b*). For the complete calculation, identification of t_0 must be carried out for the entire length of tube, and it is found that the last term in (8) is vanishingly small for small ΔX.

For larger values of $\Delta\theta$, the optimal mechanism (*B*) consists of a local strain field in the region $-\Delta X/2 < x < \Delta X/2$. As t_0 cannot be identified at a unique point of the thermoelastic history, $d\epsilon^c_{ij}$ is decomposed into two components that correspond to the extremes of $\hat{\sigma}^\theta_{ij}$. The construction is shown schematically in Fig. 11(*c*), and the corresponding upper bound produces the exact solution,

$$3/4(\sigma^p)^2+\sigma_t^2=\sigma_y^2. \tag{32}$$

For $\sigma_t > \sigma_y$, the volume V_F consists of a hoop of the tube contained within $-\Delta X/2 < x < \Delta X/2$. As a result, no *F* region exists, as the removal of this volume will not allow the transmission of σ^p between the ends of the tube, i.e., the volume V_F contains a mechanism, axial extension, which may be activated by σ^p.

5 Conclusions

Examples given in this paper allow a classification of thermal loading problems for structures subject to constant mechanical load into two broad categories. The first group, which includes the classic Bree problems, may suffer very large variations in the thermoelastic stress without danger of structural ratchetting. There exists some region of the structure after V_F has been removed through which the mechanical loads can be carried, i.e., there exists a *F* region above the classical shakedown limit. For the second group, no such region exists and a localized cyclic plastic failure mechanism is activated at the reverse plasticity limit even when applied loads are small. In all cases studied the mechanism associated with the ratchet limit consists of either the global mechanism associated with plastic collapse or a local mechanism activated in the volume of material where the thermoelastic stresses are largest. These local mechanisms are easily identified.

Although the theory, on which these calculations are based [1], does not contain the internal consistency of classical shakedown theory it does indicate a means by which structural response to thermal loading may be understood without recourse to a complete inelastic analysis.

The theory of the accompanying paper [1] and this paper

Downloaded 02 May 2010 to 171.66.16.54. Redistribution subject to ASME license or copyright; see http://www.asme.org/terms/Terms_Use.cfm

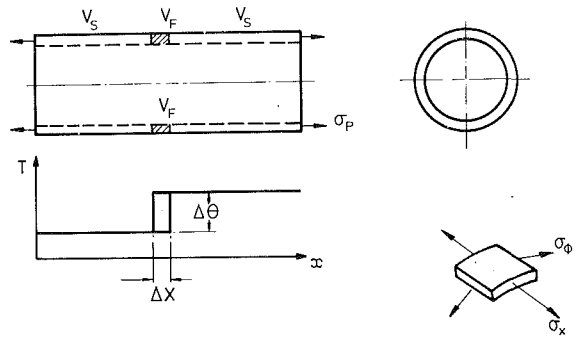


Fig. 11(*a*) Tube subjected to axial stress σ_p with temperature discontinuity traveling a short distance

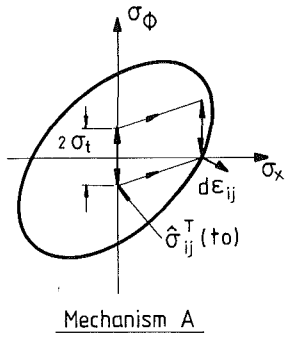


Fig. 11(*b*) For $\sigma_t < \sigma_y/2$, strain field is constant along entire length of tube

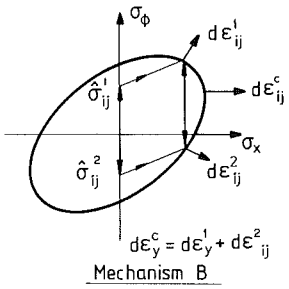


Fig. 11(*c*) For $\sigma_t > \sigma_y/2$ a local mechanism occurs in *V*

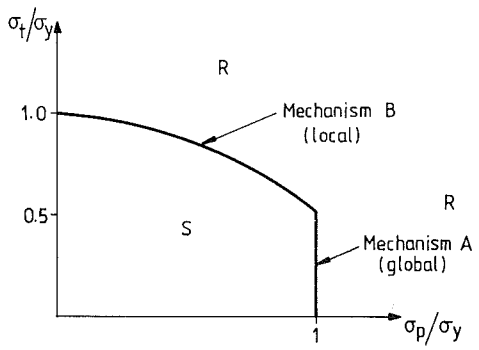


Fig. 11(*d*) Bree diagram for tube problem of Fig. 11(*a*). No *F* region exists as volume V_F contains a mechanism.

Fig. 11

provides the following conclusion concerning the effect of thermal stresses on structures.

(*a*) The use of perfect plasticity can yield a non-conservative estimate of the boundary between plastic shakedown and ratchetting regimes.

(*b*) The Bree problem is not representative of shell thermal loading problems. Where temperature differences occur along the midplane of a shell, ratchetting is much more likely to occur for low levels of primary load. The last two examples in the paper demonstrate this feature.

(*c*) In an example of a circular plate the local mechanism involved through thickness shearing of a plate element. Thin shell theory would not indicate such a mechanism and hence many finite element codes would yield an erroneous solution to this problem.

It becomes clear from these discussions that the performance of structures subjected to this type of loading is by no means well understood. The cyclic properties of the material need to be modeled more exactly than the simpler material models currently in use, and great caution must be exercised when finite element methods are used, particularly as the high-temperature design code case N47 places considerable emphasis on the use of full inelastic analysis.

The method described in this paper has been extended to the solution of cylinder problems using a finite element method [7] and to the transient Bree problem [8]. The rate of ratchet outside shakedown for a perfectly plastic material has been studied by Ponter and Cocks [9, 10].

References

1 Ponter, A. R. S., and Karadeniz, S., "An Extended Shakedown Theory for Structures That Suffer Cyclic Thermal Loading Part 1: Theory," ASME Journal of Applied Mechanics, Vol. 52, 1985, pp. 00–00.

2 Bree, J., "Elastic-Plastic Behavior of Thin Tubes Subjected to Internal Pressure and Intermittent High Heat Fluxes With Application to Fast Nuclear-Reactor Fuel Elements," *J. Strain Analysis*, Vol. 2, No. 3, 1967, pp. 226–238.

3 Koiter, W. T., "General Theorems for Elastic-Plastic Solids," *Progress in Solid Mechanics*, 2nd Ed., Hill, R., and Sneddon, I., eds., North Holland, Amsterdam, Vol. 2, 1964, pp. 167–219.

4 Hodge, P. G., *Limit Analysis of Rotationally Symmetric Plates and Shells*, Prentice-Hall, Englewood Cliffs, N.J. 1963.

5 Cocks, A. C. F., "Lower Bound Shakedown Analysis of a Simply Supported Plate Carrying a Uniformly Distributed Load and Subjected to Cyclic Thermal Loading," University of Leicester, Department of Engineering, Report No. 82-14, 1982.

6 Goodman, A. M., "The Influence of Rapid Thermal Transients on Elastic-Plastic Ratchetting," CEGB, Berkeley Nuclear Laboratories, Report No. RD/B/N 4492, 1979.

7 Ponter, A. R. S., and Karadeniz, S., "A Linear Programming Upper Bound Approach to the Shakedown Limit of Thin Shells Subjected to Variable Thermal Loading," *Journal of Strain Analysis*, Vol. 19, No. 4, 1984, pp. 221–229.

8 Ponter, A. R. S., and Karadeniz, S., "The Influence of Transient Thermal Loading on the Bree Plate, A Simplified Method of Anlaysis," *Nuclear Engineering and Design*, Vol. 80, 1984, pp. 359–374.

9 Ponter, A. R. S., and Cocks, A. C. F., "The Incremented Strain Growth of an Elastic-Plastic Body Loaded in Excess of the Shakedown Limit," ASME Journal of Applied Mechanics, Vol. 51, No. 3, 1984, pp. 465–469.

10 Ponter, A. R. S., and Cocks, A. C. F., "The Incremented Strain Growth of Elastic-Plastic Bodies Subjected to High Levels of Cyclic Thermal Loading," ASME Journal of Applied Mechanics, Vol. 51, No. 3, 1984, pp. 470–474.

APPENDIX

The Upper Bound Theorem for a Perfectly Plastic Material

We assume that the loading history corresponds to a shakedown limit, so that there exists a unique ρ_{ij} (for a strictly convex yield surface) so that

$$\phi(\sigma_{ij}) < \sigma_y \tag{B.1}$$

where

$$\sigma_{ij}(\mathbf{x},t) = \hat{\sigma}_{ij}(\mathbf{x},t) + \rho_{ij}(\mathbf{x}) \tag{B.2}$$

throughout the volume of the material. The maximum work principle may be expressed in the form

$$(\sigma_{ij} - \sigma^c_{ij})\,\dot{\epsilon}^c_{ij} \leq 0 \tag{B.3}$$

where σ^c_{ij} denotes a stress point on the yield surface at which the plastic strain rate $\dot{\epsilon}^c_{ij}$ forms a normal vector. In the most

Downloaded 02 May 2010 to 171.66.16.54. Redistribution subject to ASME license or copyright; see http://www.asme.org/terms/Terms_Use.cfm

general case, consider a history of strain $\dot{\epsilon}^c_{ij}(\mathbf{x}, t)$ that satisfies the conditions that the accumulated plastic strain,

$$d\epsilon^c_{ij} = \int_0^{\Delta t} \dot{\epsilon}^c_{ij}(\mathbf{x},t)\,dt, \tag{B.4}$$

will be compatible and gives rise to a displacement field du^c_i which satisfies displacement boundary conditions.

Identifying σ_{ij} with the shakedown solution (B.2) and integrating (B.3) over the cycle $0 \le t \le \Delta t$ and over the volume V yields the inequality:

$$\int_v D(d\epsilon^c_{ij})\,dV \ge \int_v \int_0^{\Delta t} \sigma^c_{ij}\dot{\epsilon}^c_{ij}\,dt\,dV$$

$$\ge \lambda \int_{S_p} P_i du^c_i\,dS + \int_V \int_0^{\Delta t} \hat{\sigma}^\theta_{ij}\dot{\epsilon}^c_{ij}\,dt\,dV$$

$$+ \int_v \rho_{ij} d\epsilon^c_{ij}\,dV \tag{B.5}$$

From the principle of virtual work the last term in (B.5) is zero, yielding an inequality that is determinate for prescribed $\dot{\epsilon}^c_{ij}(t)$.

For the particular class of elastic stress histories considered here, the times when plastic strain occur must be at the two extremes at $t = t_1$ and $t = t_2$. Hence we may write,

$$d\epsilon^c_{ij} = d\epsilon^1_{ij} + d\epsilon^2_{ij}, \tag{B.6}$$

$$\int_0^{\Delta t} \hat{\sigma}^\theta_{ij}\dot{\epsilon}^c_{ij}\,dt = \hat{\sigma}^\theta_{ij}(t_1)d\epsilon^1_{ij} + \hat{\sigma}^\theta_{ij}(t_2)d\epsilon^2_{ij}, \tag{B.7}$$

and

$$D = \sigma^1_{ij}d\epsilon^1_{ij} + \sigma^2_{ij}d\epsilon^2_{ij} \tag{B.8}$$

where σ^1_{ij} and σ^2_{ij} are the stresses associated with $d\epsilon^1_{ij}$ and $d\epsilon^2_{ij}$ on the yield surface.

Alternatively if we choose the positions of $d\epsilon^1_{ij}$ and $d\epsilon^2_{ij}$ so that $\sigma^1_{ij} - \sigma^2_{ij} = \hat{\sigma}_{ij}(t_1) - \hat{\sigma}_{ij}(t_2) = \Delta\sigma_{ij}$ then the corresponding quantities (17) to (18) is obtained.

Withing the range of possibilities provided by (B.5)–(B.8) for a prescribed $d\epsilon^c_{ij}$ the optimal bound is given by the constructions described in Sections 2–4.

Downloaded 02 May 2010 to 171.66.16.54. Redistribution subject to ASME license or copyright; see http://www.asme.org/terms/Terms_Use.cfm

Free Vibration of a Point-Supported Spherical Shell

T. Irie
G. Yamada
Y. Muramoto

Department of Mechanical Engineering,
Faculty of Engineering,
Hokkaido University,
Sapporo, Japan 060

An analysis is presented for the free vibration of an elastically or a rigidly point-supported spherical shell. For this purpose, the deflection displacements of the shell are written in a series of the products of the associated Legendre functions and the trigonometric functions. The dynamical energies of the shell are evaluated, and the frequency equation is derived by the Ritz method. For a rigidly point-supported shell, the Lagrangian multiplier method is conveniently employed. The method is applied to a closed spherical shell supported at equispaced four points located along a parallel of latitude; the natural frequencies and the mode shapes are calculated numerically, and the effects of the point supports on the vibration are studied.

1 Introduction

This paper presents an analysis of the nonaxisymmetric vibration of a closed spherical shell elastically or rigidly supported at several points located along a parallel of latitude. Recently, spherical shells play an important role in many industrial fields, and therefore vibration problems of these shells have been studied by many researchers. However, there are only a dozen or so papers available on the free vibration of closed spherical shells as follows. The axisymmetric vibration of isotropic shells was studied by Lamb [1], Baker [2], Kalnins [3], Wilkinson [4], Long [5], Johnson [6], and the nonaxisymmetric vibration by Silbiger [7], Shah, et al. [8], and Cohen, et al. [9]. The axisymmetric vibration of orthotropic shells was analyzed by Hoppmann and Baker [10], sandwich or layered shells by Wilkinson [11], Rath and Das [12], and the nonaxisymmetric vibration of layered shells by Shah and Frye [13], and Frye, et al. [14]. However, all of these studies are confined only to unconstrained spherical shells, and no papers have been presented for point-supported spherical shells treated here.

For the purpose of this study, the deflection displacements of a point-supported spherical shell are expressed by a series of the products of the associated Legendre functions and the trigonometric functions. The maximum kinetic and strain energies of the shell based on the Love theory are evaluated analytically, and the frequency equation is derived by the conditions for a stationary value of the Lagrange functional. For an elastically point-supported shell the strain energy of the supports is taken into account, and for a rigidly point-supported shell the Lagrangian multipliers are introduced for expressing unknown reaction forces acting at the supports.

By the application of the method, the natural freqencies (the eigenvalues of vibration) and the mode shapes are calculated numerically for a spherical shell symmetrically supported at equispaced four points, and the results are presented in some figures.

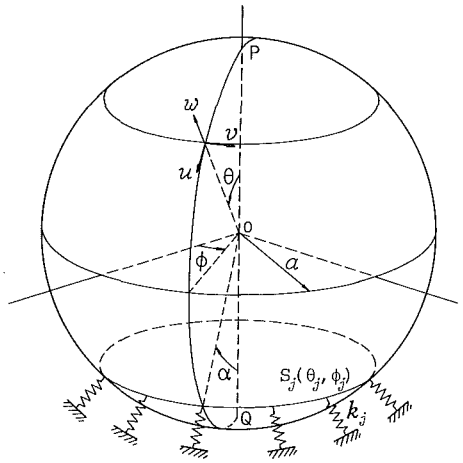


Fig 1 A spherical shell elastically supported at equispaced several points along a parallel of latitude

2 Frequency Equation of Elastically Point-Supported Spherical Shell

Figure 1 shows a thin-walled spherical shell elastically supported at equispace several points located along a parallel of latitude. With the mean radius of the shell denoted by a, spherical coordinates (a, θ, ϕ) are taken as shown in the figure. The maximum kinetic energy of the shell is written as

$$T = \frac{1}{2}\rho h a^2 \omega^2 \int_0^{2\pi} \int_0^{\pi} (u^2 + v^2 + w^2) \sin\theta d\theta d\phi \tag{1}$$

in terms of the deflection displacements u, v, and w in the meridional, latitudinal and radial directions, respectively, where ρ is the mass density, h is the wall thickness, and ω is the frequency in radians/second. Based on the Love theory, the maximum strain energy of the shell is expressed as

$$U_1 = \frac{1}{2}\int_0^{2\pi} \int_0^{\pi} \Big[D\Big\{ (u_{,\theta} + w)^2 + (u\cot\theta + v_{,\phi}\operatorname{cosec}\theta + w)^2$$

Contributed by the Applied Mechanics Division for publication in the JOURNAL OF APPLIED MECHANICS.

Discussion on this paper should be addressed to the Editorial Department, ASME, United Engineering Center, 345 East 47th Street, New York, N.Y. 10017, and will be accepted until two months after final publication of the paper itself in the JOURNAL OF APPLIED MECHANICS. Manuscript received by ASME Applied Mechanics Division, December, 1983; final revision, January, 1985.

Copyright © 1985 by ASME
Downloaded 02 May 2010 to 171.66.16.54. Redistribution subject to ASME license or copyright; see http://www.asme.org/terms/Terms_Use.cfm

$$+2\nu(u_{,\theta}+w)\,(u\cot\theta+v_{,\phi}\operatorname{cosec}\theta+w)$$
$$+\frac{1-\nu}{2}\,(u_{,\phi}\operatorname{cosec}\theta-v\cot\theta+v_{,\theta})^2\Big\}$$
$$+\frac{K}{a^2}\Big\{(u_{,\theta}-w_{,\theta\theta})^2+(u\cot\theta+v_{,\phi}\operatorname{cosec}\theta$$
$$-w_{,\theta}\cot\theta-w_{,\phi\phi}\operatorname{cosec}^2\theta)^2$$
$$+2\nu(u_{,\theta}-w_{,\theta\theta})\,(u\cot\theta+v_{,\phi}\operatorname{cosec}\theta$$
$$-w_{,\theta}\cot\theta-w_{,\phi\phi}\operatorname{cosec}^2\theta)$$
$$+\frac{1-\nu}{2}\,(u_{,\phi}\operatorname{cosec}\theta-v\cot\theta+v_{,\theta}$$
$$+2w_{,\phi}\cot\theta\operatorname{cosec}\theta-2w_{,\theta\phi})^2\Big\}\Big]\sin\theta d\theta d\phi \tag{2}$$

The maximum strain energy of J point supports is written as

$$U_2=\frac{1}{2}\sum_{j=1}^{J}\{k_u u^2(\theta_j,\phi_j)+k_v v^2(\theta_j,\phi_j)$$
$$+k_w w^2(\theta_j,\phi_j)\} \tag{3}$$

were D and K are the extensional and flexural rigidities, respectively, expressed as $D = Eh/(1-\nu^2)$ and $K = Eh^3/12(1-\nu^2)$ in terms of the Young's modulus E, Poisson's, ratio ν, and the wall thickness. The constants k_u, k_v, and k_w are the meridional, latitudinal, and radial stiffnesses of supports, respectively, and (θ_j, ϕ_j) are the coordinates of the supports S_j.

The deflection displacements of the point-supported shell are approximately expressed as

$$u=\sum_{n=1}^{N}\sum_{m=0}^{n}A_{mn}\frac{d}{d\theta}\bar{P}_n^m(\cos\theta)\begin{matrix}\cos\\ \sin\end{matrix}m\phi$$
$$v=\sum_{n=1}^{N}\sum_{m=0}^{n}B_{mn}\frac{\bar{P}_n^m(\cos\theta)}{\sin\theta}\begin{matrix}\sin\\ \cos\end{matrix}m\phi$$
$$w=\sum_{n=1}^{N}\sum_{m=0}^{n}C_{mn}\bar{P}_n^m(\cos\theta)\begin{matrix}\cos\\ \sin\end{matrix}m\phi \tag{4}$$

in terms of the normalized associated Legendre function

$$\bar{P}_n^m(\cos\theta)=\sqrt{\frac{(2n+1)(n-m)!}{2(n+m)!}}P_n^m(\cos\theta)\quad(m\geqq 1) \tag{5}$$

where the integer number m is the wave number of the latitudinal direction. The associated Legendre function is given by the following finite series:

$$P_n^m(\cos\theta)=\frac{\sin^m\theta}{2^m}\sum_{r=0}^{n-m}(-1)^r\frac{(n+m+r)!}{r!\,(m+r)!\,(n-m-r)!}\sin^{2r}\frac{\theta}{2} \tag{6}$$

It is convenient for the numerical calculation to use the normalized function of the numerically same order given in (5). In an unconstrained spherical shell, there are two classes of vibration, one of which is a purely equivoluminal motion called as the first-class vibration, and ther other is coupled membrane-bending vibration called the second-class one. Only the second-class vibration is treated here. Equations (4) present the general solutions to the second-class vibration of a closed spherical shell without any supports. By substituting the equations which are obtained by the substitution of (4) into (1)–(3) into the conditions for a stationary value of the Lagrange functional $L = T - U_1 - U_2$

$$\frac{\partial L}{\partial A_{lk}}=0,\quad \frac{\partial L}{\partial B_{kl}}=0,\quad \frac{\partial L}{\partial C_{kl}}=0$$
$$(l=1,2,\ldots,N;\ k=0,1,2,\ldots,l) \tag{7}$$

the following equations are derived:

$$\begin{bmatrix} U_{mn}^{(kl)}-\Omega^2R_{mn}^{(kl)} & \pm F_{mn}^{(kl)} & G_{mn}^{(kl)} \\ \pm F_{kl}^{(mn)} & V_{mn}^{(kl)}-\Omega^2S_{mn}^{(kl)} & \pm H_{mn}^{(kl)} \\ G_{kl}^{(mn)} & \pm H_{kl}^{(mn)} & W_{mn}^{(kl)}-\Omega^2T_{mn}^{(kl)} \end{bmatrix}\begin{Bmatrix} A_{mn}\\ B_{mn}\\ C_{mn}\end{Bmatrix}=0 \tag{8}$$
$$(n,\ 1=1,2\ldots,N;m=0,1,2,\ldots,n;k=0,1,2,\ldots,l)$$

Equations (8) are linear homogeneous equations in the unknown coefficients A_{mn}, B_{mn}, and C_{mn}. The natural frequencies of the shell are determined by calculating the eigenvalues Ω which make the determinant obtained by eliminating the unknown coefficients of (8) zero, and the mode shapes of vibration are determined from (4) by calculating the coefficients corresponding to the eigenvalues. The elements $U_{mn}^{(kl)}$, $V_{mn}^{(kl)}$, $W_{mn}^{(kl)}$, . . . of the matrix in (8) are calculated by

$$U_{mn}^{(kl)}=\delta_{mk}\Big(1+\frac{1}{12}\bar{h}^2\Big)\int_0^{\pi}\Big\{\bar{P}_n^{m\,\prime\prime}\bar{P}_l^{k\,\prime\prime}+\bar{P}_n^{m\,\prime}\bar{P}_l^{k\,\prime}\cot^2\theta$$
$$+\nu(\bar{P}_n^{m\,\prime\prime}\bar{P}_l^{k\,\prime}+\bar{P}_n^{m\,\prime}\bar{P}_l^{k\,\prime\prime})\cot\theta$$
$$+\frac{1-\nu}{2}mk\bar{P}_n^{m\,\prime}\bar{P}_l^{k\,\prime}\operatorname{cosec}^2\theta\Big\}\sin\theta\,d\theta$$
$$+\bar{k}_u\sum_{j=1}^{J}(\bar{P}_n^{m\,\prime}\bar{P}_l^{k\,\prime})_{\theta_j}\begin{pmatrix}\cos\\ \sin\end{pmatrix}m\phi\begin{pmatrix}\sin\\ \cos\end{pmatrix}k\phi)_{\phi_j}$$

$$V_{mn}^{(kl)}=\delta_{mk}\Big(1+\frac{1}{12}\bar{h}^2\Big)\int_0^{\pi}\Big\{mk\bar{P}_n^m\bar{P}_l^k\operatorname{cosec}^4\theta$$
$$+\frac{1-\nu}{2}(\bar{P}_n^{m\,\prime}-2\bar{P}_n^m\cot\theta)$$
$$\times(\bar{P}_l^{k\,\prime}-2\bar{P}_l^k\cot\theta)\operatorname{cosec}^2\theta\Big\}\sin\theta\,d\theta$$
$$+\bar{k}_v\sum_{j=1}^{J}(\bar{P}_n^m\bar{P}_l^k\operatorname{cosec}^2\theta)_{\theta_j}\begin{pmatrix}\sin\\ \cos\end{pmatrix}m\phi\begin{pmatrix}\sin\\ \cos\end{pmatrix}k\phi)_{\phi_j}$$

$$W_{mn}^{(kl)}=\delta_{mk}\int_0^{\pi}\Big[2(1+\nu)\bar{P}_n^m\bar{P}_l^k+\frac{1}{12}\bar{h}^2\{(1-\nu^2)\bar{P}_n^{m\,\prime\prime}\bar{P}_l^{k\,\prime\prime}$$
$$+(\bar{P}_n^{m\,\prime}\cot\theta-m^2\bar{P}_n^m\operatorname{cosec}^2\theta+\nu\bar{P}_n^{m\,\prime\prime})$$
$$\times(\bar{P}_l^{k\,\prime}\cot\theta-k^2\bar{P}_l^k\operatorname{cosec}^2\theta+\nu\bar{P}_l^{k\,\prime\prime})$$
$$+2(1-\nu)mk(\bar{P}_n^{m\,\prime}-\bar{P}_n^m\cot\theta)$$
$$\times(\bar{P}_l^{k\,\prime}-\bar{P}_l^k\cot\theta)\operatorname{cosec}^2\theta\}\Big]\sin\theta\,d\theta$$
$$+\bar{k}_w\sum_{j=1}^{J}(\bar{P}_n^m\bar{P}_l^k)_{\theta_j}\begin{pmatrix}\cos\\ \sin\end{pmatrix}m\phi\begin{pmatrix}\cos\\ \sin\end{pmatrix}k\phi)_{\phi_j} \tag{9}$$

$$R_{mn}^{(kl)}=\delta_{mk}\int_0^{\pi}\bar{P}_n^{m\,\prime}\bar{P}_l^{k\,\prime}\sin\theta\,d\theta$$
$$S_{mn}^{(kl)}=\delta_{mk}\int_0^{\pi}\bar{P}_n^m\bar{P}_l^k\operatorname{cosec}^2\theta\sin\theta\,d\theta$$
$$T_{mn}^{(kl)}=\delta_{mk}\int_0^{\pi}\bar{P}_n^m\bar{P}_l^k\sin\theta\,d\theta \tag{10}$$

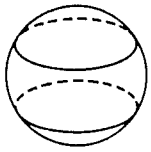
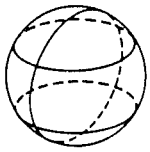
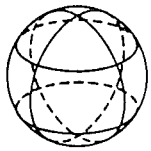
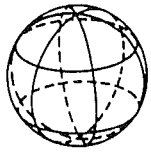
$$F_{mn}^{(kl)}=\delta_{mk}\Big(1+\frac{1}{12}\bar{h}^2\Big)\int_0^{\pi}\Big\{m\bar{P}_n^m(\bar{P}_l^{k\,\prime}\cot\theta+\nu\bar{P}_l^{k\,\prime\prime})\operatorname{cosec}^2\theta$$

Downloaded 02 May 2010 to 171.66.16.54. Redistribution subject to ASME license or copyright; see http://www.asme.org/terms/Terms_Use.cfm

Table 1 Types of vibration arising in a spherical shell symmetrically supported at equispaced four points

Type of vibration		Trigonometric functions in (4)	Signs of $F_{mn}^{(kl)}$	Signs of $H_{mn}^{(kl)}$	m
$SSS'S'$		upper	+	+	0,4,8, . . .
$SSA'A'$		upper	+	+	2,6,10, . . .
$AAS'S'$		lower	−	−	2,6,10, . . .
$AAA'A'$		lower	−	−	4,8,12, . . .
SA		upper	+	+	1,3,5, . . .
(AS)		lower	−	−	1,3,5, . . .

Table 2 Convergence characteristics of eigenvalues of vibration for an unconstrained spherical shell when the apex hole angle decreases: $\nu = 0.3$, $\bar{h} = 0.05$

θ_0	Vibration mode (m, n)			
	(0, 2)	(1, 3)	(2, 4)	(3, 5)
				
5 deg	0.7062	0.8418	0.9099	0.9881
3 deg	0.7040	0.8413	0.9137	0.9882
1 deg	0.7028	0.8410	0.9155	0.9882
0.1 deg	0.7027	0.8410	0.9158	0.9882
0 deg Exact	0.7027	0.8410	0.9158	0.9882

$$-\frac{1-\nu}{2}k(\bar{P}_n^{m\prime}-2\bar{P}_n^m\cot\theta)\bar{P}_l^{k\prime}\operatorname{cosec}^2\theta\Big\}\sin\theta\,d\theta$$

$$G_{mn}^{(kl)}=\delta_{mk}\int_0^{\pi}\Big[(1+\nu)\bar{P}_n^m(\bar{P}_l^{k\prime\prime}+\bar{P}_l^{k\prime}\cot\theta)$$

$$-\frac{1}{12}\bar{h}^2\{\bar{P}_n^{m\prime\prime}(\bar{P}_l^{k\prime\prime}+\nu\bar{P}_l^{k\prime}\cot\theta)$$

$$+(\bar{P}_n^{m\prime}\cot\theta-m^2\bar{P}_n^m\operatorname{cosec}^2\theta)(\bar{P}_l^{k\prime}\cot\theta+\nu\bar{P}_l^{k\prime\prime})$$

$$+(1-\nu)mk(\bar{P}_n^{m\prime}-\bar{P}_n^m\cot\theta)\bar{P}_l^{k\prime}\operatorname{cosec}^2\theta\}\Big]\sin\theta\,d\theta$$

$$H_{mn}^{(kl)}=\delta_{mk}\int_0^{\pi}\Big[(1+\nu)k\bar{P}_n^m\bar{P}_l^k\operatorname{cosec}^2\theta$$

$$-\frac{1}{12}\bar{h}^2\{k(\bar{P}_n^{m\prime}\cot\theta-m^2\bar{P}_n^m\operatorname{cosec}^2\theta+\nu\bar{P}_n^{m\prime\prime})\bar{P}_l^k\operatorname{cosec}^2\theta$$

$$-(1-\nu)m(\bar{P}_n^{m\prime}-\bar{P}_n^m\cot\theta)(\bar{P}_l^{k\prime}$$

$$-2\bar{P}_l^k\cot\theta)\operatorname{cosec}^2\theta\}\Big]\quad\sin\theta\,d\theta \tag{11}$$

where the following dimensionless parameters have been introduced:

$$\bar{h}=\frac{h}{a},\quad(\bar{k}_u,\bar{k}_v,\bar{k}_w)=\frac{1}{\pi D}(k_u,k_v,k_w)$$

$$\Omega^2=\frac{\rho h a^2\omega^2}{D}\ (\text{Frequency parameter}) \tag{12}$$

The symbol δ_{mk} is the Kronecker delta. The quantities $\bar{P}_n^{m\prime}$ and $\bar{P}_n^{m\prime\prime}$ express the derivatives of the function $\bar{P}_n^m(\cos\theta)$ with respect to θ, and are given by

$$\bar{P}_n^{m\prime}=-\Big[(n+1)\bar{P}_n^m\cos\theta$$

$$-\sqrt{\frac{2n+1}{2n+3}}\{(n+1)^2-m^2\}\bar{P}_{n+1}^m\Big]\operatorname{cosec}\theta$$

$$\bar{P}_n^{m\prime\prime}=\{m^2+(n+1)-(n+1)^2\sin^2\theta\}\bar{P}_n^m\operatorname{cosec}^2\theta$$

$$-\sqrt{\frac{2n+1}{2n+3}}\{(n+1)^2-m^2\}\bar{P}_{n+1}^m\cos\theta\operatorname{cosec}^2\theta \tag{13}$$

The definite integrals in (9)–(11) are calculated numerically by the Gauss-Legendre quadrature formula, since all of them cannot be expressed in simple analytical forms. Therefore, mathematical singularities arise in the integrals at the poles P and Q of the coordinate system. Usually, one would expand the integrals about the poles and patch in the integration analytically, and this is a correct procedure in handling the singularity. However, the procedure taking the region of the integrals between θ_0 and $\pi-\theta_0$ ($\theta_0 << 1$) is used here under the assumption of the presence of small holes at the poles, and the accuracy of this process is examined in Table 2. The same procedure was also employed in the paper of De Souza and Croll [15].

3 Frequency Equation of Rigidly Point-Supported Spherical Shell

Although the frequencies of a rigidly point-supported shell

Downloaded 02 May 2010 to 171.66.16.54. Redistribution subject to ASME license or copyright; see http://www.asme.org/terms/Terms_Use.cfm

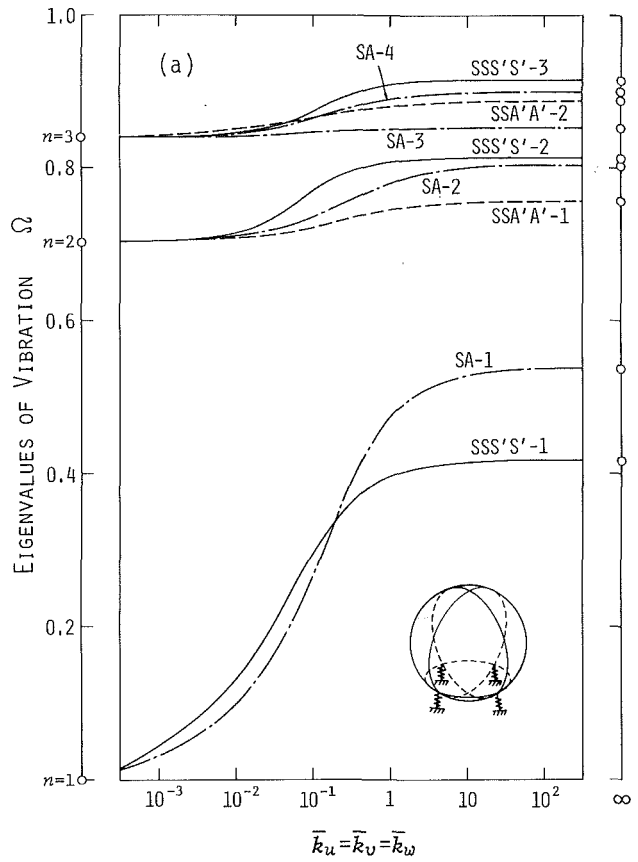


Fig. 2(*a*)

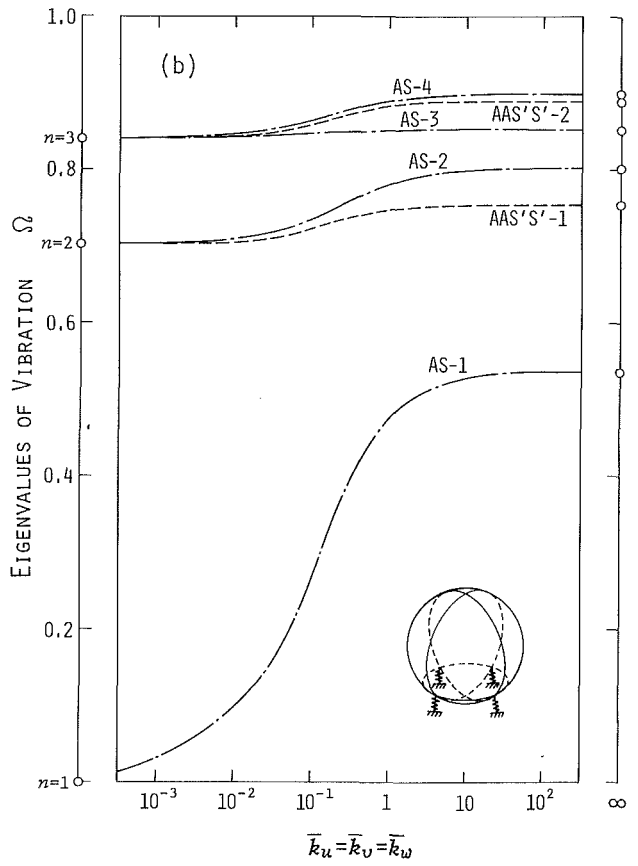


Fig. 2(*b*)

Fig. 2 Eigenvalues of vibration versus stiffness parameters of supports for elastically point-supported spherical shells: $\nu = 0.3$, $h = 0.05$, $J = 4$, $\alpha = 45$ deg ($\theta_0 = 0.1$ deg)

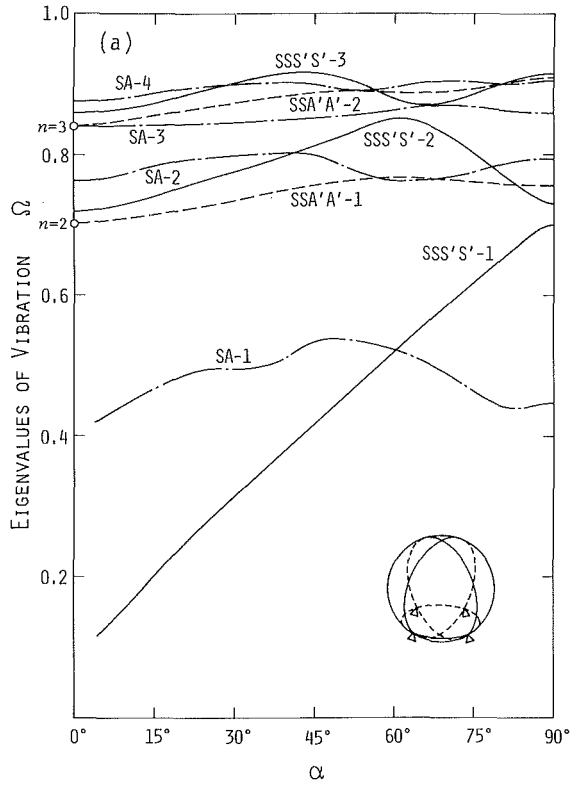


Fig. 3(*a*)

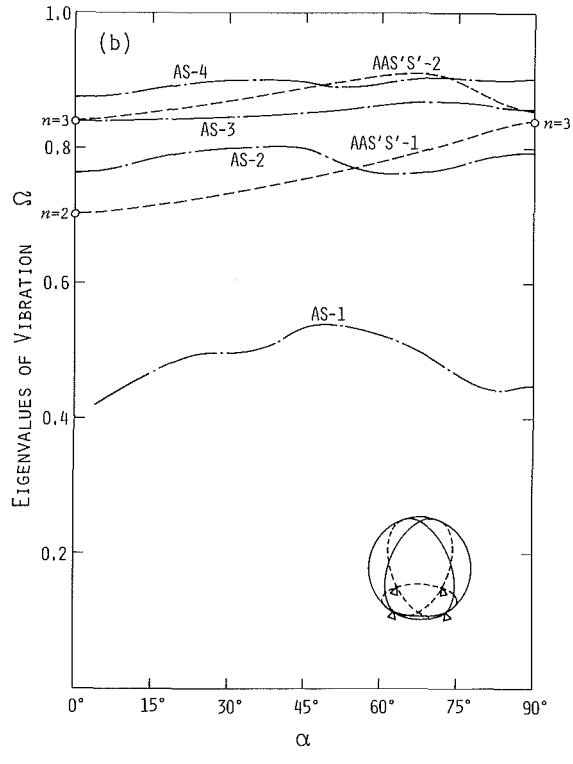


Fig. 3(*b*)

Fig. 3 Eigenvalues of vibration versus the angle of supports for rigidly point-supported spherical shells: $\nu = 0.3$, $h = 0.05$, $J = 4$ ($\theta_0 = 0.1$ deg)

are approximately calculated from (8) by taking extremely large values as the stiffness parameters ($\bar{k}_u$, $\bar{k}_v$, $\bar{k}_w$), more accurate values are determined by means of the Lagrangian multiplier method as an extension of the Ritz method. In this case, the Lagrange functional is written as

Downloaded 02 May 2010 to 171.66.16.54. Redistribution subject to ASME license or copyright; see http://www.asme.org/terms/Terms_Use.cfm

$$L = T - U_1 - \sum_{j=1}^{J} \{ \lambda_j u(\theta_j, \phi_j) + \mu_j v(\theta_j, \phi_j) + \nu_j w(\theta_j, \phi_j) \} \quad (14)$$

where λ_i, μ_i, ν_i are the Lagrangian multipliers expressing the components of the unknown reaction force acting at the supports. By substituting the equations that are obtained by the substitution of (4) into (1) and (2) into the conditions (7) and the complementary conditions expressed as

$$\frac{\partial L}{\partial \lambda_j} = 0, \quad \frac{\partial L}{\partial \mu_j} = 0, \quad \frac{\partial L}{\partial \nu_j} = 0 \quad (j = 1,2, \ldots, J) \quad (15)$$

the following frequency equation is derived:

$$\begin{bmatrix} \bar{U}_{mn}^{(kl)} - \Omega^2 R_{mn}^{(kl)} & \pm F_{mn}^{(kl)} & G_{mn}^{(kl)} & P_{mn}^{(j)} & 0 & 0 \\ \pm F_{kl}^{(mn)} & \bar{V}_{mn}^{(kl)} - \Omega^2 S_{mn}^{(kl)} & \pm H_{mn}^{(kl)} & 0 & Q_{mn}^{(j)} & 0 \\ G_{kl}^{(mn)} & \pm H_{kl}^{(mn)} & \bar{W}_{mn}^{(kl)} - \Omega^2 T_{mn}^{(kl)} & 0 & 0 & R_{mn}^{(j)} \\ P_{kl}^{(j)} & 0 & 0 & 0 & 0 & 0 \\ 0 & Q_{kl}^{(j)} & 0 & 0 & 0 & 0 \\ 0 & 0 & R_{kl}^{(j)} & 0 & 0 & 0 \end{bmatrix}$$

$$\begin{Bmatrix} A_{mn} \\ B_{mn} \\ C_{mn} \\ \lambda_j \\ \mu_j \\ \nu_j \end{Bmatrix} = 0$$

$(n, l = 1,2, \ldots, N; m = 0,1,2, \ldots, n;$

$$k = 0,1,2, \ldots, l; j = 1,2, \ldots, J) \quad (16)$$

The elements $\bar{U}_{mn}^{(kl)}$, $\bar{V}_{mn}^{(kl)}$, and $\bar{W}_{mn}^{(kl)}$ of the matrix in (16) are obtained by removing the $\bar{k}$-terms from the respective elements given in (9), and the elements $P_{mn}^{(j)}$, $Q_{mn}^{(j)}$ and $R_{mn}^{(j)}$ are calculated by

$$P_{mn}^{(j)} = \bar{P}_n^{m\prime}(\cos\theta_j) \begin{matrix}\cos \\ \sin\end{matrix} m\phi_j \quad Q_{mn}^{(j)} = \bar{P}_n^m(\cos\theta_j) \operatorname{cosec}\theta_j \begin{matrix}\sin \\ \cos\end{matrix} m\phi_j$$

$$R_{mn}^{(j)} = \bar{P}_n^m(\cos\theta_j) \begin{matrix}\cos \\ \sin\end{matrix} m\phi_j \quad (17)$$

4 Spherical Shell Symmetrically Supported at Equispaced Four Points

Consider a spherical shell supported at equispaced four points along a parallel of latitude ($\theta_j = \pi - \alpha$). As shown in Table 1, five types of vibration arise in the shell due to the structural symmetry. The symbols S and A denote symmetric and antisymmetric vibrations, respectively, with respect to a meridional plane passing through two opposite supports shown by the broken lines. While, the symbols S' and A' denote symmetric and antisymmetric vibrations, respectively, with respect to a meridional plane that equally divides the angle between two meridional planes passing through the adjacent supports. The solid lines appearing in the A and A'-type vibrations show the nodal lines where the radial deflections are zero. For each type of vibration, the trigonometric functions in (4), the double signs for the elements $F_{mn}^{(kl)}$, $H_{mn}^{(kl)}$ of the matrix in (8), and the wave number in the latitudinal direction m take the respective quantities specified in the table. The SA and AS-type vibrations have the same eigenfrequencies due to the structural symmetry of the shell.

5 Numerical Results and Discussion

In this section, the method is applied to a spherical shell elastically or rigidly supported at equispaced four points located along a parallel of latitude, and the eigenvalues of vibration Ω and the mode shapes are calculated numerically.

In the numerical calculation, a small hole is assumed at each pole for removing mathematical singularities, and also the number of terms of the series in (4) may be truncated at an appropriate finite number by considering the convergence of the numerical solution. Here, only the first eigenvalues of vibration are presented for the respective order n of the associated Legendre function given in (5).

Table 2 shows the variation of the eigenvalues of vibration when the angle θ_0 of the apex hole decreases for a spherical shell without any supports (an unconstrained shell). The eigenvalues of vibration of an unconstrained shell are independent of the wave number m in the latitudinal direction due to the spherical symmetry of the shell. However, the number m is written in this table in order for the mode shapes to be easily understood. With a decrease of the angle, the eigenvalues come to be equal to the exact values obtained analytically.

Table 3 shows the convergence characteristics of the eignvalues of vibration for a point-supported shell when the number of terms of the series in (4) increases. With an increase in number of the terms, the values converge within the range of three or four significant figures. In the present calculation, $N = 12$ are used which assures an accuracy sufficient for practical purposes. Although the accuracy of the numerical results also depends upon the number of the base points in the Gauss-Legendre quadrature formula,

Table 3 Convergence characteristics of eigenvalues of vibration for an elastically point-supported spherical shell: $\nu = 0.3$, $\bar{h} = 0.05$, $J = 4$, $\alpha = 30$ deg, $\bar{k}_u = \bar{k}_v = \bar{k}_w = 0.1$ ($\theta_0 = 0.1$ deg)

N	Number of terms	Vibration mode $SSS'S'$-1	Vibration mode $SSS'S'$-2	Number of terms	Vibration mode $SSA'A'$-1	Vibration mode $SSA'A'$-2
7	11	0.2678	0.9161	8	0.7125	0.8545
8	14	0.2581	0.9161	10	0.7124	0.8544
9	17	0.2521	0.9160	12	0.7123	0.8543
10	20	0.2482	0.9160	15	0.7122	0.8542
11	23	0.2453	0.9160	18	0.7121	0.8540
12	27	0.2431	0.9160	21	0.7120	0.8538

Downloaded 02 May 2010 to 171.66.16.54. Redistribution subject to ASME license or copyright; see http://www.asme.org/terms/Terms_Use.cfm

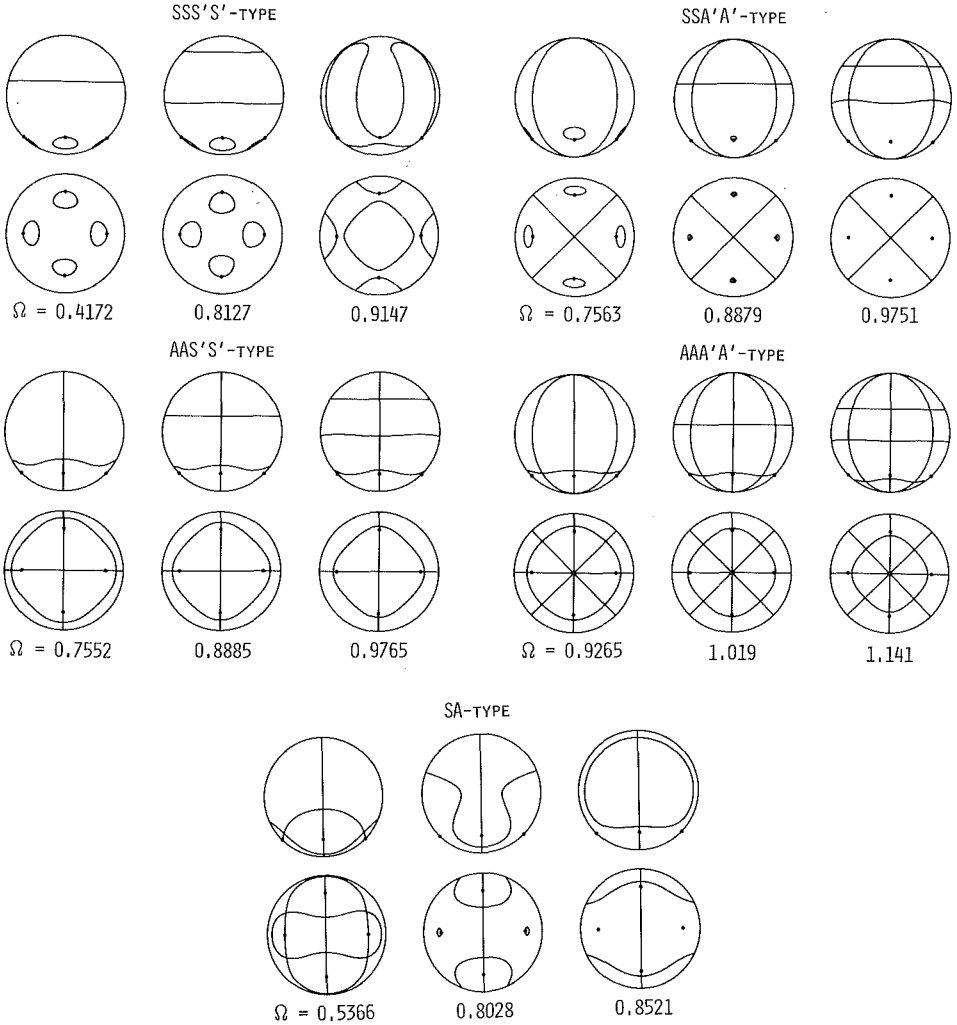


Fig. 4 Mode shapes of a rigidly point-supported spherical shell: $\nu = 0.3$, $h = 0.05$, $J = 4$, $\alpha = 45$ deg ($\theta_0 = 0.1$ deg)

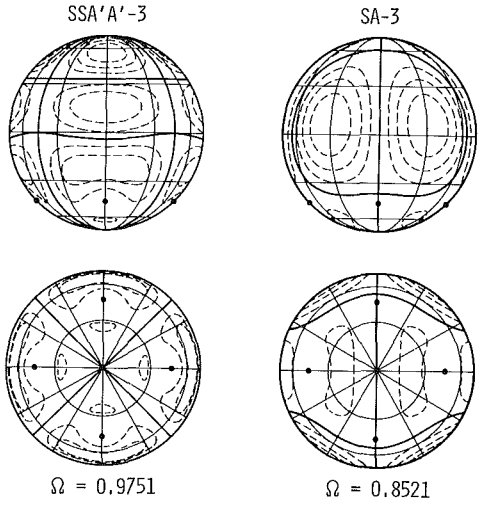


Fig. 5 Mode shapes of a rigidly point-supported spherical shell: $\nu = 0.3$, $h = 0.05$, $J = 4$, $\alpha = 45$ deg ($\theta_0 = 0.1$ deg)

sufficiently convergent values have been obtained by taking 24 base points.

Figures 2 show the eigenvalues of vibration versus the stiffness parameters $\bar{k}_u = \bar{k}_v = \bar{k}_w$ of the supports for elastically point-supported shells. The circled values on the ordinate at $\bar{k}_u = \bar{k}_v = \bar{k}_w = 0$ are the eigenvalues of an unconstrained shell. With an increase of the stiffness parameters, the eigenvalues monotonically increase and ultimately become the circled values on the ordinate at $\bar{k}_u = \bar{k}_v = \bar{k}_w = \infty$ of a rigidly point-supported shell. The eigenvalues of the $AAA'A'$-type vibration exceed the range of the values shown in these figures. The eigenvalues of the $SSS'S'$-1 and SA-1 or (AS-1) vibrations become zero with a decrease of the stiffness parameters, which represents only the translation of an unconstrained shell without presenting the vibration of the shell. The set of the SSA'-1, $AAS'S'$-1, SA-2, . . . vibrations, and the set of the SA-3 (or AS-3), $SSA'A'$-2, $AAS'S'$-2, . . . vibrations have the respective same eigenvalues of an unconstrained shell when the stiffnesss parameters become zero. In this case, the $SSA'A'$ and AAS$'S'$-type vibrations have almost equal eigenvalues independent of the vibration modes. Although the eigenvalues of the SA and AS-type vibrations have been calculated by using the different equations specified in Table 1, they are in good agreement with each other.

Figures 3 show the eigenvalues of vibration versus the angle α for rigidly point-supported shells. In the case of $\alpha = 0$ deg the shell is supported only at one of the poles, and in the case of $\alpha = 90$ deg the shell is supported at four points located on the equator. The circled values on the ordinate at $\alpha = 0$ deg are the eigenvalues of an unconstrained shell. The values of the $SSA'A'$-1, $AAS'S'$-1, SA-3, . . . vibrations of the shell of $\alpha = 0$ deg whose deflections are zero at one of the poles

Downloaded 02 May 2010 to 171.66.16.54. Redistribution subject to ASME license or copyright; see http://www.asme.org/terms/Terms_Use.cfm

coincide with those of an unconstrained shell. The eigenvalue of the $AAS'S'$-1 vibration for $\alpha = 90$ deg also coincides with that of an unconstrained shell, because the deflections are zero at the supports located on the equator. With the variation of the angle, the eigenvalues change in a wavelike manner, and hence some frequency crossings arise among the eigencurves of different types of vibration. It is considerably difficult to obtain the eigenvalues of $SSS'S'$-1 and SA-1 vibration when the angle α becomes small.

Figure 4 shows the mode shapes (the projected nodal patterns) for a rigidly point-supported shell. The points marked with • represent the location of the supports. The solid lines show the nodal lines where the radial deflections are zero. Although an unconstrained spherical shell has only nodal circles along the meridians and the parallels of latitude, point-supported shells have distorted nodal curves. The nodal lines along the parallels of latitude on the upper hemisphere opposite to the supports are not almost affected by the supports.

Figure 5 shows the mode shapes of the $SSA'A'$-3 and SA-3 vibrations which have no nodal lines passing through the supports shown in Fig. 4. Here, the thick solid lines express the nodal lines, and the broken lines do the contour lines. The thin solid lines express the meridians and the parallels of latitude at the interval of 30 deg. The radial deflection of the shell is extremely small in the vicinity of the supports.

The numerical calculations presented here were carried out on a HITAC M-280H computer of the Hokkaido University Computing Center.

6 Conclusion

The free vibration has been studied for an elastically or rigidly point-supported spherical shell.

The deflection displacements of the shell have been expressed in a series of the products of the associated Legendre functions and the trigonometric functions, and the frequency equation has been derived by the Ritz method.

By the application of the method, the eigenvalues of vibration and the mode shapes have been calculated numerically for spherical shells symmetrically supported by equispaced four points along a parallel of latitude, providing quantitative indications of the effect of the point supports on the vibration.

References

1 Lamb, H., "On the Vibrations of a Spherical Shell," *Proceedings of the London Mathematical Society*, Vol. 14, 1882, pp. 50–56.

2 Baker, W. E., "Axisymmetric Modes of Vibration of Thin Spherical Shell," *The Journal of the Acoustical Society of America*, Vol. 33, No. 12, 1961, pp. 1749–1758.

3 Kalnins, A., "Effect of Bending on Vibrations of Spherical Shells," *The Journal of the Acoustical Society of America*, Vol. 36, No. 1, 1964, pp. 74–81.

4 Wilkinson, J. P., "Natural Frequencies of Closed Spherical Shells," *The Journal of the Acoustical Society of America*, Vol. 38, No. 2, 1965, pp. 367–368.

5 Long, C. F., "Frequency Analysis of Complete Spherical Shells," *Journal of the Engineering Mechanics Division*, Proceedings of the American Society of Civil Engineers, Vol. 95, No. EM3, 1969, pp. 505–518.

6 Johnson, W., "A Note on the Radial Vibrations of an Isotropic Spherical Shells," *International Journal of Mechanical Sciences*, Vol. 16, 1974, pp. 201–207.

7 Silbiger, A., "Nonaxisymmetric Modes of Vibration of Thin Spherical Shells," *The Journal of the Acoustical Society of America*, Vol. 34, No. 6, 1962, p. 862.

8 Shah, A. H., Ramkrishnan, C. V., and Datta, S. K., "Three-Dimensional and Shell-Theory Analysis of Elastic Waves in a Hollow Sphere, Part 1 and Part 2," ASME JOURNAL OF APPLIED MECHANICS, Vol. 36, No. 3, 1969, pp. 431–444.

9 Cohen, H., Shah, A. H., and Ramakrishnan, C. V., "Free Vibrations of a Spherically Isotropic Hollow Sphere," *Acustica*, Vol. 26, 1972, pp. 329–333.

10 Hoppmann, W. H., II, and Baker, W. E., "Extensional Vibrations of Elastic Orthotropic Spherical Shells," ASME JOURNAL OF APPLIED MECHANICS, Vol. 28, No. 2, 1961, pp. 229–237.

11 Wilkinson, J. P. D., "Natural Frequencies of Closed Spherical Sandwich Shells," *The Journal of the Acoustical Society of America*, Vol. 40, No. 4, 1966, pp. 801–806.

12 Rath, B. K., and Das, Y. C., "Axisymmetric Vibration of Closed Layered Spherical Shells," *Journal of Sound and Vibration*, Vol. 37, No. 1, 1974, pp. 123–136.

13 Shah, A. H., and Frye, M. J., "Free Vibrations of Isotropic Layered Spheres," *Acustica*, Vol. 32, No. 5, 1975, pp. 291–299.

14 Frye, M. J., Shah, A. H., and McNiven, H. D., "Free Vibrations of Layered Spheres," *Acustica*, Vol. 52, No. 1, 1982, pp. 1–9.

15 De Souza, V. C. M., and Croll, J. G. A., "An Energy Analysis of the Free Vibrations of Isotropic Spherical Shells," *Journal of Sound and Vibration*, Vol. 73, No. 3, 1980, pp. 379–404.

Downloaded 02 May 2010 to 171.66.16.54. Redistribution subject to ASME license or copyright; see http://www.asme.org/terms/Terms_Use.cfm

ERRATA

Erratum on "Large Deflection Behavior of Simply Supported Laminated Panels Under In-Plane Loading," by Y. Zhang and F. L. Matthews, and published in the September 1985 issue of ASME JOURNAL OF APPLIED MECHANICS, Vol. 52, pp. 553–558.

On p. 555, equation (15) should read as follows:

$$A_I^{(1)} = (b_1 L_0^i T_1^j + b_2 L_0^j T_1^i)\ \frac{E_{22} h}{A_{22}}$$

$$A_I^{(2)} = (b_3 L_0^i T_1^j + b_4 L_0^j T_1^i)\ \frac{E_{22} h}{A_{22}} \qquad (15)$$

Copyright © 1985 by ASME
Downloaded 02 May 2010 to 171.66.16.54. Redistribution subject to ASME license or copyright; see http://www.asme.org/terms/Terms_Use.cfm

Dynamics of Viscoelastic Structures—A Time-Domain, Finite Element Formulation

D. F. Golla
Doctoral Candidate.

P. C. Hughes
Professor.

Institute of Aerospace Studies,
University of Toronto,
Toronto, Canada M3H 5T6

*Mathematical models of elastic structures have become very sophisticated: given the crucial material properties (mass density and the several elastic moduli), computer-based techniques can be used to construct exotic finite element models. By contrast, the modeling of damping is usually very primitive, often consisting of no more than mere guesses at "modal damping factors." The aim of this paper is to raise the modeling of viscoelastic structures to a level consistent with the modeling of elastic structures. Appropriate material properties are identified which permit the standard finite element formulations used for undamped structures to be extended to viscoelastic structures. Through the use of "dissipation" coordinates, the canonical "**M**, **K**" form of the undamped motion equations is expanded to encompass viscoelastic damping. With this formulation finite element analysis can be used to model viscoelastic damping accurately.*

1 Introduction

Modern computer-based techniques (such as the finite element method) enable the structural dynamicist to make highly precise calculations of the mass and stiffness properties of complex structures. These calculations, in turn, lead to quite accurate estimates of natural frequencies and mode shapes, particularly for the lower modes.

Structural damping properties, on the other hand, tend to be much less accurately calculated; indeed, one usually simply guesses at modal damping factors. This haphazard approach to structural damping belies the fact that in most applications damping is important to the structural dynamics, and in many applications it is in fact critical. Two examples may suffice to illustrate the point: for spinning (or partly spinning) spacecraft, the level of energy dissipation in the structure determines whether an initial wobbling motion grows or decays (dynamical stability); and an automatically controlled flexible spacecraft may act either unmanageable or docile (control system stability) depending on the level of damping in the "higher" vibration modes.

For example, the communications satellite shown in Fig. 1 will have its most important characteristic modes of vibration limited in amplitude by the level of damping in the long slender tower which connects the antenna reflector to the satellite's "main bus." It seems clear, then, that to assume that a damping factor, ζ, is 0.1 percent, when it is in fact 1 percent (or, for that matter, to assume $\zeta = 1$ percent when it is in fact 0.1 percent) is to commit a 1000 percent error in a crucial parameter. This state of the art is completely unacceptable.

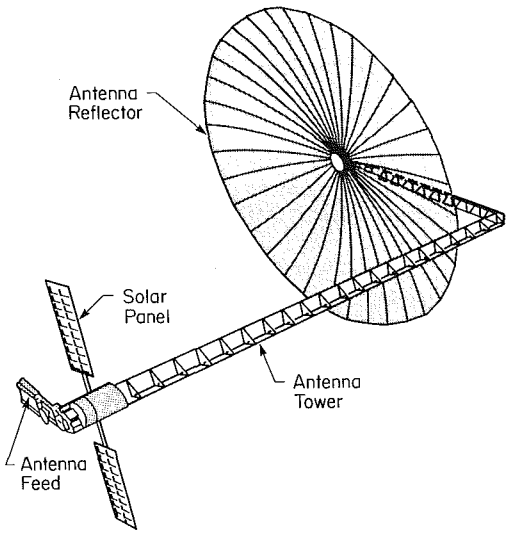


Fig. 1 Communications satellite

To bring dissipation analysis up to the same level of sophistication as mass and stiffness analysis, an equally concrete methodology is required. This paper presents one such methodology. We assume here that the structural damping is due to material viscoelasticity. Certain material constants are identified that must be known (ultimately by measurement) for each constituent material of the structure, just as known densities determine mass properties, and known elastic constants – such as Young's modulus – determine stiffness properties. These measured viscoelastic material constants permit a set of constitutive equations to be formulated for the dissipative properties over all parts of the structure.

Contributed by the Applied Mechanics Division for publication in the JOURNAL OF APPLIED MECHANICS.

Discussion on this paper should be addressed to the Editorial Department, ASME, United Engineering Center, 345 East 47th Street, New York, N.Y. 10017, and will be accepted until two months after publication of the paper itself in the JOURNAL OF APPLIED MECHANICS. Manuscript received by ASME Applied Mechanics Division, August, 1984; final revision, January, 1985.

Copyright © 1985 by ASME
Downloaded 02 May 2010 to 171.66.16.54. Redistribution subject to ASME license or copyright; see http://www.asme.org/terms/Terms_Use.cfm

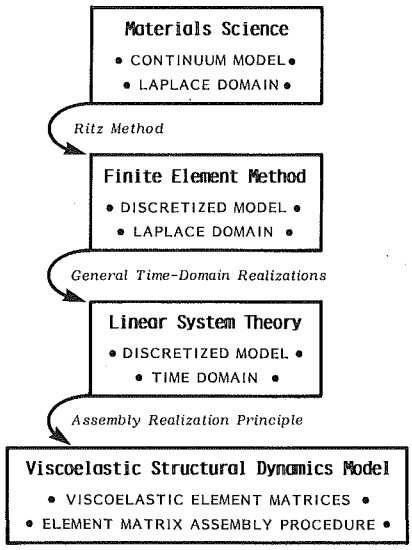


Fig. 2 Outline of viscoelastic element matrix development

It is furthermore plain that any methodology for modeling material damping that does not merge naturally with the finite element method will never be incorporated into engineering practice. The approach outlined in this paper becomes a natural extension to the finite element method.

A viscoelastic material is characterized by a constitutive relation in which the instantaneous stress depends on not only the instantaneous strain, but the strain history also. It is this latter dependence that provides energy dissipation. Time-domain equations of motion for a viscoelastic structure form a system of integrodifferential equations which are difficult to work with numerically and for this reason viscoelastic equations of motion are almost always formulated in the Laplace domain. Unfortunately, they are often wanted in the time domain.

An alternate approach is presented in this paper. Time-domain realizations of Laplace-domain motion equations will be shown to yield a linear differential formulation that includes an augmented set of generalized coordinates. In particular a second-order realization is developed that retains the important symmetry and definiteness properties of the structural system matrices. The method will also be shown to be completely amenable to treatment via the finite element method. Not only can the structural equations of motion be written in the time domain in the standard (second-order, linear differential) form, they can also be synthesized by assembling certain viscoelastic element matrices. The development of these viscoelastic element matrices is the chief contribution of this paper.

Figure 2 shows the major fields that will provide the foundation for our viscoelastic structural dynamics model, along with the major concepts and analysis techniques that lead to the development of viscoelastic element matrices. The constitutive relation for a viscoelastic material will be written as a symmetric fourth-order tensor of convolution integrals. Material properties will thus be represented by a set of relaxation functions in addition to a set of elastic constants. The most important property of the relaxation functions is that of dissipativity: Mechanical work must be done on the material for all possible strain histories.

The equations of motion of a viscoelastic structure will be formulated and discretized in the Laplace domain using a variational principle for viscoelastic continua in conjunction with the finite element method (a Ritz technique). The material properties will thus be represented by the Laplace transforms of the relaxation functions, which in turn are written as series of simple rational functions.

The key to the development of viscoelastic element matrices is in returning to the time domain with a linear differential realization. This step will require the introduction of new "dissipation" coordinates to the equations of motion. The conventional concept of a time-domain realization will then be generalized to include second-order linear differential systems. Furthermore, two special classes of realizations will be defined: "symmetrical realizations" and "linear matrix-second-order (LMSO) realizations." This will lead to the definition of "viscoelastic element matrices" which retain the important symmetry and definiteness properties familiar to, and useful in, structural dynamics.

Finally, the proposed formulation will be illustrated using both longitudinal and transverse vibrations of a simple rod. In both cases the viscoelastic element matrices are defined and assembled to form equations of motion.

2 Equations of Motion

The equation of motion governing small displacements within a viscoelastic body can be written

$$\rho(\mathbf{r})\ddot{\mathbf{u}}(\mathbf{r},t)+\underset{\sim}{\mathbf{K}}\mathbf{u}(\mathbf{r},t)=\mathbf{f}(\mathbf{r},t) \tag{2.1}$$

where $\rho(\mathbf{r})$ is the local mass density and $\underset{\sim}{\mathbf{K}}$ is a linear stiffness operator. A prescribed set of boundary conditions (also included in the symbol $\underset{\sim}{\mathbf{K}}$) determines a unique solution.

The stiffness operator $\underset{\sim}{\mathbf{K}}$ may be factored to reveal the presence of material properties. This factorization is written here in tensor notation:

$$\epsilon_{ij}=(u_{i,j}+u_{j,i})/2 \tag{2.2}$$

$$\sigma_{ij}=\int_{-\infty}^{t} G_{ijkl}(t-\tau)\,d\epsilon_{kl}(\tau) \tag{2.3}$$

$$(\underset{\sim}{\mathbf{K}}\mathbf{u})_i=-\sigma_{ij,j} \tag{2.4}$$

Of particular interest is the constitutive relation (2.3). In the case of linear elasticity the functions G_{ijkl} are simply constants (e.g., Hooke's Law) and the constitutive relation is written

$$\sigma_{ij}=G^0_{ijkl}\epsilon_{kl} \tag{2.5}$$

Furthermore, the elastic moduli G^0_{ijkl} must satisfy the symmetry relationships

$$G^0_{ijkl}=G^0_{jikl}=G^0_{ijlk}=G^0_{klij} \tag{2.6}$$

and the elasticity tensor $\mathbf{G}^0$ is positive-definite (written $\mathbf{G}^0>0$).

3 Viscoelastic Material Properties

The constitutive relation for a viscoelastic material may be written as a Stieltjes convolution (reference [1]):

$$\sigma_{ij}=\int_{-\infty}^{t} G_{ijkl}(t-\tau)\,d\epsilon_{kl}(\tau) \tag{3.1}$$

and the material properties are now represented by the functions $G_{ijkl}(t)$. We shall assume a continuous strain history with

$$\epsilon_{kl}(t)=0, \quad -\infty<t<0 \tag{3.2}$$

In other words we assume that the body is in true static equilibrium at $t=0_-$. Under these conditions we can replace the Stieltjes convolution with a Riemann convolution and write the constitutive relation

$$\sigma_{ij}=G^0_{ijkl}\epsilon_{kl}+H_{ijkl}(t)\,\epsilon_{kl}(0)+\int_0^t H_{ijkl}(t-\tau)\,\frac{\partial\epsilon_{kl}}{\partial\tau}\,d\tau \tag{3.3}$$

where $G^0_{ijkl}=\lim_{t\to\infty} G_{ijkl}(t)$ is the equilibrium elasticity and

$$G_{ijkl}(t)=G^0_{ijkl}+H_{ijkl}(t) \tag{3.4}$$

The functions $G_{ijkl}(t)$ satisfy the symmetry relationships

Downloaded 02 May 2010 to 171.66.16.54. Redistribution subject to ASME license or copyright; see http://www.asme.org/terms/Terms_Use.cfm

$$(i) \quad G_{ijkl}(t) = G_{jikl}(t) = G_{ijlk}(t)$$
$$(ii) \quad G_{ijkl}(t) = G_{klij}(t) \tag{3.5}$$

The second relationship was derived by Biot [2] using Onsager's principle for irreversible thermodynamical processes. (Onsager's principle states that the rate of entropy production is a *symmetrical* quadratic form of the generalized forces [3, pp. 387-395].) In the thermodynamical derivation by Christensen [4] this relationship is stated only for initial and final values, namely

$$G_{ijkl}(0) = G_{klij}(0)$$
$$G_{ijkl}(\infty) = G_{klij}(\infty) \tag{3.6}$$

These are necessary (but not sufficient) conditions for a viscoelastic material to dissipate energy [5]. We will use the full symmetry relationships (equation (3.5)) as did Biot. We will also assume that the functions $G_{ijkl}(t)$ all have Laplace transforms. Therefore we write the constitutive relation in the Laplace domain

$$\sigma_{ij}(s) = [G^0_{ijkl} + h_{ijkl}(s)]\epsilon_{kl}(s) \tag{3.7}$$

where

$$h_{ijkl}(s) = sH_{ijkl}(s)$$

and both $\mathbf{h}(s)$ and $\mathbf{H}(s)$ are symmetrical fourth-order tensors. We now represent viscoelastic material properties by the equilibrium elasticity constants G^0_{ijkl} and the dissipation functions $h_{ijkl}(s)$.

The most important viscoelastic material property is dissipativity. Real materials dissipate energy when they are stressed. We consider first the following definition of dissipativity [5].

Definition 3.1. A constitutive relation shall be called *dissipative* if

$$\int_0^t \sigma_{ij}(\tau) \frac{\partial \epsilon_{ij}}{\partial \tau}(\tau) d\tau \geq 0$$

for all sufficiently smooth ϵ_{ij} with $\epsilon_{ij}(0) = 0$.

While the material scientist tends to include the special case of linear elasticity within the much broader theory of linear viscoelasticity, the structural dynamicist finds it helpful to keep distinct the concepts of conservative and dissipative systems. Therefore we give the following definition:

Definition 3.2. A constitutive relation shall be called *strictly dissipative* if

$$\int_0^t \sigma_{ij}(\tau) \frac{\partial \epsilon_{ij}}{\partial \tau} d\tau > 0$$

for all sufficiently smooth ϵ_{ij}, with $\epsilon_{ij} \not\equiv 0$ and $\epsilon_{ij}(0) = 0$.

The final conditions that we impose on the functions representing viscoelastic properties are those required to produce a strictly dissipative constitutive relation. Sufficient conditions for the constitutive relation to be strictly dissipative are

$$(i) \quad G_{ijkl}(t) = G_{klij}(t)$$

and

$$(ii) \quad \mathbf{G}^0 \not< 0 \tag{3.8}$$

and

$$(iii) \quad Re\{\mathbf{H}(j\omega)\} > 0, \quad \text{all} \quad \omega$$

Here we use the new symbol $\not<$ to mean non-negative-definite.

Alternatively, we can write condition (*iii*) as follows:

$$Im\{\mathbf{h}(j\omega)\} > 0, \quad 0 < \omega < \infty \tag{3.9}$$

Having discussed the essential properties of the functions used to model a viscoelastic material we turn now to the mathematical representation of these functions. The function $h(s)$ (subscripts are dropped for convenience) is a unique material property whose mathematical representation must be chosen by the analyst. Table 1 lists a representative sampling of functions that have been used to represent viscoelastic material properties.

Table 1 Dissipation functions

Function	Author, Year
$h(s) = \sum_{i=1}^{n} \frac{a_i s}{s + b_i}$	M.A. Biot, 1955 (reference [2])
$h(s) = \frac{E_1 s^\alpha - E_0 b s^\beta}{1 + b s^\beta}$, $0 < \alpha < 1$, $0 < \beta < 1$	R. L. Bagley, P. J. Torvik, 1981 (references [6, 7])
$h(s) = as \int_0^\infty \frac{\gamma(p)}{s+p} dp$, $\gamma(p) = \begin{cases} \frac{1}{\beta - \alpha}, & \alpha \leq p \leq \beta \\ 0, & \text{otherwise} \end{cases}$	K. J. Buhariwala, 1982 (reference [8])

Bagley and Torvik [6, 7] have shown that a fractional derivative model based on molecular theory and requiring only a few parameters has excellent agreement with measured data. The function used by Biot [2], on the other hand, is amenable to the classical analysis of more than a century, namely, Laplace domain analysis of *rational* transfer functions. Moreover, its equivalence to systems of *linear differential* equations is invaluable.

Hence we use the series representation

$$h(s) = \sum_{l=1}^{v} \frac{a_l s}{s + b_l} \tag{3.10}$$

to model viscoelastic materials. With this representation we accept the potential price of generating a high-order system in return for increased analytical capability. We note that the material properties a_l and b_l must be known. These can be obtained using appropriate curve-fitting of experimental data. Just as, for example, Young's modulus and Poisson's ratio are needed for elastic analysis, a_l and b_l are needed for viscoelastic analysis.

4 The Finite Element Method

Arguably the most powerful and most popular technique for solving equations of motion (e.g., equation (2.1)) is the finite element method, which owes its mathematical justification to the method of Ritz. In the case of linear elasticity we use Hamilton's principle

$$\delta \int_{t_1}^{t_2} (T - V + W)\, dt = 0 \tag{4.1}$$

where

$$T = \frac{1}{2} \langle \dot{\mathbf{u}}, \rho \dot{\mathbf{u}} \rangle$$

$$V = \frac{1}{2} \langle \mathbf{u}, \underline{\mathbf{K}} \mathbf{u} \rangle$$

$$W = \langle \mathbf{u}, \ell \rangle$$

Downloaded 02 May 2010 to 171.66.16.54. Redistribution subject to ASME license or copyright; see http://www.asme.org/terms/Terms_Use.cfm

and where the inner product is defined as

$$\langle \mathbf{u},\mathbf{v}\rangle = \iiint_{\text{body}} \mathbf{u}^T\mathbf{v}\,dr_1\,dr_2\,dr_3$$

for any two functions $\mathbf{u}$ and $\mathbf{v}$. Now consider the Ritz approximation

$$\mathbf{u}(\mathbf{r},t) = \sum_{i=1}^{n} q_i(t)\,\mathbf{U}_i(\mathbf{r}) \tag{4.2}$$

The variational principle (4.1) yields the system of equations

$$\mathfrak{M}\ddot{\mathbf{q}} + \mathcal{K}\mathbf{q} = \mathbf{f} \tag{4.3}$$

$$m_{ij} = \langle \mathbf{U}_i, \rho\mathbf{U}_j\rangle, \quad k_{ij} = \langle \mathbf{U}_i, \underline{\mathbf{K}}\mathbf{U}_j\rangle$$

$$f_i = \langle \mathbf{U}_i, \mathfrak{f}\rangle, \quad \mathbf{q} = \text{col}\{q_i(t)\}$$

In the special case of the finite element method the mass and stiffness matrices have factorizations that are extremely important, namely,

$$\mathfrak{M} = \mathbf{P}^T\mathfrak{M}_B\mathbf{P}, \quad \mathcal{K} = \mathbf{P}^T\mathcal{K}_B\mathbf{P}$$

where

$$\mathfrak{M}_B = \text{block diag}\{\mathbf{M}_1^e, \mathbf{M}_2^e, \ldots, \mathbf{M}_m^e\}$$

$$\mathcal{K}_B = \text{block diag}\{\mathbf{K}_1^e, \mathbf{K}_2^e, \ldots, \mathbf{K}_m^e\}$$

Here $\mathbf{M}_j^e$, $\mathbf{K}_j^e$ are element mass and stiffness matrices and $\mathbf{P}$ is a pointing matrix used to assemble the element matrices. It is convenient to introduce a notation to indicate the assembly of element matrices into system matrices in a general way. Thus we write

$$\mathfrak{M} = \mathop{\mathfrak{E}}_{j=1}^{m} \mathbf{M}_j^e = \mathbf{M}_1^e \oplus \mathbf{M}_2^e \oplus \ldots \oplus \mathbf{M}_m^e$$

and (4.4)

$$\mathcal{K} = \mathop{\mathfrak{E}}_{j=1}^{m} \mathbf{K}_j^e = \mathbf{K}_1^e \oplus \mathbf{K}_2^e \oplus \ldots \oplus \mathbf{K}_m^e$$

The symbols $\oplus$ and $\mathfrak{E}$ correspond to $+$ and Σ and indicate matrix assembly rather than matrix addition. The operation of matrix assembly is an important part of the original engineering interpretation of the finite element method. That this formulation is really a Ritz method (and can therefore rest on the foundations of Ritzian theory) is the true beauty of the finite element method. The form (4.4) stems from the choice of piecewise continuous trial functions.

Consider now the case of linear viscoelasticity. The equation of motion in the Laplace domain is written

$$[s^2\rho(\mathbf{r}) + \underline{\mathbf{K}}(s)]\mathbf{u}(\mathbf{r},s) = \mathfrak{f}(\mathbf{r},s) + \rho(\mathbf{r})[s\mathbf{u}_0(\mathbf{r}) + \dot{\mathbf{u}}_0(\mathbf{r})] \tag{4.5}$$

Consider the function

$$Q(s) = s^2\langle \mathbf{u},\rho\mathbf{u}\rangle + \langle \mathbf{u},\underline{\mathbf{K}}(s)\,\mathbf{u}\rangle - 2\langle \mathbf{u},\mathfrak{f} + \rho(s\mathbf{u}_0 + \dot{\mathbf{u}}_0)\rangle \tag{4.6}$$

and the variational equation

$$\delta Q = 0 \tag{4.7}$$

in which the independent variables in the variation are the *spatial variables* only. Expanding the variation yields

$$\delta Q = 2\langle \delta\mathbf{u}, s^2\rho\mathbf{u} + \underline{\mathbf{K}}(s)\,\mathbf{u}\rangle - 2\langle \delta\mathbf{u}, \mathfrak{f} + \rho(s\mathbf{u}_0 + \dot{\mathbf{u}}_0)\rangle$$

and we can see that the stationary value of $Q(s)$ yields the same solution as equation (4.5). Note that the first two terms in equation (4.6) are not the transforms of kinetic and potential energy and equation (4.7) should not be regarded as a transformed principle of analytical dynamics. On the contrary equation (4.7) is a variational principle of a more elementary nature which quite sufficiently produces the desired solution.

The finite element method can now be used to yield discretized equations of motion in which the system matrices are assembled from element matrices. Furthermore, the element stiffness matrices may be expanded, revealing the independent viscoelastic moduli and their dissipation functions. The result of this procedure is now written using the assembly notation introduced in equation (4.4):

$$[s^2\mathfrak{M} + \mathcal{K}(s)]\mathbf{q}(s) = \mathbf{f}(s) + \mathfrak{M}(s\mathbf{q}_0 + \dot{\mathbf{q}}_0) \quad (i)$$

$$\mathfrak{M} = \mathop{\mathfrak{E}}_{j=1}^{m} \mathbf{M}_j^e \quad (ii)$$

$$\mathcal{K}(s) = \mathop{\mathfrak{E}}_{j=1}^{m} \mathcal{K}_j^e(s) \quad (iii)$$

$$\mathcal{K}_j^e(s) = \sum_{k=1}^{v} [G_k^0 + h_k(s)]\mathbf{K}_k^e \quad (iv) \tag{4.8}$$

$$h_k(s) = \sum_{l=1}^{v} a_l s/(s + b_l) \quad (v)$$

Two comments are in order about the notation. First, we have abandoned the tensor notation of the preceding section in equation (4.8) (*iv*); all independent viscoelastic moduli are now distinguished by a single subscript, $(\,)_k$. Second, we have employed an algorithmic notation to further avoid multiple subscripts: all subscripted variables and the upper limits of summation depend on all previous subscripts. For example, a_l, b_l and v in equation (4.8) (*v*) depend also on j and k.

5 Time-Domain Realizations

A realization is an important concept in linear system theory. It enables the analyst to represent a given system by an equivalent system. In their original definition of realization, Zadeh and Desoer made no reference to the state-space representation of a system. Instead, a realization was an interconnection of components of specific classes (integrators, differentiators, scalors and adders) equivalent to a given system [9, p. 95]. Since then, however, the standard linear first-order system of state equations has become the usual (although not the necessary) mathematical representation of a realization. Hence the familiar definition:

Definition 5.1. The time-domain system of state equations

$$\dot{\mathbf{x}} = \mathbf{A}\mathbf{x} + \mathbf{B}\mathbf{u}$$

$$\mathbf{y} = \mathbf{C}\mathbf{x}$$

is a *realization* of the rational transfer matrix $\mathbf{Z}(s)$ from $\mathbf{u}$ to $\mathbf{y}$ if

$$\mathbf{Z}(s) = \mathbf{C}[s\mathbf{1} - \mathbf{A}]^{-1}\mathbf{B}$$

We wish now to expand the scope of the mathematical representation of a realization. This motivates the following definitions:

Definition 5.2. The time-domain system of linear differential equations

$$\sum_{i=0}^{n} \mathbf{A}_i \frac{d^i}{dt^i}\mathbf{x} = \mathbf{B}\mathbf{u}$$

$$\mathbf{y} = \mathbf{C}\mathbf{x}$$

is a *general realization of order n* of the rational transfer matrix $\mathbf{Z}(s)$ from $\mathbf{u}$ to $\mathbf{y}$ if

$$\mathbf{Z}(s) = \mathbf{C}\left[\sum_{i=0}^{n} s^i\mathbf{A}_i\right]^{-1}\mathbf{B}$$

Downloaded 02 May 2010 to 171.66.16.54. Redistribution subject to ASME license or copyright; see http://www.asme.org/terms/Terms_Use.cfm

Definition 5.3. A general realization of order n shall be called *symmetrical* if

$$\mathbf{A}_i^T = \mathbf{A}_i, \quad i = 0, \ldots, n$$

Definition 5.4. A general second-order realization given by

$$\mathfrak{M}\ddot{\mathbf{q}} + \mathfrak{D}\dot{\mathbf{q}} + \mathcal{G}\dot{\mathbf{q}} + \mathfrak{K}\mathbf{q} + \mathcal{S}\mathbf{q} = \mathcal{B}\mathbf{u}$$
$$\mathbf{y} = \mathbf{C}\mathbf{q}$$

shall be called a *linear matrix-second-order* (LMSO) realization if

$$\mathfrak{M}^T = \mathfrak{M} > 0$$
$$\mathfrak{D}^T = \mathfrak{D} \not< 0, \quad \mathcal{G}^T = -\mathcal{G}$$
$$\mathfrak{K}^T = \mathfrak{K} \not< 0, \quad \mathcal{S}^T = -\mathcal{S}$$

We have made the substitutions

$$\mathbf{A}_2 = \mathfrak{M}, \quad \mathbf{A}_1 = \mathfrak{D} + \mathcal{G}, \quad \mathbf{A}_0 = \mathfrak{K} + \mathcal{S}$$

to enhance the significance of a LMSO realization. Since any square matrix can be written as the sum of a symmetric and skew-symmetric matrix, we have not lost generality with the substitutions $\mathbf{A}_1 = \mathfrak{D} + \mathcal{G}$ and $\mathbf{A}_0 = \mathfrak{K} + \mathcal{S}$. Note, however, that $\mathbf{A}_1$ and $\mathbf{A}_0$ can no longer be completely general matrices since we require their symmetric parts $\mathfrak{D}$ and $\mathfrak{K}$ to be non-negative-definite. Finally, note that a LMSO realization is symmetrical if $\mathcal{G}$ and $\mathcal{S}$ are both zero.

6 The Kernel of the Concept: One Displacement Variable, One Elastic Modulus, and One Dissipation-Pole Pair in $h(s)$

We now develop a symmetrical LMSO realization of the discretized Laplace-domain equation of motion for a viscoelastic structure (equation (4.8)).

To focus on the essential issues, consider the simplest case – an equation with one displacement variable (or generalized coordinate in the language of Lagrange):

$$\{s^2\mathfrak{M} + [G^0 + h(s)]\mathfrak{K}\}q(s) = f(s) + \mathfrak{M}[sq_0 + \dot{q}_0] \tag{6.1}$$

where

$$\mathfrak{M} > 0, \quad \mathfrak{K} > 0, \quad G^0 > 0$$

and

$$h(s) = \frac{a_1 s}{s + b_1} + \frac{a_2 s}{s + b_2}$$

with

$$b_2 > b_1 > 0$$

The dissipation function $h(s)$ may also be written

$$h(s) = \frac{\alpha s^2 + \gamma s}{s^2 + \beta s + \delta} \tag{6.2}$$

where

$$\alpha = a_1 + a_2, \quad \gamma = a_1 b_2 + a_2 b_1, \quad \beta = b_1 + b_2, \quad \delta = b_1 b_2$$

We begin by finding a symmetrical second order realization of $h^{-1}(s)$ in the form

$$\begin{bmatrix} M & m \\ m & 1 \end{bmatrix} \begin{bmatrix} q \\ z \end{bmatrix}^{\cdot\cdot} + \beta \begin{bmatrix} D & d \\ d & 1 \end{bmatrix} \begin{bmatrix} q \\ z \end{bmatrix}^{\cdot}$$
$$+ \delta \begin{bmatrix} K & k \\ k & 1 \end{bmatrix} \begin{bmatrix} q \\ z \end{bmatrix} = \begin{bmatrix} f_v \\ 0 \end{bmatrix} \tag{6.3}$$

[We define f_v in the Laplace domain by $f_v(s) = h(s)q(s)$.] Taking the Laplace transform of equation (6.3) and equating the transfer functions yields the following set of algebraic equations:

$$M - m^2 = 0 \quad (i)$$
$$M + D - 2md = 0 \quad (ii)$$
$$M\delta + D\beta^2 + K\delta - d^2\beta^2 - 2mk\delta = \alpha \quad (iii) \tag{6.4}$$
$$D + K - 2dk = \gamma/\beta\delta \quad (iv)$$
$$K - k^2 = 0 \quad (v)$$

A realization so defined will have the same input-output relationship as the given system. This realization will therefore be zero-state equivalent to the given system. We would also like the realization to be zero-input equivalent [9]. Thus we have constraints imposed by the initial value terms:

$$M - m^2 = 0 \quad (i)$$
$$D - d^2 = 0 \quad (ii) \tag{6.5}$$
$$m = d \quad (iii)$$

and the initial values are chosen so that

$$z_0 = -dq_0 \quad (i)$$
$$\dot{z}_0 = -d\dot{q}_0 \quad (ii) \tag{6.6}$$

Adding equation (6.5) (*ii*) to our set of equations (6.4) produces a set of six nonlinear algebraic equations in six unknown parameters (M, D, K, m, d, k) and four known parameters (α, γ, β, δ). As we shall see, equation (6.5) (*iii*) is consistent with their solution. After a little algebra these equations reduce to

$$M - m^2 = 0 \quad (i)$$
$$D - d^2 = 0 \quad (ii)$$
$$K - k^2 = 0 \quad (iii) \tag{6.7}$$
$$M + D - 2md = 0 \quad (iv)$$
$$M + K - 2mk = \alpha/\delta \quad (v)$$
$$D + K - 2dk = \gamma/\beta\delta \quad (vi)$$

Eliminating M, D, K from the final three equations yields

$$(m - d)^2 = 0 \quad (i)$$
$$(m - k)^2 = \alpha/\delta \quad (ii) \tag{6.8}$$
$$(d - k)^2 = \gamma/\beta\delta \quad (iii)$$

and solutions are now evident. A solution does not exist for an arbitrary choice of parameters (α, γ, β, δ). A solution exists only when $\gamma = \alpha\beta$, although this condition does not produce a unique solution. One of the unknowns may be arbitrarily chosen. We select d arbitrarily and write the realization thus:

$$\frac{\alpha}{\delta} \begin{bmatrix} \hat{d}^2 & \hat{d} \\ \hat{d} & 1 \end{bmatrix} \begin{bmatrix} q \\ \hat{z} \end{bmatrix}^{\cdot\cdot} + \frac{\alpha\beta}{\delta} \begin{bmatrix} \hat{d}^2 & \hat{d} \\ \hat{d} & 1 \end{bmatrix} \begin{bmatrix} q \\ \hat{z} \end{bmatrix}^{\cdot}$$
$$+ \alpha \begin{bmatrix} (1+\hat{d})^2 & (1+\hat{d}) \\ (1+\hat{d}) & 1 \end{bmatrix} \begin{bmatrix} q \\ \hat{z} \end{bmatrix} = \begin{bmatrix} f_v \\ 0 \end{bmatrix}$$

where

$$\hat{d} = d\sqrt{\delta/\alpha}$$
$$\hat{z} = z\sqrt{\delta/\alpha}$$

[Although there are two roots of equation (6.8) (*ii*) we note that the resulting solutions share a simple equivalence relationship and are therefore not fundamentally different.]

This realization of $h^{-1}(s)$ yields a symmetrical LMSO realization of the full system: The given equation

$$\{s^2\mathfrak{M} + [G^0 + h(s)]\mathfrak{K}\}q(s) = f(s) + \mathfrak{M}[sq_0 + \dot{q}_0]$$

where

$$\mathfrak{M} > 0, \quad \mathfrak{K} > 0, \quad G^0 > 0$$

and

Downloaded 02 May 2010 to 171.66.16.54. Redistribution subject to ASME license or copyright; see http://www.asme.org/terms/Terms_Use.cfm

$$h(s)=\frac{\alpha(s^2+\beta s)}{s^2+\beta s+\delta}$$

has the symmetrical LMSO realization

$$\mathbf{M}^+\begin{bmatrix} q \\ \hat{z}\end{bmatrix}^{\cdot\cdot}+\mathbf{D}^+\begin{bmatrix} q \\ \hat{z}\end{bmatrix}^{\cdot}+\mathbf{K}^+\begin{bmatrix} q \\ \hat{z}\end{bmatrix}=\begin{bmatrix} f \\ 0\end{bmatrix} \tag{6.9}$$

where

$$\mathbf{M}^+=\begin{bmatrix} \mathfrak{M} & 0 \\ 0 & 0\end{bmatrix}+\frac{\alpha\mathcal{K}}{\delta}\begin{bmatrix} \hat{d}^2 & \hat{d} \\ \hat{d} & 1\end{bmatrix} \tag{6.10}$$

$$\mathbf{D}^+=\frac{\alpha\beta\mathcal{K}}{\delta}\begin{bmatrix} \hat{d}^2 & \hat{d} \\ \hat{d} & 1\end{bmatrix} \tag{6.11}$$

$$\mathbf{K}^+=\begin{bmatrix} G^0\mathcal{K} & 0 \\ 0 & 0\end{bmatrix}+\alpha\mathcal{K}\begin{bmatrix} (1+\hat{d})^2 & (1+\hat{d}) \\ (1+\hat{d}) & 1\end{bmatrix} \tag{6.12}$$

and the initial conditions are chosen so that

$$\begin{aligned}\hat{z}_0&=-\hat{d}q_0 \qquad (i)\\ \dot{\hat{z}}_0&=-\hat{d}\dot{q}_0 \qquad (ii)\end{aligned} \tag{6.13}$$

The definiteness properties of the augmented matrices $\mathbf{M}^+$, $\mathbf{D}^+$, $\mathbf{K}^+$ are easily verified. These matrices are augmented because we have added a new coordinate ($\hat{z}$) to the system. This is a salient feature of time-domain realizations. We call these added coordinates *dissipation coordinates.*

We now turn our attention further to the dissipation function

$$h(s)=\frac{\alpha(s^2+\beta s)}{s^2+\beta s+\delta} \tag{6.14}$$

The restriction $\gamma=\alpha\beta$ in terms of the original parameters (a_1, a_2, b_1, b_2), is

$$a_2=-a_1b_1/b_2 \tag{6.15}$$

The criterion for dissipativity

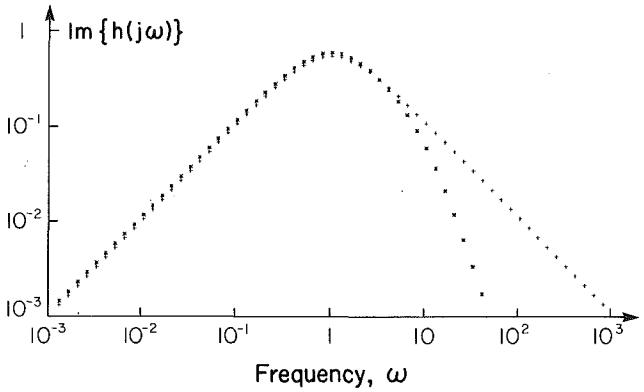
$$h(j\omega)>0, \quad 0<\omega<\infty$$

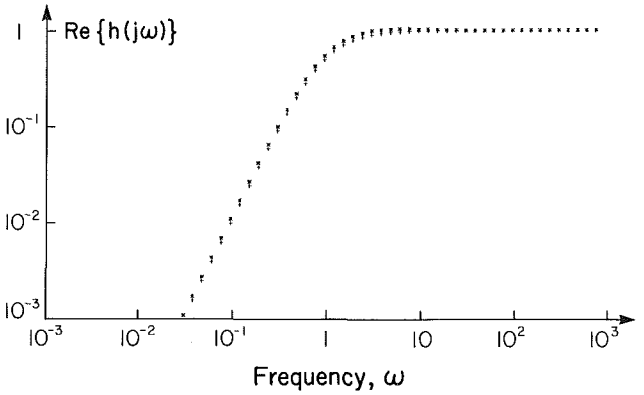
yields the two additional conditions

$$\begin{aligned}a_1b_1+a_2b_2&\geq 0 \qquad (i)\\ a_1b_2+a_2b_1&\geq 0 \qquad (ii)\end{aligned} \tag{6.16}$$

(We do not consider the trivial case $a_1 = a_2 = 0$.) The first condition dominates whenever $a_1 > 0$ (remember $b_2 > b_1 > 0$). Therefore $h(s)$ is a dissipative function provided $a_1 > 0$ ($\alpha > 0$).

The real and imaginary parts of $h(j\omega)$ are plotted in Fig. 3. These are compared to the corresponding complex parts of the single first-order term $aj\omega/(b+j\omega)$. We can see that the second-order function (equation 6.14) can provide a representation of material properties that is comparable to that of the latter function. The most noticeable difference is in the imaginary parts for frequencies higher than one decade above the peak frequency. This is not significant when considering a series of similar dissipation functions whose peaks are spaced one decade apart.





*** $h(s)=\frac{s^2+11s}{s^2+11s+10}$ +++ $h(s)=\frac{s}{s+1}$

Fig. 3 Dissipation functions

7 Viscoelastic Element Matrices

Consider now the structural model

$$\{s^2\mathfrak{M}+[G^0+h(s)]\mathcal{K}\}\mathbf{q}(s)=\mathbf{f}(s)+\mathfrak{M}[s\mathbf{q}_0+\dot{q}_0] \tag{7.1}$$

where

$$G^0>0, \quad \mathfrak{M}>0, \quad \mathcal{K}\not<0$$

and

$$h(s)=\frac{\alpha(s^2+\beta s)}{s^2+\beta s+\delta}$$

We now have more than one coordinate in $\mathbf{q}$. Using the result of the preceding section we have the symmetrical second-order realization

$$\mathbf{M}^+\begin{bmatrix} \mathbf{q} \\ \hat{\mathbf{z}}\end{bmatrix}^{\cdot\cdot}+\mathbf{D}^+\begin{bmatrix} \mathbf{q} \\ \hat{\mathbf{z}}\end{bmatrix}^{\cdot}+\mathbf{K}^+\begin{bmatrix} \mathbf{q} \\ \hat{\mathbf{z}}\end{bmatrix}=\begin{bmatrix} \mathbf{f} \\ \mathbf{0}\end{bmatrix} \tag{7.2}$$

where

$$\mathbf{M}^+=\begin{bmatrix} \mathfrak{M} & \mathbf{0} \\ \mathbf{0} & \mathbf{0}\end{bmatrix}+\frac{\alpha}{\delta}\begin{bmatrix} \hat{d}^2\mathcal{K} & \hat{d}\mathcal{K} \\ \hat{d}\mathcal{K} & \mathcal{K}\end{bmatrix}$$

$$\mathbf{D}^+=\frac{\alpha\beta}{\delta}\begin{bmatrix} \hat{d}^2\mathcal{K} & \hat{d}\mathcal{K} \\ \hat{d}\mathcal{K} & \mathcal{K}\end{bmatrix}$$

$$\mathbf{K}^+=\begin{bmatrix} G^0\mathcal{K} & \mathbf{0} \\ \mathbf{0} & \mathbf{0}\end{bmatrix}+\alpha\begin{bmatrix} (1+\hat{d})^2\mathcal{K} & (1+\hat{d})\mathcal{K} \\ (1+\hat{d})\mathcal{K} & \mathcal{K}\end{bmatrix}$$

For an unconstrained structure having rigid body modes this is not a LMSO realization since $\mathcal{K}\geq 0$ implies $\mathbf{M}^+\geq 0$. We can, however, use the spectral decomposition of the stiffness matrix to successfully define a symmetrical LMSO realization of equation (7.1). We have

$$\mathcal{K}=\mathbf{R}_e\mathbf{\Lambda}\mathbf{R}_e^T$$

where

$$\mathbf{R}_e=[\mathbf{R}_r,\mathbf{R}_f]$$

$$\mathbf{\Lambda}=\text{block diag}\,\{\mathbf{0},\mathbf{\Lambda}_f\}$$

$$\mathbf{\Lambda}_f=\text{diag}\,\{\lambda_i\}$$

Downloaded 02 May 2010 to 171.66.16.54. Redistribution subject to ASME license or copyright; see http://www.asme.org/terms/Terms_Use.cfm

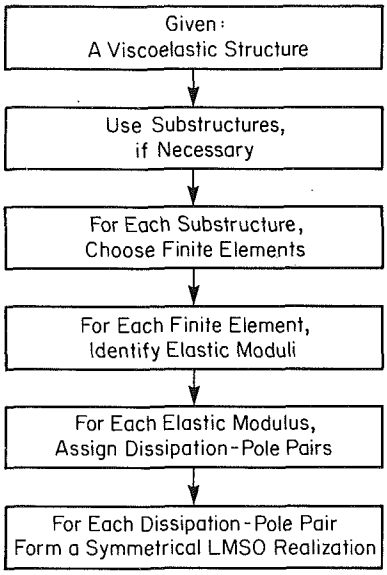


Fig. 4 Generalized method of analysis

Here $\mathbf{R}_e$ is the matrix of orthonormal eigenvectors of $\mathcal{K}$ which we partition to indicate the flexible ($\mathbf{R}_f$) and rigid ($\mathbf{R}_r$) modes. We define

$$\mathbf{R} = \mathbf{R}_f \Lambda_f^{1/2}$$

and make the substitution

$$\hat{\mathbf{z}} = \mathbf{R}\mathbf{z}$$

which effectively truncates the dissipation coordinates associated with rigid body modes.

A symmetrical LMSO realization of equation (7.1) is given by

$$\mathbf{M}^v \begin{bmatrix} \mathbf{q} \\ \mathbf{z} \end{bmatrix}^{\cdot\cdot} + \mathbf{D}^v \begin{bmatrix} \mathbf{q} \\ \mathbf{z} \end{bmatrix}^{\cdot} + \mathbf{K}^v \begin{bmatrix} \mathbf{q} \\ \mathbf{z} \end{bmatrix} = \begin{bmatrix} \mathbf{f} \\ \mathbf{0} \end{bmatrix} \tag{7.3}$$

where

$$\mathbf{M}^v = \begin{bmatrix} \mathfrak{M} & \mathbf{0} \\ \mathbf{0} & \mathbf{0} \end{bmatrix} + \frac{\alpha}{\delta} \begin{bmatrix} \hat{d}^2\mathcal{K} & \hat{d}\mathbf{R} \\ \hat{d}\mathbf{R}^T & \mathbf{1} \end{bmatrix} \tag{7.4}$$

$$\mathbf{D}^v = \frac{\alpha\beta}{\delta} \begin{bmatrix} \hat{d}^2\mathcal{K} & \hat{d}\mathbf{R} \\ \hat{d}\mathbf{R}^T & \mathbf{1} \end{bmatrix} \tag{7.5}$$

$$\mathbf{K}^v = \begin{bmatrix} G^0\mathcal{K} & \mathbf{0} \\ \mathbf{0} & \mathbf{0} \end{bmatrix} + \alpha \begin{bmatrix} (1+\hat{d})^2\mathcal{K} & (1+\hat{d})\mathbf{R} \\ (1+\hat{d})\mathbf{R}^T & \mathbf{1} \end{bmatrix} \tag{7.6}$$

and the initial conditions for the dissipation coordinates are given by

$$\mathbf{z}_0 = -\hat{d}\mathbf{R}^T\mathbf{q}_0 \tag{7.7}$$

$$\dot{\mathbf{z}}_0 = -\hat{d}\mathbf{R}^T\dot{\mathbf{q}}_0 \tag{7.8}$$

We now interpret the augmented matrices $\{\mathbf{M}^v, \mathbf{D}^v, \mathbf{K}^v\}$ as viscoelastic element matrices in the important case of the finite element method; in fact, the given matrices are just the element mass, damping, and stiffness matrices.

To give a simple example, we consider the element mass and stiffness matrices for the longitudinal vibrations of a rod:

$$\mathbf{M}^e = \mu^2 \begin{bmatrix} 2\rho 1 & \\ & 1\rho 2 \end{bmatrix}, \quad \mathbf{K}^e = E\chi^2 \begin{bmatrix} 1 & -1 \\ -1 & 1 \end{bmatrix} \tag{7.9}$$

where

$$\mu^2 = \rho Al/6, \quad \chi^2 = A/l$$

and

ρ = mass density
A = cross-sectional area of rod
l = length of element
G^0 = E = Young's modulus

In the viscoelastic case where

$$G(s) = \mathrm{E} + \frac{\alpha(s^2+\beta s)}{s^2+\beta s+\delta}$$

we have the viscoelastic element matrices

$$\mathbf{M}^v = \begin{bmatrix} 2\mu^2 & 0 & \mu^2 \\ 0 & \alpha/\delta & 0 \\ \mu^2 & 0 & 2\mu^2 \end{bmatrix} \tag{7.10}$$

$$\mathbf{D}^v = \begin{bmatrix} 0 & 0 & 0 \\ 0 & \alpha\beta/\delta & 0 \\ 0 & 0 & 0 \end{bmatrix} \tag{7.11}$$

$$\mathbf{K}^v = \begin{bmatrix} (\mathrm{E}+\alpha)\chi^2 & \alpha\chi & -(\mathrm{E}+\alpha)\chi^2 \\ \alpha\chi & \alpha & -\alpha\chi \\ -(\mathrm{E}+\alpha)\chi^2 & -\alpha\chi & (\mathrm{E}+\alpha)\chi^2 \end{bmatrix} \tag{7.12}$$

(We choose $\hat{d} = 0$ for simplicity and reorder the coordinates.)

The viscoelastic element matrices may be generalized, in three separate ways, as illustrated in Fig. 4, and then combined to analyze a general viscoelastic structure. We now illustrate these generalizations, one at a time. Furthermore, we choose $\hat{d} = 0$ for simplicitiy in all of the following.

Generalization *A*: Several Finite Elements. The assembly of several viscoelastic element matrices is written quite compactly using the assembly notation introduced earlier:

$$\mathfrak{M} = \mathop{\mathbin{\mathbf{\Sigma}}}_{j=1}^{m} \mathbf{M}_j^v, \quad \mathfrak{D} = \mathop{\mathbin{\mathbf{\Sigma}}}_{j=1}^{m} \mathbf{D}_j^v, \quad \mathcal{K} = \mathop{\mathbin{\mathbf{\Sigma}}}_{j=1}^{m} \mathbf{K}^v{}_j$$

Although simply written, there is much detail contained in the assembly process. There are three important aspects that deserve comment.

(*i*) In assembling viscoelastic element matrices, compatibility constraints are applied only to the physical coordinates (q's), exactly as in the corresponding elastic case. There are no additional compatibility constraints for the dissipation coordinates (z's); all dissipation coordinates are retained in the assembled system.

(*ii*) A rearrangement of the coordinates at the element level, as done for the simple rod example (equations (7.10)–(7.12)), can greatly facilitate matrix assembly and help minimize the bandwidth of the system matrices. To illustrate this, we assemble three of the simple rod stiffness matrices, equation (7.12).

$$\mathcal{K} = \begin{bmatrix} (\mathrm{E}+\alpha)\chi^2 & \alpha\chi & -(\mathrm{E}+\alpha)\chi^2 & & & \\ \alpha\chi & \alpha & -\alpha\chi & 0 & & 0 \\ -(\mathrm{E}+\alpha)\chi^2 & -\alpha\chi & 2(\mathrm{E}+\alpha)\chi^2 & \alpha\chi & -(\mathrm{E}+\alpha)\chi^2 & \\ & 0 & \alpha\chi & \alpha & -\alpha\chi & 0 \\ & & -(\mathrm{E}+\alpha)\chi^2 & -\alpha\chi & 2(\mathrm{E}+\alpha)\chi^2 & \alpha\chi & -(\mathrm{E}+\alpha)\chi^2 \\ & 0 & & 0 & \alpha\chi & \alpha & -\alpha\chi \\ & & & & -(\mathrm{E}+\alpha)\chi^2 & -\alpha\chi & (\mathrm{E}+\alpha)\chi^2 \end{bmatrix}$$

Downloaded 02 May 2010 to 171.66.16.54. Redistribution subject to ASME license or copyright; see http://www.asme.org/terms/Terms_Use.cfm

$\mathcal{K}$ is the assembled stiffness matrix for a simple three-element viscoelastic rod with both ends free.

(*iii*) Boundary conditions are applied only to the physical coordinates, exactly as in the corresponding elastic case. For example, the assembled stiffness matrix for a simple three-element viscoelastic rod with one end fixed is found from $\mathcal{K}$ by deleting the first row and column.

Generalization *B*: Several Moduli per Element. Given the element matrices $\mathbf{M}^e$ and $\mathcal{K}^e$ where

$$\mathcal{K}^e(s) = \sum_{k=1}^{\nu} \left[G_k^0 + \frac{\alpha_k (s^2 + \beta_k s)}{s^2 + \beta_k s + \delta_k} \right] \mathbf{K}_k^e$$

we have the corresponding viscoelastic element matrices

$$\mathbf{K}^{\nu} = \begin{bmatrix} \left[\sum_{k=1}^{\nu} (G_k^0 + \alpha_k) \mathbf{K}_k^e \right] & \alpha_1 \mathbf{R}_1 & \cdots & \alpha_\nu \mathbf{R}_\nu \\ & \alpha_1 \mathbf{1} & & 0 \\ \text{symmetric} & & \ddots & \\ & & & \alpha_\nu \mathbf{1} \end{bmatrix} \tag{7.13}$$

where

$$\mathbf{K}_k^e = \mathbf{R}_k \mathbf{R}_k^T$$

$$\mathbf{D}^{\nu} = \text{block diag} \left\{ \mathbf{0}, \frac{\alpha_1 \beta_1}{\delta_1} \mathbf{1}, \ldots, \frac{\alpha_\nu \beta_\nu}{\delta_\nu} \mathbf{1} \right\} \tag{7.14}$$

$$\mathbf{M}^{\nu} = \text{block diag} \left\{ \mathbf{M}^e, \frac{\alpha_1}{\delta_1} \mathbf{1}, \ldots, \frac{\alpha_\nu}{\delta_\nu} \mathbf{1} \right\} \tag{7.15}$$

Generalization *C*: Several Dissipation-Pole Pairs per Modulus. Given the element matrices $\mathbf{M}^e$ and $\mathcal{K}^e$ where

$$\mathcal{K}^e(s) = [G^0(s) + h(s)] \mathbf{K}^e$$

and

$$h(s) = \sum_{l=1}^{\upsilon} \frac{\alpha_l (s^2 + \beta_l s)}{s^2 + \beta_l s + \delta_l}$$

we have the corresponding viscoelastic element matrices

$$\mathbf{K}^{\upsilon} = \begin{bmatrix} \left(G^0 + \sum_{l=1}^{\upsilon} \alpha_l \right) \mathbf{K}^e & \alpha_1 \mathbf{R} & \cdots & \alpha_\upsilon \mathbf{R} \\ & \alpha_1 \mathbf{1} & & 0 \\ \text{symmetric} & & \ddots & \\ & & & \alpha_\upsilon \mathbf{1} \end{bmatrix} \tag{7.16}$$

where

$$\mathbf{K}^e = \mathbf{R}\mathbf{R}^T$$

$$\mathbf{D}^{\upsilon} = \text{block diag} \left\{ \mathbf{0}, \frac{\alpha_1 \beta_1}{\delta_1} \mathbf{1}, \ldots, \frac{\alpha_\upsilon \beta_\upsilon}{\delta_\upsilon} \mathbf{1} \right\} \tag{7.17}$$

$$\mathbf{M}^{\upsilon} = \text{block diag} \left\{ \mathbf{M}^e, \frac{\alpha_1}{\delta_\upsilon} \mathbf{1}, \ldots, \frac{\alpha_\upsilon}{\delta_\upsilon} \mathbf{1} \right\} \tag{7.18}$$

Before proceeding to numerical examples, we should discern an important principle from the foregoing discussion. Having set out to find a time-domain realization [specifically, a symmetrical LMSO realization] of the assembled Laplace-domain system given by equations (4.8), we first found realizations of the elements, and then assembled those realizations. Hence the principle:

> A realization of an assembly is an assembly of realizations.

This principle is easily verified a posteriori by taking the Laplace transform of the assembled realizations. We call this principle the assembly-realization principle. It is of fundamental importance in the derivation of viscoelastic element matrices.

8 Numerical Examples

Some numerical examples are now presented to demonstrate the use of viscoelastic element matrices in the finite element analysis of viscoelastic structures. First we look at the longitudinal free vibrations of a long, unconstrained, viscoelastic rod. The equation of motion is

$$\left\{ \rho s^2 - [\mathrm{E} + h(s)] \frac{\partial^2}{\partial x^2} \right\} u(s) = \rho (s u_0 + \dot{u}_0) \tag{8.1}$$

where

$$h(s) = \sum_{l=1}^{\upsilon} \frac{\alpha_l (s^2 + \beta_l s)}{s^2 + \beta_l s + \delta_l} \tag{8.2}$$

To nondimensionalize the equation we define the characteristic frequency

$$c = \frac{1}{L} \left(\frac{E}{\rho} \right)^{1/2} \tag{8.3}$$

(where L is the length of rod) and make the substitutions

$$t = \tau / c, \quad x = L\hat{x}, \quad u = L\hat{u}$$

$$\alpha_l = \mathrm{E}\hat{\alpha}_l, \quad \beta_l = c\hat{\beta}_l, \quad \delta_l = c^2 \hat{\delta}_l$$

We will use a relatively simple dissipation function with four terms ($\upsilon = 4$). The nondimensional material properties are listed in Table 2. Note that the eight (real) poles associated with the dissipation function start at -0.1 and increase geometrically by the common factor $\sqrt{10}$. The viscoelastic element matrices, constructed as in equations (7.10)–(7.12), are:

$$\mathbf{M}^{\upsilon} = \begin{bmatrix} 2\mu^2 & & & \mu^2 \\ & (\hat{\alpha}_1/\hat{\delta}_1) & & \\ & & (\hat{\alpha}_2/\hat{\delta}_2) & 0 \\ & & & (\hat{\alpha}_3/\hat{\delta}_3) \\ \text{symmetric} & & & (\hat{\alpha}_4/\hat{\delta}_4) \\ & & & 2\mu^2 \end{bmatrix} \tag{8.4}$$

$$\mathbf{D}^{\upsilon} = \text{diag}\{0, \hat{\alpha}_1 \hat{\beta}_1 / \hat{\delta}_1, \ldots, \hat{\alpha}_4 \hat{\beta}_4 / \hat{\delta}_4, 0\} \tag{8.5}$$

$$\mathbf{K}^{\upsilon} = \begin{bmatrix} \phi\chi^2 & \hat{\alpha}_1\chi & \hat{\alpha}_2\chi & \hat{\alpha}_3\chi & \hat{\alpha}_4\chi & -\phi\chi^2 \\ & \hat{\alpha}_1 & & & & -\hat{\alpha}_1\chi \\ & & \hat{\alpha}_2 & & 0 & -\hat{\alpha}_2\chi \\ & & & \hat{\alpha}_3 & & -\hat{\alpha}_3\chi \\ & \text{symmetric} & & & \hat{\alpha}_4 & -\hat{\alpha}_4\chi \\ & & & & & \phi\chi^2 \end{bmatrix} \tag{8.6}$$

Table 2 Nondimensional viscoelastic material properties for Young's modulus

l	$\hat{\alpha}_l$	$\hat{\beta}_l$	$\hat{\delta}_l$
1	3.0×10^{-2}	4.16×10^{-1}	3.16×10^{-2}
2	3.0×10^{-2}	4.16	3.16
3	3.0×10^{-2}	4.16×10^{1}	3.16×10^{2}
4	3.0×10^{-2}	4.16×10^{2}	3.16×10^{4}

Table 3 Eigenvalues for longitudinal vibrations of a rod

Mode number	Elastic PDE	Elastic FEM	Viscoelastic FEM	
n	$\hat{\omega}_n$	$\hat{\omega}_n$	$\hat{\omega}_n$	ζ_n
1	0	0	0	0
2	3.14	3.22	3.33	8.55×10^{-3}
3	6.28	6.93	7.19	1.01×10^{-2}
4	9.42	11.26	11.73	1.02×10^{-2}
5	12.57	13.85	14.46	9.71×10^{-3}

Downloaded 02 May 2010 to 171.66.16.54. Redistribution subject to ASME license or copyright; see http://www.asme.org/terms/Terms_Use.cfm

where

$$\phi = 1 + \sum_{l=1}^{4} \hat{\alpha}_l$$

and $\chi^2 = \mu^{-2} = m$, the number of elements in the rod.

The results of an eigenvalue analysis for a four-element rod are listed in Table 3. The natural frequencies of the corresponding elastic rod, as found from the partial differential equation (PDE) solution, and as found from a four-element finite element method (FEM) solution, are included for the purpose of comparison.

In addition to the single rigid-body mode and the four flexible-body modes, we have 32 eigenvalues on the negative real axis. These are the dissipation poles and we call the corresponding modes *dissipation modes*. They arise naturally from the dissipation coordinates with which we have augmented the system.

Consider now the free transverse vibrations of a long, cantilevered, viscoelastic rod (Fig. 5). The equation of motion is

$$\left\{A\rho s^2 + I[\mathrm{E} + h(s)]\frac{\partial^4}{\partial x^4}\right\} w(s) = A\rho(sw_0 + \dot{w}_0) \tag{8.7}$$

where

$$h(s) = \sum_{l=1}^{4} \frac{\alpha_l(s^2 + \beta_l s)}{s^2 + \beta_l s + \delta_l} \tag{8.8}$$

ρ = mass density

A = area of cross-section

I = second area moment of cross-section

E = Young's modulus

To nondimensionalize the equation we define the characteristic frequency

$$c = \frac{1}{L^2}\left(\frac{EI}{\rho A}\right)^{1/2} \tag{8.9}$$

(where L is the length of rod) and make the substitutions

$$t = \tau/c, \quad x = L\hat{x}, \quad w = L\hat{w}$$
$$\alpha_l = \mathrm{E}\hat{\alpha}_l, \quad \beta_l = c\hat{\beta}_l, \quad \delta_l = c^2\hat{\delta}_l$$

We will use the nondimensional material properties listed in Table 2.

The nondimensional elastic element matrices are given by

$$\mathbf{M}^e = \frac{\mu^2}{420}\begin{bmatrix} 156 & 22\mu^2 & 54 & -13\mu^2 \\ & 4\mu^2 & 13\mu^2 & -3\mu^4 \\ & & 156 & -22\mu^2 \\ \text{symmetric} & & & 4\mu^4 \end{bmatrix} \tag{8.10}$$

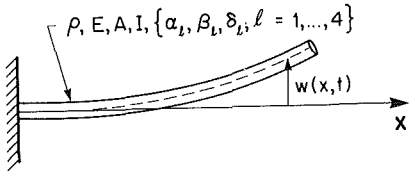


Fig. 5 Transverse vibrations of a cantilevered rod

$$\mathbf{K}^e = \begin{bmatrix} 12\chi^6 & 6\chi^4 & -12\chi^6 & 6\chi^4 \\ & 4\chi^2 & -6\chi^4 & 2\chi^2 \\ & & 12\chi^6 & -6\chi^4 \\ \text{symmetric} & & & 4\chi^2 \end{bmatrix} \tag{8.11}$$

where $\chi^2 = \mu^{-2} = m$, the number of elements that constitute the rod. The stiffness matrix has the factorization

$$\mathbf{K}^e = \mathbf{R}\mathbf{R}^T$$

where

$$\mathbf{R}^T = \begin{bmatrix} 0 & \chi & 0 & -\chi \\ 2\sqrt{3}\chi^3 & \sqrt{3}\chi & -2\sqrt{3}\chi^3 & \sqrt{3}\chi \end{bmatrix} \tag{8.12}$$

The viscoelastic element matrices are calculated from equations (7.16)–(7.18) and the coordinates are rearranged to facilitate matrix assembly. First we define the matrix partitions

$$\mathbf{M}^e = \begin{bmatrix} \mathbf{M}_{11} & \mathbf{M}_{12} \\ \mathbf{M}_{12}^T & \mathbf{M}_{22} \end{bmatrix}, \quad \mathbf{K}^e = \begin{bmatrix} \mathbf{K}_{11} & \mathbf{K}_{12} \\ \mathbf{K}_{12}^T & \mathbf{K}_{22} \end{bmatrix}$$
$$\mathbf{R}^T = [\mathbf{R}_1^T \; \mathbf{R}_2^T]$$

The viscoelastic element matrices are:

$$\mathbf{M}^v = \begin{bmatrix} \mathbf{M}_{11} & \mathbf{0} & \mathbf{0} & \mathbf{0} & \mathbf{0} & \mathbf{M}_{12} \\ & \frac{\hat{\alpha}_1}{\hat{\delta}_1}\mathbf{1} & \mathbf{0} & \mathbf{0} & \mathbf{0} & \mathbf{0} \\ & & \frac{\hat{\alpha}_2}{\hat{\delta}_2}\mathbf{1} & \mathbf{0} & \mathbf{0} & \mathbf{0} \\ & & & \frac{\hat{\alpha}_3}{\hat{\delta}_3}\mathbf{1} & \mathbf{0} & \mathbf{0} \\ & & & & \frac{\hat{\alpha}_4}{\hat{\delta}_4}\mathbf{1} & \mathbf{0} \\ \text{symmetric} & & & & & \mathbf{M}_{22} \end{bmatrix} \tag{8.13}$$

$$\mathbf{D}^v = \text{block diag}\left\{\mathbf{0}, \frac{\hat{\alpha}_1\hat{\beta}_1}{\hat{\delta}_1}\mathbf{1}, \ldots, \frac{\hat{\alpha}_4\hat{\beta}_4}{\hat{\delta}_4}\mathbf{1}, \mathbf{0}\right\} \tag{8.14}$$

$$\mathbf{K}^v = \begin{bmatrix} \phi\mathbf{K}_{11} & \hat{\alpha}_1\mathbf{R}_1 & \hat{\alpha}_2\mathbf{R}_1 & \hat{\alpha}_3\mathbf{R}_1 & \hat{\alpha}_4\mathbf{R}_1 & \phi\mathbf{K}_{12} \\ & \hat{\alpha}_1\mathbf{1} & \mathbf{0} & \mathbf{0} & \mathbf{0} & \hat{\alpha}_1\mathbf{R}_2^T \\ & & \hat{\alpha}_2\mathbf{1} & \mathbf{0} & \mathbf{0} & \hat{\alpha}_1\mathbf{R}_2^T \\ & & & \hat{\alpha}_3\mathbf{1} & \mathbf{0} & \hat{\alpha}_3\mathbf{R}_2^T \\ & & & & \hat{\alpha}_4\mathbf{1} & \hat{\alpha}_4\mathbf{R}_2^T \\ \text{symmetric} & & & & & \phi\mathbf{K}_{22} \end{bmatrix} \tag{8.15}$$

where

$$\phi = 1 + \sum_{l=1}^{4} \hat{\alpha}_l$$

Table 4 Eigenvalues for transverse vibrations of a cantilevered rod

Mode number	Elastic PDE	Elastic FEM	Viscoelastic FEM	
n	$\hat{\omega}_n$	$\hat{\omega}_n$	$\hat{\omega}_n$	ζ_n
1	3.52	3.52	3.63	8.60×10^{-3}
2	2.20×10^{1}	2.21×10^{1}	2.31×10^{1}	8.27×10^{-3}
3	6.17×10^{1}	6.22×10^{1}	6.53×10^{1}	8.42×10^{-3}
4	1.21×10^{2}	1.23×10^{2}	1.30×10^{2}	7.46×10^{-3}
5	2.00×10^{2}	2.28×10^{2}	2.42×10^{2}	3.94×10^{-3}

Downloaded 02 May 2010 to 171.66.16.54. Redistribution subject to ASME license or copyright; see http://www.asme.org/terms/Terms_Use.cfm

The eigenvalues for the first five flexible transverse vibration modes of a four-element rod are listed in Table 4. In addition to a total of eight flexible modes there are 64 eigenvalues on the negative real axis (the dissipation poles) which we do not list here.

9 Concluding Remarks

The main contribution of this paper is to show how to construct damping models for viscoelastic structures. The elusive "damping matrix" is explicitly calculated, after the system of coordinates has been augmented by the inclusion of an appropriate set of "dissipation coordinates." The kernel of the idea can be explained using a single displacement variable, a single elastic modulus, and a single pair of dissipation poles. From this fundamental result one can generalize (as shown herein) to many coordinates, many finite elements, many elastic moduli, and many pairs of dissipation poles. Admittedly, the values of certain viscoelastic material constants (the a_l and b_l) must be available, but this is completely reasonable and hardly surprising. (Could one calculate natural frequencies without knowing the elastic moduli?) It is clear that the time has come for damping characteristics to be measured and calculated, not just guessed, and that the calculations must be assimilated within the finite element method. This paper shows how to achieve these objectives.

Acknowledgments

This work was supported in part by the Natural Sciences and Engineering Research Council of Canada under Grant No. A4183, and in part by the (Canadian) Communications Research Centre.

References

1 Gurtin, M. E., and Sternberg, E., "On the Linear Theory of Viscoelasticity," *Arch. Ration. Mech. Anal.*, Vol. 11, 1962, pp. 291–356.

2 Biot, M. A., "Variational Principles in Irreversible Thermodynamics With Application to Viscoelasticity," *Physical Review*, Vol. 97, No. 6, 1955, pp. 1463–1469.

3 Soo, S. L., *Analytical Thermodynamics*, Prentice-Hall, Englewood Cliffs, N.J., 1962.

4 Christensen, R. M., *Theory of Viscoelasticity: An Introduction*, 2nd Ed., Academic Press, New York, 1982.

5 Gurtin, M. E., and Herrera, I., "On Dissipation Inequalities and Linear Viscoelasticity," *Quart. Appl. Math.*, Vol. 23, 1965, pp. 235–245.

6 Bagley, R. L., and Torvik, P. J., "Fractional Calculus—A Different Approach to the Finite Element Analysis of Viscoelastically Damped Structures," *AIAA Journal*, Vol. 21, No. 5, May 1983, pp. 741–748.

7 Bagley, R. L., and Torvik, P. J., "Fractional Calculus in the Transient Analysis of Viscoelastically Damped Structures," *Proceedings of the AIAA/ASME/ASCE/AHS 24th Structures, Structural Dynamics and Materials Conference*, Lake Tahoe, Nev., May 2–4, 1983.

8 Buhariwala, K. J., "Dynamic Response of Viscoelastic Fibre Reinforced Composite Structures," M.A.Sc. thesis, University of Toronto, Institute for Aerospace Studies, 1982.

9 Zaheh, L. A., and Desoer, C. A., *Linear System Theory*, McGraw-Hill, New York, 1963.

Downloaded 02 May 2010 to 171.66.16.54. Redistribution subject to ASME license or copyright; see http://www.asme.org/terms/Terms_Use.cfm

Nonlinear Asymptotic Solution of the Reissner Plate Equations

L. A. Taber
Assistant Professor,
Department of Mechanical Engineering,
University of Rochester,
Rochester, N.Y. 14627

Based on the Reissner plate equations for large displacements and rotations within the limits of small strain, asymptotic solutions are developed for circular plates under uniform pressure. With the boundary layer solution assumed in exponential form, the boundary conditions are applied directly at the plate edge without the need for matched asymptotic expansions. Results are presented for plates with clamped edges. When compared to the solution for the special case of von Kármán plate theory, stresses generally deviate by less than 10 percent for rotation angles up to about 30 deg.

Introduction

Large deflection of thin plates has been a popular research topic for many years. Reissner (1949) presented a set of governing equations for axisymmetric deformation of circular plates which allows arbitrarily large displacements and rotations under the restriction of small strains. Most solutions of nonlinear plate problems, however, have been based on the simpler von Kármán equations, which assume that rotations are moderate and that the surface pressure and internal shear forces always act vertically. Using the modified equations of Reissner (1963), the present work examines the effects of the horizontal components of these forces for rotation angles up to about 30 deg. In similar studies, Weinberg (1962) obtained asymptotic solutions to the Reissner equations for radial compressive loads, while Hart and Evans (1964) studied numerical solutions of these equations for vertical edge loads on annular plates.

The nature of the solution of the von Kármán equations depends on the magnitude of a load-thickness parameter β, which increases as the load increases or as the plate grows relatively thinner. For a circular plate with a uniform surface pressure, Bromberg (1956) examined the behavior for different ranges of β. He developed a regular perturbation expansion for $\beta << 1$, a power series solution for $\beta = 0(1)$, and a singular perturbation expansion for $\beta >> 1$. Other solutions to this problem are discussed in the book by Chia (1980).

This paper focuses on the case $\beta >> 1$. Although a second parameter $\alpha << \beta$ appears in the nondimensional Reissner equations, β still determines the main features of the solution. As $\beta \to \infty$, the order of the governing differential equations halves, giving the equations of Föppl-Hencky membrane theory (Föppl, 1907; Hencky, 1915), and all of the boundary conditions for a plate with clamped edges no longer can be satisfied. For β large but finite, membrane stresses dominate bending stresses everywhere except within a narrow edge zone, where the plate adjusts abruptly to the zero slope condition. To handle this situation, Bromberg (1956) followed the classical asymptotic matching procedure common to fluid mechanics whereby the radial coordinate is stretched within the "boundary layer" near the edge. Similar solutions to the von Kármán equations were studied by Chien (1948) and by Frakes and Simmonds (1985).

Here, a different type of asymptotic expansion, popular in linear thin shell theory, is explored. An a priori assumption of the boundary layer solution in exponential form allows the boundary conditions to be applied directly in the solution process, bypassing the need to stretch the coordinate for a formal matching procedure. Recently, Ranjan and Steele (1980) applied this WKB-type method to the nonlinear shell equations for moderately large rotation. The main purpose of the present research is to study its applicability to the Reissner plate equations with hopes of future application to plate and shell problems involving large strains, for which the algebra grows exceedingly tedious. To concentrate on the essentials, this paper considers only circular plates with clamped edges under uniform surface pressures.

Governing Equations

Consider a homogeneous, isotropic circular plate of radius R and thickness t. Reissner (1949, 1963) reduced the field equations for large axisymmetric deflection to the pair of coupled differential equations

$$\bar{\psi}'' + \frac{1}{r}\bar{\psi}' - \frac{1}{r^2}\bar{\psi} = \frac{Et}{r}(\cos\bar{\phi} - 1) - \frac{1}{r}(r^2 p_H)' - \nu p_H \qquad (1a)$$

$$\bar{\phi}'' + \frac{1}{r}\bar{\phi}' - \frac{1}{r^2}\cos\bar{\phi}\sin\bar{\phi} = \frac{1}{rD}(\bar{\psi}\sin\bar{\phi} - rV\cos\bar{\phi}) \qquad (1b)$$

to be solved for the deformed meridional angle $\bar{\phi}$ (Fig. 1) and the stress function

$$\bar{\psi} = rH \qquad (2)$$

with dot denoting differentiation with respect to the radial coordinate r. In these equations, E is Young's modulus, ν is Poisson's ratio, D is the plate stiffness, and H and V are the

Contributed by the Applied Mechanics Division for publication in the JOURNAL OF APPLIED MECHANICS.

Discussion on this paper should be addressed to the Editorial Department, ASME, United Engineering Center, 345 East 47th Street, New York, N.Y. 10017, and will be accepted until two months after final publication of the paper itself in the JOURNAL OF APPLIED MECHANICS. Manuscript received by ASME Applied Mechanics Division, November, 1984; final revision, March, 1985.

Copyright © 1985 by ASME
Downloaded 02 May 2010 to 171.66.16.54. Redistribution subject to ASME license or copyright; see http://www.asme.org/terms/Terms_Use.cfm

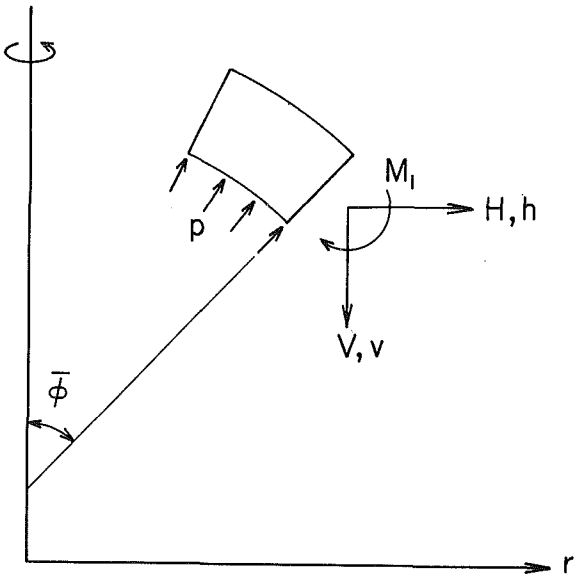


Fig. 1 Deformed plate element

horizontal and vertical stress resultants. For a uniform surface pressure p, axial equilibrium and the deformed geometry, respectively, give

$$V = pr/2; \quad p_H = p\sin\bar{\phi}, \tag{3}$$

where p_H is the horizontal component of the pressure.

Equations (1) are valid for arbitrarily large displacements and rotations so long as the strains remain small and the material obeys Hooke's law. With the introduction of nondimensional quantities

$$\alpha = 2\left(\frac{pR}{Et}\right)^{1/3}; \quad \beta = \left(\frac{pR^3}{8D\alpha}\right)^{1/2} = \frac{1}{4}[3(1-\nu^2)]^{1/2}\frac{R}{t}\alpha$$

$$x = r^2/R^2; \quad \bar{\psi} = \frac{pR^2}{\alpha}x^{-1/2}\psi; \quad \bar{\phi} = \alpha x^{1/2}\phi, \tag{4}$$

combination of equations (1), (3), and (4), and expansion in powers of α produce

$$\psi'' = -\phi^2 - \frac{\alpha^2}{4}\left[(3+\nu)\phi + 2x\phi' - \frac{x}{3}\phi^4\right] + \frac{\alpha^4}{24}\left[(5+\nu)x\phi^3 + 6x^2\phi^2\phi' - \frac{x^2}{15}\phi^6\right] + \ldots \tag{5a}$$

$$(x\phi)'' = \beta^2\left[(2\phi\psi x^{-1} - 1) - \frac{\alpha^2}{6}(2\phi^3\psi - 3x\phi^2) + \frac{\alpha^4}{120}(2x\phi^5\psi - 5x^2\phi^4)\right] - \frac{\alpha^2}{6}\phi^3 + \frac{\alpha^4}{30}x\phi^5 + \ldots \tag{5b}$$

where prime indicates differentiation with respect to x. These equations, which are accurate for $\phi \lesssim 30$ deg, can be used in most practical problems that are limited to small strain.

In terms of ϕ and ψ, the dimensionless normal stress resultants, moment resultants, and displacement components (see Fig. 1) are

$$N_1 = \frac{\bar{N}_1\alpha}{pR} = x^{-1}\psi \tag{6}$$

$$N_2 = \frac{\bar{N}_2\alpha}{pR} = 2\psi' - x^{-1}\psi + \alpha^2 x\phi + \ldots$$

$$M_1 = \frac{\bar{M}_1 R}{D\alpha} = \phi\left[1 + \nu\left(1 - \frac{\alpha^2}{6}x\phi^2 + \ldots\right)\right] + 2x\phi'$$

$$M_2 = \frac{\bar{M}_2 R}{D\alpha} = \phi\left(\nu + 1 - \frac{\alpha^2}{6}x\phi^2 + \ldots\right) + 2\nu x\phi' \tag{7}$$

$$h = \frac{Et\bar{h}\alpha}{pR^2} = x^{1/2}(N_2 - \nu N_1)$$

$$v = \frac{2\bar{v}}{\alpha R} = \int_x^1 \phi\left[1 - \frac{\alpha^2}{6}x\phi^2 + \ldots + \frac{\alpha^2}{8}(N_1 - \nu N_2)\right]dx \tag{8}$$

in which bars indicate the physical (dimensional) quantities, and 1 and 2 denote the deformed meridional and circumferential directions, respectively. The appropriate boundary conditions for a clamped edge are

$$h(1) = \phi(1) = 0 \tag{9}$$

with the regularity conditions

$$h(0) = 0, \qquad \phi(0) \quad \text{finite.} \tag{10}$$

Note that for $\alpha = 0$, equations (5)–(8) reduce to those of von Kármán's plate theory.

In terms of the stress resultants of equations (6) and (7), the direct stresses $\bar{\sigma}_{D_i} = \bar{N}_i/t$ and the bending stresses $\bar{\sigma}_{B_i} = 6\bar{M}_i/t^2$ $(i = 1,2)$ can be computed. Nondimensional stresses are given by

$$\sigma_{D_i} = \frac{\bar{\sigma}_{D_i}}{E}\left(\frac{R}{t}\right)^2 = \frac{2\beta^2}{3(1-\nu^2)}N_i$$

$$\sigma_{B_i} = \frac{\bar{\sigma}_{B_i}}{E}\left(\frac{R}{t}\right)^2 = \frac{2\beta}{[3(1-\nu^2)^3]^{1/2}}M_i. \tag{11}$$

Asymptotic Expansions

In this section, an asymptotic solution to equations (5) is developed for $\beta >> 1$. Analogous to the behavior of a shell of revolution, when β is large, membrane stresses dominate over most of the plate, with significant bending stresses confined to a narrow boundary layer adjacent to the edge. The present work, therefore, investigates a technique that is often applied to thin shells.

In linear shell problems, the particular solution of the governing equations provides the "membrane solution," which is accurate everywhere except within the edge zone. The complementary or edge-effect bending solution, which is required to satisfy the boundary conditions, is assumed a priori to be in exponential form. This procedure allows the boundary conditions to be satisfied directly at the shell edge without the need to match the membrane (interior) solution to the full boundary layer solution. While use of this technique has been confined generally to linear problems, Ranjan and Steele (1980) applied it to the nonlinear equations for moderately large rotation of a shell of revolution of which the von Kármán plate equations are a special case. The form of their *WKB*-type solution resembles that used here.

Equations (5) contain two parameters, α and β, with $\beta >> \alpha$ for a thin plate. For an asymptotic analysis, it is convenient to eliminate α through the relation $\alpha^2\beta = \lambda$, where λ is a specified constant of order unity. Thus, for a given β, the plate geometry will be restricted according to the relation

$$\frac{R}{t} = 4\left[\frac{\beta^3}{3(1-\nu^2)\lambda}\right]^{1/2} \tag{12}$$

as given by equations (4).

With $\alpha^2 = \lambda/\beta$, the solution to equations (5) is taken in the form

$$\psi = a_0 + \beta^{-1}a_1 + \beta^{-2}a_2 + \ldots + e^{\beta\xi}(\beta^{-2}b_0 + \beta^{-3}b_1 + \ldots) + e^{2\beta\xi}(\beta^{-2}c_0 + \beta^{-3}c_1 + \ldots) + \ldots$$

Downloaded 02 May 2010 to 171.66.16.54. Redistribution subject to ASME license or copyright; see http://www.asme.org/terms/Terms_Use.cfm

$$\phi = d_0+\beta^{-1}d_1+\beta^{-2}d_2+\ldots+e^{\beta\xi}(e_0+\beta^{-1}e_1 +\beta^{-2}e_2+\ldots)+e^{2\beta\xi}(\beta^{-2}f_0+\beta^{-3}f_1+\ldots)+\ldots \quad (13)$$

where the a_n and d_n terms represent the interior solution, and the exponential terms provide the edge-effect, or boundary layer, solution. All of the terms are functions of x with the decay function $\xi(x)$ defined to be zero at the edge ($x=1$) and negative for $x<1$. Thus, for $\beta>>1$, the exponential terms decay rapidly in moving away from the edge of the plate and will be neglected when the regularity conditions of equations (10) are considered.

The equations relevant to the approximate solution discussed in the next section are presented now. Substitution of equations (13) into (5) with $\alpha^2=\lambda/\beta$ and equating like powers of β in the usual fashion yield the sequence

$$a_0'' = -d_0^2$$
$$0 = 2a_0d_0x^{-1}-1 \quad (14a)$$
$$a_1'' = -2d_0d_1-\frac{\lambda}{4}\left[(3+\nu)d_0+2xd_0'-\frac{x}{3}d_0^4\right]$$
$$0 = 2x^{-1}(a_0d_1+a_1d_0)-\lambda(a_0d_0^3/3-xd_0^2/2) \quad (14b)$$
$$a_2'' = -(2d_0d_2+d_1^2)-\frac{\lambda}{4}\left[(3+\nu)d_1+2xd_1'-\frac{4x}{3}d_0^3d_1\right] +\frac{\lambda^2}{24}\left[(5+\nu)xd_0^3+6x^2d_0^2d_0'-\frac{x^2}{15}d_0^6\right]$$
$$(xd_0)'' = 2x^{-1}(a_0d_2+a_1d_1+a_2d_0)-\lambda(a_0d_0^2d_1 -xd_0d_1+a_1d_0^3/3)+\frac{\lambda^2}{120}(2xa_0d_0^5-5x^2d_0^4)\ldots \quad (14c)$$

Equations (14a) correspond to Föppl-Hencky membrane theory, which is given by the special case of $\alpha=0$, $\beta\to\infty$ in equations (5).

Next, the $\beta^2e^{\beta\xi}$ term of equation (5b) gives

$$\xi'^2 = 2a_0/x^2 \quad (15a)$$

or

$$\xi(x) = \int_1^x \frac{(2a_0)^{1/2}}{x}dx, \quad (15b)$$

and so the width of the boundary layer depends on the membrane solution. In terms of dimensional quantities, equation (15b) provides the average plate tension

$$\beta\xi = \int_R^r \left(\frac{H}{D}\right)^{1/2}dr \quad (15c)$$

which, for constant H, reduces to the edge-effect solution for a plate under a combined lateral load and a uniform inplane tension. For a shell of revolution, ξ is a function of only the applied surface load and the shell geometry (Ranjan and Steele, 1980).

With equation (15a) taken into account, the higher-order exponential terms of equations (5) yield

$$e_0'+Q_1e_0=0$$
$$e_1'+Q_1e_1=Q_2 \quad (16)$$

where

$$Q_1(x) = \frac{\xi''}{2\xi'}+\frac{1}{x}-\frac{a_1}{x^2\xi'}+\lambda\frac{d_0}{2\xi'}\left(\frac{a_0d_0}{x}-1\right)$$
$$Q_2(x) = -\frac{1}{2\xi'}\left(e_0''+\frac{2}{x}e_0'-\frac{2a_2}{x^2}e_0\right)+\frac{b_0d_0}{x^2\xi'} -\lambda\frac{e_0}{2x\xi'}(2a_0d_0d_1+a_1d_0^2-xd_1) +\lambda^2\frac{e_0}{24\xi'}(a_0d_0^4-2xd_0^3) \quad (17)$$

and

$$b_0 = -\frac{2d_0e_0}{\xi'^2}-\lambda\frac{xe_0}{2\xi'} \quad (18a)$$
$$b_1 = -\frac{1}{\xi'^2}[2(d_0e_1+d_1e_0+\xi'b_0')+\xi''b_0] -\frac{\lambda}{12\xi'^2}[2x(3\xi'e_1+3e_0'-2e_0d_0^3)+3(3+\nu)e_0] +\lambda^2\frac{x^2}{4\xi'}e_0d_0^2 \quad (18b)$$

$$c_0 = \frac{e_0^2}{4\xi'^2} \quad (19a)$$

$$c_1 = -\frac{1}{2\xi'^2}(e_0e_1+\xi''c_0+2\xi'c_0')+\frac{xd_0e_0^2}{8\xi'^2}(\lambda d_0+\lambda^2x\xi') \quad (19b)$$

with similar equations for the other terms in the series.

Solution for Plate With Clamped Edge

For a clamped edge, substitution of equations (13) into equations (8) and (9) and equating powers of β give the boundary conditions at $x=1$

$$2a_0'-(1+\nu)a_0=0$$

Table 1

n	a_{0n}	$a_{1n}, a_{2n}^{(0)}$	$a_{1n}^{(\lambda)}$
0	1	1	0
1	-0.125	0.250	$-(0.188+0.0625\nu)$
2	-0.0104	0.0521	$-(0.0208+0.00781\nu)$
3	-0.00141	0.0113	$-(3.74+1.57\nu)\times10^{-3}$
4	-2.31×10^{-4}	0.00253	$-(7.46+3.45\nu)\times10^{-4}$
5	-4.18×10^{-5}	5.85×10^{-4}	$-(1.57+0.788\nu)\times10^{-4}$
6	-8.11×10^{-6}	1.38×10^{-4}	$-(3.41+1.84\nu)\times10^{-5}$
7	-1.65×10^{-6}	3.29×10^{-5}	$-(7.61+4.39\nu)\times10^{-6}$

n	$a_{2n}^{(1)}$	$a_{2n}^{(2)}$	$a_{2n}^{(\lambda)}$	$a_{2n}^{(\lambda^2)}$
0	0	0	0	0
1	-0.0312	-0.375	$0.188+0.0625\nu$	0
2	-0.0117	-0.156	$0.0834+0.0312\nu$	$-(6.56+7.82\nu+1.30\nu^2)\times10^{-3}$
3	-0.00363	-0.0508	$0.0262+0.0110\nu$	$-(1.88+2.74\nu+0.543\nu^2)\times10^{-3}$
4	-0.00106	-0.0152	$(7.48+3.45\nu)\times10^{-3}$	$-(4.74+8.25\nu+1.84\nu^2)\times10^{-4}$
5	-3.06×10^{-4}	-0.00438	$(2.04+1.02\nu)\times10^{-3}$	$-(1.13+2.33\nu+0.572\nu^2)\times10^{-4}$
6	-8.68×10^{-5}	-0.00123	$(5.48+2.95\nu)\times10^{-4}$	$-(2.59+6.36\nu+1.70\nu^2)\times10^{-5}$
7	-2.44×10^{-5}	-3.45×10^{-4}	$(1.45+0.834\nu)\times10^{-4}$	$-(5.76+17.1\nu+4.90\nu^2)\times10^{-6}$

Downloaded 02 May 2010 to 171.66.16.54. Redistribution subject to ASME license or copyright; see http://www.asme.org/terms/Terms_Use.cfm

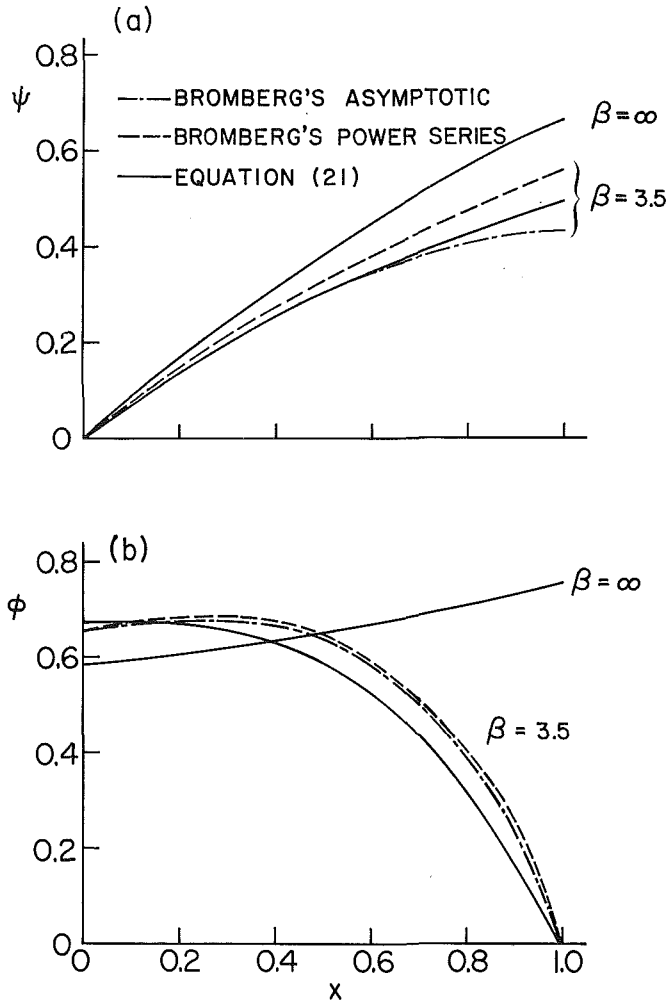


Fig. 2 Comparison of radial stress (*a*) and slope (*b*) with power series and asymptotic solutions of Bromberg (1956) for clamped edge ($\alpha = 0$)

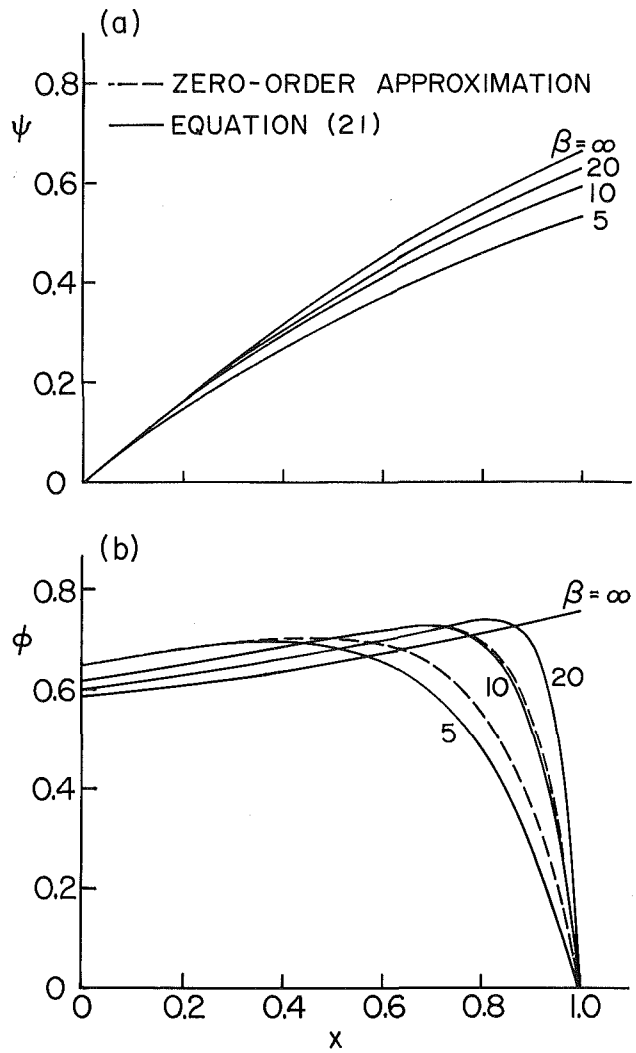


Fig. 3 Radial stress (a) and slope (b) distributions ($\alpha = 0$)

$$2(a_1' + \xi' b_0 + 2\xi' c_0) - (1+\nu)a_1 = 0 \tag{20a}$$
$$2(a_2' + b_0' + \xi' b_1 + c_0' + 2\xi' c_1) - (1+\nu)(a_2 + b_0 + c_0) = 0$$
$$\cdots$$
$$d_0 + e_0 = 0$$
$$d_1 + e_1 = 0 \tag{20b}$$
$$d_2 + e_2 + f_0 = 0$$
$$\cdots$$

As a first approximation, the series of equations (13) are truncated to

$$\psi \sim a_0 + \beta^{-1}a_1 + e^{\beta\xi}(\beta^{-2}b_0) + e^{2\beta\xi}(\beta^{-2}c_0)$$
$$\phi \sim d_0 + \beta^{-1}d_1 + e^{\beta\xi}(e_0 + \beta^{-1}e_1) \tag{21}$$

in which the inclusion of the b_0 and c_0 terms allows satisfaction of the conditions on a_1 in equations (20*a*).

As in Bromberg (1956), the interior solution, governed by equations (14), can be found in the form of the power series

$$a_0(x) = A_0 \sum_{n=0}^{\infty} a_{0n} x \left(\frac{x}{A_0^3}\right)^n \tag{22a}$$

$$a_1(x) = \sum_{n=0}^{\infty} (A_1 a_{1n} + \lambda A_0^2 a_{1n}^{(\lambda)}) x \left(\frac{x}{A_0^3}\right)^n \tag{22b}$$

$$a_2(x) = \sum_{n=0}^{\infty} (A_2 a_{2n}^{(0)} + A_0^{-3} a_{2n}^{(1)} + A_1^2 A_0^{-1} a_{2n}^{(2)} + \lambda A_0 A_1 a_{2n}^{(\lambda)} + \lambda^2 A_0^3 a_{2n}^{(\lambda^2)}) x \left(\frac{x}{A_0^3}\right)^n \tag{22c}$$

which satisfy the regularity conditions of equations (10). The second of each pair of equations (14) provide the $d_n(x)$. The constants a_{0n}, a_{1n}, $a_{1n}^{(\lambda)}$ $a_{2n}^{(0)}$, $a_{2n}^{(1)}$, $a_{2n}^{(2)}$, $a_{2n}^{(\lambda)}$, and $a_{2n}^{(\lambda^2)}$ are listed in Table 1, while A_0, A_1, and A_2 depend on the boundary conditions. For $\nu = 0.3$, substitution of equation (22*a*) into (20*a*) and subsequent iteration give $A_0 = 0.862$.

Next, with a_0 and d_0 known, equation (15*a*) gives ξ', equation (20*b*) gives $e_0(1) = -d_0(1)$, and then equations (18*a*) and (19*a*) provide $b_0(1)$ and $c_0(1)$. With these values, A_1 can be found through equations (20*a*) and (22*b*), so $a_1(x)$ and $d_1(x)$ are now known functions.

Subject to the boundary conditions of equation (20*b*), equations (16) are next solved to give

$$e_0(x) = -d_0(1)\left[\frac{a_0(1)}{a_0(x)}\right]^{1/4} x^{-1/2} \exp\left\{\int_1^x \frac{1}{\xi'}\left[\frac{a_1}{x^2} + \frac{\lambda d_0}{2}\left(1 - \frac{a_0 d_0}{x}\right)\right] dx\right\} \tag{23a}$$

and, with $b_0(x)$ and $c_0(x)$ given by equations (18*a*) and (19*a*)

Downloaded 02 May 2010 to 171.66.16.54. Redistribution subject to ASME license or copyright; see http://www.asme.org/terms/Terms_Use.cfm

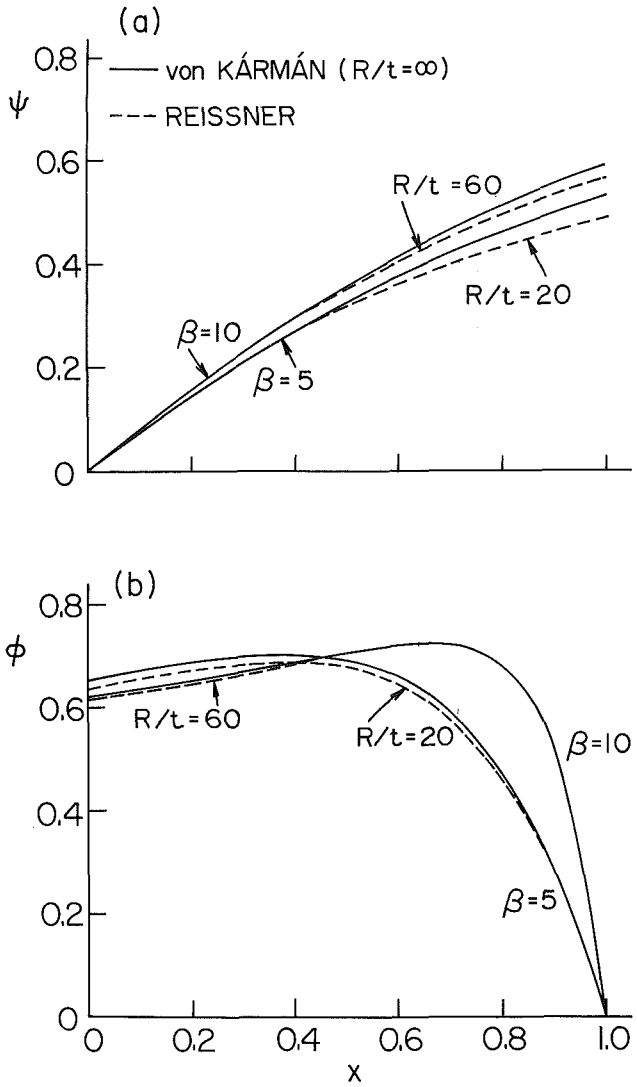


Fig. 4 Effect of R/t on radial stress (a) and slope (b)

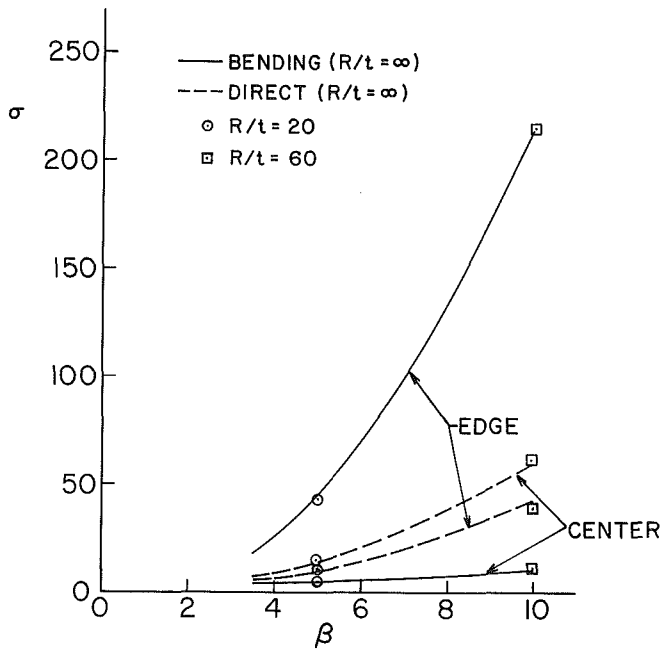


Fig. 5 Effect of R/t on direct and bending stresses

and A_2 given by a procedure similar to that outlined in the preceding paragraph,

$$e_1(x) = e_0(x)\left[\frac{d_1(1)}{d_0(1)} + \int_1^x \frac{Q_2}{e_0}\,dx\right] \tag{23b}$$

in which $Q_2(x)$ is provided by equation (17). Thus, all terms of the first approximation [equations (21)] can be computed.

As β increases, the boundary layer narrows. Therefore, when β is sufficiently large, the terms of the expansion are approximately constant within the edge zone, and so further approximation can be made by taking b_0, c_0, e_0, and e_1 as constants equal to their values at $x=1$ [see equation (21)]. In addition, equation (15b) gives

$$\xi \cong [2a_0(1)]^{1/2}(x-1). \tag{24}$$

This solution will be referred to as the "zero-order approximation."

Discussion of Results

For all of the results presented here, the integrals were evaluated numerically and $\nu=0.3$. First, the accuracy of the asymptotic solution to the von Kármán equations ($\lambda=\alpha=0$) is investigated. Radial distributions of ψ and ϕ, given by equations (21) for a clamped edge with $\beta=3.525$, are illustrated in Fig. 2. Also shown for comparison are the power series and the asymptotic solutions of Bromberg (1956), as well as the solution for $\beta=\infty$, which is given by a_0 and d_0 alone and corresponds to the membrane solution of Hencky (1915). The solution for ψ that includes only the a_0 and a_1 terms of equation (21), agrees with Bromberg's asymptotic solution but shows substantial error due to the relatively small value of β. While the exponential terms improve the accuracy of ψ somewhat, ϕ is not as accurate for the present solution. However, for $\beta \gtrsim 10$, the present and the Bromberg asymptotic solutions become virtually identical.

The boundary layer is not apparent for small values of β, but as β increases (Fig. 3), the edge zone for ϕ becomes evident as it narrows. Outside the boundary layer, the curves approach the membrane solution ($\beta=\infty$). As Fig. 3 shows, the zero-order approximation provides essentially the same values for ψ as the full solution given by equations (21). The accuracy in ϕ increases with β, and for $\beta \gtrsim 10$, this approximation is extremely accurate.

The effects of the additional terms in the Reissner plate equations ($\lambda \neq 0$) are studied next (Figs. 4 and 5). For a given β, the solution of the nondimensional von Kármán equations, represented by $R/t=\infty$, is independent of the plate geometry. But for the Reissner theory, the results depend on R/t. Since λ must be at most 0(1), only a certain range of values of R/t, given by equation (12), can be studied for each β. As shown in Fig. 4, the largest calculated difference between the Reissner and von Kármán equations (about 9 percent) occurs in ψ, in agreement with the results of Hart and Evans (1964).

Von Kármán plate theory assumes that the normal stress resultant N_1 remains approximately horizontal so that $N_1 \cong H$ at all deflections. For large rotations, however, the vertical force V contributes significantly to N_1, and so the relative magnitude of H necessary to produce N_1 grows smaller. Thus, as shown in Fig. 4, ψ is smaller in the solution of the Reissner equations, which include this contribution of V.

Finally, the nondimensional direct and bending stresses at the center and edge of the clamped plate are shown as functions of β (Fig. 5). For the values of R/t indicated, the stresses given by the von Kármán equations differ by less than 10 percent from those computed according to the Reissner equations, with the largest discrepancy occurring in the direct stresses at the edge.

Downloaded 02 May 2010 to 171.66.16.54. Redistribution subject to ASME license or copyright; see http://www.asme.org/terms/Terms_Use.cfm

Acknowledgment

This work was supported by the National Science Foundation under Grant No. MEA-8319996. The author is grateful to Professors Alfred Clark, Jr. and Richard C. Benson for their helpful discussions.

References

Bromberg, E., 1956, "Nonlinear Bending of a Circular Plate Under Normal Pressure," *Communications on Pure and Applied Mathematics*, Vol. 9, pp. 633–659.

Chia, C.-Y., 1980, *Nonlinear Analysis of Plates*, McGraw-Hill, New York, pp. 108–147.

Chien, W.-Z., 1948, "Asymptotic Behavior of a Thin Clamped Circular Plate Under Normal Pressure at Very Large Deflection," *National Tsing Hua University Scientific Reports*, Vol. 5, pp. 71–94.

Föppl, A., 1907, *Vorlesungen uber technische Mechanik*, Vol. 5, G. Teubner, Leipzig.

Frakes, J. P., and Simmonds, J. G., 1985, "Asymptotic Solutions of the von Kármán Equations for a Circular Plate Under a Concentrated Load," ASME JOURNAL OF APPLIED MECHANICS, in press.

Hart, V. G., and Evans, D. J., 1964, "Nonlinear Bending of an Annular Plate by Transverse Edge Forces," *Journal of Mathematics and Physics*, Vol. 43, pp. 275–303.

Hencky, H., 1915, "Uber den Spannungszustand in kreisrunden Platten," *Zeitschrift für Mathematik und Physik*, Vol. 63, pp. 311–317.

Ranjan, G. V., and Steele, C. R., 1980, "Nonlinear Corrections for Edge Bending of Shells," ASME JOURNAL OF APPLIED MECHANICS, Vol. 47, pp. 861–865.

Reissner, E., 1949, "On Finite Deflections of Circular Plates," *Proceedings, Symposia in Applied Mathematics*, Vol. 1, American Mathematics Society, pp. 213–219.

Reissner, E., 1963, "On the Equations for Finite Symmetrical Deflections of Thin Shells of Revolution," *Progress in Applied Mechanics* (Prager Anniversary Volume, Drucker, D. C., ed.), MacMillan, New York, pp. 171–178.

Weinberg, I. J., 1962, "Symmetric Finite Deflections of Circular Plates Subjected to Compressive Edge Forces," *Journal of Mathematics and Physics*, Vol. 41, pp. 104–115.

Downloaded 02 May 2010 to 171.66.16.54. Redistribution subject to ASME license or copyright; see http://www.asme.org/terms/Terms_Use.cfm

Load-Supporting Fluid-Filled Cylindrical Membranes

V. Namias
Department of Engineering,
Purdue University Calumet,
Hammond, Ind. 46323

When long cylindrical flexible membranes are filled with a fluid and used to support external weights, the shape they assume and the relevant geometrical and dynamical quantities are governed by a nonlinear differential equation subject to particular boundary conditions. First, a complete and exact analytical solution is obtained for an unloaded membrane. Very accurate approximate expressions are derived directly from the exact solution for the entire range of applied pressures and fluid densities. Next, the nonlinear differential equation is solved exactly under boundary conditions corresponding to the loading of the membrane. Simple asymptotic expressions are also obtained in the limit of large loads.

1 Introduction

Long cylindrical membrane containers can be used for the storage and transportation of fluids as flexible pipelines. Other applications include architectural structures such as supports for flood control [1]. This paper is an investigation of such fluid-filled membranes under various conditions of filling pressure and external loading. We consider an inextensible cylindrical membrane of negligible density, with a total fixed perimeter l, and axial length $L >> l$, so that the problem may be viewed as two-dimensional. We first discuss the unloaded membrane filled with an incompressible fluid of density ρ, under an applied pressure p_0 determined by the head of a pump at the bottom of the container. All other quantities, such as the amount M of fluid filling the membrane per unit axial length, the tension T in the membrane, the contact length C on the ground, the maximum height H, and the actual geometrical shape of the cross section will become a function of a parameter related to the known pressure p_0. In the second part of this study we load the membrane by placing an horizontal rigid plane sheet carrying various loads on its top. A second contact length C' is now formed on top as the flexible membrane is sandwiched between two horizontal planes. The original pressure, bottom contact length, and geometrical shape are altered and become functions of the applied load W; see Fig. 1.

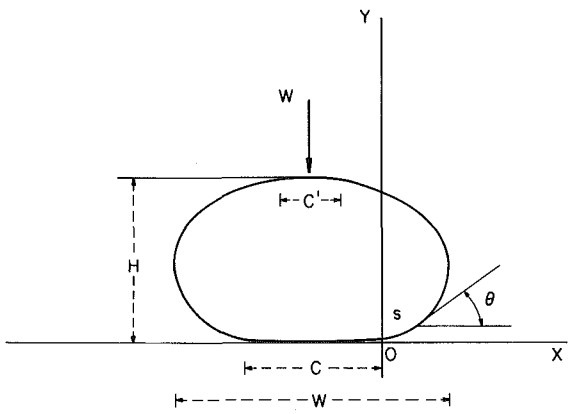


Fig. 1 Geometrical quantities in the description of the loaded membrane

2 Fluid-Filled Membrane with no External Load

The membrane is filled by a pump through an appropriate inlet hole at the bottom ($Y = 0$), at a specified pressure p_0, with a fluid of density ρ. Denoting by S the arc length from the origin and by θ the angle of the slope with respect to the X-axis, the equations governing the shape of the membrane cross section in the $(X-Y)$ plane, under equilibrium conditions, can easily be derived from the basic principles. We have

$$T\frac{d\theta}{dS} = (p_0 - p_{\text{atm}}) - \rho g Y \tag{2-1}$$

$$\frac{dX}{dS} = \cos\theta \quad \text{and} \quad \frac{dY}{dS} = \sin\theta \tag{2-2), (2-3}$$

where T represents the tension in the membrane.

It will be convenient to rewrite these equations in a dimensionless form by defining reduced quantities in the $X-Y$ plane referred to the perimeter l of the membrane. Thus, we introduce $x = X/l$, $y = Y/l$, $s = S/l$, the reduced contact length $c = C/l$, the reduced height $h = H/l$. The reduced volume will be defined as $v = V/l^2L$. Equations (2-1)–(2-3) become

$$\tau\frac{d\theta}{ds} = \beta - y \tag{2-4}$$

$$\frac{dx}{ds} = \cos\theta \quad \text{and} \quad \frac{dy}{ds} = \sin\theta \tag{2-5), (2-6}$$

Contributed by the Applied Mechanics Division and presented at the Winter Annual Meeting, Miami, Fla., November 17–21, 1985 of THE AMERICAN SOCIETY OF MECHANICAL ENGINEERS.

Discussion on this paper should be addressed to the Editorial Department, ASME, United Engineering Center, 345 East 47th Street, New York, N.Y. 10017, and will be accepted until two months after final publication of the paper itself in the JOURNAL OF APPLIED MECHANICS. Manuscript received by ASME Applied Mechanics Division, July, 1984; final revision, April, 1985. Paper No. 85-WA/APM-14.

Copyright © 1985 by ASME
Downloaded 02 May 2010 to 171.66.16.54. Redistribution subject to ASME license or copyright; see http://www.asme.org/terms/Terms_Use.cfm

where

$$\beta = \frac{1}{\rho g l}(p_0 - p_{atm}) \quad \text{and} \quad \tau = \frac{T}{\rho g l^2} \qquad (2\text{-}7), (2\text{-}8)$$

are dimensionless parameters. The same equations are also considered in a recent paper by Wang and Watson [2], where a solution is obtained only by approximation methods. It is worth noting that similar equations also arise in the theory of the elastica for the bending of flexible rods [3]. When ds is eliminated between equations (2-4) and (2-6), the resulting equation in y is easily integrated. We find, using the condition $y = 0$ at $\theta = 0$,

$$y = \beta - \sqrt{2\tau}\sqrt{a + \cos\theta} \qquad (2\text{-}9)$$

where

$$a = (\beta^2/2\tau) - 1 \qquad (2\text{-}10)$$

The condition $a > 1$ must be met to assure the reality of the radical in equation (2-9) for all angles θ. When equation (2-9) is reintroduced in (2-4), we obtain a different equation for s in terms of the variable θ.

$$\frac{ds}{d\theta} = \sqrt{\frac{\tau}{2}}\,\frac{1}{\sqrt{a + \cos\theta}} \qquad (2\text{-}11)$$

The solution is

$$s = \sqrt{\tau} k F(k, \theta/2), \qquad (2\text{-}12)$$

where

$$k = 2\sqrt{\tau}/\beta \qquad (2\text{-}13)$$

and $F(k, \theta/2)$ is the elliptic integral of the first kind with modulus k and angle $\theta/2$. The condition $a > 1$ implies $k < 1$, or $\tau < \beta^2/4$, and leads to physically meaningful results. Next, we obtain the $(x - \theta)$ equation by combining equations (2-4), (2-5), and (2-9). We find

$$\sqrt{\frac{2}{\tau}}\,\frac{dx}{d\theta} = \frac{\cos\theta}{\sqrt{a + \cos\theta}} \qquad (2\text{-}14)$$

Direct integration of equation (2-14) assuming $a > 1$ yields

$$x = \beta\left[E(k, \theta/2) - \left(1 - \frac{k^2}{2}\right)F(k, \theta/2)\right] \qquad (2\text{-}15)$$

where $E(k, \theta/2)$ is the elliptic integral of the second kind. In all these expressions, the modulus k, which appears inside and outside the elliptic integrals, depends on the tension parameter τ which is as yet unknown. The relationship between τ and β can be obtained as follows. The reduced contact length c can be found from equation (2-12). We have $1 - c = s(\theta = 2\pi)$, hence

$$1 - c = 2\sqrt{\tau} k\, K(k) \qquad (2\text{-}16)$$

where $K(k)$ is the complete elliptic integral of the first kind. We also have $x(\theta = 2\pi) = -c$, or equivalently $x(\theta = \pi) = -c/2$. Inserting this relation into equation (2-15) yields

$$-\frac{c}{2\beta} = E(k) - \left(1 - \frac{k^2}{2}\right)K(k) \qquad (2\text{-}17)$$

Eliminating c between equations (2-16) and (2-17) gives the relationship between k and β.

$$K(k) - E(k) = 1/2\beta \qquad (2\text{-}18)$$

Thus,

$$\beta = \frac{1}{2[K(k) - E(k)]} = \beta(k) \qquad (2\text{-}19)$$

This function can be inverted to yield $k = k(\beta)$.

The exact relationship between τ and β is

$$\tau = \frac{\beta^2}{4} k^2(\beta) \qquad (2\text{-}20)$$

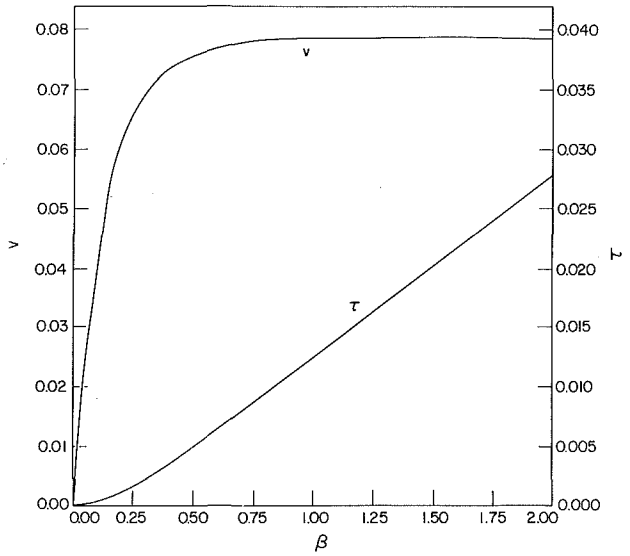


Fig. 2 Tension parameter τ and reduced volume v versus pressure parameter β under no load condition

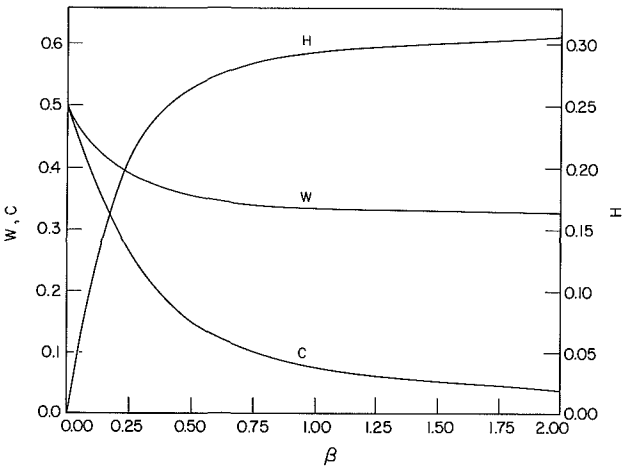


Fig. 3 Reduced height h, reduced width w, and reduced contact length c versus pressure parameter β under no load condition

All other relevant quantities can now be obtained as a function of the known parameter β. We have

$$c = 1 - \frac{4\tau}{\beta} K(2\sqrt{\tau}/\beta) \qquad (2\text{-}21)$$

$$h = y(\theta = \pi) = \beta - \sqrt{\beta^2 - 4\tau} \qquad (2\text{-}22)$$

$$w = x\left(\theta = \frac{\pi}{2}\right) - x\left(\theta = \frac{3\pi}{2}\right) = \beta\left[E\left(k, \frac{\pi}{4}\right) - E\left(k, \frac{3\pi}{4}\right)\right] -$$

$$-\beta\left(1 - \frac{k^2}{2}\right)\left[F\left(k, \frac{\pi}{4}\right) - F\left(k, \frac{3\pi}{4}\right)\right] \qquad (2\text{-}23)$$

Expressing the elliptic integrals of angle $3\pi/4$ in term of those with angle $\pi/4$, we find the equivalent result

$$w = c + 2\beta\left[E\left(k, \frac{\pi}{4}\right) - \left(1 - \frac{k^2}{2}\right)F\left(k, \frac{\pi}{4}\right)\right] \qquad (2\text{-}24)$$

which is nothing else than $w = c + 2\,x(\theta = \pi/2)$, as expected.

The reduced volume of fluid v is obtained by writing the mechanical equilibrium equation between the total Y component of the atmospheric pressure force on the exposed membrane, the weight of the fluid and the total force at the bottom of the membrane: $L\int p_{atm} dS \cos\theta + \rho g V = p_0\, C\, L$, and since $dS \cos\theta = dX$, we find

Downloaded 02 May 2010 to 171.66.16.54. Redistribution subject to ASME license or copyright; see http://www.asme.org/terms/Terms_Use.cfm

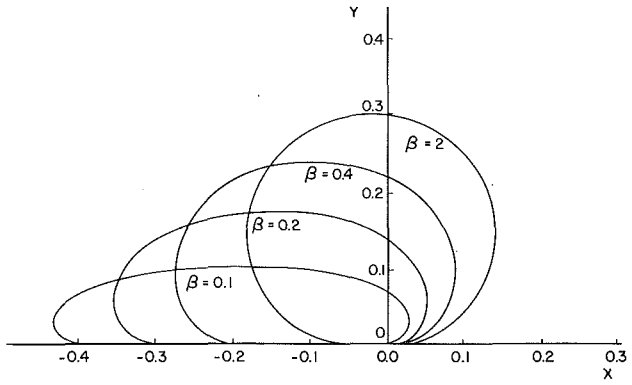


Fig. 4 Geometrical cross section of membrane for different values of the gauge pressure parameter β under no load condition

$$v=\frac{V}{l^2L}=\frac{(p_0-p_{\text{atm}})C}{\rho g\, l^2}=\beta c \tag{2-25}$$

Hence, using equation (2-21), we obtain

$$v=\beta-\beta^2k^2K(k) \tag{2-26}$$

The results have been plotted in Figs. 2 and 3.

The equation for the cross section geometrical shape can be found by eliminating θ between the following equations obtained from (2-9) and (2-15)

$$y=\beta\left[1-\sqrt{1-k^2(\beta)\sin^2\frac{\theta}{2}}\right] \tag{2-27}$$

$$x=\left\{E\left[k(\beta),\frac{\theta}{2}\right]-(1-\tfrac{1}{2}k^2(\beta))F\left[k(\beta),\frac{\theta}{2}\right]\right\} \tag{2-28}$$

While this can be done, it is preferable for the purpose of calculations and plotting to leave the equations in their parametric form. The actual shape of the cross section is shown for a few values of the pressure parameter β in Fig. 4. Even though the problem has been solved exactly, it is often desirable to obtain accurate approximate expressions in terms of more familiar functions. We first consider the case of low pressure, when β is small. As will become apparent later, this case corresponds to a modulus $k=2\sqrt{\tau}/\beta$ very near unity. When $k\sim1$, we have [6] $K(k)\sim ln(4/\sqrt{1-k^2})$ and $E(k)\sim1$. Equation (2-18) can then be easily solved for k. We obtain

$$\tau=\frac{\beta^2}{4}\left[1-16e^{-\left(\frac{1}{\beta}+2\right)}\right] \tag{2-29}$$

This result is accurate up to $\beta=0.5$, where the error is only 8 percent. When β is very small, then $\tau=\beta^2/4$, as expected. Starting with $c=1-\beta k^2K(k)$ and using the preceding approximation for k near unity, we find at once

$$c\sim\frac{1}{2}-\beta \tag{2-30}$$

We can obtain a much better approximation by replacing $K(k)$ by $1/2\beta-E(k)$, according to equation (2-18), and using $E(k)\sim1$ for $k\sim1$. The result is

$$c=\left(\frac{1}{2}-\beta\right)+16e^{-\left(\frac{1}{\beta}+2\right)}\left(\frac{1}{2}+\beta\right) \tag{2-31}$$

An even better approximation is obtained using the average of (2-30) and (2-31)

$$c=\left(\frac{1}{2}-\beta\right)+8\left(\frac{1}{2}+\beta\right)e^{-\left(\frac{1}{\beta}+2\right)} \tag{2-32}$$

This formula is good up to $\beta\simeq0.5$ where the error is only 3 percent. When equations (2-32) and (2-25) are used, one obtains an excellent approximation for the volume as well

$$v=\beta\left(\frac{1}{2}-\beta\right)+8\beta\left(\frac{1}{2}+\beta\right)e^{-\left(\frac{1}{\beta}+2\right)} \tag{2-33}$$

From equations (2-22) and (2-29) we find at once

$$h=\beta\left[1-4e^{-\left(\frac{1}{2\beta}+1\right)}\right] \tag{2-34}$$

Finally, very good approximations for the width can be found starting from equation (2-24) and using the following approximations for the elliptic integrals [6]

$$F\left(k,\frac{\pi}{4}\right)=\frac{\pi}{4}+\frac{k^2}{16}(\pi-2)+\frac{k^4}{32}(3\pi-8) \tag{2-35}$$

$$E\left(k,\frac{\pi}{4}\right)=\frac{\pi}{4}-\frac{k^2}{16}(\pi-2)-\frac{k^4}{96}(3\pi-8) \tag{2-36}$$

which are quite accurate over the entire range $0\le k\le1$. The result is

$$w=c+\frac{2\tau}{\beta}\left[1-(13-\pi)\frac{\pi}{3\beta^2}+(3\pi-8)\frac{\tau^2}{\beta^4}\right] \tag{2-37}$$

When β is very small, $\tau\simeq\beta^2/4$, and $w\simeq c+\beta/2$.

We now examine the situation when β is very large, and thus k small. The elliptic integrals can be expanded in a Taylor's series around $k=0$.

$$K(k)=\frac{\pi}{2}\left[1+\left(\frac{1}{2}\right)^2k^2+\left(\frac{1.3}{2.4}\right)^2k^4+\left(\frac{1.3.5}{2.4.6}\right)^2k^6+\ldots.\right] \tag{2-38}$$

$$E(k)=\frac{\pi}{2}\left[1-\left(\frac{1}{2}\right)^2k^2-\frac{1}{3}\left(\frac{1.3}{2.4}\right)^2k^4-\frac{1}{5}\left(\frac{1.3.5}{2.4.6}\right)^2k^6-\ldots.\right] \tag{2-39}$$

Inserting these expansions in equation (2-18), we find

$$\frac{1}{2\beta}=\frac{\pi}{2}\left[\frac{1}{2}k^2+\frac{3}{16}k^4+\frac{15}{128}k^6+\ldots.\right] \tag{2-40}$$

This series can easily be inverted and the result is

$$k^2=\frac{2}{\pi\beta}-\frac{3}{2\pi^2\beta^2}+\frac{3}{8\pi^3\beta^3}+\ldots\ldots\ldots \tag{2-41}$$

Then,

$$\tau=\frac{\beta}{2\pi}-\frac{3}{8\pi^2}+\frac{3}{32\pi^3\beta}-\frac{5}{128\pi^4\beta^2}+\ldots.. \tag{2-42}$$

Using equations (2-38), (2-41) and (2-42) in conjunction with equations (2-21) and (2-25), we find the following approximations valid for large values of β.

$$c=\frac{1}{4\pi\beta}-\frac{3}{128\pi^3\beta^3} \tag{2-43}$$

$$v=\frac{1}{4\pi}-\frac{3}{128\pi^3\beta^2} \tag{2-44}$$

Using equation (2-22), (2-23) and the expansions (2-35) and (2-36), we obtain

$$h=\frac{1}{\pi}-\frac{1}{4\pi^2\beta}-\frac{1}{16\pi^3\beta^2} \tag{2-44}$$

$$w=\frac{1}{\pi}+\frac{(\pi-2)}{8\pi^2\beta}+\frac{1}{16\pi^3\beta^2} \tag{2-45}$$

These asymptotic expressions turn out to be accurate even when $\beta<0.5$. Similar expansions, although with fewer terms have been obtained by Wang and Watson [2], by means of

Downloaded 02 May 2010 to 171.66.16.54. Redistribution subject to ASME license or copyright; see http://www.asme.org/terms/Terms_Use.cfm

approximation methods applied directly on the differential equations. As a result, the calculation of higher-order terms becomes extremely laborious. By contrast, the asymptotic expansions we have obtained from the exact solution can be obtained systematically to any desired number of terms with little mathematical labor. For small values of β, the approximate formulas obtained by Wang and Watson break down badly when $\beta > 0.2$, and no expressions are provided in the range $0.2 < \beta < 0.5$. As already indicated, the approximate formulas we have derived hold good very well up to $\beta \sim 0.5$. Consequently, the entire range of values of β has been covered by means of simple approximations.

3 Loaded Membrane

We now consider a membrane filled with a fluid to a specified pressure p_0 and resting on a horizontal surface under the effect of its own weight. The shape of the membrane is a function of the known parameter $\beta = (p_0 - p_{atm})/\rho g l$ as obtained in Section 2. A horizontal rigid plane sheet carrying variable loads W is placed on top of the membrane. The initial shape is altered by the creation of a second contact length c' at the top. All other quantities, bottom pressure, tension, height, etc. are also changed and now depend on the weight W loading the membrane. Under varying load conditions, the quantity of fluid in the membrane is fixed, and if we assume an incompressible fluid, the volume V_0 and thus the cross section area are constant. The basic differential equations governing the system are still given by (2-4)-(2-6), and the general solution given by equations (2-9), (2-12), and (2-15) continues to apply. The conditions before loading are known through the given pressure parameter $\beta_0 = (p_0 - p_{atm})/\rho g l$. The initial reduced volume v_0 is also known in terms of β_0 by means of equation (2-26). When loading takes place, then, as stated, the volume $v = v_0$ will remain unchanged. We now establish the five equations expressing the geometrical boundary conditions and the overall static equilibrium of the system in terms of the five unknowns β, τ, c, c', and h.

1. When $\theta = \pi$, $s = \frac{1}{2}(1 - c - c')$, hence equation (2-12) yields, with $k = 2\sqrt{\tau}/\beta$

$$c + c' = 1 - 2\sqrt{\tau} k\, K(k) \tag{3-1}$$

2. When $\theta = \pi$, $x = \frac{1}{2}(c - c')$, hence equation (2-15) yields

$$c' - c = 2\beta\left[E(k) - \left(1 - \frac{k^2}{2}\right)K(k)\right] \tag{3-2}$$

3. When $\theta = \pi$, $y = h$, hence equation (2-9) yields

$$h = \beta - \sqrt{\beta^2 - 4\tau} \tag{3-3}$$

4. Equilibrium of the upper flat part of the membrane yields

$$L(p_b - \rho g l h)c' l = L p_{atm} c' l + W \tag{3-4}$$

where p_b is the unknown pressure at the bottom.

We reintroduce the pressure parameter as

$$\beta = (p_b - p_{atm})/\rho g l \tag{3-5}$$

and define a dimensionless load

$$\mu = \frac{W}{\rho g L l^2} \tag{3-6}$$

so that equation (3-4) becomes

$$\beta - h = \mu/c' \tag{3-7}$$

5. Finally, equilibrium of the entire system implies

$$p_b C L = p_{atm}(C - C')L + \rho g V_0 + p_{atm} C' L + W$$

or

$$\beta c = v_0 + \mu \tag{3-8}$$

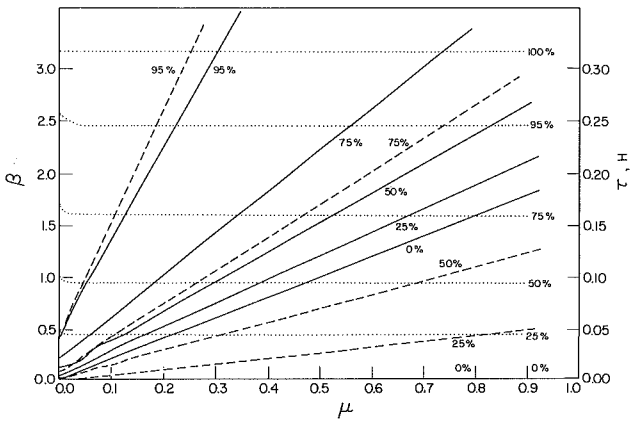


Fig. 5 Gauge pressure parameter β (solid lines), tension parameter τ (dashed lines), and reduced maximum height h (dotted lines) versus the load parameter μ, for different values of the initial reduced volume expressed as the ratio $v_0/v_{0(max)}$, or percentage of the maximum possible volume $v_{0(max)} = 1/4\pi$

We now eliminate h between equations (3-3) and (3-7) and obtain $4\tau = \beta^2 - \mu^2/c'^2$, or

$$c' = \frac{\mu}{\sqrt{\beta^2 - 4\tau}} = \frac{\mu}{\beta\sqrt{1 - k^2}} \tag{3-9}$$

We also eliminate c between equations (3-1) and (3-2) by simple addition and find, using equation (3-9) the connection between the unknown tension τ and β.

$$K(k) - E(k) + \frac{\mu}{\beta^2\sqrt{1 - k^2}} = \frac{1}{2\beta} \tag{3-10}$$

By subtracting equation (3-2) from equation (3-1), we find an expression for c:

$$c = \frac{1}{2} + \beta[(1 - k^2)K(k) - E(k)] \tag{3-11}$$

or, using equation (3-10), we obtain an alternate expression

$$c = 1 - \frac{4\tau}{\beta}K(k) - \frac{\mu}{\sqrt{\beta^2 - 4\tau}} \tag{3-12}$$

The width is $w = c + 2x(\theta = \frac{1}{2}\pi)$, i.e.,

$$w = c + 2\beta\left[E\left(k, \frac{\pi}{4}\right) + \left(1 - \frac{k^2}{2}\right)F\left(k, \frac{\pi}{4}\right)\right] \tag{3-13}$$

The distance between the two horizontal surfaces is

$$h = \beta - \sqrt{\beta^2 - 4\tau} \tag{3-14}$$

It is important to realize that none of these equations are directly usable since they contain the *two* unknowns k and β. The system of equations must be solved simultaneously, and to do so, we first eliminate c between equations (3-8) and (3-11) and introduce the following convenient combinations:

$$N = K - E \tag{3-15}$$

$$P = (1 - k^2)K - E \tag{3-16}$$

$$Q = P + N = (2 - k^2)K - 2E \tag{3-17}$$

$$R = N + P/\sqrt{1 - k^2} \tag{3-18}$$

$$S = 1 - 1/\sqrt{1 - k^2} \tag{3-19}$$

Equations (3-8) and (3-10) become

$$N\beta^2 + \mu/\sqrt{1 - k^2} = \beta/2 \tag{3-20}$$

$$P\beta^2 + \beta/2 = v_0 + \mu \tag{3-21}$$

Adding equations (3-20) and (3-21) yields a value for

$$\beta = \sqrt{(v_0 + \mu S)/Q} \tag{3-22}$$

Downloaded 02 May 2010 to 171.66.16.54. Redistribution subject to ASME license or copyright; see http://www.asme.org/terms/Terms_Use.cfm

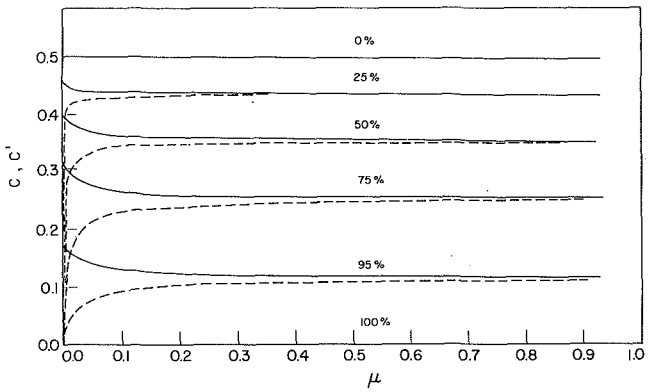


Fig. 6 Reduced bottom contact length (solid lines) and reduced top contact length (dashed lines) versus the load parameter μ, for different values of the initial reduced volume expressed as the ratio $v_0/v_{0(\max)}$ or percentage of the maximum possible volume $v_{0(\max)} = 1/4\pi$

Multiplying equation (3-20) by P and (3-21) by N and subtracting yields

$$\beta = 2(\mu R + v_0 N)/Q \tag{3-23}$$

Equating equations (3-22) and (3-23) is tantamount to eliminating β. We find

$$\sqrt{Q\left[v_0 + \mu\left(1 - \frac{1}{\sqrt{1-k^2}}\right)\right]} = 2(\mu R + v_0 N) \tag{3-24}$$

Equation (3-24) determines the relationship between k and the given load μ. It is a quadratic equation in μ whose solution is

$$\mu(k) = \frac{1}{2R^2}\left[\frac{1}{4}QS - 2v_0 RN - \sqrt{\frac{1}{16}Q^2S^2 - QSRNv_0 + QR^2 v_0}\right] \tag{3-25}$$

The function $\mu = \mu(k)$ can be inverted and its inversion yields $k = k(\mu)$. Inserting $k = k(\mu)$ into equation (3-22) or (3-23) yields $\beta = \beta(\mu)$. All other quantities can now be obtained in terms of μ. We find

$$\tau = \frac{1}{4}\beta^2(\mu)k^2(\mu) \tag{3-26}$$

$$c = \frac{v_o + \mu}{\beta(\mu)} \tag{3-27}$$

$$c' = \frac{\mu}{\beta(\mu)\sqrt{1-k^2(\mu)}} \tag{3-28}$$

$$h = \beta(\mu)[1 - \sqrt{1-k^2(\mu)}] \tag{3-29}$$

The shape after loading is obtained from equations (2-27) and (2-28), where $k = k(\mu)$ and $\beta = \beta(\mu)$. The gauge pressure parameter, the tension parameter and the reduced maximum height are plotted in Fig. 5 versus the load parameter μ, for different values of the initial reduced volume expressed as a percentage $v_0/v_{0(\max)}$, where $v_{0(\max)} = 1/4\pi$ is the maximum possible reduced volume. Figure 6 shows both reduced contact lengths versus μ. Plots of the geometrical shape of the cross section are shown in Figs. 7 and 8 for different values of the load μ and for a specified initial volume v_0. To present the effect of loading the membrane in a more suggestive and realistic way, we have shifted the geometrical shape for each loading condition, along the x-axis, in such a way as to maintain the center of symmetry of the figure at $x = 0$, under the various loads. In other words, we have plotted $y' = y(x - \frac{1}{2}c)$ instead of $y(x)$. Even though the problem has been solved exactly, it is desirable to obtain some mathematical insight into the rather complicated expression (3-25). The case $\mu = 0$

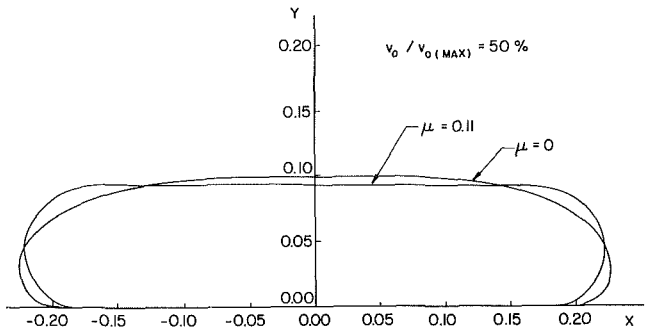


Fig. 7 Geometrical cross section of membrane for initial reduced volume ratio $v_0/v_{0(\max)} = 50$ percent, under no load ($\mu = 0$), and for $\mu = 0.11$

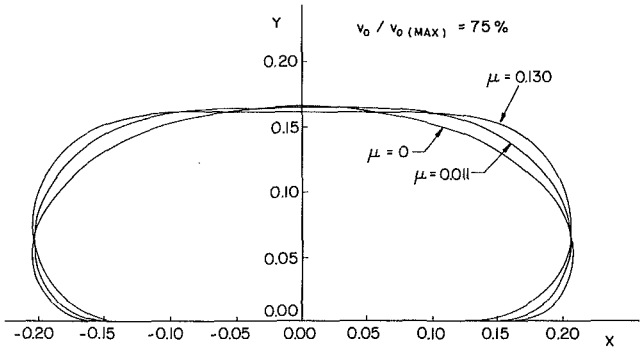


Fig. 8 Geometrical cross section of membrane for initial reduced volume ratio $v_0/v_{0(\max)} = 75$ percent, under no load ($\mu = 0$), and for $\mu = 0.011$ and $\mu = 0.13$

corresponding to no load has been discussed thoroughly in Section 2. It is possible to study the function $k(\mu)$ for small values of μ near 0, i.e., in first order in μ, but the results are rather lengthy and not particularly illuminating. Of greater interest is the situation when μ is very large, corresponding to small values of k. We use the expansions (2-38) and (2-39) in equation (3-25) and obtain a series expansion of $1/\mu$ in terms of powers of k:

$$\frac{1}{\mu} = \frac{\pi}{\sqrt{\gamma}-\gamma}k^2 + (\ldots)k^4 + (\ldots)k^6 + \ldots\ldots \tag{3-32}$$

where $\gamma = 1 - 4\pi v_0$. Series (3-32) can easily be inverted as

$$k^2 = \left(\frac{\sqrt{\gamma}-\gamma}{\pi}\right)\frac{1}{\mu} + (\ldots)\frac{1}{\mu^2} + (\ldots)\frac{1}{\mu^3} + \ldots\ldots \tag{3-33}$$

Limiting ourselves to the first order in $(1/\mu)$ in the preceding expansion, we obtain the following results valid for μ very large.

$$\beta = \frac{2\mu}{\sqrt{1-4\pi v_0}} \tag{3-34}$$

$$\tau = \frac{1}{\pi}\left(\frac{1}{\sqrt{1-4\pi v_0}} - 1\right)\mu \tag{3-36}$$

$$c = \frac{1}{2}\sqrt{1-4\pi v_0} \tag{3-36}$$

$$c' = \frac{1}{2}\sqrt{1-4\pi v_0} = c \tag{3-37}$$

$$h = \frac{1}{\pi}(1 - \sqrt{1-4\pi v_0}) \tag{3-38}$$

The shape can also be obtained for large values of μ by using the expansions

$$F(k,\phi) = \phi - \tfrac{1}{2}k^2\int_0^\phi \sin^2 t\, dt + \ldots\ldots \tag{3-39}$$

Downloaded 02 May 2010 to 171.66.16.54. Redistribution subject to ASME license or copyright; see http://www.asme.org/terms/Terms_Use.cfm

$$E(k,\phi) = \phi + \tfrac{1}{2}k^2 \int_0^\phi \sin^2 t\, dt + \ldots\ldots \quad (3\text{-}40)$$

Inserting in equations (2-27) and (2-28) and using equation (3-33) to first order in $(1/\mu)$, we find after some simplifications,

$$x = \frac{1}{2\pi}(1-\sqrt{\gamma})\sin\theta \quad (3\text{-}41)$$

$$y = \frac{1}{2\pi}(1-\sqrt{\gamma})(1-\cos\theta) \quad (3\text{-}42)$$

Hence, the equation for the geometrical shape of the nonflat part of the cross section for large μ and for $0 \le \theta \le \pi$, is

$$x^2 + \left\{y - \left[\frac{1}{2\pi}(1-\sqrt{\gamma})\right]\right\}^2 = \left[\frac{1}{2\pi}(1-\sqrt{\gamma})\right]^2 \quad (3\text{-}43)$$

and represents a semicircle of radius $(1-\sqrt{\gamma})/2\pi$, centered at $x = 0, y = (1/2\pi)(1-\sqrt{\gamma}) = (1/2\pi)(1-\sqrt{1-4\pi v_0}) = \frac{1}{2}h$, as expected. Figure 5 reveals that the gauge pressure at the bottom and the tension in the membrane increase almost linearly with the load and that the coefficient of proportionality can become very large when the membrane is filled initially to near maximum capacity. This is because under these conditions, the contact length on the ground becomes very small. Figure 6 shows that, contrary to what one may perhaps expect, the contact length on the ground decreases as the load increases, and that it is instead the top contact length which increases with increasing loads. Starting from zero, under no load conditions, the top contact length increases rapidly at first as the load increases and thereafter slowly approaches the value of the bottom contact length as the load is further increased. Both contact lengths reach a common limiting value, asymptotically. Inspection of Figs. 5 and 6 shows that the asymptotic solutions given by equations (3-34)–(3-38) are already quite good when $\mu > 0.1$. Figure 5 also shows that the maximum height h is not sensitive to the applied load and that the asymptotic value is an excellent approximation even for μ as small as 0.01. We see in Figs. 7 and 8 that beyond $\mu \sim 0.1$, the cross section has almost reached its asymptotic limit consisting of two semicircles connected by two horizontal lines, a diameter apart.

References

1 Dent, R. N., *Principles of Pneumatic Architecture*, Wiley, New York, 1972.

2 Wang, C. Y., and Watson, L. T., "The Fluid-Filled Cylindrical Membrane Container," *Journal of Engineering Mathematics*, Vol. 15, No. 2, 1981, pp. 81–88.

3 Frisch-Fay, R., *Flexible Bars*, Butterworth, Washington, 1962.

4 Irvine, H. M., *Cable Structures*, MIT Press, 1981, pp. 25–31.

5 Wang, C. Y., "The Filling of a Long Membrane Container," *J. Struct. Mech.*, Vol. 12, No. 1, 1984, pp. 1–11.

6 Abramowitz, M., and Stegun, I. A., eds., *Handbook of Mathematical Functions*, National Bureau of Standards, Applied Mathematical Series, 1968.

Downloaded 02 May 2010 to 171.66.16.54. Redistribution subject to ASME license or copyright; see http://www.asme.org/terms/Terms_Use.cfm

S. K. Datta
Professor,
Department of Mechanical Engineering,
University of Colorado,
Boulder, Colo. 80309
Fellow ASME

P. M. O'Leary[2]
Visiting Lecturer,
Department of Mechanical Engineering,
University of Colorado,
Boulder, Colo. 80309

A. H. Shah
Professor,
Department of Civil Engineering,
University of Manitoba,
Winnipeg, Canada R3T2N2

Three-Dimensional Dynamic Response of Buried Pipelines to Incident Longitudinal and Shear Waves[1]

An exact analysis is presented here for the three-dimensional dynamics of a long continuous pipeline embedded in an elastic medium. A shell model of the pipe has been used here. It is shown that the dynamic amplification of axial and hoop stresses induced in the pipe due to incident plane longitudinal and shear waves depends crucially on the ratio of rigidities of the surrounding soil and the pipe. Induced stresses are also found to have appreciable frequency dependence for certain combinations of material properties and angles of incidence. Results presented here are also applicable to buried tunnels.

Introduction

Considerable damages to buried pipelines have been found to be caused by earthquakes. Pipelines (gas, oil), sewage, and water lines are lifelines in an urban area as are roads, bridges, power lines, etc. Earthquake-induced damages to pipelines (or water and sewer lines) can cause severe hardships and losses due to fire, shortage (or lack) of water, and epidemics. For these reasons several studies have been reported in recent years that deal with the estimation of peak stresses induced in a pipeline due to earthquake-induced large ground motion and shaking for design guidelines.

The subject of this paper is the estimation of peak stresses caused by ground shaking. Most of the earlier studies in this area assumed that the modification of the free field ground motion caused by the deformation and motion of the pipeline were negligible. It was generally assumed that the pipe could be modeled as a beam on a Winkler-type foundation with spring constants independent of the frequency and wave speed of the seismic wave. Reviews of such work can be found in [1–3]. Although a shell model of the pipeline has been used in [4–6] the effect of wave propagation in the surrounding ground caused by the motion of the pipe was not taken into account.

In this paper we give exact expressions for the stiffnesses of springs representing the surrounding ground. These have been derived under the assumption that ground is linear homogeneous elastic (or viscoelastic). Once these stiffness are known equations of motion of the shell subject to displacements and stresses arising from the free field motion can be set up. In this paper we have studied in detail the peak stresses in the pipe due to incident plane longitudinal and shear waves moving at an arbitrary angle to the axis of the pipe. Earlier we studied the axisymmetric motion of a pipeline [7, 8] due to particular loading conditions. The problem studied here is completely general and includes the nonaxisymmetric modes of vibration. As special cases the plane strain motion of the shell due to plane longitudinal and shear waves moving perpendicular to the axis are obtained. These were studied earlier by several investigators [9–12].

Governing Equations

The equations that are developed here apply to pipelines as well as lined tunnels. It is assumed that the pipe (or tunnel) is infinitely long and continuous. The surrounding ground will be taken as homogeneous, isotropic, and linearly elastic[3], with Lamé constants λ, μ, and density ρ. Assuming steady state dependence on time t, the displacement $\mathbf{u}(r,\theta,x,t)$ of a point P in the ground can be taken as $\mathbf{u}(r,\theta,x)e^{-i\omega t}$ where ω is the circular frequency and r,θ,x are the cylindrical polar coordinates. The definition of the coordinates and the shell geometry are shown in Fig. 1.

$\mathbf{u}(r,\theta,x,t)$ will satisfy the equation

$$\tau^2 \nabla\nabla\cdot\mathbf{u} - \nabla\wedge\nabla\wedge\mathbf{u} = -k_2^2\mathbf{u} \tag{1}$$

where $\tau = \sqrt{2(1-\sigma)/(1-2\sigma)} = c_1/c_2, c_2^2 = \mu/\rho$, σ being

[1]Research reported here was supported in part by a grant (CEE81-20536) from the National Science Foundation, Earthquake Hazards Mitigation Program.

[2]On leave from University College, Galway, Ireland.

Contributed by the Applied Mechanics Division and presented at the Winter Annual Meeting, Miami, Fla., November 17–21, 1985 of The American Society of Mechanical Engineers.

Discussion on this paper should be addressed to the Editorial Department, ASME, United Engineering Center, 345 East 47th Street, New York, N.Y. 10017, and will be accepted until two months after final publication of the paper itself in the Journal of Applied Mechanics. Manuscript received by ASME Applied Mechanics Division, January, 1984; final revision, March, 1985. Paper No. 85-WA/APM-13.

[3] If the ground is viscoelastic then λ, μ will be complex. The analysis presented here also applies to that case.

Copyright © 1985 by ASME
Downloaded 02 May 2010 to 171.66.16.54. Redistribution subject to ASME license or copyright; see http://www.asme.org/terms/Terms_Use.cfm

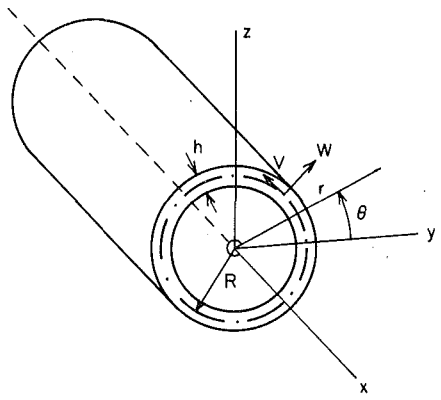


Fig. 1 Geometry of the pipeline

Poisson's ratio, ρ the density, c_1 and c_2 being, respectively, the longitudinal and shear wave speeds in the medium. To simulate traveling waves along the shell, the x-dependence of $\mathbf{u}$ will be taken as $\mathbf{u}(r,\theta)e^{i\xi x}$, where $c=\omega/\xi$ represents the speed of propagation of the incident wave along the pipe. The solution to equation (1) can be written in the form [13],

$$\mathbf{u}=\nabla\phi+\nabla\Lambda(\psi e_x)+\frac{1}{k_2}\nabla\Lambda\nabla\Lambda(\chi e_x) \tag{2}$$

where ϕ is the longitudinal wave potential, and ψ, χ are the shear wave potentials for SV and SH waves, respectively. The potentials satisfy the equations

$$\nabla^2\phi+\frac{\omega^2}{c_1^2}\phi=0;\quad \nabla^2\psi+\frac{\omega^2}{c_2^2}\psi=0;\nabla^2\chi+\frac{\omega^2}{c_2^2}\chi=0 \tag{3}$$

In equation (2), k_2 is ω/c_2.

It is easily shown [9] that solutions ϕ, ψ, χ which remain bounded as $r\to\infty$, and which represent propagating waves can be written in the form

$$\phi=\sum_0^\infty(A_n^1\cos n\theta+A_n^2\sin n\theta)K_n(\gamma r)e^{i\xi(x-ct)} \tag{4}$$

$$\psi=\sum_0^\infty(B_n^1\sin n\theta+B_n^2\cos n\theta)K_n(\delta r)e^{i\xi(x-ct)} \tag{5}$$

$$\chi=\sum_0^\infty(C_n^1\cos n\theta+C_n^2\sin n\theta)K_n(\delta r)e^{i\xi(x-ct)} \tag{6}$$

Here $\gamma=\sqrt{\xi^2-k_1^2}$, $\delta=\sqrt{\xi^2-k_2^2}$, $k_1=\omega/c_1$, $k_2=\omega/c_2$. The square roots are chosen so that for real k_1 and k_2

$$\begin{gathered}\gamma>0,\ \xi>k_1\\ \gamma=-i\gamma_1,\ 0<\xi<k_1\\ \delta>0,\ \xi>k_2\\ \delta=-i\delta_1,\ 0<\xi<k_2.\end{gathered} \tag{7}$$

Here γ_1, δ_1 are defined as

$$\gamma_1=\sqrt{k_1^2-\xi^2},\quad \delta_1=\sqrt{k_2^2-\xi^2}. \tag{8}$$

For complex c_1, c_2 (viscoelastic medium) the branches are chosen so that the solutions remain bounded and represent outgoing waves as $r\to\infty$.

The displacement $\mathbf{u}$ obtained from (1) by use of equations (4)–(6) represents the wave propagating in the ground medium caused by the motion of the pipe. The total displacement field in the ground is the sum of the free field displacement $\mathbf{u}^{(i)}$ in the absence of the pipe and $\mathbf{u}$ given by (1) and (4)–(6).

Now the boundary conditions on $\mathbf{u}$ at the interface between the shell and the ground are[4]

$$\mathbf{u}+\mathbf{u}^{(i)}=\mathbf{U},\ r=R \tag{9}$$

$$\tau_{rj}+\tau_{rj}^{(i)}=-L_{ji}U_i,\ r=R \tag{10}$$

$$(i,j)=(\wedge r,\theta,x)$$

τ_{ij} and $\tau_{ij}^{(i)}$ are the stresses associated with the displacement $\mathbf{u}$ and $\mathbf{u}^{(i)}$ respectively. $\mathbf{U}$ is the displacement of the shell middle surface. [L] is a 3 × 3 matrix operator depending on the shell theory that is used. In this paper shell has been assumed to be thin and Flugge's bending theory [14] has been used. Elements of [L] are given in Appendix *I*.

In order to derive equations governing $\mathbf{U}$ it is now necessary to write τ_{rj} in terms of $\mathbf{u}=\mathbf{U}-\mathbf{u}^{(i)}$. Using strain-displacement and stress-strain relations for the ground we can write this, for each mode n, in the form

$$\tilde{T}^\alpha=\frac{\mu}{R}[T]S_0^\alpha\quad(\alpha=1,2) \tag{11}$$

where

$$\tilde{T}^\alpha=[\tau_{rr}^\alpha,\pm\tau_{r\theta}^\alpha,\tau_{rx}^\alpha]^T,\ (r=R)$$

$$S_0^\alpha=[W_0^\alpha,\pm v_0^\alpha,u_0^\alpha]^T,\ (r=R)$$

Note that

$$w_0^\alpha=W_n^\alpha-W_n^{\alpha(i)},\ v_0^\alpha=V_n^\alpha-V_n^{\alpha(i)},\ u_0^\alpha=U_n^\alpha-U_n^{\alpha(i)}.$$

The elements of the matrix $[T]$ are given in Appendix II. $\pm$ signs corresponds to $\alpha=1$ or 2.

In writing (11) it has been assumed that the components of $\mathbf{U}$ are, dropping the factor $e^{i\xi(x-ct)}$,

$$\begin{aligned}W &= \sum_{n=0}^\infty\{W_n^1\cos n\theta+W_n^2\sin n\theta\}\\ V &= \sum_{n=0}^\infty\{V_n^1\sin n\theta+V_n^2\cos n\theta\}\\ U &= \sum_{n=0}^\infty\{U_n^1\cos n\theta+U_n^2\sin n\theta\}\end{aligned} \tag{12}$$

The components of $\mathbf{u}^{(i)}$ at $r=R$ have the same forms as the foregoing.

The physical meaning of equation (11) is clear. It says that the effect of the surrounding ground can be represented by imaginging the pipe to be supported by springs with stiffness given by the elements of $-\mu[T]$. From the expressions given in Appendix *II* it is seen that these stiffnesses depend on the material properties of the ground as well as the frequency and wavelength of the incident disturbance. The expressions for $[T]$ simplify in the limit of long wavelengths and low frequency. The limiting values of T for $\omega\to0$. $\xi\to0$ are given in Appendix *II*.

Using (11) in (10) one obtains the matrix equation for the nth modal components of U to be

$$[A-MT-\Omega^2 I]S^\alpha=-MTS^{\alpha(i)}+\tilde{T}^{\alpha(i)} \tag{13}$$

where

$$M=\mu/G,\Omega^2=\tau^2\epsilon^2 Mm\rho^*,\ \rho^*=\rho_s/\rho,\ m=h/R$$

$$S^\alpha=[W_n^\alpha,\pm V_n^\alpha,U_n^\alpha]^T$$

$$\tilde{T}^{\alpha(i)}=\frac{R}{G}[\tau_{rr(n)}^{\alpha(i)},\pm\tau_{r\theta(n)}^{\alpha(i)},\tau_{rx(n)}^{\alpha(i)}]^T\Big|_{r=R}$$

Elements of A are obtained from (I.1) in the nondimensional form as

[4]For long wavelengths and thin shells it can be verified by actual computations that the application of the boundary conditions at $r=R$ instead of at the shell-ground interface $r=R+h/2$ causes insignificant changes.

Downloaded 02 May 2010 to 171.66.16.54. Redistribution subject to ASME license or copyright; see http://www.asme.org/terms/Terms_Use.cfm

$$A_{11} = \frac{N}{6}m^3 + \frac{1}{6}n^2m^3l^2 + 2Nm + \frac{1}{6}Nm^3(1-n^2)^2 + \frac{1}{6}\mathrm{N}n^2l^2(1+\nu)m^3$$

$$A_{12} = A_{21} = 2Nnm + \frac{1}{6}nm^3l^2 + \frac{1}{12}Nnl^2(1+\nu)m^3$$

$$A_{13} = -A_{31} = i\left(-\frac{N}{6}m^3l^3 + 2N\nu lm - \frac{1}{12}m^3n^2l\right)$$

$$A_{23} = -A_{32} = iNnml(1+\nu)$$

$$A_{22} = ml^2 + 2Nn^2m + \frac{1}{4}m^3l^2$$

$$A_{33} = 2Nml^2 + mn^2(1+m^2/12)$$

Here $N = 1/1-\nu$.

Thus equation (13) is the basic equation for the forced vibration of the pipeline due to any ground shaking. Once the modal displacement components are known from (13) they are used in equation (12) to find the displacement of the shell middle surface. Then the resultant stresses in the shell are found from

$$N_{xx} = i\xi E_p U + \frac{D}{R}\xi^2 W + \frac{E_p\nu}{R}\left(W + \frac{\partial V}{\partial\theta}\right)$$

$$N_{\theta\theta} = \frac{1}{R}\left(E_p + \frac{D}{R^2}\right)\left(W + \frac{\partial V}{\partial\theta}\right) - \frac{D}{R^3}\frac{\partial}{\partial\theta}\left(V - \frac{\partial W}{\partial\theta}\right) + i\xi E_p\nu U \qquad (14)$$

In the following, numerical results are presented for these stresses when the incident field $\mathbf{u}^{(i)}$ is a plane longitudinal or a shear wave.

Numerical Results and Discussion

The object of this work is to analyze the motion of the shell excited by an incident plane seismic wave. If the incident wave is a longitudinal wave then $\mathbf{u}^{(i)}$ is given by (2) with

$$\phi = \phi^{(i)} = \frac{u_0^{(i)}}{ik_1}e^{i\xi(x-ct)}\sum_0^\infty a_n^1 J_n(\gamma_1 r)\cos n\theta$$

$$\psi = \chi = 0 \qquad (15)$$

where the constants a_n^1 are $a_0^1 = 1$, $a_n^1 = 2i^n$, $n > 0$. For incident plane SV wave, the potentials are

$$\phi = \chi = 0, \psi = \psi^{(i)}\frac{u_0^{(i)}}{ik_2\sin\theta_0}e^{i\xi(x-ct)}\sum_0^\infty b_n^1 J_n(\delta_1 r)\cos n\theta \qquad (16)$$

The b_n^1 are identical to the a_n^1. For incident SH waves, the potentials are

$$\phi = \psi = 0,\ \chi = \chi^{(i)} = \frac{u_0^{(i)}}{ik_2\sin\theta_0}e^{i\xi(x-ct)}\sum_0^\infty c_n^1 J_n(\delta_1 r)\cos n\theta \qquad (17)$$

The constants c_n^1 are identical to a_n^1.

In writing equations (15)–(17) it has been assumed that the propagation directions of the incident plane waves make an angle θ_0 with the x-axis. Thus for the incident plane longitudinal wave given by (15) ξ and k_1 are related by the relation

$$\xi = k_1\cos\theta_0 \qquad (18)$$

Then γ_1 is given by $k_1 \sin\theta_0$. For incident SV and SH waves given by (16) and (17) ξ and k_2 satisfy

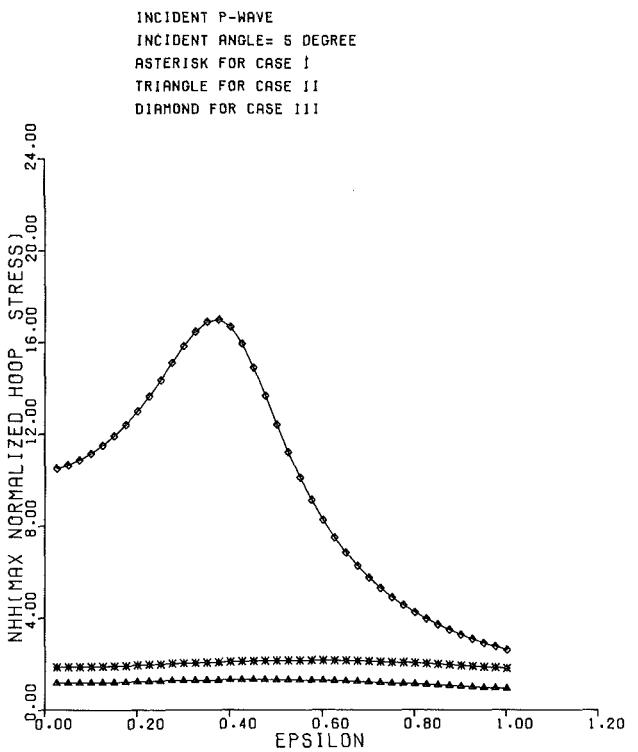


Fig. 2 Maximum hoop stress amplitude versus frequency for incident longitudinal wave

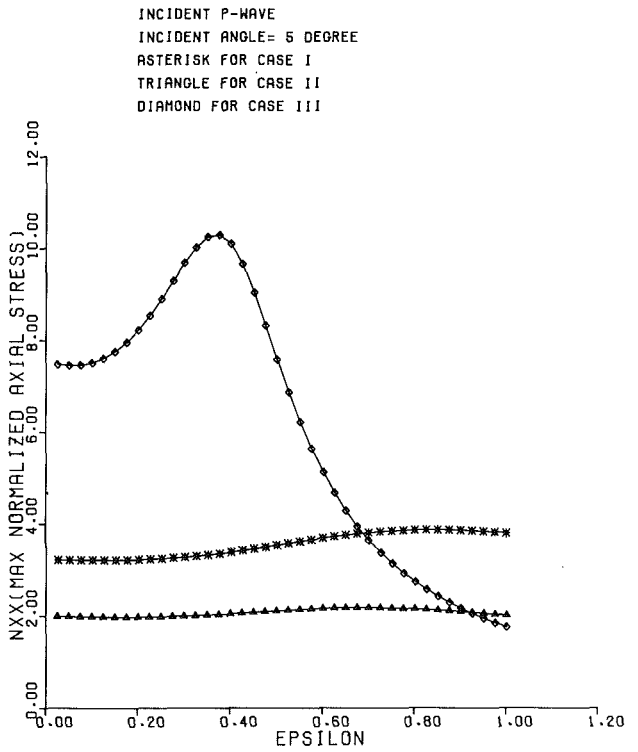


Fig. 3 Maximum axial stress amplitude versus frequency for incident longitudinal wave

$$\xi = k_2\cos\theta_0 \qquad (19)$$

δ_1 is then $k_2\sin\theta_0$.

Numerical results presented here are for the three types of waves given in the foregoing. For the incident longitudinal wave the stresses have been normalized with respect to the amplitude of the normal stress, $\sigma_0^{(i)}$, associated with the incident field. Note that

Downloaded 02 May 2010 to 171.66.16.54. Redistribution subject to ASME license or copyright; see http://www.asme.org/terms/Terms_Use.cfm

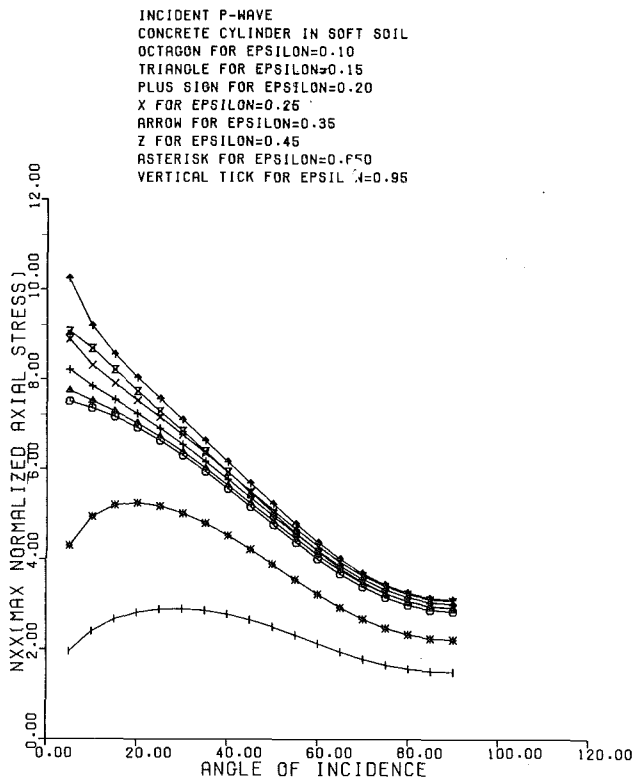


Fig. 4 Variation of maximum axial stress amplitude with the angle of incidence

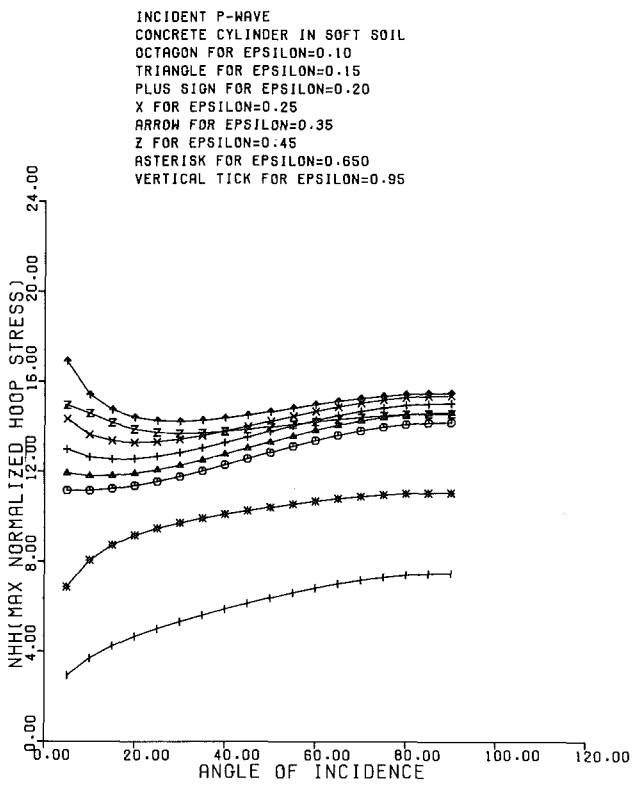


Fig. 5 Variation of maximum hoop stress amplitude with the angle of incidence

$$\sigma_0^{(i)} = \mu u_0^{(i)} k_1 \frac{C_1^2}{C_2^2} \tag{20}$$

For incident *SV* and *SH* waves the induced stresses in the pipe

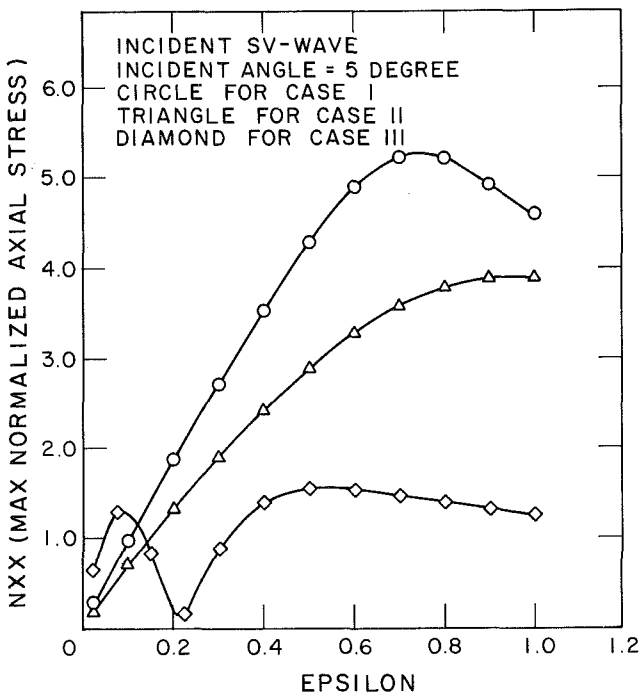


Fig. 6 Maximum axial stress amplitude versus frequency for *SV* wave incident at 5 deg

have been normalized with respect to the amplitude of the shear stress,

$$\tau_0^{(i)} = \mu u_0^{(i)} k_2 \tag{21}$$

To show the dependence of these stresses on the material properties of the pipe and the ground three representative cases have been considered here. These are:

Case *I.* Steel pipe in rock ($\rho^* = 3.0$, $\sigma = 0.25$, $M = 0.3$, $\nu = 0.25$)

Case *II.* Concrete pipe in hard soil ($\rho^* = 0.84$, $\sigma = 0.25$, $M = 0.45$, $\nu = 0.2$)

Case *III.* Concrete pipe in soft soil ($\rho^* = 0.84$, $\sigma = 0.45$, $M = 0.04$, $\nu = 0.2$)

For all cases m was taken to be 0.05.

Numerical results presented are for NXX ($= \max|N_{xx} h^{-1}/\sigma_0^{(i)}|$), or NHH ($= \max|N_{\theta\theta} h^{-1}/\tau_0^{(i)}|$). Note that the normalized stresses vary along the circumference of the pipe and reach maximum values at certain values of θ which depend on θ_0, ω, and the material properties. Since we are interested in the peak stresses, only those are presented.

Figures 2 and 3 show the variation of the peak axial and hoop stress amplitudes with frequency in the three different cases considered when the incident wave is a longitudinal wave. It is found that in the first two cases the stresses do not depend appreciably on frequency whereas, in the third the stresses increase slowly first then rapidly with increasing frequency reaching a pronounced maximum at around the frequency $f = 0.4C_1/2\pi R$ cycles /s. For a pipe of diameter 1m this corresponds to 125 Hz. This is a rather high frequency. Typically $f < 20$ Hz. For a tunnel R is much larger and then ϵ can be quite high. It is important to observe that in this example hoop stress is much larger than the axial stress at low frequencies. It can be established [15] then that for particular material and geometrical property combinations in which $\tau^2 > 4 + 2Nm(1+\nu)/M$, the peak hoop stress amplitude is greater than the axial stress amplitude. This example clearly indicates the need for a shell model and the importance of taking into account the appropriate interactions. Figures 4 and 5 show the dependence of the stresses on the angle of

Downloaded 02 May 2010 to 171.66.16.54. Redistribution subject to ASME license or copyright; see http://www.asme.org/terms/Terms_Use.cfm

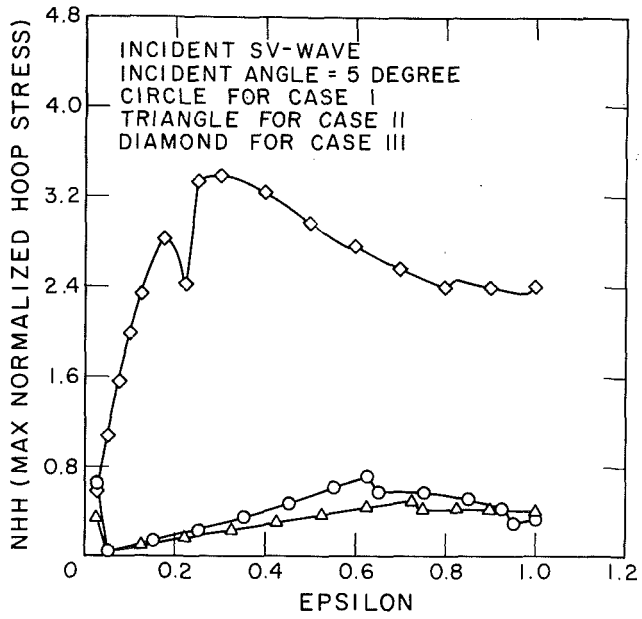


Fig. 7 Maximum hoop stress amplitude versus frequency for *SV* wave incident at 5 deg

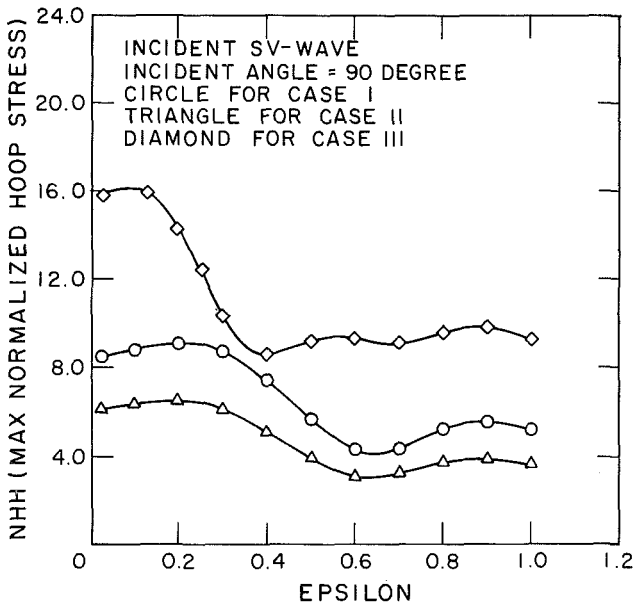


Fig. 8 Maximum hoop stress amplitude versus frequency for *SV* wave incident at 90 deg

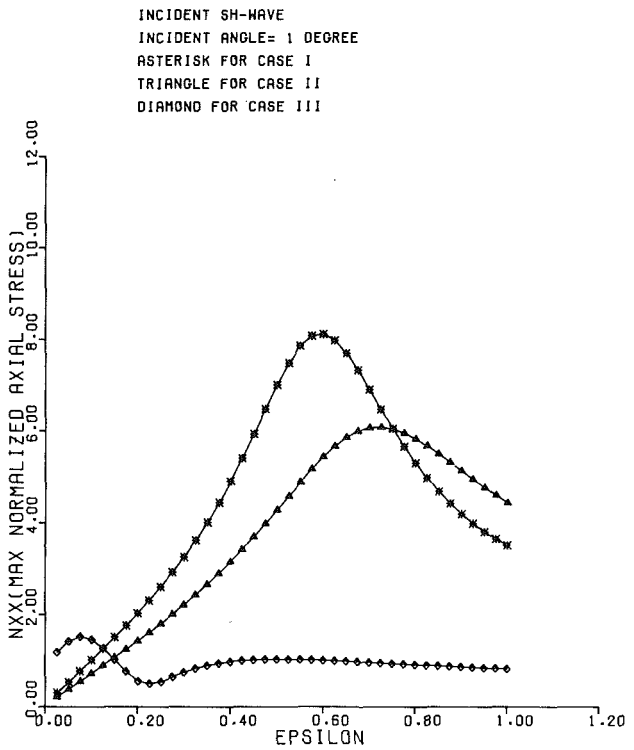


Fig. 9 Variation of maximum axial stress amplitude with frequency for *SH* wave incident at 1 deg

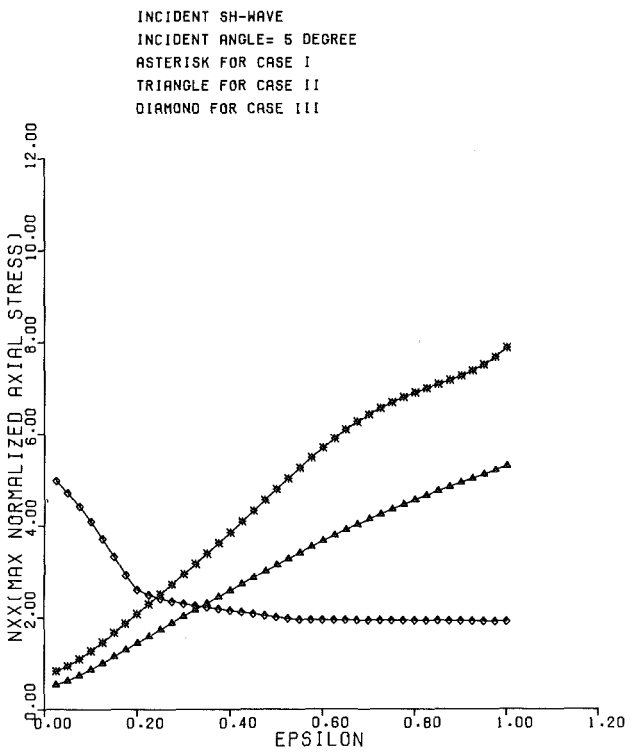


Fig. 10 Variation of maximum axial stress amplitude with frequency for *SH* wave incident at 5 deg

incidence. The results are for Case *III*. Note that except at high frequencies the axial stress continuously decrease with increasing angle of incidence. Thus the maximum axial stress is induced when the longitudinal wave is moving along the pipe. The behavior of hoop stress is much more complicated. It is seen that at low frequencies maximum hoop stress is induced when $\theta_0 = 90$ deg. However, there is a range of frequency, $f > 0.25C_1/2\pi R$ cycles/s, when the maximum hoop stress is induced for $\theta_0 = 0$ deg. Figures 2 and 3 show that both axial and hoop stresses are larger the smaller M is (except at high frequencies).

Figures 6–8 show the dependence of peak stresses on angle of incidence and frequency for *SV* wave incidence. At small angles of incidence (Figs. 6 and 7) it is found that hoop stress is larger than the axial stress when the frequency is very low. As the frequency increases the behavior of the stresses with frequency is quite different in the third case from the frist two. In the first two cases it is found that the hoop stress decreases steeply with increasing frequency, reaches a minimum at around $f > 0.05C_1/2\pi R$ Hz, then increases slowly with increasing frequency. The axial stress, on the other hand, increases rapidly with increasing frequency. Note that in the first two cases the axial stress is smaller than the hoop stress when the frequency is very low. But as the frequency increases it becomes larger. In the third case hoop stress is always larger than the axial stress. As the angle of incidence increases hoop

Downloaded 02 May 2010 to 171.66.16.54. Redistribution subject to ASME license or copyright; see http://www.asme.org/terms/Terms_Use.cfm

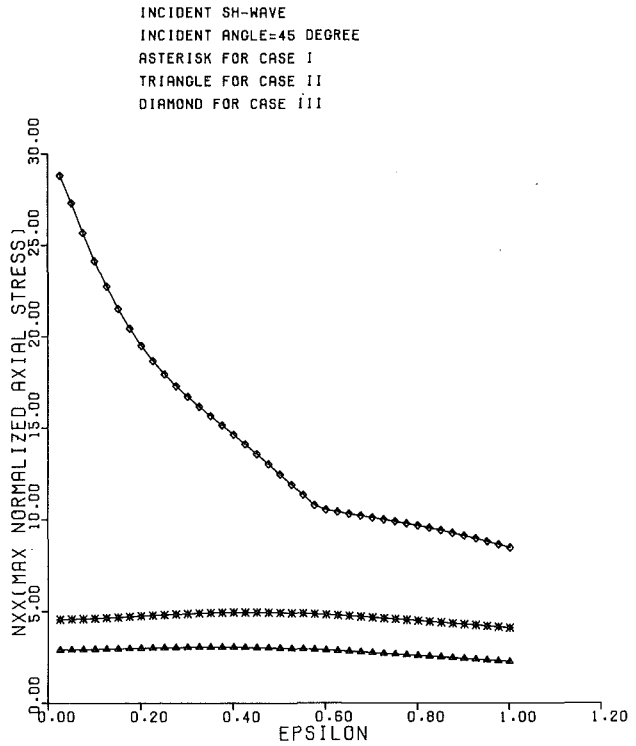


Fig. 11 Variation of maximum axial stress amplitude with frequency for *SH* wave incident at 45 deg

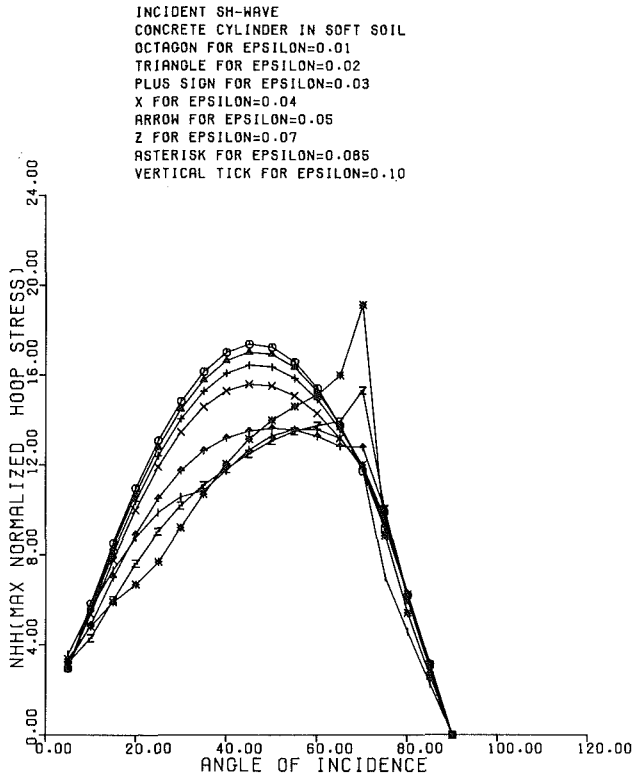


Fig. 13 Maximum hoop stress amplitude versus angle of incidence of *SH* wave

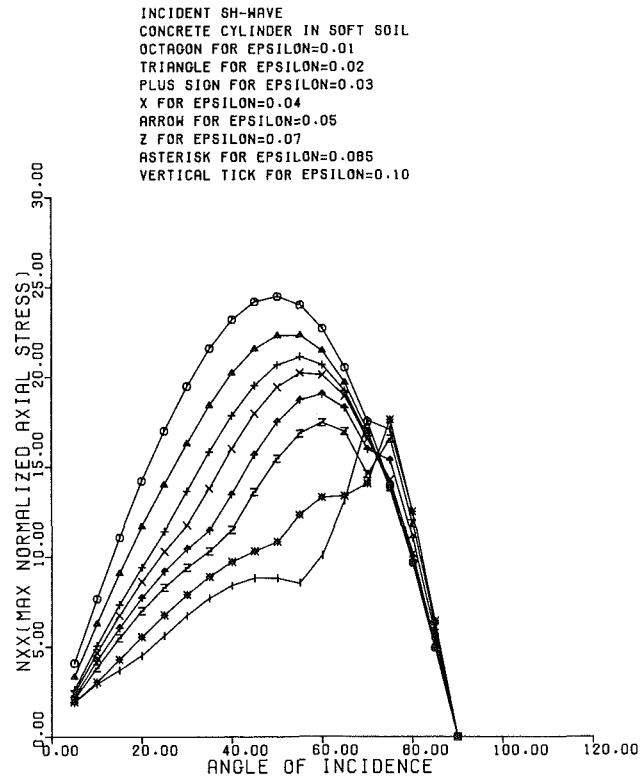


Fig. 12 Maximum axial stress amplitude versus angle of incidence of *SH* wave

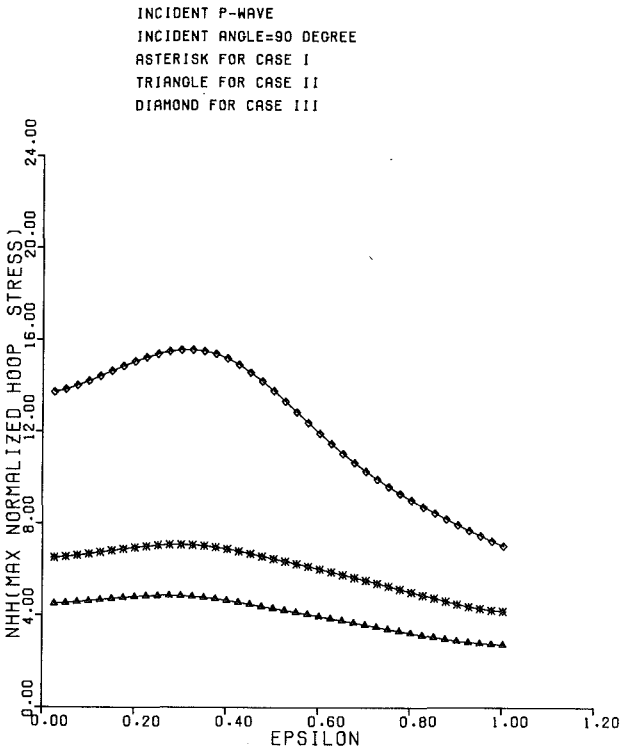


Fig. 14 Maximum hoop stress amplitude versus angle of incidence of *P* incident at 90 deg

stress also increases and becomes much larger than the axial stress. Figure 8 shows the behavior of hoop stress with frequency at $\theta_0 = 90$ deg. The dependence on M is somewhat more complicated. It is found that at small angles of incidence axial stress is larger the smaller M is at low frequencies. As the frequency increases, however, it is the largest in Case *II* and smallest in Case *III*. As the angle incidence increases it is observed that the axial stress increases with decreasing M. The same behavior is found for *NHH* for all angles of incidence.

Finally, we turn to the case of a shear wave (denoted here as *SH* wave) moving and polarized in the xy plane. Figures 9 and 10 show the variations of the axial stresses with different frequency at small angles of incidence. At very small θ_0 it is found that *NXX* in all three cases increases with frequency,

Downloaded 02 May 2010 to 171.66.16.54. Redistribution subject to ASME license or copyright; see http://www.asme.org/terms/Terms_Use.cfm

reaches a maximum, then decreases. However, in the first two cases the maxima are reached at much higher frequencies than in the third case. Note that for very small $\theta_0 (\approx 0$ deg) both *SV* and *SH* waves are the same (with a rotation of axes). But the difference between them increases rapidly as θ_0 increases (compare Figs. 6 and 10). As θ_0 increases it is seen (Figs. 10 and 11) that *NXX* decreases with frequency (initially) in Cases *I* and *II*. Figures 12 and 13 show the variations of *NXX* and *NHH* with θ_0 at different frequencies in Case *III*. A low frequencies it is found that maximum *NXX* and *NHH* occur at $\theta_0 = 45$ deg. As the frequency increases the maxima shift to higher θ_0. Note that *NXX*>*NHH* at low frequencies. However, as the frequency increases there is a narrow range of frequency in which this inequality is reversed.

Comparison of stresses induced by the three types of waves shows that in Case *III* at low angles of incidence (θ_0) maximum stresses are induced by *P* waves. In the other two cases, however, maximum stresses are caused by shear waves (except at very low frequencies). At angles of incidence near 45 deg, maximum stresses are caused by *SH* waves at low frequencies. At high frequencies, however, maximum hoop stress is caused by *P* wave and maximum axial stress by *SH* waves. For θ_0 near 90 deg, maximum hoop stress is induced by *SV* waves at low frequencies and by *P* waves at high frequencies (Figs. 8 and 14).

Conclusion

An exact three-dimensional analysis is presented here for the dynamics of a long continuous cylindrical shell (modeling a pipeline or tunnel) embedded in a homogeneous isotropic elastic medium. It is shown that proper estimation of peak stresses induced in the pipe due to longitudinal or shear waves must take into account the effect of wave propagation in the surrounding medium caused by the motion of the pipe. Expressions are given for the stiffnesses of springs supporting the pipeline which may be used to replace the surrounding ground. These stiffnesses depend on the material properties of the ground and the wavelength and frequency of the seismic disturbance.

Numerical results presented here are for incident plane waves. However, the equations derived here can be used for any other type of seismic disturbance.

Acknowledgment

Authors are grateful to the University of Colorado Computing Center for the computing time received. They also wish to thank Mr. T. Chakrabarty for help in computation.

References

1 Nelson, I., and Weidlinger, P., "Dynamic Seismic Analysis of Long Segmented Pipelines," ASME *Journal of Pressure Vessel Technology*, Vol. 101, 1979, pp. 10-20.

2 Wang, L. R. L., "Seismic Evaluation Model for Buried Lifelines," *Proc. of the 2nd ASCE Specialty Conference on Lifeline Earthquake Engineering*, Oakland, Calif. Aug. 1981, pp. 335-457.

3 Wang, L. R. L., "Role and Development of Soil Parameters for Seismic Responses of Buried Lifelines," in *Earthquake Behavior and Safety of Oil and Gas Storage Facilities, Buried Pipelines and Equipment*, PVP-Vol. 77, Ariman, T., ed., ASME, New York, 1983, pp. 312-323.

4 Hindy, A., and Novak, M., "Earthquake Response of Underground Pipelines," *Earthquake Engineering and Structural Dynamics*, Vol. 7, 1979, pp. 452-476.

5 Muleski, G. E., Ariman, T., and Aumen, C. P., "A Shell Model of Buried Pipe in a Seismic Environment," ASME *Journal of Pressure Vessel Technology*, Vol. 101, 1979, pp. 44-50.

6 Muleski, G. E., and Ariman, T., "Improved Seismic Input and Soil Models and Quasi-Static Approximation in Buried Pipes," in *Earthquake Behavior and Safety of Oil and Gas Storage Facilities, Buried Pipelines and Equipment*, PVP-Vol. 77, Airman, T., ed., ASME New York, 1983, pp. 202-208.

7 Datta, S. K., Shah, A. H., and El-Akily, N., "Dynamic Behavior of a Buried Pipe in a Seismic Environment," ASME JOURNAL OF APPLIED MECHANICS, Vol. 49, 1981, pp. 141-148.

8 Datta, S. K., Chakrabarty, T., and Shah, A. H., "Dynamic Response of Pipelines to Moving Loads," *Earthquake Engineering and Structural Dynamics*, Vol. 12, 1984, pp. 59-72.

9 Baron, M. L., and Parnes, R., "Diffraction of a Pressure Wave by a Cylindrical Shell in an Elastic Medium," *Proceedings of the 4th U.S. National Congress of Applied Mechanics*, ASME, New York, 1962, pp. 63-76.

10 Mow, C. C., and McCabe, W. L., "Dynamic Stress in an Elastic Cylinder," *ASCE Journal of Engineering Mechanics Division*, Vol. 89, 1963, pp. 21-41.

11 Mente, L. J., and French, F. W., "Response of Elastic Cylinders to Plane Shear Waves," *ASCE Journal of the Engineering Mechanics Division*, Vol. 90, 1964, pp. 103-118.

12 Garnet, H., and Crouzet-Pascal, J., "Transient Response of a Circular Cylinder of Arbitrary Thickness, in an Elastic Medium, to a Plane Dilatational Wave," ASME JOURNAL OF APPLIED MECHANICS, Vol. 34, 1966, pp. 521-531.

13 Stratton, J. A., *Electromagnetic Theory*, McGraw-Hill, New York, 1961.

14 Flügge, W., *Stresses in Shells*, Springer-Verlag, New York, 1973.

15 O'Leary, P. M., and Datta, S. K., "Dynamic Response of a Buried Pipeline at Low Frequencies," ASME *Journal of Pressure Vessel Technology*, Vol. 107, 1985, pp. 44-50.

APPENDIX *I*

$$L_{rr} = -D\xi^4 + 2\frac{GI\xi^2}{R^2}\frac{\partial^2}{\partial\theta^2} - \frac{E_p}{R^2} - \frac{D}{R^4}(1+\partial^2/\partial\theta^2)^2 + \frac{D(1+\nu)\xi^2}{R^2}\frac{\partial^2}{\partial\theta^2} + \rho_s h\omega^2$$

$$L_{r\theta} = \left(-\frac{E_P}{R^2} - \frac{2GI\xi^2}{R^2} - \frac{D(1+\nu)\xi^2}{2R^2}\right)\frac{\partial}{\partial\theta} = -L_{\theta r}$$

$$L_{rx} = i\xi\left(-\frac{D}{R}\xi^2 - \frac{E_p\nu}{R} - \frac{GI}{R^3}\frac{\partial^2}{\partial\theta^2}\right) = -L_{xr} \qquad (I.1)$$

$$L_{\theta\theta} = -Gh\xi^2 - \frac{3GI}{R^2}\xi^2 + \frac{E_p}{R^2}\frac{\partial^2}{\partial\theta^2} + \rho_s h\omega^2$$

$$L_{\theta x} = iE_p\frac{1+\nu}{2R}\xi\frac{\partial}{\partial\theta} = L_{x\theta}$$

$$L_{xx} = -E_p\xi^2 + \frac{Gh}{R^2}\left(1+\frac{I}{hR^2}\right)\frac{\partial^2}{\partial\theta^2} + \rho_s h\omega^2$$

Here $E_p = Eh/(1-\nu^2)$, $D = E_p h^2/12$, $I = h^3/12$. E is the Young's modulus, G the shear modulus, ρ_s the density, ν the Poisson's ratio, and h the thickness of the shell.

APPENDIX *II*

$$[T] = [P][Q]^{-1}$$

where

$$[Q] = \begin{bmatrix} f_n(\alpha) & nK_n(\beta) & \frac{il}{\tau\epsilon}f_n(\beta) \\ -nK_n(\alpha) & -f_n(\beta) & \frac{-il}{\tau\epsilon}nK_n(\beta) \\ ilK_n(\alpha) & 0 & -\frac{\beta^2}{\tau\epsilon}K_n(\beta) \end{bmatrix} \qquad (II.1)$$

Here $f_n(\alpha) = nK_n(\alpha) - \alpha K_{n+1}(\alpha)$. Similarly, for $f_n(\beta)$.

$$[P] = [R][Q] + S \qquad (II.2)$$

where

Downloaded 02 May 2010 to 171.66.16.54. Redistribution subject to ASME license or copyright; see http://www.asme.org/terms/Terms_Use.cfm

$$[R] = \begin{bmatrix} -2 & -2n & -2il \\ -2n & -2 & 0 \\ 2il & 0 & -n \end{bmatrix}$$

$$[S] = \begin{bmatrix} -\tau^2\epsilon^2 K_n(\alpha) & 0 & 0 \\ 0 & -\beta^2 K_n(\beta) & 0 \\ ilnK_n(\alpha) & -ilnK_n(\beta)\ \tau\epsilon f_n(\beta) & -\dfrac{\beta^2}{\tau\epsilon} nK_n(\beta) \end{bmatrix}$$

In the foregoing $\alpha = \gamma R$, $\beta = \delta R$, $\epsilon = k_1 R$, $l = \xi R$. It can be shown that $[T]$ is Hermitian.

In the limit when $\epsilon \to 0$, $l \to 0$ one obtains the following.

$\mathbf{n} = 0$

$$T_{11} = -2 = T_{22}$$

All other elements are zero.

$\mathbf{n} \geq 1$

$$[T] = \begin{bmatrix} -\dfrac{2(1+n\tau^2)}{1+\tau^2} & -\dfrac{2(n+\tau^2)}{1+\tau^2} & 0 \\ \cdots & -\dfrac{2(1+n\tau^2)}{1+\tau^2} & 0 \\ \cdots & \cdots & -n \end{bmatrix}$$

$[T]$ is symmetric.

Downloaded 02 May 2010 to 171.66.16.54. Redistribution subject to ASME license or copyright; see http://www.asme.org/terms/Terms_Use.cfm

Vibration of a Cracked Cylindrical Shell of Rectangular Planform

R. Solecki
Professor.
Mem. ASME

F. Forouhar
Research Associate.

Department of Mechanical Engineering,
University of Connecticut,
Storrs, Conn. 06268

Harmonic vibrations of a circular, cylindrical shell of rectangular planform and with an arbitrarily located crack, are investigated. The problem is described by Donnell's equations and solved using triple finite Fourier transformation of discontinuous functions. The unknowns of the problem are the discontinuities of the slope and of three displacement components across the crack. These last quantities are replaced, using constitutive equations, by curvatures and strain in order to improve convergence and to represent explicitly the singularities at the tips. The formulas for differentiation of discontinuous functions are derived using Green-Gauss theorem. Application of the boundary conditions at the crack leads to a homogeneous system of linear algebraic equations. The frequencies are obtained from the characteristic equation resulting from this system. Numerical results for special cases are provided.

1 Introduction

Numerous papers were devoted to analyses of vibrations of thin shells of various geometries (see, for example, Dym [1] and Kraus [2] for references). All reported studies however were applied to homogeneous (uncracked) shells. Apparently no investigation of vibration of cracked shells was done so far. Considerable mathematical difficulties are encountered when attempting to solve this problem formulated by a coupled system of partial differential equations describing functions with discontinuous derivatives.

Let us briefly survey related studies on statics of cracked cylindrical shells noting that almost all of the analyses refer to infinite shells. The first attempt to determine deflection, stresses, and stress intensity factor of a cracked shallow cylindrical shell is due to Folias [3] who reduced Marguerre-Reissner differential equations describing the problem to a system of dual integral equations. This in turn can be transformed to a set of coupled singular integral equations of the Cauchy type.

This technique of reducing a system of partial differential equations to a system of dual integral equations, and subsequently to a system of singular equations, seems to be the favorite of most authors of papers on statics of cracked shells.

A similar type of shell to that discussed in [3], was treated with similar mathematical devices by Copley and Sanders in [4]. Erdogan and Kibler [5] also studied shallow cylindrical shells using Marguerre-Reissner equations and reducing them to a system of singular integral equations. Their solutions however is valid, unlike Folias's solution [3], also for relatively long cracks. Keer and Watts [6] based their analysis of a complete cylindrical shell with a circumferential crack, on the equations of three-dimensional theory of elasticity. Sanders [7] used his equations to analyze an infinite cylindrical shell with a circumferential through-crack.

Few solutions exist that are based on the tenth-order shallow shell theories (Naghdi equations). These are also obtained by reducing the differential equations to singular integral equations via dual integral equations. Krenk [8] used this theory (which takes into account transverse shear deformation) to analyze cylindrical shell with an axial crack. Most recently, Delale and Erdogan [9] also investigated the effect of transverse shear on the behavior of circumferentially cracked cylindrical shell.

In [10] Delale analyzed, among others, an axially or circumferentially cracked infinite cylindrical shell. An original approach often applicable to quite general geometries, partially based on Sanders paper [11], characterizes works of Simmonds and colleagues (see, for instance, [12–14]). Finally, still another technique due to Lakshminararyana and Murthy [15] and [16] is valid for short arbitrarily located cracks in infinite shallow shells. It is based on formulating the problem in elliptic coordinates. This allows the crack edges to become coordinate lines (as a limit of an elliptic cutout). This procedure although elegant and useful in establishing closed-form expressions for local quantities would be too cumbersome, even if applicable, to deal with global quantities, because it would require manipulating infinite series of Mathieu functions.

In the static case, differential equations describing various shell theories are amenable, for certain geometries and special crack's locations, to a system of dual integral equations. These are in turn transformed into singular integral equations which are usually solved numerically. When inertia terms are included in the differential equations and when in addition the crack's location and its relative length are arbitrary, the

Contributed by the Applied Mechanics Division and presented at the Winter Annual Meeting, Miami, Fla., November 17–21, 1985 of THE AMERICAN SOCIETY OF MECHANICAL ENGINEERS.

Discussion on this paper should be addressed to the Editorial Department, ASME, United Engineering Center, 345 East 47th Street, New York, N.Y. 10017, and will be accepted until two months after final publication of the paper itself in the JOURNAL OF APPLIED MECHANICS. Manuscript received by ASME Applied Mechanics Division, June, 1984; final revision, December, 1984. Paper No. 85-WA/APM-2.

Copyright © 1985 by ASME
Downloaded 02 May 2010 to 171.66.16.54. Redistribution subject to ASME license or copyright; see http://www.asme.org/terms/Terms_Use.cfm

foregoing procedure encounters considerable difficulties or is even not applicable (in particular for infinite geometries).

In the present work it is proposed to apply integral transform to Donnell equations in an unorthodox way. Its main feature (see for instance [17, 18]) consists in expanding displacement functions discontinuous inside the region of interest into infinite series and then proceeding according to the rules of integral transformations developed previously for discontinuous functions (application of integration by parts, Green-Gauss theorem, etc.). Differential equations are transformed as the result of these operations, into algebraic equations with respect to the transforms of the unknown displacements. Application of the inversion theorem allows to determine formally the displacements that still include at this stage certain integrals depending on unknown quantities. Specifically, the unknown functions appearing in the integrands are the quantities discontinuous across the crack (discontinuities of the first kind).

In addition, depending on the boundary conditions on the shell's circumference, other unknown integrals may appear. These include certain unknown boundary quantities. The objective of the next step is the evaluation of the unknown functions in the integrands.

At this point it is very important to realize (*a*) which unknown functions are singular at the ends of their range of definition, and (*b*) what are the strengths of singularities.

Sufficient experience and information was gathered by various researchers to answer these questions. It is therefore possible to represent the unknown functions as the sum of a regular part in the form of infinite series with unknown Fourier coefficients, and of a singular part of known form multiplied by an unknown constant (the intensity factor).

Subsequently, available boundary conditions at the edge of the crack are applied. At this stage particular care must be exercised when differentiating infinite series representing functions with "inside" discontinuities: they never can be differentiated term by term. The appropriate formulas for differentiation are derived applying again generalized Green-Gauss theorem. Once all these mathematical obstacles are overcome the final result is obtained in the form of an infinite system of linear algebraic equations. In the case of natural vibration, the system is homogeneous and dependent on the unknown natural frequencies. Thus the characteristic equation is in the form of an infinite determinant equated to zero. As usual, assuming that the system is regular, one applies the method of reduction obtaining frequencies with any desired accuracy. Adaptation of this procedure to higher-order theory would not present any major difficulties.

2 Fundamental Equations

Consider a cracked shell shown in Fig. 1. It is assumed for simplification that the deflections, normal displacement, bending moments, and shear stress vanish on the contour. Validity of Donnell equations [1] is assumed:

$$\left(\frac{\partial^2}{\partial\xi^2}+\frac{1-\nu}{2}\frac{\partial^2}{\partial\eta^2}\right)u+\frac{1+\nu}{2}\frac{\partial^2 v}{\partial\xi\partial\eta}+\nu\frac{\partial w}{\partial\xi}=-q_x R^2/C \quad (1)$$

$$\frac{1+\nu}{2}\frac{\partial^2 u}{\partial\xi\partial\eta}+\left(\frac{1-\nu}{2}\frac{\partial^2}{\partial\xi^2}+\frac{\partial^2}{\partial\eta^2}\right)v+\frac{\partial w}{\partial\eta}=-q_y R^2/C \quad (2)$$

$$\nu\frac{\partial u}{\partial\xi}+\frac{\partial v}{\partial\eta}+(1+k^2\nabla^2\nabla^2)w=-q_n R^2/C \quad (3)$$

where ν is Poisson's ratio, k^2 is the thickness parameter, and C is the extensional rigidity

$$k^2=\frac{1}{12}\left(\frac{h}{R}\right)^2, \qquad C=Eh/(1-\nu^2) \quad (4)$$

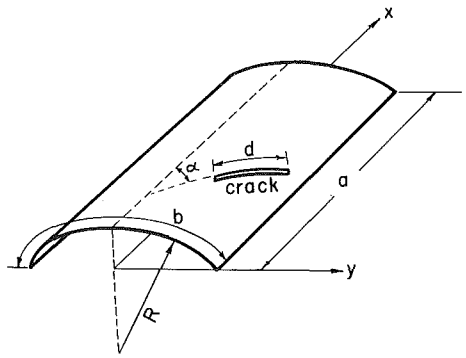


Fig. 1 Geometry of the shell

where R is the radius of curvature, h is the thickness of the shell, and where the body forces q_x, q_y, and q_n also include inertia terms. The following Fourier transforms of the displacement components u, v, and w are defined:

$$u_{mn}=\int_0^a\int_0^b u(\xi,\eta)\phi_{mn}^{(1)}\,d\xi d\eta \quad (5)$$

$$v_{mn}=\int_0^a\int_0^b v(\xi,\eta)\phi_{mn}^{(2)}\,d\xi d\eta \quad (6)$$

$$w_{mn}=\int_0^a\int_0^b w(\xi,\eta)\phi_{mn}^{(3)}\,d\xi d\eta \quad (7)$$

where

$$\phi_{mn}^{(1)}\equiv\cos\alpha_m\xi\,\sin\beta_n\eta \quad (8)$$

$$\phi_{mn}^{(2)}\equiv\sin\alpha_m\xi\,\cos\beta_n\eta \quad (9)$$

$$\phi_{mn}^{(3)}\equiv\sin\alpha_m\xi\,\sin\beta_n\eta \quad (10)$$

$\alpha_m=m\pi/\bar{a}$, $\beta_n=n\pi/\bar{b}$, $\bar{a}=a/R$, $\bar{b}=b/R$

The system of differential equations (1)–(3) is subjected to finite Fourier transformations with kernels (8), (9), and (10), respectively.

The double integrals thus obtained depend on the derivatives of u, v, and w. These integrals must be, as usual, integrated by parts to relate them to the transforms (5)–(7). In view of the discontinuities present this standard procedure is extremely tedious. The method devised in [17], based on application of Green-Gauss theorem

$$\int_s\int F_{,i}ds=\int_\Gamma Fn_i d\Gamma+\int_{\bar{\Gamma}}F\bar{n}_i d\bar{\Gamma} \quad (i=1,2,3) \quad (11)$$

is very helpful in considerably reducing the amount of manipulations. Ultimately the following system of linear algebraic equations in u_{mn}, v_{mn}, and w_{mn} is obtained, which includes integrals involving unknown discontinuities of the displacements and of the slope across the crack:

$$\left(\alpha_m^2+\frac{1-\nu}{2}\beta_n^2-\frac{R^2}{C}\rho\omega^2\right)u_{mn}+\frac{1+\nu}{2}\alpha_m\beta_n v_{mn}-\nu\alpha_m w_{mn}=A_{mn}$$

$$\frac{1+\nu}{2}\alpha_m\beta_n u_{mn}+\left(\frac{1-\nu}{2}\alpha_m^2+\beta_n^2-\frac{R^2}{C}\rho\omega^2\right)v_{mn}-\beta_n w_{mn}=B_{mn}$$

$$-\nu\alpha_m u_{mn}-\beta_n v_{mn}+\left[k^2(\alpha_m^2+\beta_n^2)^2+1-\frac{R^2}{C}\rho\omega^2\right]w_{mn}=C_{mn}$$

$$m,n=1,2,\ldots\infty \quad (12)$$

Here ω is the frequency of vibration. The quantities A_{mn}, B_{mn}, and C_{mn} appearing on the right-hand sides represent certain linear combinations (see [19] for details) of the in-

Downloaded 02 May 2010 to 171.66.16.54. Redistribution subject to ASME license or copyright; see http://www.asme.org/terms/Terms_Use.cfm

tegrals of the unknown discontinuities of the displacements Δu, Δv, and Δw and of the normal slope $\Delta\partial w/\partial n$ across the crack. The system of algebraic equations (12) is solved with respect to u_{mn}, v_{mn}, and w_{mn} and the results substituted into the inversion formulas:

$$u(\xi,\eta)=\frac{2}{\bar{a}\bar{b}}\sum_{n=1}^{\infty}u_{on}\sin\beta_n\eta + \frac{4}{\bar{a}\bar{b}}\sum_{m=1}^{\infty}\sum_{n=1}^{\infty}u_{mn}\cos\alpha_m\xi\,\sin\beta_n\eta \tag{13.1}$$

$$v(\xi,\eta)=\frac{2}{\bar{a}\bar{b}}\sum_{m=1}^{\infty}v_{mo}\sin\alpha_m\xi + \frac{4}{\bar{a}\bar{b}}\sum_{m=1}^{\infty}\sum_{n=1}^{\infty}v_{mn}\sin\alpha_m\xi\,\cos\beta_n\eta \tag{13.2}$$

$$w(\xi,\eta)=\frac{4}{\bar{a}\bar{b}}\sum_{m=1}^{\infty}\sum_{n=1}^{\infty}w_{mn}\sin\alpha_m\xi\,\sin\beta_n\eta \tag{13.3}$$

To determine the integrals of the unknown functions the boundary conditions at the crack must be applied next.

3 Boundary Conditions and Differentiation of Series Representing Discontinuous Functions

Four boundary conditions are available at the crack's edge to determine four unknown discontinuities. These are:

$$M_{nn}=0,\quad V_n=0,\quad \sigma_{nn}=0,\quad \sigma_{cn}=0 \tag{14}$$

where M_{nn} is the bending moment in the direction normal to the crack, V_n is the reduced shear force at the edge, σ_{nn} and σ_{cn} are stress components normal and tangential to the crack, respectively. Using standard expressions for cylindrical shells (see [1]) relating quantities (14) to the displacements u, v, and w and applying the formulas for directional derivatives

$$\frac{\partial}{\partial n}=\frac{\partial\xi}{\partial n}\frac{\partial}{\partial\xi}+\frac{\partial\eta}{\partial n}\frac{\partial}{\partial\eta} \tag{15}$$

one obtains from (14) the following conditions at the edge of the crack:

$$(\sin^2\alpha+\nu\cos^2\alpha)\frac{\partial^2 w}{\partial\xi^2}+(\cos^2\alpha+\nu\sin^2\alpha)\frac{\partial^2 w}{\partial\eta^2} + 2(1-\nu)\sin\alpha\cos\alpha\frac{\partial^2 w}{\partial\xi\partial\eta}=0 \tag{16.1}$$

$$\sin\alpha[1+(1-\nu)\cos^2\alpha]\frac{\partial^3 w}{\partial\xi^3}-\cos\alpha[1+(1-\nu)\sin^2\alpha]\frac{\partial^3 w}{\partial\eta^3} + \cos\alpha[(1-2\nu)\sin^2\alpha-(2-\nu)\cos^2\alpha]\frac{\partial^3 w}{\partial\xi^2\partial\eta} - \sin\alpha[1-2\nu)\cos^2\alpha-(2-\nu)\sin^2\alpha]\frac{\partial^3 w}{\partial\xi\partial\eta^2}=0 \tag{16.2}$$

$$\left(\frac{\partial u}{\partial\xi}+\nu\frac{\partial v}{\partial\eta}+\nu w\right)\sin^2\alpha+\left(\nu\frac{\partial u}{\partial\xi}+\frac{\partial v}{\partial\eta}+w\right)\cos^2\alpha - \frac{2Gh}{C}\left(\frac{\partial u}{\partial\xi}+\frac{\partial v}{\partial\eta}\right)\sin\alpha\cos\alpha=0 \tag{16.3}$$

$$-\left(\frac{\partial u}{\partial\xi}+\nu\frac{\partial v}{\partial\eta}+\nu w\right)\sin\alpha\cos\alpha + \left(\nu\frac{\partial u}{\partial\xi}+\frac{\partial v}{\partial\eta}+w\right)\sin\alpha\cos\alpha + \frac{Gh}{C}\left(\frac{\partial u}{\partial\eta}+\frac{\partial v}{\partial\xi}\right)(\cos^2\alpha-\sin^2\alpha)=0 \tag{16.4}$$

It is now necessary to differentiate series (13) in order to satisfy conditions (16). To derive proper differentiation formulae Green-Gauss theorem (11) is applied again in the way first shown in [18] (see also [20]).

Consider for instance the series (13.1) and the transform (5). To find $\partial u/\partial\xi$, Green-Gauss theorem is applied to the expression $u\,\phi^{(3)}_{mn}$ yielding

$$\iint_s\frac{\partial u}{\partial\xi}\phi^{(3)}_{mn}\,dS=-\iint_s u\frac{\partial\phi^{(3)}_{mn}}{\partial\xi}\mathrm{dS}+\int_{\bar{\Gamma}}u\phi^{(3)}_{mn}\,\bar{u}_\xi d\bar{\Gamma} \tag{17}$$

where $\bar{\Gamma}$ is the "contour" of the crack. Since $\phi^{(3)}_{mn,\xi}=\alpha_m\,\phi^{(1)}_{mn}$ therefore the foregoing becomes

$$\int_s\int\frac{\partial u}{\partial\xi}\phi^{(3)}_{mn}\,dS=-\alpha_m u_{mn}+\int_{\bar{\Gamma}}u\phi^{(3)}_{mn}\,\bar{u}_\xi d\bar{\Gamma} \tag{18}$$

The derivative of (13.1) must be of the following form:

$$\frac{\partial u}{\partial\xi}=\frac{4}{\bar{a}\bar{b}}\sum_{m=1}^{\infty}\sum_{n=1}^{\infty}g_{mn}\phi^{(3)}_{mn} \tag{19}$$

where g_{mn} are Fourier coefficients to be found. Substitution of (19) into (18) yields the desired formula

$$g_{mn}=-\alpha_m u_{mn}+\int_{\bar{\Gamma}}u\phi^{(3)}_{mn}\,\bar{u}_\xi d\bar{\Gamma} \tag{20}$$

A similar approach was used to derive expressions for other derivatives appearing in equations (16).

To derive conditional equations determining these quantities, boundary conditions (16) are applied by performing differentiation on equations (13) according to the rules explained in the previous section. After lengthy manipulations this leads to an infinite system of linear algebraic equations of the following form

$$\sum_{i-1}^{\infty}(F_{1il}U_i+F_{2il}V_i+F_{3il}W_i)+\sum_{i=2}^{\infty}F_{4il}Z_i=0 \qquad l=0,1,\ldots$$

$$\sum_{i=1}^{\infty}(F_{5il}U_i+F_{6il}V_i+F_{7il}W_i)+\sum_{i=2}^{\infty}F_{8il}Z_i=0 \qquad l=1,\ldots$$

$$\sum_{i=1}^{\infty}(F_{9il}U_i+F_{10il}V_i+F_{11il}W_i)+\sum_{i=2}^{\infty}F_{12il}Z_i=0 \qquad l=1,\ldots$$

$$\sum_{i=1}^{\infty}(F_{13il}U_i+F_{14il}V_i+F_{15il}W_i)+\sum_{i=2}^{\infty}F_{16il}Z_i=0 \qquad l=1,\ldots \tag{21}$$

Coefficients F_{1il}, F_{2il}, . . . F_{16il} are composed of double and single series with complicated general terms, some involving Fresnel integrals (due to the presence of the square roots in the denominators of equations (31); see [19]). To obtain the frequencies of natural vibration of the cracked shell one should equate to zero the characteristic determinant of the system (26).

The quantities w, u, and v appearing under the integrals are not singular and can be therefore expanded into Fourier series. However, the fact that the bending moment and the stress are square-root singular at the tips of the crack makes these Fourier series very slowly convergent. To eliminate this difficulty the procedure adopted in [18] and [20] will be generalized here. To this end the singular quantities are chosen to be the primary unknowns with "built-in" singularities:

$$\Delta\frac{\partial^2 w}{\partial n^2}=\frac{2}{d}\sum_{i=1}^{\infty}W_i\sin\frac{i\pi c}{d}+\frac{C_1}{\sqrt{c}}+\frac{C_2}{\sqrt{d-c}} \tag{22.1}$$

Downloaded 02 May 2010 to 171.66.16.54. Redistribution subject to ASME license or copyright; see http://www.asme.org/terms/Terms_Use.cfm

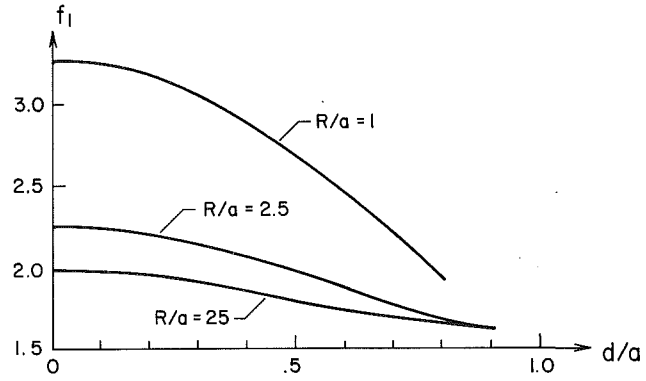


Fig. 2 The dependence of the frequency factor f for the first mode on R/a and d/a

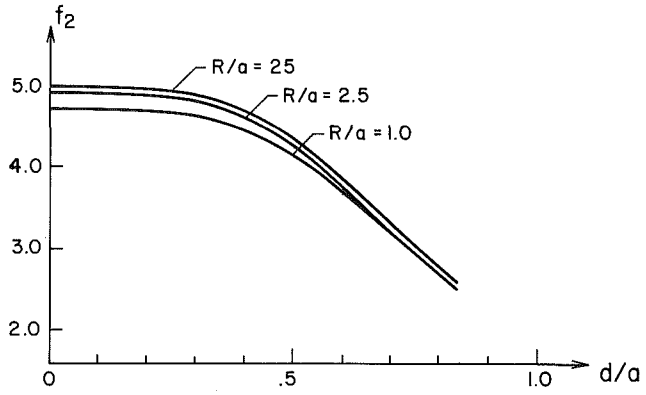


Fig. 3 The dependence of the frequency factor f for the second mode on R/a and d/a

$$\Delta\frac{\partial u}{\partial n} = \frac{2}{d}\sum_{i=1}^{\infty} U_i \sin\frac{i\pi c}{d} + \frac{C_3}{\sqrt{c}} + \frac{C_4}{\sqrt{d-c}} \tag{22.2}$$

$$\Delta\frac{\partial v}{\partial n} = \frac{2}{d}\sum_{i=1}^{\infty} V_i \sin\frac{i\pi c}{d} + \frac{C_5}{\sqrt{c}} + \frac{C_6}{\sqrt{d-c}} \tag{22.3}$$

where the unknown constants $C_1, \ldots, C_6$ are determined using continuity conditions of the displacements at the tips of the crack and by applying integration by parts. Variable "c" is measured along the crack starting at one tip. Extensive but straightforward manipulations yield finally the following expressions:

$$C_1 = -\frac{3}{\pi\sqrt{d}}\sum_{i=1}^{\infty}\frac{W_i}{i} + \frac{2}{\pi\sqrt{d}}\sum_{i=1}^{\infty}\frac{W_i}{i}$$

$$C_2 = \frac{3}{\pi\sqrt{d}}\sum_{i=1}^{\infty}\frac{W_i}{i} - \frac{4}{\pi\sqrt{d}}\sum_{i=1,3}^{\infty}\frac{W_i}{i}$$

$$C_3 = \frac{1}{\pi\sqrt{d}}\sum_{i=1}^{\infty}\frac{(-1)^i U_i}{i} - \frac{2\gamma}{R\pi\nu}d^{3/2}\left[\sum_{i=1}^{\infty}\frac{W_i}{i}\left(\frac{2}{5} - \frac{(-1)^i}{2i^2\pi^2}\right) - \frac{3}{5}\sum_{i=1,3}^{\infty}\frac{W_i}{i}\right]$$

$$C_4 = -\frac{1}{\pi\sqrt{d}}\sum_{i=1}^{\infty}\frac{U_i}{i} + \frac{2\gamma}{R\pi\nu}d^{3/2}\left[\sum_{i-1}^{\infty}\frac{W_i}{i}\left(\frac{2}{5} - \frac{1}{2i^2\pi^2}\right) - \frac{8}{15}\sum_{i=1,3}^{\infty}\frac{W_i}{i}\right]$$

$$C_5 = \frac{1}{\pi\sqrt{d}}\sum_{i=1}^{\infty}\frac{(-1)^i V_i}{i} - \frac{2\lambda}{R\pi\nu}d^{3/2}\left[\sum_{i=1}^{\infty}\frac{W_i}{i}\left(\frac{2}{5} - \frac{(-1)^i}{2i^2\pi^2}\right) - \frac{3}{5}\sum_{i=1,3}^{\infty}\frac{W_i}{i}\right]$$

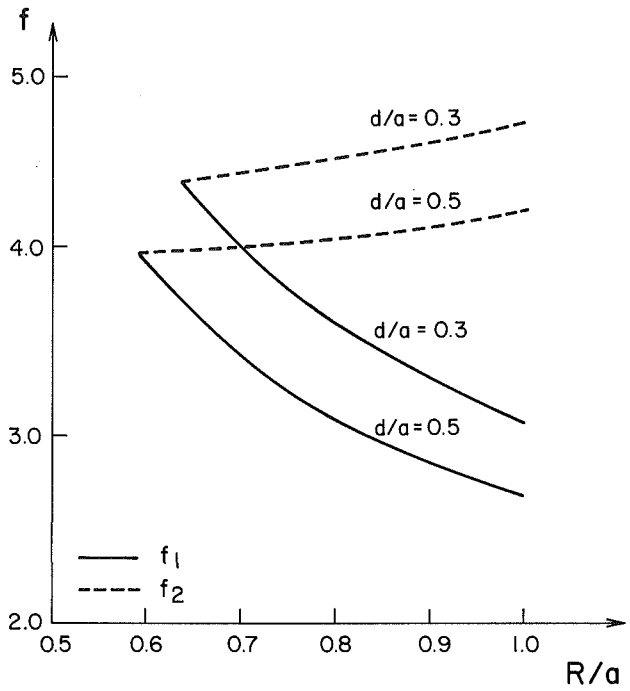


Fig. 4 The dependence of frequency factors on R/a

$$C_6 = -\frac{1}{\pi\sqrt{d}}\sum_{i=1}^{\infty}\frac{V_i}{i} + \frac{2\lambda}{R\pi\nu}d^{3/2}\left[\sum_{i=1}^{\infty}\frac{W_i}{i}\left(\frac{2}{5} - \frac{1}{2i^2\pi^2}\right) - \frac{8}{15}\sum_{i=1,3}^{\infty}\frac{W_i}{i}\right] \tag{23}$$

where $\gamma = 2\sin\alpha\cos\alpha$, $\lambda = \nu\sin^2\alpha + \cos^2\alpha$. The only unknown function that is not singular is the discontinuity of the slope across the crack. It is represented by the following series:

$$\Delta\frac{\partial w}{\partial n} = \frac{1}{d}Z_0 + \frac{2}{d}\sum_{i=1}^{\infty} Z_i \cos\frac{i\pi c}{d} \tag{24}$$

The condition that $\Delta\,(\partial w/\partial n)$ be zero at both tips leads to the following relationships:

$$Z_0 = -2\sum_{i=2,4}^{\infty} Z_i \tag{25.1}$$

$$Z_1 = -\sum_{i=3,5}^{\infty} Z_i \tag{25.2}$$

The unknown functions Δw, $\Delta(\partial u/\partial n)$, $\Delta(\partial v/\partial n)$ appearing under the integral signs in the quantities A_{mn}, B_{mn}, C_{mn} (equations (12)) are replaced now by their representations (equation (22.1)–(22.3), (23)). The discontinuities of the higher-order derivatives of the displacements are eliminated by using the conditions (14) referred to the local coordinate system $0cn$ along the crack (c, n being directions respectively tangential and normal to the crack). Thus to eliminate for instance $\Delta\,\partial^3 w/\partial^3 n$ we would use the condition

$$\Delta\frac{\partial^3 w}{\partial n^3} = -(2-\nu)\Delta\frac{\partial^3 w}{\partial c^2\partial n} \tag{26}$$

and then eliminate the dependence on "c" by integration by parts.

Finally all the quantities appearing on the right-hand sides

Downloaded 02 May 2010 to 171.66.16.54. Redistribution subject to ASME license or copyright; see http://www.asme.org/terms/Terms_Use.cfm

Table 1

	Frequency factor f_1 for the symmetric mode			Frequency factor f_2 for the antisymmetric mode		
R/a						
d/a	1.0	2.5	25	1.0	2.5	25
0.0	3.27	2.25	2.00	4.72	4.95	5.00
0.3	3.06	2.14	1.91	4.66	4.85	4.91
0.5	2.68	1.98	1.79	4.19	4.26	4.35
0.6	2.45	1.88	1.74	3.74	3.73	3.85
0.7	2.20	1.77	1.69	3.25	3.20	3.30
0.8	1.95	1.68	1.66	2.82	2.72	2.81
0.9	1.70	1.63	1.64	2.43	2.29	2.29

Table 2

d/a	R/a	1.000	0.725	0.700	0.650	Critical value of R/a in parenthesis
0.3	f_1	3.06	3.88	3.99	4.27	(0.640) 4.33
	f_2	4.66	4.43	4.40	4.33	
0.5	f_1	2.68	3.32	3.42	3.63	(0.595) 3.96
	f_2	4.19	4.01	4.00	3.98	

of equations (12) (and, after inversion, in equations (13)) depend solely on four infinite sequences of Fourier coefficients: U_i, V_i, W_i, and Z_i.

The frequency factors, $f = (\omega a^2/\pi^2)\ [12\rho(1-\nu^2)/(Eh^3)]$ have been calculated for the crack positioned at the apex, parallel to the straight edge of a shell with square planform for various d/a ratios and for three R/a ratios: $R/a = 1.0$, $R/a = 2.5$, and $R/a = 25$. (see Figs. 2 and 3 and Table 1).

The third case is equivalent to an almost flat square plate; it was chosen as the only special case of vibration of a cracked shell for which the numerical results are known. Stahl and Keer analyzed namely in [21] vibration of a rectangular plate with a crack on the symmetry line. Present results agree very well with theirs (less than 1 percent difference).

In the first and the second cases the effect of the curvature is more evident. Since no other data are available for these last cases, the frequencies of the uncracked shell with identical geometry were evaluated first. For this end the characteristic equation for an uncracked shell has been solved

$$\alpha_m^8 + \left[4\beta_n^2 - \frac{3-\nu}{1-\nu}p\right]\alpha_m^6 + \left[6\beta_n^4 - 3\frac{3-\nu}{1-\nu}p\beta_n^2 + \frac{1-\nu^2}{k^2} - \frac{p}{k^2} + \frac{2p^2}{1-\nu}\right]\alpha_m^4 + \left[4\beta_n^6 - 3\frac{3-\nu}{1-\nu}p\beta_n^4 + \beta_n^2\left(-\frac{2p}{k^2} + \frac{4p^2}{1-\nu}\right) + \frac{2p\nu^2}{k^2(1-\nu)} - \frac{3-\nu}{1-\nu}p\frac{(1-p)}{k^2}\right]\alpha_m^2 + \beta_n^8 - \frac{3-\nu}{1-\nu}p\beta_n^6 + \left(-\frac{p}{k^2} + \frac{2p^2}{1-\nu}\right)\beta_n^4 + [2p-(3-\nu)(1-\nu)p]\frac{\beta_n^2}{(1-\nu)k^2} + \frac{2p^2(1-p)}{(1-\nu)k^2} = 0 \tag{27}$$

where $p = R^2(1-\nu^2)\,\rho\omega^2/(Eh)$.

Equation (27) was solved for p and then the corresponding values of the frequency factor f have been calculated. They correspond to the case $d/a = 0.0$ in Table 1 and are helpful in determining the correctness of the behavior of the curves $R/a = 1.0$ and $R/a = 2.5$ at or near the line $d/a = 0$ (see Figs. 2 and 3). As it is seen also from these figures and from the results given in Table 1, for fixed d/a: frequency factor f_1 corresponding to the mode symmetric with respect to crack's line increases while f_2, corresponding to the mode antisymmetric with respect to the same line—decreases, with the decrease of R/a (increase of the height of shell). This phenomenon, also observed for curved arches (reference [22]) was further analyzed here. The qualitative results of this investigation are shown in Table 2 and in Fig. 4. They indicate that for given d/a there is such a value of R/a at which the antisymmetric mode becomes the fundamental mode. This critical value of R/a, which depends on d/a, is given in parenthesis in the last column of Table 2, above the corresponding common value of f_1 and f_2.

Acknowledgment

The authors gratefully acknowledge the support of the Department of the Navy, Office of the Naval Research (Contract No. N00014-81-K-0651), and that of the project monitor Dr. Nicholas Basdekas. The authors are also grateful to the reviewers of this paper for their constructive comments.

References

1 Dym, C. L., *Introduction to the Theory of Shells*, Pergamon Press, 1974.
2 Kraus, H., *Thin Elastic Shells*, Wiley, New York, 1967.
3 Folias, E. S., "An Axial Crack in Pressurized Cylindrical Shell," *Int. J. Fract. Mech.*, Vol. 1, 1965, pp. 104–113.
4 Copley, L. G., and Sanders, J. L., Jr., "A Longitudinal Crack in a Cylindrical Shell Under Internal Pressure," *Int. J. Fract. Mech.*, Vol. 5, 1969, pp. 117–131.
5 Erdogan, F., and Kibler, J. J., "Cylindrical and Spherical Shells With Cracks," *Int. J. Sol. Str.*, Vol. 12, 1967, pp. 229–237.
6 Keer, L. M., and Watts, H. A., "Mixed Boundary Value Problems for a Cylindrical Shell," *Int. J. Fract.*, Vol. 14, 1978, pp. 723–729.
7 Sanders, J. L., "Circumferential Through-Cracks in Cylindrical Shells Under Tension," ASME Journal of Applied Mechanics, Vol. 49, 1982, pp. 103–107.
8 Krenk, S., "Influence of Transverse Shear on an Axial Crack in a Cylindrical Shell," *Int. J. Fract.*, Vol. 14, 1978, pp. 123–144.

Downloaded 02 May 2010 to 171.66.16.54. Redistribution subject to ASME license or copyright; see http://www.asme.org/terms/Terms_Use.cfm

9 Delale, F., and Erdogan, F., "Transverse Shear Effect in a Circumferentially Cracked Cylindrical Shell," *Quart. Appl. Math.*, Vol. 37, 1979, pp. 239–248.

10 Delale, F., "Cracked Shells Under Skew Symmetric Loading," *Int. J. of Eng. Science*, Vol. 20, 1982, pp. 325–348.

11 Sanders, J. L., Jr., "Cutouts in Shallow Shells," ASME JOURNAL OF APPLIED MECHANICS, Vol. 37, 1970, pp. 374–383.

12 Simmonds, J. G., and Bradley, M. R., "Stress-Intensity Factors for Very Short Cracks in Arbitrary Pressurized Shells," ASME JOURNAL OF APPLIED MECHANICS, Vol. 43, 1976, pp. 657–662.

13 Latta, G. E., Simmonds, J. G., and Bradley, M. R., "Analytical and Numerical Calculation of Stress-Intensity Factors in a Pressurized Cylindrical Shell With a Clamped Crack," ASME JOURNAL OF APPLIED MECHANICS, Vol. 44, 1977, pp. 264–270.

14 Simmonds, J. G., Bradley, M. R., and Nicholson, J. W., "Stress-Intensity Factors for Arbitrarily Oriented Cracks in Shallow Shells," ASME JOURNAL OF APPLIED MECHANICS, Vol. 45, 1978, pp. 135–141.

15 Lakshminarayana, H. V., and Murthy, M. V. V., "On Stresses Around an Arbitrary Oriented Crack in a Cylindrical Shell," *Int. J. Fract.*, Vol. 12, 1976, pp. 547–566.

16 Lakshminarayana, H. V., Murthy, M. V. V., and Srinath, L. S., "On an Analytical-Numerical Procedure for the Analysis of Cylindrical Shells With Arbitrarily Oriented Cracks," *Int. J. of Fracture*, Vol. 19, 1982, pp. 257–276.

17 Solecki, R., "Bending Vibration of Simply Supported Rectangular Plates With Internal Rigid Support," *Int. J. Eng. Sci.*, Vol. 18, 1980, pp. 1309–1318.

18 Solecki, R., "Bending Vibration of a Simply Supported Rectangular Plate With a Crack Parallel to One Edge," *Eng. Fract. Mechanics*, Vol. 18, 1983, pp. 1111–1118.

19 Solecki, R., Technical Report for the Department of the Navy, ME 82-83-ONR-1.

20 Solecki, R., "Bending Vibration of a Simply Supported Rectangular Plate with an Arbitrarily Located Crack," *Eng. Fract. Mechanics*, to be published.

21 Stahl, B., and Keer, L. M., "Vibration and Stability of Cracked Rectangular Plates," *Int. J. Sol. Structures*, Vol. 8, 1972, pp. 69–92.

22 Solecki, R., and Szymkiewicz, J., "Vibration of One and Two-Dimensional Structures," in Polish, Arkady, 196.

Downloaded 02 May 2010 to 171.66.16.54. Redistribution subject to ASME license or copyright; see http://www.asme.org/terms/Terms_Use.cfm

T. P. Pawlak[1]
Engineer,
Swanson Analysis Systems, Inc.
P.O. Box 65
Houston, Pa. 15342

N. J. Salamon[1]
Professor,
Department of Engineering
Science and Mechanics,
The Pennsylvania State University,
227 Hammond Building,
University Park, Pa. 16802
Mem. ASME

F. F. Mahmoud
Professor and Vice Dean,
Mechanical Engineering Department,
Zagazig University,
Cairo, Egypt

Beams in Receding/Advancing Contact: Dundurs Problems

The response of beams constrained unilaterally by a foundation and upper barriers while under monotonic loading is treated. Several scenarios featuring gaps and clearances are solved and shown to agree with Dundurs' predictions. The solutions are generated by a numerical simulation featuring a direct incremental algorithm in conjunction with the finite element method.

Introduction

The response of beams resting on elastic foundations to static load is a classic problem thoroughly treated by Hetenyi [1]. However, even today the complicated, yet tractable nature of the problem continues to attract researchers. Several recent analytical works are referenced by Gallagher [2] who solves an integrodifferential equation for a finite beam resting on an elastic half space. And some numerical background is provided by Westbrook [3] who treated an elastic beam in the presence of rigid barriers. The fundamental problem of a finite beam resting on springs has also been solved numerically by Marks [4], Marks and Salamon [5], and Mahmoud, Salamon, and Marks [6]. Less one think the problem academic, works by Conway and Richman [7] dealing with elastic deformation of bearings and by Vaillette and Adams [8] on beam buckling in channels are examples of practical applications.

The state of these works is such that only purely receding, advancing, or stationary contact problems is addressed. But in a perspicacious paper on the philosophy of contact mechanics, Dundurs [9] was able to qualitatively predict the response of beams through concurrent receding-advancing states by employing the fundamental equations of mechanics. In doing so, he adopted a terminology that classifies contact problems into two groups: receding or advancing. This made it possible to conclude general properties of receding contacts. However for descriptive purposes, it is convenient to view the contact state in relation to change in load. Hence in this paper receding infers a decrease, advancing an increase, and stationary no change in the contact region with respect to increases in applied load. It is the present objective to quantitatively verify the behavior predicted by Dundurs for bodies in multiphase contact – hence to solve Dundurs problems.

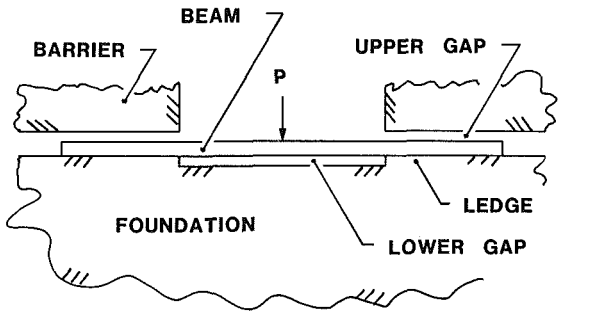


Fig. 1 Beam on foundation with gap and upper barriers

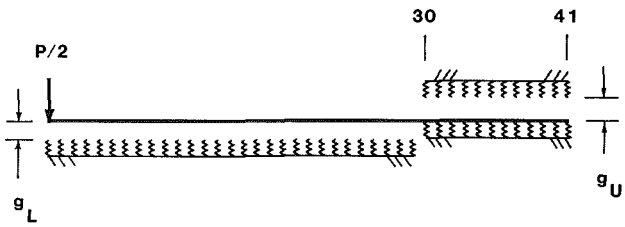


Fig. 2 The discrete beam/spring model

Several problem configurations involving a beam are solved and Fig. 1 illustrates the most complicated one. The constraints, consisting at most of a foundation and upper barrier

[1]Formerly, Graduate Student and Associate Professor respectively, Mechanical and Aerospace Engineering Department, West Virginia University, Morgantown, W.Va. 26506.

Contributed by the Applied Mechanics Division and presented at the Winter Annual Meeting, Miami, Fla., November 17-21, 1985 of THE AMERICAN SOCIETY OF MECHANICAL ENGINEERS.

Discussion on this paper should be addressed to the Editorial Department, ASME, United Engineering Center, 345 East 47th Street, New York, N.Y. 10017, and will be accepted until two months after final publication of the paper itself in the JOURNAL OF APPLIED MECHANICS. Manuscript received by ASME Applied Mechanics Division, February, 1984; final revision, October, 1984. Paper No. 85-WA/APM-3.

Copyright © 1985 by ASME
Downloaded 02 May 2010 to 171.66.16.54. Redistribution subject to ASME license or copyright; see http://www.asme.org/terms/Terms_Use.cfm

Table 1 Data for beam/spring model

Beam:	Young's modulus	$= 0.710 \times 10^{11}$ N/m^2
	Moment of inertia	$= 1.041 \times 10^{-6}$ m^4
	Half length	$= 0.381$ m
	Node spacing	$= 9.525 \times 10^{-3}$ m
Spring:	Stiffness	$= 2.627 \times 10^{6}$ N/m

with gaps, react unilaterally against the beam, that is they can only develop compression. The load P is increased monotonically causing the beam to travel through a sequence of contact states or scenarios. The solution is generated by a numerical simulation based on an extension of the work in reference [6]. The results confirm Dundurs' predictions.

Methodology

A direct, incremental algorithm was developed by Pawlak [10] and is used in conjunction with the finite element method for linear systems. The load P is applied to conventional beam elements [11] which are appropriately constrained by spring elements (the Winkler model). A symmetric half of the configuration in Fig. 1 is modeled in Fig. 2 with the undeflected beam resting in its initial state, $P=0$. This position serves as the reference for kinematic quantities which for any given set of active spring constraints are derived from the output of a linear problem. The length of each beam element is equal to the spacing between springs. The length of each spring is irrelevant.

The Simulation. The beam must always be under some constraint; initially the prescription must include attachment of at least one spring together with the slope under the load set to zero (Fig. 2). The physical system is represented by the global stiffness matrix $[K]$. Under the action of load vector $\{R\}$, which contains P, the simulation takes the following course:

1. At the mth increment in load, solve the linear system

$$\{w\}^m = [K^{(m)}]^{-1}\{R\}^m \tag{1}$$

for $\{w\}$ which contains the deflections $\{d\}$, measured positive upward, and the rotations.

2. Detect new constraints. If the detection is positve, then a scale factor $S=S_i$, which serves to position the onset of this constraint at the ith nodal location on the beam, will fall in the range $0 \le S \le 1$. Otherwise no further contacts or separations will occur and $S=1$ is set. (Details of the detection procedure are presented in the next section.)

3. Accumulate the kinematic quantities in $\{W\}$ and update the geometry or gaps $\{g\}$, that is

$$\{W\}^{m+1} = \{W\}^m + S_i\{w\}^m \tag{2}$$

and

$$\{g\}^{m+1} = \{g\} \pm S_i\{d\}^m \tag{3}$$

where the + or − sign pertains to a lower or upper gap, respectively. (Note: Initially $m=1$ and $\{W\}$ is null.)

4. Compute the residual load yet to be applied:

$$\{R\}^{m+1} = (1-S)\{R\}^m \tag{4}$$

5. If the constraint detection is positive and $S \neq 1$, then update the stiffness $[K^{(m)}]$ to $[K^{(m+1)}]$ to account for the newly connected constraint and return to step 1. Otherwise the procedure ends.

The simulation runs until either the total applied load or the number of candidate constaints is exhausted.

Constraint Detection. Contacts or separations are sensed kinematically through the scale factor $S=S_i$ such that

$$S_i = \text{Min}(\pm g/d, -D/d)_j, \quad 1 \le j \le NC \tag{5}$$

where + or − g, $g \ge 0$, is the upper or lower gap, respectively,

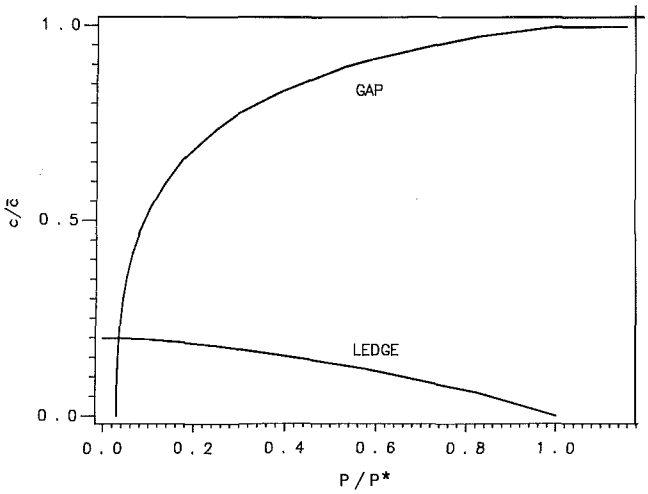


Fig. 3 Contact/load history for beam on foundation with gap (scenario A)

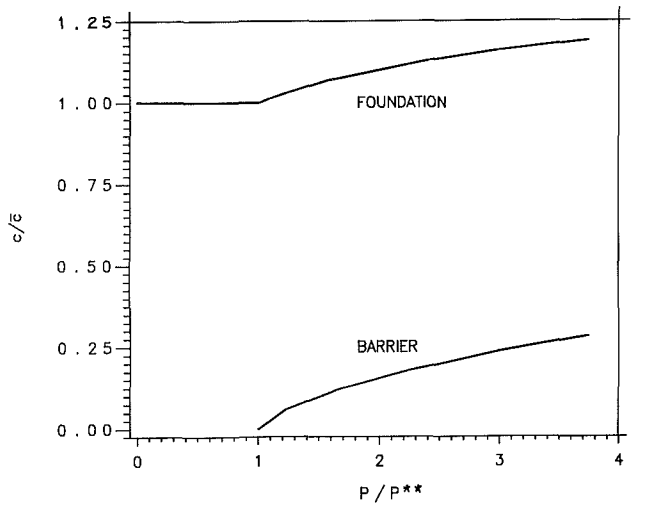


Fig. 4 Contact/load history for beam on flat foundation with upper barriers (scenario B)

and D is the accumulated deflection in $\{W\}$, all taken at node or station number j in the set of candidate constraints running from 1 to NC. The subscript i is the nodal location of the minimum. It can be proven that further contacts or separations will occur only if $0 \le S \le 1$. Hence computation of S serves as the detection mechanism.

However the computation of S alone is not sufficient. If several stations yield the same value of S, then the chosen station i is that which achieves the greatest incompatibility T_i, that is, choose i such that

$$T_i = \text{Max}(-g \pm d)_j, \quad j \epsilon I \tag{6}$$

with + taken for an upper − for a lower gap, and where j is in the set I that contains the station numbers bearing equal values of S. This is primarily of use in solving receding contact problems where $\{g\}$ is null.

Program Control. Control of the procedure is done in subroutines. A data structure is established to keep track of the contact status of each station as well as its current mode of contact, either receding or advancing. Efficiency is enhanced through use of a decision process, based in part on theoretical precepts [9], which eliminate surveying all stations during each increment. A key factor contributing to efficiency is that each spring is independent of the others. This permits determination of separation kinematically without recourse to the computation of force or stress.

Downloaded 02 May 2010 to 171.66.16.54. Redistribution subject to ASME license or copyright; see http://www.asme.org/terms/Terms_Use.cfm

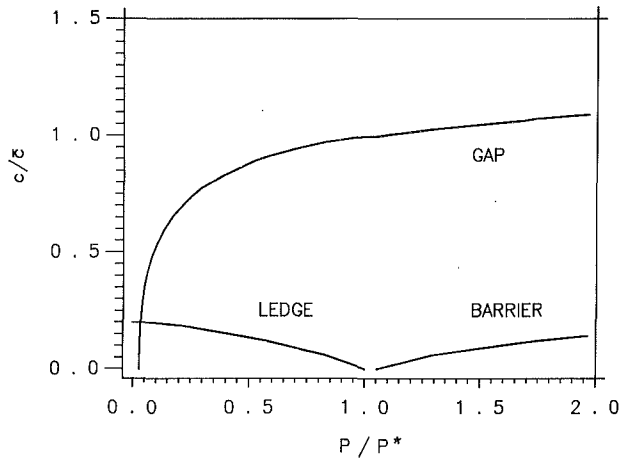


Fig. 5 Contact/load history for beam on foundation with gap and upper barriers (scenario C)

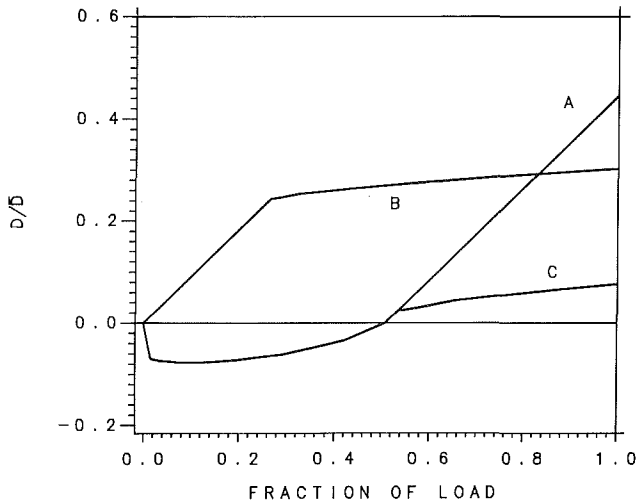


Fig. 6 Beam deflection at station 30 versus fraction of load for scenarios A, B, and C

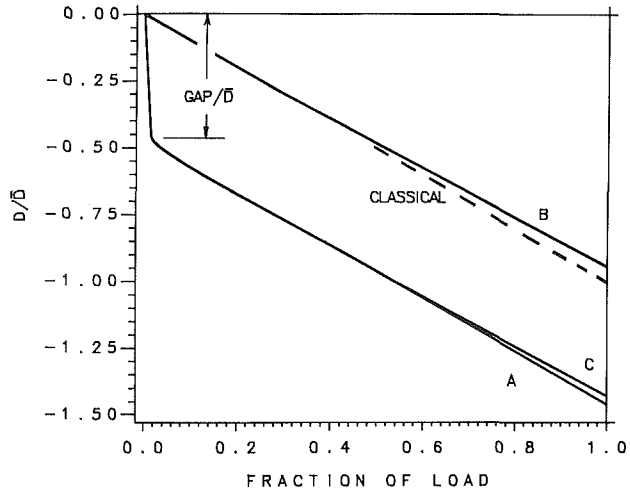


Fig. 7 Center deflection of beam versus fraction of load for scenarios A, B, and C

In essence the method employs the principles of linearity during incremental steps and superposition after them. This leads *directly* to contact-separation events in a very efficient manner. A detailed discussion of the algorithm as applied to the solution of beam and plate contact problems is provided in a journal dedicated to numerical methods [12] and, for beams only, in [10].

Results

The methodology is incorporated into a computer code to generate results for several variations of the problem illustrated in Fig. 1. Pertinent data common to all of the problems is provided in Table 1 except that the stiffness of those springs located at end-regions of the model (under the load, etc.) is halved to better approximate a continuous foundation. The beam is weightless. All problems are begun with at most two springs connected and the center slope set to zero. In what follows, c denotes the total contact length of noted portions of the beam and $\bar{c}$ denotes the total contact length for a beam on a level foundation.

To test the accuracy of the code and suitabilitj of the discretization, the classical beam-on-a-level-foundation problem was solved and compared to the exact solution for a continuous foundation [1]. In this case, with reference to Fig. 2, $g_L = 0$ and the upper barrier is removed. For the exact solution, the modulus for the continuous foundation is computed from the spring stiffness in Table 1 and is found to be 2.758×10^8 N/m^2. The computer solution yields $\bar{c} = 0.31992$ m for the total contact length and $\bar{D} = 0.004327$ m where $\bar{D}$ is the center deflection. In comparison with the exact solution, the respective errors are 0.09 percent and 0.14 percent. The contact lengths for the discrete models are interpolated values between those stations in and out of contact at the contact boundary. This provides a better approximation to the length analytically determined for a continuous foundation. Otherwise the contact length for a discrete system extends out to the last spring in contact. All subsequent results are interpolated.

Scenario A – Beam on a Gap Foundation. In Fig. 2 the upper barrier is removed and $g_L = 0.002$ m. The history of contact length versus load is illustrated in Fig. 3 where $c/\bar{c}$ is plotted against P/P^*, P^* the load required to just lift the beam off the ledge. For the short range $0 < P/P^* < 0.03$, the beam sits on the ledge in stationary contact with $c/\bar{c} = 0.199$. After touchdown in the gap, contact advances there while it simultaneously recedes along the ledge. This behavior continues until liftoff from the ledge which returns the beam to a stationary contact state with $c/\bar{c} = 1.000$ precisely. Although not illustrated, it should be noted that the beam's final configuration is identical to that of the test problem.

Scenario B – Beam on Flat Foundation With Upper Barrier. For this case the upper barrier in Fig. 2 is present with $g_U = 0.002$ m, but $g_L = 0$. The history of contact length versus load is shown in Fig. 4 where P^{**} is the load required to contact the upper barrier. While the beam is free of the barrier ($P/P^{**} < 1$), the contact remains stationary at $c/\bar{c} = 1.0$. However once contact is made with the barrier, it continues to advance along both the barrier and the foundation.

Scenario C – Beam on Gap Foundation With Upper Barrier. This is the configuration illustrated in Figs. 1 and 2 with $g_L = g_U = 0.002$ m. The history of contact length versus load is shown in Fig. 5. Although it is difficult to discern, the scenario begins with the beam in stationary contact over the load interval $0 < P/P^* < 0.03$ with $c/\bar{c} = 0.199$, precisely the same value initially attained in Fig. 3. In the interval $0.03 \le P/P^* < 1.0$, the beam advances in the gap while simultaneously receding along the ledge. Over the short load span $1.0 \le P/P^* < 1.05$ the beam is in stationary contact, free of both the ledge and the upper barrier, with $c/\bar{c} = 1.00$. This tallies with corresponding stationary contact lengths in Figs. 3 and 4. Once the upper barrier is engaged, the total process becomes advancing; at this stage the curves are similar to those in Fig. 4.

Downloaded 02 May 2010 to 171.66.16.54. Redistribution subject to ASME license or copyright; see http://www.asme.org/terms/Terms_Use.cfm

Deflection Path as a Function of Load. It is interesting to trace the deflections of the beam, denoted by D, as a function of load. In Fig. 6 the paths followed by a point on the beam at station 30 (see Fig. 2) is plotted for scenarios A, B, and C. The deflections for A and C (both feature a lower gap, but A does not include the upper barrier) are congruent until 53.6 percent of total load is reached. After this point A is free to continue to rise above the foundation; the rise is linear because the contact is stationary, whereas further rise in C is retarded by the upper barrier. Initially A and C are linear to 1.5 percent of load since the contact is stationary until the lower gap is encountered.

On the other hand, scenario B (featuring a flat foundation with upper barrier) is initially linear to 26.8 percent of load. This stationary mode of contact ends thereafter when the upper barrier is encountered.

In marked contrast, the plot of the deflections under the load for A, B, C in Fig. 7 is a picture of simplicity. The response is virtually linear throughout the loading. The upper barrier has only slight influence and the deflection of A and C differ from B roughly by the gap. Noting that under 26.8 percent of load, scenario B is equivalent to the classic beam on a flat foundation problem while at greater loads the center deflection of B is roughly approximated by linear extrapolation. Hence the center displacements of all three scenarios can be approximated knowing that for the classic flat foundation problem.

Conclusion

The qualitative predictions for concurrent receding-advancing contact problems by Dundurs [9] have been quantitatively verified for finite beams on elastic foundations. The methodology developed to do this has evolved into a simple, efficient algorithm which can be attached to any finite element or finite difference computer code [12]. For the classic problem of a beam on a continuous, elastic foundation, accuracies within 0.14 percent error were achieved for contact length and displacement under the load; however beam deflections near the contact boundary rise suddenly to 3.4 percent error for the chosen discretization. This rise in error is undoubtedly due to failure to halve the last active, discrete spring, a necessary action for accurate simulation of continuous support. Application of the algorithm to the solution of plate problems is treated in a companion paper [13].

It is interesting to note that the response for the various scenarios tallied as the beam passed through equivalent contact states. For instance the final configuration for the beam on a gap foundation is identical to that reached by a beam on a flat foundation under equal load, except that it resides in the gap. It is safe to predict that unloading would cause the beam to climb back up onto the ledges with no energy lost. Moreover should the ledges have been removed, unloading would cause the beam to duplicate the behavior of a beam on a flat foundation; it would settle down to rest in the gap. Clearly the introduction of friction will change this scenario.

While the response of the entire beam in each scenario is rather complicated, the deflection under the load is surprisingly simple. It deviates only slightly from linearity and can be approximated by the classical solution for a beam on a flat foundation plus the gap.

In closing it should be noted that the simulation could be accomplished using analytical solutions [1]. Indeed for beams the numerical algorithm is unnecessary. However these problems serve as important stepping stones for the solution of more complicated ones such as those dealing with plates, which are listed in the references.

Acknowledgment

The results reported here were obtained in the course of research supported by the National Science Foundation. In particular the first author is grateful for a graduate assistantship. The writers also thank a reviewer for helpful comments.

References

1 Hetenyi, M., *Beams on Elastic Foundation*, University of Michigan Press, Ann Arbor, Mich., 1967.

2 Gallagher, A. P., "Bending of a Free Beam on an Elastic Foundation," ASME JOURNAL OF APPLIED MECHANICS, Vol. 50, 1983, pp. 463-465.

3 Westbrook, D. R., "Contact Problems for the Elastic Beam," *Computers and Structures*, Vol. 15, 1982, pp. 473-479.

4 Marks, W. R., "Solution of Frictionless Contact Problems by a Conjugate Gradient Technique," M.S. Thesis, The University of Wisconsin, Milwaukee, Wis., 1979.

5 Marks, W. R., and Salamon, N. J., "A Modified Conjugate Gradient Method for Frictionless Contact Problems," ASME *Journal of Vibration, Acoustics, Stress, and Reliability in Design*, Vol. 105, 1983, pp. 242-246.

6 Mahmoud, F. F., Salamon, N. J., and Marks, W. R., "A Direct Automated Procedure for Frictionless Contact Problems," *International Journal for Numerical Methods in Engineering*, Vol. 18, 1982, pp. 245-257.

7 Conway, H. D., and Richman, M. W., "Flexible Thrust Pads of Fixed Inclination," ASME JOURNAL OF APPLIED MECHANICS, Vol. 50, 1983, pp. 684-686.

8 Vaillette, D. P., and Adams, G. G., "An Elastic Beam Contained in a Frictionless Channel," ASME JOURNAL OF APPLIED MECHANICS, Vol. 50, 1983, pp. 693-694.

9 Dundurs, J., "Properties of Elastic Bodies in Contact," in *The Mechanics of Contact Between Deformable Bodies*, Kalker, J. J., and de Pater, A. D., Eds., Delft University Press, 1975.

10 Pawlak, T. P., "Solution of Beam Contact Problems by a Direct Method Technique," M.S. Thesis, West Virginia University, Morgantown, W.V., 1983.

11 Cook, Robert D., *Concepts and Applications of Finite Element Analysis*, 2nd ed., J. Wiley, New York, 1981.

12 Mahmoud, F. F., Salamon, N. J., and Pawlak, T. P., "Simulation of Structural Elements in Receding/Advancing Contact," *Computers and Structures*, in press.

13 Salamon, N. J., Mahmoud, F. F., and Pawlak, T. P., "Plates in Unilateral Contact With Simple Supports: Pressure Loading," submitted for publication.

Downloaded 02 May 2010 to 171.66.16.54. Redistribution subject to ASME license or copyright; see http://www.asme.org/terms/Terms_Use.cfm

Point-Force Excitation of an Elastic Plate With an Embedded Cavity

A. Boström

A. Karlsson

Institute of Theoretical Physics,
Chalmers University of Technology,
S-412 96 Göteborg, Sweden

The propagation of elastic waves in a thick plate containing an embedded cavity is considered. The full elastodynamic equations are solved and both time-harmonic and pulse propagations are treated. The time-harmonic problem is solved using the null field approach, a method whose main characteristics are surface integral representations and expansions in spherical and planar vector wave functions. To obtain the pulse response, a Fourier integral in frequency is employed. Numerical examples are given showing the fields in both the time and frequency domains at a few selected locations on the plate surfaces when the plate is excited by a point force. Only low and intermediate frequencies are included and the pulse width is thus somewhat larger than the dimensions of the spheroidal cavity.

1 Introduction

In the present paper we consider the propagation of elastic waves in a thick plate containing an embedded spheroidal cavity. Both time-harmonic and pulse propagations are treated. The full elastodynamic equations are solved and no approximations, such as plate theory or ray methods, are used. The plate is excited by a point force on one of its surfaces and the frequency and time responses are computed at a few selected points on both surfaces. Low and intermediate frequencies are included, the highest frequency corresponds to a P wavelength about equal to the dimensions of the cavity and the pulse width of the point force is somewhat larger than the cavity.

The detection of flaws is an important problem in nondestructive evaluation, and problems similar to the present one are therefore treated by a number of authors. Problems with cavities or cracks in an elastic half space are treated by Achenbach and Brind [1, 2], Datta and El-Akily [3], Höllinger and Ziegler [4], and van der Hijden [5], and surface-breaking cracks are considered by Mendelsohn et al. [6] and Datta [7]. Transients in a plate with a symmetrically situated crack are treated by Chen [8, 9] and Itou [10]. We remark that all the work cited so far concern two-dimensional wave propagation, whereas in this paper we consider the three-dimensional problem.

To solve the time-harmonic problem we employ the null field approach and an ordinary Fourier integral then gives the pulse response. The null field approach has previously been used in a number of problems similar to the present one. Boström and Karlsson [11] compute synthetic seismograms for an inhomogeneity in a layered elastic half space, Karlsson [12] considers the two-dimensional problem of scattering of Rayleigh-Lamb modes by a flaw in a plate, and Boström and Kristensson [13] investigate the scattering of a pulsed Rayleigh wave by a cavity in an elastic half space.

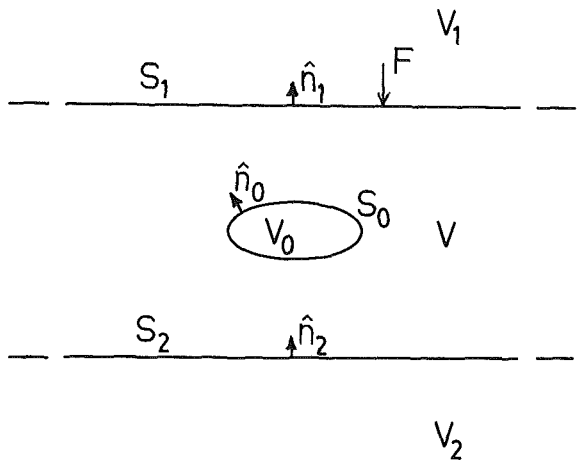


Fig. 1 The thick plate with a cavity and a point force

The computation of synthetic seismograms in reference [11] are closely related to the computations performed in the present paper. The present case is simpler in that we here consider a plate as compared to a layered elastic half space, but on the other hand, the point force used here is somewhat more complicated than the monopole (explosion) used in reference [11]. Because of the close similarities with [11] the presentation given in the following is rather brief. Section 2 gives the formal solution and Section 3 treats the source, but no explicit expressions are given. More details can be found in [11], which also lists all the explicit and lengthy expressions given by the formal solution. Finally, in Section 4 we give a few numerical examples.

2 Formal Theory

Consider an elastic plate with an embedded cavity as

Contributed by the Applied Mechanics Division and presented at the Winter Annual Meeting, Miami, Fla., November 13-17, 1985 of THE AMERICAN SOCIETY OF MECHANICAL ENGINEERS.

Discussion on this paper should be addressed to the Editorial Department, ASME, United Engineering Center, 345 East 47th Street, New York, N.Y. 10017, and will be accepted until two months after final publication of the paper itself in the JOURNAL OF APPLIED MECHANICS. Manuscript received by ASME Applied Mechanics Division, June, 1984; final revision, January, 1985. Paper No. 85-WA/APM-9.

Copyright © 1985 by ASME
Downloaded 02 May 2010 to 171.66.16.54. Redistribution subject to ASME license or copyright; see http://www.asme.org/terms/Terms_Use.cfm

depicted in Fig. 1. The top surface of the plate is denoted S_1, the bottom surface S_2, and the surface of the cavity S_0, and the unit normals $\hat{n}_\nu$, $\nu = 0, 1, 2$, of the surfaces point outward or upward as shown. The plate is denoted V, the cavity V_0, and the upper and lower half spaces V_1 and V_2, respectively. In the plate the Lamé parameters are λ and μ, the density is ρ, and the longitudinal and transverse wave speeds are $c_p = \sqrt{(\lambda+2\mu)/\rho}$ and $c_s = \sqrt{\mu/\rho}$, respectively. The surfaces S_1 and S_2 of the plate are assumed planar, although formally this restriction is not necessary. A sufficient condition on the geometry for the null field approach to be applicable is then that the circumscribed sphere of the cavity does not intersect S_1 or S_2. We choose a coordinate system with the origin inside the cavity and the z axis perpendicular to the planes S_1 ($z = z_1$) and S_2($z = z_2$).

In the present section we assume that the source is time-harmonic and we suppress the time factor $\exp(-i\omega t)$. Here we need not specify the source any further, but in the next section we will consider a pulsed point force by Fourier integration in frequency. The wave numbers are $k_p = \omega/c_p$ and $k_s = \omega/c_s$.

In the null field approach the starting point is a surface integral representation containing the free space Green's dyadic. The integral representation for the displacement vector $\mathbf{u}$ in the plate is

$$\frac{k_s}{\mu}\int_{S_0}\mathbf{u}^0\cdot(\hat{n}_0\cdot\bar{\Sigma})\,dS-\frac{k_s}{\mu}\int_{S_1}\mathbf{u}^1\cdot(\hat{n}_1\cdot\bar{\Sigma})\,dS + \frac{k_s}{\mu}\int_{S_2}\mathbf{u}^2\cdot(\hat{n}_2\cdot\bar{\Sigma})\,dS+\mathbf{u}^{inc} = \begin{cases}\mathbf{u} & \text{in } V\\ 0 & \text{in } V_0, V_1, \text{ or } V_2\end{cases} \tag{1}$$

In stating this formula the vanishing of the traction on the surfaces S_ν, $\nu = 0, 1, 2$, has been used to eliminate one term in each of the surface integrals. $\mathbf{u}^\nu$, $\nu = 0, 1, 2$, denote the surface displacement fields. The incoming field $\mathbf{u}^{inc}$ is the field from the source as if no scattering surfaces were present, i.e., as if the source was located in a homogeneous space with the material properties of the plate. The free-space Green's stress triadic $\bar{\Sigma}$ has the same relation to the Green's dyadic as the stress dyadic has to the displacement.

The stress triadic and all displacement fields are to be expanded in plane and/or spherical vector wave functions. We employ a convenient shorthand notation for the wave functions: ψ_n denotes an outgoing spherical vector wave function (it contains spherical Hankel functions and vector spherical harmonics), $Re\psi_n$ is its regular counterpart (it contains spherical Bessel functions and vector spherical harmonics), and $\phi_\uparrow$ and $\phi_\downarrow$ denote upgoing and downgoing (including evanescent) plane vector wave functions. The multiple index n contains a mode index (two S waves and a P wave) and the three indices of the spherical harmonics. The arrow on the plane wave functions similarly denotes one mode index for SH, SV, and P waves plus two continuous variables specifying the direction of propagation of the plane wave (this direction is complex for evanescent waves). The summation (and integration) convention that a repeated n (arrow) should be summed (summed and integrated) over will be used. The transformation formulas between the plane and spherical wave functions (which will soon be needed)

$$\phi_\uparrow = Re\psi_n B^\dagger_{n\uparrow} \tag{2}$$

$$\psi_n = 2\phi_\downarrow B_{\downarrow n}, \quad z>0 \tag{3}$$

thus contain a quadruple sum and a sum plus a double integral, respectively. The transformation functions $B^\dagger_{n\uparrow}$ and $B_{\downarrow n}$ are given in [11].

In this compact notation the expansions of the Green's surface traction dyadic become

$$\hat{n}_\nu\cdot\bar{\Sigma} = it_\nu(\psi_n(\mathbf{r}'))Re\psi_n(\mathbf{r}), \quad r<r', \quad \nu=0,1,2 \tag{4}$$

$$\hat{n}_\nu\cdot\bar{\Sigma} = 2it_\nu(\phi^\dagger_\uparrow(\mathbf{r}'))\phi_\downarrow(\mathbf{r}), \quad z>z', \quad \nu=0,1,2 \tag{5}$$

The superscript $\dagger$ on the plane wave function essentially reverses the direction of the wave [11]. The traction operator on surface S_ν, $\nu = 0, 1, 2$, is

$$\mathbf{t}_\nu(\mathbf{u}) = \hat{n}_\nu\lambda\nabla\cdot\mathbf{u}+2\mu\frac{\partial}{\partial n_\nu}\mathbf{u}+\mu\hat{n}_\nu\times(\nabla\times\mathbf{u}) \tag{6}$$

There are two similar counterparts to (4) and (5) valid when $r>r'$ and $z<z'$, respectively. For the incoming field we need three different expansions:

$$\mathbf{u}^{inc} = Re\psi_n a^0_n, \quad \text{in} \quad V_0 \tag{7}$$

$$\mathbf{u}^{inc} = \phi_\downarrow a^\downarrow_\uparrow, \quad \text{in} \quad V_1 \tag{8}$$

$$\mathbf{u}^{inc} = \phi_\downarrow a^2_\uparrow, \quad \text{in} \quad V_2 \tag{9}$$

The expansion coefficients a^0_n, $a^\downarrow_\uparrow$, and $a^2_\uparrow$ can be regarded as known. The surface fields on S_0, S_1, and S_2 are also expanded:

$$\mathbf{u}^0 = Re\psi_n\alpha^0_n, \quad \text{on} \quad S_0 \tag{10}$$

$$\mathbf{u}^1 = \phi_\downarrow\alpha^\downarrow_\uparrow, \quad \text{on} \quad S_1 \tag{11}$$

$$\mathbf{u}^2 = \phi_\downarrow\alpha^2_\uparrow, \quad \text{on} \quad S_2 \tag{12}$$

Other expansions are also possible and it should especially be noted that an expansion in vector spherical harmonics is often to be preferred in (10) [14, 15].

Insertion of all the expansions (4) and (5), (7)–(12) in the integral representation using the expansion (4) of the Green's surface traction dyadic in the surface integral over S_0 and the expansion (5) in the integral over S_1 and S_2, use of the transformations (2) and (3), and use of the linear independence of the spherical and plane waves in a sphere or half space, respectively, yield for the four regions V_0, V_1, V_2, V in turn:

$$iQ^0_{nn'}\alpha^0_{n'} - iB^\dagger_{n\downarrow}Q^\downarrow_{\downarrow\uparrow}\alpha^\downarrow_\uparrow + iB^\dagger_{n\downarrow}Q^2_{\downarrow\uparrow}\alpha^2_\uparrow + a^0_n = 0 \tag{13}$$

$$2iB_{\downarrow n}ReQ^0_{nn'}\alpha^0_{n'} - iQ^\downarrow_{\uparrow\downarrow}\alpha^\downarrow_\uparrow + iQ^2_{\uparrow\downarrow}\alpha^2_\uparrow + a^\downarrow_\uparrow = 0 \tag{14}$$

$$2iB_{\downarrow n}ReQ^0_{nn'}\alpha^0_{n'} - iQ^\downarrow_{\uparrow\downarrow}\alpha^\downarrow_\uparrow + iQ^2_{\uparrow\downarrow}\alpha^2_\uparrow + a^2_\uparrow = 0 \tag{15}$$

$$\mathbf{u} = \mathbf{u}^{inc} + i\psi_n ReQ^0_{nn'}\alpha^0_{n'} - i\phi_\downarrow Q^\downarrow_{\downarrow\uparrow}\alpha^\downarrow_\uparrow + i\phi_\downarrow Q^2_{\downarrow\uparrow}\alpha^2_\uparrow \tag{16}$$

Here we have introduced

$$Q^0_{nn'} = \frac{k_s}{\mu}\int_{S_0}\mathbf{t}_0(\psi_n)\cdot Re\psi_{n'}\,dS \tag{17}$$

$$Q^\downarrow_{\downarrow\uparrow} = 2\frac{k_s}{\mu}\int_{S_1}\mathbf{t}_1(\phi^\dagger_\uparrow)\cdot\phi_\downarrow\,dS \tag{18}$$

$$Q^2_{\downarrow\uparrow} = 2\frac{k_s}{\mu}\int_{S_2}\mathbf{t}_2(\phi^\dagger_\uparrow)\cdot\phi_\downarrow\,dS \tag{19}$$

$ReQ^0_{nn'}$, $Q^\downarrow_{\downarrow\uparrow}$, and $Q^2_{\downarrow\uparrow}$ are defined in the obvious ways. Equation (16) is only valid outside the circumscribed sphere to S_0, but we will only use it to calculate the fields on the surfaces of the plate so this is no further restriction of importance. Formally solving equations (13)–(15) and inserting the result into (16) we obtain

$$\mathbf{u} = \mathbf{u}^{dir} + \mathbf{u}^{anom} \tag{20}$$

where the direct field, which is the field in the absence of the cavity, is

$$\mathbf{u}^{dir} = \mathbf{u}^{inc} + \phi_\downarrow(M^\downarrow_{\downarrow\uparrow}a^\downarrow_\uparrow + M^2_{\downarrow\uparrow}a^2_\uparrow) + \phi_\downarrow(M^3_{\downarrow\uparrow}a^\downarrow_\uparrow + M^4_{\downarrow\uparrow}a^2_\uparrow) \tag{21}$$

and the anomalous field, which is the additional field due to the presence of the cavity, is

Downloaded 02 May 2010 to 171.66.16.54. Redistribution subject to ASME license or copyright; see http://www.asme.org/terms/Terms_Use.cfm

$$\mathbf{u}^{anom} = \{2\phi_\uparrow (M^1_{\uparrow\uparrow} B_{\uparrow n} + M^2_{\uparrow\uparrow} B_{\downarrow n}) + 2\phi_\downarrow (M^3_{\uparrow\uparrow} B_{\downarrow n} + M^4_{\uparrow\uparrow} B_{\downarrow n}) + \psi_n\} T^0_{nn'} c_{n'} \tag{22}$$

Here we have introduced

$$M^1_{\uparrow\uparrow} = R^2_{\uparrow\uparrow}(1 - R^1_{\uparrow\uparrow} R^2_{\uparrow\uparrow})^{-1} R^1_{\uparrow\uparrow} \tag{23}$$

$$M^2_{\uparrow\downarrow} = R^2_{\uparrow\uparrow}(1 - R^1_{\uparrow\uparrow} R^2_{\uparrow\uparrow})^{-1} \tag{24}$$

$$M^3_{\downarrow\uparrow} = (1 - R^1_{\downarrow\downarrow} R^2_{\downarrow\uparrow})^{-1} R^1_{\downarrow\uparrow} \tag{25}$$

$$M^4_{\downarrow\uparrow} = (1 - R^1_{\downarrow\downarrow} R^2_{\downarrow\uparrow})^{-1} R^1_{\downarrow\uparrow} R^2_{\downarrow\uparrow} \tag{26}$$

where

$$R^1_{\downarrow\uparrow} = -Q^1_{\downarrow\uparrow}(Q^1_{\uparrow\uparrow})^{-1} \tag{27}$$

$$R^2_{\downarrow\uparrow} = -Q^2_{\downarrow\uparrow}(Q^2_{\uparrow\downarrow})^{-1} \tag{28}$$

are the reflection operators for S_1 from below and for S_2 from above, respectively. The transition matrix for the cavity is

$$T^0_{nn'} = -ReQ^0_{nn''}(Q^0_{n''n'})^{-1} \tag{29}$$

and $c_n = -iQ^0_{nn'}\alpha^0_{n'}$ is the solution of the following equation:

$$c_n - R_{nn'} T^0_{n'n''} c_{n''} = d_n \tag{30}$$

where

$$R_{nn'} = 2B^\dagger_{n\uparrow}(M^1_{\uparrow\uparrow} B_{\uparrow n'} + M^2_{\uparrow\uparrow} B_{\downarrow n'}) + 2B^\dagger_{n\downarrow}(M^3_{\uparrow\uparrow} B_{\uparrow n'} + M^4_{\downarrow\uparrow} B_{\downarrow n'}) \tag{31}$$

$$d_n = a^0_n + B^\dagger_{n\uparrow}(M^1_{\uparrow\uparrow} a^1_\uparrow + M^2_{\uparrow\uparrow} a^2_\uparrow) + B^\dagger_{n\downarrow}(M^3_{\uparrow\uparrow} a^1_\uparrow + M^4_{\downarrow\uparrow} a^2_\uparrow) \tag{32}$$

The various quantities introduced in the preceding formal solution can be given a more or less direct interpretation. When S_1 and S_2 are planar the reflection operators R^1 and R^2 are nothing but the ordinary reflection matrices for reflection of a plane wave by an infinite plane times a two-dimensional delta function which is just an expression of Snell's law. The operators M^l, $l = 1, 2, 3, 4$, contain the same delta function times a matrix that describes the multiple reflections between the surfaces S_1 and S_2 of the plate. The last term in the direct field in (21), for instance, is thus the contribution that has been multiply reflected in the plate with the first reflection by the bottom surface and the last by the top surface. The terms in the anomalous field in (22) can be similarly interpreted and the last term there is the contribution last scattered by the cavity. The transition matrix $T^0_{nn'}$ for the cavity describes the scattering by the cavity, referred to the spherical waves, as if no other scattering surfaces were present. The multiple scattering between the cavity and the plate surfaces are described by equation (30), where the reflection matrix $R_{nn'}$ includes the effect of both plate surfaces referred to spherical waves by the transformation functions B and $B^\dagger$. The quantity d_n in (30) stems from the incoming field and includes a direct term (the first term) and terms that have been multiply reflected by the plate surfaces and transformed to spherical waves.

It should be noted that (30) has been obtained from (13)–(15) by eliminating $\alpha^1_\uparrow$ and $\alpha^2_\uparrow$ and getting an equation for α^0_n. Other orders of elimination would lead to an equation for $\alpha^1_\uparrow$ or $\alpha^2_\uparrow$, but the chosen order is strongly preferred as $\alpha^1_\uparrow$ and $\alpha^2_\uparrow$ depend on continuous variables and thus give integral equations as opposed to the algebraic equation (30).

When written in full, the various quantities of the formal solution give rise to very lengthy expressions. Except for the expansion coefficients of the incident field (and R^2, which is almost identical to R^1) these expressions are the same as those of reference [11] and are therefore not reproduced here. We will comment further on the computation of $\mathbf{u}^{dir}$ and d_n in the next section. For the other quantities we just remark that all double integrals inherent in the repeated arrows (many quantities thus contain quadruple integrals) reduce so that any given quantity contains at most one single integral.

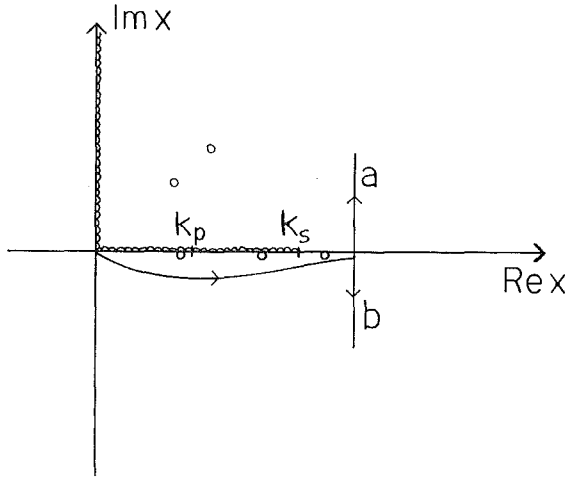


Fig. 2 Integration contours for the direct field (○ = poles, ≈ = cuts)

3 The Source

We now consider the incoming field and its source in greater detail. The source is chosen as a point force with Gaussian time dependence which acts normally on the upper surface of the plate. This source is chosen for its simplicity and because it resembles the sources usually used in nondestructive evaluation, which are, however, or greater spatial extent and are not always normally directed.

In the time domain the force is

$$\mathbf{F}(t) = -\hat{z} F_0 \delta(\mathbf{r} - \mathbf{r}_t) e^{-(t/T)^2} \tag{33}$$

where F_0 is the strength and T the pulse width. We put $\mathbf{r}_t = (x_t, 0, z_1)$ with $x_t < 0$, i.e., we locate the source on the surface S_1 and without loss of generality we place it at the negative x axis. In the frequency domain the field from the point force is easily obtained from the free space Green's dyadic [16]

$$\mathbf{u}^{inc}(\mathbf{r}) = -F_0 T k_s / (2\sqrt{\pi}\mu)\, \hat{z} \cdot \tilde{G}(\mathbf{r}, \mathbf{r}_t) e^{-\omega^2 T^2/4} \tag{34}$$

The expansion coefficients of the incoming field in plane and spherical vector waves are obtained from the corresponding expansions of the Green's dyadic (expansions similar to (4) and (5)) and we thus have

$$a^1_\uparrow = -iF_0 T k_s / (\sqrt{\pi}\mu)\, \hat{z} \cdot \phi^\dagger_\uparrow(\mathbf{r}_t) e^{-\omega^2 T^2/4} \tag{35}$$

$$a^2_\uparrow = -iF_0 T k_s / (\sqrt{\pi}\mu)\, \hat{z} \cdot \phi^\dagger_\downarrow(\mathbf{r}_t) e^{-\omega^2 T^2/4} \tag{36}$$

$$a^0_n = -iF_0 T k_s / (2\sqrt{\pi}\mu)\, \hat{z} \cdot \psi_n(\mathbf{r}_t) e^{-\omega^2 T^2/4} \tag{37}$$

When (35)–(37) are inserted into the direct field in (21) and d_n in (32) and the formal expressions are written in detail, integrals very similar to those of [11] are obtained. The integration variable is of Fourier-Hankel type and the integrands contain a Bessel function, reflection coefficients, and plane waves.

When both the source and the receiver are located on the surface S_1 the integrals in the direct field are of Sommerfeld type and they are thus very slowly converging. In reference [11] this problem was avoided by analytically extracting and integrating the slowly converging parts, but in the present case the same procedure gives remaining integrals that are not sufficiently fast converging for efficient numerical computation. The problem could be avoided by taking more terms in the analytical extraction and integration, but that procedure would be extremely cumbersome. Instead we have split the slowly convergent integral into two rapidly convergent integrals. The Bessel function in the Sommerfeld

Downloaded 02 May 2010 to 171.66.16.54. Redistribution subject to ASME license or copyright; see http://www.asme.org/terms/Terms_Use.cfm

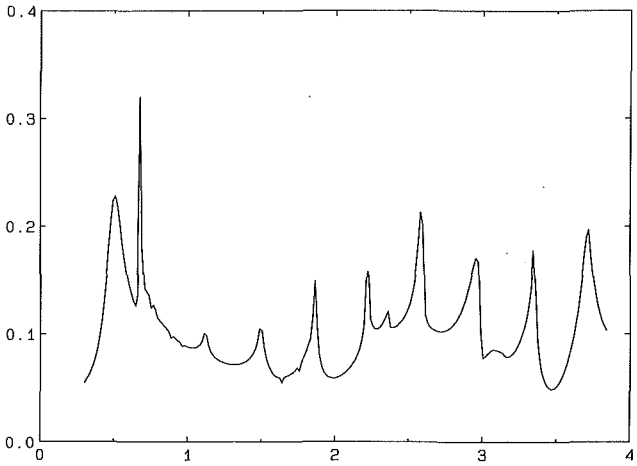


Fig. 3 Absolute value of total normal displacement as a function of $k_p b$ at $x = 0$ on the lower surface of a plate with a spherical cavity and source location $x_t = 0$

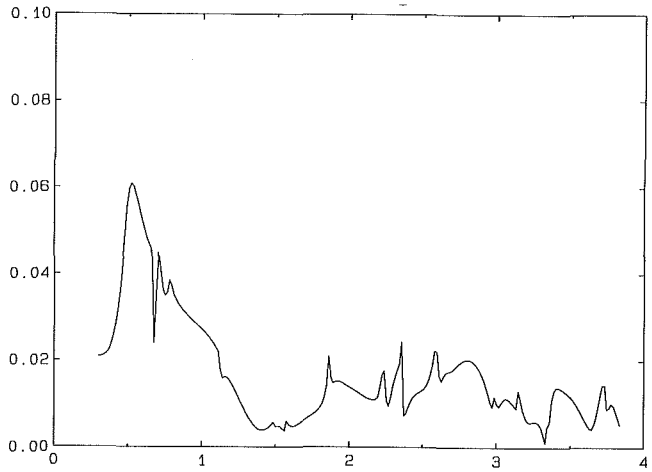


Fig. 4 Absolute value of total normal displacement as a function of $k_p b$ at $x = 0$ on the lower surface of a plate with a spherical cavity and source location $x_t = -8b$

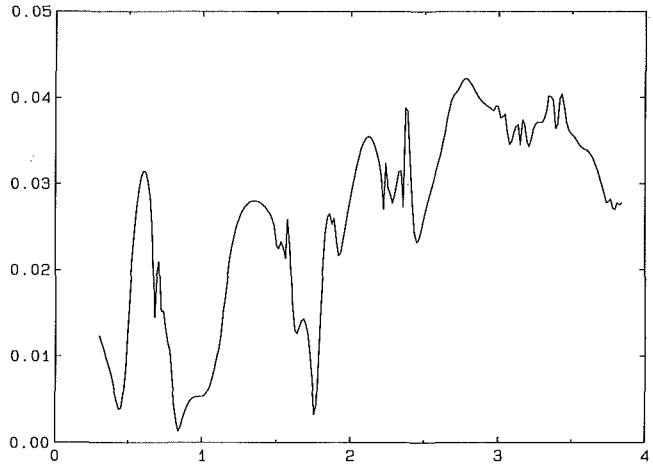


Fig. 5 Absolute value of normal displacement as a function of $k_p b$ at $x = 20b$ on the upper surface of a plate with a spheroidal cavity and source location $x_t = 0$

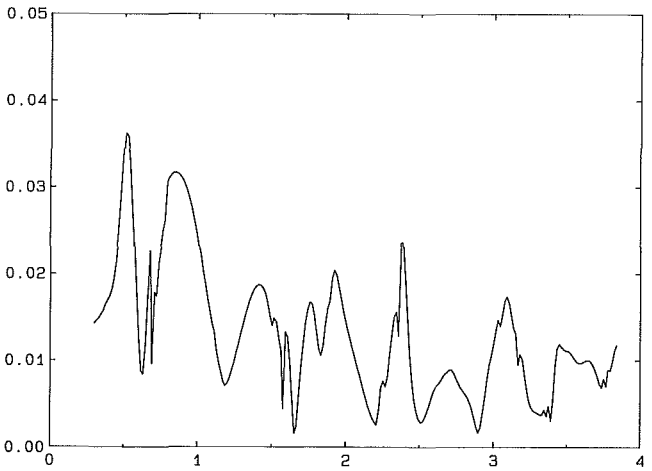


Fig. 6 Same as Fig. 5 but on the lower surface

integral is rewritten as a sum of Hankel functions $H_m^{(1)} + H_m^{(2)}$, where $H_m^{(1)}$ is exponentially decreasing in the upper half plane and $H_m^{(2)}$ in the lower. The original integral over the interval $(0, \infty)$ in the Fourier-Hankel variable x can then be split and deformed so that the part containing $H_m^{(1)}$ ($H_m^{(2)}$) is integrated along contour (*a*) (contour (*b*)) in Fig. 2. One has to be careful so that the part of contour (*a*) in the first quadrant lies to the right of all poles of the integrand. With this procedure the direct field can be computed numerically with reasonable accuracy and speed, at least for receiver locations $0 \le k_p \rho_t \le 200$, where ρ_t is the distance from the source. An alternative approach would be to write the direct field as a sum of Rayleigh-Lamb modes, cf. Karlsson [12] and Weaver and Pao [17], and this should be useful at all locations except close to the source.

Once the field in the frequency domain is computed the time-domain solution is obtained by a Fourier integration. In the numerical examples in the next section we will give the velocity field rather than the displacement field and for the velocity we have

$$\mathbf{v}(t) = 2\int_0^\infty \omega\{Re\mathbf{u}(\omega)\sin\omega t - Im\mathbf{u}(\omega)\cos\omega t\}\, d\omega \qquad (38)$$

where we have exploited the fact that $\mathbf{v}$ should be real.

4 Numerical Results

We turn to some numerical applications of the foregoing. The geometry is then further restricted by assuming the cavity to be rotationally symmetric around the z axis (the resulting simplifications are described in [11]). In the numerical examples the cavity is a sphere with radius b or an oblate spheroid with major axis b and minor axis $a = b/2$ (along the z direction). All other lengths are measured relative b. The thickness of the plate is $4b$ with the cavity symmetrically situated. We consider the two locations $x_t = 0$ and $x_t = -8b$ of the point force. The ratio between the wave speeds in the plate is $c_p/c_s = 2.11$ (corresponding to aluminum).

In the frequency domain we compute the z component (i.e., the normal component) of the displacement field on the surfaces of the plate. The field is computed at four points along the positive x axis starting at $x = 0$, i.e., immediately above or below the cavity, with a distance $10b$ between the points. The amplitude in the figures to follow is arbitrary but the same in all the figures. The weight factor $\exp(-\omega^2 T^2/4)$ from the source is naturally not included in the frequency domain computations.

The null field approach is essentially a low and intermediate frequency method so we restrict the frequency range to $0 < k_p b < 3.84$ (by an increased computer effort it should be possible to at least double this range). We compute the field at 256 frequency points equally spaced in the interval and the frequency step is thus 0.015. With this frequency interval the truncations can be limited to $l_{\max} = 14$ and $m_{\max} = 8$ (cf. [11]) meaning that the biggest matrix that needs to be inverted is of size 42×42 ($42 = 3 \times 14$). The computer cost to run the

Downloaded 02 May 2010 to 171.66.16.54. Redistribution subject to ASME license or copyright; see http://www.asme.org/terms/Terms_Use.cfm

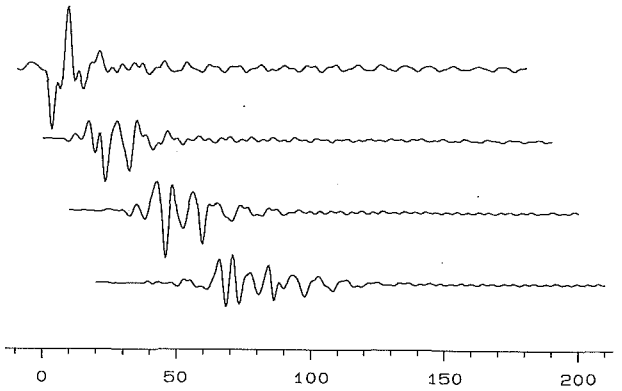


Fig. 7 Normal velocities as a function of $c_p t/b$ on the lower surface of a plate without any cavity and source location $x_t = 0$

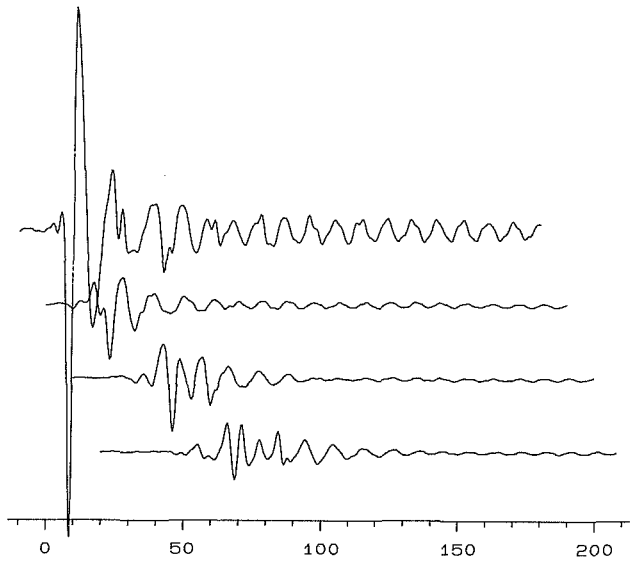


Fig. 8 Total normal velocities as a function of $c_p t/b$ on the lower surface of a plate with a spherical cavity and source location $x_t = 0$

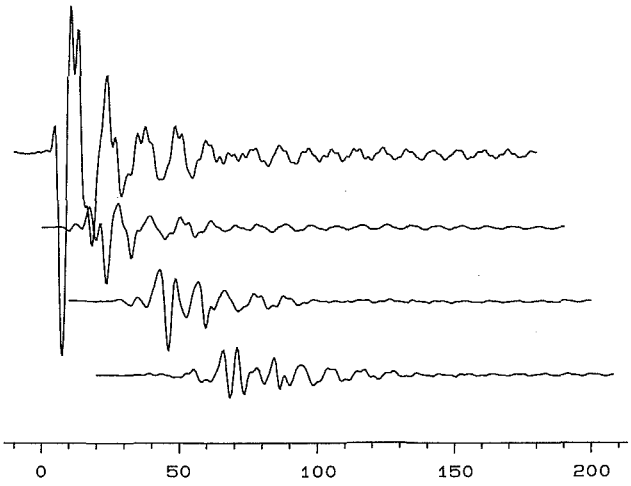


Fig. 9 Total normal velocities as a function of $c_p t/b$ on the lower surface of a plate with a spheroidal cavity and source location $x_t = 0$

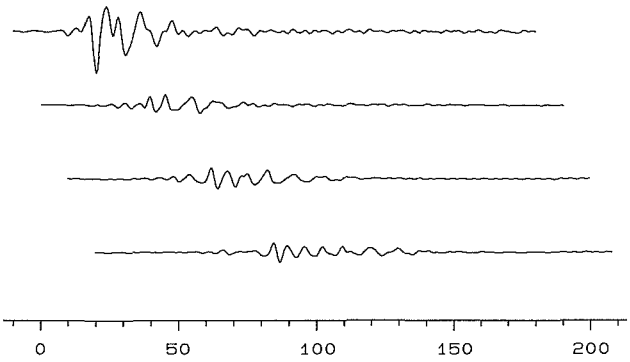


Fig. 10 Anomalous normal velocities as a function of $c_p t/b$ on the lower surface of a plate with a spherical cavity and source location $x_t = -8b$

program is considerable; to complete one run of 256 frequency points takes about 50 cpu-hours on a superminicomputer (a SEL 8780).

To check our computations as far as possible we have employed several different tests. Two good tests on the anomalous field (but not on the direct field) is reciprocity and the translated-sphere-test. Reciprocity says that if we interchange the location of the source and the receiver, the z components of the fields should be the same in the two cases. This check is satisfied with an error of less than 1 percent. A very good test is to make computations for a spherical cavity with the natural origin at the center of the sphere and compare the results with the case when the origin is translated 20 percent of the sphere radius. Although the elements of T^0, $R_{nn'}$, and d_n change considerably the fields change less than 1 percent. A good test in the time domain is causality and as will be seen later, this is mostly well satisfied. For the direct field it seems natural to try to compare to results in the literature. This has, however, not been possible because cases considered in the literature, e.g., in [17], all seems to treat a force with a time dependence in form of a unit step and our results are for a force with a rather slow time dependence (and thus a limited frequency content).

Of the numerical results we first consider the case with a spherical cavity with the point force placed immediately above the cavity at $x_t = 0$. The absolute value of the total field on the lower surface just below the cavity is shown in Fig. 3. The very periodic and pronounced peaks appearing in the figure correspond to the cutoff of the Rayleigh-Lamb modes in the plate that occur at $k_p b = 0.372\ m$ and $k_p b = 0.785\ n$ (for a plate of thickness $4b$; m and n are integers). We note that the field should actually be singular at the cutoffs.

In Fig. 4 the point force is moved to $x_t = -8b$ (two plate thicknesses away from the cavity) but the configuration is otherwise unchanged. The dependence on frequency is more varied but there are still narrow peaks at many of the cutoffs of the Rayleigh-Lamb modes. Further away from the force the frequency dependence is more irregular as seen in Figs. 5 and 6. These figures show the total field on the upper and lower plate surfaces, respectively, at a distance $20b$ (five plate thicknesses) from a force placed right above the spheriodal cavity. Comparing Figs. 5 and 6, we observe a tendency at higher frequencies for the field to be larger at the upper than at the lower surface. The probable reason for this is that at higher frequencies the force excites a rather dominating Rayleigh wave on the upper but not on the lower surface.

In the time domain we compute the normal velocity field due to the point force with Gaussian time dependence (treated in Section 3). The direct, anomalous, or total field at four points ($x = 0, 10b, 20b, 30b$) of increasing distance from the cavity are grouped together to form a "synthetic seismogram." The reason for computing the velocity field rather than the displacement field is that this suppresses the low frequencies that might otherwise be troublesome (the field at the lowest frequencies are not given in Figs. 3–6 due to possible inaccuracies as $\omega \to 0$). Due to the Gaussian time dependence of the force (note that one may equally well regard the weight factor $\exp(-\omega^2 T^2/4)$ as a filter on the

Downloaded 02 May 2010 to 171.66.16.54. Redistribution subject to ASME license or copyright; see http://www.asme.org/terms/Terms_Use.cfm

receiver with a sudden point force) we have a natural high-frequency cutoff and if we choose the pulse width T so that $c_p T/b = 1.6$ the frequency range can be restricted to $0 < \omega b/c_p < 3.84$. When computing the frequency integral in (38) we have used the simplest possible integration scheme, i.e., the trapezoidal rule (cf. [11] for comments on this; as we have no FFT algorithm implemented on our computer we have used a straightforward integration—the extra cost is immaterial since the time spent in the frequency integration is about 1 percent of the total computing time).

As the frequency integral is effectively computed as a Fourier series with fundamental frequency 0.015, the result of the integration is periodic with period T_0 where $c_p T_0/b = 2\pi/0.015 \simeq 419$. If the duration of the field at any point is longer than T_0—and this happens at least far away from the point force—then this field will be poorly represented by the Fourier series. Another problem with the frequency integral is the singularities of the frequency domain field at the cutoffs of the Rayleigh-Lamb modes. These should be integrable but the trapezoidal rule is certainly not well suited to treat singularities (the problem could be better handled by a variable step size in frequency or more easily by introducing losses in the plate material). To check the time-domain results we have used causality and we have compared the results from using 128 and 256 integration points. As seen in the following, in the time-domain results, causality is mostly rather well satisfied, even though some small noise is observed in several of the curves before the first arrival. It is hard, however, to tell whether the observed noncausalities are due to the frequency domain singularities or to an insufficient period in time. If the results from using 128 and 256 integration points are compared, only small changes are observed especially at later times. The noncausalities are also somewhat worse in the case with 128 points. These results are expected as the time period associated with 128 points is half of that for 256 points and is therefore insufficient for representing the fields at many points. In conclusion, we believe that our time-domain results are of a reasonable quality. The only remaining uncertainty of any importance is the "ringing" observed in many of the figures below (with an amplitude that is slowly decreasing with time) that may at least partly be due to inaccurately integrated singularities.

Figures 7 and 8 show the direct and total fields, respectively, on the lower plate surface for the case of a spherical cavity with a point force right above the cavity at $x_t = 0$. Figure 3 and the first curve in Fig. 8 are thus corresponding frequency and time domain results. At the point immediately below the cavity (the first curve in the figures) we note that the direct field is much smaller than the total (or anomalous) field and that there is a tremendous first arrival in the total field. We think that this is a focusing effect as all the rays from the source to the receiver touching the cavity travels the same distance. In both the direct and total field there is a clear ringing and we observe that away from the source and cavity the ringing in the total field has a lower frequency than in the direct field. If the ringing was due to inaccuracies in the integration of a singularity it seems improbable that the ringings in the direct and total field should so clearly be dominated by a single frequency that is different in the two cases.

When the cavity is an oblate spheroid instead of a sphere, but the configuration is otherwise unchanged, the field pattern is quite similar as seen from Fig. 9, which shows the total field on the lower surface (the direct field is of course the same as before, i.e., as given in Fig. 7).

If the source is moved away from the vicinity of the cavity the anomalous field becomes smaller. An example is given in Fig. 10, which shows the anomalous field on the lower plate surface when the source is moved to $x_t = -8b$ but the configuration is otherwise the same as in Figs. 7 and 8.

Acknowledgment

The present work is supported by the National Swedish Board for Technical Development (STU) and this is gratefully acknowledged.

References

1 Achenbach, J. D., and Brind, R. J., "Scattering of Surface Waves by a Subsurface Crack," *Journal of Sound and Vibration*, Vol. 76, 1981, pp. 43–56.

2 Brind, R. J., and Achenbach, J. D., "Scattering of Longitudinal and Transverse Waves by a Subsurface Crack," *Journal of Sound and Vibration*, Vol. 78, 1981, pp. 555–563.

3 Datta, S. K., and El-Akily, N., "Diffraction of Elastic Waves by Cylindrical Cavity in a Half-Space," *Journal of the Acoustical Society of America*, Vol. 64, 1978, pp. 1692–1699.

4 Höllinger, F., and Ziegler, F., "Scattering of Pulsed Rayleigh Surface Waves by a Cylindrical Cavity," *Wave Motion*, Vol. 1, 1979, pp. 225–238.

5 van der Hijden, J. H . M. T., "Diffraction of Elastic Waves by a Cylindrical Crack in a Semi-Infinite Solid (Inplane Motion)," Report 1981–11, Lab. Electromagnetic Res., Dept. Elec. Eng., Delft University of Technology, 1981.

6 Mendelsohn, D. A., Achenbach, J. D., and Keer, L. M., "Scattering of Elastic Waves by a Surface-Breaking Crack," *Wave Motion*, Vol. 2, 1980, pp. 277–292.

7 Datta, S. K., "Diffraction of *SH*-Waves by an Edge Crack," ASME JOURNAL OF APPLIED MECHANICS, Vol. 46, 1979, pp. 101–106.

8 Chen, E. P., "Impact Response of a Finite Crack in a Finite Strip Under Antiplane Shear," *Engineering Fracture Mechanics*, Vol. 9, 1977, pp. 719–724.

9 Chen, E. P., "Sudden Appearance of a Crack in a Stretched Finite Strip," ASME JOURNAL OF APPLIED MECHANICS, Vol. 45, 1978, pp. 277–280.

10 Itou, S., "Transient Response of a Finite Crack in a Strip With Stress-Free Edges," ASME JOURNAL OF APPLIED MECHANICS, Vol. 47, 1980, pp. 801–805.

11 Boström, A., and Karlsson, A., "Exact Synthetic Seismograms for an Inhomogeneity in a Layered Elastic Half Space," *Geophysical Journal of the Royal Astronomical Society*, Vol. 79, 1984, pp. 835–862.

12 Karlsson, A., "Scattering of Rayleigh-Lamb Waves From Cavities in an Elastic Plate," *Wave Motion*, Vol. 6, 1984, pp. 205–222.

13 Boström, A., and Kristensson, G., "Scattering of a Pulsed Rayleigh Wave by a Spherical Cavity in an Elastic Half Space," *Wave Motion*, Vol. 5, 1983, pp. 137–143.

14 Burden, A. D., "The Propagation of Elastic Surface Waves Along Cylindrical Cavities of General Cross Section," *Wave Motion*, Vol. 7, 1985, pp. 153–168.

15 Boström, A., "Scattering of Acoustic Waves by a Layered Elastic Obstacle in a Fluid—An Improved Null Field Approach," *Journal of the Acoustical Society of America*, Vol. 76, 1984, pp. 588–593.

16 Boström, A., and Burden, A., "Propagation of Elastic Surface Waves Along a Cylindrical Cavity and Their Excitation by a Point Force," *Journal of the Acoustical Society of America*, Vol. 72, 1982, pp. 998–1004.

17 Weaver, R. L., and Pao, Y.-H., "Axisymmetric Elastic Waves Excited by a Point Source in a Plate," ASME JOURNAL OF APPLIED MECHANICS, Vol. 49, 1982, pp. 821–836.

18 Aki, K., and Richards, P. G., *Quantitative Seismology*, Vols. 1 and 2, Freeman and Co., San Francisco, 1980.

Downloaded 02 May 2010 to 171.66.16.54. Redistribution subject to ASME license or copyright; see http://www.asme.org/terms/Terms_Use.cfm

Singular Value Decomposition for Constrained Dynamical Systems

R. P. Singh
Senior Staff Engineer,
Honeywell Inc.,
Clearwater, Fla. 33546

P. W. Likins
President,
Lehigh University,
Bethlehem, Pa. 18015

The method of singular value decomposition is shown to have useful application to the problem of reducing the equations of motion for a class of constrained dynamical systems to their minimum dimension. This method is shown to be superior to classical Gaussian elimination for several reasons: (i) The resulting equations of motion are assured to be of full rank. (ii) The process is more amenable to automation, as may be appropriate in the development of a computer program for application to a generic class of systems. (iii) The analyst is spared the responsibility for the selection of specific coordinates to be eliminated by substitution in each individual case, a selection that has no physical justification but presents abundant risk of mathematical contradiction. This approach is shown to be very efficient when the governing dynamical equations are derived via Kane's method.

Introduction

Dynamical systems of current interest are often extremely complex assemblies of rigid and flexible bodies subjected to kinematical constraints. Spacecraft provided early examples of this class of problem, and increasingly important illustrations may be found in the field of robotics, large space structures, and automatically controlled machinery. The analysis of biomechanical systems introduces a new category of problems in this class. These practical problems have in common the requirement that the analyst have the capacity to formulate equations of motion with appropriate constraint equations and solve them numerically, preferably with computer programs devised for generic classes of problems.

In operational terms, the problem of interest here is to formulate equations of dynamics and constraints in terms amenable to automatic and efficient numerical solution, without requiring the user of the computer program any extraordinary ingenuity or special insight into the inner workings of the program.

Perhaps the most satisfactory approach to the formulation of equations of motion of complex and highly constrained mechanical systems is that proposed by Kane [1–5]. However, this approach as originally presented requires the selection of a subset of the generalized velocities for elimination by substitution into kinematical equations used in the derivation of the equations of motion [1]. This selection cannot be made arbitrarily without encountering mathematical singularities. Also, systems undergoing large motion may present problems of inconsistency in the constraints such as three-dimensional loops during the system motion becoming two-dimensional or one-dimensional loops. If this approach to the formulation of a system of dynamical equations of minimum dimension is to be applied extensively to very complex systems, one must find a more systematic method for the transformation and reduction of the set. The purpose of this paper is to demonstrate that the method of singular value decomposition (SVD) [6, 7] meets all requirements.

Although the class of orthogonal decompositions known as singular value decomposition (SVD) has a long history of application to problems of observation and data reduction, and a more recent exposure in the field of multivariable control theory, there seem to be thus far very few, if any, applications in mechanics.

Dynamical Systems With Constraints

The method developed in this paper is applicable to the class of dynamical systems characterized by

$$M\ddot{q}=F(\dot{q},q,t) \tag{1}$$

subjected to kinematical constraints of the form

$$A\dot{q}=B \tag{2}$$

where q, a set of generalized coordinates, is of dimension $\nu\times 1$, M is square, and A is of dimension $m\times\nu$ for $m<\nu$. The time derivatives of the kinematic variables in q are the generalized velocities (in the Lagrangian vernacular). Of course the equations of motion for all mechanical systems can be written as equation (1). Holonomic constraints can always be written in the form of equation (2) although they often appear as written after integration; nonholonomic constraints in the class called Pfaffian or simple also take the form of equation (2).

Basically there are two conceptual approaches to solving the equations of motion of such systems. (*a*) One can introduce unknown forces or torques at the interfaces between constrained bodies (often accomplishing this symbolically with Lagrange multipliers), and then solve the dynamical equations simultaneously with the constraint equations to

Contributed by the Applied Mechanics Division for publication in the JOURNAL OF APPLIED MECHANICS.

Discussion on this paper should be addressed to the Editorial Department, ASME, United Engineering Center, 345 East 47th Street, New York, N.Y. 10017, and will be accepted until two months after final publication of the paper itself in the JOURNAL OF APPLIED MECHANICS. Manuscript received by ASME Applied Mechanics Division, February, 1984.

Copyright © 1985 by ASME
Downloaded 02 May 2010 to 171.66.16.54. Redistribution subject to ASME license or copyright; see http://www.asme.org/terms/Terms_Use.cfm

determine the constraint forces and torques as well as the kinematical variables. (*b*) Alternatively, one can use the constraint equations to reduce the dimension of the system of dynamical equations to be solved, eliminating the need to represent or solve for constraint forces or torques. This paper is concerned with the second approach to the problem, which offers the advantage of providing for solution a set of equations of minimum dimension. Only if constraint forces and torques are of explicit interest does the first approach seem appropriate. The difficulty with the second approach lies in the implementation.

In the special case of holonomic constraints, one might integrate equation (2) and solve explicitly for a subset of m of the kinematical variables in q in terms of those remaining. This might be a difficult task in general, although simple in special cases, as when $m=1$. This substitution makes m of the ν second-order equations in equation (1) redundant, and permits reduction of the set of equations to be solved to its minimum dimension, which is $\nu-m$ second-order equations. Of course this is a very special case, and generally the reduction is not so easily accomplished.

If equation (2) is nonintegrable (as for nonholonomic constraints), one cannot solve for m of the variables in q in terms of those remaining to effect the reduction through direct substitution into equation (1). One might hope to solve for a subset of m of the generalized velocities in $\dot{q}$ in terms of the other generalized velocities and the full set of generalized coordinates in q, but the result could not be substituted effectively in the second-order equations represented by equation (1). However, this obstacle can be circumvented by the conversion of equation (1) to first-order form, and this approach is particularly effective if instead of equation (1) one adopts the equivalent first-order form introduced by Kane [1]. This method will be described here in some detail to establish a standard against which the SVD approach can be compared.

Kane's Approach. Kane's formulation is expressed in terms of generalized speeds (often called derivatives of quasicoordinates) $\bar{u}_k$ defined by the nonsingular relationship

$$\bar{u}_k = \sum_{s=1}^{n} \bar{W}_{sk}\dot{\bar{q}}_s + \bar{w}_K \quad k=1, \ldots, n \tag{3}$$

where $n=\nu-m$ is the number of independent generalized velocities, reduced in number by the m constraint equations, $\bar{W}_{sk}$ and $\bar{w}_k$ are functions of q's and t and are chosen in such a way that equation (3) can be solved uniquely for $\dot{\bar{q}}_1, \ldots, \dot{\bar{q}}_n$ which comprise a subset of the generalized velocities in $\dot{q}$. In matrix terms equation (3) becomes

$$\bar{u} = \bar{W}^T\dot{\bar{q}} + \bar{w} \tag{4}$$

where $\bar{W}^T$ is the transpose of a nonsingular $n\times n$ matrix, $\dot{\bar{q}}$ is the $n\times 1$ matrix obtained by truncating the original $\nu\times 1$ matrix $\dot{q}$, and $\bar{w}$ is also of dimension $n\times 1$. In application, $\bar{W}$ may be the unit matrix, but in many problems of rotational dynamics the elements of $\bar{u}$ include the scalar components of angular velocities.

The incorporation of generalized speeds and their first derivatives into the dynamical equations is accomplished by reference to the kinematic expressions for velocities of material points, as illustrated for a system of N particles by

$$\dot{\mathbf{R}}^j = \sum_{k=1}^{n} \bar{\mathbf{V}}_k^j\bar{u}_k + \bar{\mathbf{V}}_t^j \quad j=1, \ldots, N \tag{5}$$

where boldface represents a vector, $\mathbf{R}^j$ is the inertial position vector of the jth particle, $\dot{\mathbf{R}}^j$ is the inertial velocity of the jth particle, and $\bar{\mathbf{V}}_k^j$ and $\bar{\mathbf{V}}_t^j$ are functions of q's and t. (More general expressions for continua may be found in [2].) To derive this expression in any specific applications, one must eliminate m of the generalized velocities in terms of the remaining $n(=\nu-m)$, using the constraints in equation (2). To obtain equation (5), one proceeds by expressing $\mathbf{R}^j$ as

$$\dot{\mathbf{R}}^j = \sum_{k=1}^{\nu} \frac{\partial \mathbf{R}^j}{\partial q_k}\dot{q}_k + \frac{\partial \mathbf{R}^j}{\partial t}$$

Employing the identity

$$\frac{\partial \mathbf{R}^j}{\partial q_k} = \frac{\partial \dot{\mathbf{R}}^j}{\partial \dot{q}_k}$$

one can then write

$$\dot{\mathbf{R}}^j = \sum_{k=1}^{\nu} \frac{\partial \dot{\mathbf{R}}^j}{\partial \dot{q}_k}\dot{q}_k + \frac{\partial \mathbf{R}^j}{\partial t} \tag{6a}$$

or

$$\dot{\mathbf{R}}^j = \sum_{k=1}^{m} \frac{\partial \dot{\mathbf{R}}^j}{\partial \dot{q}_k}\dot{q}_k + \sum_{k=m+1}^{\nu} \frac{\partial \dot{\mathbf{R}}^j}{\partial \dot{q}_k}\dot{q}_k + \frac{\partial \mathbf{R}^j}{\partial t} \tag{6b}$$

In the matrix form equation (6) can be written as

$$\dot{\mathbf{R}}^j = \left[\frac{\partial \dot{\mathbf{R}}^j}{\partial \dot{\bar{q}}}\right]\dot{\bar{q}} + \left[\frac{\partial \dot{\mathbf{R}}^j}{\partial \dot{q}^c}\right]\dot{q}^c + \frac{\partial \mathbf{R}^j}{\partial t} \tag{7}$$

where $\dot{\bar{q}}$ is an $n\times 1$ matrix and $\dot{q}^c$ is of dimension $m\times 1$. To eliminate $\dot{q}^c$ one must expand equation (2) as

$$[A^{mn}\,|\,A^{mm}]\begin{bmatrix}\dot{\bar{q}}\\ \dot{q}^c\end{bmatrix} = [B] \tag{8}$$

where the superscripts on A designate the number of rows and columns, respectively. The constrained generalized velocities $\dot{q}^c$ may be expressed as

$$\dot{q}^c = [A^{mm}]^{-1}([B] - [A^{mn}]\dot{\bar{q}}) \tag{9}$$

Assuming matrix A in equation (2) is of rank m (number of independent rows), it is always theoretically possible to partition $\dot{q}$ so that the last m columns of A are independent as shown in equation (9) and $[A^{mm}]^{-1}$ exists. In practice this may be difficult and this is especially the case if our objective is to devise a general purpose computer program without either burdening the user to partition A or employing a time-consuming numerical Gaussian elimination algorithm to search for m linearly independent columns. Moreover, for many dynamical systems of changing configuration the rank of A may fall below m for certain attainable states during the system motion, resulting in singularities occurring in the numerical generation and solution of the equations.

Combining equations (7) and (9) one obtains

$$\dot{\mathbf{R}}^j = \left(\left[\frac{\partial \dot{\mathbf{R}}^j}{\partial \dot{\bar{q}}}\right] - \left[\frac{\partial \dot{\mathbf{R}}^j}{\partial \dot{q}^c}\right][A^{mm}]^{-1}[A^{mn}]\right)\dot{\bar{q}} + \frac{\partial \mathbf{R}^j}{\partial t} + \left[\frac{\partial \dot{\mathbf{R}}^j}{\partial \dot{q}^c}\right][A^{mm}]^{-1}[B] \tag{10}$$

From equation (4)

$$\dot{\bar{q}} = [\bar{W}^T]^{-1}\bar{u} - [\bar{W}^T]^{-1}\bar{w} \tag{11}$$

and substituting for $\dot{\bar{q}}$ in equation (10) gives

$$\dot{\mathbf{R}}^j = \left(\left[\left[\frac{\partial \dot{\mathbf{R}}^j}{\partial \dot{\bar{q}}}\right] - \left[\frac{\partial \dot{\mathbf{R}}^j}{\partial \dot{q}^c}\right][A^{mm}]^{-1}[A^{mn}]\right][\bar{W}^T]^{-1}\right)\bar{u} - \left[\left[\frac{\partial \dot{\mathbf{R}}^j}{\partial \dot{\bar{q}}}\right] - \left[\frac{\partial \dot{\mathbf{R}}^j}{\partial \dot{q}^c}\right][A^{mm}]^{-1}[A^{mn}]\right][W^T]^{-1}\bar{w} + \frac{\partial \mathbf{R}^j}{\partial t} + \left[\frac{\partial \dot{\mathbf{R}}^j}{\partial \dot{q}^c}\right][A^{mm}]^{-1}[B] \tag{12}$$

In the preceding equation the coefficients of $\bar{u}$ represent $\bar{\mathbf{V}}_k^j$ in equation (5) and the remaining terms are $\bar{\mathbf{V}}_t^j$.

Downloaded 02 May 2010 to 171.66.16.54. Redistribution subject to ASME license or copyright; see http://www.asme.org/terms/Terms_Use.cfm

The vectors $\bar{\mathbf{V}}_k^j$ are used to generate dynamical equations from Newton's law, as illustrated for particles by the result

$$\bar{f}+\bar{f}^*=0 \tag{13}$$

where the elements of the $n\times 1$ matrices $\bar{f}_k$ and $\bar{f}_k^*$ are defined by

$$\bar{f}_k=\sum_{j=1}^{n}\mathbf{F}^j\cdot\bar{\mathbf{V}}_k^j \quad k=1,\ldots,n \tag{14}$$

and

$$\bar{f}_k^*=-\sum_{j=1}^{n}m_j\ddot{\mathbf{R}}^j\cdot\bar{\mathbf{V}}_k^j \quad k=1,\ldots,n \tag{15}$$

where $\mathbf{F}^j$ is the force on the jth particle obtained by summing all the forces, m_j is the mass and $\ddot{\mathbf{R}}^j$ is the inertial acceleration of the jth particle.

The key to utility in Kane's dynamical equations, equation (13), is the automatic elimination from $\bar{f}_k$ of any nonworking constraint forces found in $\mathbf{F}^j$, so that such forces need not be represented at all. Thus equations (13), (4), and (2) comprise $2n+m = n+\nu$ first-order equations in the $n+\nu$ variables $q_1,\ldots,q_\nu,\ u_1,\ldots,u_n$. The principal obstacle to the successful application of this formulation is the difficulty of implementing equation (9). In what follows this difficulty will be circumvented.

Singular Value Decomposition

Orthogonal decomposition of an $m\times\nu$ matrix L by singular value decomposition is closely related to the eigenvalue-eigenvector decomposition of the symmetric positive semidefinite matrices L^TL and LL^T. Let $r\le m$ be the rank of L. Then there are orthogonal matrices U and V of order $m\times m$ and $\nu\times\nu$, respectively, such that [6, 7]

$$U^TLV=\begin{bmatrix}\Sigma & 0\\ 0 & 0\end{bmatrix}=S \tag{16}$$

where $\Sigma=\text{diag}\,(\lambda_1,\lambda_2,\ldots,\lambda_r)$ and $\lambda_1\ge\lambda_2\ge\ldots\ge\lambda_r>0$.

The diagonal elements of the decomposition are called the singular values of the matrix L. The singular values are unique, although U and V are not [6, 7].

It is easy to verify that

$$V^TL^TLV=\text{diag}\,(\Sigma^2,0) \tag{17}$$

Thus $(\lambda_1^2,\ldots,\lambda_r^2)$ must be the nonzero eigenvalues of L^TL arranged in the descending order and the requirement that λ_i be non-negative completely determines the λ_i. The eigenvectors of L^TL are the columns of V. If L^TL has a multiple eigenvalue $\lambda^2>0$, the corresponding columns of V may be chosen as any orthonormal basis for the space spanned by the eigenvectors corresponding to λ^2.

From equation (16)

$$L=USV^T \tag{18}$$

Now with proper partitioning of U and V equation (18) can be expressed as

$$L=[U_1|U_2]\left[\begin{array}{c|c}\Sigma & 0\\ \hline 0 & 0\end{array}\right]\left[\begin{array}{c}V_1^T\\ \hline V_2^T\end{array}\right]=U_1\Sigma V_1^T \tag{19}$$

From the foregoing one obtains

$$U_1=LV_1\Sigma^{-1} \tag{20}$$

Thus once V_1 is chosen U_1 is obtained by equation (20). The matrices U_2 and V_2 may be any matrices with orthonormal columns spanning the null spaces of L^T and L, respectively. It is worthwhile to mention that the null space of L is the space of all vectors x such that

$$Lx=0 \tag{21}$$

With the orthogonal decomposition given by equation (18), an $\nu\times m$ matrix L^+, called the pseudoinverse of L, is defined by

$$L^+=V\left[\begin{array}{c|c}\Sigma^{-1} & 0\\ \hline 0 & 0\end{array}\right]U^T \tag{22}$$

L^+ is uniquely defined by L; it does not depend on the particular orthogonal decomposition of L [6, 7].

Application of SVD to Dynamical Systems With Constraints SVD for First-Order Equations. To avoid reliance on equation (9) in applying Kane's method to a constrained dynamical system, one must construct the counterparts of equations (3)–(5) and (13)–(15) for the unconstrained dynamical system, ignoring equation (2) in writing

$$u_k=\sum_{s=1}^{\nu}W_{sk}\dot{q}_s+w_k \quad k=1,\ldots,\nu \tag{23}$$

$$u=W^T\dot{q}+w \tag{24}$$

$$\dot{\mathbf{R}}^j=\sum_{k=1}^{\nu}\mathbf{V}_k^ju_k+\mathbf{V}_t^j \tag{25}$$

$$f+f^*=0 \tag{26}$$

$$f_k=\sum_{j=1}^{n}\mathbf{F}^j\cdot\mathbf{V}_k^j \quad k=1,\ldots,\nu \tag{27}$$

$$f_k^*=-\sum_{j=1}^{n}m_j\ddot{\mathbf{R}}^j\cdot\mathbf{V}_k^j \quad k=1,\ldots,\nu \tag{28}$$

Here the matrices u, f, and f^* have dimension $\nu\times 1$, in contrast to the previous $\bar{u}$, $\bar{f}$ and $\bar{f}^*$, which have dimension $n\times 1$, where $n=\nu-m$.

Because the constraint equations have not yet been employed, the associated nonworking constraint forces in $\mathbf{F}^j$ cannot be assured of disappearing from f_k in equation (27).

Note that including equation (2) there are $2\nu+m$ first-order equations, and if the rank of A is m they involve $2\nu+m$ unknowns $q_1,\ldots,q_\nu,\ u_1,\ldots,u_\nu$ and m scalar representations of constraint forces and torques. If the rank r of A is less than m, as may be the case, then both the number of independent constraint equations and the number of unknown scalar representations of constraint forces and torques are in fact r, not m. The objective in this section is to reduce the first-order equations to $2\nu-r$ in number, matching the count in Kane's equations, equations (13), (4), and (2) while avoiding the prospect of singularities found in equation (9).

Inversion of equation (24) provides the ν equations

$$\dot{q}=W^{T-1}u-W^{T-1}w \tag{29}$$

which upon substitution in equation (2) yields

$$[AW^{T-1}]u=B+[AW^{T-1}]w \tag{30}$$

or in simpler notation

$$Cu=D \tag{31}$$

The SVD of the $m\times\nu$ matrix C provides

$$C=USV^T \tag{32}$$

The orthogonal matrices U and V (of dimension $m\times m$ and $\nu\times\nu$, respectively) are partitioned as

$$U=[U_1|U_2] \tag{33}$$

Downloaded 02 May 2010 to 171.66.16.54. Redistribution subject to ASME license or copyright; see http://www.asme.org/terms/Terms_Use.cfm

$$V=[V_1|V_2] \tag{34}$$

where U_1 and V_1 are, respectively, $m\times r$ and $\nu\times r$ matrices; U_2 and V_2 are, respectively $m\times(m-r)$ and $\nu\times(\nu-r)$ matrices. Note that r is the rank of C as well as the rank of A.

Because $CV_2=0$, equation (31) is satisfied by

$$u=C^+D+V_2z \tag{35}$$

for any vector z; C^+ is the pseudoinverse of C. We will refer to z as the reduced vector of $(\nu-r)$ generalized speeds.

In terms of the reduced generalized speed z, $\dot{\mathbf{R}}^j$ in equation (25) becomes

$$\dot{\mathbf{R}}^j=\sum_{p=1}^{\nu-r}\sum_{k=1}^{\nu}\mathbf{V}_k^j V_{2kp}z_p+\xi_t{}^j \tag{36}$$

where ξ_t^j includes $\mathbf{V}_t^j$ and all other terms not involving z_t.

This is equivalent to premultiplying equation (26) by V_2^T, which results in a reduced set of $\nu-r$ equations in generalized speeds $u_1, \ldots, u_\nu$ and their first derivatives in the form

$$V_2{}^Tf+V_2{}^Tf^*=0 \tag{37}$$

or alternatively in the form

$$M'\dot{u}=F'(u,q,t) \tag{38}$$

where M' is $(\nu-r)\times\nu$. Differentiating equation (31) provides

$$\begin{aligned}C\dot{u}&=\dot{D}-\dot{C}u\\&=D'\end{aligned} \tag{39}$$

which upon premultiplication by U_1^T becomes

$$U_1^TC\dot{u}=U_1^TD' \tag{40}$$

Equation (19), with C replacing L, provides after premultiplication by U_1^T,

$$U_1^TC=\Sigma V_1^T \tag{41}$$

Recall that $\Sigma=\text{diag}\,(\lambda_1, \ldots, \lambda_r)$ with nonzero λ_i and the columns of V_1 are orthogonal. Hence equation (40) becomes more simply the r independent equations of constraint

$$\Sigma V_1^T\dot{u}=U_1^TD' \tag{42}$$

Equations (42), (38), and (29) provide $r+(\nu-r)+\nu=2\nu$ first-order equations in the 2ν unknowns $q_1, \ldots, q_\nu, u_1, \ldots, u_\nu$.

Of course interest focuses on the generalized coordinates $q_1, \ldots, q_\nu$ and not on the generalized speeds $u_1, \ldots, u_\nu$. These latter variables can be transformed to the reduced set of $\nu-r$ unknowns in z by use of equation (39), which by virtue of the relationship $CV_2=0$ may be written as

$$\dot{u}=C^+D'+V_2\dot{Z} \tag{43}$$

The combination of equations (43) and (35) permits the substitution of $\dot{z}$ for $\dot{u}$ and z for u among the system unknowns, with corresponding reduction of dimension. Substituting equation (43) into equation (38) provides

$$M'V_2\dot{Z}=F'-M'C^+D' \tag{44}$$

Replacing u in equation (29) by equation (35) provides

$$\dot{q}=W^{T-1}V_2z+W^{T-1}C^+D-W^{T-1}w \tag{45}$$

The combination of equations (44) and (45) is the desired first-order objective, consisting of $2\nu-r$ differential equations in the $2\nu-r$ unknowns $q_1, \ldots, q_\nu, z_1, \ldots, z_{\nu-r}$. The dimension of this system is the same as that obtained by Kane, but the potential singularity problems have been avoided. A possible disadvantage of the present formulation is the abstract character of the unknowns in z, which may have even less physical significance than the generalized speeds in u.

SVD for Second-Order Equations. An appropriate set of second-order differential equations of the system is most readily derived by using the SVD of matrix A in equation (2), the original constraint equation. As previously entertained for matrix C in equation (31), one can write

$$A=USV^T \tag{46}$$

as in equation (32), recognizing that the symbols U, S, and V in equations (46) and (32) have different values in these two equations, but retain the conceptual significance introduced originally in equation (18). Partitioning the new U and V matrices again as in equations (33) and (34), and noting the consequence $AV_2=0$, one can express $\dot{q}$ from equation (2) as

$$\dot{q}=A^+B+V_2\dot{y} \tag{47}$$

where A^+ is the pseudoinverse of A and $\dot{y}$ is an arbitrary $\nu-r$ vector, with r again the rank of A.

Substitution of equation (47) into equation (6*a*) yields

$$\dot{\mathbf{R}}^j=\sum_{p=1}^{\nu-r}\sum_{k=1}^{\nu}\frac{\partial\dot{\mathbf{R}}^j}{\partial\dot{q}_k}V_{2kp}\dot{y}_p+\sum_{s=1}^{m}\sum_{k=1}^{\nu}\frac{\partial\dot{\mathbf{R}}^j}{\partial\dot{q}_k}A_{ks}^+B_s+\frac{\partial\mathbf{R}^j}{\partial t} \tag{48a}$$

or,

$$\dot{\mathbf{R}}^j=\sum_{p=1}^{\nu-r}\mathbf{V}_p^j\dot{y}_p+\xi_t'^j \tag{48b}$$

where

$$\mathbf{V}_p^j=\sum_{k=1}^{\nu}\frac{\partial\dot{\mathbf{R}}^j}{\partial\dot{q}_k}V_{2kp} \tag{49}$$

and $\xi_t'^j$ represents the last two terms in equation (48*a*).

For a system of N particles the generalized active forces are given by

$$f_p=\sum_{j=1}^{N}\mathbf{V}_p^j\cdot\mathbf{F}^j\quad p=1, \ldots, \nu-r \tag{50}$$

Because $\mathbf{V}_p^j$ contains the pth column of matrix V_2 and columns of V_2 are the basis of the null space of A, the nonworking constraint forces make no contribution to f_p.

Similarly, the generalized inertia forces are defined by

$$f_p^*=-\sum_{j=1}^{N}\mathbf{V}_p^j\cdot m_j\ddot{\mathbf{R}}^j\quad p=1, \ldots, \nu-r \tag{51}$$

Assembling f_p and f_p^* with $\ddot{\mathbf{R}}^j$ expressed in terms of $\ddot{q}$, $\dot{q}$, and q one obtains the following matrix counterpart of equation (13) or (26)

$$M''\ddot{q}=F''(\dot{q},q,t) \tag{52}$$

where M'' is of dimension $(\nu-r)\times\nu$, $\ddot{q}$ and F'' are of dimensions $\nu\times1$ and $(\nu-r)\times1$, respectively.

Examination of equations (6*a*) and (48) reveals the following identities

$$M''=V_2^TM \tag{53}$$

and

$$F''=V_2^TF \tag{54}$$

where M and F are the matrices appearing in the equations of motion characterizing the *unconstrained* system (in the generalized coordinates $q_1, \ldots, q_\nu$) as shown by equation (1).

Differentiation of equation (2) yields

$$A\ddot{q}=B' \tag{55}$$

where

$$B'=B-\dot{A}\dot{q}.$$

Premultiplication of equation (55) by U_1^T provides the following r independent constraint equations (recalling $U_1^TA=\Sigma V_1T$)

$$\Sigma V_1\ddot{q}=U_1^TB' \tag{56}$$

Downloaded 02 May 2010 to 171.66.16.54. Redistribution subject to ASME license or copyright; see http://www.asme.org/terms/Terms_Use.cfm

Together equations (52) and (56) form the following set of ν second order equations in q

$$\begin{bmatrix} V_2^T M \\ \Sigma V_1^T \end{bmatrix} \ddot{q} = \begin{bmatrix} V_2^T F \\ U_1^T B' \end{bmatrix} \tag{57}$$

The rank of the coefficient matrix of $\ddot{q}$ in equation (57) is ν, and one may use this set of ν second-order equations for a complete simulation.

Only for holonomic system is it possible to reduce equation (57) to dimension $\nu - r$. To accomplish this reduction, one must be able to transform not only $\dot{q}$ into $\dot{y}$ as in equation (47) but also introduce the coordinate transformation

$$q = E + V_2 y \tag{58}$$

where $E = \int \mathbf{A}^+ B dt$ + constant, and similarly express $\ddot{q}$ from equation (55) in terms of $\ddot{y}$ as

$$\ddot{q} = A^+ B' + V_2 \ddot{y} \tag{59}$$

finally writing equations (52)–(54) in the form

$$V_2^T M V_2 \ddot{y} = V_2^T F - V_2^T M A^+ B' \tag{60}$$

The coefficient of $\ddot{y}$ is a symmetric positive-definite matrix with the characteristic of an "inertia matrix" for the reduced set of generalized coordinates in y. Thus equation (60) may in the case of holonomic constraints be integrated as $\nu - r$ second-order equations. For nonholonomic constraints one must forego use of equation (60), but still it is possible to combine equations (60) and (47) as a complete set of $2\nu - r$ first-order equations in the variables q and $\dot{y}$. This approach reduces the problem to the same dimension as that in the previous section, matching Kane's results. It should be noted that the variables in y and $\dot{y}$ may lack the physical significance found in q and $\dot{q}$.

Application to Complex Dynamical Systems

The motivation for this work was the development of a generic computer program for simulating spacecraft [2–5] and similar electromechanical systems [8, 9] amenable to mathematical representation as a set of flexible bodies interconnected in a topological configuration. This representation may include closed loops of bodies, prescribed motion, or other constraints that may be represented as in equation (2). The equations of motion appropriate for a set of flexible bodies in an open loop configuration appear in [2, 11]. A computer program (TREETOPS) developed to simulate the dynamic response of flexible structures in a topological tree configuration is described in [10]. The SVD techniques of the present paper are being incorporated in an extension of the TREETOPS program that permits application to constrained systems. This extension permits direct use of the dynamical equations for the less constrained system in TREETOPS, with augmentation by kinematical constraint equations and reduction of dimension by SVD. Earlier attempts to apply the approach culminating in equations (13), (4), and (2) were frustrated by repeated encounters with singularities in equation (9).

In developing such a program, attention must be given to issues of computational feasibility not addressed in this paper. For example, it is not generally a good idea to compute the singular values of A by first finding the eigenvalues of $A^T A$ [6]. Golub and Reinsch [6] have developed an extremely efficient and stable algorithm for computing the SVD. The computed U and V matrices are orthogonal to approximately the working precision of the machine. Moreover, once the decomposition of A is available, one can employ an updating scheme in the spirit of [12] to obtain the SVD of the new A rather than to compute the SVD from scratch. An excellent treatment of the computational aspects of the SVD is provided in [13].

Summary

The simulation of constrained dynamical systems as defined by equations (1) and (2) is treated in several different ways in this paper. Although one might approach the problem directly as the equivalent of a system $2\nu + m$ first-order equations, augmenting the ν generalized coordinates by m generalized constraint forces such as Lagrange multipliers, in this paper attention is focused on alternatives leading to reduction of the system dimension and avoidance of generalized constraint forces.

In the category of reduced dimension formulations, five alternative representations are presented:

1. Equations (13), (4), and (2) representing $2\nu - m$ first-order differential equations in the variables $q_1, \ldots, q_\nu, u_1, \ldots, u_{\nu-m}$, where u_i is generalized speed as suggested by Kane [1]. This formulation requires some ingenuity in the selection of generalized velocities for elimination (see equation (9)), and the potential for unacceptable singularities makes this result unacceptable for generic simulation programs. To apply the method, the rank r of the matrix A in equation (2) must be equal to the row dimension m of the matrix.

2. Equations (40), (38), and (29) representing 2ν first-order differential equations in the variables $q_1, \ldots, q_\nu, u_1, \ldots, u_\nu$, as obtained by the limited use of SVD. This equation set is of higher dimension than is required by formulation (1), but it uses the same class of variables and avoids all singularity problems automatically.

3. Equations (44) and (45) representing $2\nu - r$ first-order differential equations in the variables $q_1, \ldots, q_\nu, z_1, \ldots, z_{\nu-r}$, as obtained by the application of SVD and associated transformations. This equation set is of the same dimension as formulation (1), but it avoids all singularity problems automatically (including the case $r < m$). The variables $z_1, \ldots, z_{\nu-r}$ constitute a reduced set of generalized speeds, and may be even more abstract in interpretation than the original generalized speeds $u_1, \ldots u_\nu$.

4. Equation (57), representing ν second-order differential equations in $q_1, \ldots, q_\nu$, as obtained by the limited use of SVD. Although not of minimum dimension, this set seems attractive computationally and its variables retain their original physical significance. This set is smaller than the one obtained by employing Lagrange multipliers.

5. Equations (60) and (47), reducing to equation (60) for integrable holonomic constraints, representing $2\nu - r$ first-order equations in the variables $q_1, \ldots, q_\nu, \dot{y}_1, \ldots, \dot{y}_{\nu-r}$, as obtained by the application of SVD and associated transformations. This formulation shares many features of method 3, to which it reduces when the generalized velocities $\dot{q}_1, \ldots, \dot{q}_\nu$ are chosen as the generalized speeds $u_1, \ldots, u_\nu$.

All of these five methods have in common the elimination of nonworking constraint forces, which when included serve not only to enlarge the dimension of the dynamical system but also quite often introduce computational problems.

Selection among the several formulations presented here must depend on computational efficiencies and relative ease of interpretation. More experience with simulations is required for this evaluation.

Acknowledgments

The authors acknowledge the perceptive discussions with Dr. Robert K. Saxe of Honeywell Inc. at various stages of this research. We are also thankful to Dr. Henry Waites of NASA, MSFC, for his numerous suggestions.

Downloaded 02 May 2010 to 171.66.16.54. Redistribution subject to ASME license or copyright; see http://www.asme.org/terms/Terms_Use.cfm

References

1 Kane, T. R., and Wang, C. F., "On the Derivation of Equations of Motion," *Journal of the Society for Industrial and Applied Mathematics*, Vol. 13, 1965, pp. 487-492.

2 Singh, R. P., and Likins, P. W., "Manipulator Interactive Design with Interconnected Flexible Elements," *Proceedings of 1983 Automatic Control Conference*, San Francisco, Calif., June 1983, pp. 505-512.

3 Kane, T. R., and Levinson, D. A., "Formulation of Equations of Motion for Complex Spacecraft," *Journal of Guidance and Control*, Vol. 3, No. 2, 1980, pp. 99-112.

4 Likins, P. W., "Point-Connected Rigid Bodies in a Topological Tree," *Celestial Mechanics*, Vol. 11, 1975, pp. 301-317.

5 Huston, R. L., "Multi-Body Dynamics Including the Effects of Flexibility and Compliance," *Computers and Structures*, Vol. 14, No. 5-6, 1981, pp. 443-451.

6 Golub, G. H., and Reinsch, C., "Singular Value Decomposition and Least Square Solution," *Numer. Math.*, Vol. 14, 1970, pp. 403-420.

7 Golub, G. H., and Kahan, W., "Calculating the Singular Values and Pseudoinverse of a Matrix," *SIAM Journal of Numerical Analysis*, Vol. 2, No. 3, 1965, pp. 205-224.

8 Book, W., "Recursive Lagrangian Dynamics of Flexible Manipulator Arms via Transformation Matrices," *Proceedings of the IFAC Symposium on Computer Aided Design of Multivariable Technological Systems*, Purdue University, West Lafayette, Ind., Sept. 1982, pp. 5-18.

9 Dubowsky, S., and Gardner, T. N., "Design and Analysis of Multi-Link Flexible Mechanisms With Multiple Clearance Connections," ASME *Journal of Engineering for Industry*, Vol. 99, No. 1, 1977, pp. 88-96.

10 Vander Voort, R. J., and Singh, R. P., "A Pointing Control System Simulation and Generic Model Generator for Multi-Body Flexible Structures," *Proceedings of the Ninth DARPA Strategic and Space Symposium*, Monterey, Calif., Oct. 1983.

11 Singh, R. P., Vander Voort, R. J., and Likins, P. W., "Dynamics of Flexible Bodies in Tree Topology—A Computer Oriented Approach," *Proceedings of the AIAA Dynamics Specialist Conference*, Palm Springs, Calif., May 1984, pp. 327-337.

12 Businger, P. A., "Updating a Singular Value Decomposition," *BIT*, Vol. 10, 1970, pp. 375-385.

13 Klema, V. C., and Laub, A. J., "The Singular Value Decomposition: Its Computation and Some Applications," *IEEE Transactions on Automatic Control*, Vol. AC-25, 1980, pp. 164-176.

APPENDIX

An Illustrative Example

Figure *A*1 shows a system comprised of two particles, P and Q of mass m_1 and m_2, respectively, attached to two massless pin-connected rods of equal length L. Q is presumed to be constrained to slide along a smooth tube. Let the unit vectors **i**, **j**, and **k** (forming a triad) be fixed in an inertial reference frame I. Since this system possesses only one degree of freedom, a single generalized coordinate θ is sufficient for the specification of all admissible configurations.

The differential equation governing θ, by explicit elimination of interaction forces, is given as follows

$$(m_1 + 4m_2\mathrm{Sin}^2\theta)L^2\ddot{\theta} + 4m_2\mathrm{Sin}\theta\mathrm{Cos}\theta L^2\dot{\theta}^2 = T \qquad (A1)$$

where T (directed along **k**) is the magnitude of an external torque acting on the first link.

To illustrate the SVD technique we will assume Q to be unconstrained. An "extraneous" coordinate ψ (refer to Fig. *A*1), describing the relative rotation of the links, is introduced. The equations of motion of this two degree-of-freedom system can be written as

$$\begin{bmatrix} m_1L^2 + 2m_2L^2(1+\mathrm{Cos}\psi) & m_2L^2(1+\mathrm{Cos}\psi) \\ m_2L^2(1+\mathrm{Cos}\psi) & m_2L^2 \end{bmatrix} \begin{bmatrix} \ddot{\theta} \\ \ddot{\psi} \end{bmatrix}$$

$$+ \begin{bmatrix} -m_2L^2(2\dot{\theta}+\dot{\psi})\dot{\psi}\mathrm{Sin}\psi \\ m_2L^2\dot{\theta}^2\mathrm{Sin}\psi \end{bmatrix} = \begin{bmatrix} T \\ 0 \end{bmatrix} \qquad (A2)$$

Since the inertial velocity of Q, ${}^I\mathbf{v}^Q$, parallel to **j** is zero, the constraint equation can be written as

$${}^I\mathbf{v}^Q \cdot \mathbf{j} = 0$$

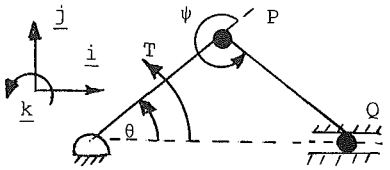


Fig. *A*1 Two link mechanism

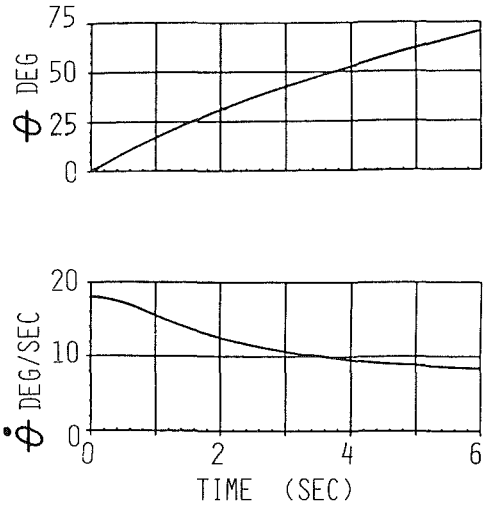


Fig. *A*2 $\theta, \dot{\theta}$ (SVD method)

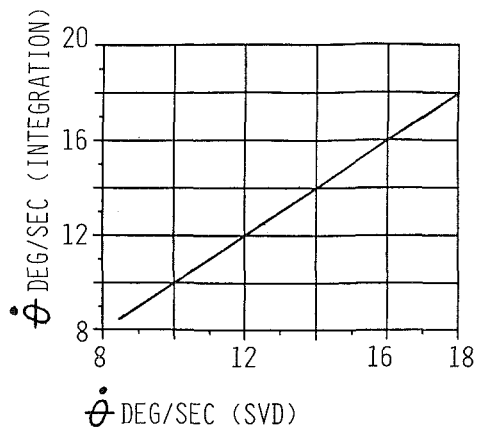


Fig. *A*3 $\dot{\theta}$ Comparison: direct integration versus SVD method

or,

$$[\mathrm{Cos}\theta + \mathrm{Cos}(\theta+\psi) \quad \mathrm{Cos}(\theta+\psi)] \begin{bmatrix} \dot{\theta} \\ \dot{\psi} \end{bmatrix} = 0 \qquad (A3)$$

Differentiation of equation (*A*3) yields

$$[\mathrm{Cos}\theta + \mathrm{Cos}(\theta+\psi) \quad \mathrm{Cos}(\theta+\psi)] \begin{bmatrix} \ddot{\theta} \\ \ddot{\psi} \end{bmatrix}$$

$$= [\dot{\theta}^2\mathrm{Sin}\theta + (\dot{\theta}+\dot{\psi})^2\mathrm{Sin}(\theta+\psi)] \qquad (A4)$$

To illustrate the use of the method under consideration, we turn to a specific case, taking $m_1 = m_2 = 0.31$ slug, $L = 1.5$ ft, $\dot{\theta}(0) = 18$ deg/sec, $\dot{\psi}(0) = -36$ deg/sec, $\theta(0) = \psi(0) = 0$, and $T = 0$.

A numerical integration of the equations of motion was performed in accordance with equations (60) and (47) of the text. Figure (*A*2) shows the values of $\theta(t)$ and $\dot{\theta}(t)$ for a duration of 6 seconds.

To check these results, equation (*A*1) was integrated. Figure (*A*3) shows the plot of $\dot{\theta}(t)$ obtained by integrating equation (*A*1) versus $\dot{\theta}(t)$ obtained by employing SVD technique. The results agree to five significant figures.

Downloaded 02 May 2010 to 171.66.16.54. Redistribution subject to ASME license or copyright; see http://www.asme.org/terms/Terms_Use.cfm

E. H. Dowell
Dean of Engineering.
Mem. ASME

Y. Kubota[1]
Visiting Scholar.

Duke University,
Durham, N.C. 27706

Asymptotic Modal Analysis and Statistical Energy Analysis of Dynamical Systems

A new derivation of the results commonly referred to as Statistical Energy Analysis (SEA) is given by studying the asymptotic behavior of classical modal analysis for a general, linear (structural) system. It is shown that, asymptotically, the response at (almost) all points of the system is the same. A numerical example is used to illustrate the way in which the asymptotic limit is approached. Both random and sinusoidal loadings are considered; for the latter an extension of the usual SEA result is obtained.

Introduction

The well-known text by Lyon [1] on Statistical Energy Analysis (SEA) is the standard reference on the subject and is highly recommended to the reader. The present authors have greatly benefitted from Lyon's discussion. As originally conceived, SEA was based on several plausible hypotheses. Various authors have considered the underlying basis for SEA and thereby advanced our understanding of it [2–4].

In the present paper, the relationship between classical modal analysis (CMA) and SEA is studied. It is shown how the results of SEA may be obtained as an asymptotic limit of CMA. The present work only considers the response of a single general linear structure under a random or sinusoidal load. However future papers will consider:

the structural-acoustic response of an enclosure bounded by a flexible wall and excited by external forces, and

two (or more) coupled structural systems.

All of these topics are addressed in reference [5] which also contains an earlier version of the present paper.

Here the emphasis is on

A new derivation of the SEA results from CMA for a single structure under random load;

The generalization of the usual SEA result to show that, asymptotically, all points on the structure have the same response. In the literature this is sometimes invoked as an assumption. Here the result is derived as part of the asymptotic limit of CMA;

A numerical example that displays the manner in which the asymptotic limit is approached for random loading; and

An extension of the usual SEA result for sinusoidal loading.

In view of the foregoing, the present results might be called more appropriately Asymptotic Modal Analysis (AMA) rather than SEA.

The important work of Crandall and his colleagues should also be cited [6–10]. Their work has been directed primarily toward those aspects of structural response under wide-band random excitation where SEA-type results of the usual sort do not hold. Both analytical and experimental work has been carried out.

Modal sum and image sum analytical methods have been used by Crandall. The modal sum methods are similar to those employed here. Image sum methods involve repeatedly using traveling waves on an infinite structure to form an appropriate cancellation of image sources to model finite plate response. Both methods have led to the identification of "intensification zones" where the local response is higher than the nearly uniform response of the rest of the structure. Special attention has been given to square and circular plates where such zones are most pronounced [6, 8, 9].

In one paper, [7, p. 386] a brief comparison is given between results obtained with the image sum method and those of SEA as obtained by Lyon. Crandall noted that, "The final result [obtained by image sum methods] can be interpreted as one of the basic principles of statistical energy analysis. . . . [It] is very nearly a simple power balance statement applied to the finite structure." However, as Crandall noted on p. 385 of [7], "The result obtained here for a string [using image sum methods] may be extended to the uniform beam, membrane and plate. It is necessary [however] to neglect the near field wave response, and (in the two-dimensional cases) to use asymptotic approximations for the far-field radiation."

In the present work, modal sum methods are used to derive the classical SEA result. Also the intensification zones, previously discovered by Crandall, et al., have been found as well.

The experimental work of Crandall, et al., was directed primarily toward the verification of intensification zones. Since the force levels used in the experiment were not

[1]On leave from Toshiba Research and Development Center, Japan.

Contributed by the Applied Mechanics Division and presented at the Winter Annual Meeting, Miami, Fla., November 17–21, 1985 of THE AMERICAN SOCIETY OF MECHANICAL ENGINEERS.

Discussion on this paper should be addressed to the Editorial Department, ASME, United Engineering Center, 345 East 47th Street, New York, N.Y. 10017, and will be accepted until two months after final publication of the paper itself in the JOURNAL OF APPLIED MECHANICS. Manuscript received by ASME Applied Mechanics Division, April, 1984; final revision, February, 1985. Paper No. 85-WA/APM-12.

Copyright © 1985 by ASME
Downloaded 02 May 2010 to 171.66.16.54. Redistribution subject to ASME license or copyright; see http://www.asme.org/terms/Terms_Use.cfm

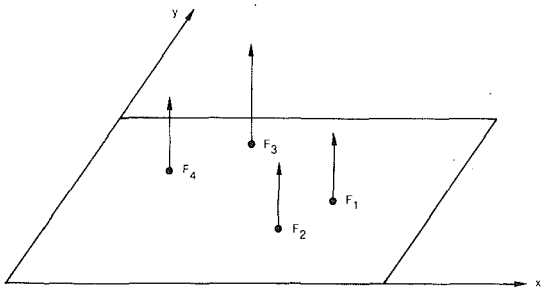


Fig. 1 Geometry of structure

calibrated, no absolute comparison between calculated and measured response levels could be made [6, 8].

In experimental work done by the present authors, and to be reported separately, the force level was calibrated and the experimental results are shown to agree with the results of AMA and SEA as the bandwidth of the excitation becomes large.

Part 1: A Linear Structure Under Random Forces

Define H_n as the modal "transfer function,"

$$H_n(\omega) \equiv \frac{1}{M_n(\omega_n^2 + 2\zeta_n i\omega_n\omega - \omega^2)}$$

From classical modal analysis [11–14] one may show that the relationship between pressure loading and the structural displacement is

$$\Phi_w(\omega;x,y) = \sum_m \sum_n \psi_m(x,y)\psi_n(x,y)H_m(\omega)H_n(-\omega) \cdot \int\int\int\int \psi_m(x,y)\psi_n(x^*,y^*) \cdot \Phi_{p_E}(\omega;x,y,x^*,y^*)dxdydx^*dy^* \quad (1)$$

Often equation (1) is approximated further, [11, 14]. Two approximations are particularly popular and useful. The first is the neglect of "off-diagonal coupling" or "joint acceptance," [1, 14]. This means omitting all terms in the double sum except those for which $m=n$. The second is the "white noise" approximation which assumes that Φ_p is slowly varying with respect to frequency relative to the rapidly varying transfer functions $H_m(\omega)$. Making both of these approximations in equation (1) we may obtain the mean square response.

$$\bar{w}^2(x,y) \equiv R_w(\tau=0;x,y) = \int_0^\infty \Phi_w(\omega;x,y)d\omega \approx \frac{\pi}{4}\sum_m \frac{\psi_m{}^2(x,y)}{M_m{}^2\omega_m{}^3\zeta_m} \int\int\int\int \psi_m(x,y)\psi_m(x^*,y^*) \cdot \Phi_{p_E}(\omega_m;x,y,x^*,y^*)dxdydx^*dy^* \quad (2)$$

Systematic Simplifications to Modal Analysis Leading to SEA

For definiteness we consider the load, p_E, to be described by many point forces, F_i (see Fig. 1). This is helpful in obtaining and understanding the results. It does not lead to any lack of generality in that any continuous spatial distribution may be represented by many point loads.

$$p(x,y,t) = \sum_{i=1}^{I} \delta(x-x_i)\delta(y-y_i)F_i(t) \quad (3)$$

The associated power spectrum is

$$\Phi_{p_E}(\omega;x,y,x^*,y^*) \equiv \sum_i \sum_j \delta(x-x_i)\delta(y-y_i)\delta(x^*-x_j^*)\delta(y^*-y_j^*)\Phi_{F_{ij}} \quad (4)$$

where $\Phi_{F_{ij}}$ is the cross-spectrum of the point loads.

Therefore equation (1) becomes

$$\Phi_w(\omega,x,y) = \sum_m \sum_n \psi_m(x,y)\psi_n(x,y)H_m(\omega)H_n(-\omega) \cdot \sum_i \sum_j \psi_m(x_i,y_i)\psi_n(x_j^*,y_j^*)\Phi_{F_{ij}}(\omega) \quad (5)$$

Thus equation (2) becomes

$$\bar{w}^2(x,y) \cong \frac{\pi}{4}\sum_m \frac{\psi_m{}^2(x,y)}{M_m^2\omega_m^3\zeta_m} \cdot \sum_i \sum_i \psi_m(x_i,y_i)\psi_m(x_j^*,y_j^*)\Phi_{F_{ij}}(\omega_m) \quad (6)$$

We now simplify equation (6) by taking a spatial average, then a modal average in an asymptotic limit. The latter is done in two closely related steps.

- Taking a spatial average over the response, equation (6) becomes (the major steps or assumptions which lead to simplifications are denoted by •)

$$<\bar{w}^2> \cong \frac{\pi}{4}\sum_m \frac{<\psi_m{}^2>}{M_m^2\omega_m{}^3\zeta_m} \sum_i \sum_j \psi_m(x_i,y_i) \psi_m(x_j^*,y_j^*)\Phi_{F_{ij}}(\omega_m) \quad (7)$$

where $<\ >$ denotes a spatial average.

Note that the point pairs x_i, y_i, $x_j{}^*$, $y_j{}^*$ obey $x_i = x_i{}^*$, $y_i = y_i{}^*$, i.e., they range over the same points on the structure. Hence the * superscript is superfluous. Note also that equation (7) per se retains a fully modal character of the classical type. We have not yet passed from the domain of modal analysis to AMA or SEA.

- *If* the number of modes is large then the right-hand side of equation (7) will tend to be dominated by terms for which $i = j$. Hence, even if the point forces are correlated, the forces behave at this stage as though they are uncorrelated. One may show (see the Appendix) that

$$A_{ij} \equiv \sum_m \psi_m(x_i,y_i)\psi_m(x_j^*,y_j^*)$$

oscillates about zero for fixed $i \neq j$ if m ranges over a large number of modes. Hence *if* it is assumed here that $<\psi_m{}^2>$, M_m, w_m, ζ_m are slowly varying with m compared to the remaining terms on the right-hand side of equation (7), then equation (7) becomes

$$<\bar{w}^2> \cong \frac{\pi}{4}\sum_m \frac{<\psi_m{}^2>}{M_m{}^2\omega_m{}^3\zeta_m} \cdot \sum_{i=1}^{I} \psi_m{}^2(x_i,y_i) \cdot \Phi_{F_{ii}}(\omega_m) \quad (8)$$

where A_{ij} for $i \neq j$ has been neglected compared to A_{ii} and A_{jj}.

- In a certain interval of frequency, $M_m{}^2$, $\omega_m{}^3$, ζ_m, $\Phi_{F_{ii}}(\omega_m)$ and $<\psi_m{}^2>$ will be slowly varying with mode number, m (see foregoing), but $\psi_m{}^2(x_i, y_i)$ will vary relatively rapidly.

Thus, in a certain interval of frequency, $\Delta\omega$,

$$<\bar{w}^2>_{\Delta\omega} \cong \frac{\pi}{4}\frac{<\psi_c{}^2>}{M_c{}^2\omega_c{}^3\zeta_c} \sum_{i=1}^{I} \Phi_{F_{ii}}(\omega_c)\sum_m \psi_m{}^2(x_i,y_i) \quad (9)$$

where the subscript c denotes the center frequency in the interval, $\Delta\omega$. $<\omega_c{}^2>$ is the spatial average of the square of the frequency whose mode is nearest ω_c.

$$\sum_{m=M}^{M+\Delta M-1} \psi_m{}^2(x_i,y_i) = C\Delta M \quad (10)$$

Downloaded 02 May 2010 to 171.66.16.54. Redistribution subject to ASME license or copyright; see http://www.asme.org/terms/Terms_Use.cfm

where C is independent of i and M provided there is a large number of modes, ΔM, in the frequency interval, $\Delta\omega$. Equation (10) is discussed more fully in the Appendix.

Thus,

$$<\bar{w}^2>_{\Delta\omega} = \frac{\pi}{4} C \frac{\Delta M}{\Delta\omega} \frac{<\psi_c{}^2>}{M_c{}^2 \omega_c{}^3 \zeta_c} \sum_{i=1}^{I} \Phi_{F_{ii}}(\omega_c)\Delta\omega \tag{11}$$

where

$$\left[\sum_{i=1}^{I} \Phi_{F_{ii}}(\omega_c)\Delta\omega\right] \equiv <\bar{F}^2>_{\Delta\omega}$$

may be identified as the total (mean square) force of the point forces in the frequency interval, $\Delta\omega$.

Finally (see the Appendix) it may be shown that (here M is the total structural mass)

$$M_c \cong M<\psi_c{}^2>$$

$$C \cong <\psi_c{}^2>$$

if there are many modes (large ΔM) in $\Delta\omega$, and thus equation (11) may be written

$$<\bar{w}^2>_{\Delta\omega} = \frac{\pi}{4} \frac{\Delta M}{\Delta\omega} \frac{<\bar{F}^2>\Delta\omega}{M^2 \omega_c{}^3 \zeta_c} \tag{12}$$

Equation (12) is the standard result for structural response used in SEA analysis.

Extension of Result for Spatial Average Response to Local Response

Equation (12) was derived starting from equation (6). As a first step a spatial average of six (6) was taken leading to (7). What is perhaps remarkable is that it can be shown that (12) is also the correct asymptotic limit for the response at (almost) any spatial point location on the structure. Thus in the asymptotic limit (almost) any point of the structure has the same response. A brief derivation of this result follows.

Consider (6) and retain only those terms for which $i=j$ since asymptotically these will be dominant. In a certain frequency interval $M_m{}^2$, $\omega_m{}^3$, ζ_m, $\Phi_{F_{ii}}(\omega_m)$ will be slowly varying with m, but $\psi_m{}^2(x,y)$ and $\psi_m{}^2(x_i, y_i)$ will vary relatively rapidly. Then (6) becomes

$$\bar{w}^2(x,y) = \frac{\pi}{4} \frac{1}{M_c{}^2 \omega_c{}^3 \zeta_c} \cdot \sum_i \Phi_{F_{ii}}(\omega_c) \sum_m \psi_m{}^2(x,y)\psi_m{}^2(x_i,y_i) \tag{13}$$

Compare (13) with (9). Equation (9) is for the spatial average response, while (13) is for the response at any (some) point, x, y.

Now it may be shown that

$$\sum_{m=M}^{M+\Delta M-1} \psi_m{}^2(x,y)\psi_m{}^2(x_i,y_i) \to [<\psi_m{}^2>]^2 \Delta M \tag{14}$$

as $\Delta M \to \infty$. This is true independent of the point of response, x, y, and the point of force application, x_i, y_i provided, of course, that these points are not near a structural boundary or near each other. Thus (12) again follows from (13). This proves that, asymptotically, all points have the same response. For a derivation of equation (14), see the Appendix. For the special case of $x, y = x_i, y_i$, a factor of $(3/2)^D$ appears on the right-hand side of (14) where $D=1$ for a beam and $D=2$ for a plate or shell. This is the concentration factor for response at the point of load application. As Crandall [6] has noted for some special structural geometries and loading points, other concentration factors may arise.

Comparison of SEA/AMA and CMA: A Numerical Example

For definiteness consider a (uniform, simply supported) beam under one or more point forces. We wish to compare the results of (6) or (7), CMA, and those of (12), SEA/AMA. To this end let us first define $\omega_{\min}$, $\omega_{\max}$ as the minimum and maximum frequencies in a frequency interval, $\Delta\omega$. Thus

$$\omega_{\max} = \omega_{\min} + \Delta\omega \tag{15}$$

Also the center frequency of the interval will be defined as

$$\omega_c = (\omega_{\min}\omega_{\max})^{1/2} \tag{16}$$

Taking the ratio of (7)-(12) one has a measure of the goodness of the asymptotic approximation, $<\bar{w}^2>_{\text{CMA}}/<\bar{w}^2>_{\text{SEA/AMA}}$. One could also use (6) to form a similar ratio. One expects the ratio to approach one asymptotically.

For a uniform, simply supported beam where $\omega_m = m^2\omega_1$, $\psi_m = \sin m\pi x/a$, the result takes on the following specific form,

$$<\bar{w}^2>_{\text{CMA}}/<\bar{w}^2>_{\text{SEA/AMA}} = \left(\frac{2}{\Delta MI}\right)(1+B)^{3/2} \sum_{m=M}^{M+\Delta M-1} \left(\frac{m_{\min}}{m}\right)^6 \sum_i \sum_i \psi_m(x_i)\psi_m(x_j) \tag{17}$$

where x_i, etc., are normalized by the beam length, a, and

$$B \equiv \Delta\omega/\omega_{\min} = \frac{\omega_{\max}}{\omega_{\min}} - 1 = \left(\frac{m_{\max}}{m_{\min}}\right)^2 - 1$$

with $m_{\min} = M$, $m_{\max} = M + \Delta M - 1$. B may be thought of as a normalized frequency bandwidth. Recall ΔM is the number of modes in a certain frequency interval of interest.

The right-hand side of (17) depends on M, ΔM, I, x_i, x_j. Now, consider equation (17) for $M/\Delta M \to \infty$. Since

$$B \to 0, \frac{m_{\min}}{m} \to 1: \quad \text{as} \quad \frac{M}{\Delta M} \to \infty$$

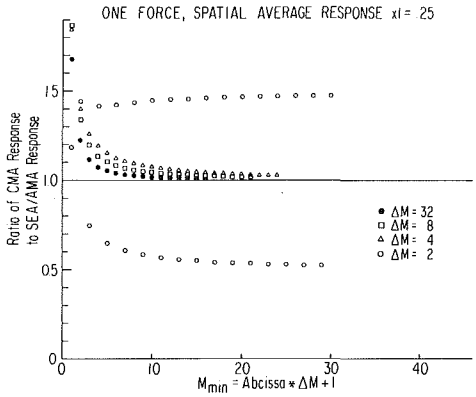


Fig. 2 Ratio of CMA response to SEA/AMA response versus minimum modal number

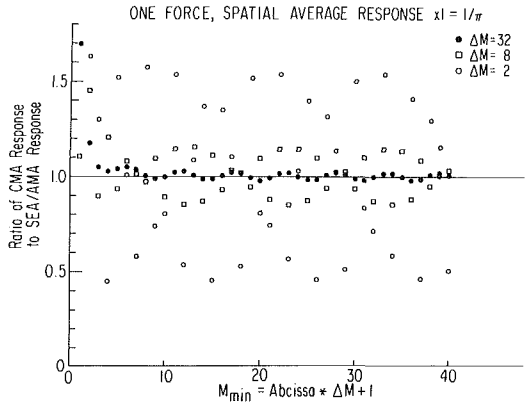


Fig. 3 Ratio of CMA response to SEA/AMA response versus minimum modal number

Downloaded 02 May 2010 to 171.66.16.54. Redistribution subject to ASME license or copyright; see http://www.asme.org/terms/Terms_Use.cfm

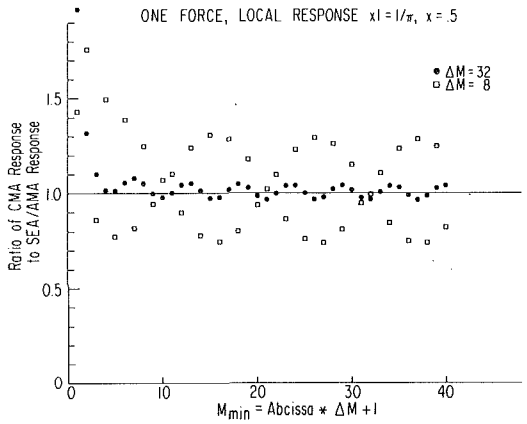


Fig. 4 Ratio of CMA response to SEA/AMA response versus minimum modal number

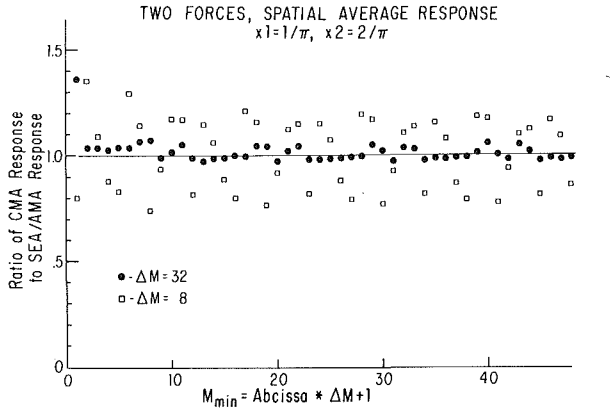


Fig. 5 Ratio of CMA response to SEA/AMA response versus minimum modal number

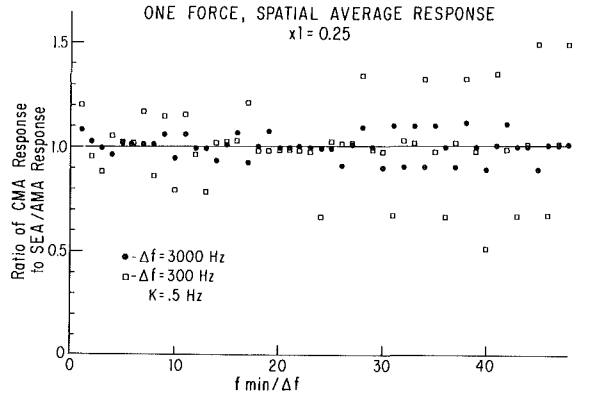


Fig. 6 Ratio of CMA response to SEA/AMA response versus ratio of minimum frequency to frequency bandwidth

equation (27) becomes

$$\frac{<\bar{w}^2>\text{CMA}}{<\bar{w}^2>\text{SEA/AMA}} \cong \frac{2}{\Delta MI} \sum_{m=M}^{M+\Delta M-1} \sum_i \sum_i \psi_m(x_i)\psi_m(x_j) \tag{17a}$$

For $I=1$ the result of the summation in equation (17a) is obtained analytically, i.e.,

$$\frac{<\bar{w}^2>\text{CMA}}{<\bar{w}^2>\text{SEA/AMA}} \cong 1 - \frac{\sin\Delta M\pi x_1 \cdot \cos(2M+\Delta M-1)\pi x_i}{\Delta M \sin\pi x_1} \tag{17b}$$

This result shows that as M varies, the ratio will oscillate about 1 with a constant amplitude which depends on ΔM and x_i. The amplitude of the oscillation about 1 will diminish as $\Delta M \to \infty$. Regarding the asymptotic behavior of equation (17b), see the Appendix. A few sample calculations have been made which are illustrative.

One Force Only: $I=1$. In Fig. 2 the ratio of CMA response to SEA/AMA response is given as for a function of M for one force location, $x_1 = 0.25$, and various ΔM. In Figs. 2–5 the horizontal coordinate is the abscissa and M = abscissa * $\Delta M + 1$. The result shows that indeed the ratio approaches 1 as $\Delta M \to \infty$. It is interesting to note that the ratio does not oscillate about 1 if $\Delta M = 4, 8, 32$. Recall that $x_1 = 0.25$ for this example. For this x_1 and $\Delta M = 4, 8, \ldots$ the sinusoidal mode shapes give rise to a repetitive result as m varies. Thus the modal average over some ΔM modes will tend monotonically toward 1. The condition is that $\Delta M x_1$ be an integer. For $x_1 = 1/4$, this implies $\Delta M = 4, 8$, etc.

If, by contrast, one chooses x_1 to be an irrational number then oscillations will always persist (since $\Delta M x_1$ will never be an integer), but these will diminish as $\Delta M \to \infty$. For example, in Fig. 3 results are shown for $x_1 = 1/\pi$. In Fig. 4, corresponding results are shown for *local* response of the point, $x = 0.5$, which were obtained from (6) and (12). These results are representative in that the asymptote is approached more rapidly for spatial average response than local response. Compare Figs. 3 and 4.

Two Forces: $I=2$. Results are shown in Fig. 5 for spatial average response with two forces whose locations are at $x_1 = 1/\pi$, $x_2 = 2/\pi$. Comparing the results of Fig. 5 with those of Fig. 3, we see that the approach of the ratio to 1 as $\Delta M \to \infty$ is less rapid for two forces than for one. This is expected.

In the examples, results were shown for various ΔM and M. In practice, however, we may wish to consider a certain frequency interval rather than a certain number of modes. Using a frequency interval, Δf, a minimum frequency, $f_{\min}$, and a natural frequency, f_m, the equation corresponding to (17) may be written as

$$\frac{<\bar{w}^2>\text{CMA}}{<\bar{w}^2>\text{SEA/AMA}} \cong \frac{2}{\Delta MI}(1+B)^{\frac{3}{2}} \sum_{m=m_{\min}}^{m_{\max}} \left(\frac{f_{\min}}{f_m}\right)^3 \sum_i \sum_i \psi_m(x_i)\psi_m(x_j) \tag{17c}$$

where

$$K \equiv \frac{h}{a^2}\sqrt{\frac{E}{12\rho}}$$

$$m_{\max} \equiv Int\left[\left(\frac{2f_{\max}}{\pi K}\right)^{\frac{1}{2}}\right]$$

$$m_{\min} \equiv Int\left[\left(\frac{2f_{\min}}{\pi K}\right)^{\frac{1}{2}}\right] + 1$$

and Int [ ] means a maximum integer that does not exceed the number in the bracket. Also

$$\Delta M = m_{\max} - m_{\min} + 1$$

$$B \equiv \frac{\Delta f}{f_{\min}}$$

$$f_m = \frac{\pi}{2} m^2 K$$

In Fig. 6, results are shown for $I=1$, $x_1 = 0.25$, $K = 0.5$ (1/sec) and various Δf. As can be seen, these results are more complicated because, for a beam, the number of modes, ΔM, *decreases* as $f_{\min}$ *increases* even for fixed Δf. Hence the ratio diverges for $f_{\min} \to \infty$ and fixed Δf. However, the ratio approaches 1 as $\Delta f \to \infty$ for fixed $f_{\min}$. This unexpected result

Downloaded 02 May 2010 to 171.66.16.54. Redistribution subject to ASME license or copyright; see http://www.asme.org/terms/Terms_Use.cfm

can be explained as follows. For a plate (the detailed results will be reported separately) the number of modes approaches a constant value as $f_{\min}$ increases. Hence no divergence occurs as $f_{\min} \to \infty$ for a plate. Moreover, as $f_{\min}$ increases sufficiently all beams will in fact become plate-like. Hence the apparent paradox is resolved.

Discussion

There are several points worthy of emphasis.

1. A systematic derivation of the SEA result as given here allows an assessment of the assumptions and consequent simplifications which are made to obtain such results.

2. In practice, a combination of classical modal analysis and SEA (or asymptotic modal analysis) may prove useful. For example, think of the total frequency interval of interest as being divided into a number of smaller intervals, $\Delta\omega$. In the lowest frequency interval, say $\Delta\omega = 0 \to \omega_1$ corresponding to $m = 1 \to M_1$, equations (6) or (7) may be used. This is the general modal result and presumes that sufficient information is available concerning the modes $m = 1$ to M_1 that these *individual* characteristics are known and worthy of retention. For $m > M_1$ (typically M_1 would be in the range 10 to 100), the individual character of the modes is no longer accurately known or worthy of retention. In higher frequency intervals, equation (22) is used where the frequency interval, $\Delta\omega$, is sufficiently large so that ΔM is sufficiently large (say greater than 10), but $\Delta\omega$ is sufficiently small so that M_m, ω_m, ζ_m and $\Phi_{F_{ii}}(\omega_m)$ do not vary rapidly. If M_m, ω_m, ζ_m *do* vary rapidly in the frequency interval, $\Delta\omega$, but $\Phi_{F_{ii}}$ does not, then one may use equation (8) in conjunction with equation (10) to develop an intermediate approximation.

It is possible, of course, that neither equations (6)–(8) nor (12) will cover adequately some range of frequency. Then one has the option of determining more modes with the required accuracy, i.e., increasing M_1, or using equations (6)–(8) in a sensitivity study with various estimates (guesses) for the modal characteristics.

It is noted that a rapid method for estimating the number of modes in a given frequency interval is highly desirable to implement the preceding strategy. Fortunately, such methods have been developed by the originators of SEA (reference [1]).

The physical interpretation of equation (12) also is worthy of emphasis. The only parameters that appear in equation (12) are:

1. $<\bar{F}^2>\Delta\omega$, the total mean square force in the frequency interval, $\Delta\omega$. The location of those forces does not appear. Nor is the cross correlation of these forces important, i.e., the mean square response is proportional to the sum of the mean square of the individual forces.

2. M, the total mass of the structure. The individual modal masses do not appear.

3. ω_c, ζ_c, the center frequency and associated critical damping ratio. The individual modal frequencies and damping rations do not appear.

4. $\Delta\omega/\Delta M$, the average separation between natural frequencies in the frequency interval, $\Delta\omega$.

Indeed, what does not appear in equation (12) is truly remarkable. In short, no individual modal characteristics appear in equation (12). Moreover the location at which the response is calculated does not appear.

Special emphasis should be given to the rule for summing forces which is implied by equation (11) et seq. Note that our definition of (mean square) force is

$$<\bar{F}^2>\Delta\omega \equiv \sum_{i=1}^{I} \Phi_{F_{ii}}(\omega_2)\Delta\omega \tag{11a}$$

This states that the forces are summed according to a sum of squares law. That is, if there are several forces, say $I = 4$, then the total force applied, F, is effectively given by

$$F^2 = F_1^2 + F_2^2 + F_3^2 + F_4^2 \tag{11b}$$

Clearly for (11*b*) to hold the forces must be uncorrelated. There are two ways this may occur. First of all, the forces, F_1, F_2, F_3, F_4 may be uncorrelated *in time*. Then (11*b*) will hold even if all forces are perfectly correlated *in space*, e.g., they all act at the same point. However, within the framework of the asymptotic analysis which leads to equation (11*a*), (11*b*) holds *even* if the forces are perfectly correlated in time. This is because, asymptotically, any two forces separated by a finite distance will be *spatially* uncorrelated as the wavelength of structural deformation tends to zero with respect to the separation distance. One should note, of course, that if the forces are applied at the same point, this can never be true. More generally, the larger the separation distance between forces the more rapidly the asymptotic results will be reached. In the mathematical derivation of equation (12), this issue arose when A_{ij} for $i \neq j$ was neglected compared to A_{ii} and A_{jj}. Recall equations (7) and (8), and see the discussion in the Appendix.

Part 2: A Linear Structure Under Sinusoidal Forces

The case of sinusoidal forces is considered next. Even though for modal methods per se the case of sinusoidal excitation is easier to analyze than that of random excitation and, moreover, the SEA result will be in a certain sense precisely the same for both random and sinusoidal forces, we chose to consider random forces first. The reason is that the derivation of the SEA result for sinusoidal forces is more delicate than that for random forces as has been appreciated, reference [1]. Moreover, we obtain a generalization of the standard SEA result which may prove useful.

For definiteness we again consider many point forces with each point force having multiple frequency content. Thus

$$p_E = \sum_i \sum_k F_{ik}\delta(x - x_i)\delta(y - y_i)e^{i\omega_k t} \tag{18}$$

where i denotes location of the ith point force and k denotes the kth frequency component. Hence, F_{ik} is the magnitude of the kth frequency component of the force at point i. Using standard methods, the temporal mean square is

$$\bar{w}^2 = 1/2 \sum_m \sum_n \sum_i \sum_j \sum_k \frac{F_{ik}F_{jk}\psi_{mi}\psi_{nj}\psi_m\psi_n}{M_m M_n [\ \ ]_m [\ \ ]_n^*} \tag{19}$$

where

$$\psi_{mi} = \psi_m(x_i, y_i)$$

$$\psi_m = \psi_m(x, y)$$

$$[\ \ ]_m = -\omega_k^2 + 2\zeta_m\omega_m i\omega_k + \omega_m^2$$

* denotes complete conjugate

Systematic Simplifications to Modal Analysis Leading to SEA (Generalized) or AMA

• Taking a spatial average over the response, equation (19) becomes

Downloaded 02 May 2010 to 171.66.16.54. Redistribution subject to ASME license or copyright; see http://www.asme.org/terms/Terms_Use.cfm

$$<\bar{w}^2> = 1/2 \sum_m <\psi_m{}^2> \sum_{i,j,k} \frac{F_{ik}F_{jk}\psi_{mi}\psi_{mj}}{M_m{}^2[\ \ldots\ ]_m[\ \ldots\ ]_m{}^*} \tag{20}$$

where the orthogonality condition (for a structure of uniform mass, or near orthogonality for slowly varying mass) has been used, viz,

$$\int\int \psi_m \psi_n dxdy = 0 \quad \text{for} \quad m \neq n \tag{21}$$

As an alternative to equation (21), one may argue that for near resonant response, $m \neq n$ will give rise to lesser response than $m = n$ because of the factors, $[\ \ldots\ ]_m\ [\ \ldots\ ]_n{}^*$, and their behavior when $\omega = \omega_m$ or ω_n.

- If the number of modes is large, then the right-hand side of equation (20) will tend to be dominated by the terms for which $i = j$. As for the case of random forces, one is assuming that $<\psi_m{}^2>$, M_m, ω_m, ζ_m are slowly varying with m compared to the remaining terms on the right-hand side of equation (20). Thus for $i \neq j$ when m ranges over a large number of modes

$$\sum_m \psi_{mi}\psi_{mj}$$

oscillates about zero and equation (20) becomes, approximately,

$$<\bar{w}^2> = 1/2 \sum_m <\psi_m{}^2> \sum_{i,k} \frac{F_{ik}\psi_{mi}^2}{M_m{}^2[\ \ldots\ ]_m[\ \ldots\ ]_m{}^*} \tag{22}$$

- When the number of natural frequencies is large in a given frequency interval, $\Delta\omega$, and when ω_k is contained within that interval, it is conservative to *assume* that at least one natural frequency, say $\omega_m{}^*$, coincides with ω_k. Moreover nearby modes, i.e., those within $\zeta_m\omega_m$ of ω_k, respond as well. This assumption has no direct counterpart in the random force case. Although, see the discussion of Lyon (reference [1]) on this point. Its consequences, however, are important as shown in the following. Note that the frequencies of response are ω_k; the mode that has natural frequency, $\omega_m = \omega_k$ is excited into resonance. Other nearby modes are excited at (slightly) off-resonance.
- For small ζ_m, resonance will occur when

$$\omega_m \cong \omega_k \tag{23}$$

Define $\Delta\omega_m$ by

$$\omega_m \equiv \omega_k + \Delta\omega_m$$

then

$$\frac{1}{[\ \ldots\ ]_m[\ \ldots\ ]_m{}^*} \cong \frac{1}{4\omega_k{}^4\zeta_m{}^2} \frac{1}{\left[\left(\frac{\Delta\omega_m}{\zeta_m\omega_k}\right)^2 + 1\right]} \tag{24}$$

where ζ_m, $\Delta\omega_m/\omega_k$ have been taken as small compared to 1. Moreover, let $\Delta\omega_m = m\Delta\omega/\Delta M$ where ΔM is the total (odd) number of modes within $\Delta\omega$, m is an index indicating each mode within that interval (using an obvious redefinition of m), and $m = -(\Delta M - 1)/2 \rightarrow (\Delta M - 1)/2$. Then equation (22) becomes

$$<\bar{w}^2>_{\Delta\omega} = 1/2 \sum_i \sum_k \sum_m \frac{<\psi_m^2>}{M_m{}^2\zeta_m{}^2} \frac{F_{ik}{}^2}{4\omega_k{}^4} \frac{\psi_{mi}{}^2}{\left[\left(\frac{m}{\epsilon}\right)^2 + 1\right]} \tag{25}$$

where

$$\epsilon = \frac{\omega_k \zeta_m \Delta M}{\Delta\omega}$$

Note that ϵ is the ratio of the modal bandwidth to the interval between two adjacent frequencies. Now to simplify equation (25) further, it is noted that [recall equation (10)] for *large* ΔM

$$\sum_{m=-(\Delta M-1)/2}^{(\Delta M-1)/2} \psi_{mi}{}^2 = C\Delta M \tag{26}$$

Therefore, the average modal value of $\psi_{mi}{}^2$ is (using a modal subscript to denote modal rather than spatial average)

$$<\psi_{mi}{}^2>_{\text{modal}} = C \tag{27}$$

Also, it may be shown that *for large* ΔM (and fixed ω_k, $\zeta_m/\Delta\omega$)

$$S\Delta M(\Delta M, \epsilon) \equiv \sum_{m=-(\Delta M-1)/2}^{(\Delta M-1)/2} \frac{1}{\left[\left(\frac{m}{\epsilon}\right)^2 + 1\right]} \rightarrow \pi\epsilon \tag{28}$$

It is interesting to note that this sum has been evaluated asymptotically by Lyon, reference [1], in a somewhat different context. For a more complete discussion see the Appendix. Physically, the asymptote $\Delta M \rightarrow \infty$ corresponds to many modes responding within a frequency interval, $\Delta\omega$, due to their finite modal bandwidth, $\zeta_m\omega_m$.

Now if ψ_{mi}^2 is approximated by its modal average, C, and assuming $<\psi_m{}^2>$, M_m, ζ_m are slowly varying with respect to m, then equation (25) becomes, upon use of equation (28),

$$<\bar{w}^2>_{\Delta\omega_k} = \frac{\pi}{8} \sum_i \sum_k \frac{F_{ik}{}^2 \Delta M_k <\psi_m{}^2>_k C_k}{\omega_k{}^3 \zeta_{ck} M_{ck}^2 \Delta\omega_k} \tag{29}$$

where the k subscript has been added to emphasize that various structural parameters are chosen to span the frequency range around the exciting (and response) frequency, ω_k. Further discussion of the derivation of equation (29) from equation (25) is given in the Appendix.

Now

$$\sum_i \frac{F_{ik}^2}{2} \equiv <\bar{F}^2>_{\Delta\omega_k}$$

is the total mean square force of frequency content ω_k. Moreover [see the Appendix and recall equation (11), et seq] if ΔM is large, then $M_{c_k} \cong M<\psi^2>_k$ and $C_k \cong <\psi^2>_k$ and thus equation (29) may be written

$$<\bar{w}^2>_{\Delta\omega_k} = \frac{\pi}{4} \sum_k \frac{\Delta M_k}{\Delta\omega_k} \frac{<\bar{F}^2>\Delta\omega_k}{M^2\omega_k{}^3\zeta_{ck}} \tag{30}$$

Equation (30) is formally the same as the result for random force excitation equation (12). However, there are some subtle distinctions in interpretation as will be discussed in the following.

Note that in the derivation of equation (30), it has been implicitly assumed that

$$\sum_m \frac{\psi_{mi}{}^2}{\left[\left(\frac{m}{\epsilon}\right)^2 + 1\right]} \rightarrow \frac{1}{\Delta M} \sum_m \psi_{mi}{}^2 \sum_m \frac{1}{\left[\left(\frac{m}{\epsilon}\right)^2 + 1\right]}$$

as $\Delta M \rightarrow \infty$

The manner in which this asymptote is approached is discussed in more detail is the Appendix. Here it is noted that if this assumption is not made (e.g., because ΔM is too small), but one still assumes that $<\psi_m^2>$, M_m, ζ_m are slowly varying with respect to m and that $M_m \cong M<\psi^2>_k$, equation (30) can be generalized to

Downloaded 02 May 2010 to 171.66.16.54. Redistribution subject to ASME license or copyright; see http://www.asme.org/terms/Terms_Use.cfm

$$<\bar{w}^2>_{\Delta\omega} = \frac{1}{4}\sum_i\sum_k \frac{<F_{ki}^2>_{\Delta\omega_k}}{M^2\omega_k{}^4\zeta_{ck}^2<\psi^2>_k} \sum_m \frac{\psi_{mi}^2}{\left[\left(\frac{m}{\epsilon}\right)^2+1\right]} \quad (31)$$

Note further that if a single mode is dominant, i.e., $m=0$, then equation (31) reduces to the well-known result for a system excited in a single resonant mode.

Discussion

Let us focus on the differences of interpretation between equation (12) and equation (30). In obtaining equation (12), many modes of the structure were assumed to be excited because of the broadband character of the random excitation force. It was then assumed that within some frequency interval of interest there were many modes (all excited), ΔM, but that M_m, ω_m, ζ_m $<\psi_m{}^2>$ were slowly varying. Clearly by choosing a large enough frequency interval, ΔM will always be large enough, but if $\Delta\omega$ is too large than ω_m, ζ_m, etc. may vary significantly and also we may lose frequency resolution in determining the response. Hence $\Delta\omega$ must be chosen to balance these competing claims.

By contrast, for sinusoidal excitation, these responses will be at the exciting frequencies, ω_k. Only those modes whose natural frequencies are near ω_k will respond significantly. Hence it is unlikely that M_m, ω_m, ζ_m, etc. will vary significantly for a given ω_k. However, whether a sufficient number of modes, ΔM, will be excited for a given ω_k for equations (30) or (31) to be a reasonable approximation is a serious question. If ΔM is not sufficiently large for equation (28) to hold, then one should use equation (31) rather than equation (30). However, for small ΔM, the presumption of $\omega_m=\omega_k$ for *some m* for each ω_k may provide a *considerable overestimate* of the response even when equation (31) is used. It should be emphasized that equation (31) may be thought of as a generalization of equation (12) as well. The reason that equation (30) [which is a limiting case of equation (31)] and equation (12) agree is that, as the number of modes becomes large within a (structural) modal bandwidth, whose bandwidth is $b\omega_s = \zeta_m\,\omega_m \approx \zeta_m\,\omega_k$, the sinusoidal force input excites those modes very nearly as though it were a broadband frequency source.

Also it might be noted that equation (31) contains within it, information on resonant versus nonresonant response. If the $m=0$ contribution dominates over all others, then resonant response may be said to dominate; if the converse is true then nonresonant response may be said to dominate. See also the discussion of Pope [15] for a related but somewhat different view.

Acknowledgment

The first author would like to thank Dr. A. V. Srinivasan for his invitation to spend some time at the United Technology Research Laboratories where this work was begun and for stimulating discussions of the material. He would also like to acknowledge Mrs. Donna Edwards, who expertly undertook some of the numerical calculations. This work was supported in part by General Motors Research Laboratory.

References

1 Lyon, R. H., *Statistical Energy Analysis of Dynamical Systems: Theory and Applications*, The MIT Press, Cambridge, Mass., 1975.

2 Zeman, J. L., and Bogdanoff, J. L., "A Comment on Complex Structural Response to Random Vibrations," *AIAA Journal*, Vol. 7, No. 7, 1969, pp. 1225–1231.

3 Woodhouse, J., "An Approach to the Theoretical Background of Statistical Energy Analysis Applied to Structural Vibration," *J. Acoust. Soc. Am.*, Vol. 69, 1981, pp. 1695–1709.

4 Clarkson, B. L., "A Structural Dynamicist Looks at Statistical Energy Analysis," *Proceedings of the Institute of Acoustics*, 1981, pp. 1–8.

5 Dowell, E. H., "Vibration Induced Noise in Aircraft: Asymptotic Modal Analysis and Statistical Energy Analysis of Dynamical Systems," R82-112447, United Technologies Research Center, Jan. 1983.

6 Crandall, S. H., "Random Vibration of One- and Two-Dimensional Structures," in *Developments in Statistics*, Vol. 2, Krishnaiah, P. R., ed., Academic Press, New York, 1979, pp. 1–82.

7 Crandall, S. H., "Structured Response Patterns Due to Wide-Band Random Excitation," in *Stochastic Problems in Dynamics*, Clarkson, B. L., ed., Pitman, London, 1977, pp. 366–389.

8 Itao, K., and Crandall, S. H., "Wide-Band Random Vibration of Circular Plates," ASME *J. Mech. Design*, Vol. 100, 1978, pp. 690–695.

9 Crandall, S. H., and Zhu, W. -Q., "Wide Band Random Excitation of Square Plates," in *Random Vibrations and Reliability*, Proc. IUTAM Symp. Frankfurt/Oder, Akademie-Verlag, Berlin, 1983, pp. 231–243.

10 Crandall, S. H., and Kulvets, A., "Source Correlation Effects on Structural Response," in *Application of Statistics*, Krishnaiah, P. R., ed., North-Holland, 1977, pp. 163–182.

11 Lin, Y. K., *Probabilistic Theory of Structural Dynamics*, McGraw-Hill, New York, 1967.

12 Lazan, B. J., *Damping of Materials and Members in Structural Mechanics*, Pergamon Press, New York, 1968.

13 Laning, J. H., and Battin, R. H., *Random Processes in Automatic Control*, McGraw-Hill, New York, 1956.

14 Powell, A., in: *Random Vibration*, Crandall, S. H., ed., Technology Press, Cambridge, Mass., 1958, Chapter 8.

15 Pope, L. D., "On the Transmission of Sound Through Finite Closed Shells: Statistical Energy Analysis, Modal Coupling, and Nonresonant Transmission," *J. Acoust. Soc. Am.*, Vol. 50, 1971, pp. 1004–1018.

16 Bolotin, V. V., "An Asymptotic Method for the Problem of Eigenvalues for Rectangular Regions," *Problems of Continuum Mechanics* (Volume dedicated to N. I. Muskhelishvili), SIAM, 1961, pp. 56–68.

APPENDIX

Sums, Averages, and Asymptotes

Various sums, averages, and asymptotes are used in the text and the more important of these are considered here. Some of these have also been considered by Crandall [6].

$$\bullet A_{ij}/A_{ii} \to 0 \quad \text{as} \quad \Delta M \to \infty \quad \text{for} \quad i \neq j$$

where

$$A_{ij} \equiv \sum_{m=M}^{M+\Delta M-1} \psi_m(x_i,y_i)\psi_m(x_j,y_j) \quad (A\text{-}1)$$

Recall equations (7) and (8).

This result simply follows from the spatial oscillations of the modes of a typical structure. Over many modes, each $\psi_m(x_i, y_i)$ is equally likely to be positive or negative; hence the product sum tends to *oscillate about* zero unless the two points i and j are the same. Of course, if the two points are close together, but not identically the same, a larger number of modes will be required for the product sum to approach its oscillatory asymptote. Also the peak of the oscillation will increase as the two points, i and j, approach each other. Nevertheless, for sufficiently large ΔM, $A_{ij}/A_{ii} \to 0$ for $i \neq j$.

$$\bullet A_{ii} \equiv \sum_{m=M}^{M+\Delta M-1} \psi_m^2(x_i,y_i) \to C\Delta M \quad (A\text{-}2)$$

as $\Delta M \to \infty$ where C is independent of i and M.

As a prototype of this relationship, consider the natural modes of a uniform, rectangular, simply supported plate of length, a, and width, b.

$$\psi_m(x,y) = \sin\frac{m_x\pi x}{a}\sin\frac{m_y\pi y}{b} \quad (A\text{-}3)$$

where m_x, m_y are the integer indices for the mth plate mode. Although this may seem to be a rather special case, recall that for a high mode (large M), the natural mode shapes will tend to be independent of

- boundary support conditions (e.g., simply supported versus clamped versus free);
- geometrical shape (e.g., rectangular versus trapezoidal); and

Downloaded 02 May 2010 to 171.66.16.54. Redistribution subject to ASME license or copyright; see http://www.asme.org/terms/Terms_Use.cfm

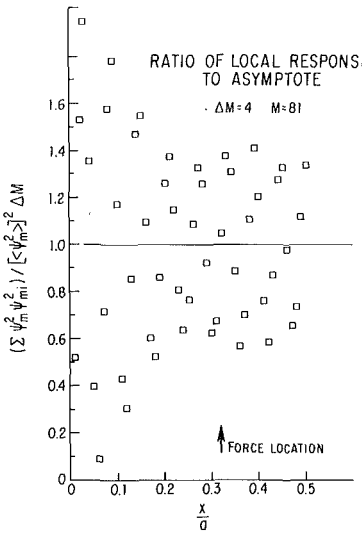


Fig. A-1(a)

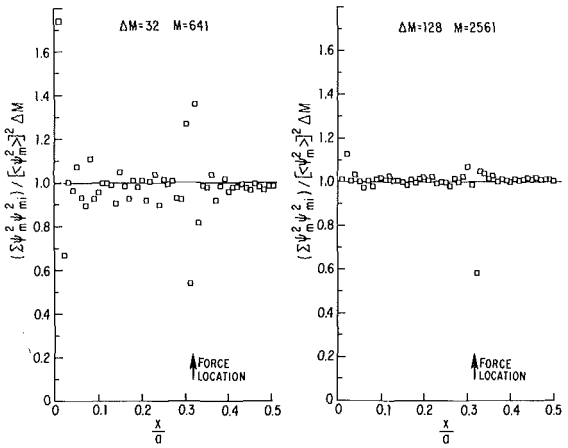


Fig. A-1(b-c)

Fig. A-1 Ratio of local response to asymptote versus response location

- mass distribution (for smoothly varying mass distributions).

See Bolotin, reference [16].

Hence equation (A-3) is, in fact, prototypical. Moreover, for our purposes, to demonstrate the validity of equation (A-2), it is sufficient to consider a one-dimensional plate (beam). The result of the summation in equation (A-2) is obtained analytically, i.e.,

$$A_{ii} \equiv \sum_{m=M}^{M+\Delta M-1} \sin^2 \frac{m\pi x_i}{a}$$

$$= \frac{1}{2}\Delta M - \frac{\sin\dfrac{\Delta M \pi x_i}{a} \cos\dfrac{(2M+\Delta M-1)\pi x_i}{a}}{2\sin\dfrac{\pi x_i}{a}} \qquad (A\text{-}4)$$

For fixed ΔM, equation (A-4) oscillates about $\Delta M/2$ as M varies. The value of A_{ii} will be bounded by

$$\frac{1}{2}\Delta M - \frac{\left|\sin\dfrac{\Delta M \pi x_i}{a}\right|}{2\sin\dfrac{\pi x_i}{a}} \le A_{ii} \le \frac{1}{2}\Delta M + \frac{\left|\sin\dfrac{\Delta M \pi x_i}{a}\right|}{2\sin\dfrac{\pi x_i}{a}} \qquad (A\text{-}5)$$

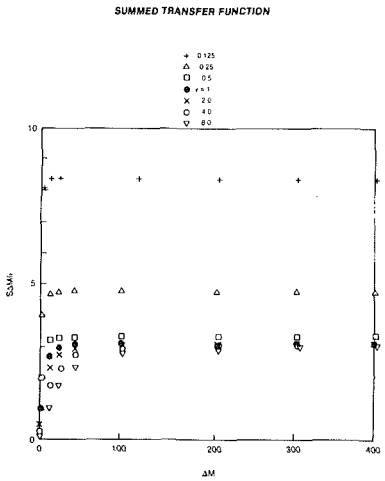


Fig. A-2 $S\Delta M/\epsilon$ versus ΔM

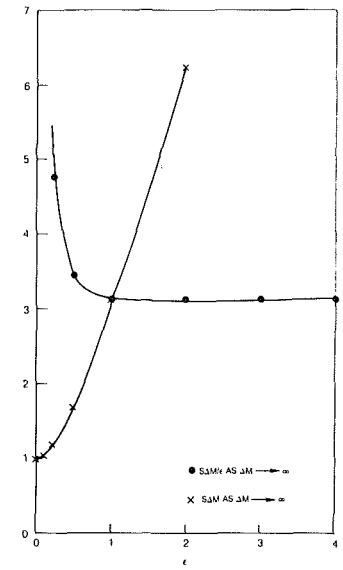


Fig. A-3 Asymptotic behavior of $S\Delta M$ versus ϵ

Hence as $\Delta M \to \infty$, A_{ii} tends to $\Delta M/2$, i.e.,

$$A_{ii} \to \frac{1}{2}\Delta M \quad \text{as} \quad \Delta M \to \infty \qquad (A\text{-}6)$$

Of course, $x_i = 0$ or a is pathological.

Equation (A-1) is considered next, again for a one-dimensional plate. The result is obtained analytically, i.e.,

$$A_{ij} = \frac{1}{2}\left[\frac{\sin\dfrac{\Delta M\pi(x_i - xj)}{2a}\cos\dfrac{\pi(2M+\Delta M-1)(x_i-xj)}{2a}}{\sin\dfrac{\pi(x_i-x_j)}{2a}}\right.$$

$$\left. - \frac{\sin\dfrac{\Delta M\pi(x_i+x_j)}{2a}\cos\dfrac{\pi(2M+\Delta M-1)(x_i+x_j)}{2a}}{\sin\dfrac{\pi(x_i+x_j)}{2a}}\right] \qquad (A\text{-}7)$$

For fixed ΔM, equation (A-7) oscillates about zero as M varies. Hence, from equations (A-5) and (A-7), the absolute value of A_{ij}/A_{ii} may be written as

Downloaded 02 May 2010 to 171.66.16.54. Redistribution subject to ASME license or copyright; see http://www.asme.org/terms/Terms_Use.cfm

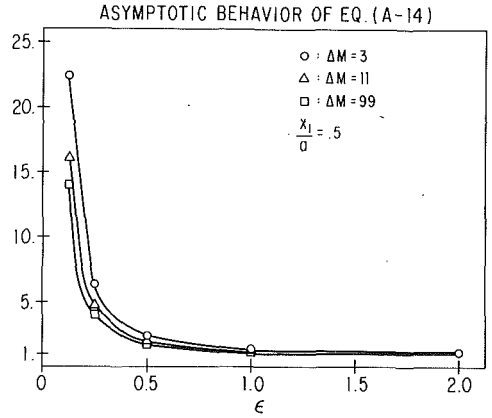


Fig. A-4 Asymptotic behavior of response to sinusoidal forces versus ϵ

$$\left|\frac{A_{ij}}{A_{ii}}\right| \leq \frac{\left|\dfrac{\sin\dfrac{\Delta M\pi(2x_i+\Delta x)}{2a}}{\sin\dfrac{\pi(2x_i+\Delta x)}{2a}}\right| + \left|\dfrac{\sin\dfrac{\Delta M\pi\Delta x}{2a}}{\sin\dfrac{\pi\Delta x}{2a}}\right|}{\Delta M - \dfrac{\left|\sin\dfrac{\Delta M\pi x_i}{a}\right|}{\sin\dfrac{\pi x_i}{a}}} \qquad (A\text{-}8)$$

where $\Delta x = x_j - x_i$. Hence as $\Delta M \to \infty$, A_{ij}/A_{ii} tends to zero.

The asymptotic behavior of equation (A-6) suggests the definition of a modal average of the mode shapes (squared). It is worthy of note that the modal average of the mode shapes (squared) for a single spatial point is equal to the spatial average of a single (high number) mode (squared), i.e.,

$$\cdot \sum_{m=M}^{M+\Delta M-1} \frac{\psi_m^2(x_i,y_i)}{\Delta M} = \frac{\iint \psi_M^2(x,y)dxdy}{\iint dxdy} \equiv <\psi_M^2> \qquad (A\text{-}9)$$

for any i as $\Delta M \to \infty$ as $M \to \infty$

This readily follows from equation (A-3). Recall equation (11), et seq. Also, in the same spirit, one may show that

$$\cdot \iint m_p \psi_M^2\, dxdy = M_p <\psi_M^2> \qquad (A\text{-}10)$$

for $M \to \infty$

where m_p is the (smoothly varying) plate mass/area and M_p is the total plate mass.

$$\cdot \sum_{m=M}^{M+\Delta M-1} \psi_m{}^2(x,y)\psi_m{}^2(x_i,y_i) \to [<\psi_m{}^2>]^2 \Delta M \qquad (A\text{-}11)$$

as $\Delta M \to \infty$

Again, without loss of generality, it is sufficient to consider a one-dimensional plate. Equation (A-11) then follows from the use of (A-3) in (A-11). In Figs. A-1(*a*), (*b*), and (*c*), the ratio of the two sides in (A-11) is shown for various ΔM and M for $x_i = a/\pi$. As can be seen, for $\Delta M \to \infty$, the ratio approaches 1. The exceptional situations are when $x = x_i$, $a - x_i$, 0, and a in which cases (A-11) does not follow. For $x = x_i$, $y = y_i$, the right-hand side of (A-11) is multiplied by $(3/2)^D$ where $D = 1$ or 2 for one or two dimensions, respectively, for large ΔM. Also see Crandall [6].

Perhaps the most subtle of the various sums and averages that are used in the text are the following (recall equation 28):

$S\Delta M(\Delta M, \epsilon)$

$$\equiv \sum_{m=-(\Delta M-1)/2}^{(\Delta M-1)/2} \frac{1}{\left[\left(\dfrac{\Delta\omega_m}{\zeta_m\omega_k}\right)^2 + 1\right]} \to \pi \frac{\omega_k}{\Delta\omega} \Delta M \zeta_m \qquad (A\text{-}12)$$

as

$$\Delta M \to \infty, \frac{\omega_k \zeta_m \Delta M}{\Delta\omega} \to \infty$$

Using $\Delta\omega_m = m\Delta\omega/\Delta M$ [recall equation (24) et seq], equation (A-12) becomes

$$S\Delta M \equiv \sum_{m=-(\Delta M-1)/2}^{(\Delta M-1)/2} \frac{1}{\left[\left(\dfrac{m}{\epsilon}\right)^2 + 1\right]} \to \pi\epsilon \qquad (A\text{-}13)$$

for $\epsilon \to \infty$ and $\Delta M \to \infty$

where

$$\epsilon \equiv \frac{\omega_k \zeta_m \Delta M}{\Delta\omega}$$

It is of interest to plot $S\Delta M$ versus ΔM for various ϵ to observe how the asymptote is approached. This is done in Fig. A-2. $S\Delta M$ may be thought of as the summed (normalized) transfer function for those resonant modes whose natural frequencies, ω_m, are within the effective frequency range, $\zeta_m\omega_\kappa$, of the exciting frequency ω_k. As is seen in Fig. A-2, the asymptote is approached more slowly as $\epsilon \to \infty$. Hence, the practical use of the asymptote is dependent on ϵ being large, say greater than 1, but not too large. For example, a large ΔM but small ζ_m would be appropriate. In Fig. A-3, $S\Delta M$ and $S\Delta M/\epsilon$ are plotted for $\Delta M \to \infty$ and various ϵ. This perhaps more clearly demonstrates the asymptotic behavior of $S\Delta M$ for large and small ϵ.

Finally consider the asymptote,

$$\cdot \sum_m \frac{\psi_{mi}{}^2}{\left[\left(\dfrac{m}{\epsilon}\right)^2 + 1\right]} \to \frac{1}{\Delta M} \sum_m \psi_{mi}{}^2 \sum_m \frac{1}{\left[\left(\dfrac{m}{\epsilon}\right)^2 + 1\right]} \qquad (A\text{-}14)$$

as $\Delta M \to \infty$

In Fig. A-4, the ratio of the right-hand side of (A-14) to the left-hand side is shown versus ϵ for various fixed ΔM. Recall ϵ is proportional to ΔM, see equation (25) et seq. In all results shown the lowest mode in the summation is taken to be the first beam mode. Note that the ratio approaches unity more rapidly as ΔM and ϵ increase. Note further that as ΔM increases, this implies increasing ϵ as well.

Downloaded 02 May 2010 to 171.66.16.54. Redistribution subject to ASME license or copyright; see http://www.asme.org/terms/Terms_Use.cfm

C. Pierre
Graduate Research Assistant,
Duke University,
Durham, N.C. 27706

A. A. Ferri
Visiting Scholar,
Duke University

E. H. Dowell
Dean of Engineering,
Duke University,
Durham, N.C.
Mem. ASME

Multi-Harmonic Analysis of Dry Friction Damped Systems Using an Incremental Harmonic Balance Method

A multi-harmonic, frequency domain analysis of dry friction damped systems is presented which uses an incremental harmonic balance method. When compared with time domain solution methods, it is found that the incremental harmonic balance method can yield very accurate results with some advantages over the time domain methods. Both one and two degree-of-freedom systems are studied.

1 Introduction

Many mechanical systems of interest are damped with the aid of dry friction. In some applications, for example turbomachinery and space structures, dry friction is the most important source of mechanical damping. The analysis of such systems is difficult due to the nonlinear nature of the damping law. The most widely used and the simplest model of dry friction, Coulomb damping, still presents formidable difficulties to the analyst. The Coulomb damping model assumes that when sliding occurs between two bodies in contact, the friction force is constant in magnitude and is directed so as to oppose the relative movement. The magnitude is assumed to be proportional to the normal force between the two bodies. Although the Coulomb model of dry friction renders the governing equations of motion piecewise linear, global solutions to forced excitation are difficult to obtain.

A number of techniques have been used in the past by various researchers. Among the earliest work is that of Den Hartog [1] where an "exact," steady-state, time domain solution is found for a single degree-of-freedom system. This method was later applied to a two degree of freedom with one dry friction damper by Yeh [2]. The exact method provides good results, but becomes impractical when dealing with many degrees of freedom and many dry friction dampers. It is also limited by the complications that arise in studying multi-stick motion (motion with more than two stops per cycle).

Other time domain methods have been investigated, for example [3]–[6]. These methods use numerical integration in time combined with some conditions to check for and simulate sticking. The numerical integration methods offer the advantages of being able to handle multiple sticking, multiple degrees of freedom and very complicated damping laws. There are, of course, some drawbacks to numerical integration. If a time step is chosen which is too large, it is possible to generate erroneous time histories which appear completely reasonable and well behaved. The automatic generation of parameter studies through numerical integration is difficult since the duration of the transient and the necessary size of the time step vary as the parameters change. For this reason, parameter studies, such as frequency response curves, are most often generated in a "point-by-point" manner.

Because of the nature of the dry friction nonlinearity, frequency domain analyses have in the past been limited to a single harmonic approximation. Global solutions to Coulomb damped systems require that the algebraic sign of the relative velocity be known over one cycle of oscillation, i.e., that sign (x') be known explicitly. When x' is approximated by a Fourier sum involving more than one harmonic, sign (x') can not be expressed in closed form. Nonetheless, the one harmonic approximation has been used by many researchers, for example [7]–[11]. This method has been shown to give adequate results for continuous slip motion, but not for stick-slip motion where higher harmonics become important.

In this paper, a multi-harmonic, frequency domain analysis of dry friction damped systems under forced harmonic excitation is presented. The analysis uses the incremental harmonic balance (IHB) method as described by Lau [12], [13] and outlined below. Incremental harmonic balance has been used to study a variety of problems in nonlinear dynamics. Here, the method is modified to analyze dry friction. The main advantage of applying an incremental approach to problems involving dry friction is that the sign function can be expanded for small increments in the motion.

The method is first applied to a one degree of freedom system with combined viscous and dry friction damping. The results are compared with those of existing time domain techniques and excellent agreement is found. Depending on the number of harmonics used in the analysis, the method

Contributed by the Applied Mechanics Division and presented at the Winter Annual Meeting, Miami, Fla., November 17–21, 1985, of THE AMERICAN SOCIETY OF MECHANICAL ENGINEERS.

Discussion on this paper should be addressed to the Publishing Department, ASME, United Engineering Center, 345 East 47th Street, New York, N.Y. 10017, and will be accepted until two months after final publication of the paper itself in the JOURNAL OF APPLIED MECHANICS. Manuscript received by ASME Applied Mechanics Division, June, 1984; final revision, December, 1984. Paper No. 85-WA/APM-16.

Copyright © 1985 by ASME
Downloaded 02 May 2010 to 171.66.16.54. Redistribution subject to ASME license or copyright; see http://www.asme.org/terms/Terms_Use.cfm

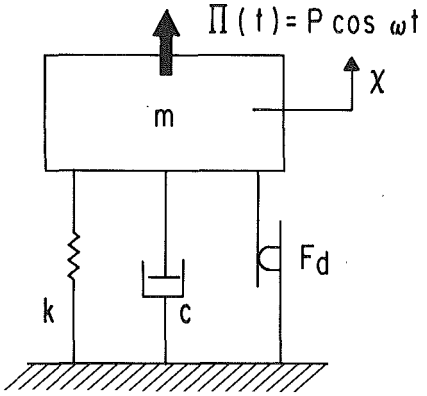


Fig. 1 Single degree of freedom dry friction damped system

gives good results even for motion with multiple sticking. It is also shown that the technique can be applied to multi-degree-of-freedom systems with multiple dry friction dampers. As an illustration, the case of a two degree of freedom system with two dry friction dampers is studied.

2 Method of Analysis: IHB Method

2.1 Nondimensionalized Equation of Motion. Consider a one degree of freedom system with combined viscous and dry friction damping under forced harmonic excitation of period $2\pi/\omega$: $\Pi(t) = P\cos\omega t$. The system is shown in Fig. 1.

The governing equation of motion is:

$$mx'' + F_d \text{sign} x' + cx' + kx = P\cos\omega t \tag{1}$$

where $' = d/dt$, F_d is given by a coefficient of friction times normal force to the sliding surfaces, and c is the viscous damping coefficient. Then, introducing:

- the force ratio $F = P/F_d$
- the dimensionless displacement $f = xk/F_d$
- the free vibration natural frequency of the spring-mass system $\omega_0 = (k/m)^{1/2}$
- the damping ratio $\zeta = c\omega_0/2k$

Equation (1) may be written as:

$$\frac{1}{\omega_0^2} f'' + \text{sign} f' + \frac{1}{\omega_0} 2\zeta f' + f = F\cos\omega t \tag{2}$$

Finally, considering the dimensionless time $\tau = \omega t$ and the reduced vibration natural frequency $\Omega = \omega/\omega_0$, equation (2) becomes:

$$\Omega^2 \ddot{f} + \text{sign}\dot{f} + 2\zeta\Omega\dot{f} + f = F\cos\tau \tag{3}$$

where $\dot{} = d/d\tau$

2.2 Incremental Harmonic Balance Method. The IHB method used to solve equation (3) was initially proposed by Lau in [12]. A great advantage of the method, among others, is that it deals easily with strong nonlinearities. The IHB method was used to treat a cubic type nonlinearity in [12], [13], and [14]. Nevertheless, the sign nonlinearity introduced by dry friction damping is of an entirely different kind, and its treatment requires further development of the IHB method.

The first step of the IHB method is a Newton-Raphson procedure: the current state of vibration corresponding to the excitation parameters Ω_0 and F_0 is denoted by $f_0(\tau)$. A neighboring state is reached through a parameter incrementation:

$$\begin{aligned} f &= f_0 + \Delta f \\ \Omega &= \Omega_0 + \Delta\Omega \\ F &= F_0 + \Delta F \end{aligned} \tag{4}$$

The next step is to substitute the expansions (4) into equation (3) and, neglecting the nonlinear terms of Δf, $\Delta\Omega$, and ΔF, to obtain a linearized incremental equation. The latter step is quite straightforward for a cubic (or any continuous) nonlinearity [12], [13]. With dry friction damping in the system, one has to establish a first order Taylor expansion of the nonlinear term sign $(\dot{f}_0 + \Delta\dot{f})$ of equation (3), which is obtained as follows.

The sign function may be expressed as:

$$\text{sign}(u) = -1 + 2H(u) \tag{5}$$

where $H(u)$ is the unit step function:

$$H(u) = \begin{cases} 0 & , u<0 \\ 1/2 & , u=0 \\ 1 & , u>0 \end{cases} \tag{6}$$

It is well known that the derivative of $H(u)$ is the Dirac delta function $\delta(u)$, which may be defined as:

$$\int_{-\infty}^{+\infty} \delta(x-a)g(x)dx = g(a) \tag{7}$$

Hence:

$$\frac{d}{du}\text{sign}(u) = 2\frac{d}{du}H(u) = 2\delta(u) \tag{8}$$

Rigorously, δ and H should be regarded as generalized functions whose derivatives are defined through distribution theory. Equation (8) is a well known result which may be found in books treating this subject [15], [16].

A first order Taylor expansion of the sign function is obtained using (8):

$$\text{sign}(u + \Delta u) = \text{sign}(u) + 2\delta(u)\Delta u \tag{9}$$

Then the nonlinear term of equation (3) may be expanded:

$$\text{sign}(\dot{f}_0 + \Delta\dot{f}) = \text{sign}\dot{f}_0 + 2\delta(\dot{f}_0)\Delta\dot{f} \tag{10}$$

and the linearized incremental equation obtained from (3), (4), and (10) is:

$$\begin{aligned} &\Omega_0^2\Delta\ddot{f} + [2\delta(\dot{f}_0) + 2\zeta\Omega_0]\Delta\dot{f} + \Delta f \\ &\qquad = R - 2\Omega_0\ddot{f}_0\Delta\Omega - 2\zeta\dot{f}_0\Delta\Omega + \cos\tau\Delta F \end{aligned} \tag{11a}$$

where:

$$R = -[\Omega_0^2\ddot{f}_0 + 2\zeta\Omega_0\dot{f}_0 + \text{sign}\dot{f}_0 + f_0 - F_0\cos\tau] \tag{11b}$$

R is the corrective term which goes to zero when the solution is reached.

Although equation (11) is linear, it has variable coefficients and thus is difficult to solve. Hence, an approximate solution will be obtained by assuming a periodic solution and using Galerkin's procedure, which is the second step of the method. The functions f_0 and Δf can be written as:

$$f_0(\tau) = \sum_{k=1,3}^{2N-1} (a_k \text{sink}\tau + b_k \text{cosk}\tau) \tag{12}$$

$$\Delta f(\tau) = \sum_{k=1,3}^{2N-1} (\Delta a_k \text{sink}\tau + \Delta b_k \text{cosk}\tau) \tag{13}$$

corresponding to a solution of period $2\pi -$ the forcing period. The even harmonics are identically zero, as can be shown by considering equation (3). N is the number of harmonics taken into account.

Galerkin's method is used with Δa_k's and Δb_k's as generalized coordinates:

$$\int_0^{2\pi} [\Omega_0^2\Delta\ddot{f} + (2\delta(\dot{f}_0) + 2\zeta\Omega_0)\Delta\dot{f} + \Delta f] \begin{bmatrix} \text{sink}\tau \\ \cdot \\ \cdot \\ \cdot \\ \text{cosk}\tau \end{bmatrix} d\tau$$

Downloaded 02 May 2010 to 171.66.16.54. Redistribution subject to ASME license or copyright; see http://www.asme.org/terms/Terms_Use.cfm

$$= \int_0^{2\pi} [R - 2\Omega_0 \ddot{f}_0 \Delta\Omega - 2\zeta \dot{f}_0 \Delta\Omega + \cos\tau \Delta F] \begin{bmatrix} \sin k\tau \\ \cdot \\ \cdot \\ \cdot \\ \cos k\tau \end{bmatrix} d\tau \qquad (14)$$

Let us define the amplitude vector by $\mathbf{a} = (a_1, \ldots, a_{2N-1}, b_1, \ldots, b_{2N-1})^T$ and its corresponding increment by $\Delta\mathbf{a} = (\Delta a_1, \ldots, \Delta b_1, \ldots)^T$ where bold face denotes a vector and T denotes a transpose. An incremental system of $2N$ linear equations in terms of the Δa_k's and the Δb_k's is obtained from equation (14):

$$[C]\Delta\mathbf{a} = \mathbf{R} + \Delta\Omega\mathbf{Q} + \Delta F\mathbf{P} \qquad (15)$$

where:

$$[C] = \begin{bmatrix} [C_1] & [C_{12}] \\ \hline [C_{21}] & [C_2] \end{bmatrix} \quad \mathbf{R} = \begin{bmatrix} \mathbf{R}_1 \\ \hline \mathbf{R}_2 \end{bmatrix} \quad \mathbf{Q} = \begin{bmatrix} \mathbf{Q}_1 \\ \hline \mathbf{Q}_2 \end{bmatrix} \quad \mathbf{P} = \begin{bmatrix} \mathbf{P}_1 \\ \hline \mathbf{P}_2 \end{bmatrix}$$

The expressions for $[C]$, $\mathbf{P}$, $\mathbf{Q}$, and $\mathbf{R}$ are given in detail in the Appendix, and the linear parts of the matrices and vectors are straightforward to obtain. Nevertheless, it is worth studying in detail the nonlinear parts of the elements of $[C]$ and of the components of $\mathbf{R}$.

Typically, these nonlinear terms are expressed by:

$$[C_1]_{ij}^{NL} = \int_0^{2\pi} 2\delta(\dot{f}_0) j \cos j\tau \sin i\tau \, d\tau \qquad (16)$$

$$\mathbf{R}_{1i}^{NL} = -\int_0^{2\pi} \text{sign}(\dot{f}_0) \sin i\tau \, d\tau \qquad (17)$$

similar expressions exist for $[C_{12}]^{NL}$, $[C_{21}]^{NL}$, $[C_2]^{NL}$ and $\mathbf{R}_2^{NL}$.

The evaluation of the latter integrals requires a knowledge of the zeros of the function $\dot{f}_0$. In the computer program, this is achieved at each iteration through a subroutine that uses the bisection and secant methods on the trigonometric function $\dot{f}_0$. It is interesting to note that, if N harmonics are considered for the amplitude, the maximum number of zeros for $\dot{f}_0$ is $2(2N-1)$. Let $\tau_1, \ldots, \tau_M$ be the M zeros of $\dot{f}_0$, and $s_1, s_2, \ldots, s_{M+1}$ be the sign of $\dot{f}_0$, respectively, in the intervals $[\tau_0, \tau_1] \ldots [\tau_M, \tau_{M+1}]$, with $\tau_0 = 0$ and $\tau_{M+1} = 2\pi$. Then Integral (17) is expressed by:

$$\mathbf{R}_{1i}^{NL} = \sum_{m=0}^{M} s_{m+1} \frac{1}{i} [\cos(i\tau_{m+1}) - \cos(i\tau_m)] \qquad (18)$$

Because of the presence of the Dirac function, there is no contribution to Integral (16), except at the instants τ_1 through τ_M. Integral (16) can be evaluated by considering the new variable $\dot{f}_0$, and one obtains:

$$[C_1]_{ij}^{NL} = \sum_{m=1}^{M} 2j \cos(j\tau_m) \sin(i\tau_m) \frac{1}{|\ddot{f}_0(\tau_m)|} \qquad (19)$$

2.3 Algorithm and Convergence. A current state of vibration of the system is defined by a triplet (f, Ω, F) solution of equation (3). From equation (12), one may note that the displacement f is represented in an equivalent manner by the converged amplitude vector $\mathbf{a}$, and may be characterized by its norm $A = \|\mathbf{a}\|$, the so-called total amplitude. Here the Euclidian norm is considered, whose square is proportional to the energy of the vibration.

One is primarily interested in the frequency response curves of the system for a constant force level, that is, the curves A versus Ω with F as a parameter, which implies $\Delta F = 0$ in equation (15). Then the frequency response curves may be obtained by incrementing Ω from point to point. This is the Ω-incrementation option, i.e., Ω remains constant through the iterative process at every point $\Delta\Omega = 0$. Hence, at every iteration, one has to solve:

$$[C]\Delta\mathbf{a} = \mathbf{R} \qquad (20)$$

which is done by matrix inversion.

Another possibility is to increment the total amplitude A from point to point. In this case, A remains constant through the iterative process, and one has to solve at every iteration:

$$\begin{cases} [C]\Delta\mathbf{a} = \mathbf{R} + \Delta\Omega\mathbf{Q} \\ \|\mathbf{a} + \Delta\mathbf{a}\| = \|\mathbf{a}\| \end{cases} \qquad (21)$$

A convenient method to solve the nonlinear system (21) is proposed in [14] and the reader is referred there for more details.

Depending on the local shape of the response curve, one of these two approaches is used. Hence, in order to obtain a point on a response curve, the set of linear equations (20) – possibly System (21) – is solved at each iteration, providing the data for the next iteration. The corrective vector $\mathbf{R}$ and the amplitude vector $\mathbf{a}$ – possibly the frequency Ω – are updated at each iteration. Convergence is reached when $\|\mathbf{R}\|$ is smaller than the convergence parameter.

An important feature of the computer program is that the number N of temporal harmonics used in the analysis may be varied from one run to another, since N is an element of the data for the program.

Although there is no theoretical limitation to the number of harmonics, there is obviously a computer time – hence, a cost – limitation. The required CPU time grows geometrically with the number of harmonics. Practically, a calculation with three harmonics is very affordable, while using six harmonics for the analysis can only be performed for a few cases that require an exceptional accuracy. As a rule, three harmonics – the first, third, and fifth – are usually used to obtain a very good accuracy at a very reasonable cost.

The above method leads to a very good convergence in most cases. Nevertheless, at very low frequency and low force level – i.e., when substantial sticking occurs – convergence may be very difficult to obtain. For in the sticking regions, flat portions of the time histories have to be approximated by a Fourier series representation. In these cases, a very small change in the amplitude vector $\mathbf{a}$ often implies a change in the number of zeros of $\dot{f}_0$, hence also implying a quite large change in the residue vector $\mathbf{R}$ due to the presence of the sign function. Another reason for the sensitivity of $\mathbf{R}$ is that, for a flat portion of a time history, the term sign $(\dot{f}_0)$ should be identically equal to zero, which is not the case if one uses a Fourier series representation, and no matter how small the amplitude of the velocity is, the corresponding contribution to the term sign $(\dot{f}_0)$ in $\mathbf{R}$ is always either 1 or -1.

In order to circumvent this problem, a multi-dimensional secant method [17] is used to solve directly the equations $\mathbf{R} = \mathbf{0}$ when the Newton-Raphson procedure fails to converge. Through the combined use of these two methods, convergence is achieved in all cases.

3 Results

The IHB method can be used to obtain easily plots of amplitude versus frequency of excitation. The amplitudes of vibration may be expressed either as peak amplitudes per cycle or as the norm of the vector of harmonic components. When the norm of the harmonic components is used, the amplitude is indicative of the total energy of the motion. The effect of various parameters on frequency response curves can be systematically studied. Here, the influence of force am-

Downloaded 02 May 2010 to 171.66.16.54. Redistribution subject to ASME license or copyright; see http://www.asme.org/terms/Terms_Use.cfm

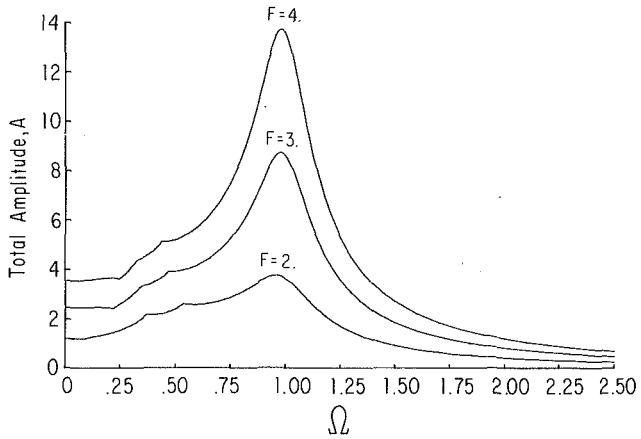


Fig. 2 Frequency response for various levels of force and $\zeta = .1$

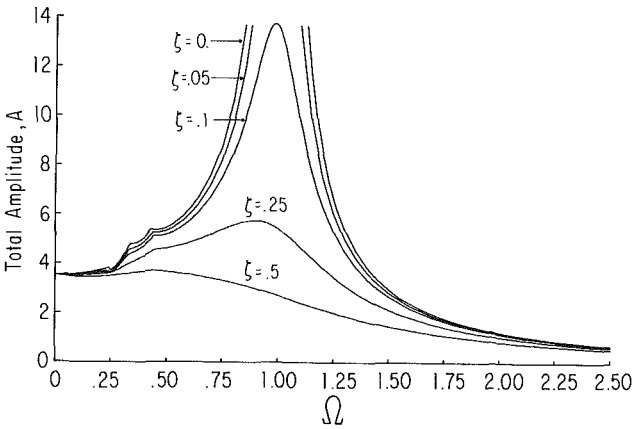


Fig. 3 Influence of viscous damping on the frequency response, for $F = 4$.

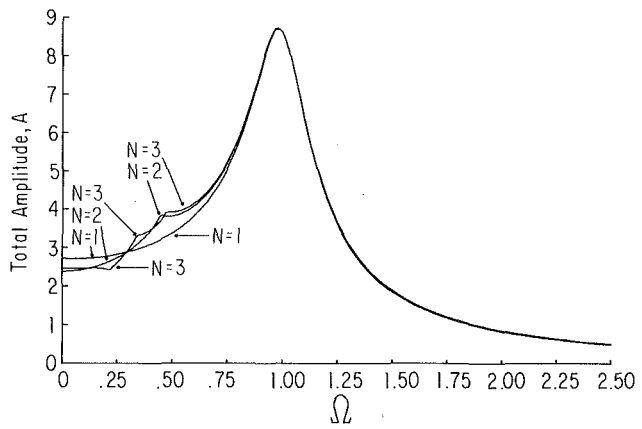


Fig. 4 Influence of the number of harmonic terms on the frequency response, for $F = 3.$ and $\zeta = .1$

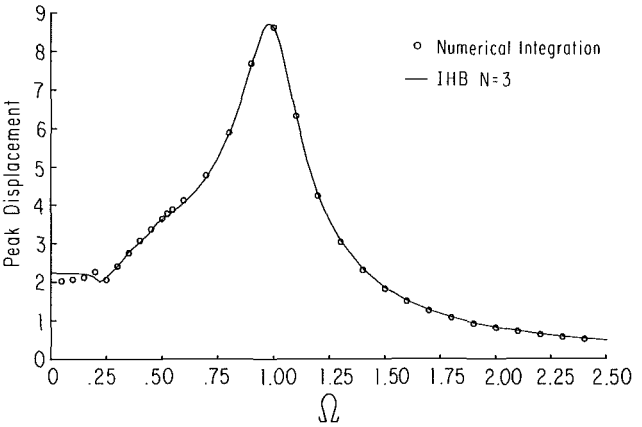


Fig. 5 Comparison of peak displacements for 3 harmonic IHB and time integration methods, for $F = 3.$ and $\zeta = .1$

plitude, viscous damping and number of harmonics included in the IHB method is studied.

The frequency response for a viscous damping ratio of 0.1 and for various levels of force is shown in Fig. 2. Three harmonics are used and the total amplitude A, as defined before, refers to the norm of the vector of harmonic components. Due to the nondimensionalization explained above, F represents the ratio of exciting force to dry friction force. Therefore, an increase in force level may be thought of as a decrease in the amount of dry friction. As discussed above, the IHB method uses an initial guess of the amplitude vector and iterates until convergence is achieved. In the generation of the above curves, the rate of convergence is improved by choosing the initial guess of the amplitude vector to be the converged vector from a nearby frequency. Specifically, as the frequency is incremented (or decremented), the previous solution for **a** is used as the initial guess for the current frequency step. The size of the frequency step can vary over the frequency range, $0-2.5$. When sticking begins to occur a smaller step size was found to be necessary to maintain a fast convergence rate.

Figure 3 shows the dependence of the frequency response on the amount of viscous damping. A force of $F = 3$ and three harmonics are used. The accuracy of the results shown in Figs. 2 and 3 will be discussed subsequently. Figure 4 shows the effect of varying the number of harmonics on the frequency response results. The one harmonic result is exactly the solution that would have been obtained by first order harmonic balance or equivalent first order frequency domain techniques. It is seen that for the range of frequencies where stickfree motion exists, $\Omega > .5$, there is little difference between the results for different numbers of harmonics. As sticking becomes more pronounced, $0 < \Omega < .5$, more harmonics are necessary to approximate the motion.

The accuracy of the multi-harmonic IHB method was tested by comparing the results against those of existing time domain analyses. In this case, a fourth order Runge-Kutta numerical integration routine was used to provide an accurate basis for comparison. The results can be compared in terms of amplitudes, phases and waveshapes of the motion. Figure 5 shows the frequency response curve for $F = 3.0$, $\zeta = 0.1$, calculated by the two methods. The amplitude used as a basis of comparison is the peak displacement per cycle. Comparing the total amplitudes at various frequencies would also be possible, however it would require calculating the mean squared value of the time domain solution at each frequency of comparison. Recall that the norm of the amplitude vector is proportional to the total energy of the motion. Specifically, $MS = 1/2 \ \|a\|^2$, hence, $\|a\| = \sqrt{2}\text{RMS}$. As seen in Fig. 5, excellent agreement is observed except at very low frequencies, $\Omega < 0.2$, where the maximum difference is about 10 percent. The low frequency motion is characterized by the presence of many sticking regions, or stops, per cycle. As Ω approaches zero, the number of stops per cycle grows without bound [3]. This would account for the relatively poor agreement of the two methods at low frequencies.

It is interesting to compare the frequency response curves of total amplitude and peak displacement. In Fig. 6 the total and peak amplitudes are compared for the case $F = 3$, $\zeta = 0.1$, number of harmonics $= 3$. One can see that the two curves virtually coincide for $\Omega > 0.5$ and diverge somewhat for $\Omega < 0.5$. As verified by numerical integration, the system begins to stick at approximately this frequency. To simulate

Downloaded 02 May 2010 to 171.66.16.54. Redistribution subject to ASME license or copyright; see http://www.asme.org/terms/Terms_Use.cfm

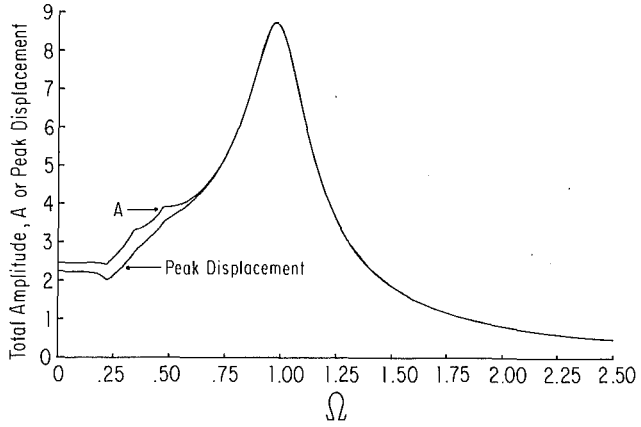


Fig. 6 Comparison of total amplitude and peak displacement, for $F = 3.$, $\zeta = .1$, and $N = 3$

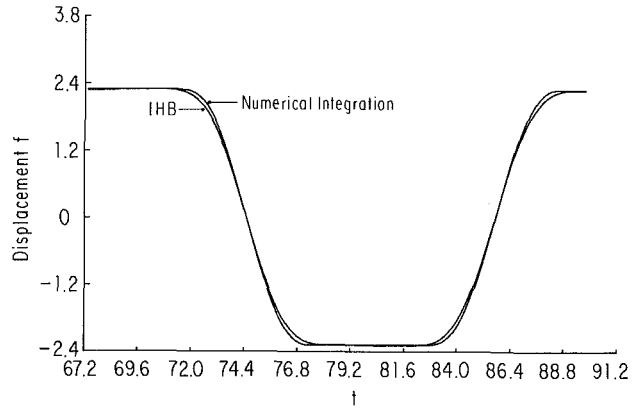


Fig. 7 Comparison of time histories for 3 harmonic IHB and time integration, for $F = 3.$, $\Omega = .28$, and $\zeta = .1$.

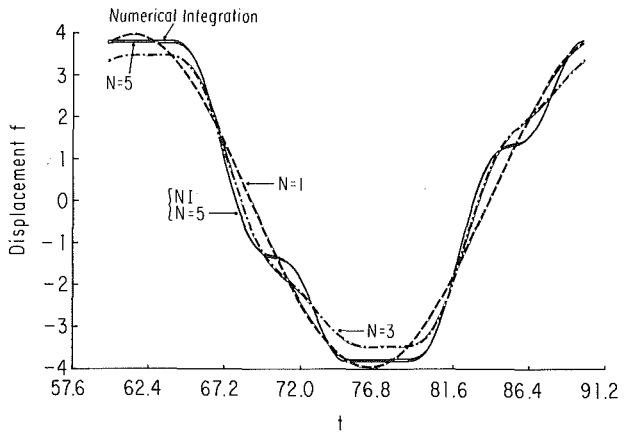


Fig. 8 Comparison of time histories for 1,3, and 5 harmonic IHB and time integration, for $F = 4.$, $\Omega = .21$, and $\zeta = 0$

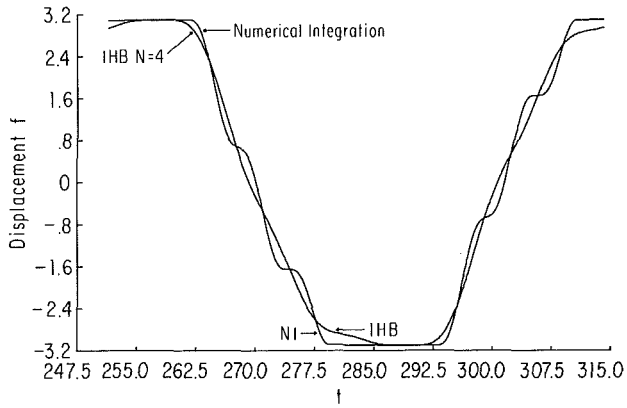


Fig. 9 Comparison of time histories for 4 harmonic IHB and time integration, for $F = 4.$, $\Omega = .1$, and $\zeta = 0$

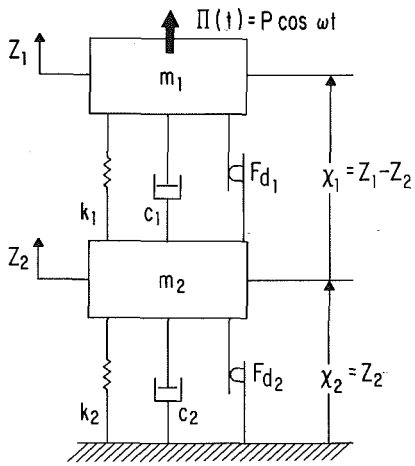


Fig. 10 Two degree of freedom dry friction damped system

sticking, the harmonics must add in such a way that a "flat-topped" displacement waveform is produced. This necessitates that the total amplitude be greater than the peak displacement. One can also see that on the frequency response of total amplitude, there are two slight sub-resonances which are not present on the peak displacement curve. These sub-resonances are caused by an effective decrease in the amount of Coulomb damping at those frequencies. This decrease is due to an increase in the percentage of sticking time per cycle, while there is no appreciable increase in peak displacement. The sub-resonances reflect the increase in energy, or in the MS displacement, at those frequencies.

An important check on the accuracy of the IHB method is a comparison of the IHB predicted waveforms for displacement and the waveforms obtained from numerical integration. This determines how well the IHB method can predict the occurrence and duration of sticking. The IHB results are converted to time histories, and are compared to the time histories generated by numerically integrating equation (3) until steady-state is achieved. Since both methods assume a forcing of $F\cos\tau$, the two time histories should not only display similar waveforms for displacement, but should also be in phase with each other. For this reason, a comparison of waveform between the two methods also provides a comparison of phase prediction.

In Fig. 7, time histories are compared for the case where $F = 3.0$, $\Omega = 0.28$, $\zeta = 0.1$. Three harmonics are used in the IHB analysis. The amplitude, waveform and phase are seen to be in excellent agreement. It is seen that, even for as few as three harmonics, the IHB results closely simulate the flat-topped waveform which characterizes sticking. The waveforms for the case $F = 4.$, $\Omega = 0.21$, $\zeta = 0$ and various numbers of harmonics are shown in Fig. 8. It is seen that one harmonic alone does not provide accurate data for amplitude, phase and waveform. With three harmonics used in the IHB analysis, there is good agreement in amplitude and phase, but multiple stickings and inflections per cycle are not predicted. As more harmonics are added, the IHB results converge to the numerical integration result. Figure 9 is an example of a case where many stops and/or inflections take place over one cycle. Again good agreement in amplitude and phase is observed. The three harmonic IHB result resembles a smooth three frequency fit to the relatively jagged numerical in-

Downloaded 02 May 2010 to 171.66.16.54. Redistribution subject to ASME license or copyright; see http://www.asme.org/terms/Terms_Use.cfm

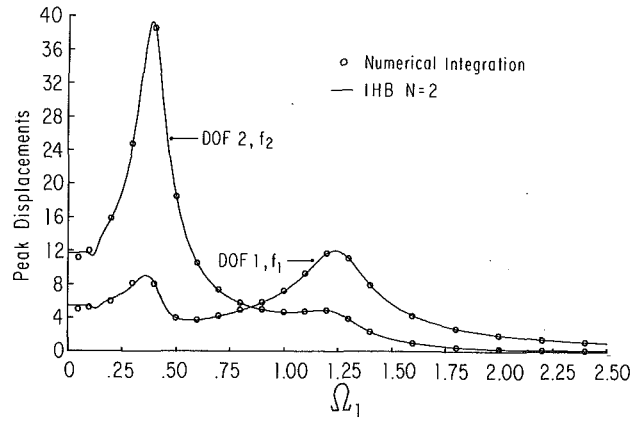


Fig. 11 Comparison of peak displacements for 2 harmonic IHB and time integration methods, for a 2 DOF system. $F=6.$, $\Omega_2/\Omega_1=2.$, $\zeta_1=.05$, $\zeta_2=.2$, $\beta=2.$, $\mu=.5$.

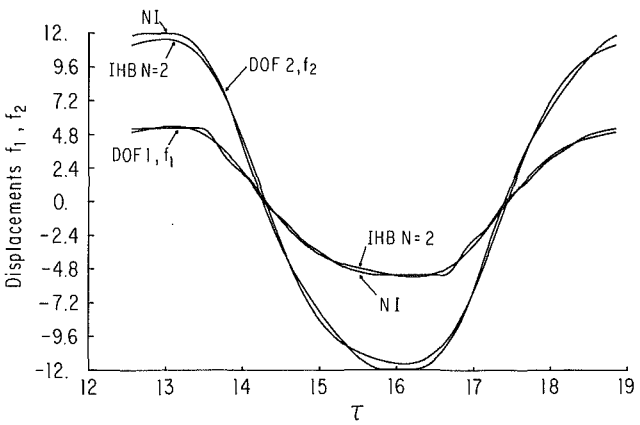


Fig. 12 Comparison of time histories for 2 harmonic IHB and time integration, for a 2 DOF system, at $\Omega_1=.1$. $F=6.$, $\Omega_2/\Omega_1=2.$, $\zeta_1=.05$, $\zeta_2=.2$, $\beta=2.$, $\mu=.5$.

tegration result. This would imply that IHB should not be used when fine details of multiple stop motion are desired. It should also not be used if accurate values for percentage of stick per cycle are needed.

There are a number of advantages to the IHB method over other existing techniques. The method yields accurate results directly in the frequency domain with frequency content and means square value readily displayed. Numerical integration, on the other hand, requires additional effort to obtain the frequency content – by means of a Fast Fourier Transform. Frequency response plots and other parameter variations can be easily produced with the IHB method by incrementing a particular parameter and using information from the previous step to increase the rate of convergence at each point. The capability to consider multi-harmonics allows it to give good results, in terms of amplitude, phase and waveform, even for cases where stick/slip motion occurs. Since the algorithm is developed for any number of harmonics the user can specify the number of harmonics desired as an input parameter and is only limited by computation time considerations. Unlike the numerical integration techniques, the IHB method also provides a means of determining when it has converged. Convergence is indicated by the relative magnitude of the residue vector. When the norm of this vector is small, the best estimate of the actual solution has been obtained for the number of harmonics considered. The method has a number of advantages over the exact method of solution as well. The IHB algorithm is valid for all types of stick/slip motion, while the exact method requires a different algorithm depending on the number of stops per cycle. Motion with multiple sticks per cycle would be quite difficult to solve for exactly, since the number of unknowns grows with each additional stop per cycle. The situation is further complicated since, as seen in [3], the frequency ranges over which different numbers of stops per cycle occur grow smaller as the number of stops per cycle increases. The algorithms dealing with many stops per cycle, therefore, would only be valid over very small ranges of frequency. The exact method also appears to be not easily extended to systems with multi-degrees-of-freedom and multiple dry friction dampers. Indeed the case of multiple dry friction dampers has not yet been attempted with the exact method, to the authors' knowledge. In the following section, the IHB method is applied to a two degree-of-freedom system with two dry friction dampers to illustrate the extension to multi-DOFs.

4 IHB Analysis of a Two Degree-of-Freedom System

The extension of the IHB method to analyze the two degree-of-freedom system with two dry friction dampers shown in Fig. 10 is straightforward. Note that an appropriate choice of coordinates is essential to being able to expand the sign terms for small increments. The governing equations of motion for this system are given by:

$$\begin{cases} m_1x_1''+m_1x_2''+c_1x_1'+k_1x_1+F_{d_1}\,\mathrm{sign}x_1'=P\cos\omega t \\ m_2x_2''-c_1x_1'+c_2x_2'-k_1x_1+k_2x_2-F_{d_1}\,\mathrm{sign}x_1'+F_{d_2}\,\mathrm{sign}x_2'=0 \end{cases} \tag{22}$$

After nondimensionalizing, they become:

$$\begin{cases} \Omega_1^2\ddot{f}_1+\dfrac{\mu}{\beta}\Omega_2^2\ddot{f}_2+2\zeta_1\Omega_1\dot{f}_1+\mathrm{sign}\dot{f}_1+f_1=F\cos\tau \\ \Omega_2^2\ddot{f}_2-2\zeta_1\beta\Omega_1\dot{f}_1+2\zeta_2\Omega_2\dot{f}_2-\beta\mathrm{sign}\dot{f}_1+\mathrm{sign}\dot{f}_2 \\ \qquad -\beta f_1+f_2=0 \end{cases} \tag{23}$$

Where the new parameters introduced are defined as follows:

$$f_i=\frac{x_ik_i}{F_{d_i}} \quad \omega_i^2=\frac{k_i}{m_i} \quad \zeta_i=\frac{c_i\omega_i}{2k_i} \quad \Omega_i=\frac{\omega}{\omega_i} \quad i=1,2$$

$$\beta=\frac{F_{d_1}}{F_{d_2}} \quad \mu=\frac{m_1}{m_2} \quad F=\frac{P}{F_{d_1}} \quad \tau=\omega t \tag{24}$$

The IHB method is applied to the above system yielding a system of the same form as (15)

$$[C]\Delta\mathbf{a}=\mathbf{R}$$

where now **a** represents the sine and cosine portions of the two displacements. The dimension of the above system is $4*N$. For example, if two harmonics are considered for f_1 and f_2, $[C]$ will be 8×8. Computationally, this would be equivalent to taking 4 harmonics in the one DOF case. However, usually one expects the latter case to converge less rapidly because of the higher harmonic content of the solution.

An extensive study of the two-degree-of-freedom dry friction damped system is probably deserving of a paper in and of itself. Here, we study only a particular set of parameter values to demonstrate the performance of the IHB method.

Figure 11 shows the frequency response curves for each of the two degrees of freedom, for the case: $F=6.$, $\zeta_1=.05$, $\zeta_2=.2$, $\beta=2.$ $\mu=.5$, $\Omega_2/\Omega_1=2$. The solid line represents the IHB results with the peak displacements plotted versus Ω_1. The peak displacements calculated by numerical integral are represented by circles. Only two harmonics per DOF are

Downloaded 02 May 2010 to 171.66.16.54. Redistribution subject to ASME license or copyright; see http://www.asme.org/terms/Terms_Use.cfm

considered in the IHB analysis. It is seen that very good agreement exists between the two sets of results. Figure 12 compares the time histories generated from the coefficients of the IHB analysis with those generated from numerical integration at $\Omega_1 = 0.1$. At this frequency, both dry friction dampers undergo two stops per cycle. Though only two harmonics are considered for each DOF, it is still seen that good agreement in waveforms and phase can be obtained.

5 Conclusion

The IHB method has been successfully applied to dry friction damped systems of one and two degrees of freedom. The expansion of the sign nonlinearity for small increments in its argument is the key to making this multi-harmonic, frequency domain solution technique possible. The method is found to be very accurate when compared with existing time domain techniques. Though the method can consider any number of harmonics, there is, naturally, a tradeoff between level of accuracy and computational cost. In general, three temporal harmonics were found to be adequate for good accuracy at a reasonable cost.

Quantitative comparisons of computer costs between the IHB method and numerical integration reveal that there is no clear cost advantage of one method over the other. The relative computational performance depends on many factors including: frequency range, amount of sticking present, desired level of accuracy, number of frequency points desired (for frequency response plots) and the value of other parameters (ζ,F) which among other things determines the duration of the transient.

Although it does not provide detailed information on stick/slip motion, the IHB method does provide good results for amplitude and phase. All types of stick/slip motion, i.e., any number of stops per cycle, may be studied using a single algorithm. This makes the method very advantageous for the generation of frequency response cycles and other types of parameter studies.

References

1 Den Hartog, J. T., "Forced Vibrations with Combined Coulomb and Viscous Friction," *Trans ASME*, 1931, Paper APM-53-9, pp. 107-115.

2 Yeh, G. C. K., "Forced Vibrations of a Two-Degree-of-Freedom System with Combined Coulomb and Viscous Damping," *J. Acoustical Soc. of America*, Vol. 39, 1966, pp. 14-24.

3 Pratt, T. K., and Williams, R., "Non-Linear Analysis of Stick/Slip Motion," *J. Sound and Vibration*, Vol. 74, No. 4, 1981, pp. 531-542.

4 Zmitrowicz, A., "A Vibration Analysis of a Turbine Blade System Damped by Dry Friction Forces," *Int. J. Mech. Sci*, Vol. 23, No. 12, 1981, pp. 741-761.

5 Hunt, D., Adams, W., and Bock, T., "Dynamic Analysis of Structures with Friction Forces at Sliding Junctures," *J. Spacecraft*, Vol. 21, No. 2, 1984, pp. 175-179.

6 Shearer, J. L., "Digital Simulation of a Coulomb-Damped Hydraulic Servosystem," ASME *Journal of Dynamic Systems, Measurement and Control*, Vol. 105, No. 4, 1983, pp. 215-221.

7 Sinha, A., and Griffin, J. H., "Friction Damping of Flutter in Gas Turbine Engine Airfoils," *AIAA J. Aircraft*, Vol. 20, No. 4, 1983, pp. 372-376.

8 Sinha, A., and Griffin, J. H., "Effects of Static Friction on the Forced Response of Frictionally Damped Turbine Blades," ASME *Journal of Engineering for Gas Turbines and Power*, Vol. 106, No. 1, 1984, pp. 65-69.

9 Dowell, E. H., "The Behavior of a Linear, Damped Modal System with a Nonlinear Spring-Mass-Dry Friction Damper System Attached," *J. of Sound and Vibration*, Vol. 89, No. 1, 1983, pp. 65-84.

10 Ferri, A. A., and Dowell, E. H., "The Behavior of a Linear, Damped Modal System with a Non-Linear Spring-Mass-Dry Friction Damper System Attached, Part II," To be published in the *J. of Sound and Vibration*.

11 Jezequel, L., "Structural Damping by Slip in Joints," ASME *Journal of Vibration, Acoustics, Stress, and Reliability in Design*, Vol. 105, No. 4, 1983, pp. 497-504.

12 Lau, S. L., Cheung, Y. K., and Wu, S. Y., "A Variable Parameter Incremental Method for Dynamic Instability of Linear and Nonlinear Elastic Systems," ASME JOURNAL OF APPLIED MECHANICS, Vol. 49, Dec. 1982, pp. 849-853.

13 Lau, S. L., Cheung, Y. K., and Wu, S. Y., "Incremental Harmonic Balance Method with Multiple Time Scales for Aperiodic Vibration of Nonlinear Systems," ASME JOURNAL OF APPLIED MECHANICS, Vol. 50, December 1983, pp. 871-876.

14 Pierre, C., and Dowell, E. H., "A Study of Dynamic Instability of Plates by an Extended Incremental Harmonic Balance Method," To be published in the ASME JOURNAL OF APPLIED MECHANICS.

15 Schwartz, L., *Théorie des distributions*, Hermann, Paris, 1966.

16 Lighthill, M. J., *Introduction to Fourier Analysis and Generalized Functions*, Cambridge University Press, 1958.

17 Wolfe, Phillip, "The Secant Method for Simultaneous Non-linear Equations," Communications of the ACM, Vol. 2, 1959.

APPENDIX

$$[C_1]_{ij} = \int_0^{2\pi} [-\Omega_0^2 j^2 \sin j\tau + 2\delta(\dot{f}_0) j \cos j\tau + 2\zeta\Omega_0 j \cos j\tau + \sin j\tau] \sin i\tau d\tau$$

$$[C_{12}]_{ij} = \int_0^{2\pi} [-\Omega_0^2 j^2 \cos j\tau - 2\delta(\dot{f}_0) j \sin j\tau - 2\zeta\Omega_0 j \sin j\tau + \cos j\tau] \sin i\tau d\tau$$

$$[C_{21}]_{ij} = \int_0^{2\pi} [-\Omega_0^2 j^2 \sin j\tau + 2\delta(\dot{f}_0) j \cos j\tau + 2\zeta\Omega_0 j \cos j\tau + \sin j\tau] \cos i\tau d\tau$$

$$[C_2]_{ij} = \int_0^{2\pi} [-\Omega_0^2 j^2 \cos j\tau - 2\delta(\dot{f}_0) j \sin j\tau - 2\zeta\Omega_0 j \sin j\tau + \cos j\tau] \cos i\tau d\tau$$

$$\mathbf{R}_{1_i} = \int_0^{2\pi} -[\Omega_0^2 \ddot{f}_0 + \operatorname{sign}\dot{f}_0 + 2\zeta\Omega_0 \dot{f}_0 + f_0 - F_0 \cos\tau] \sin i\tau d\tau$$

$$\mathbf{R}_{2_i} = \int_0^{2\pi} -[\Omega_0^2 \ddot{f}_0 + \operatorname{sign}\dot{f}_0 + 2\zeta\Omega_0 \dot{f}_0 + f_0 - F_0 \cos\tau] \cos i\tau d\tau$$

$$\mathbf{Q}_{1_i} = \int_0^{2\pi} [-2\Omega_0 \ddot{f}_0 - 2\zeta \dot{f}_0] \sin i\tau d\tau$$

$$\mathbf{Q}_{2_i} = \int_0^{2\pi} [-2\Omega_0 \ddot{f}_0 - 2\zeta \dot{f}_0] \cos i\tau d\tau$$

$$\mathbf{P}_{1_i} = \int_0^{2\pi} \cos\tau \sin i\tau d\tau$$

$$\mathbf{P}_{2_i} = \int_0^{2\pi} \cos\tau \cos i\tau d\tau$$

Downloaded 02 May 2010 to 171.66.16.54. Redistribution subject to ASME license or copyright; see http://www.asme.org/terms/Terms_Use.cfm

Stochastic Response of Nonlinear Dynamic Systems Based on a Non-Gaussian Closure[1]

R. A. Ibrahim
Associate Professor.
Mem. ASME

A. Soundararajan
Graduate Student.

H. Heo
Graduate Student.

Texas Tech University,
Department of Mechanical Engineering,
Lubbock, Texas 79409

The random response of nonlinear dynamic systems involving stochastic coefficients is examined. A non-Gaussian closure scheme is outlined and employed to resolve an observed contradiction of the results obtained by other techniques. The method is applied to a system possessing nonlinear damping. The stationary response is obtained by numerical integration of the closed differential equations of the moments (up to fourth order). An interesting feature of the numerical results reveals the existence of a jump in the response statistic functions. This new feature may be attributed to the fact that the non-Gaussian closure more adequately models the nonlinearity, and thus results in characteristics that are similar to those of deterministic nonlinear systems. The results are compared with solutions derived by the Gaussian closure and stochastic averaging method.

1 Introduction

The random response analysis of dynamic nonlinear systems is not a simple task and depends on several factors such as the type of nonlinearity inherent to the system and the nature of the excitation. In particular the complexity of the analysis is recognized for nonlinear systems that are subjected to random parametric excitation. In most cases it is not possible to derive a solution for the response transition probability described by the Fokker Planck equation. Furthermore, the differential equations of the response statistic functions (such as moments, semi-invariants, or quasimoments) form an infinite coupled set in which the differential equations of a certain order moment contain higher-order moment terms.

With reference to random parametric vibration of nonlinear systems, approximate solutions were obtained (Ibrahim, 1978) by employing a Gaussian closure scheme (based on the assumption that the response is "nearly" Gaussian). However, these solutions were found in contradiction with those obtained by using the Stratonovich stochastic averaging method (Ariarathnam, 1980 and Ibrahim and Soundararajan, 1983). It was found that the nontrivial solution obtained by using the Gaussian closure exists for all excitation levels defined by the domain $D/2\zeta > 1$, while the stochastic averaging solution exists for $D/2\zeta > 2$, where $2D$ is the spectral density of the parametric excitation and ζ is the linear damping factor of the system.

The application of Gaussian closure schemes to nonlinear systems with random Gaussian coefficients is not valid since the response is not Gaussian distributed. A proper treatment of the infinite hierarchy problem is to develop a non-Gaussian closure scheme to truncate the differential equations of the response statistical functions to an acceptable degree of approximation. The validity of this approach can be examined by inspecting the properties of the response statistics of all orders involved in the analysis, such as the non-negativeness of even order moments and whether the moments satisfy Schwarz's inequality.

Although the concept of developing an asymptotic expansion of a non-Gaussian probability density was established 40 years ago (Cramer, 1946) in a form of Edgeworth or Gram-Charles expansion, it has not been employed until recently in nonlinear control and dynamic systems. Kuznetsov, et al. (1960), Stratonovich (1963), and Bover (1978) developed Edgeworth expansions in terms of quasimoments for one and multidimensional processes. Sperling (1979) established a set of linear differential equations for the response quasimoments of discrete nonlinear systems excited by white noise. Dashevskii (1967), Dahevskii and Liptser (1967), Nakamizo (1970), and Assaf and Zirkle (1976) derived truncated asymptotic expansion in terms of the semi-invariants. It was indicated that the expansion is successful if it converges as the order of semi-invariant increases. Beaman and Hedrick (1981) extended the statistical linearization technique to a nonlinear set of stochastic differential equations of the Itô type. Their approach assumes an expansion of a multidimensional probability density function in terms of derivatives of multidimensional Gaussian probability density function.

The non-Gaussian approaches were employed to analyze the response of first and second-order nonlinear systems with constant coefficients and subjected to external random excitation (Bover, 1978, Assaf and Zirkle, 1976, Crandall, 1980,

[1]This research is supported by a grant from the National Science Foundation under grant no. MEA-8313572.

Contributed by the Applied Mechanics Division and presented at the Winter Annual Meeting, Miami, Fla., November 17–21, 1985 of The American Society of Mechanical Engineers.

Discussion on this paper should be addressed to the Editorial Department, ASME, United Engineering Center, 345 East 47th Street, New York, N.Y. 10017, and will be accepted until two months after final publication of the paper itself in the Journal of Applied Mechanics. Manuscript received by ASME Applied Mechanics Division, June, 1984; final revision, December, 1984. Paper No. 85-WA/APM-6.

Copyright © 1985 by ASME
Downloaded 02 May 2010 to 171.66.16.54. Redistribution subject to ASME license or copyright; see http://www.asme.org/terms/Terms_Use.cfm

1981). These applications were confined to one-dimensional processes and claimed to be not robust procedures (Crandall and Zhu, 1983). However, the response of several vibrating systems is repesented by a mulitdimensional process and, therefore, there is a strong need to develop a reliable and versatile procedure to handle problems involving various types of nonlinearties and random parametric coefficients. One of the main purposes of this investigation is to implement the basic work of Assaf and Zirkle to establish such a procedure.

This paper outlines a first-order non-Gaussian closure scheme based on the Edgeworth asymptotic expansion in terms of the semi-invariants. The procedure is demonstrated by an example of a dynamic system with linear-plus-cubic damping and subjected to parametric random excitation. The numerical results indicate that the system response statistics are bounded. The mean square of the system displacement is found to be closer to the stochastic averaging solution than the Gaussian closure response, for excitation levels exceeding a critical level below which the system does not oscillate. Another interesting feature of the non-Gaussian closure solution is that all the response statistics exhibit a jump in their values at a critical excitation level. The jump phenomenon was not predicted by other methods.

2 Analysis of the Stochastic Response

Consider the dynamic response of a nonlinear system, subjected to parametric random excitation, described by the differential equation of motion

$$\ddot{Y}+Y=\psi\{Y,\dot{Y},\ddot{Y},W(\tau)\} \tag{1}$$

where Y is the response displacement (nondimensional), a dot denotes differentiation with respect to the time parameter $\tau=\omega_n t$, ω_n is the system natural frequency, and t is the real time. The function $\psi\{\ \}$ encompasses terms of small order such as the linear damping force, all types of nonlinearties (such as stiffness, damping, and inertia), and the parametric random excitation $W(\tau)$. $W(\tau)$ is a stationary wide-band random process and may appear as a coefficient of linear and nonlinear terms. This excitation is assumed to have zero mean with a smooth spectral density $2D$ up to some frequency $\omega >> \omega_n$. In this case, equation (1) may be approximated by a set of equivalent Itô equations and the response coordinates (displacement and velocity) will constitute a Markov process. Introducing the transformation $Y=X_1$ and $\dot{Y}=X_2$ and removing $\ddot{Y}$ from ψ by successive elimination, equation (1) can be written in terms of the two first-order differential equations

$$\dot{\mathbf{X}}=\mathbf{f}(\mathbf{X},\tau)+\mathbf{G}(\mathbf{X},\tau)\mathbf{W}(\tau) \tag{2}$$

where the elements of the vector $\mathbf{f}$ and the matrix $\mathbf{G}$ are linear and nonlinear functions of the state coordinates $\mathbf{X}$.

If $W(\tau)$ is approximated as a physical white noise in the sense of Gray and Caughey (1965) then it can be written as the "formal" derivative of the Brownian motion process $B(\tau)$ as

$$W(\tau)=\sigma dB(\tau)/d\tau \tag{3}$$

where $\sigma^2=2D$.

Equation (2) can be written as a stochastic differential equation of Stratonovich type

$$dX_i=f_i(\mathbf{X},\tau)d\tau+\sum_{j=1}^{2}G_{ij}(\mathbf{X},\tau)dB_j(\tau)\quad i=1,2 \tag{4}$$

Alternatively equation (2) may in turn be transformed into the Itô type equation

$$dX_i=\left\{f_i(\mathbf{X},\tau)+\frac{1}{2}\sum_{k=1}^{2}\sum_{j=1}^{2}G_{kj}(\mathbf{X},\tau)\frac{\partial G_{ij}(\mathbf{X},\tau)}{\partial X_k}\right\}dt$$

$$+\sum_{j=1}^{2}G_{ij}(\mathbf{X},\tau)dB_j(\tau) \tag{5}$$

where the double summation expression is due to the Wong-Zakai (1965) correction term, which is a result of replacing the real random excitation by a white noise process.

The dynamic response statistic functions can be expressed in terms of moments, semi-invariants, or quasimoments. These three functions are related by definite relationships defined by Kendall and Stuart (1969) and Crandall (1980). For random Gaussian processes it is known that all semi-invariants of order greater than the second are zero. The same is applied to quasimoments since third, fourth, and fifth-order quasimoments are identical to the corresponding central-semi-invariants as shown by Bover (1978). If the process is non-Gasssian, the higher-order semi-invariants $\lambda_{n>2}$ do not vanish. However, their contribution diminishes as their order increases if the process is slightly deviated from Gaussian. Thus one would expect that the first few higher order semi-invariants will give an adequate measure of the deviation of the process from being Gaussian. Accordingly, it is possible to describe the probability density function of a non-Gaussian process in terms of a truncated Edgeworth expansion. This expansion is analogous to a certain extent to the asymptotic approximation techniques used frequently in deterministic nonlinear mechanics.

The basic ingredients of the truncated Edgeworth expansion are the response semi-invariants which can be expressed in terms of the response moments. The differential equations of the moments and semi-invariants can be generated by using the Itô rule of stochastic differential (Arnold 1974):

$$d\Phi(\mathbf{X})=\left\{\frac{\partial\Phi(\mathbf{X})}{\partial X_i}\right\}^T\{d\mathbf{X}\}+\frac{1}{2}\text{Trace}\,\mathbf{GQG}^T\left[\frac{\partial^2\Phi(\mathbf{X})}{\partial X_i\partial X_j}\right]dt \tag{6}$$

where $\Phi(\mathbf{X})$ is a general scalar function of the response coordinates, $Qd\tau=E[d\mathbf{B}(\tau)\ d\mathbf{B}(\tau)^T]$, and T denotes transpose.

Taking expectation for both sides of equation (6) and dividing by $d\tau$, gives

$$\frac{d}{dt}E[\Phi]=E\left[\left\{\frac{\partial\Phi}{\partial X_i}\right\}^T\{\mathbf{f}(\mathbf{X},\tau)\}\right]+\frac{1}{2}E[\text{Trace}\,\mathbf{GQG}^T\boldsymbol{\Phi}_{xx}] \tag{7}$$

For two-dimensional Markov process the differential equations of the moments are obtained if Φ is expressed in the form

$$\Phi(\mathbf{X})=(X_1^kX_2^l) \tag{8}$$

The differential equations of the semi-invariants can also be generated if $\Phi(\mathbf{X})$ is written in terms of the characteristic function

$$E[\Phi(\mathbf{X})]=E[\exp(i\theta_1X_1+i\theta_2X_2)]$$

$$=\int_{-\infty}^{\infty}\int_{-\infty}^{\infty}\exp(i\theta_1X_1+i\theta_2X_2)\text{p}(\mathbf{X})\,dX_1\,dX_2 \tag{9}$$

where θ_i are arbitrary real valued parameters and $i=\sqrt{-1}$.

For the purpose of the present analysis the relationships between the joint semi-invariants and the joint moments are derived. The following relations are used:

$$\lambda_3[X_iX_jX_k]=E[X_iX_jX_k]-\sum^{3}E[X_i]E[X_jX_k]$$

$$+2E[X_i]E[X_j]E[X_k]$$

$$\lambda_4[X_iX_jX_kX_l]=E[X_iX_jX_kX_l]-\sum^{4}E[X_i]E[X_jX_kX_l]$$

Downloaded 02 May 2010 to 171.66.16.54. Redistribution subject to ASME license or copyright; see http://www.asme.org/terms/Terms_Use.cfm

$$+2\sum^{6} E[X_i]E[X_j]E[X_kX_l]-\sum^{3} E[X_iX_j]E[X_kX_l]$$

$$-6E[X_i]E[X_j]E[X_k]E[X_l]$$

$$\lambda_5[X_iX_jX_kX_lX_m]=E[X_iX_jX_kX_lX_m]$$

$$-\sum^{5} E[X_i]E[X_jX_kX_lX_m]$$

$$+2\sum^{10} E[X_i]E[X_j]E[X_kX_lX_m]$$

$$-6\sum^{10} E[X_i]E[X_j]E[X_k]E[X_lX_m]$$

$$+2\sum^{15} E[X_i]E[X_jX_k]E[X_lX_m]-\sum^{10} E[X_iX_j]E[X_kX_lX_m]$$

$$+24E[X_i]E[X_j]E[X_k]E[X_l]E[X_m]$$

$$\lambda_6[X_iX_jX_kX_lX_mX_n]=E[X_iX_jX_kX_lX_mX_n]$$

$$-\sum^{6} E[X_i]E[X_jX_kX_lX_mX_n]$$

$$+2\sum^{15} E[X_i]E[X_j]E[X_kX_lX_mX_n]$$

$$-6\sum^{20} E[X_i]E[X_j]E[X_k]E[X_lX_mX_n]$$

$$+24\sum^{15} E[X_i]E[X_j]E[X_k]E[X_l]E[X_mX_n]$$

$$-\sum^{15} E[X_iX_j]E[X_kX_lX_mX_n]$$

$$-6\sum^{45} E[X_i]E[X_j]E[X_kX_l]E[X_mX_n]$$

$$-\sum^{10} E[X_iX_jX_k]E[X_lX_mX_n]$$

$$+2\sum^{15} E[X_iX_j]E[X_kX_l]E[X_mX_n]$$

$$+2\sum^{60} E[X_i]E[X_jX_k]E[X_lX_mX_n]$$

$$-120E[X_i]E[X_j]E[X_k]E[X_l]E[X_m]E[X_n] \tag{10}$$

where numbers over summation signs refer to the number of possible terms generated in the form of the indicated expressions without allowing permutation of indices. For example

$$\sum^{3} E[X_i]E[X_jX_k]=E[X_i]E[X_jX_k]$$

$$+E[X_j]E[X_iX_k]+E[X_k]E[X_iX_j]$$

The authors have also derived seventh and eighth-order relations but they are not listed here due to space limitations.

The non-Gaussian probability density function as expressed in terms of the Edgeworth expansion is

$$p(X_1,X_2)=\overset{*}{p}(X_1,X_2)\Big\{\sum_{n=0}^{\infty}\frac{\rho^n}{n!}H_n(y_1/\sigma_1)H_n(y_2/\sigma_2)$$

$$+\sum_{i+j=3}\frac{1}{i!j!}\frac{\lambda_{ij}}{\sigma_1^i\sigma_2^j}\sum_{n=0}^{\infty}\frac{\rho^n}{n!}H_{n+i}(y_1/\sigma_1)H_{n+j}(y_2/\sigma_2)$$

$$+\sum_{i+j=4}\frac{1}{i!j!}\frac{\lambda_{ij}}{\sigma_1^i\sigma_2^j}\sum_{n=0}^{\infty}\frac{\rho^n}{n!}H_{n+i}(y_1/\sigma_1)H_{n+j}(y_2/\sigma_2)$$

$$\frac{1}{2}\sum_{\substack{i+j=3\\ r+s=4}}\frac{1}{i!j!r!s!}\frac{\lambda_{ij}}{\sigma_1^i\sigma_2^j}\frac{\lambda_{rs}}{\sigma_1^r\sigma_2^s}$$

$$\sum_{n=0}^{\infty}\frac{\rho^n}{n!}H_{n+i+r}(y_1/\sigma_1)H_{n+j+s}(y_2/\sigma_2)\Big\} \tag{11}$$

where $p^*(X_1,X_2)$ is the Gaussian probability density function of the two random proceses X_1 and X_2,

$$y_i=X_i-m_i,\ \rho=E[y_1y_2]/\sigma_1\sigma_2$$

is the correlation coefficient

$$\sigma_i=C_{ii}=E[(X_i-m_i)^2],\ m_i=E[X_i],$$

and $H_n(\ )$ is the Chebychev-Hermite polynomial defined by (Cramer, 1946):

$$H_n(X)=(-1)^n\exp(X^2/2)\frac{d^n}{dx^n}\{\exp(-X^2/2)\},\ H_0(X)=1 \tag{12}$$

The non-Gaussian probability density function given by (11) should be strictly positive. If this condition is violated for a particular problem one may consider the Gram-Charlier expansion (Beaman and Hedrick, 1981), otherwise, numerical simulation such as Monte Carlo method may be used.

For dynamic systems with quadratic nonlinearity the differential equations of the response moments of order n will contain moments of order $n+1$. If cubic nonlinearity is included the nth order moment equations will contain moments of order $(n+2)$, and so on. Thus the first-order non-Gaussian closure can be established by setting fifth-order semi-invariants to zero for the case of quadratic nonlinearity, or setting fifth and sixth-order semi-invariants to zero for the case of cubic nonlinearity, and so on. Second-order non-Gaussian approximation can be obtained by generating differential equations of the response moments up to fifth order and setting sixth-order semi-invariants to zero for the case of quadratic nonlinearity. For the case of cubic nonlinearity, seventh and eighth-order semi-invariants are equated to zero.

3 Application

This section demonstrates the application of the non-Gaussian closure to nonlinear systems subjected to random parametric excitation. These systems are encountered in various practical applications such as beams under random axial loads, liquid propellant sloshing under random vertical accelerations, uncoupled ship rolling motion in random sea waves. The response of these systems may be described by the differential equation of motion

$$\ddot{Y}+(2\zeta+\beta Y^2)\dot{Y}+[1+W(\tau)]Y=0 \tag{13}$$

where ζ and β are linear and nonlinear damping coefficients. Stiffness and inertia nonlinearities will not be considered. Equations (13) may be written in the state vector form

$$\dot{X}_1=X_2$$
$$\dot{X}_2=-X_1-(2\zeta+\beta X_1^2)X_2-X_1W(\tau) \tag{14}$$

where the coordinate transformation described in Section 2 is

Downloaded 02 May 2010 to 171.66.16.54. Redistribution subject to ASME license or copyright; see http://www.asme.org/terms/Terms_Use.cfm

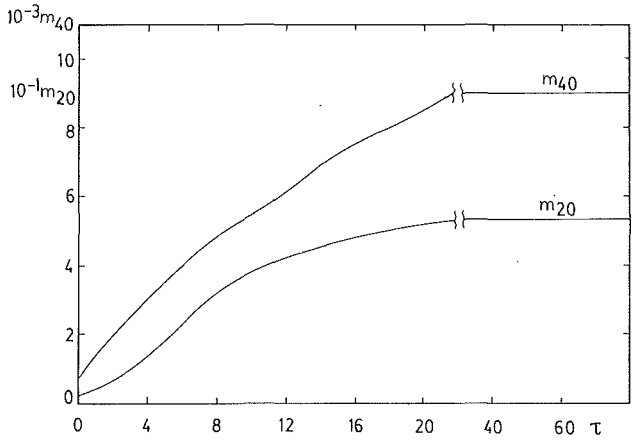


Fig 1 Transient and steady-state time history response as obtained by numerical integration (mean-square m_{20} and fourth-order moment m_{40} of the response displacement), $\zeta = 0.02$, $\beta = 0.01$, $D/2\zeta = 15$

used. It is not difficult to show that the general differential equation of the response joint moments, $m_{k,l} = E[X_1^k X_2^l]$ of system (14) is given in the form

$$\dot{m}_{kl} = km_{k-1,l+1} - 2\zeta l m_{kl} - \beta l m_{k+2,l} - l m_{k+1,l-1} + Dl(l-1)m_{k+2,l-2} \tag{15}$$

It is seen that a moment equation of order $n = k+l$ is coupled with moments of order $n+2$. The first-order non-Gaussian solution will be obtained by considering moment equations up to fourth order.

The first-order moment equations are:

$$\begin{aligned} \dot{m}_{10} &= m_{01} \\ \dot{m}_{01} &= -2\zeta m_{01} - \beta m_{21} - m_{10} \end{aligned} \tag{16}$$

The second-order moment equations are:

$$\begin{aligned} \dot{m}_{11} &= m_{02} - 2\zeta m_{11} - \beta m_{31} - m_{20} \\ \dot{m}_{20} &= 2m_{11} \\ \dot{m}_{02} &= -4\zeta m_{02} - 2\beta m_{22} - 2m_{11} + 2Dm_{20} \end{aligned} \tag{17}$$

The third-order moment equations are:

$$\begin{aligned} \dot{m}_{30} &= 3m_{21} \\ \dot{m}_{03} &= -6\zeta m_{03} - 3\beta m_{23} - 3m_{12} + 6Dm_{21} \\ \dot{m}_{21} &= 2m_{12} - 2\zeta m_{21} - \beta m_{41} - m_{30} \\ \dot{m}_{12} &= m_{03} - 4\zeta m_{12} - 2\beta m_{32} - 2m_{21} + 2Dm_{30} \end{aligned} \tag{18}$$

and the fourth-order moment equations are:

$$\begin{aligned} \dot{m}_{40} &= 4m_{31} \\ \dot{m}_{04} &= -8\zeta m_{04} - 4\beta m_{24} - 4m_{13} + 12Dm_{22} \\ \dot{m}_{31} &= 3m_{22} - 2\zeta m_{31} - \beta m_{51} - m_{40} \\ \dot{m}_{13} &= m_{04} - 6\zeta m_{13} - 3\beta m_{33} - 3m_{22} + 6Dm_{31} \\ \dot{m}_{22} &= 2m_{13} - 4\zeta m_{22} - 2\beta m_{42} - 2m_{31} + 2Dm_{40} \end{aligned} \tag{19}$$

It is seen that the last two sets of moment equations contain fifth and sixth-order moment terms. To close these equations the corresponding fifth and sixth-order semi-invariants are equated to zero. Thus fifth and sixth-order moments in (18) and (19) can be expressed in terms of lower-order moments. This procedure results in transforming the linear differential equations (18) and (19) into a set of nonlinear first-order moment equations. In view of relations (10) the degree of nonlinearity reaches sixth order. The resulting 14 coupled differential equations are solved by numerical integration by using the CSMP (Continuous System Modeling Program) algorithm.

For various sets of small initial conditions, and for excitation levels $D/2\zeta$ well above a certain critical value, the

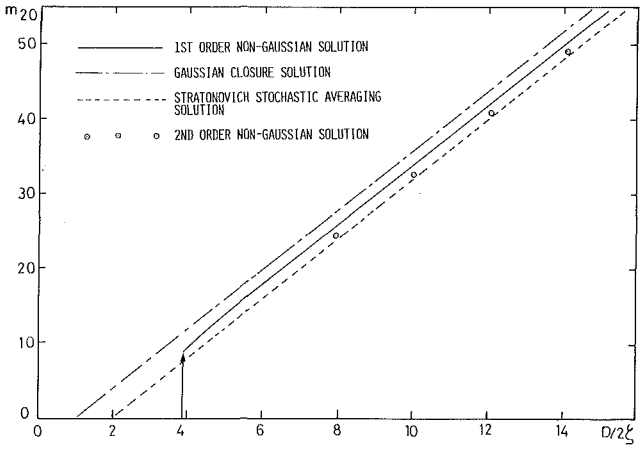


Fig. 2(*a*) Mean-square response as obtained by different solutions

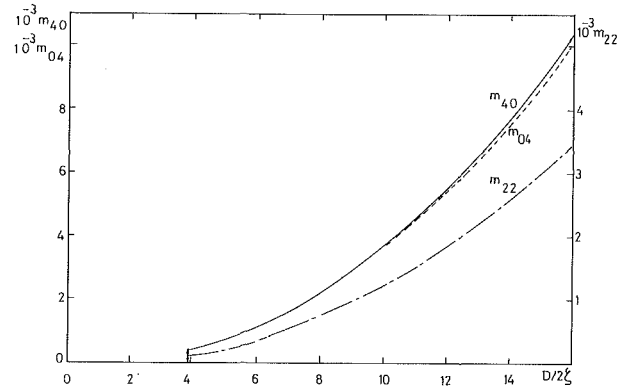


Fig 2(*b*) Fourth-order response moments

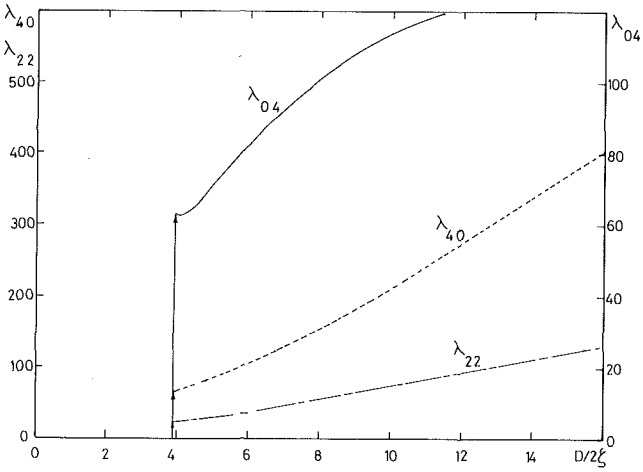


Fig 2(c) Fourth-order response semi-invariants

Fig. 2 First-order non-Gaussian stationary response statistics for system parameters $\zeta = 0.02$, $\beta = 0.01$

time history response indicates that the response moments of even order grow monotonically with time until they reach a steady state of bounded level governed mainly by the nonlinear damping force. A sample of the transient and steady state response is shown in Fig. 1. The odd order moments are not displayed and they reach zero level in the steady-state region. These results indicate that the system response is stationary and the system oscillates randomly about its equilibrium position.

For excitation levels $1 < D/2\zeta < (D/2\zeta)_{cr}$, and for any set of small initial conditions the numerical integration blows up,

Downloaded 02 May 2010 to 171.66.16.54. Redistribution subject to ASME license or copyright; see http://www.asme.org/terms/Terms_Use.cfm

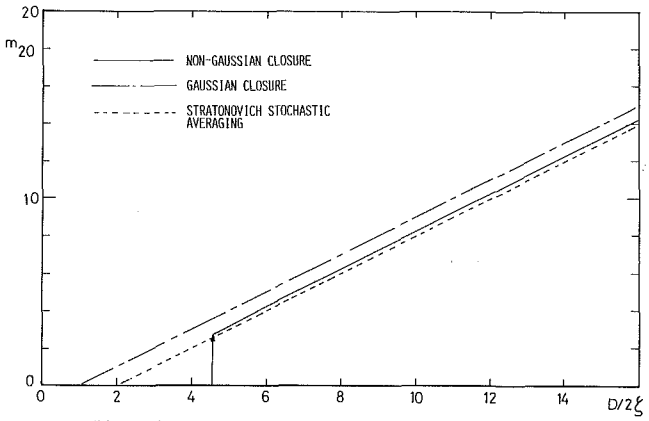


Fig. 3(*a*) Mean-square response of three solutions

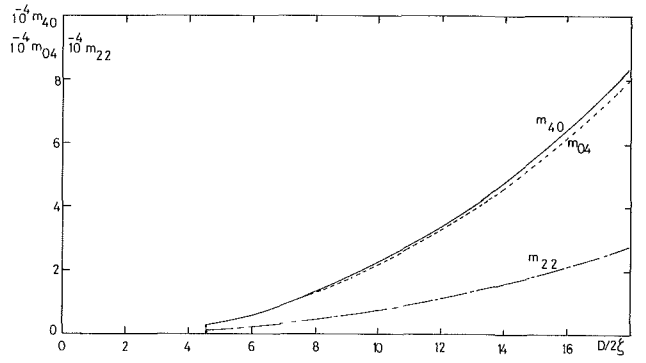


Fig 3(*b*) Fourth-order response moments

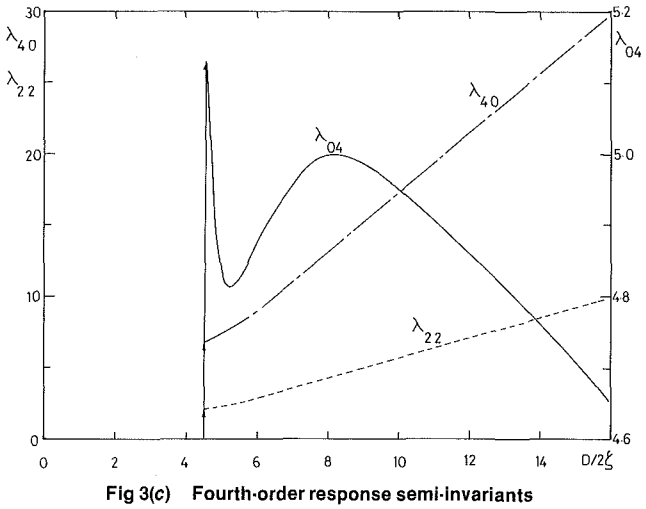


Fig 3(*c*) Fourth-order response semi-invariants

Fig. 3 First-order non-Gaussian Stationary Response statistics for system parameters $\zeta = 0.05, \beta = 0.1$

which may imply that real responses are not possible. For excitation levels $D/2\zeta < 1$ the system response moments decay to a state of rest. Physically this means that the excitation level is too small to overcome the system damping forces.

The stationary mean square response m_{20} is plotted in Figs. 2(*a*) and 3(*a*) as function of the excitation level $D/2\zeta$ for two sets of damping constants $(\zeta, \beta) = (0.02, 0.01)$ and $(0.05, 0.1)$, respectively. It is seen that the mean square increases almost linearly with $D/2\zeta > (D/2\zeta)_{cr}$. These figures provide a comparison between the results of three different methods: the non-Gaussian solution (n-G), the Gaussian closure solution (G), and the Stratonovich stochastic averaging solution (S). Solutions (G) and (S) were obtained by

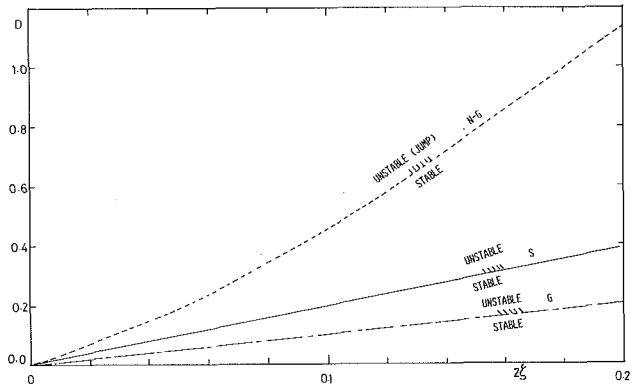


Fig. 4 Comparison of stability-instability boundaries of non-Gaussian (N-G), Stratonovich (S), and Gaussian (G) solutions

Ariaratnam (1980). It is seen that the first-order non-Gaussian solution lies between the (G) and (S) solutions. The degree of departure from the G and S solutions is mainly governed by the linear damping ratio ζ. As ζ increases the n-G mean-square response becomes closer to the *S* solution. The limiting effect of the nonlinear damping parameter β on the response is common for the three solutions.

Second-order approximation is examined by generating differential equations for the fifth and sixth-order moments, and setting seventh and eighth-order joint semi-invariants to zero. The details of the analysis is not reported in this paper because of length limitations. The results are shown by small circles in Fig. 2(*a*). It is seen that the second-order approximation gives better results.

However, unlike the G and S solutions, which give instability boundaries $D/2\zeta = 1$ and 2, respectively, the non-Gaussian solution exhibits a new feature which is manifested by a jump in all even-order response statistics (considered in the analysis) at a critical excitation level $(S/2\zeta)_{cr}$. The value of $(D/2\zeta)_{cr}$ is governed by the linear damping ratio ζ.

The jump phenomenon has motivated the authors to extend the analysis to derive the stationary solution by setting the left-hand side of equations (16)–(19) to zero. The following stationary solution of the resulting algebraic equations is obtained

$$m_{10} = m_{01} = 0$$
$$m_{11} = m_{21} = m_{31} = 0 \qquad (20a)$$

From the CSMP results the zero solution of

$$m_{12} = m_{30} = m_{03} = 0 \qquad (20b)$$

is enforced, and yields

$$m_{22} = K m_{20}, \quad K = \frac{D/2\zeta - 1}{\beta/2\zeta}$$
$$m_{40} = 3K m_{20} \qquad m_{02} = m_{20},$$
$$m_{13} = m_{20}\left\{3\beta m_{20}(3K - 2m_{20}) - 2\left(3\frac{D}{2\zeta} - 1\right)K\right\}, \qquad (20c)$$

where m_{20} is obtained by solving for the roots of the polynomial

$$m_{20}^4 + b_1 m_{20}^3 + b_2 m_{20}^2 + b_3 m_{20} + b_4 = 0 \qquad (20d)$$

where the coefficients b_i are given in the Appendix.

The roots of equation (20*d*) are determined numerically by using the IMSL subroutine ZPOLR (Zeros of a Polynomial with Real coefficients). All the roots of (20*d*) are found complex within an excitation level range defined by the region $1 < D/2\zeta < (D/2\zeta)_{cr}$. The imaginary value of the mean square is characterized physically by a nonoscillatory zero amplitude. At $D/2\zeta = 1$ the corresponding root is zero and for $D/2\zeta < 1$

Downloaded 02 May 2010 to 171.66.16.54. Redistribution subject to ASME license or copyright; see http://www.asme.org/terms/Terms_Use.cfm

the roots are negative, which implies that the system is completely dormant.

The jump phenomenon defines the beginning of a distinct regime of the system response characterized by a continuous random motion for all excitation levels greater than the critical level. This conclusion is supported by the experimental observations reported by Baxter (1971) and Roberts (1980). These experimental investigations reported three characteristic forms of the response: (*i*) zero motion response over the whole observation period, (*ii*) partially developed random motion with periods of zero motion, and (*iii*) continuous random motion. The partially developed regime was noticed to dominate with reducing excitation level. Furthermore, it was difficult to make a precise determination of the changeover from the partially developed motion to zero motion. This difficulty has recently been discussed by Bolotin (1984, p. 273) in connection with the experimental investigation of stochastic stability of parametric excited systems.

Figures 2(*b*) and 3(*b*) show the fourth-order moments m_{40}, m_{04}, and m_{22} as function of the excitation level. These moments increase nonlinearly with the excitation level $D/2\zeta > (D/2\zeta)_{cr}$. The corresponding fourth-order semi-invariants are shown in Fig. 2(*c*) and 3(*c*). The existence of these semi-invariants reflects the fact that the response is non-Gaussian. The response statistic functions displayed in Figs. 2 and 3 are adequate to construct the first-order non – Gaussian probability density function.

The instability boundary that defines the location of the jump is plotted in Fig. 4. Figure 4 also shows another two instability boundaries obtained by the Gaussian closure and Stratonovich stochastic averaging solutions. The nonlinear damping coefficient does not affect the stability boundaries, a fact that was verified by Nevel'son and Khas'miniskii (1966).

4 Conclusions

A first-order non-Gaussian closure scheme is developed and employed successfully for nonlinear systems subjected to random parametric excitation. The results were found to be more accurate than the Gaussian closure solution. Unlike other techniques, such as the Gaussian closure or the Stratonovich averaging method, the present procedure predicts the jump phenomenon of the response statistic at a critical excitation level. The critical excitation level defines a boundary that is higher than the mean-square stability boundaries derived by other methods.

More accuracy was obtained by using a second-order non-Gaussian closure. The numerical integration gave one real solution and there was no possibilty for multiple solutions.

Acknowledgment

This research is supported by a grant from the National Science Foundation under research grant no. MEA-8313572 for which the authors are very grateful.

References

Ariaratnam, S. T., 1980, "Bifurcation in Nonlinear Stochastic Systems," *New Approaches to Nonlinear Problems in Dynamics*, Holmes, P. J., ed., SIAM, Philadelphia, pp. 470-474.

Arnold, L., 1974, *Stochastic Differential Equations: Theory and Applications*, John Wiley & Sons, New York.

Assaf, Sh. A., and Zirkle, L. D., 1976, "Approximate Analysis of Nonlinear Stochastic Systems," *Int. J. Control*, Vol. 23, No. 4, pp. 477-492.

Baxter, G. K., 1971, "The Nonlinear Response of Mechanical Systems to Parametric Random Excitation," Ph.D. Thesis, Syracuse University, Syracuse, N.Y.

Beaman, J. J., and Hedrick, J. K., 1981, "Improved Statistical Linearization for Analysis of Nonlinear Stochastic Systems, Part I: An Extended Statistical Linearization Technique," ASME JOURNAL OF APPLIED MECHANICS, Vol. 48, pp. 14-21.

Bolotin, V. V., 1984, *Random Vibrations of Elastic Systems*, Martinus Nijhoff Publishers, The Netherlands.

Bover, D. C. C., 1978, "Moment Equations for Nonlinear Stochastic Systems," *J. Math. Anal. Appl.*, Vol. 65, No. 2, pp. 306-320.

Cramer, H., 1946, *Mathematical Methods of Statistics*, Princeton University Press, Princeton, New Jersey.

Crandall, S. H., 1980, "Non-Gaussian Closure for Random Vibration of Nonliner Oscillators," Int. J. Nonlinear Mech., Vol. 15, pp. 303-313.

Crandall, S. H., 1981, "Non-Gaussian Closure Techniques for Stationary Random Vibration," *Proceedings of the IX-th Int. Conf. on Nonlinear Oscillations*, Kiev.

Crandall, S. H., and Zhu, W. Q., 1983, "Random Vibrations: A Survey of Recent Developments," ASME JOURNAL OF APPLIED MECHANICS, Vol. 50, pp. 953-962.

Dashevskii, M. L., 1967, "Approximate Analysis of the Accuracy on Nonstationary, Nonlinear Systems, Using the Method of Semi-Invariants," *Automation and Remote Control*, Vol. 28, No. 11, pp. 1673-1690.

Dashevskii, M. L., and Lipster, R. Sh., 1967, "Application of Conditional Semi-Invariants in Problems of Nonlinear Filtering of Markov Processes," *Automation and Remote Control*, Vol. 28, No. 6, pp. 63-74.

Gray, A. H., and Gaughey, T. K., 1965, " A Controversy in Problems Involving Random Parametric Excitation," *J. Math. Phys.*, Vol. 44, No. 3, pp. 288-296.

Ibrahim, R. A., 1978, "Stationary Response of a Randomly Parametric Excited Nonlinear System," ASME JOURNAL OF APPLIED MECHANICS, Vol. 45, pp. 910-916.

Ibrahim, R. A., and Soundararajan, A., 1983, "Nonlinear Parametric Liquid Sloshing Under Wide-Band Random Excitation," *J. Sound and Vib.*, Vol. 91, No. 1, pp. 119-134.

Kendall, M., and Stuart, A., 1969, *The Advanced Theory of Statistics*, Vol. 1, Distribution Theory, Charles Griffin, London.

Kuznetsov, P. I., Stratonovich, R. L., and Tikhonov, V. I., 1960, "Quasi-Moment Functions in the Theory of Random Processes," *Theory Probab. Appl.*, Vol. 5, pp. 80-97.

Nakamizo, T., 1970, "On the State Estimation for Nonlinear Dynamic Systems," Int. J. Control, Vol. 11, No. 4, pp. 683-695.

Nevel'son, M. B., and Khas'miniskii, R. Z., 1966, "Stability of Stochastic Systems," *Prob. Information Transformation*, Vol. 2, No. 3, pp. 61-74.

Roberts, J. W., 1980, "Random Excitation of a Vibratory System With Autoparametric Interaction," *J. Sound and Vibration*, Vol. 69, pp. 101-116.

Sperling, L., 1979, "Analysis of Stochastically Excited Nonlinear Systems Using Differential Equations for Generalized Quasimoment Functions," *Z. Angew Math. Mech. (ZAMM)*, Vol. 59, No. 4, pp. 169-176.

Stratonovich, R. L., 1963, *Topics in the Theory of Random Noise*, Vol. I, Gordon & Breach, New York.

Wong, E., and Zakai, M., 1965, "On the Relation Between Ordinary and Stochastic Differential Equations," *Int. J. Eng. Sci.*, Vol. 3, No. 2, pp. 213-229.

APPENDIX

Coefficients of equation (20*d*)

$$b_1 = -\frac{3}{2}K + \frac{8}{3\beta}$$

$$b_2 = \frac{1}{\beta}\left[-4K\zeta + \frac{K_1}{6} + \frac{1}{9\beta}(K_2+1)\right]$$

$$b_3 = \frac{1}{\beta^2}\left(-\frac{1}{6}KK_2 + \frac{4}{9}\zeta K_1 - \frac{K}{6}\right),$$

$$b_4 = \frac{1}{54\beta^3}\left[K_1K_2 + 3K(D-2\zeta\right]$$

where

$$k_1 = 2\zeta\left(\frac{3D}{2\zeta} - 1\right)K, \qquad K_2 = 1 + 12\zeta^2.$$

Downloaded 02 May 2010 to 171.66.16.54. Redistribution subject to ASME license or copyright; see http://www.asme.org/terms/Terms_Use.cfm

Journal of Applied Mechanics

Brief Notes

A Brief Note is a short paper that presents a specific solution of technical interest in mechanics but which does not necessarily contain new general methods or results. A Brief Note should not exceed 1500 words *or equivalent* (a typical one-column figure or table is equivalent to 250 words; a one line equation to 30 words). Brief Notes will be subject to the usual review procedures prior to publication. After approval such Notes will be published as soon as possible. The Notes should be submitted to the Technical Editor of the JOURNAL OF APPLIED MECHANICS. Discussions on the Brief Notes should be addressed to the Editorial Department, ASME, United Engineering Center, 345 East 47th Street, New York, N. Y. 10017, or to the Technical Editor of the JOURNAL OF APPLIED MECHANICS. Discussions on Brief Notes appearing in this issue will be accepted until two months after publication. Readers who need more time to prepare a Discussion should request an extension of the deadline from the Editorial Department.

Stability of Annular Sector Plates With Clamped Radial Edges

I. E. Harik[1]

Introduction

The most important problems encountered with sector plates are bending, vibrations, and stability. Recent articles have dealt with the bending [1, 2] and free vibration [3] of sector plates for various edge conditions. Research on the stability of these plates appears to have been rather scarce. Solutions are only available for the case where the straight (radial) edges are simply supported [4–8].

In this Note, a semianalytical solution is presented for the problem of in-plane stability of a sector plate having clamped radial edges. The circumferential edges can have any combination of boundary conditions.

Analysis

A truncated circular sector plate of constant thickness t, with a subtended angle γ, is considered (see Fig. 1). Within the classical small deflection theory of thin plates, the governing differential equation in polar coordinates of a sector element is expressed as [6]

$$\nabla^2\nabla^2 W(r,\theta) = \frac{t}{D}\left\{\sigma_r \frac{\partial^2 W(r,\theta)}{\partial r^2} + \sigma_\theta\left[\frac{1}{r}\frac{\partial W(r,\theta)}{\partial r} + \frac{1}{r^2}\frac{\partial^2 W(r,\theta)}{\partial \theta^2}\right] + 2\tau_{r\theta}\left[\frac{1}{r}\frac{\partial^2 W(r,\theta)}{\partial r\partial\theta} - \frac{1}{r^2}\frac{\partial W(r,\theta)}{\partial\theta}\right]\right\} \quad (1)$$

in which

$$\nabla^2 = \frac{\partial^2}{\partial r^2} + \frac{1}{r}\frac{\partial}{\partial r} + \frac{1}{r^2}\frac{\partial^2}{\partial\theta^2} \quad (2)$$

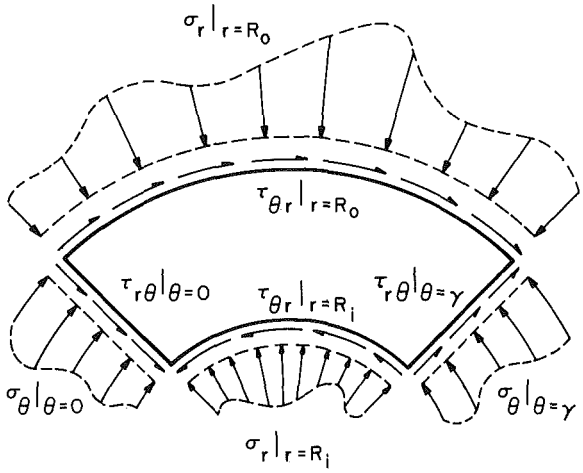


Fig. 1 Annular sector plate subjected to edge forces

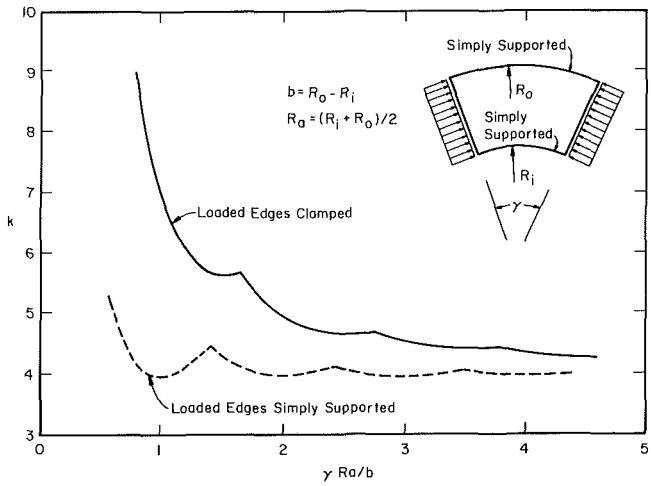


Fig. 2 Buckling coefficient for sector plate with simply supported circular edges

$W(r,\theta)$ is the normal deflection of the plate, σ_r, σ_θ, and $\tau_{r\theta}$ are the radial, tangential, and shear stresses, respectively, and D is the elastic rigidity of the plate.

The transverse deflection W is assumed to be of the form

[1]Assistant professor, Department of Civil Engineering, University of Kentucky, Lexington, KY 40506.

Manuscript received by ASME Applied Mechanics Division, July 1983, final revision, January, 1985.

Copyright © 1985 by ASME
Downloaded 02 May 2010 to 171.66.16.54. Redistribution subject to ASME license or copyright; see http://www.asme.org/terms/Terms_Use.cfm

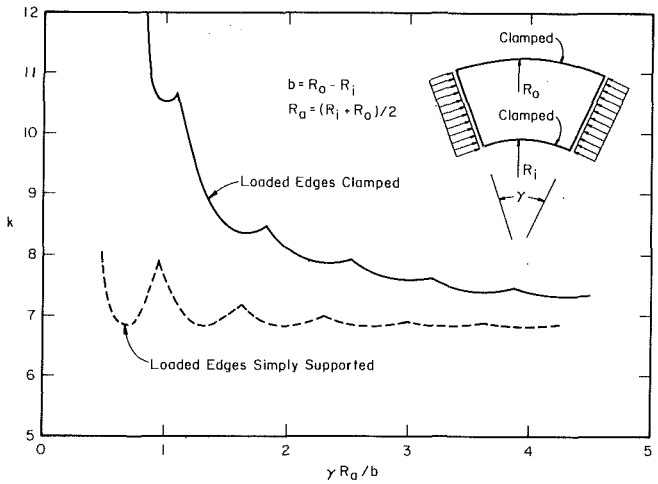


Fig. 3 Buckling coefficient for sector plate with clamped circular edges

$$W(r,\theta) = \sum_{m=1}^{\infty} F_m(r)\, G_m(\theta) \tag{3}$$

in which

$$G_m(\theta) = \cosh(\eta_m\theta) - \cos(\eta_m\theta) - E_m[\sinh(\eta_m\theta) - \sin(\eta_m\theta)] \tag{4}$$

$$E_m = \frac{\cosh(\lambda_m) - \cos(\lambda_m)}{\sinh(\lambda_m) - \sin(\lambda_m)} \tag{5}$$

$$[\eta_m = \lambda_m/\gamma, \lambda_m = 4.7300, 7.8532, 10.9960, \ldots, (2m+1)\pi/2]$$

$F_m(r)$ are the radial functions, and $G_n(\theta)$ are the basic functions along the θ-direction (eigenfunctions for a vibrating beam with both ends fixed [9]). The basic functions satisfy two of the following orthogonality relationships:

$$\left.\begin{aligned} &\int_0^{\gamma} G_n G_m\, d\theta = 0 \\ &\int_0^{\gamma} G_n G_m''\, d\theta \neq 0 \\ &\int_0^{\gamma} G_n G_m''''\, d\theta = 0 \end{aligned}\right\} \quad n \neq m \tag{6}$$

Substituting equation (2) into equation (1), multiplying both sides of the resulting equation by $G_n(\theta)$, integrating with respect to θ from 0 to γ and disregarding the radial and shear stresses, then the mth harmonic component of equation (1) reduces to

$$\frac{d^4F_m}{dr^4} + \frac{2}{r}\frac{d^3F_m}{dr^3} - (1 + 2\eta_m^2 g_{2m})\left(\frac{1}{r^2}\frac{d^2F_m}{dr^2} - \frac{1}{r^3}\frac{dF_m}{dr}\right)$$

$$+ (\eta_m^4 - 4\eta_m^2 g_{2m})\frac{F_m}{r^4} = \frac{t\sigma_\theta}{D}\left(\frac{1}{r}\frac{dF_m}{dr} - \eta_m^2 g_{2m}\frac{F_m}{r^2}\right) \tag{7}$$

in which

$$\eta_m^2 g_{2m} = \eta_m^2 g_{2mm}\,|_{m=n} + \eta_m^2 g_{2mn}\,|_{m\neq n} \tag{8}$$

$$\eta_m^2 g_{2mm} = -\frac{\int_0^{\gamma} G_m'' G_m\, d\theta}{\int_0^{\gamma} G_m^2\, d\theta} \tag{9}$$

$$\eta_m^2 g_{2mn} = -\frac{\sum_{n=1}^{\infty} \frac{1}{(\eta_m^4 - \eta_n^4)} \int_0^{\gamma} (G_n'''' G_m'' - G_n'' G_m'''')\, d\theta}{\int_0^{\gamma} G_m^2\, d\theta} \tag{10}$$

$$\eta_m^4 = \frac{\int_0^{\gamma} G_m'''' G_m\, d\theta}{\int_0^{\gamma} G_m^2\, d\theta} \tag{11}$$

In the r-direction, the plate is divided into a discrete number of pivotal points along a nodal line. Writing the equations at the discrete pivotal points yields the following simultaneous equations in compact matrix form:

$$[B]\{W\} = k[A]\{W\} \tag{12}$$

Equation (12), in typical eigenvalue form, may be written as

$$[A]^{-1}[B]\{W\} = k[I]\{W\} \tag{13}$$

where k is the buckling coefficient for which nontrivial solutions of equation (13) exist.

Application

The results on buckling of rectangular plates are well documented [10], but the same cannot be said to be true about annular sector plates. The only available results are for sector plates whose radial edges are simply supported [4–8].

The present method is applied on an annular sector with varying width $(b = R_o - R_i)$ to average radius $[R_a = (R_o + R_i)/2]$ ratios. The clamped straight edges are compressed with a uniformly distributed load (σ_θ = constant) over their width. Figures 2 and 3 show the variation in the buckling coefficient k with aspect ratio $\gamma R_a/b$ for simply supported and clamped circular edges. Results are also presented for the case where the loaded edges are simply supported [5], using the same method with the appropriate eigenfunctions.

The magnitude of the buckling coefficient was unchanged for different curvature ratios ($b/R_a = 0.001, 0.1, 0.5$). Similar findings were presented for the case of simply supported radial edges [4–6].

Acknowledgment

The author wishes to express his gratitude to Mr. Raghuram Ekambaram for his help in generating the numerical and graphical results.

References

1 Harik, I. E., "Bending of Transversally Loaded Orthotropic Rectangular and Sector Plates," Civil Engineering Report No. WSUCE0183, Wayne State University, Detroit, Mich., Feb. 1983.

2 Harik, I. E., "Analytical Solution to Orthotropic Sector," *Journal of Engineering Mechanics*, Vol. 110, No. 4, Apr. 1984, pp. 554–568.

3 Mukhopadhyay, M., "A Semi-Analytical Solution for Free Vibration of Annular Sector Plates," *Journal of Sound and Vibration*, Vol. 63, No. 1, 1979, pp. 87–95.

4 Harik, I. E., and Ekambram, R., "Elastic Buckling of Simply Supported Sector Plates," *SECTAM XII, Twelfth Conference on Theoretical and Applied Mechanics*, held at Callaway Gardens, Pine Mountain, Georgia, May 10–11, 1984, pp. 120–123.

5 Harik, I. E., and Ekambaram, R., "Local Buckling in Curved Box Members," *Seventh International Conference on Cold-Formed Steel Structures*, held at St. Louis, Missouri, Nov. 13–14, 1984, pp. 565–579.

6 Culver, C. G., and Frampton, R. E., "Local Instability of Horizontally Curved Members," *Journal of The Structural Division, ASCE*, Vol. 96, No. ST2, Feb. 1970, pp. 245–265.

7 Kopackova, M., and Jira, J., "Analysis of Plate in the Form of Annular Sector Under the Action of In-Plane Forces," *ACTA Technica CSAV*, Vol. 23, No. 1, 1978, pp. 51–57.

8 Rubin, C., "Stability of Polar Orthotropic Sector Plates," ASME JOURNAL OF APPLIED MECHANICS, Vol. 45, June 1978, pp. 448–450.

9 Flügge, W., *Handbook of Engineering Mechanics*, McGraw-Hill, New York, 1962.

10 Column Research Committee of Japan, *Handbook of Structural Stability*, Corona Publishing, Tokyo, Japan, 1971.

Downloaded 02 May 2010 to 171.66.16.54. Redistribution subject to ASME license or copyright; see http://www.asme.org/terms/Terms_Use.cfm

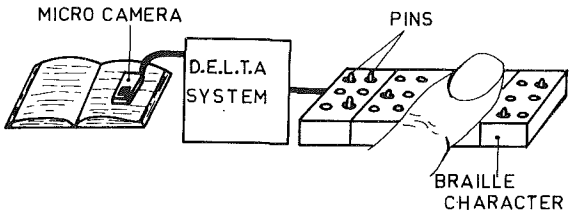


Fig. 1 Scheme of the braille reading system

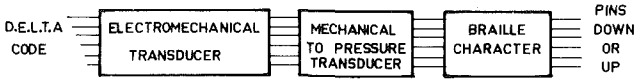


Fig. 2 Scheme of the translation system with the pneumatic interface

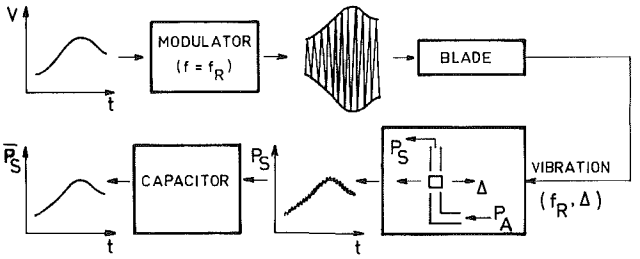


Fig. 3 Principle of the transducer with: f_R: resonant frequency of the blade, Δ: amplitude vibration, and P_A: constant supply pressure

Electric-to-Pneumatic Transducer and its Use for Reading Braille

R. Caen[1] and C. Fonade[1]

The motivation for development of the transducer was the necessity to realize a functional terminal part of a braille reading system (see Fig. 1). The electronic and computing parts of the system, which can recognize printed character forms and which can convert these into signals representing braille characters, has been realized by the research team "Vision par calculateur" (Conter and Valobra, 1980) headed by Professor Bruel (1980).

A mechanical system with a pneumatic interface was designed which satisfied the following five conditions (refer to Fig. 2):

(*a*) Adjustable pin height to suit the user.

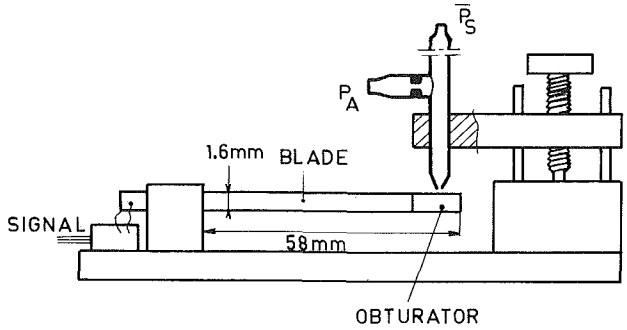
(*b*) Capability to receive information without lifting the finger from the pins.

(*c*) Low-noise level associated with movement of the pins.

(*d*) Reasonable total cost.

(*e*) Possibility of further development for translation of a full printed page.

The desired speed of movement of the pins dictated the choice of a piezoelectric "blade" as the electromechanical converter, and a potentiometer or an interrupting jet system as the mechanical-to-pressure transducer. The configuration and size of the system has been calculated for a reaction delay time of much less than 0.2 seconds. Finally, because of a hysteresis problem that was encountered in the use of the piezoelectric system and because a low-energy level to drive the blade was required, an amplitude modulation process at the resonant frequency of the blade was chosen (Caen and Fonade, 1982–1983).



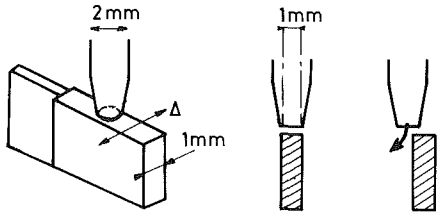


Fig. 4 Potentiometer system and typical geometric parameters

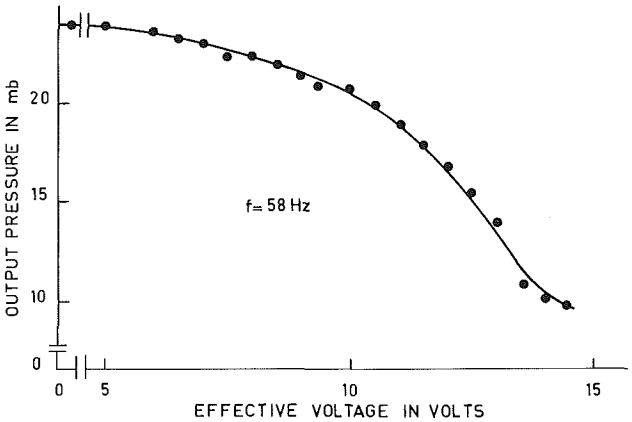


Fig. 5(*a*) Amplitude to pressure (*f* constant)

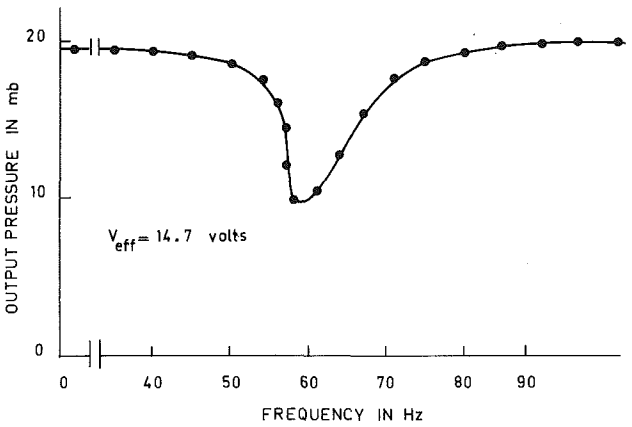


Fig. 5(*b*) Frequency to pressure (*V* constant); $\bar{P}_S$ is measured with a water column manometers

Fig. 5 Relationship between electric signal and pressure

The principle of the transducer is illustrated in Fig. 3, with an interrupting jet flow system as an example. Details of the relationship between the blade and the pneumatic devices, along with typical results, are shown in Figs. 4–7. The schematic in Fig. 3 is based on a behavior in the linear part of Figs. 5(*a*) and 7(*a*).

[1]Docteur ès Sciences and Maître de Conférence, Institut National Polytechnique de Toulouse, Institut de Mecanique des Fluides, Laboratoire Associé au C.N.R.S., 2, rue Camichel, 31071 Toulouse Cedex, France.

Manuscript received by ASME Applied Mechanics Division, November, 1984; final revision, February, 1985.

Downloaded 02 May 2010 to 171.66.16.54. Redistribution subject to ASME license or copyright; see http://www.asme.org/terms/Terms_Use.cfm

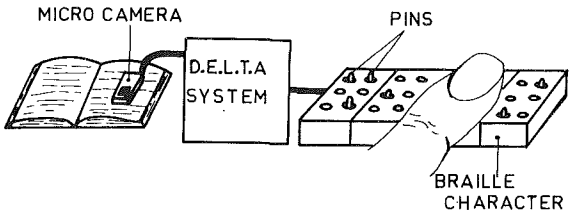


Fig. 1 Scheme of the braille reading system

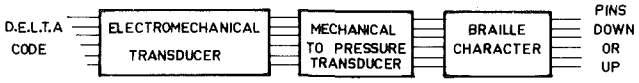


Fig. 2 Scheme of the translation system with the pneumatic interface

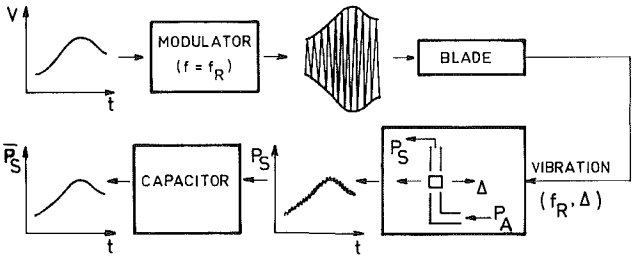


Fig. 3 Principle of the transducer with: f_R: resonant frequency of the blade, Δ: amplitude vibration, and P_A: constant supply pressure

Electric-to-Pneumatic Transducer and its Use for Reading Braille

R. Caen[1] and C. Fonade[1]

The motivation for development of the transducer was the necessity to realize a functional terminal part of a braille reading system (see Fig. 1). The electronic and computing parts of the system, which can recognize printed character forms and which can convert these into signals representing braille characters, has been realized by the research team "Vision par calculateur" (Conter and Valobra, 1980) headed by Professor Bruel (1980).

A mechanical system with a pneumatic interface was designed which satisfied the following five conditions (refer to Fig. 2):

(*a*) Adjustable pin height to suit the user.

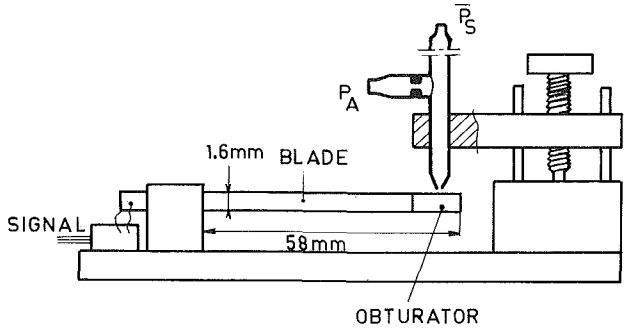
(*b*) Capability to receive information without lifting the finger from the pins.

(*c*) Low-noise level associated with movement of the pins.

(*d*) Reasonable total cost.

(*e*) Possibility of further development for translation of a full printed page.

The desired speed of movement of the pins dictated the choice of a piezoelectric "blade" as the electromechanical converter, and a potentiometer or an interrupting jet system as the mechanical-to-pressure transducer. The configuration and size of the system has been calculated for a reaction delay time of much less than 0.2 seconds. Finally, because of a hysteresis problem that was encountered in the use of the piezoelectric system and because a low-energy level to drive the blade was required, an amplitude modulation process at the resonant frequency of the blade was chosen (Caen and Fonade, 1982–1983).



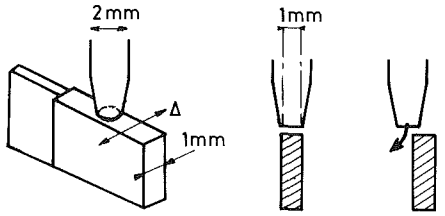


Fig. 4 Potentiometer system and typical geometric parameters

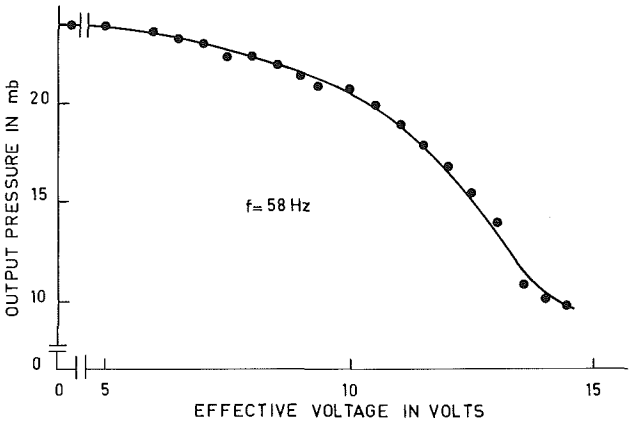


Fig. 5(*a*) Amplitude to pressure (*f* constant)

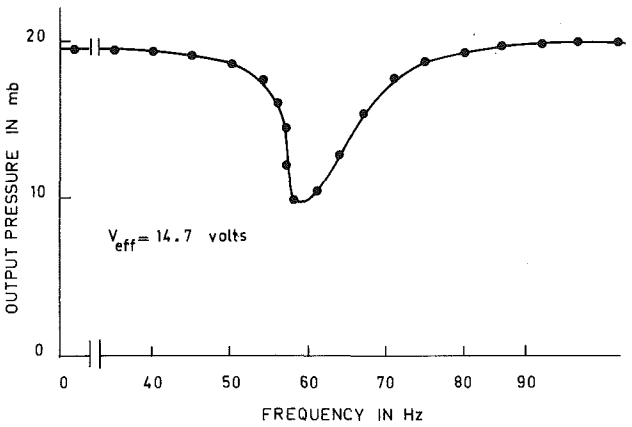


Fig. 5(*b*) Frequency to pressure (*V* constant); $\bar{P}_S$ is measured with a water column manometers

Fig. 5 Relationship between electric signal and pressure

The principle of the transducer is illustrated in Fig. 3, with an interrupting jet flow system as an example. Details of the relationship between the blade and the pneumatic devices, along with typical results, are shown in Figs. 4–7. The schematic in Fig. 3 is based on a behavior in the linear part of Figs. 5(*a*) and 7(*a*).

[1]Docteur ès Sciences and Maître de Conférence, Institut National Polytechnique de Toulouse, Institut de Mecanique des Fluides, Laboratoire Associé au C.N.R.S., 2, rue Camichel, 31071 Toulouse Cedex, France.

Manuscript received by ASME Applied Mechanics Division, November, 1984; final revision, February, 1985.

Copyright © 1985 by ASME
Downloaded 02 May 2010 to 171.66.16.54. Redistribution subject to ASME license or copyright; see http://www.asme.org/terms/Terms_Use.cfm

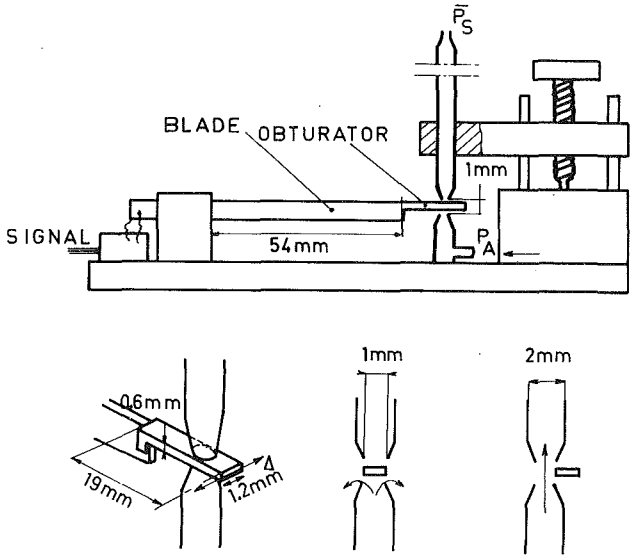


Fig. 6 Interrupting jet system and typical geometric parameters

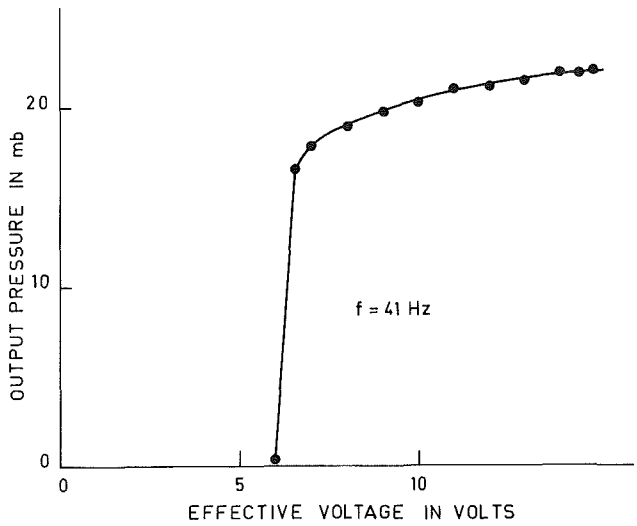


Fig. 7(*a*) Amplitude to pressure (*f* constant)

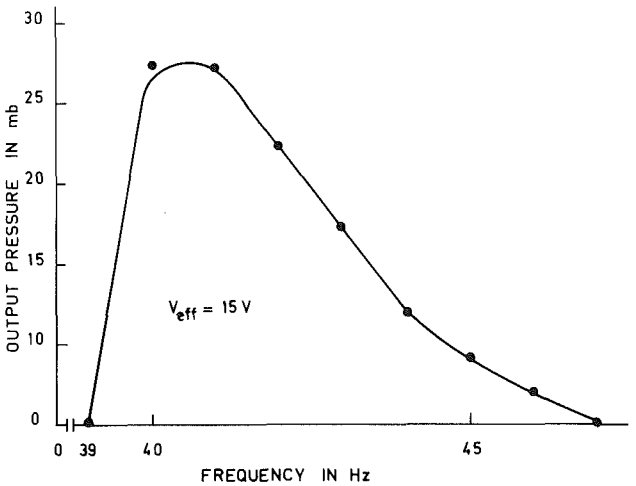


Fig. 7(*b*) Frequency to pressure (*V* constant)

Fig. 7 Relationship between electric signal and pressure

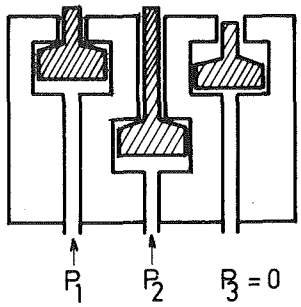


Fig. 8 Character display unit (half a view). Distance between pins must be less than 3 mm.

The shapes of these curves may be modified by changing the geometric parameters (e.g., distances to blade, nozzle diameters, width of the blades, etc.). Signs of the slopes can be opposite to those shown if slotted obturators are used.

Figures (5*b*) and 7(*b*) show that it is possible to convert an electrical frequency into a pneumatic pressure, which can be very useful, particularly for speed control processes. The ratio P_S/P_A depends on the distance between the nozzles and the obturators, and it is close to 2 in our experiments.

In the braille reading system, the transducer is followed by a character display unit, inside of which six small pistons are moved by the pressure (see Fig. 8). It is a binary system whereby an electronic gate is opened or closed by the braille code coming from the computer. Pressure and vibration of the blades are interrelated. It can be seen from the steep slope at the beginning of the curve in Fig. 7(*a*) that the interrupting jet device is more suitable for this application.

The type of system considered here seems to be desirable when users wish to "read" a printed text without hearing a spoken version of it. The future full-page version of the system will allow the user to "read" graphs and drawings, for example.

Acknowledgments

This work was supported by a grant from Delegation Generale de la Recherche Scientifique et Technique. The authors wish to thank Mr. Khattab for his participation in the measurements reported.

References

Conter J., and Valobra M., 1980, "Etude et réalisation d'un Dispositif Électronique de Lecture de Texte Pour Aveugles. Project D.E.L.T.A. Système Portatif Multifonte," Thèse de Docteur-Ingénieur, Université de Toulouse.

Caen R., and Fonade Ch., 1982–1983, "Procédé de Conversion d'une Grandeur Électrique en Une Grandeur Pneumatique ou Hydraulique et Convertisseur Pour sa Mise en Oeuvre," Demandes de Brevets, 82 12434 et 83 08675.

Long Wavelength Elastic Scattering From a Planar Distribution of Inclusions

J. Baik[1,2] and R. B. Thompson[2]

Introduction

The elastic wave scattering from a planar array of inclusions is an important problem in the nondestructive evaluation of bonds between similar or dissimilar materials. The long wavelength regime is of particular interest because of the microscopic dimensions often exhibited by the in-

[1]Present address: Tristar Semiconductor, Inc., 5150 Great America Parkway, Santa Clara, CA 95050.

[2]Ames Laboratory, Iowa State University, Ames, Iowa 50011

Manuscript received by ASME Applied Mechanics Division, March 15, 1985; final revision May 31, 1985.

Downloaded 02 May 2010 to 171.66.16.54. Redistribution subject to ASME license or copyright; see http://www.asme.org/terms/Terms_Use.cfm

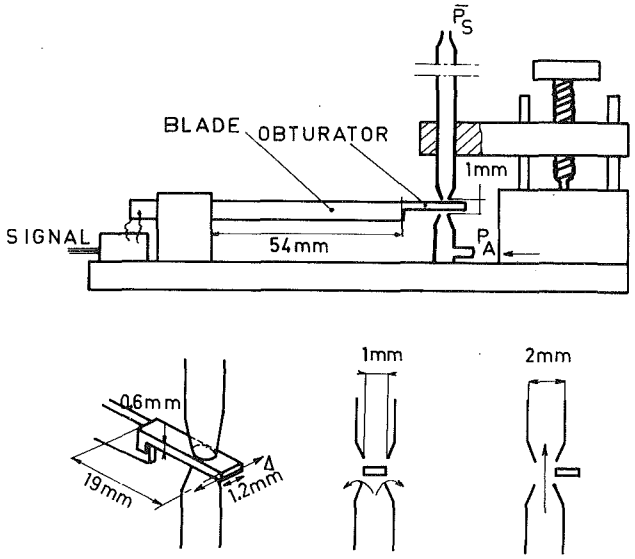


Fig. 6 Interrupting jet system and typical geometric parameters

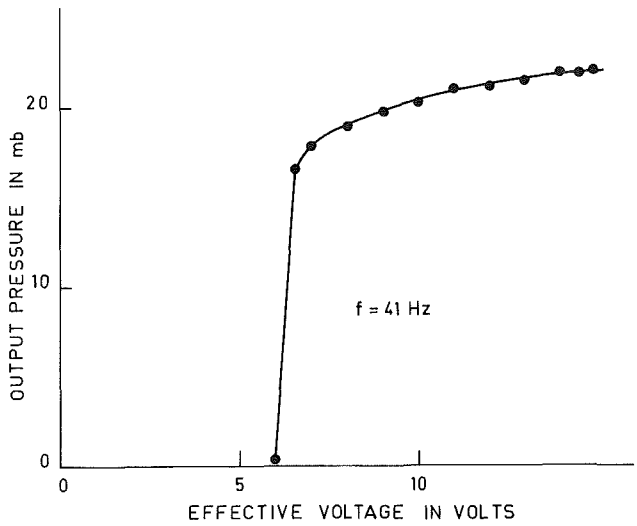


Fig. 7(*a*) Amplitude to pressure (*f* constant)

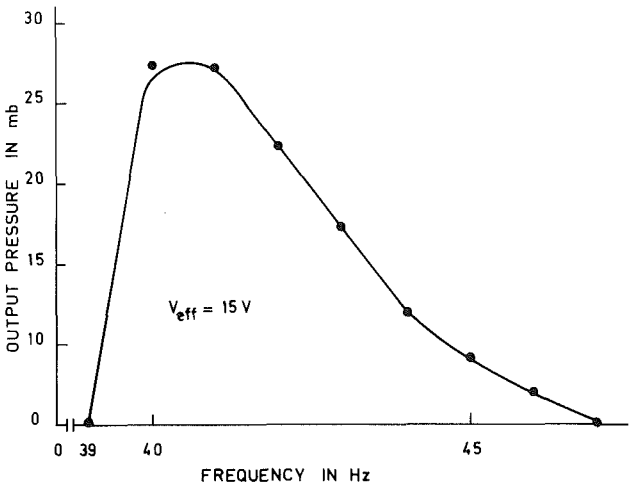


Fig. 7(*b*) Frequency to pressure (*V* constant)

Fig. 7 Relationship between electric signal and pressure

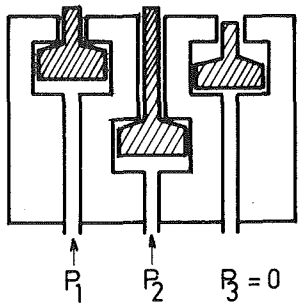


Fig. 8 Character display unit (half a view). Distance between pins must be less than 3 mm.

The shapes of these curves may be modified by changing the geometric parameters (e.g., distances to blade, nozzle diameters, width of the blades, etc.). Signs of the slopes can be opposite to those shown if slotted obturators are used.

Figures (5*b*) and 7(*b*) show that it is possible to convert an electrical frequency into a pneumatic pressure, which can be very useful, particularly for speed control processes. The ratio P_S/P_A depends on the distance between the nozzles and the obturators, and it is close to 2 in our experiments.

In the braille reading system, the transducer is followed by a character display unit, inside of which six small pistons are moved by the pressure (see Fig. 8). It is a binary system whereby an electronic gate is opened or closed by the braille code coming from the computer. Pressure and vibration of the blades are interrelated. It can be seen from the steep slope at the beginning of the curve in Fig. 7(*a*) that the interrupting jet device is more suitable for this application.

The type of system considered here seems to be desirable when users wish to "read" a printed text without hearing a spoken version of it. The future full-page version of the system will allow the user to "read" graphs and drawings, for example.

Acknowledgments

This work was supported by a grant from Delegation Generale de la Recherche Scientifique et Technique. The authors wish to thank Mr. Khattab for his participation in the measurements reported.

References

Conter J., and Valobra M., 1980, "Etude et réalisation d'un Dispositif Électronique de Lecture de Texte Pour Aveugles. Project D.E.L.T.A. Système Portatif Multifonte," Thèse de Docteur-Ingénieur, Université de Toulouse.

Caen R., and Fonade Ch., 1982–1983, "Procédé de Conversion d'une Grandeur Électrique en Une Grandeur Pneumatique ou Hydraulique et Convertisseur Pour sa Mise en Oeuvre," Demandes de Brevets, 82 12434 et 83 08675.

Long Wavelength Elastic Scattering From a Planar Distribution of Inclusions

J. Baik[1,2] and R. B. Thompson[2]

Introduction

The elastic wave scattering from a planar array of inclusions is an important problem in the nondestructive evaluation of bonds between similar or dissimilar materials. The long wavelength regime is of particular interest because of the microscopic dimensions often exhibited by the in-

[1]Present address: Tristar Semiconductor, Inc., 5150 Great America Parkway, Santa Clara, CA 95050.

[2]Ames Laboratory, Iowa State University, Ames, Iowa 50011

Manuscript received by ASME Applied Mechanics Division, March 15, 1985; final revision May 31, 1985.

Copyright © 1985 by ASME
Downloaded 02 May 2010 to 171.66.16.54. Redistribution subject to ASME license or copyright; see http://www.asme.org/terms/Terms_Use.cfm

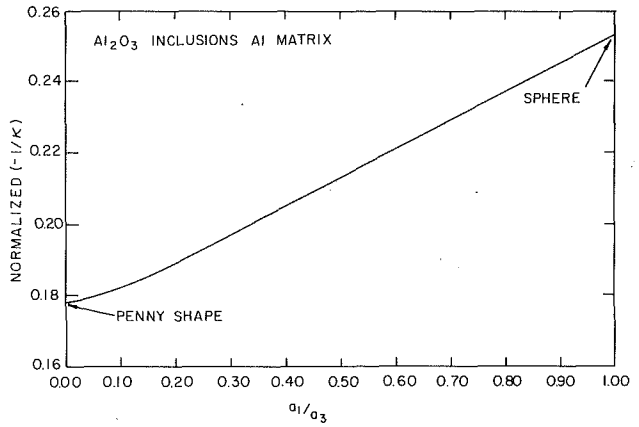


Fig. 1 Normalized compliance per inclusion ($-\mu/NV\kappa$) versus ellipticity for Al_2O_3 in Al

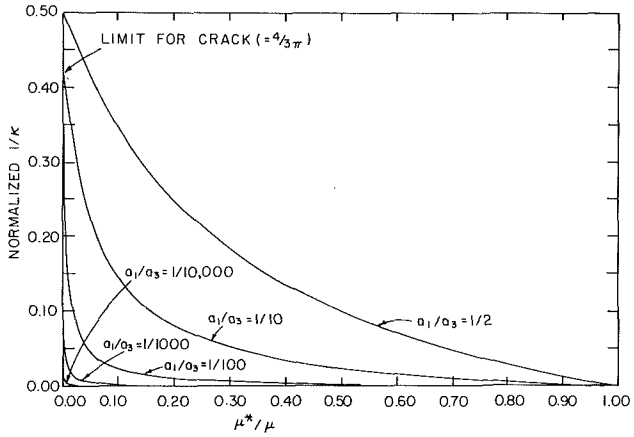


Fig. 2 Normalized compliance per inclusion ($\mu/NV_1\kappa$) versus relative shear modulus of inclusion

clusions and limits placed on the interrogating frequency by wave attenuation mechanisms. In recent studies of the scattering from interfaces containing cracks (Thompson et al., 1983 and 1984; Angel and Achenbach, 1985) a set of modified boundary conditions have been shown to lead to correct expressions for the long wavelength scattering. The present paper extends those results to the problem of a low density planar array of ellipsoidal inclusions.

Analysis

In the quasi-static spring model for ultransonic scattering from interfacial cracks (Thompson et al., 1983 and 1984) continuity of displacement is replaced by the boundary condition

$$[\sigma(0^+)+\sigma(0^-)]/2 \simeq \kappa[U(0^+)-U(0^-)] \tag{1}$$

where U is the dynamic displacement perpendicular to the interface, σ is the associated stress component, κ is the distributed stiffness of the interface, and the coordinates 0^+ and 0^- refer to the opposite sides of the interface. Equation (1) is selected to reproduce the far field displacements under a static load σ_1. Hence, κ is deduced in accordance with the relationship

$$\kappa = \sigma_{11}/\Delta_I \tag{2}$$

where $\Delta_I/2$ is the increase in displacement of a point far from a cracked interface relative to that for an uncracked interface. Expressions for Δ_I are available for a wide range of crack geometries (Tada et al., 1973).

For this case of interfacial cracks, $\sigma(0^+) = \sigma(0^-)$ is the second boundary condition employed. Comparison of reflection and transmission coefficients deduced from the boundary conditions to exact elastodynamic solutions for a periodic array of strip cracks shows good agreement when the elastic wavelength is large with respect to the period (Angel and Achenbach, 1985). These boundary conditions are energy conservant. The significance of energy loss, as would occur for random positioning of the cracks due to incoherent scattering of energy, has not been fully established.

For the case of inclusions, the inertial effects of a change in density must also be considered. The continuity of stress must be replaced by the relationship

$$-m\omega^2[U(0^+)+U(0^-)]/2 \simeq \sigma(0^+)-\sigma(0^-) \tag{3}$$

where ω is the angular frequency of the time harmonic elastic wave field and m is the excess in mass per unit area at the interface. To lowest order in frequency, the reflection and transmission coefficients are given by

$$R = j\omega(Z/2\kappa - m/2Z)/[1+j\omega(Z/2\kappa + m/2Z)] \tag{4}$$

$$T = 1/[1+j\omega(Z/2\kappa + m/2Z)] \tag{5}$$

where Z is the acoustic impedance (density times wavespeed) of the host material.

The utility of this approximate solution lies in the fact that the Δ_I can be deduced from static elasticity solutions for a variety of geometries for which the full elastodynamic solutions are intractable. Results for cracks have been discussed elsewhere (Thompson et al., 1983 and 1984, Angel and Achenbach, 1985, Baik and Thompson, 1985). This paper extends these to the case of sparsely distributed inclusions.

When the unincluded area is large, the inclusions' responses are nearly non-interacting and their individual deformations may be approximated by the static displacement solution of Eshelby for a single inclusion in an unbounded medium (Eshelby, 1961). At distances far from the interface with respect to the inclusion separation, the extra displacement due to the inclusions can be shown to be given by

$$\Delta_I/2 = N\int U_I dA \tag{6}$$

where N is the number of inclusions per unit area, U_I is the difference in the far field displacements of an included and unincluded materials, as predicted for the isolated inclusion by Eshelby, and the area integral is to be evaluated in the far field of the isolated inclusion. Combination of equations (2) and (6), along with explicit expressions for U_I as a function of σ_{11}, leads to the result

$$\kappa = \frac{3(1-\nu)}{4_\pi a_3^2 a_1 N}\left[(1-\nu)\frac{e_{11}{}^T}{\sigma_{11}} + 2\nu\frac{e_{33}{}^T}{\sigma_{11}}\right]^{-1} \tag{7}$$

where ν is Poisson's ratio and the inclusions are assumed to be oblate spheroids with semi-axes a_1 perpendicular to the interface and a_3 in the plane of the interface. The $e_{11}{}^T$ are the "equivalent inclusion" strains as defined by Eshelby. They depend on the elastic moduli of the host and included material and on the aspect ratio of the inclusion, but not on the absolute inclusion dimensions. The excess mass is given by $m = NV(\rho_1 - \rho_0)$ where V is the volume of an individual inclusion, ρ_1 is its density, and ρ_0 is the density of the host medium.

Numerical Results

The variation of the interfacial stiffness with inclusion parameters is illustrated by the plots in Figs. 1 and 2. Figure 1 illustrates the variation of κ with the ellipticity of the inclusions. In this example, the moduli were chosen to correspond to estimates of the polycrystalline elastic constants of Al_2O_3 inclusions ($\lambda^* = 142$GPa, $\mu^* = 162$GPa) in an Al matrix ($\lambda = 59.3$GPa, $\mu = 26.1$GPa.) Since the inclusion is stiffer than the matrix, negative values of κ occur. The abscissa is a normalized compliance per inclusion, ($-\mu/NV\kappa$),

Downloaded 02 May 2010 to 171.66.16.54. Redistribution subject to ASME license or copyright; see http://www.asme.org/terms/Terms_Use.cfm

where $V = 4\pi a_3{}^2 a_1/3$ is the volume of a single inclusion. This quantity varies by 42% as the inclusion shape ranges from penny shaped to spherical.

Figure 2 shows the compliance per inclusion ($\mu/NV_1\kappa$), normalized now by the volume of a circumscribing sphere, $V_1 = 4\pi a_3{}^3/3$, versus the shear modulus of the inclusion relative to that of the host (μ^*/μ). A Poisson's ratio of 1/3 is assumed for both materials, and the inclusion is taken to be softer than the host. Of particular interest is the transition to the crack limit of $4/3\pi$. For highly oblate inclusions, the modulus required to approach the crack response varies directly with the ratio a_1/a_3. Thinner inclusions require a smaller modulus before they can have a substantial compliance.

Discussion

These results for κ, coupled with the readily computed values of m, should provide a useful approximation in studying the interaction of elastic waves with inclusion layers. A particularly important application would appear to be the nondestructive evaluation of bonded layers.

Acknowledgment

This work was performed for the U.S. Department of Energy, Office of Basic Energy Sciences, Division of Materials Sciences, under contract No. W-7405-Eng-82.

References

Angel, Y. C., and Achenbach, J. D., 1985, "Reflection and Transmission of Elastic Waves by a Periodic Array of Cracks," ASME JOURNAL OF APPLIED MECHANICS, Vol. 107, pp. 33–41.

Baik, J. M., and Thompson, R. B., 1985, "The Elastic Compliance of Imperfect Interfaces: Review and Relationship to Ultrasonic Scattering," *Review of Progress in Quantitative NDE*, Vol. 4, Thompson, D. O., and Chimenti, D. E., eds., Plenum Press, New York, pp. 133–144.

Eshelby, J. D., 1961, "Elastic Inclusions and Inhomogeneities," *Progress in Solid Mechanics*, Vol. II., Ch. III, Sneddon, I. N., and Hill, R., eds., North-Holland, Amsterdam, pp. 89–140.

Tada, U., Paris, P., and Irwin, G., 1973, *The Stress Analysis of Cracks Handbook*, Del Research Corporation, St. Louis.

Thompson, R. B., Skilling, B. J., Zachary, B. J., Schmerr, L. W., and Buck, O., 1983, "Effects of Crack Closure on Ultrasonic Transmission," *Review of Progress in Quantitative Nondestructive Evaluation*, Vol. 2, Thompson, D. O., and Chimenti, D. E., eds., Plenum Press, New York, pp. 325–343.

Thompson, R. B., and Fiedler, C. J., 1984, "The Effects of Crack Closure on Ultrasonic Scattering Measurements," *Review of Progress in Quantitative Nondestructive Evaluation*, Vol. 3, Thompson, D. O., and Chimenti, D. E., eds., Plenum Press, New York, pp. 207–215.

Moving Load on Initially Stressed Orthotropic Cylindrical Shells Filled With Liquid

S. Chonan[1]

Introduction

This note is concerned with the dynamic response of infinitely long, axially stressed, fluid-filled orthotropic cylindrical shells subjected to an axisymmetric moving load. It is the purpose of this note to study to what extent the shell response is affected by the internal fluid medium. The critical load speed for which a resonance effect occurs in the system is obtained and the profile of the bending moment in the shell is shown graphically for a subcritical load speed. The results are compared with those of empty orthotropic shells.

Governing Equations

Consider an infinitely long, fluid-filled orthotropic cylindrical shell with initial axial stress. The x coordinate is along the shell axis and the r coordinate is in the direction of the shell radius. The θ coordinate is normal to x and r. The resultant force of the initial stress is denoted by T. The shell is subjected to an axisymmetric load $p(x,t)$, so that the θ component of the displacement vanishes. The displacements of the shell in the r and x directions are denoted by w and u, and the corresponding displacements of fluid by w_f and u_f. Furthermore, the rotation angle of the shell in the xr plane is denoted by ψ. The fluid pressure on the inner shell surface is given by $p_F(x,t)$. In this case the equations of motion of the shell are suitable modifications of those given in reference [1] and are written as

$$[(E_x + T)\partial^2/\partial x^2 - m_\rho \partial^2/\partial t^2]u + [(E_\nu/R)\partial/\partial x]w + [-(D_x/R)\partial^2/\partial x^2 + (I_\rho/R)\partial^2/\partial t^2]\psi - \eta_x(1 + h/2R)(\partial/\partial t)[u - (h/2)\psi] = 0, \quad (1)$$

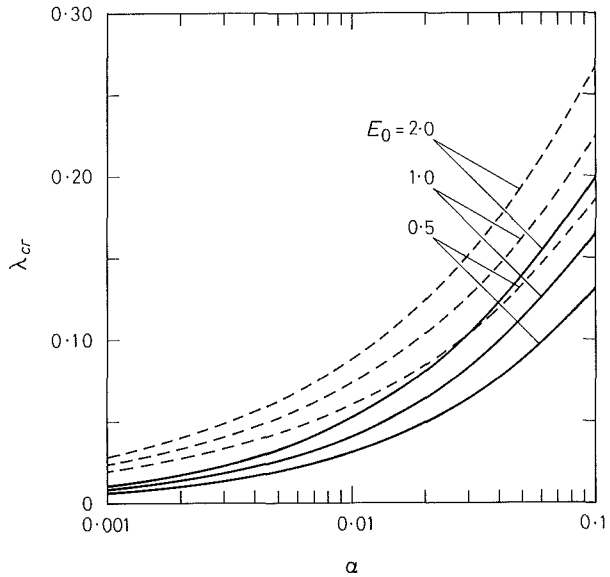


Fig. 1 The first non-dimensional critical speed λ_{cr} versus thickness-to-radius ratio α. $\epsilon = 0$; ——, $\rho' = 0.36$ (fluid-filled shell); – – – –, $\rho' = 0$ (empty shell).

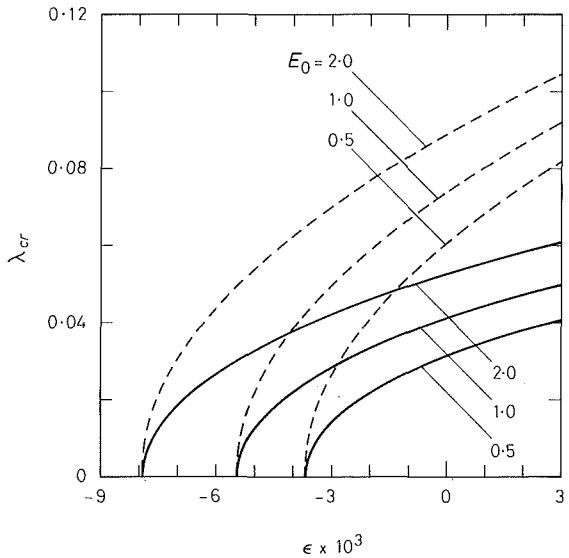


Fig. 2 The first non-dimensional critical speed λ_{cr} versus initial stress parameter ϵ. $\alpha = 0.01$; ——, $\rho' = 0.36$ (fluid-filled shell); – – – –, $\rho' = 0$ (empty shell).

[1]Associate Professor, Department of Mechanical Engineering, Tohoku University, Sendai, Japan

Manuscript received by ASME Applied Mechanics Division, July 7, 1982; final revision November 14, 1984.

Downloaded 02 May 2010 to 171.66.16.54. Redistribution subject to ASME license or copyright; see http://www.asme.org/terms/Terms_Use.cfm

where $V = 4\pi a_3{}^2 a_1/3$ is the volume of a single inclusion. This quantity varies by 42% as the inclusion shape ranges from penny shaped to spherical.

Figure 2 shows the compliance per inclusion ($\mu/NV_1\kappa$), normalized now by the volume of a circumscribing sphere, $V_1 = 4\pi a_3{}^3/3$, versus the shear modulus of the inclusion relative to that of the host (μ^*/μ). A Poisson's ratio of 1/3 is assumed for both materials, and the inclusion is taken to be softer than the host. Of particular interest is the transition to the crack limit of $4/3\pi$. For highly oblate inclusions, the modulus required to approach the crack response varies directly with the ratio a_1/a_3. Thinner inclusions require a smaller modulus before they can have a substantial compliance.

Discussion

These results for κ, coupled with the readily computed values of m, should provide a useful approximation in studying the interaction of elastic waves with inclusion layers. A particularly important application would appear to be the nondestructive evaluation of bonded layers.

Acknowledgment

This work was performed for the U.S. Department of Energy, Office of Basic Energy Sciences, Division of Materials Sciences, under contract No. W-7405-Eng-82.

References

Angel, Y. C., and Achenbach, J. D., 1985, "Reflection and Transmission of Elastic Waves by a Periodic Array of Cracks," ASME JOURNAL OF APPLIED MECHANICS, Vol. 107, pp. 33–41.

Baik, J. M., and Thompson, R. B., 1985, "The Elastic Compliance of Imperfect Interfaces: Review and Relationship to Ultrasonic Scattering," *Review of Progress in Quantitative NDE*, Vol. 4, Thompson, D. O., and Chimenti, D. E., eds., Plenum Press, New York, pp. 133–144.

Eshelby, J. D., 1961, "Elastic Inclusions and Inhomogeneities," *Progress in Solid Mechanics*, Vol. II., Ch. III, Sneddon, I. N., and Hill, R., eds., North-Holland, Amsterdam, pp. 89–140.

Tada, U., Paris, P., and Irwin, G., 1973, *The Stress Analysis of Cracks Handbook*, Del Research Corporation, St. Louis.

Thompson, R. B., Skilling, B. J., Zachary, B. J., Schmerr, L. W., and Buck, O., 1983, "Effects of Crack Closure on Ultrasonic Transmission," *Review of Progress in Quantitative Nondestructive Evaluation*, Vol. 2, Thompson, D. O., and Chimenti, D. E., eds., Plenum Press, New York, pp. 325–343.

Thompson, R. B., and Fiedler, C. J., 1984, "The Effects of Crack Closure on Ultrasonic Scattering Measurements," *Review of Progress in Quantitative Nondestructive Evaluation*, Vol. 3, Thompson, D. O., and Chimenti, D. E., eds., Plenum Press, New York, pp. 207–215.

Moving Load on Initially Stressed Orthotropic Cylindrical Shells Filled With Liquid

S. Chonan[1]

Introduction

This note is concerned with the dynamic response of infinitely long, axially stressed, fluid-filled orthotropic cylindrical shells subjected to an axisymmetric moving load. It is the purpose of this note to study to what extent the shell response is affected by the internal fluid medium. The critical load speed for which a resonance effect occurs in the system is obtained and the profile of the bending moment in the shell is shown graphically for a subcritical load speed. The results are compared with those of empty orthotropic shells.

[1]Associate Professor, Department of Mechanical Engineering, Tohoku University, Sendai, Japan

Manuscript received by ASME Applied Mechanics Division, July 7, 1982; final revision November 14, 1984.

Governing Equations

Consider an infinitely long, fluid-filled orthotropic cylindrical shell with initial axial stress. The x coordinate is along the shell axis and the r coordinate is in the direction of the shell radius. The θ coordinate is normal to x and r. The resultant force of the initial stress is denoted by T. The shell is subjected to an axisymmetric load $p(x,t)$, so that the θ component of the displacement vanishes. The displacements of the shell in the r and x directions are denoted by w and u, and the corresponding displacements of fluid by w_f and u_f. Furthermore, the rotation angle of the shell in the xr plane is denoted by ψ. The fluid pressure on the inner shell surface is given by $p_F(x,t)$. In this case the equations of motion of the shell are suitable modifications of those given in reference [1] and are written as

$$[(E_x + T)\partial^2/\partial x^2 - m_\rho \partial^2/\partial t^2]u + [(E_\nu/R)\partial/\partial x]w + [-(D_x/R)\partial^2/\partial x^2 + (I_\rho/R)\partial^2/\partial t^2]\psi - \eta_x(1 + h/2R)(\partial/\partial t)[u - (h/2)\psi] = 0, \quad (1)$$

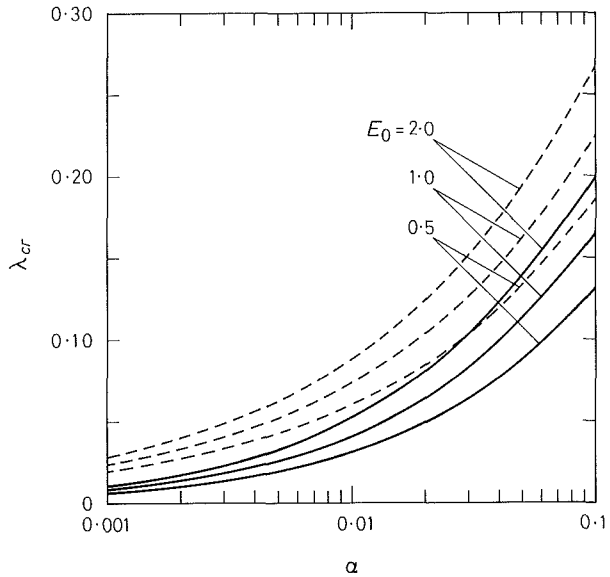


Fig. 1 The first non-dimensional critical speed λ_{cr} versus thickness-to-radius ratio α. $\epsilon = 0$; ——, $\rho' = 0.36$ (fluid-filled shell); – – – –, $\rho' = 0$ (empty shell).

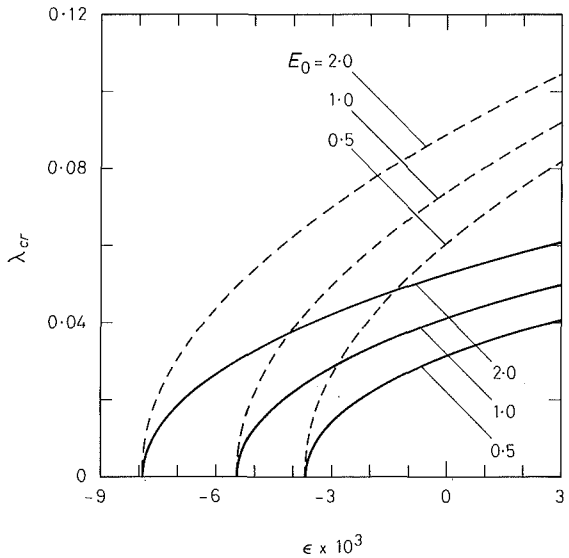


Fig. 2 The first non-dimensional critical speed λ_{cr} versus initial stress parameter ϵ. $\alpha = 0.01$; ——, $\rho' = 0.36$ (fluid-filled shell); – – – –, $\rho' = 0$ (empty shell).

Copyright © 1985 by ASME
Downloaded 02 May 2010 to 171.66.16.54. Redistribution subject to ASME license or copyright; see http://www.asme.org/terms/Terms_Use.cfm

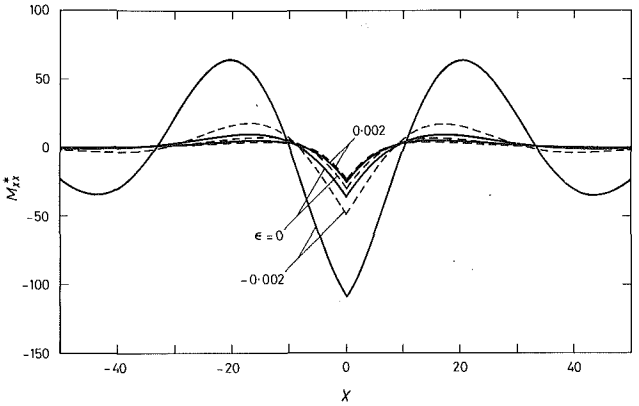


Fig. 3 Variation of bending moment profile with increasing initial stress parameter ϵ. $\lambda = 0.02$, $\alpha = 0.01$, $E_0 = 0.5$; ——, $\rho' = 0.36$ (fluid-filled shell); – – –, $\rho' = 0$ (empty shell).

$$[(E_\nu/R)\partial/\partial x]u + [-(G_x+T)\partial^2/\partial x^2 + (1/R^2)(E_\theta + D_\theta/R^2) + m_\rho \partial^2/\partial t^2]w + [G_x \partial/\partial x]\psi + \eta_r(1+h/2R)(\partial/\partial t)w = (1+h/2R)p(x,t) + (1-h/2R)p_F(x,t), \quad (2)$$

$$[(D_x/R)\partial^2/\partial x^2 - (I_\rho/R)\partial^2/\partial t^2]u + [-G_x\partial/\partial x]w + [-D_x\partial^2/\partial x^2 + G_x + I_\rho \partial^2/\partial t^2]\psi - \eta_x(h/2)(1+h/2R)(\partial/\partial t)[u-(h/2)\psi] = 0, \quad (3)$$

where

$$E_x = E_{x0}h,\ E_\theta = E_{\theta 0}h,\ E_\nu = E_{\nu 0}h,\ G_x = \kappa G_{x0}h,$$
$$D_x = E_{x0}h^3/12,\ D_\theta = E_{\theta 0}h^3/12,\ m_\rho = \rho h,\ I_\rho = \rho h^3/12.$$

Here, E_{x0}, $E_{\theta 0}$, $E_{\nu 0}$ and G_{x0} are the moduli of elasticity, κ $(=\pi^2/12)$ is the shear coefficient, h, R and ρ are the thickness, mean radius and mass density of the shell, and t the time; η_r and η_x are the coefficients of external damping for the radial and tangential movements of the outer shell surface.

For the fluid medium, the linear acoustic equation is used. In this case, if one represents the velocities of the fluid as

$$\partial w_f/\partial t = -\partial\phi/\partial r,\ \partial u_f/\partial t = -\partial\phi/\partial x, \quad (4,5)$$

ϕ satisfies

$$[\partial^2/\partial r^2 + (1/r)\partial/\partial r + \partial^2/\partial x^2 - (1/c_f^2)\partial^2/\partial t^2]\phi = 0, c_f^2 = K_f/\rho_f \quad (6)$$

where K_f and ρ_f are the bulk modulus and mass density. The fluid pressure p_f is given by

$$p_f = \rho_f \partial\phi/\partial t. \quad (7)$$

At the interface between the shell and the fluid, the pressure and the normal velocities are continuous, i.e.,

$$(\partial/\partial t)w(x,t) = (\partial/\partial t)w_f(r,x,t)\,|_{r=R-(h/2)}, \quad (8)$$

$$p_F(x,t) = p_f(r,x,t)\,|_{r=R-(h/2)}. \quad (9)$$

The shell is assumed to be acted upon by a moving load

$$p(x,t) = -P\delta(x-ct), \quad (10)$$

where δ is the Dirac delta function, and c the load speed.

The procedure of determining the solution by applying the complex Fourier transform method is the same as the one outlined in references [2] and [3], and is not repeated here. In the following the numerical results obtained are shown.

Numerical Results and Discussion

The results that follow are for the physical parameters $E_{x0} = 7.7\times10^{10}\ N/m^2$, $G_{x0} = 2.7\times10^{10}\ N/m^2$, $E_{\nu 0} = 2.3\times10^{10}\ N/m^2$, $K_f = 0.2\times10^{10}\ N/m^2$, $\rho = 2.8\times10^3\ kg/m^3$, $\rho_f = 1.0\times10^3\ kg/m^3$, and $\eta_x = \eta_r = 0$. Non-dimensional parameters are introduced in the figures: $M_{xx}^* = [12/Ph]M_{xx}$, $X = (x-ct)/h$, $\lambda = [\rho/E_{x0}]^{1/2}c$, $E_0 = [1/E_{x0}]E_{\theta 0}$, $\alpha = h/R$, $\epsilon = [1/E_{x0}h]T$, $\rho' = \rho_f/\rho$. Here, M_{xx}^* is the dimensionless moment per unit length of the shell cross-section perpendicular to the x-axis, X is the dimensionless moving coordinate, λ is the dimensionless load speed, E_0 is the orthotropy coefficient, α is the thickness-to-radius ratio of the shell, ϵ is the dimensionless initial axial stress, and ρ' is the mass ratio of the fluid and the shell.

Figure 1 shows the nondimensional critical load speed $\lambda_{cr}(=[\rho/E_{x0}]^{1/2}c_{cr})$ for which a resonance effect occurs in the system. λ_{cr} is plotted as a function of α both for the fluid-filled and the empty shells. When $\lambda = \lambda_{cr}$, one has the solution of the form [2, 3]

$$\int_{-\infty}^{\infty} [g(s)/(s-\alpha)^2(s+a)^2]ds.$$

It blows up, and one encounters a resonance in the sense that the amplitudes of the various quantities in the system increase beyond bound all along the shell. Clearly λ_{cr} of the fluid-filled shell is lower than that of the empty shell. This comes from the inertia effect of the internal fluid. It is also observed that λ_{cr} increases with an increase of E_0. In the figure $\lambda_{cr} = 0.1$ corresponds to Mach number $M = 1.46$.

Figure 2 shows the variation of λ_{cr} with increasing ϵ for $\alpha = 0.01$. λ_{cr} decreases monotonically and reaches zero as the compressive axial force increases. The critical speeds of the fluid-filled and the empty shells become zero at the same value of the axial load. This is due to the fact that the inertia effect of the fluid decreases with a decrease of the load speed and its effect on the shell finally vanishes when the load speed becomes zero.

Figure 3 shows the moment profile of an orthotropic shell for a load speed $\lambda = 0.02$. The results were obtained by applying the residue theorem to the inverse integral. The load speed is lower than the critical speed for all the values of ϵ under consideration. In that case the singular points of the integrand for the fluid-filled shell are given by $s = m_1 \pm in_1$, $-m_1 \pm in_1$, $\pm in_2$,- - -, $\pm in_\infty$. For the empty shell they are reduced to $s = m_1 \pm in_1$, $-m_1 \pm in_1$. The response curves of the fluid-filled shell were obtained by taking into account the first 40 residues. The 40th residue was 10^{-3} times as large as the first residue. For the subcritical load speed, the M_{xx}^* is distributed symmetrically with respect to the position of the applied load ($X = 0$). It takes on a maximum value under the load. The maximum moment increases when the shell is subjected to a compressive axial force. It is also observed that the response amplitude of the fluid-filled shell is greater than that of the empty shell.

References

1 Baker, E. H., and Herrmann, G., "Vibration of Orthotropic Cylindrical Sandwich Shells under Initial Stress," *AIAA Journal*, Vol. 4, 1966, pp. 1063-1070.

2 Achenbach, J. D., and Sun, C. T., "Moving Load on a Flexibly Supported Timoshenko Beam," *International Journal of Solids and Structures*, Vol. 1, 1965, pp. 353-370.

3 Herrmann, G., and Baker, E. H., "Response of Cylindrical Sandwich Shells to moving Loads," ASME JOURNAL OF APPLIED MECHANICS, Vol. 34, 1967, pp. 81-86.

Axial Stress-Time History Measurements in Impulsively Loaded Aluminum Rods Using the Double Gauge Technique

Z. Rosenberg[1], M. Mayseless[1], and Y. Partom[1]

[1] A. D. A., Haifa, Israel.

Manuscript received by ASME Applied Mechanics Division, November 20, 1984; final revision April 30, 1985.

Downloaded 02 May 2010 to 171.66.16.54. Redistribution subject to ASME license or copyright; see http://www.asme.org/terms/Terms_Use.cfm

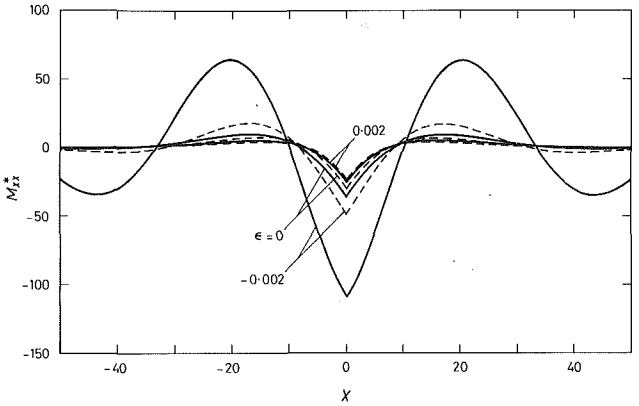


Fig. 3 Variation of bending moment profile with increasing initial stress parameter ϵ. $\lambda = 0.02$, $\alpha = 0.01$, $E_0 = 0.5$; ——, $\rho' = 0.36$ (fluid-filled shell); – – –, $\rho' = 0$ (empty shell).

$$[(E_\nu/R)\partial/\partial x]u + [-(G_x+T)\partial^2/\partial x^2 + (1/R^2)(E_\theta + D_\theta/R^2) + m_\rho \partial^2/\partial t^2]w + [G_x \partial/\partial x]\psi + \eta_r(1+h/2R)(\partial/\partial t)w = (1+h/2R)p(x,t) + (1-h/2R)p_F(x,t), \quad (2)$$

$$[(D_x/R)\partial^2/\partial x^2 - (I_\rho/R)\partial^2/\partial t^2]u + [-G_x\partial/\partial x]w + [-D_x\partial^2/\partial x^2 + G_x + I_\rho \partial^2/\partial t^2]\psi - \eta_x(h/2)(1+h/2R)(\partial/\partial t)[u-(h/2)\psi] = 0, \quad (3)$$

where

$$E_x = E_{x0}h,\ E_\theta = E_{\theta 0}h,\ E_\nu = E_{\nu 0}h,\ G_x = \kappa G_{x0}h,$$
$$D_x = E_{x0}h^3/12,\ D_\theta = E_{\theta 0}h^3/12,\ m_\rho = \rho h,\ I_\rho = \rho h^3/12.$$

Here, E_{x0}, $E_{\theta 0}$, $E_{\nu 0}$ and G_{x0} are the moduli of elasticity, κ $(=\pi^2/12)$ is the shear coefficient, h, R and ρ are the thickness, mean radius and mass density of the shell, and t the time; η_r and η_x are the coefficients of external damping for the radial and tangential movements of the outer shell surface.

For the fluid medium, the linear acoustic equation is used. In this case, if one represents the velocities of the fluid as

$$\partial w_f/\partial t = -\partial\phi/\partial r,\ \partial u_f/\partial t = -\partial\phi/\partial x, \quad (4,5)$$

ϕ satisfies

$$[\partial^2/\partial r^2 + (1/r)\partial/\partial r + \partial^2/\partial x^2 - (1/c_f^2)\partial^2/\partial t^2]\phi = 0, c_f^2 = K_f/\rho_f \quad (6)$$

where K_f and ρ_f are the bulk modulus and mass density. The fluid pressure p_f is given by

$$p_f = \rho_f \partial\phi/\partial t. \quad (7)$$

At the interface between the shell and the fluid, the pressure and the normal velocities are continuous, i.e.,

$$(\partial/\partial t)w(x,t) = (\partial/\partial t)w_f(r,x,t)\,|_{r=R-(h/2)}, \quad (8)$$

$$p_F(x,t) = p_f(r,x,t)\,|_{r=R-(h/2)}. \quad (9)$$

The shell is assumed to be acted upon by a moving load

$$p(x,t) = -P\delta(x-ct), \quad (10)$$

where δ is the Dirac delta function, and c the load speed.

The procedure of determining the solution by applying the complex Fourier transform method is the same as the one outlined in references [2] and [3], and is not repeated here. In the following the numerical results obtained are shown.

Numerical Results and Discussion

The results that follow are for the physical parameters $E_{x0} = 7.7\times10^{10}\ N/m^2$, $G_{x0} = 2.7\times10^{10}\ N/m^2$, $E_{\nu 0} = 2.3\times10^{10}\ N/m^2$, $K_f = 0.2\times10^{10}\ N/m^2$, $\rho = 2.8\times10^3\ kg/m^3$, $\rho_f = 1.0\times10^3\ kg/m^3$, and $\eta_x = \eta_r = 0$. Non-dimensional parameters are introduced in the figures: $M_{xx}^* = [12/Ph]M_{xx}$, $X = (x-ct)/h$, $\lambda = [\rho/E_{x0}]^{1/2}c$, $E_0 = [1/E_{x0}]E_{\theta 0}$, $\alpha = h/R$, $\epsilon = [1/E_{x0}h]T$, $\rho' = \rho_f/\rho$. Here, M_{xx}^* is the dimensionless moment per unit length of the shell cross-section perpendicular to the x-axis, X is the dimensionless moving coordinate, λ is the dimensionless load speed, E_0 is the orthotropy coefficient, α is the thickness-to-radius ratio of the shell, ϵ is the dimensionless initial axial stress, and ρ' is the mass ratio of the fluid and the shell.

Figure 1 shows the nondimensional critical load speed $\lambda_{cr}(=[\rho/E_{x0}]^{1/2}c_{cr})$ for which a resonance effect occurs in the system. λ_{cr} is plotted as a function of α both for the fluid-filled and the empty shells. When $\lambda = \lambda_{cr}$, one has the solution of the form [2, 3]

$$\int_{-\infty}^{\infty} [g(s)/(s-\alpha)^2(s+a)^2]ds.$$

It blows up, and one encounters a resonance in the sense that the amplitudes of the various quantities in the system increase beyond bound all along the shell. Clearly λ_{cr} of the fluid-filled shell is lower than that of the empty shell. This comes from the inertia effect of the internal fluid. It is also observed that λ_{cr} increases with an increase of E_0. In the figure $\lambda_{cr} = 0.1$ corresponds to Mach number $M = 1.46$.

Figure 2 shows the variation of λ_{cr} with increasing ϵ for $\alpha = 0.01$. λ_{cr} decreases monotonically and reaches zero as the compressive axial force increases. The critical speeds of the fluid-filled and the empty shells become zero at the same value of the axial load. This is due to the fact that the inertia effect of the fluid decreases with a decrease of the load speed and its effect on the shell finally vanishes when the load speed becomes zero.

Figure 3 shows the moment profile of an orthotropic shell for a load speed $\lambda = 0.02$. The results were obtained by applying the residue theorem to the inverse integral. The load speed is lower than the critical speed for all the values of ϵ under consideration. In that case the singular points of the integrand for the fluid-filled shell are given by $s = m_1 \pm in_1$, $-m_1 \pm in_1$, $\pm in_2$,- - -, $\pm in_\infty$. For the empty shell they are reduced to $s = m_1 \pm in_1$, $-m_1 \pm in_1$. The response curves of the fluid-filled shell were obtained by taking into account the first 40 residues. The 40th residue was 10^{-3} times as large as the first residue. For the subcritical load speed, the M_{xx}^* is distributed symmetrically with respect to the position of the applied load $(X = 0)$. It takes on a maximum value under the load. The maximum moment increases when the shell is subjected to a compressive axial force. It is also observed that the response amplitude of the fluid-filled shell is greater than that of the empty shell.

References

1 Baker, E. H., and Herrmann, G., "Vibration of Orthotropic Cylindrical Sandwich Shells under Initial Stress," *AIAA Journal*, Vol. 4, 1966, pp. 1063-1070.

2 Achenbach, J. D., and Sun, C. T., "Moving Load on a Flexibly Supported Timoshenko Beam," *International Journal of Solids and Structures*, Vol. 1, 1965, pp. 353-370.

3 Herrmann, G., and Baker, E. H., "Response of Cylindrical Sandwich Shells to moving Loads," ASME JOURNAL OF APPLIED MECHANICS, Vol. 34, 1967, pp. 81-86.

Axial Stress-Time History Measurements in Impulsively Loaded Aluminum Rods Using the Double Gauge Technique

Z. Rosenberg[1], M. Mayseless[1], and Y. Partom[1]

[1] A. D. A., Haifa, Israel.

Manuscript received by ASME Applied Mechanics Division, November 20, 1984; final revision April 30, 1985.

Copyright © 1985 by ASME
Downloaded 02 May 2010 to 171.66.16.54. Redistribution subject to ASME license or copyright; see http://www.asme.org/terms/Terms_Use.cfm

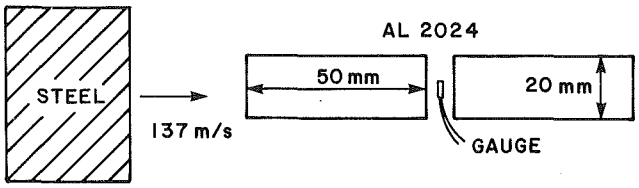


Fig. 1 Schematic representation of the rigid wall impacting an instrumented rod

The purpose of this Brief Note is to present experimental stress-time histories along the centerline of impulsively loaded aluminum rods. The measurement is based on the double gauge technique in which we use both a manganin stress gauge and a constantan strain gauge at the same location in the rod. The strain gauge record enables one to eliminate the strain contribution to stress gauge resistance change and have a stress-time history. The measured stress history is compared to a calculated one using two-dimensional Lagrangian code and the agreement between them is good.

Introduction

The transient response of impulsively loaded cylindrical bars has been the subject of numerous investigations for over a century. Most of the experimental work in this field has been based on strain measurements at various locations along the impacted bar. Some works were published in which thin quartz discs were inserted inside the bar in an attempt to measure stress-time histories. As emphasized by Habberstad et al. (1972), these gauges suffer from two major limitations: (a) mechanical impedance mismatch between gauge and bar and (b) relatively poor time resolution because of gauge thickness.

In a recent paper by Rosenberg et al. (1984a), we have demonstrated the feasibility of using commercial manganin stress gauges to measure stress-time histories inside impulsively loaded long rods. We have shown there that owing to the simple uniaxial stress state which exists for long rods (length to diameter ratio of at least 10) it is possible to use the same calibration curve for the gauge which we determined recently in planar impact experiments as given by Rosenberg et al. (1980). The stress waves which we measured in Rosenberg et al. (1984a) were the elastic waves which propagate at bar velocities along the long rod. In order to perform stress measurements during dynamic plastic deformation, one has to embed the stress gauge closer to the impact end of the bar (say two to five diameters). At these close distances, the bar deforms considerably and so does the embedded stress gauge. In order to have a meaningful stress-time history from such a deforming piezoresistive gauge we have to work with the double-gauge technique, which was presented in Rosenberg et al. (1984b), for axially symmetric impacts.

The purpose of the present note is to demonstrate the usefulness of the double-gauge technique by measuring the stress-time history inside impulsively loaded short rods near the impacted end.

We shall briefly describe the double-gauge technique after which we present experimental results of the stress-time histories in the middle of 2024-T351 aluminum rods at a distance of 2.5 diameters from the impact end. These measured histories are then compared to calculated ones using a 2-D elasto-plastic Lagrangian code.

Experimental Techniques

The basic idea behind the double gauge technique is that when a piezoresistive gauge is placed in a complex stress field,

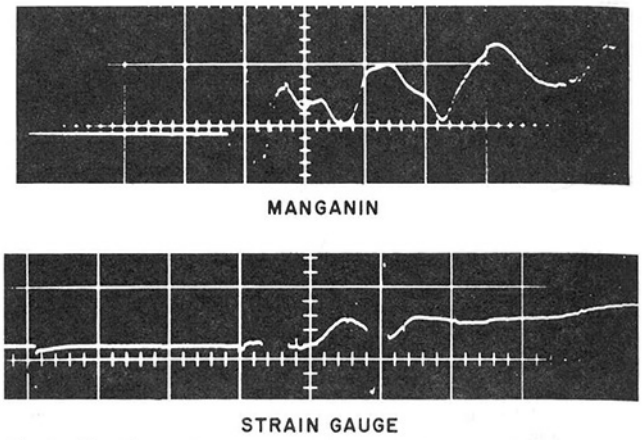


Fig. 2 Experimental gauge record from a typical experiment. In both records, time sweep is 2 μs/div.

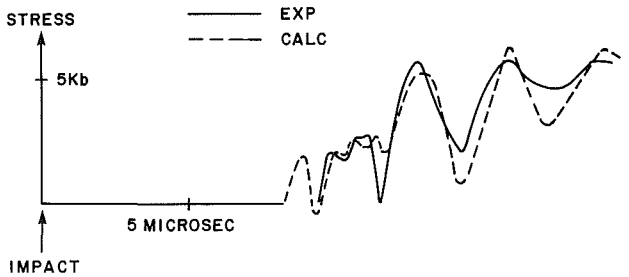


Fig. 3 The reduced stress-time history and the calculated one

its electrical resistance changes are due to both the stress which acts on it (through its specific resistivity) and the strains it experiences, which tend to change its length and cross section. By using two well-calibrated piezoresistive gauges, one on top the other, it is possible to eliminate the strain contribution to their resistance-time signals. We have used manganin and constantan as the two gauges in Rosenberg et al. (1984b) and used these two gauges also for the present study.

The two gauges were inserted between two aluminum rods (2024-T351, 20 mm in diameter and 50 mm long) as shown in Fig. 1. The gauges are manufactured by Micro-Measurements (manganin type LM-SS-12CH-048 and constantan type CEA-13-1250W-120). The thickness of each gauge is about 5μm and with their packages their thickness is 0.05 mm. In order to isolate the gauge and its leads from the metallic rod, we added two 25 μm mylar sheets on both sides of the gauge so that the total thickness of the gauge layer between the rods was about 0.1 mm. The gauges with the mylar sheets were bonded to the rods with Hysol 0151 clear epoxy resin.

One can embed the two gauges as was done in Rosenberg et al. (1984b) but instead of inserting one gauge above the other, we found it easier to perform two identical experiments with one gauge per shot. The various details concerning manganin gauge calibration and their constant-current power supply can be found in Rosenberg et al. (1980) so that we will not repeat them here. Their piezoresistance coefficient (under uniaxial strain conditions) is about 2×10^{-3} (ohm/ohm)/kg, while that of the constantan gauges is zero (these gauges are used as strain gauges because of the fact that their electrical resistivity is insensitive to both temperature and pressure).

Due to this behavior of the constantan gauge, we can get the longitudinal strain of the gauge in a straightforward manner (see Rosenberg et al. (1984b):

$$\epsilon_L = \sqrt{R/R_0} - 1 \tag{1}$$

Downloaded 02 May 2010 to 171.66.16.54. Redistribution subject to ASME license or copyright; see http://www.asme.org/terms/Terms_Use.cfm

where R is the measured resistance of the gauge and R_0 is its initial value, and ϵ_l is the longitudinal strain in the gauge (along the current direction).

In the experiments which we describe here, we assume that owing to the fact that the two gauges (manganin and constantan) are situated at the same point inside the rod, and due to their similarity in shape, they experience the same stress and strain fields. Thus, by eliminating the longitudinal strain ϵ_L from the manganin gauge record, we have the axial stress-time history at the gauges' location.

Calculation Scheme

In order to follow the complex nature of the stress-time histories, at the center of the rod, we used our 2D Lagrangian elastoplastic code – DISCO – which was described by Kivity and Tsur (1978). The code is similar to the well known HEMP code and we used an underformable rigid wall with full sliding across the interface in order to describe the impact. The constitutive model which we used in order to describe material behavior is the Phase Model which was described recently by Partom and Schanin (1979) and Partom (1980).

The axial stresses were calculated near the center line of the rod and an average was taken over four computational cells in order to simulate the lateral dimensions of the gauges, which are about 3×3 mm.

Results and Discussion

Two typical records are shown in Fig. 2 where one can clearly see the complex behavior of both the strain and stress histories. Both records have a very noisy part for the first 1 μs after wave arrival to the gauge location. The noise is probably due to large tensile stresses, as the code calculation has shown. After about 1 μs, however, the two gauges show a relatively smooth behavior for about 10 microseconds. The wave nature of the manganin gauge record is due to the lateral reverberations across the rod diameter of the release waves following the deformation of the rod. The time between two consecutive extrema in the gauge record matches the time needed to sound waves to travel back and forth along the bar radius. Similar characteristics of stress histories were also noted by Karnes and Bertholf (1969) in their calculations of rod impacts.

The reduced axial stress-time history from the two gauges is shown in Fig. 3 together with the calculated one. As we can see, the agreement between the two is good and the general behavior of the stress signal is similar to the manganin gauge record (Fig. 2) which means that the strain corrections were not too large. The peak stresses (both measured and calculated) histories are near 6 kb which is about twice the yield strength of the material (for 2024-T351 we measured $y_0 = 3.4$ kb in simple tension experiments.

The relative minima of the stress histories show quite a large discrepancy between calculated and experimental records. We do not know the reason for this, but we think that it has to do with the modelling of the dynamic plastic response of the aluminum alloy. This response is probably not accurately modelled, especially with the several loading-unloading cycles which the material experiences. Thus, we conclude that the various features of the stress histories show good agreement which can be improved by a better modelling (Bauschinger effect, etc.) of the rod material.

Conclusions

We have measured the axial stress-time histories inside impulsively loaded aluminum rods near the impacted end (2.5 diameters). The measurement is achieved by using the double gauge technique which is most appropriate for axially symmetric stress fields. The measured stress signal is in good agreement with the calculated one and both show the expected stress reverberations with stress extrema reaching 6 kb which is about twice the static yield strength for this aluminum.

The double gauge technique can be used to determine such stress histories at various points along the centerline of the rod enabling one to calibrate computer codes and test constitutive models.

Acknowledgments

The authors wish to thank Mr. R. Kreif and Mr. D. Mazar for their technical help in performing the shots.

References

1 Habberstad, J. L., Hoge, K. G., and Foster, J. E., 1972, "An Experimental and Numerical Study of Elastic Strain Waves on the Centerline of a 6061-TG Aluminum Bar," ASME JOURNAL OF APPLIED MECHANICS, 39, 386–371.

2 Karnes, C. H., and Bertholf, L. D., *Inelastic Behavior of Solids*, M. L. Kamninen, W. F. Adler, A. R. Rosenfield, and R. I. Jaffee eds., McGraw-Hill, N.Y. 501–519.

3 Kivity, Y., and Tsur, D., 1978, "Study of Projectile Formation in Lined Shallow Cavity Charges," *Proc. of the 4th Int. Symp. on Ballistics*, Monterey, CA., Oct. 17–19.

4 Partom, Y., and Schanin, J., 1979, "Calibration of Nonlinear Viscoelastic Response," Msc. Thesis of J. Schanin, Technion-ISRAEL Institute of Technology.

5 Partom, Y., 1980, "Calculation of Viscoplastic Response," *Physical Nonlinearities in Structural Analysis*, J. Hult and J. Lemaite, eds. Senlis, pp. 207–211.

6 Rosenberg, Z., Mayseless, M., and Partom, Y., 1984a, "The Use of Manganin Stress Transducers in Impulsively Loaded Long Rod Experiments," ASME JOURNAL OF APPLIED MECHANICS, Vol. 51, pp. 202–204.

7 Rosenberg, Z., Partom, Y., Mayseless, M., and Falcovitz, J., 1984b, "Determination of Stress Time Histories in Axially Symmetric Impacts with the Two-Gauge Technique," *Journal of Applied Physics*, Vol. 56, pp. 1434–1438.

8 Rosenberg, Z., Yaziv, D., and Partom, Y., 1980, "Calibration of Foil Like Manganin Gauges," *Journal of Applied Physics*, Vol. 51, pp. 3702–3705.

Solutions of Multiple Crack Problems of Elastic Half-Plane

Y. Z. Chen[1]

Introduction

As a counterpart to the singular integral equation approach in crack problem [1–4], the Fredholm integral equation approach for the multiple crack problems of elastic half-plane is used in this note. Using the elementary solution obtained and taking some density distributions of the elementary solution along each crack, the proposed problem can be easily converted into a system of Fredholm integral equation. We found that the proposed approach is very effective, efficient and interesting.

Analysis

According to Muskhelishvili's work [5], resultant forces and displacements can be expressed as follows

$$-Y+iX=\eta_1\varphi(z)+z\overline{\varphi'(z)}+\overline{\psi(z)}, \quad \eta_1=1 \tag{1}$$

$$2G(u+iv)=-(\eta_2\varphi(z)+z\overline{\varphi'(z)}+\overline{\psi(z)}), \quad \eta_2=-\kappa \tag{2}$$

where G is the shear modulus of elasticity, $\kappa=(3-\nu)/(1+\nu)$ for plane stress and $\kappa=3-4\nu$ for plane strain conditions, ν is the Poisson's ratio, and $\varphi(z)$, $\varphi'(z)=\Phi(z)$, $\psi(z)$, $\psi'(z)=\Psi(z)$ are analytic functions.

If two pairs of the concentrated forces (P_{pair} and Q_{pair} in Fig. 1) are applied at a prescribed point $(s, 0)$ of both edges of a single crack in an infinite plate, after some manipulations one easily obtains the following solution [6]

$$\Phi_p(z)=-\frac{P-iQ}{2\pi i}\frac{X(s)}{X(z)(z-s)}, \tag{3}$$

[1] Associate Professor, Division of Engineering Mechanics, P.O. Box 80, Jiangsu Institute of Technology, Zhenjiang, Jiangsu, 212003, People's Republic of China.

Manuscript received by ASME Applied Mechanics Division, June 27, 1984; final revision February 20, 1985.

Downloaded 02 May 2010 to 171.66.16.54. Redistribution subject to ASME license or copyright; see http://www.asme.org/terms/Terms_Use.cfm

where R is the measured resistance of the gauge and R_0 is its initial value, and ϵ_l is the longitudinal strain in the gauge (along the current direction).

In the experiments which we describe here, we assume that owing to the fact that the two gauges (manganin and constantan) are situated at the same point inside the rod, and due to their similarity in shape, they experience the same stress and strain fields. Thus, by eliminating the longitudinal strain ϵ_L from the manganin gauge record, we have the axial stress-time history at the gauges' location.

Calculation Scheme

In order to follow the complex nature of the stress-time histories, at the center of the rod, we used our 2D Lagrangian elastoplastic code – DISCO – which was described by Kivity and Tsur (1978). The code is similar to the well known HEMP code and we used an underformable rigid wall with full sliding across the interface in order to describe the impact. The constitutive model which we used in order to describe material behavior is the Phase Model which was described recently by Partom and Schanin (1979) and Partom (1980).

The axial stresses were calculated near the center line of the rod and an average was taken over four computational cells in order to simulate the lateral dimensions of the gauges, which are about 3×3 mm.

Results and Discussion

Two typical records are shown in Fig. 2 where one can clearly see the complex behavior of both the strain and stress histories. Both records have a very noisy part for the first 1 μs after wave arrival to the gauge location. The noise is probably due to large tensile stresses, as the code calculation has shown. After about 1 μs, however, the two gauges show a relatively smooth behavior for about 10 microseconds. The wave nature of the manganin gauge record is due to the lateral reverberations across the rod diameter of the release waves following the deformation of the rod. The time between two consecutive extrema in the gauge record matches the time needed to sound waves to travel back and forth along the bar radius. Similar characteristics of stress histories were also noted by Karnes and Bertholf (1969) in their calculations of rod impacts.

The reduced axial stress-time history from the two gauges is shown in Fig. 3 together with the calculated one. As we can see, the agreement between the two is good and the general behavior of the stress signal is similar to the manganin gauge record (Fig. 2) which means that the strain corrections were not too large. The peak stresses (both measured and calculated) histories are near 6 kb which is about twice the yield strength of the material (for 2024-T351 we measured $y_0 = 3.4$ kb in simple tension experiments.

The relative minima of the stress histories show quite a large discrepancy between calculated and experimental records. We do not know the reason for this, but we think that it has to do with the modelling of the dynamic plastic response of the aluminum alloy. This response is probably not accurately modelled, especially with the several loading-unloading cycles which the material experiences. Thus, we conclude that the various features of the stress histories show good agreement which can be improved by a better modelling (Bauschinger effect, etc.) of the rod material.

Conclusions

We have measured the axial stress-time histories inside impulsively loaded aluminum rods near the impacted end (2.5 diameters). The measurement is achieved by using the double gauge technique which is most appropriate for axially symmetric stress fields. The measured stress signal is in good agreement with the calculated one and both show the expected stress reverberations with stress extrema reaching 6 kb which is about twice the static yield strength for this aluminum.

The double gauge technique can be used to determine such stress histories at various points along the centerline of the rod enabling one to calibrate computer codes and test constitutive models.

Acknowledgments

The authors wish to thank Mr. R. Kreif and Mr. D. Mazar for their technical help in performing the shots.

References

1 Habberstad, J. L., Hoge, K. G., and Foster, J. E., 1972, "An Experimental and Numerical Study of Elastic Strain Waves on the Centerline of a 6061-TG Aluminum Bar," ASME JOURNAL OF APPLIED MECHANICS, 39, 386–371.

2 Karnes, C. H., and Bertholf, L. D., *Inelastic Behavior of Solids*, M. L. Kamninen, W. F. Adler, A. R. Rosenfield, and R. I. Jaffee eds., McGraw-Hill, N.Y. 501–519.

3 Kivity, Y., and Tsur, D., 1978, "Study of Projectile Formation in Lined Shallow Cavity Charges," *Proc. of the 4th Int. Symp. on Ballistics*, Monterey, CA., Oct. 17–19.

4 Partom, Y., and Schanin, J., 1979, "Calibration of Nonlinear Viscoelastic Response," Msc. Thesis of J. Schanin, Technion-ISRAEL Institute of Technology.

5 Partom, Y., 1980, "Calculation of Viscoplastic Response," *Physical Nonlinearities in Structural Analysis*, J. Hult and J. Lemaite, eds. Senlis, pp. 207–211.

6 Rosenberg, Z., Mayseless, M., and Partom, Y., 1984a, "The Use of Manganin Stress Transducers in Impulsively Loaded Long Rod Experiments," ASME JOURNAL OF APPLIED MECHANICS, Vol. 51, pp. 202–204.

7 Rosenberg, Z., Partom, Y., Mayseless, M., and Falcovitz, J., 1984b, "Determination of Stress Time Histories in Axially Symmetric Impacts with the Two-Gauge Technique," *Journal of Applied Physics*, Vol. 56, pp. 1434–1438.

8 Rosenberg, Z., Yaziv, D., and Partom, Y., 1980, "Calibration of Foil Like Manganin Gauges," *Journal of Applied Physics*, Vol. 51, pp. 3702–3705.

Solutions of Multiple Crack Problems of Elastic Half-Plane

Y. Z. Chen[1]

Introduction

As a counterpart to the singular integral equation approach in crack problem [1–4], the Fredholm integral equation approach for the multiple crack problems of elastic half-plane is used in this note. Using the elementary solution obtained and taking some density distributions of the elementary solution along each crack, the proposed problem can be easily converted into a system of Fredholm integral equation. We found that the proposed approach is very effective, efficient and interesting.

Analysis

According to Muskhelishvili's work [5], resultant forces and displacements can be expressed as follows

$$-Y+iX=\eta_1\varphi(z)+z\overline{\varphi'(z)}+\overline{\psi(z)}, \quad \eta_1=1 \tag{1}$$

$$2G(u+iv)=-(\eta_2\varphi(z)+z\overline{\varphi'(z)}+\overline{\psi(z)}), \quad \eta_2=-\kappa \tag{2}$$

where G is the shear modulus of elasticity, $\kappa=(3-\nu)/(1+\nu)$ for plane stress and $\kappa=3-4\nu$ for plane strain conditions, ν is the Poisson's ratio, and $\varphi(z)$, $\varphi'(z)=\Phi(z)$, $\psi(z)$, $\psi'(z)=\Psi(z)$ are analytic functions.

If two pairs of the concentrated forces (P_{pair} and Q_{pair} in Fig. 1) are applied at a prescribed point $(s, 0)$ of both edges of a single crack in an infinite plate, after some manipulations one easily obtains the following solution [6]

$$\Phi_p(z)=-\frac{P-iQ}{2\pi i}\frac{X(s)}{X(z)(z-s)}, \tag{3}$$

[1] Associate Professor, Division of Engineering Mechanics, P.O. Box 80, Jiangsu Institute of Technology, Zhenjiang, Jiangsu, 212003, People's Republic of China.

Manuscript received by ASME Applied Mechanics Division, June 27, 1984; final revision February 20, 1985.

Copyright © 1985 by ASME
Downloaded 02 May 2010 to 171.66.16.54. Redistribution subject to ASME license or copyright; see http://www.asme.org/terms/Terms_Use.cfm

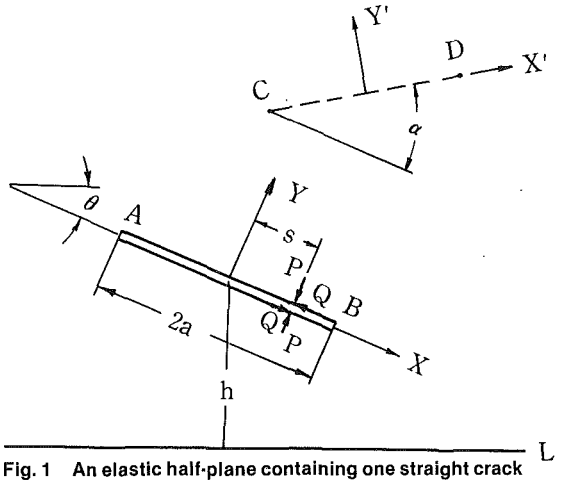


Fig. 1 An elastic half-plane containing one straight crack

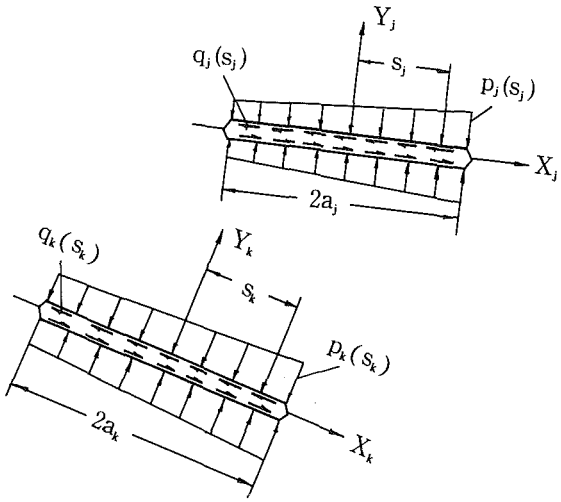


Fig. 2 Multiple crack problems in an elastic half-plane

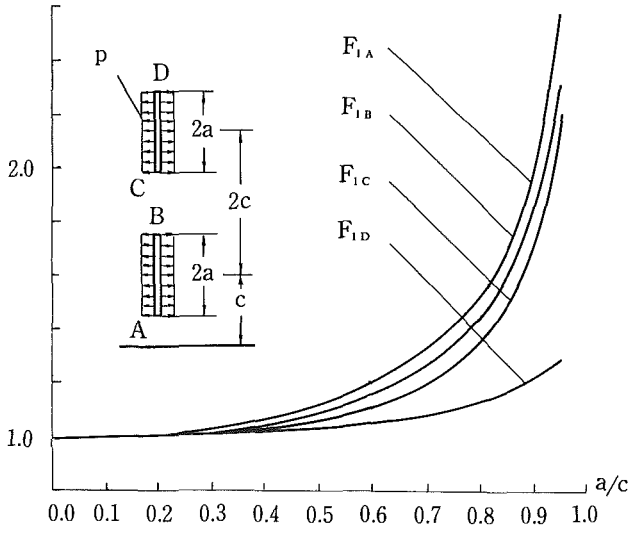


Fig. 3 Stress intensity factors for two cracks in series, where $F_{1A} = K_{1A}/(p\sqrt{\pi a})$, $F_{1B} = K_{1B}/(p\sqrt{\pi a})$, $F_{1C} = K_{1C}/(p\sqrt{\pi a})$, $F_{1D} = K_{1D}/(p\sqrt{\pi a})$

$$\Psi_p(z) = -\frac{P+iQ}{2\pi i}\frac{X(s)}{X(z)(z-s)} - \Phi_p(z) - z\Phi_p'(z), \qquad (4)$$

where

$$X(z) = \sqrt{(z^2-a^2)}, \quad X(s) = i\sqrt{(a^2-s^2)}. \qquad (5)$$

Note that, the subscript p in (3) and (4) means that the two complex potentials $\Phi_p(z)$ and $\Psi_p(z)$ are the first (or principal) part of the elementary solution. Clearly, the corresponding tractions along the boundary of the half-plane are not equal to zero.

If the boundary of a half-plane is traction free (Fig. 1), from (1) and the condition along the free boundary L we have

$$\eta_1\overline{\varphi(t)} + \bar{t}\varphi'(t) + \psi(t) = 0 \quad t\epsilon L \qquad (6a)$$

or

$$\eta_1\overline{\Phi(t)}d\bar{t} + \Phi(t)d\bar{t} + \bar{t}\Phi'(t)dt + \Psi(t)dt = 0. \quad t\epsilon L \qquad (6b)$$

Furthermore, if one uses the following relations along the boundary L

$$\bar{t} = At + B, \quad d\bar{t} = Adt \qquad (7)$$

where $A = exp\,(-2i\theta)$, $B = 2ih\ exp\ (-i\theta)$, then condition (6b) becomes

$$\eta_1\overline{\Phi(t)} + \Phi(t) + [(At+B)\Phi'(t) + \Psi(t)]/A = 0. \quad t\epsilon L \qquad (8)$$

It is easy to verify that the following complex potentials

$$\Phi(z) = \Phi_p(z) + \Phi_c(z), \quad \Psi(z) = \Psi_p(z) + \Psi_c(z) \qquad (9)$$

satisfy (8), if one takes

$$\Phi_c(z) = \bar{W}(Az+B)/\eta_1 \qquad (10)$$

$$\Psi_c(z) = -A[\eta_1\bar{\Phi}_p(Az+b) + \bar{W}(Az+B)/\eta_1] - A(Az+B)\bar{W}'(Az+B)/\eta_1, \qquad (11)$$

where

$$W(z) = -\Phi_p(z) - [(Az+B)\Phi_p'(z) + \Psi_p(z)]/A. \qquad (12)$$

In (9) two complex potentials $\Phi_c(z)$ and $\Psi_c(z)$ are the second part (or complement) of the elementary solution. Finally, $\Phi(z)$ and $\Psi(z)$ are called the elementary solutions for the multiple crack problems of the half-plane. Along the crack line AB and the fictitious line CD in Fig. 1, the normal and tangential tractions corresponding to the potentials $\Phi(z)$ and $\Psi(z)$ are [5, 6]

$$\sigma_{yy} + i\sigma_{xy} = (P+iQ)\delta(t-s) + \overline{\Phi_c(t)} + \bar{t}\Phi_c'(t) + \Psi_c(t) + \Phi_c(t), \quad t\epsilon AB \qquad (13)$$

$$\sigma_{y'y'} + i\sigma_{x'y'} = \Phi(z) + \overline{\Phi(z)} + exp(2i\alpha)(\bar{z}\Phi'(z) + \Psi(z)). \quad z\epsilon CD \qquad (14)$$

Now the multiple crack problem shown in Fig. 2 with the given normal and tangential forces $p_k(s_k)$ and $q_k(s_k)$ can be considered as a superposition of N single crack problems with the undetermined normal and tangential forces/densities $P_k(s_k)$ and $Q_k(s_k)$ along each crack. Furthermore, using the elementary solution obtained and principle of superposition, a system of Fredholm integral equations for $P_k(s_k)$ and $Q_k(s_k)$ is obtained as follows

$$P_k(s_k) + \sum_{j=1}^{N}\int_{-a_j}^{a_j} P_j(s_j)f_{nn,jk}(s_j,s_k)ds_j + \sum_{j=1}^{N}\int_{-a_j}^{a_j} Q_j(s_j)f_{tn,jk}(s_j,s_k)ds_j = p_k(s_k), \qquad (15)$$

$$Q_k(s_k) + \sum_{j=1}^{N}\int_{-a_j}^{a_j} P_j(s_j)f_{nt,jk}(s_j,s_k)ds_j + \sum_{j=1}^{N}\int_{-a_j}^{a_j} Q_j(s_j)f_{tt,jk}(s_j,s_k)ds_j = q_k(s_k), \qquad (16)$$

$$[s_k] < a_k, \quad k = 1,2,\ldots N$$

The meanings of the above kernels f_{nn}, f_{tn}, f_{nt} and f_{tt} can be found from [6–8].

Downloaded 02 May 2010 to 171.66.16.54. Redistribution subject to ASME license or copyright; see http://www.asme.org/terms/Terms_Use.cfm

After the system of the integral equations (15) and (16) is solved, the stress intensity factors at the crack tips can be obtained from

$$K_{A,j}=K_{1A,j}-iK_{2A,j}=-\int_{-a_j}^{a_j}(P_j(s_j)-iQ_j(s_j))\sqrt{[(a_j-s_j)/(a_j+s_j)(\pi a_j)]}ds_j,$$
(for left tip) (17)

$$K_{B,j}=K_{1B,j}-iK_{2B,j}=-\int_{-a_j}^{a_j}(P_j(s_j)-iQ_j(s_j))\sqrt{[(a_j+s_j)/(a_j-s_j)(\pi a_j)]}ds_j,$$
(for right tip) (18)

Clearly, if $\eta_1=1$ is replaced by $\eta_2=-\kappa$ in all above equations, then the multiple crack problems of elastic half-plane with fixed boundary can also be solved.

Numerical Results

For the sake of brevity, we present only one set of obtained numerical results. In computation the following Chebyshev quadrature rule is used

$$\int_{-a}^{a}G(t)dt=(\pi a/M)\sum_{m=1}^{M}G(t_m)\sin((2m-1)\pi/2M).$$
$$t_m=a\cos((2m-1)\pi/2M) \quad (19)$$

As a result of using (19), the integrals shown in (17) and (18) convert into summations and the integral equations (15) and (16) convert into a system of algebraic equations. In the condition of $M=9$ and free boundary of half-plane, the calculated numerical results of SIF values for the case of two cracks in series are plotted in Fig. 3.

Acknowledgments

The author is grateful for support from the Science Fund of the Chinese academy of Sciences.

References

1 Erdogan, F., Gupta, G. D., and Cook, T. S., "Numerical Solution of Singular Integral Equations," *Methods of Analysis and Solution of Crack Problems*, Sih, G. C., ed., Noordhoff International Publishing, Leyden, 1973.

2 Erdogan, F., "Mixed Boundary Value Problems in Mechanics," *Mechanics Today* 5, Nemat-Nasser, S., ed., Pergamon Press, New York, 1978.

3 Panasyuk, V. V., Savruk, M. M., and Datsyshyn, A. P., "A General Method of Solution of Two-dimensional Problems in the Theory of Crack," *Engineering Fracture Mechanics*, Vol. 9, 1977, pp. 481–497.

4 Ioakimidis, N. D., and Theocaris, P. S., "A System of Curvilinear Cracks in an Isotropic Elastic Half-plane," *International Journal of Fracture*, Vol. 15, 1979, pp. 299–309.

5 Muskhelishvili, N. I., *Some Basic Problems of the Mathematical Theory of Elasticity*, P Noordhoff Ltd., Groningen, Holland, 1953.

6 Chen, Y. Z., "Solutions of Multiple Crack Problems of a Circular Plate or an Infinite Plate Containing a Circular Hole by Using Fredholm Integral Equation Approach," *International Journal of Fracture*, Vol. 25, 1984, pp. 155–168.

7 Chen, Y. Z., "Reducing Crack Problems of a Circular Plate or an Infinite Plate Containing a Circular Hole into Fredholm Integral Equation," *International Journal of Fracture*, Vol. 23, 1983, pp. R101-104.

8 Chen, Y. Z., "Solutions of Multiple Crack Problems of a Circular Region for Antiplane Elastic Problem or Torsion Problem by Using Fredholm Integral Equation Approach," *International Journal of Fracture*, Vol. 25, 1984, pp. R15–19.

Downloaded 02 May 2010 to 171.66.16.54. Redistribution subject to ASME license or copyright; see http://www.asme.org/terms/Terms_Use.cfm

Journal of Applied Mechanics

Discussion

Theory of Orthotropic and Composite Cylindrical Shells, Accurate and Simple Fourth-Order Governing Equations[1]

C. W. Bert[2]. The author is to be congratulated on extending his accurate, yet simple equations for isotropic circular cylindrical shells to orthotropic ones. However, the discusser would like to add a word of caution relative to the validity of the author's equation (16). This expression for the shear modulus in terms of the orthotropic elastic moduli and Poisson's ratios was attributed to Huber [21]. Apparently, Huber proposed it for use in predicting the shear modulus of reinforced concrete. However, for the three modern fiber-reinforced composite materials and Douglas fir, as listed in the author's Table 2, equation (16) leads to errors from +51.4 percent (glass/epoxy) to +508 percent (graphite/epoxy) in the shear modulus. The simple expression, $G = 1/2\, E_2$, leads to errors from 50.2 percent (boron/epoxy) to −67.9 percent (Douglas fir). Thus, the latter expression would be preferable in the case of the composite materials, but not Douglas fir.

Author's Closure

The authors would like to express sincere thanks to Professor Bert for his keen interest and pertinent comments on our paper. We welcome the opportunity to further elaborate that the employment of the relation (16), $G=\sqrt{E_1E_2}/2(1+\sqrt{\nu_1\nu_2})$ for the shear modulus G has an insignificant effect on the accuracy of the solutions of the governing differential equations deduced in the paper, despite the inaccuracy of the relation (16). This property of composites is of importance in the development of the present theory. It is an elegant property of composites.

As is known, no general exact relation such as the relation $G=E/2(1+\nu)$ for isotropic materials, can be deduced among elastic constants of orthotropic or anisotropic materials. Nevertheless, the relation (16) $G=\sqrt{E_1E_2}\,/\,2(1+\sqrt{\nu_1\nu_2})$ was recommended by Huber (1923) for use in the application of the theory of anisotropic plates to reinforced concrete slabs. It is also shown by Panc (1975), based on theoretical considerations, that the expression (16) may be used as an approximation. However, for modern fiber-reinforced composite materials as listed in Table 2, the use of the relation (16) can lead to a substantial percentage of errors in the shear modulus as compared with test data (*assume those test data are accurate*). In the course of our investigation, the following results were observed from which the issue regarding the validity of the relation (16) may be resolved.

1. In the governing differential equation (14), only coefficients k_2 and K are affected by the value of the shear modulus G. It can be easily shown that the percentage of errors in the coefficients k_2 and K are much smaller than the percentage of errors in the shear modulus G when the relation (16) is employed in calculating k_2, K, and G. Thus the application of (16) has much less effect on the accuracy of the solutions of the governing differential equations deduced in the paper than its effect on the shear modulus G.

2. Employing the relation (16) in the coefficient k_2 of the middle term $\partial^8/\partial\alpha^4\partial\beta^4$ (*only in this term*) of equation (14), equation (14) may be written as a pair of fourth-order governing equations (18). As Tables 3–8 show, the differences between either the real or imaginary parts of the characteristic roots of the original eighth-order equation (14) and the pair of fourth-order equations (18) are negligibly small (less than 0.5 percent). This indicates that equation (18) is equally as accurate as the original equation (14). As shown in the paper, equation (18) reduces to the well-known governing differential equation for orthotropic plates.

3. Tables 3–8 show that the differences between either the real or imaginary parts of the characteristic roots of the original equation (14) and the pair of fourth-order equations (26) which is deduced from (18) are also negligibly small, less than 0.5 percent. Thus, despite the employment of the relation (16) in (26) and (18), both (26) and (18) are just as accurate as the original equation (14). Equation (26) should be preferred in application because it is much simpler than equation (18) and yet has the same accuracy as equations (18) and (14). For the composite materials listed in Table 2, the relation (16) leads to errors of +51.4 percent (glass/epoxy) to +508 percent (graphite/epoxy) in the shear modulus. However, the errors in the characteristic roots of equations (18) and (26) are negligibly small and thus the accuracy of the characteristic roots are practically unaffected by the substantial errors in the shear modulus. This result is quite surprising in composites and useful in applications.

4. Tables 3–8 also show that the characteristic roots obtained from the fourth-order governing equations (27), (29), and (30) are excellent approximations of the roots obtained from equation (14).

5. Stresses, moments, and displacements are obtained from equations (8), (12), and (13). These original equations (8), (12), and (13) are unaffected by the relation (16) since it is not employed in equations (8), (12), and (13).

6. Accurate particular solutions should be calculated from equations (14), (18), or (26).

[1] By S. Cheng and F. B He and published in the December, 1984, issue of the ASME JOURNAL OF APPLIED MECHANICS, Vol. 51, pp. 736–744.

[2] Perkinson Professor of Engineering, University of Oklahoma, Norman, Okla. 73019. Fellow ASME.

Copyright © 1985 by ASME
Downloaded 02 May 2010 to 171.66.16.54. Redistribution subject to ASME license or copyright; see http://www.asme.org/terms/Terms_Use.cfm

Conclusions

Finally, the following conclusions may be drawn. Although the relation (16) is inaccurate and can lead to large errors in the shear modulus G, nevertheless the use of the relation in the governing differential equations can still yield very accurate final solutions. This justifies the employment of the relation (16) and establishes the accuracy as well as the validity of these simple fourth-order governing equations deduced in the paper. It also illustrates that the value of the shear modulus given by the relation (16) has less effect on the solutions of the governing equation than that of moduli of elasticity. This property of composite shells is important as it can be employed to resolve what was originally a difficult problem and leads us to the deduction of these simple and accurate equations. All in all, it is a remarkable property of shell theory, especially with regard to composite shells.

This Closure may serve as an amendment or appendix to the authors' paper. Thanks to Professor Bert again for his valuable discussion.

The Constitutive Theory for Fluid-Filled Porous Materials[1]

R. W. Zimmerman.[2] In her interesting article on fluid-filled porous materials [1], the author makes the statement that "for many practical problems, the fluid can be assumed to be incompressible." While incompressibility is often a useful assumption in fluid mechanics, the applicability of this concept of fluid-filled porous materials is actually quite limited. To see why this is so, consider the following expression for the "undrained" bulk modulus K_u;

$$K_u = \frac{K_s(K_\phi + K_f) - \phi K_\phi (K_s - K_f)}{(K_\phi + K_f) + \phi(K_s - K_f)} \tag{1}$$

This expression is equivalent to Carroll's [2] expression for K_u, with his porosity modulus C replaced by K_ϕ for notational consistency. It is clear from (1) that K_s and K_ϕ are natural standards against which the bulk modulus of the pore fluid must be measured. For typical geological materials saturated with water or liquid hydrocarbons, K_s will be *larger* than K_f by a factor of at least ten. As explained in [2], a good estimate for K_ϕ in the case of spherical pores is $4G_s/3$, which is of the same order of magnitude as K_s, and is therefore also much larger than K_f. Actual porous rocks such as sandstones or tuffs will have porosity moduli smaller than $4G_s/3$, reflecting the greater compliance of non-spherical pores, but these moduli will still be of the same order of magnitude as K_f, and cannot be neglected in (1).

To illustrate by way of an example, consider the following values taken from a study by Murphy [3] of a Fort Union sandstone:

$$\phi = 0.085,$$
$$K_s = 35.0 \text{ GPa},$$
$$K_\phi = 0.85 \text{ GPa}.$$

Evaluating the undrained bulk modulus for the three cases of water saturation ($K_f = 2.25$ GPa), air saturation ($K_f = 8 \times 10^{-4}$ GPa), and saturation with an incompressible fluid ($K_f \to \infty$), the following values are arrived at:

$$K_u(\text{water}) = 18.0 \text{ GPa},$$
$$K_u(\text{air}) = 7.12 \text{ GPa},$$
$$K_u(\text{incompressible pore fluid}) = 38.3 \text{ GPa}.$$

The undrained bulk modulus for the case of water saturation is seen to be closer to the *drained* modulus (7.12 GPa) than to the modulus predicted for the limiting case of an incompressible pore fluid! The assumption of fluid incompressibility is therefore a very poor one in this case, and it should be noted that most liquid hydrocarbons are slightly *more* compressible than water. Examination of values of K_s and K_ϕ for commonly occurring geological materials will show that the above example is by no means exceptional, but is typical. The limiting case of an incompressible pore fluid is of some use only for cracked, low porosity crystalline rocks, for which both ϕ and K_ϕ are very low.

References

1 Katsube, N., "The Constitutive Theory for Fluid-Filled Porous Materials," ASME JOURNAL OF APPLIED MECHANICS, Vol. 52, 1985, pp. 185–189.

2 Carroll, M. M., "Mechanical Response of Fluid-Saturated Porous Materials," *Proceedings of the 15th International Congress of Theoretical and Applied Mechanics*, Rimrott, F. P. J., and Tabarrok, B., eds., 1980, North-Holland, New York.

3 Murphy, W. F., "Acoustic Measurements of Partial Gas Saturation in Tight Sandstones," *Journal of Geophysical Research*, Vol. 89, 1984, pp. 11549–11559.

Author's Closure

The author would like to thank Dr. Zimmerman for his useful comments on the practicality of the assumption of fluid incompressibility. The author wishes to correct the word from "many" to "some" on her statement.

The author would like to add that the general case when the fluid is compressible has been investigated and the intention is to include the formulations for the case when the fluid is incompressible as a special case only.

[1] By N. Katsube and published in the March, 1985, issue of the ASME JOURNAL OF APPLIED MECHANICS, Vol. 52, pp. 185–189.

[2] Department of Mechanical Engineering, University of California, Berkeley, Calif. 94720. Assoc. Mem. ASME.

Downloaded 02 May 2010 to 171.66.16.54. Redistribution subject to ASME license or copyright; see http://www.asme.org/terms/Terms_Use.cfm

Conclusions

Finally, the following conclusions may be drawn. Although the relation (16) is inaccurate and can lead to large errors in the shear modulus G, nevertheless the use of the relation in the governing differential equations can still yield very accurate final solutions. This justifies the employment of the relation (16) and establishes the accuracy as well as the validity of these simple fourth-order governing equations deduced in the paper. It also illustrates that the value of the shear modulus given by the relation (16) has less effect on the solutions of the governing equation than that of moduli of elasticity. This property of composite shells is important as it can be employed to resolve what was originally a difficult problem and leads us to the deduction of these simple and accurate equations. All in all, it is a remarkable property of shell theory, especially with regard to composite shells.

This Closure may serve as an amendment or appendix to the authors' paper. Thanks to Professor Bert again for his valuable discussion.

The Constitutive Theory for Fluid-Filled Porous Materials[1]

R. W. Zimmerman.[2] In her interesting article on fluid-filled porous materials [1], the author makes the statement that "for many practical problems, the fluid can be assumed to be incompressible." While incompressibility is often a useful assumption in fluid mechanics, the applicability of this concept of fluid-filled porous materials is actually quite limited. To see why this is so, consider the following expression for the "undrained" bulk modulus K_u;

$$K_u = \frac{K_s(K_\phi + K_f) - \phi K_\phi (K_s - K_f)}{(K_\phi + K_f) + \phi(K_s - K_f)} \tag{1}$$

This expression is equivalent to Carroll's [2] expression for K_u, with his porosity modulus C replaced by K_ϕ for notational consistency. It is clear from (1) that K_s and K_ϕ are natural standards against which the bulk modulus of the pore fluid must be measured. For typical geological materials saturated with water or liquid hydrocarbons, K_s will be *larger* than K_f by a factor of at least ten. As explained in [2], a good estimate for K_ϕ in the case of spherical pores is $4G_s/3$, which is of the same order of magnitude as K_s, and is therefore also much larger than K_f. Actual porous rocks such as sandstones or tuffs will have porosity moduli smaller than $4G_s/3$, reflecting the greater compliance of non-spherical pores, but these moduli will still be of the same order of magnitude as K_f, and cannot be neglected in (1).

To illustrate by way of an example, consider the following values taken from a study by Murphy [3] of a Fort Union sandstone:

$$\phi = 0.085,$$
$$K_s = 35.0 \text{ GPa},$$
$$K_\phi = 0.85 \text{ GPa}.$$

Evaluating the undrained bulk modulus for the three cases of water saturation (K_f = 2.25 GPa), air saturation ($K_f = 8 \times 10^{-4}$ GPa), and saturation with an incompressible fluid ($K_f \to \infty$), the following values are arrived at:

$$K_u(\text{water}) = 18.0 \text{ GPa},$$
$$K_u(\text{air}) = 7.12 \text{ GPa},$$
$$K_u(\text{incompressible pore fluid}) = 38.3 \text{ GPa}.$$

The undrained bulk modulus for the case of water saturation is seen to be closer to the *drained* modulus (7.12 GPa) than to the modulus predicted for the limiting case of an incompressible pore fluid! The assumption of fluid incompressibility is therefore a very poor one in this case, and it should be noted that most liquid hydrocarbons are slightly *more* compressible than water. Examination of values of K_s and K_ϕ for commonly occurring geological materials will show that the above example is by no means exceptional, but is typical. The limiting case of an incompressible pore fluid is of some use only for cracked, low porosity crystalline rocks, for which both ϕ and K_ϕ are very low.

References

1 Katsube, N., "The Constitutive Theory for Fluid-Filled Porous Materials," ASME JOURNAL OF APPLIED MECHANICS, Vol. 52, 1985, pp. 185–189.

2 Carroll, M. M., "Mechanical Response of Fluid-Saturated Porous Materials," *Proceedings of the 15th International Congress of Theoretical and Applied Mechanics*, Rimrott, F. P. J., and Tabarrok, B., eds., 1980, North-Holland, New York.

3 Murphy, W. F., "Acoustic Measurements of Partial Gas Saturation in Tight Sandstones," *Journal of Geophysical Research*, Vol. 89, 1984, pp. 11549–11559.

Author's Closure

The author would like to thank Dr. Zimmerman for his useful comments on the practicality of the assumption of fluid incompressibility. The author wishes to correct the word from "many" to "some" on her statement.

The author would like to add that the general case when the fluid is compressible has been investigated and the intention is to include the formulations for the case when the fluid is incompressible as a special case only.

[1] By N. Katsube and published in the March, 1985, issue of the ASME JOURNAL OF APPLIED MECHANICS, Vol. 52, pp. 185–189.

[2] Department of Mechanical Engineering, University of California, Berkeley, Calif. 94720. Assoc. Mem. ASME.

Copyright © 1985 by ASME
Downloaded 02 May 2010 to 171.66.16.54. Redistribution subject to ASME license or copyright; see http://www.asme.org/terms/Terms_Use.cfm

Journal of Applied Mechanics

Book Reviews

Computational Methods for Transient Analysis. Edited by Ted Belytschko and Thomas J. R. Hughes. North-Holland, The Netherlands, 1983. 523 Pages. Price $69.00.

REVIEWED BY P. BURGERS[1]

This book is a review of many topics fundamental to dynamic numerical analysis, and in particular to finite elements, although some chapters do discuss finite difference methods. The areas covered, in order of presentation, are an overview of transient finite element and difference methods, a detailed compendium of transient algorithms with a heavy emphasis on their stability, techniques of performing partitioned analyses of coupled systems, dynamic boundary element methods, dynamic relaxation, dynamic and spatial dispersion of discretised systems, methods of modeling infinite bodies with finite meshes for dynamic transient problems, explicit dynamic finite difference methods, implicit finite element methods and finally combined Lagragian-Eulerian (ALE) finite element methods. Each chapter has been written by different experts in the particular field but the editing has been thorough so that the cross referencing is quite good.

The introductory chapter was written by Belytschko and serves as very readable background material for the rest of the book, apart from a questionable statement on the most appropriate stress rate to use in finite elements. There is a brief but interesting presentation of 'hour-glass' control of finite elements and then short introductions to other topics in the book. The second chapter, by Hughes, discusses time integration algorithms and their stability in great detail, bringing together many results in dynamic numerical analysis in one place. The majority of the discussion is on linear symmetric systems, these being the ones that have received the most study. This chapter will serve very well as a starting point for anybody interested in getting a good background into the more theoretical side of numerical dynamics. The chapter on dispersion by discretised systems by Schreyer compliments this chapter very well and together they give a good all round review, although it would have been very interesting if the chapter on dispersion had continued in the detail that it started with. As with all the other chapters, there is a detailed reference list of recent work in the area so interested readers can pursue the subject further.

The history and current state of the art (as used by the authors) on the analysis of coupled systems by partitioning the system into a number of subsystems, each with degrees of freedom associated with a single system is presented by Park and Felippa. Examples of this are solid structures interacting with fluid systems or the pore fluid flow through soil. The suitability of the method with linear subsystems or even mildly nonlinear systems seems clear, but it is not obvious to the reviewer that this is true for highly nonlinear systems, e.g. if the problem involves large strains. This chapter is quite comprehensive (and lengthy) and will serve as a good starting point for a newcomer to the area. Modeling of infinite bodies by discretised methods always leads to difficulties. Chapter seven on 'silent boundary' methods in dynamics, by Cohen and Jennings, considers this problem in great detail. The difficulty is that the numerical problem must draw energy out of the mesh through the boundaries. A number of techniques are discussed with the advantages and disadvantages summarized.

The remaining chapters discuss implicit methods in dynamics, such as the BFGS algorithm, dynamic relaxation, explicit Lagrangian finite differences. In final chapter the problem of mesh distortion due to deformation or flow is considered using an arbitrary Lagragian-Eulerian formulation. The concept is very attractive – use a mesh that models the deformation in the best manner for all times of interest and still retains the ease of modeling boundaries that comes with the Finite Element method. The example used to illustrate the technique (which gives an automatic mesh rezoning using the same number of elements) is for fluid-solid interaction. However the idea is possibly suitable for problems just involving a single material type with regions of large deformation, such as seen in forging and extrusion problems. The problem of determining a suitable mapping for the mesh as a function of time remains but the idea certainly has great potential.

In summary this first volume in the series *Computational Methods in Mechanics* published by North-Holland makes for a broad review of the area of numerical dynamics which would be of benefit to both novices and experts in the field.

Random Vibrations of Elastic Systems. By V. V. Bolotin. Martinus Nijhoff, The Hague, 1984. 468 Pages. Price $86.00.

REVIEWED BY S. H. CRANDALL[1]

This masterly monograph on the theory of random vibration is a translation of the 1979 Russian edition. The author is the leading contributor to this theory in the Soviet Union. His book *Statistical Methods in Structural Mechanics* (Russian editions in 1961 and 1965, English translation in 1969) contained an excellent introduction to the subject at the time when activity in this field was just beginning to blossom.

Random vibration as the name of a technical discipline has come to mean the study of the random fields or processes which are the excitations and responses of deterministic dynamic systems. The discipline arose about thirty years ago out of the need to solve three distinct aerospace problems with the common thread of random excitation: turbulent buffeting

[1] Hibbitt, Karlsson & Sorensen, Inc., Providence, Rhode Island 02906. Assoc. Mem. ASME.

[1] Ford Professor of Engineering, Massachusetts Institute of Technology, Cambridge, Mass. 02139.

Copyright © 1985 by ASME
Downloaded 02 May 2010 to 171.66.16.54. Redistribution subject to ASME license or copyright; see http://www.asme.org/terms/Terms_Use.cfm